

*Carnegie
Institution*

OF WASHINGTON

Year Book 74

1974-1975

*Carnegie
Institution*

OF WASHINGTON

Year Book 74

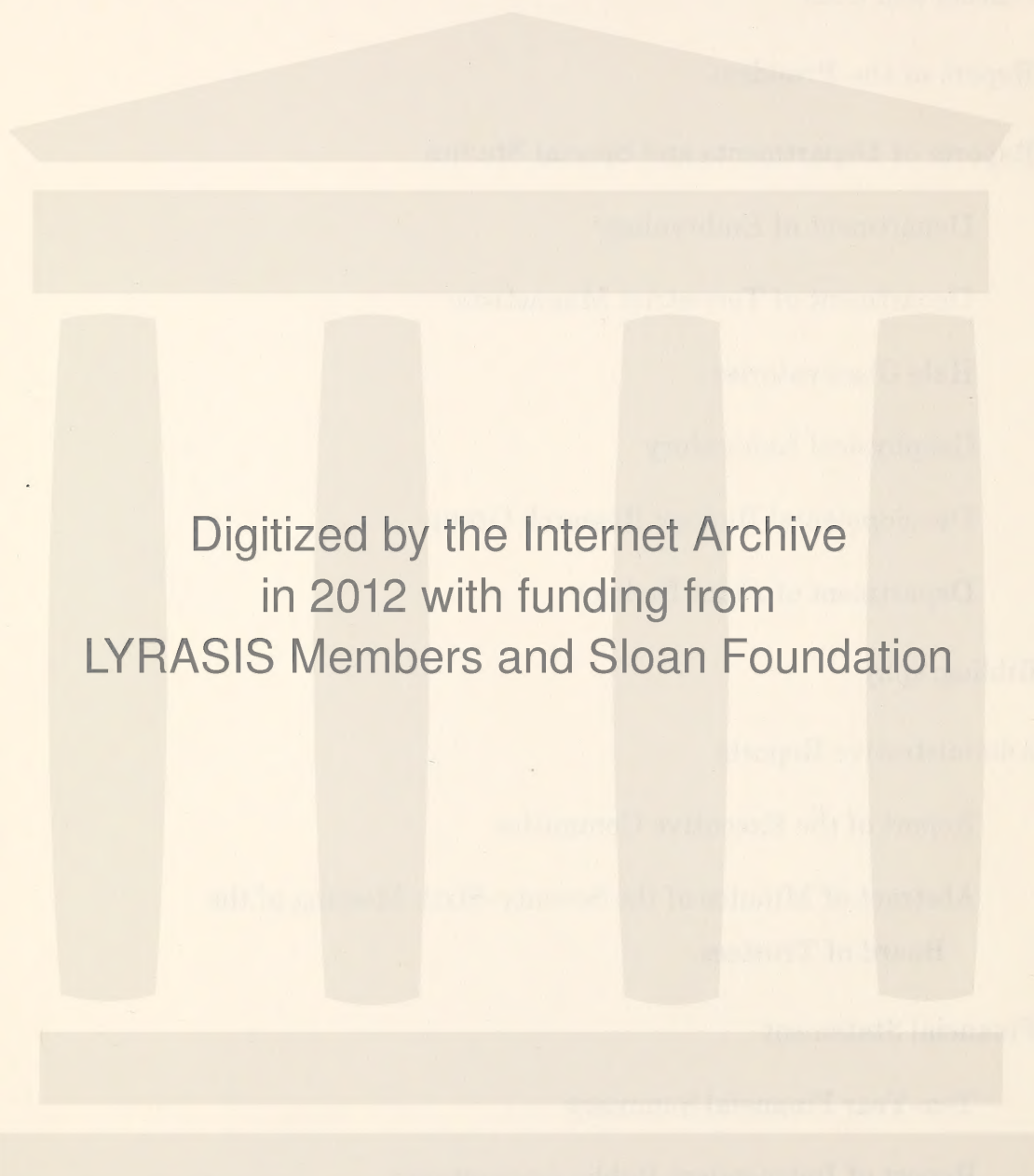
1974-1975



Library of Congress Catalog Card Number 3-16716
The John D. Lucas Printing Company, Baltimore, Maryland
Issued December 1975

Contents

	<i>page</i>
Officers and Staff	v
Report of the President	1
Reports of Departments and Special Studies	1
Department of Embryology	3
Department of Terrestrial Magnetism	105
Hale Observatories	303
Geophysical Laboratory	379
Developmental Biology Research Group	651
Department of Plant Biology	737
Bibliography	-815
Administrative Reports	817
Report of the Executive Committee	819
Abstract of Minutes of the Seventy-Sixth Meeting of the Board of Trustees	821
Financial Statement	823
Ten-Year Financial Summary	825
Report of Independent Public Accountants	826
Articles of Incorporation	841
By-Laws of the Institution	845
Index of Names	851



Digitized by the Internet Archive
in 2012 with funding from
LYRASIS Members and Sloan Foundation

President and Trustees

PRESIDENT

Philip H. Abelson

BOARD OF TRUSTEES

William McChesney Martin, Jr.
Chairman

Frank Stanton
Vice-Chairman

William T. Golden
Secretary

Eric Ashby¹
Lewis M. Branscomb
John T. Connor²
John Diebold²
Michael Ference, Jr.
Carl J. Gilbert
Hanna H. Gray
Crawford H. Greenewalt
William C. Greenough²
Patrick E. Haggerty³
Caryl P. Haskins
William R. Hewlett
Keith S. McHugh⁴
Henry S. Morgan
William I. Myers
Walter H. Page
Robert M. Pennoyer
Richard S. Perkins
William M. Roth
Robert C. Seamans, Jr.
Charles P. Taft⁵
Charles H. Townes
Juan T. Trippe
James N. White

Alfred L. Loomis⁶
Garrison Norton
Trustees Emeriti

¹ Resigned June 1974.

² Elected May 1975.

³ Resigned June 1975.

⁴ Resigned September 1974; designated Trustee Emeritus May 1975; died June 7, 1975.

⁵ Resigned April 1975; designated Trustee Emeritus May 1975.

⁶ Died August 11, 1975.

Former Presidents and Trustees

PRESIDENTS

Daniel Coit Gilman	1902-1904	Vannevar Bush	1939-1955
John Campbell Merriam	1921-1938	Robert Simpson Woodward	1904-1920
<i>President Emeritus</i>	1939-1945	Caryl P. Haskins	1956-1971

TRUSTEES

Alexander Agassiz	1904-05	Robert A. Lovett	1948-71
George J. Baldwin	1925-27	Seth Low	1902-16
Thomas Barbour	1934-46	Wayne MacVeagh	1902-07
James F. Bell	1935-61	Andrew W. Mellon	1924-37
John S. Billings	1902-13	John Campbell Merriam	1921-38
Robert Woods Bliss	1936-62	Margaret Carnegie Miller	1955-67
Amory H. Bradford	1959-72	Roswell Miller	1933-55
Lindsay Bradford	1940-58	Darius O. Mills	1902-09
Omar N. Bradley	1948-69	S. Weir Mitchell	1902-14
Robert S. Brookings	1910-29	Andrew J. Montague	1907-35
Vannevar Bush	1958-71	William W. Morrow	1902-29
John L. Cadwalader	1903-14	Seeley G. Mudd	1940-68
William W. Campbell	1929-38	William Church Osborn	1927-34
John J. Carty	1916-32	James Parmelee	1917-31
Whitefoord R. Cole	1925-34	Wm. Barclay Parsons	1907-32
Frederic A. Delano	1927-49	Stewart Paton	1916-42
Cleveland H. Dodge	1903-23	George W. Pepper	1914-19
William E. Dodge	1902-03	John J. Pershing	1930-43
Charles P. Fenner	1914-24	Henning W. Prentis, Jr.	1942-59
Homer L. Ferguson	1927-52	Henry S. Pritchett	1906-36
Simon Flexner	1910-14	Gordon S. Rentschler	1946-48
W. Cameron Forbes	1920-55	David Rockefeller	1952-56
James Forrestal	1948-49	Elihu Root	1902-37
William N. Frew	1902-15	Elihu Root, Jr.	1937-67
Lyman J. Gage	1902-12	Julius Rosenwald	1929-31
Walter S. Gifford	1931-66	William W. Rubey	1962-74
Cass Gilbert	1924-34	Martin A. Ryerson	1908-28
Frederick H. Gillett	1924-35	Henry R. Shepley	1937-62
Daniel C. Gilman	1902-08	Theobald Smith	1914-34
John Hay	1902-05	John C. Spooner	1902-07
Barklie McKee Henry	1949-66	William Benson Storey	1924-39
Myron T. Herrick	1915-29	Richard P. Strong	1934-48
Abram S. Hewitt	1902-03	William H. Taft	1906-15
Henry L. Higginson	1902-19	William S. Thayer	1929-32
Ethan A. Hitchcock	1902-09	James W. Wadsworth	1932-52
Henry Hitchcock	1902	Charles D. Walcott	1902-27
Herbert Hoover	1920-49	Frederic C. Walcott	1931-48
William Wirt Howe	1903-09	Henry P. Walcott	1910-24
Charles L. Hutchinson	1902-04	Lewis H. Weed	1935-52
Walter A. Jessup	1938-44	William H. Welch	1906-34
Frank B. Jewett	1933-49	Andrew D. White	1902-16
Samuel P. Langley	1904-06	Edward D. White	1902-03
Ernest O. Lawrence	1944-58	Henry White	1913-27
Charles A. Lindbergh	1934-39	George W. Wickersham	1909-36
William Lindsay	1902-09	Robert E. Wilson	1953-64
Henry Cabot Lodge	1914-24	Robert S. Woodward	1905-24
Carroll D. Wright	1902-08		

Under the original charter, from the date of organization until April 28, 1904, the following were *ex officio* members of the Board of Trustees: the President of the United States, the President of the Senate, the Speaker of the House of Representatives, the Secretary of the Smithsonian Institution, and the President of the National Academy of Sciences.

OFFICE OF ADMINISTRATION

1530 P Street, N.W., Washington, D.C. 20005

Philip H. Abelson	<i>President</i>
James W. Boise	<i>Bursar; Secretary-Treasurer, Retirement Trust; Executive Secretary to the Finance Committee</i>
Marjorie H. Walburn	<i>Assistant to the President</i>
Sheila A. McGough	<i>Publications Officer; Editor</i>
Kenneth R. Henard	<i>Assistant Bursar; Assistant Treasurer, Retirement Trust</i>
Joseph M. S. Haraburda	<i>Assistant to the Bursar</i>
Richard E. Hewitt	<i>Administrative Officer for Services</i>

Marshall Hornblower	<i>Counsel</i>
---------------------	----------------

STAFF MEMBERS IN SPECIAL SUBJECT AREAS

Roy J. Britten

Alfred D. Hershey

Tatiana Proskouriakoff

DISTINGUISHED SERVICE MEMBER IN SPECIAL SUBJECT AREA

Barbara McClintock

RESEARCH ASSOCIATE AT LARGE

Harry E. D. Pollock

Report OF
THE *President*

MANY PEOPLES OF THE WORLD are beginning to learn the hard way what a few observers have known for a long time—exponential growth of any kind cannot go on indefinitely. For more than a hundred years much of the world has experienced an unprecedented era of fast growth in the use of energy and raw materials. In addition, since World War II exponential growth of population has been ubiquitous, with especially high rates prevailing in less developed countries. The inevitable cessation of rapid growth of population will not occur suddenly or universally but rather on a country by country basis. In contrast, changes in the world situation with respect to energy in the form of hydrocarbons have been dramatic.

For more than two decades, until the end of 1973, the use of petroleum in the United States, Japan, and Western Europe increased rapidly. In the developed countries hydrocarbons became the principal source of energy, and many observers have pointed to a worldwide correlation between consumption of energy and standard of living. In the United States, the annual rate of increase was 4%–5%. In the other highly developed countries, the rate was even faster. These countries enjoyed great prosperity. During the past two years, consumption of energy in all these places has decreased. Some economists argue that increased costs of oil represent only about 2% of the gross national product and hence should not affect the economy much. Perhaps so. But maybe the effects reverberate through the economy in ways that are not altogether understood, for example, people turning away from 2-ton automobiles.

Perhaps there is a lesson to be learned from the lowly bacterium *Escherichia coli*. When a simple solution containing a food—glucose—and some inorganic salts is inoculated with *E. coli*, the bacteria enjoy a period of exponential growth. Starting with, for example, a population of 10^3 per milliliter, growth proceeds with a doubling time of 53 minutes. That is, after such an interval, the population increases to 2×10^3 per milliliter, and after a like period, to 4×10^3 . This doubling goes on with clocklike precision for a period of about 18 hours—more than 20 doubling times during which the population increases more than a millionfold. At that point, if bacteria had brains, traditions, written history, and econometricians, they would confidently expect a continuation of a society geared to exponential growth. However, in the course of only a fraction of a doubling time, exponential growth stops and the bacterial culture goes into a static state followed by a decline. This, despite the fact that almost all conditions for growth, such as food supply, are adequate. There is little to be gained from pursuing analogies, but one point should be emphasized. In any biological system, including those involving humans, exponential growth can stop suddenly, to be followed by a declining state.

Exponential economic growth in the United States may be restored. But it will not be restored to the precise conditions existing in 1973. The country faces a decade or more of adjustments to a new set of realities, both internal and external. The world situation is especially complex in that limiting factors are becoming apparent in energy, food, and raw materials. Moreover, constraints among these major factors are interactive. The key factor is energy. Given sufficient and inexpensive quantities of it, modern technology could provide ample food and materials. However, the world faces major problems as economies based on oil change to those utilizing other sources of energy.

One by one the oil producers of the rest of the world will repeat the experience

of the United States. After many years of exponential growth, domestic production reached a peak in 1970. During 1974 and 1975, production declined at the rate of 5% per year. This occurred despite a quadrupling of the price for new oil. Energy problems of the United States have been compounded by falling supplies of natural gas, the leading domestic source of energy. Production of this fuel at one time also followed an exponential growth curve, later tapering off and declining in 1974 and 1975, at the annual rate of 6%–8%.

Prospects are poor for an overall improvement in these trends during the next five years. Oil is scheduled to flow in the Alaska pipeline in late 1977, but this will arrest only briefly the decay in national production. Some analysts believe optimistically that higher prices and more drilling activity and enhanced tertiary recovery will bring out additional supplies, but the record of the past two years provides no basis for such optimism. Similar remarks apply to prospects for natural gas during the next five years. Thus, the most realistic estimate is that present declining trends will continue. On this basis, in 1980 one would expect a domestic production of 7 million barrels of oil a day and 13 trillion cubic feet of gas a day. In 1974, the corresponding figures were 8.8 million and 21 trillion, respectively.

Taken together, oil and gas supplied 75.7% of United States energy consumption in 1974. Thus simultaneous failure of the two sources is a serious problem. It is not practical to meet more than a small fraction of the shortfall of natural gas by imports. Fair prospects exist for an expansion of domestic supplies of natural gas after a period of perhaps five years. However, in the meantime, if energy consumption is to be maintained, let alone increased, the nation must turn to other sources. Of these, by far the most convenient is oil. Thus, considerable pressure is likely to build to expand greatly imports of oil. But this would entail increased vulnerability and balance of payments problems. Experience in 1973–1974 demonstrated that the United States is vulnerable when its imports exceed 20% of consumption. In late 1975, they were 38%, which amounted to about 6 million barrels a day. Merely to maintain the present level of consumption of energy based on hydrocarbons would require an annual expansion of imports of about 1 million barrels of oil a day.

Oil and natural gas are crucial to most societal needs and to the functioning of the economy, e.g., merely to name a few uses—petroleum products for cars, buses, trains, and planes, and for agriculture. Natural gas is a feedstock for fertilizers and petrochemicals. It is the main source of energy for industry, and it supplies the heat needed by 55% of the nation's homes. Hydrocarbons are so essential that it is questionable whether the economy can grow when supplies of these fuels are static or contracting. Ultimately, the country must shift to other energy sources, such as coal, oil shale, wood, and solar and nuclear power. Such shifts will have profound effects on the economy and on the shape of society, and will not be accomplished without various kinds of trauma.

The magnitude of the changes is not easy to visualize from the vantage point of the present. After all, houses are warm and there is gasoline at the pumps. However, perspective can be gained by surveying briefly the past century or so. Just a little over a hundred years ago the nation's principal source of energy was wood. It was used in homes and in locomotives. The principal source of energy for factories was water power, and so most of the manufacturing was located near streams such as those in New England. Most of the population lived on farms. About a hundred years ago a major shift toward coal occurred. This led to a tremendous industrial boom in Pittsburgh and the Middle West—a development in which Andrew Carnegie was a leader. This was soon accompanied by

production and use of electricity. An important offshoot was the electric streetcar. As cities grew, their pattern was influenced by the new form of transportation.

By 1920 a new phenomenon was well under way—the creation of a mobile society based on the internal combustion engine and on petroleum. Tractors and other machinery revolutionized agriculture. At one time, more than 90% of the population were engaged in farming. Today, only about 4% are so employed. Such a shift had inevitable social consequences.

Around 1950 another important development occurred—a great expansion in the use of natural gas. Much of this fuel is obtained as a by-product of petroleum production. Originally the gas was burned as a nuisance. Then its value was perceived and exploited. At first the price was very small. Natural gas was much cheaper and, of course, cleaner than coal and more convenient to use. In consequence, total consumption of coal in the United States remained about the same for 25 years while other factors of the economy expanded and prospered. As a corollary, Appalachia endured more than two decades of stagnation. At the same time, Houston and the Gulf Coast prospered and the region became the locale of great petrochemical complexes based on cheap energy and cheap feedstocks.

During the past two years there has been a fundamental change in the realities governing energy. Not so many years ago foreign residual oil was delivered to the East Coast for \$1.40 a barrel (42 gallons). This was equivalent in cost to \$0.23 per million BTU. At that time, crude oil in Texas fetched \$3.00 a barrel. Appalachian coal at the mine mouth brought from \$4 to \$8 a ton, i.e., from \$0.17 to \$0.34 per million BTU. Today, foreign residual oil is priced at about \$10 a barrel. Coal as an energy source is much cheaper than oil or natural gas, and Appalachia is booming. New England, which is poorly endowed with indigenous energy, is experiencing depression and high unemployment. The Gulf Coast continues to prosper because of high returns on its petroleum and natural gas. However, its earlier marked advantages of cheap energy and feedstocks have disappeared. It is as yet too early to identify the next great centers of industrial expansion. However, it is certain that society and the economy will undergo transformations of a magnitude comparable to those that occurred earlier in this century.

Much depends on the choices that are made. For example, how large a role will the various sources fill? Can suitable replacements for the hydrocarbons be produced? Will it be possible to maintain a mobile society? In principle, the answers to the last two questions are yes. But in practice, the costs may require considerable modifications in the use of mobile machinery. Likely sources of the energy are coal, shale, or wood. If liquids from coal were used, the fluid would not be burned in a gasoline engine but in something resembling a diesel. To supply such fuel, chemical complexes costing on the order of \$100 billion would be required. If the choice were shale oil, an enormous and not altogether welcome concentration of facilities would be centered in Colorado and Utah. If fluids derived from trees or plants were employed, they would likely take the form of ordinary alcohol. In that case, a motor not too different from that of the present might be employed, though one might expect substantial improvement on it. If trees were used as the basic source of energy, the southeastern and northwestern parts of the country would be especially favored.

Another imponderable is the role of nuclear power, including the breeder. Of late there has been increasing resistance within the United States to expansion of nuclear power even though this is at present the cheapest method of generating

electricity. In principle, nuclear plants could be located in virtually every state, and costs would not be much different in the various regions. Nuclear energy shares with several other forms, such as geothermal and wind, the handicap that the product is in the form of electricity. Electricity has many useful characteristics, but it fills directly only a small fraction of the total energy needs. If liquid fuels were made by a process involving electricity, they would be very costly.

One can multiply examples of the consequences of decisions about energy within the United States. These effects will be profound. Capital expenditures for energy-related plants will be enormous, but they are only part of the capital costs. Creation of new facilities in new localities will involve concomitant construction of housing and all that entails in the way of supporting facilities such as roads and schools. Many older communities will be impoverished as factories move and young people leave. Given a prosperous United States with a growing economy such changes could be managed. However, prospects for a growing economy during the next decade or more are not good. During that time, domestic production of oil and natural gas will continue to decline. Attrition of supplies of natural gas will cause great difficulties for industry, which derives more than half its energy from this source. Thus the United States faces a difficult period of attempting to live with dislocations due to failure of supplies of hydrocarbons, attendant unemployment, and huge costs of welfare.

A period of heavy federal deficit spending is hardly a favorable time to engage in a huge program of private capital expenditures. The paralyzing effects of such a situation were felt in 1975. High interest rates drove up the total costs of construction of new energy facilities. (In some instances, the time required to go on-stream is close to ten years.) In consequence, many energy projects were delayed or cancelled, including nuclear, shale oil, and gasification plants. They all would have helped ease forthcoming shortages of hydrocarbons, and the shale and gasification plants would also have supplied invaluable new practical learning experiences.

The outlook is not all dismal. At least some parts of industry are moving to adapt to the evolving situation. Many companies have found ways to cut consumption of energy while maintaining production. During the past four years one major organization has reduced its consumption per unit product by 27%. Another important development is the trend toward lighter, less fuel-consuming automobiles. As the current inventory of more than 100 million automobiles is slowly replaced, demand for petroleum will be substantially reduced.

Another aspect in which there has been some progress is the potential utilization of coal. This fuel could in principle replace much of the hydrocarbons that are burned to produce heat for boilers and for industrial processing. During 1975 there were many announcements of plans to open new mines, thus leading toward increasing production. At the same time, ability to use coal was being improved. An important environmental constraint is the high sulfur content of many eastern coals, but this year a number of processes were developed to ameliorate this problem. One of them was an intriguing method combining standard coal washing with a following separation of coal into two fractions, one very low in sulfur and the other containing a moderate amount. The very low fraction can be burned under utility boilers and meet clean air standards for new plants. The other fraction can be burned in the older plants or in plants having flue gas desulfurization equipment. Separation into two fractions is done through the use of a magnetite-water suspension with specific gravity delicately adjusted to cause one fraction to float and the other to sink.

In its efforts to utilize new energy sources, the United States, with its great

supplies of coal and oil shale, has many alternatives. It has considerable geothermal energy potential, great competence in nuclear energy, and tremendous resources of forests and farms, and abundant usable solar energy.

Most other countries are not so fortunate and they have limited choices. For example, a major result of the high prices and forthcoming depletion of oil has been to expedite a worldwide rush to go nuclear. Consider the position of a country such as France which has very limited deposits of coal and modest amounts of oil. It has rich soil, but this has been devoted to agriculture. If France wishes to enjoy amenities that energy can bring, it must expand nuclear facilities. This it has been doing, and it has developed local uranium isotope processes while pioneering in successful operation of a breeder reactor.

Consider South America, which has little coal and which has oil of consequence in only a few countries. Much of the continent might use energy derived from plants and trees. But in practice, there is likely to be a tendency to follow the example of Brazil, which is going nuclear in a big way. Another country in the news is Iran, at the moment a large exporter of oil. However, the spectre of depletion is already apparent, and prudence seems to dictate to the Shah the necessity of acquiring nuclear plants and technology. Many others will follow. This is an unwelcome prospect for the United States. Can or will these proliferating installations be monitored effectively? Will terrorists acquire the making of nuclear weapons? In principle, the risks could be reduced by international agreements involving inspections, and efforts to achieve safeguards should certainly be made. However, in practice the world is embarked on a dangerous course.

For the long pull, a much more satisfactory approach applicable to many areas would be to harvest the sun's energy in a variety of ways. The amounts of solar energy impinging on the earth are tremendous. In even so profligate a country as the United States, annual use of energy amounts to about one thousandth that received each year from the sun. Some trees fix through photosynthesis as much as 2%-3% of the energy falling on them. Thus, in principle, United States energy needs could be met by devoting a small fraction of the land to tree farms. In the tropics, where growth conditions are often even more favorable, prospects for a large renewable energy source are excellent. If exploited, it would decrease pressure toward nuclear proliferation. It would appear desirable for the United States to encourage and assist such developments.

One of the effects of the successful actions of the oil cartel has been to place very heavy burdens on the majority of the less developed countries—those that have little or no oil. The burden is at least twofold. They pay greatly increased prices for oil, but in addition their imports from countries such as Japan and those of Western Europe cost more. The example of the successful oil cartel plus financial strains has caused many countries to seek means of obtaining higher prices for their raw materials. Thus far such efforts have not been very successful. However, the lesson of oil has not been lost on companies in the United States. Some attention has always been devoted to assuring supplies of key raw materials. That attention is now keener than ever. Analysis shows that our principal vulnerabilities lie in the effects of sudden denial of some crucial material, such as chrome or tungsten. Adequate stockpiles of such materials should be maintained. Given sufficient time, technology can overcome the effects of most shortages. One simple approach is to analyze the uses of a given substance in terms of the functions it serves. For some substances, it will be found that another, more abundant material can be used instead.

Prospects for additional supplies of raw materials are mixed. In the mineral field, geologic knowledge is being advanced by the concept of plate tectonics and by the use of the Earth Resources Technology Satellite and deep sea exploration. Thus, discovery of new resources will be fostered. However, ability to exploit discoveries is handicapped by environmental constraints, by limited ability to exploit public lands, and by soaring costs of energy. The winning of mineral values is often energy-intensive.

Today many of the materials employed are nonminerals—wood products, plastics, and other synthetics. The economy is especially dependent on items derived from natural gas and petroleum. The annual tonnage of such synthetics is somewhat less than that of steel, but in volume they surpass it. Most of the basic feedstocks for these materials could be derived from wood or plants. At one time the nation's supplies of ethyl alcohol, acetone, and butanol were produced by fermentation of grain or molasses. The three chemicals are or could be used as a substantial fraction of the inputs for plastics and other synthetics. The key starting materials for fermentation are sugars. A convenient and comparatively cheap one is glucose, which can be obtained from the starch of grains or the cellulose of trees by hydrolysis. Wood itself could be modified chemically to form a useful substitute for many plastics. These examples merely illustrate a part of the potential of renewable resources for replacing hydrocarbons. Demand for feedstocks currently derived from oil or natural gas could also be satisfied in considerable measure by chemicals from coal. Basic and applied research designed to exploit the feedstock potential of renewable resources and coal are likely to provide highly useful information and lead to important practical results. For several decades the existence of cheap petrochemicals served to make other sources noncompetitive and hence relatively uninteresting. The scarcity and high prices of hydrocarbons have created new opportunities. When the old sources are looked at in the light of modern technology by scientists employing present-day powerful experimental tools, new opportunities will become apparent.

The vulnerability of the United States to stoppage of foreign imports could also be lessened if greater efforts were devoted to employing common materials such as those derivable from ordinary rocks. Such efforts would not only lessen the need to import, they would also be beneficial to the rest of the world. Thus the developments of the past two years are pointing toward efforts to use the abundant minerals of the earth's crust and materials that can be formed from them.

Another major manifestation of exponential growth has been the population explosion. For a time, it seemed that the "Green Revolution" and other agricultural developments might keep pace with expanding populations. But even Mexico, the cradle of a successful Green Revolution, is now a net food importer. For a time it was an exporter, but the inexorable growth of population has eaten up the surplus. The situation varies greatly from region to region. Some of the less developed countries are still food exporters. Others are self-sufficient and possess untilled but suitable land. In most countries, yields are not nearly so high as in the United States. Thus it would appear that overall food production might be increased very substantially. However, the high cost of energy and fertilizers as well as social factors such as lack of economic incentives have restrained production. At the same time, population continues to grow. In consequence, world food production is no longer abundantly sufficient. Countries that were once major exporters no longer are. Today, North America and Australia are the only continents that are net exporters of food products. As for the

United States, the situation has changed considerably during the past several decades. During the 'fifties and much of the 'sixties, there was an unwelcome surplus of food production leading to costly governmental programs to hold down acreage and to pay for storage of huge amounts of carry-over grains. During the 'seventies, matters changed drastically. Stockpiles of grains disappeared, idle land was farmed, and bumper crops were sold at substantial prices. The change in the demand for United States grain provides dramatic evidence that expanding world population is in the process of coming up against a barrier to further exponential growth—the food barrier.

For the United States, this great turn of events is important. In the fiscal year ended June 30, 1975, this country exported agricultural products valued at \$21.6 billion. This sum is comparable to the cost of oil imports in 1974 (\$25.0 billion), and indeed were it not for the huge export revenues obtained from agriculture the United States would have had problems with its balance of payments.

As we look ahead, a further tightening of world food supplies will increase revenues and provide an extremely valuable bargaining tool in the world political game. However, food shortages and perhaps famines are likely to put the United States in unenviable moral predicaments. At times this country may find itself having to decide which people will starve. Moreover, as United States imports of oil increase and as the oil cartel raises its prices, the United States might feel compelled to respond by raising prices of food exports to pay for the oil. This might give the United States the appearance of a nation that would squeeze funds from starving people in order to go for joyrides.

Obviously, the United States must place first priority on putting its own house in order and caring for its own people. But the United States has enormous resources of land, raw materials, and trained people. Through improvements in agriculture, the sustainable yields could be substantially increased. Through improvements in forestry and forest management, very substantial increases—a factor of two or more beyond present production—might be attained. In addition, both agriculture and forestry could ultimately enjoy additional factors of improvement by continuing basic research. Progress that is made in the United States is likely to be of worldwide application. Thus, we might assist others in the best fashion, that is, by helping them to help themselves. Another way we would do ourselves a favor while benefiting others is by using indigenous energy sources to such an extent that oil imports could be diminished. This would remove pressure from prices and extend the lifetime of world supplies.

The problems of changing the mix of domestic energy supplies are largely economic, political, and environmental, with technological barriers of significant but moderate importance. In 1975 a large amount of basic and especially applied research was being carried out or financed by government, notably by the Energy Research and Development Administration and by the National Science Foundation. This work is important and should be pursued vigorously. However, the big bottleneck is the delay in applying on a large scale what is already known. For example, this country should implement well-known methods of conservation. It should substitute coal for oil and gas. It should exploit resources of natural gas in tight geological formations in the Rocky Mountains and in the Appalachian Basin. It should proceed with construction of prototype facilities for synthetic fluids from coal. It should conduct full-size in situ retorting of oil shale.

In 1975, some people were beginning to understand that it would be prudent to take decisive steps with respect to energy, materials, and food. But there was

by no means general awareness of the long lead times involved in effective implementation.

That the United States and other countries face a decade and more of difficult adjustments to cessation of the kind of exponential growth characteristic of the 'fifties and 'sixties is certain. But even the rough outline of the course those adjustments will follow is uncertain, for the crucial elements in determining the course are the people and their leaders. If the spirit of a people is crystallized by an event like the attack on Pearl Harbor, they will demand and get leadership. Then what previously looked like great problems become readily manageable. Before December 1941, the technological achievements of World War II seemed impossible. Indeed, given this nation's condition in 1975, with clashing objectives and parochial demands, the accomplishments of World War II would require several decades. But such a situation cannot and must not prevail indefinitely.

When the mood for decisive action crystallizes, the nation's leaders will again find it necessary to effect at least a partial mobilization of intellectual, scientific, technologic, and industrial resources. Obviously, the precise relationships will differ from those of World War II, for the problems and needs are different. But there is one lesson of World War II that should be remembered. The nation's scientists and engineers constitute an enormous intellectual reserve. During ordinary times, scientists pursue knowledge at its frontiers. Much of what they do looks esoteric, and indeed applications may be long in coming. But there is a highly practical side to most scientists. They are problem solvers. They are accustomed to analyze complex situations and to identify do-able pieces. Those that perform effectively are highly trained, experts in limited fields but possessed of broad fundamental knowledge. With their knowledge and experience, many scientists can rather quickly tackle new problems in fields quite different from their previous activities.

These remarks about the adaptability of scientists are especially relevant to the Carnegie Institution. During World War II, contributions of the Carnegie staff such as Vannevar Bush and Merle Tuve to the national effort were enormous. In total, the contributions were of a magnitude far out of proportion to the numbers involved. This resulted in part because of excellence of the staff, but in addition it came about because of policies and traditions that have long determined the character of the staff and its work. The Institution has been guided by Andrew Carnegie's desire that the staff seek knowledge for the benefit of mankind. This guideline has found expression in the broad choices that individual staff members make. While giving top priority to seeking fundamental knowledge, they have maintained a broad awareness of societal needs and practical applications. In consequence, over the years many important applications of Carnegie discoveries have been made.

One way that scientists achieve and demonstrate excellence is by opening up or exploiting new areas for investigation. During the present era, progress in science has often been associated with opportunities created by new techniques, equipment, or instrumentation. Carnegie scientists, with their versatile and practical bent, have made more than their share of innovations in techniques, equipment, and in instrumentation. That contributions of this kind are continuing is demonstrated by the record of the past few years. This will be exemplified in the discussion that follows of highlights of the past year of work and events at the various departments of the Institution.

The Year in Review

GEOPHYSICAL LABORATORY

In its mission of attempting to understand processes involved in the formation and evolution of the earth, the Geophysical Laboratory has often pioneered. Since its beginning in 1906, the laboratory has introduced many new concepts, techniques, and experimental equipment. As some questions were answered, new tools were created that led investigators to study yet other puzzles and indeed to formulate completely new topics for research. During the past few years, scientists at the laboratory have been particularly innovative with respect to equipment and technique.

One example is the development this past year of equipment capable of achieving pressures of 500,000 atmospheres at a temperature of 2500°C. Such a pressure corresponds to that at about 1000 kilometers depth in the earth, whereas the temperature is greater than that of the white-hot filament of an electric light. Development of this equipment is a remarkable achievement in itself. However, what is perhaps more noteworthy is the creation of means of simultaneously measuring the pressure and temperature, and monitoring effects with spectrophotometers, x rays, and Mössbauer effect behavior of samples under these extreme conditions. These developments were conducted principally by Peter M. Bell and Ho-Kwang Mao.

A striking feature of the pressure equipment is its low cost and simplicity. Most of the approaches to high pressure research have involved massive equipment with the experimental sample inaccessible to the observer while it is under high pressure. The new apparatus permits visual inspection and other direct observations of the sample while under pressure. The method of producing the pressure is to use the space between opposing diamond anvils. The sample is heated by absorbing the energy of a laser beam to which the diamond anvils are transparent.

The new equipment makes the high temperature chemistry of the earth's deep interior accessible to study. Results from the new equipment will be followed avidly by theoretical geophysicists seeking to understand such processes of the earth's interior as those giving rise to the motion of tectonic plates. The new knowledge that will arise is also likely to lead to important practical results,

much as the studies of P. W. Bridgman at Harvard were ultimately extended by the General Electric Company to the commercial synthesis of diamonds.

Ho-Kwang Mao, David Virgo, and Carnegie Fellow Frank E. Huggins have designed, built, and tested Mössbauer equipment adapted to use in conjunction with the special conditions of the high-pressure diamond cell. Observations can be conducted successfully on 10-microgram samples. These scientists point out that ability to conduct Mössbauer studies at high temperatures and pressures is particularly important because of the ubiquitous occurrence of iron in the earth's crust and mantle. Moreover, iron is the only transition element of major abundance.

Thus, iron can be expected to give rise to most, if not all of the complications associated with crystal-field and charge-transfer phenomena, variable valence and spin states, and the electrical and magnetic properties of cations in minerals likely to be found in the mantle. For this reason, Mössbauer studies of minerals containing iron under the pressures and temperatures of the mantle are expected to be especially informative. Furthermore, Mössbauer data as a function of pressure can be related to pressure-induced changes in the crystal chemistry and the magnetic, spin, and valence properties of iron in minerals, on which may be based interpretations of pressure-induced phenomena within the earth.

Sometimes a substantial contribution is made by putting together in a new context simple techniques which when combined create a powerful new capability. This is true of a major advance in radioactive dating achieved at the Geophysical Laboratory with collaboration of the Department of Terrestrial Magnetism.

Various clocks based on decaying radioactivity have been known for many years. Until about ten years ago their accuracy was about 1%–2%. This was useful but, for example, in the dating of old rocks (3000 million years) an error of 30–60 million years was common. This level of accuracy is not adequate for many purposes. Subsequent improvement of electronic circuitry in mass spectrometers at the Department of Terrestrial Magnetism and elsewhere created a potential for better measurement of isotope abundances. However, the potential was not being fully realized because of tiny amounts of adventitious impurities in reagents, in distilled water, and in the dust of laboratories. An example is the dating of zircons which contain uranium that decays to lead. In principle, the zircon can be dated by measuring the ratio of the atoms of lead that have been formed to the atoms of parent uranium now present. The amount of radioactive lead to be determined is often of the order of a few micrograms or less. The accidental addition of a few hundredths of a microgram of ordinary lead results in a serious error in the measurement. Quantities of this kind are ubiquitous, if only because of the large-scale use of tetraethyl lead in gasoline and consequent aerosols from motor exhausts. Thus laboratories, glassware, and reagents are contaminated. Through an effort sparked by Thomas E. Krogh with Gordon L. Davis and former Carnegie Fellow James M. Mattinson, techniques were developed that cut the contamination to a low level. Reagents were purified by molecular distillation, and a new procedure using a Teflon bomb eliminated the need for extensive chemical processing. Preparation of a pure sample of ^{205}Pb to use as a quantitative tracer was also helpful. The net effect was that for the first time Krogh and colleagues could measure mineral ages of 3000 million years with an accuracy of $\pm 1\text{--}2$ million years. The equipment involved is simple and cheap and will be duplicated elsewhere. It will facilitate accurate dating and detailed reconstruction of important Precambrian events, some of which hold the key to early evolution of life and some of which created many of the world's most important mineral deposits.

For many years petrologists have been well aware of the role of comparatively small amounts of water in altering the properties of rocks, particularly at the high temperatures and pressures prevailing in the earth's interior. Among the effects are large changes in strength and melting points. In addition, water can cause changes in chemical relationships among the silicates. Water also probably has a role in explosive volcanism. In spite of this background of knowledge of one volatile, H_2O , petrologists have not fixed much attention on a second volatile, CO_2 .

When the role of volatiles is considered, emphasis is usually placed on water, not only because of the large amount in the oceans but also because of its abundance in some rocks. The working hypothesis is that the water now in the oceans originated deep in the earth. Because the amount of water in the oceans is much greater than the amount of CO_2 in carbonate rocks, attention has focused on water. However, if one takes seriously the concept of tectonic plates and the attendant underthrusting, one would be led to assume that large amounts of carbonate have been and are being recycled. Indeed, in areas where tectonic plates have collided, the amount of CO_2 underthrust as carbonates might exceed that of H_2O present in any form.

During the past two years, David H. Eggler has placed a spotlight on the roles of CO_2 and has opened up what may well become a most significant area for research and understanding. Eggler has found that CO_2 dissolves in silicate melts and that it plays a significant part in the fractionation of magma toward silica-undersaturated compositions. The solubility of CO_2 is dependent on pressure. Thus a sudden release of pressure could give rise to a sudden release of CO_2 with important physical and chemical sequelae.

In this year's Report, Hatten S. Yoder, Jr., Director of the Geophysical Laboratory, has outlined some results of this year's work on CO_2 . Carnegie Fellow Bjørn O. Mysen obtained infrared spectra on quenched CO_2 -saturated liquids and demonstrated that CO_2 enters these liquids both as discrete CO_2 molecules and as the carbonate anion. Increasing temperature increases the proportion of total carbon entering the melt as carbonate anion, as does increasing basicity of the silicate melt. Highly polymerized (acid) melts such as the melt of albite composition dissolve the least CO_2 (1–2 weight percent) according to Mysen, and at temperatures near the albite- CO_2 liquidus the only carbon dioxide species in the melt is molecular CO_2 . Less polymerized silicate melts such as the melt of diopside composition display a large CO_3^{2-} absorption band under all conditions investigated. Infrared measurements indicate that the CO_3^{2-} ion is more important in hydrous than in H_2O -free silicate melts. Increasing basicity, temperature, and pressure also result in increasing total CO_2 solubility in all compositions studied ($\text{CaMgSi}_2\text{O}_6$, $\text{NaAlSi}_3\text{O}_8$, $\text{NaAlSi}_2\text{O}_6$, NaAlSiO_4 , natural olivine nephelinite, tholeiite, and andesite).

On the basis of his present studies, Mysen places emphasis on the low solubility of CO_2 compared with that of H_2O and also on how strong the dependence of CO_2 solubility is on temperature, pressure, and silicate chemistry. These results together with phase equilibrium data on model mantle CO_2 - H_2O systems can aid in understanding the fractionation of tholeiitic magmas to compositions containing normative nepheline and larnite. It is proposed by Mysen that CO_2 -rich vapors can evolve from silicate magmas during ascent in the upper mantle. The development of such a CO_2 -rich vapor presents a means of generating nephelinitic magmas by partial melting of a peridotite upper mantle; previous models have lacked the mechanism to generate a CO_2 -rich vapor.

The origin of kimberlite, containing initially the three principal minerals

olivine, calcite, and phlogopite, depends greatly on the role of CO_2 and H_2O . In the course of studying the system $\text{CaO-MgO-SiO}_2\text{-CO}_2$, Eggler discovered another invariant point that bears directly on the generation of kimberlite. The invariant point is formed by the intersection of the decarbonation reaction $\text{dolomite} + \text{enstatite} = \text{forsterite} + \text{diopside} + \text{CO}_2$ with the melting curve of the assemblage $\text{diopside} + \text{forsterite} + \text{carbonate}$ at a pressure between 25 and 30 kbar. Because of these relationships, the subsolidus phase assemblage of a simple peridotite composition at 30 kbar is not $\text{diopside} + \text{forsterite} + \text{orthopyroxene} + \text{CO}_2$ but $\text{forsterite} + \text{orthopyroxene} + \text{diopside} + \text{dolomite}$. The latter assemblage melts to a carbonate-rich liquid at a temperature hundreds of degrees below the solidus of volatile-free peridotite. Pressure release by tectonic processes could, therefore, trigger melting that yields kimberlitic liquids at relatively low temperature. It had previously been thought that such melts could form only by fractionation of more silica-rich partial melts. Eggler also proposes, on the basis of these phase equilibria, a new concept of the low-velocity zone beneath the oceans where partial melting results from the presence of small amounts of CO_2 rather than H_2O .

DEPARTMENT OF TERRESTRIAL MAGNETISM

George W. Wetherill became Director of the Department of Terrestrial Magnetism in April 1975. He came from the University of California at Los Angeles where he had been Professor of Geophysics and Geology. Wetherill was a staff member at the department from 1953 to 1960 before going to UCLA.

A graduate of the University of Chicago, Wetherill received bachelor's degrees in philosophy (1948) and physics (1949). He earned the M.S. degree in 1951 and the Ph.D. in 1953, both in physics. From 1951 to 1953 he was an Atomic Energy Commission Predoctoral Fellow, doing thesis research on spontaneous fission of uranium and thorium and nuclear processes in nature. Before that he was a research assistant at the University of Chicago, where he worked on the 170-inch synchrocyclotron.

While he was a staff member at the Department of Terrestrial Magnetism, Wetherill participated in a joint DTM-Geophysical Laboratory project to re-determine the decay constants of rubidium and potassium—standards that are fundamental to the measurement of geologic time. Wetherill's main contribution to this effort was his determination of the concentration and isotopic composition of inert gases such as argon by mass spectrometric isotope dilution. His formulation of the systematics of complex data for open systems is the basis of modern age determinations using the lead-uranium method. He has contributed extensively to the definition and assignment of age provinces in ancient Precambrian shield areas.

Wetherill has been a principal investigator of lunar samples from Apollo 11 to 17 since 1969. He has done major theoretical work on the origin of meteorites by studying the dynamics of stray bodies in the solar system.

Ellis T. Bolton, the former Director, continues with the Institution as a senior staff member. He is currently Carnegie Institution of Washington Professor of Marine Studies at the University of Delaware.

Bolton succeeded Merle A. Tuve as Director of the Department of Terrestrial Magnetism in 1966. He had joined the Carnegie Institution in 1949 as a fellow at DTM and had served as staff member, chairman of the Biophysics Section, and associate director. Although his training at Rutgers University (B.S., 1943; Ph.D., 1950) was in immunology and its use in indicating the degree of related-

ness between species, at DTM he shifted his attention to biosynthesis in bacteria and in small molecules that are the precursors of proteins and nucleic acids. His work in these areas helped clarify the pathways by which sulfur is incorporated into amino acids and the role of the Krebs cycle in the incorporation of carbon from CO_2 into amino acids and nucleotides.

Bolton also contributed to development of the competition method for analysis of the inhibition of synthesis now called "feedback" control. Later he turned to studies of macromolecules and the more complex particles found in cells. He demonstrated the role of magnesium in stabilizing ribosomes, developed means of purifying ribosomes and animal virus, and showed the difference in composition between different sizes of ribosomes. An important contribution of Bolton's work was the development, with B. J. McCarthy and B. H. Hoyer, of an agar gel method for isolating single strands of DNA. This technique for analyzing relationships between living things has created new possibilities for study in medicine, differentiation, taxonomy, and evolution.

At the Mariculture Laboratory of the College of Marine Studies, University of Delaware, Bolton is part of an interdisciplinary group of biologists, chemists, and engineers engaged in research and development efforts to determine feasibility of large scale growing of filter-feeding marine invertebrates—oysters. The study is progressing well.

Bolton commenced his work at Delaware in September 1974. From that time until April 1975, L. Thomas Aldrich served as acting director of the department. He carried on cheerfully and effectively, managing to perform vital administrative functions while maintaining his personal research program.

This department has a long history and tradition of developing and maintaining excellent instrumentation. Much of the current research is made possible by its special facilities.

For example, the mass spectrometers at the department have capabilities equaled by few elsewhere. Their ion sources have been so improved that high precision isotopic measurements can be conducted on a few nanograms of sample. The electronics of the instruments are excellent and are coupled with computer averaging techniques. In consequence, it is possible to measure isotope ratios to a standard deviation of .005 percent. This capability together with the techniques developed by Thomas E. Krogh and Gordon L. Davis at the Geophysical Laboratory make feasible new accuracy in zircon dating. The capability also facilitated obtaining significant findings on the strontium isotope content of mid-ocean ridge basalts.

According to plate tectonic theory, new oceanic lithosphere is produced at mid-ocean ridges by addition of material from deeper within the earth's mantle. The surface manifestations of this material are the mid-ocean ridge basalts (MORB), obtained by dredging and drilling of the sea floor. Previous work, primarily based on young dredge haul samples, showed that MORB is distinguishable from other basalts, by both its trace element concentrations and its strontium isotopic composition. It was not clear from this earlier work that the difference was an essential characteristic of MORB or reflected biased sampling of rocks of a particular age. Stanley R. Hart reports results from older (15–40 million year) samples of MORB from the South Atlantic, obtained by drilling, which show that the characteristic differences between MORB and other basalts extend back in time.

These differences between MORB and other basalts such as those produced in volcanic island arcs are examples of a fundamental problem which dominates current geochemical discussions of the mechanisms by which material is trans-

ferred from the deeper interior of the earth to the surface regions: that various basaltic rocks, all presumably derived from the mantle, exhibit different chemical and isotopic characteristics. Further examples are given in the report by Hart and Carnegie Fellow William M. White, collaborating with J. G. Schilling, concerning basalts from the mid-Atlantic ridge, the Azores, and Iceland. The most obvious explanation is that the mantle is chemically heterogeneous on both a local and a global scale. If true, a new field of "mantle geology" directed toward an understanding of the basic principles governing these heterogeneities is opened.

Further examples of the capabilities of the department staff in developing instrumentation are represented in contributions by I. Selwyn Sacks. Details have been described earlier. His wide amplitude, wide frequency seismometer and highly sensitive strainmeter are achieving increasing acceptance. The potentialities of the strainmeter are still being investigated, but the indications are that it will have very important practical applications. This year ten of the meters were installed by the Japanese Government in and near a probable earthquake site. The Japanese are urgently seeking means of predicting earthquakes, and their assessment of the potential usefulness of the Sacks strainmeter in comparison with other approaches has been favorable.

The wide amplitude, wide frequency seismometers have made feasible an investigation conducted this year on seismic events attending the subduction of tectonic plates.

The tectonic environment of the Andes and the adjacent portions of the South Atlantic Ocean are complementary to those of the mid-ocean ridges. Here down-going slabs of oceanic lithosphere plunge hundreds of kilometers beneath the continental lithosphere, resulting in the seismically active "Benioff zone," volcanism, and the formation of mountain belts. The relationships between these processes have been the subject of a continuing combined geophysical and geochemical investigation. Sacks and Carnegie Fellow J. Arthur Snoke report seismic studies of lithospheric plate motions in both South America and Japan. The seismic work suggests a new hypothesis for the generation of the thick lithosphere which distinguishes continents from ocean basins: that the cool down-going slab of oceanic lithosphere freezes out aesthenosphere in the "wedge" defined by the intersection of the continental plate and the down-going oceanic plate. In combination with migration of the ocean trench associated with the down-going slab, this could provide a mechanism for increasing the mass of continental lithosphere over geological time.

Vera C. Rubin, W. Kent Ford, Jr., and Norbert Thonnard have drawn a very interesting conclusion from their study of the apparent anisotropy in the distribution of a particular class of galaxies as indicated by both optical and radio data: that the best interpretation of their observations requires our galaxy, as well as its local neighbors, to be moving at a velocity of about 500 kilometers per second with respect to the reference frame defined by the distant galaxies. The direction of this motion is perpendicular to the direction of the nearest large cluster of galaxies, the Virgo cluster, and the velocity corresponds to the orbital velocity of a body at the distance of our galaxy from the Virgo cluster. Therefore, the data are consistent with the idea that in some sense our galaxy is in orbit about the Virgo cluster, although not in the usual way, as the 10^{11} year period of such an orbit is much greater than the age of the galaxies. These observations are inconsistent with the generally accepted isotropic distribution of 3°K cosmic blackbody radiation background. The discrepancy appears to be outside the observational errors of both sets of measurements, and represents an important problem for further investigation.

Timely accomplishment of the observations mentioned above would not have been possible without the Carnegie image tube developed by Ford at DTM. Continued improvements in these devices and systems for utilizing them have been made by Ford. In addition, he reports advances in developing a new type of detector especially suitable for photometric work. This detector eliminates use of the photographic plate and provides the imaging data in digital form.

In atomic physics, the intensity of production of characteristic x-ray line spectra by heavy ion bombardment yielded a simple exponential dependence on the atomic number of the target atom. Surprisingly, it appeared that current theories do not yield this result, even though its simple form strongly suggests that a theoretical explanation should be possible. Louis Brown and his co-workers have derived a simple expression which fits the observed exponential dependence of the line spectra on Z , as well as predicting the x-ray energy spectrum of the continuum radiation. Although this does not yet represent a complete theory for the problem, the agreement with observed data indicates that the approach taken is on the right track.

In nuclear physics, the nuclear structure of ^{16}O and ^{10}B were successfully investigated by formation of the compound nucleus by bombardment of ^{15}N and ^9Be with polarized protons. The former nucleus is of astrophysical interest as $^{15}\text{N}(p,\alpha)^{12}\text{C}$ and $^{15}\text{N}(p,\gamma)^{16}\text{O}$ are competing steps in the CNO cycle of stellar energy production.

During this report year, organized activities of the Biophysics Section were concluding. This meant the ending of a highly successful, highly productive 30 year experiment. This year's Report of the Department of Terrestrial Magnetism contains a compact history of the experiment written by Richard B. Roberts. In it he outlines the origins of the Biophysics Section, describes its evolution, and points to some of its major accomplishments.

At the conclusion of World War II, Tuve became director of the department and brought about a reorientation of its program. In particular, nuclear physics had received a tremendous emphasis from the development of the atom bomb and seemed destined to be carried out by large groups with unlimited funds. In contrast, biophysics appeared to be more suitable for small groups and (with the advent of tracers) due for a burst of progress. In addition, prewar experience had demonstrated that physicists could contribute to biology not only in technique but in the planning of experiments. Tuve therefore decided to reduce the emphasis on nuclear physics and to initiate a Biophysics Section. At this initial stage the group included Abelson (chairman), Dean Cowie, and Roberts, all trained in physics. In addition, the group was fortunate to have with them H. H. Darby and W. R. Duryee as guest investigators who provided a much needed wealth of biological experience.

The experiments of the first years, 1947 to 1951, were largely exploratory; they included such diverse topics as capillary permeability, and the effects of ultraviolet radiation, vitamin B_{12} , and various ions on biological material. The biological materials used ranged from humans to bacterial viruses, but following Robert's participation in the bacteriophage course at Cold Spring Harbor there was a steadily increasing use of the bacterium *Escherichia coli* as biological material.

By 1952 the group had been expanded with the addition of Bolton and Roy J. Britten and interest of the group had focused on the synthesis of amino acids and nucleotides by *E. coli*. This subject was studied intensively through 1955, culminating in the publication of the book *Studies of Biosynthesis in E. coli*. This book was well received generally and was considered to be a "bible" by some

microbiologists. From that time on, the Biophysics group was an important contributor to the flourishing field of molecular biology during its most exciting years. In his write-up, Roberts points to the productivity of the small Biophysics Section. One measure is three books and 200 or more papers.

A better measure lies in the listing of significant findings: (1) isotopic competition method; (2) flow patterns in metabolism in *E. coli*; (3) feedback inhibition; (4) demonstration that nascent protein is attached to ribosomes; (5) virus purification on DEAE columns; (6) patterns of ribosome synthesis; (7) proof that newly formed RNA in bacteria is one-third messenger, two-thirds ribosomal precursor; (8) agar column for nucleic acid reactions; (9) messenger isolation; (10) application of nucleic acid interaction to measure relatedness of species and degree of divergence; (11) homology of DNA in *E. coli* and lysogenic virus; (12) detailed studies of divergence in virus, bacteria, algae, vertebrates, rodents, and primates; (13) application of nucleic acid reactions to cancer virus investigations; (14) demonstration that DNA remains identical but RNAs differ in different tissues and stages of development; (15) extensive studies of nucleic acid reaction kinetics; (16) discovery of repeated DNA; (17) properties of repeated DNA; (18) involvement of catecholamines and peptides in learning and memory.

At the conclusion of his summary, Roberts ends on this thoughtful note.

"We are pleased to have participated in this exciting period in the development of biology. We believe that we did make significant contributions and that, since some of us will carry on in different places, our history is not complete. We are especially pleased to note the contributions being made by 22 Fellows who received a part of their training with us."

HALE OBSERVATORIES

It is premature to celebrate the successful completion of the Irénée du Pont Telescope, for there is work that remains. However, most of the tasks have been completed and very successfully. For example, the figuring of the main mirror has been finished, and tests show that it is excellent. The mirror has been shipped to Chile and it has arrived on Las Campanas safely. The telescope itself was thoroughly shop-tested in Los Angeles, subsequently shipped to Chile, and installed without problems in its dome on Las Campanas.

Construction of a major observatory on a mountain 5000 miles distant is a demanding task that requires close coordination of many engineering and construction activities. The telescope was designed by the staff of the Hale Observatories, led by Bruce H. Rule as chief engineer and project officer. The late Ira S. Bowen made innovative contributions to the optical design. Testing of the telescope and design of auxiliary instruments are, as expected, requiring much additional effort on the part of staff members. Large demands are also made on the administrative staff.

A novel control system for the du Pont Telescope has been created by J. T. Fridenberg of Caltech's Astroelectronics Laboratory with close collaboration of staff members of the Hale Observatories. A prototype has been tested on the 1.5 meter telescope on Palomar Mountain.

The telescope automatic control system was designed to control large observatory telescopes with a degree of sophistication equal to that provided by a typical general purpose computer. By making use of modern microprocessor modules, the control system operates the telescope independently of the data acquisition or

other associated functions. This distributive processing technique isolates the control functions from problems often encountered with single computer control. A telescope so controlled avoids operational interruptions that normally occur when a computer control system is off-line.

In addition to responsibilities in connection with the new Irénée du Pont Telescope and to meeting requirements for new equipment, the staff must devote part of their time to ensuring that the various existing telescopes and their many pieces of auxiliary apparatus are maintained in good condition. This is essential if both the local astronomers and the many guests are to function effectively. In spite of these burdens, which are shared by a staff of limited size, the research productivity of the Hale Observatories is excellent. This year much attention has been devoted to studies of galaxies—their structure, dynamics, clustering, and evolution. Horace W. Babcock, Director of the Hale Observatories, notes that a review of research topics reported upon for the past year shows that some twenty different investigations related to galaxies are in progress or have just been completed.

A galaxy such as our own, which includes the sun and the Milky Way, contains many millions of stars that occupy a relatively flat, disk-shaped region of space. Edwin P. Hubble classified the shapes of galaxies according to a bifurcated scheme with a sequence of forms branching from elliptical into normal spirals and barred spirals. Later Olin J. Eggen, Donald Lynden-Bell, and Allan R. Sandage introduced the concept that galaxies were formed by contraction and collapse of a primordial gas cloud to a plane.

J. Richard Gott III and Trinh X. Thuan of the California Institute of Technology have developed a more detailed analysis of events during galaxy formation. They analyzed the competing effects of dissipation and turbulent viscosity, using a model of cloud formation in the early protogalaxy. Numerical models, including both stars and gas, were used to simulate the collapse. The stars and gas collapsed together until they reached the plane, whereupon the gas formed a disk and the stars continued in elliptical orbits to form a spheroidal halo. Some oscillations of the disk are expected before equilibrium is reached. Models may be used to relate galaxial parameters to the original size and angular momentum of the cloud. In general, if star formation in the early protogalaxy is essentially complete by the time of maximum collapse, an elliptical galaxy is formed. If a significant amount of gas remains at this stage, it will dissipate its energy to form a disk-like spiral. Observed properties of ellipticals and spirals imply that ellipticals formed out of larger perturbations of the primordial gas cloud than did spirals, giving the ellipticals greater densities and shorter collapse times. If early star formation is rapid and dependent upon the square of the density, ellipticals are expected to complete their star formation by the time of maximum collapse, while spirals are not. Protogalaxies arising from larger initial density fluctuations cluster more readily, accounting for the preferential occurrence of ellipticals in large clusters.

The best hope for advancing knowledge of the chemical composition and chemical evolution of galaxies lies in the interpretation of the spectra of the regions of ionized interstellar gas within them. Leonard T. Searle has recently surveyed the strength of emission lines that are probes of ionization structure in a number of H II regions in the galaxies M31, M101, and M51. He has carried out a systematic survey of the behavior of the infrared lines of [S III] and is collaborating with G. Shields of the University of Texas in the interpretation of the data. The observed behavior of the [S III] lines is not in accord with the

predictions of the simple ionization-structure models that have so far been used to interpret the spectra of H II regions. Unexpectedly, large density fluctuations within the emitting regions are indicated. It is already clear that the low excitation that is characteristic of regions situated in the inner spiral arms of galaxies is not simply a consequence of an enhanced oxygen abundance, as had earlier seemed likely.

Observations bearing on the distribution of metallicity in the Andromeda Spiral, M31, were obtained by M. Schwarzschild of Princeton University in collaboration with J. Beverley Oke. They used the multichannel spectrometer on the Hale Telescope to obtain energy distributions at several locations in the central bulge of M31. The results can be interpreted as an increase of the heavy element abundance toward the nucleus of the spiral. Beyond a radius of 2', no further abundance changes were observed; but at 7'.5 and 10' from the center of M31 along the major axis, there is evidence for young hot stars.

Sandage completed analysis of redshifts and photometry of selected groups and clusters of galaxies in the southern hemisphere. He found that when aggregates of galaxies having populations in the range of 20 to 300 are examined, the mean absolute magnitude of the first-ranked galaxy varies by only about 0.15 mag. This suggests that the absolute magnitude of the first-ranked galaxy is determined by some physical upper limit in the galaxy formation process that is independent of the statistics relating to other members of the cluster.

James E. Gunn and Oke have continued their separate programs to discover faint clusters of galaxies and to measure the redshifts and absolute spectral-energy distributions of the brightest members of these clusters. The first aim is to produce a list of clusters found under well-controlled conditions within a definite limit of apparent magnitude. Hundreds of clusters were identified on plates obtained in the course of an initial survey with the 1.2-meter Schmidt telescope. Spectrophotometric observations of a few show that redshifts are typically between 0.20 and 0.35. A deeper survey, conducted with a 90-mm image tube at the prime focus of the 5-meter telescope, has produced a sample of about 30 very faint clusters of galaxies that typically have redshifts larger than 0.40.

In addition to work on galaxies, other studies were conducted at the Hale Observatories. A few examples follow.

George W. Preston, Arthur H. Vaughan, Jr., and former Carnegie Fellow Richard E. White have completed their investigation of Hg isotopy anomalies in the mercury stars. Wavelengths of Hg II λ 3984 in 30 stars are distributed rather uniformly from the value for the terrestrial mix of isotopes to a value that implies a preponderance of ^{204}Hg . The wavelengths are loosely correlated with effective temperature. Relative isotopic abundances derived from partially resolved profiles of λ 3984 in ι Coronae Borealis, χ Lupi, and HR 4072 suggest that simple mass-dependent fractionation has occurred in all three stars. This indicates that an isotope separation process rather than exotic nucleosynthesis is responsible for the isotope anomalies. Accordingly, a scheme has been devised whereby isotopic compositions can be inferred from a comparison of stellar wavelengths and equivalent widths of λ 3984 with those calculated for a family of fractionated isotopic mixes. For one star, 46 Aquilae, Preston reports a wavelength for the Hg II line that corresponds to pure ^{204}Hg .

Jesse L. Greenstein has continued the colorimetric search for white dwarfs, especially those with late-type spectra and colors, using the multichannel spectrophotometer on the Hale Telescope. The rarity of yellow and red degenerate stars continues to contradict the simple theory of cooling of the core of a

degenerate object. Although numerous objects have been found cooler than 8000°K , none have been found cooler than about 4500°K (EG 202). A few have relatively strong metallic lines, but at wavelengths longer than $\lambda\ 5500$ they prove to be relatively blue objects. The reasonable possibilities seem to be that (1) the cooling becomes rapid below effective temperature 5500°K and the stars disappear into the black dwarf stage, or (2) some physical mechanism delays cooling of old white dwarfs.

James A. Westphal and Jerome Kristian have continued to refine and test the application of SIT television camera tubes for two-dimensional (image) photometry. The level of photometric precision obtained at the telescope is close to the 1% limit expected from laboratory tests of the system. Over a range of 10 magnitudes, from 12 to 22, it is possible with the SIT-Vidicon to reproduce with highly satisfactory precision a broad-band sequence established with photomultipliers. The limits are not intrinsic, but at magnitude 22 the signal is completely dominated by the sky. SIT measurements should be accurate to fainter levels, although fainter photoelectric standards are not available. In a ten-minute exposure, stars are measurable fainter than $V = 24$ mag, with progressively lower precision attributable to photon statistics. Currently, the 1% limit for precision of the SIT system is due primarily to seemingly random variations of the order of 0.5% in the background.

The same SIT system used in image photometry has been employed by Westphal and Kristian for several programs of low- and high-resolution spectroscopy. When used with a small spectrograph, there are two important features of the SIT detector that make it particularly suitable for faint objects. The reproducibility of the transfer function allows accurate sky subtraction, while the two-dimensional format permits the spectra of the sky and object-plus-sky to be recorded simultaneously. The sky-subtraction process functions well and produces difference spectra that are limited essentially by photon noise. The SIT-Vidicon has also been applied successfully as a detector at the coude spectrograph of the Mount Wilson 2.5-meter telescope, where it has been used by Robert J. Brucato to study stellar line profiles and by C. P. Wilson to measure velocity dispersions and rotations of the central regions of galaxies. Cooling of the tube to -90°C makes possible exposure times of several hours.

An experimental grating spectrograph equipped with a cooled integrating SIT-Vidicon camera is nearing completion under Gunn's direction. The system is being interfaced with a PDP-11/40 minicomputer to give real time capability for addition, averaging, reduction, and display of spectra.

A new f/60 infrared photometer has been put into operation on the Mount Wilson 1.5-meter telescope. Signal modulation is obtained by wobbling the Cassegrain secondary of the telescope. The system provides a very satisfactory level of performance for the study of infrared radiation from molecular clouds, H II regions, and external galaxies.

DEPARTMENT OF PLANT BIOLOGY

Located not far from the center of the Stanford University campus, this department is ideally situated for botanical research. Within easy range are such diverse environments as the hot, dry Death Valley; the cool, moist coastal zone; and the alpine Sierras. The department has transplant gardens in these regions and an extremely well-equipped mobile laboratory to utilize the diverse plant resources.

On the Stanford campus, the department has extensive facilities on a 10-acre plot of ground. This year comprehensive renovation of the headquarters building and construction of new facilities were completed, providing excellent additional laboratory space. The department is now in position to interact even more effectively with Stanford and is already doing so through joint efforts on teaching and research.

The total joint enterprise has at its disposal unique experimental capabilities. These are in part a result of collaboration between Olle Björkman and Joseph Berry of the department and Professor H. A. Mooney of Stanford. The equipment includes controlled growth chambers and a mobile laboratory. Thus it is possible to duplicate at the laboratory most of the various natural conditions that plants encounter, ranging from those of Death Valley to the conditions of the coastal regions. In addition, it is possible to create combinations of environmental variables which do not exist in natural environments, such as extremely high temperatures together with very high humidities or high CO₂ concentrations.

The mobile laboratory has all the measuring and control systems needed for continuous and simultaneous measurement of such parameters as rates of CO₂, O₂, and H₂O vapor exchange and a host of other relevant variables, and is also equipped with a small dedicated computer. A most valuable feature of the on-board data acquisition and processing system in addition to providing greatly improved speed, flexibility, convenience, and accuracy in data collecting is that the immediate processing of the data enables observation of important plant responses to a change in a certain factor or combination of factors with sufficient speed to permit further study and manipulation of these responses.

When not in use in the field, the mobile laboratory is docked next to the controlled growth facilities and is there employed as an integral part of the stationary laboratory. Having a single sophisticated instrument package which can be used both in laboratory and in field eliminates extensive cross-calibration efforts, saving both time and funds, and giving the same precise base line to measurements made under both circumstances.

These major items are only part of the resources at the Department of Plant Biology. The completion of new construction has provided additional laboratory space. At the same time, David C. Fork and Carnegie Fellow Tetsuo Hiyama have developed and built new pieces of equipment that permit detailed examination of processes of photosynthesis with control of intensity, wavelength, and time to periods as short as 2×10^{-7} seconds. This equipment, together with apparatus developed earlier by C. Stacy French, represents an inventory of powerful tools for investigation of photobiology.

During the report year, department staff lived with the disruption attendant to extensive construction and renovation. Nevertheless, the staff enjoyed a productive year in teaching and research.

Björkman, together with Mooney and James Ehleringer, a Stanford graduate student, continued studies in progress last year on the photosynthetic properties of plants from contrasting thermal environments. Direct measurement of photosynthesis corresponded well with previous growth studies, indicating that the temperature dependence of dry matter production is closely related to the temperature dependence of photosynthetic capacity, whether the plant studied used the C₃ or C₄ pathway of carbon fixation, and whether it was a native of a cool coastal climate or the extremes of temperature found in the bottom of Death Valley. When the various plants were all grown under similar conditions, whether warm or cool, some showed the capability of adapting the photosynthetic

machinery to growth under temperature regimes far removed from normal, while others did not. Plants which could perform excellently under the most extreme conditions, however, seemed the least adaptive.

Further studies by Björkman indicate that the high temperature inhibition of photosynthesis is not caused by a decrease in stomatal conductance, nor by temperature-induced alteration of diffusive transport of CO₂ fixation sites within the cells. Neither is it caused by a general breakdown of cellular integrity, since inhibition of respiration cannot be detected until temperatures are raised significantly above those at which inhibition of photosynthesis is found. Under rate-limiting light intensities, however, the quantum yield for photosynthesis falls off sharply at the temperature at which inhibition of photosynthesis is first found. Likewise, the quantum yield of the extraordinary desert plant *Tidestromia oblongifolia*, which can flourish at a temperature of 47°C, is sharply reduced when the plant is grown at lower temperature, e.g., 22°C. The cause cannot be alteration of any barriers to CO₂ movement into the cell, nor reduction in chlorophyll, protein, or carboxylation enzymes. Björkman hypothesizes that the membrane properties which permit photosynthesis at high temperatures preclude their effective function at low temperatures.

Fork, Joseph A. Berry, and Ms. Garrison then heat-treated leaves of *Tidestromia* and examined various properties of chloroplasts isolated from them. It was clear that photosystem II electron transport was strongly inhibited by treatments which did not affect photosystem I. The temperature at which this effect is first noted corresponds fairly well with the temperature at which inhibition of photosynthesis is first observed. Changes in the fluorescence kinetics of intact leaves also occur at temperatures at which thermal inhibition of photosynthesis is found. These results also implicate system II. Overall fluorescence yield is also affected by temperature, but transitions in fluorescence yield occur at temperatures significantly above those at which damage to photosynthesis occurs. Likewise, studies on ion leakage show that cell permeability is also normal at temperatures above which photosynthetic damage occurs. It is clear that photosynthetic membranes are more sensitive than the plasma membrane to thermal injury.

Carnegie Fellows Norio Murata and John H. Troughton, together with Fork, grew the blue-green alga *Anacystis nidulans* under different temperatures selected to bring about known variation in the fatty acid composition of their membranes. Studies using electron spin resonance spectrometry on isolated fragments suggested that in cells grown at higher temperatures, the marked change in the environment of the spin label with increasing temperature occurred at higher temperatures. Maximum fluorescence yield also occurred at higher temperatures for cells grown at higher temperatures, as was the case for lamellar fragments or for structures formed by reaggregation of extracted galactolipids and chlorophyll *a*. Fluorescence of the extracted chlorophyll alone, however, or extracted phycobilins, showed no effect of growth temperature. Thus the changes observed in fluorescence yield in intact cells must be produced by interaction between the pigments and membrane lipids. The changes are probably caused by transition of membrane lipids between the liquid-crystalline state and the mixed solid, liquid-crystalline state.

Further studies on electron transport as indicated by P700 reduction, oxygen evolution, and the shift of the thylakoid membranes from pigment state 1 to pigment state 2 also gave clear evidence of the membrane phase transition at roughly the same temperatures. These studies complement those by the physio-

logical ecology group on temperature effects on photosynthesis under conditions of thermal inhibition.

Fork and Jeanette Brown have continued studies on light-induced shifts in carotenoid absorption in a wide variety of different algal groups. Included were representatives of a newly identified algal group, the *Eustigammatophyceae*, plants containing only chlorophyll *a*, β -carotene, and a major xanthophyll. Both light-minus-dark difference spectra and kinetics of the changes were examined. It is clear that such shifts occur in virtually all photosynthetic organisms, with the blue-green algae standing as the single exception. Further study is needed, however, to understand the physicochemical events which underlie these changes.

Brown has continued studies on the properties of chlorophyll-protein complexes isolated from higher plants. One of these, CPI, is rich in P700 and contains only chlorophyll *a*. CPI is considered to be the reaction center chlorophyll. The other complex, CPII, contains all of the chlorophyll *b*, plus an equimolar concentration of chlorophyll *a*. Studies with Suzanne Acker and Jacques Duranton at the French Atomic Energy Center, Saclay, near Paris, show clearly that CPI is metabolically isolated from the rest of the chlorophyll-containing membranes in the plastid. Its pigments are both synthesized and degraded more slowly than the rest of the pigments.

Fluorescence emission spectra at room temperature and at -190°C were measured for both CPI and CPII. Dilution of CPII did not alter the fluorescence emission spectra whether excitation occurred with 420 nm or 470 nm light (preferential chlorophyll *a* or chlorophyll *b* excitation, respectively). Thus the two chlorophylls are clearly on the same protein (though not necessarily on the same polypeptide chain), since otherwise dilution would have decreased energy transfer between chlorophyll *b* and chlorophyll *a*.

William F. Thompson, who joined the department this year, has initiated extensive studies of plant nucleic acids, concentrating particularly on DNA hybridization techniques. Studies on reaggregation of pea DNA suggest that the genome is organized with many clusters of repetitive sequences.

Winslow R. Briggs, Director of the Department of Plant Biology, has been able to resume work started last year in the laboratory of Professor Rainer Hertel, University of Freiburg, Germany, on a promising candidate for the phototropic photoreceptor. With a Visiting Investigator, Jack Freeberg, he has obtained evidence for a light-induced absorbance change in a membrane fraction from corn coleoptiles. The change, which decays in the dark, suggests the light-induced reduction of a flavoprotein with subsequent reduction of a *b*-type cytochrome. Though other workers have seen such changes and related them to the phototropic photoreceptor, the present work represents the first demonstration of such changes outside the fungi, and the first suggestion that the pigment is membrane-associated. Robert Brain, a Stanford undergraduate visiting the laboratory during the summer of 1975, has been able to show the same changes in a membrane fraction from the fungus *Neurospora crassa*.

DEPARTMENT OF EMBRYOLOGY

In his introduction to the Report of the Department of Embryology, the Director, James D. Ebert, stresses the communal nature of the scientific enterprise, emphasizing both the interactions of the department with other laboratories and the interactions of staff members, fellows, and students within the department. He takes as one of his prime examples the way in which new

insights into gene structure have emerged through the use of restriction enzymes. The accomplishments of the department in the isolation of genes, in which Donald D. Brown has pioneered, are well known. In significant advances reported this year, the newly emerging technology of restriction enzymes has played a major part. This technology was not developed in the department, but several staff members and fellows have been quick to apply it critically to their problems. In this continuing study of the "anatomy" of the DNA which codes for 28S and 18S ribosomal RNA (termed ribosomal DNA or rDNA), a pivotal role has been played by Peter K. Wellauer, a Fellow of the National Cystic Fibrosis Research Foundation, along with staff members Donald Brown, Igor B. Dawid, and Ronald H. Reeder. In *Xenopus laevis*, about 450 copies of these genes are present on each of two chromosomes in every cell. Earlier studies revealed that these genes can be isolated completely free of the rest of the cell's DNA. Studies in the department and elsewhere have shown that rDNA is composed of multiple repeating units which are tandemly linked end to end. About two-thirds of each repeating unit is a gene region which serves as the template for the transcription of 28S and 18S ribosomal RNA. The remaining one-third of each repeating unit is not transcribed into RNA, has no known function, and is called the "spacer" region.

Within a cell, all 900 copies of the transcribed gene region appear to be identical, both in length and in nucleotide sequence, suggesting that cells have some mechanism for maintaining these hundreds of copies identical within close tolerances. The recent unexpected finding was that the spacer regions between the genes come in a variety of lengths. As many as seven different spacer sizes have been found on a single chromosome alternating with gene regions of constant length.

The existence of heterogeneous spacer lengths in rDNA was discovered by the use of a site-specific restriction endonuclease called EcoRI. EcoRI is one of a newly described class of enzymes which recognize specific short nucleotide sequences in the DNA and will cut the DNA only at the site of those sequences. In rDNA, the EcoRI recognition site occurs just twice in each repeating unit. Cutting the DNA at these two sites produces two fragments per repeating unit—one fragment containing only gene sequences and the other containing all of the spacer plus some gene region on each end. Electrophoresis of these fragments on agarose gels separates them according to size and reveals that the spacer-containing fragments come in different size classes while the gene fragment is homogeneous in size.

When EcoRI is used to cut rDNA isolated from individual frogs, it is found that the pattern of spacer length can vary from one individual to the next. This has made it possible to use rDNA spacer pattern as a genetic marker, that is, to select two frogs which have different spacer patterns, mate them, and observe how the spacer patterns are transmitted to the progeny.

Dana Carroll, a Fellow of the U.S. Public Health Service, also working with Donald Brown, has used a similar approach in further investigating the nature and organization of heterogeneity in the oocyte-type 5S DNA of *Xenopus laevis*. Again, not only is the existence of heterogeneity confirmed, but it is shown to be located in the AT-rich portion of the spacer.

In these examples at least, length heterogeneity results from the presence of variable amounts of reiterated simple sequences in nontranscriber spacer, with the region of variable length being close, if not adjacent, to the 3' end of the transcription unit.

Carroll's findings are a part, albeit a key part, of a larger undertaking by Donald Brown and his colleagues, namely the exploration of the "dual 5S DNA system" of *Xenopus*. The *Xenopus* genome contains at least two kinds of 5S DNA. "Somatic" 5S DNA appears to be made in all cells. "Oocyte" 5S DNA synthesis is "turned off" in somatic cells. Key questions concerning gene regulations are thus posed. Donald Brown and E. Jordan describe further progress in isolating 5S DNAs; and in a study related closely to Carroll's, Carnegie Fellow Ronald Brown has analyzed in detail the spacer sequence adjacent to the 3' end of the 5S DNA transcription unit. It is thought that the end of the gene itself and the first two spacer nucleotides may be at least part of the "termination signal" for RNA polymerase.

Significant progress is again reported by Douglas M. Fambrough and his colleagues, especially graduate student Peter Devreotes, U.S. Public Health Service Fellow Katherine Tepperman, and Professor Daniel Drachman of The Johns Hopkins University School of Medicine.

For several years Fambrough and his co-workers have been focusing on the differentiation of the skeletal muscle plasma membrane and the organization of skeletal muscle fibers. Many of their studies have centered upon the acetylcholine receptors of skeletal muscle, since they appear in the plasma membrane as readily detected functional molecules early in muscle development; are later confined to a small area of cell surface, the postsynaptic surface of the neuromuscular junction; and in denervated skeletal muscle reappear all over the surface of each muscle fiber. Because acetylcholine receptors can be readily identified not only by their function but also through the use of a radioactive probe which binds to them with extreme tenacity (iodinated α -bungarotoxin), they can be studied in ways which are unique. The group's working hypothesis includes the following elements. Acetylcholine receptors are synthesized by the normal protein synthesizing machinery. Newly synthesized receptor components occur as organized macromolecular structures of molecular weight about 250,000 daltons incorporated into internal cell membranes. These "precursors" are then inserted into the plasma membrane, the population of precursors being enough to support two hours of new receptor incorporation into plasma membrane without any new protein synthesis. Once in the plasma membrane, the receptors are functional molecules and are free to interact with the radiolabeled probe. Plasma membrane receptors are degraded by a random-hit process which is energy-dependent and proteolytic, probably involving internalization of membrane containing receptors and then degradation by lysosomal enzymes. During the past year, the group has developed techniques which will allow direct testing of several aspects of this model of the life history of receptor molecules. They have also devised a method for continuous monitoring of receptor degradation in organ-cultured skeletal muscle and have begun extending findings to adult mouse muscle.

Drachman and Fambrough earlier investigated the disease myasthenia gravis. They have now studied another human disease, congenital myotonic dystrophy, in which the muscle pathology suggested the possible participation of denervation. Since the appearance of extrajunctional acetylcholine receptors is a sensitive marker for denervated skeletal muscle surface, Drachman and Fambrough have used the radiolabeled probe for acetylcholine receptors on biopsy specimens from patients with congenital myotonic dystrophy. Biopsy material from two patients with the denervating disease amyotrophic lateral sclerosis has also been examined.

During 1974-1975, Richard Pagano was joined by two postdoctoral Carnegie

Fellows, Leaf Huang and Masatoshi Takeichi. Together with Ebert's colleague, Keiko Ozato, joint Carnegie-Marine Biological Laboratory Fellow, they have vigorously extended their explorations of phospholipid-cholesterol dynamics in mammalian cells. Their objective is to understand the dynamic movements which cellular phospholipids and cholesterol can undergo in cell membranes and the effects which perturbations in these motions can have on cellular activity. Among their studies described in the body of the Director's Report, two are especially noteworthy. They have combined their earlier knowledge of the interactions of cell membranes and lipid vesicles with the technique of high resolution electron microscope autoradiography to determine the surface distribution of one lipid component, phosphatidyl choline, on Chinese hamster fibroblasts. Second, in cooperation with Ozato and Ebert, they have begun to examine the effects of cell surface lipid perturbations on lymphocyte activation.

Pagano's and Huang's findings bear directly on the possibility of using lipid vesicles, into which appropriate macromolecules have been reconstituted, to "transplant" a foreign membrane protein (or other marker) into the plasma membrane of an intact host cell. They have been able to clarify the relative contributions of the various "pathways" a lipid vesicle can take in its interaction with a mammalian cell. The major pathways of lipid incorporation in vesicle-treated cells are fusion of vesicle and cell and exchange of lipids between vesicle and cell. Pagano and Huang have established that the fusion process is dominant at 37°C, while at 2°C (or with energy depleted cells), exchange of lipids between vesicles and cells is important. Finally, they have demonstrated that intact vesicles are *not* being engulfed by cells in a process resembling phagocytosis.

Ebert and associates have been engaged in fundamental studies of immune mechanisms. The immune response to foreign antigen is an orderly series of defensive actions. These include lymphoid cell recognition of the antigen as foreign, differentiation of lymphocytes into cytotoxic (killer) cells, proliferation of these cells, stimulation of humoral antibody production, and, at the appropriate time, suppression of the immune response, which otherwise could get out of hand. Thymus-derived lymphoid cells (T cells) play a primary role in this sequence.

Last year, Ebert and associates described a useful biological system for studying the behavior of lymphocytes in the immune response. This consisted of a population of T cells exposed to different mitogens, one of which was Concanavalin A (ConA). With this tool it was possible to assemble evidence supporting an affirmative answer to such questions as: Do lymphocytes differentiate into killer cells for all antigens by the same mechanism? If so, is the sensitization by specific alloantigens simply a triggering of the lymphocyte proliferation and concomitant transformation?

This year Ozato, Ebert, and W. H. Adler, a Visiting Investigator, have continued to study T cell recognition. They also have established conditions under which suppression of the immune response can be studied. In their experimental system, soluble ConA had a suppressor effect. So did spleen cells and lymph node cells "coated" with ConA. Contrary to expectation, however, "coated" thymocytes were inactive. Modification of the cell surface by ConA was assumed to be the immediate cause of the observed differences. This hypothesis was supported by the results of studies by Ozato and Ebert using further modifications of lymphocyte surfaces.

Studies by Ozato, Huang, and Ebert are now going forward on the nature of binding of mitogens to lymphocytes in an attempt to delineate the relation between cell surface events and subsequent DNA synthesis.

DEVELOPMENTAL BIOLOGY RESEARCH GROUP

The activities of this group are largely carried out in Southern California by faculty, graduate students, and postdoctoral fellows associated with California Institute of Technology. A key individual is Roy J. Britten, who is a staff member of the Carnegie Institution and a Senior Research Associate of Caltech.

The Developmental Biology Research Group was established as a result of a scientific collaboration starting in 1967 between Britten (at the time a member of the Biophysics Section of the Department of Terrestrial Magnetism) and Eric Davidson (then at Rockefeller University). Each had independently inferred that the repetitive DNA sequences, which are ubiquitous in higher organism DNA, were involved in the regulation of genetic activity.

By 1969 Britten and Davidson were convinced that an extensive experimental program would be required if their concept of the regulation of genetic activity were to be properly tested. They concluded that a large group would be required with the potentiality not only to investigate the sequence structure of DNA but also to prepare pure and well-characterized RNA from well-defined stages of development and to make use of these molecules for subtle studies of their sequence relationship and spatial relationship of the sequences in the DNA. When Davidson was offered an appointment at Caltech, the decision was made to set up laboratories there.

The work of the new group was initiated late in the spring of 1971 at Pasadena and early in the fall at the nearby Kerckhoff Marine Laboratory. Much of the effort of the group has been devoted to a thorough investigation of the sequence organization of the genome of higher organisms. The rationale offered by Britten and Davidson for this choice was : (1) The process which underlies all the other levels of control and regulation in the cell must be the control of the expression of the genetic information present in the DNA. (2) Thus the control of the transcription of the DNA sequences of structural genes into messenger RNA is probably fundamental. (3) The control of transcription requires molecular recognition of each of the many genes coordinately expressed in a given tissue or cell state. (4) It therefore appears likely that each set of genes (batteries) for which transcription is coordinately initiated at a given stage of development should have a battery-specific similar DNA sequence near the structural gene sequence itself.

This year the DNA of 14 species representing several phyla has been tested for interspersion of repeated sequences with single-copy sequences. A very similar pattern was observed in 12 of the species. *Drosophila* and honey bee were different. In all the other species the majority of the single copy DNA (65%–80%) occurs in lengths of 1000–3000 nucleotide pairs separated by short repeats with a typical length of 300 nucleotide pairs. It is now known that most genes are single-copy DNA sequences and the observed single-copy lengths are those expected for structural genes coding for proteins made up of 300–1000 amino acid residues. The measurements made this year also show that many structural genes have adjacent repeated sequences.

The concept that repeated sequences regulate gene expression through transcription control previously led to the prediction that repeated sequences would be found adjacent to structural genes in the DNA. This prediction has been borne out by the following measurements. Preparations were made of single-copy DNA sequences adjacent to repetitive sequences. This DNA was shown to be a specific sequence class containing about one-third of the total single-copy DNA. Messenger RNA from developing sea urchin embryos was found to

hybridize almost as effectively (80% or more) with this DNA preparation as with whole single-copy DNA. This observation bears out a prediction by Britten and Davidson made from their concepts of genetic regulation and also prepares the ground for an examination of the specificity of the adjacent repetitive sequences in relation to the state of differentiation of the tissues being studied.

LOSSES . . .

I regret that I must report the death of Keith S. McHugh on June 7, 1975. Mr. McHugh was a trustee of the Institution from December 1950 to September 1974, when he resigned for reasons of health. He was named trustee emeritus in May 1975 at the annual meeting of the board. Mr. McHugh was an active participant in the work of the board of trustees, serving on the auditing committee since 1952 and as chairman since 1954; he was chairman of the nominating committee for two separate terms. He was also at various times a member of the finance and executive committees.

His business experience and his record of public service made Mr. McHugh a great asset to the Institution. He was president of the New York Telephone Company from 1949 to 1959. In 1959 he left the telephone company to head the New York State Department of Commerce. During 1959–1966 he initiated a program for attracting commerce and industry to the state, which succeeded in reversing the movement of major companies out of New York.

Mr. McHugh was appointed to 50 commissions, boards, and special committees in New York, including the New York Job Development Authority (chairman), the planning coordination board of the Governor's Office for Regional Development (chairman), the Science and Technology Foundation (director), the Special Cabinet Committee on Civil Rights, the Atomic Energy Coordinating Council, the Air Pollution Control Board, and the Water Resources Commission. In 1967 he became chairman of the executive committee of Action for Transportation, Inc., and in 1968 he headed a post-Vietnam committee to plan social and economic transition after the war.

At the national level, Mr. McHugh was deputy administrator of the National Recovery Administration and a member of the National Security Resources Board. He was awarded Certificates of Appreciation by the Department of Defense for his work on the War Production Board and the Board of War Communications during World War II. He was also a member of the Commission on Revision of Armed Services Pay.

Mr. McHugh was born at Fort Collins, Colorado, on February 25, 1895. He graduated from the University of Wisconsin in 1917 with a B.S. degree in chemical engineering. During World War I, he was a captain in the U.S. Army in France.

I must also report, with regret, the death of trustee emeritus Alfred L. Loomis on August 11, 1975. Mr. Loomis became a trustee of the Institution in December 1934 and was a member of the board until his resignation in April 1973. In May 1973 he was designated trustee emeritus. He was a member of the finance committee from 1934 to 1971, except for the war years, and a member of the auditing committee from 1956 to 1971. He was a valuable adviser to the Institution in scientific as well as fiscal matters.

Successful in three fields—physics, law, and finance—Mr. Loomis was known

primarily for his scientific achievements. He graduated from Yale University in 1909 with a bachelor's degree and a reputation as an inventor with great skill in mathematics and science. He then attended Harvard Law School, graduating *cum laude* in 1912. By 1915 he was a member of the law firm of Winthrop & Stimson in New York. During World War I Mr. Loomis served as a major in the army and helped develop the Aberdeen chronograph, a device that measures projectile velocity. After the war he became a highly successful investment banker and vice president of Bonbright & Company.

In 1928 he established the Loomis Laboratories, which developed, among other things, the electroencephalograph, a device that records electrical impulses transmitted by the brain. He also worked on the electronic centrifuge for which he and Dr. Edmund Newton Harvey of Princeton received the Wetherill Medal of the Franklin Institute in 1935. In 1930 he established the Loomis Institute for Scientific Research, and in 1933 retired completely from business to pursue his scientific interests.

During World War II, Mr. Loomis headed the radar research division of the Office of Scientific Research and Development under the direction of Carnegie president Vannevar Bush. Mr. Loomis was a pioneer in the development of loran, the electronic navigational aid. For his war work he received the Medal of Merit from the United States government and His Majesty's Medal for Service in the Cause of Freedom from the government of Great Britain.

Mr. Loomis was born in New York, New York, on November 4, 1887. He was a founder and trustee of the RAND Corporation, an adviser of the Lawrence Radiation Laboratories, and a life member emeritus of the Corporation, Massachusetts Institute of Technology.

This year three members of the board of trustees have resigned, and the Institution feels their loss. They are Charles P. Taft, Eric Ashby, and Patrick E. Haggerty.

The loss of The Honorable Charles P. Taft is a great one, but it is reassuring that he will continue his long association with the Institution as a trustee emeritus and that we will still benefit from his guidance and friendship. Mr. Taft was a trustee of the Institution from December 1936 to April 1975—one of the longest terms ever served by a trustee. That alone makes his trusteeship remarkable, but more than that, we will remember and value his faithful service on many committees over the years, giving the Institution the benefit of his wisdom and experience.

The Institution will also miss The Rt. Hon. Lord Ashby of Brandon, a trustee since May 1967, who resigned in June 1974. Although distance and his duties as Master of Clare College and Vice-Chancellor of The University of Cambridge prevented Lord Ashby from taking an active part in the committee work of the board of trustees, he has been and will continue to be a good friend of the Institution and an important link with the British scientific and educational communities.

Patrick E. Haggerty, chairman of Texas Instruments Incorporated, elected in May 1974, was a valuable addition to our board of trustees. I am sorry that he found it necessary to resign from the board in June 1975 because of the many contributions he could have made to the work of the board and of the Institution.

. . . AND GAINS

The most notable of the gains this year is the election of three new trustees at the annual meeting of the board in May 1975. They are John T. Connor, John Diebold, and William C. Greenough.

John T. Conner is chief executive officer and chairman of the board of Allied Chemical Corporation. He was Secretary of Commerce under President Lyndon Johnson from 1965 to 1967, when he joined Allied Chemical. During World War II he was general counsel to the Office of Scientific Research and Development, and after the war was counsel to the Office of Naval Research and special assistant to the Secretary of the Navy for two years. He was awarded the Presidential Certificate of Merit for his service in 1948. He joined Merck and Co. in 1947 as general attorney and was president and director from 1955 until his appointment as Secretary of Commerce.

Mr. Connor graduated *magna cum laude* from Syracuse University in 1936 and earned a J.D. degree from Harvard Law School in 1939.

John Diebold is chairman of the board of the Diebold Group, Inc., a management consulting firm, and of John Diebold, Inc., a management and investment firm; he founded both companies. He is a member of the Council on Foreign Relations, the Hudson Institute, and the National Planning Association. In 1963 he was appointed to the U.S. delegation to the United Nations science conference in Geneva. He is a member of two National Science Foundation groups: the advisory committee on ethical and human values of science and technology and the industrial panel on science and technology.

Mr. Diebold received a B.S. degree from the U.S. Merchant Marine Academy in 1946; a B.A. in economics, with high honors, from Swarthmore College in 1949; and an M.B.A., with distinction, from Harvard University in 1959.

William C. Greenough joined the Teachers Insurance and Annuity Association (TIAA) in 1941, became its president in 1957, chairman and president in 1963, and chairman and chief executive officer in 1967. He has held the same executive positions in the College Retirement Equities Fund (CREF) since it was formed as an adjunct to TIAA in 1952. He is a member of The Rockefeller University Council and a director of the New York Stock Exchange, the Dry Dock Savings Bank, and the Turner Construction Company.

Dr. Greenough received the A.B. degree from Indiana University in 1935, and the University presented him with the Distinguished Service Award in 1960 and an LL.D. degree in 1965. He earned the M.A. and Ph.D. degrees from Harvard University in 1938 and 1949. In 1951 he received the Elizur Wright Award for his study *A New Approach to Retirement Income*.

The following honors have been awarded to Staff Members during the past year.

James D. Ebert, Director of the Department of Embryology, was elected to the Institute of Medicine of the National Academy of Sciences. He was awarded an honorary D.Sc. degree by Indiana University. Dr. Ebert was also Regent's Lecturer at the University of California in the spring of 1975.

Winslow R. Briggs, Director of the Department of Plant Biology, was elected to the American Academy of Arts and Sciences.

Allan R. Sandage of the Hale Observatories received an honorary D.Sc. degree

from Miami University, Oxford, Ohio. Dr. Sandage was awarded the Catherine Wolfe Bruce Gold Medal by the Astronomical Society of the Pacific.

Donald D. Brown of the Department of Embryology delivered the Jessup Lectures at Columbia University.

C. Stacy French, Director Emeritus of the Department of Plant Biology, received an honorary doctoral degree from the University of Göteborg, Sweden.

Henrietta H. Swope is a former Staff Member of the Hale Observatories who retired in 1968 but remains engaged in post-retirement studies. This year she was honored by Barnard College, which presented her with the Distinguished Alumnae Award, and by the University of Basel (Switzerland), which awarded her an honorary doctoral degree.

J. Eric Thompson,* Staff Member in archaeology with the Division of Historical Research from 1935 to 1959, was named Knight of the British Empire in the New Year's Honours Lists. Sir Eric also received the Order of the Quetzal from the Republic of Guatemala.

* Died September 9, 1975.

FACULTY, FELLOWS, AND STUDENTS

1974-1975

DEPARTMENT OF EMBRYOLOGY
Baltimore, Maryland*Director*

James D. Ebert

Staff Members

Donald D. Brown
Igor B. Dawid
Douglas M. Fambrough
Kenneth J. Muller
Richard E. Pagano
Ronald H. Reeder
Yoshiaki Suzuki

Fellows

Ronald D. Brown
Dana Carroll
Scott Emmons
Toru Higashinakagawa
Leaf Huang
John F. Morrow
Seigo Ohi
Tokindo Okada
Keiko Ozato
Aileen K. Ritchie
Masatoshi Takeichi
Katherine Tepperman
William B. Upholt
Peter K. Wellauer

Assistant Investigator

Peter J. Stambrook

Students

Sandra L. Biroc
Peter Devreotes
Marc Friedman
Carol Kaushagen
Jose Ramirez
Changlin A. Wey

GEOPHYSICAL LABORATORY
Washington, D.C.*Director*

Hatten S. Yoder, Jr.

*Carnegie Institution
Distinguished Professor*

Elburt F. Osborn

Emeritus Research Associate

Emanuel G. Zies

Staff Members

Peter M. Bell
Francis R. Boyd, Jr.
Felix Chayes
John R. Cronin
Gordon L. Davis
David H. Eggler
Larry W. Finger
John D. Frantz
P. Edgar Hare
Thomas C. Hoering
T. Neil Irvine
Thomas E. Krogh
Ikuo Kushiro
Ho-Kwang Mao
Douglas Rumble III
David Virgo

Fellows

Jagannadham Akella
Richard J. Arculus
John I. Hedges
Floyd N. Hodges
Frank E. Huggins
Bruce R. Lipin
Robert H. McCallister
Gifford H. Miller
Karlis Muehlenbachs
Bjørn O. Mysen
Yasuo Nakamura
Howard R. Naslund
Yoshikazu Ohashi
Martin G. Seitz
Rosemary J. Vidale
E. Bruce Watson

Students

Dora Lee
Noreen Tuross

HALE OBSERVATORIES

Pasadena, California

Director

Horace W. Babcock

Associate Director

J. Beverley Oke

Staff Members

Halton C. Arp
 Edwin W. Dennison
 Jesse L. Greenstein
 James E. Gunn
 Robert F. Howard
 Jerome Kristian
 Robert B. Leighton
 Guido Münch
 Gerry Neugebauer
 George W. Preston
 Bruce H. Rule
 Allan R. Sandage
 Wallace L. W. Sargent
 Maarten Schmidt
 Leonard T. Searle
 Stephen A. Sackett
 Arthur H. Vaughan, Jr.
 James A. Westphal
 Harold Zirin

Staff Associates

Eric E. Becklin
 Robert J. Brucato
 Michael W. Werner

Fellows

Ermanno F. Borra
 Michael H. Hart
 Francois Schweizer
 Pieter van der Kruit
 Christopher P. Wilson
 Hirokazu Yoshimura
 Robert J. Zinn

Carnegie-Chilean Fellows

Eduardo Hardy
 Maria Teresa Ruiz

Student Observers

Jill Bechtold
 Steven V. W. Beckwith

Frances Cordova
 Jonathan H. Elias
 Richard F. Green
 Paul Hickson
 John G. Hoessel
 John P. Huchra
 John Kormendy
 Philip Massey
 Jorge Melnick
 William C. Friedhorsky
 Douglas M. Rabin
 Anneila I. Sargent
 William L. Sebok
 Edwin L. Turner
 Barry E. Turnrose
 William E. Westbrook
 Theodore B. Williams
 Steven P. Willner

DEPARTMENT OF PLANT BIOLOGY

Stanford, California

Director

Winslow R. Briggs

Staff Members

Joseph A. Berry
 Olle Björkman
 Jeanette S. Brown
 David C. Fork
 Malcolm A. Nobs
 William F. Thompson

Emeritus

C. Stacy French, Director
 William M. Hiesey, Staff Member

Fellows

Steven J. Britz
 William G. Hagar
 Tetsuo Hiyama
 John M. Mackenzie
 Bruce E. Mahall
 Norio Murata
 Charles Rogler
 Heather G. Strong
 John H. Troughton

Students

Daniel J. Cosgrove
 James Ehleringer

DEPARTMENT OF
TERRESTRIAL MAGNETISM
Washington, D.C.

Director

George W. Wetherill

Associate Director

L. Thomas Aldrich

Distinguished Service Member

Merle A. Tuve

Emeritus

Scott E. Forbush

Staff Members

George E. Assousa

Manuel N. Bass

Ellis T. Bolton

Louis Brown

Dean B. Cowie

W. Kent Ford, Jr.

Stanley R. Hart

Albrecht W. Hofmann

Bill H. Hoyer

David E. James

Alan T. Linde

Nancy R. Rice

Richard B. Roberts

Vera C. Rubin

I. Selwyn Sacks

Norbert Thonnard

Kenneth C. Turner

Fellows

John Bannister

Charles L. Bennett

Arturo Cuyubamba

Michael B. Davis

Charles Doering

Antonio Flores

George H. Pepper

Charles J. Peterson

J. Arthur Snoke

John W. Warner III

William M. White

Student

David Westpfahl, Jr.



Reports of Departments and Special Studies

Department of Embryology

Department of Terrestrial Magnetism

Hale Observatories

Geophysical Laboratory

Developmental Biology Research Group

Department of Plant Biology

Department of Embryology

Baltimore, Maryland

James D. Ebert

Director

Carnegie Institution of Washington Year Book 74, 1974-1975

Contents

Introduction	7
Developmental Genetics by Gene Isolation: The Dual 5S DNA System	12
Purification and characterization of new 5S DNAs from <i>Xenopus laevis</i> and <i>Xenopus mulleri</i>	13
Nucleotide sequences adjacent to the 5S RNA genes	13
The arrangement of length heterogeneity in 5S DNA of <i>Xenopus laevis</i>	14
Transcription of 5S DNA	19
<i>Xenopus laevis</i> - <i>Xenopus mulleri</i> hybrid animals	19
The Molecular Basis, Arrangement, and Inheritance of Length Heterogeneity in <i>Xenopus laevis</i> Ribosomal DNA	19
The organization of sequences within the spacer of <i>Xenopus laevis</i> ribosomal DNA	20
The arrangement of length heterogeneity in amplified and chromosomal rDNA	22
The inheritance of rDNA spacer length heterogeneity	25
Conclusion	26
Chromosomal Proteins and the Control of Gene Function	26
The association of ribosomal genes with histones in cultured cells	27
Analysis of the proteins of isolated ribosomal gene chromatin	28
Iodination of <i>Xenopus</i> histone F _{2a1} in chromatin	33
The Regulation of Fibroin Genes	36
Morphological observations of silk gland nuclei during development	36
Preparation of assay probes for detecting fibroin mRNA synthesized in vitro	38
Fibroin mRNA synthesis in a pulse-labeled silk gland	39
Fibroin mRNA synthesis in isolated silk gland nuclei	41
Localization of Fibroin Genes in Silk Gland Cells of <i>Bombyx mori</i>	42
Attempts to Isolate the Fibroin Gene of <i>Bombyx mori</i>	45
Biogenesis of Mitochondria	46
Mapping studies on mitochondrial DNA of <i>Xenopus laevis</i> and <i>Xenopus mulleri</i> ..	46
Physical mapping of 4S RNA genes on mitochondrial DNA	47
A comparative study of the mitochondrial genomes of the sheep and the goat	48
Mitochondrial DNA and RNA in <i>Drosophila</i>	49
Phospholipid-Cholesterol Dynamics in Mammalian Cells	53
Interactions of phospholipid vesicles with mammalian cells	54
Studies of mechanism	54
A proposed mechanism for vesicle-cell interactions	59
Interaction of phospholipid vesicles with mouse lymphocytes in vitro	60
Spatial distribution of cell surface lipids	64
Intercellular exchange of lipids	65
Lipid perturbations and lymphocyte activation	66
Studies on Skeletal Muscle Plasma Membranes	67
Characterization of receptor pools	68
Turnover of receptors in denervated adult muscle	74
Iodination of membrane proteins of muscle cells	78

An investigation of the involvement of denervation in the human skeletal muscle diseases amyotrophic lateral sclerosis and congenital myotonic dystrophy	81
Signaling in the Nervous System: Synaptic Morphology of Specific Neurons in the Leech	85
Mouse Lymphocytes as Tools for the Study of Mitogenic Events and Regulatory Processes Associated with the Cell Membrane	88
Regulation of transplantation immunity by T lymphocytes	88
Modification of the lymphocyte surface by ConA	90
The study of ConA binding sites on murine thymic lymphocytes	93
Enhancement of surface permeability of thymocytes by ConA	94
The Collection of Human Embryos	97
Developmental stages in human embryos	97
Development of the nervous system	98
Staff Activities	98
Bibliography	101
Personnel	103

INTRODUCTION

On an earlier occasion I wrote, in part, "In recent years it has become increasingly fashionable for directors of laboratories to stress that their organizations are 'where the action is,' with increasing emphasis on the interactions of society and technology underlying our social concerns." This posture is fully consonant not only with currently increasing emphasis on contract-supported, directed research and the decline in grants for unfettered basic investigations, but with today's cry for the dissolution of peer review mechanisms. According to current dogma, self-serving scientists are incapable of assessing the long-term societal consequences of their research. The Department of Embryology has been privileged to play a major role in research that has provided the underpinning for advances in biology and medicine which have had a significant impact in promoting human welfare. I have addressed this question on other occasions. It will suffice to say here that we have not neglected our societal responsibilities. Yet when I hear the expression, "where the action is," I still think not of technology but of basic science, which we need today more than ever before.

At a time when basic science is questioned, *even ridiculed*, how can we ourselves best understand, and best explain to others, the guiding spirit of our work, which as Alfred Hershey once wrote, "... is scarcely evident in a day to day record of it." I believe, with Hershey, that we must repeatedly stress the communal nature of scientific effort. Important gains made in our Department have contributed to advances made by others; all too often, however, we fail to stress the obverse truism, that important conceptual and technical gains made in laboratories other than our own are vital to our own progress. It is in this light that we may best give the lie to the argument that duplication of research

places the entire scientific enterprise in jeopardy. As Hershey put it, "duplication of effort—is a virtually nonexistent bugbear."

This lesson, which must be restated repeatedly, is brought home by a look at Donald Brown's present interests. For several years they were generated almost exclusively by his technical ingenuity, single-mindedness, and tenacity, and by his own belief that it should be possible to isolate and characterize the genes of higher organisms, and attain an eventual understanding of the mechanisms regulating their action. Still further advances are recounted in the pages to follow, but it is now possible to see more clearly how crucial to these new directions have been major findings in other laboratories on two fronts: the use of restriction enzymes for elucidating the molecular fine structure of genes; and of the newer methodology for covalently linking DNAs of different organisms; for example, fragments of DNA from the frog, *Xenopus laevis*, or the silkworm, *Bombyx mori*, may be linked to a bacterial plasmid, enabling the replication of animal DNA sequences in bacteria.

I would be less than honest if I did not say that almost without exception the staff, fellows, and students in the Department have enjoyed a productive year. This "admission," however, makes my next task well-nigh impossible. How does one extract from such an impressive record of accomplishment and happy associations the year's "highlights"? One has to admit further that he is guided in part by his personal taste; but beyond that I have chosen to point up two classes of findings—those in which answers have been provided to specific questions, and those which have increased the number of valid questions.

New insights into gene structure have emerged through the use of restriction enzymes. Unexpected features of the structure of the ribosomal genes have

been discovered recently by a group including postdoctoral Fellow Peter Wellauer and Staff Members Ronald Reeder, Igor Dawid, and Donald Brown, who have been studying the "anatomy" of the DNA which codes for 28S and 18S ribosomal RNA (termed ribosomal DNA or rDNA). In *Xenopus laevis*, about 450 copies of these genes are present on each of two chromosomes in every cell. Earlier studies revealed that these genes can be isolated completely free of the rest of the cell's DNA. Work in the Department and elsewhere has shown that rDNA is composed of multiple repeating units tandemly linked end to end. About two-thirds of each repeating unit is a gene region which serves as the template for the transcription of 28S and 18S ribosomal RNA. The remaining one-third of each repeating unit is not transcribed into RNA, has no known function, and is called the spacer region.

Within a cell, all 900 copies of the transcribed gene region appear to be identical both in length and in nucleotide sequence, suggesting that cells have some mechanism for maintaining these hundreds of copies identical within close tolerances. The recent, unexpected finding is that the spacer regions between the genes come in different lengths. As many as seven different spacer sizes have been found on a single chromosome alternating with gene regions of constant length.

The existence of heterogeneous spacer lengths in rDNA was discovered by the use of a site-specific restriction endonuclease called EcoRI. EcoRI is one of a newly described class of enzymes which recognize specific short nucleotide sequences in the DNA and will cut the DNA *only* at the site of those sequences. In rDNA the EcoRI recognition site occurs just twice in each repeating unit. Cutting the DNA at these two sites produces two fragments per repeating unit—one fragment containing only gene sequences and the other containing all of the spacer plus some gene region on each

end. Electrophoresis of these fragments on agarose gels separates them according to size and reveals that the spacer-containing fragments come in different size classes while the gene fragment is homogeneous in size.

When EcoRI is used to cut rDNA isolated from individual frogs, it is found that the pattern of spacer length can vary from one individual to the next. This has made it possible to use the rDNA spacer pattern as a genetic marker, that is, to select two frogs which have different spacer patterns, mate them, and observe how the spacer patterns are transmitted to the progeny.

Dana Carroll has used a similar approach in further investigating the nature and organization of heterogeneity in the oocyte-type 5S DNA of *Xenopus laevis*. Again, not only is the existence of heterogeneity confirmed, but it is shown to be located in the AT-rich portion of that spacer.

In these examples, at least, length heterogeneity results from the presence of variable amounts of reiterated simple sequences in nontranscribed spacer, with the region of variable length being close, if not adjacent, to the 3' end of the transcription unit.

It is hoped that experiments of this sort will eventually reveal the mechanism whereby a cell can conserve hundreds of apparently identical gene regions while allowing them to be interspersed with heterogeneous, less conserved spacer regions.

Carroll's findings are a part, albeit a key part, of a larger undertaking by Brown and his colleagues, namely the exploration of the dual 5S DNA system of *Xenopus*. The *Xenopus* genome contains at least two kinds of 5S DNA. "Somatic" 5S DNA appears to be made in all cells. "Oocyte" 5S DNA synthesis is "turned off" in somatic cells. Key questions concerning gene regulation are then posed. Donald Brown and E. Jordan describe further progress in isolating 5S DNAs; and in a study related closely to

Carroll's, Ronald Brown has analyzed in detail the spacer sequence adjacent to the 3' end of the 5S DNA transcription unit. It is thought that the end of the gene itself and the first two spacer nucleotides may be at least part of the termination signal for RNA polymerase.

Significant progress is again reported by Douglas Fambrough and his colleagues, especially graduate student Peter Devreotes, postdoctoral Fellow Katherine Tepperman, and Fambrough's collaborator at the Johns Hopkins University School of Medicine, Daniel Drachman.

For several years the group has been focusing on the differentiation of the skeletal muscle plasma membrane and the organization of skeletal muscle fibers. In previous Year Books they have reported not only on the appearance and maturation of several plasma membrane properties related to the specialized functions of skeletal muscle during development but also on some of the changes in plasma membrane properties which characterize denervated adult skeletal muscle and are reminiscent of the properties of embryonic muscle. They have also reported on some characteristics of abnormal muscle, namely in the muscular dysgenic mouse and in humans with the disease myasthenia gravis. Many of their studies have focused upon the acetylcholine receptors of skeletal muscle, since the receptors appear in the plasma membrane as readily detected functional molecules early in muscle development, they are later confined to a small area of cell surface—the postsynaptic surface of the neuromuscular junction—and in denervated skeletal muscle they appear all over the surface of each muscle fiber. Because acetylcholine receptors can be readily identified not only by their function but also through the use of a radioactive probe which binds to them with extreme tenacity (iodinated α -bungarotoxin), they can be studied in ways that are unique. Thus the group continues to understand more each year about the

number and distribution of acetylcholine receptors in the plasma membrane in various physiological states, their rate of synthesis and destruction, and the mechanism by which they are incorporated into the plasma membrane of muscle fibers and later removed and degraded by the fibers.

Fambrough and his co-workers have continued to pursue their studies on the mechanisms of synthesis, incorporation into plasma membrane, and degradation of acetylcholine receptors. Their working hypothesis includes the following elements. Acetylcholine receptors are synthesized by the normal protein synthesizing machinery, this synthesis being sensitive to inhibition by puromycin and by cycloheximide. Newly synthesized receptor components occur as organized macromolecular structures of molecular weight about 250,000 daltons (when solubilized in detergent solution) incorporated into internal cell membranes (of unknown type and location). These precursors are then inserted into the plasma membrane, the population of precursors being enough to support two hours of new receptor incorporation into plasma membrane without any new protein synthesis. Once in the plasma membrane the receptors are functional molecules and are free to interact with the radio-labeled probe, iodinated α -bungarotoxin. Plasma membrane receptors are degraded by a random-hit process which is energy dependent and proteolytic, probably involving internalization of membrane containing receptors and then degradation by lysosomal enzymes. During the past year the group has developed techniques which will allow direct testing of several aspects of this model of the life history of receptor molecules. They have also devised a method for continuous monitoring of receptor degradation in organ-cultured skeletal muscle and have begun extending their findings to adult mouse muscle.

Drachman and Fambrough have also investigated another human disease, con-

genital myotonic dystrophy, in which the muscle pathology suggested the possible participation of denervation. Since the appearance of extrajunctional acetylcholine receptors is a sensitive marker for denervated skeletal muscle surface, they have used the radio-labeled probe for acetylcholine receptors on biopsy specimens from patients with congenital myotonic dystrophy. They have also examined biopsy material from two patients with the denervating disease amyotrophic lateral sclerosis.

During 1974–1975 Richard Pagano was joined by two postdoctoral Fellows, Leaf Huang and Masatoshi Takeichi. Together with Ebert's colleague, Keiko Ozato, they have vigorously extended their explorations of phospholipid-cholesterol dynamics in mammalian cells. Their objective is to understand the dynamic movements which cellular phospholipids and cholesterol can undergo in cell membranes, and the effects which perturbations in these motions can have on cellular activity. Among their studies described in the body of the Report, two are especially noteworthy. They have combined their earlier knowledge of interactions of cell membranes and lipid vesicles with the technique of high resolution electron microscope autoradiography to determine the surface distribution of one lipid component, phosphatidylcholine, on Chinese hamster fibroblasts. Second, in cooperation with Ozato and Ebert, they have begun to examine the effects of cell surface lipid perturbations on lymphocyte activation.

Ozato and Ebert, with the collaboration of William Adler of the Gerontology Research Center, National Institutes of Health, have continued to focus on mouse lymphocytes in their studies of mitogenic events regulated by processes associated with the cell membrane.

Two significant discoveries have emerged. First, the regulation by two mitogens, Concanavalin A (ConA) and bacterial lipopolysaccharide (LPS), of the mixed lymphocyte reaction (MLR)

and the generation of cytotoxic lymphocytes was studied in congenic-resistant mice using cortisone-resistant thymocytes (CRT) as responding cells. LPS enhanced the generation of cytotoxic lymphocytes selectively when suboptimal concentrations of alloantigens were given followed by a selective augmentation in the MLR. Mitogenic concentrations of ConA, on the other hand, suppressed the generation of cytotoxicity regardless of antigen dose. The mechanism of suppression could not be ascribed to suppressor T cells, since the addition to the culture of syngeneic CRT activated by ConA did not change the immune response. Prospective suppressor cells that can be activated by ConA were found to be located in lymphoid organs other than thymus, because suppression occurred in CRT mixed lymphocyte cultures by ConA-activated spleen cells or ConA-activated lymph node cells. These cells also suppressed MLR. Suppressor activity was resistant to mitomycin C treatment and sensitive to anti- θ antibody plus complement. ConA-activated thymocytes, on the contrary, amplified the proliferation of the responding cells.

In an attempt to modulate the recognition processes that occur on lymphocyte membranes in mixed lymphocyte cultures, responding cortisone-resistant thymocytes or stimulating spleen cells (treated with mitomycin C) were pretreated with native ConA (N-ConA) or succinyl ConA (S-ConA). Highly significant cell proliferation was observed in *syngeneic* combinations when either the responding cells or the stimulating cells were treated with ConA, although ConA alone was never mitogenic. In *allogeneic* combinations the proliferative response on day 3 was five to seven times higher than in the normal MLR by the ConA pretreatment of either partner. The triggering of proliferation was dependent on two factors: (1) The presence of spleen cells as the stimulating cells (thymocytes were much less effective).

(2) The presence of ConA molecules (the effect was blocked by the specific inhibitor of ConA, α Mannopyranoside) on either one of the partners. The optimal concentration of S-ConA was about twice that of N-ConA. Even more striking was the observation that cultures in which either one of the partners was pretreated with ConA in allogeneic combinations showed a strong suppression (60% to 80% inhibition) in the subsequent generation of the cytotoxic lymphocytes (CL). The ConA concentration required to trigger proliferation corresponded to that for suppressing the generation of CL. ConA pretreatment did not exhibit cytotoxic activity toward syngeneic tumor cells.

It is a special pleasure to report the arrival, as this report is being written, of Staff Member Kenneth J. Muller. Muller, trained in neurobiology at Massachusetts Institute of Technology and Harvard Medical School, comes prepared to devote himself, for the foreseeable future, to the study of synaptic transmission and integration in the central nervous system, using, at least at the outset, the leech *Hirudo medicinalis* as his experimental object. His brief statement, "Signaling in the nervous system: Synaptic morphology of specific neurons in the leech," based on work performed jointly with U. J. McMahan of Harvard Medical School, will serve to introduce him and his subject.

Mention has already been made of the contributions of several Fellows: Peter Wellauer, having completed his third year in the Department (in 1974–1975 under the auspices of the National Cystic Fibrosis Research Foundation), will spend most of 1975–1976 at California Institute of Technology before returning to his native Switzerland; late in the spring of 1975, Dana Carroll moved to the Department of Microbiology at the University of Utah School of Medicine; Ronald Brown will join the University of Cincinnati. Fellows Katherine Tepperman, Leaf Huang, Masa-

toshi Takeichi, and Keiko Ozato will continue their associations with the Department in 1975–1976, the first two as Fellows of the U.S. Public Health Service; Takeichi, as a Carnegie Fellow; and Ozato, supported jointly by Carnegie and the Marine Biological Laboratory.

In addition to Ronald Brown and Dana Carroll, two other postdoctoral Fellows have been associated with Donald Brown: John Morrow and Scott Emmons, both Fellows of the National Cystic Fibrosis Research Foundation. Morrow, who has already taken up new responsibilities at Harvard Medical School, reports some progress in his attempts to isolate the fibroin gene of *Bombyx mori*. Emmons is trying to develop an assay system which can be used to examine the transcription products synthesized using pure 5S DNA as a template in vitro.

In addition to Wellauer, postdoctoral Fellows in Dawid's program include Seigo Ohi and William Upholt. Upholt has centered his attention on comparing the mitochondrial genome of the sheep and goat. He is leaving (August 31, 1975) to join the research staff of the University of Chicago. Ohi, whose appointment is also drawing to a close, has continued to pursue an important technical objective, the covalent attachment of ferritin to 4S RNA for the visualization of 4S RNA/DNA complexes in the electron microscope.

Also completing a two-year stay is Toru Higashinakagawa, a joint Carnegie-Mitsubishi Fellow. He will return to his post at the Mitsubishi-Kasei Institute of Life Sciences in Tokyo.

Aileen Ritchie has continued her studies with Douglas Fambrough as a Fellow of the Muscular Dystrophy Associations of America, Inc.

In the summer and fall of 1974 and again in the spring of 1975 the Department was privileged to have the company (all too briefly) as a Senior Carnegie Fellow of Professor Tokindo Okada of

Kyoto University, with whose laboratory the Department has long enjoyed a highly productive association.

Extramural collaborators continue to play an important role in the research of the Department. This year the group included W. H. Adler, Daniel Drachman, and U. J. McMahan, already mentioned; A. Forsheit and N. Davidson of the California Institute of Technology; George Brownlee of the MRC Unit of Molecular Biology, Cambridge; and Hayden Coon of the National Cancer Institute.

Graduate students continued to be an integral part of the Department's life. Those whose contributions are presented specifically in the Report are Carol

Kaushagen, J. L. Ramirez (both with Dawid), Sandra Biroc (with Reeder), and, as cited above, Peter Devreotes. Ms. Biroc has accepted a postdoctoral appointment at the University of California, Davis.

Mentioning Davis, California, takes us naturally to the Carnegie Embryological Collection, which was moved there in July 1973. The Collection is now housed, as Ronan O'Rahilly and Ernest Gardner put it, in "Carnegie Village," in a delightful setting halfway between the School of Medicine and the California Primate Research Center. Work is already well under way, but a "formal" opening is being planned for November 1975.

DEVELOPMENTAL GENETICS BY GENE ISOLATION: THE DUAL 5S DNA SYSTEM

D. D. Brown, R. D. Brown, D. Carroll, S. Emmons, and E. Jordan

Much of our attention is now focused on the dual 5S DNA system of *Xenopus*. Our long-term goals are to purify the two kinds of 5S DNA from the genomes of *X. laevis* and *X. mulleri* (and perhaps other species of *Xenopus* as well), to sequence regions in their spacer DNAs which may have regulatory functions, and to reconstruct their transcriptional controls in vitro.

Xenopus synthesizes at least two kinds of 5S ribosomal RNA. Somatic cells produce one type, termed *somatic* 5S RNA. The predominant 5S RNA synthesized by *oocytes* differs from the somatic 5S RNA by six nucleotides. However, some somatic 5S RNA as well as small amounts of other 5S RNAs are synthesized in *oocytes*. Thus a control mechanism exists which appears to shut off *oocyte* 5S RNA genes in somatic cells. In previous Reports we have described the isolation of 5S DNAs (the DNAs coding for the 5S RNAs) from *X. laevis* and *X. mulleri*. These DNAs have been sequenced in

part. The *X. laevis* 5S DNA contains only *oocyte*-type genes; the purified *X. mulleri* 5S DNA has been identified as *oocyte*-type 5S DNA as well.

We describe progress toward our goal of isolating other 5S DNA components from the *Xenopus* genome. Dana Carroll has demonstrated that 5S DNA "repeats" of different lengths can be adjacent in the genome, a finding similar to that described for rDNA in another section of this Report (P. K. Wellauer *et al.*, this Report). Ronald Brown has analyzed the spacer sequence adjacent to the 3' end of the 5S DNA transcription unit. The AT-rich spacer begins immediately at the 3' end of the gene. The end of the gene itself and the first two spacer nucleotides are proposed to be at least part of the termination signal for RNA polymerase. Scott Emmons has begun to develop an assay system which can be used to examine the transcription products synthesized using pure 5S DNA as a template.

PURIFICATION AND CHARACTERIZATION OF
NEW 5S DNA FROM *Xenopus laevis* AND
Xenopus mulleri

D. D. Brown, E. Jordan, R. D. Brown,
and D. Carroll

The purified 5S DNAs we have been studying for several years code for oocyte-type 5S RNA. We have predicted that somatic 5S RNA will be transcribed from a completely different DNA component. These genes should be present in multiple copies and band as satellite DNA. We have detected and purified a new DNA component containing 5S RNA genes from the genome of each of the two *Xenopus* species we have been using. The new 5S DNAs contain about 10% as many 5S RNA genes per cell as do the oocyte 5S DNAs. The new *X. laevis* 5S DNA has been purified and characterized in some detail; the new *X. mulleri* 5S DNA is still only about 60% pure and has not been characterized.

The new *X. laevis* 5S DNA is purified by four density gradient steps. It has been characterized by thermal denaturation, analytical ultracentrifugation, denaturation mapping, and restriction enzyme digestion. Table 1 compares characteristics of the new 5S DNA component with those of oocyte-type 5S DNA from *X. laevis*.

The spacer regions of the two 5S DNAs have little if any homology by hybridization criteria. Moreover, studies

of the new 5S DNA demonstrate that the gene sequence is not oocyte-type. Although it contains some sequences predicted for the somatic-type 5S RNA, the new 5S DNA has some different sequences as well. Our tentative conclusion is that we have isolated a 5S DNA component containing a gene which codes for a 5S RNA different from both the oocyte-type and the somatic-type 5S RNAs.

A new 5S DNA from *X. mulleri* has been partly purified. It is a trace component of the genome, containing only a small fraction of the number of 5S RNA genes compared to the oocyte-type 5S DNA. Sequence studies have not yet been carried out.

NUCLEOTIDE SEQUENCES ADJACENT TO
THE 5S RNA GENES

R. D. Brown

The sequences adjoining the 3' end of the genes coding for oocyte-type 5S RNA from *X. laevis* and *X. mulleri* have been compared. 5S RNA was hybridized to the coding strand of the 5S DNA. This hybrid was used as a template for *E. coli* DNA polymerase I, utilizing two important properties of this enzyme. First, the enzyme requires a primer for nucleic acid synthesis. It will initiate synthesis on the hybrid only by adding nucleotides to the 3' terminus of the 5S RNA. Second, in the presence of Mn^{++}

TABLE 1. Characteristics of the Newly Isolated 5S DNA from *X. laevis*
Compared to Oocyte 5S DNA

	Oocyte-5S DNA	New 5S DNA
Buoyant density in CsCl	1.692	1.701
Strand separation in alkaline CsCl	yes	no
Repeat length (base pairs)	620-810	350
Approximate number of repeats/haploid DNA	~24,000	~2,000
% 5S DNA of total DNA	~0.7	~0.03
Restriction Enzyme Sensitivity (cleavages/repeat)		
EcoRI	resistant	resistant
Hind III	one	resistant
Hae III	three	four
Type of gene	oocyte-5S RNA	unknown 5S RNA

individual ribonucleotides may be polymerized into the growing DNA chain along with the other three deoxyribonucleotides. This "ribosubstitution" introduces sites into the DNA which may be cleaved specifically with alkali or RNase.

The first few nucleotides adjacent to each gene were sequenced by the analysis of limited synthesis with only one or two deoxynucleotides present in the reaction mixture. The terminal sequence of *X. laevis* and *X. mulleri* 5S RNA is GCUU_{OH}. Limited synthesis led to the conclusion that the sequences added to this terminus were TTCA on the *X. laevis* 5S DNA and TT(A or C)G on the *X. mulleri* template. At the third nucleotide after the gene, the two spacer sequences diverge and the *X. mulleri* sequence is heterogeneous. We assume that sequences important for the termination of RNA synthesis are likely to be conserved in the two *Xenopus* species. If this is true then the termination signal must end two nucleotides after the gene and is likely to contain at least the two terminal nucleotides of the gene sequence itself: (gene) 5'-TTTT-3'

3'-AAAA-5' (spacer).

The heterogeneity of the *X. mulleri* sequence adjacent to the gene has prevented further sequencing of this region. It has been possible to show, however, that the nucleotide following the first G residue is heterogeneous and may be T, A, or C and possibly also G. The *X. laevis* sequence in this region has been more readily analyzed. Short extension products, ribosubstituted with rGTP and digested with T₁ RNase, contain at least

the 3' proximal sequence, rCrUrUTTCAAArG(T), plus the oligonucleotides TTTTCAAArG(T) and T₃₋₅G(A). These sequences are essentially identical to portions of those determined by Brownlee and Brown (*Year Book* 73, p. 12) to be the AT-rich portion of the 5S DNA spacer region. In Fig. 1, they are aligned with one of the most common sequences that derive from this portion of the spacer. We conclude that the AT-rich region of the *X. laevis* spacer is immediately adjacent to the 3' end of the gene (see also Fig. 3).

THE ARRANGEMENT OF LENGTH HETEROGENEITY IN 5S DNA OF *Xenopus laevis*

D. Carroll

We have been investigating the nature and organization of heterogeneity in the oocyte-type 5S DNA of *X. laevis*. Last year, we reported the existence of repeat length heterogeneity, which was discovered by analysis of Hind III restriction enzyme digests of 5S DNA. We have confirmed the existence of this heterogeneity and its location in the AT-rich portion of the spacer by examining digestion products of the 5S DNA produced by another enzyme, Hae III. This enzyme cleaves DNA at the sequence 5'-GGCC-3'. There are two of these sequences within the 5S RNA gene, between positions 8 and 9 and positions 66 and 67. When the actual digest is analyzed by gel electrophoresis (Fig. 2), four fragments are observed, so the enzyme also

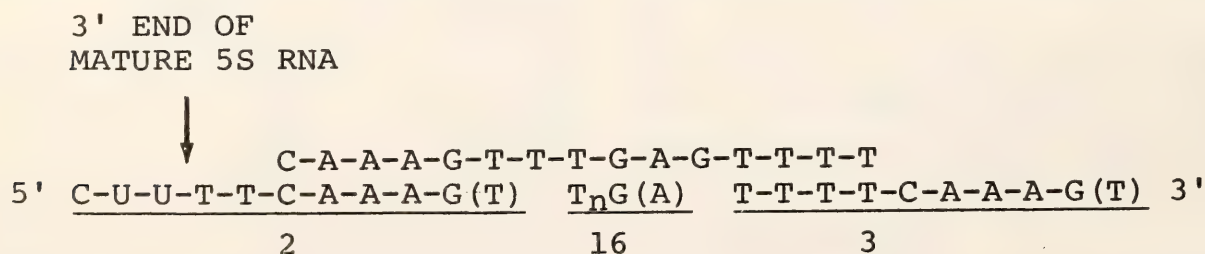


Fig. 1. Spacer sequences adjacent to the 3' end of the 5S rRNA gene in *X. laevis*. Three oligonucleotides adjacent to the gene are aligned with one of the most abundant spacer sequences found previously within the A-T rich spacer region (see *Year Book* 73). The previous sequencing was done on the strand opposite to the one drawn here.

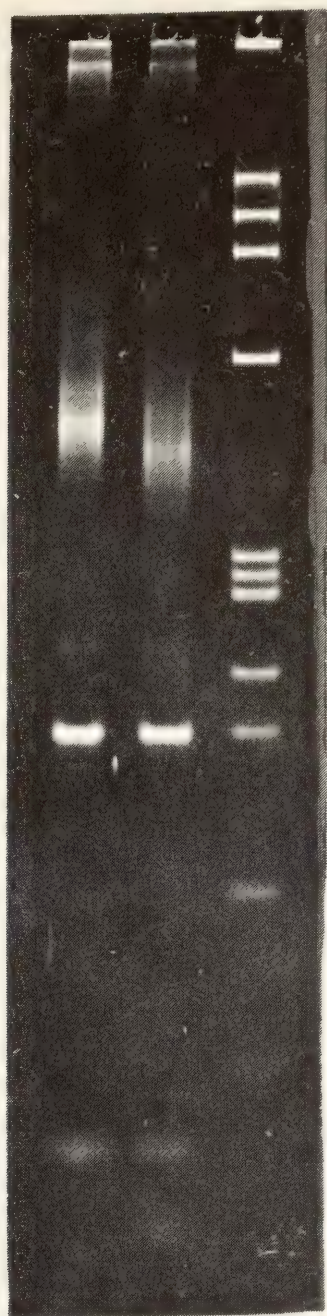


Fig. 2. Electrophoresis in a 6% polyacrylamide gel of *X. laevis* 5S DNA digested with Hae III (left) and Hae III + Hind III (center). A sample of bacteriophage ϕ X174 RF DNA digested with Hae III is included (right) for molecular weight standards. Electrophoresis is from top to bottom.

makes two cuts in the spacer. The smallest fragment is 58 base pairs long, the presumed intragenic piece. A homogeneous fragment of 180 base pairs and a heterogeneous collection of DNA molecules averaging approximately 450 base pairs are generated. These heterogeneous fragments separate on gels into distinct sub-bands with the same mass distribution and average sub-band separation (14 base pairs) observed for the repeat-length fragments generated by Hind III.

Co-digestion of 5S DNA with Hae III and Hind III (Fig. 2) yields the 58 and 180 base-pair fragments unchanged. The ~ 450 base-pair collection of heterogeneous length molecules are shortened to ~ 400 base pairs, and a new homogeneous fragment of 45 base pairs appears.

Our current model of *X. laevis* 5S DNA (Fig. 3) comes from the restriction enzyme data and nucleotide sequencing (see the preceding report by R. D. Brown). The length heterogeneity resides entirely within the AT-rich spacer; repeat units appear to differ from each other by the number of internal (15-mer) repeats they contain. The arrangement of this heterogeneity will help to distinguish between sudden and gradual mechanisms of tandem gene evolution (P. K. Wellauer *et al.*, this Report).

We have investigated the possibility that some of the heterogeneity might be due to differences between animals, as observed in the case of the ribosomal DNAs. 5S DNA was isolated from four frogs, and Hind III digests of each were analyzed by gel electrophoresis. The 5S

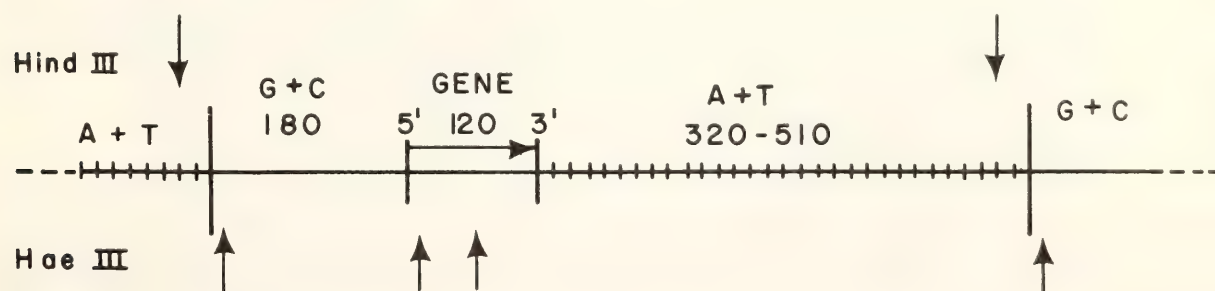


Fig. 3. A model of the repeating unit of *X. laevis* 5S DNA, indicating the location of the cutting sites for Hind III and Hae III.

DNA purified from individual animals was as heterogeneous in repeat lengths as the pooled 5S DNA.

To analyze the heterogeneity of 5S DNA repeat lengths along single molecules, we joined fragments of 5S DNA with a bacterial plasmid DNA. We discovered first that the tetracycline-resistant plasmid, PSC101, has a single Hind III site, very close to its EcoRI site, which had been used for the insertion of foreign DNA. We then demonstrated that stable insertions could be made at the Hind III site without affecting the viability of the plasmid. Fragments from a complete Hind III digest of 5S DNA were joined to Hind III-digested PSC101 DNA with *E. coli* polynucleotide ligase, and the mixture was used to transform tetracycline-sensitive *E. coli*. Individual tetracycline-resistant clones were isolated and hybrid plasmids purified and analyzed. As expected, the single repeat of 5S DNA from each clone was homogeneous and different in length from those derived from other clones (Fig. 4).

We then prepared hybrid plasmids containing several repeat units of 5S DNA. To ensure that all the repeats in a single plasmid were adjacent in the genome, a partial Hind III digest of 5S DNA was prepared and fractionated by gel electrophoresis. The bands containing 4 and 5 repeats were excised from the gel and the DNA eluted. After checking, by electron microscope measurements, that each preparation contained only DNA of the expected size, they were joined to PSC101 and used for transformation. As before, hybrid plasmid DNA was prepared from individual clones. We checked to see that these plasmids had the anticipated structure. The plasmids were cut with EcoRI (5S DNA has no EcoRI site; while the single site in PSC101 is very close to the Hind III insertion point), partially denatured with alkali, and prepared for electron microscopy. Each molecule showed the characteristic 5S repeating structure,



Fig. 4. Electrophoresis in a 2.0% polyacrylamide, 0.5% agarose composite gel of Hind III digests of hybrid plasmids containing single-repeat units of 5S DNA. From left: three individual plasmids, a mixture of the three, and total 5S DNA.

with the appropriate number of bubbles, covalently joined to the plasmid (Fig. 5).

The distribution of repeat length within these plasmids—and therefore within the chromosomal segments—was analyzed by electrophoresis of their Hind III

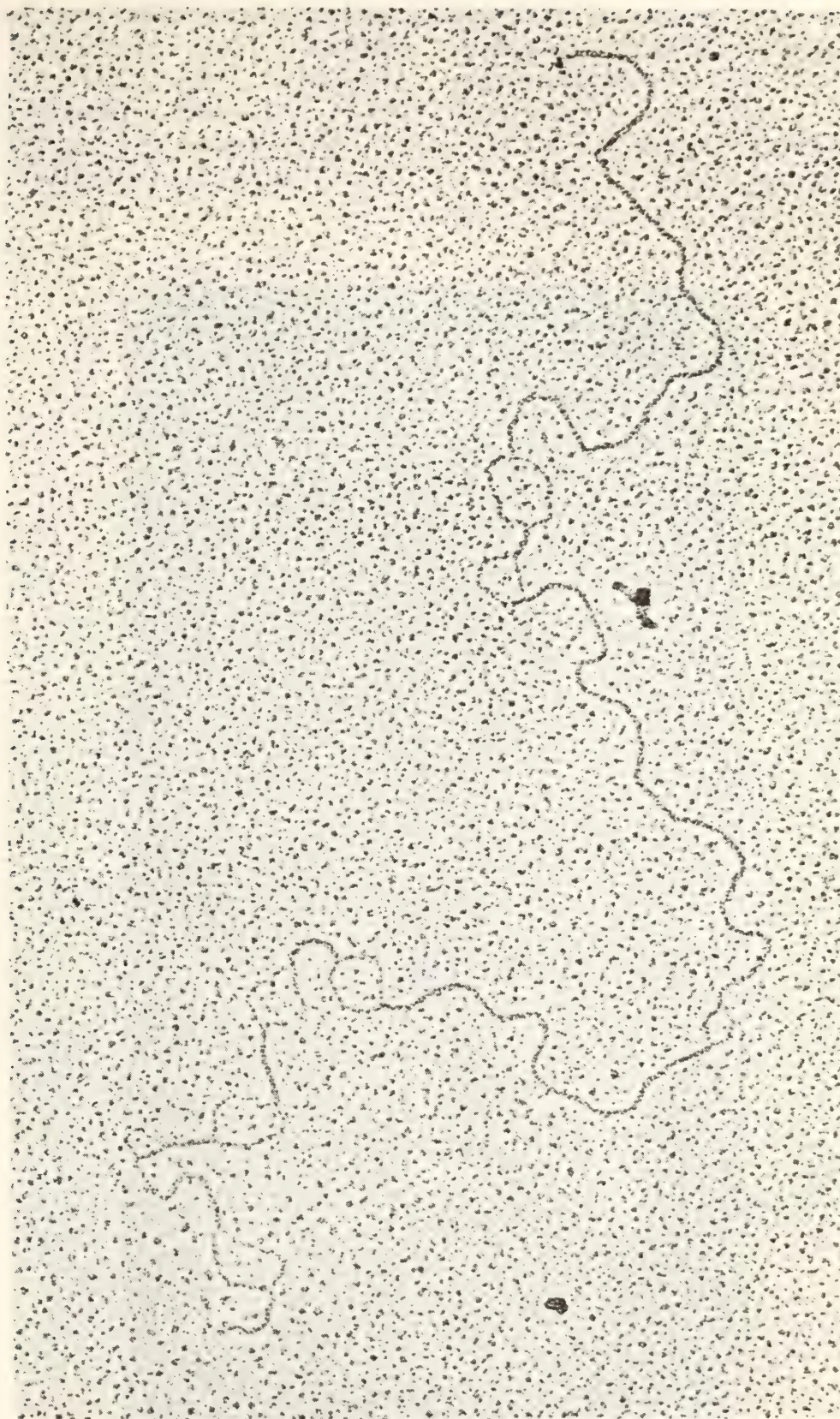


Fig. 5. A partially denatured molecule of a hybrid plasmid DNA in covalent linkage with 5-repeat units of 5S DNA. The circular molecule has been linearized by EcoRI cleavage. The PSC101 portion is at the top, as shown, and contains three denatured regions. The 5S DNA repeats are seen at the bottom.

digests. Each plasmid yielded a characteristic pattern with several different 5S DNA repeat units (Fig. 6). Therefore, adjacent repeat units are not in general identical; and sudden correction mechanisms (such as the hypothetical master-slave mechanism) cannot be operating in this DNA.

A "gradual" mechanism of tandem evolution which has proceeded by unequal crossing-over has several attractive features: (1) It does not require the postulation of any unknown mechanism. (2) It can spread or eliminate variants. (3) The presence of multiple repeats (both full repeats and internal, 15-mer

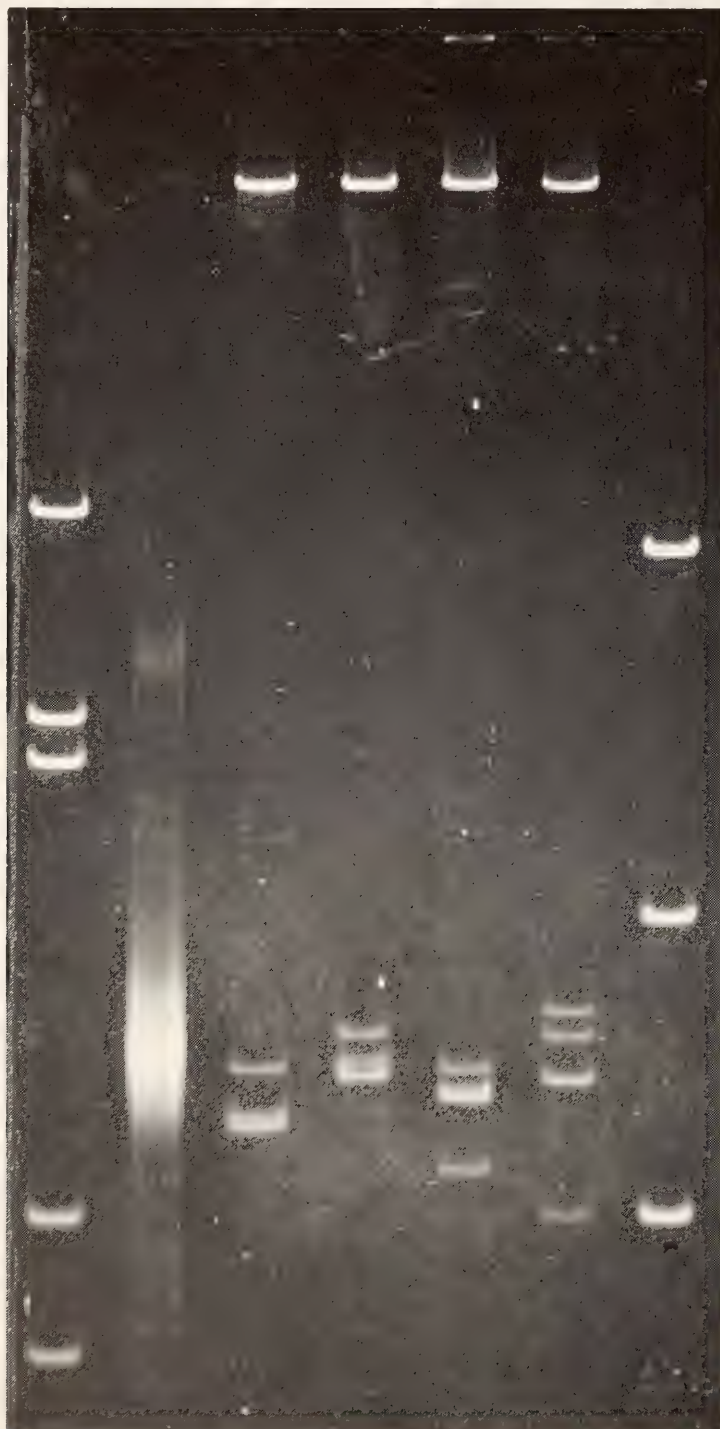


Fig. 6. Electrophoresis (as in Fig. 4) of Hind III digests of hybrid plasmids containing 4 and 5 repeat units of 5S DNA. From left: a Hind III digest of SV40 DNA, total 5S DNA, two different 4-repeat plasmids, two different 5-repeat plasmids, a Hae III digest of SV40 DNA.

repeats) may increase the crossover frequency compared to nonreiterated DNA. (4) Any crossover may be unequal not only with respect to full repeat units but also with respect to internal repeats. In fact, recombination with out-of-phase pairing of the 15-mers would generate exactly the type of repeat length heterogeneity we observe.

TRANSCRIPTION OF 5S DNA

Scott Emmons

To understand the control of gene expression in eukaryotes it will be necessary to reconstruct their transcription in vitro. We are attempting to find out in this way how the 5S genes of *Xenopus* are expressed.

The 5S genes are transcribed in vivo by some form of RNA polymerase III (Weinmann and Roeder, *Proceedings of the National Academy of Sciences*, 71, 1790-1794, 1974), and the properties of this enzyme purified from *Xenopus* have been studied extensively (Sklar, Schwartz, and Roeder, *ibid*, 72, 348-352, 1975). However, when presented with isolated 5S DNA, this enzyme does not make 5S RNA (Roeder, personal communication). The problem therefore is to find a different form of either the enzyme or the template which endows the system in vitro with the specificity existing in vivo. In beginning our search, we are developing an assay for correct initiation of transcription at the beginning of the 5S gene. Our scheme involves the use of restriction enzyme fragments of 5S DNA from *Xenopus mulleri* which carry the first few nucleotides of the 5S

gene. These will be used as hybridization probes of transcripts made from *Xenopus laevis* 5S DNA in vitro. It is hoped that in this way a sensitive and specific assay for authentic transcription in vitro may be developed.

Xenopus laevis-*Xenopus mulleri* HYBRID ANIMALS

D. D. Brown and E. Jordan

In *Year Book 72* (p. 11) and *Year Book 73* (p. 9), we described the use of hybrid animals to "introduce heterogeneity" into the ribosomal DNA locus. When F_1 animals were backcrossed with wild-type *Xenopus* of either species, only a very few wild-type segregants were found. This evidence supported the notion that extensive homologue exchange must have occurred in the F_1 germ cells. These experiments have not been continued for three reasons: (1) An independent method for demonstrating crossing-over between the *laevis* and *mulleri* rDNA could not be devised and nondisjunction could not be ruled out. (2) Extensive crossing-over between rDNA in the two species might not mimic the normal rate of crossing-over between homologues of one species. (3) New methods for analyzing crossing-over within a single species became available, involving restriction enzyme digestion of purified ribosomal DNA, a technique that gives a kind of "fingerprint" of rDNA in a single nucleolar organizer locus. Results of these experiments are described for *X. laevis* ribosomal DNA elsewhere by P. K. Wellauer *et al.* (this Report).

THE MOLECULAR BASIS, ARRANGEMENT, AND INHERITANCE OF LENGTH HETEROGENEITY IN *Xenopus laevis* RIBOSOMAL DNA

P. K. Wellauer, R. H. Reeder, I. B. Dawid, and D. D. Brown

Tandem ribosomal genes are separated from each other by spacers of unknown function. Most of the sequence of these spacers evolves at a high rate between

species of *Xenopus*, suggesting that the function of spacers does not rely on a specific nucleotide sequence. Yet the multiple spacers in a tandem array of genes

and spacers resemble each other closely; they have evolved together. In the experiments reported here, we have sought to obtain detailed information about the organization of spacer sequences and to distinguish between two general models which would account for this tandem evolution in the ribosomal DNA of *Xenopus*. *Sudden correction mechanisms* predict that a mutation in one repeat will be spread to adjacent repeats in a single event. Examples of this are the "master-slave" mechanism and the expansion and contraction of multiple repeats. One likely "sudden" mechanism is by "rolling circle" replication in which one repeat is replicated continually, giving rise to many identical tandem repeats. *Gradual mechanisms* such as multiple unequal cross-overs between homologues and/or sister chromatids predict a gradual scrambling of new sequences that arose by mutations, fixing some in the population and eliminating others. We have attempted to distinguish between these two general mechanisms by analyzing the newly discovered length heterogeneity within the multiple repeats of ribosomal DNA. We have asked: (1) What is the molecular basis of this length heterogeneity? (2) How is it arranged within a single nucleolar organizer? and (3) Is the pattern of length heterogeneity inherited "intact" or is it "scrambled" in a single generation? *Sud-*

den correction mechanisms predict tandem homogeneity. Slow mechanisms permit scrambling of heterogeneity between adjacent repeats.

THE ORGANIZATION OF SEQUENCES WITHIN THE SPACER OF *Xenopus laevis* RIBOSOMAL DNA

Each repeating unit of ribosomal DNA (rDNA) consists of a gene region that is transcribed into the 40S ribosomal RNA precursor plus a nontranscribed spacer region (Fig. 7). While all 40S RNA regions in *X. laevis* are identical at the resolution provided by our present technology, the spacers vary in length (*Year Book 73*, p. 35). To study the basis of these length variations we took advantage of the development by Morrow *et al.* (*Proceedings of the National Academy of Sciences*, 71, 1743, 1974) of a method of linking fragments of rDNA to a bacterial plasmid and then cloning and replicating the hybrid plasmid in *E. coli*. The restriction endonuclease EcoRI cuts rDNA at two sites, yielding two fragments of DNA from each repeating unit. The smaller of these is homogeneous and comprises most of the transcribed region. The larger of the two contains all of the nontranscribed spacer. Since the spacer regions are heterogeneous in length, this fragment also varies in size. Four cloned spacer-containing fragments of different lengths were used in this study. Two of

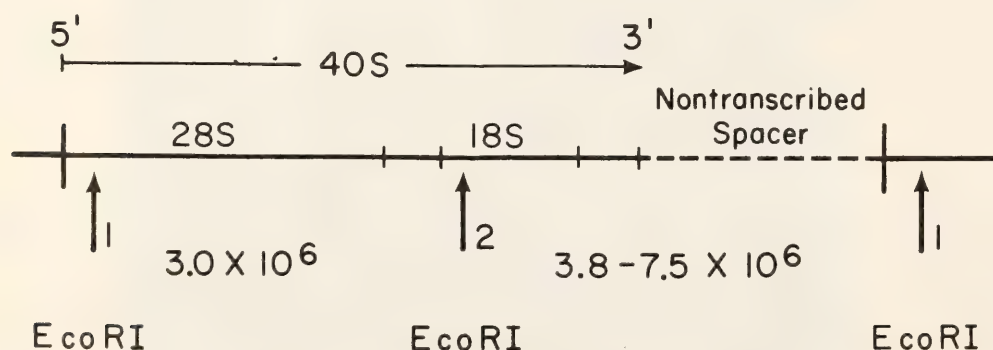


Fig. 7. Model of one repeating unit of *Xenopus laevis* ribosomal DNA. The repeat begins at the 5'-end of the 40S transcription unit. The 40S precursor region contains the 28S and 18S genes plus two transcribed spacers (see *Year Book 73*, 45). The length variability is restricted to the nontranscribed spacer. The restriction endonuclease EcoRI cuts each rDNA repeat at two sites as indicated by the arrows.

these with molecular weights of 3.9 and 4.2×10^6 had been generated by Morrow and his colleagues and two more (molecular weights of 5.4 and 6.6×10^6) were prepared by similar methods.

These cloned homogeneous rDNA fragments were analyzed by homoduplex and heteroduplex mapping in the electron microscope. The main conclusion of this work is that the spacer region is composed to a large extent of internally repetitious units. These subrepeats are limited to two regions of the spacer (designated A and C in Fig. 9). We do not know the size of the subrepeats, but they are probably less than 50 nucleotides.

The evidence for internal repetition within the nontranscribed spacer is based on the following observations. If two cloned rDNA molecules of different lengths had identical, unique sequences except for an extra DNA piece which accounted for their difference, a heteroduplex between the two molecules should always result in a double-stranded region corresponding in length to the shorter strand and a single-stranded loop at a fixed position, the point where additional sequences are present in the longer strand. However, heteroduplexes between rDNA fragments showed multiple loops and the position of these loops varied, as illustrated in Fig. 8. This situation can be explained if the region within which loops occur is tandemly repetitious. Loops with variable positions have been ob-

served by Busse and Baldwin (*Journal of Molecular Biology*, 65, 401, 1972) in heteroduplex molecules involving bacteriophage DNAs with duplications. Measurements of heteroduplexes between cloned rDNA molecules defined two distinct regions (A and C) of repetitive DNA (Figures 8 and 9), separated by a segment in which no repetitiveness could be detected (region B). In addition, the spacer segment adjacent to the 5'-end of the transcription unit (region X) is devoid of loops in heteroduplex molecules and therefore is presumed to lack sequence repetition. From its location in the repeat, region X probably contains various control sequences which are involved in RNA transcription.

The length heterogeneity between repeats is confined to regions A and C of the spacer. Thus, long rDNA repeats have more copies of subrepeats than do short rDNA repeating units. Confirmation of this idea has been obtained from thermal denaturation profiles of cloned rDNA fragments of different lengths. Part of the hyperchromicity occurred within one very sharp transition. The fraction of the total hyperchromicity that occurred in this transition increased from the shortest to the longest rDNA fragment. This hypersharp melting transition represents primarily the denaturation of region A. Such hypersharp melting curves are characteristic of simple sequence DNAs like satellite DNAs.

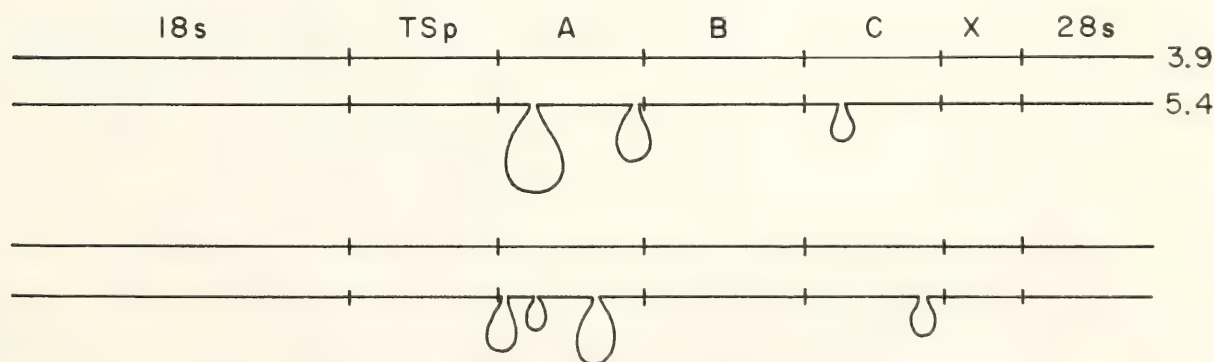


Fig. 8. Model for heteroduplex molecules between rDNA fragments of 3.9 and 5.4×10^6 daltons. Since regions A and C are composed of small subrepeats, loops formed in these regions can occur at various positions by association of the strands in different registers.

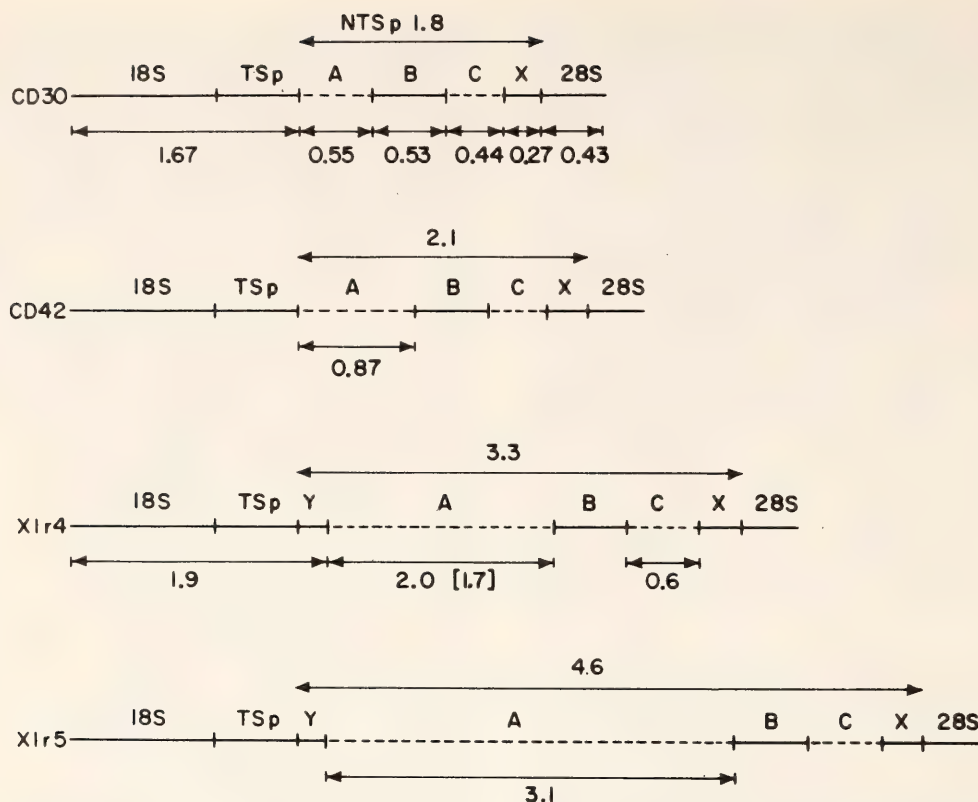


Fig. 9. Models for the four cloned rDNA fragments which were studied. The molecular weights of the fragments are: CD30, 3.9×10^6 ; CD42, 4.2×10^6 ; Xlr4, 5.4×10^6 ; Xlr5, 6.6×10^6 . The size of each region is given in CD30 and again in the larger fragments whenever a change in the size of a particular region was found. TSp stands for transcribed spacer, NTSp for nontranscribed spacer.

THE ARRANGEMENT OF LENGTH HETEROGENEITY IN AMPLIFIED AND CHROMOSOMAL rDNA

In this section we address several questions which arise from the finding that *X. laevis* rDNA contains spacers of various lengths. We ask whether length heterogeneity occurs in single individuals and within one nucleolar organizer, and if this occurs, whether repeating units of different lengths are arranged in blocks of like units or whether they may be scrambled. We further compare the distribution and arrangement of different size classes of spacers in chromosomal and amplified rDNA.

Figure 10 shows representative electrophoretic patterns of rDNAs which had been purified from individual frogs and digested with EcoRI restriction endonuclease. Each pair of gels compares amplified and chromosomal rDNA from a single frog; each pair displays two patterns of about the same complexity.

There are a few generalizations that can be drawn from these experiments.

First, bands that are visualized in amplified rDNA in most cases correspond to bands in chromosomal rDNA, indicating that no additional heterogeneity is introduced during amplification. The only exception to this rule found so far is shown in gel *b* of Fig. 10.

Second, the gel analysis demonstrates that there may be strong selection for certain repeats during amplification. For instance, the chromosomal rDNA in gel *a* (Fig. 10) shows two strong bands of spacer containing rDNA fragments with molecular weights of about 4.0 and 5.0×10^6 plus a faint band at about 4.5×10^6 . The amplified rDNA derived from this chromosome has only one strong band at 5.0×10^6 plus two faint bands at 4.0 and 4.5×10^6 . In one chromosome the most abundant class of repeating units may become amplified, while in another chromosome a rare class of repeats will undergo amplification. This

observation may also explain the electrophoretic patterns shown in gel *b*, since one could argue that the additional band which is observed in amplified rDNA from this frog may be present in chromosomal rDNA as well but at too low an intensity to be seen.

Third, although we do not know the reasons for this selective amplification, we can demonstrate that it must be genetically determined. Gels *c* and *d* (Fig. 10) show that sibling frogs which inherited the same chromosome amplify their rDNA in the same way.

These observations raise the question whether the *intramolecular* arrangement of length heterogeneity is the same in amplified and in chromosomal rDNA. We approached this problem in the following way. Long single strands from two preparations each of amplified and chromosomal rDNA were hybridized with an excess of the cloned 3.9×10^6

spacer-containing rDNA fragment, and the molecules were analyzed in the electron microscope. Representative micrographs and tracings of two such heteroduplex molecules are presented in Figs. 11 and 12. The amplified rDNA molecule (Fig. 11) displays three and the chromosomal rDNA molecule (Fig. 12), two heteroduplex regions which are separated by segments of single-stranded DNA. One heteroduplex region plus one single-stranded region add up to one rDNA repeating unit. The three heteroduplexes in the amplified rDNA were identical in size, whereas the heteroduplexes in the chromosomal rDNA differed. Measurements of a large number of strands from the two preparations of *amplified* rDNA demonstrate that, within the limits of this technique, between 87% and 98% of nearest neighbor repeats are identical in size within one particular strand of DNA. On the other hand, only between



Fig. 10. Comparison of EcoRI digests of amplified (A) and chromosomal (C) rDNA from individual frogs which contain a single nucleolar organizer (heterozygous frogs carrying the anucleolate mutation). The rDNAs were isolated from four separate frogs, digested with EcoRI restriction endonuclease, and the fragments electrophoresed on 1% agarose gels. The rDNAs from each frog are grouped together. Gels *a* and *b* show the patterns of two sibling frogs which inherited different chromosomes; gels *c* and *d* show two siblings which inherited the same chromosome; gel *e* contains Hind III digested phage λ DNA. Molecular weights of the fragments are multiplied by 10^{-6} .

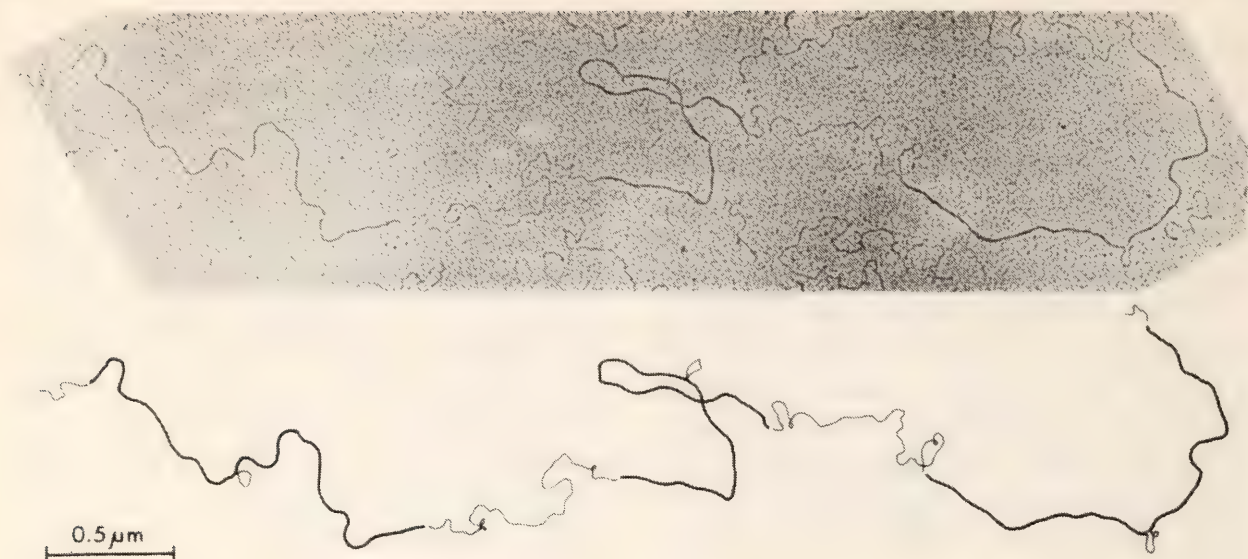


Fig. 11. Electron micrograph and tracing of a molecule of amplified rDNA. This molecule displays three full repeating units of identical size. Single strands of rDNA were hybridized with a threefold excess of the 3.9×10^6 spacer-containing fragment and were examined by electron microscopy.

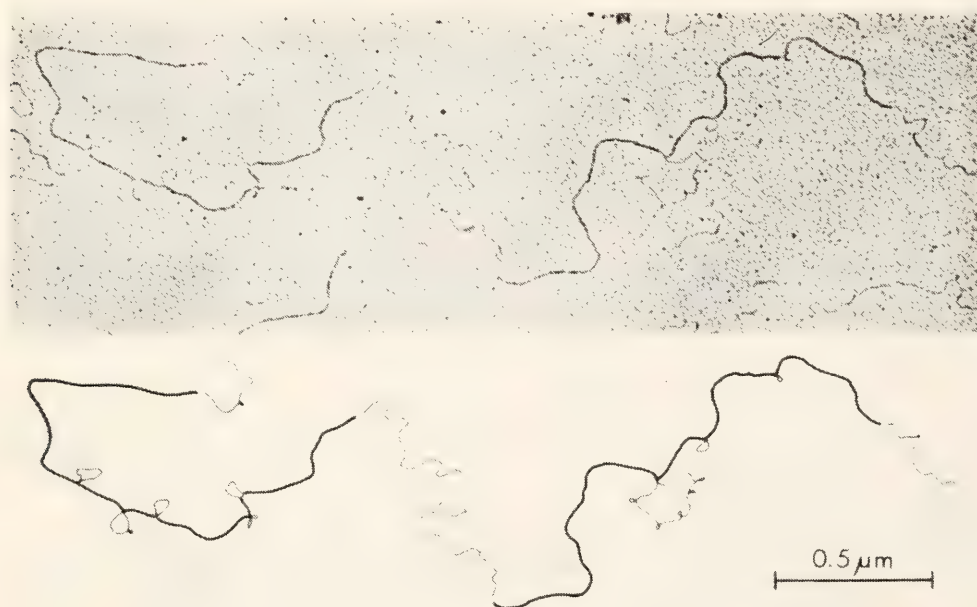


Fig. 12. Electron micrograph and tracing of a molecule of chromosomal rDNA. The two repeating units in this molecule are of different lengths. The molecule was analyzed as described in the legend to Fig. 11.

30% and 50% of the nearest neighbor repeating units of chromosomal rDNA are identical in size. In both samples of chromosomal rDNA, 30% identical nearest neighbor repeats would be present if repeats of different size classes were arranged at random in these DNAs. Therefore, in one of the chromosomal rDNAs analyzed, the arrangement of length heterogeneity is compatible with random expectation.

The main conclusion from these experiments is that the intramolecular arrangement of length heterogeneity is fundamentally different in amplified and in chromosomal rDNA. The observation that most if not all repeating units within one molecule of amplified rDNA are homogeneous in size is compatible with a rolling circle mechanism for amplification. The data also support a model in which predominantly single repeating

units are copied or excised from chromosomal rDNA during the initial amplification event.

THE INHERITANCE OF rDNA SPACER LENGTH HETEROGENEITY

We have begun a series of experiments to learn how rDNA spacer patterns are inherited. In particular, we are interested in observing how stable the spacer patterns are and what types of changes might be detectable from one generation of animals to the next. Such experiments might give clues to the mechanism by which homogeneous and conserved gene regions are maintained interspersed with more rapidly evolving and variable length spacer regions.

So far about 50 progeny from three separate matings have been analyzed. The restriction enzyme patterns of purified chromosomal rDNA of the parents and selected offspring from one mating are shown in Fig. 13. In this cross a female heterozygous for the anucleolate mutation (1-1) was mated with a wild-type male (11). To simplify analysis, only heterozygous offspring (1-1) were studied. The rDNA fragments of all but two of the offspring fall into two groups of different fragment patterns (Fig. 13c, d). The sum of these two patterns gives the pattern of the male parent's rDNA and therefore represents the normal segregation of the two male chromosomes. Since only 1-1 offspring were analyzed, the female's single rDNA-containing chromosome was excluded from the selected progeny.

Two of the offspring had spacer patterns which were related to the two major classes but differed significantly. One of these patterns differed from the pattern shown in Fig. 13c, by having its 5.1×10^6 class of spacer fragments doubled in quantity compared to the other spacer classes. In the other unusual case the pattern was similar to that shown in Figure 7d, but it contained an extra band at 4.3×10^6 . At present we do not know how either of these unusual

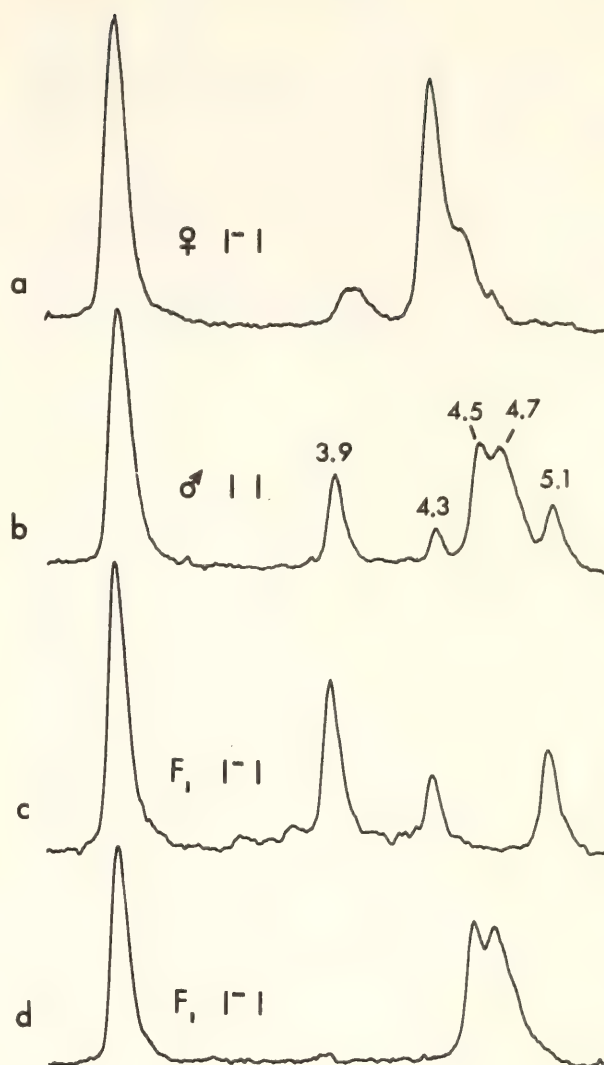


Fig. 13. EcoRI fragment patterns of chromosomal rDNA from parents and offspring of a single mating. A female heterozygous for the anucleolate mutation (1-1) was mated with a wild-type male (11) and offspring bearing the mutant chromosome were analyzed. Chromosomal rDNA was isolated from each frog, digested with EcoRI, and the digest electrophoresed on a 1% agarose gel. After staining with ethidium bromide, the gel was photographed and the photograph traced in a densitometer. Densitometer traces are shown of rDNA from (a) the female parent; (b) the male parent; (c) one class of offspring; (d) the other major class of offspring. The spacer-containing bands are identified by $MW \times 10^{-6}$.

patterns arose. Unequal crossing over (either homologue or sister chromatid exchange) seems unlikely, since it would require the spacer size classes to be arranged in homogeneous blocks in the chromosome. The heteroduplex analysis described earlier in this report suggests

that such homogeneous blocks do not occur.

The general conclusion at this stage is that the spacer patterns are usually transmitted from one generation to the next without detectable alteration. In order to understand the mechanism that gives rise to occasional changes in rDNA restriction pattern, we are now analyzing additional crosses.

CONCLUSION

These experiments provide partial or complete answers to the three questions posed in the introduction. (1) Length heterogeneity exists only within specific regions of the nontranscribed spacer region. The greatest variation in length lies within the spacer region adjacent to the 3'-end of the transcription unit. Those regions which are heterogeneous in length consist of simple, highly reiterated sequences. Fewer or greater numbers of these sequences account for the length variation between spacers. (2) Single nucleolar organizers having several hundred tandem repeats can consist of as many as seven distinguishable repeat lengths. Analysis of adjacent repeats by heteroduplex mapping shows

extensive scrambling of this heterogeneity. Thus, in a high proportion of the repeats, the length of one repeat is different from that of its neighbor. In contrast, the multiple repeats along a single molecule of amplified rDNA are homogeneous in length. This is in good agreement with the observations of others that amplification occurs by a rolling circle mechanism. (3) The characteristic repeat length heterogeneity within a nucleolar organizer is generally inherited without change by the progeny. This was found to be the case in all but two animals from three matings.

We conclude that the explanation for length heterogeneity in rDNA is the same as that for 5S DNA: it is caused by the presence of variable amounts of reiterated simple sequences in the nontranscribed spacer. This region of variable length, like the one in spacer regions of 5S DNA, is close to if not adjacent to the 3'-end of the transcription unit. Adjacent repeats of rDNA like those in 5S DNA (D. Carroll, this Report) are frequently of different lengths. This rules out the "sudden" correction mechanisms in their extreme form and supports the crossing-over model as the means by which tandem repeating sequences evolve together.

CHROMOSOMAL PROTEINS AND THE CONTROL OF GENE FUNCTION

*R. H. Reeder, T. Higashinakagawa, and S. Biroc
with the assistance of E. Hogan*

In *Year Book 73*, p. 28, Higashinakagawa reported the isolation of highly purified ribosomal gene chromatin from *Xenopus* oocytes that are active in ribosomal RNA synthesis. This year he reports his first efforts at characterizing the proteins associated with the active ribosomal genes. He has found a significant amount of histone in the ribosomal gene chromatin, and at least some of this histone appears to be bound to the actively transcribed gene regions.

Eventually we hope not only to produce a complete catalogue but also to map the locations of all the proteins associated with these genes, both when they are transcribed actively and when they are inactive.

Parallel experiments have been done with the ribosomal gene chromatin from *Xenopus* cultured cells. It was not possible to physically isolate the ribosomal gene chromatin. However, experiments using limited DNase digestion of isolated

nuclei have shown that the ribosomal genes are partially protected from DNase in a manner similar to the bulk of the chromatin, thus providing indirect evidence that the active ribosomal genes in cultured cells are also associated with histones.

In a separate line of research, Biroc has examined the accessibility of histone tyrosines in chromatin to reaction with radioactive iodine. The reactivity to iodine changes in a specific manner as the chromatin structure is progressively taken apart. These studies lay the groundwork for detection of possible conformational differences of histones on active versus inactive chromatin.

THE ASSOCIATION OF RIBOSOMAL GENES WITH HISTONES IN CULTURED CELLS

R. H. Reeder

This year has seen an explosion in the literature on the structure of chromatin of eukaryotic organisms. The finding, in several laboratories, that chromatin possesses a repeating subunit structure has been especially compelling. Histones have been shown to be associated with the DNA chain, forming a structure that, in the electron microscope, resembles beads on a chain. Each bead consists of about 200 base pairs of DNA plus a specific cluster of histone molecules. When chromatin is digested briefly with a nonspecific DNase such as micrococcal nuclease, the DNA in the bead is relatively resistant to attack, while the DNA connecting the beads is relatively open. Thus, brief DNase digestion results in cleaving most of the DNA into 200 base-pair fragments or oligomers. These observations suggest an indirect method of learning whether or not specific genes are associated with histones. One can treat unfractionated chromatin (or isolated nuclei) with DNase, separate the resultant DNA fragments by gel electrophoresis, and locate fragments containing a specific gene by molecular hybridization with a radioactive RNA specific

for that gene. If the gene in question is cut into 200 base-pair pieces or higher order oligomers, that can be taken as good evidence that it is associated with histones.

We have used this protocol to study the genes for 18S and 28S ribosomal RNA in *Xenopus* cultured cells. Nuclei labeled with ^3H -thymidine were isolated from cells that had been seeded in roller bottles four days before and were growing maximally. This particular cell line is not contact inhibited and grows until it exhausts the medium. Aliquots of the nuclei were digested with various amounts of micrococcal nuclease, and the DNA fragments were purified and electrophoresed on acrylamide gels cross-linked with ethylene diacrylate. Figure 14 shows the distribution of the ^3H -labeled DNA fragments after three different degrees of DNase digestion. As reported by others, the bulk of the DNA is cut into an oligomeric series of fragments. To locate the ribosomal genes in such gels, each gel was sliced, each slice was hydrolyzed with alkali to liberate the DNA, and the DNA from each slice was hybridized in solution with ^{32}P -labeled ribosomal RNA. After hybridization the hybrids were trimmed with RNase and caught on a nitrocellulose filter to be counted. The distribution of the ^{32}P label in Fig. 14 shows that the ribosomal genes were cut into the same fragment sizes as was the bulk DNA, strongly implying that they are associated with histones in a manner similar to that of the bulk chromatin. Other experiments (not shown) indicate that the spacer region of the ribosomal DNA is also associated with histones. One problem in interpreting these results is that we have no direct measure of what fraction of the ribosomal genes are actively transcribed even in a rapidly growing cell. One might argue that the active genes are only a fraction of the approximately 900 ribosomal genes in the cell and that they are preferentially destroyed very early during DNase di-

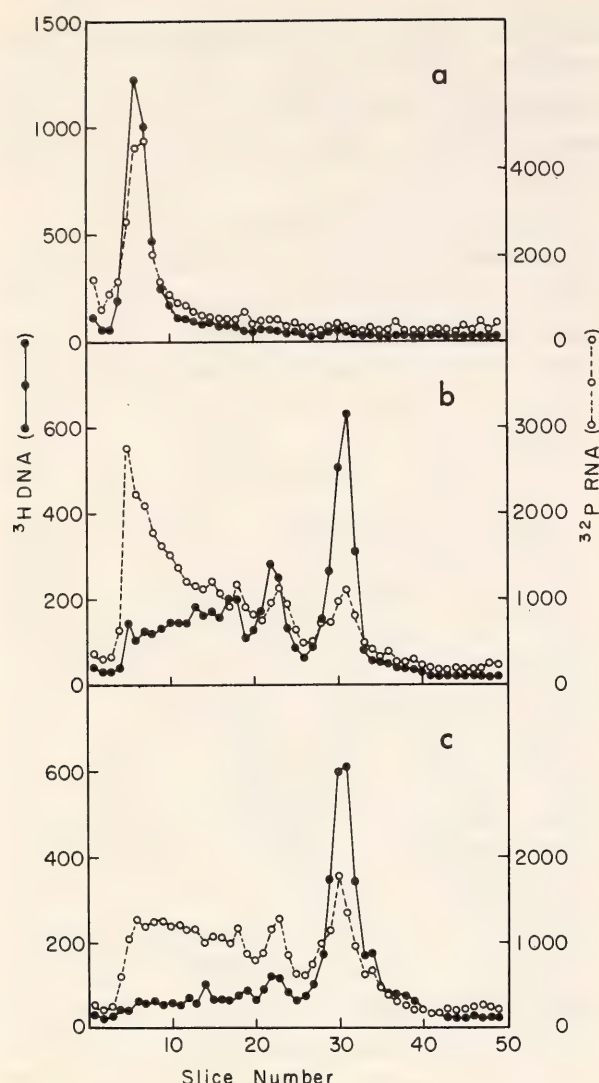


Fig. 14. Hybridization of cultured cell nuclear DNA fragments with ribosomal RNA. Cultured *Xenopus* cells were grown for 4 days in roller bottles and labeled overnight with ^3H thymidine, and nuclei were isolated. Aliquots were digested with increasing amounts of micrococcal nuclease in 0.01 M Tris pH 8, 0.01 M NaCl, 5 mM MgCl_2 for 10 min at 37°C . The DNA fragments were purified and electrophoresed on 6% acrylamide tube gels cross-linked with ethylene diacrylate. The gels were sliced, each slice hydrolyzed with alkali, and the DNA in each slice hybridized with ^{32}P rRNA. The hybrids were trimmed with RNase and caught on nitrocellulose filters in 3 M NaCl. (a) 16% digestion of the bulk DNA, (b) 33% digestion, (c) 41% digestion. The major peak at about slice no. 30 has a size of 135–185 base pairs depending upon the strength of DNase digestion.

gestion. If that were true, then Fig. 14 would be telling us only about the remaining inactive genes. This interpretation seems unlikely, since control experiments have shown that the ribosomal

genes are progressively destroyed by DNase, as a "smooth function" of digestion time. We cannot detect the rapid early loss of a fraction of these genes. Furthermore, nuclei from young active cells and from old cells that have exhausted the medium and have stopped growing both show the same linear kinetics of ribosomal gene digestion by DNase.

Another possible artifact could have arisen if histones were able to rearrange during the isolation and digestion of the nuclei. This artifact has been partially ruled out by an experiment in which a trace amount of radioactive deproteinized DNA was mixed with a large excess of unlabeled nuclei and the mixture digested with DNase. While the unlabeled DNA in the nuclei was digested into the usual oligomeric fragments, the deproteinized radioactive DNA was rapidly destroyed without being cut into any discrete size classes, suggesting that rearrangement of histones is not a serious artifact in these experiments.

In summary, therefore, we feel that the most likely interpretation of these experiments is that histones are associated with active ribosomal genes.

ANALYSIS OF THE PROTEINS OF ISOLATED RIBOSOMAL GENE CHROMATIN

T. Higashinakagawa

Ribosomal gene chromatin has been isolated in a highly purified state from the nucleoli of *Xenopus laevis* oocytes (Year Book 73, p. 28). By this technique we are now able to provide chromatin of 75%–80% purity routinely—and occasionally even of 95%–100% purity. Since the nucleolus is an indicator of active ribosomal RNA synthesis, analysis of this chromatin should give us information about the proteins on active genes, just as studies with bulk DNA chromatin should tell about the proteins on inactive genes. We have begun to analyze the protein moiety of rDNA chromatin with special attention to the presence or absence of histones.

Ribosomal gene chromatin was dissolved in SDS and electrophoresed on an SDS-polyacrylamide slab gel together with proteins of various origins for the purpose of comparison (Fig. 15). As shown in Fig. 16, this particular prepara-

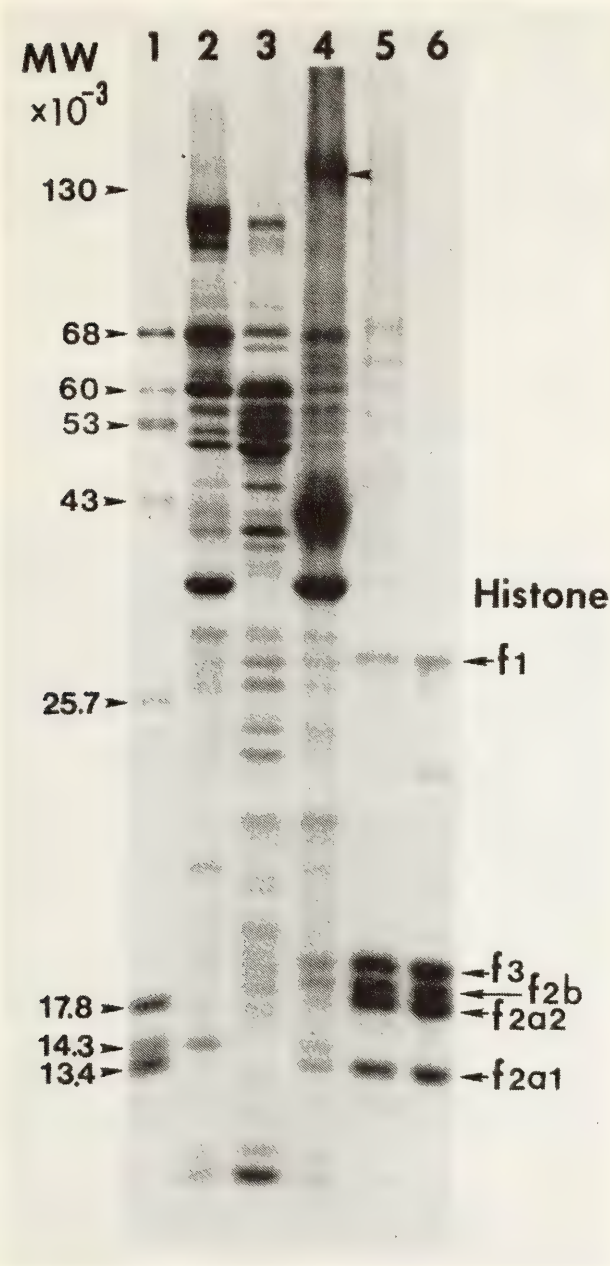


Fig. 15. SDS-polyacrylamide gel electrophoresis pattern of ribosomal gene chromatin proteins. Ribosomal gene chromatin and proteins from other sources were dissolved by heating in SDS and β -mercaptoethanol and electrophoresed on a slab gel of 15% polyacrylamide-0.1% SDS. (1) Molecular weight markers, (2) total nucleolar protein, (3) ribosomal protein, (4) ribosomal gene chromatin protein, (5) *Xenopus* bulk DNA chromatin protein, (6) *Xenopus* acid extracted histone. An arrow in slot (4) points to the possible RNA polymerase I subunit.

tion happened to possess no detectable amount of bulk chromosomal DNA when examined in an analytical CsCl density gradient; it was therefore almost 100% pure ribosomal gene chromatin. The ribosomal gene chromatin clearly contains histones F_{2a1} , F_{2a2} , F_{2b} and F_3 (Fig. 14, slot 4). There is no discrete band which corresponds to histone F_1 in this gel. Another band of interest is visible in the high molecular weight region of the gel (marked by the arrow). This rather strong band has almost the same mobility as that of the *E. coli* RNA polymerase $\beta\beta'$ subunits, and hence may possibly represent a subunit of the RNA polymerase I molecule. Almost all other protein bands coincide with ribosomal protein or total nucleolar protein and are present in such large amounts in the nucleolus that they are unlikely to be specifically bound to the ribosomal DNA. At this resolution we can detect no other rDNA-specific protein that is present in the same abundance as histones. Our techniques are not yet sufficiently sensitive to detect proteins which may be present in only a few copies per rDNA repeating unit.

We wished to measure the histone-to-DNA ratio in rDNA chromatin. Since the yield of this chromatin is low (0.1–0.2 μ g of rDNA from one frog), conventional analytical procedures are difficult to apply. However, we have developed a procedure in which electrophoresis is carried out in 2 mm diameter gel columns, and in this way 0.5–1.0 μ g of histones can be visualized and quantitated by staining. Figure 17 shows the electrophoretogram of the ribosomal gene chromatin protein carried out in such a small gel column. By comparison with a gel like the one shown in Fig. 15, each histone component can be assigned on this gel as indicated in the figure. The amount of histone was estimated from the area under the stained peaks while the amount of DNA as well as the percentage of rDNA (purity) was measured in an analytical CsCl density gradient

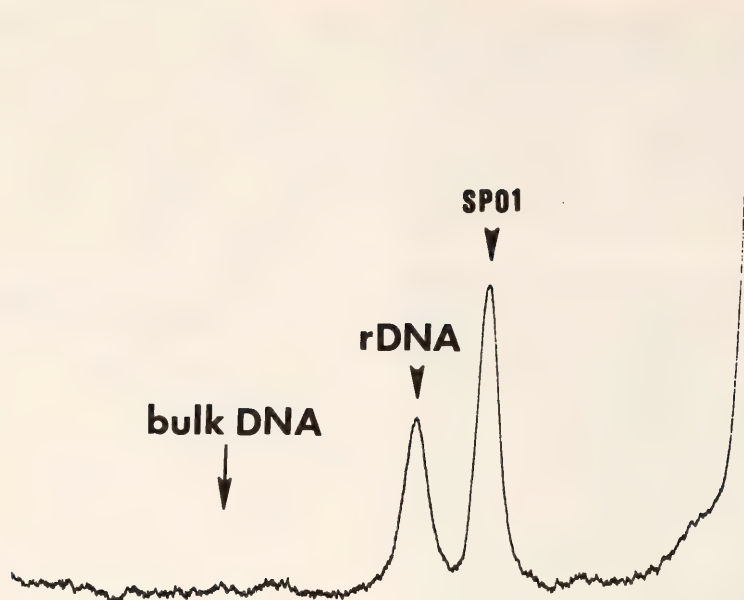


Fig. 16. Analytical CsCl density gradient profile of DNA from the ribosomal gene chromatin analyzed in Fig. 15. Virtually no bulk DNA is detectable, showing that this is almost 100% pure ribosomal gene chromatin.

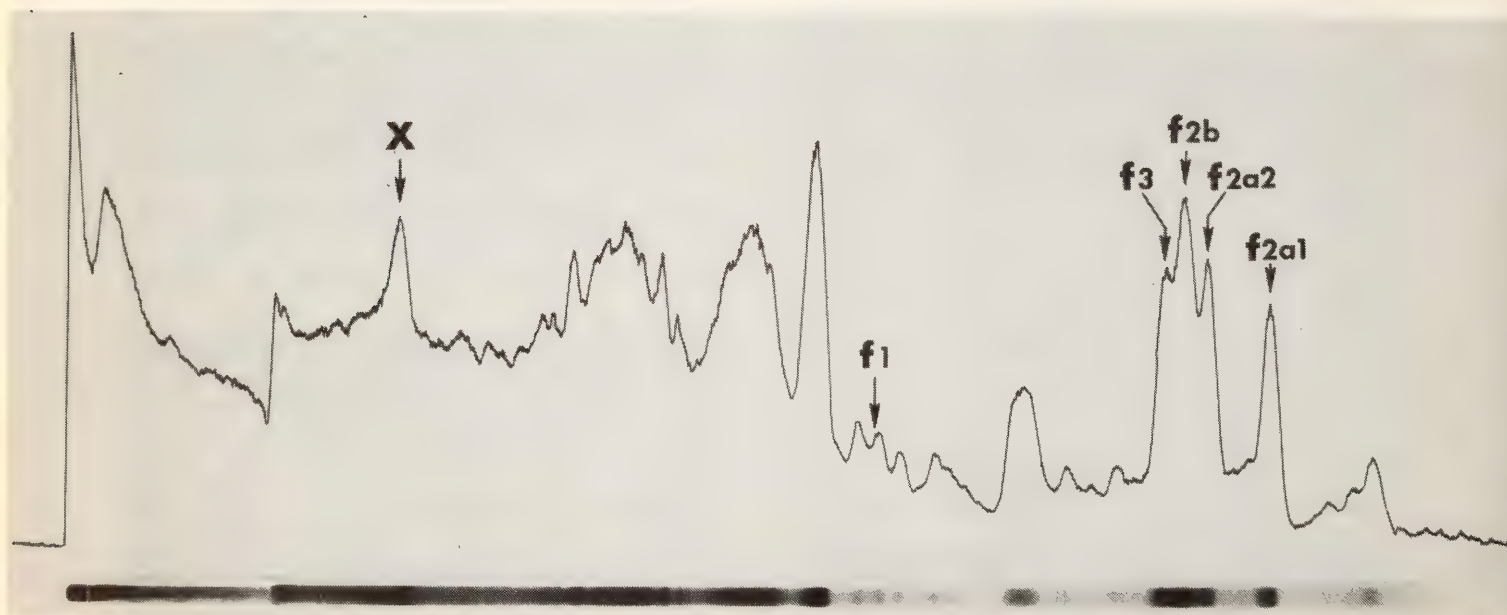


Fig. 17. SDS-polyacrylamide gel electrophoresis pattern of ribosomal gene chromatin protein carried out in a 2 mm diameter gel column. The conditions of electrophoresis were the same as in Fig. 15. This gel corresponds to experiment 3 in Table 2. "X" indicates the location of the possible RNA polymerase I subunit.

like that shown in Fig. 16. The entire measurement was calibrated by constructing a standard curve using bulk DNA chromatin prepared from *Xenopus* cultured cells under exactly the same conditions. The results of these experiments are summarized in Table 2.

The amount of F_{2a1} is smaller than is found in bulk *Xenopus* chromatin. This

also seems to be the case with the sum of F_{2a2} , F_{2b} , and F_3 . Due to some uncertainty in the overall recovery of histones, we regard this measurement as a minimum estimate of the amount of histone on the ribosomal DNA. Obviously, these results corroborate the finding shown in Fig. 15.

The presence of histones in active

TABLE 2. Composition of Ribosomal DNA Chromatin

Expt. No.	Bulk DNA (μg)	rDNA (μg)	Purity (%)	Relative Histone Abundance* on rDNA	
				F _{2a1}	F _{2a2} + F _{2b} + F ₃
1	0.22	0.82	79	0.30	0.36
2	0.26	0.86	77	0.34	0.37
3	0.86	2.73	76	0.46	0.66

* Both bulk DNA chromatin containing a known amount of DNA (determined by Model E analysis) and ribosomal DNA chromatin were electrophoresed under identical conditions, and the area under their histone bands determined. Relative histone abundance is expressed as the ratio of histone areas in rDNA chromatin (after subtracting the area contributed by contaminating bulk DNA chromatin) to the histone area in bulk chromatin containing an equivalent amount of DNA.

ribosomal DNA chromatin could be interpreted in several ways. For example, it is possible that the histones do not belong there and were accidentally picked up during isolation. Alternatively, they may belong on the rDNA but are only located on the nontranscribed spacer region, not on the transcribed gene region. A third, and most interesting, possibility is that they are also associated with the active gene regions. To explore these possibilities we have studied the action of micrococcal nuclease on isolated nucleoli.

If histones are associated with rDNA within the nucleolus, we should be able to digest the nucleoli and isolate protected fragments similar to the protected fragments we described from cultured cell nuclei. By hybridization of these fragments with ribosomal RNA we should be able to determine if they are derived from the gene region, the spacer region, or both. Accordingly, oocyte nucleoli were isolated, divided into three aliquots, and digested with increasing amounts of micrococcal nuclease. After deproteinization, each aliquot of DNA fragments was labeled with ³²P, using a DNA polymerase exchange reaction. Control experiments have shown that this labeling method does not alter the electrophoretic mobility of the DNA. The labeled fragments were then electro-

phoresed on a 6% polyacrylamide slab gel and located by autoradiography. Micrococcal nuclease fragments from whole nuclei and restriction enzyme fragments from SV 40 viral DNA were also labeled and run under the same conditions for comparison. The results are shown in Fig. 18.

Digestion of nucleoli with small amounts of nuclease (lane 1) results in the appearance of DNA bands with sizes of about 135, 280, and 400 base pairs, plus some higher molecular weight material. These bands are similar in size to those derived from whole nuclei. We take their appearance as good evidence that histones are bound to the rDNA in a specific manner and are not just loosely associated with nucleoli due to an isolation artifact. In other experiments we have observed that the size of the nuclease-derived bands changes with increasing digestion; we assume this accounts for the size difference seen in Fig. 18 between the nuclear and nucleolar fragments. With longer digestion (lanes 2 and 3) the larger bands disappear and a series of smaller bands appear. Small fragments similar to these have been interpreted by other investigators as resulting from nuclease attack *within* the histone-DNA complex and are additional evidence that histones are associated with the rDNA.

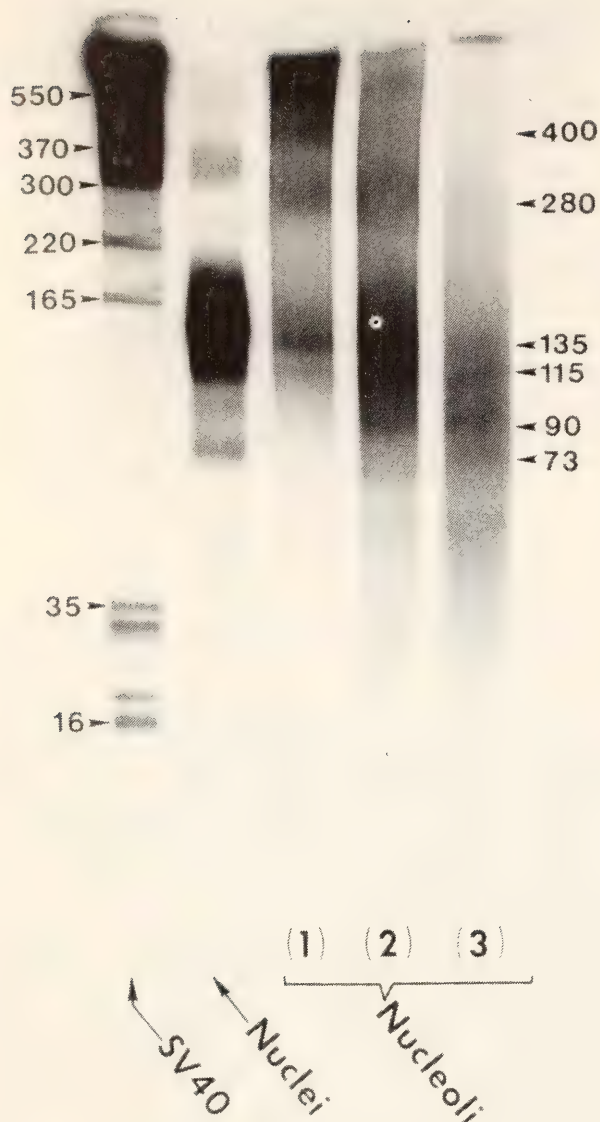


Fig. 18. Electrophoresis of nucleolar DNA fragments after partial nuclease digestion. Isolated nucleoli (72% rDNA purity) were digested with increasing amounts of micrococcal nuclease. The DNA fragments were deproteinized and labeled with ^{32}P , using *E. coli* DNA polymerase, and a portion of each was run on a 6% acrylamide slab gel cross-linked with bis acrylamide. The gel was then dried down and autoradiographed. SV40 viral DNA digested with restriction enzyme Hae III and DNA fragments from whole nuclei digested with micrococcal nuclease were labeled and run at the same time for comparison. DNA sizes are given in base pairs. The sizes of the 16–35 base-pair fragments of SV40 DNA are only approximations.

To determine if the ribosomal DNA fragments were coming from the gene or spacer region, the rest of each sample was electrophoresed in tube gels of 6%

acrylamide cross-linked with ethylene diacrylate. The gels were then sliced and the DNA from each slice was hybridized to saturation with ^3H -rRNA. The results are shown in Fig. 19. After low nuclease digestion (Fig. 19a) the ^3H -rRNA hybridizes with all size classes of ^{32}P -labeled fragments. Resolution of the various bands is not as good in diacrylate cross-linked gels, but the hybridization clearly follows the major peaks. From

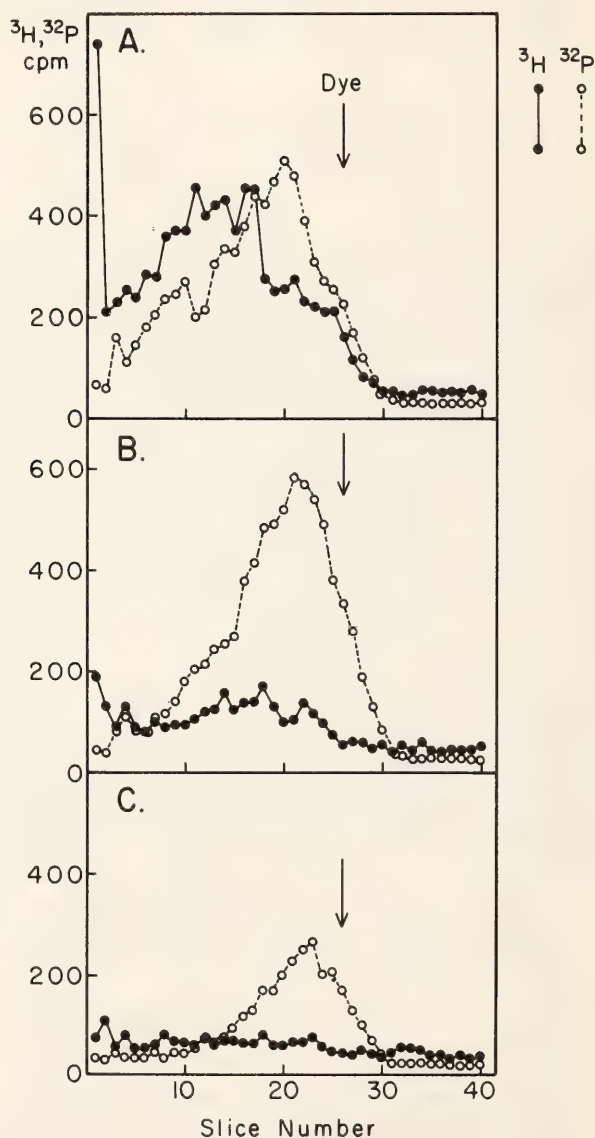


Fig. 19. Hybridization of nucleolar DNA fragments with ribosomal RNA. The remainder of each nucleolar DNA sample shown in Fig. 18 was electrophoresed on a 6% acrylamide tube gel as described in Fig. 14 and hybridized with ^3H -labeled ribosomal RNA. Panels A, B, and C correspond to lanes 1, 2, and 3, respectively, of Fig. 17. They show the results in increasing degrees of nuclease digestion.

the known specific activity of the ^3H -rRNA we can say that about 50% of the gene region present in the rDNA before digestion has been recovered in the gel (Fig. 19a). Since there undoubtedly were losses during digestion, labeling with ^{32}P , and subsequent electrophoresis, this result indicates that a large fraction of the gene region is associated with histones.

Upon stronger digestion (Fig. 19 b and c) the gene region disappears rapidly, while a fraction of the ^{32}P -labeled DNA disappears more slowly. Since the DNA in this nucleolar preparation was 72% rDNA, it is probable that this more slowly degraded fraction is largely spacer sequences.

The apparent presence of histones on actively transcribed ribosomal genes is somewhat surprising; especially so in view of the well-entrenched theory that histones function as repressors of genetic information. It is a sufficiently important observation that we intend to attempt to verify it as soon as possible by independent methods. If our present interpretation is correct, interesting questions are immediately raised concerning the manner in which RNA polymerase is able to traverse histone-covered DNA. The intriguing possibility is also raised that histones on active genes are different in conformation, secondary modification, or some other measurable parameter from histones on inactive DNA. This possibility is also open to experimental exploration.

IODINATION OF *Xenopus* HISTONE $\text{F}_{2\text{a1}}$ IN CHROMATIN

S. Biroc

Xenopus histone $\text{F}_{2\text{a1}}$ has four tyrosine residues, all of which can react with radioactive iodine under appropriate conditions. However, when histone $\text{F}_{2\text{a1}}$ is complexed in native chromatin, all four tyrosines are not equally reactive, suggesting that their individual reactivity depends upon their accessibility from

the external milieu and further suggesting that we can use reactivity to iodine as a probe of the three-dimensional arrangement of $\text{F}_{2\text{a1}}$ in chromatin.

It was first necessary to determine the location of the *Xenopus* $\text{F}_{2\text{a1}}$ tyrosines along the amino acid chain. *Xenopus* $\text{F}_{2\text{a1}}$ has not been sequenced; however, it appears to have a sequence nearly identical to the known sequence of calf thymus $\text{F}_{2\text{a1}}$. The molecules of both species co-migrate on acid-urea or SDS acrylamide gels. They have the same number of tyrosine residues. After iodination and tryptic digestion they both yield identical iodinated tryptic peptide maps. Since, in general, $\text{F}_{2\text{a1}}$ is the most evolutionarily conserved protein that is known, we believe it is safe to use the amino acid sequence of calf thymus $\text{F}_{2\text{a1}}$ to order the tyrosines of *Xenopus* $\text{F}_{2\text{a1}}$. Figure 20 shows the electrophoretic separation of the iodinated (tyrosine-containing) tryptic peptides from *Xenopus* $\text{F}_{2\text{a1}}$ and shows where they are located within the complete molecule.

The influence of chromatin structure on the reactivity of each of these tyrosine residues was examined in the following manner. Chromatin from *Xenopus* cultured cells was iodinated in various concentrations of NaCl ranging from zero to 2 M. Each mixture also contained a known amount of the free amino acid L-tyrosine to serve as an internal standard. After iodination the specific activity of the L-tyrosine was measured as well as the specific activity of each of the four $\text{F}_{2\text{a1}}$ peptide tyrosines. The specific activity of each peptide tyrosine was divided by the specific activity of the free tyrosine to calculate the reactivity index of the peptide tyrosine. A reactivity index of less than 1.0 indicated that the peptide tyrosine was less accessible to iodination than the free tyrosine, and a reactivity index greater than 1.0 indicated it was more accessible than free tyrosine. The reactivity indices of each $\text{F}_{2\text{a1}}$ tyrosine are plotted against NaCl concentration in Fig. 21. In very low

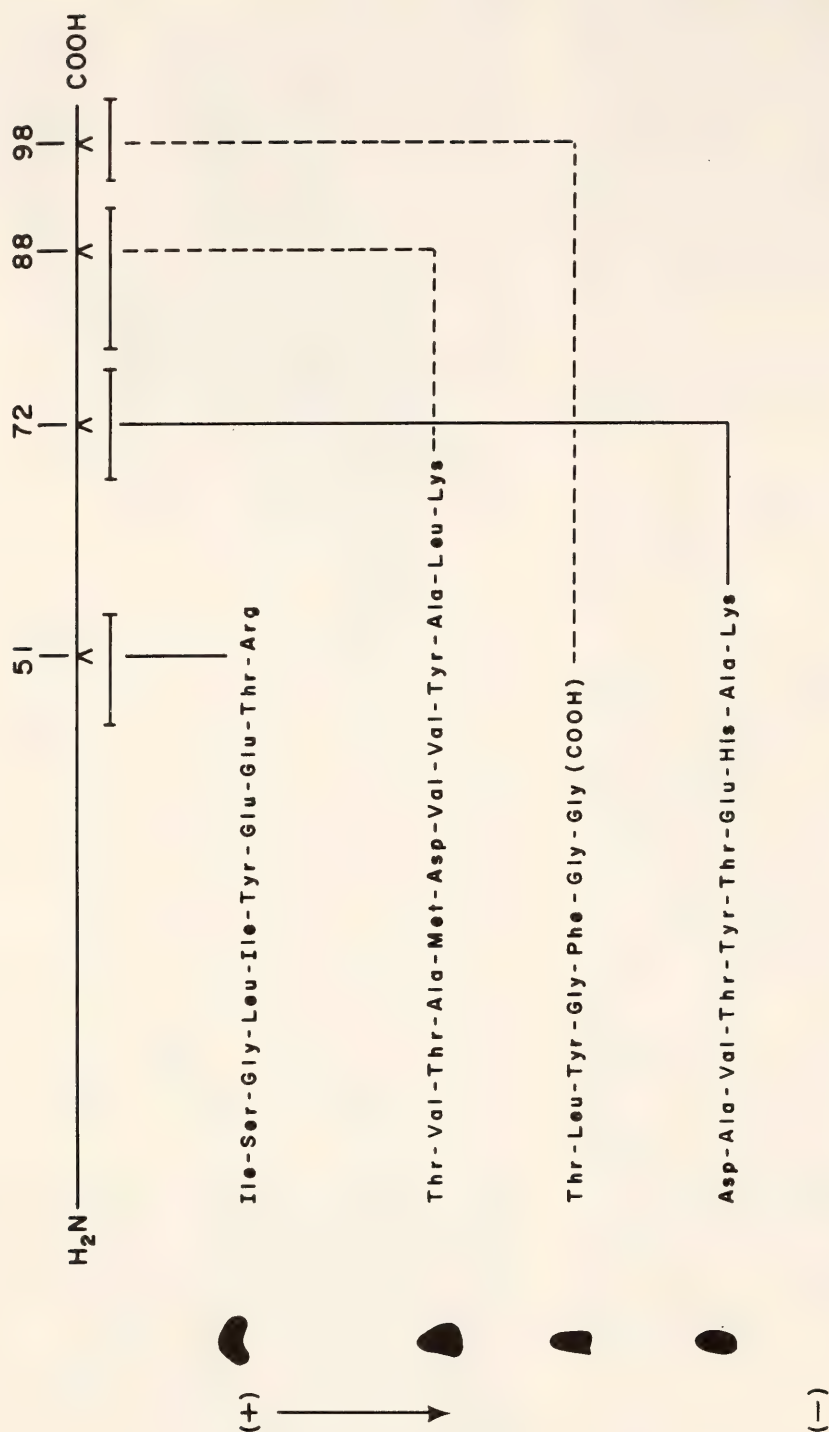


Fig. 20. Location of iodinated tyrosine peptides in *Xenopus* F_{2a1} histone. *Xenopus* F_{2a1} was iodinated, digested with trypsin, electrophoresed at pH 3.5, and the iodinated tyrosine peptides located by autoradiography. The peptides were identified by a variety of procedures including electrophoresis at various pH's and cyanogen bromide cleavage. Assignments were made assuming that the *Xenopus* peptides have the same amino acid sequence as those from calf thymus.

ionic strength, where chromatin presumably is in its normal nondenatured conformation, all four tyrosines were less reactive than free tyrosine. Tyrosines 98 and 72 barely reacted at all, while tyrosines 51 and 88 were about one-third as reactive as the internal standard. Pre-

sumably all four are more or less "buried" within the chromatin structure. As the salt concentration is raised, two interesting observations can be made. (1) At 0.5 M NaCl tyrosines 98, 72, and 51 remain unaffected. However, tyrosine 88 has increased to almost maximal reactiv-

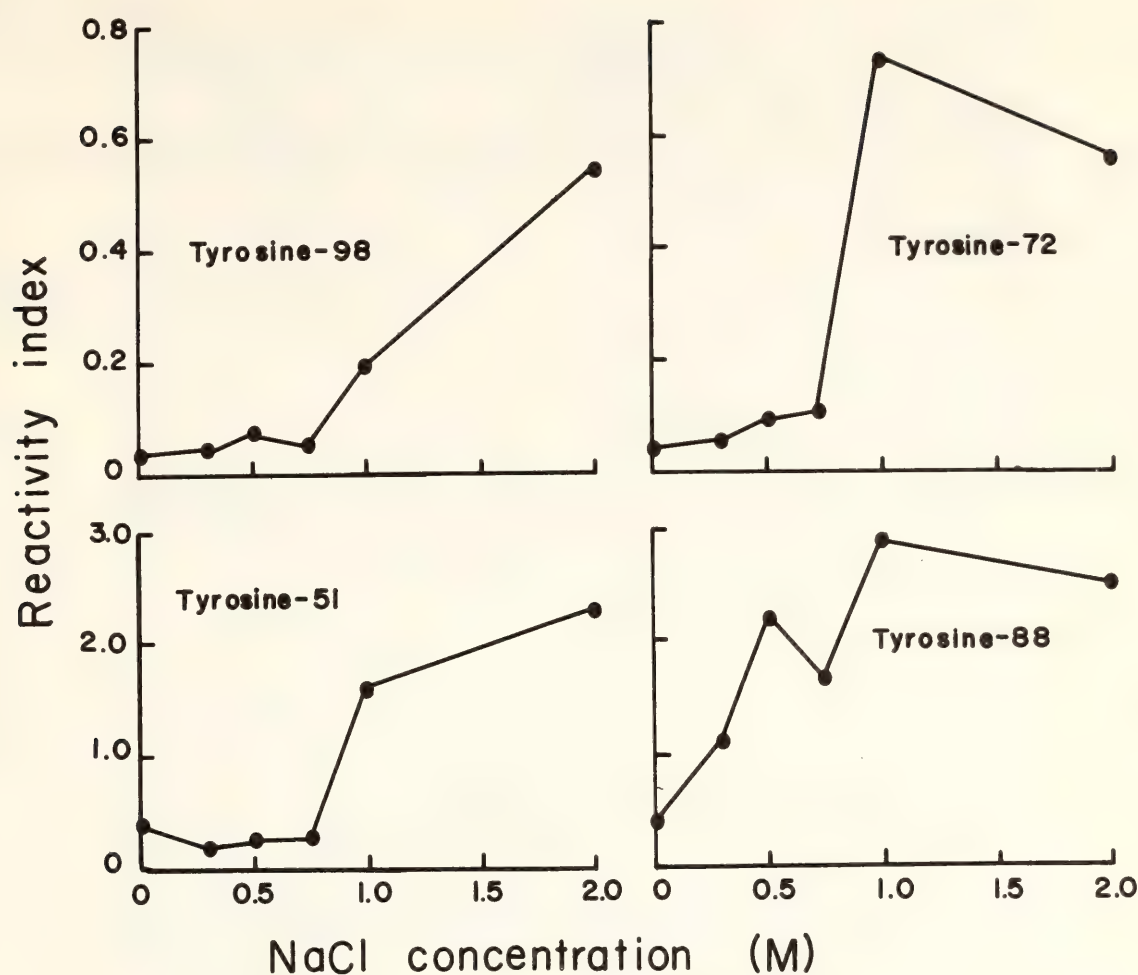


Fig. 21. Reactivity of histone F_{2a1} tyrosines iodinated in chromatin in increasing NaCl concentrations. *Xenopus* chromatin was dissolved in (1) 5 mM Tris, 1 mM EDTA, (2) 0.3 M NaCl, (3) 0.5 M NaCl, (4) 0.75 M NaCl, (5) 1.0 M NaCl, and (6) 2.0 M NaCl, and then iodinated in the presence of an internal standard. The histones were extracted and electrophoresed on acid/urea gels. The radioactive F_{2a1} was eluted from the gel piece, trypsin-digested and electrophoresed at pH 3.5 to determine how much radioactivity was associated with each tyrosine. The specific activity of each peptide tyrosine was compared to the specific activity of free tyrosine for each respective NaCl concentration. Reactivity index is plotted as a function of NaCl concentration for each F_{2a1} tyrosine.

ity in this salt. Control experiments showed that histone F₁ was completely dissociated from the chromatin at 0.5 M NaCl, while the other four histones remained bound to the DNA. This suggests the possibility that tyrosine 88 is involved in interaction with histone F₁. Alternatively, removal of F₁ may allow a conformational change in the chromatin that exposes tyrosine 88. (2) Raising the NaCl concentration to 2.0 M causes an increase in the reactivity of the other tyrosines so that at 2.0 M NaCl all four have undergone a five- to tenfold in-

crease over their reactivity in low ionic strength.

These experiments demonstrate that the iodination reaction is a sensitive probe for detecting changes in the association state (or conformation) of histone F_{2a1}. The fact that we are finding histones on actively transcribed genes raises the likelihood that those histones may be in a different conformation than histones on inactive genes. In future experiments we hope to use the iodination reaction as a tool to search for such conformational differences.

THE REGULATION OF FIBROIN GENES

Y. Suzuki and P. Giza

We have been studying the regulation of fibroin gene action in the silkworm *Bombyx mori*. Our goal is to understand which cellular constituents are responsible for the selective transcription of the genes in the posterior silk gland. Our approach is to isolate chromatin, RNA polymerase, and whatever regulatory factors may occur in the posterior gland, and to attempt to reproduce faithful transcription of fibroin genes in vitro.

Toward this goal, several studies have been initiated and are reported here: (1) morphological observations of silk gland nuclei during development; (2) efforts to prepare probes for detecting fibroin mRNA sequences synthesized in vitro; (3) pulse-labeling experiments in vivo; and (4) the isolation of nuclei and the synthesis of fibroin mRNA in vitro.

An unexpected and encouraging observation was the fact that in RNA preparations labeled in vivo for only 30 minutes the synthesis of fibroin mRNA comprised 10% to 15% of the total radioactive transcripts in the late fifth instar. This quantitation is possible because of the unique nature of the fibroin mRNA sequences (*Year Book 73*, p. 24). Ours is the first quantitative measurement of a single messenger RNA in pulse-labeled material by a direct chemical method. Similar results have been obtained with isolated silk glands in organ culture, indicating that the posterior silk gland is a self-regulatory organ for fibroin gene transcription in the late fifth instar. Although the silk gland nuclei possess a convoluted and ramified structure, which makes their isolation difficult, to say the least, the unusual predominance of fibroin mRNA synthesis in the pulse-labeled material has compelled us to attempt the fourth study, the isolation of nuclei and the synthesis of fibroin mRNA in vitro. This approach would narrow the localization of the

regulatory factors for fibroin gene transcription.

MORPHOLOGICAL OBSERVATIONS OF SILK GLAND NUCLEI DURING DEVELOPMENT

P. Giza and Y. Suzuki

Before attempting to isolate silk gland nuclei for transcription in vitro we felt that a better understanding of nuclear morphology was essential. It is known that silk gland nuclei undergo dramatic changes in appearance as the larva matures, suggesting that the isolation of intact nuclei could present difficulties. Accordingly, silk glands were studied from late embryos (about 1.5 day before hatching) through the late fifth instar. All preparations shown in Fig. 22 are fixed, Feulgen-stained, whole mounted silk glands at the larval stages indicated.

The shape of the nuclei from late embryos (not shown here) to early third instar is not unusual compared to nuclei of other eukaryotic cells. However, the silk gland nucleus is very much elongated and occupies a large portion of the cellular volume. During the middle to late third instar the nuclei begin to ramify at both ends of the elongated nuclear structure. The process continues through the fourth and fifth instars and culminates in the extremely complex structure shown in Fig. 22f. This nuclear ramification is associated with significant increases in cellular DNA, a process termed "polyploidization."

Pondering this complex structure (Fig. 22f) one must ask, how are 400,000 sets of genomes in the posterior gland cell in the fifth instar organized structurally and functionally? We do not see a typical "polytene" structure. It has been generally accepted that the nuclei present an amorphous "interphase-like" appearance, but convincing data are scant. Therefore, we have studied the nucleus

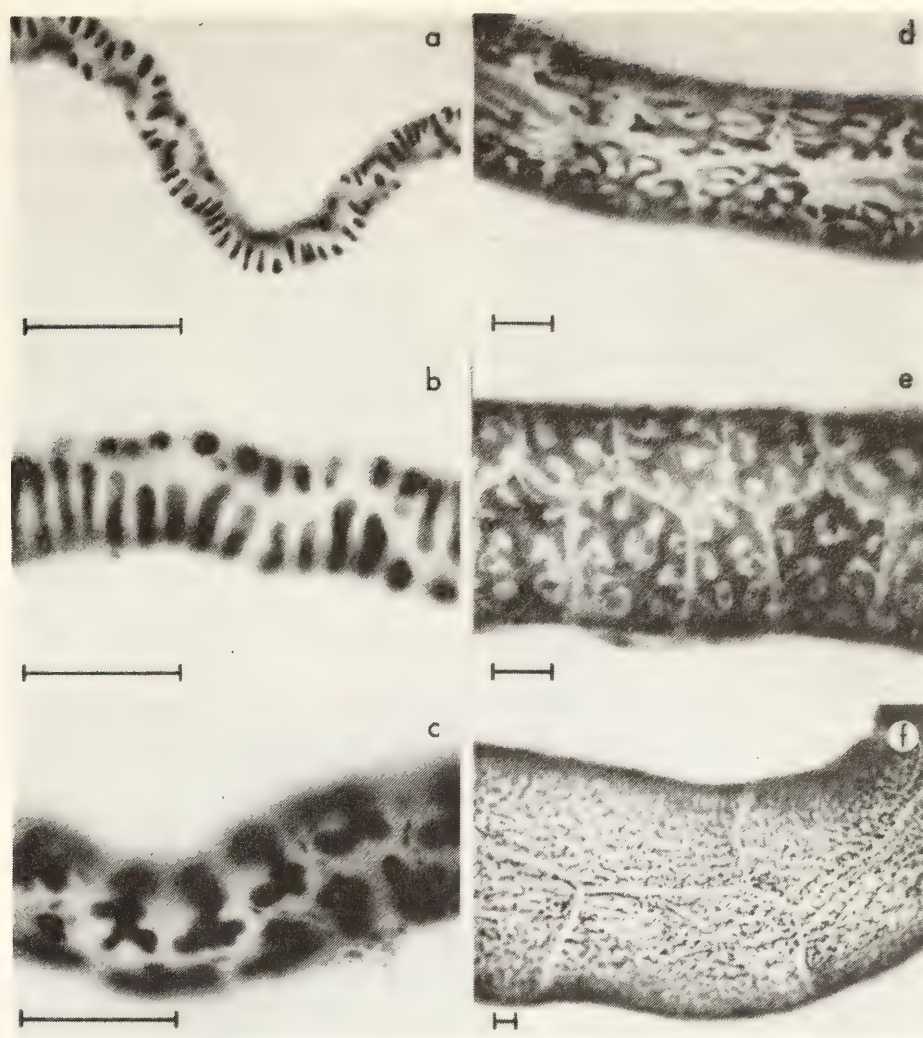


Fig. 22. Morphological changes in silk gland nuclei during development. They are all posterior glands except one middle gland (1e). Preparations were fixed, stained by the Feulgen-Schiff reaction, dehydrated, and mounted in Harleco Synthetic Resin. The bars are 100 μ m. (a) first instar (2 days after hatching), (b) second instar (3 days after first ecdysis), (c) third instar (4 days after second ecdysis), (d) fourth instar (4 days after third ecdysis), (e) fourth instar (2 days after third ecdysis), (f) fifth instar (7 days after fourth ecdysis). Figure 22e is displayed to show hexagonal cell boundaries clearly.

by high power microscopy after Feulgen staining. To our surprise we have observed a large number of Feulgen-positive granules, somewhat like individual "chromosomes," in the polyploid nucleus (Fig. 23). The size and shape of these granules are quite similar to those of individual chromosomes in spermatocytes. In fact, the overall staining of the nucleus appears to be due to the individual staining of thousands of these granules. These structures have been seen throughout the nucleus and have now been observed in embryonic through third instar nuclei. Whether they persist throughout larval development or are

present only at certain periods is not known. We also do not know if the granules are present in the fourth and fifth instars, because these nuclei are thick and stain darkly with little internal detail. Very preliminary results have revealed that the number of granules is increasing during silk gland development; the approximate number is a product of the polyploid number and the haploid chromosome number. These observations and interpretations are reminiscent of Geitler's early studies of endomitosis some 40 years ago. Recently, C. Thomas (this Report) has shown that the fibroin genes and ribosomal DNA are

PREPARATION OF ASSAY PROBES FOR
DETECTING FIBROIN mRNA
SYNTHESIZED IN VITRO

Y. Suzuki

In order to detect nascent or fragmented fibroin mRNA in mixtures of various RNA species, we need hybridization probes like fibroin genes or complementary DNA synthesized by reverse transcriptase. Although the optimal probe will probably be supplied by fibroin gene purification and amplification of the gene linked with a plasmid in bacteria, other approaches are being explored.

The poly rC-cellulose column that was described in *Year Book 73*, p. 24, has been found to be unsatisfactory.

E. coli DNA polymerase is known to synthesize DNA from RNA templates. Therefore, using purified fibroin mRNA (>90% pure) as template and oligo dT as a primer, complementary DNA was synthesized. The cDNA was hybridized with radioactive total cellular RNA from the posterior gland, and from the hybrid thus formed, RNA was recovered and digested with RNase T₁, and the digest was fractionated with DEAE-Sephadex. The profile was characteristic of a 50% pure fibroin mRNA, suggesting either that impurities in the template mRNA preparation were transcribed preferentially or that transcripts of noncoding regions of the mRNA make up about half of the short sequence synthesized. The latter possibility was verified by the following experiment. Reverse transcription was carried out using oligo dT-cellulose as a primer. The cDNA-oligo dT-cellulose thus obtained was packed into a jacketed column and hybridized with the radioactive total cellular RNA from posterior gland. The hybrid was eluted with thermal elution, and the radioactive RNA was tested for its T₁ fingerprint. The profile was characteristic of pure fibroin mRNA. The result indicates that, although the reverse transcript is composed of complementary

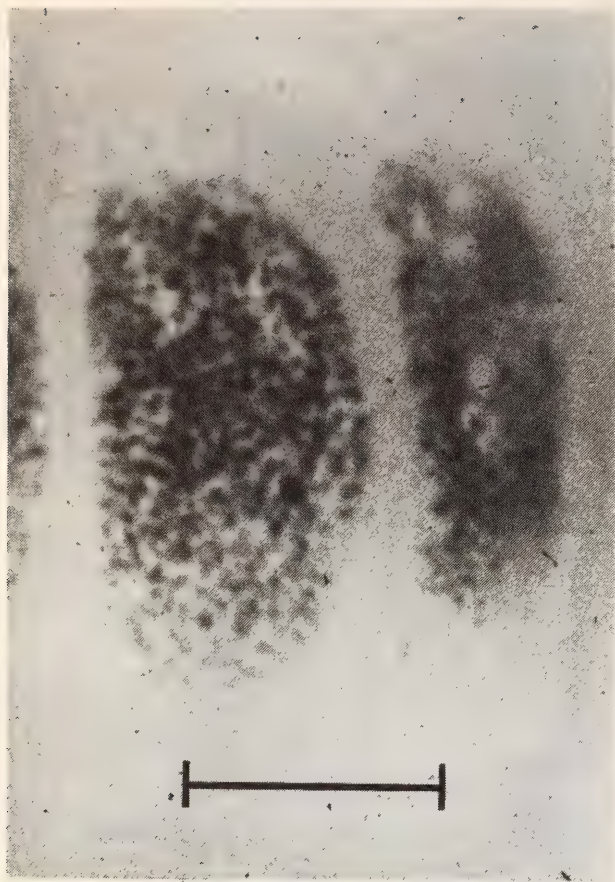


Fig. 23. Feulgen positive granules in silk-gland nuclei. Middle silk-gland nuclei of early first instar. The bar is 10 μ m.

distributed randomly in the nucleus in all stages and in the middle as well as the posterior silk gland. It is also known that thousands of nucleoli are distributed throughout the nucleus. We can now ask whether the fibroin genes can be detected on single granules at a frequency of 1 out of 28 granules, thereby providing definitive identification of the granules as individual chromosomes, because *B. mori* has 28 haploid chromosomes which are round and indistinguishable from each other. We know, too, that there is one fibroin gene per haploid complement. Thus, the following picture of chromosomal organization in the silk gland nucleus emerges. Multiple endomitotic replications of individual chromosomes are followed by random segregation of the replicated chromosomes, each individual chromosome maintaining its independence.

sequences of noncoding and coding regions to fibroin mRNA, a longer fibroin mRNA sequence than the cDNA has been trapped, and the cDNA column is useful for purifying fibroin mRNA.

It is known that fibroin genes bind more actinomycin D than the bulk of *B. mori* DNA and can be partially purified by actinomycin D/CsCl centrifugation. This technique has been employed for the quantification of fibroin genes and the structural analysis of the genes using purified fibroin mRNA as an assay probe. We have asked whether the total cellular RNA of the late fifth instar can be used for hybridization and whether the RNA recovered from the fibroin gene region is pure fibroin mRNA. The T₁ fingerprint of the RNA was identified as pure fibroin mRNA, indicating that the partially purified genes suffice to remove pure mRNA from the total cellular RNA. However, when the total cellular RNA of earlier stages of the fifth instar was employed, the fingerprint of the hybridization RNA showed some impurities, imposing limits on usefulness of the technique.

FIBROIN mRNA SYNTHESIS IN A PULSE-LABELED SILK GLAND

Y. Suzuki

It has been generally believed that in eukaryotes a specific single mRNA would be difficult to detect by direct chemical methods like base composition or sequence analysis. We wondered whether this generalization held for fibroin mRNA too; fibroin genes comprise only 0.002% of the *B. mori* genome, and, in fact, in our earliest studies fibroin mRNA was not detectable in pulse-labeled RNA, but was detectable only after several hours of incubation. However, the methods employed several years ago were sucrose gradient centrifugation of RNA and base composition analysis of the fractionated RNA, the sensitivity of which was not satisfactory.

The quantitative data listed in Tables

3 and 4 indicate that the number of fibroin mRNA molecules/gene accumulated by 6 days of the fifth instar is about four times that of rRNA molecules/gene; and that by 12 hours of labeling, mRNA synthesis is highly predominant, about 16 times greater than rRNA synthesis. These results suggest that the mRNA is more rapidly synthesized (and less stable) than rRNA and could possibly be detected by chemical methods in pulse-labeled materials. Therefore, using Bio-Gel column fractionation and sequence analysis (*Year Book* 73, p. 20), fibroin mRNA synthesis in a pulse-labeled material has been re-investigated. Posterior silk glands were labeled in vivo or in organ cultures in vitro with ³H-uridine or ³²PO₄³⁻ for 30 min, and the RNA was fractionated by Bio-Gel column (Fig. 24). The peak,

TABLE 3. The Posterior Silk Gland RNA Accumulated by 6 Days of the Fifth Instar

	Amount μg/Cell	Number of Molecules/ Cell*	Number of Molecules/ Gene†
rRNA	3.90	1.08×10^{12}	1.17×10^4
Fibroin mRNA	0.17	1.82×10^{10}	4.55×10^4

* Molecular weight of 28S plus 18S rRNA is about 2.2×10^6 , and that of fibroin mRNA is 5.7×10^6 .

† *B. mori* genome carries 230 rDNA genes and one fibroin gene per haploid set. The cell is about 4×10^5 -ploid.

TABLE 4. Predominant Synthesis of Fibroin mRNA over rRNA during Different Time Intervals in Late Fifth Instar

	Number of RNA Molecules/Gene	
	Number of rRNA Molecules/Gene	
	rRNA	Fibroin mRNA
30 min	1.0	>20
12 hr	1.0	15.9
6 days	1.0	3.9

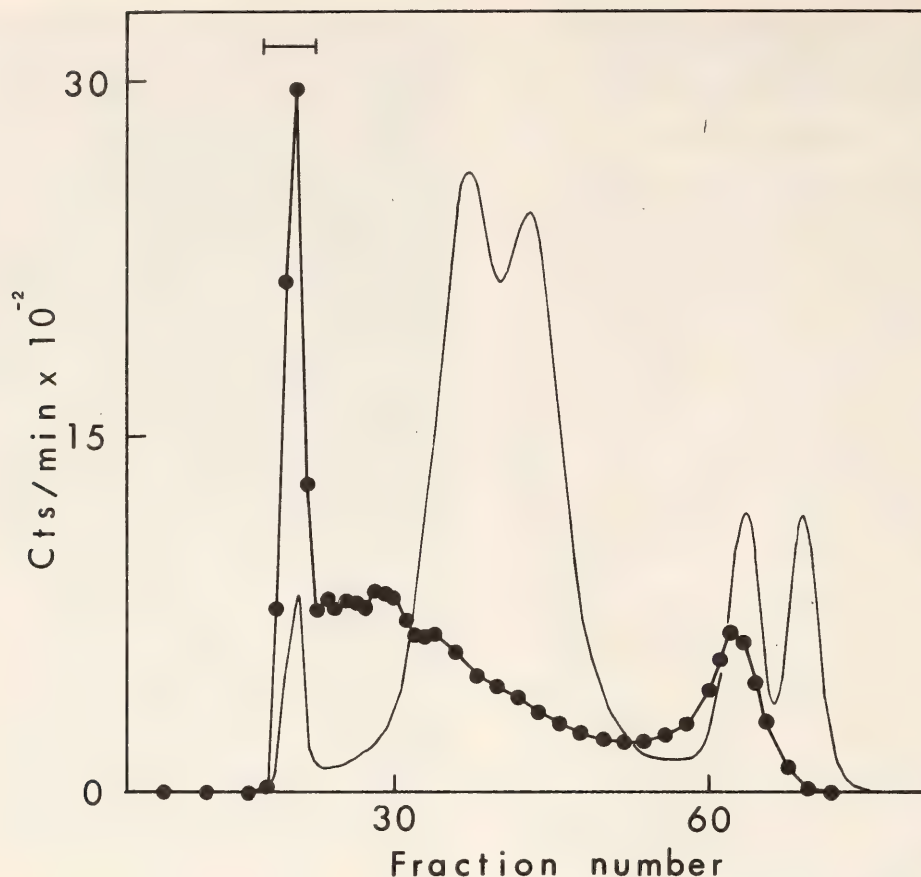


Fig. 24. Fractionation of RNA synthesized in the posterior silk gland in 30 min on a Bio-Gel A-50m column. Two pairs of posterior glands were dissected at 6 days of the fifth instar, and incubated with ^3H -uridine for 30 min at 26°C . RNA was extracted and applied to a Bio-Gel column (2.6×70 cm). A 0.3 ml aliquot out of each 5.4 ml fraction was taken and counted for its acid-insoluble counts. Circles, ^3H cts/min; solid line, A_{260} monitored by a Gilson spectrophotometer.

which appeared in the void volume of the column, had about 26% of the total radioactivity. This includes any recovered fibroin mRNA and any digested with RNase T_1 . The resulting oligonucleotides were fractionated on DEAE-Sephadex (Fig. 25). The oligonucleotide profile shown in Fig. 25 is characteristic of fibroin mRNA with some impurities. From the approximate purity and the fraction of radioactivity in the void volume peak of Fig. 24, it was calculated that fibroin mRNA synthesized during a 30 min pulse-labeling period comprises about 13% of the total radioactive transcripts. From these results we conclude that mRNA is more rapidly synthesized and is less stable than rRNA (Table 4), and that the regulatory factors for fibroin gene transcription reside in the posterior gland *per se* and not in the hemolymph.

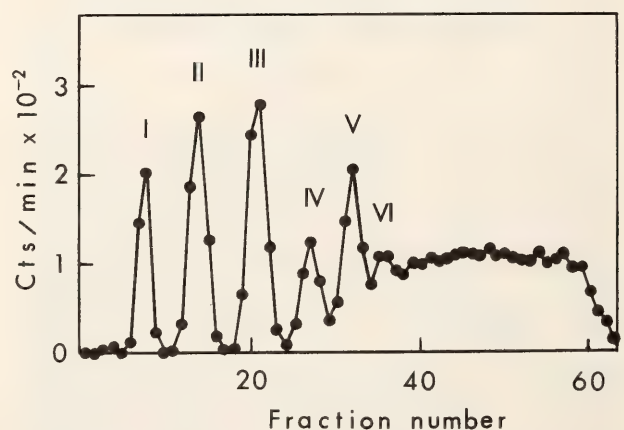


Fig. 25. RNase T_1 fingerprint of fibroin mRNA fraction from pulse labeled material. RNA was labeled *in vivo* with $^{32}\text{P}\text{O}_4^{3-}$ for 40 min, extracted, and fractionated by a Bio-Gel A-50m column. The void volume peak from the column like the one in Fig. 24 was recovered and digested with RNase T_1 , and the digest was fractionated on a DEAE-Sephadex A25 column (0.9×12 cm). Circles, ^{32}P cts/min; Roman numerals indicate the position of oligonucleotides by carrier RNA.

FIBROIN mRNA SYNTHESIS IN ISOLATED SILK GLAND NUCLEI

Y. Suzuki and P. Giza

Our morphological observations of nuclei suggested that third instar nuclei might be appropriate for the isolation of intact nuclei. After a few trials, we abandoned the idea because too little material was obtained to process further.

Gentle disruption of the silk gland cells from the fifth instar larvae has been unsuccessful.

Finally, the posterior silk glands from fifth instar larvae were homogenized with a Dounce loose-fitting homogenizer in the presence of 0.2% NP40, and cytoplasmic materials were eliminated by repeated centrifugations in the presence of NP40 and one centrifugation through 2.2 M sucrose. Typical examples of the nuclei isolated by this method are shown in Fig. 26. Although the originally convoluted and ramified nuclei (Fig. 22) have been fragmented, the fragmented nuclei maintain their integrity to a surprising extent, and even branched structures are seen (Fig. 26). Chemical analyses have revealed that DNA recovery is about 60%, and more than 95% of the cytoplasmic RNA is eliminated. In the isolated nuclei, the ratios of DNA, RNA, and protein are 1.0:1.5:4.6, indicating that both RNA and protein contents are higher than those in the nuclei of other organisms.

RNA synthesis was carried out with these isolated nuclei at 25°C, and the incorporation was linear for 30 min, gradually slowing, but still increasing even after 90 to 120 min. The RNA was extracted and fractionated on a Bio-Gel A-50 m column. Figure 27 shows both the radioactivity profile and cold RNA absorbance, which is mostly due to contaminating cytoplasmic RNA. Relatively high molecular weight RNAs were synthesized in vitro, and about 35% of the radioactivity resides in a region of greater than 28S rRNA. The cold RNA profile showed that there was little RNA degradation during incubation. The frac-



Fig. 26. Isolation of nuclear fragments from extremely ramified nuclei of posterior silk gland. The nuclear fragments were isolated from the posterior glands at 3 days of the fifth instar by the method described in the text, and stained by the Feulgen-Schiff reaction. Three typical examples of these are shown. The bar is 100 μ m.

tion in the void volume of Fig. 27 was recovered and analyzed for its RNase T₁ fingerprint. The profile was characteristic of very impure fibroin mRNA. The fraction was also hybridized to the act D/CsCl fractionated DNA, and the T₁ fingerprint of the RNA from the fibroin gene region was found to be characteristic of fibroin mRNA with some

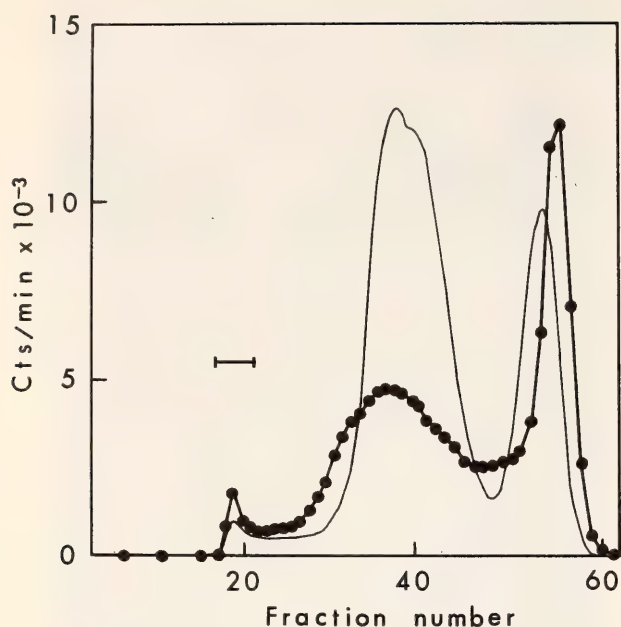


Fig. 27. Fractionation of RNA synthesized in isolated posterior silk gland nuclei on a Bio-Gel A-50m column. Nuclear fragments isolated from two pairs of posterior silk glands at 6 days of the fifth instar were incubated with ^3H -UTP for 30 min at 25°C . RNA was extracted, passed through a Sephadex G25 column, and applied to the Bio-Gel column (1.6×73 cm). A $25 \mu\text{l}$ aliquot out of each 2.7 ml fraction was taken and counted. Circles, ^3H cts/min; solid line, A_{260} monitored by a Gilson spectrophotometer.

impurities. These results demonstrate that *some* fibroin mRNA has been synthesized in fragmented nuclei. However, the amount is less than that observed

in pulse-labeling experiments *in vivo*. Therefore, the results suggest that we are losing regulatory factors *in vitro*. Our next objective is to recover them.

LOCALIZATION OF FIBROIN GENES IN SILK GLAND CELLS OF *Bombyx mori*

C. Thomas

Radioactive iodinated silk fibroin messenger RNA and ribosomal RNA have been used as probes to localize their genes in tissue sections of *Bombyx mori* by hybridization *in situ*.

Gene localization is made easier in silk gland cells by the polyploidization that occurs during larval development: At the end of the fifth instar, each nucleus in the posterior or the middle gland cells has about 0.5×10^6 haploid equivalents of DNA.

This study was undertaken to determine whether the location of a gene is related to its state of activity. Whereas ribosomal genes are active in all silk gland cells throughout larval life, the fibroin genes are active only in posterior silk gland cells during larval feeding stages.

The specificity of iodinated fibroin

mRNA as a probe for the gene was tested by hybridization with DNA that had been fractionated in an actinomycin-CsCl gradient.

In *Year Book 73*, p. 16, preliminary experiments suggested a preferential localization of fibroin genes in the posterior silk gland cells close to the nuclear membrane; ribosomal genes were randomly distributed throughout cells of the posterior and middle silk glands. The intracellular distribution of the fibroin genes was reconstructed by serial sections of posterior and middle silk gland cells from the second to the late fifth instar. Feeding and molting periods were also compared. *Whether fibroin genes were functioning (Fig. 28) or not (Fig. 29), they were distributed randomly throughout the nucleus and had no obvious association with any visible nuclear structure.*

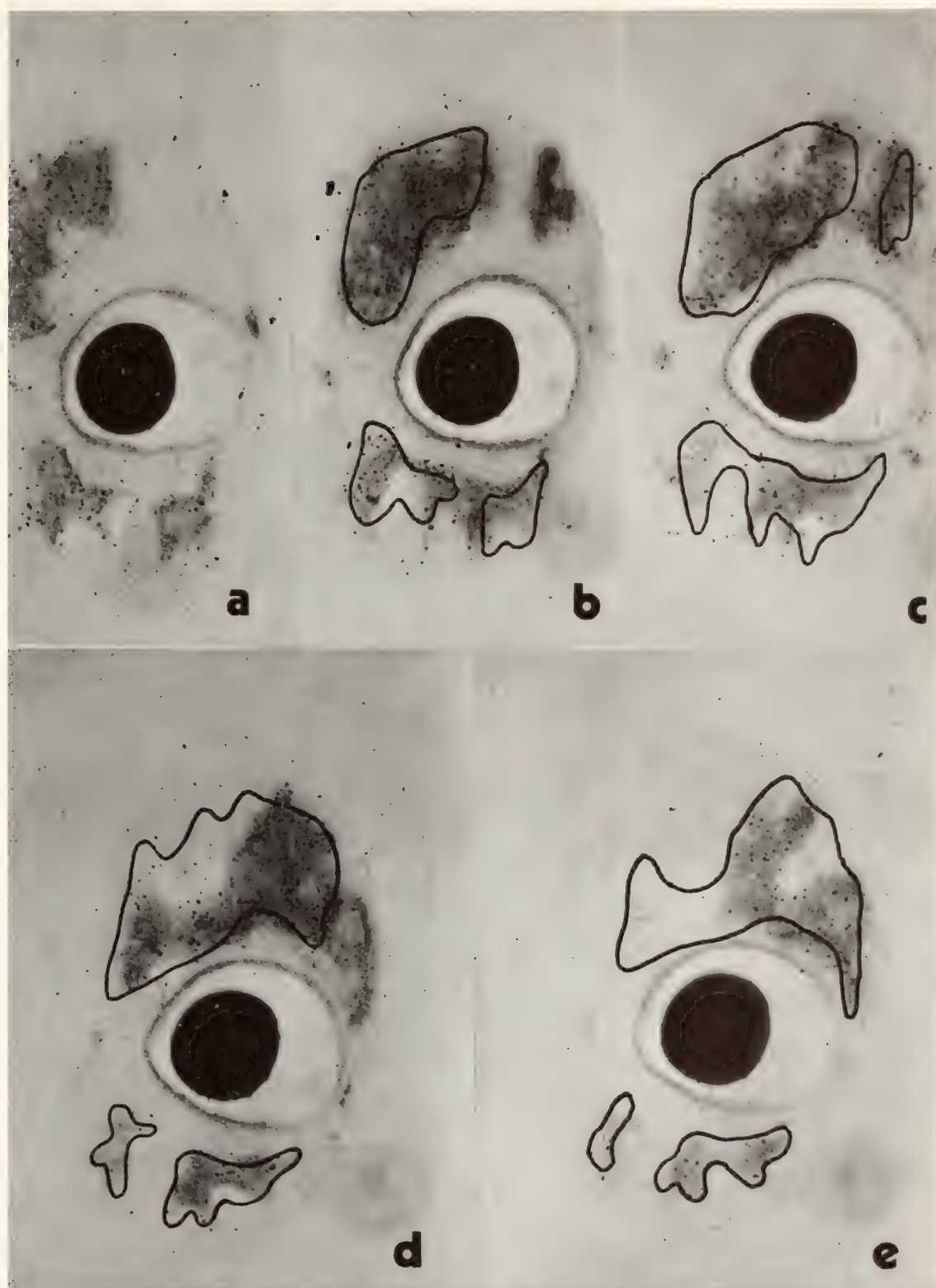


Fig. 28. Localization of fibroin genes in five serial sections of the posterior silk gland during the third instar. A complete nucleus is included within these sections; the nuclear outline of the preceding section is delineated in each section. Hybridization reaction included 0.1 $\mu\text{g/ml}$ ^{125}I -mRNA (3×10^7 cpm/ μg), 50 $\mu\text{g/ml}$ carcass RNA and 100 $\mu\text{g/ml}$ *E. coli* sRNA.

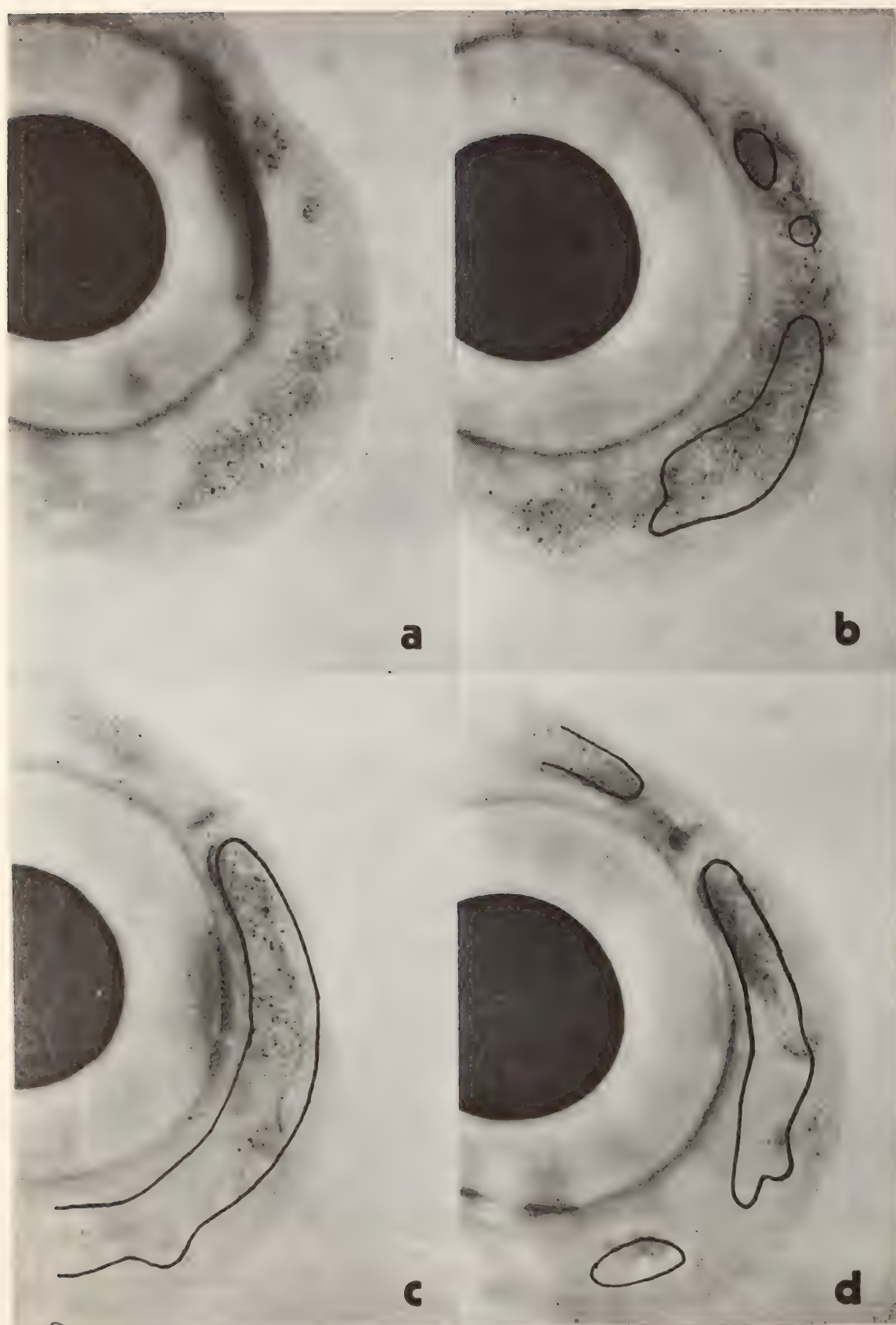


Fig. 29. Localization of fibroin genes in four serial sections of the middle silk gland during the third instar. A complete nucleus is included within these sections. Same conditions as for Fig. 28.

ATTEMPTS TO ISOLATE THE FIBROIN GENE OF *Bombyx mori*

J. Morrow

The goal of this project is the isolation of the silk fibroin gene and the DNA adjoining it in the silkworm genome. The approach is to purify DNA containing the fibroin gene from the rest of the DNA of *B. mori*. Subsequently the small amount of purified DNA will be replicated in *Escherichia coli* after covalent attachment to a bacterial plasmid.

Since the DNA encoding the structure of fibroin protein has a molecular weight of about 9×10^6 daltons, a larger fragment containing the gene must be isolated. The size chosen was 25×10^6 daltons. *Bombyx* DNA was sheared to this size by stirring at a constant speed.

The DNA molecules containing the fibroin gene were then separated from most other DNA by actinomycin D-CsCl equilibrium centrifugation (*Year Book* 73, p. 15). Three successive gradient separations gave a 27-fold purification of the gene with 33% yield. Purification was assayed by hybridization of the DNA to radioactive fibroin messenger RNA. The results indicated that little more could be achieved by further repetition of the actinomycin D-CsCl banding. Other gradients do not appear promising for isolation of this gene. At this molecular weight, the fragments containing the gene are not separated from the main band of *Bombyx* DNA in Ag^+ - Cs_2SO_4 gradients. Previous work showed that the same should be true of Hg^{2+} - Cs_2SO_4 gradients.

The *Bombyx* DNA and plasmid DNA must have complementary termini in order to be joined to form a recombinant plasmid. Complementary termini are formed by cleavage of DNA with some restriction enzymes (sequence-specific endonucleases found in bacteria). For this and other reasons, digestion of the fibroin gene and environs by several restriction enzymes was studied.

Total *Bombyx* DNA of molecular weight 60×10^6 was digested by an excess of a particular enzyme. The DNA was then fractionated on a gradient, and the fibroin gene fragments were located by hybridization to radioactive fibroin mRNA. The rate of sedimentation in a sucrose gradient, relative to a marker of known molecular weight, was used as a measure of the molecular weight of the gene fragments. The amount of neighboring DNA still joined to the gene was estimated from its equilibrium buoyant density in an actinomycin D-CsCl gradient.

The results indicate that the average molecular weight of gene fragments was $7-8 \times 10^6$ after Hind III digestion and that they contained a small amount of neighboring DNA. It is probable that the Hind III enzyme either does not cleave at any of the sites or else cleaves at one site within the gene and near the ends of the gene. After EcoRI digestion, the gene fragments had an average molecular weight of roughly 15×10^6 and retained a large amount of neighboring DNA. Tentatively we conclude that this enzyme cleaves once within the gene but not within a considerable distance outside the gene. Results of similar experiments indicate that the Hind II enzyme cleaves near the ends of the gene but not within it.

Isolation of the Hind III gene fragments would not provide the desired neighboring DNA sequences. The EcoRI gene fragments are also unsuitable for isolation for two reasons. Their buoyant density in actinomycin D-CsCl does not permit extensive purification from other *Bombyx* DNA. Their large molecular weight suggests that it would be difficult or impossible to join them to plasmid DNA through EcoRI cohesive ends because of the low probability of cycliza-

tion of large DNA molecules. This problem may be overcome by use of longer cohesive termini.

After 27-fold purification of the fibroin gene by actinomycin D–CsCl gradients, one DNA molecule in every 400 contains the fibroin gene. Present work is directed toward joining this partly purified DNA

to a bacterial plasmid through synthetic poly dA and poly dT termini. These termini can be polymerized on the respective DNAs by the enzyme, terminal transferase. Isolation of the gene will then consist of finding the occasional recombinant clone containing the fibroin gene.

BIOGENESIS OF MITOCHONDRIA

I. B. Dawid, C. Kaushagen, J. L. Ramirez, S. Ohi, and W. B. Upholt

Our work has been centered on the physical mapping of the mitochondrial DNA molecule (mtDNA). In all metazoan animals this DNA is a circular molecule with a molecular weight between 10 and 12×10^6 . Some of the functions of mtDNA have been elucidated: This DNA codes for one large and one small mitochondrial ribosomal RNA molecule (rRNA) which, together with a number of proteins, form the distinct mitochondrial ribosome. In addition, mtDNA codes for several smaller (4S) RNAs, most, if not all, of which are transfer RNAs (tRNAs) and are involved in mitochondrial protein synthesis. Together, rRNA and tRNA sites occupy about 20% to 25% of the mtDNA molecule. The remaining parts of the mtDNA may code for messenger RNAs for mitochondrial proteins. A site of particular interest in mtDNA is the origin of replication. This site may be visualized in the electron microscope as a displacement loop (D-loop), in which a short third strand of DNA is duplexed with one of the parent strands, displacing the other strand (see Kasamatsu and Vinograd, *Annual Review of Biochemistry*, 43, 695, 1974). This D-loop structure provides a convenient reference point in mapping studies.

Some technical approaches of particular value to mapping experiments have been pursued (*Year Book 73*, p. 47), in particular the use of bacterial restriction endonucleases and the covalent attachment of ferritin to 4S RNA for the

visualization of 4S RNA/DNA complexes in the electron microscope.

MAPPING STUDIES ON MITOCHONDRIAL DNA OF *Xenopus laevis* AND *Xenopus mulleri*

J. L. Ramirez

Here the primary approach involves the use of restriction endonucleases to provide reference points for the mapping of mitochondrial genes and for the origin of replication in the mitochondrial DNA. It is known that EcoRI makes two and three cuts in *X. laevis* and *X. mulleri* mtDNA, respectively. (*Year Book 73*, p. 51). The two *X. laevis* fragments constitute 87% and 13%, and the three *X. mulleri* fragments are 43%, 39%, and 17% of their respective genomes.

Endonuclease I from *Serratia marcescens* (Sma I) makes a single cut in *X. mulleri* mtDNA and none in mtDNA of *X. laevis*, or in any other of seven animal mtDNAs tested.

The position of the D-loop (which marks the replication origin) with respect to the restriction sites was determined by electron microscopy. DNA samples were fixed with glyoxal, which blocks branch migration of the D-loop in the fragments; then they were fully or partially digested with restriction endonucleases, and examined by electron microscopy. Maps obtained for the two mtDNAs are shown in Fig. 30 a and b. In *X. laevis* (Fig. 30a) EcoRI makes one of its two cuts within the D-loop,

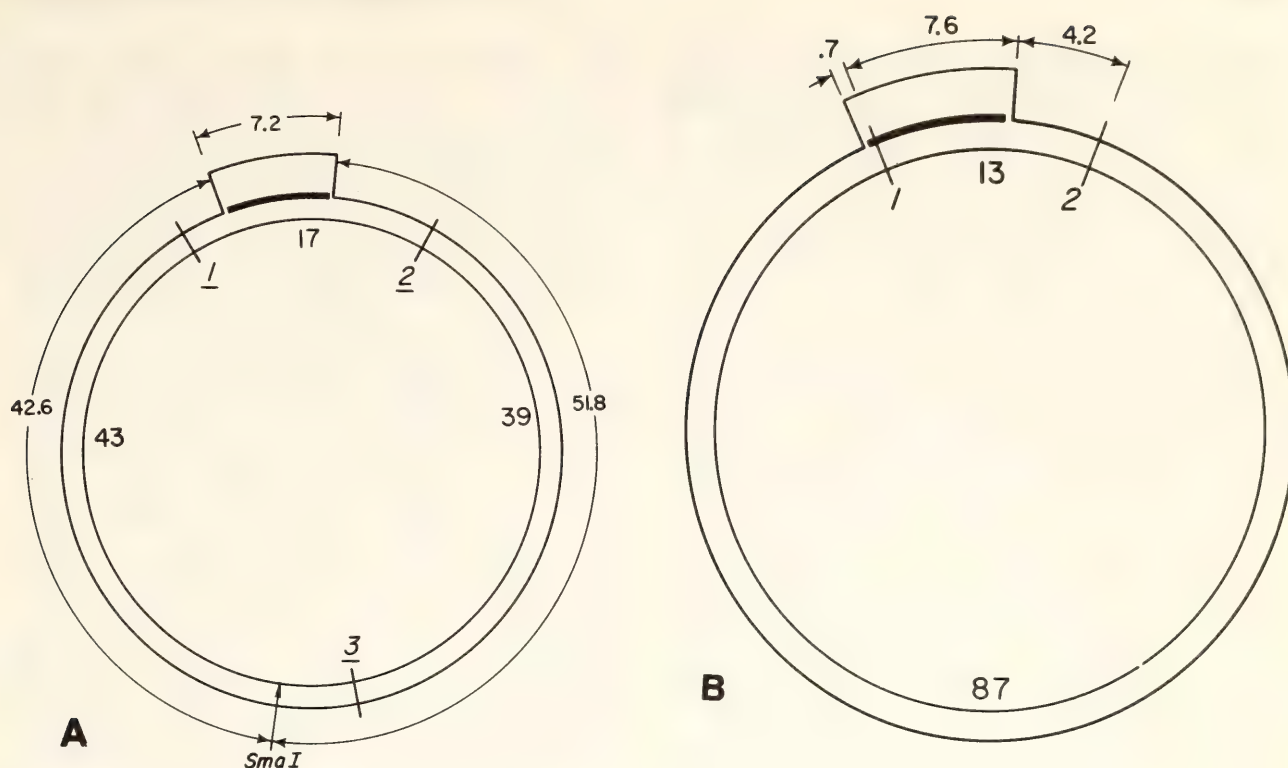


Fig. 30. Physical maps of mtDNAs; (a) *X. laevis*, (b) *X. mulleri*. EcoRI sites are represented by underlined numbers. The different regions are expressed as percent of the length of the total genomes. The distance from EcoRI site 3 to the *Sma* I site is 5.3% of genome length. The D-loop is schematically drawn at the top of each map, with the displacement strand shown as a thick line.

producing "H-forms." These forms consist of the two EcoRI double-stranded fragments bound together by the single-strand part of the D-loop.

In *X. mulleri* mtDNA the D-loop was mapped first in relation to the single *Sma* I site (Fig. 30b). Next, the D-loop was located in an EcoRI digest and found in the smallest fragment (17% fragment). Gel electrophoretic analysis showed that the *Sma* I site is within the largest EcoRI fragment (43% fragment). From these observations the three EcoRI sites, the *Sma* I site, and the D-loop could be oriented with respect to each other (Fig. 30b). This map was confirmed by our analysis of D-loop containing mtDNA fragments derived by partial digestion with EcoRI.

PHYSICAL MAPPING OF 4S RNA GENES ON MITOCHONDRIAL DNA

S. Ohi and I. B. Dawid

We have continued to work toward the physical mapping of 4S RNA genes

on mitochondrial DNA. Most, if not all, of the mitochondrial 4S RNA molecules are tRNAs which are specific for the mitochondrial protein-synthesizing system. Since the visualization of tRNA in a hybrid with DNA depends on the tagging of the tRNA with a bulky component like ferritin, we reported last year an effort to link covalently tRNA to ferritin through an RNA-Hg-S-ferritin bond (*Year Book* 73, p. 49). Although we observed effective coupling, the complex formed was not stable enough to permit further work; a model complex, tRNA-Hg-S-BI-lysine, degraded exponentially, the half-life being about 18 hr at 4°C.

An alternative method to covalently link tRNA to ferritin has been reported by Wu and Davidson (*Journal of Molecular Biology*, 78, 1, 1973), and we have successfully reproduced their method. The method makes use of the Schiff base reaction; tRNA 3'-dialdehyde generated by NaIO_4 oxidation is reacted with epsilon- NH_2 groups of lysine in ferritin and the conjugate is sub-

sequently stabilized by NaBH_4 reduction. The purified complex was stable over several months under storage at -20°C .

Having the adduct in hand, we then moved to the mapping of 4S RNA genes on *Xenopus laevis* mtDNA. Purified H-strand prepared by the poly(IG) method was hybridized with the small and large rRNAs together with ferritin-coupled 4S RNAs (fer-4S RNA). Excess ferritin and fer-4S RNA were removed by electrophoresis on a 3% agarose gel. In another experiment, the sample was simply diluted to reduce the background. Two heteroduplex molecules with interpretive tracings are shown in Fig. 31. The position of fer-4S RNAs is presently being mapped relative to the positions of the small and large rRNA duplex regions. It is already apparent that one of the 4S RNA genes is located between the small and large rRNA genes (see Fig. 31a). Similar observations have been reported by Wu, Davidson, Attardi, and Aloni in HeLa cells (*Journal of Molecular Biology*, 71, 81-93, 1972). The mapping on the L-strand will be carried out in reference to the specific cutting site of the EcoRI restriction enzyme.

A COMPARATIVE STUDY OF THE MITOCHONDRIAL GENOMES OF THE SHEEP AND THE GOAT

W. B. Upholt

Several aspects of the mitochondrial genetic system can be studied by comparing closely related mtDNAs. These include the mechanisms of the maintenance of the genetic information during evolution of a genome which is present in many identical copies, the correlation of the rate of nucleotide change of specific sequences with the function of the sequences, and the role of nucleotide sequence and secondary structure in the control of expression and replication of mtDNA.

Previous studies of mtDNA evolution in *X. laevis* and *X. mulleri* have shown

that about 20% to 30% of the mitochondrial genome, apparently that coding for the mitochondrial ribosomal and transfer RNAs, is the most highly conserved portion. The remainder of the mitochondrial genome has diverged considerably more rapidly (*Year Book* 70, p. 44). To compare these more rapidly diverging regions in some detail, more closely related species are needed which have homologies in this region but which show measurable differences as well. After a comparison of published data for the relatedness of the nuclear genome of different species and preliminary comparisons of different mtDNAs (see *Year Book* 71, pp. 22-24), the goat and the sheep were selected for further studies. Preliminary RNA-DNA hybridization experiments suggested that sheep and goat mtDNAs are more closely related than those of *X. laevis* and *X. mulleri* or of mouse and rat, but less related than the mtDNAs of subspecies of the mouse (*Year Book* 71, pp. 22-24).

Goat and sheep mtDNAs were compared by an analysis of the fragments obtained after digestion with several restriction endonucleases. EcoRI, which recognizes a sequence of six bases, gives five fragments with goat mtDNA and three with the sheep mtDNA. Two of the sheep fragments co-migrate with two of the goat fragments in agarose gels, indicating that three EcoRI sites in sheep and goat mtDNAs occur at identical sites. This was confirmed by mapping the order of the fragments as described below. When these two mtDNAs were digested with Hind III restriction endonuclease, which recognizes a different six-nucleotide sequence, two sites out of four were in common. Hae III endonuclease, which recognizes a tetranucleotide sequence, yielded 41 fragments larger than 200 nucleotide pairs; 13 of these appeared identical in sheep and goat mtDNA. The frequency of occurrence of common fragments in digests of these mtDNAs by these restriction enzymes is consistent with approximately 10% se-

quence divergence between sheep and goat mtDNAs.

The order of the EcoRI fragment in goat and sheep mtDNA (Fig. 32) has been mapped by electron microscopy according to the following procedure. Goat mtDNA was digested with EcoRI, and the mixture of five fragments was denatured and annealed with denatured, intact (singly nicked) sheep mtDNA. Heteroduplex molecules were formed between one circular strand of sheep mtDNA and between one to five goat fragments. Double-stranded regions could be distinguished from single-stranded regions of DNA in the electron micrographs. The order of the goat fragments could be determined from heteroduplex molecules in which two to four of the goat fragments were present. Since every goat EcoRI fragment has a distinct size, each duplex region could be assigned to one or to a combination of several of these fragments. The single small region of lowest homology between sheep and goat mtDNA (see below) was helpful as an additional reference point. This approach, with modifications, can be used to map the order of restriction fragments in their parent molecule.

Replication of most mtDNAs begins at a specific site (the D-loop) by the unidirectional extension of a short displacement fragment. In the sheep mtDNA, the D-loop was found in approximately 30% of the closed, circular mtDNA molecules; it was 4.4% of the mitochondrial genome in length. The position of the D-loop was measured with respect to EcoRI site 1 (Fig. 32).

Sequence homology between sheep and goat mtDNA was studied by heteroduplex mapping in the electron microscope. Regions of low homology are visualized as single-stranded loops, and homologous regions form duplex DNA. The degree of homology required for the formation of a stable duplex depends on the concentration of formamide and salt in the spreading solution. When spread from 50% formamide, sheep-goat mtDNA

heteroduplex molecules show a single heterology loop which is 1.7% of the mitochondrial genome in length. The location of this loop was mapped relative to the EcoRI sites, and in this way relative to the D-loop. As shown in Fig. 33, the heterology region overlaps one end of the D-loop. When the spreading was carried out in the presence of 60% formamide, the original heterology loop increased in length, and a second loop formed which appeared to overlap the other end of the D-loop. These observations show that the most rapidly diverging regions in sheep and goat mtDNA overlap, or at least are very close to, the two ends of the D-loop.

The sequence divergence between sheep and goat mtDNAs is at a low but easily measurable level, indicating that further comparative studies of these DNAs should provide interesting information on the functional organization and evolution of mammalian mtDNA.

MITOCHONDRIAL DNA AND RNA IN *Drosophila* *C. Kaushagen*

The characterization of mitochondrial ribosomal RNA (mt-rRNA) from *Drosophila melanogaster* (Year Book 72, p. 43) has been continued. Base composition analysis was performed on ^{32}P mt-rRNA prepared from Schneider's cultured *Drosophila melanogaster* embryonic cell line no. 2, grown in medium supplemented with $^{32}\text{PO}_4$. The ^{32}P RNA was purified on a sucrose-SDS gradient and then run on 5% acrylamide gels in 98% formamide. These gels were sliced, counted, and the ^{32}P RNA was eluted. Aliquots of this RNA were hydrolyzed overnight in 0.3 N NaOH at 37°C. The four nucleotides were separated by high voltage paper electrophoresis, and the percentage of radioactivity in each nucleotide was determined. The remaining ^{32}P mt-RNA eluted from formamide gels was run on aqueous 2.4% acrylamide gels, eluted, and also analyzed for base composition. Since these values were

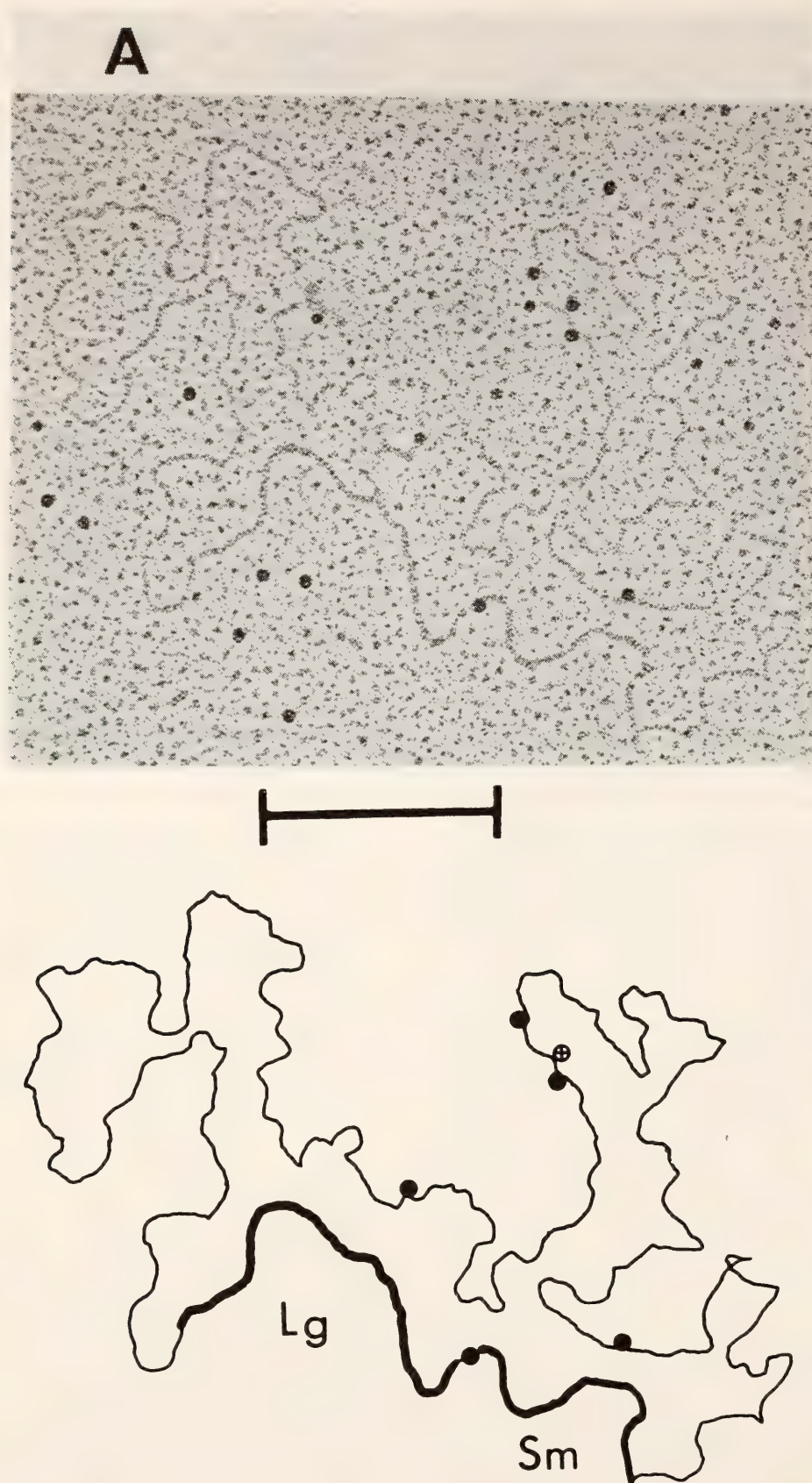
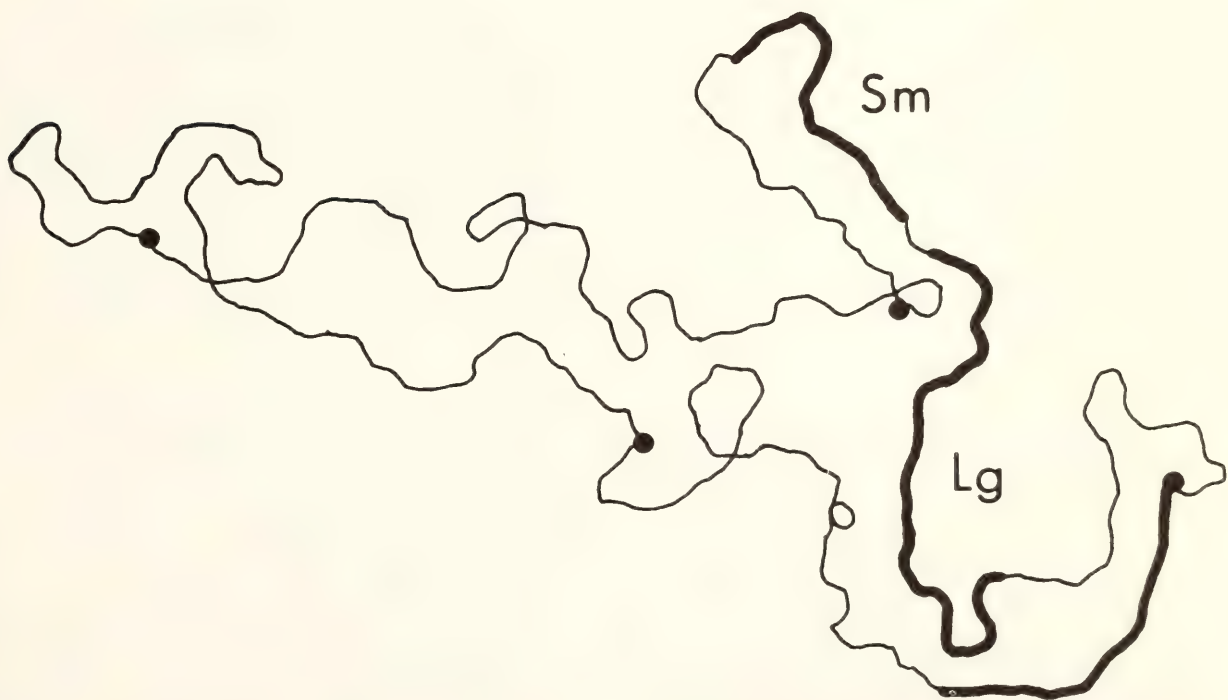
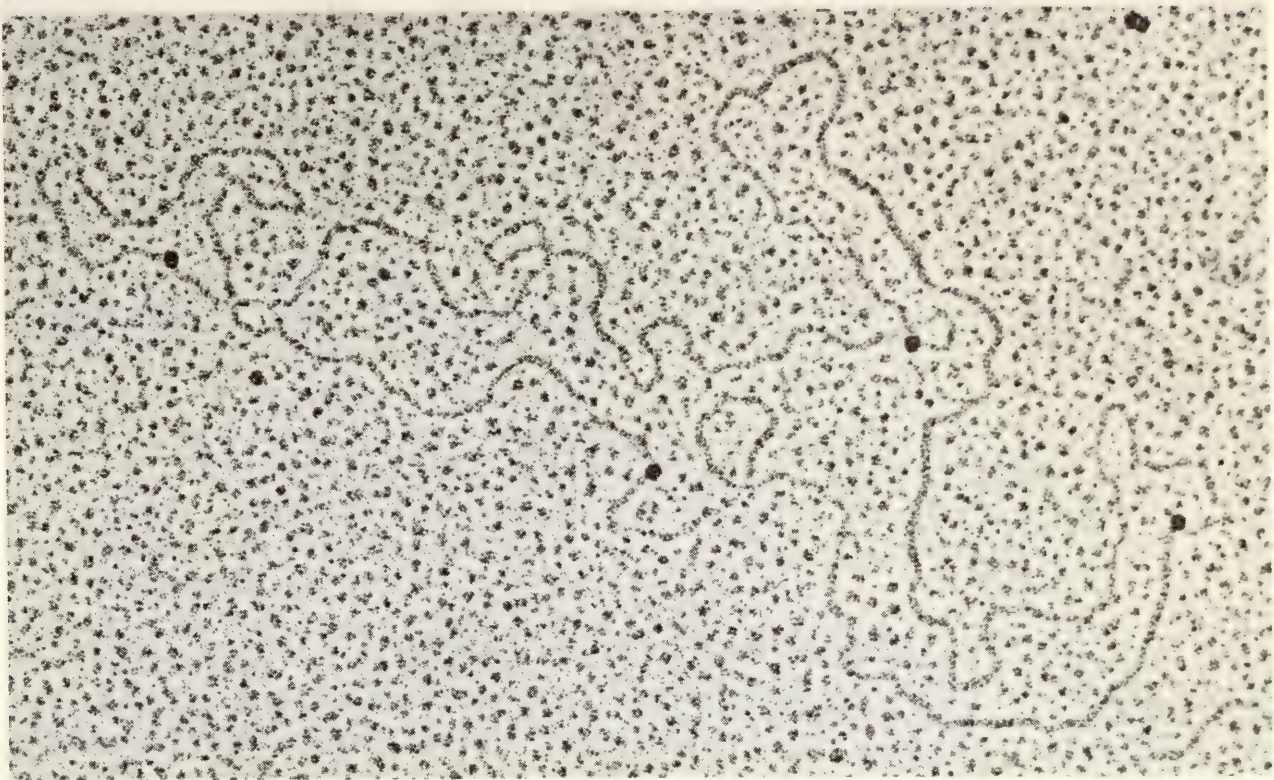


Fig. 31. Electron microgram and interpretive tracing of heteroduplexes formed by hybridization between mitochondrial fer-4S RNA, small and large rRNAs, and the H-strand of *X. laevis* mtDNA. Hybridization was carried out at 37°C in the presence of 40% formamide for 2 hr at $[Na^+] = 0.5 M$. The concentration of each component during the incubation was as follows: DNA = 2 $\mu g/ml$, fer-4S RNA = 40 $\mu g/ml$, small rRNA = 2 $\mu g/ml$, large rRNA

B



$= 4 \mu\text{g/ml}$. The duplex regions between mtDNA and the large (Lg) and small (Sm) rRNAs are indicated. Closed circles indicate ferritin-4S RNA hybrids with the DNA, and open circles are probable fer-4S RNA/DNA hybrids. Ferritin background was reduced (A) by dilution, and (B) by gel-electrophoresis. Bar equals 0.5×10^6 dalton double-stranded molecular weight.

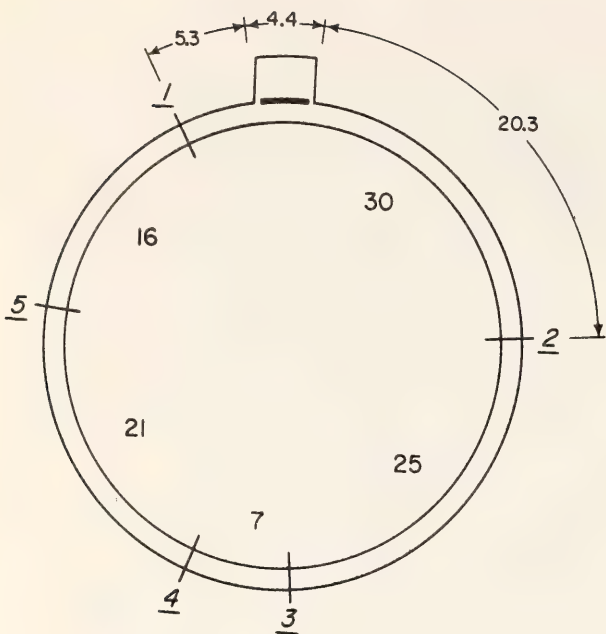


Fig. 32. Composite map of EcoRI sites of the goat and sheep mtDNAs. Underlined numbers (1-5) show the positions of the EcoRI sites in goat mtDNA. The sheep mtDNA is cut by EcoRI at sites 1, 4 and 5. Numbers inside the map show the percent of the entire goat genome in each of the goat fragments. At the top of the map, the sheep D-loop is represented and its position with respect to the EcoRI cut 1 is shown.

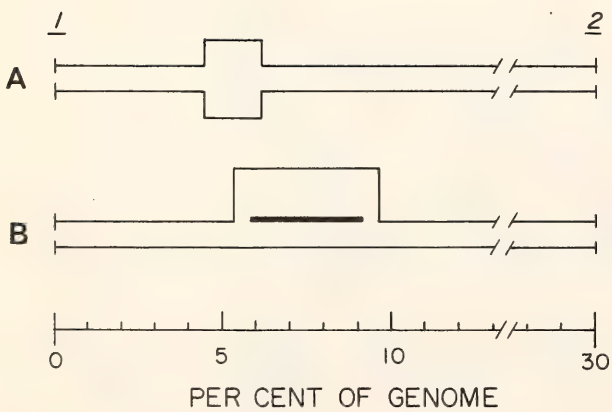


Fig. 33. Positions of D-loop and region of lowest homology (heterology loop) between the sheep and goat mtDNAs in reference to EcoRI sites 1 and 2 in goat mtDNA. (A) diagrammatic representation of the position and size of the heterology loop; (B) diagrammatic representation of the position of the sheep D-loop.

nearly identical to those determined for the RNA eluted from the formamide gels, the ^{32}P mt-rRNAs were considered homogeneous, and the base composition data were averaged (Table 5).

The composition of these rRNAs is quite unusual in that it is lower in its content of guanylic and cytidylic acids (GC) than any other rRNA from mitochondria or any other source studied previously. This result is interesting in two ways. First, the low GC content correlates with the unusual behavior of the *Drosophila* mt-rRNAs during gel electrophoresis (see *Year Book* 72, p. 43). Second, there is a correlation between GC content of cytoplasmic and mitochondrial rRNAs in *Drosophila*. *Drosophila* cytoplasmic rRNAs have a GC content of about 40% which is considerably lower than that of most other metazoan animals. The mt-rRNAs in other animals have a GC content of about 40%, i.e., lower than the cytoplasmic rRNAs in the same animals and similar to *Drosophila* cytoplasmic rRNA. In *Drosophila*, the mt-rRNAs have an even lower GC content, and the difference in composition between cytoplasmic and mitochondrial rRNAs is maintained. It will be interesting to look for a functional or evolutionary basis for these relations.

In preparation for mapping these mt-rRNAs on the mtDNA of *D. melanogaster*, closed-circular mtDNA was prepared from embryos by ethidium bromide-CsCl gradients. Open-circular mtDNA was prepared from this material by singly nicking it with DNase. Denaturation maps of nicked mtDNA were generated in an effort to establish one reference point on the circular DNA molecule. Denaturation was accomplished by incubation at high pH in the presence of 12.5% formaldehyde and 25 mM EDTA. The solution was then neutralized and spread for electron microscopy. Denaturations performed at several pH's revealed that one region representing about 25% of the molecule denatures completely even at the lowest pH where

TABLE 5. Nucleotide Composition of Large and Small mt-rRNAs of *Drosophila melanogaster* (mole percent of nucleotides, mean \pm standard deviation)

RNA	N	Cytidylic Acid	Adenylic Acid	Guanylic Acid	Uridylic Acid	% G + C
Lg	3	7.0 \pm 0.2	40.5 \pm 1.2	10.8 \pm 0.1	41.8 \pm 1.0	17.7 \pm 0.2
Sm	4	8.4 \pm 0.7	40.0 \pm 0.9	12.7 \pm 0.4	39.1 \pm 1.2	21.0 \pm 0.4
28S	5	17.5 \pm 0.3	29.9 \pm 0.9	22.1 \pm 1.1	30.5 \pm 0.7	37.5 \pm 1.2
18S	5	18.4 \pm 0.7	28.6 \pm 0.2	23.4 \pm 0.8	29.5 \pm 0.6	42.0 \pm 0.6

Lg and Sm refer to the large and small mitochondrial rRNAs (see *Year Book* 72, p. 43), and 28S and 18S are the cytoplasmic rRNAs. The base composition determined for the cytoplasmic rRNAs are similar to those reported previously from several other laboratories.

TABLE 6. Extent of Denaturation of *D. melanogaster* mtDNA at Various pH's (Mean \pm standard deviation)

pH	Number of Molecules Measured	Percent of Length in Single-Stranded Regions	Percent of Length in Largest Denaturation Bubble
10.6	20	32.1 \pm 2.5	26.4 \pm 1.7
10.75	12	44.5 \pm 7.1	25.4 \pm 2.5
10.9	14	57.3 \pm 5.7	28.2 \pm 4.1
11.05	100

any denaturation occurs. This region remains the same length even at pH's where up to 60% of the molecule is denatured in other regions (Table 6). This one large denaturation "bubble" will be used as a reference point for mapping the mt-rRNAs.

Drosophila mtDNA has also been cut

with Hind III and EcoRI restriction endonucleases, yielding three and four fragments, respectively. The molecular weights of the Hind III fragments were determined in the electron microscope; they are 5.24, 3.60, and 3.01×10^6 . An analysis of partially denatured restriction fragments is currently under way.

PHOSPHOLIPID-CHOLESTEROL DYNAMICS IN MAMMALIAN CELLS

R. E. Pagano, L. Huang, M. Takeichi, and K. Ozato
with the technical assistance of E. Asch, D. Somerville, and W. Duncan

The investigations being carried out in this laboratory are concerned with the dynamic movements cellular phospholipids and cholesterol can undergo in the membranes of mammalian cells and the effects perturbations in these motions can have on cellular activity. The basic premise of these studies is that these

membrane components are not merely static structural elements of cells, but rather because of their ability to undergo dynamic movements, both within single cells and between contiguous cells, they are candidates for control mechanisms which participate in the regulation of cell growth and differentiation.

To test the relation between membrane lipid dynamics and biological functions of cells, one needs, first, information about the spatial distribution of cell surface lipid components (and cholesterol). Taking advantage of some of the properties of vesicle-cell interactions described below (see also *Year Book 73*, p. 52) and the technique of high resolution electron microscopic autoradiography, we have begun to determine the surface distribution of one lipid component, phosphatidyl choline, on cultured Chinese hamster fibroblastic cells.

If cell lipids and cholesterol levels can in some way regulate cellular activity, then a static picture of the patterns of distribution of various lipid components over cell surfaces is only a first step in understanding the mechanism. A second essential step is to learn if, and how, these membrane components can move between cells, and whether such movements result in significant compositional changes in the surface membrane of a given cell. Finally, it will be necessary to delineate the possible effects which alterations in the composition of cell surface lipids can have on regulating cellular activity. For this purpose we have chosen to investigate the effects of cell surface lipid perturbations on lymphocyte activation.

Details of our studies on each of these topics are presented in separate sections which follow.

INTERACTIONS OF PHOSPHOLIPID VESICLES WITH MAMMALIAN CELLS

Studies of Mechanism

*R. E. Pagano and L. Huang
with the assistance of E. Asch*

The use of artificially generated lipid vesicles (liposomes or phospholipid dispersions) has recently been reported by several laboratories for producing a variety of modifications in the physiology of mammalian cells. These include the use of vesicles as carriers to cells of entrapped materials, promoting agents

for cell fusion, and as tools for modifying the lipid composition of the membranes of intact cells. The possible molecular mechanisms by which lipid vesicles produce their varied effects, however, have not been fully determined. Furthermore, many of the studies have been complicated by factors which make mechanistic interpretations difficult if not impossible. For example, some studies on drug entrapment have been carried out in whole animals or in serum-containing medium—conditions which could favor the reorganization of the lipid vesicles into other structures. Others have utilized lipid vesicles prepared by mechanical dispersion of a mixed lipid system in an aqueous phase—a technique which is known to produce a heterogeneous collection of multicompartmented structures of widely varying size and shape.

In *Year Book 73*, p. 52, we presented our observations on the characteristics of the uptake of phospholipid by cultured Chinese hamster V79 cells upon incubation in a simple, balanced salt solution, with chemically and physically well-defined unilamellar lipid vesicles. In that report, detailed studies on the mechanism of this uptake were presented, which demonstrated that the major pathway of lipid uptake by these cultured cells at 37°C is a vesicle-cell fusion mechanism. In the present study, we show that an additional pathway, lipid exchange, may account for the remaining lipid uptake.

Chinese hamster V79 cells were grown in roller bottles in a culture medium containing radio-labeled palmitic acid. This method effectively labels the cellular glycerolipids and phospholipids with tritium. After a sufficient growth period the monolayer of cultured cells was washed extensively with Gey's solution and incubated for one hour at 37°C with ^{14}C -DOL (0.05 $\mu\text{Ci}/\text{mg}$) unilamellar vesicles (1 mg phospholipid/ml Gey's). Following this incubation, the supernatant was removed and briefly centrifuged to remove any whole cells or frag-

ments which were detached from the roller bottles during the course of the incubation. The supernatant from this centrifugation was then concentrated to a small final volume on an Amicon ultrafiltration device. The concentrated suspension was then applied to a Sepharose 4B column and the effluent monitored by absorbance measurements at 280 nm, and determinations of ^{14}C -cpm and ^3H -cpm.

In Fig. 34, the elution profile of the unilamellar vesicle fraction prior to interaction with cells is shown. It is seen to consist of a broad symmetrical peak, both in absorbance and in ^{14}C -cpm, centered about fraction number 36. Fig. 35 shows the profiles of absorbance at 280 nm, ^3H -cpm and ^{14}C -cpm for a suspension of ^{14}C -DOL vesicles following interaction with the ^3H -labeled cells. The profile of absorbance consists of four distinct peaks. The first peak, corresponding to the column void volume, represents a material of high molecular weight ($\pm 20 \times 10^6$ daltons), e.g., cellular fragments or lipoprotein aggregates,

which were not removed from the vesicle suspension by low-speed centrifugation. The second peak, centered about fraction 36, represents the unilamellar lipid vesicles. Both peaks are seen to contain ^3H -cpm and ^{14}C -cpm. The remaining two peaks of absorbance have no detectable amounts of radioactivity associated with them and probably correspond to soluble proteins. In the control experiment in which the lecithin vesicles were not incubated directly with the cells but rather with a simple salt solution that had been in contact with the ^3H -labeled cells, a similar profile of absorbance vs. fraction number was obtained (Fig. 36). The first two major peaks are again seen to contain both ^3H and ^{14}C , but the relative amounts are considerably different from those given in Fig. 35. Qualitatively similar results to those presented in Figures 34–36 were also obtained with cells whose lipids were radio-labeled by growth on $2\text{-}^3\text{H}$ -glycerol.

Fractions 35–48 from the column represented by the profile in Fig. 35 were

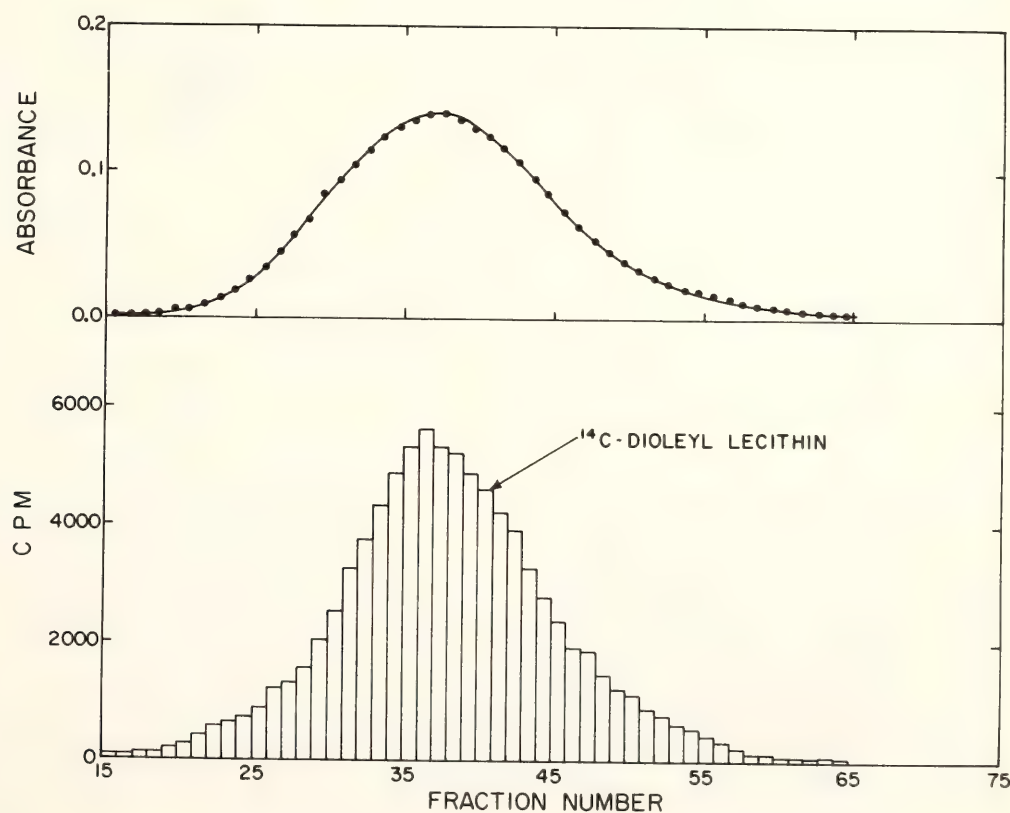


Fig. 34. Elution profile of unilamellar fraction of ^{14}C -DOL vesicles chromatographed on Sepharose 4B (2.5×40 cm). Absorbance at 280 nm, and ^{14}C -cpm vs. fraction number.

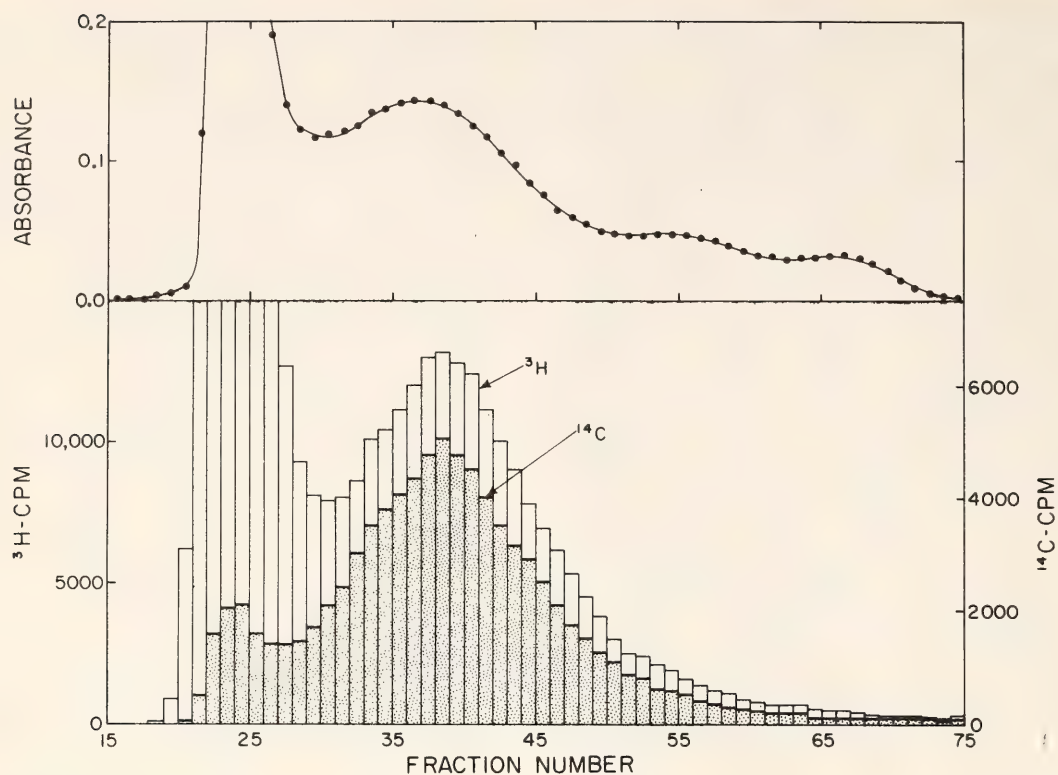


Fig. 35. Elution profile of unilamellar ^{14}C -DOL vesicles following a 1 hr incubation at 37°C with Chinese hamster V79 cells. Cell lipids were labeled with ^3H by growth on ^3H -palmitic acid. Absorbance at 280 nm, ^3H -cpm, and ^{14}C -cpm are plotted vs. fraction number.

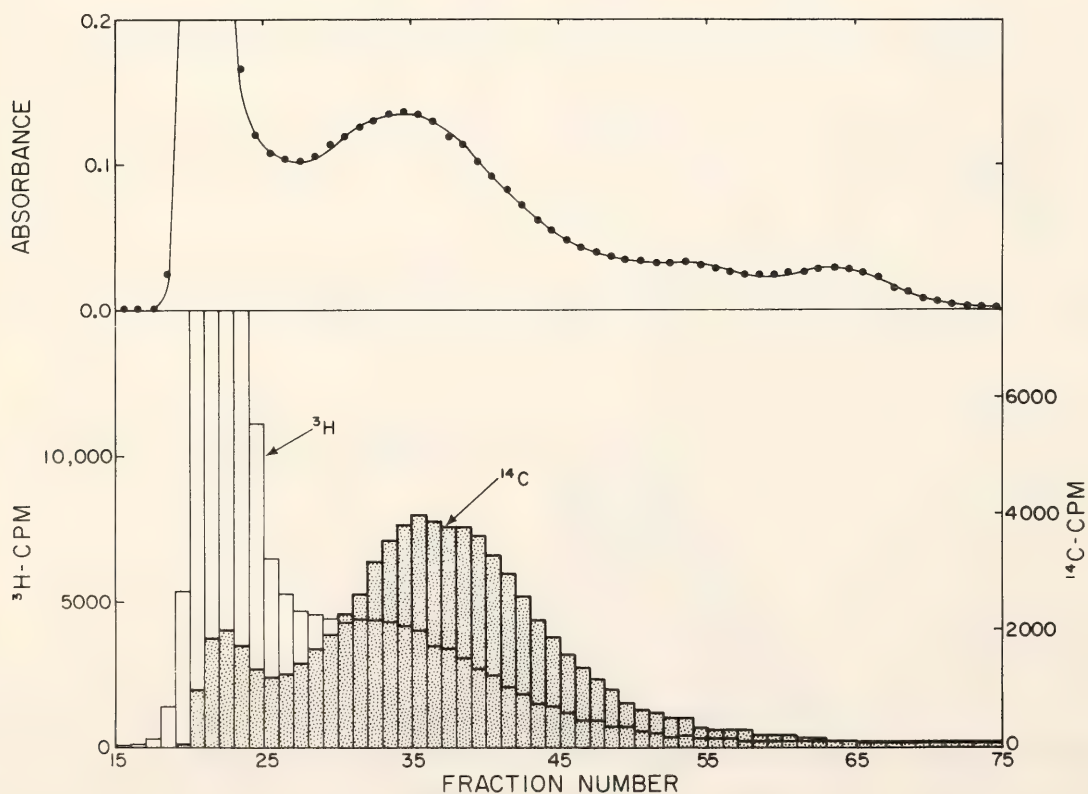


Fig. 36. Cells were incubated for 1 hr at 37°C in Gey's solution containing no vesicles. The supernatant was then used for a 1 hr incubation at 37°C with ^{14}C -DOL vesicles and chromatographed on Sepharose 4B as in Fig. 35.

pooled and the lipids subsequently extracted with 2/1:chloroform/methanol. Analysis of the extracted lipids by thin layer chromatography (TLC) revealed six major spots (A-F, Figure 37). Spot C was identified as phosphatidyl choline, and F corresponded to cholesterol and other less polar lipids, e.g., triglycerides. The remaining spots were not firmly identified but are most probably lyso-phosphatidyl choline (spot A), sphingo-myelin (spot B), and glycolipids (spots D and E). A similar two-dimensional chromatogram was obtained from the lipids extracted from pooled fractions 34-47 of the column represented in Fig. 36.

The spots from each thin layer plate were subsequently scraped from the TLC plate and analyzed for both ³H and ¹⁴C.

The results of this analysis are given in Table 7. It is seen that all spots from both plates contain ³H and ¹⁴C, with the possible exception of the less polar lipids, spot F, which is very high in ³H-cpm and contains practically no ¹⁴C. Furthermore, it is seen that the ratio ¹⁴C-cpm/³H-cpm, of spots A through F varies considerably. If the ratio of the total ¹⁴C-cpm to total ³H-cpm scraped from each plate is made, it is seen that this number (0.40 for TLC-I, and 1.22 for TLC-II) agrees well with the corresponding ¹⁴C-cpm/³H-cpm ratio of the samples which were applied to each plate (0.39 for TLC-I and 1.29 for TLC-II). These numbers also agree well with the ratios of the pooled samples prior to chloroform-methanol extraction, indicating that no preferential extraction of the lipids occurred.

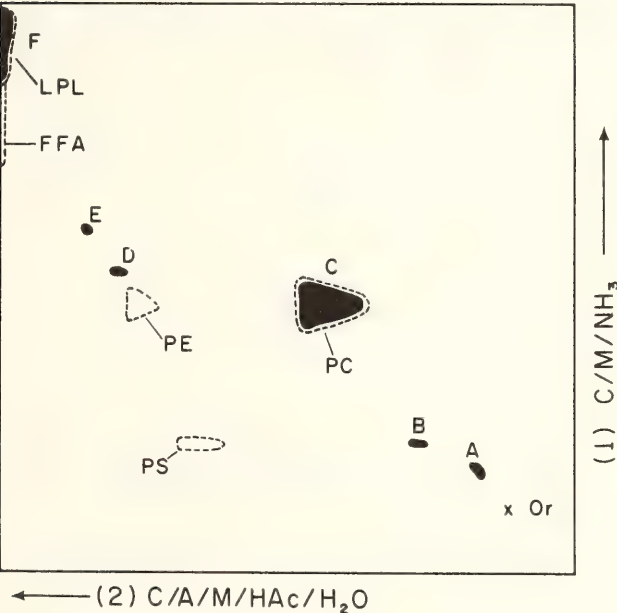


Fig. 37. Two dimensional thin-layer chromatogram on silica gel of lipids extracted from ¹⁴C-labeled vesicles which were incubated with ³H-labeled cells (Fig. 35; fractions 35-45). Chromatograms were developed in solvent systems (1) chloroform-methanol-28% ammonia (65: 25: 5, v/v) and (2) chloroform-acetone-methanol-acetic acid-water (6: 8, 2: 2: 1, v/v). Six major spots were observed (A-F); the dashed lines show the position of known standards (PC = phosphatidyl choline; PS = phosphatidyl serine; PE = phosphatidyl ethanolamine; FFA = free fatty acids; LPL = less polar lipids, e.g., cholesterol, triglycerides) developed under identical conditions. Or = origin.

TABLE 7. Radioactive Analysis of Two-Dimensional Thin-Layer Chromatograms (TLC) of Lipids Extracted From ¹⁴C-DOL Vesicles Following Their Incubation with ³H-labeled Chinese Hamster V79 Cells

Spot	³ H-cpm	¹⁴ C-cpm	¹⁴ C-cpm/ ³ H-cpm
<i>TLC-I: Vesicles Incubated Directly with Cells</i>			
Or	34	28	0.8
A	45	122	2.7
B	918	33	0.04
C	3807	5559	1.5
D	96	605	6.3
E	28	68	2.4
F	11124	19	0.002
Total from plate:	16052	6434	0.40
Applied to plate:	0.39
Pooled samples			
before extraction:	0.36
<i>TLC-II: Vesicles Incubated with Supernatant (See text)</i>			
Or	12	14	1.2
A	32	97	3.0
B	281	41	0.1
C	3237	6172	1.9
D	198	964	4.9
E	47	105	2.2
F	2257	16	0.007
Total from plate:	6064	7409	1.22
Applied to plate:	1.29
Pooled samples			
before extraction:	1.19

All of the observations cited above suggest that during the course of vesicle-cell incubation some of the cell lipids become an integral part of the phospholipid vesicles with no significant change in vesicle size. These results can best be explained in terms of an exchange process in which lipid molecules from the cell surface and vesicle are interchanged, with no *net* transfer of cellular lipid to the vesicles. The data in Fig. 36 show that when lipid vesicles are incubated with a balanced salt solution containing the lipids and proteins normally given off by cells placed in a protein-free medium, a smaller fraction of the cell lipids become associated with the lipid vesicles. Thus, the contribution of exchange between lipids in the cell supernatant and the vesicles is small relative to the vesicle-cell lipid exchange.

If an exchange is involved in the interaction of lipid vesicles with cultured cells, it is reasonable to assume that in

vesicles comprised of several lipid components, these components might exhibit different rates of exchange with the cell membrane lipids. The use of mixed vesicles comprised of ^{14}C -cholesterol and ^3H -lecithin shows (see Fig. 38), however, that regardless of the mole fraction of cholesterol in lecithin, the two components enter the cell at the same rate when the vesicle-cell incubation is carried out at 37°C . Since only about 10% of the lipid uptake at 37°C can be accounted for by an exchange mechanism, while the remainder is most likely due to vesicle-cell fusion, this finding is not surprising. At 2°C , where fusion is largely suppressed, the differential exchange of lipids between vesicles and cells becomes important, with cholesterol entering the cell more slowly than lecithin.

The actual mechanism of the vesicle-cell lipid exchange demonstrated here remains to be elucidated. The exchange process might be the result of one or

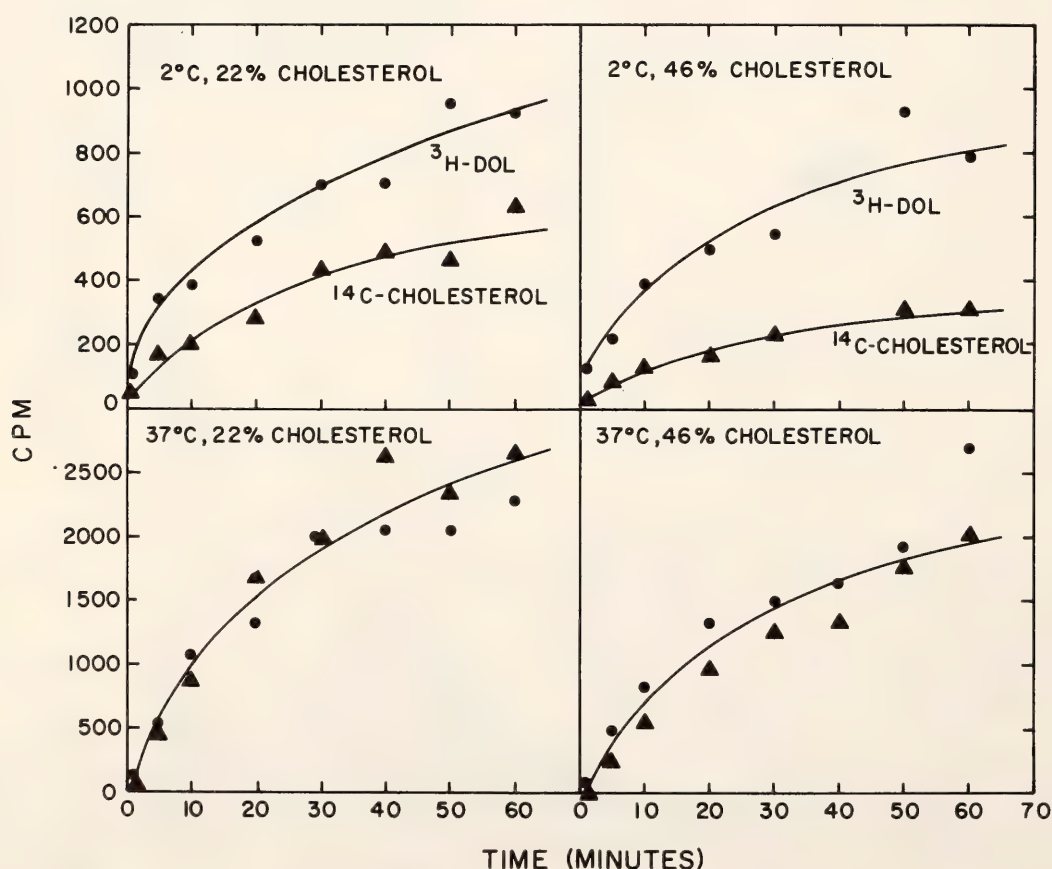


Fig. 38. Uptake of ^3H -dioleoyl lecithin (circles) and ^{14}C -cholesterol (triangles) by V79 cells from mixed vesicles, containing either 22 or 46 mole % cholesterol. The ratio, ^3H -cpm/ ^{14}C -cpm in the applied vesicle suspension was 1.0. The ordinate is the observed cpm per 10^7 cells.

more of the following: (1) a physical transfer of lipid components between membranes when cell and vesicle come into momentary contact; (2) an exchange mechanism involving an enzymatic transfer of acyl chains from the exogenously supplied lecithin to other plasma membrane lipids, and *vice-versa*; or (3) a carrier mechanism involving specific phospholipid exchange proteins which could transfer lipids between the vesicles and cells. These possibilities will be explored in future studies.

A Proposed Mechanism for Vesicle-Cell Interactions

The results of our previous studies on vesicle-cell fusion (*Year Book 73*, p. 52) as well as the present observations have led us to consider a two-step mechanism for vesicle-cell interactions as given in Fig. 39. This proposed mechanism can simultaneously account for both vesicle-cell fusion and some vesicle-cell lipid exchange. In this scheme, when a lipid bilayer vesicle collides with the plasma membrane of the cell (Fig. 39A), an intermediate structure (Fig. 39B), is formed in which the outer monolayer of vesicle lipids becomes an integral part of the outer monolayer of the plasma membrane lipid bilayer, with the aqueous interior of the vesicle and its surrounding inner monolayer of lipids splitting or dividing the bilayer of the plasma membrane. A similar type of structure has been postulated to explain the penetration of echinoderm eggs by oil droplets studied in the 1930's by Chambers and Kopac. The driving force for generation of the intermediate structure shown in Fig. 39B would be the reduction in free energy of the system by elimination of the relatively high-energy lipid bilayer vesicle/water interface and its replacement with a lower-energy cytoplasm/intermediate/water interface. During the lifetime of the intermediate, the outer monolayer vesicle lipids would be free to diffuse laterally in the plane of the plasma membrane and intermix with the

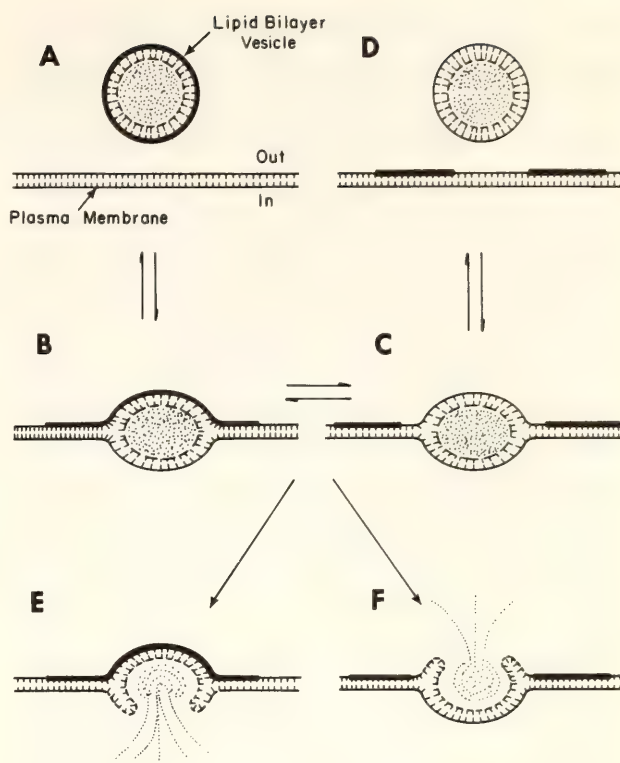


Fig. 39. Schematic diagram of proposed mechanism for interaction of unilamellar vesicles with the plasma membrane of a cultured cell at 37°C. The outer monolayer of vesicle lipids is represented by a heavy black line, and the inner monolayer, by a thin dashed line. (A) Lipid bilayer vesicle containing sequestered material collides with the cell membrane to form an intermediate structure as given in (B). In this structure, the outer monolayer of lipids from the vesicle may mix with the outer monolayer of lipids in the plasma membrane to give the intermediate structure shown in (C). Either intermediate (B or C) can revert to an intact vesicle, (A or D), or rupture as shown in (E) or (F). Rupture toward the cell interior would be recorded as a fusion event (E), whereas rupture toward cell exterior (F) would transfer all the vesicle lipids to the cell without any transfer of the trapped contents. Rupture is depicted only for the intermediate structure shown in (B).

cell lipids as depicted in Fig. 39C. The intermediate structures in Fig. 39 B and C could pinch off to give intact vesicles containing the original complement of vesicle lipids (Fig. 39A) or vesicles containing cell lipids and vesicle lipids (Fig. 39D). The latter case would be measured as a molecular exchange event. According to this scheme, the cell lipids would be confined to the outer monolayer of the newly generated bilayer vesicle. The

intermediate structures (Fig. 39 B or C) could also rupture. If the rupture occurs toward the cytoplasm (Fig. 39C), the discharge of the vesicular aqueous contents will be registered as a fusion event, and the vesicle lipids will be added symmetrically to both sides of the plasma membrane. Such a process might be mediated by an enzymatic reaction, e.g., a phospholipase activity in the cytoplasm. If the intermediate structures rupture toward the outside, there will be no association of the trapped contents with the cell, and both the inner and the outer monolayer vesicle lipids will be added to the outer monolayer of the plasma membrane of the cell.

The proposed mechanism is consistent with the following experimental observations of vesicle-cell interactions. First, it was observed that while small molecules such as sucrose can leak out of the *vesicle* during its interaction with cells, no simultaneous leakout of metabolite (e.g., ^3H -deoxyglucose) from the *cell* occurs. This is contrary to observations of natural membrane fusions which have been demonstrated to be leaky processes. This discrepancy can be explained in terms of the proposed model by requiring that any transient leak formed during vesicle-cell fusion occur during the formation of the intermediate structure (Fig. 39B) and not during actual discharge of the vesicular contents into the cytoplasm of the cells. A second observation, given in another report, demonstrating a lack of fusion of large (>1500 Å) multilamellar vesicles with cells, is also consistent with the proposed model. We argue that the intermediate structure (Fig. 39B) is unable to form in the large vesicles because of their relatively low surface energy.

It should eventually be possible to further test the scheme proposed in Fig. 39 if electron microscopic techniques of sufficient resolution directly reveal the existence of the postulated intermediate structures. The use of vesicles which have an asymmetric distribution of radio-

labeled lipid may also prove useful. In the interim, it is hoped that the results presented in this study will prove beneficial, not only in dealing with the cellular modification phenomena produced by lipid vesicles but also in considering natural membrane fusion processes.

INTERACTION OF PHOSPHOLIPID VESICLES WITH MOUSE LYMPHOCYTES IN VITRO

L. Huang, K. Ozato, and R. E. Pagano

Last year we reported (*Year Book* 73, p. 83) that pretreatment of mouse lymphocytes with phospholipid vesicle suspensions significantly enhanced the mitogenic activity of these cells in vitro. We have now examined this interaction in more detail.

First, we investigated the kinetics of phospholipid uptake by mouse lymphocytes. Vesicles comprised of ^3H -egg yolk lecithin (EYL) were prepared in Gey's salt solution by ultrasonic irradiation. The uptake of lipid by mouse (CBA or C57 Black) thymus or spleen cells was studied both at 37°C and 0°C . As shown in Fig. 40, microgram quantities of EYL became cell-associated in a 60 min incubation at 37°C . The uptake was linear with incubation time and showed a strong temperature dependence. Spleen cells were more effective in uptake than thymus cells.

In order to study the influence of lipid fluidity on the phospholipid uptake by lymphocytes, vesicles comprised of dimyristoyl lecithin (DML) were prepared and used for uptake studies. These vesicles have their phase transition temperature (T_c) at about 25°C as compared with those of EYL vesicles at -10°C . Therefore, vesicles prepared from EYL are in a fluid liquid-crystalline state both at 37°C and 0°C . The result of an uptake experiment using DML vesicles is shown in Fig. 41. At 37°C , the amount of lecithin uptake by thymus cells was comparable to that by EYL vesicles (Fig. 40). In contrast to the findings with EYL vesicles, however, the uptake

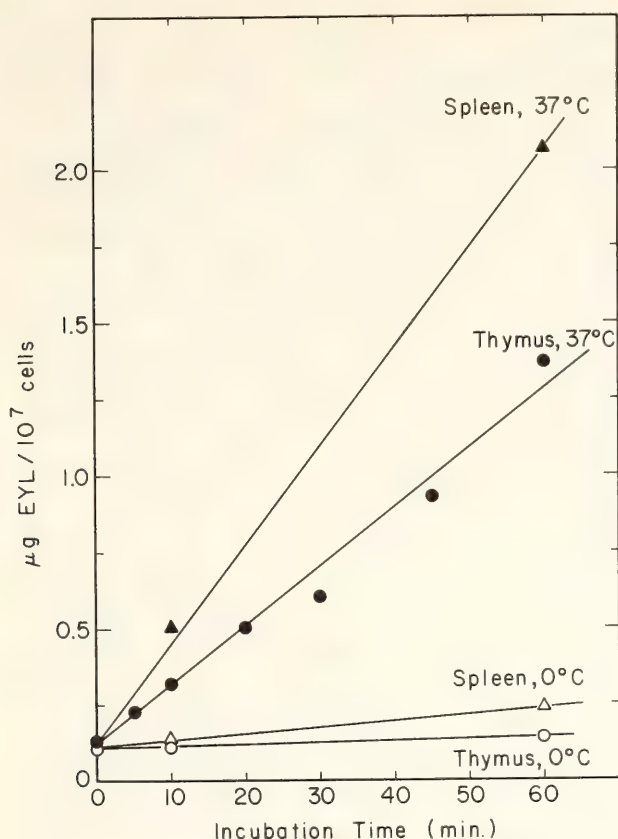


Fig. 40. Uptake of ^3H -EYL (1.0×10^6 cpm/mg) by mouse lymphocytes in vitro. EYL vesicle concentration = 1 mg/ml; 1×10^7 cells/ml in Gey's solution. Circles: thymus cell; triangles: spleen cells. Open symbols: 0°C incubation; filled symbols: 37°C incubation.

of DML was greatly enhanced at 0°C . Therefore, we conclude that the lecithin uptake process is much more effective below the thermal phase transition of the exogenous lipid, a phenomenon also observed in uptake studies in which Chinese hamster fibroblastic cells (Year Book 73, p. 56) were used.

In order to further characterize the uptake of phospholipid by lymphocytes, a series of experiments using EYL vesicles under different conditions was performed; the results are summarized in Table 8. Divalent cations such as Ca^{+2} , Mn^{+2} and Zn^{+2} stimulated the uptake process at nontoxic concentrations (judged by the trypan blue dye exclusion test). Mg^{+2} ions, however, showed no effect up to a concentration of 5 mM. Low (mitogenic) doses of Concanavalin A (ConA) and succinyl-ConA reduced

the incorporation of ^3H -EYL into thymocytes; lower doses, however, were less inhibitory. Inhibitors of energy metabolism (NaN_3) and monovalent cation transport (ouabain) only slightly reduced the uptake, while an inhibitor of cellular motility (cytochalasin B) showed no significant effect. Fixation of cells by glutaraldehyde strongly inhibited the uptake process. Mild enzyme treatment of cells prior to incubation with vesicles exhibited various positive or negative effects. Proteolytic digestion with trypsin but not with pronase significantly reduced the incorporation of phospholipid into thymocytes without cytotoxic effects. On the other hand, treatment of cells with phospholipases A and D resulted in enhancement of the uptake of EYL. Neurominidase treatment was ineffective. In order to determine whether phospholipid vesicles are incorporated into

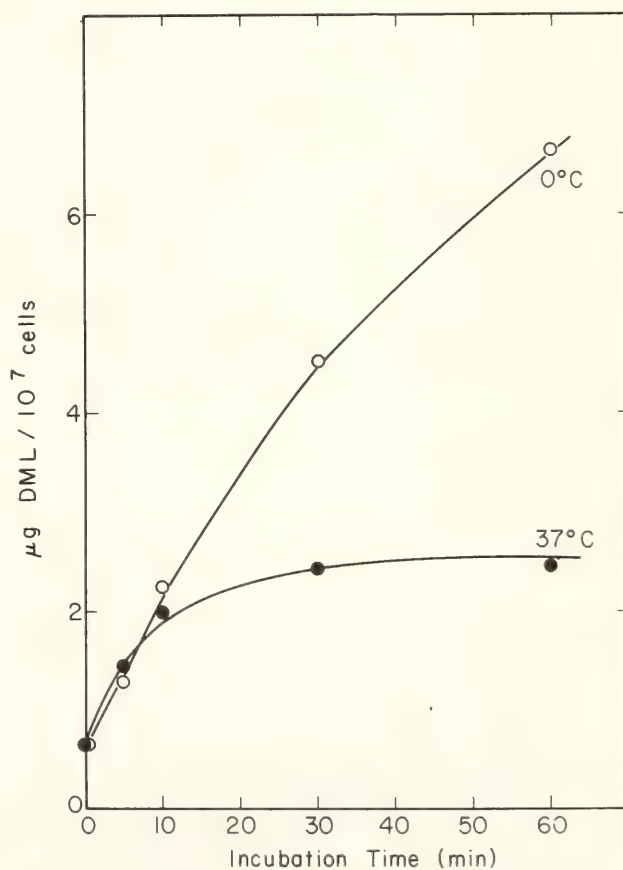


Fig. 41. Uptake of ^3H -DML (4.5×10^6 cpm/mg) by mouse thymocytes in vitro. 1×10^7 cells/ml; 1 mg DML/ml in Gey's solution. Open circles: 0°C incubation, filled circles: 37°C incubation.

TABLE 8. Effect of Mitogens, Metabolic Inhibitors, Divalent Cations, and Enzyme Treatment on the Uptake of ^3H -EYL by Mouse Thymocytes

Treatment	Uptake of ^3H -EYL (% of Control)
Control	100
ConA* (2 $\mu\text{g}/\text{ml}$)	70
ConA (20 $\mu\text{g}/\text{ml}$)	76
ConA (200 $\mu\text{g}/\text{ml}$)	88
Suc-ConA* (2 $\mu\text{g}/\text{ml}$)	81
Suc-ConA (20 $\mu\text{g}/\text{ml}$)	85
Suc-ConA (200 $\mu\text{g}/\text{ml}$)	97
NaN_3^\dagger ($10^{-2}M$)	96
Cytochalasin B ‡ ($10^{-4}M$)	107
Ouabain ‡ ($10^{-3}M$)	89
Glutaraldehyde* (2%)	35
Ca^{+2} § (5 mM)	147
Mg^{+2} (5 mM)	103
Mn^{+2} (0.5 mM)	129
Zn^{+2} (0.1 mM)	107
Trypsin (0.01%)	46
Pronase (0.001%)	105
Phospholipase A (0.01%)	316
Phospholipase D (0.1%)	208
Neuraminidase (0.0001%)	116

* 1×10^7 cells/ml in Gey's solution were pretreated with various reagents at 37°C for 30 min (15 min for all enzyme treatments). After two washes, cells were incubated with ^3H -EYL vesicle suspensions (1 mg/ml in Gey's solution) for 60 min at 37°C .

† Present in pretreatment as well as during incubation with vesicles.

‡ Present only during incubation with vesicles.

§ All experiments with divalent cations were carried out in Ca^{+2} , Mg^{+2} -free Gey's (CMFG). Controls for these experiments were also in CMFG.

lymphocytes as intact structures, i.e., both phospholipid and the trapped aqueous content of the vesicles become cell-associated, we conducted the following experiment.

Vesicles containing ^3H -inulin trapped inside ^{14}C -EYL were prepared and used in an uptake experiment. As shown in Fig. 42, ^3H -inulin uptake matched nearly perfectly with that of ^{14}C -EYL at 37°C , strongly suggesting that intact vesicles are being incorporated into the cells. Since the incorporation was insensitive to an inhibitor of energy metabolism

(NaN_3), it is unlikely that a process such as endocytosis is responsible for the vesicle uptake. Also, in electron microscopic autoradiograms of thin sections through vesicle-treated lymphocytes, neither attached vesicles nor radio-labeled lipids were localized exclusively on the cell surface. The possibility that intact vesicles adsorbed on the surface membrane of cells was therefore excluded. At present, fusion of phospholipid vesicles with lymphocyte plasma membrane seems most likely the major pathway for their incorporation at 37°C , although definitive proof awaits further experimentation. At 0°C , uptake of trapped ^3H -inulin was negligible (Fig. 42), excluding any mechanism involving the incorporation of intact vesicles.

Another possible mechanism for lipid uptake by vesicle-treated lymphocytes is the exchange of individual lipid molecules between vesicles and the cell surface. Such a possibility is supported by the following experimental results. When vesicles composed of ^{14}C -EYL and ^3H -cholesterol (1:1 molar ratio) were prepared and used in uptake experiments, the rate of entry into lymphocytes for ^3H -cholesterol at 37°C was about twice the expected rate for cholesterol and EYL molecules had they been incorporated into the cells together (Fig. 43). This finding suggests that in addition to vesicle-cell fusion, individual molecules, especially cholesterol, can be incorporated into cells by an exchange mechanism.

Electron microscopic autoradiographic studies of mouse lymphocytes incubated with a variety of radioactively labeled lipid vesicles are in progress. An autoradiogram obtained following 1 hr incubation at 37°C with ^3H -EYL vesicles is shown in Fig. 44A. The radio-labeled lipid is seen to be distributed into both the plasma membrane and internal structures in the cell. This finding is in qualitative agreement with biochemical analysis of fractionated cells. By contrast, autoradiograms of cells treated 1 hr at

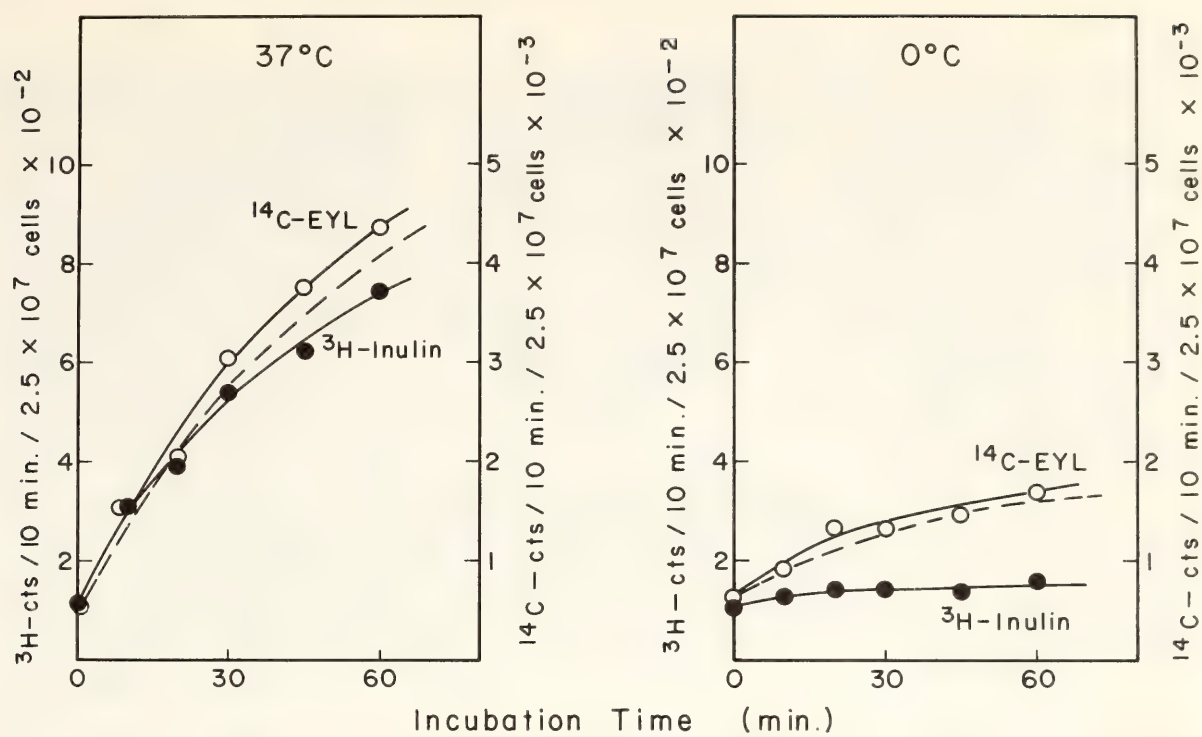


Fig. 42. Incubation of mouse thymocytes with phospholipid vesicles generated from ^{14}C -EYL (2.12×10^5 cpm/mg) and containing sequestered ^3H -inulin (500 mCi/g). Dashed curve represents the expected amount of ^3H -inulin uptake calculated from the observed ^{14}C -lipid uptake and the ^3H -cpm/ ^{14}C -cpm ratio of the applied vesicles (0.187). 2.5×10^7 cells/ml; 1 mg EYL/ml in Gey's solution.

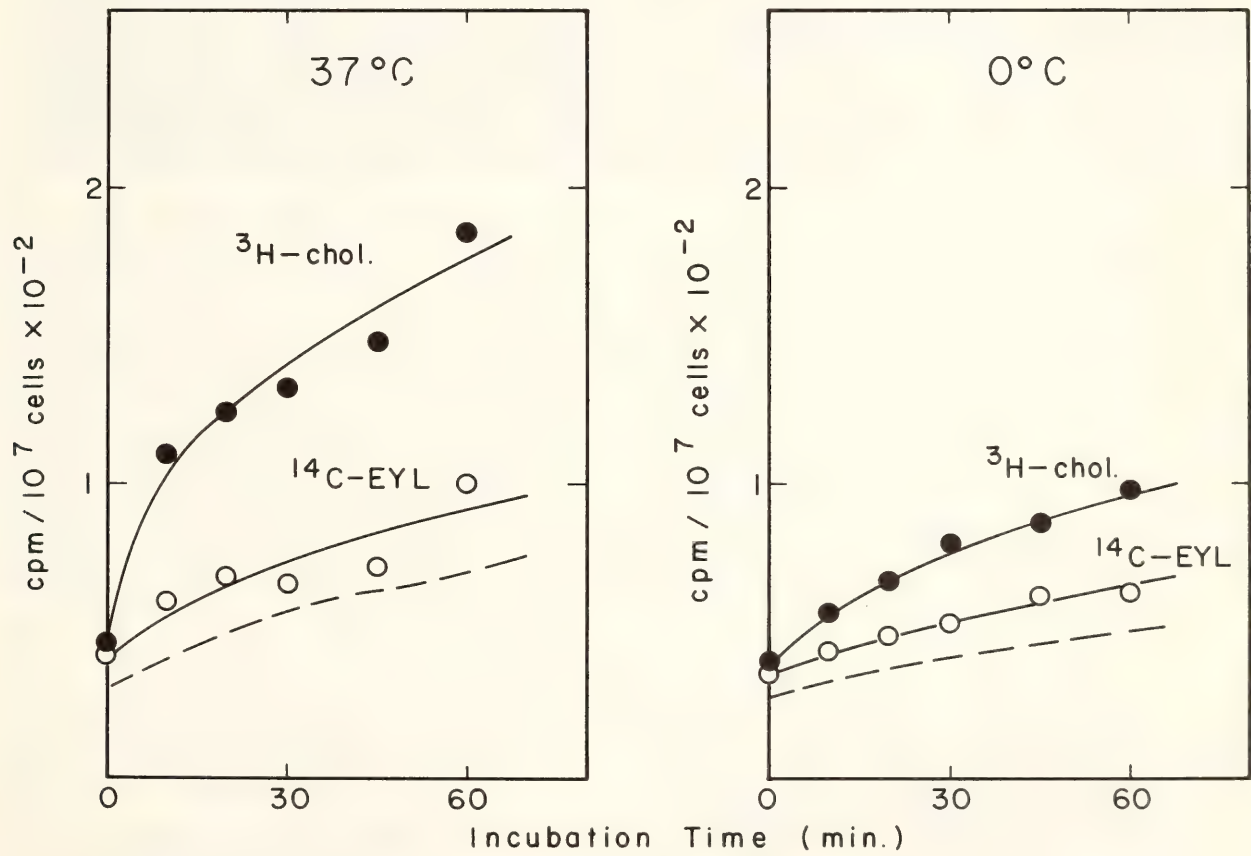


Fig. 43. Uptake of ^{14}C -EYL (2.4×10^5 cpm/mg) and ^3H -cholesterol (4.64×10^5 cpm/mg) by mouse lymphocytes from EYL vesicles containing 50 mole % cholesterol. Dashed curve represents the expected amount of ^3H -cholesterol uptake calculated from the observed ^{14}C -EYL uptake and the ^3H -cpm/ ^{14}C -cpm ratio of the applied vesicles (0.75). 1×10^7 cells/ml; 0.5 mg EYL/ml in Gey's solution.

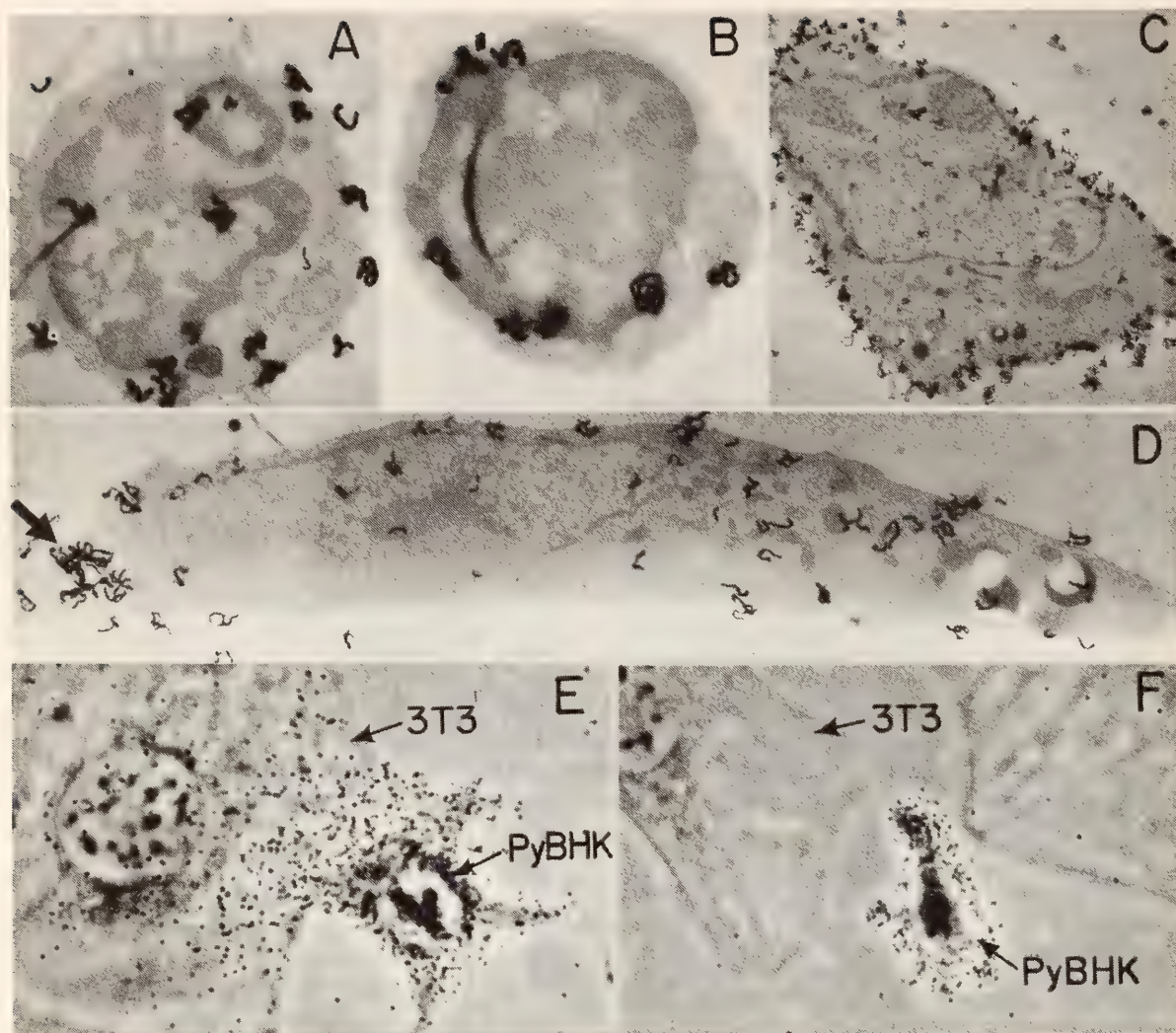


Fig. 44. (A) EM autoradiogram of normal thymic lymphocyte incubated 1 hr at 37°C with ^3H -EYL vesicles. (B) EM autoradiogram of normal thymic lymphocyte incubated 1 hr at 37°C with vesicles comprised of 1:1 EYL/ ^3H -cholesterol. Note accumulation of label on nuclear membrane. (C) EM autoradiogram of Chinese hamster V79 cell incubated with ^3H -dimyristoyl lecithin vesicles 1 hr at 2°C. Thin sections were made parallel to culture dish on which cells were grown. (D) EM autoradiogram of Chinese hamster V79 cell incubated with ^3H -dimyristoyl lecithin vesicles 1 hr. Thin sections were made perpendicular to culture dish. Note accumulation of label at edge of cell (arrow). (E) Phospholipid transfer between *contiguous* cells. A polyoma virus-transformed baby hamster kidney cell (Py-BHK) was labeled with radioactive ^3H -sphingomyelin vesicles and allowed to grow on a tissue culture plate containing unlabeled mouse 3T3 cells. The grains over cells mark the sites of radioactive decay and approximate location of a labeled lipid molecule. (F) Same as (E) except the labeled and unlabeled cells are not in contact. Note lack of transfer between cells.

37°C with vesicles comprised of 1:1 EYL/ ^3H -cholesterol (Fig. 44B) show that the labeled cholesterol is largely internalized, and resides almost exclusively on the nuclear membrane of treated cells. Cell fractionation studies to determine whether the exogenously supplied cholesterol has been appreciably metabolized to some other component are in progress.

SPATIAL DISTRIBUTION OF CELL SURFACE LIPIDS

*M. Takeichi and R. E. Pagano
with the assistance of W. Duncan*

The two-dimensional distribution of phospholipids and cholesterol in the plane of the cell membrane is thought to be governed by several general physical

principles which have been elucidated in model systems and in studies of prokaryotic organisms. These include the two-dimensional phase separation of membrane lipids, the presence of specific "boundary lipids" which surround specialized membrane proteins requiring a particular environment, and packing constants which are imposed because of the existence of structures with very small radii of curvature. In order to test some of these ideas in animal cell membranes, which are known to be exceedingly complex compositionally as well as functionally, we are attempting to elucidate the spatial distribution of exogenously supplied radioactive phospholipids introduced into cultured mammalian cells by the techniques of vesicle interaction, described elsewhere in this Report.

Chinese hamster V79 cells were incubated with vesicles composed of ^3H -dimyristoyl lecithin for 1 hr at 2°C or 37°C . The cells were then washed, fixed, sectioned, and prepared for electron microscope autoradiography. Figure 44C shows an autoradiogram obtained when cells labeled at 2°C were sectioned parallel to the culture dish on which the cells were grown. The level is seen to be homogeneously distributed over the cultured cell surface. Similar results were obtained for cells labeled at 37°C , except that some internalization of the label occurred. In sections made perpendicular to the culture dish, however, an inhomogeneous pattern of labeling was found in which the lipid label accumulated between contacting cells (not shown) and at the edges of contact of individual cells with the substrate (Fig. 44D, arrow). Little of the lipid label was found on the upper surface of the cell exposed to the bathing medium or on the under, attached surface of the cultured cell.

These observations demonstrate that the spatial distribution of one membrane lipid may not be random. Future experiments to determine the lateral distribution of each of the major lipid classes,

and the variation of this distribution with the degree of unsaturation of the fatty acid moiety of the phospholipid are in progress.

INTERCELLULAR EXCHANGE OF LIPIDS

M. Takeichi and R. E. Pagano

The surface membranes of a wide variety of cell types have the capacity of forming junctions which are permeable to cytoplasmic constituents. Thus the intercellular exchange of soluble components is thought to be one type of intercellular communication which can exist in a collection of cells comprising a cell mass or tissue. We are interested in the possibility that membrane constituents, namely cellular phospholipids and cholesterol molecules, can exchange between cells when two cells come into contact. If lipid molecules were exchanged and mixed between two cells with different plasma membrane lipid compositions, the properties of the surface membranes of one or both of these cells could be modified as a result of the exchange. This in turn might result in altered cellular activity if there is a relation between membrane dynamics and the biological functions of cells. The following experiments were done to obtain basic information about the existence of an intercellular lipid exchange mechanism.

Various types of cells (baby hamster kidney (BHK), polyoma virus-transformed BHK (PyBHK), mouse L cells, Balb/c 3T3 cells) were labeled by incubation with ^3H -sphingomyelin (SPHM) lipid vesicles. These cells were then seeded into nonlabeled cell cultures. Under the appropriate experimental conditions, the labeled cells adhered to the culture dish, and some of them made contact with nonlabeled cells. Such cultures were then fixed and examined autoradiographically at the light microscope level. The autoradiograms of these cultures show that the ^3H -label is transferred to originally nonlabeled cells within 60 min after mixing of the donor

and recipient cells. Figure 44E demonstrates that lipid transfer has occurred between a labeled PyBHK and an unlabeled 3T3 cell which have come into contact. In Fig. 44F, where no cell-cell contact was made, no transfer of label took place. Experiments in which labeled and nonlabeled cells were mixed in a pellet demonstrated that no transfer of labeled ³H-SPHM occurred, suggesting that junctions formed by normal biological processes are required for the intercellular exchange of lipids, and that artificial physical contact of cells is ineffective for this purpose.

Further experiments to clarify the biological significance of the intercellular exchange of membrane lipids and the mechanism by which this exchange is accomplished are in progress. Particular attention is being focused on the possibility that specific phospholipid exchange proteins at the cell surface may act as carriers for the movement of lipids between cells.

LIPID PERTURBATIONS AND
LYMPHOCYTE ACTIVATION

*K. Ozato and L. Huang
with the assistance of D. Somerville*

In *Year Book 73*, p. 83, we reported that the pretreatment of T-lymphocytes with liposomes could enhance the mitogenic response to ConA. We have extended our study to test the effect of six different lipid vesicle types on mitogenic responses in both T-cells and B-cells, in an attempt to delineate the relationship between the altered lipid composition of the cells and mitogenic response. T-cell response to ConA was tested in cortisone-resistant thymocytes. B-cell response was tested in spleen cells using the B-cell specific mitogen LPS. Cells were exposed to liposome solutions for 20 min at room temperature. Excess vesicles were removed, and cells were then stimulated with mitogens. Table 9 shows the mitogenic response on day 2. We found that egg yolk lecithin (EYL),

TABLE 9. Effect of Different Liposomes on Mitogenic Response

Experimental Group		³ H-TdR Incorporation (cpm/culture)
I. ConA*	Control (RPMI 1640)	6089
	EYL (1 mg/ml)	7455
	EYL-cholesterol (0.5 mg/ml)	8363
	EYL-cholesterol oleate (0.1 mg/ml)	8627
	DPL (1 mg/ml)	5401
	DML (0.5 mg/ml)	9233
	DML (0.5 mg/ml)	19815
	DLL (0.1 mg/ml)	1413
	No ConA	23
II. LPS	Control	5986
	EYL (1 mg/ml)	6062
	EYL-cholesterol (0.5 mg/ml)	8214
	EYL-cholesterol oleate (0.1 mg/ml)	18023
	DPL (1 mg/ml)	7454
	DLL (0.1 mg/ml)	79
	No LPS	210

* Mitogenic responses to ConA or to LPS were tested using cortisone-resistant thymocytes or spleen cells, respectively. Cells were treated with different liposomes diluted in RPMI 1640 at room temperature for 20 min. After washing, cells were resuspended in fresh medium. Then ConA (1 μg/ml) or LPS (5 μg/ml) was added. ³H-TdR (1 μCi/ml) was added to the culture 2 days after plating and cells were labeled for 18 hr. Each value represents mean of duplicate.

EYL-cholesterol, EYL-cholesterol oleate, and dimyristoyl (DML) could enhance the mitogenic response in both T- and B-cells when the optimal doses of pretreatment were performed. DPL (dipalmitoyl lecithin) and DLL (dilauryl lecithin) showed no appreciable enhancement. In the T-cell system DML showed the most significant enhancing effect (about threefold). In the B-cell system the cholesterol oleate showed remarkable enhancement, again about three to four times higher incorporation being noted. Liposomes did not change the optimal doses of mitogens when either suboptimal or superoptimal concentrations of mitogens were employed.

Biochemical analysis of the stimulated lymphocytes as well as electron microscopic autoradiographic studies are in progress to determine whether a correla-

tion exists between the enhancement of the mitogenic response and the degree of internalization of the exogenously supplied lipids.

STUDIES ON SKELETAL MUSCLE PLASMA MEMBRANES

*D. M. Fambrough, P. N. Devreotes, A. K. Ritchie, and K. Tepperman
with technical assistance of S. Cherry, A. Mabin, and W. Duncan*

Our interest for the past several years has been in the differentiation of the skeletal muscle plasma membrane and the organization of skeletal muscle fibers. In previous Year Books we have reported on the appearance and maturation of several plasma membrane properties related to the specialized functions of skeletal muscle during development. We have also reported on some of the changes in plasma membrane properties which characterize denervated adult skeletal muscle and are reminiscent of the properties of embryonic muscle, and on some characteristics of abnormal muscle, namely in the muscular dysgenic mouse and in humans with the disease myasthenia gravis. Many of our studies have focused upon the acetylcholine receptors of skeletal muscle, since they appear in the plasma membrane as readily detected functional molecules early in muscle development, are later confined to a small area of cell surface (the postsynaptic surface of the neuromuscular junction), and in denervated skeletal muscle reappear all over the surface of each muscle fiber (as is the case in the embryonic state). Because acetylcholine receptors can be readily identified not only by their function but also through the use of a radioactive probe which binds to them with extreme tenacity (iodinated α -bungarotoxin), they can be studied in ways which are unique. Thus we have been able to learn a great deal about their number and distribution in the plasma membrane in various physiological states, their rates of synthesis and destruction, and the mechanism by which they are incorpor-

ated into the plasma membrane of muscle fibers and later removed and degraded by the fibers. Comparable data for other identified plasma membrane proteins in higher organisms are not yet available.

In the past year we pursued our studies on the mechanisms of synthesis, incorporation into plasma membrane, and degradation of acetylcholine receptors. The working hypothesis we had formulated in previous years includes the following elements. Acetylcholine receptors are synthesized by the normal protein synthesizing machinery (although we do not yet know whether synthesis takes place upon membrane-bound or free polysomes) and their synthesis is sensitive to inhibition by puromycin and by cycloheximide. Newly synthesized receptor components occur as organized macromolecular structures of molecular weight about 250,000 daltons (when solubilized in detergent solution) incorporated into internal cell membranes (of unknown type and location). These "precursors" are then inserted into the plasma membrane, the population of precursors being enough to support two hours of new receptor incorporation into plasma membrane without any new protein synthesis. Once in the plasma membrane the receptors are functional molecules and are free to interact with the radio-labeled probe, iodinated α -bungarotoxin. Plasma membrane receptors are degraded by a random-hit process which is energy-dependent and proteolytic, probably involving internalization of membrane containing receptors and then degradation by lysosomal enzymes. During the past year we developed techniques

that will allow direct testing of several aspects of our model of the "life history of receptor molecules." We also devised a method for continuous monitoring of receptor degradation in organ-cultured skeletal muscle and have begun extending our findings to adult mouse muscle.

We have also investigated another human disease, myotonic dystrophy, in which the muscle pathology suggested the possible participation of denervation. Since the appearance of extrajunctional acetylcholine receptors is a sensitive marker for denervated skeletal muscle surface, we have used our radio-labeled probe for acetylcholine receptors on biopsy specimens from patients with myotonic dystrophy. We have also examined biopsy material from two patients with the denervating disease amyotrophic lateral sclerosis.

Eager to extend our studies to other specific membrane proteins, we have begun to probe for other skeletal muscle plasma membrane markers which might be used to investigate the metabolism of the plasma membrane.

CHARACTERIZATION OF RECEPTOR POOLS

P. N. Devreotes and D. M. Fambrough

Last year we described two classes of acetylcholine receptors in addition to the class functionally defined as surface receptors. Our description was based on several observations. After a brief (20 min at 0.1 $\mu\text{g}/\text{ml}$) incubation of cultured chick embryo myotubes with α -bungarotoxin, the cells are rendered physiologically insensitive to ionophoretically applied acetylcholine. After this treatment, however, there is a significant number of receptors which have not been complexed with α -bungarotoxin. These receptors are revealed by solubilization of the pretreated myotubes in 1% Triton X-100 followed by interaction of the detergent extract with ^{125}I - α -bungarotoxin. There are about 40% as many additional receptors as there are rapidly saturable surface receptors. By several biochemi-

cal criteria, which include the kinetics of interaction with α -bungarotoxin, protection from α -bungarotoxin by $10^{-3}M$ curare, and sucrose gradient sedimentation, the additional receptors are indistinguishable from the rapidly saturating surface receptors. If one continues to incubate the intact myotubes with α -bungarotoxin, the percentage of additional receptors revealed by Triton X-100 solubilization is eventually reduced from 40% to 10%. Apparently, a class of receptors containing 30% as many receptors as does the surface interacts only slowly with extracellular α -bungarotoxin; while another class, containing 10% as many receptors as does the surface, cannot interact with α -bungarotoxin prior to extraction of the myotubes. The smaller class disappears rapidly in cells pretreated with 10 $\mu\text{g}/\text{ml}$ puromycin and is likely to be the precursor of the surface receptors. The larger, slowly interacting class we have called "hidden" and its function is unknown. In cultured rat myotubes the two classes taken together are much larger than in chick and equal 100% as many receptors as there are rapidly saturable surface receptors. Our interpretation of the receptor classes and their possible relationships taken from these and other observations is summarized in Fig. 45. This model has been published in *Journal of Cell Biology*, 65, 335, 1975.

INTERRELATIONSHIP OF RECEPTOR CLASSES

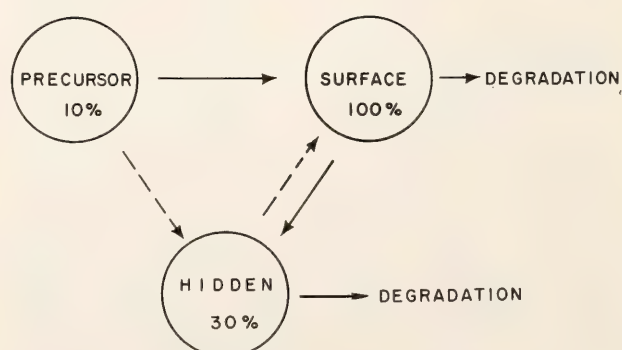


Fig. 45. Hypothetical interrelationships between receptor classes.

Our goals in the past year have been to extend our understanding of the nature and relationships of the receptor classes defined above. Specifically, we have undertaken an electron microscope autoradiographic investigation of the "hidden" receptors. Perhaps the slow interaction with α -bungarotoxin is related to their subcellular location. In addition, we have developed a technique to directly label the acetylcholine receptor through its amino acid precursors. This technique will soon be used to explore the interrelationships of the receptor classes.

In our initial discussion of the "hidden" receptors it was stated that while the "surface" receptors are rapidly saturated with α -bungarotoxin the "hidden" receptors interact only slowly with extracellular α -bungarotoxin. Therefore, careful analysis of the kinetics of interaction of ^{125}I - α -bungarotoxin with intact myotubes should reveal two components. Figure 46 shows such an analysis. In this experiment a 30-fold excess of α -bungarotoxin was used and therefore we would expect the kinetics to follow those of a pseudo-first order reaction. The data have been normalized so that 100 equals the number of surface receptors and therefore 130 equals the number of surface plus hidden receptors. Most of the receptors (about 100 on the normalized scale) interact with α -bungarotoxin rapidly ($t_{1/2} = 7$ min), while the remainder (about 30 on the normalized scale) interact more slowly ($t_{1/2} = 1$ –2 hr). Also illustrated in Fig. 46 are the kinetics of interaction of ^{125}I - α -bungarotoxin with intact myotubes at 4°C. At 4°C only as many receptors as there are surface receptors (100 on the normalized scale) interact with ^{125}I - α -bungarotoxin even after very long interaction times (24 hr). This experiment suggests that at 4°C the hidden class of receptors does not bind α -bungarotoxin. Accordingly, we defined as another criterion for surface receptors that the receptors interact with α -bungarotoxin at 4°C.

To determine whether the slowly interacting hidden class has a unique subcellular location, we prepared autoradiograms on thin sections of myotubes and examined cells labeled at 4°C and at 37°C. We predicted that at 4°C all the grains would represent receptors in the plasma membrane and thus be located at the cell perimeter. We predicted that at 37°C, in addition to the grains at the perimeter an extra 30% would have another subcellular localization. Unexpectedly, in myotubes saturated with ^{125}I - α -bungarotoxin at 37°C only a small fraction ($\sim 30\%$) of the acetylcholine receptors are associated with the perimeter of the cell (Fig. 47). From this observation it must be concluded that the rapidly saturating receptors we have functionally defined as "surface" are not located *exclusively* at the cell perimeter since, if they were, about 75% of the grains should be located there. For myotubes saturated at 37°C we examined more than 1200 grains over 14 different cells in two independent preparations, and 55%–86% of the grains have *not* been located at the cell perimeter. Although we do not have quantitative data at this time, we have determined qualitatively that in autoradiographs of cells labeled at 4°C many of the grains are also *not* located at the cell periphery. The unexpected distribution of "surface" receptors has complicated our analysis of the autoradiograms. Since many of the "surface" receptors can be located in what appears to be the interior of the cell, we would like to label the surface of the cell by an independent method. At present, several dyes and stains which would nonspecifically label the external surface of the plasma membrane are under consideration.

Figure 48 shows the kinetics of disappearance, during puromycin treatment, of the class of receptors we have suggested to be the precursor of the surface receptors. Also shown is the simultaneous incorporation of new re-

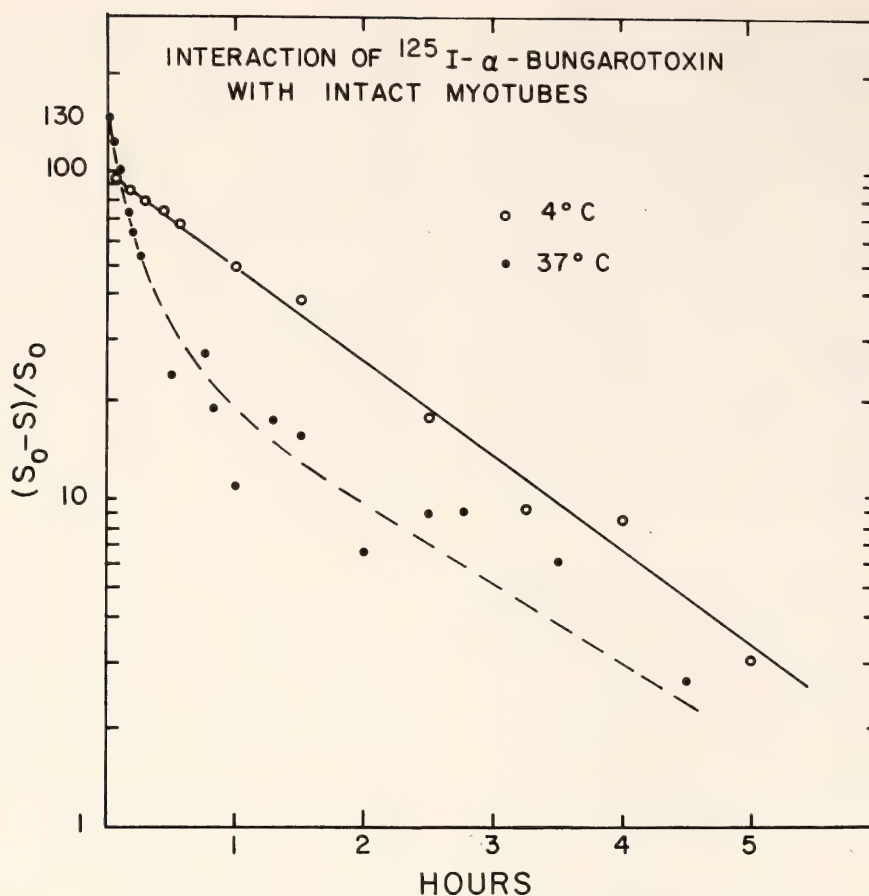


Fig. 46. Kinetics of α -bungarotoxin binding. Large sets of identical 5-day cultures were equilibrated in growth medium at 4°C and at 37°C. At each of the time-points ^{125}I - α -bungarotoxin was added to four cultures so that the concentration of α -bungarotoxin was 0.2 $\mu\text{g}/\text{ml}$. The time indicated is the time of preincubation of each set of four cultures with α -bungarotoxin. At the termination of the experiment all the cultures were rinsed by immersion in a large bath of wash medium (Hanks 0.5% BSA, pH 7.2). The cultures were then extracted with 1% Triton X-100 and assayed for radioactivity in a Packard Auto-Gamma Scintillation Spectrometer. The value expressed is the mean of the four cultures in each set. The experiment was repeated three times.

ceptors into the surface class. At present, these matched kinetics are the strongest evidence supporting the conclusion that these receptors are precursors of the surface receptors. Because of the indirect nature of this experiment, we wish to directly label the precursor and follow the incorporation of the label into the surface. In addition, an important question concerning the mechanism of incorporation of new proteins into the surface membrane might be resolved by directly labeling the receptor. In Fig. 48 the kinetics of disappearance of the precursor and the appearance of new receptors appear to follow linear, zero-order kinetics. If this were accurate, it

would imply an assembly-line type mechanism such that a newly synthesized receptor would spend a 2 hr transit time before its incorporation into the surface. On the other hand, if the kinetics were first-order exponentials, it would imply that a newly synthesized receptor would have equal probability of being incorporated into the surface as a receptor which had been synthesized 2–3 hr earlier. We believe our puromycin kinetic data are not sufficiently accurate to resolve the linear and exponential models. However, if the receptor were directly labeled through its amino acid precursors and *some* labeled receptors appeared on the surface prior to 2 hr, the linear

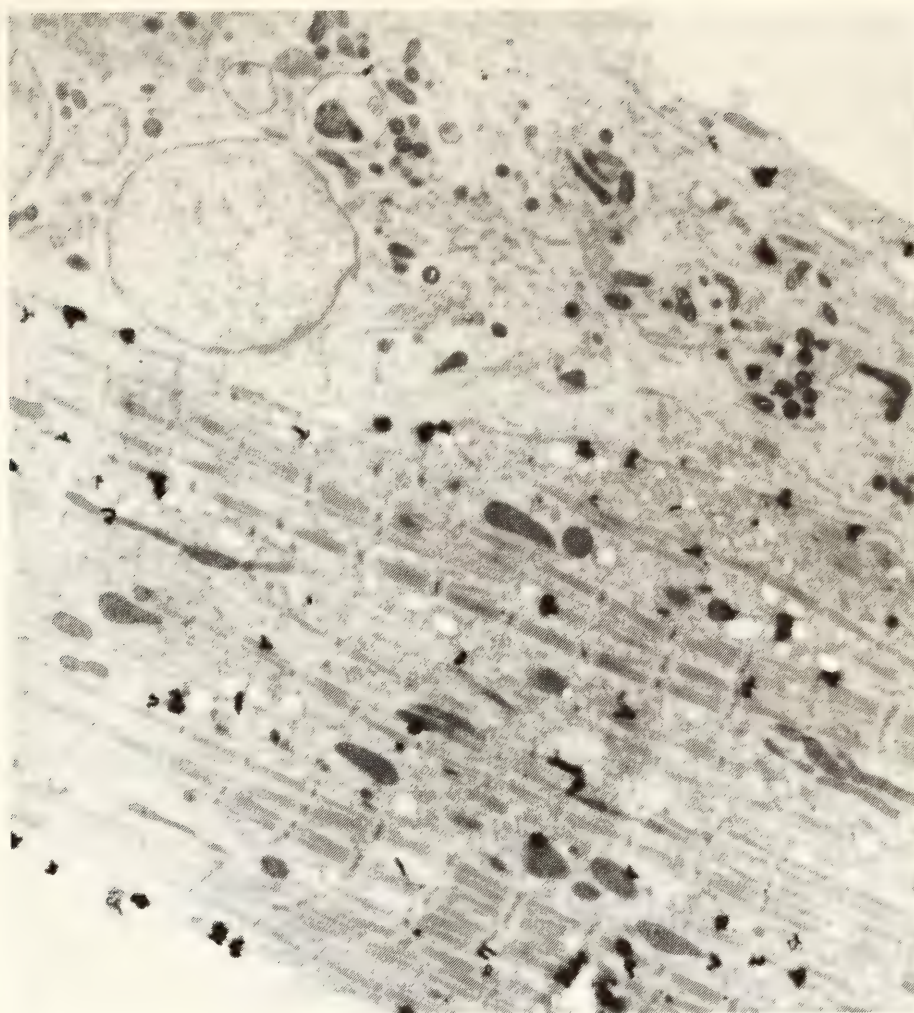


Fig. 47. Electron microscope autoradiograph of receptor distribution in myotube. Several 5-day myogenic cultures were labeled with ^{125}I - α -bungarotoxin for 6 hr at 37°C . After rinsing to remove unbound ^{125}I - α -bungarotoxin, the cultures were fixed overnight in 2% glutaraldehyde at 4°C . The cultures were osmicated, stained in uranyl acetate, dehydrated, and embedded in Epon. Thin (gold interference color) sections were prepared and collected on Formvar carbon-coated grids. The grids were coated with a thin film of Ilford L-4 nuclear track emulsion and exposed for about a month at 4°C . Grids were developed in Microdol-X. Background was about 0.2 grain/ $100\ \mu^2$.

assembly-line model would be ruled out.

To label the acetylcholine receptor with radioactive amino acids seemed impractical from two points of view. Large quantities of high specific-activity amino acids would be expensive, and complete purification of the labeled receptor would be necessary before its radioactivity could be rigorously verified. We decided, therefore, to band the receptor by equilibrium density sedimentation and then to look for a shift in density of newly synthesized receptors following incorporation of amino acids containing stable isotopes. Amino acid mixtures contain-

ing the stable isotopes ^2H , ^{13}C , and ^{15}N can be obtained from Merck, Sharpe and Dohme. In addition, since the position of the receptor in the gradient is monitored by specified ^{125}I - α -bungarotoxin binding, no purification step is necessary. Metrizamide, a tri-iodinated benzamido derivative of glucose, provides a convenient medium to density-band the receptor, since it does not disrupt the α -bungarotoxin-receptor interaction at concentrations with a density of up to $1.5\ \text{g}\cdot\text{m}^{-3}$. Our preliminary attempts to shift the density of newly synthesized receptors with ^2H amino acids and to de-

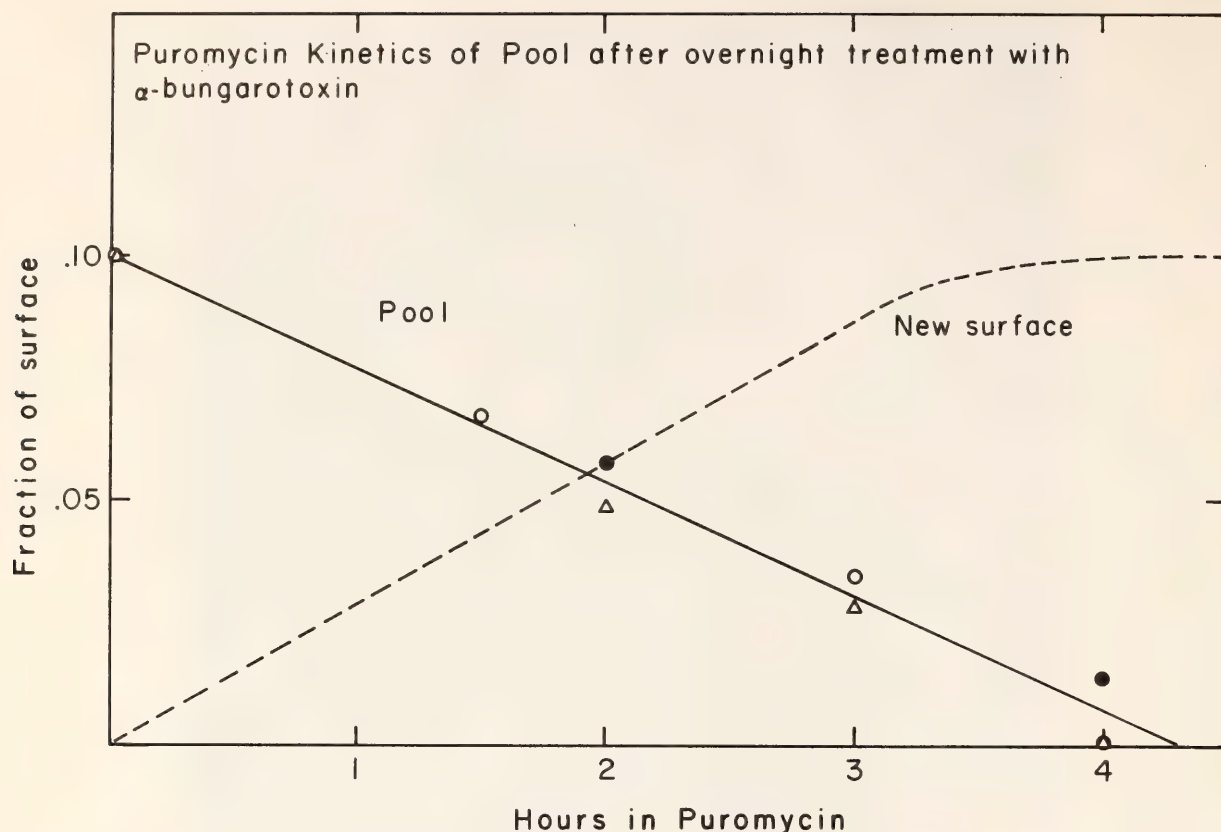


Fig. 48. Kinetics of pool disappearance and new receptor appearance. Decrease of "precursor" in presence of puromycin. All cultures were incubated overnight with 0.5–1.0 $\mu\text{g/ml}$ unlabeled α -bungarotoxin. The next day sets of 5–6 cultures were pretreated with 20 $\mu\text{g/ml}$ puromycin for the indicated times. All cultures were then washed to remove unbound α -bungarotoxin. In one experiment (open circles), sets were immediately extracted in 1% Triton X-100. In the other two experiments (filled circles, open triangles) the cells were scraped from the dish, homogenized by 25 strokes of a Dounce (pestle B) homogenizer (in 10 mM Tris at 0°C), and centrifuged at $50,000 g \times 30'$. The pellets were extracted with 1% Triton X-100, 10 mM Tris, pH 7.8. Each of the extracts was incubated with 0.01 $\mu\text{g/ml}$ ^{125}I - α -bungarotoxin for 1 hr at room temperature. The complexes formed were freed of unbound α -bungarotoxin by Bio-Gel P-60 chromatography. The fractions in the excluded peak were pooled, and an aliquot was taken for analysis by velocity sedimentation in sucrose gradients. In all cases the area under the 10S peak in the gradient was measured. For each experiment, all values were normalized so that the control value equaled 0.10 of the surface. Incorporation was measured after cells were first saturated with unlabeled α -bungarotoxin for about 15 hr. The actual plateau level reached in this experiment was about 8% of the total surface, but it has been normalized to 0.10 for comparison with the pool decrease.

test the density shift in spontaneously formed metrizable gradients were successful. The density shift produced, however, was quite small (6-drop separation–40-drop half-width of bands). Shortly thereafter, another group reported equilibrium density sedimentation studies of bacterial enzymes in metrizable gradients. The authors observed that since metrizable, being highly viscous, approaches its equilibrium concentration gradient very slowly, it is possible to preform a stable metrizable gradient

and to centrifuge at very high fields (350,000 g) in order to rapidly equilibrate the macromolecular species (in our case, the acetylcholine receptor). In our initial attempts using a preformed metrizable gradient ($dp/dr = 0.03 \text{ g}\cdot\text{cm}^{-4}$) we observed greater separations of "heavy" and "light" receptors (see Fig. 49a). By appropriate manipulation of the preformed gradient ($dp/dr = 0.015 \text{ g}\cdot\text{cm}^{-4}$) it should be possible to double this separation. In addition, we have shifted the density of receptors by

incorporation of amino acids containing ^{13}C (see Fig. 49b). Since we can purchase amino acids substituted with all three heavy isotopes (^2H , ^{13}C , ^{15}N) on the same amino acid, and thus add the

shifts seen in Fig. 49 a and b, it should be possible to observe large separations of "heavy" and "light" receptors (40-drop separation—40-drop half-width of bands).

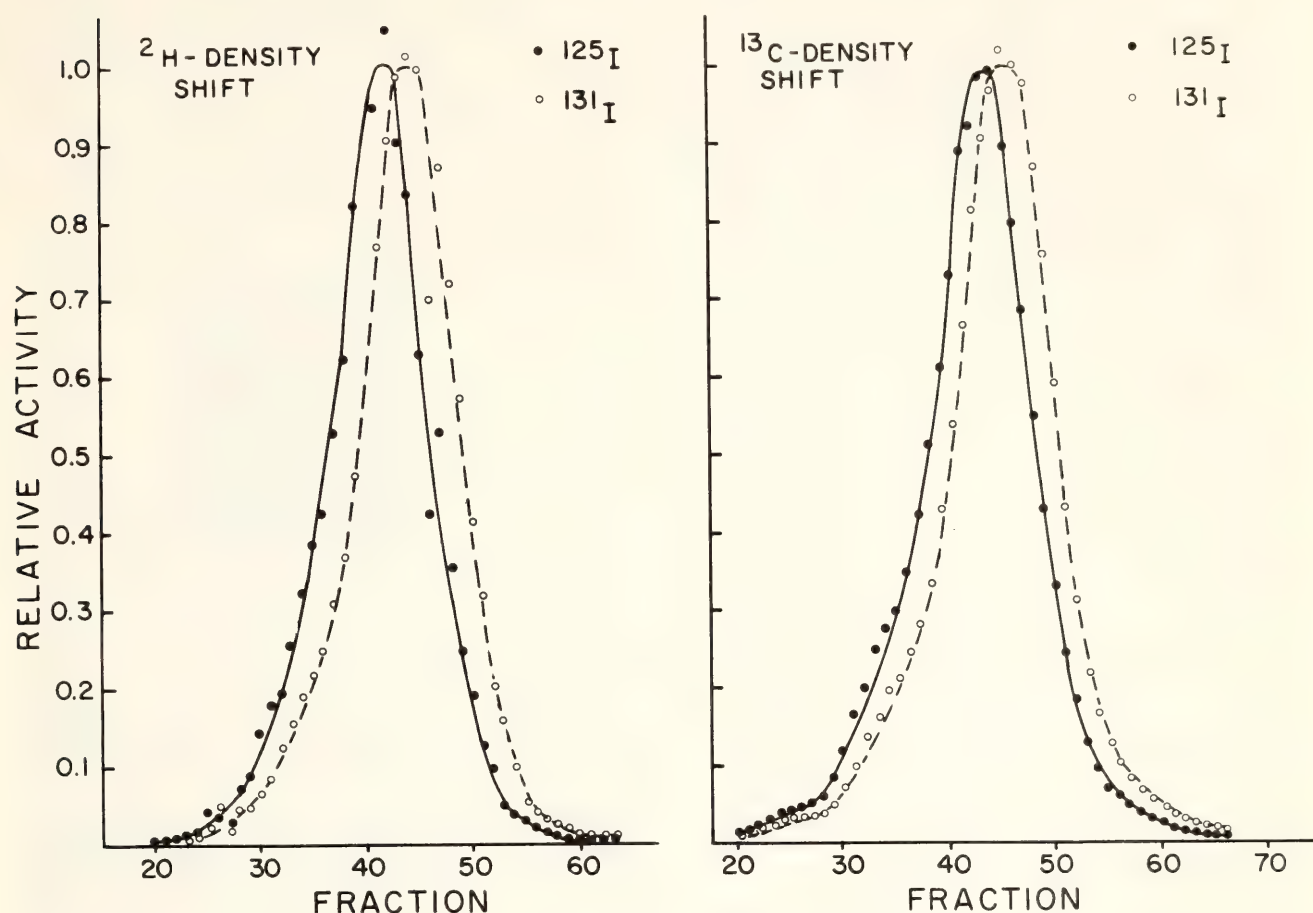


Fig. 49. Density shift of newly synthesized receptors. Several large 5-day cultures were incubated with $0.2\ \mu\text{g}/\text{ml}$ unlabeled α -bungarotoxin overnight. After 16 hr of incubation the medium was switched to one containing amino acids substituted with ^2H (a) or ^{13}C (b) (preparation of the medium is described below) but still containing $0.2\ \mu\text{g}/\text{ml}$ unlabeled α -bungarotoxin. After 5 more hours of incubation the cultures were washed to remove unbound α -bungarotoxin and incubated in "heavy" medium for an additional 2 hr. During the final 30 min of incubation ^{125}I - α -bungarotoxin was added to the cultures such that the concentration was $0.2\ \mu\text{g}/\text{ml}$. The cultures were washed at 4°C , the cells scraped from the culture dishes, homogenized in 10 mM Tris, and centrifuged at 17,000 rpm for 45 min. The pellet was extracted in a small volume of 1% Triton-10 mM Tris. An aliquot of the extract was mixed with a marker of ^{131}I - α -bungarotoxin-receptor complexes which were extracted from an independent set of cultures. The mixture was loaded in a thin band on a step metrizamide gradient containing 0.95 ml of each of five concentrations: 40%, 35%, 30%, 25%, 20% (W/W) of metrizamide. The solvent for the metrizamide was deuterium oxide. Centrifugation was carried out in a Beckman SW65 Rotor for 15 hr at 54,000 rpm at 4°C . Gradients were collected by puncturing the bottom of the tube. One hundred four-drop fractions were collected from each gradient into scintillation vials. Radioactivity was monitored simultaneously on appropriate channels for ^{125}I and ^{131}I . After correction for crossover between the channels the data were plotted, and smooth curves were drawn through each peak (peak fractions contained at least 800 cpm). Data were then normalized to the highest point on the smooth curve; some points are therefore greater than one. Heavy medium was our normal growth medium except that 16 of the amino acids were substituted by an ^2H or ^{13}C amino acid mixture and serum normally added to the medium was exhaustively dialyzed against Hanks. Amino acid mixtures were obtained from Merck, Sharp and Dohme and were either 98% atom purity ^2H or 80% atom purity ^{13}C .

TURNOVER OF RECEPTORS IN DENERVATED ADULT MUSCLE

D. M. Fambrough and P. N. Devreotes

Last year we reported that the rate of degradation of α -bungarotoxin bound to acetylcholine receptors in denervated rat diaphragm muscle in organ culture was a first-order exponential process with a half-time of about 24 hr. It was not possible to establish the identity between degradation of toxin and degradation of receptor, as was done for chick muscle in tissue culture, because of the much greater technical difficulties in working with adult muscle. Nevertheless, by analogy with cultured muscle, it seems almost certain that degradation of toxin is associated with degradation of receptor in adult denervated skeletal muscle as well. This hypothesis would be strengthened if it could be shown that the degradation of α -bungarotoxin bound to extrajunctional acetylcholine receptors in adult muscle were similar to degradation in tissue cultured muscle in its sensitivity to various metabolic inhibitors and other environmental conditions. Exploration of factors influencing the degradation of α -bungarotoxin in denervated adult skeletal muscles was begun, but the rat diaphragm proved to be a poor experimental material because it cannot be isolated as a viable muscle without also including a large amount of other (intercostal) muscle and portions of several ribs, which serve as the area of insertion of the diaphragm onto the body wall. Since these tissues also bind α -bungarotoxin, they contribute to the observed degradation in a way that is difficult to control from one preparation to the next and also difficult to evaluate for any given preparation. Thus a thin, easily denervated and easily dissected skeletal muscle with insertions onto long tendons was sought. The mouse extensor digitorum longus (EDL), a muscle in the lower hindlimb, was selected. This muscle has been used in many denervation and reinnervation studies.

Our experiments on acetylcholine receptor metabolism in tissue culture utilized the constancy of total receptor number from one culture dish to the next, and often 20 to 50 culture dishes would be used in constructing a kinetic curve. When working with adult skeletal muscles it is not possible to dissect out 20 to 50 muscles simultaneously; that would take several hours and require the sacrifice of many animals. Therefore, the next step in investigating receptor metabolism in adult skeletal muscles was to devise a method for obtaining an entire kinetic curve from one or a few muscles. We have not yet developed means to measure accumulation of acetylcholine receptors or incorporation of new receptors into plasma membrane in single adult muscles. Such measurements are complicated by the long time needed for saturation of a muscle with α -bungarotoxin and removal of the unbound toxin. However, we have been able to measure degradation of toxin previously bound to acetylcholine receptors continuously for periods of 24 hr or longer. This was accomplished by maintaining the muscle in a perfusion chamber which fits into the well of a gamma detector. The gamma radiation produced by decay of ^{125}I , which is a measure of the number of α -bungarotoxin receptor complexes in the muscle, is continuously monitored. When iodinated α -bungarotoxin is degraded, the resultant ^{125}I -tyrosine diffuses out of the muscle and is carried out of the gamma well by the perfusion solution. The loss of radiation from the muscle is due almost exclusively to degradation of α -bungarotoxin. Since degradation is very sensitive to temperature, the gamma well and the perfusion solutions and associated pumps are housed in an incubator to maintain a constant 37°C. Some details of the perfusion chamber are illustrated in Fig. 50.

Figure 51 illustrates the loss of radiation from 8-day denervated mouse EDL muscle after exposure to ^{125}I -labeled α -bungarotoxin. The curve consists of three

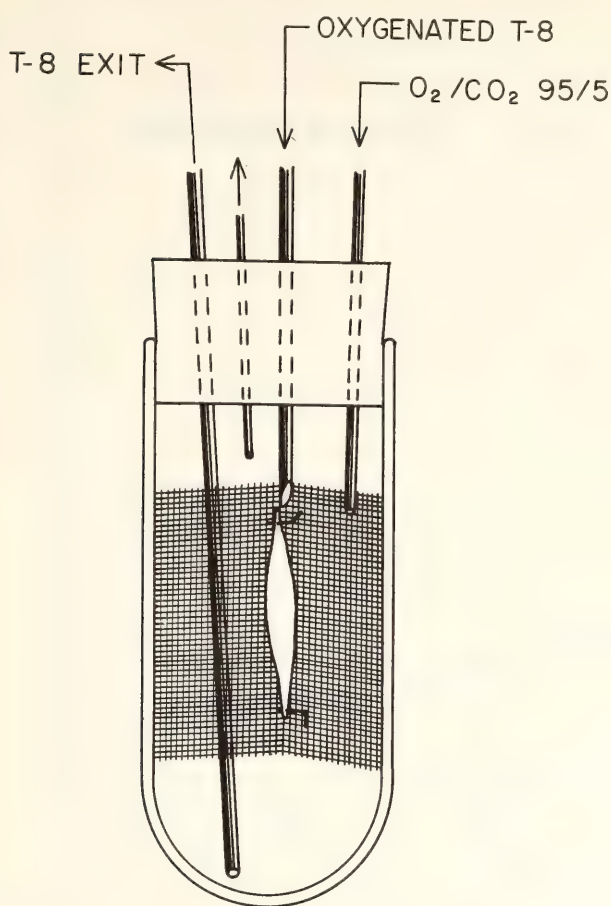


Fig. 50. Perfusion chamber for the growth of adult mouse muscle. The chamber consists of a glass test tube and silicone rubber stopper through which pass stainless steel tubes for delivery and removal of medium and oxygen. The muscle is pinned to a stainless steel grid support.

first-order exponentials. The first represents the washout of free bungarotoxin from the extracellular spacer of the muscle. The second has a total duration of about 5 or 6 hr and represents the loss of a variable but always rather small fraction of the total radioactivity. Its meaning is not known. Finally, the long third exponential represents the degradation of bound α -bungarotoxin and release of the radio-labeled degradation product from the muscle. Some assumptions are required for calculation of the half-time for degradation of α -bungarotoxin. The major assumption is what fraction of the total radioactivity is associated with this exponential. It is known that the α -bungarotoxin associated with acetylcholine receptors that

occur at the former neuromuscular junction is degraded at a much slower rate than is extrajunctionally bound α -bungarotoxin. In the mouse EDL the extrajunctional acetylcholine receptors constitute roughly 60% to 90% of total receptors during the first few weeks following denervation. Another portion of the bound α -bungarotoxin is associated with material that cannot be solubilized with the detergent Triton X-100. Whether or not this toxin is associated with insoluble receptors and what the rate of loss of toxin from this set of binding sites is are unknown. If this insoluble material is assumed *not* to be receptor, and the loss of radioactivity from these sites is assumed to be slow compared to degradation of toxin bound to extrajunctional receptors, then a half-time for degradation is about 20 hr. If *all* the radioactivity remaining in the muscle at the end of the second exponential (Fig. 51) were associated with extrajunctional receptors, then the half-time for degradation would be about 30 to 35 hr. Judging from the data on tissue cultured rat and chick muscle and from the data of Chang and Huang on degradation of toxin associated with rat diaphragm in vivo, we think a half-time of about 20 hr seems most reasonable.

Among the first experiments we performed with the perfused EDL muscle is a test of the dependence of degradation on metabolic energy. In this experiment, illustrated in Fig. 52, the rate of degradation was measured for many hours and then $10^{-3}M$ dinitrophenol was added to the perfusion medium to interfere with ATP synthesis by the muscle. The introduction of dinitrophenol resulted in a tenfold decrease in the rate of loss of radioactivity from the muscle, confirming that the process is an energy-requiring one. An analogous experiment with cultured chick muscle was reported in *Year Book 73*, p. 64.

We have also been able to demonstrate that the acetylcholine receptors appearing in extrajunctional plasma membrane

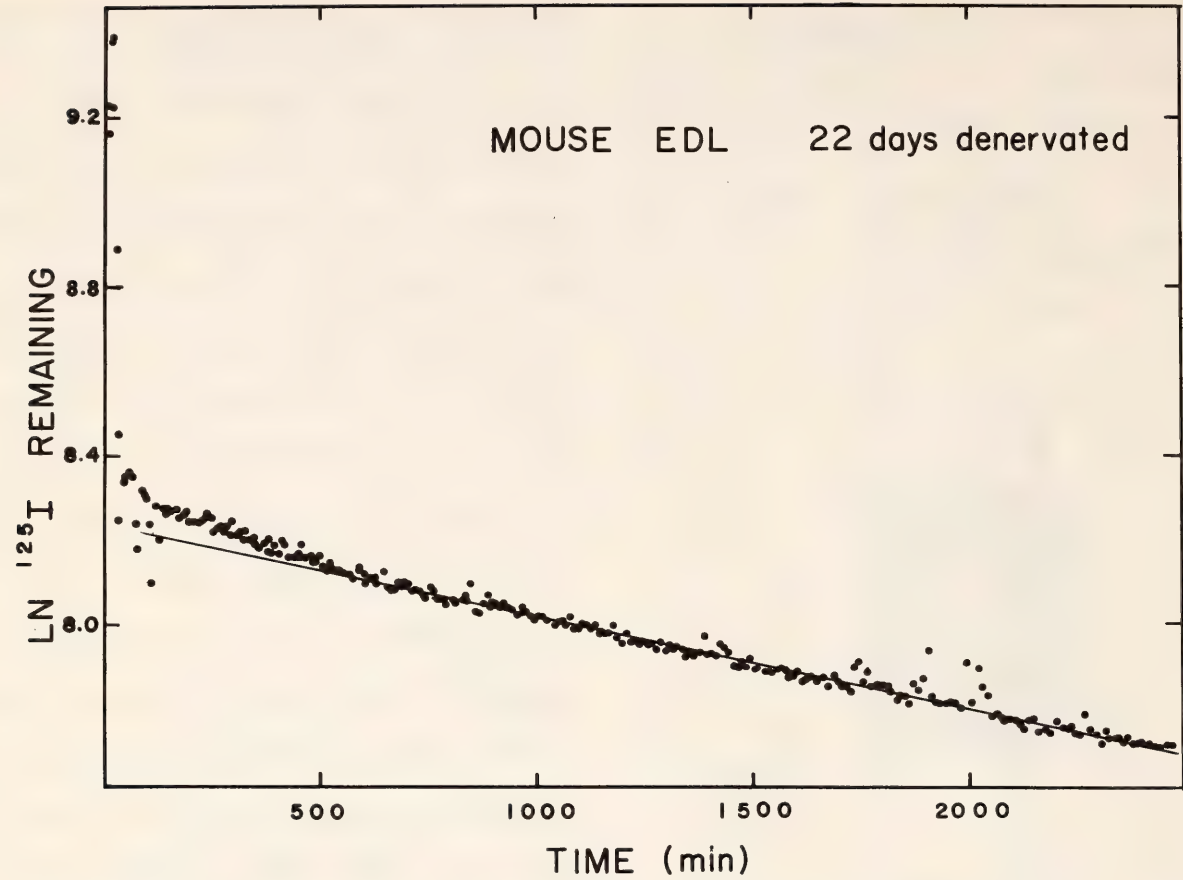


Fig. 51. Release of radioactivity from 22-day denervated mouse EDL muscle in organ culture, following brief incubation of muscle with ¹²⁵I- α -bungarotoxin. Details of culture and monitoring of radioactivity are in text.

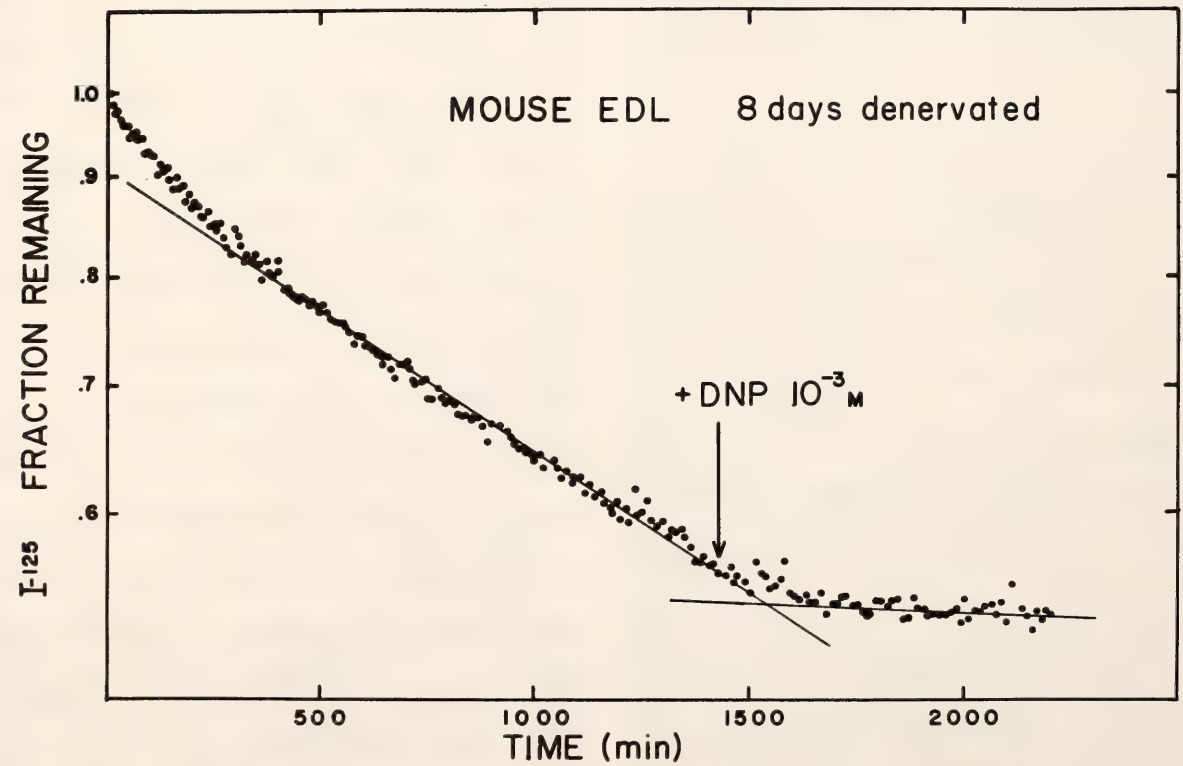


Fig. 52. Effect of 2, 4-dinitrophenol on the release of radioactivity from 8-day denervated mouse EDL, following brief incubation with ¹²⁵I- α -bungarotoxin. Measurements begin after the washout of most of the unbound α -bungarotoxin.

after denervation are synthesized *de novo*. This was accomplished using essentially the same experimental procedures as were used to demonstrate the incorporation of isotopically labeled amino acids into acetylcholine receptors in cultured chick skeletal muscle. The lower leg muscles of 10 mice were denervated by cutting the right sciatic nerve. Five days later the EDL muscles were removed and maintained in organ culture. During the first 3 hr in organ culture the culture medium contained 1 $\mu\text{g}/\text{ml}$ α -bungarotoxin and all of the amino acids of the Trowell T-8 medium were fully deuterated in the non-exchangeable hydrogens. Thus, all of the existing acetylcholine receptors on the EDL muscle fibers were blocked by unlabeled α -bungarotoxin and the newly synthesized receptors should have incorporated the isotopically labeled amino acids in their polypeptide chains. Then the unlabeled α -bungarotoxin was removed by washing the muscles with many changes of medium over a 2 hr period. Then the organ cultures were maintained overnight in culture medium, still with deuterated amino acids. The next day the new surface acetylcholine receptors were labeled with ^{125}I - α -bungarotoxin by incubation for 1 hr and muscles were thoroughly washed to remove unbound bungarotoxin. The muscles were homogenized in 1% Triton X-100, 10 mM Tris buffer to solubilize the labeled receptors, and the homogenates were centrifuged at 10,000 $\times g$ for 30 min to sediment insoluble material. The supernatant, containing the solubilized receptors, was concentrated by pressure dialysis, layered on a 5% to 20% sucrose gradient containing 1% Triton X-100, and centrifuged for 4 hr at 62,000 rpm in a Beckman SW-65 rotor at 20°C. The 10S peak from such gradients contained the ^{125}I - α -bungarotoxin labeled, deuterium-containing receptors. ^{131}I - α -bungarotoxin labeled control receptors were prepared from EDL muscles denervated for the same length of time but maintained in the animals

until they were removed for incubation with the ^{131}I -labeled α -bungarotoxin. The purification of these control receptors was identical to that for the deuterated receptors.

The receptors synthesized by EDL muscles during maintenance in organ culture with deuterated amino acids in the medium and the receptors from control denervated muscle, now containing different iodinated α -bungarotoxin labels, were mixed and layered on stepwise gradients of metrizamide-deuterium oxide and centrifuged for 4 days at 33,000 rpm in a Beckman No. 40 fixed angle rotor, which banded the receptors in a spontaneously formed gradient. The resultant fractionation of receptors is illustrated in Fig. 53. The receptors from the muscles grown in organ culture with deuterated amino acids were clearly more dense than those from control muscles, proving that deuterated amino acids had been incorporated into the newly appearing receptors in organ culture. Thus it is proved that acetylcholine receptors are synthesized *de novo* and incorporated into the extrajunctional plasma membranes of denervated skeletal muscle fibers.

Some years ago we were able to show that when denervated skeletal muscle was maintained in organ culture denervation, supersensitivity developed just as it does in denervated muscle in vivo. When protein synthesis was blocked by inclusion in the culture medium of either puromycin or cycloheximide (both inhibitors of protein synthesis), the appearance of extrajunctional chemosensitivity was blocked. Work in several laboratories demonstrated that there is a large increase in the total number of receptors after denervation, and we have shown that the receptors at the former neuromuscular junction remain at a high concentration there. Thus there was a good deal of evidence to suggest that denervation supersensitivity to acetylcholine results from the synthesis of new acetylcholine receptors. Nevertheless, it

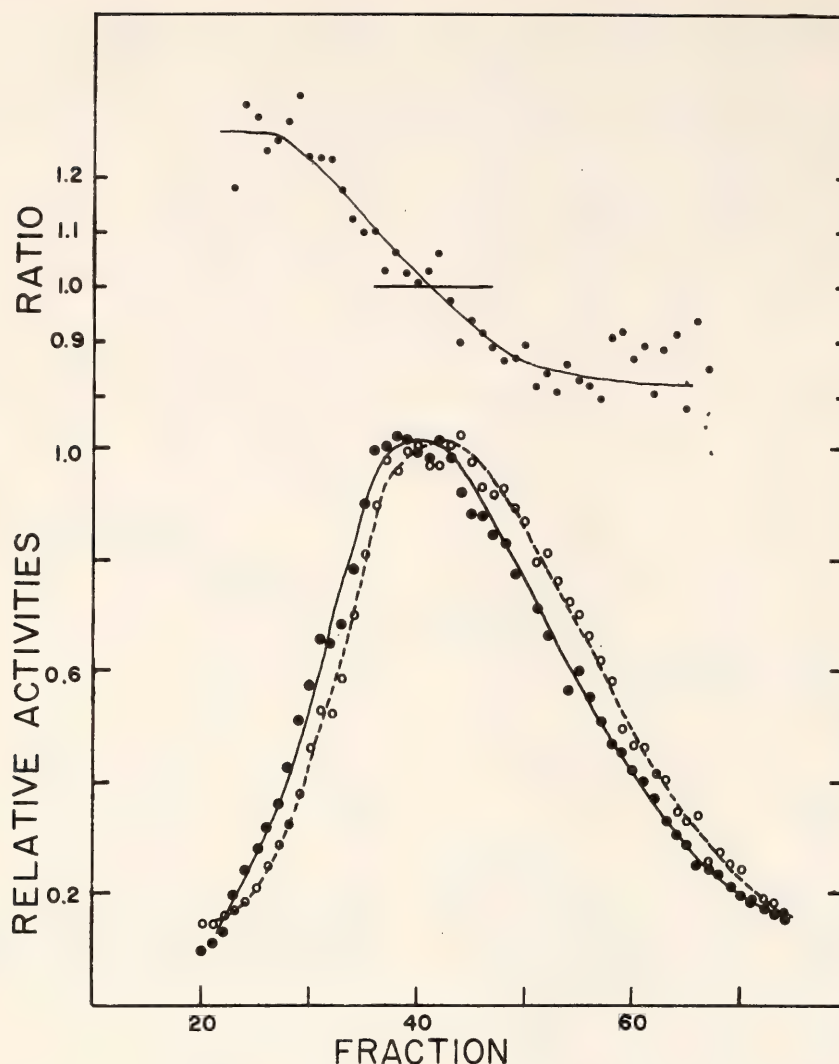


Fig. 53. Equilibrium density gradient sedimentation of 6-day denervated mouse EDL acetylcholine receptors. ^{131}I - α -bungarotoxin-receptor complexes from 6-day denervated muscle (open circles). ^{125}I - α -bungarotoxin-receptor complexes appearing during 15 hr in organ culture in medium containing ^3H -amino acids (filled circles). α -bungarotoxin-receptor complexes were extracted from the muscle by homogenization in 1% Triton, 10 mM Tris buffer, pH 7.8, and prepurified by sucrose gradient velocity sedimentation. The ratio of ^{125}I to ^{131}I values is shown above for peak fractions.

was still possible that all the receptors involved in denervation supersensitivity were already present as "latent" receptors whose activation was dependent upon protein synthesis. This hypothesis, however unlikely, has now been ruled out. As it stands now, the appearance of acetylcholine receptors in extrajunctional membranes of denervated skeletal muscle and the metabolism of these receptors appear to be qualitatively like the corresponding phenomena in tissue-cultured embryonic skeletal muscle and even surprisingly similar in quantitative aspects.

IODINATION OF MEMBRANE PROTEINS OF MUSCLE CELLS

K. Tepperman

One protein of the muscle cell membrane, the acetylcholine receptor, has been studied in detail by many research groups; and its synthesis, appearance in the plasma membrane, and degradation have been described in this laboratory. In order to develop a better understanding of plasma membranes, in terms of their structure and their metabolism, it would be useful to conduct similar studies with other membrane proteins. One

means of identifying a specific group of membrane proteins is to iodinate cells using lactoperoxidase and $^{125}\text{I}^-$. This method has been shown to specifically label proteins on the surface of the plasma membrane in red blood cells, L cells and several other cell types. Iodination is a useful tool in describing the organization of the plasma membrane, since it can be used in studying the size and accessibility of surface proteins. In addition, the turnover of iodinated cell-surface proteins can be monitored by following the loss of iodinated proteins from the cell surface. In the past year, iodination of plasma membrane proteins of cultured muscle cells was carried out using lactoperoxidase, a peroxide generating system, and $\text{Na } ^{125}\text{I}$. After iodination the cells were removed from culture plates by several different methods. The proteins were solubilized in SDS buffer and separated by polyacrylamide gel electrophoresis on slab gels. Gels were stained to reveal the major protein bands and then dried and autoradiographed. Figures 54 and 55 show densitometer traces of autoradiographs of 7.5% and 15% acrylamide gels. Gels of different acrylamide concentrations are required to obtain maximum resolution of different size classes of polypeptides. For each of these gels, iodinated chick muscle cells in tissue culture were extracted directly in a buffer containing 4 M urea, 1% SDS and 10 mM Tris, pH 6.8. Similar protein distributions were obtained when the proteins were first precipitated with TCA, washed with acetone, and then extracted in SDS buffer. Analysis of the different gels suggests that there are at least 15 clearly distinguishable iodinated bands, some of which may represent more than one polypeptide. They range in molecular weight from approximately 12,000 daltons to approximately 230,000 daltons, with the large molecular weight polypeptide showing the largest single amount of ^{125}I .

In order to determine whether any of

the iodinated bands could be nonspecifically bound serum proteins, bovine serum albumin was (^{125}I) iodinated by the chloramine T method and incubated with cultured muscle cells for several hours. After incubation cells were rinsed by methods used routinely after iodination. All the ^{125}I -BSA could be removed, suggesting that nonspecifically bound proteins are probably not contributing to the protein pattern. In addition ^{125}I -BSA was used as a standard on SDS gels and did not coincide with any major iodinated band.

Experiments were also done to test whether one sensitive membrane property, the resting potential, was changed as a result of iodination. Resting membrane potentials of cultured chick myotubes were monitored by Aileen Ritchie during the iodination reaction. At an iodide concentration of 10^{-6}M , the concentration used in the labeling experiments, the resting membrane potential remained at normal levels. It required a concentration of 10^{-4}M iodide to significantly decrease resting potentials.

Preliminary experiments have been done using rat muscle cells in culture for iodination. In these experiments, cells were iodinated in suspension after removal from plates by collagenase. SDS gel analysis of the proteins from these cells shows some radioactive components similar in molecular weight to those from chick cells. However, the large molecular band seen on autoradiographs of chick proteins is absent. Further experiments must be done to determine whether this difference is a species difference or a difference due to the preparation method.

In some experiments, cells were preincubated with α -bungarotoxin before iodination. The cells were then analyzed both on SDS gels and on sucrose gradients. On gels, no peak of iodination occurred at a molecular weight corresponding to bungarotoxin. On sucrose gradients, there was no iodinated 10S peak corresponding to the position of the ACh

receptor on either the toxin-treated or control plates. This indicates that neither the ACh receptor nor the α -bungarotoxin bound to it exhibit significant iodination, although the ACh receptor has been esti-

mated to represent approximately 1% of the cell surface protein. This result may be important in determining the limits of the iodination reaction for identifying specific proteins.

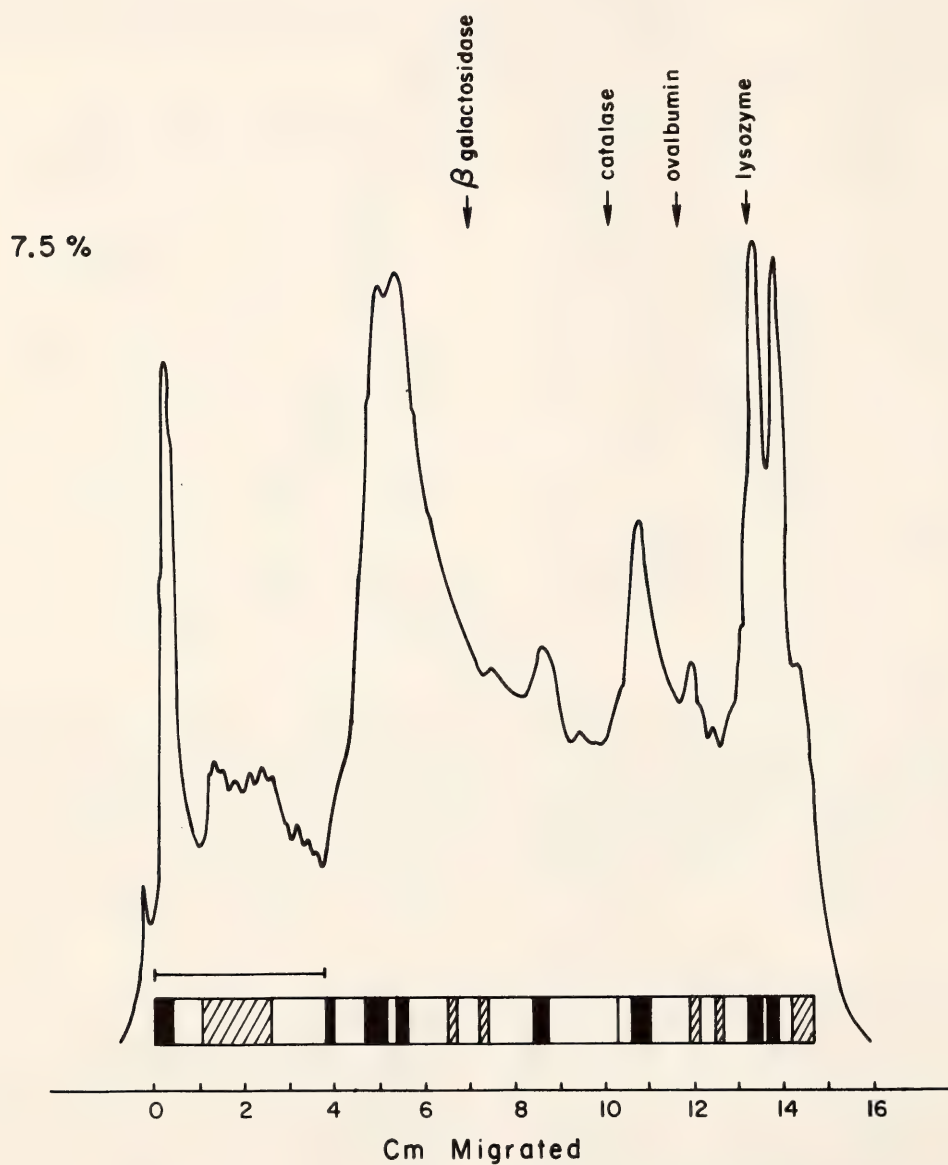


Fig. 54. Distribution of iodinated proteins on a 7.5% SDS acrylamide gel. Iodinated chick skeletal muscle cells were extracted in 4 M urea, 1% SDS, 10 mM Tris, pH 6.8, boiled in the presence of mercaptoethanol, and layered onto a Bio-Gel P-2 column to remove free ^{125}I . A portion of the excluded peak was then layered onto a stacking gel, 3% acrylamide, 0.2% bisacrylamide, pH 6.8, over a running gel, 7.5% acrylamide, 0.2% bisacrylamide, pH 8.8. Electrophoresis was carried out at 3.3v/cm for 2 hr, then at 6.6v/cm for 4 hr. Gels were stained, then dried and autoradiographed. The figure shows a densitometer trace of the autoradiogram. Also shown is a schematic drawing of the gels. Above the drawing, a measuring bar indicates the length of the stacking gel. Migration is from left to right. Positions of four molecular weight markers are shown: lysozyme (MW 14,800), ovalbumin (MW 43,000), catalase (MW 60,000) and β -galactosidase (MW 130,000).

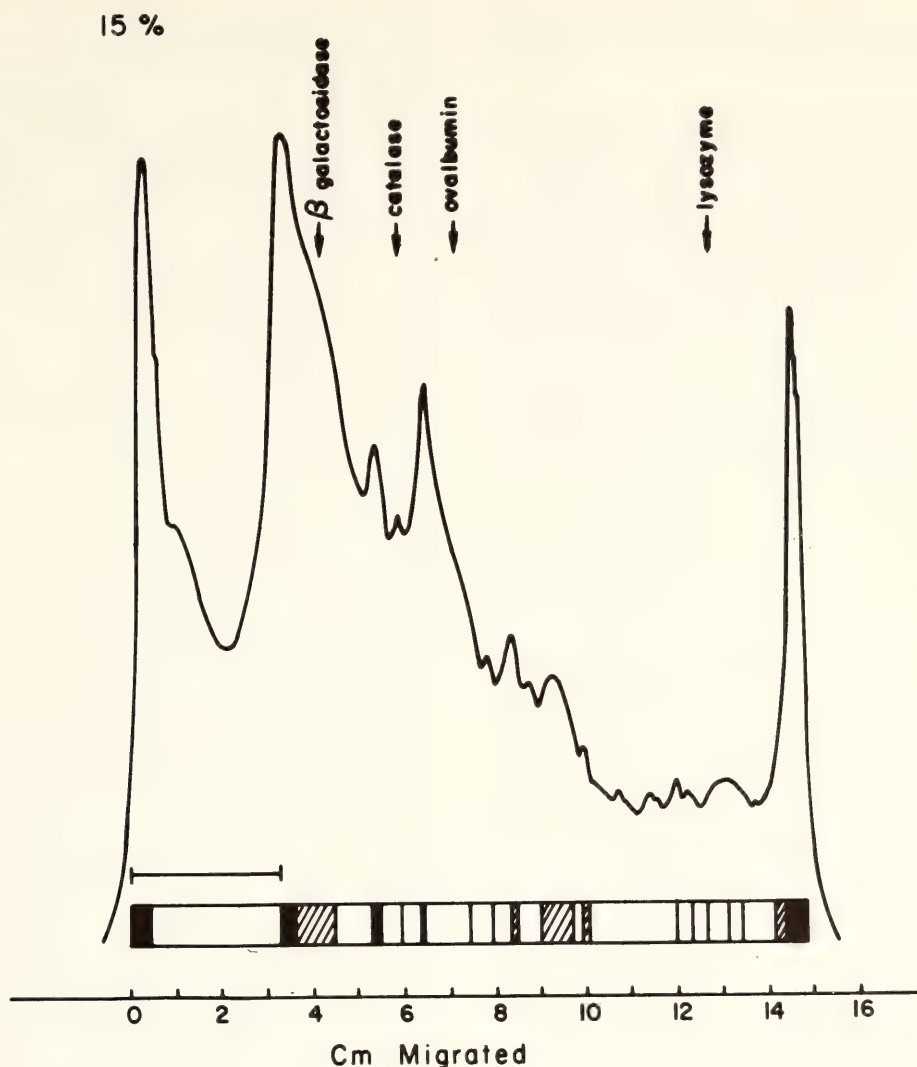


Fig. 55. Distribution of iodinated proteins on a 15% acrylamide gel. A fraction of the protein extract described in Fig. 54 was layered onto a stacking gel of 6% acrylamide, 0.2% bisacrylamide, pH 6.8, over a running gel of 15% acrylamide, 0.2% bisacrylamide. Gels were electrophoresed and prepared as in Fig. 54.

AN INVESTIGATION OF THE INVOLVEMENT
OF DENERVATION IN THE HUMAN
SKELETAL MUSCLE DISEASES
AMYOTROPHIC LATERAL SCLEROSIS AND
CONGENITAL MYOTONIC DYSTROPHY

*D. M. Fambrough in collaboration with
D. B. Drachman**

The muscular dystrophies constitute a heterogeneous group of progressive muscle disorders which are usually inherited and are characterized by typical clinical patterns of weakness. Classically, the muscular degeneration has been thought

* Department of Neurology, The Johns Hopkins University School of Medicine.

to result from some primary defect inherent in the muscle fiber, although such an abnormality has not yet been identified in any of the dystrophies. More recently, the possibility has been raised that abnormalities of the motor nerves might be fundamental to the pathogenesis of the dystrophies. This concept is based chiefly on similarities in the histopathology and physiological properties of denervated and dystrophic human muscle: "myopathic" histological features are often present in muscle of patients with disorders of the motor nerves; and fibrillations and the reduction in the number of functional motor units have

been reported in a variety of neuromuscular disorders, including the dystrophies.

Of the group of muscular dystrophies, we elected to study myotonic dystrophy, since its features most closely resemble those of denervation. The muscular weakness is predominantly *distal*, as occurs also in peripheral neuropathies. Histologically, the affected muscle fibers show *atrophy* similar to that seen in denervation rather than destruction or denervation. With histochemical techniques the Type I fibers are found to be preferentially involved, which has been thought to represent a selective denervation effect.

The present investigation was designed to test the denervation hypothesis further by applying to human dystrophic muscle a widely accepted criterion of denervation: a high density of extrajunctional acetylcholine receptor sites. Nine patients ranging in age from 19 to 55 years with typical myotonic dystrophy gave informed consent for this study. All the myotonic dystrophy patients had family histories consistent with an autosomal dominant pattern of inheritance and manifested a characteristic pattern of weakness as well as clinical electromyographic and histological features of this disorder. As controls, two patients with amyotrophic lateral sclerosis (ALS) gave informed consent for this study. ALS is well known to be a disease involving progressive denervation of skeletal muscle fibers. Denervated rat diaphragm muscle was also used as a control.

Several techniques were used to assess the occurrence of extrajunctional acetylcholine receptors. All the techniques involved the binding of ^{125}I -labeled α -bungarotoxin to acetylcholine receptors in thin muscle strips obtained from biopsy specimens. Biopsy specimens were dissected and incubated in medium containing ^{125}I - α -bungarotoxin as described in *Year Book* 72, p. 56, for biopsies of myasthenia gravis patients. Specimens

were thoroughly washed to remove unbound α -bungarotoxin and fixed in glutaraldehyde. In some cases single muscle fibers were dissected from the specimens after staining for the enzyme acetylcholinesterase (to reveal the locations of neuromuscular junctions). These were mounted on microscope slides, and autoradiographs were made. In most cases small bundles of muscle fiber segments were used in determinations of the average density of extrajunctional acetylcholine receptors by a scintillation counting method described for denervated rat skeletal muscle in *Year Book* 73, p. 61. Finally, samples of all the biopsies were embedded in plastic and $1\text{ }\mu\text{m}$ cross sections were cut and processed for autoradiography.

Autoradiographs of whole mounted single muscle fibers sites on muscle fibers of patients with myotonic dystrophy (after incubation with iodinated α -bungarotoxin) revealed a normal pattern of bungarotoxin binding. Each fiber displayed one small area of densely packed silver grains, reflecting the binding of a very large number of α -bungarotoxin molecules in the area of the endplate. The extrajunctional surface of each fiber was virtually devoid of grains (approximately background level). These autoradiographs are interpreted to suggest that, qualitatively, the acetylcholine receptors in the muscle fibers are distributed just as they are in the muscle fibers of normal, innervated adults. Autoradiographs of denervated muscle fibers prepared in the same way show a high density of extrajunctional grains, indicative of a high level of extrajunctional acetylcholine receptors. Most of the muscle fibers examined in the present study by whole-mount autoradiography were fibers of approximately normal diameter. However, several very small caliber fibers were also examined (see Fig. 56), and they too appeared to be normal in grain distribution.

In Table 10, values for the number of α -bungarotoxin binding sites per endplate



Fig. 56. Autoradiogram of small-caliber human muscle fiber from patient with myotonic dystrophy, after incubation of biopsy with ¹²⁵I- α -bungarotoxin. Note dense accumulation of silver grains at neuromuscular junction and paucity of grains over distant extrajunctional areas.

and the density of extrajunctional sites on the average muscle fiber (both values obtained from scintillation counting) are presented. While there is a fair amount of variation in values from different patients, this variation may reflect normal variability, and all values for end-plate α -bungarotoxin binding sites are above values previously reported for myasthenia gravis patients and similar to values reported for normal adults. The density of extrajunctional α -bungarotoxin binding sites is in all cases low when compared with values of 500 to 700 sites per μm^2 obtained for 14-day denervated rat diaphragm fibers. The values for myotonic dystrophy patients are thus not consistent with high extrajunctional acetylcholine receptor density. The data in Table 10 indicate that the average muscle fiber in myotonic dystro-

phy patients lacks a high density of extrajunctional acetylcholine receptors, but these data could not reveal the presence of a small population of muscle fibers with a very high density of extrajunctional acetylcholine receptors. Therefore, it was necessary to examine each of the muscle fibers in biopsy specimens to determine whether or not a denervated population of muscle fibers existed. For this analysis, cross sections of biopsied muscle (after incubation with iodinated α -bungarotoxin) were examined after autoradiography. Since we could not be sure of the sensitivity of detection of denervated fibers by this technique, we also examined autoradiographs of denervated rat diaphragm muscle and of muscle biopsy specimens from two patients with amyotrophic lateral sclerosis (ALS). All of the small-caliber fibers seen in the autoradiographs of ALS muscle (Figure 57A) and all of the denervated rat muscle fibers were overlain by numerous silver grains. The densities for denervated rat skeletal muscle and for ALS denervated fibers were qualitatively similar, suggesting that the density of acetylcholine receptors in atrophic ALS muscle fibers must be on the order of several hundred sites per μm^2 . The grain density over atrophic fibers in areas devoid of large fibers seemed somewhat higher than the grain density over atrophic fibers in areas of muscle containing large numbers of large caliber

TABLE 10. Acetylcholine Receptors* in Muscles of Patients with Myotonic Dystrophy

Patient	Sites per Junction (mean + S.E.M.)	Extra-junctional Density (receptor/ μm^2)
1	$5.21 \pm 0.83 \times 10^7$	22
2	$2.75 \pm 0.26 \times 10^7$	20
3	$4.54 \pm 0.41 \times 10^7$	12
4	$1.78 \pm 0.53 \times 10^7$	1
5	$1.49 \pm 0.10 \times 10^7$	6
6	$2.59 \pm 0.22 \times 10^7$	11

* ¹²⁵I- α -bungarotoxin binding sites.

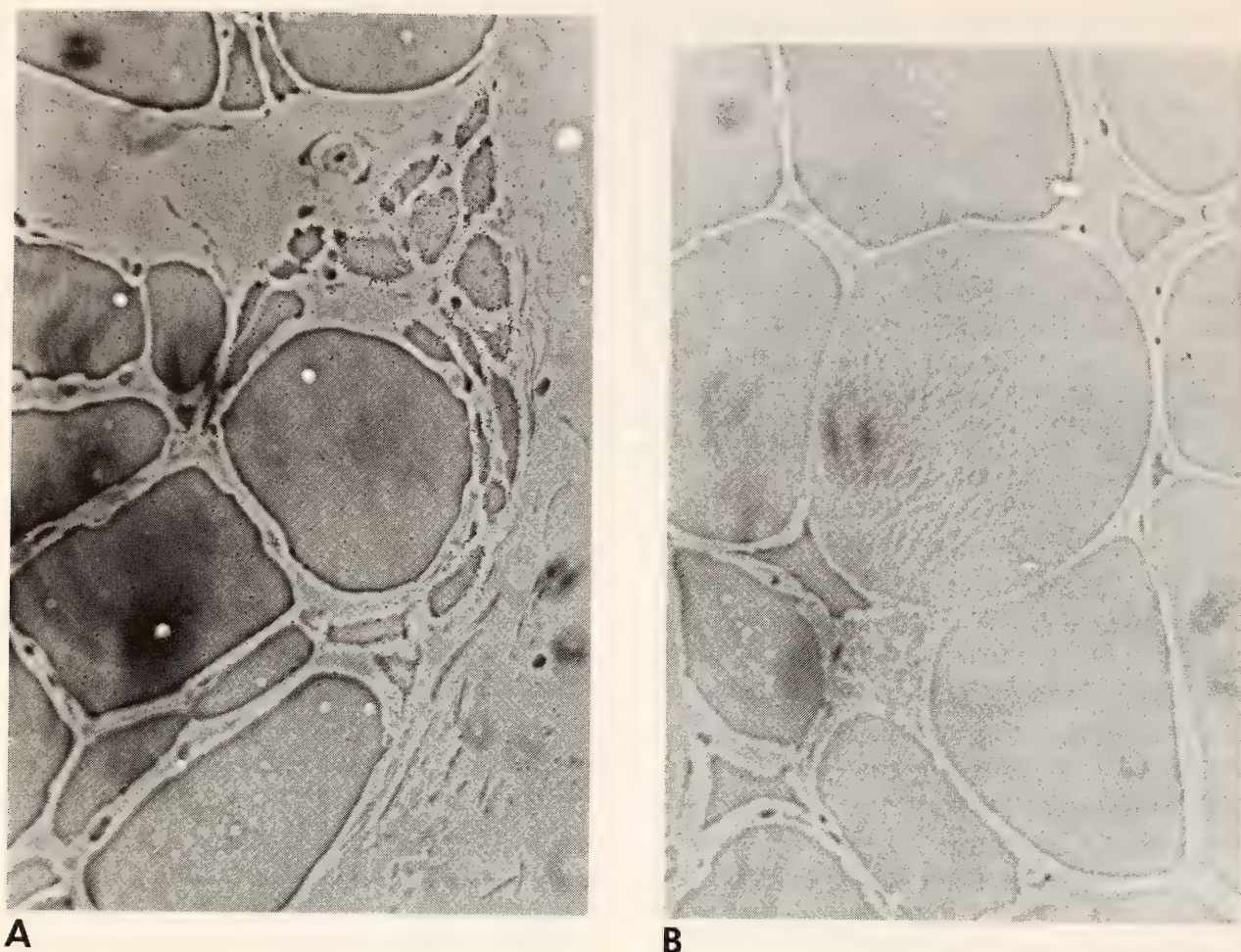


Fig. 57. Autoradiograms of cross-sections of human muscle biopsies after incubation with ^{125}I - α -bungarotoxin. (A) amyotrophic lateral sclerosis (ALS); (B) congenital myotonic dystrophy. Note high grain density over small caliber fibers in ALS biopsy.

fibers as well. This may reflect the longer period of denervation of the muscle fibers, which results in a greater accumulation of acetylcholine receptors in the areas with widespread atrophy.

In contrast to the ALS and denervated rat muscle, the muscles of myotonic dystrophy patients did not contain any fibers which displayed large numbers of extrajunctional α -bungarotoxin binding sites (Fig. 57B). We examined several hundred small caliber fibers as well as about ten times that many larger caliber fibers in autoradiograms of muscles from patients. Also, grain counts were made of the perimeter area of 137 small caliber fibers and 86 large caliber fibers. The average grain densities were very similar and the absolute grain densities were so low that statistical analysis of indi-

vidual fibers was not meaningful. The grain density for large caliber fibers was 0.73 per 100 μm^2 and that for the small caliber fibers was 0.82 per 100 μm^2 . These densities approximate the density of grains that occurred as background on these slides. In contrast to these negative data for myotonic dystrophy patients, grain counts for a biopsy of one ALS patient, done together with the congenital myotonic dystrophy material, revealed a grain density over atrophic fibers which was 3 per 100 μm^2 higher than the grain density over the large, presumably still innervated fibers.

The results of this study demonstrate that there is no population of skeletal muscle fibers in myotonic dystrophy muscles which displays a high extrajunctional acetylcholine receptor density.

Since an increase in extrajunctional receptors has been found to be an invariable consequence of denervation of mammalian muscle fibers, our findings suggest that there is not a significant population of denervated muscle fibers in myotonic dystrophy.

These data do not *prove* that denervation is not involved in myotonic dystrophy. One possibility is that some fibers are denervated for only a short time and are quickly re-innervated by neighboring motor nerves. If this were the case, the small fibers should nevertheless be the "denervated" ones in transition between one motor unit and another and should therefore show an increase in acetylcholine receptors. The absence of such an increase in the atrophic fibers

is perhaps the strongest argument against the denervation hypothesis. Another possibility is that spontaneous muscle activity prevents a denervation-like increase in extrajunctional receptors in denervated muscle fibers of myotonic dystrophy patients. It has been shown experimentally that electrical stimulation of denervated skeletal muscle can largely prevent or reverse the development of extrajunctional acetylcholine sensitivity. Could the spontaneous activity of myotonic muscles have a similar effect? Although the amount of activity of myotonic muscles has not been quantitatively measured, it would seem to be far less than the regular, continual stimulation required to prevent the denervation effect.

SIGNALING IN THE NERVOUS SYSTEM: SYNAPTIC MORPHOLOGY OF SPECIFIC NEURONS IN THE LEECH

*K. J. Muller, in collaboration with Uel J. McMahan**

The central nervous system of the leech *Hirudo medicinalis* provides a favorable preparation for studying a variety of fundamental neurobiological problems, particularly those dealing with synaptic transmission and integration. Its organization is so simple and reliable that a single neuron impaled with microelectrodes in one animal is found to perform like a corresponding cell in another. The central nervous system of the leech consists of a chain of identical segmental ganglia; each ganglion controls the stereotypic patterns of behavior of its body segment. Of the 350 neurons in each ganglion, the functions of about 100 have been identified. Most of the sensory and motor neurons can be recognized from animal to animal by the relatively constant shapes and positions of their cell bodies. Synaptic contacts between some mechanosensory and motor neurons have been characterized

physiologically and shown to mediate reflexive behavior. It has also been possible experimentally to make permanent changes in the synaptic interactions between certain neurons. In order to complement these physiological studies, over the past year we have examined in some detail the structure of specific neurons with the aim of locating and characterizing their synapses.

The synapses of cells in the ganglion are between neuronal processes that form an intricate meshwork, the neuropil, in the center of the ganglion. This arrangement has made it difficult to trace the origins of particular profiles seen in the electron microscope and even to follow the continuity of selectively stained processes in the light microscope. We have therefore injected horseradish peroxidase through a recording micropipette into specific neurons to mark their finest processes. Peroxidase forms a dense reaction product that is visible in the injected neurons' cytoplasm throughout the ganglion; ultrastructural details are

* Department of Neurobiology, Harvard Medical School.

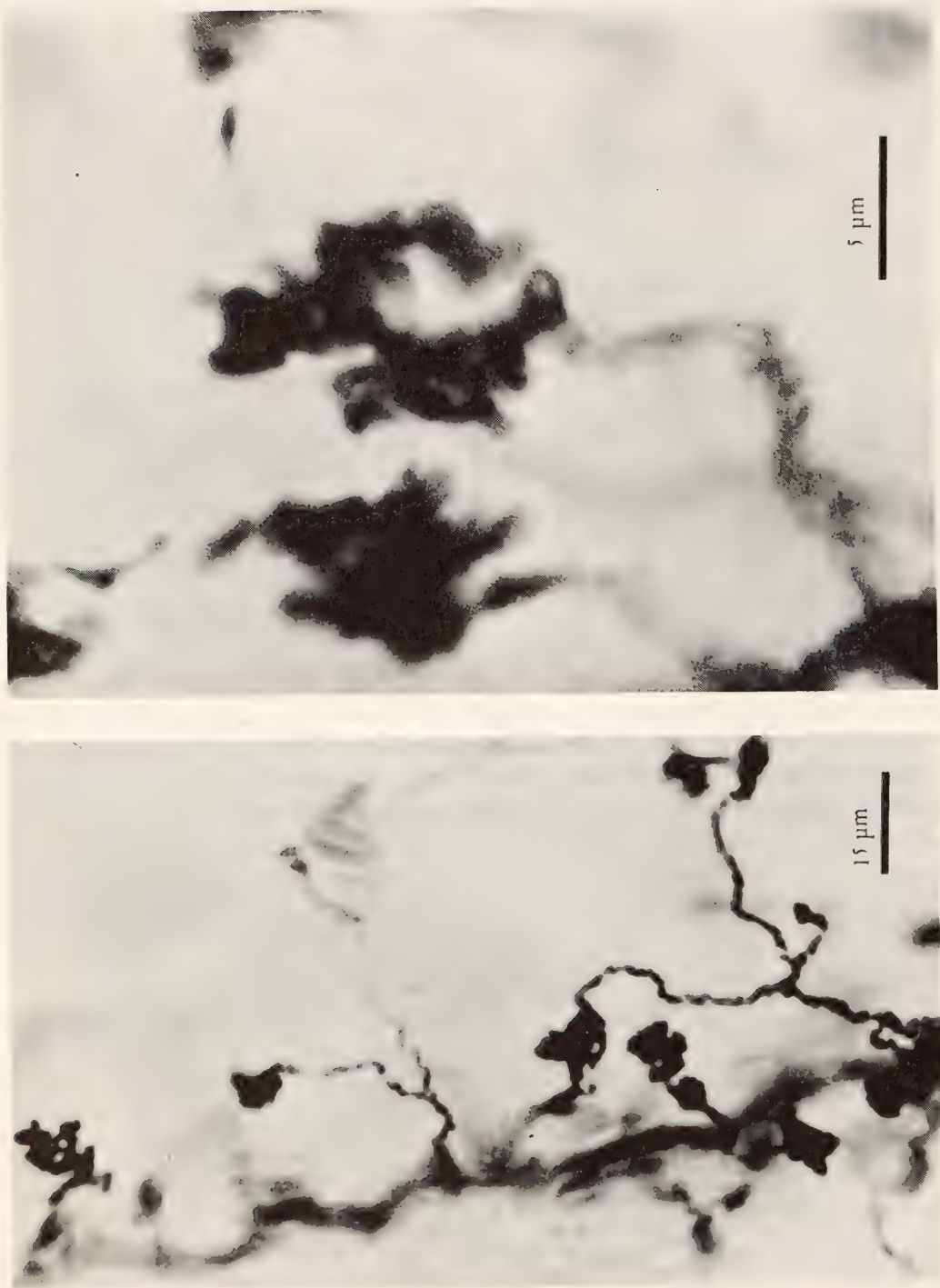


Fig. 58. Processes of a pressure sensory neuron in the leech. The cell was injected with horseradish peroxidase and the ganglion reacted with benzidine dihydrochloride, dehydrated, and mounted whole. At the ends of the fine processes that emerge from the main trunk are clusters of fingerlike swellings, shown enlarged on the right. The clusters are the sites of dozens of synaptic contacts.

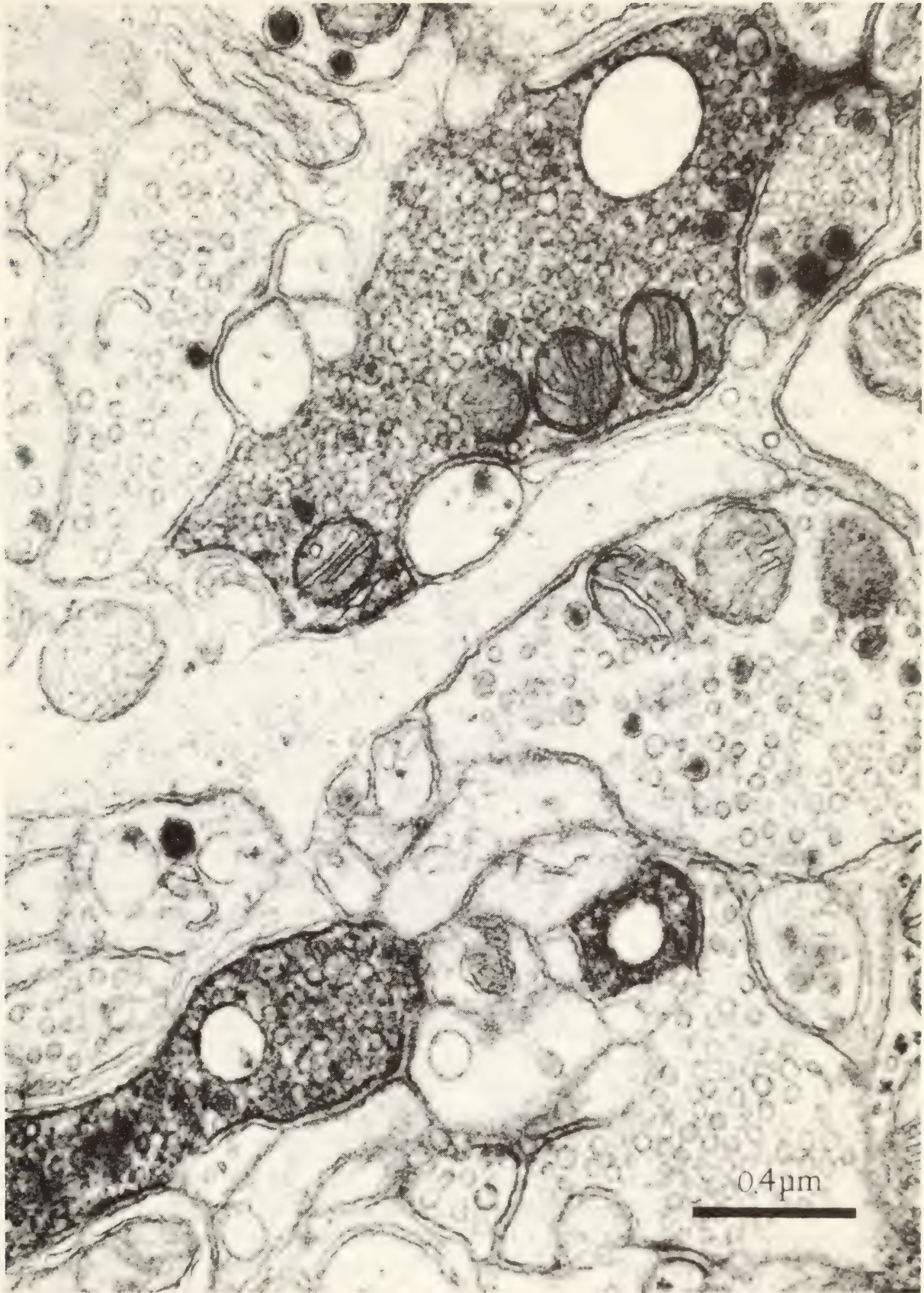


Fig. 59. A cell as in Fig. 58 reacted with diaminobenzidine tetrahydrochloride and prepared for electron microscopy. Synaptic vesicles are visible in the injected processes, and at the lower left the sensory neuron is making synaptic contact with two unidentified processes.

preserved so that synaptic components can be recognized electron-microscopically and correlated with structures seen in the light microscope. We have found that each type of mechanosensory or motor neuron has a distinctive distribution of synapses and processes within the ganglion. Figure 58, for example, shows light micrographs from the whole mount of an injected pressure sensory neuron as its main process passes through the neuropil. Fine branches emerge from the main trunk; at their tips and along their length are clusters of fingerlike processes that are in sites of dozens of synapses, one of which is illustrated in the electron micrograph in Fig. 59. Prominent swellings also occur along the fine processes of other sensory neurons. These varicosities are the sites of con-

centrations of vesicles; the arrangement of membrane specializations indicates that they are presynaptic "terminals." Some of the vesicle-containing varicosities are also postsynaptic. Motoneuron processes are studded with spines a few microns long and a fraction of a micron in diameter. The motoneurons do not contain prominent clusters of vesicles but receive extensive synaptic contact by varicosities, chiefly upon their spines and small branches.

Armed with a detailed description of identified neurons in the normal animal, it should be possible to trace the regeneration of connections and to detect any morphological basis for physiological and behavioral changes that can be produced by experimental manipulation of the leech and its nervous system.

MOUSE LYMPHOCYTES AS TOOLS FOR THE STUDY OF MITOGENIC EVENTS AND REGULATORY PROCESSES ASSOCIATED WITH THE CELL MEMBRANE

K. Ozato, W. H. Adler, J. D. Ebert, and L. Huang
assisted by Delores Somerville and Bessie Smith*

REGULATION OF TRANSPLANTATION IMMUNITY BY T LYMPHOCYTES: EFFECTS OF MITOGENS

*K. Ozato, J. D. Ebert, and W. H. Adler**

We have continued to explore the mechanism of T cell recognition. Since the recognition of alloantigens is achieved by cell to cell interaction, which is difficult to analyze directly, we have used simple probes to approach the problem, that is, we have modified the immune response by the mitogens Concanavalin A (ConA) and bacterial lipopolysaccharide (LPS). Previously we had established an experimental model system in which the proliferative response (mixed lymphocyte reaction (MLR)) and the generation of cytotoxic lymphocytes (GCL) could be assayed. To be confi-

dent that we were dealing with T cells, we used cortisone-resistant thymocytes as the responding cells, thereby excluding contamination by B cells or their product, anti H-2 antibody, which are known to interfere with T cell mediated immunity. We focused on appropriate combinations of strains in which the gene products other than H-2 antigens were avoided; thus we chose the B10 vs. B10.D2 system (H-2^b vs. H-2^d). We found that the B cell mitogen LPS (added at the initiation of culture) enhanced the generation of cytotoxic lymphocytes when the responding cells were stimulated with suboptimal doses of alloantigens (Fig. 60). On the other hand, mitogenic concentrations of ConA (5 and 10 $\mu\text{g}/\text{ml}$) suppressed cytotoxic activity regardless of alloantigen dose. These effects were found to affect the early events of lymphocyte differentiation; the addition of mitogens 24 hr after the initi-

* Gerontology Research Center, National Institutes of Health, Baltimore, Maryland.

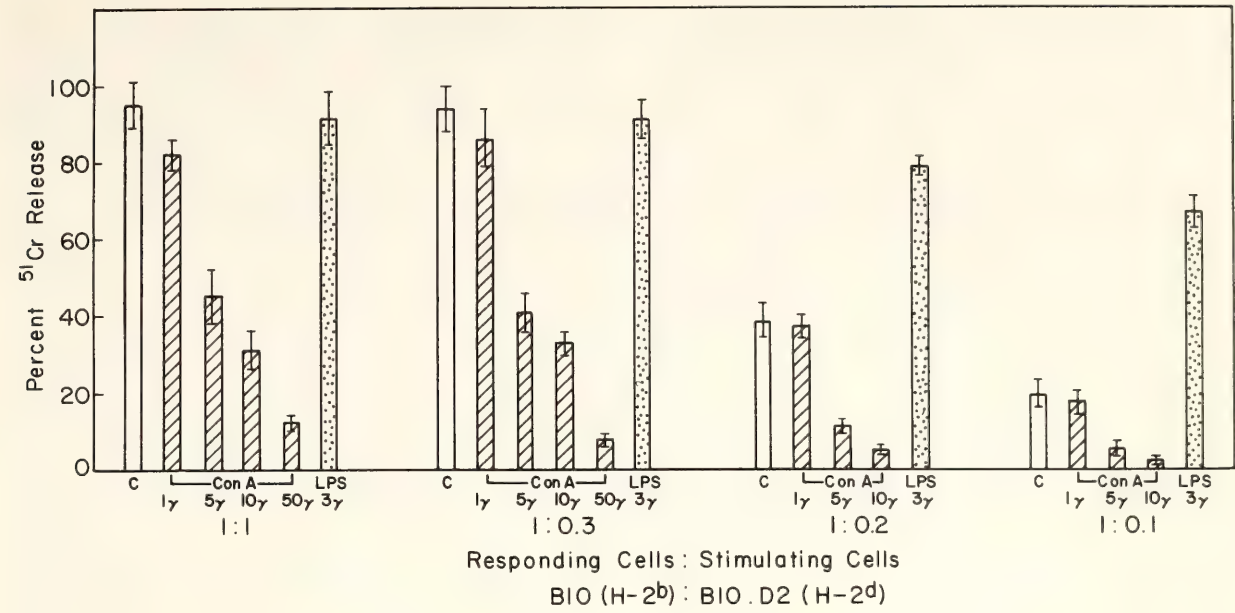


Fig. 60. Effect of ConA or LPS on the generation of cytotoxic lymphocytes (B10 vs. B10.D2). 1×10^7 cortisone-resistant thymocytes were sensitized with B10.D2 spleen cells at different cell ratios (expressed as responding vs. stimulating cells). ConA at the concentrations indicated or LPS ($3 \mu\text{g}/\text{ml}$) was added at the initiation of culture. Cytotoxic activity per chamber on day 5 is expressed as percent ^{51}Cr -release from target cells (P815). Each column represents the mean of duplicates \pm standard deviation.

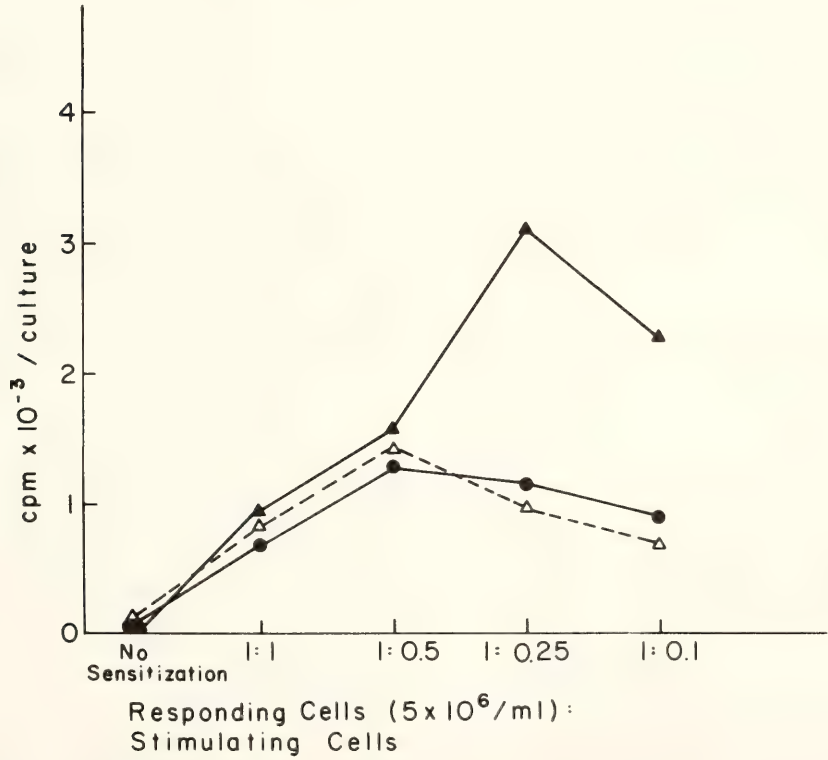


Fig. 61. Effect of LPS on the proliferative response on day 3 to allogeneic stimulation. 1.25×10^6 B10 CRT were cultured with B10.D2 spleen cells at different cell ratios. LPS was added at the initiation of the cultures (filled triangles) or at 24 hr thereafter (open triangles). Controls are indicated by filled circles. Cells were labeled with ^3H -TdR ($1 \mu\text{Ci}/\text{ml}$) for 18 hr at different time-points. Each value represents the mean of triplicates.

ation of culture induced neither enhancement nor suppression. Selective enhancement of the GCL by LPS in lower doses of alloantigens was observed in the MLR, too (Fig. 61). The response was about twice as high. Taking into account the previous finding that LPS lowers the mitogenic doses of ConA in T cells, LPS appears to potentiate T lymphocytes when suboptimal doses of stimulatory alloantigens are given.

In this work considerable effort was devoted to exploring the mechanism of suppression, especially to determining the possible involvement of suppressor T cells. Recently it has been shown that both antibody response and T cell-mediated immunity are regulated, so as not to "overshoot" the response, by the lymphoid population itself, in most cases by T cells, which have been termed "suppressor T cells." Since the suppressor cell concept could give a clue to the nature of immunological tolerance, we asked whether suppressor T cells might play a role in our system. ConA-activated thymocytes were tested for their ability to suppress the generation of cytotoxic activity comparably with soluble ConA. We tested three different lymphocytes with regard to suppressor activity. The results are shown in Table 11. Spleen cells or lymph node cells

stimulated by ConA could significantly suppress the GCL when they were added at a ratio of 1/10. Suppression was dependent on the presence of T cells because anti- θ treatment in the presence of complement completely abolished the activity. It was independent of cell division, however, for mitomycin C treatment did not impair the activity. Most remarkably, however, thymocytes stimulated by ConA did not suppress the immune response. Thus we can draw two conclusions: First, although transplantation immunity can be regulated by suppressor T cells, not all T lymphocytes function as suppressors: *Thymocytes were inactive*. Second, the mechanism of suppression observed in our experimental system is not attributable to suppressor T cells, since we have used only thymocytes as the responding cells. Therefore, the modifications of the lymphocyte surface by ConA are assumed to be the immediate cause.

MODIFICATION OF THE LYMPHOCYTE SURFACE BY CONA

K. Ozato and J. D. Ebert

The finding that suppressor T cells are not responsible for the suppression just described led us to explore further the possibility that the interaction of the ConA molecule with the lymphocyte surface can modify the subsequent immune response.

Therefore, further modifications of lymphocyte surfaces were carried out both on responding lymphocytes (cortisone resistant thymocytes) and on stimulating lymphocytes (mitomycin C-treated allogeneic or syngeneic spleen cells), by "coating" lymphocytes with native (tetravalent) ConA and succinyl (divalent) ConA. Coating of the cells with ConA alone did not induce a mitogenic response. We discovered that when the responding cells were coated with ConA, the proliferative response to allogeneic cells was enhanced 5 to 7 times. A comparable enhancement was noted

TABLE 11. Effect of ConA-Activated Cells on the Generation of Cytotoxic Lymphocytes*

Experimental Group	Percent ^{51}Cr -Release
Control	89.3 ± 7
ConA-activated thymocytes added	90.1 ± 4
ConA-activated spleen cells added	26.0 ± 2
ConA-activated lymph node cells added	23.8 ± 3

* 1×10^7 B10 cortisone-resistant thymocytes were sensitized with 5×10^6 B10.D2 spleen cells treated with mitomycin C. ConA-activated lymphocytes (1×10^6) obtained 48 hr after incubation were added to the culture. Cytotoxic activity per chamber on day 5 is expressed as the percent Cr^{51} release from P815 target cells (mean of duplicate \pm SD).

even when stimulating cells were coated with ConA (Fig. 62). Perhaps the most striking observation was that lymphocytes treated with ConA could manifest

a highly significant proliferation in syngeneic combinations. This response was observed by coating either responding or stimulating cells (Table 12). Native

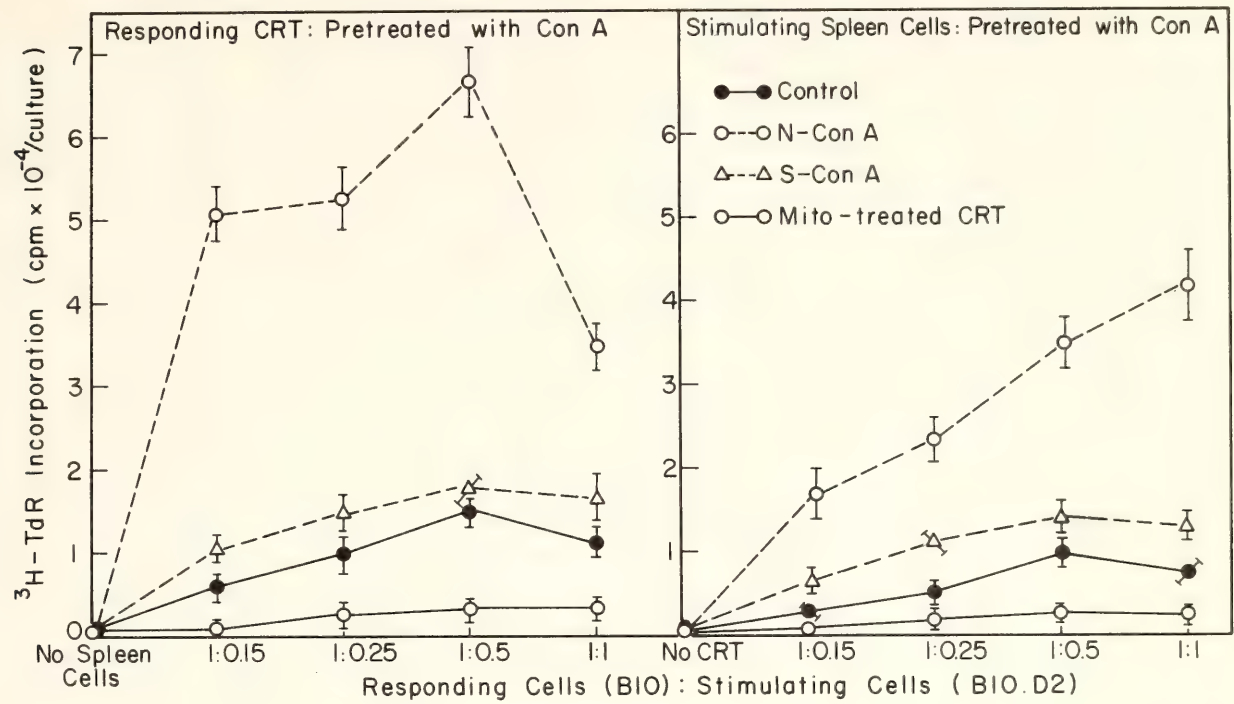


Fig. 62. Left: Proliferative response by ConA-pretreated cortisone-resistant thymocytes. 1.7×10^6 normal B10 cortisone-resistant thymocytes or B10 cortisone-resistant thymocytes pretreated with $50 \mu\text{g/ml}$ of native ConA or succinyl ConA were sensitized with different numbers of allogeneic spleen cells (B10.D2), expressed as the ratio of responding to stimulating cells. $^3\text{H-TdR}$ ($1 \mu\text{Ci/ml}$) was added 52 hr after the initiation of culture. Cells were labeled for 18 hr. Cortisone-resistant thymocytes pretreated with native ConA followed by subsequent treatment of mitomycin C were also tested. Each value indicates the average of triplicate culture \pm standard deviation (SD). Right: Proliferative response by cortisone-resistant thymocytes sensitized with spleen cells coated with ConA in the one-way MLC. 1.7×10^6 normal B10 cortisone-resistant thymocytes were sensitized with varying numbers of normal B10.D2 spleen cells or spleen cells pretreated with $50 \mu\text{g/ml}$ of native ConA or succinyl ConA. Cortisone-resistant thymocytes treated with mitomycin C were also sensitized with native ConA pretreated spleen cells. $^3\text{H-TdR}$ ($1 \mu\text{Ci/ml}$) was added 52 hr after the initiation of culture. Cells were labeled for 18 hr. Each value indicates the average of triplicate culture \pm SD.

TABLE 12. Effect of ConA Coating of Lymphocytes on Triggering in Syngeneic Combination

Responding Cells Pretreated with ConA*	$^3\text{H-TdR}$ Incorporation	Stimulating Cells Pretreated with ConA†	$^3\text{H-TdR}$ Incorporation
Control	197 \pm 10	control	94 \pm 4
Native ConA	21272 \pm 1018	native ConA	20393 \pm 1205
Succinyl ConA	1613 \pm 502	succinyl ConA	2790 \pm 212

* Responding cortisone-resistant thymocytes (B10.D2) were treated with $50 \mu\text{g/ml}$ of ConA for 30 min, after which they were washed, resuspended in fresh medium, mixed with syngeneic spleen cells, and treated with mitomycin C.
† Stimulating spleen cells (B10.D2) were pretreated with $50 \mu\text{g/ml}$ of ConA for 30 min, after which they were treated with mitomycin C. They were then mixed with cortisone-resistant thymocytes. $^3\text{H-TdR}$ ($1 \mu\text{Ci/ml}$) was added 52 hr after culture. The values represent mean of duplicate \pm SD.

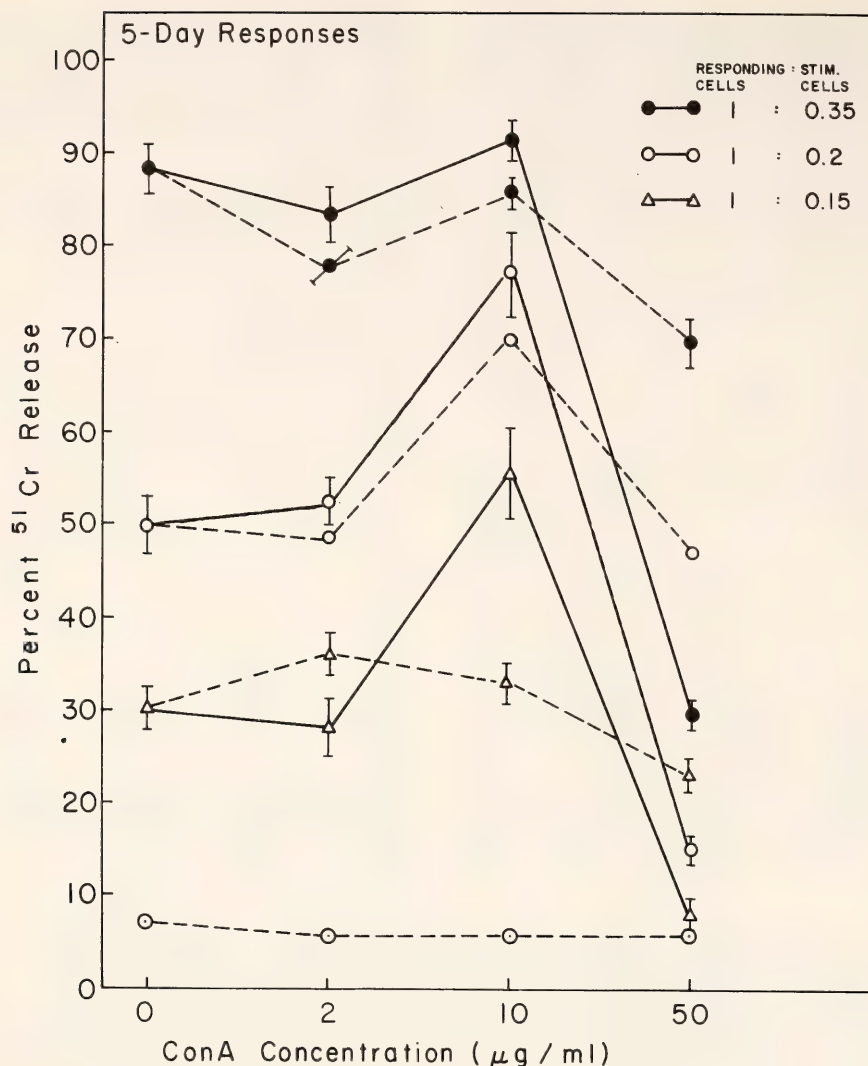


Fig. 63. GCL by cortisone-resistant thymocytes pretreated with ConA. 1×10^7 B10. Cortisone-resistant thymocytes treated with varying concentrations of native ConA (solid lines) or succinyl ConA (dotted lines) were sensitized with different numbers of B10.D2 spleen cells (expressed as the ratio of responding to stimulating cells). Cytotoxic activity per chamber on day 5 is expressed as percent of ⁵¹Cr-release from target P815 cells (mean of duplicate \pm SD).

ConA was much more effective than succinyl-ConA. We confirmed that when spleen cells are used as stimulators, all the syngeneic combinations tested (H-2^k, H-2^b, H-2^d) showed the response. Although syngeneic cells have not been considered to be stimulatory, our findings show that under those conditions, T cells may be stimulated in the syngeneic combination. We look to a further study of this syngeneic response for possible clues to the understanding of self-recognition.

The consequences of membrane modi-

fication were studied further. The capability of GCL was completely suppressed when either responding or stimulating cells were modified by ConA. The severe suppression seemed to be related somehow to the accelerated proliferative response, since only at doses where proliferation was enhanced was the suppression of GCL demonstrated (Fig. 63). Thus it is clear that the immune response of the lymphocytes whose cell surface has been modified is regulated in both the proliferative and effector phases.

THE STUDY OF CONA BINDING SITES ON
MURINE THYMIC LYMPHOCYTES

K. Ozato and J. D. Ebert

Last year we reported (*Year Book* 73, p. 81) the nature of the thymocyte response to the T cell-specific mitogen, ConA. We dealt especially with the synergistic effect of a B cell-specific mitogen, bacterial lipopolysaccharide (LPS). Thereafter, we studied the binding of mitogens to lymphocytes to try to delineate the relationship between cell surface events and subsequent DNA synthesis. First native ConA was labeled with tritium by acetylation to visualize the binding. We have now compared two groups of thymocytes—cortisone-resistant thymocytes and normal thymocytes that are different in their mitogenic responsiveness, the former being about seven times more vigorous than the latter

in mitogenic responsiveness to ConA. Our results show that these two lymphocytes have an almost identical binding capacity for ConA at both 0°C and 37°C, that is, they have the same binding sites with the same kinetic properties (Fig. 64). According to our calculations, there are about 7×10^5 receptors on one thymocyte. The number of receptors per thymocyte appeared to be far greater than that required for mitogenic stimulation, for the saturation dose for binding was 600-fold higher than the mitogenic dose ($1 \mu\text{g/ml}$). We further investigated whether ConA binding could be inhibited or otherwise modified by other mitogens such as LPS or phytohemagglutinin-p (PHA-P). In the responsiveness to ConA tested in the thymocyte system, LPS showed a cooperative role, while PHA-P was inhibitory. Thus, these two reagents were considered useful

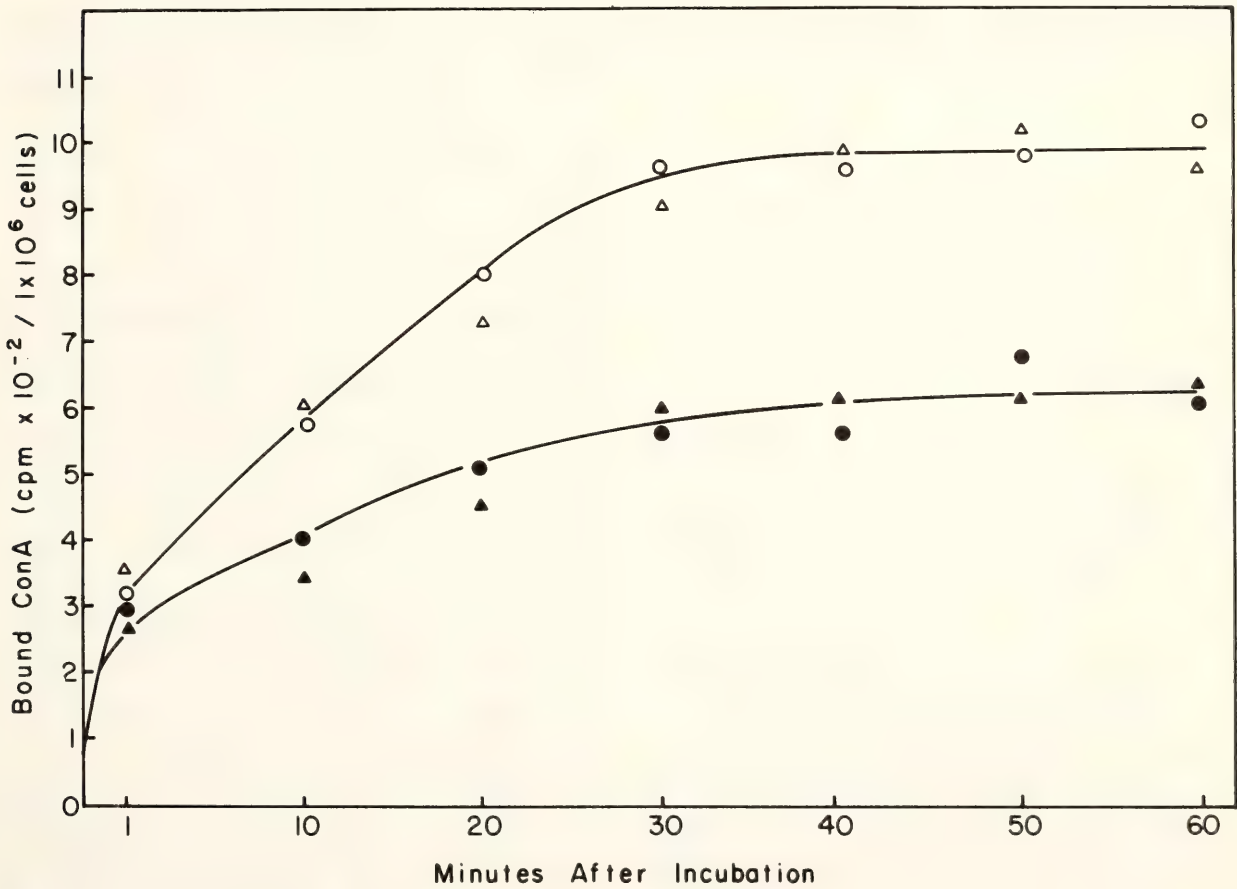


Fig. 64. Kinetics of ^3H -ConA binding to thymocytes. Thymocytes (1×10^6 cells in 0.2 ml) were labeled with $50 \mu\text{g/ml}$ of ^3H -ConA for various periods at 37°C (open triangles, cortisone resistant; open circles, normal) or at 0°C (filled triangles, cortisone resistant; filled circles, normal). Each value represents the average of triplicates.

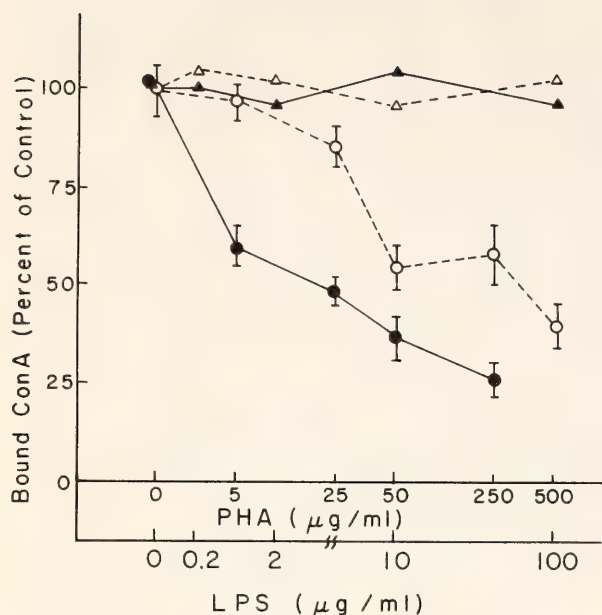


Fig. 65. Effect of LPS or PHA-P pretreatment on the binding of ^3H -ConA to thymocytes. Thymocytes were pretreated with various concentrations of LPS for 30 min, then labeled with 50 $\mu\text{g}/\text{ml}$ (filled triangles) or 100 $\mu\text{g}/\text{ml}$ (open triangles) of ^3H -ConA. In another series thymocytes were pretreated with various concentrations of PHA-P before they were labeled with 50 $\mu\text{g}/\text{ml}$ (filled circles) or 100 $\mu\text{g}/\text{ml}$ (open circles) of ^3H -ConA.

probes for exploring the binding of mitogens in relation to subsequent triggering of proliferation. As shown in Fig. 65, we found that when thymocytes were pretreated with PHA-P, the subsequent binding to ConA was significantly reduced, whereas LPS did not change the binding property. Thus, the inhibition of mitogenic response to ConA by PHA-P might be attributable to the hampering of ConA binding to thymocytes.

ENHANCEMENT OF SURFACE PERMEABILITY OF THYMOCYTES BY CONA

K. Ozato, L. Huang, and J. D. Ebert

The binding of mitogens to lymphocytes provides an attractive experimental model system to investigate signals from the cell membrane for the triggering of DNA synthesis. The influx of Ca^{+2} has been proposed as a secondary message

for signaling the onset of proliferation (Luckasen *et al.*, 1974). To obtain more detailed information about the uptake of Ca^{+2} , we studied the relations between the binding of mitogens to thymocytes and the transport of substances across the cell membrane.

As shown in Fig. 66, the T-cell mitogens PHA and ConA enhanced ^{45}Ca uptake almost equally in cortisone-resistant and normal thymocytes. The B-cell mitogen, LPS, did not change ^{45}Ca uptake. The increase in ^{45}Ca uptake, however, did not correspond to the dose-response relationship of ConA mitogenicity. No detectable enhancement was found at mitogenic concentrations (1 $\mu\text{g}/\text{ml}$). Significant enhancement was demonstrated only at higher concentrations. The uptake of ^{45}Ca increased linearly at least for 60 min of incubation (Fig. 67) and was entirely dependent on the presence of ConA, since the increment of uptake ceased immediately after the specific ConA inhibitor, α -MM, was added. Interestingly, ConA not only affects Ca^{+2} uptake, but also enhances the uptake of CrO_4^- in thymocytes (Fig. 68). The enhancement was again observed at ConA concentrations higher than mitogenic doses. Moreover, we discovered that the binding of ConA to thymocytes changes permeability of trypan blue, a dye with a molecular weight of about 960 which is widely used for viability testing. After 40 min incubation of cells in the presence of 50 $\mu\text{g}/\text{ml}$ of ConA, approximately 20% to 40% of the cells were stained (Table 13). These stained cells were not dead but merely reflecting a transient increase in surface permeability. This conclusion was based on the following observation. Thirty minutes after incubation when a significant fraction of the cell population became stainable, α -MM was added to the incubation mixture, and the dye exclusion test was performed 10 and 30 min later (Table 13). By this treatment, most of the cells were no longer stainable. Strong agglutination by ConA was

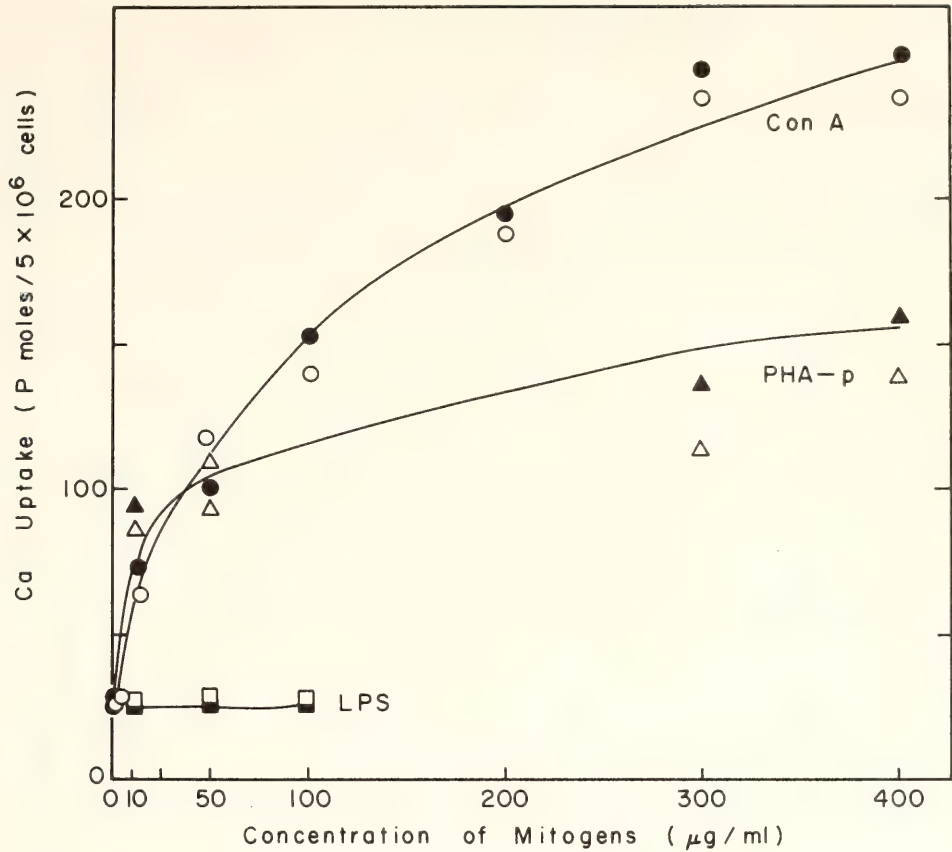


Fig. 66. Effect of mitogens on ⁴⁵Ca uptake by thymocytes. 5 × 10⁶ normal thymocytes (open symbols) or cortisone-resistant thymocytes (filled symbols) (both from CBA strain) in 0.2 ml RPMI 1640 containing various concentrations of mitogens were incubated in the presence of 1 μCi ⁴⁵Ca for 40 min.

also reversed. To test whether this permeability change induced by ConA is also valid for larger molecules, we have examined the uptake of ¹⁴C-inulin which has a molecular weight of 5000 to 7000. No detectable increase in inulin uptake was observed at ConA concentrations up to 100 μg/ml. Thus, the size of the “pores” on the thymocyte surface induced by ConA binding is likely to fall between the sizes of trypan blue and inulin.

In conclusion, we believe it is premature to hypothesize that Ca⁺² influx is directly responsible for the lymphocyte activation by mitogens in the system we have studied because increase in Ca⁺² uptake does not occur at mitogenic doses and because the uptake of other molecules and ions is also stimulated by mitogen binding.

TABLE 13. Effect of ConA on Dye Exclusion by Thymocytes

ConA Concentration	Stained Cells (%)*			
	0 min	20 min	40 min	60 min
Control	1.8	2.0	2.7	2.3
ConA (10 μg/ml)	1.2	1.5	23.4	31.6
†ConA (10 μg/ml) + MM	3.4	3.0
ConA (50 μg/ml)	2.0	2.1	38.6	48.1
†ConA (50 μg/ml) + MM	2.9	3.7

* 5 × 10⁶ normal thymocytes in 0.2 ml of RPMI 1640 in the presence of ConA were incubated at 37°C. 0.1 ml trypan blue (0.5% in PBS) was added at the time-points indicated. More than 200 cells were counted for each sample. Each value represents mean of duplicate.

† α-MM (10⁻¹ M) was added to the cell suspension in the presence of ConA 30 min after the incubation. Dye exclusion test was performed at the time-points indicated.

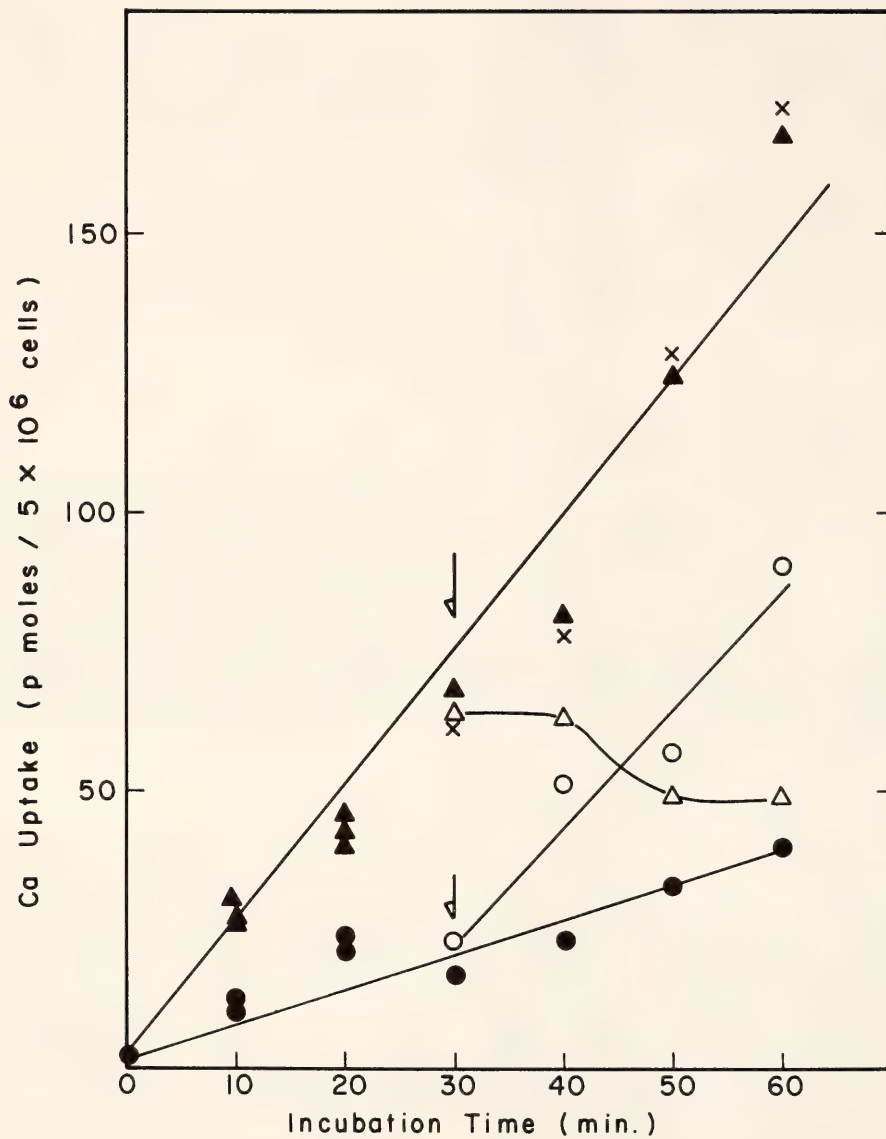


Fig. 67. Kinetics of ^{45}Ca uptake by thymocytes: Effect of inhibitors. 5×10^6 normal thymocytes were incubated in 0.2 ml RPMI 1640 containing $1 \mu\text{Ci } ^{45}\text{Ca}$ in the presence (filled triangles) or absence (open circles) of ConA ($50 \mu\text{g/ml}$). $\alpha\text{-MM}$ ($10^{-1}M$) (open triangles) or galactose ($10^{-1}M$) (X—X) was added 30 min after incubation (upper arrow) to ConA containing cell suspensions. ConA ($50 \mu\text{g/ml}$, open circles) was added to control cell suspensions 30 min after incubation (lower arrow).

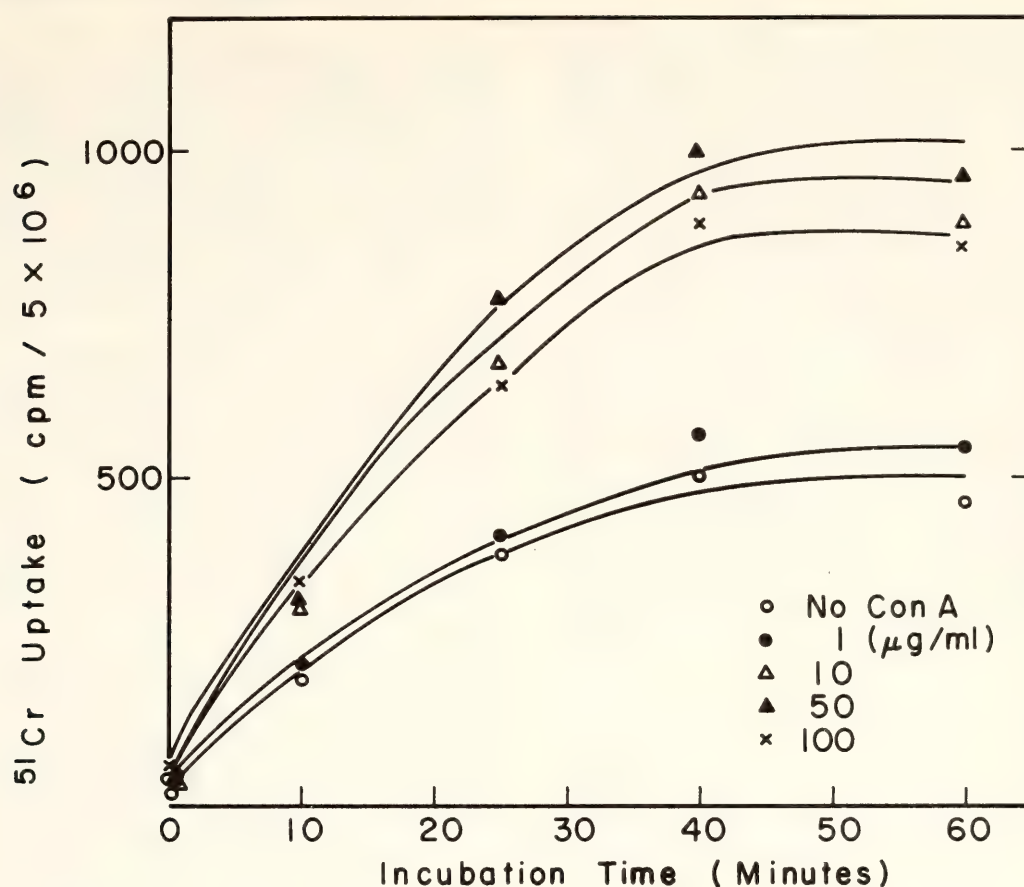


Fig. 68. Kinetics of $^{51}\text{CrO}_4$ uptake by thymocytes. 5×10^6 normal thymocytes were incubated in 0.2 ml RPMI 1640 containing $1 \mu\text{Ci Cr}^{51}$ in the presence of various concentrations of ConA.

THE COLLECTION OF HUMAN EMBRYOS

R. O'Rahilly and E. Gardner

The Carnegie Embryological Collection (including the Bluntschli material), which was moved to Davis in July 1973, has now been installed in "Carnegie Village," a group of half a dozen buildings at the University of California, in a delightful setting halfway between the School of Medicine and the California Primate Research Center. The transfer was made on 11 June 1974, and a formal opening is being planned for November 1975. Several visitors have studied the Collection during the past year, including Arthur T. Hertig, who, with John Rock, contributed so many of the early human embryos to the Collection.

Forty-nine specimens, more than a dozen of which belong to the embryonic period, were acquired during the year.

All inquiries concerning the Collection

should be addressed to Professor R. O'Rahilly or Professor E. Gardner, Carnegie Laboratories of Embryology, University of California, Davis, California 95616.

DEVELOPMENTAL STAGES IN HUMAN EMBRYOS

Work continues on the revision of stages 10 to 23 and on the tabulation of the timing and sequence of developmental events in staged human embryos. A detailed account of the development of the limbs by O'Rahilly and Gardner has been submitted for publication. Preliminary work by Alexander Barry has been begun on the establishment of a computer catalogue of all the prenatal mammalian material.

An interesting sequel to Blechschmidt's *Die pränatalen Organsysteme des Menschen* (Hippokrates Verlag, Stuttgart, 1973), in which the Carnegie system of staging was adopted, is Gasser's *Atlas of Human Embryos* (Harper and Row, Hagerstown, Md., 1975), in which photomicrographs in some 15 staged embryos (14 of which belong to the Carnegie Collection) are reproduced. A number of drawings are also included. In stage 23 (8 postovulatory weeks), for example, 38 photomicrographs of Carnegie embryo No. 4570 (30.7 mm C.-R.) are shown with detailed labels and drawings to indicate the levels of the sections.

DEVELOPMENT OF THE NERVOUS SYSTEM

Work continues on the "Developmental Neurobiology of Primates," for which a research grant was awarded to Ernest Gardner, as mentioned in last year's Report. A chapter on "The developmental anatomy and histology of the human central nervous system" is being prepared by O'Rahilly and Gardner for the *Handbook of Clinical Neurology*, edited by P. J. Vinken and G. W. Bruyn (North Holland Publishing Co., Amster-

dam). Volumes 26 and 27 on "Congenital Malformations of the Brain and Skull" are being edited by N. C. Myrianthopoulos. An article on "The Dandy-Walker and Arnold-Chiari malformations" by Gardner, O'Rahilly, and Prolo is due to appear in the *Archives of Neurology*. A paper on "The prenatal development of the human eye" by O'Rahilly has been accepted for publication in *Experimental Eye Research*. An account of "The nerve supply and conducting system of the human heart at the end of the embryonic period proper" has been submitted for publication.

Witold Wozniak, Medical Academy of Poznan, Poland, spent a month in Davis studying the development of the human nervous system. He prepared projection drawings and photomicrographs of the brain at stage 21 (7½ postovulatory weeks), and it will be of interest to compare in detail the level of development with that at stage 23 (8 weeks), already under investigation by Gardner and O'Rahilly. Wozniak is also engaged in a study of the developing human spinal cord with the aid of both light and electron microscopy.

STAFF ACTIVITIES

The dissemination of research findings, through presentations at conferences and meetings of learned societies, publications, and teaching serves several functions: It provides an opportunity for criticism and exchange, leading ultimately to verification of discovery, and advance—the word "ultimately" being crucial, for verification may be preceded by failure, reexamination and redirection.

Teaching promotes another crucial role: it enables our staff to attract new investigators of high quality by creating an awareness of the forces impinging upon and fostering innovation. Here our concern is not so much with increasing the number of developmental biologists as it is with providing enrichment and

rare opportunities for intellectual growth for gifted young men and women by the preceptorial approach, long the hallmark of enlightened postdoctoral education.

International conferences and symposia in which members of the Department participated during the year included the following: The Fifth Conference, "De la Physique Théorique à la Biologie (Versailles, France); a symposium on Mechanism of Synaptic Action, in connection with the International Congress of Physiological Sciences (Jerusalem, Israel); a Conference on Ribosomes (St. Johns, Newfoundland); a Conference on Tests of Teratogenicity *in vitro* (Woods Hole, Massachusetts); a Symposium on Cancer Biology at the

Given Institute of Pathobiology (Aspen, Colorado); the Conference on Recombinant DNA Molecules (Asilomar, California); the Ninth Leukocyte Culture Conference (Williamsburg, Virginia); and a Conference on Selected Aspects of Developmental Genetics (Iowa City, Iowa).

Among the other conferences engaging the interest of members of the group, the following should be mentioned: The University of Minnesota Symposium on the Interface between Molecular Biology and -Medicine (Minneapolis); the New York Academy of Sciences' Conference on Human Uses of Molecular Genetics; Five Gordon Research Conferences, dealing with Biological Regulatory Mechanisms, Chromatin, Developmental Biology, Lipid Metabolism, and Nucleic Acids; the UCLA-ICN Winter Symposium on DNA Replication (Squaw Valley, California); and a Symposium on Excitable Cells in Tissue Culture (Atlantic City).

Lectures were presented on a number of campuses, including Albert Einstein College of Medicine; Case Western Reserve University; Colorado State University; Columbia University; Duke University School of Medicine; Emory University; Erindale College; Hebrew University, Jerusalem; Loyola College; McGill University; Moravian College; Princeton University; Saint Louis University; Stanford University; State University of New York at Buffalo; Temple University; the Universities of California at Berkeley and Santa Barbara; Chicago, Cincinnati, Colorado, Maryland, Missouri, North Carolina, Paris, Pennsylvania, Rochester, Tennessee, Texas, Virginia, Wisconsin and Yale Universities.

Special presentations included The Jessup Lectures at Columbia University and a series of lectures as Regents' Lecturer at the University of California.

Members of the group also spoke at hospitals and research centers, among them the CNRS Laboratory, Gif-sur-

Yvette, France; the Cold Spring Harbor Laboratory; Institute for Cancer Research; Marine Biological Laboratory; M. D. Anderson Hospital; National Institutes of Health; National Jewish Hospital; and Weizmann Institute.

Members of the Department took part in meetings of learned societies, including, in addition to those already mentioned, the American Association for the Advancement of Science, American Association of Anatomists, American Society of Biological Chemists, American Society for Cell Biology, American Philosophical Society, American Physiological Society, American Society for Microbiology, Biophysical Society, Federation of American Societies for Experimental Biology, National Academy of Sciences, Society for Developmental Biology, Society of General Physiologists, and Society for Neuroscience.

Advisory and consultative services included membership on the editorial boards of *Anales del Desarrollo*, *Cell*, *Developmental Biology*, *Journal of Embryology and Experimental Zoology*, *Excerpta Medica* (section on Human Developmental Biology), *Current Topics in Developmental Biology*, *Oceanus*, and *Quarterly Review of Biology*.

Members of the staff also acted in these capacities: Chairman, Assembly of Life Sciences, National Academy of Sciences-National Research Council; Member of the Board of Governing Trustees and the Board of Scientific Overseers, Jackson Laboratory; Trustee, President, and Director, Marine Biological Laboratory; Member of the Corporation, Woods Hole Oceanographic Institution; and Trustee of International Medical Congress, Ltd.

Other posts occupied by members of the Department include the following: in the American Institute of Biological Sciences, member, Council of Past Presidents; in the Institut de la Vie, Chairman, World Committee on the Formative Weeks of Human Life; in the National Academy of Sciences, member, Commit-

tee on Science and Public Policy; member, Coordinating Committee for Air Quality Studies; and member, Committee on Energy; in the National Institutes of Health, member, Board of Scientific Counselors, National Institute of Child Health and Human Development, member, Gerontology Research Center Resources Advisory Committee, member, Physiological Chemistry Study Section; and member-elect, Cell Biology Study Section; and in the Society for Developmental Biology, President.

Members of the Department served on several visiting committees, including those for the Departments of Biology at Brookhaven National Laboratory, Harvard University, Massachusetts Institute of Technology, and Princeton University, and the External Advisory Committee of the University of Chicago's Cancer Research Center.

Staff members taught in the EMBO course on Molecular Genetics of Higher Organisms at Port-Cros, France, and in courses at the Marine Biological Laboratory, as well as at Johns Hopkins (in the Departments of Biology, Biophysics and Pediatrics).

Seminars

The roster of speakers at the seminars organized by the Department to serve all those working in developmental biology in the region included: Bruce Alberts (Princeton University); E. X. Albuquerque (University of Maryland); T. Blumenthal (Indiana University); Charles Boder (Geneva); Diana Card (University of California, Los Angeles); David Clayton (Stanford University); Marco Crippa (Geneva); James Darnell (Rockefeller University); Laura de Francesco (University of California, San Diego); Marshall Edgell (University of North Carolina); Sharyn Endow (Yale University); David Harrison (Jackson Laboratory); Clyde Hutchinson (University of North Carolina); Lawrence Kedes and Lawrence Korn (both of Stanford University); A. A. Kroon (Groningen); Richard Novick (Public Health Research Institute); Tokindo Okado (Kyoto University); Arnold Revzin (University of Oregon); Robert Roeder (Washington University); T. Thomas (University of Georgia) and H. Wahn (Wayne State University).

BIBLIOGRAPHY

- Adler, W. H., *see* Ozato, K.
- Brown, D. D., and R. Stern, Methods of gene isolation. *Ann. Rev. Biochem.*, 43, 667-693, 1974.
- Brown, D. D., *see also* Brown, R. D., Brownlee, G. C., Forsheit, A. B., Lizardi, P., and Wellauer, P. K.
- Brown, R. D., and D. D. Brown, The nucleotide sequence adjoining the 3' end of the genes coding for 5S ribosomal RNA in *Xenopus*. *Fed. Proc.*, 34, 608 (abstract), 1975.
- Brownlee, G. C., E. M. Cartwright, and D. D. Brown, Sequence studies of the 5S DNA of *Xenopus laevis*. *J. Mol. Biol.*, 89, 703-718, 1974.
- Carroll, D., *see* Wellauer, P. K.
- Cartwright, E. M., *see* Brownlee, G. C.
- Coon, H. G., *see* Dawid, I. B.
- Davidson, N., *see* Forsheit, A. B.
- Dawid, I. B., I. Horak, and H. G. Coon, The use of hybrid somatic cells as an approach to mitochondrial genetics in animals. *Genetics*, 78, 459-471, 1974.
- Dawid, I. B., *see also* Leister, D. E., Wellauer, P. K., and Wu, G.-J.
- Deutch, A., *see* Wellauer, P. K.
- Devreotes, P. N., and D. M. Fambrough, Acetylcholine receptor turnover in membranes of developing muscle fibers. *J. Cell Biol.*, 65, 335-358, 1975.
- Devreotes, P. N., *see also* Fambrough, D. M.
- Ebert, J. D., Birth defects: the present and the future. In *Birth Defects*, A. G. Motulsky, W. Lenz and F. J. E. Ebeling, eds. Excerpta Medica, pp. 10-17, Amsterdam, 1974.
- Ebert, J. D., *see also* Ozato, K., and Stambrook, P. J.
- Fambrough, D. M., Acetylcholine receptors: revised estimates of extrajunctional receptor density in denervated rat diaphragm. *J. Gen. Physiol.*, 64, 468-472, 1974.
- Fambrough, D. M., and P. N. Devreotes, Synthesis and degradation of acetylcholine receptors in cultured chick skeletal muscle. In *Exploratory Concepts in Muscular Dystrophy II*, A. T. Milhorat, ed. Excerpta Medica, Amsterdam, pp. 55-67, 1975.
- Fambrough, D. M., *see also* Devreotes, P. N.
- Forsheit, A. B., N. Davidson, and D. D. Brown, An electron microscope heteroduplex study of the ribosomal DNAs of *Xenopus laevis* and *Xenopus mulleri*. *J. Mol. Biol.*, 90, 301-314, 1974.
- Gardner, E., and R. O'Rahilly, Le cerveau à la fin de la période embryonnaire vraie. *Bull. Ass. Anat.*, 58, 109-114, 1974.
- Gardner, E., *see also* O'Rahilly, R.
- Gasser, R. F., *Atlas of Human Embryos*, Harper and Row, Hagerstown, Md., 318 pp., 1975.
- Higashinakagawa, T., and R. H. Reeder, Purification and preliminary characterization of active ribosomal gene chromatin. *Federation Proceedings*, 34, 581 (abstract), 1975.
- Higashinakagawa, T., *see also* Wellauer, P. K.
- Horak, I., *see* Dawid, I. B.
- Huang, L., *see* Pagano, R. E.
- Kelley, D. E., *see* Wellauer, P. K.
- Leister, D. E., and I. B. Dawid, Physical properties and protein constituents of cytoplasmic and mitochondrial ribosomes of *Xenopus laevis*. *J. Biol. Chem.*, 249, 5108-5118, 1974.
- Lizardi, P. M., and D. D. Brown, The length of the fibroin gene in the *Bombyx mori* genome. *Cell*, 4, 207-215, 1975.
- Lizardi, P. M., R. Williamson, and D. D. Brown, The size of fibroin messenger RNA and its polyadenylic acid content. *Cell*, 4, 199-205, 1975.
- O'Rahilly, R., and E. Gardner, Les stades de développement de l'embryon humain. *Bull. Ass. Anat.*, 58, 177-182, 1974.
- O'Rahilly, R., *see also* Gardner, E.
- Ozato, K., W. H. Adler, and J. D. Ebert, The effect of concanavalin A and bacterial lipopolysaccharides on mixed lymphocyte cultures and generation of cytotoxic effector lymphocytes. *Federation Proceedings*, 34, 1005 (abstract), 1975.
- Pagano, R. E., L. Huang, and C. Wey, Interaction of lipid vesicles with cultured mammalian cells. *Nature*, 252, 166-167, 1974.
- Perry, R., *see* Wellauer, P. K.
- Ramsey, E. M., *The Placenta of Laboratory Animals and Man*, Holt, Rinehart and Winston, Inc., New York, 196 pp., 1975.
- Reeder, R. H., Ribosomes from eukaryotes: genetics. In *Ribosomes*, P. Lengyel, M. Nomura and A. Tissières, eds., Cold Spring Harbor, 489-518, 1974.

- Reeder, R. H., *see also* Higashinakagawa, T., and Wellauer, P.
- Sachs, H. G., *see* Stambrook, P. J.
- Stambrook, P. J., H. G. Sachs, and J. D. Ebert, The effect of potassium on the cell membrane potential and the passage of synchronized cells through the cell cycle. *J. Cell Physiol.*, **85**, 283-292, 1975.
- Stambrook, P. J., and R. Williamson, Error frequency in 5S RNA from cells grown in 5-Bromodeoxyuridine. *Eur. J. Biochem.*, **48**, 297-302, 1974.
- Suzuki, E., *see* Suzuki, Y.
- Suzuki, Y., and E. Suzuki, Quantitative measurements of fibroin messenger RNA synthesis in the posterior silk gland of normal and mutant *Bombyx mori*. *J. Mol. Biol.*, **88**, 393-407, 1974.
- Wellauer, P. K., and I. B. Dawid, Secondary structure maps of ribosomal RNA and DNA I. *J. Mol. Biol.*, **89**, 379-395, 1974.
- Wellauer, P. K., I. B. Dawid, D. E. Kelley, and R. P. Perry, Secondary structure maps of ribosomal RNA II. *J. Mol. Biol.*, **89**, 397-407, 1974.
- Wellauer, P. K., and R. H. Reeder, A comparison of the structural organization of amplified ribosomal DNA from *Xenopus mulleri* and *Xenopus laevis*. *J. Mol. Biol.*, **93**, 151-161, 1975.
- Wellauer, P. K., R. H. Reeder, D. Carroll, D. D. Brown, A. Deutch, T. Higashinakagawa, and I. B. Dawid, Amplified ribosomal DNA from *Xenopus laevis* has heterogeneous spacer lengths. *Proc. Nat. Acad. Sci., USA*, **71**, 2823-2827, 1974.
- Wey, C., *see* Pagano, R. E.
- Williamson, R., *see* Lizardi, P., and Stambrook, P. J.
- Wu, G.-J., and I. B. Dawid, *In vitro* transcription of *Xenopus* mitochondrial deoxyribonucleic acid by homologous mitochondrial ribonucleic acid polymerase. *J. Biol. Chem.*, **249**, 4412-4419, 1974.

PERSONNEL

Year Ended June 30, 1975

(including those whose services began or ended during the year)

Research Staff

Donald D. Brown, Biochemistry
Igor B. Dawid, Biochemistry
James D. Ebert, Director
Douglas M. Fambrough, Biochemistry
Kenneth J. Muller, Neurobiology
Richard E. Pagano, Biophysics
Ronald H. Reeder, Biochemistry
Yoshiaki Suzuki, Biochemistry

Assistant Investigator

Peter J. Stambrook

Research Associates (extramural)

Bent G. Böving, Detroit, Michigan
Robert L. DeHaan, Atlanta, Georgia
Ernest Gardner, Davis, California
Arthur T. Hertig, Boston, Massachusetts
Irwin R. Konigsberg, Charlottesville, Virginia
Ronan O'Rahilly, Davis, California

Fellows

Ronald D. Brown, Fellow of Carnegie Institution of Washington
Dana Carroll, Fellow of U.S. Public Health Service
Scott Emmons, Fellow of the National Cystic Fibrosis Research Foundation
Toru Higashinakagawa, Joint Fellow of Carnegie Institution of Washington and Mitsubishi-Kasei Institute
Leaf Huang, Fellow of Carnegie Institution of Washington
John F. Morrow, Fellow of the National Cystic Fibrosis Research Foundation
Seigo Ohi, Fellow of Carnegie Institution of Washington
Tokindo Okada, Senior Fellow of Carnegie Institution of Washington
Keiko Ozato, Joint Fellow of Carnegie Institution of Washington and Marine Biological Laboratory

Aileen K. Ritchie, Fellow of Muscular Dystrophy Associations of America, Inc.
 Masatoshi Takeichi, Fellow of Carnegie Institution of Washington
 Katherine Tepperman, Fellow of the U.S. Public Health Service
 William B. Upholt, Fellow of Carnegie Institution of Washington
 Peter K. Wellauer, Fellow of the National Cystic Fibrosis Research Foundation

Students

Sandra L. Biroc, Graduate, Johns Hopkins University
 Peter Devreotes, Graduate, Johns Hopkins University
 Marc Friedman, Graduate, Johns Hopkins University
 Carol Kaushagen, Graduate, Johns Hopkins University
 Jose Ramirez, Graduate, Johns Hopkins University
 Changlin A. Wey, Graduate, Johns Hopkins University

Visiting Investigators and Extramural Collaborators

W. H. Adler, Baltimore, Maryland
 George Brownlee, Cambridge, England
 John W. Chase, Boston, Massachusetts
 Hayden G. Coon, Bethesda, Maryland
 N. Davidson, Pasadena, California
 Daniel B. Drachman, Baltimore, Maryland
 Michael Edidin, Baltimore, Maryland
 A. Forsheit, Pasadena, California
 J. W. S. Harris, London, England
 Uel J. McMahan, Boston, Massachusetts

Christian Thomas, Brussels, Belgium
 Witold Wozniak, Poznan, Poland

Student Assistant

Gail Anderson, Johns Hopkins University

Clerical and Technical Staff

Elaine S. Asch, Senior Technician
 Judith M. Biemiller, Secretary
 James H. Blackwell, Custodian
 Paul Blackwell, Custodian (part time)
 Julia L. Certain, Librarian (part time)
 Huei-Wen Chen, Technician
 Sally S. Cherry, Technician
 William J. Cleary, Recorder
 William H. Duncan, Senior Technician
 Ernestine V. Flemmings, Laboratory Helper
 Paul Giza, Technician
 Richard D. Grill, Photographer
 Virginia S. Hicks, Laboratory Helper
 Mary E. Hogan, Technician (part time)
 John E. Jones, Custodian
 Eddie D. Jordan, Senior Technician
 June M. Lam, Secretary
 Alice H. Mabin, Laboratory Helper
 Thomas F. Malooly, Business Manager
 Thomas F. Miller, Custodian
 Ann N. Murphy, Secretary
 Joyce I. Patterson, Laboratory Helper
 John Pazdernik, Jr., Building Engineer
 Betty Lou Phebus, Bookkeeper-Clerk
 Martha L. Rebbert, Senior Technician
 Adrienne Robinette, Secretary
 John J. Sexton, Custodian
 Bessie H. Smith, Laboratory Helper
 Delores V. Somerville, Senior Technician
 John L. Wiser, Machinist

Department of Terrestrial Magnetism

Washington, District of Columbia

George W. Wetherill
Director

Contents

Introduction	109
Astrophysics	113
Galaxies	113
Observational cosmology	113
Observations of late-type southern galaxies	118
Internal motions in barred spiral galaxies	120
The velocity field of the peculiar galaxy NGC 1275	123
Ionized gas in the nuclear bulge of M31	125
Large-scale structures in our Galaxy	126
Search for shell structure in association with old galactic supernova remnants in neutral hydrogen and formaldehyde	126
Zeeman splitting of the 21-cm line of neutral hydrogen in supernova remnant shells	129
Magellanic stream gas	131
A search for very high velocity clouds	131
The structure of globular clusters	133
Equipment development	135
Image tube systems	135
The intensifier-image dissector scanner	137
The pointing of our 60-ft Derwood radio telescope	138
A new receiver for the IAR	139
Acknowledgments	139
Activities of the Instituto Argentino de Radioastronomía	139
Nuclear and Atomic Physics	141
Introduction	141
Continuum and characteristic x rays produced with potassium ions	141
The $^{15}\text{N}(p,\alpha)^{12}\text{C}$ reaction excited with polarized protons	146
The $^9\text{Be}(p,n)^9\text{B}$ reaction excited with polarized protons	148
A return to $^4\text{He}(p,p)^4\text{He}$	149
Miscellany	150
Biophysics	150
Introduction	150
Properties of human DNA sequences containing poly(dA) or poly(dT)	151
Relationships of some African monkeys as determined by their single-copy DNA sequence homologies	158
A special class of related repeated sequences in mouse and rat DNAs	159
Are there mouse satellite sequences in main-band RNA?	161
Repeated DNA and speciation	164
A distinctive feature of the human genome	165
Protein-protein interactions	165
Historical review of Biophysics Section	172
Geochemistry and Geophysics	180
Diffusion of Ca and Sr in a basalt melt	183
The partitioning of rare earth elements between garnet and liquid at high pressures: preliminary experiments	189
An assessment of local and regional isotopic equilibrium in a partially molten mantle	195
Kinetic processes and thermal history of rocks	210
Deep Sea Drilling Project Leg 34 basalts and ocean ridge basalts: a geochemical comparison	218

Geochemistry of the Azores and the mid-Atlantic ridge: 29°N to 60°N	224
Secondary minerals in oceanic basalt	234
Immiscibility and ancient and modern volcanism	240
Early evolution of the central Andean volcanic arc	247
Strontium isotopic composition of late Cenozoic central Andean volcanic rocks: a disequilibrium melting model	250
Anomalous island arc asthenosphere and continental growth	256
Determination of the subducting lithosphere boundary by use of converted phases .	266
Seismic source studies	273
Archambeau's elastodynamical source-model solution	274
The implications of moving boundaries in elastodynamics	278
Multiple rupture earthquakes and the determination of source parameters	281
Borehole strainmeters: long-term stability and sensitivity to dilatancy	287
Electrical conductivity studies in South America	291
Local seismic net in southern Peru	293
Cosmic-ray research	293
 Bibliography	 296
 Personnel	 299

INTRODUCTION

The end of this report year comes at a time of change at the Department of Terrestrial Magnetism. The successful completion of our 30-year program in biophysics and the arrival of a new director represent discontinuities likely to reopen fundamental questions concerning the long-range goals of the Department. It thus seems a good time to reaffirm our commitment to certain approaches to scientific knowledge which have characterized scientific research at DTM.

One of these is a loosely organized form of group research which occupies a middle ground between a disciplined "team" with clear lines of authority, and a collection of individuals competing among themselves for individual rewards in the form of promotions, financial support, students, or scientific recognition. Another is a lack of inhibition in pursuing investigations into areas which might conventionally be regarded as lying outside one's field of competence. While the dangers of this are too obvious to discuss, there are also limitations to the extent an interdisciplinary team of specialized workers can replace a scientist personally responsible for all aspects of a scientific investigation. We have found that the alternative of encouraging mature scientists to enlarge their areas of competence well beyond their previous boundaries can be rewarded by the identification of new questions, and by opening up new approaches to older areas of study. While this characteristic is not unique to DTM, our endowed financial support is especially suited to taking the risks involved, avoiding the inhibitions arising from a need for short-term results and from the conservatism resulting from increasing demands for accountability on the part of federal funding agencies.

The Department may therefore be viewed as an educational institution of a special sort, not limited by conventional division into faculty and students, even though we do possess these standard at-

tributes. This conventional division is most appropriate to the task of transmitting existing knowledge from one generation to another. However, in our case the knowledge is newly generated by our work, and we must first prepare ourselves to receive this new knowledge and then assimilate it ourselves before transmitting this newly won knowledge to another group of "students," those who learn from our scientific publications, presentations in scientific meetings and from this Report.

Geophysics and Geochemistry

The work of the Department in the earth sciences continues to exploit and extend the unification of terrestrial processes resulting from the establishment of plate tectonics in the mid-1960's. These processes are most clearly expressed in the oceanic regions of the earth. As a consequence, much of the geochemical work in recent years has involved study of oceanic rocks, in contrast to our earlier work, which was concentrated almost entirely on continental material. In 1973-1974 one of our staff members, S. R. Hart, served as chief scientist aboard the deep-sea drilling vessel, the *Glomar Challenger*, on Leg 34 of the Deep Sea Drilling Project, and another of our group, M. N. Bass, served as a member of the scientific staff on that cruise.

According to plate tectonic theory, new oceanic lithosphere is produced at mid-ocean ridges by addition of material from deeper within the earth's mantle. The surface manifestations of this material are the mid-ocean ridge basalts (MORB), obtained by dredging and drilling of the sea floor. Previous work, primarily based on young dredge haul samples, showed that MORB is distinguishable from other basalts by both its trace element concentrations and its strontium isotopic composition. It was not clear from this work whether this was an essential char-

acteristic of MORB or reflected biased sampling of rocks of a particular age. Hart reports results obtained on older (15–40 m.y.) samples of MORB from the South Atlantic, obtained by drilling, which show that the characteristic differences between MORB and other basalts extend back into time.

These differences between MORB and other basalts such as those produced in volcanic island arcs are examples of a fundamental problem which dominates current geochemical discussions of the mechanisms by which material is transferred from the deeper interior of the earth to the surface regions. This is that various basaltic rocks, all presumably derived from the mantle, exhibit different chemical and isotopic characteristics. Further examples of this are given in the report by White, Hart, and Schilling concerning basalts from the mid-Atlantic ridge, the Azores, and Iceland. The most obvious explanation of this is that the mantle is chemically heterogeneous on both a local and a global scale. If true, this opens up a new field of "mantle geology" directed toward an understanding of the basic principles governing these heterogeneities.

An alternative to the hypothesis of major mantle heterogeneity is that the differences between the various basalts are primarily a consequence of chemical and isotopic disequilibrium on a mineralogical scale during the production of the basaltic magma by partial melting of the mantle. Hart and Hofmann argue against this disequilibrium hypothesis as an explanation of the differences between MORB and other basalts. Their reasoning invokes in an essential way the results of new and refined diffusion studies by Hofmann, as well as trace element partition studies, such as those reported here by Shimizu and Kushiro.

The tectonic environment of the Andes and the adjacent portions of the South Atlantic Ocean are complementary to those of the mid-ocean ridges. Here down-going slabs of oceanic lithosphere

plunge hundreds of kilometers between the continental lithosphere, resulting in the seismically active Benioff zone, volcanism, and the formation of mountain belts. The relationships between these processes have been the subject of a continuing combined geophysical and geochemical investigation. Sacks and Snoke report seismic studies of lithospheric plate motions in both South America and Japan, while Aldrich reports related studies of electrical conductivity of the earth's interior in the Andes. The seismic work suggests a new hypothesis for the generation of the thick lithosphere which distinguishes continents from ocean basins. This is that the cool, down-going slab of oceanic lithosphere freezes out aesthenosphere in the wedge defined by the intersection of the continental plate and the down-going oceanic plate. In combination with migration of the ocean trench associated with the down-going slab, this could provide a mechanism for increasing the mass of continental lithosphere over geological time.

Investigations reported by James, Brooks, and Cuyubamba are directed toward extending our knowledge of processes in this region back in time by geochemical and isotopic investigation of the earliest (185 m.y. old) volcanic rocks of the Andes. These earliest rocks differ from the younger volcanics in that they appear to have been more directly derived from oceanic lithosphere. The isotopic compositions of strontium from the younger rocks suggest derivation by partial remelting of continental lithosphere. More detailed examination of the strontium isotopic data for the younger rocks shows that it cannot be explained in terms of equilibrium melting of a homogeneous mantle. James presents evidence to support a disequilibrium melting model for these Andean rocks, in spite of the arguments of Hart and Hofmann against a similar model for the generation of the oceanic basalts.

A recurring theme in DTM geochemical studies has been the search for in-

formation concerning the earlier history of the earth, and much of our previous work in geochronology was motivated by that interest. At present the primary question relating to the older rocks of the earth is the extent to which our newly won knowledge of plate tectonics can be extrapolated to much earlier periods of earth history. Earlier work by Hart and co-workers at DTM supported the idea that 2.7 b.y. Archean volcanic rocks were in many ways analogous to certain modern arc volcanics, but that the higher geothermal gradient at that time resulted in a greater proportion of rocks produced by extensive but shallow partial melting. In this Report Brooks infers that this would also produce a larger number of rocks derived from magmas exhibiting liquid immiscibility and presents evidence that this was the case.

The interpretation of seismic data depends in an essential way on interaction between observation, experiment, and physical theory. We have built up our strength in the theoretical area in recent years. In this Report, Snoke, Linde, and Sacks address the problem of relating the observed seismograms to the source mechanism. They point out major difficulties with previous solutions to this problem and show that it may prove possible to remove some of these difficulties by considering models in which the seismic strain release occurs through multiple ruptures rather than a single rupture.

Astrophysics

In our work in astrophysics, combining both radio and optical observations, attention is centered on distant galaxies and their motions, on dynamical problems in our own Galaxy, and in the development of the advanced instrumentation which will be needed for future extension of this work.

Rubin, Ford, and Thonnard have drawn a very interesting conclusion from their study of the apparent anisotropy in the distribution of a particular class

of galaxies as indicated by both optical and radio data. This is that the best interpretation of their observations requires our Galaxy, as well as its local neighbors, to be moving at a velocity of about 500 km/sec with respect to the reference frame defined by the distant galaxies. The direction of this motion is perpendicular to the direction of the nearest large cluster of galaxies, the Virgo cluster, and the velocity corresponds to the orbital velocity of a body at the distance of our Galaxy from the Virgo cluster. Therefore, the data are consistent with the idea that in some sense our Galaxy is in orbit about the Virgo cluster, although not in the usual way, as the 10^{11} year period of such an orbit is much greater than the age of the galaxies. These observations are inconsistent with the generally accepted isotropic distribution of 3°K cosmic black body radiation background. The discrepancy appears to be outside the observational errors of both sets of measurements and represents an important problem for further investigation.

Many of the optical observations of Rubin, Ford, and Peterson and the radio observations of Thonnard and Turner are directed toward understanding the velocity field within a galaxy, particularly in galaxies of selected types, such as the barred spirals and the unusual galaxy NGC 1275, possibly two galaxies in collision. Some of this work was done at the radio astronomical facility of the Instituto Argentino Radioastronomía (IAR) in Argentina, established jointly by the Carnegie Institution, Argentine universities, and Argentine scientific agencies. In addition, Kumar has studied the optical emission spectrum of a "bulge" of ionized gas extending outward from the nucleus of the nearby Andromeda galaxy, M31. These measurements support the hypothesis that this gas is ionized by extremely hot stars near the end of stellar evolution which are in the process of becoming white dwarfs.

Within our own Galaxy, radio studies

have been made of supernova remnants. Supernovae and their remnants are of great interest because of their relationship to the final stages of stellar evolution, to pulsars and neutron stars, their major contribution to the synthesis of the elements, as a mechanism for returning stellar matter to the interstellar medium, and as sources of cosmic rays. Assousa, in collaboration with others, has searched for the radio frequency lines of formaldehyde in expanding neutral hydrogen shells associated with these remnants. Although formaldehyde absorption was detected, their work showed that this was neither associated with the expanding shells nor with the remnants themselves. Turner has made use of Zeeman splitting in the 21-cm hydrogen line of the expanding shells to measure the strength of the interstellar magnetic field. In one remnant he showed that this field was less than 3 microgauss, whereas in another case a possible positive result of about 5 microgauss was found.

In other work directed toward our own Galaxy and its neighborhood, Tuve and his co-workers have searched for very high velocity hydrogen clouds which would be indicative of the Galaxy being an open system, either receiving material from intergalactic space or expelling material from the Galaxy. No such phenomena were found. Peterson reports work on a very distant globular cluster associated with our Galaxy. Comparison of the size of the cluster with the tidal "Roche limit" for disruption by the general galactic gravitational field is used to show that this cluster is in a very eccentric orbit about the galactic center.

Many of the observations mentioned above would not have been possible without the Carnegie image tube developed at DTM by W. K. Ford, Jr. Continued improvements in these devices and systems for utilizing them have been made by Ford. In addition he reports advances in developing a new type of detector especially suitable for photometric work. This detector eliminates use of the pho-

tographic plate and provides the imaging data in digital form.

Biophysics

Although it is planned that some work in biophysics will continue beyond this year, it will be on a diminishing scale. It therefore seemed a good time to summarize the many distinguished achievements of this group during the past 30 years. This has been done by R. B. Roberts, one of the founding members of the group. He traces the evolution of the DTM Biophysics Section from a group of enthusiastic nuclear physicists with little background in biology through their increasing biological sophistication, and enumerates 18 significant findings made by the nine staff members and numerous resident associates, fellows, and technical assistants associated with this program. All this work was done in the context of the revolutionary advances being made in biochemistry during this time, as a consequence of new understanding of the genetic mechanism in living cells and the role of nucleic acids. It is a testimony to the viability of the approach to science taken by the Institution and the Department that a small group with modest funding and few professional credentials in this area were able to play such a significant role in a large and expanding field of science.

During this year studies of DNA in human, primate, rat, and mouse cells have continued. Bonner has worked on a promising method for isolating genetically important human DNA segments. Hoyer has used the thermal stability of reassociated DNA obtained from different primates to determine the relative times of their evolutionary divergence. By use of this method he infers that the group of African monkeys studied represents an evolutionary group more homogeneous than that formed by man, orangutan, and gibbon but less homogeneous than man, chimpanzee, and gorilla.

N. Rice and other members of the group have been working on the relation-

ship between repeated DNA sequences (families) and evolutionary processes. In Rice's work the puzzling result is found that two species can possess homogeneous families which are only loosely related to each other, and alternative hypotheses are proposed to explain this result. Roberts and co-workers report preliminary work supporting the hypothesis that family formation is necessary for speciation.

Cowie is working at present at the Pasteur Institute in Paris, continuing work on metabolism in *Escherichia coli*. He reports results on the modification of enzyme activity as a consequence of enzyme-antibody binding.

Nuclear and Atomic Physics

One of the older fields of research still very active at DTM is the study of atomic and nuclear phenomena by bombardment with accelerated charged ions. This work is carried out by L. Brown and his colleagues G. H. Pepper and L. G. Arnold, and also involves collaboration with several workers associated with our astrophysics group, N. Thonnard and C. K. Kumar.

In the atomic physics area, the intensity of production of characteristic x-ray line spectra by heavy ion bombardment yielded a simple exponential dependence

on the atomic number of the target atom. Surprisingly, it appeared that current theories do not yield this result, even though its simple form strongly suggests that a theoretical explanation should be possible. Brown and his co-workers have derived a simple expression which fits the observed exponential dependence of the line spectra on Z , as well as predicting the x-ray energy spectrum of the continuum radiation. Although this does not yet represent a complete theory for the problem, the agreement with observed data indicates that the approach taken is on the right track.

In the area of nuclear physics, the nuclear structure of ^{16}O and ^{10}B was successfully investigated by formation of the compound nucleus by bombardment of ^{15}N and ^9Be with polarized protons. The former nucleus is of astrophysical interest as $^{15}\text{N}(p,\alpha)^{12}\text{C}$ and $^{15}\text{N}(p,\gamma)^{16}\text{O}$ are competing steps in the CNO cycle of stellar energy production.

The results found for the energy levels of ^{10}B by $^9\text{Be}(p,n)^{10}\text{B}$ are satisfying in that they are in agreement with the prediction of the shell model as well as with some earlier work. However, they are in disagreement with our earlier measurements of $^9\text{Be}(p,p)^9\text{Be}$. The latter data are being reanalyzed in order to try to understand this difference.

ASTROPHYSICS

G. E. Assousa, E. T. Ecklund, W. K. Ford, Jr., C. K. Kumar, C. A. Little, C. J. Peterson, V. C. Rubin, N. Thonnard, K. C. Turner, M. A. Tuve, and J. W. Warner

Collaborators

B. Balick, L. K. De Noyer, J. W. Erkes, J. Graham, C. Heiles, M. S. Roberts, and R. Sanders

Astronomers at DTM are principally observers, using optical or radio telescopes as the problems demand, and turning to the development of more advanced instruments as the need for them is indicated. Major studies of the past year relate to external galaxies and large structures in our Galaxy, and are discussed below.

GALAXIES

OBSERVATIONAL COSMOLOGY

W. Kent Ford, Jr., Vera C. Rubin, and Norbert Thonnard

For the past several years, we have been collecting data for an all-sky sample of Sc I galaxies, i.e., "standard candles," to answer the question, Is the

Hubble expansion isotropic as observed from the Galaxy? Curiously, the answer to this question had not explicitly been sought previously in an observational program by optical astronomers. In collaboration with Dr. Morton S. Roberts, National Radio Astronomy Observatory,* and Dr. John A. Graham, Cerro Tololo Inter-American Observatory, we have now obtained optical velocities, 21-cm velocities, HI fluxes, magnitudes, and colors for almost 200 galaxies, and the analysis of the observed expansion is presently being completed. The anisotropy reported earlier (Rubin, Ford, and Rubin, 1973; *Year Book* 73, 885, 1974) persists at about the 4.5σ level. From a detailed study of the form of the velocity variation across the sky for galaxies with $3500 < V < 6500 \text{ km s}^{-1}$ (distances about 60 to 120 Mpc), we believe that the apparent isotropy can best be interpreted as a motion of our Galaxy with respect to this sample of galaxies. The velocity of the sun is $V = 647 \pm 144 \text{ km s}^{-1}$ toward $\alpha = 39^\circ \pm 24^\circ$, $\delta = +57^\circ \pm 12^\circ$, which corresponds to galactic coordinates $l = 137^\circ$, $b = -2^\circ$. If we remove from this motion the velocity of our sun relative to the Local Group of galaxies, then the velocity of our Galaxy and the Local Group of galaxies becomes $V = 494 \pm 150 \text{ km s}^{-1}$, toward $l = 164^\circ$, $b = -3^\circ$.

This location for the apex of the galactic motion means that the Galaxy is moving edge on, and that the motion is not far from the plane defined by the distribution of bright galaxies and small nearby groups, the Supergalactic Plane. Moreover, the motion is approximately orthogonal to the direction of the Virgo cluster, the nearest large cluster of galaxies, of which we may be an outlying member. Hence we have no component of motion toward or away from the Virgo cluster, nor has the presence of the excess

mass toward Virgo slowed the expansion in our region of space. A schematic diagram of this motion is shown in Fig. 1. Our program galaxies are too distant to enable us to tell if our Local Group is rotating about the Virgo cluster. At our present distance from Virgo, about 20 Mpc, a bound orbit would have $V \sim 500 \text{ km s}^{-1}$, with a period of revolution of some 10^{11} years, or ten times the estimated age of the universe. Hence the concept of a bound orbit has no meaning, unless it relates to an earlier age of the expanding universe, when our Galaxy was closer to Virgo. From our study we cannot define the size of our co-moving group, nor draw any conclusions concerning systematic motions of the galaxies nearer than 60 Mpc. We initially chose a sample for study which is sufficiently distant so that the velocities are unaffected by local irregularities within the local supercluster, yet not so distant that any velocity irregularity is masked by the large Hubble expansion.

A motion of our Galaxy as large as $647 \pm 144 \text{ km s}^{-1}$ as observed from the sun is of considerable interest to cosmologists because it conflicts with present determinations of the isotropy of the 3° black body radiation. The early history of the universe is contained in the spectrum and the directionality of the 3° cosmic background radiation. The most generally accepted theory assumes that the universe started some 15 billion years ago at a singularity, the Big Bang, and has been expanding and cooling ever since. At present, the radiation field from the Big Bang has cooled to 3°K ; the corresponding peak wavelength of the photons is about 1 or 2 mm. To study the isotropy of this radiation field from the earth is very difficult because of the radiation of the earth's atmosphere and the Galaxy, which are both considerably above 3° . It is only slightly less difficult from balloons. However, results by a number of groups (discussed in Peebles, 1971) indicate that the radiation field is extremely isotropic, from which an upper

*The National Radio Astronomy Observatory is operated by Associated Universities for Research in Astronomy, Inc., under contract with the National Science Foundation.

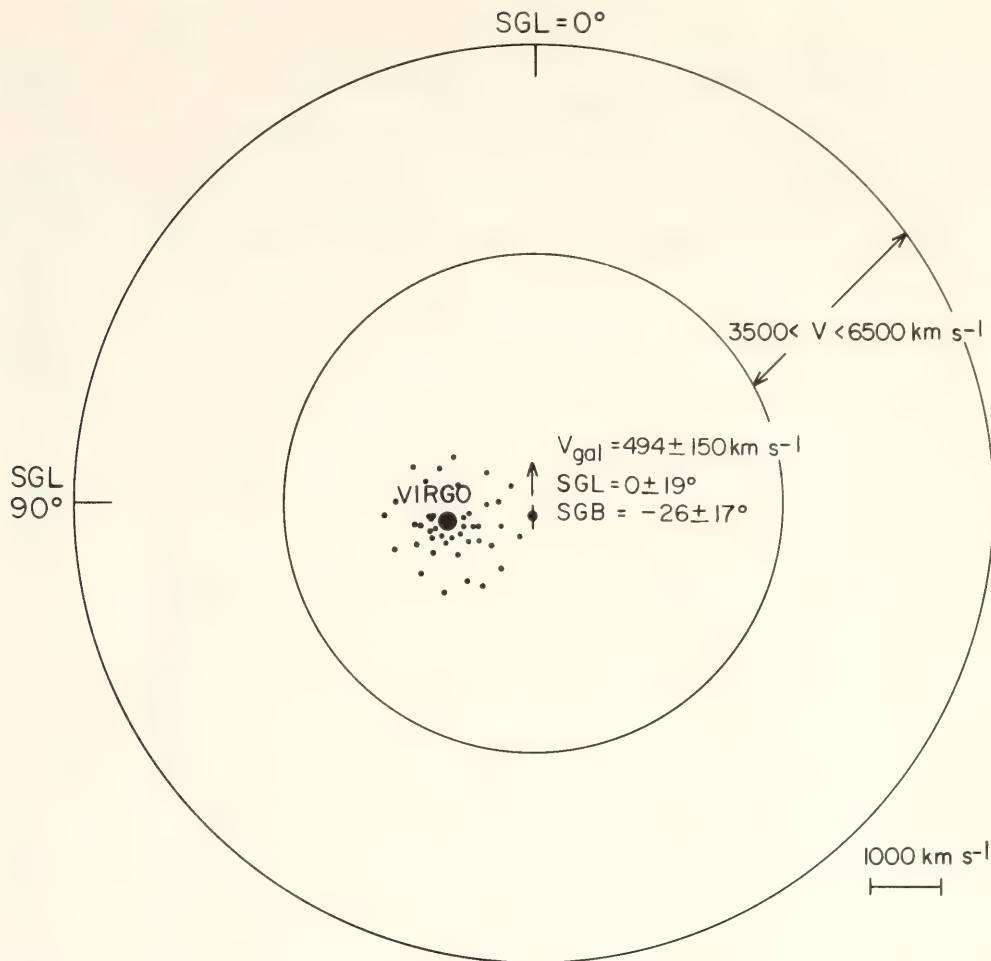


Fig. 1. Schematic drawing in plane of supergalaxy. Our Galaxy is shown moving edge on toward $SGL = 0^\circ$, approximately orthogonal to the Virgo cluster. The Sc I galaxies in the study are located in a spherical shell with $3500 < V < 6500 \text{ km s}^{-1}$.

limit to the motion of the sun of about 300 km s^{-1} is inferred. If future experiments confirm the isotropy of the radiation field, then the resolution of the conflict between the velocity we have detected and the low velocity inferred from the 3° radiation may be a major step in our understanding of the universe.

Alternative explanations of the observed anisotropy might be a Hubble constant which varies as a function of position on the sky, or a mean absolute magnitude for Sc I galaxies which varies as a function of position. In either case, however, the observations require a minimum value on one region of the sky, increasing smoothly to a maximum value 180° away. Such a cosine variation is the natural result of a motion, and hence we feel this latter explanation is the most acceptable. Velocity studies of a more distant sample of galaxies could distin-

guish between these two interpretations, and we are making plans to extend the study to both nearer and more distant galaxies.

Enroute to the conclusion of our Sc I study, we used the extensive body of data to carry out a considerable number of statistical analyses, much in the spirit of early studies of statistics of stars. From the variation of velocity, magnitudes, and colors of the galaxies, we mapped the large-scale distribution of absorbing material in our Galaxy. This is the first time that a complete sample of galactic velocities has been employed in such a determination, and the result is a completely independent determination of the coefficient of galactic extinction, A_B . We obtain $A_B = 0.14 \pm 0.04$, which supports the low value for galactic extinction which is derived from stellar colors.

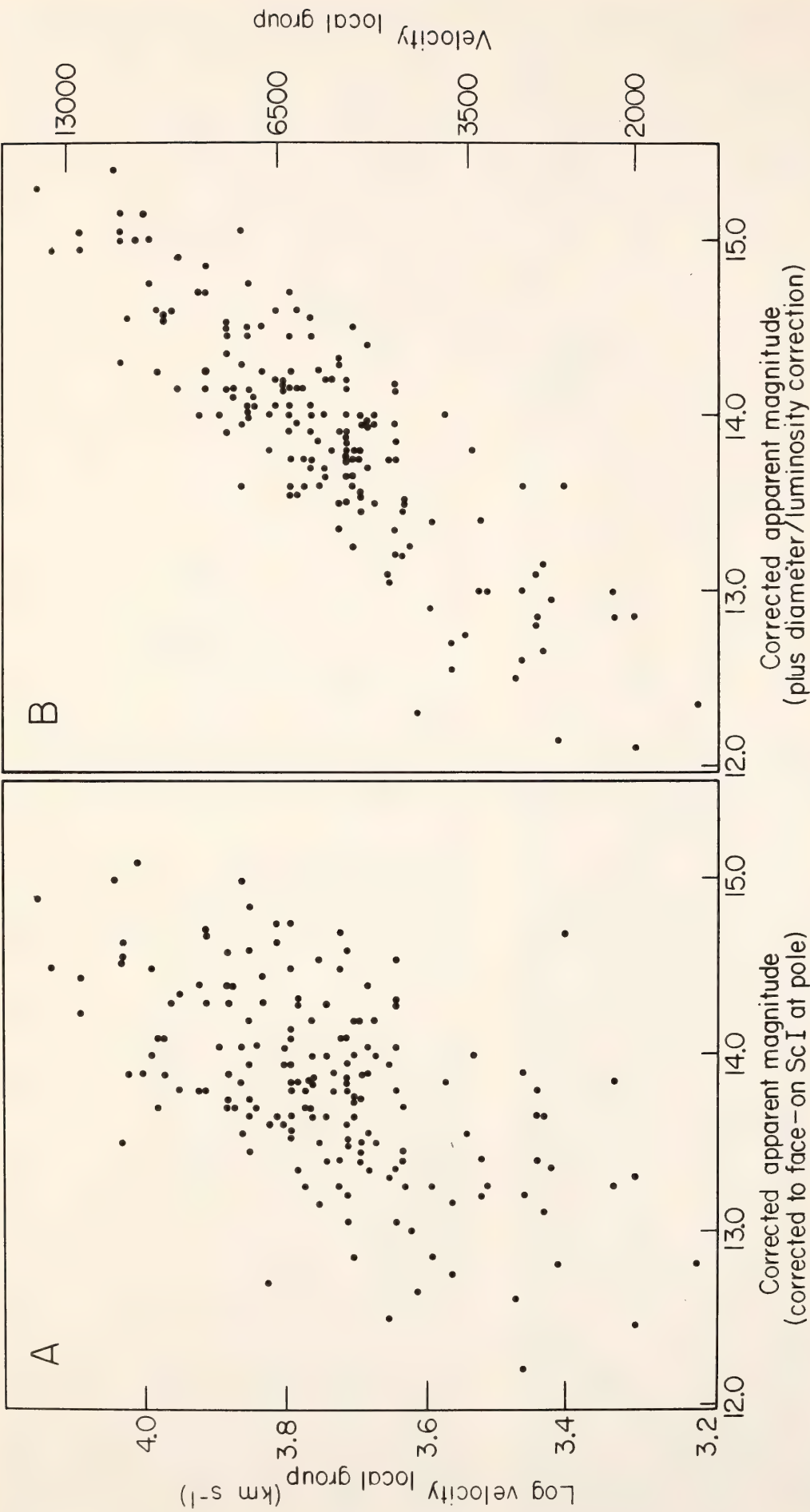


Fig. 2. Hubble diagrams for program galaxies: (A) Log of observed velocity, corrected for the motion of the sun relative to the local group, plotted against observed magnitude, corrected to face on Sc I at the pole. (B) As in (A), except that apparent magnitude is also corrected for the linear diameter/luminosity relation.

We have also detected a very strict relation between intrinsic luminosity of an Sc I galaxy and its diameter, a relation which can be used to assign a more exact luminosity to each galaxy. Formerly, it had been assumed in statistical

studies that all Sc I galaxies have the same mean absolute magnitude, $M = M_o$, with a dispersion of $\sigma_{M_o} \sim 0^m.5$. Now, however, by considering the linear diameter of the galaxy, we can make a better estimate of the absolute magnitude of

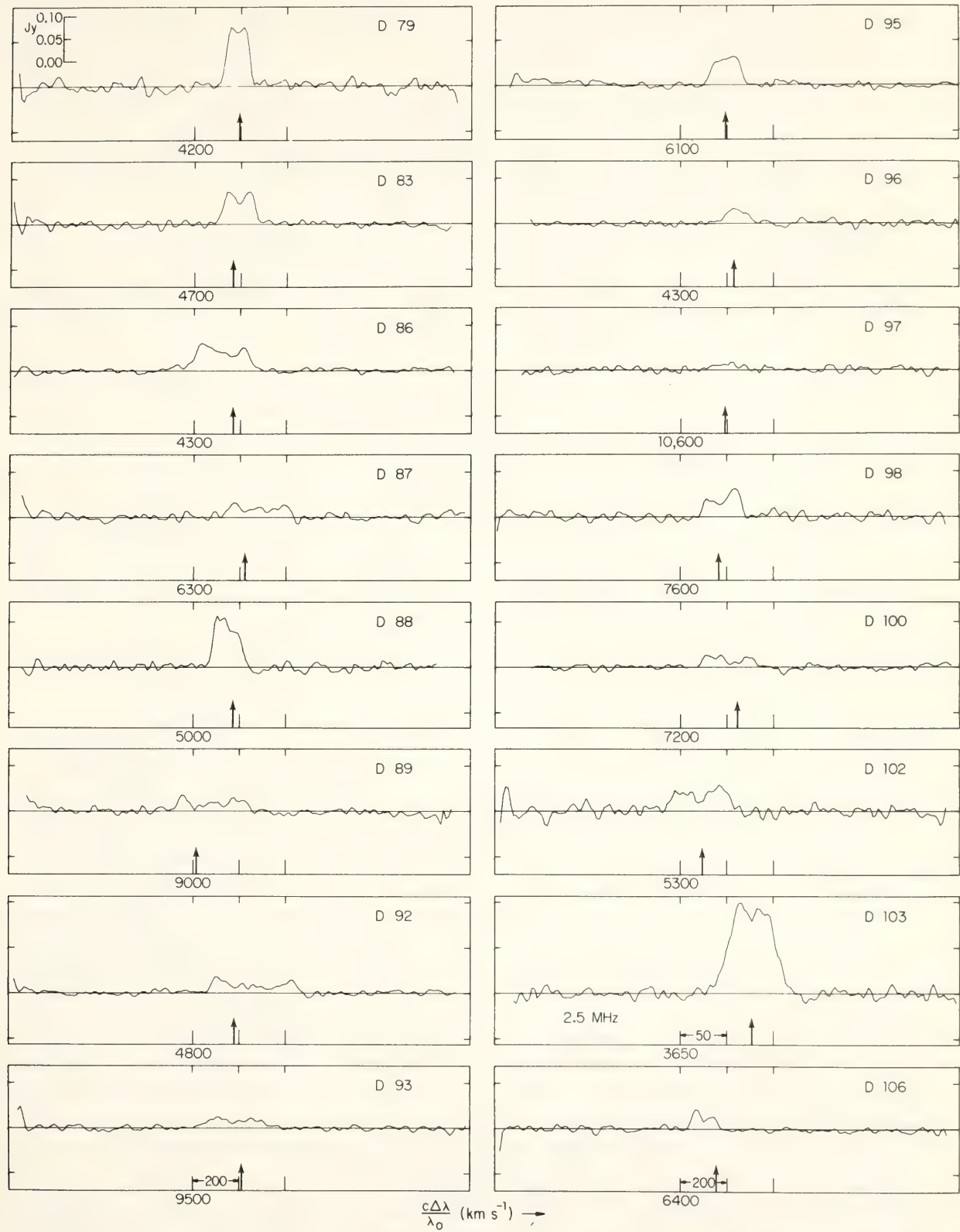


Fig. 3. Representative sample of 21-cm hydrogen line velocity profiles for Sc I galaxies. The abscissa gives the 21-cm flux in Janskies ($1 \text{ Jy} = 10^{-26} \text{ w m}^{-2} \text{ Hz}^{-1}$), while the ordinate is the heliocentric velocity in km sec^{-1} . The arrows indicate the observed optical velocities.

each galaxy. This enables us to get a more accurate estimate of the distance of each galaxy by comparing its observed magnitude with its assigned intrinsic luminosity. The variation is such that an Sc I galaxy with diameter 20 kpc is intrinsically 0.7 magnitudes fainter than one of 40 kpc; one of 60 kpc is 0^m4 brighter. While the relation between galaxy diameter and luminosity has been discussed several times since it was explicitly noted by Hubble (1936), no use of the relation had been made. We show in Fig. 2A and 2B the Hubble diagram for our program galaxies, before and after application of the correction for the diameter/luminosity effect. The very significant decrease in the scatter ($\sigma_{M_0} < 0^m4$) of the diagram is due to the application of this correction.

We are analyzing our 21-cm neutral hydrogen line observations of the Sc I sample and therefore can only mention some preliminary results. The success of the observations in itself is impressive. Of 137 galaxies observed, in only two were we not able to detect any hydrogen emission. In five galaxies the signal was confused by a companion galaxy in the telescope beam, and for five others the detection was questionable and was not included in our analysis. We therefore have 125 Sc I galaxies with a good determination of the total hydrogen flux. Because these galaxies are all much smaller in diameter than the telescope beam, no errors should arise due to partly resolved sources. The analysis of the hydrogen contents of such a large, well-defined set of galaxies should be invaluable in helping us to better understand the properties of spiral galaxies.

In Fig. 3 a representative sample of hydrogen line profiles is shown for 16 Sc I galaxies. The arrow indicates the observed optical velocity. For the 120 galaxies with both optical and 21-cm velocities, the mean difference $V_{\text{opt}} - V_{21 \text{ cm}}$ is only 3 km/sec, with $\sigma = 36$ km/sec. The ratio of optical luminosity to neutral hydrogen luminosity varies by no more

than a factor of 3, indicating that the neutral hydrogen luminosity can also be used as an indicator of the "brightness" of the galaxy. We therefore use the 21-cm luminosity as a second distance indicator, in the same manner as the optical magnitudes. Because galactic extinction will not affect the 21-cm magnitudes, the close correlation of the optical and 21-cm luminosities confirms the validity of the correction for absorption which we use, and, more importantly, helps to rule out galactic absorption as a source of the anisotropy.

References

- Hubble, E., *The Realm of the Nebulae*, New Haven: Yale University Press, p. 48, 1936.
 Peebles, P. J. E., *Physical Cosmology*, Princeton: Princeton University Press, Ch. 2, 1971.
 Rubin, V. C., W. K. Ford, Jr., and J. S. Rubin, A curious distribution of radial velocities of Sc I galaxies with $14.0 \leq m \leq 15.0$, *Astrophys. J. (Lett.)*, 183, L111, 1973.

OBSERVATIONS OF LATE-TYPE SOUTHERN GALAXIES

Norbert Thonnard and Kenneth C. Turner

Of importance in understanding the contents and structure of galaxies has been a comparison of their neutral hydrogen content and velocity distribution with their optical morphology. From the width of the hydrogen line profile and the inclination of the galaxy on the plane of the sky, it is possible to obtain an independent determination of the total mass of the galaxy. The ratio of hydrogen to optical luminosity and the total hydrogen mass are important parameters in understanding the properties of different galaxy types. The systematic study of large numbers of galaxies at 21 cm has until recently been undertaken only from northern hemisphere observations. In contrast, the Australian observatories have focused on the detailed study of the

velocity field of individual galaxies that were large enough to be resolved by their $13\frac{1}{2}$ arc min beam (Shabbrook and Robinson, 1967). Observations of galaxies at 21 cm from the southern hemisphere, especially with telescope beams that are large compared to the galaxy size, are important to further our understanding of galaxies.

We therefore continued our program of 21-cm hydrogen line observations of late-type galaxies in the southern sky following the installation of a redesigned receiver front-end on the 30-meter CIW-IAR radio telescope in Parque Pereyra, Argentina. Even though the receiver noise temperature had improved by 25%, we still had difficulty observing these faint signals because the system stability

and base-line curvature continued to be a problem. To remove the instrumental base line (approx. 8°K), we had to spend 6 minutes out of every 12-minute integration cycle observing a point away from the galaxy which we later subtracted from the "on" profile.

We observed 11 galaxies. Two of these, in which we had detected 21-cm hydrogen line emission for the first time during our first observing run (*Year Book 71*, p. 243, 1972), were large enough that we mapped them this time to determine the total extent of the neutral hydrogen. In Fig. 4 are shown representative profiles of three galaxies. Typical integration times for each object averaged about 90 minutes "on" and 90 minutes "off."

A-255 is a late barred spiral, classified

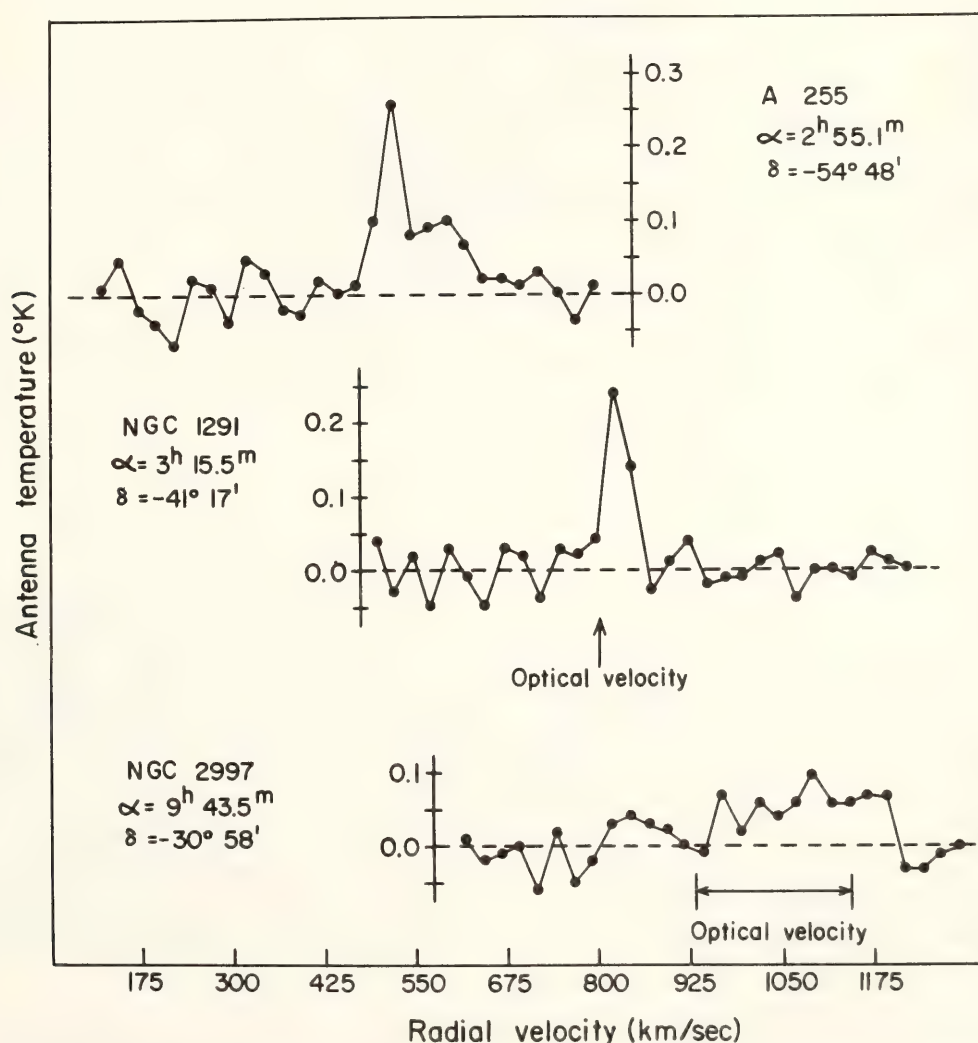


Fig. 4. 21-cm neutral hydrogen line profiles for three southern galaxies. The abscissa gives the antenna temperature in degrees Kelvin; the ordinate gives the observed velocity corrected to the local standard of rest in km/sec. Where known, published optical velocities are indicated.

as an SBd by de Vaucouleurs and de Vaucouleurs (1964). This galaxy has no published optical or 21-cm velocity; therefore, the radial velocity of 555 km/sec is a new value.

NGC 1291 is an interesting galaxy. Perrine (1922) described it as a "fuzzy ball" with a faint outer spiral structure of approximately one and one half turns. In the Shapley-Ames catalog it is classified as an elliptical and by de Vaucouleurs as a ringed barred S0/a galaxy. De Vaucouleurs (1963) obtained an optical radial velocity of 802 km/sec. On the Palomar Sky Survey prints, except for the faint outer ring, this object looks like a normal barred S0 galaxy. It has been found that as one goes along the Hubble sequence from irregular (late-type) to elliptical (early-type) galaxies, the fraction of matter in the form of neutral hydrogen as compared to total galaxy mass decreases to vanishing amounts; no 21-cm hydrogen line radiation has yet been found in elliptical galaxies, and the detection for "normal" S0's is still debatable (Gallagher, Faber, and Balick, 1975). All of this would make it quite surprising to find neutral hydrogen in this galaxy, but the good agreement between the original detection of 21-cm emission with $V_r = 833$ km/sec (Lewis, 1970), our present observation of $V_r = 828$ km/sec and the optical velocity of $V_r = 802$ km/sec makes the detection of hydrogen emission from NGC 1291 quite certain. Whether the surprisingly high neutral hydrogen content warrants reclassification of this galaxy or is a characteristic of the ringed structure, can only be settled by more observations on similar objects.

NGC 2997 is a typical Sc galaxy similar to M101. An optical spectrum taken by Pastoriza (1967) shows a rather steep velocity gradient, not at all inconsistent with our 21-cm profile. Also, using an inclination of 24° determined from the ratio of major to minor axes and a typical maximum rotational velocity of 275 km/sec for an Sc galaxy, one calcu-

lates a profile width of 224 km/sec, which is in good agreement with the observed width of approximately 250 km/sec.

References

- de Vaucouleurs, G., and A. de Vaucouleurs, Classification and radial velocities of bright southern galaxies, *Mem. R. Astron. Soc.*, 68, 69, 1963.
- de Vaucouleurs, G., and A. de Vaucouleurs, *Reference Catalogue of Bright Galaxies*, Austin: University of Texas Press, 1964.
- Gallagher, J. S., S. M. Faber, and B. Balick, H I in early-type galaxies. I. observations. Submitted for publication, *Astrophys. J.*, 1975.
- Lewis, B. M., Neutral hydrogen in the S0 galaxy NGC 1291, *Observatory*, 90, 264, 1970.
- Pastoriza, M. G., Spectra of peculiar nuclei in galaxies, *Observatory*, 87, 225, 1967.
- Perrine, C. D., Notes on four interesting nebulae, *Mon. Not. R. Astron. Soc.*, 82, 486, 1922.
- Shabbrook, R. R., and B. S. Robinson, 21-cm observations of NGC 300, *Aust. J. Phys.*, 20, 131, 1967.

INTERNAL MOTIONS IN BARRED SPIRAL GALAXIES

W. Kent Ford, Jr., Charles J. Peterson,
Vera C. Rubin, and Norbert Thonnard

In the past 15 years, rapid progress has been made in understanding the dynamics of spiral galaxies, principally because of advances in observing technology. For nearby galaxies, the velocity field can be mapped in detail by measuring the line-of-sight velocities of the excited gas surrounding the hot, young blue stars. Unfortunately, the observation and understanding of barred spiral galaxies have remained difficult, principally because the bars consist of old, relatively faint cool stars with little or no excited gas. Hence, the velocity field

within the bar and its relation to spiral structure in general remain unknown. With the availability of the 4-meter telescope and advanced image tubes, we are attempting to learn more about the dynamics of barred spiral galaxies.

NGC 5383 is one of the few bright barred spiral galaxies in the northern sky, and therefore it is a natural candidate for observation in our continuing program to study the velocity fields in

barred spiral galaxies. We have used a Carnegie image tube on the Kitt Peak 4-meter spectrograph to obtain spectra at very high spatial and velocity resolution in NGC 5383. We show in Fig. 5 a photograph of the galaxy taken with a Carnegie image tube at the Cassegrain focus of the 4-meter telescope, and spectra in three position angles across the galaxy. The emission lines of $H\alpha$, $[N II]$, and $[S II]$ arise from the ex-

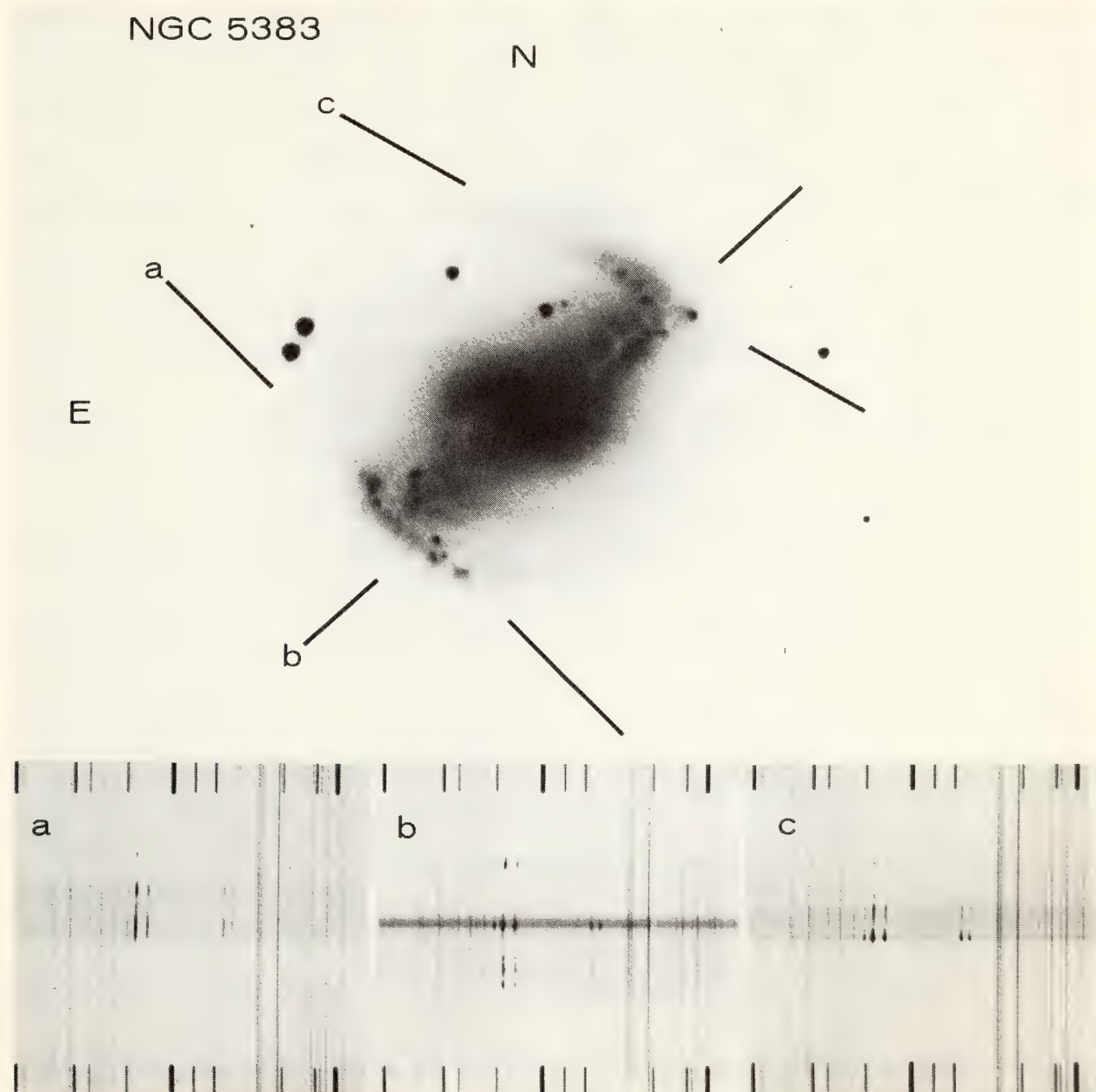


Fig. 5. Reproduction of a plate of NGC 5383, taken at the Cassegrain focus of the Kitt Peak 4-m telescope with a Carnegie image tube, plus N_2 -baked IIIa-J plate, exposure 12 min. Lines indicate positions of spectrograph slit for spectra *a*, *b*, *c*. All spectra taken with Carnegie image tube plus 4-m Cassegrain spectrograph, N_2 baked IIIa-J plates, exposures 125, 85, and 107 min; original dispersion 56 Å/mm. Comparison spectral lines are Ne + A. Lines completely crossing spectra are emission lines of the night sky.

cited gas surrounding hot young stars, and a study of their velocities allows us to map the velocity field of the excited gas. We now have observed emission line spectra with the spectrograph slit in nine different positions.

In order to determine the velocities of the stellar population in the bar, we have obtained spectra along the bar in the blue spectral region. We are presently completing the measurement and reduction of this extensive plate material. In conjunction with the study, the Dutch radio astronomers are using the Westerbork (Holland) aperture synthesis radio telescope at 21-cm to map the velocity field of the neutral hydrogen in NGC 5383. Intercomparison of the optical and radio results is expected to be valuable in helping us to understand the dynamics of barred spiral galaxies.

NGC 3351 is a bright barred spiral galaxy in the Leo group of galaxies, typical of those barred spirals in which the outer arms form a complete ring like the Greek letter theta. The galaxy is oriented

on the sky so that our line of sight is almost along the bar. Hence, noncircular motions along the bar should be detectable. Our study of the *nucleus* of this galaxy is now complete (Rubin *et al.*, 1975a) and shows the nucleus to consist not of a single central concentration but a ring of emission regions about 350 pc from the center. The ring is rotating, with $V_{\text{rot}} = 126 \pm 16 \text{ km s}^{-1}$, and also contracting toward the center, with $V_{\text{con}} = 34 \pm 11 \text{ km s}^{-1}$.

With the Kitt Peak 4-meter telescope, we have obtained spectra with the spectrograph slit tangent to the *outer* ring in 12 position angles. Figure 6 shows the measured hydrogen emission line velocities around the ring, plotted as a function of angular position in the plane of the galaxy. If the outer arms are rotating only, the observed velocities will vary as a sinusoid, with a phase defined by the galaxy/observer geometry and an amplitude proportional to the rotational velocity. The dashed line is a least-squares sinusoidal fit which gives a heliocentric

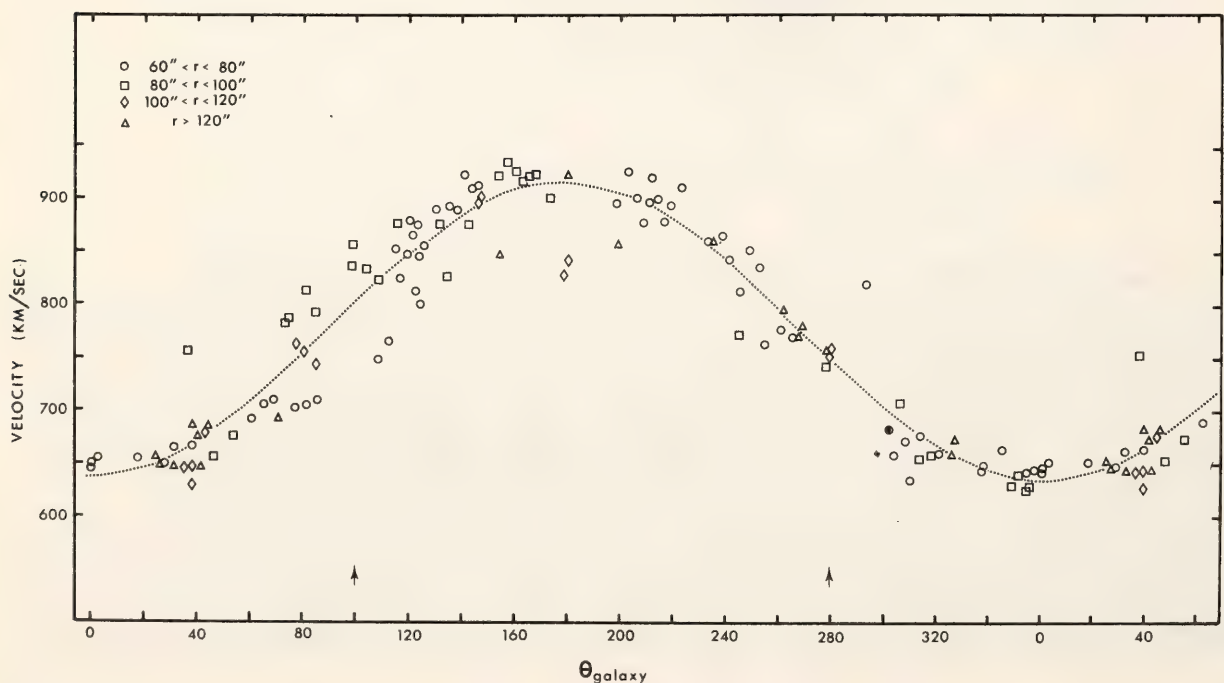


Fig. 6. Observed velocities as a function of angular position in the plane of the galaxy NGC 3351. Data are divided into four groups according to radial distance from the nucleus. The dotted line is a least-squares sinusoidal fit with systemic velocity 775 km/sec and amplitude $V(R) \sin i = 139 \pm 4 \text{ km/sec}$, corresponding to $V = 216 \pm 6 \text{ km s}^{-1}$ in the plane of the galaxy, $3 < R < 6 \text{ kpc}$. Velocity data for $0^\circ < \theta_{\text{galaxy}} < 60^\circ$ has been repeated at the right edge of the graph. The two arrows mark the position angle of the bar.

systemic velocity of $780 \pm 3 \text{ km s}^{-1}$, in excellent agreement with the optical and 21-cm central velocities of 779 ± 8 and $779 \pm 3 \text{ km s}^{-1}$. The rotational velocity is $V(R)\sin i = 139 \pm 4 \text{ km s}^{-1}$ corresponding to a rotation in the plane of the galaxy $V_{\text{rot}} = 216 \pm 6 \text{ km s}^{-1}$ at the distance of the ring, $3 < r < 6 \text{ kpc}$; the phase indicates that there are no significant expansion or contraction motions in the outer ring, but rotation only. The mass within 9 kpc is $\geq 5 \times 10^{10} M_{\odot}$.

To understand the dynamics of barred spiral systems, it is necessary to know the velocity structure of the bar. However, with one possible exception, there are no emission regions in the bar. Measurement of relatively sharp stellar absorption features (Ca I λ 4226, Fe I 4325, $H\gamma$, $H\beta$, Mg I λ 5183, plus other lines) shows that the rotation within the bar is of uniform angular velocity. The small velocity gradient observed along the bar is consistent with only circular motion in the bar. The study is continuing.

NGC 6764 is a relatively nearby, but previously unstudied, barred spiral galaxy. A 4-m spectrum revealed that the nuclear emission lines are about 750 km s^{-1} broad, which places it in the class of Seyfert galaxies, those galaxies with rapidly rotating clouds of ionized gas in their nuclei. Measured velocities just outside the nucleus indicate that there are streaming motions both into and out of the nucleus. The details of the velocity field have been published elsewhere (Rubin *et al.*, 1975b).

References

- Rubin, V. C., W. K. Ford, Jr. and C. J. Peterson, Evidence for contraction in the nuclear ring of the barred spiral galaxy NGC 3351, *Astrophys. J.*, **198**, 39, 1975a.
 Rubin, V. C., N. Thonnard, and W. K. Ford, Jr., Observations of NGC 6764, a barred Seyfert galaxy, *Astrophys. J.*, **198**, 31, 1975b.

THE VELOCITY FIELD OF THE PECULIAR GALAXY NGC 1275

W. Kent Ford, Jr., Charles J. Peterson,
and Vera C. Rubin

NGC 1275 is one of the most peculiar galaxies known. Ever since the discovery that it is an intense source of radio radiation, astronomers have been attempting to understand its nature. Its structure has been variously interpreted as the result of a collision between two galaxies (Baade and Minkowski, 1954) or the aftermath of a violent outburst in the nucleus of a single galaxy (Burbidge, Burbidge, and Sandage, 1963). The excited gas appears at two velocities, one at $V \sim 5200 \text{ km s}^{-1}$ in agreement with the velocity determined from the stellar absorption lines (Humason, 1932, and our spectra), and the other at $V \sim 8200 \text{ km s}^{-1}$. Interest in this object has been restimulated by the recent discovery (deYoung, Roberts, and Saslaw, 1973) of 21-cm hydrogen absorption, with a velocity corresponding to the high velocity system. If this is interpreted as two galaxies in collision, then the galaxy at $V \sim 8200 \text{ km s}^{-1}$ must lie along the line of sight between us and the galaxy at $V \sim 5200 \text{ km s}^{-1}$, and must be falling into the lower velocity galaxy.

We have obtained new observational material with the Kitt Peak 4-meter image tube spectrograph to map the velocity field at higher spatial and velocity resolution than has been done formerly to see if an optical study can help clarify the nature of NGC 1275. This higher resolution reveals much greater structure in the velocity field than had been previously found (Burbidge and Burbidge, 1965). A spectrum taken $7''\text{N}$ of the nucleus is shown in Fig. 7; $H\alpha$ in the two velocity systems is marked. The very high degree of complexity in the relative line strengths of the two systems, in the velocity gradients, in the discontinuities in the lines, and even in the discontinuities in the weak continuum, all suggest that it will not be

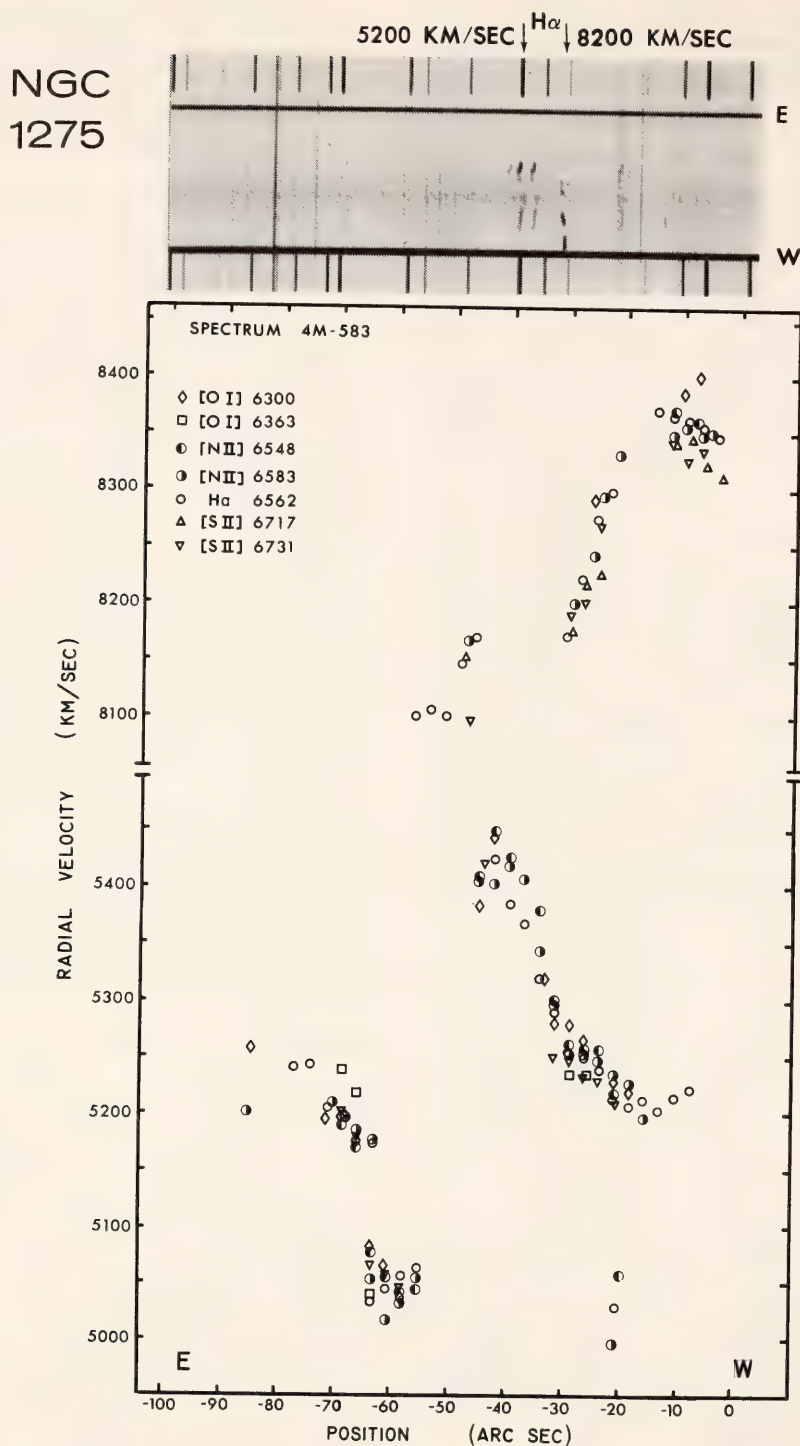


Fig. 7. Emission line velocities in NGC 1275 measured on 4m-583; spectrograph slit was offset $\sim 7''$ N at position angle 92.5° . Reproduction of spectrum is shown above, taken with Carnegie image tube plus 4-m Cassegrain spectrograph, N_2 -baked IIIa-J plates, exposure 230 min; original dispersion 56 \AA/mm . The location of $H\alpha$ in the two velocity systems is marked by arrows.

easy to understand this object. Our observations are continuing.

References

- Baade, W., and R. Minkowski, On the identification of radio sources, *Astrophys. J.*, 119, 215, 1954.
- Burbidge, E. M., G. R. Burbidge, and A. R. Sandage, Evidence for the occurrence of violent events in the nuclei of galaxies, *Rev. Mod. Phys.*, 35, 947, 1963.
- Burbidge, E. M., and G. R. Burbidge, Optical evidence suggesting the oc-

currence of a violent outburst in NGC 1275, *Astrophys. J.*, 142, 1351, 1965.
 de Young, D. S., M. S. Roberts, and W. C. Saslaw, Detection of 21-centimeter hydrogen absorption in the high velocity component of the radio galaxy Perseus A, *Astrophys. J.*, 185, 809, 1973.
 Humason, M. L., The emission spectrum of the extra-galactic nebula NGC 1275, *Publ. Astron. Soc. Pac.*, 44, 267, 1932.

IONIZED GAS IN THE NUCLEAR BULGE OF M31

C. Krishna Kumar

The relation of the chemical composition of the interstellar material in a galaxy to the past history of the evolution and dynamics of stars in the galaxy continues to be a major question in the understanding of the universe. Only for nearby galaxies is there sufficient spatial

resolution to permit the investigation of these questions as a function of position in a galaxy. Earlier studies by Rubin and Ford (1971) indicated the presence of ionized gas (Fig. 8) in the nuclear bulge extending out to 2 kpc from the nucleus of M31. This gas is diffuse in spatial distribution and the measured radial velocities of the $H\alpha$ and $[N II]$ 6583 Å lines have been used by Ford and Rubin for kinematical investigations. Here we report on the intensities of the lines emitted by this gas and explore the consequences.

The principal emission lines that are seen in the spectra are the $[O II]$ 3727–29 Å doublet, $[O III]$ 5007 Å, $H\alpha$, the $[N II]$ 6548–83 Å doublet, and the $[S II]$ 6717–31 Å doublet. A spectrum of the nuclear bulge of M31, taken with the Carnegie image tube plus the Kitt Peak 4-m spectrograph is shown in Fig. 8. The lines are weak (e.g., $W(6563 \text{ Å}) \approx 1 \text{ Å}$), and we have measured the

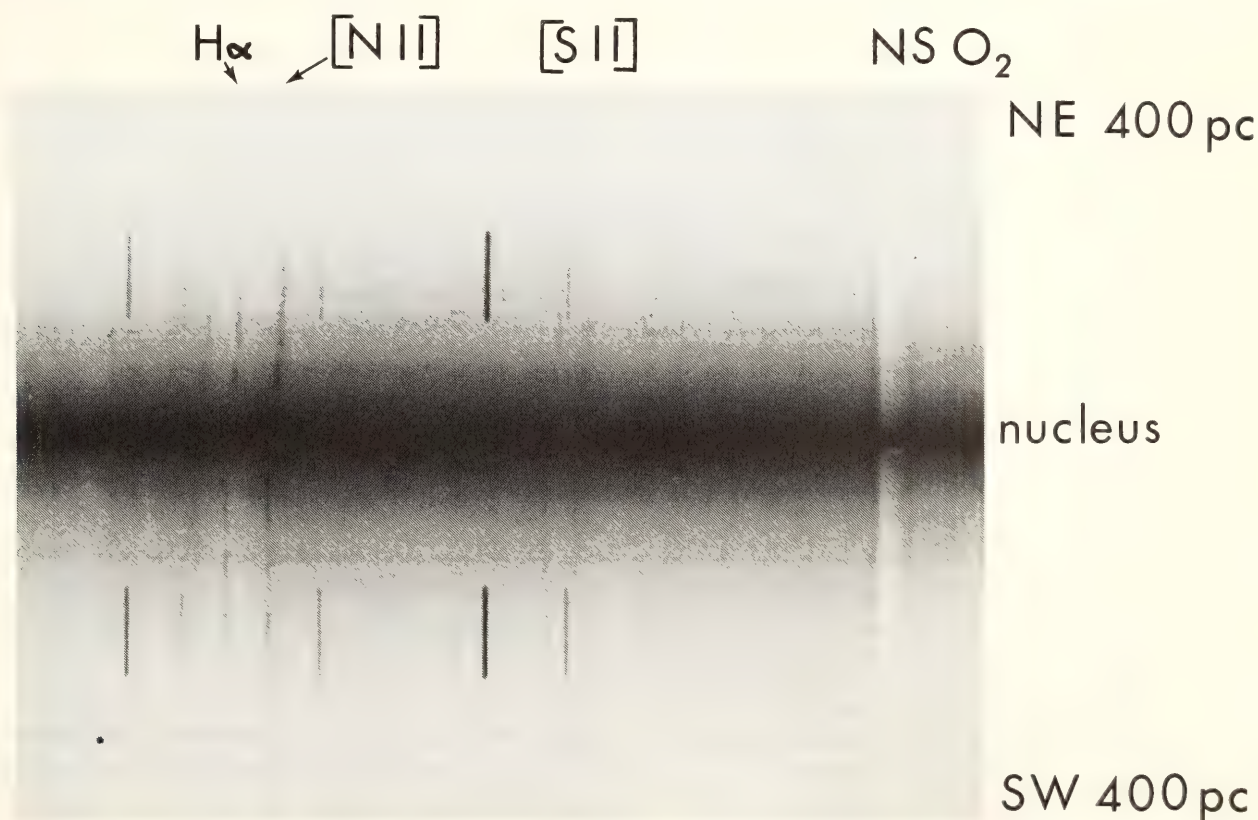


Fig. 8. Spectrum along major axis in nuclear bulge of M31, showing emission lines from diffuse gas superimposed upon continuum produced by integrated starlight. Carnegie image tube plus 4-m Cassegrain spectrograph, plus N_2 -baked IIIa-J plates, exposure 120 min; original dispersion 28 Å/mm. Absorption lines crossing plate at right are night sky absorption lines from O_2 (1-0 band).

intensities of these lines between 50 pc and 100 pc distance from the nucleus only. The intensities of the lines corrected for the underlying stellar absorption in the case of $H\alpha$ and [S II] 6717 Å (due to Ca I) and for interstellar extinction with $E(B - V) = 0^m.11$ are given below.

Line	Intensity
[O II] 3727–29	0.6
[N II] 6548–84	1.6
[O III] 5007	2.5
[O I] 6300	<0.25
[S II] 6717–31	0.6
$H\alpha$	1.0

The intensity ratio of the [S II] lines 6717/6731, as well as earlier measurements by Münch (1960) of the 3727/3729 ratio of [O II], indicates low electron densities ($\leq 50 \text{ cm}^{-3}$). The observed line intensities cannot be attributed to conventional time-independent H II regions, particularly because of the large strength of the [S II] lines. On the other hand, the emission spectrum bears a strong resemblance to the spectra of supernova remnants (SNR) such as the Cygnus loop. Because the velocity dispersion in the central regions is about $150\text{--}200 \text{ km s}^{-1}$, one might expect cloud-cloud collisions to simulate the spectrum of the Cygnus loop, which is expanding at 140 km s^{-1} . However, in galactic SNR the [O III] 5007 Å line is weaker than the [O II] 3726–29 Å doublet by about a factor of 3, whereas in M31 we find the opposite. Furthermore, an excess ultraviolet flux ($\lambda < 2500 \text{ Å}$) has been observed in M31 by the orbiting astronomical observatory. There is sufficient theoretical as well as observational justification to attribute this UV flux to stars that are about to become white dwarfs. The observed UV excess in M31 is sufficient to influence the ionization equilibrium of the gas we are studying, and hence simple cloud collisions cannot be the sole agents for ionizing and exciting the interstellar gas. One can hope to learn about the evolution of the hot (T_e

$\approx 60,000^\circ\text{K}$) pre-white dwarf stars from observations of the ionized gas. Already our observations rule out the possibility that these stars shine for about 10^7 years at high temperatures. If these stars lose most of their energy by neutrino emission, as has been suggested, they would live for only 10^5 years, in which case one has to use a time-dependent model for the ionization of the gas by these hot stars. The spectral line intensities we have measured are consistent with this model. A qualitative prediction of this model is that at increasing distance from the nucleus the [O III] 5007/ $H\alpha$ line ratio should decrease, possibly accompanied by an increase in the [O I] 6300/ $H\alpha$ line ratio. It is to be noted that the cloud collision model makes no such prediction. We plan to secure further observations to check this and carry out time-dependent model calculations if the data warrant them.

References

- Münch, G., Expanding motions in interstellar gas in the nuclear region of Messier 31, *Astrophys. J.*, **131**, 250, 1960.
 Rubin, V. C., and W. K. Ford, Jr., Radial velocities and line strengths of emission lines across the nuclear disk of M31, *Astrophys. J.*, **170**, 25, 1971.

LARGE-SCALE STRUCTURES IN OUR GALAXY

SEARCH FOR SHELL STRUCTURE IN ASSOCIATION WITH OLD GALACTIC SUPERNOVA REMNANTS IN NEUTRAL HYDROGEN AND FORMALDEHYDE

George E. Assousa

The study of the neutral hydrogen distribution in the vicinity of old galactic supernova remnants (SNR) is part of our effort in both the northern and southern hemispheres to understand the effects of the SNR on the interstellar medium. Thus our observations have led to the discovery of expanding fragmen-

tary shells surrounding the SNR's HB21 (Assousa and Erkes, 1973), S147 (Assousa, Balick, and Erkes, *Year Book 73*, p. 899), and W44 (Knapp and Kerr, 1974; Sato, 1974). Examination of the neutral hydrogen distribution from the Assousa, Balick, Erkes SNR survey (*Year Book 73*, p. 899) has also shown evidence for similar partial shell distributions in the vicinity of the Cygnus Loop and W41.

The discovery of the shell structure in the neutral hydrogen prompted us, in collaboration with Carl Heiles of the University of California, Berkeley, and Robert Sanders from the National Radio Astronomy Observatory, to examine the SNR's HB21 and S147 for the presence of H₂CO to determine the likelihood of molecular formation in these cool accreted shells. It was hoped that the detection of formaldehyde in these clouds would: (1) test the hypothesis that molecules can form behind isother-

mal shocks and therefore could be associated with regions in which hydrodynamical disturbances have occurred. This could, for example, be an explanation of dense molecular line regions near the galactic center; (2) allow detailed kinematic mapping of expanding SNR shells.

The H₂CO observations were carried out at 6 cm with the 85-foot antenna at the Hat Creek Radio Observatory. The beamwidth is 10' at 6 cm, and beam efficiency is 0.79. A cooled parametric amplifier gave a system noise temperature of 60°K and the 100-channel filter bank was used with 30 kHz filters giving a total window of 3 MHz or a velocity coverage of 187 km/sec. Peak-to-peak noise for the 30 kHz filters is 0.04° to 0.06°K.

A total of 144 positions for S147 and 126 for HB21 were covered in 0.33° grids in *l* and *b* except near the edges of HB21, where in directions perpendicular to the

TABLE 1. List of Supernova Remnants Observed for H₂CO

Name	<i>l</i> (degrees)	<i>b</i> (degrees)	Diameter (arc minutes)	Detection of H ₂ CO
Kepler	4.5	6.8	3	No
	5.3	-1.1	14	Yes
KE67	18.8	0.3	13	Yes
	20.0	-0.2	8	Yes
W41	23.1	-0.3	15	Yes
KE73	27.4	-0.0	32	Yes
KE79	33.7	0.0	9	Yes
	35.6	0.0	11	Yes
CTB 72	41.9	-4.1	125	No
3C386	47.0	10.6	3	No
W66	78.1	1.8	8	Yes
W63	82.2	5.4	68	No
HB21	89.1	4.7	130	No
3C434.1	94.0	1.0	18	No
CTB1	117.3	0.1	30	No
NGC 7822	118.1	5.0	20	Yes
CTA1	119.4	9.8	120	No
HB3	132.4	2.2	110	Yes
3C129	160.4	0.1	6	No
HB9	160.4	2.8	140	No
VRO 42.05.01	166.2	4.3	50	No
S147	180.8	-2.2	200	No
IC443	188.9	3.1	45	Yes
0607 + 17	193.3	-1.5	80	No
CTB37A	348.5	0.1	7	Yes

edge of the remnant the spacing was 10 arc minutes. No absorption line could be observed in either set of profiles.

To further test possible association of H_2CO with SNR's, 23 additional galactic remnants were observed. All objects are listed in Table 1. Twelve remnants showed possible to definite lines. Of these, five large remnants were observed in de-

tail, CTB72, W63, NGC 7822, HB3, and PKS0607+17. Two, NGC 7822 (Fig. 9), and HB3 (Fig. 10), showed absorption lines at several positions along the remnant. For these sources, the depth of the absorption line varies with position, but there is no apparent change in the line's central velocity.

From this we conclude that: (1) be-

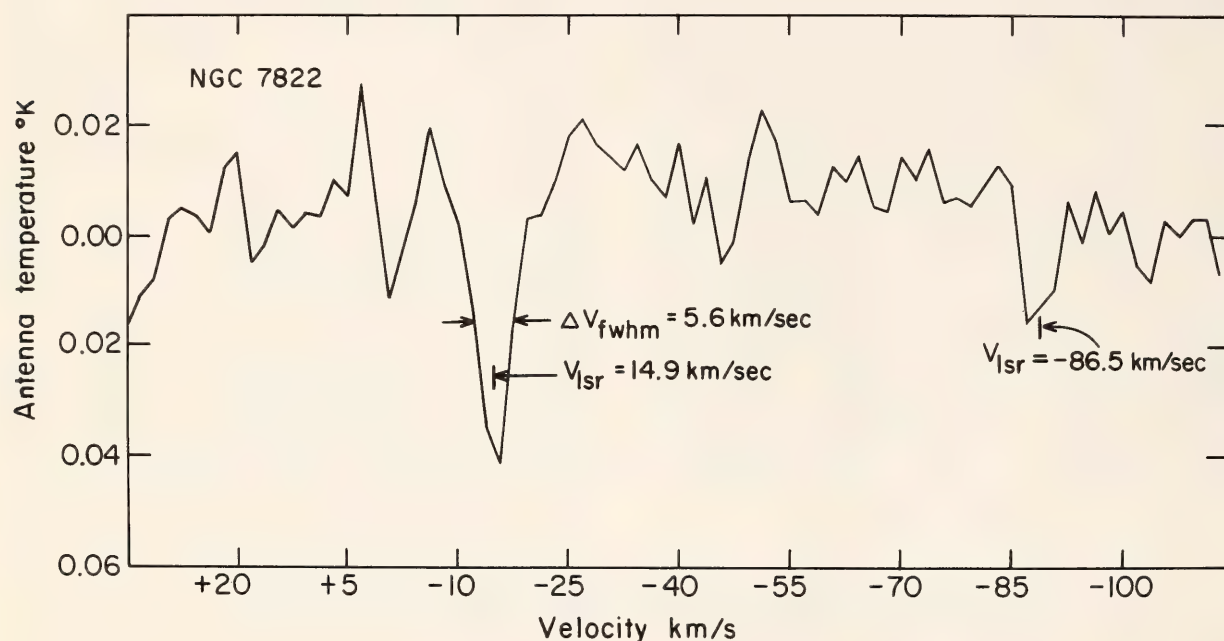


Fig. 9. H_2CO absorption spectrum in the direction of NGC 7822. The primary feature is 5.6 km/sec wide and appears at $v_{\text{lsr}} = -14.9$ km/sec. A weaker feature appears at $v_{\text{lsr}} = -86.5$ km/sec.

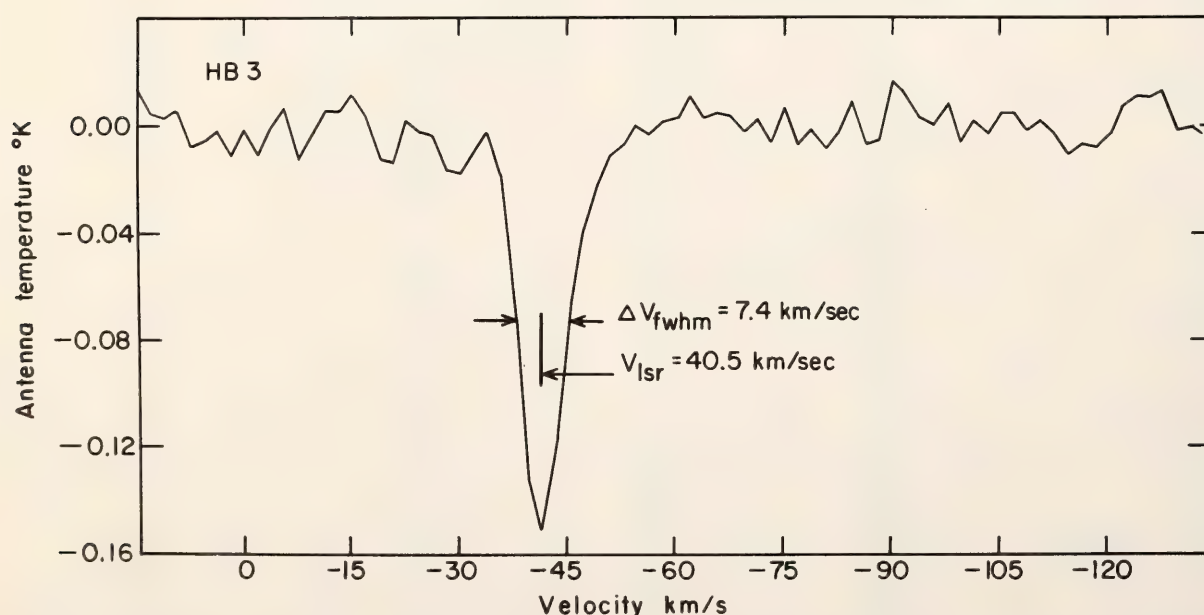


Fig. 10. H_2CO absorption spectrum in the direction of HB3. A prominent feature, 7.4 km/sec wide, appears at $v_{\text{lsr}} = -40.5$ km/sec.

cause there is no velocity variation, the absorption could not be taking place in any possible expanding shell associated with the remnant; (2) based on the detailed observations of the large remnants there appears to be no association between the H_2CO observed and any of the remnants; (3) the variation in depth of the absorption features observed indicates either structure in the continuum source or the absorbing clouds. We are currently studying these absorption features with the hope that we can determine the nature of the excitation (Evans *et al.*, 1975).

References

- Assousa, G. E., and J. W. Erkes, An expanding shell of neutral hydrogen surrounding the supernova remnant HB 21, *Astron. J.*, 78, 885, 1973.
- Evans II, N. J., B. Zuckerman, G. Morris, and T. Sato, Interstellar H_2CO I. Absorption studies, dark clouds, and the cosmic background radiation, *Astrophys. J.*, 196, 433, 1975.
- Knapp, G. R., and F. J. Kerr, A cold HI shell around the supernova remnant W44, *Astron. Astrophys.*, 33, 463, 1974.
- Sato, F., Neutral hydrogen associated with W44, *Publ. Astron. Soc. Jpn.*, 26, 459, 1974.

ZEEMAN SPLITTING OF THE 21-CM LINE OF NEUTRAL HYDROGEN IN SUPERNOVA REMNANT SHELLS

Kenneth C. Turner

The problem of measuring the interstellar magnetic field has been an extremely difficult one. Indirect methods lead us to infer that it is quite small, on the order of a few microgauss, but no really satisfactory direct determinations exist, except in a few special objects, which do not permit us to obtain a value for the general field (Verschuur, 1970).

The discovery of expanding HI shells around some supernova remnants

(SNR's) (Erkes, *Year Book* 68, p. 368; Assousa *et al.*, *Year Book* 73, p. 899) offers an interesting possibility, however. Theories of the evolution of SNR's predict that the general interstellar magnetic field may be considerably amplified as the SNR compresses the medium surrounding it. We therefore chose two promising candidates, HB21 and W44, and attempted to detect the Zeeman splitting of the 21-cm hydrogen line in the shells surrounding them. The component of the magnetic field along the line of sight will produce opposite frequency shifts of the radiation of opposite circular polarization. The total shift is very small, only 2.8 Hz/microgauss, so a very narrow line must be observed for very long integration times, with considerable care taken to avoid instrumental effects.

In collaboration with Linda K. Denoyer from the University of Illinois, Urbana, and Joseph W. Erkes from Dudley Observatory, Albany, observations were made on the 140-foot telescope of the National Radio Astronomy Observatory with a specially designed "Zeeman" feed which switches between the two opposite circular polarizations. No field was detected in the HB21 shell. Using a three standard deviation confidence limit, we may say $B_{\text{shell}} < 12$ microgauss. Applying a theoretical amplification factor of 4, we can then estimate that the general interstellar magnetic field in this region must be less than 3 microgauss.

The situation in the direction of W44 is much more complicated, as shown in Fig. 11. A theoretical curve corresponding to 5 microgauss is shown fitted to a portion of the spectrum. The fit is not unique, however, and this observation is still under study.

Reference

- Verschuur, G. L., Further measurements of the Zeeman effect at 21-centimeters and their limitations, *Astrophys. J.*, 161, 867, 1970.

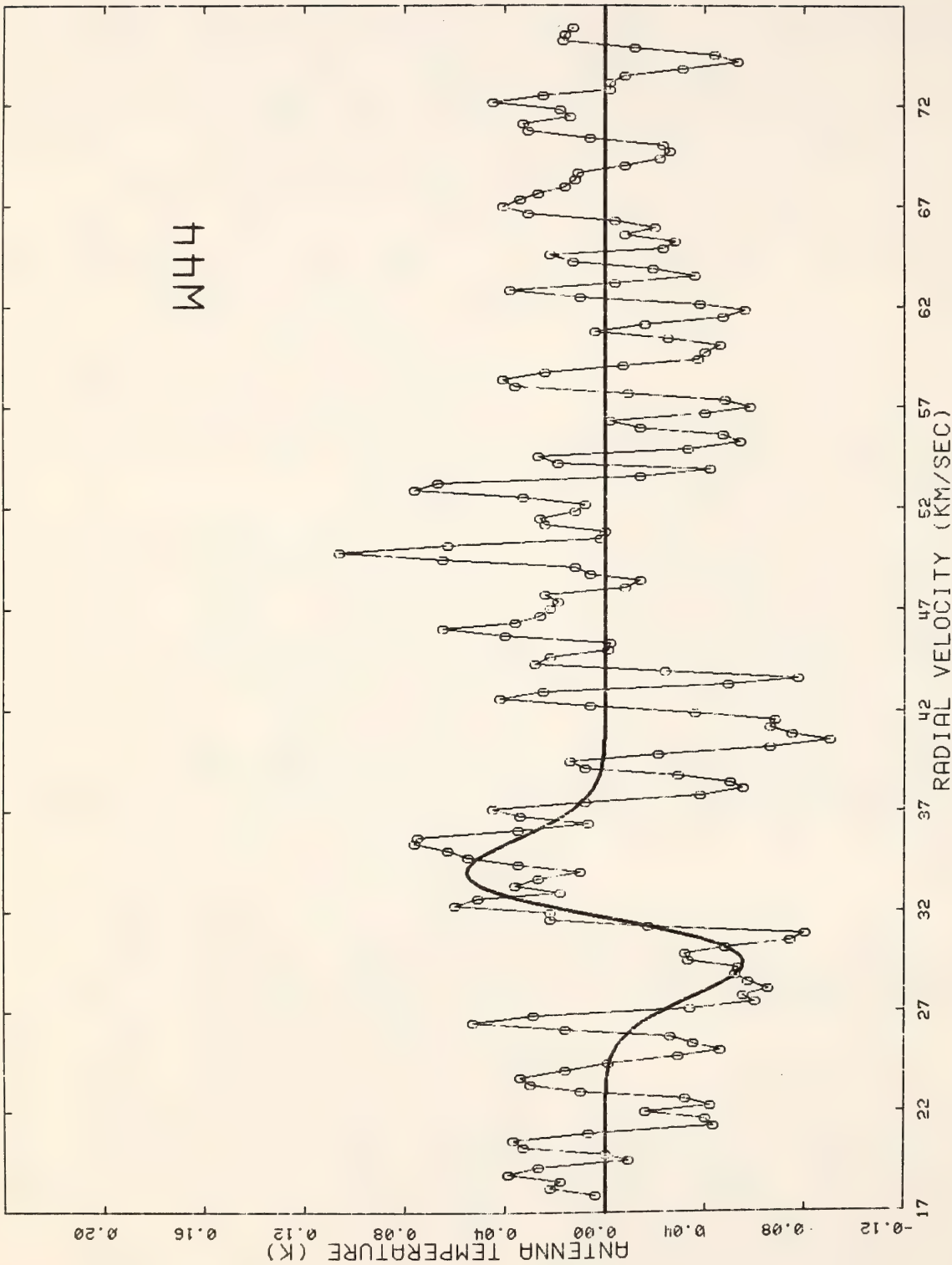


Fig. 11. Difference spectrum of the two circular polarizations in the direction of the supernova remnant W44. The solid line is a theoretical Zeeman spectrum corresponding to a magnetic field of about 5 microgauss.

MAGELLANIC STREAM GAS

Kenneth C. Turner

The problem of the history and dynamics of the Magellanic Clouds is an interesting and complicated one. These two galaxies, usually classified as irregulars, are our two nearest neighbors in space, being only some 60 kpc from our own Galaxy. Indeed, they are sufficiently near that our Galaxy exerts an order of magnitude more gravitational force on each cloud than they do on each other. We would therefore expect this to be a very disturbed system, and such is indeed the case. Not only is the velocity field of each cloud quite complicated (being, in general, multiple valued), but a considerable amount of neutral hydrogen exists between the two clouds (J. V. Hindman *et al.*, 1963, and *Year Book* 67, p. 290, and 68, p. 366). Arguments have been made attempting to relate this material to possible histories of the Galaxy-Magellanic Cloud System (see K. C. Turner *et al.*, *Year Book* 67, p. 290, and references cited in I. Mirabel and K. C. Turner, 1973).

The discovery of the Magellanic Stream (Mathewson *et al.*, 1974), a very long stream of neutral hydrogen extending from the general direction of the Magellanic Clouds to well past the South Galactic Pole, obviously has a very important bearing on these arguments, and it was thought important to confirm this discovery and to obtain profiles of this material for detailed dynamical analysis.

Figure 12 shows spectra observed in the direction of the brightest concentrations near the Magellanic Clouds. Here the material is readily detectable, having velocities not far from those associated with the Clouds themselves. Farther away, near the South Galactic Pole, however, the material has radial velocities near those of our local galactic gas. However, our wide velocity resolution, chosen for high sensitivity, together with

some base-line problems to be discussed in another section of this Report, made it impossible to make a clear division between Local and Stream hydrogen.

References

- Hindman, J. V., R. X. McGee, A. W. L. Carter, E. C. J. Holmes, and M. Beard, A low resolution hydrogen-line survey of the Magellanic system, *Aust. J. Phys.*, 16, no. 4, 552-569, 1963.
 Mathewson, D. S., M. N. Cleary, and J. D. Murray, The Magellanic Stream, *Astrophys J.*, 190, 291, 1974.
 Mirabel, I., and K. C. Turner, A search for neutral hydrogen remnants of strong tidal disruption of the Small Magellanic Cloud, *Astron. Astrophys.*, 22, 437, 1973.

A SEARCH FOR VERY HIGH VELOCITY CLOUDS

*Merle A. Tuve, Charles A. Little,
and Everett T. Ecklund*

A cumulative search has continued through the year for hydrogen clouds of very high velocities of approach, which might be clouds from outer space "falling" into our Galaxy, or, conversely, clouds of very high velocities of recession, if they are explosively expelled in some way from, for example, the center of our Galaxy. As indicated in the Report for last year, a routine was established for searching selected sky points from zero velocity to -800 km/sec and from zero to $+800$ km/sec. A 53-channel receiver is used, modified to give each channel a velocity width of 16 km/sec (to half-power points) and spaced by 16 km/sec. The 60-foot parabolic antenna has a half-power width of 0.87° on the sky.

Observations are made at even 10° intervals in galactic longitude from 0° through 350° . At each longitude, observations are made at galactic latitudes 00° , 04° , 08° , 12° , 20° , 24° , 28° , 40° ,

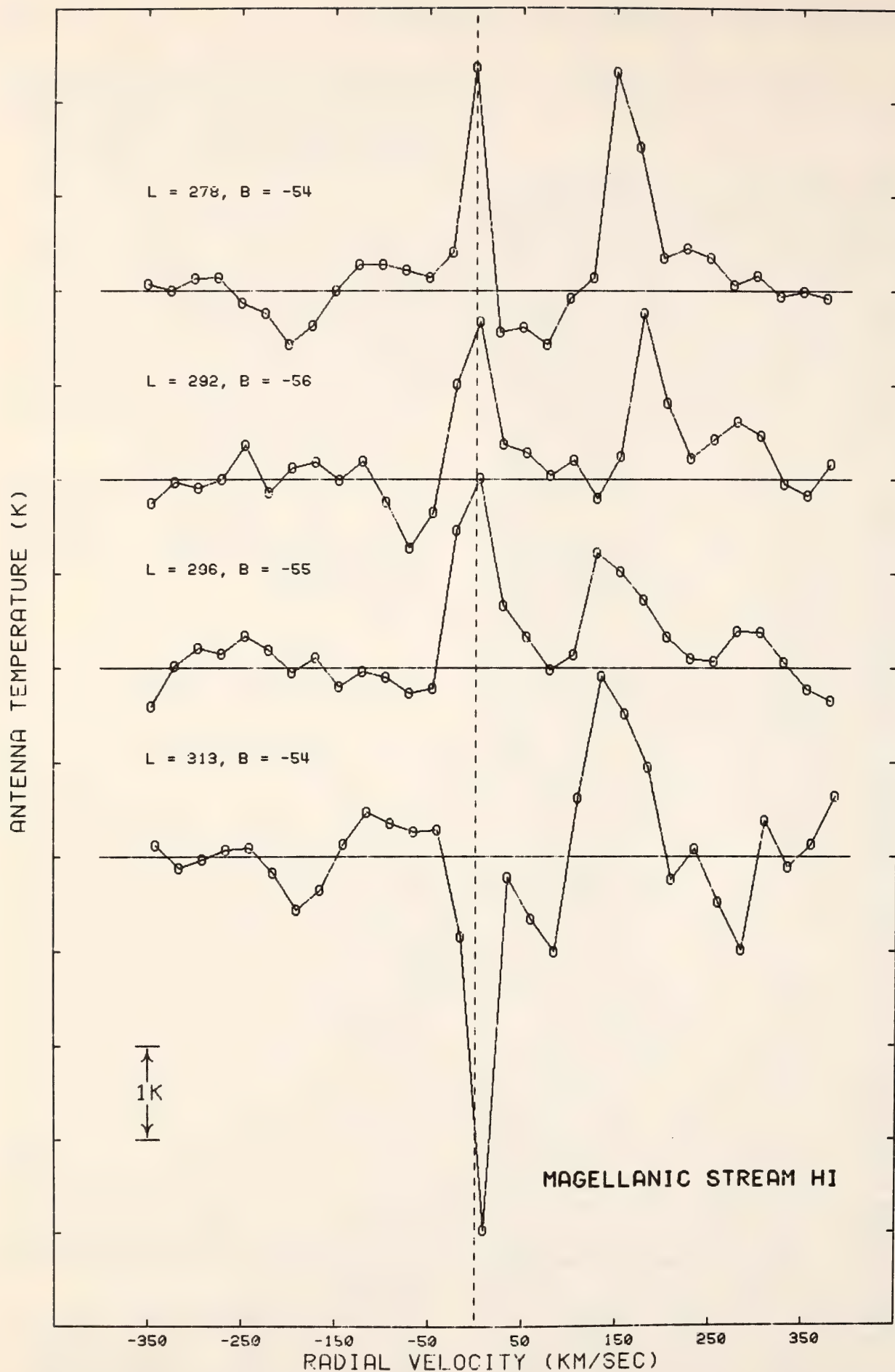


Fig. 12. Relative spectra of Magellanic Stream neutral hydrogen (cold sky reference spectrum has been subtracted). Deviations from zero near zero velocity represent changes in the amount of local hydrogen between the stream point and the reference point. Stream gas velocity is near 175 km/sec in the local standard of rest.

48°, 52°, 60°, and at the same list of negative latitudes. Thus, 21 sets of observations are made for each galactic longitude for which the listed points rise above the horizon. Of 756 possible points, about 580 rise above the horizon at this latitude, and about 540 of these had been observed by May 1975. For each sky point four runs are made, two receding and two approaching. Each run is the average of three independent integrations of 80 seconds each on each channel. The overall receiver noise temperature is a bit high (about 300°K) in average runs, and the tuning curve of the parametric amplifier and other receiver circuits varies some from day to day (or hour to hour, if adjustments are made). From critical inspection one concludes that a diffuse cloud of great velocity spread (say 200 or 400 km/sec) would fail to be identified if its emission raised the antenna temperature only $\frac{1}{2}^\circ$ or 1° K; it would simply appear to be a modest change in curvature of the base line. However, a cloud of moderately wide velocity spread (150 km/sec or less) would show as a distinct bulge in the (curved) base line if it contributed $\sim 3^\circ$ K to the antenna temperature. Careful examination of hundreds of records indicates that a cloud of small velocity spread, ~ 50 km/sec or less, would clearly be noticed if it gave rise to an antenna temperature of $\frac{1}{2}^\circ$ K or more.

To date, no confirmed example of such a cloud has been found. A list of about 20 suspected examples remains for re-examination among the many small deviations in the routinely observed curves, which have been studied and repeated. It should also be noted that a small accumulation of neutral hydrogen on one side of the Galaxy, swept up by galaxy motion through a very low density of neutral hydrogen in outer space (if such exists) would not be detected if it gave rise to an antenna temperature of only a few degrees, because other effects, such as antenna "spillover" (maximum 8°K)

change, cause changes in the base-line level.

It thus appears from our modest survey that hydrogen clouds from outer space falling toward our Galaxy are not a conspicuously frequent occurrence in space, and clouds expelled from our Galaxy at high velocities are also hard to find, if they exist.

THE STRUCTURE OF GLOBULAR CLUSTERS

Charles J. Peterson

Among the most spectacular objects of our Galaxy are the 120 globular clusters, nearly spherical systems each of which contains up to 10^6 stars. The globular clusters were formed early in the history of the Galaxy; their distribution in space and their kinematical properties hold clues to the processes involved in the formation of the Galaxy as a whole. These systems, because of their apparently simple structure, also provide a basic test for dynamical theory. Theoretical studies (King, 1966) show that a cluster may be defined in terms of three parameters: a total mass, a core radius, and a limiting radius. The core radius is the radius at which the surface density of stars has dropped to one-half that of the central value; it is closely related to the potential energy with which the cluster formed (e.g., a small core radius indicates a tightly bound cluster). The limiting radius defines the "edge" of the cluster. It is not an intrinsic property of the cluster but is set by the external gravitational field of the Galaxy at that point of the cluster's orbit where the galactic tidal forces are strongest. This point is at the closest approach of the cluster to the center of the Galaxy and is called the perigalacticon distance.

Of particular interest are the very distant clusters which, because of their uncertain relation to the Galaxy at the time of their discovery, were designated "intergalactic tramps." Until recently, these distant clusters had been little

studied because of the faintness of their individual stars. One of these objects, Palomar 2, is of particular interest because it is observed in the anticenter of our Galaxy, and hence a study of its orbit, stellar composition, and colors may teach us also about the outer regions of our Galaxy. Pal 2 has an estimated distance modulus of 19 or 20 (McCarthy and Treanor, 1964) and thus is between 60 and 100 kpc from the sun or 70 to 110 kpc from the center of the Galaxy. Pal 2 therefore is located at least twice

as far from the center as the generally adopted radius of our Galaxy (which is of the order of 30 kpc; the sun is about 10 kpc from the center).

As part of a long-term study of the properties of globular clusters (Peterson, 1974; Peterson and King, 1975) and as a start of a study of Pal 2, star counts have been made on two plates of this cluster, one plate taken with the 84-inch (Lynds) and one at the prime-focus of the 4-meter telescope (Rubin and Ford). Approximately 600 cluster stars are

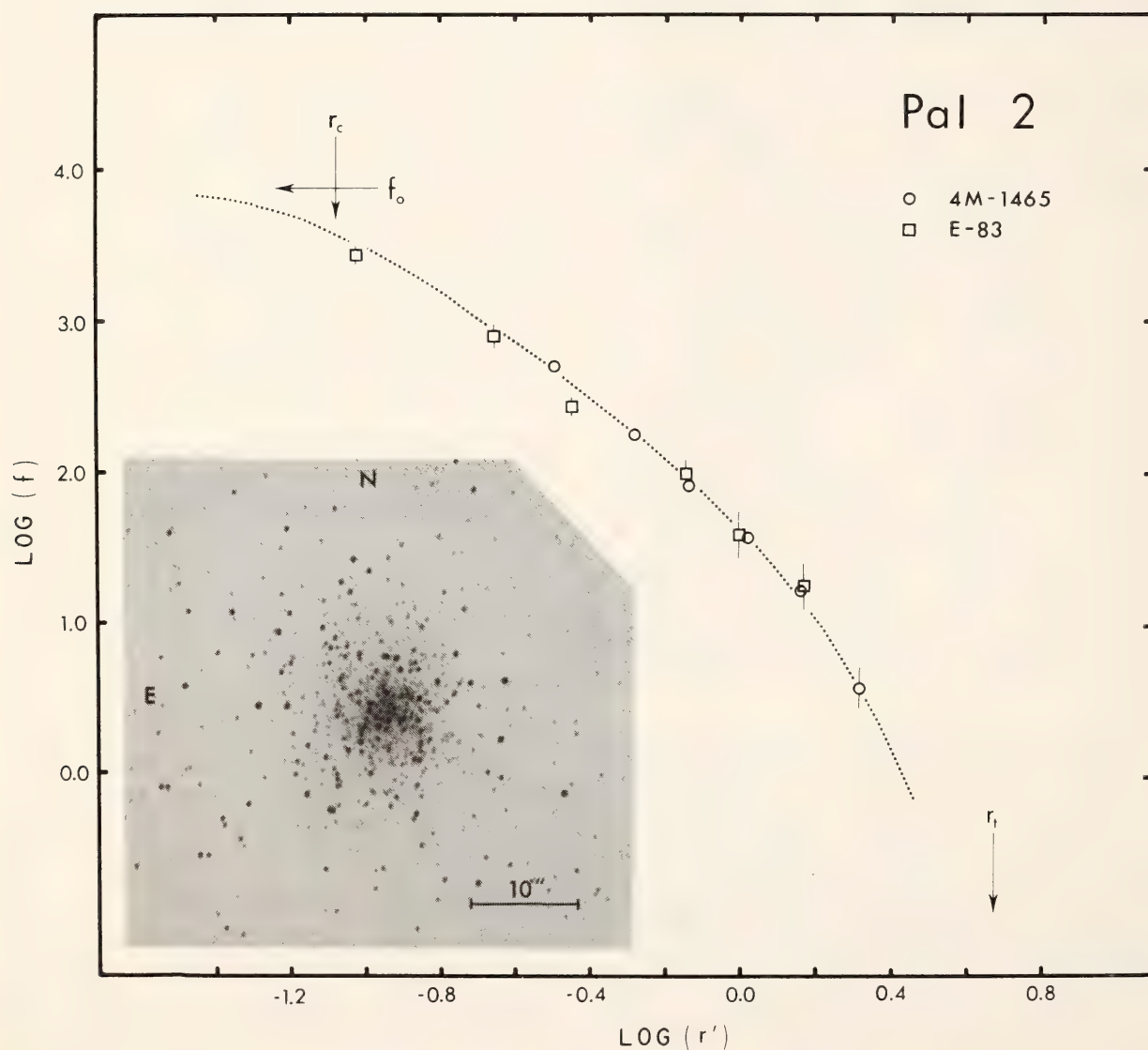


Fig. 13. Surface density versus radius from star counts of two plates (E-83, 84" Kitt Peak telescope; 4M-1465, 4-meter Mayall telescope) in the distant globular cluster Palomar 2. The dashed line is a theoretical model curve from King (1966) with core radius $\log r_c' = -1.08$; tidal radius $\log r_t' = 0.67$; and concentration parameter $c = \log (r_t'/r_c') = 1.75$. The insert is a copy of a 4-m prime focus plate of Palomar 2, taken on N_2 -baked 0-127 plate, exposure 70 min; original scale $12''/\text{mm}$.

countable within a radius of 5' on a one-hour exposure at the Mayall telescope. The surface density profile (Fig. 13) can be fitted quite well by a theoretical profile computed from a self-consistent dynamical model (King, 1966) for a concentration class $c = \log(r_c/r_t) \geq 1.75$, where r_c is the core radius and r_t is the limiting or tidal radius. The latter radius is relatively insensitive to model curves and is $r_t = 4.7 \pm 0.2$ (for $c = 1.75$) corresponding to a tidal radius of $r_t = 80\text{--}140$ parsecs at the estimated distance of the cluster. From the tidal radius we can determine the closest approach of the cluster to the center of the Galaxy. This distance is much smaller (by at least a factor of 5) than the presently observed distance for Pal 2. Hence Pal 2 must orbit the Galaxy in a greatly elongated orbit, which carries it to vast distances from the Galactic Center.

References

- King, I. R., The structure of star clusters. III. Some simple dynamical models, *Astron. J.*, 71, 64, 1966.
- McCarthy, M. F., and P. J. Treanor, Infrared observations of Abell 2, *Ric. Spectrosc. Lab. Astrosfis. Specola Vaticana*, 6, 511, 1964.
- Peterson, C. J. Distribution of orbital eccentricities of the globular clusters, *Astrophys. J. (Lett.)*, 190, L17, 1974.
- Peterson, C. J., and I. R. King, Observed radii and structural parameters in globular clusters, *Astron. J.*, 80, 427, 1975.

EQUIPMENT DEVELOPMENT

IMAGE TUBE SYSTEMS

W. Kent Ford, Jr.

During the past two years, greatly improved versions of the Carnegie image tube have become available for astronomical observations. These cascaded image intensifiers, RCA type C33063

EP3, are in large part a result of a two-year development program undertaken at RCA for the Institution and supported by a grant to the Department of Terrestrial Magnetism from the National Science Foundation. With the completion of this development effort, our emphasis has shifted somewhat from the testing and evaluation of prototype tubes to the design and construction of optimum systems incorporating the improved tubes and to observing with them. An excellent opportunity for this was provided by my joint Carnegie-AURA appointment to Kitt Peak National Observatory as a Visiting Resident Scientist.

The gain of an image intensifier is derived from the quantum efficiency of the photocathode that converts the optical input to an electronic image. Various image tubes store and detect the electrons which contain the pictorial information by different means. In the cascaded intensifier, primary photoelectrons are accelerated through 10 to 15 kilovolts and focused on an efficient electron multiplier consisting of a phosphor-photocathode sandwich. The secondary photoelectrons that are thus created are in turn accelerated and focused on a phosphor screen which then displays an intensified optical image. This intensified image is recorded on a photographic emulsion with a transfer lens.

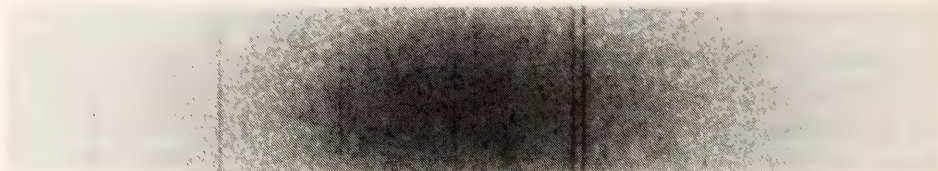
In a high-gain image intensifier, each primary photoelectron produces an optical scintillation consisting of tens of thousands of photons of which only a few percent are collected by the transfer lens. Nevertheless, these photoelectron scintillations are sufficiently bright to be recorded as a clump of blackened grains in the developed photographic plate; the certainty of detection of any individual scintillation is proportional to its brightness. Image intensifiers with a radiant power gain of $100,000\times$ or greater, when used with a fast transfer lens, produce individually detectable scintillation images and hence are particularly useful

in recording an image consisting of a very few photoelectron events in the absence of any background. Such high-gain systems have also been used to great advantage in faint object spectroscopy by Lynds and others at Kitt Peak by moving the photographic plate perpendicular to the dispersion to provide widening of the spectrum. Without this plate-widening mechanism the bright scintillations in the spectrum of a stellar object tend to overexpose or saturate the plate with relatively few photoelectrons, and consequently only high contrast

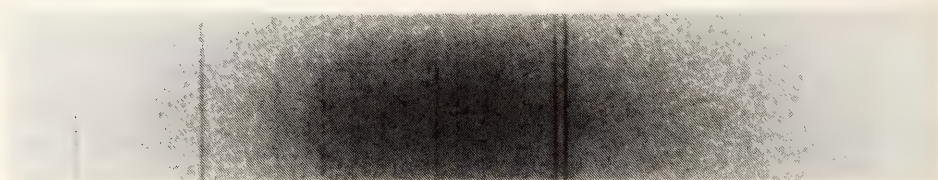
features of the spectrum are detected. The moving-plate scheme is particularly useful in obtaining widened spectra with a high signal-to-noise ratio of faint point source objects as it permits convenient use of a very small entrance aperture, which is necessary in order to discriminate against the night sky background. The technique, however, is limited to point source objects, since any spatial information is lost in the widening process.

In order to obtain high signal-to-noise spectra of extended objects having low

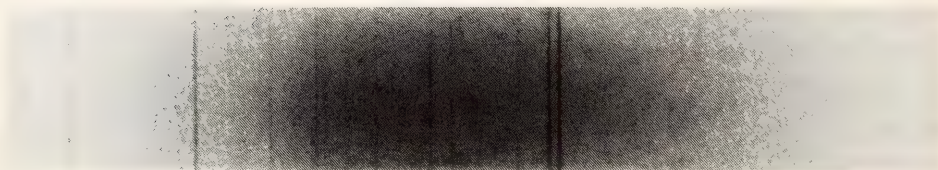
10 sec F 1.0



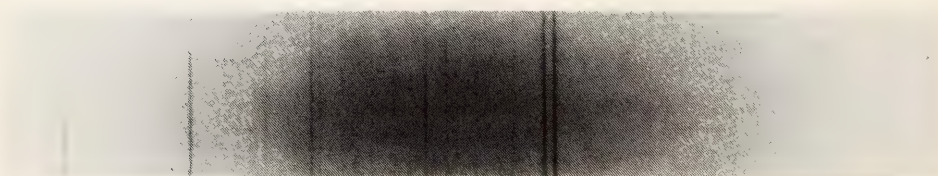
20 sec F 1.4



40 sec F 2.0



80 sec F 2.8



160 sec F 4.0

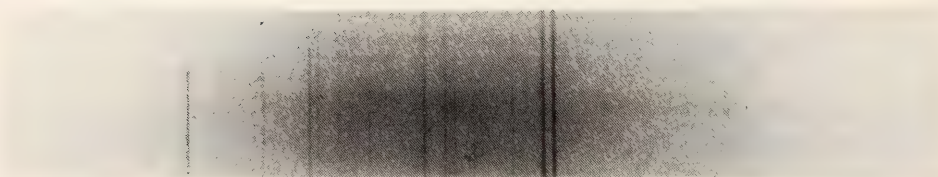


Fig. 14. Test sequence with image intensifier illustrating method of improving signal-to-noise ratio in exposures to approximately the same optical density by averaging more photoelectron scintillations.

surface brightness, some other technique is required. A two-stage cascaded intensifier such as the RCA C33063 operating at 28 or 30 kilovolts has sufficient gain (radiant power gain of 15,000 to 20,000 \times) that with an f/1 transfer lens the statistical fluctuation or quantum noise due to the accumulation of individual photoelectrons is recorded even on a fine-grain emulsion. This system is fast but noisy, since each photoelectron scintillation is statistically contributing many blackened grains to the exposure. The plate appears very grainy in uniformly exposed portions, and weak features in the image are lost in the large density fluctuations. To improve the signal-to-noise ratio, more photoelectron scintillations must be integrated in a longer exposure. If this is done with the fast transfer lens, the plate will be excessively dense; it is usually more expedient simply to stop-down the transfer lens so that the optical density of the recorded image is near optimum for the particular emulsion.

This situation is illustrated by a series of test exposures reproduced in Fig. 14 and by the various examples of long-slit galaxy spectra in other portions of this Report. The test spectra are of a continuum source (a tungsten lamp) mixed with an emission source (helium, argon, and neon discharge lamps). The exposures are with a two-stage Carnegie image tube, RCA C33063 EP3 S/N 8-7-2-1, and are recorded on an N₂ baked IIIaJ plate through a Repro-Nikkor 85 mm f/1 transfer lens. On this plate the transfer lens is changed by one stop and the time doubled for each exposure. The improvement in the detectability of weak lines is evident.

THE INTENSIFIER-IMAGE DISSECTOR SCANNER

W. Kent Ford, Jr.

The accuracy of measurement of intensities is limited in the photographic readout of image intensifiers by calibra-

tion problems associated with nonlinear photographic process. To circumvent these problems we have continued our work on the electrical readout of intensifiers with an image dissector along the lines described in some detail in *Year Book 71* (p. 221). The method is based on the fact that photoelectron scintillations as displayed at the output of a high-gain intensifier have a lifetime associated with the persistence of the phosphor screens. By sampling each picture element in a line image with an image dissector (an electrically scanned photomultiplier) with a repetition rate comparable to the decay time, a histogram of the occurrence of photoelectron events can be accumulated in a digital signal averager.

The work thus far may be summarized as follows: The image dissector, lens coupled to the two-stage image intensifier, operates with the efficiency predicted for the particular dissector photocathode quantum efficiency. This efficiency is adequate for repetitive single-line scans and is probably useful for two-line scans of spectra of star-plus-sky and sky. The efficiency is below that of an ideal photoelectron counter because of the decay characteristic of the phosphors. The system is satisfactorily free of fixed pattern noise due to the lens rather than fiber optic coupling of the intensifier and dissector. The present data acquisition system operates in an increment memory by one mode for each detected photoelectron scintillation rather than the add scaler count to memory contents mode that has been very successfully used at Lick Observatory by Robinson and Wampler. We have shown that the statistical noise associated with the recorded data is just the noise associated with the number of counts per channel.

The intensifier-image dissector scanner appears to be one of the best of the available digital detectors. Because of the persistence of the phosphors that are used as the storage element, the effectiveness of the device is limited to only

a few lines or possibly a small-format area array. The advantages of our particular device are the relative freedom of fixed-pattern noise, good resolution, and good statistical counting properties.

THE POINTING OF OUR 60-FT DERWOOD RADIO TELESCOPE

E. T. Ecklund, N. Thonnard, and K. C. Turner

With the ever increasing amount of radio interference we have been experiencing at low frequencies at our radio astronomy observatory in Derwood, Maryland, it has been clear for some time that our observational future there lies at short wavelengths (~ 15 mm) where there are few sources of interference and where only very nearby sources will be troublesome due to the line-of-sight propagation of these short wavelengths. We have developed a good receiver at these frequencies and have undertaken various observational programs. As reported in *Year Book 73* (p. 919), we have readjusted the surface of the antenna and more than doubled its efficiency. But, at such short wavelengths, a 60-foot antenna has a half-power beam-width of only 0.058° , and our pointing has been poor enough that so

far we have only been able to study sources that could be seen in "real time."

Before investing a lot of time and money to install more accurate position indicators on our antenna, we wanted to determine where the weak links in the pointing were and how rigid the feed support and paraboloid were. Strain gauges consisting of music wire and a special scale readable from any attitude were wired from the edge of the paraboloid to the focus and vertex and across both sides of the paraboloid. On a cloudy, still day, the telescope was moved in all directions and with a small telescope the reading of the strain gauges was taken. This enabled us to calculate the actual position of the focal point relative to the paraboloid at any attitude. It was gratifying to discover that the antenna itself and the feed support are very rigid. In Fig. 15 are plotted the measured deflections of the focus relative to the paraboloid versus the angle from the zenith the antenna is pointing to. The deflections are only a function of the zenith angle and can be fitted to the equation (solid line)

$$\Delta\theta = 0.0187 \sin(Z)$$

which can be easily introduced as a simple correction. Measurements made of

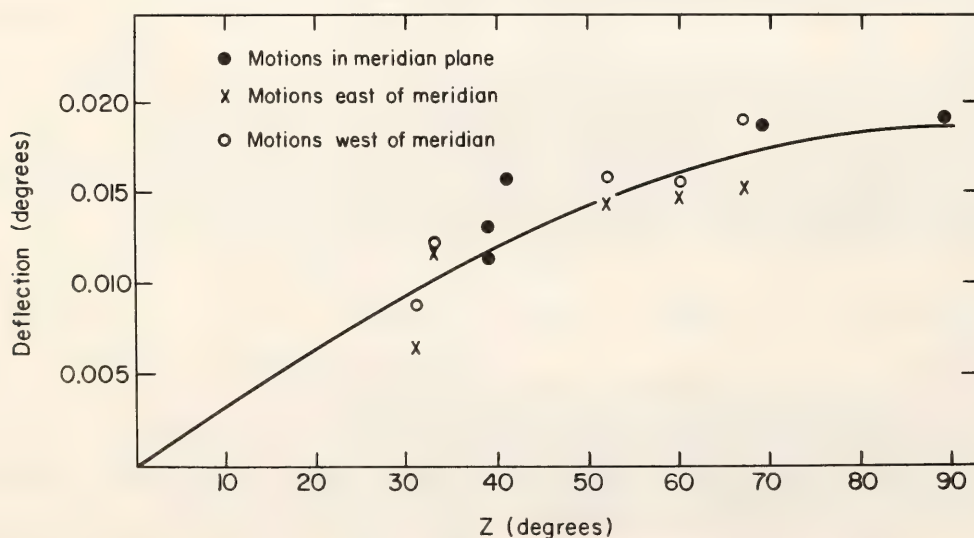


Fig. 15. Angular deflection of the feed support relative to the focal point of the 60-ft Derwood paraboloid for different antenna positions as a function of angular distance from the zenith Z . The solid curve has been fitted to the data and gives the deflection as $\Delta\theta = 0.0187 \sin Z$.

the edge of the dish relative to the polar axis indicate that the deflections are also less than 0.02% in this plane, indicating that most of the pointing problems we have been encountering are probably due to large deflections in the large driving gear and in the position encoders themselves, which are coupled to the driving gear. If after a few more measurements we can confirm that there are no large and unusual deflections between the polar and declination axes and the paraboloid itself, then we feel that by placing an accurate angle encoder on the polar and declination axes we will be able to utilize the antenna to its full capability at short wavelengths.

A NEW RECEIVER FOR THE IAR

N. Thonnard and K. C. Turner

Because of the serious stability and base-line problems experienced while using the present receiver at the Instituto Argentino de Radioastronomía to study very faint signals, and as our scientific interests are moving toward research that will require much improved sensitivity and stability, it has been decided to design and construct a completely new system that will take advantage of the many technological advances made since the development of our original hydrogen-line receiver.

Our present system may be thought of as being divided into three parts. The front end, consisting of parametric amplifier, switch, feed horn, mixer, temperature control apparatus, etc., all installed at the focus of the telescope, will be replaced by a completely new, modern system. Dimensional and thermal stability, as well as low noise, will be emphasized to ensure that the system does not vary with telescope position and time.

The intermediate frequency part, consisting of IF amplifiers, 2nd mixers, and filter banks, we propose to leave unchanged. The back end, which converts the output energy of the filters to numerical values, will be completely rede-

signed. In place of the present system of tuned amplifiers, diode phase detectors, and large integrating capacitors with a mechanical readout switch, the proposed system will sample the slightly integrated output of the filters directly, performing the synchronous detection and integration digitally in a small on-line computer, which will also continuously measure the gain of the system. This will eliminate many additional possibilities of instability and instrumental drift and increase the flexibility of observing procedures.

A joint proposal, by the DTM and the Instituto Argentino de Radioastronomía, to the National Science Foundation and the Agencia Ejecutivo Argentino has been made to perform this modernization, and to make observations of southern spiral galaxies and high-velocity clouds as an international effort under the joint agreement for scientific cooperation signed by Argentina and the U.S.

ACKNOWLEDGMENTS

This year again, the astronomers at DTM acknowledge with thanks the generous allotments of telescope time from Kitt Peak National Observatory, National Radio Astronomy Observatory, and Hat Creek Radio Observatory.

The development of the high-gain image tube and the work on the digital system have been supported in large part by a grant from the National Science Foundation.

ACTIVITIES OF THE INSTITUTO ARGENTINO DE RADIOASTRONOMÍA

Ever since the early 1960's when the Instituto Argentino de Radioastronomía was established in a cooperative venture between the Carnegie Institution of Washington, the Argentine Consejo Nacional de Investigaciones Científicas e Técnicas, the Comisión de Investigaciones Científicas de la Provincia de Buenos Aires, and the Universities of La Plata and Buenos Aires, relations be-

tween our institutions have been warm and cordial, weathering the problems that plague any international cooperative venture, due primarily to the confidence that between friends and colleagues difficulties can always be worked out. That this continuing collaboration bears fruit in both hemispheres is demonstrated by this brief outline of IAR activities, as well as the research described in more detail elsewhere in this Report.

Instrumentation

During 1974 several minor changes in the 21-cm line receiver were made. A new parametric amplifier pump system was installed, using a Gunn diode, which results in a more reliable operation of the front end. The low-frequency section of the local oscillator was redesigned and built with integrated circuits. It will be used to drive the Fairchild phase-lock oscillator. Several power sources were replaced by solid-state units. Some work was done with a new front end using the same type of paramp as the one actually in use. In the last months of the year, the new installation for the receiver room was worked on. Several temperature controllers were designed and built to replace those in the front end and filter banks. Work was also done on the design of low-noise 30 MHz preamplifiers and 100 KHz band-width IF amplifiers.

21-cm Work

F. R. Colomb, M. Gil, and R. Morras have extended their observations around the south celestial pole. They have finished the observations and final reduction of the region $290^\circ \leq l \leq 314^\circ$; $-17^\circ \leq b \leq -27^\circ$; with $\Delta l = \Delta b = 1^\circ$. In these surveys they found several intermediate negative velocity clouds (IVC). The survey is now in the final stage of preparation for publication.

F. R. Colomb, W. Pöppel, and C. Heiles of the University of California continued the observations for the hydrogen survey at low velocities (-50

$\leq v \leq +50$ km/sec) of the southern hemisphere. They completed about 30% of the observations.

F. R. Colomb, R. Morras, and W. G. L. Pöppel made an attempt to detect Comet Kohoutek (1973) in the continuum and in the line, with negative results.

New Personnel

E. Bajaja returned from Leiden, The Netherlands, where he was working on H I line observations of galaxies with the new Westerbork synthesis radio-telescope. T. Gergely returned from Maryland, U.S.A., where he received his Ph.D.; he is now studying supernova remnants. M. Caponi returned from Maryland, U.S.A., where she received her Ph.D.; she is studying theoretical aspects of galactic structure.

Two fellowships were awarded by the Provincial Research Council to Margarita Franco and Carlos Alberto Olano, who have begun investigations at the Institute under the supervision of Drs. F. R. Colomb, E. Bajaja, W. Pöppel, and I. Mirabel. Three new technicians, Ing. A. J. Sanz, Ing. J. J. Mignacco, and Enrique Eduardo Hurrell are now engaged in the design and maintenance of our equipment, under the supervision of E. M. Filloy.

H. O. Morganti began work in the photography laboratory preparing drawings for publications. S. Acero was engaged for the operation of the radio telescope.

I. F. Mirabel and M. Franco have finished the study of a neutral hydrogen structure at $l = 8^\circ$, $b = -5.5^\circ$ with a radial velocity of -218 km/sec. This feature was probably ejected from the galactic nucleus.

I. F. Mirabel, W. G. L. Pöppel, and E. R. Vieira completed the study of an object discovered by Cugnon near $l = 349^\circ$, $b = +3^\circ$. The results will be published in *Astrophysics and Space Science*.

W. G. L. Pöppel and E. R. Vieira of

the Instituto de Física, of the Universidade Federal de Rio Grande do Sul, Brazil, completed the observations and reductions of their large survey for the region $240^\circ \leq l \leq 372^\circ$, $+3^\circ \leq b \leq +17^\circ$. The first part of their atlas of profiles and contour maps ($360^\circ \leq l \leq 372^\circ$) has been published (Carnegie Inst. Wash. Pub. No. 633). The rest will follow. Using the atlas, a study of the southern extension of a near cloud observed by R. Sancisi and H. van Woerden (1970) was started by C. A. Olano and W. G. L. Pöppel, as well as an analysis of the general motions of gas in the region $348^\circ \leq l \leq 372^\circ$ by M. Franco and W. G. L. Pöppel.

Observations were made to detect neutral hydrogen in three galactic clusters by W. G. L. Pöppel and M. D. Vota and in six small dark clouds by M. Gordon and W. G. L. Pöppel.

Reference

Sancisi, R., and H. van Woerden, An elongated neutral-hydrogen emission feature in Scorpius and Ophiuchus, *Astron. Astrophys.*, 5, 135, 1970.

NUCLEAR AND ATOMIC PHYSICS

L. Brown, G. H. Pepper, N. Thonnard, C. K. Kumar, and L. G. Arnold

INTRODUCTION

L. Brown

Two completely different modes of research originated from work with the Van de Graaff machine during the past year. Investigations with heavy ion-induced x rays are in the confused state typical of a new field of study. For various reasons most experiments by others have been conducted at energies well beyond the capabilities of our machine, e.g., 200 MeV Kr, and our examination of the low-energy region showed an aspect of this phenomenon so extreme and so simple that it seemed to cry for explanation. This led us to a theoretical clue: an equation that reproduces the

Z-dependence of all the experiments known to us as well as the shape of the spectrum of the heavy-ion continuum. Our formula is by no means the complete explanation, but it has made successful predictions. It points toward a different, heretofore untried mechanism.

Investigations with the beam of polarized protons are typical of research having an advanced theoretical framework on which to build. Theory and experiment are used together to determine the structure of nuclei, and the work is slow and tedious. The experiments are often in energy regions of isotopic structure that have seen little activity in years, regions that yield information only to new measuring techniques. During the past year we have probed the structure of two fundamental isotopes, ^{10}B and ^{16}O . In one we suspected no anomalies and found one; in the other we suspected one and found another.

CONTINUUM AND CHARACTERISTIC X RAYS PRODUCED WITH POTASSIUM IONS

L. Brown, N. Thonnard, and C. K. Kumar

The creation of vacancies in the electron shells of atoms by the impact of point charges is fairly well understood. The probability that an electron, a proton or one of the light nuclei will eject an electron from the K or L shell can be calculated for a wide range of velocity and atomic number, provided any electrons of the projectile are much less tightly bound than those of the target. These calculations, based on the Born and the binary encounter approximations, fail when applied to collisions in which the electron shells of target and projectile interact. Theoretical attempts to describe collisions of this kind generally start with Fano and Lichten's proposal (1965) that the wave functions of the separated atoms transform through molecular orbitals into the wave functions of an atom having a nucleus made of the target and projectile nuclei in close proximity. This way of picturing

collisions has explained the results of several experiments but has not led to a quantitative theory of vacancy production with $Z_1 \sim Z_2 > 10$ (for a review, see Garcia *et al.*, 1973). It was for this reason that we undertook the experiment described in the last Annual Report (Year Book 73, p. 929).

A result that particularly impressed us was the exponential dependence on target atomic number, Z_2 , of the emission of potassium K lines. A change in yield of nearly three decades was shown in Fig. 43 of Year Book 73 as Z_2 took on values from 21 to 30; the atomic number of the projectile is 19. At the time no theory could account for this; an adaptation of the molecular orbital model has since been proposed by Meyerhof *et al.* (private communication), but it is based on an empirical equation and fails to reproduce the strong Z dependence of our results. We have developed a formula that does reproduce the relative Z dependence of the data just cited as well as the results of all similar experiments known to us.

In the lower right of Fig. 16 is shown schematically how the energies of the wave functions of the separated atoms K and Sc (right) transform through molecular wave functions to form briefly a united atom with $Z = 19 + 21$ (left). If the wave functions make this transformation adiabatically, the electrons of the two 1s shells of the heavy and light atom will form, respectively, the 1s and 2p shells of the united atom when the two nuclei are in close proximity and reform themselves on separation. This predicts no K-shell vacancies and hence no x-ray emission. Experiments showed early that the light collision partner emits copious amounts of characteristic x-rays, the heavy partner relatively few. This has been taken as evidence that the $2p\sigma$ molecular orbital is ionized, and various ideas have been proposed for doing this but none has yielded quantitative results.

Figure 16 also shows the energies of

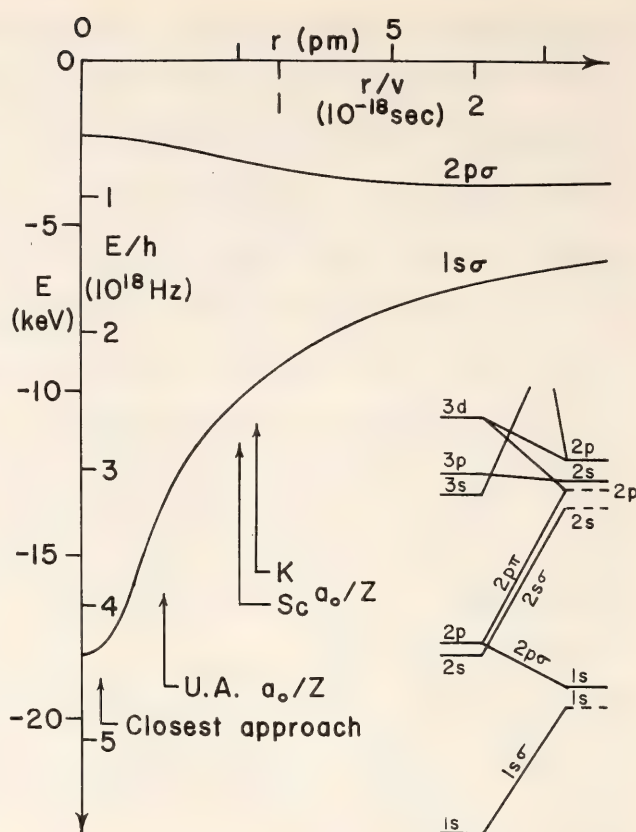


Fig. 16. Energy levels of the diatomic system K + Sc. In the lower right is the correlation diagram for the inner shells. The united atom structure is at the left; the separated atom structures are at the right with Sc denoted by dashed lines and K by solid lines. The remainder of the figure shows the energies of $1s\sigma$ and $2p\sigma$ molecular orbitals as functions of the internuclear separation, which has been converted to units of time through the ion velocity.

the $1s\sigma$ and $2p\sigma$ molecular orbitals as functions of internuclear distance. The energy is also shown in units of electron oscillation frequency and the distance of separation in units of time obtained through the ion velocity. This demonstrates that the transformations of the $1s\sigma$ cannot be adiabatic because the electron executes only a few oscillations as r decreases below 5 pm. The consequences of this violation cannot be stated with certainty, but it is reasonable to expect electrons trying to follow the $1s\sigma$ orbital to undergo quantum jumps, which will frequently (perhaps always) be radiationless transitions that eject from the $2p\sigma$ or higher orbitals. This method of ejecting electrons in atomic collisions is the novel part of our proposal.

The collision times are short compared with the times of spontaneous electromagnetic transitions, so such a process must be induced if it is to be effective. We have assumed the stimulating field to result from the motion of the projectile nucleus acting on electrons whose average position is given by the expec-

tation value of the united atom radius. The Fourier transform of this time-varying field gives the frequency spectrum of the virtual photons with which the electron may interact. Assuming that Auger transitions in the $1s\sigma$ orbital are stimulated in proportion to the amplitude of this spectrum yields a formula

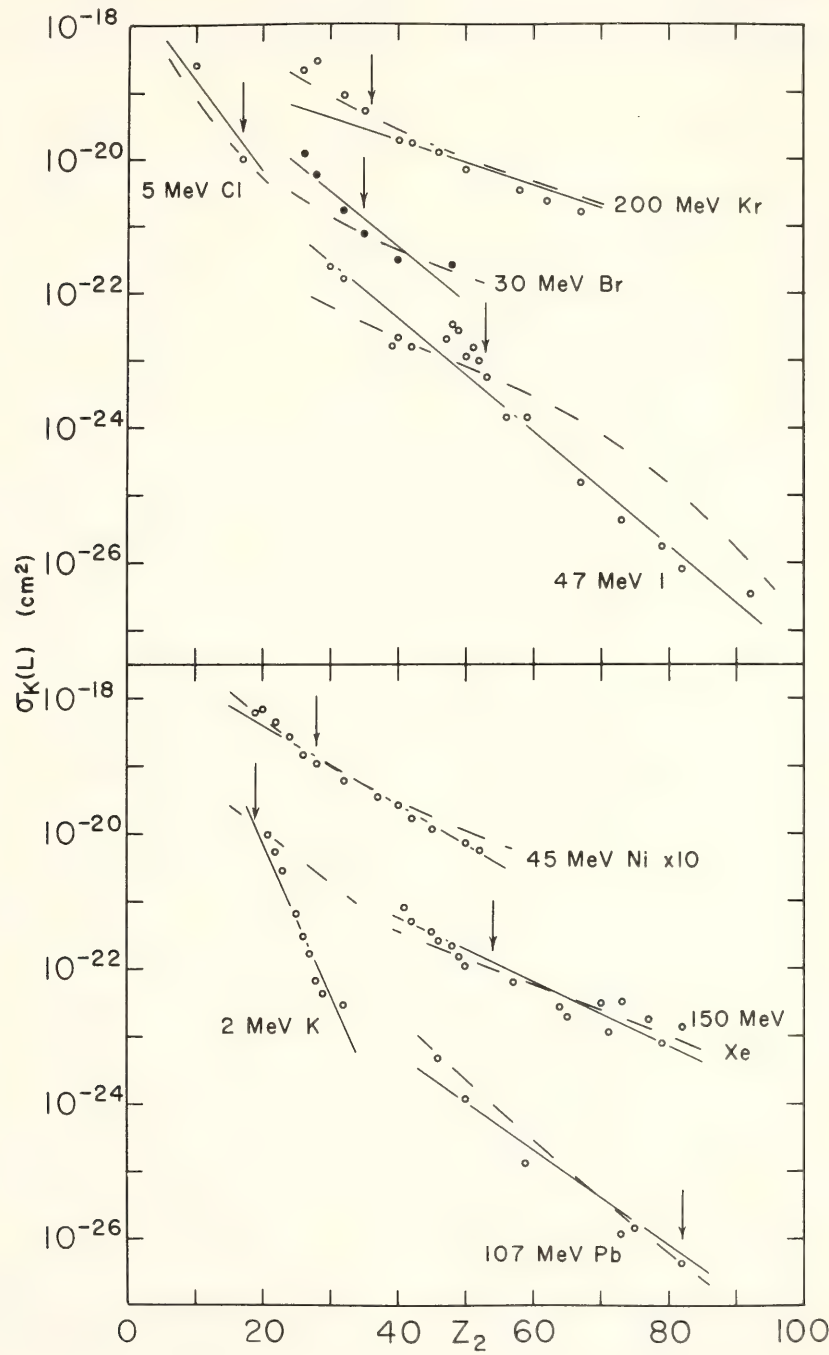


Fig. 17. Cross sections for K-vacancy production as function of Z_2 for eight experiments. The value given is for the emission by the light collision partner. Solid and open circles distinguish nearby data. The projectile and incident energy are indicated for each group. Vertical arrows indicate Z_1 . The 2 MeV K points are from the experiment described in *Year Book 73*, p. 929; the 5 MeV Cl are from Winters *et al.* (1975); the 45 MeV Ni are from Kubo *et al.* (1973); the 150 MeV Xe are from Gippner *et al.* (1974a); the remainder are from Meyerhof *et al.* (private communication). The dashed curves are from an empirical equation by Meyerhof *et al.* (1974); the full curves are from Equation 1.

for the relative probability $I(Z_2)$ of ejecting an electron from the $2p\sigma$ orbital

$$I(Z_2) \propto \exp\left(-\frac{3e^2 Z_1 + Z_2}{4\hbar v}\right) \quad (1)$$

where e is the electronic charge; \hbar , the reduced Planck constant; and v , the projectile velocity.

The characteristic x-rays of these collisions are superimposed on a continuum

whose origin is not yet certain. One proposal, discussed in *Year Book 73*, p. 929, suggests that the continuum results from transitions to vacancies in the molecular orbitals. The energy of the orbital is a function of the internuclear distance, as illustrated in Fig. 16, so a continuum of photon energies results. Recent work by Greenberg *et al.*, 1974, and Thoe *et al.* (1975) indicates that this continuum is

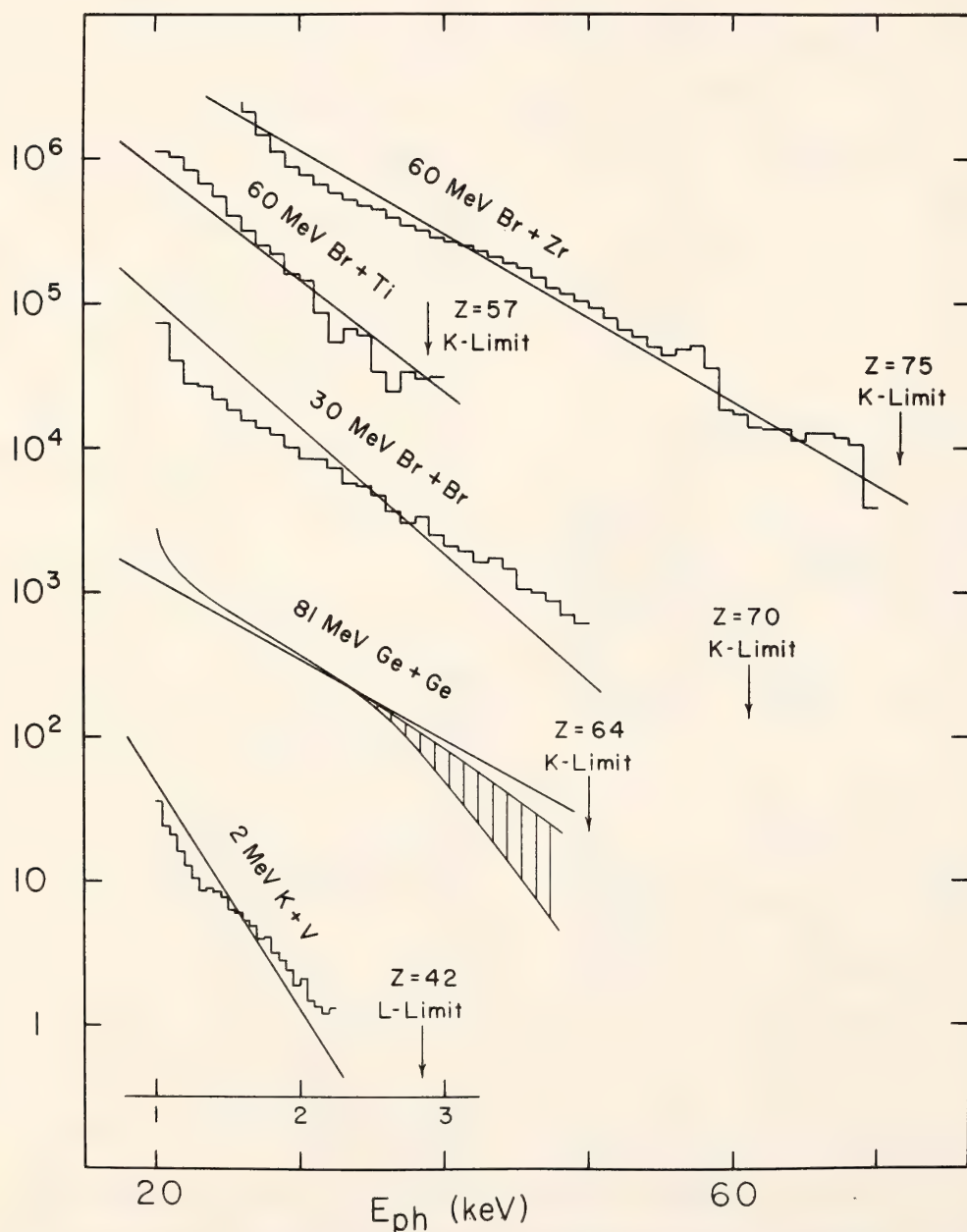


Fig. 18. X-ray continuum yield per unit energy interval in arbitrary units as a function of photon energy. Vertical arrows indicate the united atom limit. The top three measurements are from Meyerhof *et al.* (1974); the fourth, which has pulse-height analyzer points reproduced by a curve and a shaded region, is from Gippner *et al.* (1974b); and the bottom, which has a different (1 to 3 keV) energy scale from the other four, is from the experiment described in *Year Book 73*, p. 929. The straight lines are from Equation 2 with $n = 2$ for the 2 MeV K on V, and $n = 1$ for the others.

stimulated. The time-varying field we assumed to induce the radiationless transitions should also induce transitions in the molecular orbitals, if they have vacancies to be filled. This assumption yields a formula for the relative intensity $I(E)$ of the continuum as a function of photon energy E

$$I(E) \propto \exp\left(-\frac{3n^2}{2} \frac{a_0}{Z_1 + Z_2} \frac{E}{\hbar v}\right) \quad (2)$$

where a_0 is the Bohr radius and n the principal quantum number. Continua have been observed in what seem to be two bands: one that should terminate on the K shell of the united atom, and the other on the L shell. The former uses $n = 1$ in Equation 2; the latter, $n = 2$.

Figure 17 shows a wide range of characteristic x-ray cross-section measurements resulting from heavy ion collisions. The solid lines show the application of Equation 1; the dashed curves are from the empirical equation of Meyerhof *et al.*, private communication. Equation 1 was derived when only the 2 MeV K^+ and the 47 MeV I^+ data were at hand; the remaining measurements allowed its predictive capabilities to be tested. Figure 18 shows measurements of x-ray continua with solid lines from Equation 2. As the comparisons in Figs. 17 and 18 show, the two equations account for relative values of the Z dependence of characteristic emission and the E dependence of continuum emission rather well. One cannot calculate cross sections with them at present, or the dependence of the data on the projectile energy, although the relative dependence is satisfactory at all energies tested.

These two formulae result from the same starting assumption and appear to link together two different observations of the same collision. The anomalous nature of these collisions was recognized more than seven years ago, and the absence of any other quantitative explanation forces further study of the two formulae. The interpretation we attach to Equation 1—that of stimulated Auger

transitions—is new to atomic physics and has potentially a wider applicability in atomic collisions than just the production of K-shell vacancies.

References

- Fano, U., and W. Lichten, Interpretation of Ar^+-Ar collisions at 50 keV, *Phys. Rev. Lett.*, **14**, 627, 1965.
- Garcia, J. D., R. J. Fortner, and T. M. Kavanagh, Inner-shell vacancy production in ion-atom collisions, *Rev. Mod. Phys.*, **45**, 111, 1973.
- Gippner, P., K. H. Kaun, W. Neubert, F. Stary, and W. Schulze, Excitation of K X-rays by bombardment of thick solid targets with 150 MeV Xe ions, Joint Institute for Nuclear Research, E7-7688, Dubna, 1973a.
- Gippner, P., K. H. Kaun, F. Stary, W. Schulze, and Yu. P. Tretyakov, Quasimolecular K X-ray excitation by bombardment of Ge atoms with Ge ions, *Nucl. Phys.*, **A230**, 509, 1974b.
- Greenberg, J. S., C. K. Davis, and P. Vincent, Evidence for quasimolecular K X-ray emission in heavy ion collisions from the observation of the X-ray directional anisotropy, *Phys. Rev. Lett.*, **33**, 473, 1974.
- Kubo, H., F. C. Jundt, and K. H. Purser, Target Z dependence of projectile K X-ray production cross sections in high energy, heavy ion-atom collisions, *Phys. Rev. Lett.*, **31**, 674, 1973.
- Meyerhof, W. E., T. K. Saylor, S. M. Lazarus, A. Little, B. B. Triplet, L. F. Chase, Jr., and R. Anholt, Molecular-orbital K X-ray formation in heavy ion collisions, *Phys. Rev. Lett.*, **32**, 1279, 1974.
- Meyerhof, W. E., T. K. Saylor, S. M. Lazarus, A. Little, B. B. Triplet, R. Anholt, L. F. Chase, Jr., and P. D. Bond, K vacancy production in heavy ion collisions, private communication.
- Thoe, R. S., I. A. Sellin, M. D. Brown, J. P. Forester, P. M. Griffin, D. J. Pegg, and R. S. Peterson, Observation of large and strongly energy dependent

directional anisotropies in noncharacteristic K x rays emitted in heavy ion collisions, *Phys. Rev. Lett.*, **34**, 64, 1975.

Winters, L., M. D. Brown, L. D. Ellsworth, T. Chiao, E. W. Pettus and J. R. Macdonald, K X-ray production in single collisions of chlorine and sulfur ions, *Phys. Rev.*, **A11**, 174, 1975.

THE $^{15}\text{N}(\text{p},\alpha)^{12}\text{C}$ REACTION EXCITED WITH POLARIZED PROTONS

G. H. Pepper, L. Brown, and L. G. Arnold

In the isotope ^{16}O , a group of five levels located in the energy region from 12.3 to 13.3 MeV excitation energy stands out as pure compound nuclear states when observed through the reaction $^{15}\text{N}(\text{p},\alpha)^{12}\text{C}$. This region includes the isobaric analogs of the ground and first three excited states of ^{16}N and ^{16}F . At low energies the cross section is small because of the Coulomb barrier; at higher energies it is very small for about 1.5 MeV because no states are excited. Reference to the limited energy level diagram of Fig. 19 (from Ajzenberg-Selove, 1971) would seem to belie these remarks, because it shows more than five states, but $^{15}\text{N}(\text{p},\alpha)^{12}\text{C}$ can proceed only through intermediate states that are 0^+ , 1^- , 2^+ , 3^- , 4^+ , \dots , a consequence of the conservation of angular momentum and parity. States with other values of J^π are invisible to it.

In addition to furnishing information about the structure of ^{16}O this reaction is also the last one in the carbon-nitrogen cycle through which main-sequence stars with temperatures hotter than our sun burn hydrogen. Details of the reaction in the proton energy range of a few hundred keV are important for predicting the reaction rates at thermonuclear energies. The resonance at 0.34 MeV is very near this energy range and the four near 1 MeV cannot be neglected.

Three questions about the structure of ^{16}O in this region need answers. First, the location of the 2^+ state at 13.1 MeV

is uncertain by ± 0.15 MeV; there may in fact be two such states. Second, there is evidence from other light nuclei that some states of given J^π have orbital angular momentum admixtures of $\Delta l = 2$. The ground state of the deuteron was the first example of this; *Year Book 73*, p. 920, describes just such an occurrence in the structure of ^4He . The presence of a d-wave admixture ($\Delta l = 2$) in the two 1^- states would alter the manner of extrapolating these resonances to low energies. Third, there is reason to question whether the assignment $T = 0$ and $T = 1$ to the pair of 3^- states at 13.13 and 13.26 MeV is valid. The $T = 1$ would be the analog of the second excited state of ^{16}N and ^{16}F . The 13.13 MeV state shows up strongly in $^{12}\text{C}(\alpha,\alpha)^{12}\text{C}$ and weakly in $^{15}\text{N}(\text{p},\alpha)^{12}\text{C}$; the 13.26 MeV state is just the opposite—behavior that is normal for such T assignments—but the relative magnitudes and their γ -decays to $T = 0$ states bring this into question and cause one to suspect that the analog state is the pair, not just one of them. Some states in the mass 8 system, which were the subject of previous investigation (see *Year Book 70*, p. 333, and *Year Book 71*, p. 247), exhibit similar features. Exciting the reaction with polarized protons should answer the first two questions, and once we are certain of the structure, the matter of the isospin of the 3^- states can be studied through calculations that couple the two through the isospin term of the nuclear potential.

We measured six angular distributions of polarization analyzing power for proton energies from 0.34 to 1.21 MeV, all at energies where differential cross-section data were available. The results are described through an expansion of Legendre functions (see *Year Book 73*, p. 921, for the defining equations). The experimentally determined coefficients A_i of the associated functions, which describe the analyzing power, are shown in Fig. 20. Their rapid change as functions of proton energy complicates the analy-

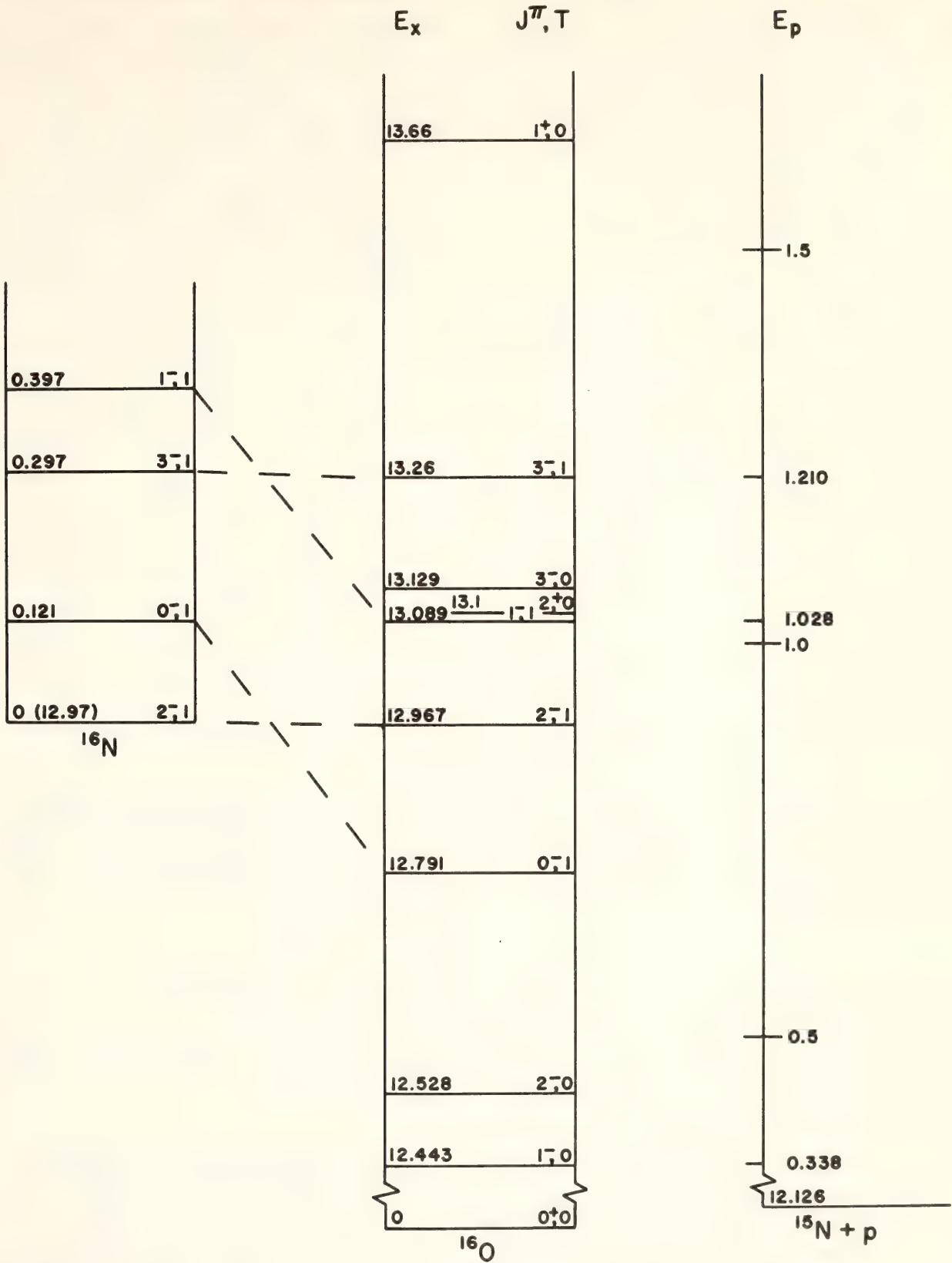


Fig. 19. Limited energy level diagram for ^{16}O and isobar diagram for $A = 16$. Levels, as they were thought to exist prior to our experiment, are indicated by horizontal lines with the energy in MeV above the ground state at the left and two quantum numbers descriptive of the state at the right—the angular-momentum-parity and the isospin. The energies of ^{16}N have been shifted vertically to eliminate the neutron-proton mass differences and the Coulomb energy. Levels that are presumed to be isospin multiplets are connected by dashed lines. A scale at the right gives proton energy for $^{15}\text{N}(p,\alpha)^{12}\text{C}$ in MeV. Only levels with $J^\pi = 0^+, 1^-, 2^+, 3^-, \dots$ can be observed with this reaction and $T = 1$ states will show up much less strongly than $T = 0$ states.

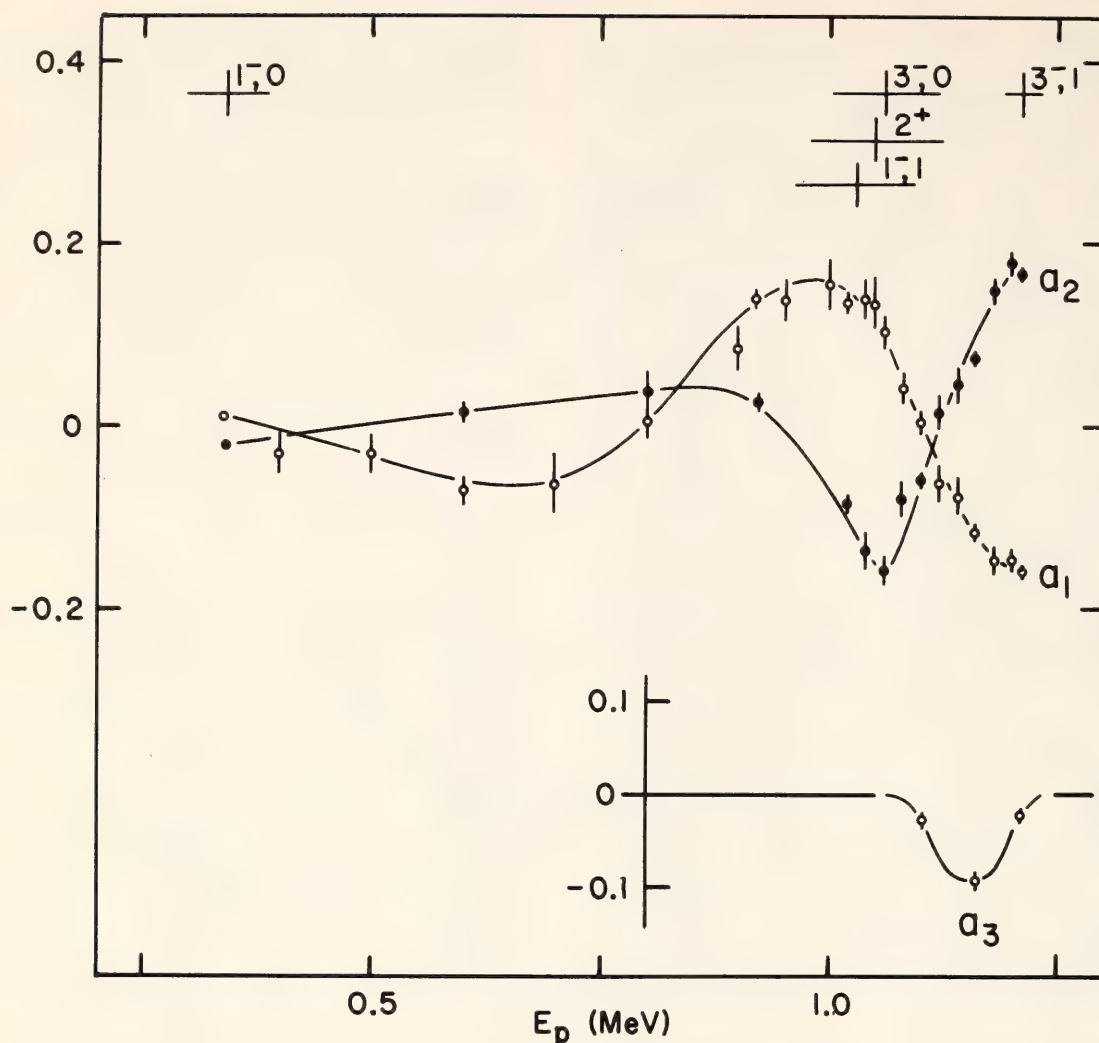


Fig. 20. Coefficients of the associated Legendre functions that describe the measured analyzing power of $^{15}\text{N}(p,\alpha)^{12}\text{C}$. These coefficients can be calculated theoretically, if the structure of the compound nucleus, in this case ^{16}O , is known. The location of resonances accepted at the time this work began are indicated with crosses; the vertical line is the resonance energy; the horizontal gives the width.

sis, so as a further aid we measured the analyzing power in small energy steps at the angles where the functions $P_2^1(\theta)$ and $P_3^1(\theta)$ are zero. The analyzing power for the 0.34 MeV resonance, the 12.44 MeV 1^- state, is evidence that it has a small d-wave admixture. The 1^- state at 13.09 MeV shows pronounced polarization effects, which can be explained as interference from the nearby 3^- and 2^+ states as well as a small d-wave admixture. The 3^- at 13.26 MeV shows polarization effects resulting from its interference with 1^- and 2^+ states. Theoretical calculations of the coefficients, which should establish the structure accurately, are under way.

Reference

Ajzenberg-Selove, F., Energy levels of light nuclei $A = 16-17$, *Nucl. Phys.*, A166, 1, 1971.

THE $^9\text{Be}(p,n)^9\text{B}$ REACTION EXCITED WITH POLARIZED PROTONS

L. Brown, U. Rohrer, and L. G. Arnold

In *Year Book 72*, p. 191, we described our study of ^{10}B with $^9\text{Be}(p,p)^9\text{Be}$ using polarized protons. For proton energies below 2 MeV (8.4 MeV excitation energy, see Fig. 10, p. 192, *Year Book 72*) we were able to demonstrate an unambiguous and simple structure. Above 2 MeV proton energy there were differential

cross-section data at only one angle and this lack prevented the phase-shift analysis from giving as clear a picture of the structure there. At 2.56 MeV proton energy (8.89 MeV excitation energy) lie two excited states, degenerate in energy within experimental error. Marion (1956) showed that one, observed through ${}^9\text{Be}(p,\alpha\gamma){}^6\text{Li}$, was 2^+ and the other, observed through ${}^9\text{Be}(p,n){}^9\text{B}$, was 3^+ . Later Altman *et al.* (1962) concluded after examining the relative neutron and proton reduced widths that the latter state must be 3^- .

Our phase shift analysis clearly favored the 2^+ and 3^+ at 2.56 MeV and was unable to fit the data with 2^+ and 3^- . We have completed the measurement of the angular distribution of the analyzing power of ${}^9\text{Be}(p,n){}^9\text{B}$ at four energies that span the structure in question as well as two energies well above it. The coefficients of the associated Legendre functions are shown in Fig. 21 and give a

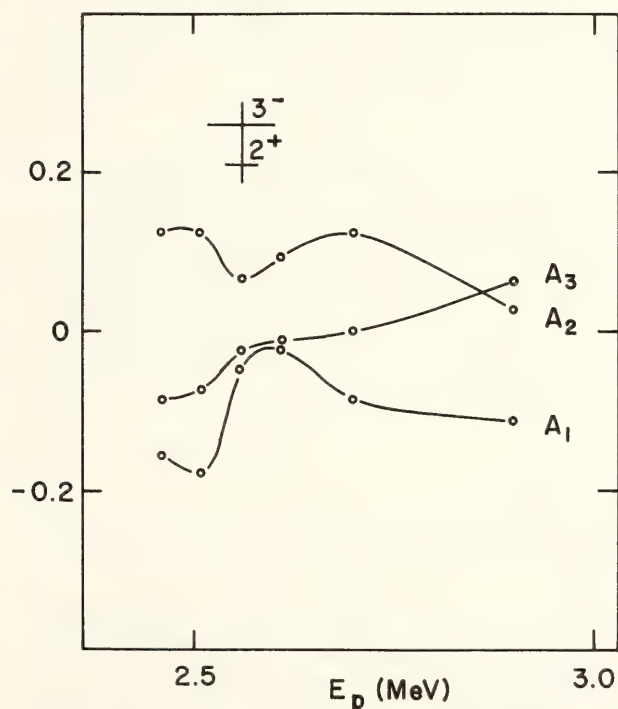


Fig. 21. Coefficients of the associated Legendre functions that describe the analyzing power of ${}^9\text{Be}(p,n){}^9\text{B}$. At 2.56 MeV proton energy are two states degenerate in energy, a 2^+ of width 38 keV and a 3^+ or 3^- of width 85 keV. These data rule out the 3^- because the interference of two states of the same parity leads to $A_1 = A_3 = 0$ over the range of the resonances.

clear answer to the question of parity assignment. If the two states have the same parity, the odd coefficients will be zero across the 85 keV wide resonance, a condition not satisfied. In addition, a nonzero A_3 coefficient requires the presence of d waves in both the proton and neutron channels. The 3^- assignment is favored. The shell model predicts a 3^- state in ${}^{10}\text{B}$ near 8.89 MeV excitation energy that has a nearly pure $d_{5/2}$ configuration. The absence of an A_4 coefficient is consistent with a 3^- state that is a pure configuration.

The results of the ${}^9\text{Be}(p,n){}^9\text{B}$ analysis require us to examine again the results of our earlier study of ${}^9\text{Be}(p,p){}^9\text{Be}$ near 2.56 MeV. By using the shell model predictions for the 3^- state as a guide, we hope to clarify the matter.

References

- Altman, A., W. M. MacDonald, and J. B. Marion, Nucleon reduced widths and charge independence, *Nucl. Phys.*, **35**, 85, 1962.
 Marion, J. B., Excited states in ${}^{10}\text{B}$, *Phys. Rev.*, **103**, 713, 1956.

A RETURN TO ${}^4\text{He}(p,p){}^4\text{He}$

L. Brown and G. H. Pepper

In *Year Book 73*, p. 927, we described the present status of ${}^4\text{He}(p,p){}^4\text{He}$, which was the first experiment we undertook with the polarized proton beam (see *Year Book 65*, p. 72). The phase shifts describing this interaction are given by various parameterizations, each capable of reproducing all measurements over a 20 MeV range with accuracies around 1%. We use this interaction from time to time to verify the polarization of our beam, and this time continued it for a few weeks at the request of R. L. Walter of Duke University who hoped he would be able to distinguish between the various parameterizations. The matter has a special significance because measurements in our energy range should be able

to decide the existence of a d-wave admixture to the ground state of ^4He for which Plattner *et al.* (1975) have advanced evidence, evidence resting primarily on our old data. The measurements we just completed tend to favor one of the parameterizations, but a clear answer requires accuracies five times better than we generally run, which means running 25 times longer. This experiment will probably be postponed until the current of our polarized beam is correspondingly greater, or until we are convinced the results justify the expenditure of time.

Reference

- Plattner, G. R., R. D. Viollier, and K. Alder, Evidence for the D State of ^4He , *Phys. Rev. Lett.*, **34**, 830, 1975.

MISCELLANY

In December G. H. Pepper participated in measurements of K- and L-shell x-ray cross sections produced with 7–35 MeV lithium ions at the Tandem Accelerator Laboratory of Florida State University. This work was undertaken to test theories for creating inner-shell vacancies through direct interaction, i.e., where the projectile may be considered a point charge. Analysis is not complete but the K-shell data seem to indicate a need for relativistic wave functions in

high-Z targets when struck by low-velocity projectiles.

During September A. J. Ratkowski of New York University used the alkali beam of the DTM Van de Graaff to measure the energy dissipated by electronic collisions when these projectiles were stopped in silicon crystals. The targets were silicon surface-barrier detectors that registered inherently the electronic excitation through the separation of electron-hole pairs. The results follow the theory of Lindhard *et al.* (1963 *a*, *b*, 1968) for the stopping of slow, heavy atomic projectiles in matter.

References

- Lindhard, J., M. Scharff, and H. E. Schiott, Range concepts and heavy ion ranges, (Notes on Atomic Collisions, II), *Mat. Fys. Medd. Dan. Vid. Selsk.*, **33**, No. 14, 1963*a*.
Lindhard, J., V. Nielsen, M. Scharff, and P. V. Thomsen, Integral equations governing radiation effects (Notes on Atomic Collisions, III), *Mat. Fys. Medd. Dan. Vid. Selsk.*, **33**, No. 10, 1963*b*.
Lindhard, J., V. Nielsen, and M. Scharff, Approximation method in classical scattering by screened Coulomb fields, (Notes on Atomic Collisions, I), *Mat. Fys. Medd. Dan. Vid. Selsk.*, **36**, No. 10, 1968.

BIOPHYSICS

T. I. Bonner, D. B. Cowie, B. H. Hoyer, N. R. Rice, and R. B. Roberts

INTRODUCTION

As in the past several years, much of the work of the Biophysics Section has dealt with the DNA of eukaryotic cells. Bonner is attempting to isolate DNA segments which are transcribable *in vivo* and which therefore represent essentially all of the gene regions. He is exploiting the observation that RNAs from several species have been found to contain short (~ 25 nucleotides) transcribed runs of

poly(adenylic acid). The complementary DNA molecules can in principle be isolated simply by taking that fraction of total denatured DNA which binds to a column of poly(A) or poly(U), to isolate the partner DNA strand.

Hoyer is continuing his study of relatedness among the primates and reports on experiments measuring similarity of single-copy DNA among several rather closely related African monkeys.

Repeated DNA has also been examined, and a preliminary finding of a family present in human but not in chimp DNA is reported.

Repeated sequences in rat and mouse DNAs are the subject of Rice's report. She has found a small class (about 1% of total DNA) of repeated mouse (or rat) DNA which reassociates to higher thermal stability with homologous DNA rather than with heterologous DNA. How these two species can each possess rather homogeneous families which are only loosely related to each other is an evolutionary puzzle of great interest.

Cowie, working at the Pasteur Institute with Georges Cohen and Paolo Truffa-Bachi, has continued his study of the *Escherichia coli* allosteric enzyme aspartokinase I—homoserine dehydrogenase I. Work has centered on the conformational changes induced in the enzyme when it binds to specific antibodies and on the effects of the enzyme's ligands on this antibody coupling.

Finally, in the hope that it will be of general interest, we include Roberts's account of the remarkable history of the Biophysics Section—from the early days when radioisotopes for biological experiments were produced by DTM's cyclotron, through periods concentrating on metabolic pools, ribosomes, and DNA. The group is now disbanding, and we offer this as tribute to the section of which we are pleased and privileged to have been members.

PROPERTIES OF HUMAN DNA SEQUENCES CONTAINING POLY(dA) OR POLY(dT)

T. I. Bonner

The messenger RNA of the cellular slime mold (*Dictyostelium discoideum*) contains a short sequence of poly(adenylic acid) of about 25 nucleotides in addition to the longer poly(A) sequence (in this case about 100 nucleotides) which is commonly found at the 3' end of eukaryotic messenger RNAs (Jacobson *et al.*, 1974). In contrast to the long poly(A) sequence which is added to the

precursor nuclear RNA after it is transcribed, the short poly(A) is transcribed from DNA. Furthermore, in at least half of the messenger RNA molecules, the short poly(A) is separated by no more than 25 nucleotides from the long poly(A) at the 3' end of the molecule. This result suggests that the short poly(A) sequence functions as a terminator of the transcriptional unit. If the presence of short poly(A) sequences with similar properties were common throughout the eukaryotes, it could prove to be a very useful tool in the study of gene expression.

There is evidence that these sequences are indeed common. Bishop *et al.* (1974) have studied the amount of poly(dA) present in the genomes of several eukaryotes. While they found substantial quantities of poly(dA), they concluded that there was much too little poly(dA) of sufficient length for the long poly(A) in messenger RNAs to be encoded by the DNA. However, if one studies their results it is apparent that the genomic poly(A) reacts with poly(U) to form hybrids which melt approximately 20°C lower than hybrids of synthetic poly(A) with poly(U). Assuming that the lowering of the melting temperature is due to the short length of the genomic poly(A) and not to the presence of other bases within the poly(A), the length must be about 20–30 nucleotides. With an average length of 25 nucleotides, the amount of poly(A) in rat DNA implies about 140,000 poly(A) sequences per genome or one poly(A)₂₅ sequence per approximately 20,000 nucleotide pairs.

It has also been shown (Nakazato *et al.*, 1974) that the heterogeneous nuclear RNA of a human cell line contains about one poly(A) sequence of 20–40 nucleotides per molecule. Furthermore, the short poly(A) sequences are clearly the result of transcription, while the long poly(A) sequences are not. However, they do not find any short poly(A) in cytoplasmic RNA, an observation which is not consistent with the short poly(A)

being near the end of the message unless the long poly(A) is formed by elongation of the short poly(A).

The discussion above clearly suggests that the occurrence of large numbers of 20–30 nucleotide poly(A) sequences is a common feature of eukaryotic DNAs. It also appears likely that these sequences occur approximately once per transcriptional unit, although it is not clear whether they are usually located within the messenger sequences. The isolation of DNA sequences containing the short poly(A) stretches and the complementary sequences containing short poly(T) stretches could be useful for several reasons. First, the short poly(T)-containing sequences should be enriched in expressible sequences, thus allowing more sensitive measurements of differences in expression between different cell populations. Second, the isolated sequences should represent only one strand of the DNA and should thus be incapable of self-reaction. This property alone would be a great technical convenience. Third, the isolated sequences could be useful, especially if the short poly(A) sequence is located at the 3' end of the message, in the mapping of the sequence organization of the genome using the poly(A) sequence as a reference point.

In principle the isolation can be accomplished simply by reacting denatured DNA with synthetic poly(A) or poly(U) that is covalently bound to a matrix such as agarose. Thus, the sequences containing poly(dT) can be bound to a poly(A)-agarose column. The bound sequences should include those from which short, poly(A)-containing RNA molecules are transcribed. Unfortunately, the bound fraction may also include some sequences that are representative of the other DNA strand, since it is known (Molloy *et al.*, 1972) that there are also short U-rich regions in RNA.

Column Properties

Since the poly(A) and poly(T) stretches in the DNA are expected to be

short, their thermal stabilities when reacted with long molecules of poly(A) or poly(U) will be quite low. For this reason one must do the reactions under higher salt and lower temperature conditions than usual. However, going too far in this direction would allow non-specific reactions to take place. The conditions we have used, namely 0.28 M PB at 25°C, provide a reasonable compromise. Human DNA of 2300 nucleotides median length binds 7%–14% compared to an expected value of 6%, assuming that human DNA contains the same amount of short poly(A) as rat and that the poly(A) sequences are not clustered. However, *Escherichia coli* DNA, which contains about 30 times less poly(A) (Bishop *et al.*, 1974), binds about 20 times less DNA to the column even in the presence of human DNA bound to the column. This result shows that the reaction criterion is not so low as to allow the nonspecific binding of the *E. coli* DNA directly to the column or even secondarily to the bound human DNA.

I have used two different binding procedures. In the first procedure the DNA was alkali denatured, then brought to 0.28 M PB and loaded on the poly(A)-agarose, or poly(U)-agarose, column so that the sample volume was entirely within the column volume. After 10–15 minutes the column was washed with more 0.28 M PB, and the bound DNA was eluted with solutions containing at least 70% formamide and less than 0.09 M PB. The second procedure used a column of 1 cm diameter by 3 cm height of either poly(U) or poly(A)-agarose through which the sample was passed at a rate of about 1 ml/min. The first procedure gives as much as twice as much binding as the second. However, when labeled poly(dA) of 38 nucleotides average length or poly(dT) of 48 nucleotides average length is bound using the second procedure, 96% binds to the column. Thus, the increase in binding using the first procedure must be due to the re-

association of molecules that cannot directly bind to the column with those that can. Since the only substantial difference between the two procedures is approximately 10 minutes of incubation time, the reassociation must involve sequences that are highly repetitive under our very relaxed incubation conditions. This explanation is supported by the observation that of the DNA which binds to a poly(A)-agarose column in 15 minutes only 55%–65% will bind a second time, while a third binding gives 80%–90%. This pattern of binding indicates that rapidly reassociating sequences not containing poly(T) are being successively removed. Thus two or three binding steps are necessary to purify the poly(A)- or poly(T)-containing sequences to a reasonable extent. As we shall see later, most of the molecules that bind to the column contain highly repeated sequences.

Since the poly(A) and poly(U) that are covalently bound to the agarose are nominally about 1500 nucleotides long, which is considerably longer than the

longest poly(A) stretches in natural RNAs, the whole length of a poly(A) or poly(U) sequence in a bound RNA or DNA molecule should be base-paired. And since the stability of the hybrid depends on the base-paired length, we should be able to differentiate the bound sequences on the basis of the poly(A) or poly(U) length by using a gradient elution from the column. To test the column properties in this regard we have used ^{32}P -labeled RNA from HeLa cells, which should provide us with at least two size classes of poly(A) sequences, about 25 nucleotides and about 200 nucleotides. When this RNA was bound to a poly(U)-agarose column, the total binding was nearly 2% and the elution pattern typically was as shown in Fig. 22. There is a pronounced peak at about 65% completion of the gradient which must correspond to the long poly(A) sequences. The peak at about 11% completion, which is somewhat less pronounced than usual, corresponds to the short poly(A) sequences, as can be seen in Fig. 23 which shows the elution pattern of DNA

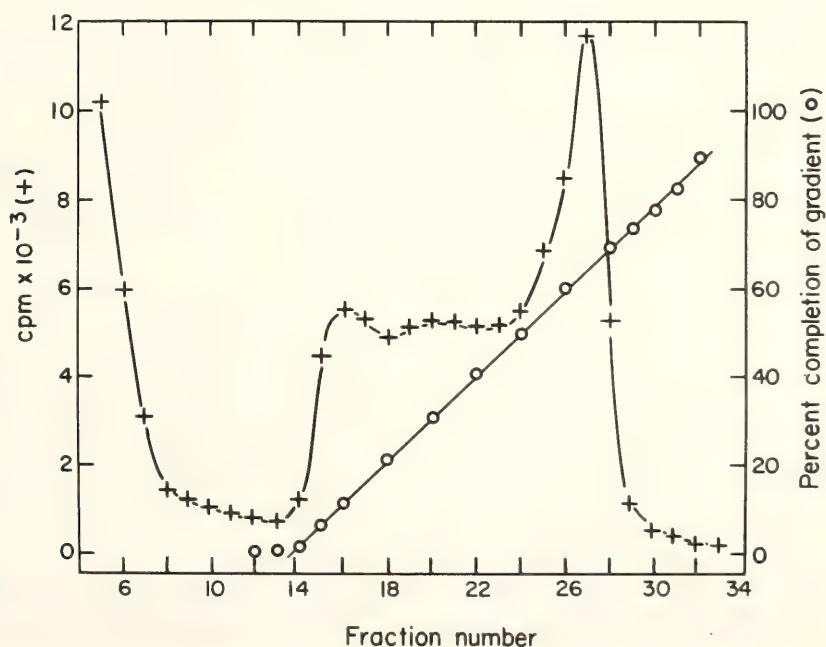


Fig. 22. Gradient elution of ^{32}P -labeled HeLa RNA from a poly(U)-agarose column. ^{32}P -HeLa RNA was bound to a 1 cm \times 3 cm poly(U)-agarose column in 0.28 M PB, 10^{-3} M EDTA at 25°C by passing the sample through the column at a rate of approximately 1 ml/min. The elution of bound RNA was done with a linear gradient which varied from 0.28 M PB, 10^{-3} M EDTA (solution A) at the beginning to 90% formamide, 0.01 M PB, 0.01 M EDTA (solution B) at the finish. The refractive index of individual fractions was measured to determine the percentage of solution B in the fraction.

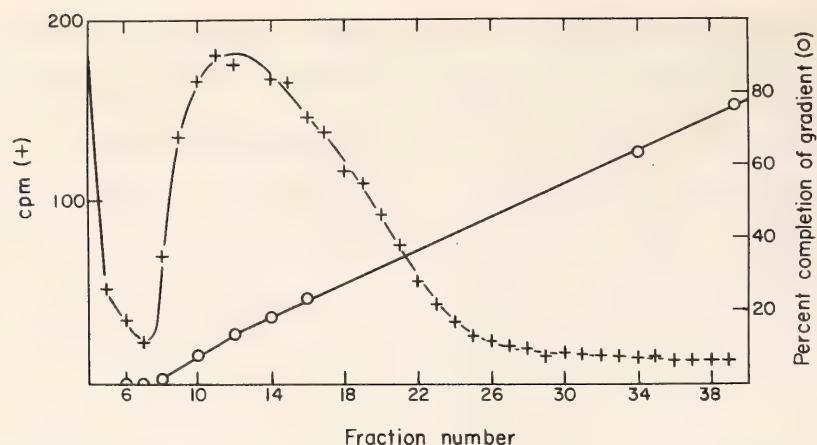


Fig. 23. Gradient elution of human DNA from a poly(U)-agarose column. ^3H -labeled DNA was alkali denatured, brought to 0.28 M PB and then bound to and eluted from a poly(U)-agarose column as described in Fig. 22.

sequences binding to the same column. In order to determine how well the position in the elution gradient characterizes the poly(A) sequence length, fractions were selected from the early, middle, and late portions of the gradient and were again bound to and eluted from the column. As shown in Fig. 24, at least 75% of the counts that bind elute within two fractions of their original position. However, the binding of all three fractions is only about 50%, which suggests that there was substantial degradation

between the first binding and the second binding. The important point is that neither early nor middle fractions have an appreciable amount of RNA eluting in the late portion of the gradient. This means that they have negligible amounts of long poly(A)-containing molecules. Hence, essentially all of the long poly(A) sequences must be base-paired over their entire length. The only likely reason that elution position would not be directly related to the poly(A) sequence length is the possibility that base-pairing occasionally occurs over less than the full poly(A) length. Since this does not happen to the long poly(A) sequences, one can assume that the elution position is indeed a good indicator of poly(A) length.

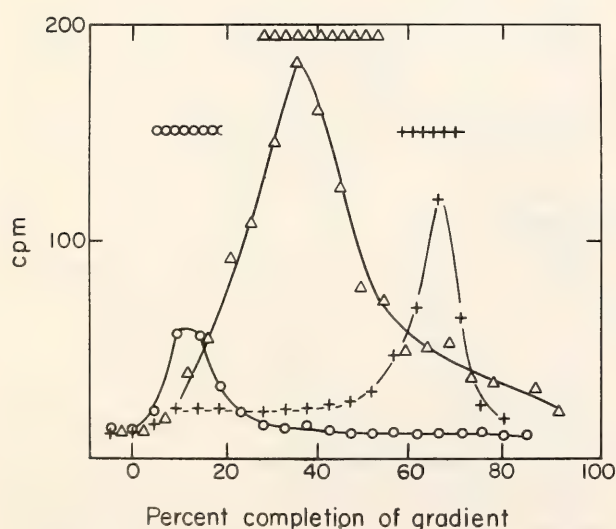


Fig. 24. Rechromatography of selected gradient fractions. Fractions were selected from the early, middle, and late portions of gradients similar to the gradient of Fig. 22, bound to the poly(U) column and eluted again. The horizontal bars above the peaks indicate the positions of the fractions in the initial gradient.

The labeled RNA also allows us to determine whether the short U-rich regions in RNA have sufficiently different binding or elution properties that they can be distinguished from the poly(T) sequences in DNA which are complementary to the poly(A)₂₅ sequences of RNA. When RNA is bound to a poly(A)-agarose column, the midpoint of the gradient elution occurs at 21% of completion as compared to the midpoint at 18% completion for the DNA bound to poly(U)-agarose shown in Fig. 23. This small difference could well be due to the increased stability of the rU:rA base pairs for the RNA compared to rU:dA

base pairs with the DNA. Thus it appears that we will be unable to distinguish between DNA sequences (or other complements) corresponding to RNA poly(U) and DNA sequences (or their complements) complementary to RNA poly(A).

Properties of Poly(A)- or Poly(U)-Binding DNAs

As I mentioned earlier, when DNA is bound to the columns a substantial fraction of the bound DNA will not bind to the column a second time. Presumably these are DNA molecules containing highly repeated sequences complementary to molecules that actually bind to the column because of their poly(A) or poly(U). Two successive bindings to the column usually produce a DNA fraction capable of binding a third time with nearly 90% efficiency. Such fractions, which should represent reasonably pure poly(A)- or poly(U)-containing sequences, amount to 5-7% of the total DNA whose initial median size is 2300

nucleotide pairs. DNA that has bound twice to a poly(A) column, and from which the instantaneously reassociating fraction (11%) has been removed, reassociates with and without an excess of unlabeled DNA as shown in Fig. 25. In the presence of unlabeled DNA the reassociation of the poly(T)-containing sequences indicates that 64% of the molecules contain repeated sequences with an average repetition frequency of about 75,000. For comparison, the kinetics of unfractionated DNA of 2300 NTP median length indicates that 46% of the unfractionated molecules contain repeated sequences with an average repetition frequency of 34,000. Thus the poly(T)-containing sequences appear to be enriched in highly repeated sequences. The kinetics of poly(T)-containing sequences prepared from DNA of 385 nucleotide average length shows nearly as much repeated DNA (about 55%) and with nearly as great a repetition frequency (about 50,000). Thus, it is

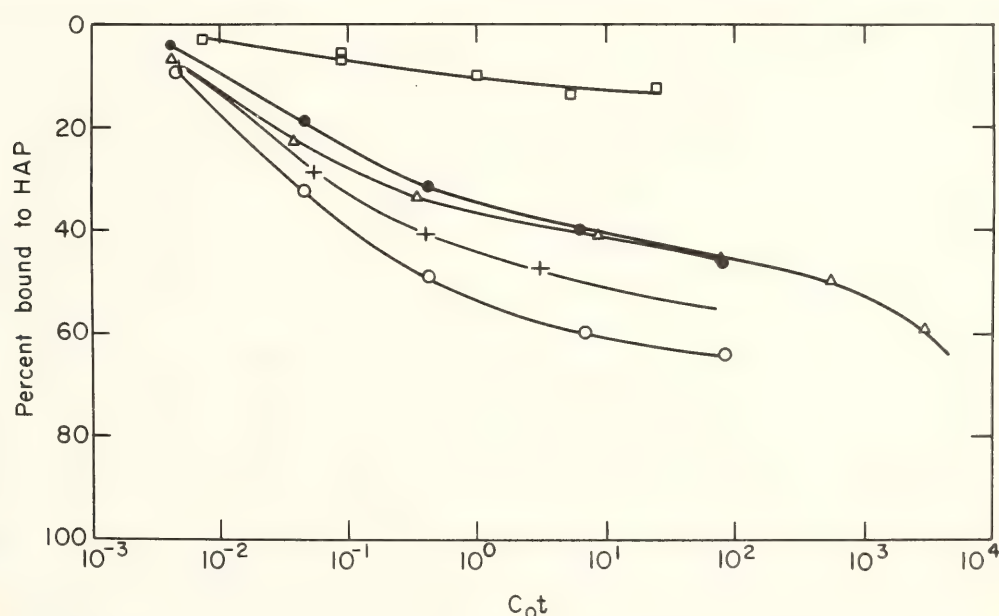


Fig. 25. Reassociation kinetics of poly(T)-containing DNA. The reassociation of various DNA fractions in 0.14 M PB at 60°C (or the equivalent) are shown as the fraction of labeled DNA binding to hydroxyapatite. Reassociation was measured in the presence of a large excess of human DNA of 450 NTP average length for the following DNAs: (a) 2300 NTP DNA which bound twice to poly(A) columns and was stripped of "instantaneously reassociating" DNA, indicated by open circles; (b) unfractionated DNA of 2300 NTP median length, solid circles; (c) 385 NTP DNA which bound to poly(A) column, plusses; and (d) poly(T)-primed complementary DNA, triangles. In addition, we show the self-reaction of fraction a as open squares. The self-reaction C_0t values have been multiplied by a factor of 15 to correct for sequence enrichment (see text).

clear that more than half of the poly(T) sequences in the genome are within about 350 nucleotides of a highly repeated sequence. The estimate of about 140,000 poly(T) sequences in the rat genome includes both poly(T) sequences that would occur as poly(U) in RNA and poly(T) sequences which would be transcribed into poly(A) sequences. Thus, the data suggest that perhaps one or the other of these two groups is adjacent to a single family of repeated sequences.

Figure 25 also shows the kinetics of self-reaction of the poly(T)-containing sequences. The actual C_0t values obtained using the specific activity of the DNA have been multiplied by a factor of 15 to correct for the fact that the sequences, which represent only 5%–7% of the genome, are more concentrated than they would be if the same amount of DNA from the whole genome were present. It is quite conceivable that these C_0t values could be in error by as much as a factor of 2. With this in mind, the data appear to be consistent with the interpretation that about 20% of the repeated sequences are capable of self-reacting with about the same kinetics as were evident in the presence of excess unlabeled DNA. This result suggests that there is still a contamination of sequences not containing poly(T) amounting to about 10% of the repeated sequences or about 6%–7% of the total preparation. This level of contamination would be consistent with the fact that only 88% of this DNA preparation will bind to the poly(A) column.

An initial test to see whether the poly(T)-containing sequences are enriched in expressed sequences was performed by reacting the same preparation of DNA with excess RNA from WI-38 cells to $R_0t = 2200$. Even though this R_0t value is an order of magnitude less than is necessary to reach saturation with total single-copy DNA (Hoyer's unpublished results), 13% of the DNA molecules react with the RNA.

Polymerase Copying

If we take poly(T)- or poly(A)-containing sequences and use them as template for a DNA polymerase in the presence of poly(A) or poly(T) as primer, we should be able to generate complementary DNA (cDNA) representative of the sequences in one direction or the other from the poly(A) or poly(T) region. The various possibilities are illustrated in Fig. 26. Let A and B represent the sequences at the 3' and 5' ends of the poly(U) region in an RNA molecule and let C and D represent the sequences which are at the 3' and 5' ends of the short poly(A) region in an RNA molecule. Furthermore, let the complementary sequences be denoted as A' , B' , C' , and D' . Then poly(T)-containing template DNA contains the RNA-like sequences A and B and the RNA-complementary sequences C' and D' as illustrated in the second line of Fig. 26. Since the DNA polymerase starts at the priming poly(A) sequences and proceeds in the 5' to 3' direction, the polymerase product will include just the sequences B' and C . Of these only the sequences B' can react with RNA. Similarly, as shown in the third line of Fig. 26, poly(A)-containing template DNA contains the RNA-like sequences C and D and the RNA-complementary sequences A' and B' . Thus, the polymerase product contains the sequences A and D' . If, as suggested by the slime mold, the short poly(A) sequence in RNA occurs near the 3' end of messenger RNA, then the sequence class D' should be complementary to messenger RNA, and the sequence class C should be largely spacer DNA.

In an effort to disentangle the properties of the sequence classes A , B , C and D , I have begun to prepare cDNA from poly(A)-binding and poly(U)-binding DNAs. I have used the DNA polymerase from *Micrococcus luteus* and have labeled the polymerase product by supplying ^{32}P -labeled dGTP to the reaction mixture. The use of label in dGTP al-

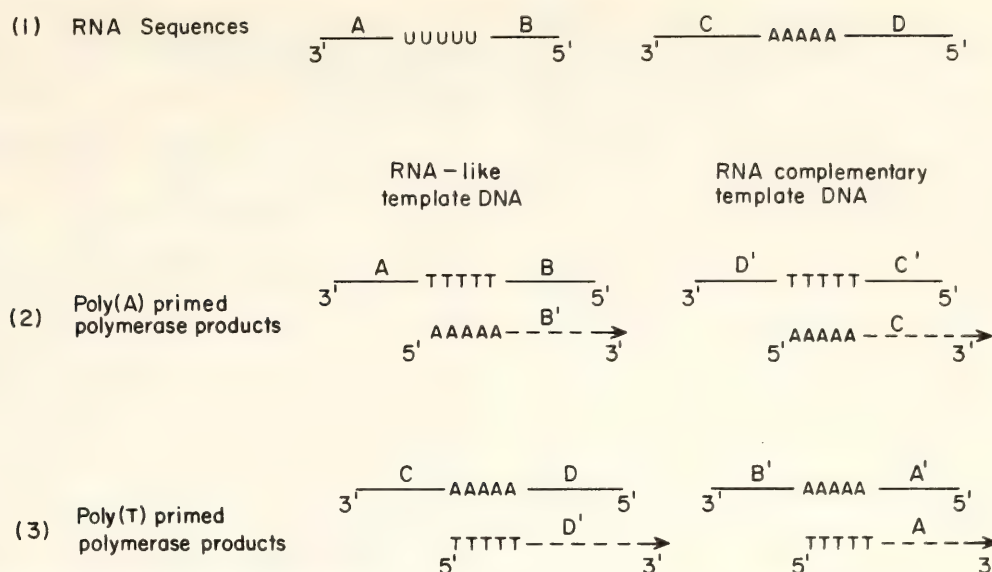


Fig. 26. Possible DNA polymerase products from poly(A)- or poly(T)-containing templates. We denote the sequences at the 3' and 5' ends of poly(U) and short poly(A) sequences which occur in RNA by the letters *A*, *B*, *C*, and *D* as shown in the first line of the figure. The complementary sequences are denoted *A'*, *B'*, *C'*, and *D'*. The remainder of the figure shows the various possible types of poly(A)- or poly(U)-binding template sequences and their polymerase products. In all cases, AAAAA and TTTTT represent poly(A) and poly(T) sequences of about 25 nucleotides. The polymerase products are indicated by dashed lines with arrows indicating the direction of copying.

allows one to measure the incorporation of deoxyribonucleoside triphosphates into DNA without having to worry about the formation of poly(A), poly(T), or poly(AT). In the initial attempt using (dT)₁₂₋₁₈ to prime poly(U)-binding template sequences, incorporation was measured by denaturing the polymerase product and binding to HAP at 50°C in 0.042 *M* PB. The ³²P-labeled material that eluted in 0.14 *M* PB was taken to be a single-stranded polymerase product, while the material that eluted in 0.42 *M* PB was assumed to be a product containing a hairpin loop caused by the polymerase reversing direction and using the previous product as a template. The 0.42 *M* PB fraction was discarded, and the 0.14 *M* PB was further purified by binding to a poly(A) column. At this point there was 47 times as much product in the poly(T)-primed case as in the unprimed control reaction.

Even though the poly(T)-primed DNA probably contained a significant amount of DNA which is too short to form a stable product at 60°C in 0.14 *M* PB, the kinetics of this DNA in the

presence of an excess of unlabeled DNA was studied. As the results in Fig. 25 show, at least 45% of this DNA contains repeated sequences. When reassociated with WI-38 RNA to $R_0t = 2000$, about 15% of the DNA reacts with RNA. The question whether reacting sequences are repeated or are single-copy is of considerable importance. According to our discussion above, the sequences which react with RNA must be of the class D' which, if the short poly(A) sequences are near the 3' end of messenger RNA, must be complementary to messenger RNA. Since messenger RNA sequences are almost entirely single-copy, a large fraction of repeated sequences would indicate that the short poly(A) sequences are not predominately near the 3' end of messenger RNA. A very tentative answer to this question was obtained by reacting the poly(T)-primed DNA with RNA to $R_0t = 2600$. The product was treated with S1 nuclease to remove unreacted sequences, and the remaining 3% of the DNA was reacted with DNA to $C_0t = 15$. The results indicate that at least 75% of the S1-resistant DNA contains

repeated sequences. A more definite answer will require reacting the DNA with the RNA to a R_{ot} of 20,000–40,000 so that all the DNA that can react with the DNA has an opportunity to do so.

I intend to pursue the use of the cDNA from poly(A)– and poly(T)–containing DNA templates in order to determine the properties of the adjacent sequences. The question of the location of the short poly(A) sequences in RNA is of particular interest since it bears heavily on usefulness of the poly(T)–containing sequences as probes for transcriptional studies.

References

- Bishop, J. O., M. Robash, and D. Evans, Polynucleotide sequences in eukaryotic DNA and RNA that form ribonuclease-resistant complexes with polyuridylic acid, *J. Mol. Biol.*, **85**, 75–86, 1974.
- Jacobson, A., R. A. Firtel, and H. F. Lodish, Transcription of polydeoxythymidylate sequences in the genome of the cellular slime mold, *Dictyostelium discoideum*, *Proc. Nat. Acad. Sci. USA*, **71**, 1607–1611, 1974.
- Molloy, G. R., W. L. Thomas, and J. E. Darnell, Occurrence of uridylate-rich oligonucleotide regions in heterogeneous nuclear RNA of HeLa cells, *Proc. Nat. Acad. Sci. USA*, **69**, 3684–3688, 1972.
- Nakazato, H., M. Edmonds, and D. W. Kopp, Differential metabolism of large and small poly(A) sequences in the heterogeneous nuclear RNA of HeLa cells, *Proc. Nat. Acad. Sci. USA*, **71**, 200–204, 1974.
- DNA sequences when single-copy, radioactive fragments were reassociated with unfractionated, unlabeled DNA fragments derived from homologous or heterologous monkey species. The rationale and methodology are essentially described in *Year Book 69*, pp. 488–500, and *Year Book 71*, pp. 260–262.
- These studies provide information on the present status of the relationships of some African monkeys and provide some further insight into their evolutionary divergence times. Since these monkeys have similar generation times, the relative thermostabilities of their reassociated sequences may be assumed to have a direct relationship to their times of divergence (see *Year Book 69*, pp. 488–500).
- The radioactive single-copy DNA sequences were derived from tissue culture cells from the green monkey (*Cercopithecus sabaeus*) or the rhesus monkey (*Macaca mulatta*). Single-copy, radioactive DNA from the South American capuchin monkey (*Cebus capucinus*) was included as a common reference.
- The unlabeled DNA fragments used were prepared from the tissues of rhesus and green monkeys as well as the capuchin monkey. In addition, DNA fragments derived from the tissues of the baboon (*Papio anubis*), the cynomolgus monkey (*Macaca fascicularis*), and the Indochinese bear macaque (*Macaca arctoides*) were used in heterologous reassociations. The unlabeled DNA fragments included the single-copy as well as the repeated DNA fragments.
- The results in Table 2 indicate that the rhesus monkey is more closely related to the other macaques and the baboon than is the green monkey. Also, the green monkey and the rhesus monkey are uniformly diverged from the species tested because the $\Delta T_{e_{50}}$'s within each group are similar.
- If previous DNA homology data are taken into account and the divergence times used are realistic (*Year Book 69*, pp. 492–493), it can be inferred that the

RELATIONSHIPS OF SOME AFRICAN MONKEYS AS DETERMINED BY THEIR SINGLE-COPY DNA SEQUENCE HOMOLOGIES

Bill H. Hoyer and N. W. van de Velde

We have examined the relationships of several of the African monkeys on the basis of the thermostabilities of their

TABLE 2. Divergence of Some African Monkeys as Indicated by the Thermostabilities of Radioactive Single-Copy DNA Fragments Reassociated with Unlabeled Homologous or Heterologous DNAs

Source of unlabeled DNA	Source of Radioactive DNA Fragments and the ΔT_{e50} * of the Reassociated DNAs	
	<i>Cercopithecus sabeus</i>	<i>Macaca mulatta</i>
<i>C. sabeus</i>	0	2.4
<i>M. Mulatta</i>	2.4	0
<i>M. arctoides</i>	2.2	1.8
<i>M. fascicularis</i>	2.3	2.0
<i>Papio anubis</i>	2.5	2.2

* ΔT_{e50} is determined graphically as described in *Year Book 71*, pp. 260–261; the larger the number indicated, the greater the sequence divergence. The radioactive DNA fragments were reacted with excess unlabeled DNA; self-reaction of the radioactive DNA was about 1%. The reaction was allowed to proceed to $C_{ot} = 20,000$ at 60°C and 0.14 M PB, and the unique sequences were prepared as indicated in *Year Book 71*, pp. 260–261. *Escherichia coli* ³²P-DNA was included as an internal standard.

African monkeys diverged between 15 and 30 million years ago. Data derived from the radioactive single-copy capuchin DNA sequences indicate a ΔT_{e50} of 11°C for both green and rhesus monkeys, a result in good agreement with previous findings with green monkey indicator sequences (*Year Book 69*, pp. 492–493).

The African monkeys examined here form an evolutionary group somewhat more homogeneous than that formed by man, orangutan, and gibbon but less homogeneous than the group formed by man, chimpanzee, and gorilla.

A SPECIAL CLASS OF RELATED REPEATED SEQUENCES IN MOUSE AND RAT DNAs

Nancy Reed Rice

There are several known cases of related satellites occurring within a single species or in closely related species (Sutton and McCallum, 1972; Rice and Straus, 1973; Gall and Atherton, 1974; Cooke, 1975). In each case heterogeneity within a satellite appears quite limited (it has a high T_m after reassociation), yet it is clearly dissimilar from its counterparts (cross product has a low T_m). How two diverging species can each

possess homogeneous families which are only loosely related to each other is an unsolved and highly intriguing puzzle.

Between more distantly related species, where satellites show no cross-homology at all, those repeated sequences which are related exhibit about the same thermal stability when reassociated with heterologous as with homologous DNA (Rice, 1972). It is as though a particular family in each of two diverging lines accumulates base changes at about the same rate, resulting in the same average heterogeneity within each at present. Stavnezer (1971), however, has reported that there is a fraction of repeated mouse (or rat) DNA which reassociates to higher thermal stability with homologous than with heterologous DNA, thus mimicking the satellite findings. I here report results confirming his observation.

The experiments can be summarized as follows: (1) A high thermal stability fraction of mouse-repeated ³H-DNA is prepared (mouse satellite having previously been removed). (2) ³H-DNA which appears to reassociate instantaneously is removed from this fraction. (3) That part of the fraction able to reassociate with repeated sequences of rat DNA is isolated in double-stranded

form and treated with S1 nuclease, thus removing all ^3H -DNA segments which are not base paired with the rat DNA. (4) S1-resistant ^3H -DNA is reassociated with repeated sequences of rat or mouse DNAs and the thermal stability of the products determined.

In one such experiment, mouse L cell ^3H -DNA from which the satellite had been removed following Ag^+ - Cs_2SO_4 centrifugation (as described in Fig. 30 of the accompanying report) was reduced in piece size to 300 nucleotide pairs by sonication, and reassociated to C_0t 22 in 0.14 M PB at 50°C. Twenty-six percent of the total bound to HAP, and the 14% of the total which eluted above 70° was employed in subsequent steps. Instantaneously reassociating material (23%) was removed from the latter material by incubation to C_0t 4×10^{-5} and passage through HAP. This high thermal stability fraction of mouse DNA, which I shall refer to as Fraction A, yields a product of predominantly high thermal stability when reassociated with unlabeled mouse DNA but one of considerably lower stability with rat DNA (C_0t 4.5 in each case), as shown in Fig. 27. The 63% of Fraction A able to reassociate with rat DNA was isolated in double-stranded form from HAP (0.4 M PB elution of bound material), dialyzed, and treated with S1 nuclease for 2 hours under the high-salt, 37°C conditions of Hutton and Wetmur (1973). Forty-one percent of the radioactivity was rendered dialyzable. Nondialyzable material (Fraction B) was divided in half, reassociated with either mouse or rat DNA to C_0t 16 in 0.14 M PB at 50°, applied to HAP, and eluted in 5°C steps in 0.14 M PB (Fig. 28). The extent of reaction of Fraction B with mouse and rat DNAs was very similar (80% and 74%, respectively), but the two melting profiles are quite different (T_m with mouse DNA about 73°C, with rat DNA about 65°C). Thus, it seems clear that at least some of Fraction B is able to pair with low stability with rat DNA

and with considerably higher stability with mouse DNA. As Fraction B comprises about 4% of total mouse DNA, this subclass amounts to at least 1% of total DNA.

The same format was followed in an

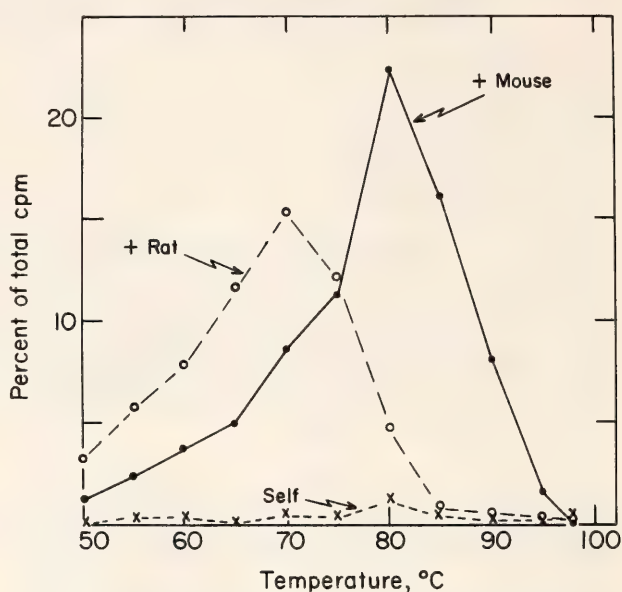


Fig. 27. Reassociation of mouse Fraction A ^3H -DNA (prepared as described in text) with mouse and rat DNAs to C_0t 4.5 in 0.14 M PB at 50°C. Eighty percent of the ^3H -DNA reassociated with mouse DNA and 63% with rat DNA; self-reaction totalled 4%. Bound material was eluted from HAP in 5°C steps in 0.14 M PB, 0.02% SLS.

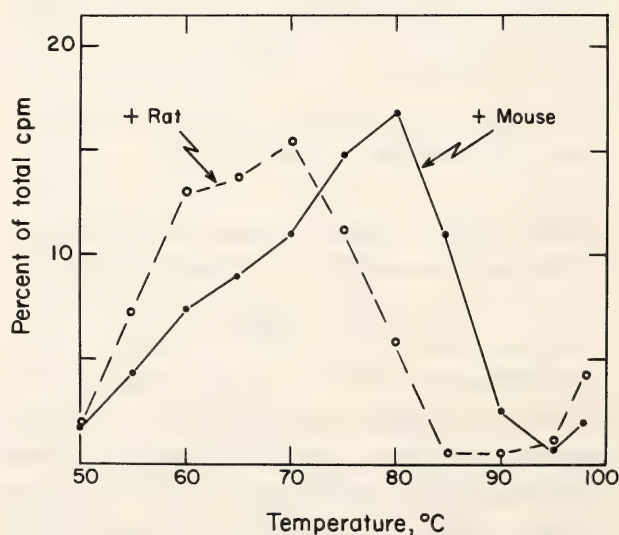


Fig. 28. Reassociation of mouse Fraction B ^3H -DNA (prepared as described in text) with mouse and rat DNAs to C_0t 16 in 0.14 M PB at 50°C. Eighty percent of the ^3H -DNA reassociated with mouse DNA and 74% with rat DNA. Bound material was eluted from HAP in 5°C steps in 0.14 M PB, 0.02% SLS.

experiment with rat ^{14}C -DNA. Twenty-two percent of the total DNA eluted from HAP above 70° following incubation to C_0t 3. Instantaneous binding material (25%) was removed by passage through HAP after incubation to C_0t 2×10^{-5} . Forty-seven percent of the resulting Fraction A was able to reassociate with mouse DNA after incubation to C_0t 1 at 50°C in 0.14 M PB . This material was isolated in double-stranded form and S1-treated as above. Fifty-three percent of the radioactivity was rendered dialyzable. The nondialyzable Fraction B was reassociated with rat or mouse DNA to C_0t 5 (86% and 77% reassociation, respectively) and the two thermal elution profiles determined (T_m with rat DNA about 76°C , with mouse DNA about 68°C) as shown in Fig. 29. Here again Fraction B constitutes about 4% of total rat DNA, and the differentially melting subclass somewhat less.

As with related satellite DNAs, these results imply an evolutionary history involving more than simple random mutation since divergence from the last common ancestor—for in that case ho-

mologous and heterologous melting profiles would be identical. One possible explanation is a mechanism that could maintain a high degree of similarity within a family of repeated sequences in each species. The last common ancestor would have possessed a family, also of limited heterogeneity, the whole of which is the source of the modern rat and mouse families. In each of the diverging lines, members of the family have effectively evolved together. Alternatively, the present rat and mouse families might be amplifications of only two or more individual (and nonidentical) members of a family possessed by the last common ancestor.

References

- Cooke, H. J., Evolution of the long range structure of satellite DNAs in the genus *Apodemus*, *J. Mol. Biol.*, **94**, 87, 1975.
- Gall, J. G., and D. D. Atherton, Satellite DNA sequences in *Drosophila virilis*, *J. Mol. Biol.*, **85**, 633, 1974.
- Hutton, J. R., and J. G. Wetmur, Length dependence of the kinetic complexity of mouse satellite DNA, *Biochem. Biophys. Res. Comm.*, **52**, 1148, 1973.
- Rice, N. R., Change in repeated DNA in evolution, in *Brookhaven Symposia in Biology*, No. 23, H. H. Smith, ed., Gordon and Breach, New York, p. 44, 1972.
- Rice, N. R., and N. A. Straus, Relatedness of mouse satellite DNA to DNA of various *Mus* species, *Proc. Nat. Acad. Sci. USA*, **70**, 3546, 1973.
- Stavnezer, E., Ph.D. thesis, Johns Hopkins University, 1971.
- Sutton, W. D., and M. McCallum, Related satellite DNAs in the genus *Mus*, *J. Mol. Biol.*, **71**, 633, 1972.

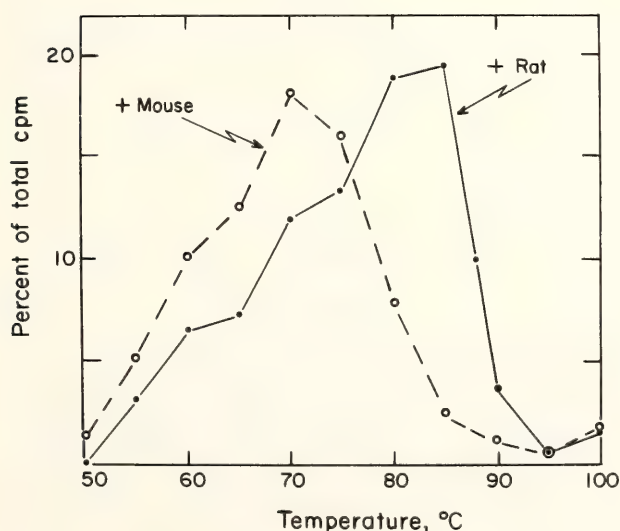


Fig. 29. Reassociation of rat Fraction B ^{14}C -DNA (prepared as described in text) with rat and mouse DNAs to C_0t 5 in 0.14 M PB at 50°C . Eighty-six percent of the ^{14}C -DNA reassociated with rat DNA and 72% with mouse DNA. Bound material was eluted from HAP in 5°C steps in 0.14 M PB , 0.02% SLS.

ARE THERE MOUSE SATELLITE SEQUENCES IN MAIN-BAND RNA?

Nancy R. Rice

Mouse satellite DNA, which is composed of several million very similar

copies of a sequence of 50–100 nucleotides (Waring and Britten, 1966; Rice, 1974), is known to be localized around the centromeres of the mouse chromosomes (Jones, 1970; Pardue and Gall, 1970). Satellite sequences exist in a tightly clustered arrangement. From studies of the effect of molecular weight on percent satellite observable in CsCl density gradients, it was concluded that other, interspersed sequences can account for no more than about 10% (and possibly much less) of total isolated satellite DNA (Rice, 1974). How did such a highly nonrandom arrangement arise? Did mouse satellite originate in one or more noncentromeric regions and eventually, through rapid translocation, become concentrated at the 20 centromeres? Or did it originate in its present locations, from which dispersal by translocation must be quite slow? One approach to this problem is to investigate in a number of different DNAs how the interspersion of satellite and main-band sequences varies with satellite age. I here report progress toward quantifying the extent of such interspersion for mouse satellite DNA.

In the appropriate Ag^+ - Cs_2SO_4 density gradient, DNA molecules consisting solely of satellite DNA fail to bind Ag^+ , while the rest of mouse DNA binds significantly and hence increases in density (Fig. 30). Molecules that consist of partly satellite and partly nonsatellite would be expected to show intermediate binding and to be separable in varying degrees from pure satellite. Hence, one measure of the extent to which satellite sequences are interspersed is the degree to which they can be found linked to non-satellite DNA in such density gradients.

Experimentally I have asked whether nonradioactive main-band DNA contains sequences able to reassociate with trace amounts of isolated mouse satellite ^3H -DNA. From the extent of such reassociation at defined C_0t , the satellite content of the unlabeled DNA can be calculated. Fifty-five μg main-band DNA from the

gradient shown in Fig. 30, for example, was reassociated in $C_0t\ 6 \times 10^{-2}$ in the presence of satellite ^3H -DNA ($0.01\ \mu\text{g}$, $C_0t\ 10^{-5}$, self-reaction, 22%), and 64% of the ^3H cpm were found to bind to hydroxyapatite. From the simple second-order reassociation curve of isolated satellite presented in last year's report (instantaneous binding, 7%; final extent of reassociation, 95%), it follows that there is about eightfold higher satellite content in the incubation mix than in the satellite ^3H -DNA alone and that therefore the main-band DNA contains $7 \times .01 = .07\ \mu\text{g}$ satellite, or $.07/55 = .13\%$ satellite. All main-band DNAs from several other gradients yielded similar results, incubation to $C_0t\ 10^{-2}$

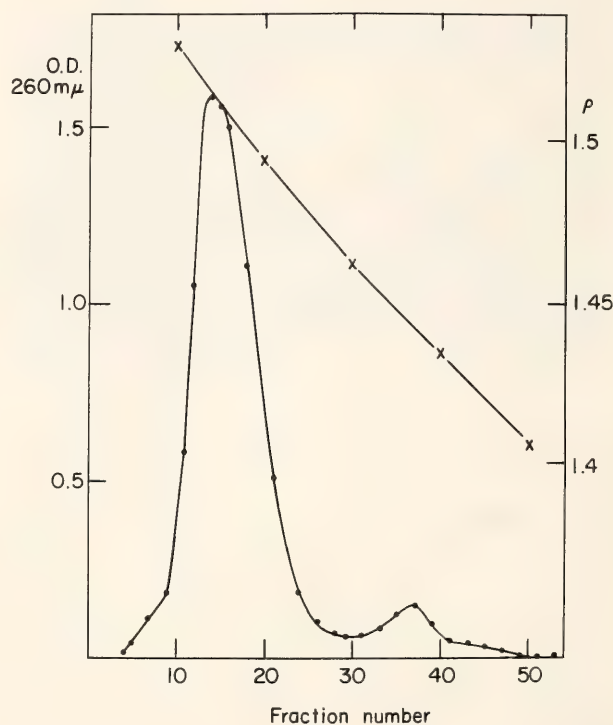


Fig. 30. 2.3 mg mouse DNA in 0.01 M sodium tetraborate, $\text{pH}\ 8.9$, was incubated with AgNO_3 at $\text{Ag}^+/\text{DNA-P} = 0.3$ for several hours at room temperature. Cs_2SO_4 was added to give a refractive index of 1.3722, and the solution was divided among four 40 rotor tubes and centrifuged at 33,000 rpm for 3 days at 19°C . Fractions were collected following tube puncture, and $\text{O.D.}_{260\text{ m}\mu}$ measured after dilution with 0.01 M Tris, $\text{pH}\ 8.8$. (solid circles) Main band DNA (fractions 7–23 in the above gradient) from all four tubes was pooled and dialyzed against 0.01 M Tris, 0.01 M NaCl, 0.001 M EDTA (TNE). Crosses represent density (g/cm^3).

to 6×10^{-2} in the presence of satellite ^3H -DNA resulting in 37–79% of ^3H cpm binding to HAP. Thus, satellite comprises 0.1% to about 0.7% of these main-band DNAs, amounting to up to 10% of total cellular satellite content.

Since this apparent interspersion may result from technical problems of centrifuging and fractionating, I have asked to what extent these satellite sequences remain in main-band DNA through a second cycle of centrifugation. Main-band DNA of Fig. 30, for example, was recentrifuged in a CsCl density gradient, and fractions across the gradient were assayed for satellite content as above. As shown in Fig. 31, the distribution of satellite is clearly different from that of main-band DNA. Satellite sequences are of lower than average density, about 80% of the total occurring in the less dense half of the DNA, and about 50% in the least dense quarter. Since *pure* satellite exhibits very similar banding behavior in such gradients, it is clear that the initial estimate of interspersion is much too high.

Recentrifuging main-band DNA from Fig. 30 in a second Ag^+ - Cs_2SO_4 gradient is even more decisive. As shown in Fig. 32 the majority of satellite sequences bind little or no Ag^+ and appear quite apart from the main-band DNA. Since these molecules traveled *with* main-band DNA in the first gradient, it appears that most of the apparent interspersion results from technical limitations. Satellite content of this second main band is about six times lower than that of the first, and thus amounts to about 0.3% of total cellular satellite DNA. I would predict that a third centrifugation cycle will reduce this even further. For the present, however, taking 0.3% as the upper limit for satellite interspersion, it can be calculated that up to about 15,000 of the more than four million satellite sequences could be linked to nonsatellite molecules.

References

Bond, H. E., W. G. Flamm, H. E. Burr, and S. B. Bond, Mouse satellite DNA, further studies on its biological and

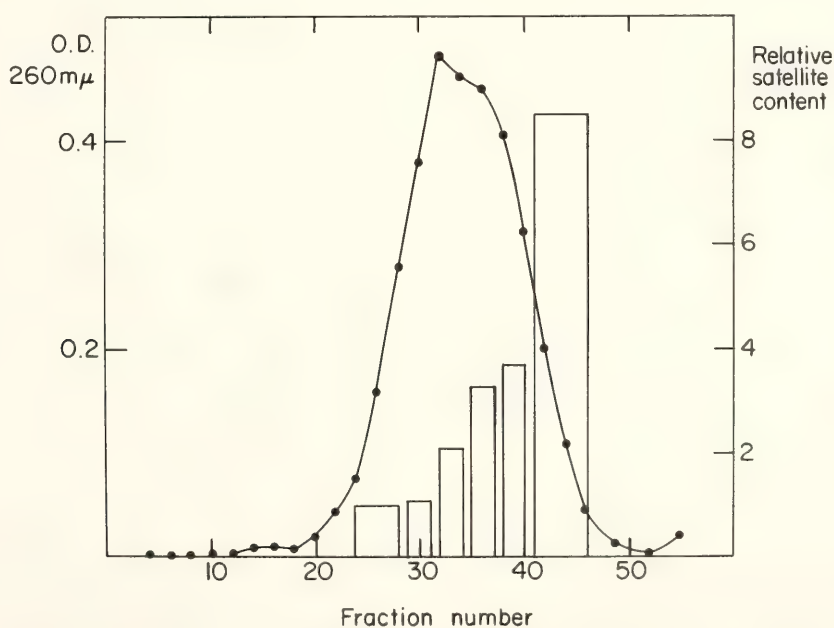


Fig. 31. 300 μg main-band DNA from Fig. 30 was dialyzed against TNE and then centrifuged in a preparative CsCl density gradient for 3 days at 33,000 rpm at 19°C in the 40 rotor. Fractions were collected following tube puncture. $\text{O.D.}_{260\text{m}\mu}$ of diluted fractions was determined, and indicated fractions were pooled and dialyzed against 0.01 M phosphate buffer (PB). Each pool was reassociated with 0.01 μg mouse satellite ^3H -DNA (self-reaction 22%, C_{ot} 10^{-5}) in 0.14 M PB at 50°C , and the extent of binding of ^3H cpm to hydroxyapatite determined. Satellite content of each pool was calculated as described in the text.

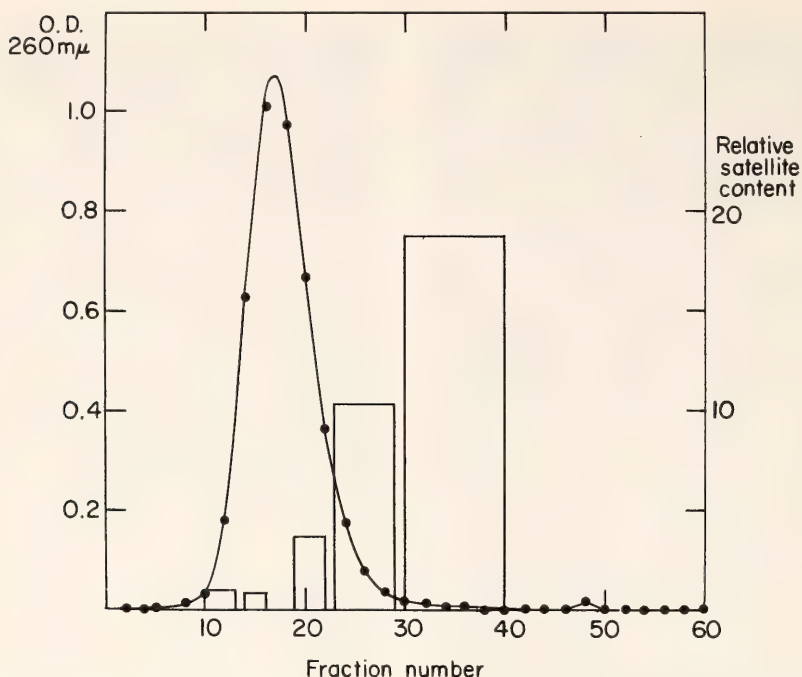


Fig. 32. 300 μ g main-band DNA from Fig. 30 was dialyzed against TNE, then against several changes of 0.002 M sodium tetraborate. The solution was brought up to 0.01 M sodium tetraborate, incubated with AgNO_3 at $\text{Ag}^+/\text{DNA-P} = 0.3$ for several hours at room temperature, then centrifuged with Cs_2SO_4 at 33,000 rpm for 3 days at 19°C. Fractions were collected following tube puncture. Diluted fractions of O.D._{260 mμ} were pooled, dialyzed against TNE, and assayed for satellite content as described in Fig. 31.

physical characteristics and its intracellular location, *J. Mol. Biol.*, **27**, 289, 1967.

Jones, K. W., Chromosomal and nuclear location of mouse satellite in individual cells, *Nature*, **225**, 912, 1970.

Pardue, M. L., and J. G. Gall, Chromosomal localization of mouse satellite DNA, *Science*, **168**, 1356, 1970.

Rice, N. R., Fine structure in mouse satellite DNA, *Carnegie Inst. Wash. Year Book* **73**, p. 1088, 1974.

Waring, M., and R. J. Britten, Nucleotide sequence repetition: a rapidly reassociating fraction of mouse DNA, *Science*, **154**, 791, 1966.

REPEATED DNA AND SPECIATION

*R. B. Roberts, N. R. Rice,
and N. W. van de Velde*

Year Book 64 reports the discovery of repeated DNA, and the same Report includes consideration of the role of repeated DNA in evolution. *Year Book 65* points out that the formation of a new family is a more drastic and possibly

more significant event than the slow changes produced by accumulation of mutations. The suggestion is made that family formation may be related to sudden evolutionary changes such as bursts of speciation. This theme is elaborated in *Year Book 67* which quotes G. C. Simpson who indicates that sudden drastic changes are evident in the fossil record.

This year a report by S. M. Stanley provided the clue for a partial test of the hypothesis that family formation is necessary (but perhaps not sufficient) for speciation. He has calculated that the rate of speciation is three times more rapid in mammals than in molluscs. Accordingly, if family formation is necessary for speciation, we would expect to find three times more repeated DNA in mammals than in molluscs.

Accordingly, we have extracted DNA from clams and oysters to determine whether this expectation is borne out. Preliminary measurements show relatively little repeated DNA in these organisms, 14% in the oyster and 19%

in the clam (compared to 30%–50% in most mammals). Furthermore, these low figures may be too high if the DNA used is contaminated by DNA from bacteria or other microorganisms growing within the molluscs.

Thus, the early results are consistent with the hypothesis that family formation is necessary for speciation. Measurements of many other organisms would be needed to establish a firm correlation between the rate of speciation and the rate of family formation. Ordinarily we would not include such preliminary observations in our report. However, as this may be the last report of the Biophysics Section, they are included in the hope that someone may be stimulated to carry out the needed work.

Reference

Stanley, S. M., A theory of evolution above the species level, *Proc. Nat. Acad. Sci. USA*, **72**, 646, 1975.

A DISTINCTIVE FEATURE OF THE HUMAN GENOME

Bill H. Hoyer, Richard B. Roberts, Nancy R. Rice, and Neltje W. van de Velde

Other evidence is consistent with the hypothesis that the formation of new families may be necessary for the formation of new species. In several closely related rodents, families of DNA sequences are found which react to form highly stable complexes with homologous DNA but which react to give only quite unstable complexes with the DNA of the near relative. This situation has been described in *Year Book* **71**, p. 264; **72**, p. 197; and **73**, p. 1098. This year we have examined the human DNA to determine whether it contained any such DNA different from the DNA of the closely related chimpanzee.

Highly radioactive human DNA was incubated to C_0t 100 and then adsorbed on hydroxyapatite and eluted in 2.5° temperature steps. The material which was highly stable (eluting at 87.5°) was

collected and any instantaneous binding material removed by passing through the column after an extremely short incubation. The resulting fraction was then reacted with an excess of nonradioactive DNA from human, chimpanzee, or *E. coli*. After incubation to C_0t 100 the three different samples were adsorbed to the column and eluted by a temperature gradient. The elution diagrams showed two major peaks, one at 72° and one at 85°. Both are present after incubation with *E. coli* DNA and can be attributed to self-reaction among the tracer molecules. Incubation with chimpanzee DNA increases only the 72° peak, while incubation with human DNA results in a large increase in the 85° peak. We believe that this fraction is due to a new family of DNA sequences which was formed after (or possibly as the cause of) the divergence of the human and chimpanzee lines.

This experiment has been repeated in slightly different circumstances three times but much remains to be done. Ordinarily such preliminary observation would not be reported at this time. However, it is of considerable interest to find a fraction of the human DNA (approximately 1%) that does differ markedly from that of chimp. The bulk of human DNA differs from chimpanzee in only 1% of the nucleotides. Since these findings may not be followed up in this laboratory, we considered that the results should be reported.

PROTEIN-PROTEIN INTERACTIONS

Dean B. Cowie, Georges N. Cohen,
and Paolo Truffa-Bachi**

Cellular activities are regulated by two main mechanisms. One, operating at the genetic level, controls the rate of translation of genetic material into specific messenger RNAs and has been the subject of many studies which can be

*Institut Pasteur, Service de Biochimie Cellulaire, Paris, France.

grouped under the generic name induction-repression mechanisms. The second regulates the activity of already synthesized proteins by modifying them either covalently (phosphorylation, adenylation, ADP-ribosylation, etc.) or by changing their conformation by an allosteric transition under the influence of small ligands which act as modulators or transducers. These covalent or conformational changes lead to an increase or decrease of catalytic activity, always in the "interest" of the cell economy. We have been interested in the latter mechanism for several years and have chosen to study the conformational changes caused by ligand binding (the ligand being either substrates or feedback inhibitor) to aspartokinase I-homoserine dehydrogenase I of *Escherichia coli*, an enzyme occupying a key position in the biosynthesis of several essential metabolites.

The ways to detect changes are numerous, from the ones that detect gross conformational changes, such as optical rotatory dispersion or hydrogen-deuterium exchange, to those which detect

changes in the environment of specific aromatic residues, by difference spectroscopy or fluorescence. Many of these methods have been applied to the enzyme under study. We have focused our attention on the conformational changes brought about by the reaction of the protein with specific antibodies, and on qualitative and quantitative effects of the various ligands of the protein on this reaction.

Activity of the Antibody-bound Enzyme

Antibody binding inhibits the activity of some enzymes completely, some partially, and others not at all. In some instances, antibody-induced enzyme activation has been reported (Cinander, 1967; Cowie *et al.*, 1961).

We have investigated the interaction of the allosteric enzyme aspartokinase I-homoserine dehydrogenase I (AKI-HDHI) with antibodies specific for this protein. This report concerns some of the characteristics of this antibody-antigen complex in terms of the activity of the homoserine dehydrogenase and

TABLE 3. Reduction of Homoserine Dehydrogenase Activity upon Binding of Aspartokinase I-Homoserine Dehydrogenase I to its Specific Immunoabsorbent*

Experiment Number	Units Bound Enzyme	Units Enzyme Activity on the Column (maximum)	Percent
1	3000	525	18
2	2300	520	23
3	2200	320	28
4	1950	300	41
5	1100	400	36
6	1000	250	25
7	1050	450	43
8	1000	215	22
9	1300	430	33
10	1550	300	19
			av. = 28.8

* Various nonsaturating quantities of AKI-HDHI were loaded on the immunoabsorbent column in buffer (0.5 ml–2.0 ml, pH 7.2). Buffer washes (70–300 ml) were then percolated through the column, and the HDH activity of the eluate fractions assayed. The total activity found in the eluates is subtracted from the units loaded on the column to determine the units of antibody-bound enzyme. The quantity of eluted enzyme is usually only a few percent of the quantity loaded. The column volume was 2.0 ml, and the diameter of the column was 2 cm. HDH activity of the antibody-bound enzyme was determined by percolating substrate solution through the column at a fixed rate (see text).

its threonine sensitivity. HDH activity is measured in the direction $\text{HS} \rightarrow \text{ASA}$ by the method of Patte *et al.*, using HDH substrate solution: 10 ml *M* Tris, pH 9.0; 25 ml *M* KCl; 10 ml 2.5 *M* L-homoserine; and 10 mg NADP.

Immunoabsorbent columns were prepared containing antibodies specific for AKI-HDHI (Cowie *et al.*, 1973). Usually a column was loaded with a non-saturating quantity of purified enzyme and washed with buffer (20 mM potassium phosphate, pH 7.2, and 0.15 *M* KCl) to remove unbound enzyme. The homoserine dehydrogenase activity and the threonine sensitivity of the antibody-bound enzyme can be easily determined by flowing substrate solution (in the presence or absence of feedback inhibitor) through the column and measuring, immediately after elution, the absorbency of the eluates at 340 nm. The enzyme activity on the column can be calculated from the absorbency values and the flow rate of the substrate solution (Feldmann *et al.*, 1972; Cowie *et al.*, 1974). From the kinetic studies presented below it can be seen that this immunoabsorbent method has unique advantages for the study of slow kinetic reactions.

Table 3 demonstrates that only a portion of activity of the homoserine dehydrogenase loaded on the column remains active. Figure 33 shows that a maximum of enzyme activity is observed soon after the substrate solution is added to the column. In some instances, where the initial observed enzyme activity exceeds 25% of the load (Table 3), there is a slow decrease in the column activity until a value is reached equal to approximately 25% of the activity of the load (Fig. 33). The activity of the antibody-bound enzyme does not appear to be sensitive to enzyme concentration (over the range studied, Table 3).

The antibody-bound enzyme is only slightly sensitive to L-threonine inhibition. Figure 33 shows that there is approximately a 10% inhibition when the substrate solution is supplemented with

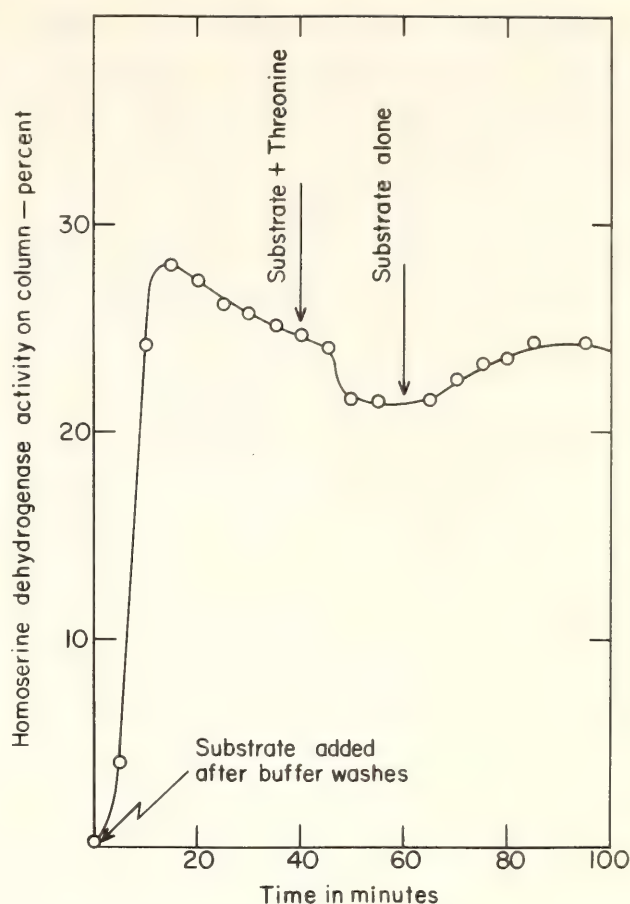


Fig. 33. Homoserine dehydrogenase activity observed on the antibody column during percolation with substrate solution. After loading with a non-saturating quantity of HDH, the column was washed for 70 minutes (300 ml buffer, pH 7.2) before the percolation with substrate solution was started. After 40 minutes the substrate solution was supplemented with L-threonine (2×10^{-3} *M* final concentration); at 60 minutes unsupplemented substrate solution was employed. The flow rate of the substrate solution was 0.9 ml/min, and samples were taken every 5 minutes. At the time the substrate solution was first added to the antibody column the quantity of bound HDH was 2200 units; the percentages given are the observed HDH activities on the column relative to this quantity of bound enzyme. Other column details are as given in Table 3.

L-threonine (final concentration 2×10^{-3} *M*). Restoration of the antibody-bound enzyme activity (—10%) occurs when the threonine is removed.

During the passage of substrate through the column there is little removal of active homoserine dehydrogenase from the antibody-enzyme complex. This can be shown by measuring the change in absorbency, with time, of each eluate fraction after the initial

absorbency determination has been made. Only a few percent of the activity of the enzyme load appears in the eluate washes, and for the most part in the early eluate fractions.

It is evident that the antibody-bound enzyme exists in a conformational state quite different from that of the free enzyme in buffer—where the threonine inhibition is 70% and the enzyme, in the absence of threonine, is fully active.

When the same type of kinetic experiments are repeated with the substrate solution supplemented with 2×10^{-3} M L-threonine, completely different results are obtained.

Figure 34 shows that under these conditions the homoserine hydrogenase activity of the antibody-bound enzyme can

initially be as much as 50% of the activity of the free enzyme. Furthermore, *removal* of the threonine from the percolating substrate solution results in a slow *inactivation* of the antibody-enzyme complex, which then can be partially reactivated by addition of threonine to the substrate solution.

These results suggest that the enzyme, loaded and bound to the antibody (in buffer at pH 7.2) can slowly assume a new conformation state which *in presence of threonine* and the other ligands contained in the substrate solution (at pH 9.0) is *more active* than the free enzyme in the presence of the same amount of threonine. That threonine plays a major role in such a conformational transition can be demonstrated

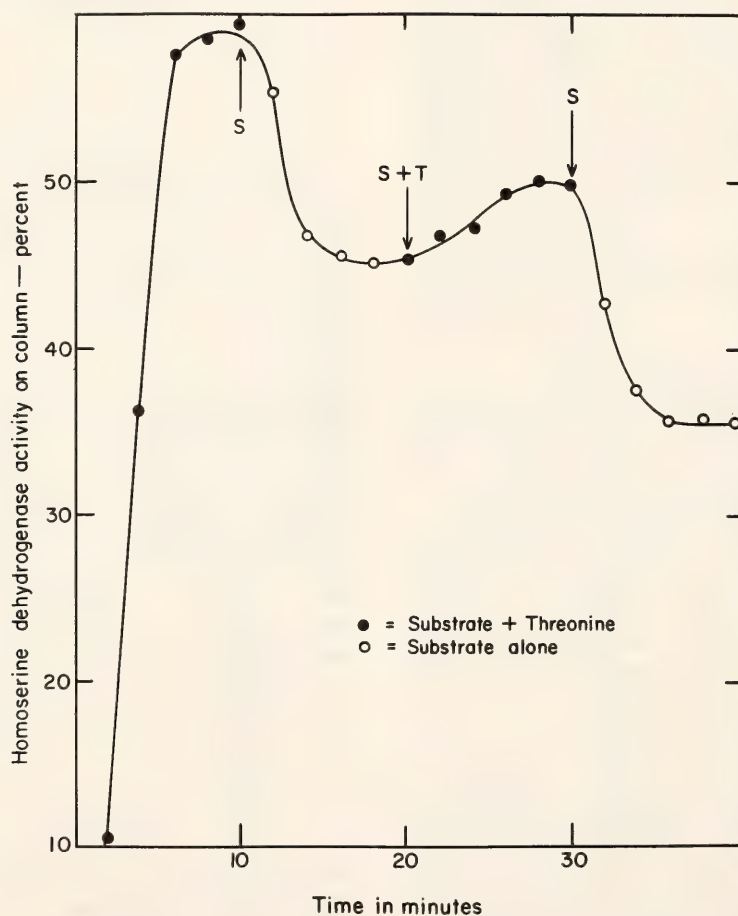


Fig. 34. Homoserine dehydrogenase activity observed on the antibody column following percolation with threonine supplemented (2×10^{-3} M) substrate solution. Buffer wash procedure as in Fig. 33. At the times indicated, unsupplemented (or threonine-supplemented) substrate solutions were used for further percolation. A continuous flow rate of 2.7 ml/minute was used, and samples were taken every 2 minutes. The quantity of bound HDH at the end of the buffer wash was 1400 units. The percentages given in this figure are the observed HDH activities relative to this quantity of bound enzyme. Other column details are as given in Table 3.

by the data of Fig. 34 in which only the removal of threonine from the substrate solution causes a reduced activity of the antibody-enzyme complex.

A more dramatic presentation of the phenomenon is shown in Fig. 35. Here, repeated oscillations in enzyme activity are produced by the alternative removal and restoration of threonine to the substrate solution.

It should be noted that the effect of the threonine supplementation diminishes with time. In addition, the time required to go from the most to the least active conformational state is of the order of 10 minutes. In these experiments, the flow rate of the percolating substrate solution was 2.3 ml per minute; the volume of the column was 2.0 ml; and each sample took 2 minutes to collect. Thus, in less than a minute all of the individual enzyme-antibody complexes were exposed to each change of environmental conditions.

During the course of this experiment

there was some loss of active enzyme to the eluates. The total active enzyme lost during the 90 minutes amounted to 10% of the quantity of enzyme initially bound to the antibody column.

The results reported above are markedly different from those reported last year (Cowie *et al.*, 1974) when similar studies were carried out. The only experimental difference between the two sets of experiments is the buffer wash procedure which was added to this year's studies. Very little enzyme is eluted by the buffer wash, and it has been concluded that the time the enzyme remains bound to the antibodies (before assaying with substrate solution) has a significant bearing on the state of the enzyme. This conclusion is supported by the following observations.

The minimal time consumed by the buffer wash procedure was 70 minutes. When a nonsaturating load of enzyme is added to the column in buffer and allowed to stand for 70 minutes before

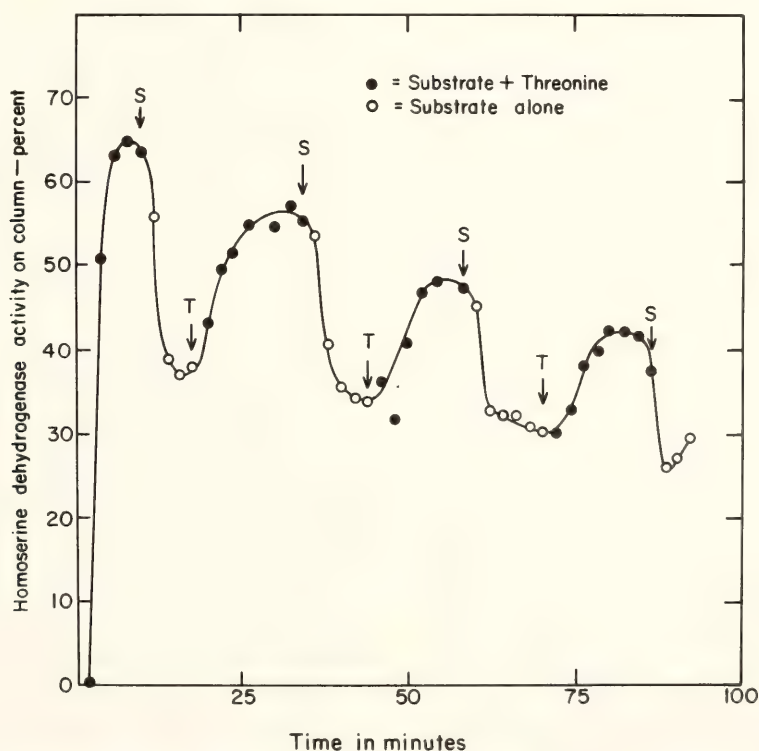


Fig. 35. Homoserine dehydrogenase activity observed on the antibody column following percolation with threonine-supplemented ($2 \times 10^{-3} M$) substrate solution. Buffer wash procedure as in Fig. 33. At times indicated, supplemented or threonine-supplemented substrate solutions were used for percolation. A continuous flow rate of 2.3 ml/minute was used, and samples were taken every 2 minutes. The quantity of bound HDH at the end of the buffer wash was 1400 units. The percentages given in this figure are the observed HDH activities relative to this quantity of bound enzyme. Other column details are as given in Table 3.

assaying with substrate solution, the characteristics of the antibody-bound enzyme are found to be identical to those shown in Fig. 33. The HDH activity was about 25% of the activity of the enzyme load and only slightly sensitive to threonine.

Additional studies, investigating the state of the antibody-bound enzyme immediately after the enzyme has been loaded on the column, gave results typical of those shown in Fig. 36.

A maximum of enzyme activity is observed soon after the flow of substrate solution is initiated. This is followed by a rapid loss of antibody-bound enzyme activity which eventually decreases asymptotically to a slower rate. The maximal enzyme activity observed on the column varies between 55% and 70% and depends upon the flow rate of substrate solution. The optical density of the eluate increased with time, showing that enzyme is released from the column (Fig. 36 inset).

The biphasic nature of the data (Fig. 36) indicates that the loss of activity of the antibody-bound enzyme involves more than a single process. The appearance of active enzyme in the eluates indicates that some dissociation of the enzyme from antibody binding does occur when substrate solution (at pH 9.0) is percolated through the column. However, sufficient active enzyme is not recovered in the eluate fractions to account for the loss of activity of the antibody-enzyme complex. During the first 30 minutes of this experiment the *observed* loss of the column activity (maximum value, 56% of load activity) dropped by 31% of the activity loaded on the column. Over this period of percolation of substrate, only 15% of the total load of enzyme activity was recovered in the eluate fractions.

Initially the antibody-bound enzyme is sensitive to threonine; however, during the inactivation process, there is a corresponding decrease in threonine sensitivity. At the end of 50 minutes the

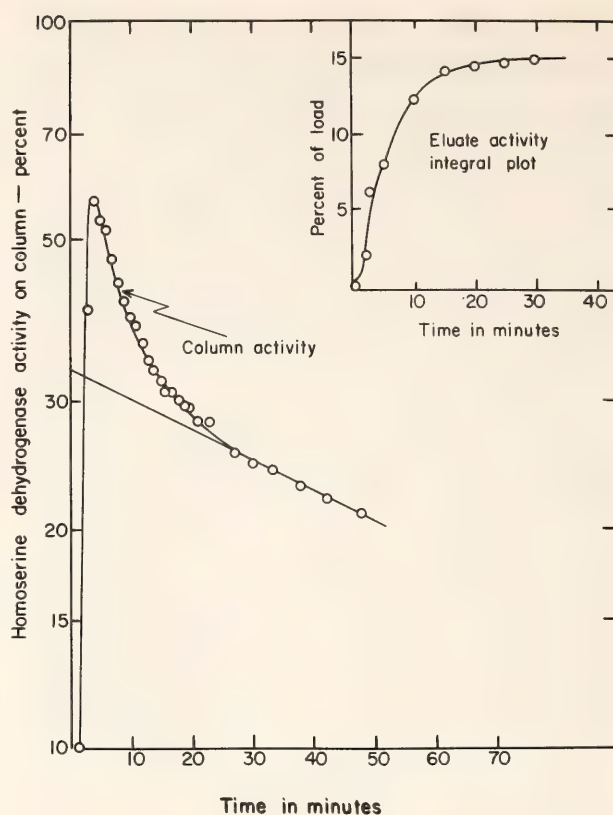


Fig. 36. Homoserine dehydrogenase activity observed on the antibody column following percolation with substrate solution which was added immediately after loading the column with HDH. The buffer wash procedure was eliminated. The flow rate was 2.7 ml/minute, and samples were taken every minute. The inset figure shows the cumulative values of actual enzyme appearing in the eluate during the course of the experiment. The percentages given in this figure are the observed HDH activities relative to the activity of the load of 2800 units of HDH. Other column details are as given in Table 3.

threonine inhibition is only about 10%.

The above results suggest that as soon as the antibody-enzyme complex is formed, inactivation of HDH is initiated. Furthermore, the substrate solution (pH 9.0) dissociates a portion of the enzyme from the antibodies, a process not observed when buffer (pH 7.2) is percolated through the column. The activity of the enzyme-antibody complex, even in buffer at pH 7.2, however, decreases from the time the enzyme becomes bound to the antibody column.

Figure 37 shows the results of another experiment in which substrate solution, supplemented with $2 \times 10^{-3} M$ L-threonine, is percolated through the col-

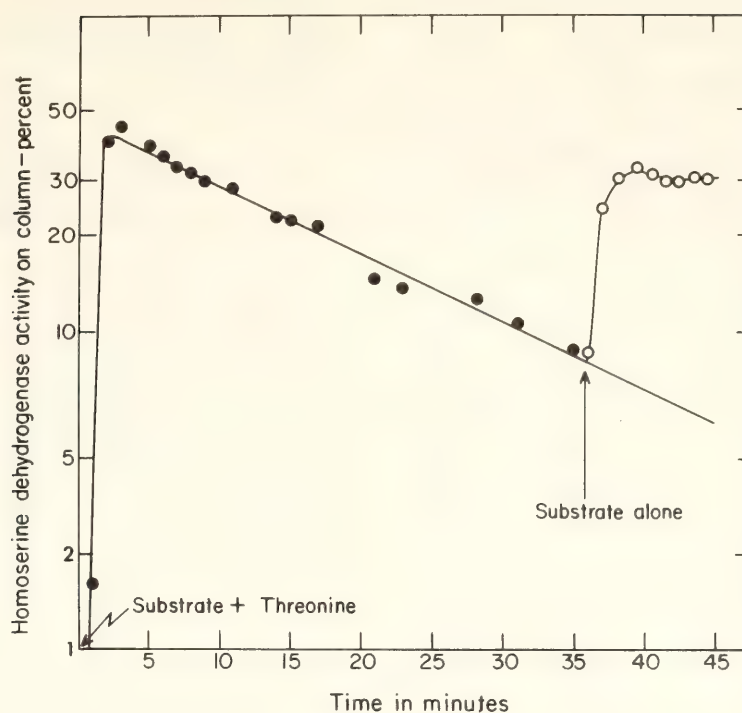


Fig. 37. Homoserine dehydrogenase activity observed on the antibody column following percolation with threonine-supplemented ($2 \times 10^{-3} M$) substrate solution. The buffer wash procedure was eliminated. The flow rate was 2.7 ml/minute, and samples were taken every minute. At 36 minutes unsupplemented substrate solution was used. The percentages given in this figure are the observed HDH activities relative to the activity of the load of 900 units of HDH. Other column details are as given in Table 3.

umn immediately after the addition of a nonsaturating enzyme load. Under these conditions, the loss of activity of the antibody-enzyme complex can be represented as a single exponential. Furthermore, removal of the threonine from the substrate results in an increase of HDH activity (Fig. 37). This increase reaches a value which, when compared to the activity on the column immediately before the removal of threonine, shows that the activity remaining on the column is normally inhibitable by threonine. The same degree of recovery of enzyme activity with the removal of threonine from the substrate solution occurs over the entire course of the experiment. Thus, other than the overall loss of enzyme activity on the column, the antibody-enzyme complex reacts to threonine just like the soluble enzyme.

As in the previous experiment, Fig. 36, the recovery of active enzyme in the eluate fractions is inadequate to compensate for the observed loss of column

HDH activity. About 15% of the activity was eluted during the first 36 minutes of substrate percolation; the decrease in column activity over the same period of time was 33%. This indicates that either inactive protein is being eluted or that the antibody-bound enzyme is being inactivated during the time of the experiment (or that both processes are occurring). Since the quantity of protein eluted in these experiments is so low, its determination depends upon the use of labeled enzyme preparations. Such a study is now under way.

One can conclude from these studies that there are conditions under which the antibody-enzyme complex can behave like the free enzyme in solution. This conformation is observed before the enzyme has had sufficient time to undergo a conformational change imposed upon it by its antibodies and is observable following loading of the enzyme on the antibody column and

percolating immediately with substrate solution (\pm L-threonine).

Conversely, if the enzyme is allowed to react for a sufficient time with the antibodies, it undergoes gradually an irreversible conformational change, resulting eventually in the loss of 75% to 80% of the original activity and in the loss of its sensitivity to threonine. During the process of the temporal inactivation by the antibodies the addition of threonine retards the ultimate formation of the irreversible configuration, producing a paradoxical increase in the apparent conformation of the enzyme less susceptible to antibody inactivation.

The use of antibodies has allowed us to probe some of the conformational changes of the enzyme other than those imposed upon it by the allosteric equilibria which can be displaced by its specific ligands. It is also felt that such studies may provide some information regarding the antigen-antibody reaction itself.

References

- Cinander, B., Antibodies to enzymes—a discussion of the mechanisms of inhibition and activation, *Proc. 2nd Meeting of the Federation of European Biochemical Societies*, p. 85, Vienna, Austria, April 21–24, 1965.
- Cowie, D. B., S. Spiegelman, R. B. Roberts, and J. D. Duerksen, Ribosome-bound-galactosidase, *Proc. Nat. Acad. Sci. USA*, **47**, 114–122, 1961.
- Cowie, D. B., P. Truffa-Bachi, J. M. Costrejean, M. C. Py, and G. N. Cohen, A preliminary immuno-chemical study of *E. coli* aspartokinase I-homoserine dehydrogenase I. *Biochem. Biophys. Res. Comm.*, **53**, 188–193, 1973.
- Cowie, D. B., G. N. Cohen, and P. Truffa-Bachi, Protein-protein interaction, in *Carnegie Inst. Wash. Year Book* **73**, pp. 1064–1088, 1974.
- Feldmann, K., H. Zeisel, and E. Helmreich, Interaction between native and chemically modified subunits of matrix-bound glycogen phosphorylase, *Proc. Nat. Acad. Sci. USA*, **69**, 2278–2282, 1972.

HISTORICAL REVIEW OF BIOPHYSICS SECTION

R. B. Roberts

Formation of the Section

At this time, when the 30-year existence of the Biophysics Section is in the final stage of termination, it seems appropriate to look back at its history and accomplishments. A Biophysics Section was first authorized by Vannevar Bush in 1946 during M. A. Tuve's first year as Director of the Department. Its origins can be traced further back. The first publication in the area of biophysics appeared in 1931 on "Biological Effects of Gamma Rays." This subject was timely in anticipation of the exposure of laboratory workers to intense sources of radiation which would be produced when the disintegration of nuclei by artificially accelerated particles was achieved (1932).

Following this discovery and the discovery of artificial radioactivity (1934), nuclear physics equipment and techniques became very attractive to the biological community. During the late 1930's the Department had available two of the relatively scarce accelerators, and there is no wonder that biologists wanted to share these facilities. Effects of gamma rays, neutrons, and charged particles on all sorts of biological material needed study. More importantly, radioactive isotopes of most elements could be produced and used as tracers to answer questions previously unapproachable. Many such experiments were carried out using the two Van de Graaff accelerators then in operation. As examples, fruit flies were bombarded with neutrons for Demerec; in 1938 ^{24}Na was produced and used to study the flow of material from mother to embryo in rats (this study is now reprinted in *Classic Papers in Obstetrics and Gynecology*);

^{11}C was used to study the uptake of CO_2 in photosynthesis in 1940.

In fact, these activities infringed seriously on the time available for nuclear physics. Tuve then persuaded Bush to provide funds for the construction of a large cyclotron with capacity to provide tracers for the entire Carnegie Institution and the Washington area. The design of this machine and the associated laboratory was started in early 1939. The war years then intervened, but the cyclotron was completed in 1942. It was used during the war to produce radioactive isotopes of arsenic and antimony for studies of tropical medicine for the Navy, and later to produce isotopes for general distribution.

At the conclusion of the war Tuve became Director of the Department and brought about a reorientation of the Department's program. In particular, nuclear physics had received a tremendous emphasis from the development of the atom bomb and seemed destined to be carried out by large groups with unlimited money. In contrast, biophysics appeared to be more suitable for small groups and (with the advent of tracers) due for a burst of progress. In addition, our prewar experience had demonstrated that physicists could contribute to biology not only in technique but in the planning of experiments. Tuve therefore decided to reduce the emphasis on nuclear physics and to initiate a Biophysics Section. At this initial stage the group included P. H. Abelson (chairman), D. B. Cowie, and Roberts, all trained in physics. In addition, we were fortunate to have with us H. H. Darby and W. R. Duryee as guest investigators who provided a much needed wealth of biological experience.

The experiments of the first years (1947–1951) were largely exploratory, including such diverse topics as capillary permeability and the effects of ultraviolet radiation, vitamin B_{12} , and various ions on biological material. The biological materials used ranged from humans to

bacterial viruses, but following one staff member's participation in the bacteriophage course at Cold Spring Harbor there was a steadily increasing use of the bacterium *Escherichia coli* as the best suited to our interests (see CIW Publ. 624, pp. 656–690, 692–695).

Biosynthesis of Small Molecules

By 1952 our interests had focused on the synthesis of amino acids and nucleotides by *E. coli*, and this subject was studied intensively through 1955, culminating in the publication of *Studies of Biosynthesis in E. Coli*. During this period the method of isotopic competition was introduced and used extensively. As an example of this method, bacteria are provided with radioactive glucose as a carbon source, and an appropriate nonradioactive amino acid is added to the medium as a competitor. After a period of growth the cells are harvested; their proteins are isolated, and the amino acids of the proteins examined. Radioactivity does not appear in the amino acid that was added or in the other amino acids derived from it. From such results it is possible to deduce the pathways of synthesis in the cell and to calculate the flow along each pathway. Such calculations demonstrated the importance of the Krebs's Cycle (previously recognized as a component of carbohydrate catabolism) in the synthetic activities.

Furthermore, the replacement of one carbon source by another was not simply due to dilution but to the abrupt termination of synthetic activities no longer needed. These changes were described at the time as a chemical response and contrasted to the biological response of a reduction in the synthesis of enzymes that were no longer needed. These two processes are now termed "feedback inhibition" and "enzyme repression." The results of these years are described in CIW Publication 607, *Studies of Biosynthesis in Escherichia coli* (1955).

Metabolic Pools

Having a quite complete flow pattern for carbon in *E. coli*, we chose not to continue this work in other organisms but to investigate the properties of the "pools" in which the small building blocks of protein and nucleic acids are held in the cell prior to incorporation into the macromolecules. These compounds are concentrated by the cells, and it appeared that the mechanisms for their concentration might be related to the machinery for synthesis. This subject was investigated in both *E. coli* and yeast. It turned out to be extremely complicated: Some amino acids competed with others for entry into the cell; some compounds were incorporated into macromolecules without equilibrating with pools already present in the cell. The results had to be interpreted in terms of what we called a carrier molecule. The term "permease" (used by the Pasteur group and now generally accepted) was distasteful to us because at that time there was little evidence that an enzyme was involved.

These studies turned out to yield little information concerning the mechanisms of macromolecular synthesis, but the knowledge of the properties of the pools and the kinetic delays that they introduce was essential to the proper interpretation of later studies of protein and ribosome synthesis. They are included in the material of CIW Publication 624, *Studies in Macromolecular Biosynthesis*, 1964.

Experimental work on the properties of the pool did not terminate abruptly; in fact, further information became essential and our last paper on pools was not published until 1963. After 1957, however, interest shifted increasingly to larger components of the cell. At that time the literature carried reports that a fraction had been isolated from disrupted animal cells which contained ribonucleoprotein particles mixed with fragments of membranes. This fraction had also been shown to be rich in newly

formed protein. Similar ribonucleoprotein particles (now termed ribosomes) had been found in bacteria. Our attention shifted to these particles and their possible involvement in protein synthesis.

Macromolecules

By 1959 methods had been developed to keep the particles stable for fractionation either by sedimentation or on DEAE columns. However, we found no indication that the particles carried newly formed protein. The difficulty lay in the small quantity and rapid turnover of the nascent protein. Further experiments were carried out (with the participation of K. McQuillen) in which the period allowed for protein synthesis was decreased from minutes to a few seconds and the nascent protein was clearly shown in association with the ribosomes. This experiment showed for the first time that the machinery of protein synthesis consisted of ribosomes and not the other components of the microsome fraction. Further work along these lines (with S. Spiegelman) showed a small fraction of beta-galactosidase associated with ribosomes. Furthermore, these ribosomes could be precipitated by addition of antibody to the enzyme followed by addition of antibody to the first antibody. Thus a method was available to select a particular class of ribosome. Currently this procedure is used in radioimmunoassays and RNA messenger isolation.

Numerous other studies of ribosomes culminated in a series of four papers which described the kinetics of synthesis of ribosomes including both the nucleic acid and the protein components. Two sequential classes of precursors (which we called eosomes and neosomes) were clearly observable and seemed to account for most of the newly formed RNA of the cell.

Just at that time the messenger theory of Monod was promulgated. This theory predicted that newly formed RNA had only a transient existence and was

broken down after serving as template for protein synthesis. The base composition of the newly formed RNA was predicted to be similar to DNA and different from ribosomal RNA and RNA of DNA-like composition that had been observed under special conditions. This did not agree with our observations that most newly formed RNA was ribosomal precursor. This discrepancy was resolved by a series of experiments (Midgley) that measured the composition of RNA in a series of bacteria of different DNA compositions. The RNA changed in composition with time of exposure to the tracer, indicating that roughly one-third was DNA-like RNA and had a rapid turnover. The remaining two-thirds of the RNA was stable ribosome precursor. These findings should have settled the issue; one-third of the newly formed RNA had the properties predicted for messenger. However, for a number of years thereafter, newly formed RNA was considered to be entirely messenger by most workers in the field.

More direct evidence was needed to convince the doubters since measurements of composition could detect the messenger but did nothing to isolate it. Bolton and McCarthy then devised a method for immobilizing single-stranded DNA by trapping it in agar. RNA could then be incubated with the single-stranded DNA, and RNA strands could be bound to its complementary DNA. This procedure allowed the separation of messenger RNA from ribosomal RNA since there were relatively few sites where the ribosomal RNA could be bound. Unbound RNA was then washed out and the bound RNA recovered by washing with a different solution or at a higher temperature. Messenger RNA was isolated in useful quantities free from the much more abundant ribosomal RNA. This method brought about a notable advance in the study of DNA-RNA interactions as the earlier methods were either tedious or not generally applicable.

The development of the agar column brought about a major shift in the program of the section as it rapidly became apparent that here was a procedure which allowed exploration of entirely new areas. These developments will be described below.

In addition to the main theme of ribosomes, ribosome synthesis, and messenger RNA outlined above, many other aspects of protein synthesis were studied concurrently. These include work on enzyme induction and the incorporation of analogs. This experimental work (up to the use of the agar column) is gathered together in *Studies in Macromolecular Biosynthesis*, CIW Publication 624 (1964).

Nucleic Acid Interactions

The procedure for trapping DNA in agar was developed in the spring of 1962, and its use in isolating messenger RNA is briefly mentioned in *Year Book 61*. In the following year the method was used extensively. The kinetics of synthesis of messenger RNA was observed, and the relative proportions of different classes of messenger RNA were estimated. The reaction specificity was determined, and it was found that unrelated RNA would not bind, but RNA from closely related species did bind to some extent.

The first experiments used RNA to bind to a DNA column; subsequently DNA-DNA reactions were investigated. This technique was utilized to show both the degree of relatedness among different bacteria and the homology between *E. coli* DNA and the DNA of its lysogenic phage lambda.

Reports in the literature stated that renaturation of DNA from animals did not occur. This result seemed plausible because of the much larger genome and the corresponding dilution of individual genes. In spite of this, highly successful experiments were conducted using animal DNAs. The report in *Year Book 62* includes measurements showing the degree of relatedness for various organisms,

from *E. coli* to man (see Table 4). Within the first year the versatility of the method and its application to a wide variety of problems including taxonomy and evolution had been demonstrated.

The following year saw further use and development of the agar column. Competition was introduced as an additional tool. Here the similarity of two nucleic acids is shown by their ability to react with one another as well as to compete for a limited number of binding sites on the entrapped DNA. Thus, a large excess of *E. coli* DNA has no effect on the binding of human DNA to human DNA trapped in the agar. However, a large excess of nonradioactive human DNA will reduce the binding of radioactive human DNA. And so will a large excess of monkey DNA (although to a lesser extent). The degree of competition indicates the degree of similarity. One great advantage of this system is that radioactive DNA from each species is not needed.

Competition was used to show that the DNAs from various organs of mouse are identical but the RNAs of these organs are quite different. This finding provided experimental support to the theory of development that the genes of different tissues are the same, but their expressions differ.

Competition was also used to extend the studies of relatedness among the

bacteria and their phages and among animals. The evolutionary significance is shown in the relationship between the degree of divergence among DNAs as observed by these techniques and the time (estimated by evolutionists) since the divergence of the species (see Fig. 38).

The application of the technique to a medical problem is also reported. In cooperation with D. Axelrod, DNA complementary to polyoma virus DNA was observed in mouse DNA and the amount was strikingly increased in DNA derived from mouse tumors induced by polyoma. This approach is widely used at present in the search for human tumor viruses.

The experimental results obtained with the agar column are reviewed in *Molecular Genetics*, edited by J. H. Taylor, Academic Press, New York (1967).

Repeated DNA

In 1965 the studies of nucleic acid interactions took on a new aspect. Ever since the first use of the agar column for mammalian DNA, a puzzle remained as to why it worked at all. The mammalian genome being 500 times larger than *E. coli* DNA, its DNA should re-nature 500 times slower than bacterial DNA (at the same concentration). Yet this did not happen. Perhaps some mysterious property of the agar accelerated the reaction. Renaturation was then

TABLE 4. Binding of DNA Fragments from Animals and Bacteria to Denatured DNA Embedded in Agar

DNA in Agar	Percent ³² P-DNA Bound Relative to the Homologous DNA		
	Human	Mouse	<i>E. coli</i>
Human	100	25	...
Mouse	25	100	0
Rat	15	75	...
Hamster	15	60	...
Guinea pig	15	15	...
Rabbit	15	15	...
Calf	25	10	0
Salmon	5	10	0
<i>E. coli</i>	0	0	100

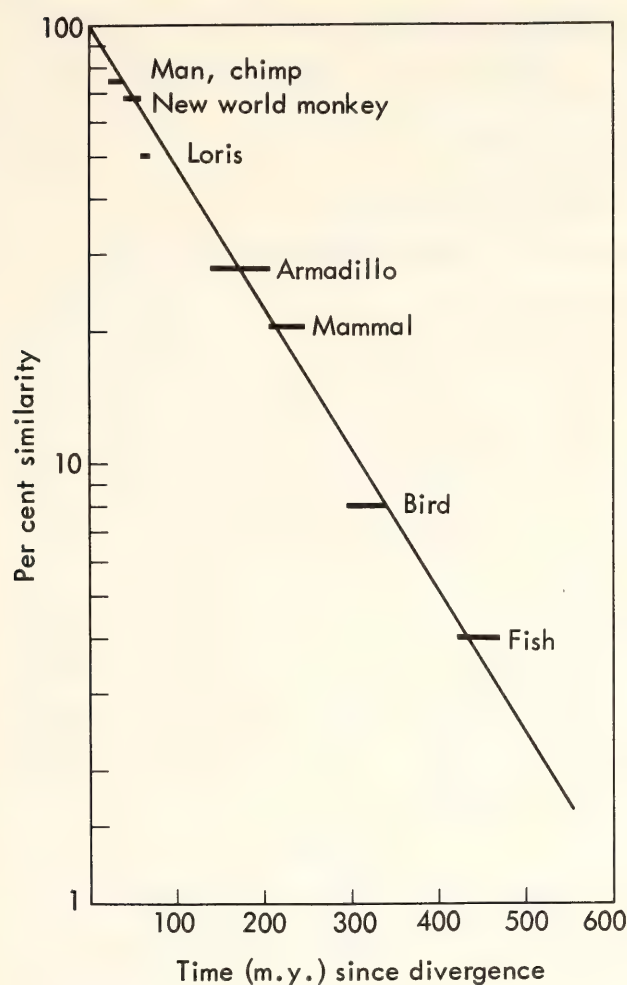


Fig. 38. Relationship between polynucleotide similarity and time of evolutionary divergence.

tested in solution, and it proceeded as rapidly as in agar. Careful studies of the renaturation rate showed that a fraction of mouse DNA reacted more rapidly than *E. coli* DNA instead of 500 times slower.

This finding brought Britten to the realization that a large fraction of the mouse DNA must be composed of a large number of copies of the same (or very similar) sequences. In fact, calculations indicated that the rapidly renaturing fraction (about 10% of the total) contains about one million copies of a short sequence of DNA. Of the remaining DNA, roughly half is found in families of 1000 to 100 members, and the rest has only one or very few copies per genome.

These results answered one question but raised a host of others. How widely was this repeated DNA distributed

through the various species of organisms? How did it originate? What role did it have in evolution? A new technique was provided for fractionating DNA according to its rate of renaturation. What were the properties of these fractions? The earlier agar experiments appeared to have observed only the repeated DNA and its products. Would unique DNA have given the same results? Were the members of the families identical or just similar enough to react?

Since 1965 a large share of the efforts of the Biophysics Section have been devoted to answering these questions. Those amenable to direct proof have been answered; but others are more elusive, requiring an accumulation of indirect evidence. Thus, an early survey showed repeated DNA in more than 50 species throughout the range of phylla, and it seemed quite safe to conclude that repeated DNA made up a large fraction of the genomes of all eukaryotic organisms. Next, the unique sequences were examined and a portion was found to be transcribed. Breaking the DNA into fragments of different sizes showed that the repeated fraction was distributed as short sequences scattered throughout the genome. By 1969 a summary of properties of repeated DNA was reported (see Table 5).

Subsequent developments include: (1) isolation of the ribosomal genes of *E. coli*; (2) formulation of a theory for the role of repeated DNA in controlling the expression of DNA; (3) demonstration that messenger RNA (isolated from polysomes) is mainly transcribed from unique DNA; (4) measurement of the rates of divergence of unique and repeated DNA in rodents and primates; (5) study of the relatedness of the DNAs among bacteriophage, blue-green algae, and plants; (6) measurement of the effect of mismatching on the kinetics of DNA reassociation; and (7) analysis of properties of the fraction of eukaryotic DNA that appears to reassociate instantaneously.

TABLE 5. Observed Properties of Repeated DNA Sequences

1. Occurrence	Observed in all tested species above the fungi.
2. Quantity	From 20% to 80% of the total nuclear DNA.
3. Frequency	From 50 to 2,000,000 related sequences per family.
4. Precision	All degrees of thermal stability seen in reassociated repeated DNA.
5. Arrangement	Scattered throughout the length of the genome.
6. Age	Several hundred million years up to very recent time.
7. Variety	Patterns of frequency and precision vary widely even among vertebrates.
8. Expression	RNA complementary to some repeated DNA sequences has been observed in every cell type examined.
9. Control of Expression	Different sets of repeated sequences are transcribed in different tissues and stages of development.

The Brain

Beginning in 1955 the Biophysics Section has carried on a collaborative program with Drs. L. B. and J. B. Flexner of the University of Pennsylvania in studies of the brain. The central theme of this work has been to determine the biochemical basis of long-term memory. Behavior patterns can be inherited (e.g., bird songs) and thus must be transmitted to the progeny by DNA. Furthermore, the DNA is expressed in the phenotype by the kinds and quantities of protein synthesized. Possibly then, some behavior patterns develop independently but others require a stimulus from the environment for their maturation. However, both could have the same basic mechanism. Thus we attempted to test the hypothesis that protein synthesis, or protein synthesizing systems, provided a mechanism for memory formation.

The early work applied the methods developed for study of protein synthesis in bacteria to the mouse brain. It was observed that synthesis proceeded at a rapid pace in the brain and that sufficient newly formed protein was available to account for new connections among neurons. Next, it was found that puromycin (a protein-synthesis inhibitor) could disrupt memory even when injected weeks after the initial training. This appeared to support the hypothesis.

Soon thereafter, however, a stronger inhibitor of protein synthesis (acetoxycycloheximide) had no effect on memory (if injected a day after training). The hypothesis seemed to have failed.

Later it was found that memory could be restored in puromycin-treated mice by a number of different procedures, including injection of water into the brain or the use of adrenergic stimulating drugs, or simply by leaving the mouse in the cold (which stimulates the adrenergic system). Radioactive puromycin-peptides were found in the brain even months after the administration of puromycin, and the procedures which restored memory also reduced the level of puromycin-peptides in the synaptosome fraction to levels that were not memory inhibiting. Puromycin blockage appeared to be caused by the formation of puromycin-peptides, which adsorbed to receptor sites and blocked certain synapses. Presumably these are receptors for catecholamines as the puromycin has a structural resemblance to these compounds.

Thus, experiments designed to demonstrate a role for protein synthesis in memory formation ended in implicating the catecholamines. Furthermore, other classes of compounds are involved. A small injection of vasopressin (or related small peptides) can protect the

memory from puromycin blockage. The end of this story is not yet in sight.

Possibly, protein synthesis is necessary for the final consolidation of long-term memory, but this process continues during the week or so after training when the memory trace seems to be spreading throughout the brain. Unfortunately, this hypothesis cannot be tested at present because prolonged inhibition of protein synthesis is lethal.

Most of these experiments were carried out at the University of Pennsylvania by the Flexners. Active experimental work was a minor effort of the Biophysics Section in the period 1966–1974. Roughly 20 papers have been published, and the results up to 1969 are summarized in *Quarterly Review of Biophysics*, 1969.

Conclusion

This brief history has attempted to trace the main themes followed by the section during its 30 years. The past was emphasized because its individual events are largely forgotten by now and the significant findings are merged into the general story of molecular biology. The recent work is not quite ripe for such historical treatment. Neither was it possible to do justice to the many fascinating offshoots that have been followed. The development of methods and techniques, too, has been ignored. For example, the pressure cell was first built to release phage from infected bacteria before lysis; this was achieved elsewhere a short time later. Our attempts failed because the pressure cell was too effective and disrupted the phage. The same efficiency kept us from observing polysomes in spite of hundreds of observations of

the ribosomes from bacteria passed through the cell. The polysomes, too, were disrupted.

The product of this small group can be measured by the three books and 200 or more papers published. A better measure can be found in a listing of significant findings: (1) Isotopic competition method. (2) Flow patterns of metabolism in *E. coli*. (3) Feedback inhibition. (4) Demonstration that nascent protein is attached to ribosomes. (5) Virus purification on DEAE columns. (6) Patterns of ribosome synthesis. (7) Proof that newly formed RNA in bacteria is one-third messenger, two-thirds ribosomal precursor. (8) Agar column for nucleic acid reactions. (9) Messenger RNA isolation. (10) Application of nucleic acid interaction to measure relatedness of species and degree of divergence. (11) Homology of DNA in *E. coli* and lysogenic virus. (12) Detailed studies of divergence in viruses, bacteria, algae, vertebrates, rodents, and primates. (13) Application of nucleic acid reactions to cancer virus investigations. (14) Demonstration that DNA remains identical but RNAs differ in different tissues and stages of development. (15) Extensive studies of nucleic acid reaction kinetics. (16) Discovery of repeated DNA. (17) Properties of repeated DNA. (18) Involvement of catecholamines and peptides in learning and memory.

We are pleased to have participated in this exciting period in the development of biology. We believe that we did make significant contributions and that, since some of us will carry on in different places, our history is not complete. We are especially pleased to note the contributions being made by 22 Fellows who received a part of their training with us.

Staff

P. H. Abelson, 1946–1953
D. B. Cowie, 1946–
R. B. Roberts, 1947–
E. T. Bolton, 1949–1966
R. J. Britten, 1951–1971

B. J. McCarthy, 1958–1964
D. E. Kohne, 1965–1971
N. R. Rice, 1968–
B. H. Hoyer, 1968–

Resident Associates and Senior Fellows

D. Axelrod
G. N. Cohen
H. H. Darby
E. H. Davidson
W. R. Duryee
J. B. Flexner
L. B. Flexner

A. Gelderman
M. A. Martin
F. T. McClure
K. McQuillen
M. Miranda
I. Z. Roberts
S. Spiegelman

P. Szafranski

Fellows

A. I. Aronson
R. J. Avery
J. A. Boezi
T. I. Bonner
D. J. Brenner
T. J. Byers
J. A. Chiscon
E. H. Creaser
M. Davis
J. D. Duerksen
N. J. Grady

Y. Kato
E. S. Kempner
J. J. Leahy
H. M. Lenhoff
S. Lövtrup
J. E. Midgley
A. V. Rake
R. A. Shleser
N. A. Straus
D. G. Wallace
M. J. Waring

Technical Assistants

E. Aldous
R. E. Bresnahan
M. Chamberlin
J. H. Eames
E. F. French
L. Gazze
J. M. George
J. Gray
W. Griffin
D. Johnson
M. L. Kelley
S. Lohman

M. Melean
B. D. North
P. Paul
L. Prager
P. Roddy
M. K. Sands
A. Shirven
J. Smith
E. Stern
N. van de Velde
B. P. Walton
J. Young

GEOCHEMISTRY AND GEOPHYSICS

*L. T. Aldrich, M. Bass, L. Beach, C. Brooks, K. D. Burrhus, M. Dodson, S. E. Forbush,
S. R. Hart, A. Hofmann, D. E. James, A. T. Linde, I. S. Sacks, N. Shimizu,
A. Snoke, and W. White*

Collaborators

*C. Aguirre, J. Bannister, M. Casaverde, A. Cuyubamba, G. L. Davis, S. del Pozo,
D. W. Evertson, R. C. Fletcher, A. Flores, L. Gélinas, A. A. Giesecke, T. E. Krogh, I. Kushiro,
Y. Motoya, L. Ocola, H. Okada, G. Olafsson, J. E. Ramirez, A. Rodriguez B.,
J. G. Schilling, H. Sigtryggsson, D. Simoni, R. Stefansson, S. Suyehiro, L. Tamayo,
and Y. Yamagishi*

One of the goals in understanding the earth and its history is to learn about the physical and chemical properties of rocks that characterize the various provinces and domains of the earth's surface

and interior. Over the past 30 years members of this Department have played a major role in initiating and advancing research on the isotopic composition and age of rocks and on the seismic structure

of the crust and uppermost mantle. With every advance in knowledge has come deeper appreciation of the earth's complexity and the scale of its inhomogeneity. With passing time, the studies of the Department centered increasingly on investigating the differences between various regions of the globe with the aim of answering the question "Is there structure and pattern to the complexities we observe?"

The theories of sea-floor spreading and plate tectonics have provided a conceptual framework in which the history and processes of crust and mantle can be better understood. As a result, ideas and concepts have evolved rapidly over the past several years. Of special importance has been the restructuring of earth sciences as once widely separated disciplines in geology, geochemistry, and geophysics have merged to provide more unified approaches to resolving long-standing problems.

The blurring of distinctions between geochemistry and geophysics has been evident over the past year in this Department as our attention has focused on the problem of the structure and composition of the earth's mantle. Staff Members and Fellows with widely divergent backgrounds, but drawing on each other's expertise, are joined in several common efforts to understand mantle inhomogeneity and how it bears on plate dynamics, the formation of magmas, and the evolution of crust and mantle.

Most of the geochemical studies reported here are concerned with questions of chemical and isotopic variation in oceanic basalts and island arc andesites as indicators of gross mantle inhomogeneity. Studies in geophysics span a range of topics from upper mantle structure in subduction zones to theoretical investigations of earthquake source models. A common goal of the studies in geophysics is to determine the physical properties of rocks within the crust and mantle, the stresses to which they are subjected, and the manner in which

they yield to these stresses. Reports by Bass, by Forbush, and by Aldrich and colleagues pertain to areas of geochemistry and geophysics other than those just outlined and emphasize the personal and diverse research interests of the members of the Department.

Research by Hofmann and by Shimizu and Kushiro provides fundamental information on the way in which trace elements distribute themselves in the mantle. Hofmann's report gives kinetic data on rates of diffusion of Sr and Ca that bear directly upon the question of the degree of trace element homogenization one would expect between mineral phases in a partially melted mantle. Shimizu and Kushiro's report is another in a continuing series demonstrating how certain trace elements and rare earth elements are partitioned between crystal and liquid phases during partial melting of mantle material. Knowledge of partitioning coefficients provides a means of inferring mantle compositions from the compositions of the derivative magmas. Dodson's report on the kinematics of metamorphic reactions provides further insight into the rates at which mineralogical changes occur in rocks with changing thermal regime.

Reports by Hofmann and Hart, by Hart, and by White, Hart, and Schilling deal with the problem of the origin of mid-ocean ridge and oceanic island basalts. The two groups of volcanic rocks exhibit distinct differences in trace element and isotopic composition. Various and conflicting theories have been proposed to explain the differences, and the controversy now has resolved itself into two contrary views: One holds that the compositional differences are due to disequilibrium melting of a homogeneous mantle in which mineral phases are not in isotopic equilibrium with one another; the other holds that the magmas of oceanic islands are derived from mantle of composition fundamentally different from that which supplies the mid-ocean ridges. The reports presented here pro-

vide strong support for the latter view. The authors support the idea that certain oceanic islands overlie mantle plumes or diapirs and that the source material of these magmas was therefore derived from deep within the mantle.

Brooks addresses the question of the variation of mantle composition with time. His studies on magma immiscibility, showing it to be a rare phenomenon today but common in ancient rocks, suggest that both the composition of the earth's mantle and its thermal regime may have been significantly different in Archean time.

James, Brooks, and Cuyubamba carry the study of mantle inhomogeneity to the continents. They show that for the central Andean volcanic arc, the magmas of Mesozoic time were derived from a mantle source of fundamentally different composition from that which supplied the magmas of late Cenozoic time. James, in a discussion of a model for disequilibrium melting of the thick ancient continental lithosphere of western South America, shows that the high $^{87}\text{Sr}/^{86}\text{Sr}$ ratios of the late Cenozoic andesites and dacites could be due to varying degrees of partial melting of isotopically unequilibrated phlogopite in rigid lithospheric mantle.

Sacks' investigations of upper mantle structure beneath the Japan arc shed light on how thick continental lithospheric plates may be formed. He shows that rigidity of the asthenosphere is abnormally high in that wedge of mantle overlying the descending plate and situated between trench and volcanic arc. He hypothesizes that in this zone, high rigidity asthenosphere is being "frozen" out of normal asthenosphere and added to the base of the island arc lithosphere. This process would create a lithospheric "root" similar to that observed beneath South American and other continental areas. Snoke and Sacks in a companion paper on structure in subduction zones show how converted and reflected seismic phases can be used to map the top of

the downgoing slab in regions where the seismicity is ambiguous or nonexistent.

Snoke has successfully resolved a major controversy over incompatible differences between various earthquake source models. Source models are commonly used to infer fault dimensions and stress release of an earthquake from the measured far-field radiation spectrum. Critical to any such study is whether the model is consistent with observation. A model proposed by Archambeau appeared to be in better agreement with some observations than are other source models. Snoke shows, however, that the effects predicted by Archambeau's model are due to nonphysical behavior and are therefore spurious. Archambeau's model is shown to be equivalent to other source models. Linde, Sacks, and Snoke seek to answer the question of why the observed spectra from earthquake radiation differ from those predicted by models. They show that multiple rupture (all source models assume simple rupture) during an earthquake can produce some of the spectral effects observed. This in turn can lead to serious errors in the calculation of apparent stress release and fault dimensions.

The discovery by workers in the Soviet Union and in the United States that earthquakes are preceded by a long period of dilatancy in the region of the eventual rupture has given added impetus to borehole strainmeter studies. Sacks, Snoke, and others report on the sensitivity of the borehole strainmeters to the detection of precursory dilatancy and calculate the distances from the fault at which dilatancy could be observed for different fault lengths and noise levels.

Aldrich and colleagues report on the results of continuing studies of the electrical conductivity anomaly beneath the Andes of South America. They have extended their investigations into Chile and Argentina and have obtained more detailed observations in Peru and Bolivia. Preliminary results indicate that

the electrical conductivity structure beneath southern Peru and Bolivia is complex and distinctly different from the conductivity structure observed in central Chile.

The reports end with that of Forbush and Beach who demonstrate that cosmic-ray diurnal anisotropy is due to reversals in the sun's poloidal magnetic field. With this demonstration they are able to conclude that all variations in cosmic-ray intensity, except those of meteorological cause, are due to solar mechanisms.

The studies described in the reports that follow reflect the highly personal and individual approach to research at the DTM and testify to the soundness of Merle Tuve's proposition that a small group of scientists, working together in shared interest, pursuing their individual goals, can make significant contributions to knowledge.

DIFFUSION OF CA AND SR IN A BASALT MELT

Albrecht W. Hofmann

Interest in diffusion measurements has recently increased because of the current controversy in the literature over the validity of using chemical and isotopic differences in oceanic basalts as indicators of compositional differences in the source mantle (e.g., Hart *et al.*, 1973; O'Hara, 1973, 1975; O'Nions and Pankhurst, 1974; Flower *et al.*, 1975). Those who deny the validity of these indicators assume that the source is homogeneous on a large scale and explain all chemical and isotopic variation found in the volcanic rocks as the result of differences in the melting and crystallization process (for a more detailed discussion see the companion reports by Hofmann and Hart and by James). All parties to the argument agree that partial melting in an initially homogeneous mantle and subtraction of the melt (by intrusion) leads to an inhomogeneous residue. If the mantle convects, as it must if the present concepts of plate tectonics are

approximately correct, it seems likely that the inhomogeneous residue will be transported to a location where melting occurs again (for a contrary view, see Ringwood, 1974). It is therefore important to determine whether and on what scale the mantle can be rehomogenized by the combined process of convection and diffusion. The results reported below confirm the prediction made in last year's Report that diffusion distances in a partially molten mantle are limited to tens or hundreds of meters and that rehomogenization of larger scale inhomogeneities (tens of kilometers) is highly unlikely.

Diffusion data are also important in determining the structure of silicate melts and in understanding crystallization processes. However, a considerably larger body of data will be needed before applications in these areas can be realized. The present report is a continuation and expansion of work started last year (see *Year Book* 73, pp. 935-941).

Experimental Methods

Only aspects of the methods will be described which differ from those reported last year (Hofmann, *Year Book* 73, pp. 935-941). Continued difficulties in obtaining leak-free and bubble-free diffusion couples resulted in several changes in technique: (1) In most of the experiments the radioactive tracer was applied in the form of a thin source at the open end of a platinum tube filled with quenched basalt glass (olivine tholeiite flow from Kilauea, 1921), rather than in the form of an infinitely extended source (referred to as diffusion couple). (2) Most of the experiments were made using the beta emitter ^{45}Ca and the results were analyzed by autoradiography rather than particle counting. This permitted a rough evaluation of the convective contribution to the total transport. (3) A new well-type NaI (3 inch diameter, 1×2 inch well) afforded improved resolution and counting geometry for gamma-ray spectrometry of

^{85}Sr -doped charges. This makes it possible to analyze the activity profile of ^{85}Sr in the basalt-filled tubes by counting either the sectioned material itself or the residual activity in the tube after grinding.

The results obtained by the thin-source technique, though different in some details, confirm the order of magnitude of the results obtained by the diffusion-couple technique. This is encouraging in view of the fact that measured diffusion coefficients in solid silicates frequently differ by several orders of magnitude, depending on the experimental technique (see, for example, Gilletti, 1974).

Thin-source diffusion runs were prepared as follows: Two-mm Pt tubing was filled with olivine tholeiite basalt melt by capillary action or by applying suction at about 1400°C . The quenched tubes were then cut into pieces 0.5 to 2.5 cm long and reannealed at the approximate intended run temperature. In the temperature range employed (1250° to 1450°C), the melt is held in the horizontally suspended, open-ended tubes by surface tension. A final anneal for about 1 minute at 1000°C caused the glass to devitrify and shrink so that the end surfaces were concave and had a dull appearance. Several drops of ^{45}Ca or ^{85}Sr chloride solution were then dried on one or both free ends of basalt, and the prepared charge was suspended at above-liquidus temperatures in a Pt-wound furnace in air for durations of up to several days. This produced diffusion gradients of up to 1.5 cm long.

To determine the activity profile of ^{45}Ca (β^- , 0.255 MeV, $t_{1/2} = 165$ days) in the basalt after the high-temperature diffusion experiment, the glass-filled Pt tube was mounted with epoxy cement in a groove on the surface of an aluminum block. This assembly was hand ground and polished to remove the upper half of the tube and to expose a flat, polished section parallel to the long axis of the tube. The polished block was then ex-

posed for several days to a nuclear-emulsion plate (Ilford emulsion type K.5, 25 $\text{m}\mu$ thick), and the density of the developed image was scanned using a microdensitometer with chart recorder output. Two typical records are shown in Fig. 39.

Charges doped with ^{85}Sr were analyzed by consecutive sectioning in a manner similar to that described in *Year Book* 73, pp. 935–941. Improvements were made by using the above-mentioned new detector crystal and by employing the residual activity directly in the data analysis (Frischat and Oel, 1966).

One advantage of the improved analytical methods is that deviations of the measured activity profile from an ideal diffusion profile are easily detected. Such deviations must be attributed to transport mechanisms other than volume diffusion, because in tracer diffusion any concentration dependence of the diffusion coefficient is assumed to be negligible.

Results

Typical activity profiles are shown in Figs. 39 and 40 for thin-source diffusion of ^{45}Ca and ^{85}Sr , respectively. Figure 39 also shows the deviations from "ideality" encountered in diffusion runs of short duration. The comparison shows that a transport process other than volume diffusion is dominant during the early stages of a run. Some convection near the open ends of the tube is likely during the initial heating of the charge. In addition, the distribution of tracer is uneven (Fig. 41a). In order to minimize the effects of poorly controlled initial and boundary conditions, a study of the time dependence of the transport distance was made at $1310 \pm 10^\circ\text{C}$. The results, in terms of apparent diffusion coefficients, are shown in Fig. 42. This and the much closer correspondence of long-run profiles to "ideal" diffusion profiles (Fig. 39) indicate clearly that volume diffusion becomes the dominant transport process in runs lasting several hours or days.



Fig. 39. ^{45}Ca activity in basalt as a function of distance in two thin-source experiments. The activity is determined by microdensitometry from a nuclear emulsion. The solid lines are calculated diffusion profiles for diffusion from an infinitely thin source into a semi-infinite medium. Run durations (and temperatures) are 12.1 hours at 1309°C (a) and 47.75 hours at 1390°C (b). Similar deviations between measured profile and the calculated line are evident in all runs of short duration.

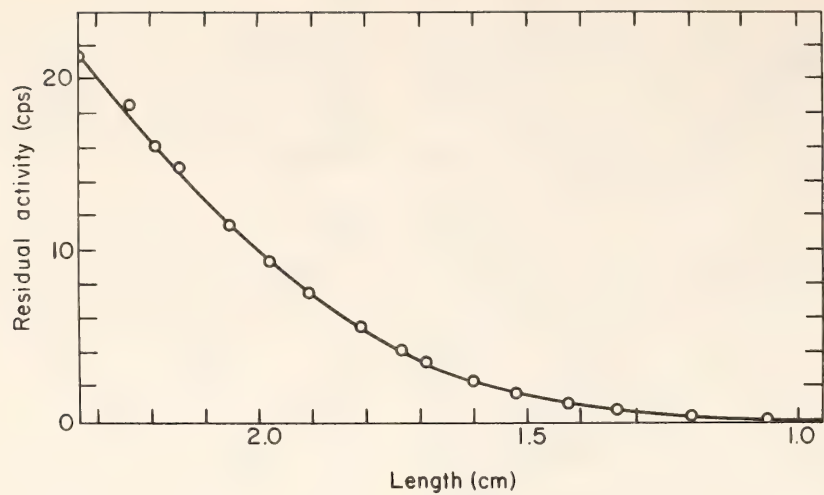


Fig. 40. Residual ^{85}Sr activity versus length determined by successive removal of basalt glass and counting of the remaining basalt rod. The line is a calculated curve for ideal thin-source diffusion into a semi-infinite medium.

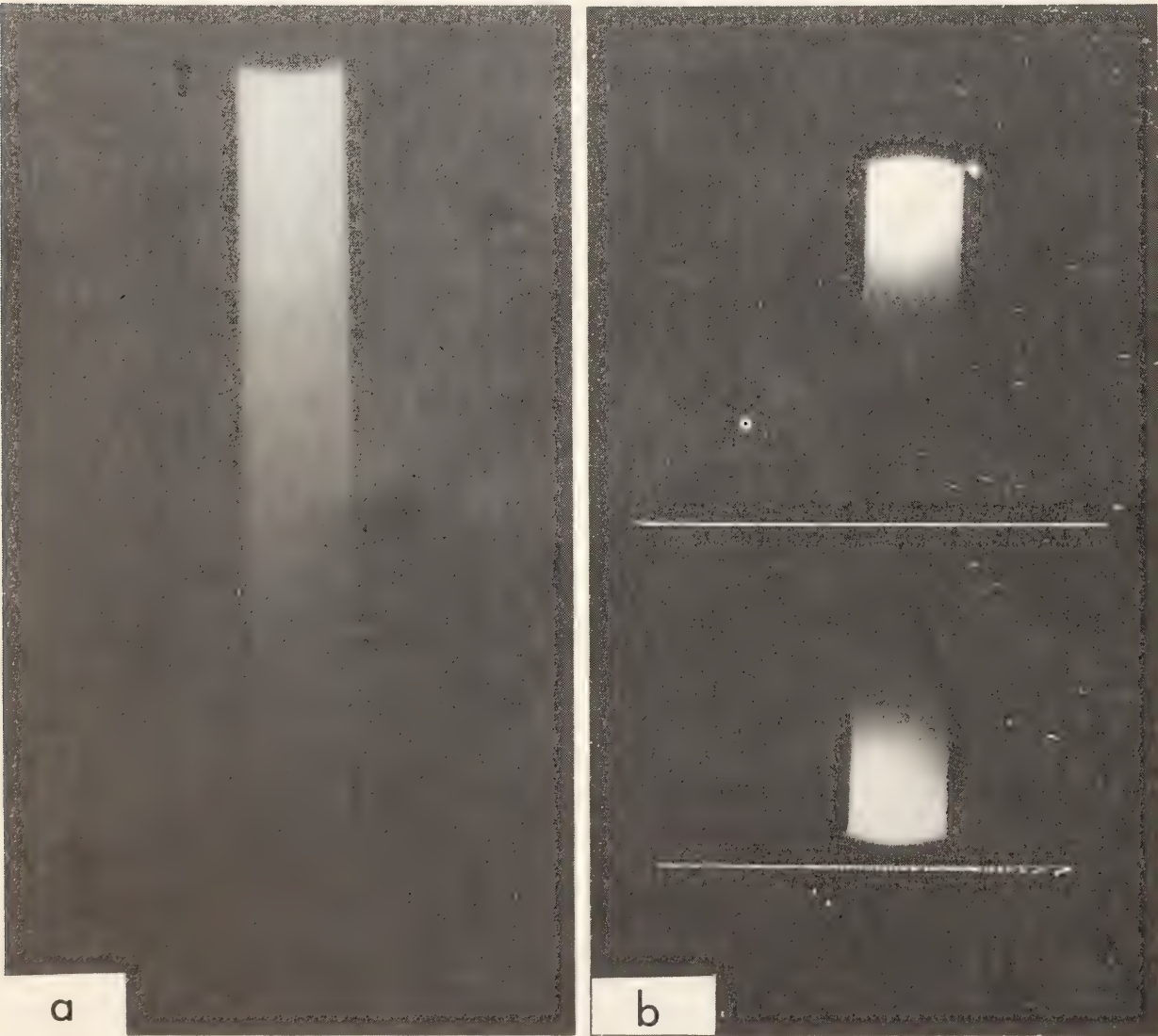


Fig. 41. Images of beta particle tracks on nuclear emulsions: *a*, taken from a 89-hr diffusion run at 1309°C ; *b*, taken from a 3.8-hr diffusion run at 1305°C .

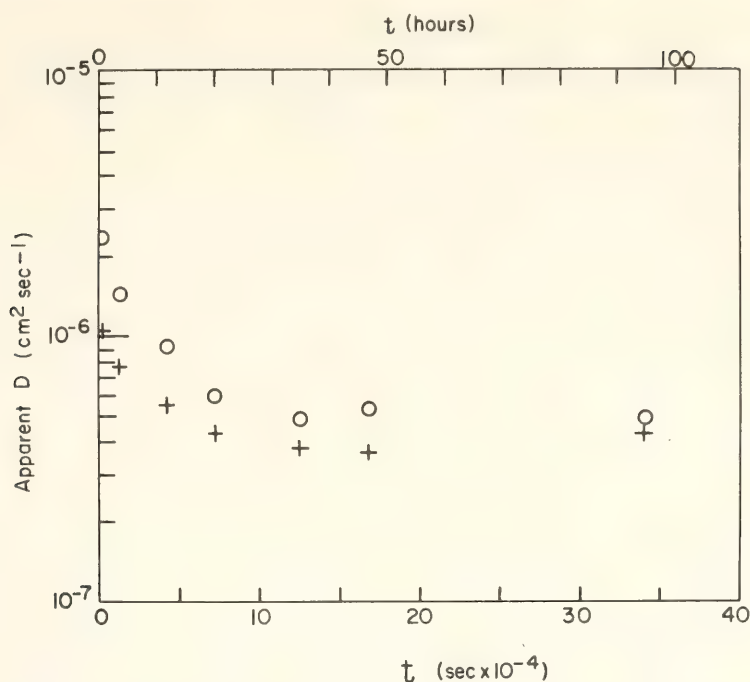


Fig. 42. Apparent diffusion coefficients at $1310 \pm 10^\circ\text{C}$ as a function of run duration, determined from two points in each activity profile. These are measured at $A/A_0 = 0.1$ (crosses) and $A/A_0 = 0.5$ (circles), where A_0 is the activity at the origin. The percent difference between the two apparent D values is an indication of the misfit between the measured profile and an ideal diffusion profile from a thin source. This difference decreases from about 100% for short times to less than 10% for long run times.

The temperature dependence of the diffusion coefficient for ^{45}Ca is shown in Fig. 43, which also gives the results of Medford (1973) on Ca diffusion in mugearite for comparison. The differences between the two sets of data may be because of the difference in matrix composition of the two melts employed; or it may be because Medford measured chemical interdiffusion of calcium with other components of the basalt, whereas the present experiments were designed to measure Ca-tracer diffusion.

Figure 44 shows the results of the experiments for ^{85}Sr diffusion. In this case there is a discrepancy between the results obtained by the couple method (as described in last year's Report) and the new thin-source data. It had been estimated (Hofmann, *Year Book*, 73, p. 938) that the preliminary data on diffusion couples were accurate within a factor of 2, so the new results may not differ *significantly* from the previous ones. Additional experimentation is clearly needed to obtain a better estimate

of the temperature dependence and to demonstrate that the two techniques yield concordant results.

The order of magnitude of the diffusion coefficients of both Sr and Ca is such that equilibration of the melt phase on a centimeter scale in a partially molten mantle requires only a few years, but equilibration on a kilometer scale requires more than one lifetime of the earth. Diffusion in solid silicates tends to be slower by several orders of magnitude (see Hofmann and Hart, this Report), so that equilibration in an all-solid mantle is restricted to an even smaller scale.

Acknowledgments

The high-temperature experiments were done at the Geophysical Laboratory with help and advice from the staff and Fellows. The basalt sample was supplied by H. S. Yoder, Jr. Financial support was given by the National Science Foundation, Grant no. GA-40250.

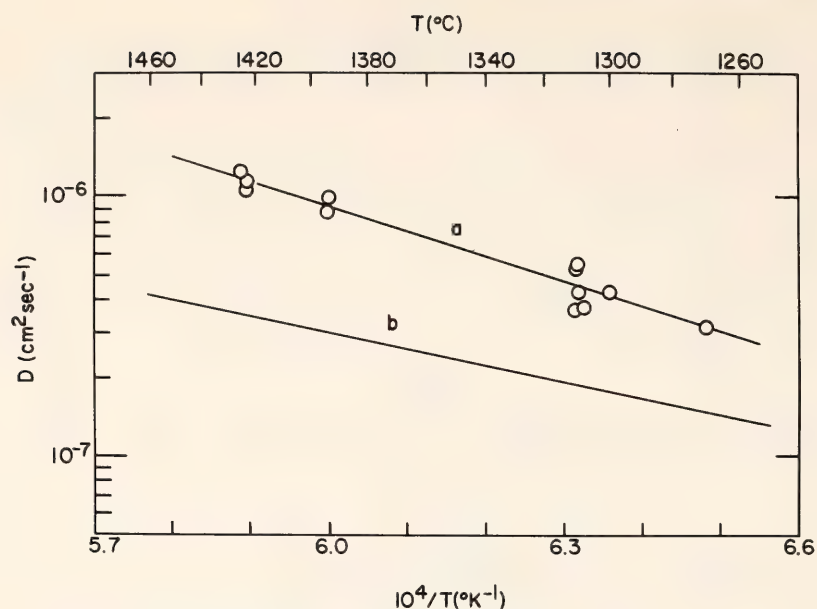


Fig. 43. Arrhenius plot ($\log D$ versus $1/T$) for ^{45}Ca -tracer diffusion in olivine tholeiite melt. The line a is the (visual) best fit through the measured values of the diffusion coefficient. Its slope corresponds to an activation energy of 44 kcal/mole. Line b is taken from Medford (1973) and represents Ca diffusion in a mugearite melt.

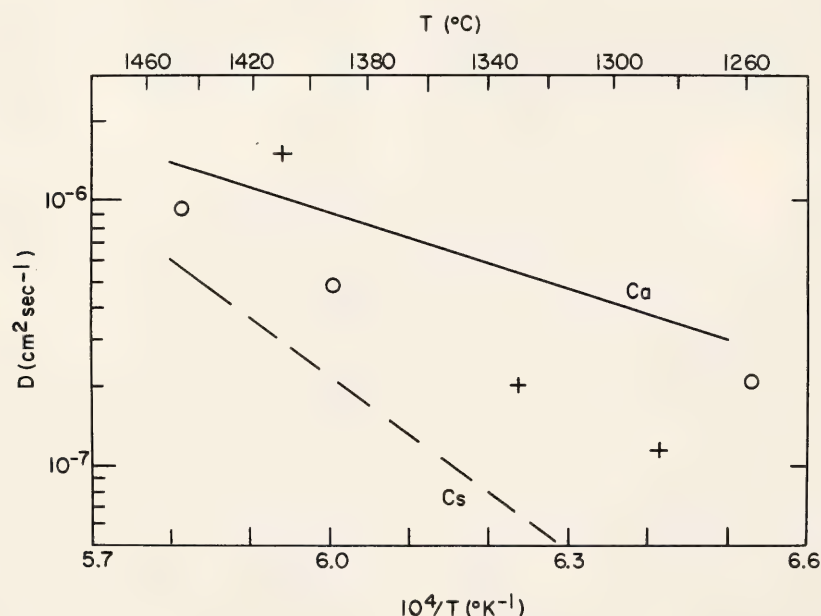


Fig. 44. Arrhenius plot for ^{85}Sr -tracer diffusion in olivine tholeiite melt. Crosses and circles represent D values from diffusion couples and thin-source experiments, respectively. The line labeled Ca represents ^{45}Ca -tracer diffusion and is taken from Fig. 43. The line labeled Cs represents Cs-tracer diffusion in a synthetic basalt-like melt determined by Winchell and Norman (1969).

References

- Flower, M. F. J., H. U. Schmincke, and R. N. Thompson, Phlogopite stability and the $^{87}\text{Sr}/^{86}\text{Sr}$ step in basalts along the Reykjanes Ridge, *Nature*, **254**, 404–406, 1975.
- Frischat, G. H., and H. J. Oel, Eine Restaktivierungsmethode zur Bestimmung von Selbst diffusions—Koeffizienten in Festkörpern, *Z. Angew. Phys.*, **20**, 195–201, 1966.
- Giletti, B. J., Diffusion related to geochronology, in *Geochemical Transport and Kinetics*, A. W. Hofmann, B. J. Giletti, H. S. Yoder, Jr., and R. A. Yund, eds., *Carnegie Inst. Wash. Publ.* **634**, pp. 61–76, 1974.

- Hart, S. R., J. G. Schilling, and J. L. Powell, Basalts from Iceland and along the Reykjanes Ridge: Sr isotope geochemistry, *Nature*, 246, 104–107, 1973.
- Medford, G. A., Calcium diffusion in a mugearite melt, *Can. J. Earth Sci.*, 1D, 394–402, 1973.
- O'Hara, M. J., Non-primary magmas and dubious mantle plume beneath Iceland, *Nature*, 243, 507–508, 1973.
- O'Hara, M. J., Is there an Icelandic mantle plume?, *Nature*, 253, 708–710, 1975.
- O'Nions, R. K., and R. J. Pankhurst, Petrogenetic significance of isotope and trace element variations in volcanic rocks from the mid-Atlantic, *J. Geol.*, 15, 603–634, 1974.
- Ringwood, A. E., The petrological evolution of island arc systems, *J. Geol. Soc. London*, 130, 183–204, 1974.
- Winchell, P., and J. H. Norman, A study of the diffusion of radioactive nuclides in molten silicates at high temperatures, in *High Temperature Technology*, third International Symposium 1967, 1969.

THE PARTITIONING OF RARE EARTH
ELEMENTS BETWEEN GARNET AND LIQUID
AT HIGH PRESSURES: PRELIMINARY
EXPERIMENTS

N. Shimizu and I. Kushiro

The interpretation of the trace element abundances of volcanic rocks in terms of fractional crystallization and/or partial melting models rests upon a knowledge of the partitioning of the trace elements between liquid and solid phases in these processes. The partitioning of rare earth elements (REE) between garnet and liquid is particularly important for explaining the enrichment of light REE relative to heavy REE in alkali basalts and kimberlites as these light REE enriched patterns have been ascribed to equilibration with garnet (e.g., Gast, 1968; Schilling and Winchester, 1969; Kay and Gast, 1973).

Experimental evidence has been needed to show the applicability of the partition coefficients of REE measured for natural garnet-liquid pairs (Schnetzer and Philpotts, 1970; Philpotts *et al.*, 1972) to partial melting of garnet lherzolite or crystallization of garnet of the liquidus of basaltic magmas at high pressures.

The composition chosen for the study is diopside 30% (by weight), pyrope 70%. The mixture of this composition studied by O'Hara and Yoder (1967) is used here as the starting material. A composite solution containing eight REE was added to the powdered material in a Pt crucible and dried on a hot plate. It was then fused at 1500°C in air to make a homogeneous glass starting material for high-pressure runs. Concentrations of REE in the starting material are given in Table 6 and are about 15 to 40 times chondritic average. They are within the range of concentrations observed for natural basalts. 15 to 20 mg of the powdered material were sealed into platinum capsules with 3.5 to 10.2 wt% of water. Ten runs were carried out at 30 kb at temperatures between 1175° and 1450°C for 2 hours in a solid-media high-pressure apparatus. The best run product was obtained at 1275°C with about 9 wt% water. It consisted of euhedral garnet crystals 10 to 30 μm in diameter (about 25% of the charge), clear glass, quench crystal (dendritic or feathery), and a trace amount of forsterite. In order to evaluate equilibrium relationships between garnet and liquid (glass and quench crystal), the major element composition of garnet was determined by an electron microprobe. The garnet composition (SiO_2 , 44.5; Al_2O_3 , 23.1; MgO , 27.1; CaO , 3.94; total, 98.64) was found to be quite homogeneous from one grain to another, indicating that equilibrium was closely approached at least for the major elements.

The run product was then pulverized with two-bottle distilled acetone in an agate mortar and processed with the differential dissolution technique (DDT)

TABLE 6. REE Concentrations and Partition Coefficients (*D*)

	GAR (ppm)*	LIQ (ppm)*	D (GAR/LIQ)†	SM (ppm)*
Ce	0.905	44.0	0.021	31.9
Nd	1.14	13.2	0.087	9.82
Sm	0.810	3.73	0.217	2.91
Eu	0.458	1.42	0.320	1.15
Gd	2.86	5.75	0.498	4.94
Dy	5.18	4.84	1.06	4.94
Er	5.20	2.60	2.00	3.33
Yb	10.68	2.65	4.03	4.90

* GAR, garnet; LIQ, liquid; SM, starting material.

† Plotted as curve *A* in Fig. 46.

developed (Shimizu and Hart, 1973) for separation of phases in a similar experimental study of the partitioning of LIL trace elements between clinopyroxene and liquid at high pressures (Shimizu, 1974). Rare earth elements (REE) were analyzed in the separated phases by isotope dilution using spike solutions provided by Dr. J. A. Philpotts. Total blanks were 0.1 ng for Ce and 0.01 to 0.06 ng for the other REE and were negligible except for Ce in garnet for which a correction of about 12% was required. We consider that the concentrations reported in Table 6 are reliable to 5%.

In this preliminary study, the variation of partition coefficients with *P*, *T*, and composition was not investigated. Several runs were carried out at identical *P* and *T* (30 kb, 1275°C) and almost identical water content (about 9 wt%) to test the DDT with different concentrations of HF. The concentrations of REE in the liquid phase (glass and quench crystal) were obtained from the first-step dissolution as in the previous study, and those in garnet were obtained for the sample remaining after five consecutive HF treatments. Although the separation technique (DDT) was found to be excellent in the previous study on clinopyroxene-liquid (Shimizu, 1974), in which only clinopyroxene and clear glass were observed, a serious difficulty was encountered in the present experiments in part due to the presence of quench

crystal together with glass. The presence of a trace amount of forsterite is, however, believed to be of very minor importance. During the course of the DDT treatments, it was observed that a part of the quench crystals was hard to dissolve in dilute HF (5% for example) and that a part of the garnet was dissolved after several steps of treatment with 15% HF. When some part of the liquid phase remains after the HF treatments, it causes an anomalously high concentration of light REE in the solid phase in a manner similar to a matrix impurity in a mineral separate of phenocryst-matrix pairs and thus increases the apparent partition coefficients. The effect can be significant if the true equilibrium partition coefficients are small (<1). For heavy REE, on the contrary, the presence of quench crystal impurity would decrease the concentrations and thus lower the apparent partition coefficients. The magnitude of the impurity effect may be estimated by simple calculations. If the true partition coefficient for Ce is 0.01, presence of 1% liquid phase would increase the concentration by a factor of 2 and thus increase the partition coefficient by the same magnitude. In contrast, the same amount of liquid phase would decrease the Yb content of garnet only by 0.7% and thus have no significant effect, if the true partition coefficient for Yb is around 4.

Comparison of the several runs (two of them are shown in Fig. 45 as curves

A and B) suggests that this is the case in the present experiments. Curve A was obtained for the run product which contained the smallest amount of quench crystal and which was treated with 10% HF (which seemed to be an optimum

concentration of the acid in the present experiments). Curve B is an example of a less successful separation in part due to an abundance of quench crystal and to use of dilute HF (5%). It should be noted that these curves appear to be

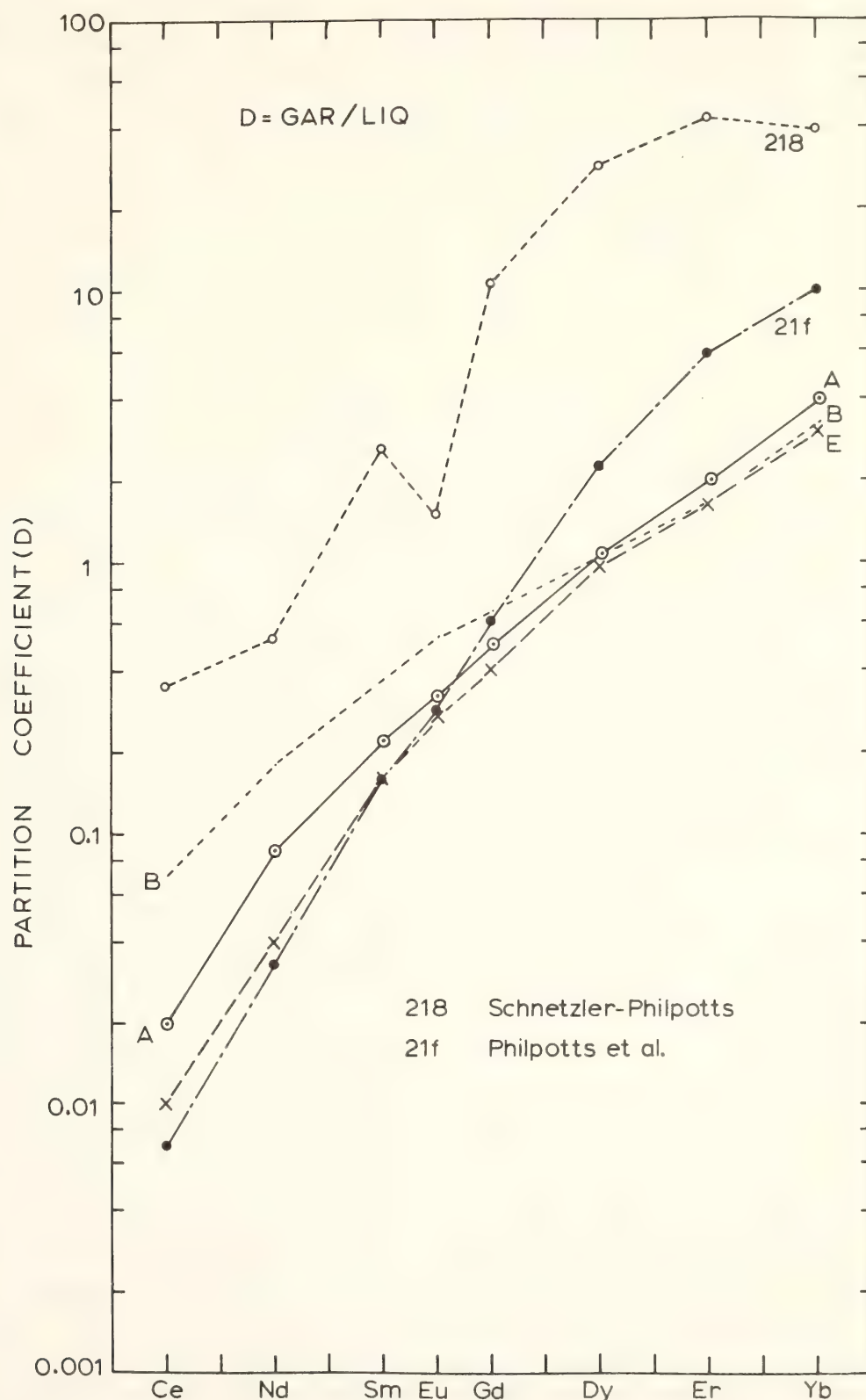


Fig. 45. Partition coefficients of REE between garnet and liquid. A and B, this study (see text); 218, Schnetzler and Philpotts (1970); 21f, Philpotts *et al.* (1972); E, estimate (Shimizu, 1975).

rotating around Dy for which the partition coefficient is close to 1. Although the values for A seem to be best in the present experiments, we still are not sure that the phase separation was complete. Therefore, we suggest that the partition coefficients for the light REE, particularly that for Ce, should be regarded as upper limits. The partition coefficient for Ce may have to be reduced by a factor of 2 (to 0.01) if the final purity of the garnet phase is 99%. Nevertheless, we suggest that the values for the heavy REE, which are of particular importance for the REE geochemistry of volcanic rocks, are reliable, since the effect of impurity seems to be small, as mentioned above.

In Fig. 45 the partition coefficients obtained for natural garnet-liquid pairs are plotted for comparison. The values for 218 (Schnetzler and Philpotts, 1970) are for the almandine-rich garnet phenocryst-dacitic matrix pair. They are significantly higher than the experimental values for all REE. Although the causes of these differences are not well understood, it should be noted that the chemical compositions as well as P and T are grossly different between the almandine-dacite pair and the present experiments. Better agreement is obtained for a garnet megacryst-host basalt from Kakanui, New Zealand.

In recent papers (e.g., Allègre *et al.*, 1973; Kay and Gast, 1973; Frey *et al.*, 1974; Shimizu, 1975), the partition coefficients for GAR-LIQ are estimated from CPX-LIQ and GAR-CPX relationships. It has been shown (Philpotts *et al.*, 1972; Shimizu, 1975) that the partitioning of REE between garnet and clinopyroxene is rather constant over a range of chemical composition and estimated P and T . This seems to justify combining the natural CPX-GAR relationships and CPX-LIQ partitioning (particularly those of Grutzeck *et al.*, 1973, or Schnetzler and Philpotts, 1970) to estimate GAR-LIQ partition coefficients. Curve E in Fig. 45 shows an

example of the estimated partition coefficients obtained in this manner. The experimental values are in excellent agreement with the estimated ones.

It is clear from Fig. 45 that REE of larger ionic radii are rejected more strongly from garnet (relative to liquid). This relationship is better illustrated in Fig. 46, where the partition coefficients (now defined as $(\text{REE}/\text{Mg})_{\text{GAR}}/(\text{REE}/\text{Mg})_{\text{LIQ}}$, plotted as the natural logarithm) are plotted against the ionic radii (values from Whittaker and Munstus, 1970: 8-fold coordination, assuming that REE substitute for Mg by analogy with Y-garnet). The present results define a straight line for REE ranging from Yb to Nd, while the point for Ce is significantly lower. The major element composition of the liquid phase was calculated by material balance, based on garnet composition (probe data) and starting material and on proportions of garnet and liquid estimated from REE material balance (26% garnet and 74% liquid; trace amount of forsterite was neglected).

It is noted that the partition coefficients for Yb and Er are larger than that of Mg despite their considerably larger ionic radii. This situation appears to be similar to the plagioclase-liquid system, in which the partition coefficient of Sr is higher than that of Ca, Sr having a larger ionic radius than Ca (Higuchi and Nagasawa, 1969). It has been suggested that Sr would be of a more suitable size in the plagioclase structure than Ca (Higuchi and Nagasawa, 1969). By analogy, it may be suggested that the heavy REE (Yb and Er) are more suitable elements in the garnet structure than Mg.

Considering that the partition coefficient for Ce is an upper limit, the deviation of Ce from the straight line (Fig. 46) seems significant. The deviation is related to the ionic radius in such a way that for ions larger than Ca (the radius of Ca = 1.20Å), being equal to that of Nd), the energetics of substitution may

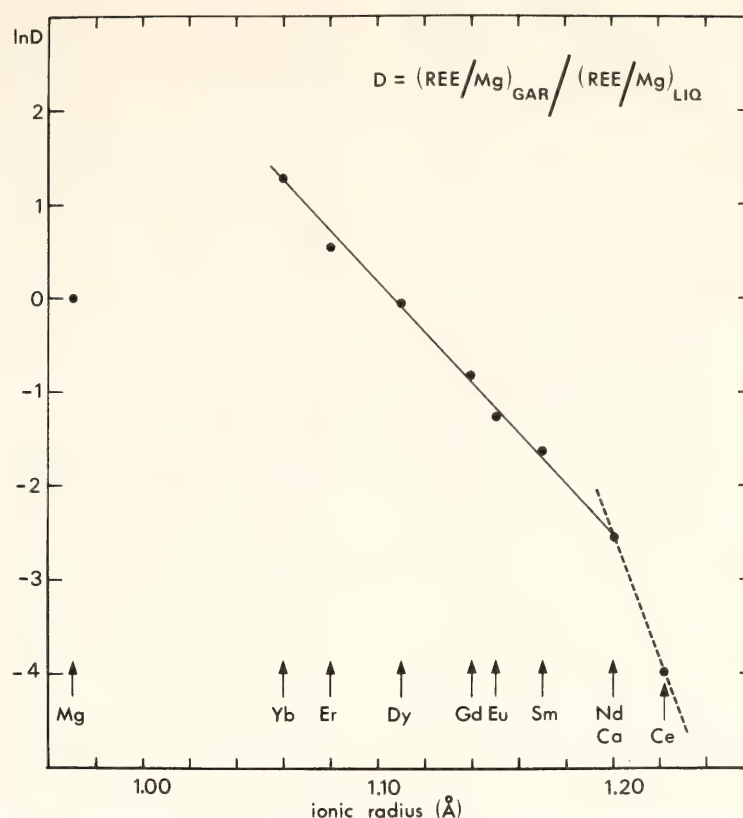


Fig. 46. $\ln D$ vs ionic radii (8-fold coordination, from Whittaker and Muntus (1970)).

be different from that for the smaller REE. The estimated partition coefficient for La (Frey *et al.*, 1974) of 0.004 is on the extension of the Nd-Ce line. The higher oxidation state of Ce^{4+} as a reason for the deviation mentioned above may be ruled out because Ce^{4+} has a smaller ionic radius than Ce^{3+} .

The arguments given above would be valid only for pyrope-rich garnet. For grossularite-andradite garnet, the sites available for REE are larger because Ca is the host ion. It would be possible then to expect that quite a different partition pattern would be observed for the grossularite-liquid system than that of the present experiments.

Agreement between the present results and the garnet-liquid partition coefficients estimated for natural systems suggests that these values can be used to calculate the REE patterns of liquids produced by partial melting of garnet lherzolite and to assess the effect of "eclogite fractionation" (O'Hara and Yoder, 1967). An example of this application is found in Shimizu and Arculus

(1975), who examined partial melting and fractional crystallization models (including eclogite fractionation) based on the partition coefficients reported here for the REE variations observed for a suite of basanitoids-alkali olivine basalts from Grenada, Lesser Antilles. They concluded that the observed variations (a factor of 6 for Ce and constant Yb) may be best explained by various degrees of partial melting of garnet lherzolite.

O'Hara (1968) stated that the higher K_2O content of alkali basalt compared to tholeiite may be explained by a small degree of partial melting (5% for alkali basalt and 20% for tholeiite) followed by extensive eclogite fractionation (50%, compared with no eclogite fractionation for tholeiite) and subsequent olivine fractionation (40%, same for tholeiite), starting with the mantle with K_2O as low as 0.025%. If these figures are to be taken as representative, relatively small variations in heavy REE (8–15 times chondrite) between tholeiite and alkali basalts suggests that a high partition coefficient of heavy REE (Yb) between

garnet and liquid (such as 40, Schnetzler and Philpotts, 1970) is difficult to reconcile with the observation. For example, 50% eclogite fractionation could result in depletion of Yb in the residual liquid of more than 4 orders of magnitude if $D_{\text{Gar}}^{\text{Yb}} = 40$ and eclogite consists of 50% garnet and 50% clinopyroxene.

O'Hara (1970) suggested that the chemical composition of partial melts and solid residua can be satisfactorily explained by garnet lherzolite-garnet harzburgite inclusions in kimberlite (GLIK/GHR model). This implies that a significant amount of garnet is present in the solid residua (in fact, some garnet harzburgite inclusions contain more than 5% garnet). If this were the typical circumstance for partial melting of the mantle, and if the REE patterns of basaltic magmas represent partial melts, then calculations suggest that a very high partition coefficient of heavy REE (Yb) between garnet and liquid (such as 40) is difficult to reconcile with the petrologic models. For example, a liquid in equilibrium with a solid containing garnet (5% of the original solid, for example) would be depleted in Yb by a factor of about 2 relative to the initial solid. If the mantle has REE abundances of 2–4 times chondrite, the above liquid must have Yb content of 1–2 times chondrite, being much too low for any erupted magmas.

References

- Allègre, C. J., R. Montigny, and Y. Bottinga, Cortège ophiolitique et cortège océanique, géochimie comparée et mode de genèse., *Bull. Soc. Geol. Franç.*, 15, 461–477, 1973.
- Frey, F. A., W. B. Bryan, and G. Thompson, Atlantic ocean floor: geochemistry and petrology of basalts from Legs 2 and 3 of the Deep Sea Drilling Project, *J. Geophys. Res.*, 79, 5507–5527, 1974.
- Gast, P. W., Trace element fractionation and the origin of tholeiitic and alkaline magma types, *Geochim. Cosmochim. Acta.*, 32, 1057–1086, 1968.
- Grutzeck, M. W., S. J. Kridelbaugh, and D. F. Weil, REE partitioning between diopside and silicate liquid, *Eos*, 54, 1222, 1973.
- Higuchi, H., and H. Nagasawa, Partition of trace elements between rock-forming minerals and the host volcanic rocks, *Earth Planet. Sci. Lett.*, 7, 281–287, 1969.
- Kay, R. W., and P. W. Gast, The rare earth content and origin of alkali-rich basalts, *J. Geol.*, 81, 653–682, 1973.
- O'Hara, M. J., The bearing of phase equilibria studies in synthetic and natural systems on the origin and evolution of basic and ultrabasic rocks, *Earth Sci. Rev.*, 4, 69–133, 1968.
- O'Hara, M. J., Upper mantle composition inferred from laboratory experiments and observations of volcanic products, *Phys. Earth Planet. Int.*, 3, 236–245, 1970.
- O'Hara, M. J., and H. S. Yoder, Jr., Formation and fractionation of basic magmas at high pressures, *Scott. J. Geol.*, 3, 67–117, 1967.
- Philpotts, J. A., C. C. Schnetzler, and H. H. Thomas, Petrogenetic implications of some new geochemical data on eclogitic and ultrabasic inclusions, *Geochim. Cosmochim. Acta*, 36, 1131–1166, 1972.
- Schilling, J. G., and J. W. Winchester, Rare earth contribution to the origin of Hawaiian lavas, *Contrib. Mineral. Petrol.*, 23, 27–37, 1969.
- Schnetzler, C. C., and J. A. Philpotts, Partition coefficients of rare earth elements between igneous matrix material and rock-forming mineral phenocryst, II, *Geochim. Cosmochim. Acta*, 34, 331–340, 1970.
- Shimizu, N., An experimental study of the partitioning of K, Rb, Cs, Sr and Ba between clinopyroxene and liquid at high pressures, *Geochim. Cosmochim. Acta*, 38, 1789–1798, 1974.
- Shimizu, N., Rare earth elements in garnets and clinopyroxenes from garnet

- lherzolite inclusions in kimberlites, *Earth Planet. Sci. Lett.*, **25**, 26–32, 1975.
- Shimizu, N., and R. J. Arculus, Rare earth element concentrations in a suite of basanitoids and alkali olivine basalts from Grenada, Lesser Antilles, *Contrib. Mineral. Petrol.*, in press, 1975.
- Shimizu, N., and S. R. Hart, Differential dissolution technique (DDT): chemical separation of crystals from glass, in *Carnegie Inst. Wash. Year Book 72*, pp. 268–270, 1973.
- Whittaker, E. J. W., and R. Muntus, Ionic radii for use in geochemistry, *Geochim. Cosmochim. Acta*, **34**, 945–956, 1970.

AN ASSESSMENT OF LOCAL AND REGIONAL ISOTOPIC EQUILIBRIUM IN A PARTIALLY MOLTEN MANTLE

A. W. Hofmann and S. R. Hart

Introduction

The isotopic composition of Sr and Pb has been used to set constraints on the origin and the composition of the source material of volcanic rocks. Gast (1960) pioneered this approach and showed by comparing meteoritic and terrestrial $^{87}\text{Sr}/^{86}\text{Sr}$ ratios and trace element abundances that the earth (or at least the upper mantle and crust) is depleted in alkalis relative to chondritic meteorites. Starting with the work of Hurley *et al.* (1962) and Faure and Hurley (1963), the initial $^{87}\text{Sr}/^{86}\text{Sr}$ ratio was used to determine, for example, whether granites were derived from the crust or the mantle. Gast, Tilton, and Hedge (1964) for the first time showed that there are consistent differences between individual oceanic islands in the isotopic composition of lead and strontium, and they concluded that there are regional variations in the composition of the upper mantle. Hedge and Peterman (1970) and Hart (1971) compared $^{87}\text{Sr}/^{86}\text{Sr}$ ratios from ocean floor basalts (i.e., rocks derived from mid-ocean ridges) with ratios

from oceanic islands and showed that the isotopic ratios from the ocean floor are systematically lower. More recent work has shown that although significant regional differences do exist, the ocean floor basalts are the most nearly constant in their Sr-isotopic composition of all the volcanic rocks investigated. The $^{87}\text{Sr}/^{86}\text{Sr}$ ratios of these rocks usually vary within the narrow range 0.7025–0.7035, with the large majority having values less than 0.7030. In contrast, the $^{87}\text{Sr}/^{86}\text{Sr}$ ratios of oceanic island basalts are higher and much more variable. The pattern that emerges from these results is one of distinct groupings of basalts from the different environments in terms of isotopic compositions. This is illustrated in Fig. 47, where $^{87}\text{Sr}/^{86}\text{Sr}$ ratios of basalts are shown for rocks derived from the ocean floor and from ocean islands. These results imply that the mantle is compositionally inhomogeneous both laterally and vertically because volcanoes situated near a mid-ocean ridge usually erupt lavas that differ in isotopic composition from the mid-ocean ridge material itself. If these conclusions are valid, they constrain the choice of convection patterns in the mantle. For example, models that call for derivation of *all* volcanic rocks from the same convecting upper mantle must be rejected. On the other hand, models that call for derivation of mid-ocean ridge material from a partially molten upper mantle and derivation of oceanic islands from plumes or blobs rising from deeper within the mantle are consistent with the isotope data (see also Schilling, 1973).

Until recently the interpretation outlined above has in general been accepted as valid by isotope geochemists and ignored by petrologists and geophysicists. Now, presumably for the purpose of circumventing the consequences of these restrictions, the basic assumption of all conclusions based on isotopic data has been challenged. This is the assumption that the isotopic composition of the

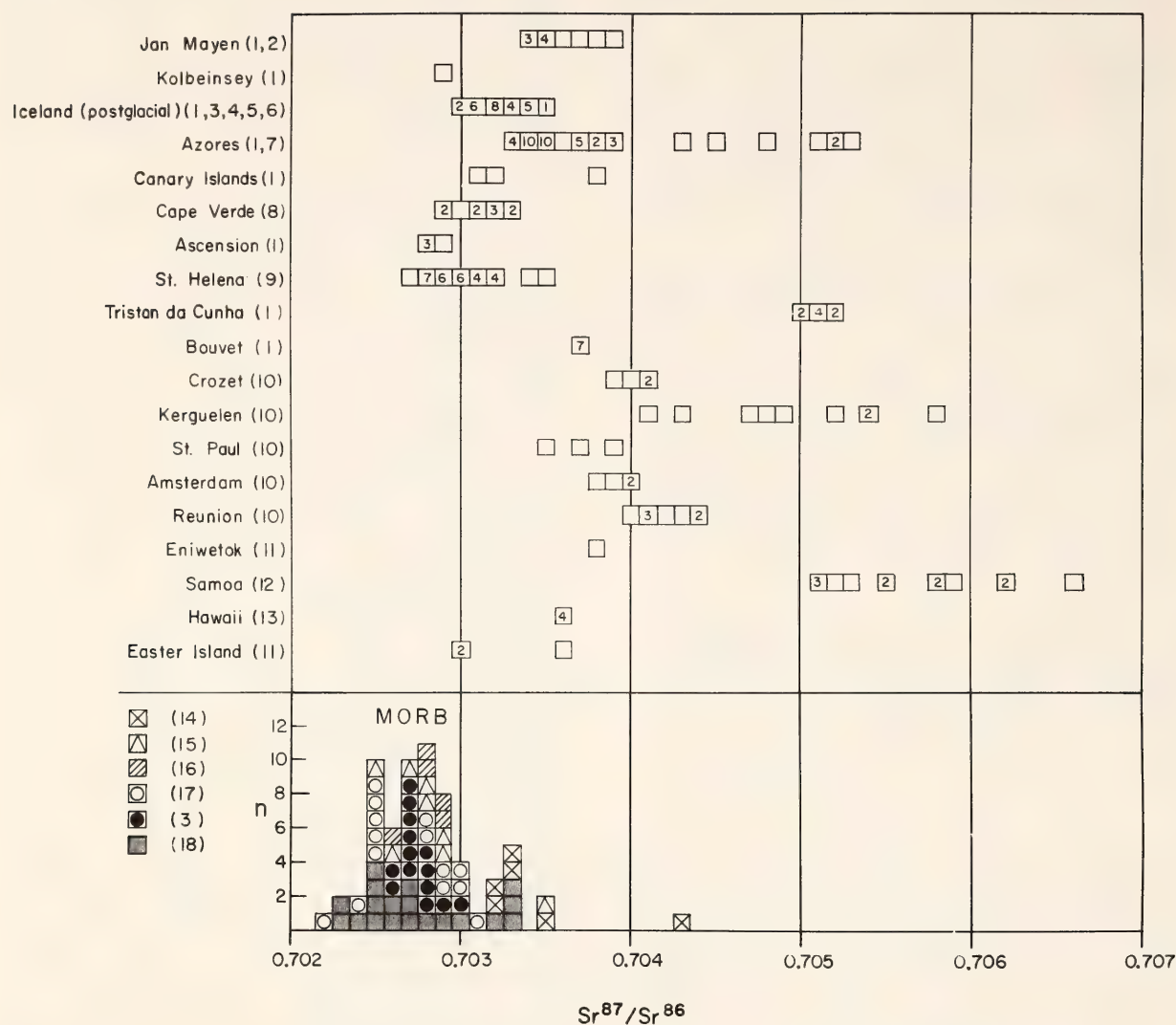


Fig. 47. Comparison of $^{87}Sr/^{86}Sr$ ratios from mid-ocean ridge basalts (MORB) and from oceanic islands. The MORB data are plotted as a frequency diagram (number of samples (n) versus $^{87}Sr/^{86}Sr$) below the horizontal line. The island data are arranged geographically in the sequence North Atlantic, South Atlantic, Indian, and Pacific Oceans. The number of samples for each value of $^{87}Sr/^{86}Sr$ (rounded to four significant figures) is indicated on the figure; a blank square represents one sample. The following data have been omitted: (1) all island-arc data; (2) all analyses published prior to 1970 (because of less uniform analytical precision of these older analyses); (3) analyses of samples from the Reykjanes Ridge between 0 and 200 km from Iceland (because this region is similar to Iceland itself with respect to isotopic and trace element composition), see reference 3 below; (4) one anomalously low value given by reference 17 (because reanalyses of the sample failed to confirm this value); (5) all data for mid-Atlantic ridge samples by White *et al.*, this Report) (because the results are shown elsewhere in this Report, and because inclusion of these data would aggravate the problem inherent in this type of frequency plot, namely, weight the data excessively with a large number of analyses from one area, the Azores platform). The key on the left-hand side identifies the islands and the references for islands and ocean-floor samples. The references are indicated by a number in parentheses and by the following list: (1) O'Nions and Pankhurst, 1974; (2) Lussiaa-Berdou-Polve and Vidal, 1973; (3) Hart *et al.*, 1973; (4) Sun and Jahn, 1975; (5) O'Nions *et al.*, 1973; (6) O'Nions and Grönvold, 1973; (7) White *et al.*, 1975; (8) Klerkx *et al.*, 1974; (9) Grant *et al.*, 1974; (10) Hedge *et al.*, 1973; (11) Hedge and Peterman, 1970; (12) Hedge *et al.*, 1972; (13) Hart, 1973; (14) Subbarao and Hedge, 1973; (15) Subbarao, 1972; (16) Hart *et al.*, 1972; (17) Hedge and Peterman, 1970; (18) Hart, 1975.

erupted material is representative of the source material in the mantle. This condition is met if there is isotopic equilibrium between the melt and the solid residue in the source region so that the isotopic ratios either remain constant or change in such a manner that the effect can be calculated (e.g., from the known age of the rock) or cancelled by simple normalization for fractionation. Those who have challenged this assumption prefer to make a different assumption, namely that the source mantle is compositionally uniform. O'Hara (1973, 1975) proposed that the different magmas on Iceland and the Reykjanes Ridge "were derived from a homogeneous source, [and that] the differences could arise from fractional crystallization during the ascent of the lava." He further suggested that "isotope ratios had changed during the manifest fractional crystallization." Flower *et al.* (1975) "are reluctant as yet to accept the two-mantle-source model because it is essentially defeatist," and attempt to show that $^{87}\text{Sr}/^{86}\text{Sr}$ variation in the basalts "is not irreconcilable with a single mantle composition." They do this by postulating that phlogopite, because of its high Rb/Sr ratio, is a source of unequilibrated radiogenic ^{87}Sr which is added to the melt only as the phlogopite itself enters the melt phase. O'Nions and Pankhurst (1974) also find an inhomogeneous mantle more difficult to accept than disequilibrium melting and propose specific models of disequilibrium melting to account for the observed isotopic variations. Earlier suggestions of disequilibrium melting were made by Gast *et al.* (1964) and by Peterman *et al.* (1970), though only in reference to partial fusion of a xenolith caught in the host basalt immediately prior to eruption, and by Harris *et al.* (1972), who used the evidence of isotopic disequilibrium within xenoliths to infer that such disequilibrium might persist during partial melting and basalt genesis. Disequilibrium within xenoliths or between xenolith and

host basalt appears to be common (Allsopp *et al.*, 1969; Compston and Lovering, 1969; Cooper and Green, 1969; Dasch and Green, 1975; Hutchison and Dawson, 1970; Kudo *et al.*, 1972; Laughlin and Brookins, 1971; Leggo and Hutchison, 1968; Lovering and Tatsumoto, 1968; Manton and Tatsumoto, 1971; Morioka and Kigoshi, 1975; O'Neil *et al.*, 1970; Paul, 1971; Peterman *et al.*, 1970; Stuckless and Ericksen, 1975; Stueber and Ikramuddin, 1974; Stueber and Murthy, 1966; Stull and McMillan, 1973; Zartman and Tera, 1973). Because the original relationship of these xenoliths to the host basalt is not known, extrapolation from the xenolith data to the behavior of the actual melting region remains dubious.

In this controversy, relatively little attention has been given to the processes by which the mantle might be homogenized. It is obvious that the process of withdrawing a partial melt leaves a solid residue that is depleted in some of its components. Because of this, the mantle regions that are the source of volcanism must become chemically different from adjacent regions. The question then arises, Is there a plausible mechanism by which these regions are rehomogenized? Some authors deny this (Dickinson and Luth, 1971; Ringwood, 1974) because they view the residue as a refractory solid that cannot be equilibrated with undepleted mantle because solid-state diffusion in silicates is known to be very slow. Others (Armstrong, 1968; O'Nions and Pankhurst, 1974) assume that mantle convection combined with diffusion will rehomogenize an inhomogeneous mantle. The new diffusion data in melts given in the companion report by Hofmann (this Report) bear on this question.

Most of the participants of this discussion (O'Hara is one exception) accept the conclusion that the variability in isotopic composition of fresh volcanic rocks reflects isotopic inhomogeneities of the source. The issue is the length (or

volume) scale of these inhomogeneities. Two extreme cases may be distinguished: (1) a mantle that is uniform on a regional scale (when comparing samples that are representative of 10 to 1000 km³ volumes) but at the same time is not in chemical and isotopic equilibrium on a local (centimeter or less) scale; (2) a mantle that is locally equilibrated but is inhomogeneous on a regional scale. Case 1 would be produced by very efficient mechanical stirring and extremely inefficient (or absent) chemical diffusion. Case 2 would be produced by inefficient mechanical stirring combined with local diffusion or recrystallization processes that lead to local chemical and isotopic equilibrium between individual mineral grains or, more importantly in the present context, between the melt phase and residual crystals.

In this report we argue the merits of case 2 for a partially molten mantle. For this purpose, we examine the regional pattern of isotopic compositions in oceanic rocks, the constraints set by isotopic model ages, and the shortcomings of published models that are based on the assumption of case 1. In addition we apply available kinetic data to estimate the length scale of equilibration in a partially molten mantle. We are led to the conclusion that the isotopic composition of oceanic volcanic rocks is indeed representative of the source and that the mantle is inhomogeneous (on a regional scale) both horizontally and vertically.

Evidence Based on Analytical Data from Volcanic Rocks

The idea of a chemically heterogeneous mantle received its first strong verification from the Sr and Pb isotope work of Faure and Hurley (1963), Hedge and Walthall (1963), and Gast, Tilton, and Hedge (1964). Recent high precision isotopic work has not markedly changed the picture, though it has added considerable detail to earlier findings. We will restrict our discussion to oceanic volcanics, as there is less possibility that

crustal contamination is involved in these cases. There is no convincing evidence of crustal contamination in any of the oceanic volcanic isotopic data and, as will be pointed out later, the lead isotope data appear to preclude any significant contamination. Other evidence, such as the striking uniformity of Sr isotope ratios for recent tholeiites from the whole length of the active volcanic zone in Iceland (Hart *et al.*, 1973), also suggests involvement of crustal contaminants is minimal or absent.

The lead isotope data of oceanic volcanic rocks have been recently summarized by Sun and Hanson (1975). In addition, we have collected most of the recent high precision Sr isotope data (that is, data published since 1970) for oceanic islands and mid-ocean ridges, and these data are summarized in Fig. 47. This figure simply demonstrates again the well-known variability of Sr isotope ratios in oceanic rocks and emphasizes the clear-cut difference between mid-ocean ridge basalts (MORB) and island basalts. The demarcation between ridge basalts and island basalts occurs at a ⁸⁷Sr/⁸⁶Sr value of about 0.7030. Very few island basalts have values below 0.7030; two exceptions are St. Helena and Ascension Islands, which are significantly below 0.7030. There are a number of ridge basalts with values higher than 0.7030, but these are invariably associated either with seawater alteration or proximity to hot spots or plumes. For example, some of the high values reported by Hedge and Peterman (1970) are probably altered, as judged by petrographic descriptions and Rb and Cs contents reported in Kay, Hubbard, and Gast (1970). Other high values occur in samples probably affected by nearby hot spots; for example, the samples from 45°N on the mid-Atlantic ridge appear to be related to the Azores hot spot (White, Hart, and Schilling, 1975), while samples from the mid-Indian Ocean ridge (Subbarao and Hedge, 1973) are probably related to

either the Reunion hot spot or to the triple junction on the mid-Indian Ocean ridge. To our knowledge, there is no well-documented Sr isotope ratio on fresh MORB which is higher than 0.7030, when only ridge segments well removed from hot spots are considered.

This, then, is the type of data which demonstrates isotopic heterogeneity from the sub-oceanic mantle. By itself, it does not settle the question of whether that heterogeneity is on a mineralogical (= local) scale or on a larger, regional scale. If the isotopic differences between ridge basalts reflect regional mantle heterogeneities, then it would appear difficult to keep these sources distinct in a convecting mantle, as islands may occur very close to ridges. This problem was posed by Hart (1971) and has recently been the main consideration leading O'Nions and Pankhurst (1974) to consider disequilibrium melting models as an alternative to the generally accepted idea of a regionally heterogeneous mantle. Another, and in our opinion more plausible, solution to this problem is given by a vertically stratified mantle. A specific model (see for example, Schilling, 1973, and Sun and Hanson, 1975) of such a mantle may consist of a convecting upper mantle that is chemically depleted by previous melting and a more "juvenile" lower mantle, which may or may not convect separately. Mid-ocean ridge basalts with their low $^{87}\text{Sr}/^{86}\text{Sr}$ ratios and depleted alkalies and other trace elements are derived from the upper mantle; oceanic island basalts with their higher $^{87}\text{Sr}/^{86}\text{Sr}$ ratios and their less depleted trace element character are derived from plumes or isolated diapiric intrusions that rise from the lower mantle with relatively little chemical interaction with the upper mantle. A model like this, however, requires many plumes or diapirs, as all oceanic islands and probably many seamounts will require derivation from a mantle source that is chemically distinct from the spreading ridge mantle.

One aspect of the isotopic data that bears on the problem of scale of the mantle heterogeneities is the marked uniformity of Sr isotopic ratios for basalts from a given geographic area despite large variations in the other chemical constituents of the basalt. For example, tholeiites from the whole length of the neo-volcanic zone on Iceland are isotopically uniform (within the limits of measurement) despite considerable variation in other trace element concentrations (Hart *et al.*, 1973; Hart and Schilling, 1973). With rather limited sampling, we have already demonstrated potassium contents ranging from 150 ppm to 2000 ppm (and an even larger range is shown by the data of Sigvaldason, 1974), with like variations in other LIL (large ion lithophile) element concentrations such as Rb, Cs, and Ba. This phenomenon can be extended to some of the alkali basalts on Iceland, which have Sr isotope ratios similar to the tholeiites despite their markedly different chemical character. If a small-scale disequilibrium model (corresponding to case 1 in the "Introduction") is invoked to explain the Sr isotopic data from Iceland, this model must at the same time explain how such diverse chemical characteristics are obtained from a chemically homogeneous mantle. While O'Nions and Pankhurst (1974) suggest that the Sr isotopic characteristics of oceanic basalts may be explained by disequilibrium melting models, they do not show how such a model can be made compatible with the isotopic uniformity coupled with chemical diversity of basalts from Iceland. A similar situation exists in the region of the Azores hot spot (White, Hart and Schilling, 1975), where tholeiites dredged from the Azores platform have Sr isotope ratios identical to those of the alkali basalts from the nearby islands, despite rather large differences in chemical character.

A related phenomenon is that most islands show considerable uniformity of Sr isotope abundances, whereas separate

islands will have distinctly different Sr ratios. This can be seen for the various islands of the Azores group (White, Hart, and Schilling, 1975), as well as other islands in the Atlantic (O'Nions and Pankhurst, 1974). In other words, if disequilibrium melting of a regionally homogeneous mantle is envisaged, it has to be carried out in such a way that Sr isotope ratios show inter-island but not intra-island variations. It is conceivable and has been vigorously argued by O'Hara (1973, 1975) that the intra-island chemical differences are the result of different degrees of fractional crystallization. In this case, the isotopic composition of the residual melts could remain constant despite their chemical diversity. Nevertheless, this does not solve the basic problem of obtaining the isotopic uniformity in the first place, namely at the melting stage through a disequilibrium process. If the melts are to be isotopically uniform but different from this source, the extent of reaction between solid and (disequilibrium) melt fractions must be remarkably uniform for all batches of magma within each island. At the very least, both the rate of melt production and the degree of partial melting would have to be uniform.

In disequilibrium melting models, phlogopite generally plays a key role (O'Nions and Pankhurst, 1974; Flower, Schmincke, and Thompson, 1975). The crucial question here is of course whether phlogopite can remain out of isotopic equilibrium for times of the order of 10^7 to 10^9 years, and whether it can remain as a residual phase during any significant degree of melting. We will address the first part of this question below; the second part requires experimental verification. Here, we only point out that the amount of phlogopite in the mantle should not be treated as an unconstrained variable. For example, O'Nions and Pankhurst (1974) consider 5% phlogopite in their mantle model. Is this reasonable? Phlogopite contains about

8% potassium, and the overall K content of the postulated mantle rocks is directly related to phlogopite content. A peridotite containing 5% phlogopite will have a K content of 4000 ppm. This is probably 10 times the K content of almost any mantle-derived ultramafic rock yet analyzed, and 4 to 5 times the K content of chondrites. Ever since Gast's (1960) classic paper it has been accepted that the earth's crust and upper mantle are depleted in alkalis relative to chondrites. A K content of 4000 ppm implies heat production of at least 4–5 times the chondritic value (or more, if a terrestrial K/U ratio is assumed); a model for a sub-oceanic mantle with this level of heat production would be seriously out of step with estimates based on observed heat flow. The arguments of Gast (1960) and subsequent workers need not be restated here, and we add only that unless entirely new evidence is introduced, the chondritic K value of $\sim 0.08\%$ must be considered an upper limit for the terrestrial K abundance. Consequently, if we consider a mantle with a maximum of 1% phlogopite as the source of the melts, a very small degree of partial melting will consume all the available phlogopite, unless the phlogopite is far more refractory than is indicated by experimental studies on phlogopite stability (Yoder and Kushiro, 1969; Modreski and Boettcher, 1973; Forbes and Flower, 1974).

Evidence Derived from Time Constraints

It is obvious that time considerations are important in this discussion, because isotopic and trace element equilibrium or disequilibrium will be strongly dependent on kinetic factors. Any serious chemical model for the mantle must be consistent with the fact that the observed heterogeneities have persisted for times of the order of 1–3 billion years. The most persuasive evidence for this is the general alignment of volcanic lead isotope data along a secondary isochron of about 2 billion-year slope. This argu-

ment was originally presented by Gast, Tilton, and Hedge (1964) and Tatsu-moto (1966a, 1966b). Since that time, numerous papers have added Pb isotope data from a variety of volcanic environments, and have gradually improved the precision of the isotopic data (see, for example, Sun and Hanson, 1975). Data from oceanic islands and oceanic ridges, when plotted on a $^{206}\text{Pb}/^{204}\text{Pb}$ versus $^{207}\text{Pb}/^{204}\text{Pb}$ diagram, fall along a linear trend which, interpreted as a secondary isochron, has an age of ~ 2.0 billion years. These lead data require derivation of lead from sources which have maintained separate and distinct U/Pb systems for this length of time. Unless one of these sources is considered to be crustal (i.e., sediment, seawater, etc.), the source of the Pb isotope heterogeneities must reside in the mantle. One argument against sediment involvement is the near absence of sediments in the vicinity of the mid-ocean ridge. Direct involvement of seawater lead is also unlikely, because the concentration of Pb in seawater is on the order of 30,000 times lower than in basalt, and interaction with the very large volumes of seawater required would change the oxygen isotopic composition of the basalt profoundly. Another argument can be made from recent comparisons between volcanic leads and ocean sediment leads (Sinha and Hart, 1972; Church and Tilton, 1973; Meijer, 1975). In general, oceanic sediment leads (and presumably seawater Pb as well, Chow and Patterson, 1962) lie along a linear trend which is subparallel to the oceanic volcanic lead line, but which has significantly higher values of $^{207}\text{Pb}/^{204}\text{Pb}$. Thus the crustal lead available for contamination of ocean volcanic rocks does not fall either along or on an end-member to the oceanic trend, but above it (on a $^{207}\text{Pb}/^{204}\text{Pb}$ – $^{206}\text{Pb}/^{204}\text{Pb}$ plot) and subparallel to it.

Because only one radioactive parent isotope is involved in the Sr isotope system, one cannot make the same argu-

ment as with the lead. However, as shown by Sun and Hanson (1975), the oceanic volcanic Sr data fall approximately along a 2.0 b.y. isochron when plotted on a Rb-Sr isochron diagram. This age is meaningful only if the Rb/Sr ratio of the volcanic liquid is the same as that of the source. However, for the age of the mantle heterogeneities to be substantially less than this 2.0 b.y. value, it is necessary to postulate a very systematic type of disequilibrium melting which can produce liquids with Rb/Sr ratios that are systematically lower than in the source so that the approximate isochron relationship is preserved. Equilibrium melting involving residual phlogopite is not an effective way of producing liquids with Rb/Sr ratios significantly lower than the source (retention of 2% phlogopite after melting of a source containing an original 5% phlogopite will decrease the Rb/Sr ratio of the liquid by only 20% relative to the starting material).

Evidence for mantle heterogeneity (on some scale) exists not only from Pb and Sr isotope evidence, but also from trace element ratios and abundances. While one cannot prove that the trace element heterogeneities have also existed for a long time period, as one can for the lead isotope data, it is probably reasonable to consider all of the heterogeneities as being related to the same processes. After all, the Pb and Sr isotopic variations are generated by variations in U/Pb and Rb/Sr, and these four trace elements are similar in general behavior to the many other trace elements for which mantle heterogeneity is postulated (K, Cs, Ba, REE, etc.). Thus we feel that any discussion of mechanisms for generating a particular trace element pattern in volcanic rocks should be compatible with the constraints imposed by time. For example, O'Nions and Pankhurst (1974) consider a model in which disequilibrium melting of phlogopite peridotite occurs, with the disequilibrium having persisted for only 20 m.y. Obvi-

ously, it is much easier to conceive of inter-mineral disequilibrium lasting for 20 m.y. than for 2000 m.y. We argue that models such as proposed by O'Nions and Pankhurst be considered only if they are consistent with disequilibrium on a time scale of approximately 2000 m.y.

O'Hara's (1973, 1975) explanation for the trace element and isotopic variations between tholeiites from Iceland and those from the Reykjanes Ridge requires special discussion, because he assumed a uniform mantle source for the entire region and relied entirely on fractional crystallization to explain all the chemical variation. Hart *et al.* (1973) explained the Sr isotope data from these basalts as due to large-scale heterogeneities in the mantle. O'Hara (1973) first discounted the isotopic evidence by alluding to the implicit "assumption that these isotopes cannot be fractionated." Actually, the question of whether Sr isotopes can be fractionated in nature or not is irrelevant, because all Sr isotope analyses are routinely corrected for all isotopic fractionation effects, be they natural or laboratory induced. O'Hara (1975) clarified his earlier statement, stating the process was one involving a change of isotope ratio "during manifest fractional crystallization." Presumably this refers not to isotope fractionation but to generation of radiogenic ^{87}Sr during histories in variable Rb/Sr environments. To produce the observed difference in Sr isotope ratios of the Iceland-Reykjanes Ridge basalts (0.7027 versus 0.7030) would require aging for 15 m.y. in an environment having a Rb/Sr ratio of 0.5. The oldest rocks in Iceland are about 15 m.y. old (O'Nions and Pankhurst, 1973), so this is a reasonable upper limit for the age of a Rb/Sr subsystem. However, the Rb/Sr ratio of 0.5 is at least 10 times the highest ratio observed in any of the basalts from Iceland. O'Hara's model will only work if one assumes that the Rb source which supported the growth of ^{87}Sr in Icelandic

basalts is now hidden. O'Hara's model is even more difficult to defend when the Pb isotope data are considered as well. Sun and Jahn (1975) have shown that the Sr isotope variation between Iceland and the Reykjanes Ridge is paralleled by a variation in Pb isotope abundances. The Pb isotope data form a linear trend similar to that commented on above for oceanic volcanics in general, with an inferred age of about 1.5 b.y. Obviously, short-term fractionation models such as O'Hara's do not explain the recent Iceland isotopic data nor the more general body of geochemical data (of which Iceland is only a specific case) that has been available for over ten years.

Evidence for Mineral Disequilibrium

Perhaps the closest analog to possible mantle material is found in the ultramafic nodules which are erupted in alkali basalts and other undersaturated basalt types. The large majority of these nodules appear isotopically different from their host basalts (these findings are based on at least 19 different publications covering about 100 separate nodules). Most of these studies involved Sr isotope data; however, lead isotope studies on nodule suites (e.g., Zartman and Tera, 1973) also indicate disequilibrium between nodules and host basalt. Because of the absence of any systematic relationship between nodules and host, the authors of these studies have generally concluded that the nodules are not related genetically to their host basalt but are probably accidental inclusions.

In addition to disequilibrium between nodule and host basalt, 10 of the studies have analyzed the constituent minerals of the nodules (usually olivine, orthopyroxene, and clinopyroxene) and in nearly all cases disequilibrium was also found to exist between the minerals of a given nodule. Again, most of these studies relied on Sr isotope data; however, similar results were reported for Pb isotope abundances by Zartman and Tera (1973) and by Morioki and Kigoshi (1975).

Generally, the olivine and orthopyroxene have higher $^{87}\text{Sr}/^{86}\text{Sr}$ ratios than coexisting clinopyroxene; in some cases the differences are very large. For example, a nodule from Victoria, Australia (Dasch and Green, 1975), contained olivine with $^{87}\text{Sr}/^{86}\text{Sr} = 0.713$, orthopyroxene = 0.7060, clinopyroxene = 0.7029, total bulk nodule = 0.7040, and host basalt = 0.7045. While this particular case nicely illustrates the Sr isotope disequilibrium that is frequently found between minerals in nodules, it also illustrates some of the unanswered problems. A mineralogical mode was reported for this nodule, and when the individual mineral analyses are used to reconstruct the whole rock, the Sr and Rb concentrations are lower by a factor of about 3 than the directly analyzed whole rock nodule, while the resulting $^{87}\text{Sr}/^{86}\text{Sr}$ ratio (0.7055) is higher than the bulk nodule. This implies that some phase or material is present in the nodule which was not analyzed but which has relatively high Rb and Sr contents, and an 87/86 ratio lower than 0.7040. While this question does not directly affect the concept of mineral disequilibrium in nodules, it does show that nodules are complex systems and allows room for speculation about possible contaminating effects of such material on separated minerals. It should be noted that although most nodules that have been studied come from basalts erupted through continental terrains, disequilibrium has been proven in at least one case for an oceanic site, Hawaii (Zartman and Tera, 1973; Stueber and Ikramuddin, 1974).

Inter-mineral disequilibrium in ultramafic nodules does not demonstrate, however, that the mantle in magma source regions will show similar disequilibrium. Because most of these nodules are not cogenetically related to their host basalt, and because their constituent minerals are not in equilibrium, little can be said about the depth from which they come, or whether they do in

fact come from a mantle region which is presently acting as a source for magmas. They could come from the uppermost mantle levels of the lithosphere where temperatures have been relatively low (500° – 600°C) for long periods of time (subcontinental lithosphere is essentially protected against high temperatures and reworking by virtue of the overlying continent). Even in Hawaii (where the observed isotopic disequilibrium is less than most of the continental occurrences), the lithosphere is probably 10^8 years, or older. One obvious test of the possibility that most nodules have not been at magmatic temperatures for a long time would be to analyze nodules from an area of very young lithosphere—for example, an island which is very close to a spreading ridge. If disequilibrium exists in such nodules, one can be fairly sure of their recent high-temperature history. Nevertheless, even at temperatures just below the solidus, the equilibration rate is expected to be much lower than in a partially molten state. This point is explained more fully below.

Application of Kinetic Data

Although reliable experimental studies on the kinetics of reactions and diffusion are scarce, the available data all appear to point to local equilibrium, at least if grain diameters are on the order of 1 cm or less and if the time available for melting is on the order of a few thousand years or more. Several lines of evidence lead to this conclusion:

1. Melting experiments conducted with natural or artificial peridotite systems generally attain equilibrium within hours or days (e.g., Mysen and Boettcher, 1975). The melting process forces all major residual solid phases to change composition. Thus, zoned crystals can be observed when equilibrium has not been attained. The slowest possible process for this change in composition is probably volume diffusion. The actual process in the presence of a melt is likely to be dissolution into the melt and re-

precipitation of the melt-equilibrated solid, whenever the coherency stress with the crystal between initial and equilibrated composition is sufficiently large (Petrović, 1973). If the rate-limiting step is diffusion, the equilibration time can be extrapolated to coarser grained material. Typical grain diameters used in electron microprobe examination of experimental materials are about 50 μm . An extrapolation to 1 cm requires a time factor of about 40,000, so that the time for equilibration is on the order of a hundred years.

2. Direct determinations of diffusion coefficients are available for some of the phases of interest. These are shown in Fig. 48. It appears from these results that at 1000°C, the probable lower temperature limit for melting in the mantle, $D = 10^{-13} \text{ cm}^2 \text{ sec}^{-1}$ may be taken as a lower limit for cation diffusion in mantle minerals. This means that a sphere of 1 cm diameter will equilibrate with a well-mixed melt phase in less than 4×10^4 years. The word "equilibrate" is used here in the sense that the actual mass transfer between crystal and environment is 99% of that required for complete equilibration.

3. Sr diffusion in phlogopite is critical to several of the nonequilibrium-melting models proposed by O'Nions and Pankhurst (1974) and Flower *et al.* (1975) because, if present, phlogopite is expected to be the major contributor of radiogenic strontium in the mantle. If some of this ^{87}Sr can be retained in the phlogopite before and during partial melting, or if it does not equilibrate with the non-radiogenic strontium of another phase such as clinopyroxene, the $^{87}\text{Sr}/^{86}\text{Sr}$ ratio of the melt may either increase or decrease as the degree of melting increases, depending on the particular process of nonequilibrium melting. To the best of our knowledge, the radiogenic argon and strontium of all mica minerals is either lost or equilibrated with the environment during any high-grade metamorphic event. This is borne out by radiometric

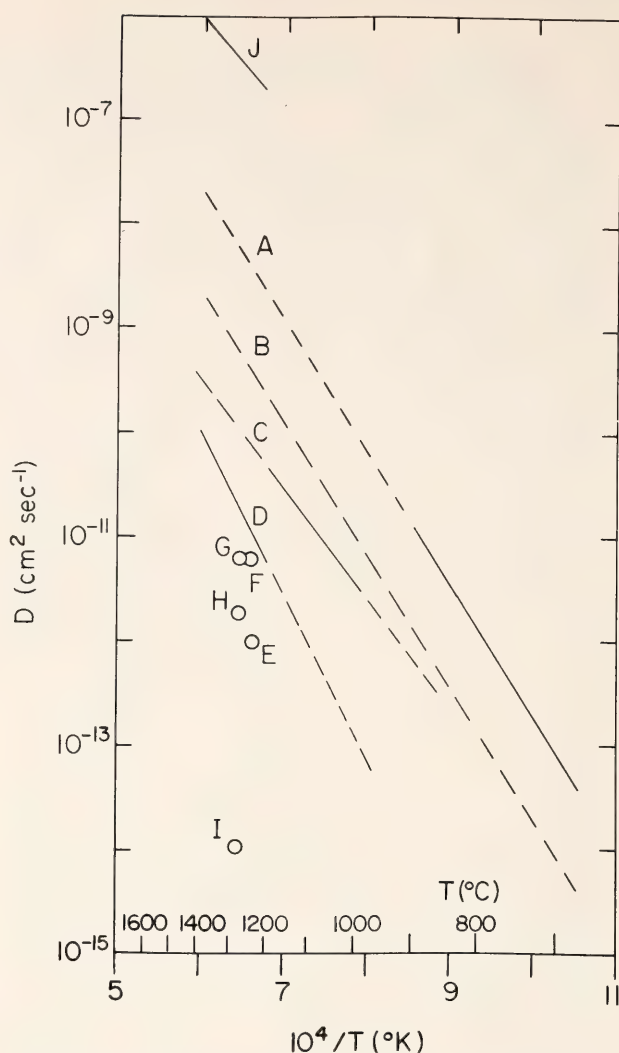


Fig. 48. Arrhenius plot ($\log D$ versus $1/T$) for diffusion in silicates relevant to mantle rocks. Solid lines are experimentally determined; dashed lines are inferred or extrapolated. A, Ar in phlogopite (Giletti, 1974b); B, Sr in phlogopite estimated from line A and from data by Hart (1964); C, Fe-Mg interdiffusion in olivine ($F_{0.87}$; $f_{\text{O}_2} = 10^{-12}$ atm) from Buening and Busek (1973); D, Fe-Mg interdiffusion in olivine ($F_{0.90}$) from Misener (1974); E, U in diopside (Seitz, 1973); F, Al in diopside (Seitz, 1973); G, H, and I, oxygen in enstatite, diopside, and forsterite, respectively (Muehlenbachs, 1974); J, Ca in basalt (Hofmann, this Report).

age determinations by numerous authors, and it is true even for short-term heating during contact metamorphism (e.g., Hart, 1964; Hanson and Gast, 1967). From this evidence alone it appears extremely unlikely that phlogopite can retain measurable amounts of radiogenic strontium at temperatures above 1000°C. To obtain an approximate time for Sr equilibrium between phlogopite and its

environment, we extrapolate the diffusion measurement of Giletti (1974b) on argon in phlogopite to higher temperatures and estimate that the diffusion coefficient for Sr is no more than a factor of 10 lower. This estimate is derived from the well-determined relative behavior of Sr and Ar in biotite (Hart, 1964; Hanson and Gast, 1967). Giletti's results are used instead of other published data because his measurements are the only ones in which the mica was stable under the experimental conditions. The estimated diffusion coefficients for Sr in phlogopite are shown in Fig. 48. The resulting maximum time for Sr equilibration between phlogopite and melt at 1000°C is about 1200 years for a sphere or 1900 years for a cylinder of 1 cm diameter.

Studies of trace element partitioning (e.g., Philpotts and Schnetzler, 1970; Shimizu, 1974; Hart and Brooks, 1974) have shown that clinopyroxene is probably the major Sr-bearing phase in the upper mantle. Slow diffusion in clinopyroxene might therefore inhibit overall equilibration even if diffusion in phlogopite and other phases is rapid. Argon retention in pyroxenes is known to be higher than in micas, and it is conceivable that the strontium in clinopyroxene does not equilibrate with the melt; we are therefore planning to determine Sr diffusion in clinopyroxene experimentally. It should be remembered, however, that extraordinarily small diffusion coefficients ($D < 10^{-15} \text{ cm}^2 \text{ sec}^{-1}$) are required for disequilibrium to persist between liquid and a coarse-grained solid (grain diameter $> 1 \text{ cm}$) for a time span of one million years or more.

If one accepts a diffusion coefficient of $10^{-13} \text{ cm}^2 \text{ sec}^{-1}$ at 1000°C, the apparent disequilibrium in mantle xenoliths is not altogether surprising, if one assumes that the xenolith existed in a fluid-free environment before being caught up by the rapidly intruding melt. In an all-solid peridotite, Sr isotopic equilibration between phases is inhibited by two fac-

tors: (1) the extremely low concentration of Sr in olivine and orthopyroxene, the two major phases present; and (2) the potentially much greater distance over which strontium must diffuse through solid material. To illustrate the first factor we imagine a clinopyroxene grain separated from a phlogopite grain by a barrier of olivine. If the intrinsic mobility of Sr in all three phases is the same but the concentration in the olivine is lower by a factor of 500 (see partitioning data by Hart and Brooks, 1974), the rate of exchange or flux through the olivine barrier is reduced by a factor of 500. The second factor is important because diffusion times vary with the square of the diffusion distance. Wilshire and Jackson (1975) show examples of compositionally inhomogeneous xenoliths that would require diffusion over distances of 10 cm or more for homogenization to occur. Once a sufficient amount of melt is present to wet all the grain boundaries, then barriers to internal equilibration are removed since the melt phase acts as a short circuit between the solids because diffusion is several orders of magnitude faster in the silicate melt than in the solids (see Fig. 48). Consequently, the presence of a melt phase may be necessary to the establishment of local equilibrium in the mantle.

This leaves the question of large-scale rehomogenization in the mantle. O'Nions and Pankhurst (1974) argue the case for local disequilibrium for short-lived processes (e.g., accumulation of radiogenic Sr in phlogopite equivalent to an age of 20 m.y.). At the same time they believe that, on a regional (kilometer) scale, the mantle will be homogenized by the combined effects of diffusion and convection. The times involved for this process are presumably somewhere between 10^8 and 5×10^9 years. As pointed out above, diffusion distances vary with the square root of time. Using again $D = 10^{-13} \text{ cm}^2 \text{ sec}^{-1}$, a characteristic distance of $Dt = \sim 60 \text{ cm}$ is obtained for a diffusion time of 10^9 years. Larger

scale homogenization is therefore out of the question for an all-solid mantle. This statement must be qualified by adding that we assume that mantle convection without diffusion is not effective in producing large-scale homogeneous mantle corresponding to case 1 discussed in the introduction. We infer this qualitatively from the present-day surface kinematics of plate movement, which point to large convection cells (on the order of 1000 km) and slow turnover time ($\sim 10^8$ years). Even models that consider two scales of convection (Richter and Parsons, 1975) envision small rolls greater than 100 km in diameter. In the presence of a melt, the diffusion coefficients and, therefore, the distances are substantially higher, but even in this case, regional homogenization is achieved only by rather vigorous stirring. The characteristic distance for a partially molten mantle, calculated using $D = 10^{-6} \text{ cm}^2 \text{ sec}^{-1}$ as an upper limit for the diffusivity (see companion report by Hofmann), is $\sqrt{Dt} = 1 \text{ km}$. It is therefore difficult, for example, to see how a subducted oceanic crust of 5 km thickness can ever be equilibrated with the surrounding mantle as proposed by Armstrong (1968). Extensive mixing appears to be plausible only in environments where very large shear strains are encountered, for example, within the diapiric intrusion of partially molten material. On the other hand, little or no isotopic exchange is expected to occur between separate diapirs, even if they are in close proximity.

We conclude that the observed isotopic patterns of oceanic volcanic rocks are altogether unsurprising: (1) Individual oceanic islands frequently show constant isotopic composition regardless of rock type (Hart *et al.*, 1973; O'Nions and Pankhurst, 1974) because of mixing during diapiric rise of the source material. Each diapir samples a different portion of a heterogeneous mantle. (2) Mid-ocean ridge material is more uniform on a larger scale than oceanic islands because much larger volumes of source

rock are sampled and homogenized during separation of the melt from its solid residue and intrusion to the surface. (3) The depleted nature of mid-ocean ridge material relative to ocean-island material requires a vertically stratified mantle. If the two types of material happen to extrude in close mutual proximity, they will nevertheless retain their isotopic identities. (4) The processes of subduction and production of oceanic islands give rise to a heterogeneous mantle. Rehomogenization by convection and diffusion is unlikely because diffusion is too slow, and models that require a homogeneous mantle appear to be unrealistic. (5) Once a heterogeneous mantle is accepted there is no need to postulate local disequilibrium during melting or isotopic changes (as proposed by O'Hara, 1973, 1975) during subsequent fractional crystallization. (6) The geophysical consequences of a stratified mantle need further exploration. The stratification may be stabilized by the relatively greater density of "fertile" mantle as compared with "depleted" mantle (O'Hara, 1975), and the two or more layers may form separate convection systems. Intrusion from the lower, fertile layer through the depleted layer would then require a small amount of partial melting at the top of the fertile layer or an adiabatic rise of plumes from even greater depths. Again, such a plume would be partially molten by the time it encounters the depleted upper mantle.

We agree with O'Nions and Pankhurst (1974) that the isotopic data do not by themselves prove or disprove the existence of plumes; but if our conclusions regarding local equilibrium are confirmed by further experimental work on kinetics, the isotopic data can serve as a powerful constraint on the choice of convection pattern in the mantle.

References

- Allsopp, H. L., L. O. Nicolaysen, and P. Hahn-Weinheimer, Rb/K ratios and Sr-isotopic compositions of minerals

- in eclogitic and peridotitic rocks, *Earth Planet. Sci. Lett.*, **5**, 231–244, 1969.
- Armstrong, R. L., A model for Sr and Pb isotope evolution in a dynamic earth, *Rev. Geophys.*, **6**, 175–199, 1968.
- Buening, D. K., and P. R. Buseck, Fe-Mg lattice diffusion in olivine, *J. Geophys. Res.*, **78**, 6852–6862, 1973.
- Chow, T. J., and C. Patterson, The occurrence and significance of lead isotopes in pelagic sediments, *Geochim. Cosmochim. Acta*, **26**, 263–308, 1962.
- Church, S. E., and G. R. Tilton, Lead and strontium isotopic studies in the Cascade Mountains; bearing on andesite genesis, *Geol. Soc. Am. Bull.*, **84**, 431–454, 1973.
- Compston, W., and J. F. Lovering, The strontium isotopic geochemistry of granulitic and eclogitic inclusions from the basic pipes at Delegate, Eastern Australia, *Geochim. Cosmochim. Acta*, **33**, 691–699, 1969.
- Cooper, J. A., and D. H. Green, Lead isotope measurements on lherzolite inclusions and host basanites from western Victoria, Australia, *Earth Planet. Sci. Lett.*, **6**, 69–76, 1969.
- Dasch, E. J., and D. H. Green, Strontium isotope geochemistry of lherzolite inclusions and host basaltic rocks, Victoria, Australia, *Am. J. Sci.*, **275**, 461–469, 1975.
- Dickinson, W. R., and W. C. Luth, A model for plate tectonic evolution of mantle layers, *Science*, **174**, 400–404, 1971.
- Faure, G., and P. M. Hurley, The isotopic composition of strontium in oceanic and continental basalts: application to the origin of igneous rocks, *J. Petrol.*, **4**, 31–50, 1963.
- Flower, M. F. J., H.-U. Schmincke, and R. N. Thompson, Phlogopite stability and the $^{87}\text{Sr}/^{86}\text{Sr}$ step in basalts along the Reykjanes Ridge, *Nature*, **254**, 404–406, 1975.
- Forbes, W. C., and M. F. J. Flower, Phase relations of titanphlogopite, $\text{K}_2\text{Mg}_2\text{TiAl}_2\text{Si}_6\text{O}_{20}(\text{OH})_4$: a refractory phase in the upper mantle? *Earth Planet. Sci. Lett.*, **22**, 60–66, 1974.
- Gast, P. W., Limitations on the composition of the upper mantle, *J. Geophys. Res.*, **65**, 1287–1297, 1960.
- Gast, P. W., G. R. Tilton, and C. Hedge, Isotopic composition of lead and strontium from Ascension and Gough Islands, *Science*, **145**, 1181–1185, 1964.
- Giletti, B. J., Studies in diffusion I: argon in phlogopite mica, in *Geochemical Transport and Kinetics*, A. W. Hofmann, B. J. Giletti, H. S. Yoder, Jr., and R. A. Yund, eds., *Carnegie Inst. Wash. Publ.* **634**, pp. 107–115, 1974.
- Grant, N. K., J. L. Powell, J. V. Walther, and F. R. Burkholder, The isotopic composition of strontium in lavas from St. Helena, South Atlantic, submitted to *Earth Planet. Sci. Lett.*, 1974.
- Hanson, G. N., and P. W. Gast, Kinetic studies in contact metamorphic zones, *Geochim. Cosmochim. Acta*, **31**, 1119–1153, 1967.
- Harris, P. G., R. Hutchison, and D. K. Paul, Plutonic xenoliths and their relation to the upper mantle, *Philos. Trans. R. Soc. London, Ser. A*, **271**, 313–323, 1972.
- Hart, S. R., The petrology and isotopic-mineral age relations of a contact zone in the Front Range, Colorado, *J. Geol.*, **72**, 493–525, 1964.
- Hart, S. R., K, Rb, Cs, Sr and Ba contents and Sr isotope ratios of ocean floor basalts, *Philos. Trans. R. Soc. London, Ser. A*, **268**, 573–587, 1971.
- Hart, S. R., Submarine basalts from Kilauea rift, Hawaii: Nondependence of trace element composition on extrusion depth, *Earth Planet. Sci. Lett.*, **20**, 201–203, 1973.
- Hart, S. R., LIL geochemistry of Leg 34 basalts, *Initial Reports of the Deep Sea Drilling Project*, **34**, in press, 1975.
- Hart, S. R., and C. Brooks, Clinopyroxene-matrix partitioning of K, Rb, Cs, Sr and Ba, *Geochim. Cosmochim. Acta*, **38**, 1799–1806, 1974.
- Hart, S. R., W. E. Glassley, and D. E.

- Karig, Basalts and sea-floor spreading behind the Mariana Island arc, *Earth Planet. Sci. Lett.*, 15, 12-18, 1972.
- Hart, S. R., and J.-G. Schilling, The geochemistry of basalts from Iceland and the Reykjanes Ridge, *Carnegie Inst. Wash. Year Book* 72, p. 259, 1973.
- Hart, S. R., J.-G. Schilling, and J. L. Powell, Basalts from Iceland and along the Reykjanes Ridge: Sr isotope geochemistry, *Nature, Phys. Sci.*, 246, 104-107, 1973.
- Hedge, C. E., and Z. E. Peterman, The strontium isotopic composition of basalts from the Gordo and Juan de Fuca Rises, northeastern Pacific Ocean, *Contrib. Mineral. Petrol.*, 27, 114-120, 1970.
- Hedge, C. E., Z. E. Peterman, and W. R. Dickinson, Petrogenesis of lavas from western Samoa, *Geol. Soc. Am. Bull.*, 83, 2709-2714, 1972.
- Hedge, C. E., and F. G. Walthall, Radiogenic strontium-87 as an index of geologic processes, *Science*, 140, 1214-1217, 1963.
- Hedge, C. E., N. D. Watkins, R. A. Hildreth, and W. P. Doering, $^{87}\text{Sr}/^{86}\text{Sr}$ ratios in basalts from islands in the Indian Ocean, *Earth Planet. Sci. Lett.*, 21, 29-34, 1973.
- Hurley, P. M., H. Hughes, G. Faure, H. Fairbairn, and W. Pinson, Radiogenic strontium-87 model for continent formation, *J. Geophys. Res.*, 67, 5315-5336, 1962.
- Hutchison, R., and J. B. Dawson, Rb, Sr and $^{87}\text{Sr}/^{86}\text{Sr}$ in ultrabasic xenoliths and host-rocks, Lashaine Volcano, Tanzania, *Earth Planet. Sci. Lett.*, 9, 87-92, 1970.
- Kay, R., N. J. Hubbard, and P. W. Gast, Chemical characteristics and origin of oceanic ridge volcanic rocks, *J. Geophys. Res.*, 75, 1585-1613, 1970.
- Klerkx, J., S. Deutsch, and P. De Paepe, Rubidium, strontium content and strontium isotopic composition of strongly alkalic basaltic rocks from the Cape Verde Islands, *Contrib. Mineral. Petrol.*, 45, 107-118, 1974.
- Kudo, A. M., D. G. Brookins, and A. W. Laughlin, Sr isotopic disequilibrium in lherzolites from the Peurco Necks, New Mexico, *Earth Planet. Sci. Lett.*, 15, 291-295, 1972.
- Laughlin, A. W., and D. G. Brookins, Chemical and strontium isotopic investigations of ultramafic inclusions and basalt, Bandera Crater, New Mexico, *Geochim. Cosmochim. Acta*, 35, 107-113, 1971.
- Leggo, P. J., and R. Hutchison, A Rb-Sr isotope study of ultrabasic xenoliths and their basaltic host rocks from the Massif Central, France, *Earth Planet. Sci. Lett.*, 5, 71-75, 1968.
- Lovering, J. F., and M. Tatsumoto, Lead isotopes and the origin of granulite and eclogite inclusions in deep-seated pipes, *Earth Planet. Sci. Lett.*, 4, 350-356, 1968.
- Lussia-Berdou-Polve, M., and P. Vidal, Initial strontium isotope composition of volcanic rocks from Jan Mayen and Spitzbergen, *Earth Planet. Sci. Lett.*, 18, 333-338, 1973.
- Manton, W. I., and M. Tatsumoto, Some Pb and Sr isotopic measurements on eclogites from the Roberts Victor Mine, South Africa, *Earth Planet. Sci. Lett.*, 10, 217-226, 1971.
- Meijer, A., Pb and Sr isotopic data bearing on the origin of lavas from the Mariana arc system, submitted to *Bull. Geol. Soc. Am.*, 1975.
- Misener, D. J., Cationic diffusion in olivine to 1400°C and 35 K bar, in *Geochemical Transport and Kinetics*, A. W. Hofmann, B. J. Giletti, H. S. Yoder, Jr., and R. A. Yund, eds., *Carnegie Inst. Wash. Publ.* 634, pp. 117-125, 1974.
- Modreski, P. J., and A. L. Boettcher, Phase relations of phlogopite in the system $\text{K}_2\text{O}-\text{MgO}-\text{CaO}-\text{Al}_2\text{O}_3-\text{SiO}_2-\text{H}_2\text{O}$ to 35 kilobars: a better model for micas in the interior of the earth, *Am. J. Sci.*, 273, 385, 1973.
- Morioki, M., and K. Kigoshi, Lead isotopes and age of Hawaiian lherzolite

- nodules, *Earth Planet. Sci. Lett.*, **25**, 116–120, 1975.
- Muehlenbachs, K., and I. Kushiro, Oxygen isotope exchange and equilibrium of silicates with CO₂ or O₂, in *Carnegie Inst. Wash. Year Book 73*, pp. 232–236, 1974.
- Mysen, B. O., and A. L. Boettcher, Melting of a hydrous mantle: II. Geochemistry of crystals and liquids formed by anatexis of mantle peridotite at high pressures and high temperatures, as a function of controlled activities of water, hydrogen, and carbon dioxide, *J. Petrol.*, in press, 1975.
- O'Hara, M. J., Non-primary magmas and dubious mantle plume beneath Iceland, *Nature*, **243**, 507–508, 1973.
- O'Hara, M. J., Is there an Icelandic mantle plume? *Nature*, **253**, 708–710, 1975.
- O'Neil, J. R., C. E. Hedge, and E. D. Jackson, Isotopic investigations of xenoliths and host basalts from the Honolulu volcanic series, *Earth Planet. Sci. Lett.*, **8**, 253–257, 1970.
- O'Nions, R. K., and K. Grönvold, Petrogenetic relationships of acid and basic rocks in Iceland: Sr isotopes and rare-earth elements in late and postglacial volcanics, *Earth Planet. Sci. Lett.*, **19**, 397–409, 1973.
- O'Nions, R. K., and R. J. Pankhurst, Secular variation in the Sr-isotope composition of Icelandic volcanic rocks, *Earth Planet. Sci. Lett.*, **21**, 13–21, 1973.
- O'Nions, R. K., and R. J. Pankhurst, Petrogenetic significance of isotope and trace element variations in volcanic rocks from the mid-Atlantic, *J. Petrol.*, **15**, 603–634, 1974.
- O'Nions, R. K., R. J. Pankhurst, I. B. Fridleifsson, and S. P. Jakobsson, Strontium isotopes and rare-earth elements in basalts from Heimaey and Surtsey volcanic eruption, *Nature*, **243**, 213–214, 1973.
- Paul, D. K., Strontium isotope studies on ultramafic inclusions from Dreiser Weiher, Eifel, Germany, *Contrib. Mineral. Petrol.*, **34**, 22–28, 1971.
- Peterman, Z. E., I. S. E. Carmichael, and A. L. Smith, Strontium isotopes in quaternary basalts of southwestern California, *Earth Planet. Sci. Lett.*, **7**, 381–384, 1970.
- Petrović, R., The effect of coherency stress on the mechanism of the reaction albite + K⁺ \rightleftharpoons K-feldspar + Na⁺ and on the mechanical state of the resulting feldspar, *Contrib. Mineral. Petrol.*, **41**, 151–170, 1973.
- Philpotts, J. A., and C. C. Schnetzler, Phenocryst-matrix partition coefficients for K, Rb, Sr, and Ba, with applications to anorthosite and basalt genesis, *Geochim. Cosmochim. Acta*, **34**, 307–322, 1970.
- Richter, F. M., and B. Parsons, On the interaction of two scales of convection in the mantle, *J. Geophys. Res.*, **80**, 2529–2541, 1975.
- Ringwood, A. E., The petrological evolution of island arc systems, *J. Geol. Soc. London*, **130**, 183–204, 1974.
- Schilling, J.-G., Iceland mantle plume: geochemical evidence along Reykjanes Ridge, *Nature*, **242**, 565–571, 1973.
- Seitz, M. G., Uranium and thorium diffusion in diopside and fluorapatite, in *Carnegie Inst. Wash. Year Book 72*, pp. 586–588, 1973.
- Shimizu, N., An experimental study of the partitioning of K, Rb, Cs, Sr and Ba between clinopyroxene and liquid at high pressures, *Geochim. Cosmochim. Acta*, **38**, 1789–1798, 1974.
- Sigvaldason, G. E., Basalts from the center of the assumed Icelandic mantle plume, *J. Petrol.*, **15**, 497–524, 1974.
- Sinha, A. K., and S. R. Hart, A geochemical test of the subduction hypothesis for generation of island arc magmas, in *Carnegie Inst. Wash. Year Book 71*, pp. 309–312, 1972.
- Stuckless, J. S., and R. L. Erickson, Strontium isotope geochemistry of the volcanic rocks and associated mafic and ultramafic nodules from the Ross Island area, Antarctica (Abs.) *Eos*, **56**, 471, 1975.
- Stueber, A. M., and M. Ikramuddin,

Rubidium, strontium in ultramafic nodule minerals and host basalts, *Geochim. Cosmochim. Acta*, 38, 207–216, 1974.

Stueber, A. M., and V. R. Murthy, Strontium isotope and alkali element abundances in ultramafic rocks, *Geochim. Cosmochim. Acta*, 30, 1243–1259, 1966.

Stull, R. J., and K. McMillan, Origin of lherzolite inclusions in the Malapai Hill basalt, Joshua Tree National Monument, California, *Geol. Soc. Am. Bull.*, 84, 2343–2350, 1973.

Subbarao, K. V., The strontium isotopic composition of basalts from the East Pacific and Chile Rises and abyssal hills in the eastern Pacific Ocean, *Contrib. Mineral. Petrol.*, 37, 111–120, 1972.

Subbarao, K. V., and C. E. Hedge, K, Rb, Sr and $^{87}\text{Sr}/^{86}\text{Sr}$ in rocks from the mid-Indian oceanic ridge, *Earth Planet. Sci. Lett.*, 18, 223–228, 1973.

Sun, S. S., and G. N. Hanson, Evolution of the mantle: geochemical evidence from alkali basalt, *Geology*, 3, 297–302, 1975.

Sun, S. S., and B. Jahn, Lead and strontium isotopes in post-glacial basalts from Iceland, *Nature*, 255, 527–530, 1975.

Tatsumoto, M., Genetic relations of oceanic basalts as indicated by lead isotopes, *Science*, 153, 1094–1101, 1966a.

Tatsumoto, M., Isotopic composition of lead in volcanic rocks from Hawaii, Iwo Jima, and Japan, *J. Geophys. Res.*, 71, 1721–1733, 1966b.

Wilshire, H. G., and E. D. Jackson, Problems in determining mantle geotherms from pyroxene compositions in ultramafic rocks, *J. Geol.*, 83, 313–329, 1975.

Yoder, H. S., Jr., and I. Kushiro, Melting of a hydrous phase: phlogopite, *Am. J. Sci.*, 267A, 558, 1969.

Zartman, R. E., and F. Tera, Lead concentration and isotopic composition in five peridotite inclusions of probable mantle origin, *Earth Planet. Sci. Lett.*, 20, 54–66, 1973.

KINETIC PROCESSES AND THERMAL HISTORY OF ROCKS

Martin H. Dodson

Introduction

Kinetic processes in minerals and rocks have been little used for geothermometry, in spite of their very great sensitivity to temperature. The scarcity of reliable kinetic data applicable to geologic situations has been partly responsible for this state of affairs. Another factor is the lack of an adequate body of theory to relate kinetic processes to thermal history. In view of the rapid increase in quantity and quality of kinetic data now becoming available, it appears timely to review some theoretical relationships related to kinetics in slowly cooling systems, and to present some new relationships concerning kinetic processes during thermal pulses produced by igneous intrusions in their host rocks. The application of these relationships both to loss of radiogenic daughter products and to false petrochemical equilibria will be discussed.

Published Work

Gentner, Goebel, and Präg (1954) solved the differential equations for simultaneous production and diffusion of radiogenic daughter product in a cooling cubic crystal; they used the result in inferring a cooling history for the Stassfurt salt deposits from K-Ar and U-He ages. Wagner and Reimer (1972) combined data on fission-track annealing with fission-track ages to infer the low-temperature cooling history of the Alps. Dodson (1973) discussed the concept of closure temperature in cooling geochronological and petrological systems, and found a simple relationship between it and cooling rates. Wood (1964) and Goldstein and Short (1967) calculated cooling rates of iron meteorites by numerical modeling of the nickel concentration profiles across taenite lamellae. Lasaga and Richardson (1975) found

analytic solutions for diffusion-controlled exchange between adjacent mineral phases in a cooling metamorphic assemblage, and applied them to Fe-Mg exchange between garnet and cordierite; their method permits the use of various temperature-time relationships during cooling. Seifert and Virgo (1975) estimated the cooling rate of a natural anthophyllite from the Fe-Mg order-disorder relationships. Mineral ages in contact zones have been studied by Hart (1964) and Hanson and Gast (1967), among others, using numerical methods to model the kinetics of isotopic losses. Brandt (1974) made the surprising claim, backed by theoretical analysis, that it is possible to infer temperatures in contact zones from isotopic losses without a knowledge of the parameters governing the rate of loss; a partial analysis of this claim is presented below.

Approximations to Thermal History

At sufficiently high temperatures any given kinetic process will go so rapidly, in relation to the rate of change of temperature, that equilibrium will be continuously maintained. At sufficiently low temperatures, the process will go so slowly that no change can occur over geological time. In neither of these situations will kinetics tell us anything about thermal history except, perhaps, lower or upper limits to temperatures. However, in the transitional temperature range between those two extremes, kinetic processes will go part way towards equilibrium, and the system under consideration will then contain a quantitative record of some aspect of that part of the thermal history.

The transitional temperature range is fairly narrow because of the temperature sensitivity of kinetic processes. Over this limited range it generally will be appropriate to describe the rate/temperature relationship by the Arrhenius law:

$$k(T) = k_0 \exp(-E/RT) \quad (1)$$

where $k(T)$ is the rate constant at absolute temperature T ; R is the gas constant; k_0 is the frequency factor; and E , the activation energy characteristic of the process. For volume diffusion we replace $k(T)$ and k_0 by $D(T)/a^2$ and D_0/a^2 , a being a characteristic dimension of the system.

The form of the Arrhenius relationship makes it desirable to describe thermal history in terms of the reciprocal of absolute temperature, which can then be expressed as a Taylor series in time t , i.e.,

$$T^{-1}(t) = T_0^{-1} + \frac{dT^{-1}}{dt}(t - t_0) + \frac{d^2T^{-1}}{dt^2} \frac{(t - t_0)^2}{2!} \dots \quad (2)$$

in which T_0 and the differential coefficients are taken at time $t = t_0$. Because we are concerned with the limited transitional temperature range, we can confine our attention to the following approximations:

(1) Slow cooling:

$$\begin{aligned} T^{-1} &\simeq T_0^{-1} + \frac{dT^{-1}}{dt}(t - t_0) \\ &= T_0^{-1} - \dot{T}(t - T_0)/T^2 \end{aligned} \quad (3)$$

(2) Thermal pulse:

$$\begin{aligned} T^{-1} &\simeq T_{\max}^{-1} \\ &+ \frac{d^2T}{dt^2} \frac{(t - t_0)^2}{2!} \\ &= T_{\max}^{-1} \\ &- \ddot{T}(t - t_0)^2/2T_{\max}^2 \end{aligned} \quad (4)$$

Equation 4 corresponds to a parabolic approximation symmetrical about the peak of the pulse at $t = t_0$.

In all cases investigated it is necessary that the kinetic processes under consideration be so slow at ambient temperatures as to cause negligible changes over geological periods.

Slow Cooling

The closure of a cooling petrological system is illustrated in Fig. 49. The ordinate x represents a chemical parameter (e.g., ^{18}O abundance, or an Fe^{2+} -Mg ordering parameter) whose equilibrium value varies directly with temperature according to curve A . In the high temperature range equilibrium is maintained continuously, and the actual value of x , represented by curve B , follows curve A very closely. In the transitional range curve B departs from curve A , though x still changes toward the equilibrium value. Eventually, curve B asymptotically approaches a constant value of x , which corresponds to the observed closure temperature T_c .

For radiogenic isotopes an analogous situation exists (Dodson, 1973). Curve A corresponds to the total amount of radiogenic daughter produced up to any time, and curve B to the *deficit* of radiogenic daughter product in the mineral,

which is the difference between curve A and curve C . The important difference between geochronological and petrochemical systems is that in the former we must estimate T_c from kinetic parameters and cooling rates, whereas in the latter we can directly measure T_c .

Differential equations for curve B have been solved by Dodson (1973) for two simple cases, namely, first-order chemical reaction, and volume diffusion of a minor component between a geometrically simple isotropic body and an infinite, mobile reservoir. In both cases the boundary conditions (represented by curve A) are assumed to vary linearly with time, and therefore with $1/T$, over the transitional temperature range. The cooling rate (T) is taken into account in a cooling time constant τ , which is defined by a dimensionless form of Equation 3

$$\frac{E}{RT} = \frac{E}{RT_0} + \frac{t}{\tau} \quad (5)$$

By differentiating this we find

$$\tau = -RT^2/E\dot{T} \quad (6)$$

From Equations 1 and 4 we find

$$k(t) = k(0)e^{-t/\tau} \quad (7)$$

so τ is the time required for the rate constant to diminish to $1/e$ of any given value.

Use of Equation 7 makes tractable the integration of the appropriate linear differential equations, leading to the following results:

$$\frac{E}{RT_c} = \ln(A\tau k_0) \quad (8a)$$

$$\frac{E}{RT_c} = \ln(A\tau D_0/a^2) \quad (8b)$$

in which A is 1.8 for first-order kinetics, and 8.7, 27, or 55 for volume diffusion from a plane slab, cylinder, or sphere, respectively.

Combining Equations 6 and 8 we obtain

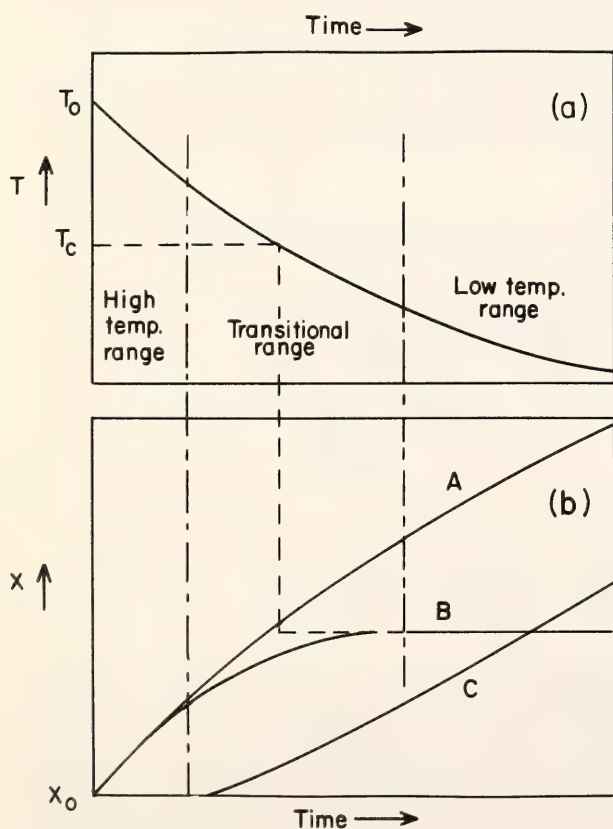


Fig. 49. Definition of closure temperature T_c . A , equilibrium value of X . B , actual value of X . C , Accumulation of radiogenic isotope ($= A - B$).

$$\begin{aligned} & E/RT_c \\ & = \ln [-ART_c^2 (k_0, D_0/a^2)/E\dot{T}] \quad (9) \end{aligned}$$

which can be solved iteratively for T_c or E , and directly for \dot{T} or frequency factor. In the former case a rather precise result is obtained from relatively imprecise values of cooling rate; conversely, rather large errors in T , k_0 , etc. would result from relatively small errors in T_c or E .

For geochronological systems in young orogenic belts a precise thermal history can in principle be obtained. For a given locality, each system provides an equation relating T_c and \dot{T} at the time corresponding to the measured age. In the simplest case, a single system together with the present-day temperature will yield a linear approximation to cooling history. For n systems an n th degree polynomial in time could be fitted to the data, in principle.

Use of geochemically observed values of T_c (e.g., apparent ^{18}O paleotemperatures) to determine cooling rate will be less satisfactory. Very precise observations of T_c are needed; the activation energy must also be known very well; and errors in A or frequency factor will be propagated directly to the estimated cooling rate. It may be more satisfactory to use Equation 9 to compare cooling rates derived from a given kinetic system, rather than to determine absolute values.

More Complex Kinetics

Examination of the differential equations for closure of cooling systems suggests that solutions will only take the form of Equation 8 with constant A if the differential equation is linear. However, Dodson (1975b) shows that Equation 8, with a suitably chosen value of A , may well be a useful approximation for more complex kinetic systems—provided the rate constant has dimensions 1/time, the value of A is given within a factor of about 2 by $2/kt_{1/2}$, where $t_{1/2}$ is the time required for 50% approach to

equilibrium at constant temperature with rate constant k . For the order-disorder kinetics studied by Seifert and Virgo (1974, 1975) this approach yields $A = 10$. Given their observed T_c of 270°C , $E = 61.6$ kcal/mole, and $k_0 = 8.6 \times 10^{17} \text{ yr}^{-1}$, we obtain a cooling rate of 13°C per million years. Numerical solution of the rate equations is in progress and should indicate how good this simple approach is and to what extent A is a function of τk_0 . It should be noted that in second or higher-order kinetics the quantity $kt_{1/2}$ is not uniquely defined as it is in first-order kinetics.

Kinetic Effects of a Thermal Pulse

In a zone surrounding any igneous intrusion the rocks are subjected to transient heating. The peak temperature reached during the heating falls off away from the intrusion, and the time of the heating tends to increase. A simple approximation to the effective heating time of such a thermal pulse will be derived here.

In studying diffusion phenomena with time-varying diffusion coefficients, standard solutions of the diffusion equation can be used simply by replacing the dimensionless time Dt/a^2 by

$$(1/a^2) \int_0^t D(u) du.$$

In general, for any kinetic effect expressible in the form

$$x = k(t)f(x, t) \quad (10)$$

in which $k(t)$ has dimensions 1/time, a solution can be obtained in which the dimensionless parameter $\int_0^t k(u) du$ takes the place of time.

For a thermal pulse we can define its effective duration τ_p as follows:

$$\tau_p = \frac{1}{D_{\max}} \int D(t) dt \quad (11)$$

where D_{\max} is the value of the diffusion coefficient at the maximum temperature. The limits of integration are not well

defined, but they are not critical provided the process is slow enough to be geologically negligible at ambient temperatures.

Assuming a rapid diminution in the rate coefficient with diminishing temperature, we can express $D(t)$ as a function of time by using the Taylor approximation given in Equation 4. We thus have

$$\begin{aligned} \int D(t) dt &\simeq D_{\max} \int \exp \left[-\frac{E}{R} \cdot \frac{d^2 T^{-1}}{dt^2} \frac{(t - t_0)^2}{2} \right] dt \\ &= D_{\max} \sqrt{-2RT_{\max}^2/E\ddot{T}} \int e^{-u^2} du \end{aligned}$$

Integrating from $-\infty$ to ∞ , we obtain

$$\begin{aligned} \int D(t) dt &\simeq D_{\max} \sqrt{-2\pi RT_{\max}^2/E\ddot{T}} \quad (12) \end{aligned}$$

so that:

$$\tau_p \simeq \sqrt{-2\pi RT_{\max}^2/E\ddot{T}} \quad (13)$$

The approximation upon which Equation 13 is based is illustrated in Fig. 50. It has been tested by numerical integration over the thermal history shown (which is the pulse shape due to an instantaneous plane source of heat at $x = 0, t = 0$). Selected results are shown in Table 7. The magnitude of the error in the approximation can be seen to range from $\sim 100\%$ at $E = 10$ kcal/mole to $\sim 10\%$ at $E = 60$ kcal/mole. Changing pulse height has little effect on these errors. (Very small errors were found in previous numerical tests quoted by Dodson (1975a) and are probably due to modeling a pulse symmetrical about T_{\max} , in which case the third-order term in the Taylor expansion is zero.) For many purposes this degree of approximation will be sufficient; however, an improved approximation is being sought.

Finite difference approximations to d^2T/dt^2 can be found. The simplest second-difference approximation is $T =$

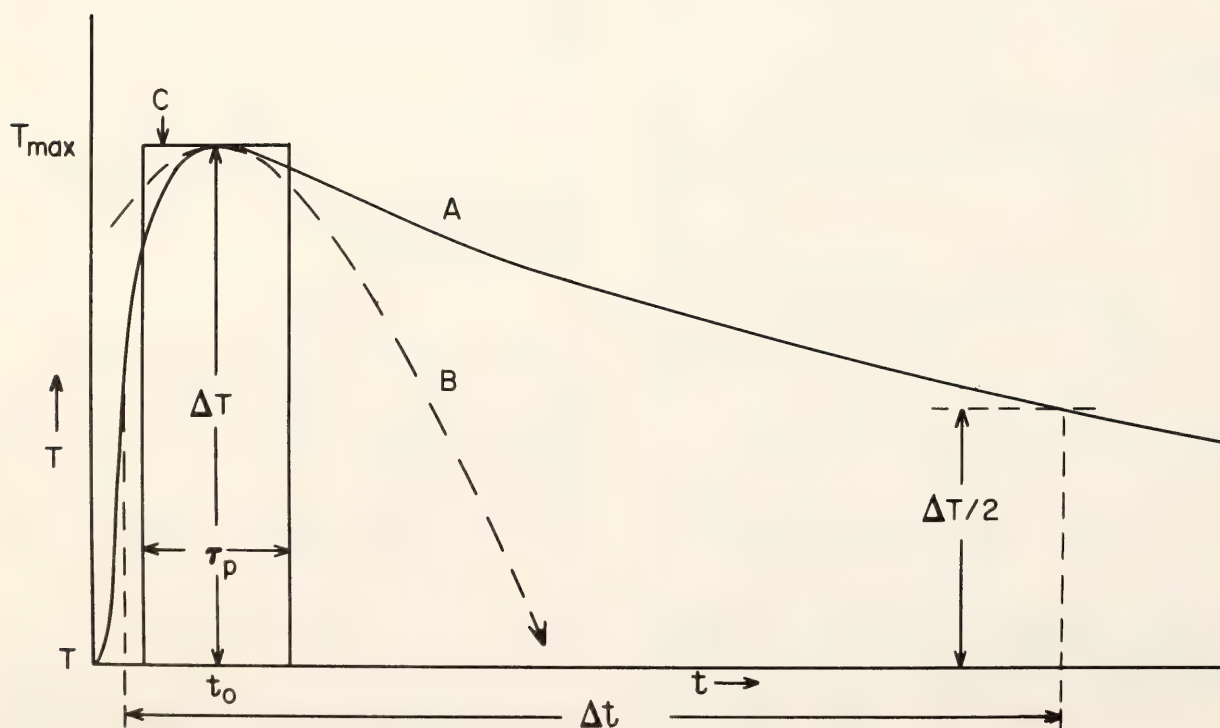


Fig. 50. A, thermal pulse due to an instantaneous plane source. B, Taylor approximation to A. C, equivalent square pulse for $E = 30$ kcal/mole (See Table 7).

TABLE 7. Relation between Effective Pulse Duration τ_p Calculated by Equation 20 and by Numerical Integration, for Pulse Shape $\Delta T = Bt^{-1/2} e^{-1/t}$ with $T_a = 300$, $B = 600$

Activation Energy (kcal/mole)	τ_p (Equation 20)	τ_p (numerical integration)
10	3.48	>5.5*
20	2.46	3.34
30	2.01	2.43
60	1.42	1.56

* The numerical integral converges very slowly for $E = 10$ kcal/mole. Also the rate constant at ambient temperature is too large relative to that at T_{\max} (290°C) to be neglected over all but very short geological periods.

$4\Delta T/\Delta t^2$ where Δt is the duration measured at half the maximum pulse height ΔT (Fig. 50). This gives too low a value for the strongly asymmetrical pulse of Fig. 50, for which we find empirically $T \simeq 9\Delta T/\Delta t^2$. In general we can write

$$T = S_p \Delta T / \Delta t^2, \quad (14)$$

S_p being a constant dependent upon pulse shape.

We can now derive a simple expression for the peak temperature which must be reached to attain a given approach towards equilibrium, say 50%. We can call this the threshold temperature T_{th} and write

$$G_{50} = D_{\max} \tau_p / a^2 \\ = D_0 \exp(-E/RT_{th}) \tau_p / a^2 \quad (15)$$

where G_{50} is a factor dependent on the diffusion geometry, and is equal to 0.2, 0.06, and 0.03 for planar, cylindrical, and spherical geometry (see Crank, 1956). We can thus write

$$\frac{E}{RT_{th}} \\ = \ln(G_{50}^{-1} \tau_p D_0 / a^2) \quad (16)$$

The similarity to Equation 8 for slow cooling is noteworthy. One may substitute for τ_p by Equations 13 and 14, and solve iteratively for T_{th} , the result being fairly insensitive to the argument of the logarithmic expression.

It may well be possible to make adequate estimates of Δt directly from ther-

mal models or indirectly from the distribution of apparent ages.

Diffusion of components other than radiogenic isotopes may be treated in a similar way. Although the equilibrium conditions are in general temperature dependent, and therefore will change with time, they can reasonably be regarded as constant to a first approximation during the significant period near the top of the pulse. Initial conditions would have to be determined outside the contact zone. For diffusion processes some knowledge of the initial concentration profile of the diffusing component will be needed.

Brandt's Method for Thermal Pulses

Brandt (1974) suggested that temperatures in contact zones could be inferred from diffusive losses of radiogenic isotopes without prior knowledge of the diffusion parameters. Here the results so far obtained in a critical study of Brandt's method (which is not yet complete) will be summarized.

Brandt assumes the thermal pulse to be of constant duration τ , the peak height $\Delta T(x)$ being given by

$$\Delta T(x) = \Delta T_0 e^{-kx} \quad (17)$$

where x is the distance from the contact; k and ΔT_0 are undetermined. He then substitutes Equation 17 in the Arrhenius equation, to express the quantity $D\tau/a^2$ (which he calls the Fourier number Fo) as a function of x ; this quantity is in-

ferred directly from the observed diffusion losses, assuming a simple model. Brandt then shows that the natural logarithm of F_0 plotted against x will have a point of inflection at distance x_{inf} at which the absolute temperature T_{inf} is twice the ambient temperature T_a . Two further observed quantities, namely, the value of $d(\ln F_0)/dx$ at the point of inflection, and the ratio of F_0 at that point to F_0 at the contact, make it possible to determine the parameters ΔT_0 and k , defining the pulse height as a function of x , and the activation energy E .

It is not easy to give a physical interpretation of Brandt's rather elaborate mathematical procedure. However, one may make the general comment that it is an attempt to combine the laws governing diffusion at particular locations with those governing the transfer of heat among those locations.

An attempt has been made to generalize Brandt's method to other temperature profiles. If we write

$$\Delta T = \Delta T_0 f(kx) \quad (18)$$

where $f(kx)$ is a known function of x except for the single unknown parameter k , we can proceed along parallel lines to Brandt and find the point of inflection in the curve of Fourier number versus distance. This will yield the following equations:

$$\begin{aligned} & T_a/T_{\text{inf}} \\ &= (1 - f''/2f'^2)_{x=x_{\text{inf}}} \quad (19a) \end{aligned}$$

$$\begin{aligned} & T_a/\Delta T_0 \\ &= (2f'^2/f'' - f)_{x=x_{\text{inf}}} \quad (19b) \end{aligned}$$

Equation 19b relates the two unknowns ΔT_0 and k to the known T_a and x_{inf} . Two additional equations needed analogous to Brandt's Equations 11 and 12 are:

$$\ln \frac{F_{01}}{F_{02}} = \frac{E}{RT_2} - \frac{E}{RT_1} \quad (20)$$

$$\frac{1}{F_0} \frac{dF_0}{dx} = \frac{d(\ln F_0)}{dx}$$

$$= -\Delta T_0 \frac{E}{RT_{\text{inf}}^2} kf'(kx) \quad (21)$$

in which T_{inf} , T_1 , and T_2 are related by Equation 18 to ΔT_0 , k , and the known distances x_{inf} , x_1 , and x_2 . The distances x_1 and x_2 would be selected to yield the most precise observable estimate of $\ln(F_{01}/F_{02})$. (The quantity F_0 at the contact, used by Brandt, will generally be indeterminate, since total loss of radiogenic isotopes normally occurs there at the time of intrusion.)

Equations 19b, 20, and 21, in conjunction with Equation 18, are sufficient in principle to solve the problem. The two questions to be answered are: "How sensitive is the result to errors in the observations?" and "How sensitive is the method to the assumed form of $f(kx)$?" To the first question one may answer, qualitatively, that the position of the point of inflection and the gradient of the curve at that point will not be determinable very precisely, either by graphical or numerical methods; besides errors of measurement, there are inhomogeneities in the heated rock to be considered. The latter can be seen clearly in the results of Hanson and Gast (1967) on the Snowbank Lake granite in the aureole of the Duluth gabbro. To answer the second question, one can try one or two simple tests. For example, if we use instead of Equation 18

$$\Delta T \propto (kx)^n$$

in which n is negative, we find on differentiating and substituting in Equation 19a that $T_a/T_{\text{inf}} = (1 + 1/n)/2$. Now for the temperature profile due to an instantaneous plane source (see Table 7) we find $n = -1$, so no point of inflection could be observed. Taking $n = -2$, we get $T_{\text{inf}} = 4T_a$. These results suggest that the calculation will be very sensitive to the form of $f(kx)$.

Brandt's assumption that the pulse is of constant duration is rather unsatisfactory. Using the approximation of Equation 13 and the pulse shape given in

Table 7, we can show that the effective pulse duration varies approximately as x^2 . However, if we knew the precise form of the temperature profile we would presumably know how the effective pulse duration varies, so we could, in principle, derive rather more elaborate versions of Equations 19b–21.

As an alternative to the procedure discussed above we may suppose that we have a thermal model in which the linear dimensions of the contact zone are known in terms of the thermal properties of the rock and the size of the intrusion causing the thermal pulse. Then we can write $\Delta T = \Delta T_0 f(P, kx)$, in which k is known, and P is some other parameter of the thermal model (e.g., latent heat, or a parameter describing the effect of fluids on heat transfer in the contact zone). Then P and ΔT_0 would be determinable, in principle.

Conclusions and Warning

The various approaches to cooling history and to thermal pulses discussed here are idealizations. While they provide a guide to the study of the relationship between kinetic processes and thermal history, the uncertainties of extrapolation of kinetic data to low temperatures, particularly in the mechanisms operative over long periods at low temperatures, call for great caution in interpretation. It is reasonable to hope, however, that by testing these relationships on a number of different kinetic systems in various environments we shall discover eventually those systems which are most promising for use in geothermometry.

References

Brandt, S. B., A new approach to the determination of temperatures of intrusives from radiogenic argon loss in contact aureoles, in *Geochemical Transport and Kinetics*, A. W. Hofmann, B. J. Giletti, H. S. Yoder, Jr., and R. A. Yund, eds., *Carnegie Inst. Wash. Publ. 634*, pp. 295–298, 1974.

- Crank, J., *Mathematics of diffusion*, Oxford, Clarendon Press, 1956.
- Dodson, M. H., Closure temperature in cooling geochronological and petrological systems, *Contrib. Mineral. Petrol.*, **40**, 259–276, 1973.
- Dodson, M. H., Diffusion effects of a thermal pulse (Abstr.), *Eos*, **56**, 472, 1975a.
- Dodson, M. H., Arrhenius processes in cooling solids, in preparation, 1975b.
- Gentner, W., K. Goebel, and R. Präg, Vergleichende Messungen nach der Kalium-Argon und Uran-Helium Methode, *Geochim. Cosmochim. Acta*, **5**, 125–136, 1954.
- Goldstein, J. I., and J. M. Short, Cooling rates of 27 iron and stony-iron meteorites, *Geochim. Cosmochim. Acta*, **31**, 1001–1023, 1967.
- Hanson, G. N., and P. W. Gast, Kinetic studies in contact metamorphic zones, *Geochim. Cosmochim. Acta*, **31**, 1119–1153, 1967.
- Hart, S. R., The petrology and isotopic mineral age relations of a contact zone in the Front Range, Colorado, *J. Geol.*, **72**, 493–525, 1964.
- Lasaga, A. C., and S. M. Richardson, A mathematical model of diffusion in retrograde metamorphism (Abstr.), *Eos*, **56**, 459, 1975.
- Seifert, F., and D. Virgo, Temperature dependence of intra-crystalline Fe^{2+} -Mg distribution in a natural anthophyllite, *Carnegie Inst. Wash. Year Book 73*, pp. 405–411, 1974.
- Seifert, F., and D. Virgo, Kinetics of the Fe^{2+} -Mg order-disorder reaction in anthophyllites; quantitative cooling rates, *Science*, **188**, 1107–1109, 1975.
- Wagner, G. A., and G. M. Reimer, Fission track tectonics: the tectonic interpretation of fission track apatite ages, *Earth Planet. Sci. Lett.*, **14**, 263–268, 1972.
- Wood, J. A., The cooling rate and parent planets of several iron meteorites, *Icarus*, **3**, 429–459, 1964.

DEEP SEA DRILLING PROJECT LEG 34
BASALTS AND OCEAN RIDGE BASALTS:
A GEOCHEMICAL COMPARISON

S. R. Hart

Introduction

Basalt produced at mid-ocean ridges (MORB) has been recognized for several years as being distinctly different from basalts produced in other tectonic environments. While the differences are small, they are nevertheless adequate for distinguishing MORB from other basalts, and there is currently considerable debate over the explanation of these differences. While the geographic variation of MORB chemistry is well studied, largely from dredge hauls along the ridges, the variation back in time is only poorly understood. Older MORB usually are accessible only by drilling, and frequently this older material is badly altered. Leg 34 of the Deep Sea Drilling Project (DSDP) drilled three sites on the Nazca plate, between the East Pacific Rise and the Peru-Chile trench. The basalts drilled on this leg, covering an age range of about 15–40 m.y., are less altered than most DSDP basalts and provide an ideal suite of samples to compare with zero-age MORB. This paper will present such a comparison, utilizing major elements, the LIL (large-ion lithophile) trace elements, and Sr isotope ratios.

Technique and Results

Major element analyses were performed by microprobe on glass samples from sites 319 and 320, leg 34; no glass was available from site 321.

Analyses of K, Rb, Cs, Sr, Ba, and the rare earth elements (REE) were carried out on a few selected samples by isotope dilution, and Sr concentration on a complete suite of leg 34 samples was determined by x-ray fluorescence. The Sr isotopic ratios were performed on a 6-inch automated mass spectrometer. In addition to the leg 34 samples, LIL-element

and Sr isotopic data on a large number of young MORB dredge samples and various oceanic island and island arc samples are reported for comparison purposes.

Discussion

Sr concentrations. Sr is relatively insensitive to alteration by seawater (Hart, 1969; Pearce and Cann, 1973; Thompson, 1973) and so may be used for the leg 34 basalts to characterize inter- and intra-site variations. The data are plotted as a function of depth at the three sites in Fig. 51. While there is some overlap between sites, each site has a relatively distinct range of Sr concentration, with site 320 having the highest average concentration (126 ppm); site 321, the lowest (92 ppm); and site 319, an intermediate value (111 ppm). At site 320 there is a slight tendency for Sr concentration to increase with depth; the other two sites do not show any clear trend with depth. Even single cooling units

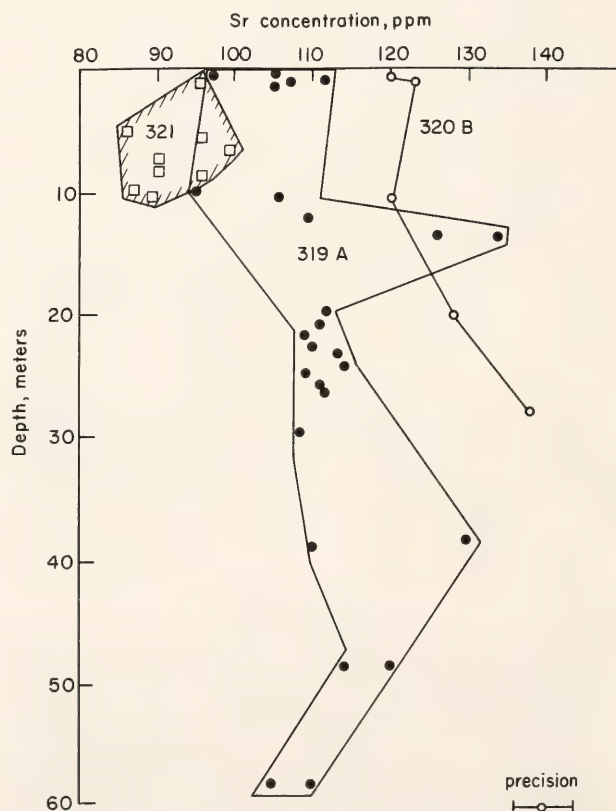


Fig. 51. Strontium concentration versus depth, sites 319, 320, and 321, leg 34. Precision estimate of $\pm 3\%$ shown at bottom.

may show considerable variation, as in the unit at site 319 between 11 m and 30 m. While most of this unit shows values in the range 105–115 ppm, three samples fall above 125 ppm. These high values may be related to local accumulation of plagioclase phenocrysts. Overall, the Sr concentrations of leg 34 basalts are within the range of typical MORB, and significantly lower than Sr concentrations found in subalkaline tholeiites from oceanic islands or island arcs where concentrations are typically greater than 200 ppm. In relatively fresh rocks, Sr concentrations can be used to discriminate MORB from basalts from almost all other environments (one exception being Iceland, where low-Sr tholeiites are also found, Hart *et al.*, 1973).

Rare earth element patterns. Of the various LIL elements, the REE are the most insensitive to seawater alteration (Philpotts *et al.*, 1969). The REE patterns for glass samples from sites 319 and 320 are shown in Fig. 52, along with two samples of MORB which represent the upper and lower limits of all MORB analyzed to date (Kay *et al.*, 1970). The site 319 and 320 patterns show the light REE depletion typical of most MORB, with no significant europium

anomaly. There is a tendency for depletion of the heavy REE in these two leg 34 basalts, and this is not common in MORB. REE patterns of the type shown in Fig. 52 are not diagnostic of MORB, since light-depleted patterns may also be found in tholeiites from island arcs and some oceanic islands such as Iceland.

K, Rb, Cs, and Ba concentrations. These elements are all susceptible to sea water alteration, with Cs being one of the most strongly affected of all elements. However, in fresh glasses such as those from sites 319 and 320, the alkali data should be reliable (Table 8). The sample from site 321 was not a glass, but a holocrystalline sample with relatively low water content. The low Cs content of this sample suggests it is relatively free from alteration effects. The samples from all three sites are low in alkalis and Ba, and show the high ratios of K/Rb, K/Cs, and K/Ba that are typical of MORB. In fact, the site 319 glass is lower in K (382 ppm) than any other MORB thus far analyzed by accurate techniques. There appears to be a trend of increasing K and Ba concentration (and decreasing K/Rb, K/Ba ratio) with age represented by the three samples of Table 8 (site 319, 20 m.y.;

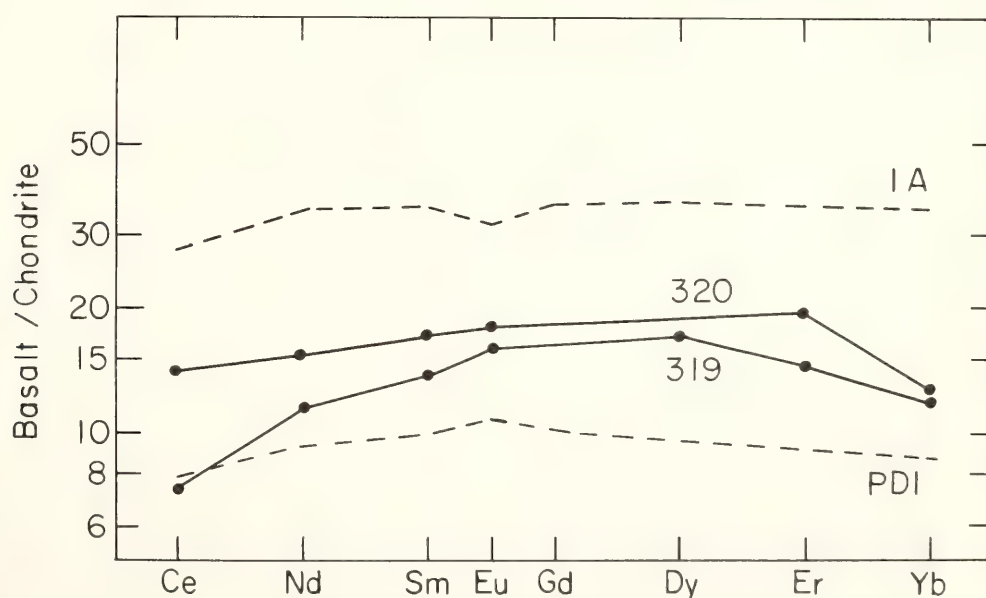


Fig. 52. Rare earth element patterns for two glass samples, 319A-2-1, 27–30, and 320B-3-1, 101–105. Shown for comparison are the highest and lowest patterns (dashed lines) reported for MORB, from Kay *et al.*, 1970. Note the lack of significant europium anomaly in the leg 34 samples.

TABLE 8. LIL Element Contents, Leg 34 Basalts

	3194-2-1 Interior	(27-30) Glass	320B-3-1 (101-105) Glass	321-14-1 (42-45)	Average MORB*
K (ppm)	1892	382	707	1131	1064
Rb (ppm)	5.17	0.188	0.665	1.334	1.02
Cs (ppm)	0.19	0.0085	0.0084	0.0226	.013
Sr (ppm)	95 (XRF)	97.1	107.6	86 (XRF)	124
Ba (ppm)	2.79	1.323	6.73	16.38	12.2
K/Rb	366	2032	1063	850	1046
K/Cs	9940	45,000	84,000	50,000	81,000
K/Ba	678	288	105	69	109
⁸⁷ Sr/ ⁸⁶ Sr +	0.70309	0.70266	0.70246	0.70288	0.70265
H ₂ O (total, %)	0.44	...	0.23	0.63	...
H ₂ O† (%)34

* Average of 22 fresh basalts from four different ridges (Hart, 1975).

† Precision $2\sigma = \pm 0.01\%$ relative to 0.70800 E + A standard.

site 320, 30 m.y.; site 321, 40 m.y.); more analyses would be required to see if this effect is real.

To contrast the K, Rb, and Ba data of leg 34 basalts with other MORB and basalts from other tectonic environments, concentration of these elements has been plotted using the data of Table 8 and data from Hart (1975) in Figs. 53 and 54. In the K/Rb-K plot (Fig. 53), site 319 falls slightly outside the field of MORB (due to the low K content); sites 320 and 321 fall in the central part of the MORB field. In general, MORB cannot be distinguished from arc tholeiites on the basis of K-Rb relationships. The leg 34 basalts do fall outside the arc tholeiite field, though they show the same general trend of decreasing K/Rb with increasing K content that is shown by arc tholeiites, MORB, and the Reykjanes Ridge-Iceland suite.

In the K-Ba plot (Fig. 54), site 319 again falls outside the MORB field (showing the highest K/Ba ratio yet recorded for any basalt), while sites 320 and 321 fall within the MORB field. The K/Ba ratio appears to be an excellent diagnostic parameter (in fresh samples) for distinguishing MORB from arc tholeiites and oceanic island tholeiites

(such as Iceland and Hawaii). While the leg 34 samples show a trend of negative slope on this plot (as they did in Fig. 53), there is not as clear a trend in the arc tholeiite data. The Reykjanes Ridge-Iceland data show a trend of negative slope similar to the leg 34 samples. Whether this is a trend which reflects mantle chemistry directly, or is a result of differentiation or mixing processes, is unknown at this time. The Reykjanes Ridge-Iceland trend has been interpreted by Schilling (1973) as mixing of two chemically different types of mantles (or of magmas from two different mantles).

Sr isotope ratios. The data for the three leg 34 samples (Table 8) are compared in Fig. 55 with data from other MORB (Hart, 1975) and with data on basalts from other tectonic environments (unpublished data). On this plot, all three leg 34 sites fall within the MORB field. As has been noted before (Tatsunoto *et al.*, 1965; Hart, 1971; Hart *et al.*, 1973), MORB generally have ⁸⁷Sr/⁸⁶Sr ratios lower than 0.7030, whereas most other basalts have ratios higher than 0.7030. There are several exceptions: Basalts from the mid-Atlantic ridge at 45°N have ratios of 0.7033 (Hart, 1975),

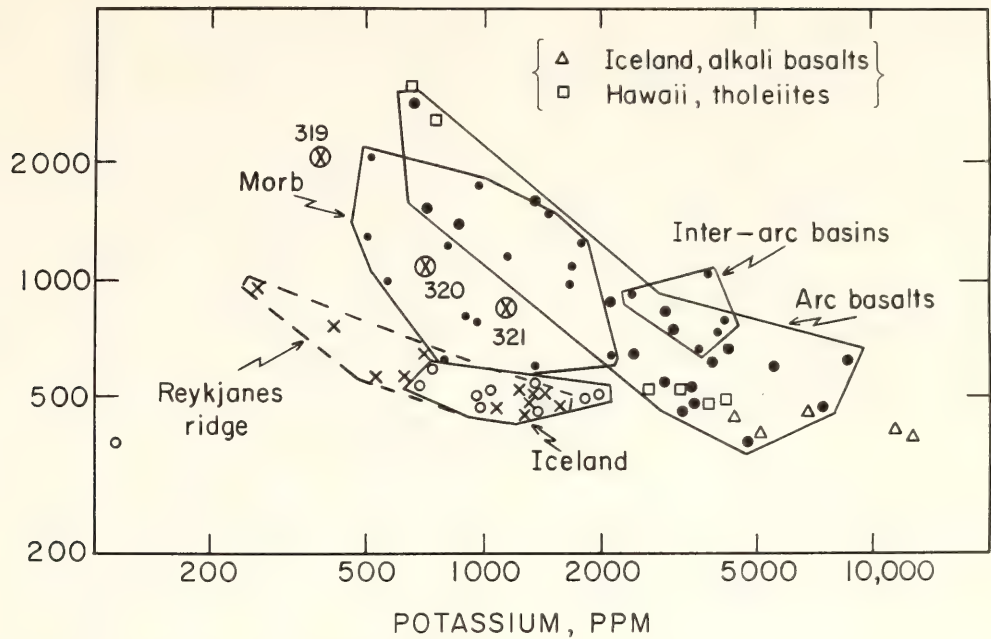


Fig. 53. K/Rb ratio versus K concentration of three leg 34 basalts compared with zero-age MORB (mid-ocean ridge basalt); island arc tholeiites; tholeiites from the Reykjanes Ridge, Iceland, and Hawaii; and five tholeiites from the marginal sea behind the Marianna Island arc. The MORB data is from Hart (1975); samples from 46°N on the mid-Atlantic ridge have not been plotted. Most of the other data are unpublished. The Iceland sample with very low K content is a Mg-rich basalt from the Reykjanes Peninsula.

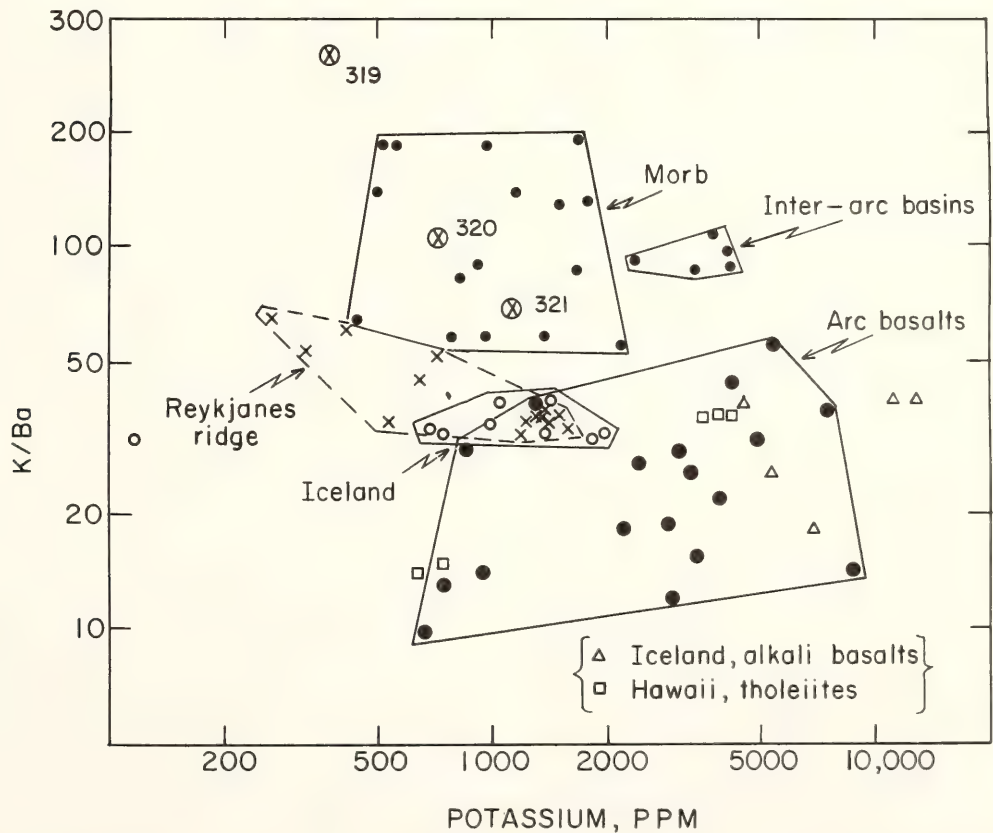


Fig. 54. K/Ba ratio versus K concentration of three leg 34 basalts compared with basalts from other tectonic environments. See Fig. 53 legend for additional details.

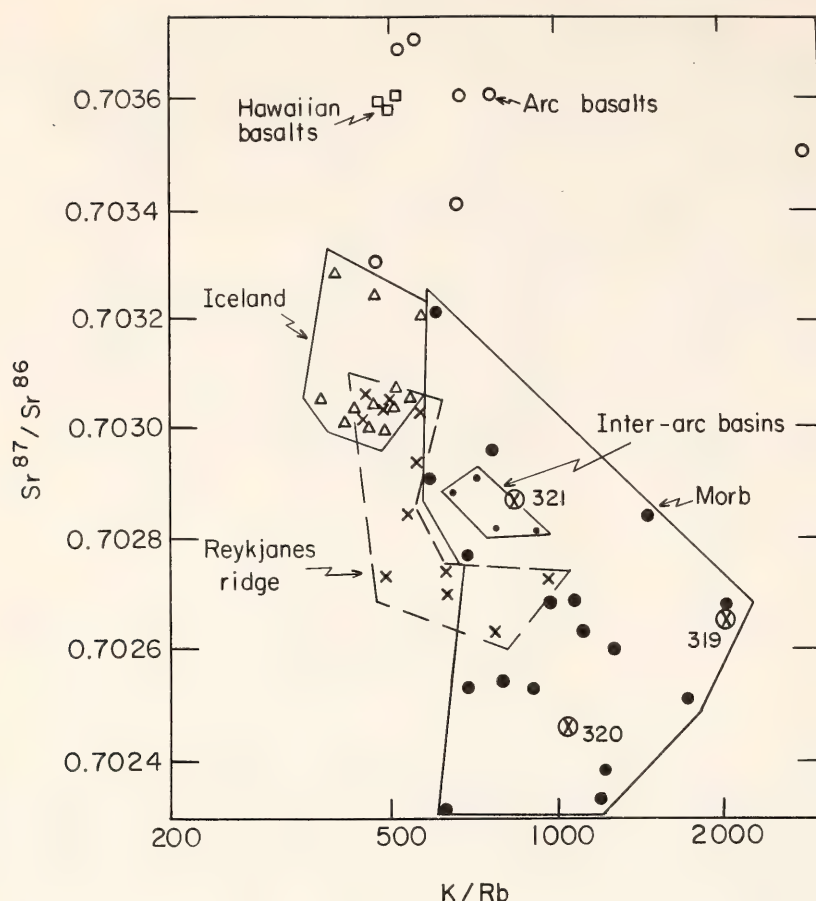


Fig. 55. $^{87}\text{Sr}/^{86}\text{Sr}$ ratio versus K/Rb ratio for three leg 34 basalts compared with basalts from other tectonic environments. See Fig. 53 legend for additional details.

and several basalts from the Indian Ocean have ratios in the range 0.7030–0.7034 (Hart, 1975; Hedge *et al.*, 1973). In addition, several oceanic islands have values as low as 0.7028 (St. Helena, Grant *et al.*, 1974; Ascension, O’Nions and Pankhurst, 1974). Oceanic island basalts generally have $\text{K/Rb} < 600$, so in a plot like Fig. 55 the MORB fields and oceanic island fields remain separated (except for the peculiar “undepleted” basalts at 45°N on the mid-Atlantic ridge). It should be noted that there is a real variation in the $^{87}\text{Sr}/^{86}\text{Sr}$ of MORB from different localities, with well-documented values as low as 0.7023 (Fig. 55), contrary to the statement by O’Nions and Pankhurst (1974) that MORB tend to be very uniform at a value of 0.7029. An exceptionally low value of 0.7012 was reported by Hedge and Peterman (1970) for MORB from the Gordo Rise; reanalysis of powder from the same sample at DTM gave a more normal value of 0.7024.

The differences between Sr isotope ratios in MORB and other basalts (for example, those from oceanic islands) have been ascribed to derivation from a mantle which is chemically heterogeneous (Tatsumoto *et al.*, 1965). Further work, in particular a detailed study of basalts from Iceland and the Reykjanes Ridge (Hart *et al.*, 1973) has been similarly interpreted. The only serious alternative to this heterogeneous mantle model is the one proposed by O’Nions and Pankhurst (1974) which invokes isotopic disequilibrium or heterogeneity on a mineralogical scale. Because of the isotopic differences between basalts from the three leg 34 sites, they would normally be interpreted as being derived from chemically different mantle. In other words, many of the major and trace element differences between the leg 34 basalts may be primary, and a reflection of chemical differences in the mantle which supplied each of the sites. While some of the observed differences

may be a result of crystal fractionation effects, there would be no need to explain all the differences in this way. Whether or not one can also explain the trace element and isotopic differences in terms of a mineral disequilibrium model (such as that of O'Nions and Pankhurst, 1974) must await further quantitative development of such models. Detailed arguments against disequilibrium melting models are given in a companion paper in this Report (Hofmann and Hart).

Alteration effects. One test was made of the effect of seawater alteration on a drilled basalt. A core fragment from site 319A (see Table 8), which contained both a chilled glass margin and a holocrystalline interior, was analyzed.

The K content of the altered interior is 5 times and the Rb content 25 times that of the fresh glass (despite a water content for the interior sample of only 0.44%), and the K/Rb and K/Cs ratios are drastically lowered (factors of 5 in both cases). The Ba concentration has doubled in the altered interior, while the Sr concentration is not significantly changed. The Sr isotope ratio is considerably higher in the altered portion (0.7031 versus 0.7027), presumably due to exchange with seawater Sr (Hart *et al.*, 1974) which has a $^{87}\text{Sr}/^{86}\text{Sr}$ ratio of about 0.7091. In general, these effects are similar to those reported in other studies (Hart, 1969; Philpotts *et al.*, 1969; Thompson, 1973; Hart *et al.*, 1974) except that the interior portion of this sample would not be judged to be highly altered on the basis of its H_2O content alone.

References

- Grant, N. K., J. L. Powell, J. V. Walther, and F. R. Burkholder, The isotopic composition of strontium in lavas from St. Helena, South Atlantic, submitted to *Earth Planet. Sci. Lett.*, 1974.
- Hart, S. R., K, Rb, Cs content and K/Rb, K/Cs ratios of fresh and altered submarine basalts: *Earth Planet. Sci. Lett.*, 6, 295, 1969.
- Hart, S. R., K, Rb, Cs, Sr, and Ba contents and Sr isotopic ratios of ocean floor basalts: *Philos. Trans. R. Soc. London, Ser. A*, 268, 573, 1971.
- Hart, S. R., LIL-element geochemistry, leg 34 basalts: *Initial Reports of the Deep Sea Drilling Project, 34*, in press, 1975.
- Hart, S. R., J. G. Schilling, and J. L. Powell, Basalts from Iceland and along the Reykjanes Ridge: Sr isotope geochemistry, *Nature, Phys. Sci.*, 246, 104, 1973.
- Hart, S. R., A. J. Erlank, and E. J. D. Kable, Sea floor basalt alteration: Some chemical and Sr isotopic effects, *Contrib. Mineral. Petrol.*, 44, 219, 1974.
- Hedge, C. E., and Z. E. Peterman, The strontium isotopic composition of basalts from the Gordo and Juan de Fuca Rises, Northeastern Pacific Ocean, *Contrib. Mineral. Petrol.*, 27, 114, 1970.
- Hedge, C. E., N. D. Watkins, R. A. Hildreth, and W. P. Doering, $\text{Sr}^{87}/\text{Sr}^{86}$ ratios in basalts from islands in the Indian Ocean, *Earth Planet. Sci. Lett.*, 21, 29, 1973.
- Kay, R., N. J. Hubbard, and P. W. Gast, Chemical characteristics and origin of oceanic ridge volcanic rocks, *J. Geophys. Res.*, 75, 1585, 1970.
- O'Nions, R. K., and R. J. Pankhurst, Petrogenetic significance of isotope and trace element variations in volcanic rocks from the Mid-Atlantic, *J. Petrol.* 15, 603, 1974.
- Pearce, J. A., and J. R. Cann, Tectonic setting of basic volcanic rocks determined using trace element analyses, *Earth Planet. Sci. Lett.*, 19, 290, 1973.
- Philpotts, J. A., C. C. Schnetzler, and S. R. Hart, Submarine basalts: Some K, Rb, Sr, Ba, rare-earth H_2O and CO_2 data bearing on their alteration, modification by plagioclase, and possible source materials, *Earth Planet. Sci. Lett.*, 7, 293, 1969.
- Schilling, J. G., Iceland mantle plume:

geochemical study of the Reykjanes Ridge, *Nature*, 242, 565, 1973.

Tatsumoto, M., C. E. Hedge, and A. E. J. Engel, Potassium, rubidium, strontium, thorium, uranium, and the ratio of strontium-87 to strontium-86 in oceanic tholeiitic basalt, *Science*, 150, 886, 1965.

Thompson, G. A geochemical study of the low-temperature interaction of sea-water and oceanic igneous rocks, *Eos*, 54, 1015, 1973.

GEOCHEMISTRY OF THE AZORES AND THE MID-ATLANTIC RIDGE: 29°N TO 60°N

William M. White, Stanley R. Hart,
and Jean-Guy Schilling

Introduction

Mid-ocean ridge basalts (MORB) are remarkable for their low abundances of large ion lithophile elements (LIL) such as K, Rb, Cs, Sr, Ba, and REE, and their low isotopic ratios of Sr and Pb, as well as their general petrochemical uniformity. The low concentrations of LIL, as well as other "incompatible" elements and the low large-ion/small-ion ratios, such as Rb/K and La/Sm in MORB, are generally thought to be due to their derivation from a mantle severely depleted in these elements by previous episodes of melting (Gast, 1968). The depleted character of MORB—which are, with very few exceptions, tholeiites—contrasts strongly with that of tholeiitic and alkali basalts erupted on oceanic islands. As both mid-ocean ridge (MOR) and oceanic island volcanics are mantle derived, this contrast implies significant mantle heterogeneity and differences in mantle evolution which warrant further investigation into their nature.

The Azores archipelago, which is the locus of the triple junction of the North American, Eurasian, and African plates, is an excellent example of the contrasting petrochemistry of oceanic island

lavas and MOR lavas. Although several recent papers have dealt with the tectonic evolution of the Azores (Krause and Watkins, 1970; Machado *et al.*, 1972; McKenzie, 1972), the evolution of the region is still poorly understood. There is a moderate amount of petrological data from the islands, but trace element and isotope data are scarce.

Schilling (1975) has shown that basalts erupted along the Mid-Atlantic ridge (MAR) transect of the Azores platform have anomalously high (La/Sm)_{E.F.} ratios and that there is a gradation from high (La/Sm)_{E.F.} values on the Azores platform (39°N) to (La/Sm)_{E.F.} values typical of MORB at about 33°N. He has interpreted this as being the result of a mantle plume (Morgan, 1971) rising beneath the Azores and mixing southward along the ridge with the low-velocity layer source of normal ridge basalts.

We report here the results of a Sr-isotope and alkali and alkaline earth trace element study of lavas erupted along the MAR from 29°N to 60°N, on the Azores Islands and in the Terceira trough. The study documents geochemical variation in the region and provides a test of hypotheses of Azores evolution, particularly the plume hypothesis. We also examine the relationship of tholeiitic basalt erupted on the MAR to the alkali lavas erupted on the Azores Islands.

Sampling and Analytical Procedure

We analyzed 77 basalt samples from 63 dredge stations along the MAR from 29°N to 60°N, shown in Fig. 56, and 41 samples from the Azores Islands and the Terceira trough, shown in Figs. 57 and 58. Thirty-nine stations along the ridge and two stations in the Terceira trough were dredged by R. V. Trident of the University of Rhode Island during cruises TR89, TR100, TR119, TR122, TR123, and TR154. Samples from other stations were provided by several other investigators. Island samples were collected by two of us (White and Schill-

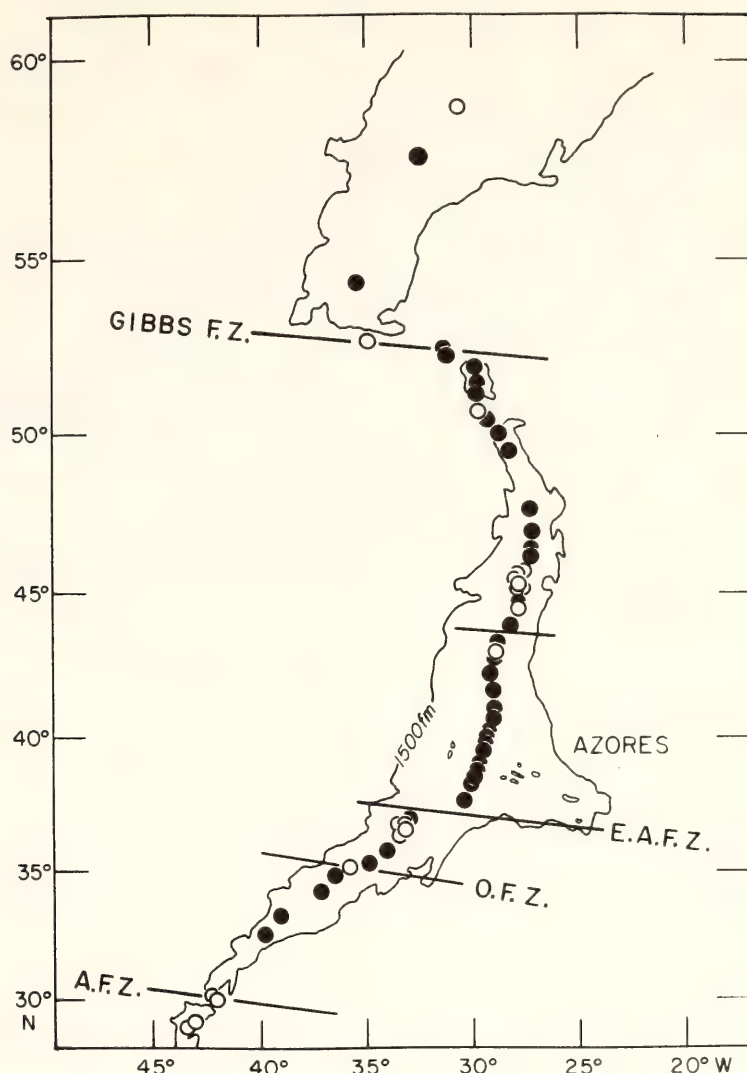


Fig. 56. Map of the study area. Solid circles designate *R. V. Trident* dredge stations; open circles designate other dredge stations.

ing) and by M. D. Tapia. Nearly all the samples analyzed from the ridge are tholeiitic basalts. A few transitional and mildly alkaline basalts occur at 35° and 45°N (Aumento, 1968; Muir and Tilley, 1964; Schilling, 1975, and unpublished analyses), while lavas from the Azores Islands are alkaline.

$^{87}\text{Sr}/^{86}\text{Sr}$ ratios were measured using DTM's automated 6-inch mass spectrometer. K, Rb, Cs, Ba, and in seven cases, Sr were analyzed by isotope dilution. Details of the procedure and precision of the isotope dilution analysis have been given elsewhere (Hart and Brooks, 1974). The remaining Sr analyses were done by x-ray fluorescence at the Geophysical Laboratory (precision: $\pm 3\%$ at 100 ppm, 2 sigma).

Results

Geochemical variation along the ridge.

The $^{87}\text{Sr}/^{86}\text{Sr}$ profile of basalts erupted along the ridge is shown in Fig. 59. Two distinct maxima are apparent, one at 44°–45°N, the other over the Azores platform (39°N). The maximum over the Azores platform (about 0.70345) appears slightly higher than that at 45°N (about 0.70340). The transition zones north of 45° and south of 39°N are relatively gentle, with the $^{87}\text{Sr}/^{86}\text{Sr}$ ratios decreasing to typical ridge values of 0.70250 to 0.70270. Ten analyzed samples from the FAMOUS (French American Mid Ocean Undersea Studies) region, situated in the geochemical transition zone south of the Azores, have intermediate values.

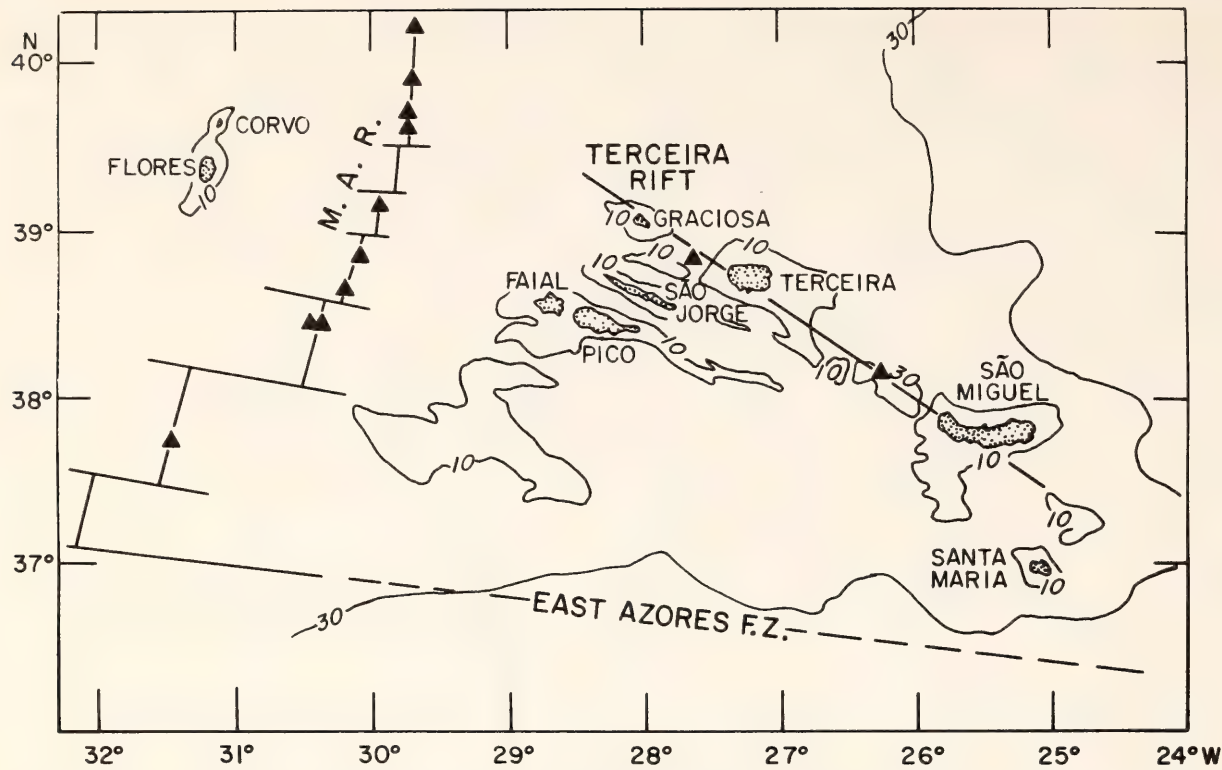


Fig. 57. Map of the Azores Islands. Triangles indicate location of *R. V. Trident* dredge stations. 1000-meter and 3000-meter bathymetric contours are shown.

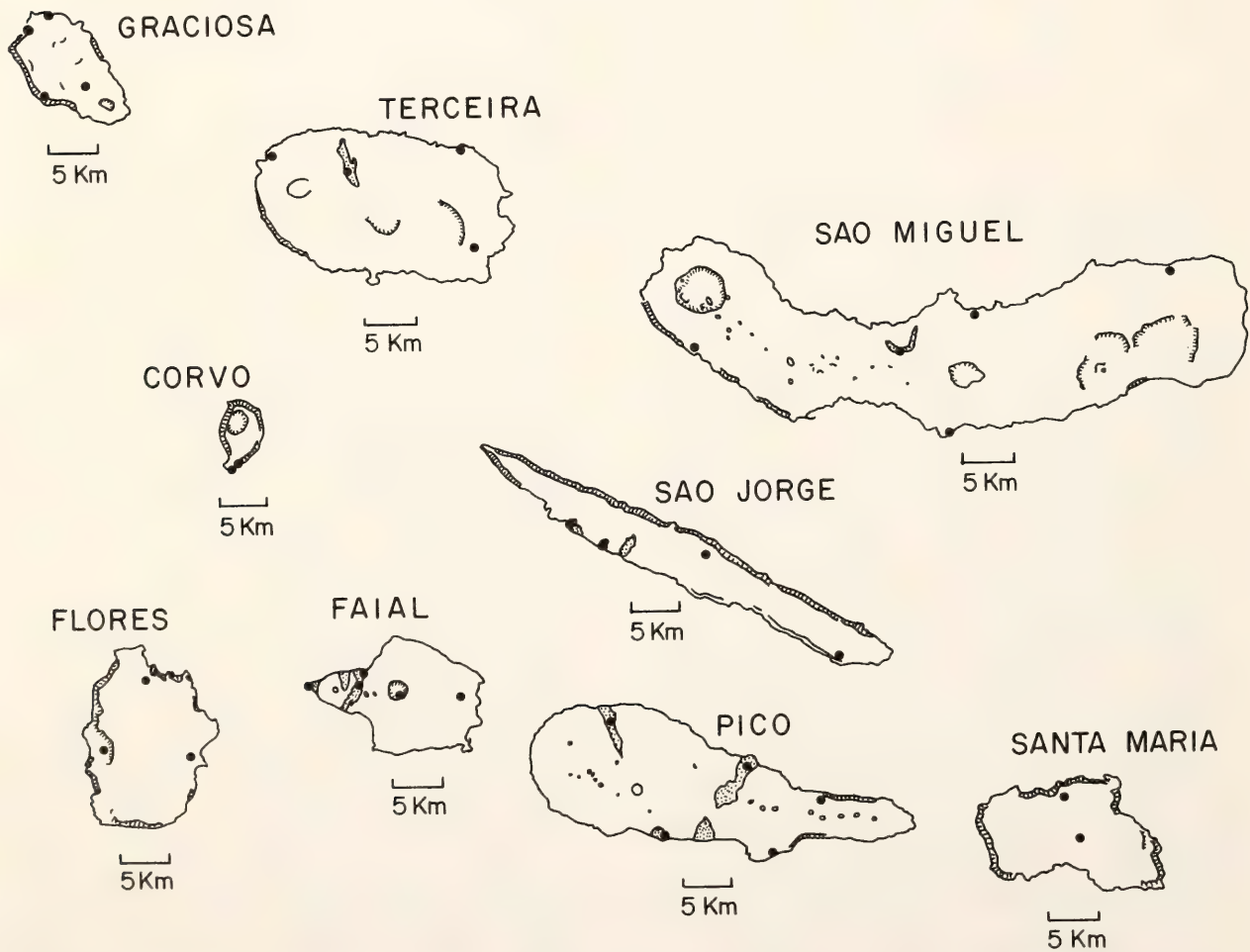


Fig. 58. Sample location maps for Azores Islands. Solid circles designate sample locations. Dotted areas are historical lava flows.

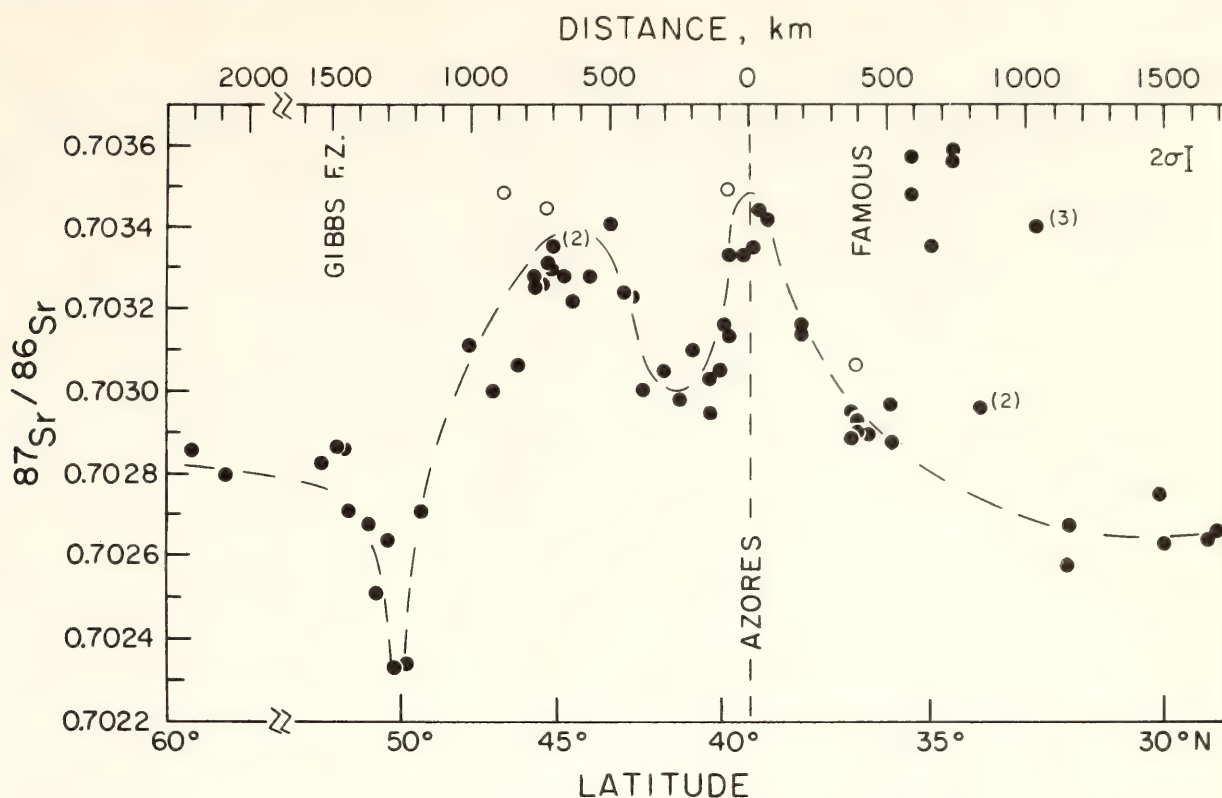


Fig. 59. Variation of $^{87}\text{Sr}/^{86}\text{Sr}$ vs. radial distance from the center of the Azores platform (39°N , 30°W). Open symbols indicate values suspected of having changed due to post-eruptive alteration. (2) indicates two or more identical analyses. (3) indicates three identical analyses.

Figure 60 shows the variation of K and Ba along the ridge; profiles of Rb, Cs, and Sr are similar. A comparison of Figs. 59 and 60 shows that the variation of the concentrations of these elements is quite similar to the variation of $^{87}\text{Sr}/^{86}\text{Sr}$ though some differences exist. Trace element concentrations in basalts from the Azores platform are much higher than in those from the 45°N area, whereas the $^{87}\text{Sr}/^{86}\text{Sr}$ values from the two areas are quite similar. The “saddle” in the $40^\circ\text{--}43^\circ\text{N}$ area dips relatively lower for the trace elements than for the $^{87}\text{Sr}/^{86}\text{Sr}$ ratios. Basalts from the Gibbs Fracture Zone tend to be somewhat high in their trace element content.

The variations of Ba/K and Rb/K along the ridge are similar; the former is shown in Fig. 61. While this profile exhibits a broad maximum over the Azores region, there are striking contrasts between the variation of Ba/K and $^{87}\text{Sr}/^{86}\text{Sr}$, notably the lack of a saddle between the Azores and 45°N . In

addition, while the decrease of $^{87}\text{Sr}/^{86}\text{Sr}$ and trace element concentrations along the ridge south of the Azores is linear or slightly concave upward, the decrease of Ba/K is distinctly convex upward. The decrease of $(\text{La}/\text{Sm})_{\text{E.F.}}$ is more or less linear (Schilling, 1975).

$^{87}\text{Sr}/^{86}\text{Sr}$ values for samples from the 35°N Oceanographer Fracture Zone area are anomalously high. In basalts from stations TR119 8D and 7D this anomalous character includes trace element and major element chemistry as well. However, these basalts are vesicular (20% vesicles) with sediment in the vesicles, and high $^{87}\text{Sr}/^{86}\text{Sr}$ values could be due to sediment contamination. Similarly, basalts from station V30 RD7 (one analysis) show evidence in thin section of alteration and have somewhat high H_2O contents. Finally, $^{87}\text{Sr}/^{86}\text{Sr}$ values for station TR123 4D (33°N) are also anomalously high. These samples are quite unusual in composition, with extremely low LIL-element con-

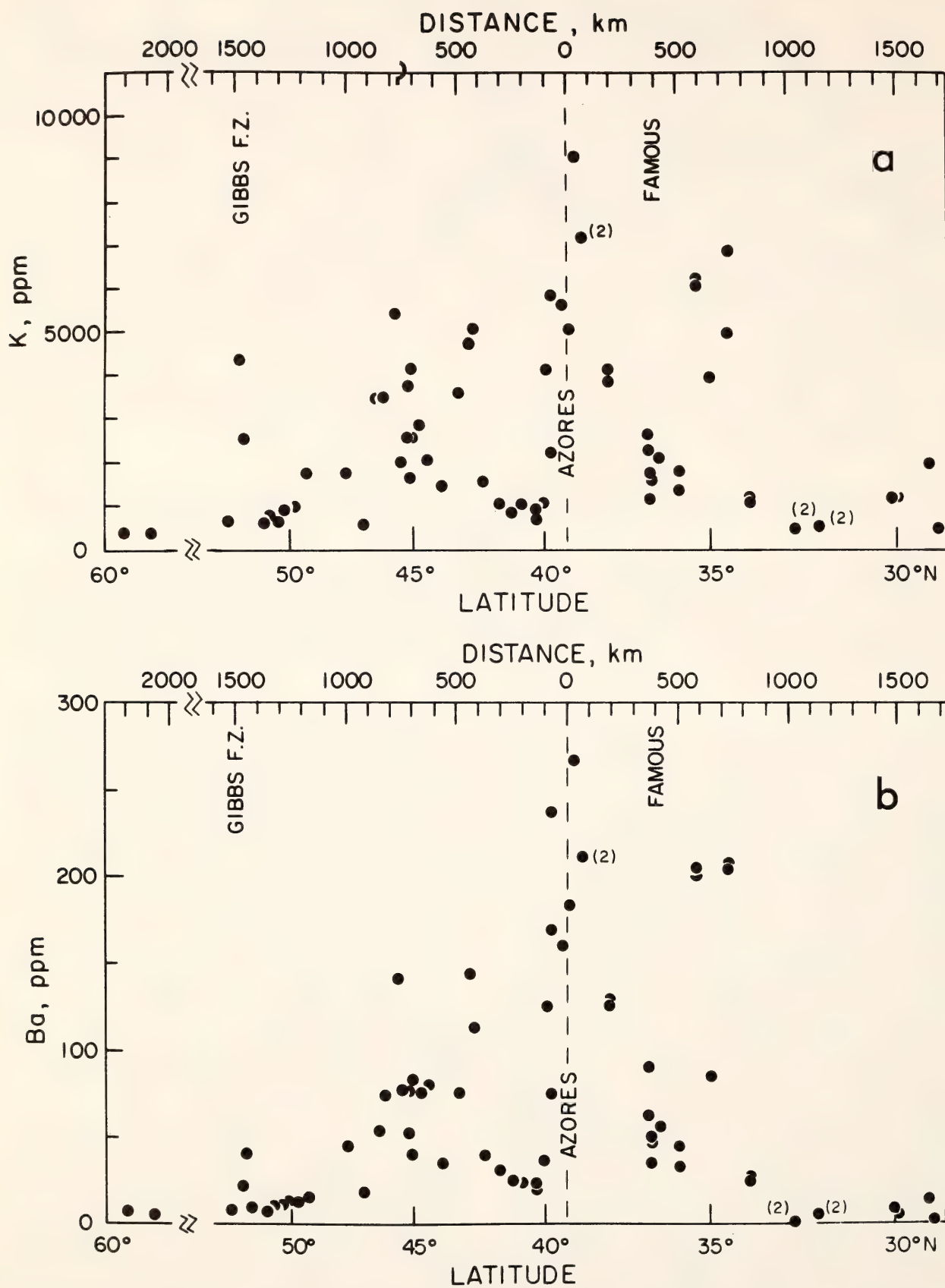


Fig. 60. *a*, variation of K (ppm) vs. radial distance from the center of the Azores platform. *b*, variation of Ba (ppm) vs. radial distance from the center of the Azores platform. Symbols are the same as for Fig. 59.

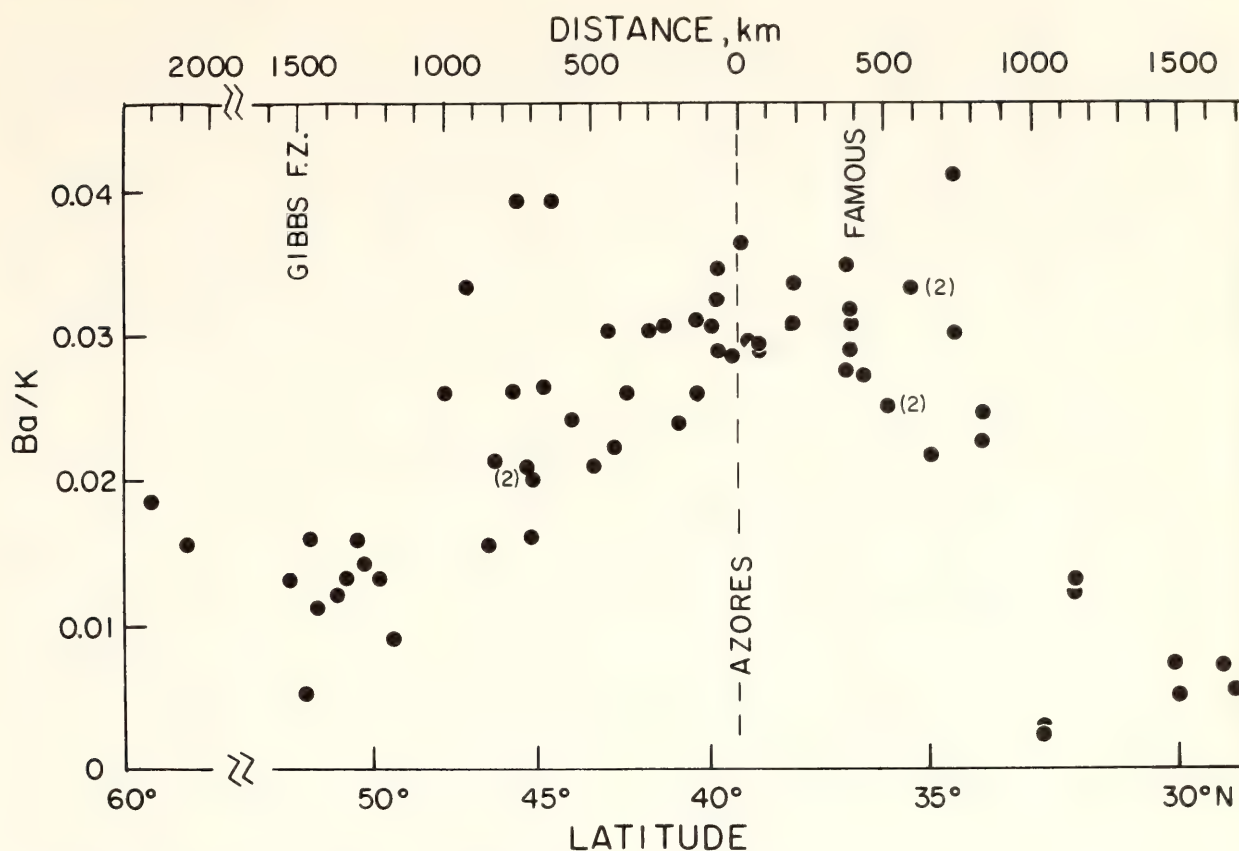


Fig. 61. Variation of Ba/K vs. radial distance from the center of the Azores platform. Symbols are the same as for Fig. 59.

tents and low trace element ratios such as La/Sm and Rb/K. They tend to be picritic, and relatively Al rich.

Basalts from the region of 50°N have $^{87}\text{Sr}/^{86}\text{Sr}$ values (0.70233) among the lowest yet obtained from MOR, while their trace element chemistry is very close to the average for MORB. These low values are an important feature of the profile, although their significance is not yet clear.

Azores Islands and the Terceira trough. The samples from the Azores Islands and the Terceira trough vary from alkali basalts to highly differentiated commendites. The $^{87}\text{Sr}/^{86}\text{Sr}$ ratios in these lavas show wide variation: 0.70332 to 0.70525; however, all but six values fall in the range 0.70332 to 0.70394, and over half the samples studied have values less than 0.70354. Our discussion of Azores Island geochemistry will center on $^{87}\text{Sr}/^{86}\text{Sr}$ results, as major element analysis necessary for the interpretation of the trace element data is

not yet available for all the samples. The isotope data are plotted against longitude in Fig. 62.

Flores and Corvo, both volcanically extinct, lie along a N-S trending submarine ridge and are the only two islands west of the MAR. $^{87}\text{Sr}/^{86}\text{Sr}$ values from these two islands range from 0.70332 to 0.70352, with no apparent isotopic differences between the two islands. Faial and Pico, both of which have had several historical eruptions, are aligned along a submarine ridge, which apparently extends to Sao Miguel (Krause and MacGregor, 1975). $^{87}\text{Sr}/^{86}\text{Sr}$ ratios from these islands range from 0.70347 to 0.70394, the values from Faial tending to average somewhat higher than those from Pico. Sao Jorge, a young, active, linear volcano lies along a submarine ridge which also apparently extends to Sao Miguel (Krause and MacGregor, 1975), and has $^{87}\text{Sr}/^{86}\text{Sr}$ in the range 0.70332–0.70338.

Graciosa, Terceira, and Sao Miguel lie

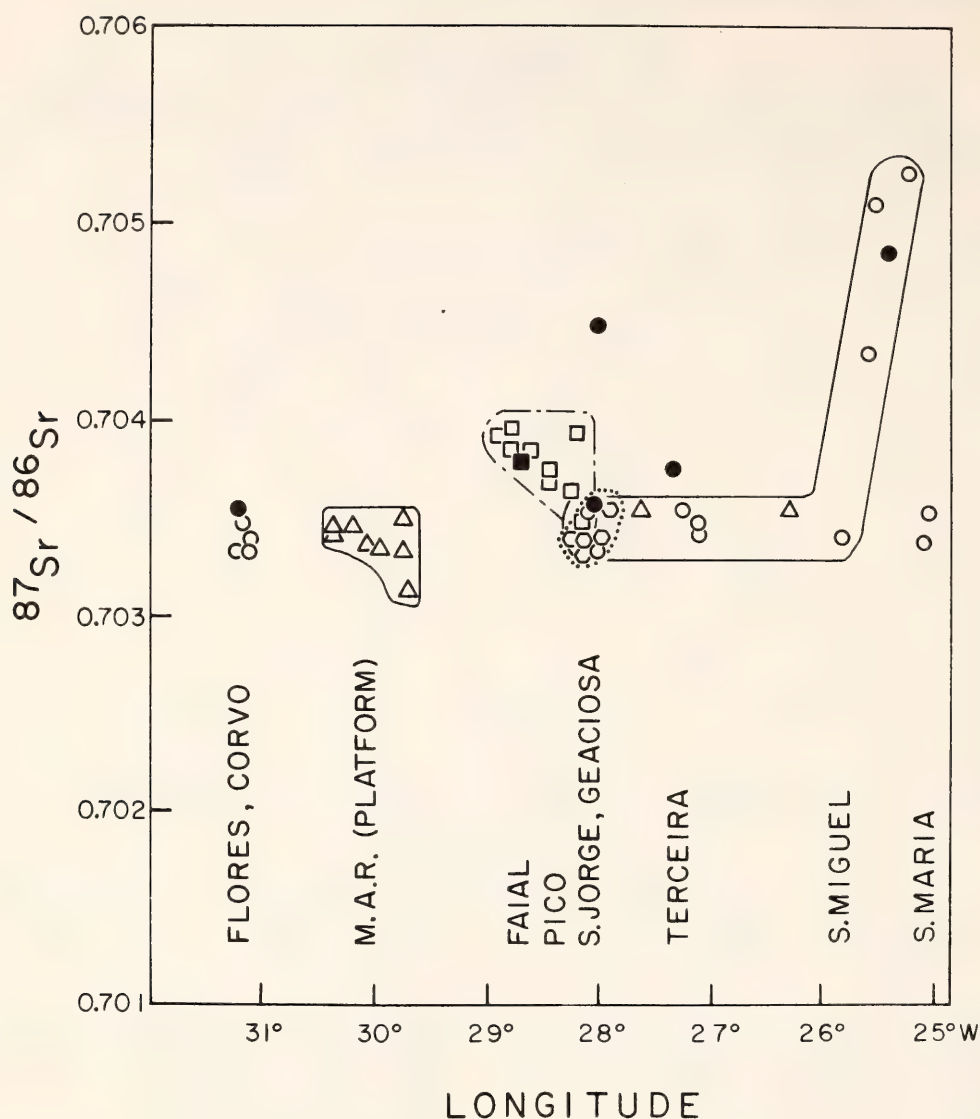


Fig. 62. Variation of $^{87}\text{Sr}/^{86}\text{Sr}$ vs. longitude across the Azores plateau. Triangles denote dredge stations; squares denote samples from Faial and Pico; hexagons denote samples from Sao Jorge; circles denote samples from Flores, Corvo, Santa Maria, Graciosa, Terceira, and Santa Maria. Open symbols are basalts and trachybasalts; closed symbols are trachytes. Solid line encloses samples from the MAR and the Terceira line; dotted line encloses samples from Sao Jorge. Dashed line encloses samples from Faial and Pico.

along the Terceira trough, which may be a secondary spreading center (Krause and Watkins, 1970). There have been several historic eruptions on Sao Miguel and Terceira, and numerous submarine eruptions reported from the trough; although there have been no eruptions on Graciosa, evidence suggests it is still active (Machado, 1967). $^{87}\text{Sr}/^{86}\text{Sr}$ ratios from Graciosa, Terceira, and submarine basalts from the trough fall in the range 0.70336–0.70345, with the exception of two commendites from Graciosa and Terceira, which have higher ratios.

The high Rb/Sr ratios (around 10) in

these two commendites suggest that the $^{87}\text{Sr}/^{86}\text{Sr}$ ratios are the result of ^{87}Sr accumulation due to Rb decay since differentiation of the magma. If the initial ratios of these two samples were near the average for the two islands (about 0.70350), then the apparent ages are 2.5 m.y. for the Graciosa commendite and 0.75 m.y. for the Terceira sample. Field relationships suggest these ages are reasonable.

Sao Miguel, which is apparently the intersection of the Terceira, Sao Jorge, and Faial-Pico tectonic features, is geochemically anomalous. One basalt from

the western third of the island (trending NW–SE) has an $^{87}\text{Sr}/^{86}\text{Sr}$ ratio of 0.70337, while four values from the eastern two-thirds of the island (trending E–W) range from 0.70434 to 0.70525.

Samples from Santa Maria, which is not aligned along any tectonic feature and which clearly is the oldest of the islands, yielded $^{87}\text{Sr}/^{86}\text{Sr}$ ratios of 0.70336 to 0.70352.

Discussion and Conclusions

Comparison with Iceland. Maximal values for $^{87}\text{Sr}/^{86}\text{Sr}$ and $(\text{La}/\text{Sm})_{\text{E.F.}}$, 0.70345 and 2.8, respectively, from the ridge transect of the Azores platform are considerably higher than values from the ridge transect across Iceland, 0.70305 and 1.3 for $^{87}\text{Sr}/^{86}\text{Sr}$ and $(\text{La}/\text{Sm})_{\text{E.F.}}$, respectively (Hart *et al.*, 1973). $^{87}\text{Sr}/^{86}\text{Sr}$ and $(\text{La}/\text{Sm})_{\text{E.F.}}$ values from 45°N are slightly lower than those from the Azores platform. In addition, while the Iceland–Reykjanes Ridge transition zone between the undepleted Icelandic basalts and the depleted ridge basalts extends only some 400 km, the transition zone between the Azores platform and the “normal” ridge to the south extends some 1000 km. Thus the geochemical anomaly beneath the Azores is greater in both magnitude and extent.

The marked isotopic uniformity along the central neovolcanic zones of Iceland (Hart *et al.*, 1973) is not duplicated in the MAR transect of the Azores platform, as the $^{87}\text{Sr}/^{86}\text{Sr}$ values begin decreasing within 100 km north and south of the center of the platform.

Variation patterns in the Azores. Initial $^{87}\text{Sr}/^{86}\text{Sr}$ ratios from six of the islands fall in the narrow range of 0.70332 to 0.70354, similar to—though on the average slightly higher than— $^{87}\text{Sr}/^{86}\text{Sr}$ ratios of basalts from the MAR transect of the platform. $^{87}\text{Sr}/^{86}\text{Sr}$ ratios tend to conform to the geographical distribution of the islands; that is, islands lying along the same tectonic feature tend to have similar $^{87}\text{Sr}/^{86}\text{Sr}$ ratios with the obvious exception of eastern Sao

Miguel. As Fig. 62 indicates, there is no systematic change in $^{87}\text{Sr}/^{86}\text{Sr}$ ratios longitudinally away from the ridge.

Faial, Pico, and particularly Sao Miguel are the only islands where reliable $^{87}\text{Sr}/^{86}\text{Sr}$ ratios are markedly dissimilar from those of the adjacent MAR. All the samples are fresh and the high $^{87}\text{Sr}/^{86}\text{Sr}$ ratios cannot be explained by post-eruptional alteration. The situation is somewhat analogous to that of the Snaefells Peninsula in Iceland, where lavas are erupted with distinctly higher $^{87}\text{Sr}/^{86}\text{Sr}$ ratios (0.70325) than those of the central neovolcanic zones (0.70304) (Hart *et al.*, 1973). However, the magnitude of the difference is considerably greater in the present case. Why lavas with such greatly differing isotopic ratios can be erupted on a single island while variation along the ridge is so gradual over distances up to 1000 km, remains an enigma.

Mantle geochemistry and the plume hypothesis. A clear analogy exists between the results presented here and those from the Reykjanes Ridge (Hart *et al.*, 1973). Schilling (1973) has interpreted the geochemical variation along the Reykjanes Ridge as being the result of the upwelling of a mantle plume beneath Iceland and its mixing with the depleted mantle source of MAR basalts. Additional geophysical and geochemical evidence supports this interpretation (Francis, 1973; Vogt and Johnson, 1973; Hart *et al.*, 1973). O'Hara (1973, 1975) has challenged this interpretation and has suggested that isotope ratios such as $^{87}\text{Sr}/^{86}\text{Sr}$ and $^{206}\text{Pb}/^{204}\text{Pb}$ may be changed somehow during fractional crystallization, but he has not suggested a mechanism to produce such changes. The island isotope data presented here show no systematic variation with differentiation, and, as there is no evidence in the literature to support O'Hara's suggestion, we consider it improbable that the Sr isotope ratios can be affected by fractional crystallization.

Recently it has been suggested that

isotopic equilibrium may not be achieved during the melting process and that this disequilibrium may explain the observed variation in $^{87}\text{Sr}/^{86}\text{Sr}$ along the Reykjanes Ridge (Sigvaldason *et al.*, 1974; O'Nions and Pankhurst, 1974). O'Nions and Pankhurst (1974) have presented a model for disequilibrium melting of a phlogopite-bearing mantle. Their model predicts that for small degrees of melting, the $^{87}\text{Sr}/^{86}\text{Sr}$ ratio of the melt would be significantly higher than that of the source, and that the $^{87}\text{Sr}/^{86}\text{Sr}$ ratio of the melt would decrease with increasing degree of melting. Thus, according to this model, liquids produced by small degrees of melting, such as nephelinites (Green, 1970) and alkali basalts, should have higher $^{87}\text{Sr}/^{86}\text{Sr}$ ratios than tholeiites produced by larger degrees of melting by the same source. But on Oahu, nephelinites have ratios similar to or slightly lower than tholeiites (Powell and Delong, 1966). In the present case, most alkali lavas from the Azores Islands have $^{87}\text{Sr}/^{86}\text{Sr}$ ratios similar to those of tholeiites from the MAR transect of the Azores platform. Furthermore, as U and Th are not concentrated in phlogopite, disequilibrium melting of a phlogopite-bearing mantle cannot explain the variation of lead isotopes along the Reykjanes Ridge (Sun *et al.*, 1975) or the observed enrichment in radiogenic Pb in Azores Islands lavas (Sun and Hanson, 1975; Oversby and Gast, 1968). Thus, while we agree that the possibility of disequilibrium melting needs further investigation, the model presented by O'Nions and Pankhurst (1974) does not satisfactorily explain the observed variation of radiogenic isotopes in oceanic lavas. For further discussion of the disequilibrium melting hypothesis, see the accompanying paper (this Report) by Hofmann and Hart.

Therefore, we tentatively conclude that the observed geochemical variation along the Ridge is due to geochemical variation in the mantle source. The observed variation along the Ridge is con-

sistent with the Azores mantle plume hypothesis as considered by Schilling (1975), although geochemical studies alone cannot prove the existence of plumes, which are essentially dynamical concepts. The data would fit alternative models such as a vertically or horizontally inhomogeneous static mantle. However, static mantle models have difficulty explaining how the mantle underlying spreading ridges can produce basaltic magmas of uniform composition, apparently indefinitely. Static models also have difficulty explaining the gradual transitions observed along the MAR and Reykjanes Ridge.

It is unclear whether the 45°N area represents a separate anomalous mantle, or is in some way associated with the anomalous mantle beneath the Azores, or whether the isolated anomalous regions at 35°N and 33°N can be accounted for by the plume hypothesis.

If the plume interpretation is correct, then our results indicate that there is no diminution of the plume's geochemical effect longitudinally as far as Sao Miguel and Santa Maria. Its effect therefore is not radially symmetrical as $^{87}\text{Sr}/^{86}\text{Sr}$ ratios begin decreasing along the MAR within 100 to 200 km from the center of the platform. Our analyses include both historical flows and flows from some of the oldest volcanic sequences of the archipelago (Santa Maria and NE Sao Miguel; Abdel-Monem *et al.*, 1968) and reveal no particular systematic change with time. Hence, the plume must have been present beneath the Azores for at least the last 4 to 6 m.y.

Lavas from 6 of the Azores Islands all have initial $^{87}\text{Sr}/^{86}\text{Sr}$ ratios which fall within the range of $^{87}\text{Sr}/^{86}\text{Sr}$ ratios in basalts from the MAR transect of the Azores platform. This implies that alkali basalts on these islands are being derived from a mantle geochemically similar to that which is feeding volcanism along the MAR transect of the platform. However, higher values on Faial, Pico,

and Sao Miguel imply considerable local mantle heterogeneity in this region.

At present we have no adequate explanation for the differences between LIL, LIL ratio, and $^{87}\text{Sr}/^{86}\text{Sr}$ profiles presented here. However, our investigation into these differences centers on these possibilities: variable degree of partial melting and/or crystal fractionation, variation in source mineralogy, second-order variation in mantle geochemistry, and mixing models which might account for the observed differences. These differences may be important clues to magmatic processes and mantle dynamics in this region.

This work represents a part of the doctoral dissertation of one of us (William White) at the University of Rhode Island and much of the discussion presented here is preliminary in nature.

References

- Abdel-Monem, A., L. A. Fernandez, and G. A. Boone, Pliocene-Pleistocene minimum K-Ar ages of older eruptive centers, Eastern Azores (abstr.), *Trans. Am. Geophys. Union*, 49, 363, 1968.
- Aumento, F., The mid-Atlantic Ridge near 45°N. II. Basalts from the area of Confederation Peak, *Can. J. Earth Sci.*, 5, 1-21, 1968.
- Francis, T. J. G., The seismicity of the Reykjanes Ridge, *Earth Planet. Sci. Lett.*, 18, 119-124, 1973.
- Gast, P. W., Trace element fractionation and the origin of tholeiitic and alkaline magma types, *Geochim. Cosmochim. Acta.*, 32, 1057-1086, 1968.
- Green, D. H., The origin of basaltic and nephelinitic magmas, *Trans. Leicester Liter. Philos. Soc.*, 64, 26-54, 1970.
- Hart, S. R., and C. Brooks, Clinopyroxene matrix partitioning of K, Rb, Cs, Sr, and Ba, *Geochim. Cosmochim. Acta*, 28, 1799-1806, 1974.
- Hart, S. R., J-G. Schilling, and J. L. Powell, Basalts from Iceland and along the Reykjanes Ridge; Sr isotope geochemistry, *Nature, Phys. Sci.*, 246, 104-107, 1973.
- Krause, D. C., and B. A. McGregor, Azores plateau submarine geology, *Geol. Soc. Am. Bull.*, in press, 1975.
- Krause, D. C., and N. D. Watkins, North Atlantic crustal genesis in the vicinity of the Azores, *Geophys. J. R. Astron. Soc.*, 19, 261-283, 1970.
- Machado, F., J. Quintino, and J. H. Monteiro, Geology of the Azores and the mid-Atlantic Rift, *Twenty-fourth Int. Geol. Congr.*, Sec. 3, pp. 134-142, 1972.
- McKenzie, D. P., Active tectonics of the Mediterranean region, *Geophys. J. R. Astron. Soc.*, 30, 109-185, 1972.
- Morgan, W. J., Convection plumes in the lower mantle, *Nature*, 230, 42-43, 1971.
- Muir, I. D., and C. E. Tilley, Basalts from the northern part of the rift zone of the mid-Atlantic Ridge, *J. Petrol.*, 5, 409-434, 1964.
- O'Hara, M. J., Non-primary magmas and dubious mantle plume beneath Iceland, *Nature*, 243, 507-508, 1973.
- O'Hara, M. J., Is there an Icelandic mantle plume? *Nature*, 253, 708-710, 1975.
- O'Nions, R. K., and R. J. Pankhurst, Petrogenetic significance of isotope and trace element variation in volcanic rocks from the mid-Atlantic, *J. Petrol.*, 15, 603-634, 1974.
- Oversby, V. M., and P. W. Gast, Lead isotope compositions and uranium decay series disequilibrium in recent volcanic rocks, *Earth Planet. Sci. Lett.*, 5, 199-206, 1968.
- Powell, J. L., and S. E. Delong, Isotopic composition of strontium in volcanic rocks from Oahu, *Science*, 153, 1239-1242, 1966.
- Schilling, J-G., Iceland mantle plume: Geochemical study of the Reykjanes Ridge, *Nature*, 242, 565-571, 1973.
- Schilling, J-G., Azores mantle blob: rare earth evidence, *Earth Planet. Sci. Lett.*, 25, 103-115, 1975.

- Sigvaldason, G. E., S. Steinthorsson, N. Oskarsson, and P. Imsland, Compositional variation in recent Icelandic tholeiites and the Kverkfjoll hot spot, *Nature*, 251, 579–582, 1974.
- Sun, S. S., and G. N. Hanson, Evolution of the mantle: geochemical evidence from alkali basalts, *Geology*, 3, 297–302, 1975.
- Sun, S. S., M. Tatsumoto, and J-G. Schilling, Mantle mixing along the Reykjanes Ridge axis: lead isotopic evidence, submitted to *Science*, 1975.
- Vogt, P. R., and G. L. Johnson, A longitudinal seismic reflection profile of Reykjanes Ridge: part II—implications for the mantle hotspot hypothesis, *Earth Planet. Sci. Lett.*, 18, 49–58, 1973.

SECONDARY MINERALS IN OCEANIC BASALTS

Manuel N. Bass

The results of a study of the secondary minerals in basalts cored during Leg 34 of the Deep Sea Drilling Project were combined with earlier results on basalts from Leg 17 (Bass *et al.*, 1973a, 1973b) and the many extant observations on dredged basalts to construct a composite picture of the progressive development of secondary minerals in oceanic basalts during late magmatic and deuterite processes, and during subsequent low-temperature processes when the rocks were exposed to open, oxygenated bottom waters (the so-called "seawater alteration") and to pore waters, the oxygen contents of which varied with time (diagenesis).

For mnemonic purposes, we can distinguish four groups of processes: (1) late magmatic-deuterite; (2) sea-water alteration (pre-burial); (3) nonoxidative diagenesis (post-burial, limited oxidation); and (4) oxidative diagenesis (post-burial, intense oxidation).

These four discrete stages are an oversimplification since, prior to burial, stages 2, 3, and 4 proceed simultaneously.

The interior portions of unfractured blocks, whose exteriors are bathed in open bottom water and are undergoing sea-water alteration in a direct sense, are subject at successively inward levels, to stages 4 (oxidation superimposed on earlier hydration) and 3 (hydration with limited oxidation). The successive levels, which in part control the color zonation seen in joint blocks of oceanic basalt, reflect the fact that water is available in abundance and diffuses relatively fast, whereas oxygen supply is limited and its inward progress is retarded either by a slow diffusion rate, or, more likely, by its consumption by readily oxidized primary and secondary phases. The degree to which the concurrent processes penetrate into a given igneous body or pile of flows depends on the porosity and permeability of the system. At an actively spreading ridge crest these are controlled by pillow structure, vesicles and diktytaxitic vugs, primary cooling cracks and tectonic effects; and the alteration zones penetrate into essentially fresh rock. In old crust reexposed on tectonic ridges and in troughs of fracture zones, the early porosity and permeability have been decreased by deposition of veins and amygdulites during burial, and increased by tectonic fracturing during burial and especially during the subsequent activity that led to reexposure of the rocks. Processes 3 and 4 continued during the burial of the rocks, as discussed more fully below. Following reexposure, process 2 is renewed on exposed surfaces and a new wave of concurrently developing zones sweeps through the old rocks, superimposing themselves on any earlier alteration zones developed during the earlier history of the rocks. It is this type of complex history that is recorded in many or most old rocks dredged from fracture zones. For the remainder of this discussion we ignore the multi-stage complications consequent on reexposure after a long history of burial and focus on the alteration of rocks formed at the ridge crest and subsequently buried, but

not reexposed, and of sills injected into such rocks after burial.

Following burial, process 2 (seawater alteration) is terminated, but processes 3 and 4 proceed as before, penetrating natural joint blocks in successive waves recorded as visible color zones which reflect various secondary minerals. The reducing capacity of the system is low, and redox potentials relatively high, so oxidation effects produced during earlier stages, such as sea-water alteration of exposed surfaces, are not reversed after burial. In other words, the rocks seem, for the most part, always to retain the most oxidized state they have attained. Near an active ridge crest, joints are numerous and open, and pore fluids penetrate easily to the surfaces of the joint blocks. After burial the development of veins and amygdules is accelerated, and fracture porosity tends to decrease. Near the ridge crest the tectonic activity connected with the spreading process creates new fractures and tends to counteract the sealing effect of veins. Away from the crest the tectonic activity diminishes; vein deposition dominates; porosity is sealed; fractures are healed; and thereby the bulk density and elasticity of oceanic crustal layers 2 and 3 increase. The rate of further alteration then tends to be dominated more and more by diffusion, and successive steps in the alteration process are more faithfully recorded as visible zones or replacement effects (pseudomorphs). In a highly fractured system one would have to study many joint blocks to reconstruct the sequence of events. In the nonpillowed, less fractured, massive portions of flows, and in sills injected far from ridge crests, that are thereby not subject to severe tectonism, diffusion dominates from the start and the diffusion fronts tend to parallel the generally flat-lying flow or sill boundaries. Thus, Deep Sea Drilling Project (DSDP) holes tend to penetrate the alteration zones at a high angle and core recovery is best in such unfractured rocks. These cores provide the least am-

biguous cases in which to study the successive effects of nonoxidative and oxidative diagenesis, namely those resulting from processes 3 and 4. I had earlier studied samples from sills cored during Leg 17 (hole 169 in particular, and possibly holes 167 and 170 as well). I was especially fortunate to participate in Leg 34 during which, for the first time, cores of massive flows of mid-ocean ridge basalts (MORB) were recovered, yielding the best cores from that leg. The old (Cretaceous) sills from Leg 17 and the relatively young (Miocene to late Eocene) massive flows from Leg 34 complement each other in age, thus allowing the composite picture to be drawn in considerable detail.

Before outlining that picture, however, one additional factor needs to be discussed, namely susceptibility to alteration of the various primary and secondary phases. This affects the rate of alteration, the rate of development of distinct alteration zones, and the clarity of those zones. The main phases in virtually all holocrystalline oceanic basalts are clinopyroxene (mainly augite) and plagioclase. Subordinate phases are titanomagnetite, olivine, and interstitial glass. Volumetrically the chilled glass surfaces of flows and pillows are minor, but they assume great significance because of the frequency with which they are recovered in cores and dredges, and their unique importance in marking surfaces of discrete igneous cooling units, be they pillow, flows, or sills. Of these various phases, clinopyroxene and plagioclase are most resistant to seawater alteration and diagenesis. Only in rocks as old as Cretaceous does one begin to see alteration of plagioclase, either to an aluminous smectite, seen only along cracks or in selected zones, or to a monoclinic K-feldspar pseudomorph, the extent of development of which depends on the supply of potassium, which in turn depends on the abundance of smectite which rapidly takes up K in exchange sites and must be virtually saturated

(i.e., at equilibrium with pore waters) before K is available to partake in replacement of plagioclase. Clinopyroxene likewise shows almost no alteration in rocks younger than Cretaceous. In them it is replaced under nonoxidative conditions by smectite. The alteration is greatly accelerated by high activities of carbonate ion species, so that highly altered clinopyroxene is generally associated with abundant carbonate. By the time clinopyroxene and plagioclase begin to show alteration, all other primary phases have been extensively altered, and the progress of that alteration can be followed in the relatively young rocks cored during Leg 34. Titanomagnetite is oxidized at high temperatures to Ti-poor magnetite and ilmenite, and at low temperatures to titaniferous maghemomagnetite and maghemite. Olivine is replaced by smectite under nonoxidative conditions, and is either wholly removed or replaced by porous, earthy Fe oxide under oxidative conditions. Smectite rims around earthy Fe oxide cores in pseudomorphs after olivine record a composite history. Fe-rich olivine, which is restricted to the matrices of holocrystalline MORB, alters much more rapidly than early, Mg-rich olivine. Hence, the existence of groundmass olivine in MORB, though permitted by known phase relations, was not firmly established until rare remnants and much more abundant pseudomorphs after it were found in the massive, diabasic-textured MORB cored during Leg 34 at sites 319 and 321. Interstitial glass is presumably richer in Fe and water in coarser grained, more slowly cooled rocks, and hence, is more rapidly altered than is the relatively Mg-rich glass of chilled selvages. The interstitial glass is altered to a green or blue-green, relatively Fe-rich smectite, and alters even more rapidly than associated olivine if one may judge from the relative frequency and abundance of fresh remnants of these phases. The glassy, relatively Mg-rich selvages of pillows and flows alter progressively

through golden yellow to orange isotropic palagonite; to red isotropic, highly oxidized palagonite; or red-to-orange fibropalagonite (a dense aggregate of poorly crystallized smectite crystallites).

Late magmatic-deuteric products. Late hydrous products of the magmatic stage include rare biotite (and possibly amphibole). Quench products include interstitial hydrous glass and possibly quench smectite. Deuteric products include Ti-poor magnetite and maghemomagnetite with ilmenite lamellae pseudomorphic after titanomagnetite; paper-thin veins of chlorite and minor talc; rare iddingsite; and possibly smectite after olivine and interstitial glass. Minor talc may accompany smectite after olivine.

Products of sea-water alteration. Palagonite and fibropalagonite are the most prominent products of this stage. Other products formed concurrently just below or inward from the surfaces of joint blocks are most readily recognized in those blocks, one of the surfaces of which is a chilled glassy selvage. In and just inward from the glass selvage, olivine and interstitial glass are altered to earthy Fe oxide where they are exposed to abundant oxygen. Where access of oxygen is retarded and an early hydration front has passed through, the olivine is altered to smectite and the interstitial glass to golden yellow palagonite or fibropalagonite. A later wave of oxidation may replace remnant olivine by Fe oxide to give composite pseudomorphs, and convert the altered glass from golden yellow to brown, orange, or red. Still further inward the interstitial glass is hydrated but not oxidized, and is replaced by relatively well-crystallized green or blue-green smectite which is difficult to assign with certainty to the stage of seawater alteration (pre-burial) or diagenesis.

Fe and Mn oxides formed during seawater alteration are x-ray amorphous near the surfaces of joint blocks. As little as two of three centimeters inward, however, dark veins give x-ray patterns of

todorokite, birnessite (which may have formed directly or replaced todorokite), and, rarely, goethite. The crystallinity seems to be a function of rapidity of crystallization, hence of rates of nucleation and crystal growth. Phillipsite veins are frequently found in those rocks which record seawater alteration, but, except well inward from surfaces, the veins are believed to have formed after burial since phillipsite appears to be unstable in open seawater. Carbonate is minor or rare in the phillipsite and Mn oxide veins and appears to have formed primarily after burial.

Products of nonoxidative diagenesis. Interstitial glass is replaced by green to blue-green smectite (some of which may be of quench origin). Groundmass olivine is wholly replaced, and phenocrystic olivine is partially (along cracks and edges) to wholly replaced by similar smectite. The high ferric Fe content of the blue-green smectite in veins associated with the altered olivines and glass (Table 9) suggests that limited oxidation occurs at this stage, but not enough to produce independent ferric Fe phases. Titanomagnetite may undergo some oxidation toward maghemomagnetite.

Veins are composed mainly of green to blue-green smectite, magnesian calcite, aragonite, and a mixture of pyrite and marcasite. Lesser constituents are celadonite, chlorite, talc, and mixed-layer clay minerals. The chemical constituents of the smectite are probably derived from the immediate wall rocks since smectite veins seem to die out individually and collectively toward contacts of cooling units. The relatively high ferric Fe content (Table 9) suggests some oxidation, but limited in extent, so that the smectite lattice accommodates the ferric Fe and independent ferric Fe phases do not form. The crystallization of smectite keeps the activity of Mg ions depressed to levels at which the nucleation of calcite is not inhibited. The textural and compositional relations of the carbonates suggest that aragonite formed stably or metastably and later than magnesian calcite; for instance, the aragonite is clear, unetched, and often idioblastic, suggesting that its rate of inversion to calcite was effectively nil. From this fact it is inferred that as smectite crystallization slowed, the activity of Mg ions in pore fluids rose, the nucleation of calcite ceased, its growth

TABLE 9. Wet Chemical Analysis of Green Vein Smectite
Formed during Nonoxidative Diagenesis, Hole 321,
Core 14, Section 3, 80–100 cm.

	Original (%)	Corrected* (%)
SiO ₂	42.60	42.33
TiO ₂	1.01	1.04
Al ₂ O ₃	6.57	6.03
Fe ₂ O ₃	8.93	9.15
FeO	4.51	4.62
MnO	0.03	0.03
MgO	16.70	17.11
CaO	0.27	0.00
Na ₂ O	1.27	1.18
K ₂ O	0.76	0.78
H ₂ O+	6.81	6.98
H ₂ O—	10.29	10.55
P ₂ O ₅	0.20	0.20
TOTAL	99.95	100.00
Cl 72 ppm		

* 2.37 Plagioclase (An₅₅) subtracted, normalized to 100% (H. Onuki, Analyst).

slowed radically or stopped, and ultimately, aragonite formed. Concurrently a second generation of chlorite (presumably Mg-rich) began to form. It is intimately intergrown with late, light-blue (presumably Mg-rich) smectite, which often occupies the centers of thick smectite veins. Thus, while oxygen, H_2O and CO_2 appear to be added, little if any material appears to be lost, so that a vertical section through a cooling unit should yield the original, nonvolatile composition of the unit. Like smectite

veins, the carbonate veins die out toward surfaces of cooling units.

The origin of the sulfides is an unsolved puzzle in two ways. Biological reduction of pore-water sulfate is an inadequate source of sulfur. The host rock is an adequate source, but the mechanism of its mobilization is unknown. The reason for the coexistence of two sulfides is likewise unknown, despite the fact that the coexistence is a long-known fact of many low-temperature sulfide occurrences. In the Cretaceous rocks from Leg

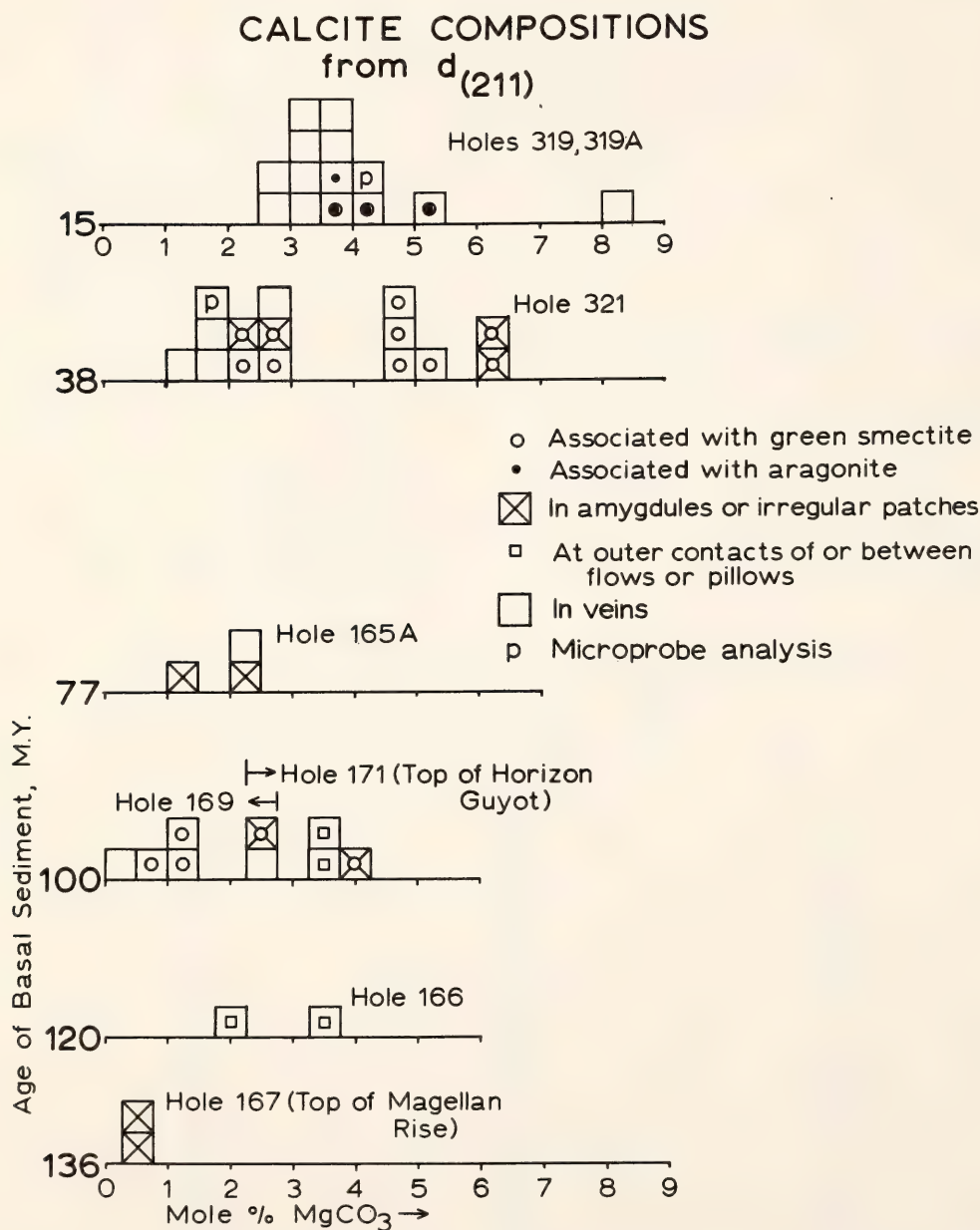


Fig. 63. Compositions of secondary calcites from basalts cored during legs 17 and 34 plotted against ages of basal sediments. The empty large squares refer to calcites associated with ferric oxides and/or oxidized smectites; note that they tend to be lower in Mg than those associated with aragonite and green smectite.

17 no marcasite was found, but its presence cannot be excluded since the Leg 17 rocks are mostly oxidatively altered and little sulfide of any sort survives. Therefore, the presently known occurrences of marcasite in oceanic crustal basalts of Miocene and late Eocene ages do not provide an adequate basis for speculations on its rate of inversion to pyrite at low temperatures.

Mn oxides formed at this stage of alteration are mainly or solely todorokite, which is fairly well crystallized, presumably as a result of slow rate of crystallization. Phillipsite formation at this stage was restricted to chilled surfaces. A possible reason is the inability

of phillipsite to compete effectively with smectite, celadonite, and talc for the limited available dissolved silica in the interior of the cooling units, and its much more effective competition near glassy surfaces, the alteration of which provided relatively abundant free silica and few or no competing phyllosilicates.

Products of oxidative diagenesis. The advent of oxygen behind sharp, diffusion-controlled oxidation fronts inaugurates oxidative diagenesis. Any remnant olivine is oxidized to earthy Fe oxide, and titanomagnetite to titaniferous maghemite and maghemite. The outermost, Fe-rich rims of clinopyroxene may be oxidized. Smectite is oxidized,

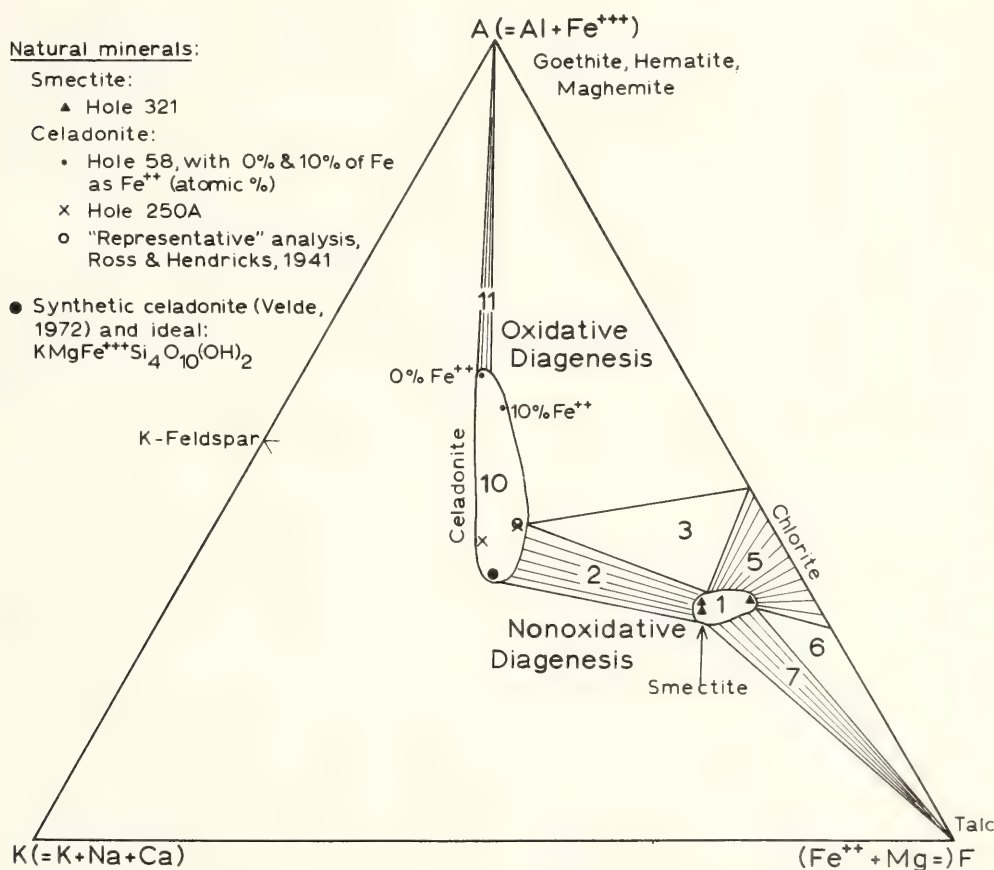


Fig. 64. Modified AKF diagram (quartz generally absent) showing the diagenetic phyllosilicate assemblages in oceanic crustal basalts. In some respects the diagram is an overlay of an ACF on an AKF diagram. The chlorite field is guesswork deployed for convenience of illustration. Calcite- and aragonite-bearing assemblages are not shown. The calcite and aragonite would plot at the apex K, which is also the apex C of the ACF overlay. They commonly coexist with smectite and talc, less consistently with chlorite and celadonite. These assemblages and those observed to contain four phyllosilicates could be plotted only by separation of one of the composite components shown, in order to create a three-dimensional tetrahedral volume. This could be done without violation of phase-rule restrictions. The oxidation states of the phyllosilicates shown increase monotonically from the base toward the apex A.

and charge balance is preserved by expulsion of ferric Fe as a red, brown, or yellow dust which pigments the intrinsically colorless resulting smectite. Except for some celadonite, the formation of which is limited by the supply of K, no new phyllosilicates form. Sulfides are oxidized, resulting in limonite stains in host rock adjacent to formerly sulfide-bearing veins. The limonite is the most readily visible sign of the oxidative alteration. Aragonite inverts to Mg-poor calcite. Magnesian calcite adjusts progressively toward stabler calcites poorer in Mg, a change which appears better correlated with oxidation than with the age of the host rock (Fig. 63).

Phillipsite continues to form. If joints and veins are opened and admit Si-rich pore fluids from the surfaces of cooling units to the interiors, phillipsite and Mg-poor calcite may form drusy vugs in the interiors of cooling units where the crystallization may be slow enough to form well-crystallized birnessite, either by oxidation of earlier todorokite or by direct precipitation of birnessite. Fairly well-crystallized goethite may form under similar circumstances.

The observed phase assemblages can be plotted in a modified AKF diagram (Fig. 64) without violating the requirements of the mineralogical phase rule, suggesting that both the oxidative and nonoxidative mineral assemblages, viewed separately, closely approximate equilibrium assemblages. The rarity of phyllosilicates crystallized directly from solution during oxidative diagenesis precludes at this time a decision as to whether the goethite-smectite or celadonite-chlorite tie-line is stable under those conditions, but the Fe-pigmented, oxidized smectites suggest that it is goethite-smectite.

References

- Bass, M. N., R. Moberly, J. M. Rhodes, C. S. Shih, and S. E. Church, Volcanic rocks cored in the central Pacific, Leg 17, Deep Sea Drilling Project, *Initial Reports, Deep Sea Drilling Project*, 17, 429–503, 1973a.
- Bass, M. N., R. Moberly, J. M. Rhodes, C. S. Shih, and S. E. Church, Volcanic rocks cored in the central Pacific, Leg 17, Deep Sea Drilling Project, *Trans. Am. Geophys. Union*, 54, 991–995, 1973b.
- IMMISCIBILITY AND ANCIENT AND MODERN VOLCANISM
- C. Brooks and L. Gélinas*
- Archean volcanics from the Canadian Shield have long been the subject of major element, trace element, and isotopic studies in this laboratory and the results have been reported in previous Reports. As part of this broad geochemical program, we have often digressed into topics that show promise of furnishing information on the type and nature of ancient magmatism (e.g., the trace element and isotopic composition of relic pyroxenes from Archean volcanics (*Year Book* 73, p. 967). This study is another of these digressions, and in this case we are attempting to understand ancient magmatism in the light of immiscibility, a process of igneous differentiation which may leave distinct and unusual imprints in the products of volcanism.
- Many of the globule-like textures found in igneous rocks have been found to be demonstrably immiscible with their enclosing fractions (e.g., Philpotts and Hodgson, 1968; Ferguson and Currie, 1972). Most of these examples come from mafic alkaline intrusives; however, surprisingly, some have been unearthed in tholeiitic associations. For instance Roedder and Weiblen (1971) report the occurrence of two immiscible silicate liquids (one enclosed as droplets in another and quenched to form two immiscible glasses) in volcanic rocks from Hawaii, California, Greenland, and Canada. Similar observations have been made in the high-alumina olivine-tholeiite of Hat Creek, California (Anderson and Gottfried, 1971) and in the tholei-

* Génie Minéral, Ecole Polytechnique, Montréal, Québec, Canada.

itic Deccan Traps (De, 1974). De (1974) also suggested that the trend of differentiation in the Upper Zone of the Layered Series of the Skaergaard Intrusion was in part controlled by liquid immiscibility, and this was subsequently verified experimentally by McBirney (1975). Further evidence linking immiscibility and tholeiitic magmatism has been advanced by Gélinas *et al.* (1975), who explain the origin of variolitic lavas in tholeiitic suites of Canadian Archean volcanic piles by liquid immiscibility.

It would seem, therefore, that some form of association exists between liquid immiscibility and tholeiitic magmas. In many cases this association links immiscible splitting to only the late stages in magmatic history; however, the tholeiitic Archean variolites of Canada, the komatiitic Archean variolites of South Africa (Ferguson and Currie, 1972), and the Skaergaard intrusion of Greenland all involve immiscibility on a much grander scale. Are these examples merely artifacts of some peculiar geologic conditions, or is immiscibility a ubiquitous phenomenon that continually shadows tholeiitic magmatism, awaiting only the right physicochemical conditions before manifesting itself?

The purpose of this study is to examine this question by an appraisal of certain ancient and modern volcanic suites representative of the main classes of volcanism (tholeiitic, calcalkaline, alkaline) with the aim of (1) evaluating the possible link between tholeiitic magmatism and immiscibility, and (2) comparing the main classes of volcanism in the light of susceptibility to immiscibility. It will be revealed that not only is there a good case for tholeiitic magmas to be more commonly associated with immiscibility than either the calcalkaline or alkaline volcanics, but also that there is a stronger likelihood of encountering evidences of immiscibility in the more ancient volcanics, as a result of a polarized, time-dependent proneness of certain magmas to undergo liquid segregation.

Proposed Miscibility Gaps

Grieg (1927) showed that of the major rock-forming oxides, Na_2O , K_2O , and Al_2O_3 are miscible with SiO_2 whereas CaO , FeO , MgO , and Fe_2O_3 are immiscible with SiO_2 at high SiO_2 concentrations. Grieg presented a pseudo-ternary diagram of $(\text{CaO} + \text{MgO} + \Sigma\text{FeO} + (\text{TiO}_2))$ versus $(\text{Na}_2\text{O} + \text{K}_2\text{O} + \text{Al}_2\text{O}_3)$ versus SiO_2 to show the limited extent of the primitive immiscibility field in the polycomponent system. In this system, Grieg's primitive field is restricted to a narrow zone high on the silica portion of the $(\text{CaO} + \text{MgO} + \Sigma\text{FeO} + (\text{TiO}_2))$ - SiO_2 edge (Fig. 65). Although experimentally verified, Grieg considered immiscibility unlikely as a process in the origin of igneous rocks, on the bases that: (1) The experimentally-established minimum temperatures were too high (nearly 1700°C); (2) No igneous rocks approached the compositions found to show immiscibility in the laboratory; and (3) The textural evidence for immiscibility in natural rocks could be readily assigned to other processes. It was not until Roedder (1951) described silicate immiscibility in the system leucite-fayalite-silica, and in the parent quaternary system K_2O - FeO - Al_2O_3 - SiO_2 (1953), at much lower temperatures (minimum $< 1100^\circ$), and in compositions much closer to igneous rocks, that the geological possibility of immiscibility became reasonable.

In the development of knowledge concerning this second field of immiscibility (denoted PMG in Fig. 65), both Holgate (1954) and Roedder (1956) noted that two systems relevant to silicate melts display flat liquidus surfaces which according to Grieg (1927) are indicative of possible metastable fields of liquid immiscibility. These systems are $\text{NaAlSi}_3\text{O}_8$ - FeO - SiO_2 (Bowen and Schairer, 1938), where the fayalite field displays a flat liquidus surface, and KAlSi_2O_6 - $\text{CaMgSi}_2\text{O}_6$ - SiO_2 (Schairer and Bowen, 1938), where the plateau-shaped diopside field shows a peculiar inverse curvature. With

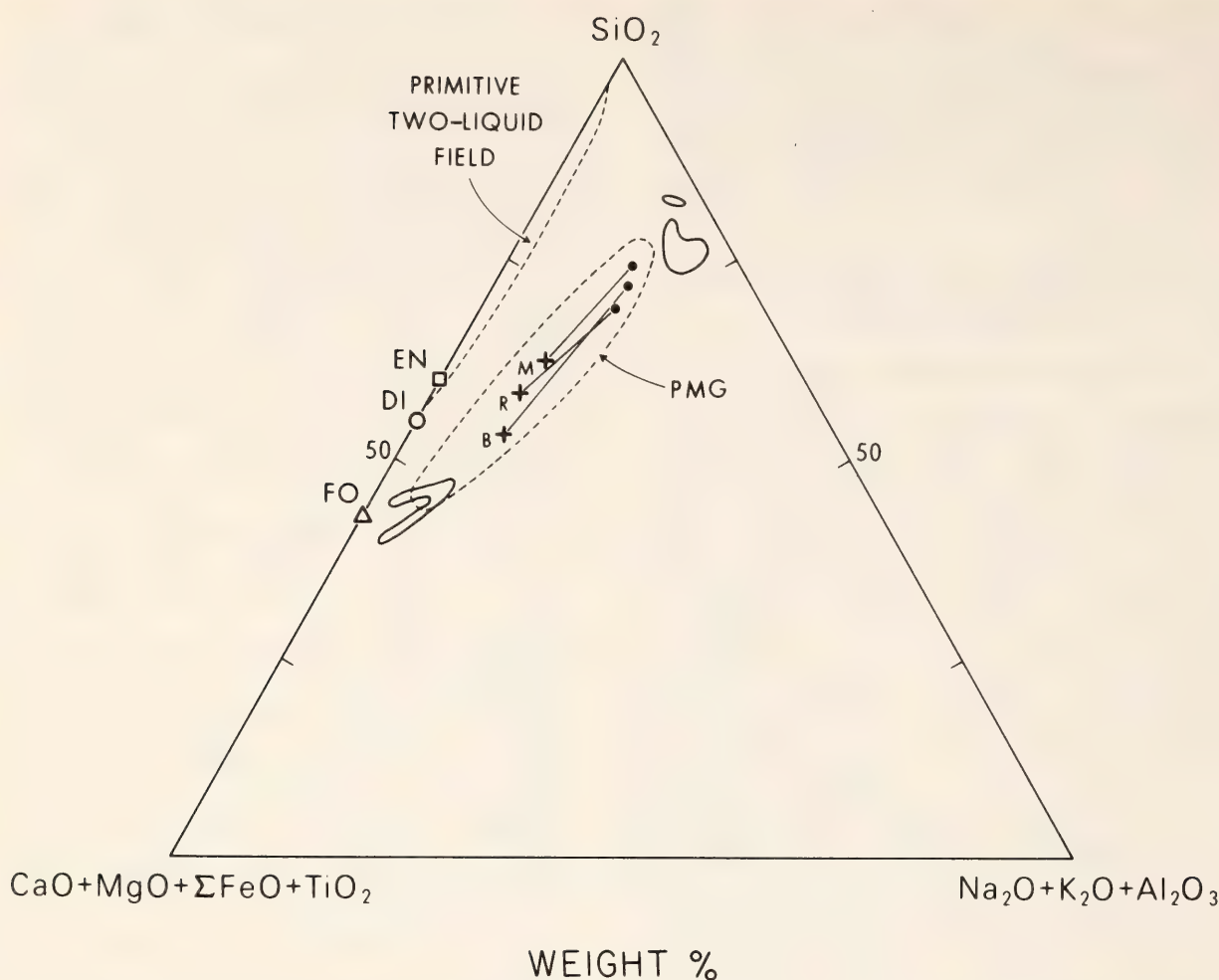


Fig. 65. Pseudo-ternary diagram showing location of the primitive and proposed miscibility gaps (latter denoted as PMG). Tie-lines within the PMG join experimentally established liquid-immiscible fractions (data from Roedder and Weiblen (*R*), 1970; Massion and Van Groos (*M*), 1973; McBirney (*B*), 1975). The open fields are for lunar glass inclusions ($N = 50$) of Roedder and Weiblen.

the aid of Grieg's (1927) pseudo-ternary diagram, Holgate (1954) presented Roedder's (1951) stability field of immiscibility within the system leucite-fayalite-silica, together with the locations of the axes of the metastable miscibility gaps for the systems $\text{NaAlSi}_3\text{O}_8\text{-FeO-SiO}_2$ and $\text{KAlSi}_3\text{O}_8\text{-CaMgSi}_2\text{O}_6\text{-SiO}_2$. The coincidence of these axes with Roedder's field of immiscibility was striking.

The final validity of this field was obtained in the laboratory. Roedder and Weiblen (1970), Ferguson and Currie (1972), Massion and Van Groos (1973) and McBirney (1975) have obtained during experiments immiscible liquid pairs which plot within the PMG shown in Fig. 65. Hence, the PMG can be considered confidently as a verified, geologi-

cally-applicable two-liquid field. Presumably, magmas with compositions plotting in or on the flank of the PMG would be prone to split into two liquids, and we use this property throughout our evaluation of the volcanic rock series.

Because we use the PMG in our appraisal of volcanic rock suites, it is pertinent here to consider some of the more important properties of this field as revealed on the pseudo-ternary diagram of Fig. 65. The PMG is an extended ellipsoid that roughly parallels the silica-cafemic oxides boundary. This means that a magma composition plotting on the alkaluminous side of the PMG would be driven into the PMG by any processes leading to a relative decrease in the alkali and alumina contents of that

magma. If this process also leads to a lower alumina-to-alkalies ratio, then immiscible splitting is even further favored, although as pointed out by Watson and Dickey (1975) the ratio, more appropriately, should be alumina-to-alkalies plus water. These features have importance in the discussion to follow.

Volcanic Rock Suites and the PMG

Phenocryst-free, rapidly cooled volcanic rocks can be used to tell much about the composition of their parent magma. In gathering data from the literature we have undoubtedly included numerous phenocryst-bearing volcanic rocks; however, this is of secondary importance since we are primarily interested in liquid compositions, and these may be either original melt compositions or compositions of late, residual liquids. The procedure used has been to assemble data from different tectonic regimes and to establish composite fields for the main classes of volcanism.

The composite fields for modern vol-

canics are plotted in Fig. 66. These volcanics define a vast domain on the right flank of the PMG, with their respective positions being controlled by their relative alkali-plus-alumina contents. Successively from the alkali-alumina corner towards the PMG, the suites encountered are alkaline, calcalkaline, low-K calcalkaline, and tholeiitic. The only modern suite to overlap the PMG is the tholeiite suite, and on dissection, it is found to do so only for the more silicic low-K tholeiites of island arcs. No other modern volcanic suite approaches the PMG, although the low-K and normal calcalkaline fields closely parallel the boundary of the PMG.

The composite Archean tholeiite and low-K calcalkaline suites are shown in Fig. 67B. The ancient tholeiite suite is essentially identical with the modern tholeiite suite (Fig. 67A) and most especially with the low-K tholeiite suite of island arcs. Both of these suites overlap the PMG at higher SiO_2 concentrations, with the ancient suite displaying a slight trend to even higher SiO_2 contents than

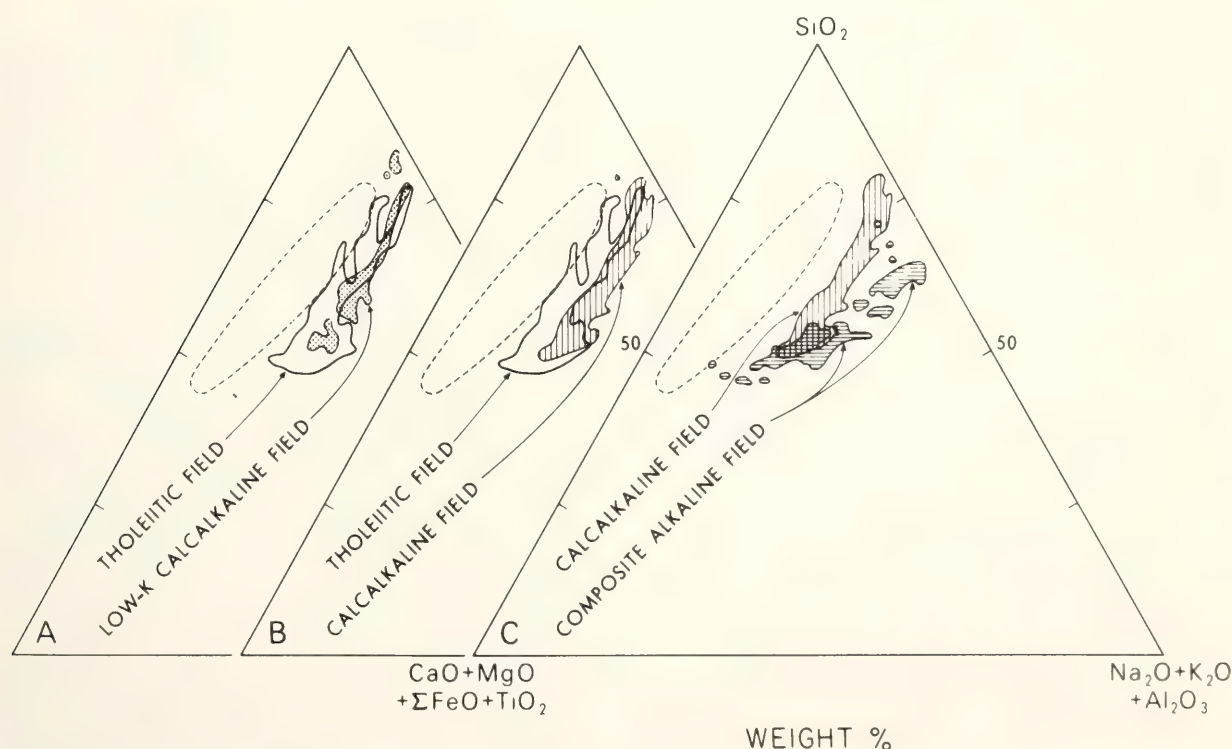


Fig. 66. Composite fields for modern volcanics in relationship to the PMG. The alkaline, calcalkaline, low-K calcalkaline, and tholeiitic suites are based on 119, 73, 168, and 284 analyses, respectively (data sources too numerous to identify).

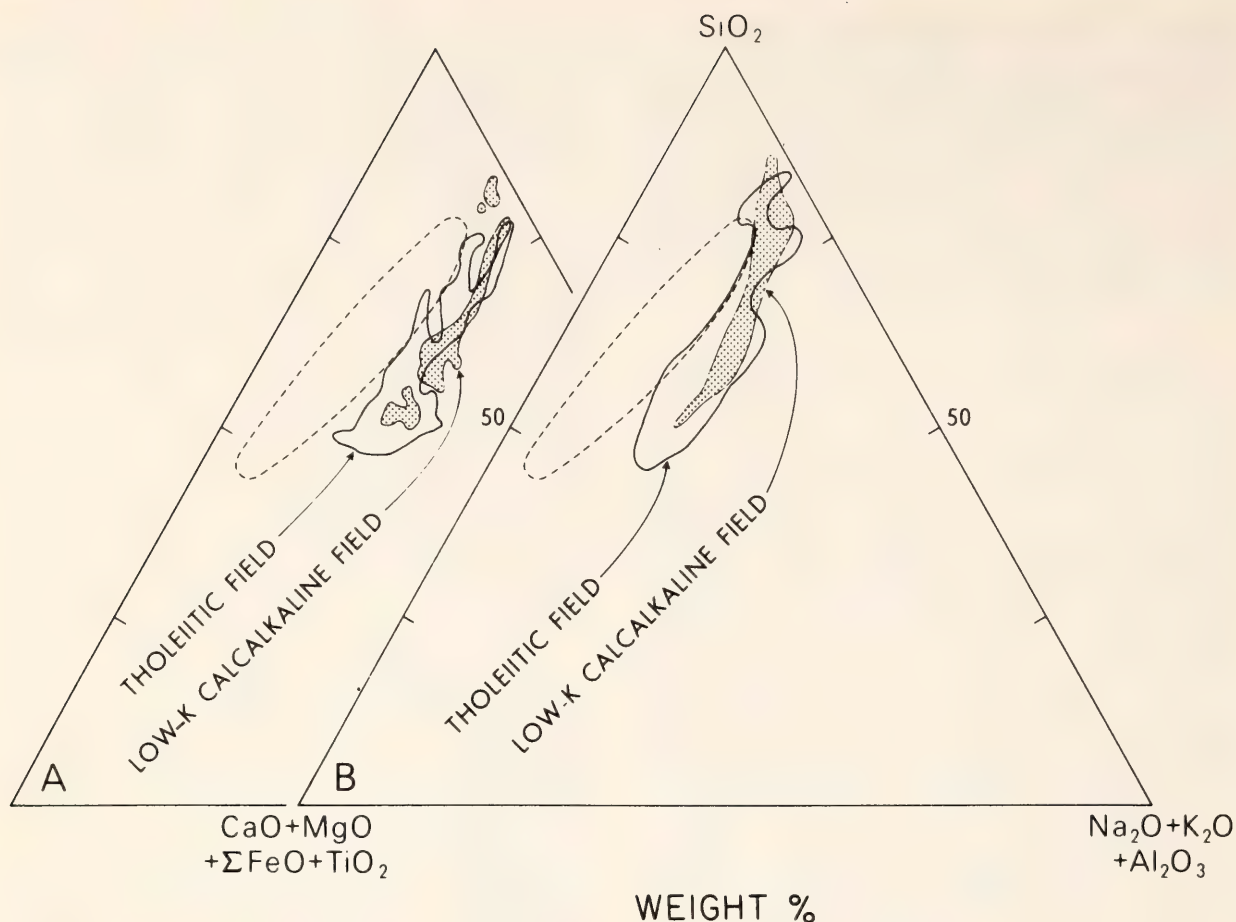


Fig. 67. Composite fields for modern (A) and ancient (B) tholeiitic and low-K calcalkaline fields with respect to the PMG. The fields are based on 345 (A) and 122 (B) analyses (data source, Gélinas *et al.*, 1975).

those encountered in the modern examples.

The composite, ancient low-K calcalkaline field differs from the modern field. While the modern field never approaches the PMG, the ancient is positioned significantly closer to the PMG and actually touches it at high SiO_2 concentrations. For the most part the ancient volcanics possess lower alumina plus alkalis than their modern chemical counterparts.

Discussion

It remains to relate these observations to immiscibility. On examining the abundance of textural evidence indicative of immiscibility, it is clear that Archean terranes contain many examples, whereas there are few in modern terranes. The best examples of immiscibility found in Archean terranes are the variolitic lavas

of Canada and South Africa, and they are widespread. Is this a real phenomenon indicating a varying susceptibility of tholeiitic and ancient calcalkaline magmas to undergo liquid immiscibility with time? There is evidence to suggest that this may be so.

Lower alumina and alkali contents result in rock fields plotting in the PMG. It has been suggested (e.g., Hart *et al.*, 1970) that because of a higher geothermal gradient, high rates of convective upwelling and reduced lithospheric thickness were probable in the Precambrian. Extensive and relatively shallow partial melting is a direct prediction of such thermal considerations, and this has already been used in discussing the origin of komatiite (e.g., Viljoen and Viljoen, 1969; Brooks and Hart, 1974; Cawthorn and Strong, 1974). Because extensive partial melting produces magmas with

lower alkali and alumina contents, this model implies that the production of immiscibility-prone magmas was more common in the Archean than today.

Further support for encountering immiscibility-prone magmas early in Earth's history is provided by models of mantle water content over time. Strong and Stevens (1974), in discussing the change in Earth's behavior at the Archean-Proterozoic boundary, postulate that the differences between Archean and younger sections result from a water-pressure effect on the peridotite solidus. With degassing of the mantle, smaller and smaller degrees of partial melting of mantle material occur. This is in direct accord with the previously discussed thermal model. However, water not only has a role in partial melting considerations, it has been shown to have a direct effect on the field of immiscibility.

Holgate (1954) proposed that the field of immiscibility was enlarged at high water pressure, and as pointed out by Watson and Dickey (1975) water as a liquidus depressant has been found necessary in many cases of experimental verification of the process (e.g., Philpotts and Hodgson, 1968; Philpotts, 1971; Ferguson and Currie, 1972). Arguments can be advanced for both wet and dry Archean volcanism; because (a) the Canadian Archean of 2.7 b.y. contains abundant andesites, and (b) the Archean tholeiites most closely resemble low-K island arc tholeiites, we are inclined to believe that the volcanism during the formation of the Archean metavolcanic belts may have been wet. Whatever the water content, however, this model, involving decreasing water contents in the accessible mantle with time, again favors immiscibility in Archean volcanic rocks relative to those of younger terranes.

It would seem, on the basis of this evaluation of ancient and modern volcanic suites, that a direct link between magmatism and immiscibility exists for certain tholeiitic and ancient calcalkaline magma compositions. These compositions

are mostly in the intermediate-to-felsic range, a fact reminiscent of Grieg's (1927) experimental observation that CaO, FeO, MgO and Fe₂O₃ show incomplete miscibility with SiO₂ at high SiO₂ concentrations.

An important question relates to whether the potential immiscibility in ancient and modern tholeiitic magmas (and in ancient low-K calcalkaline magmas) is restricted to the late-stage residual liquids only, or whether it involves much of the magma. The previous discussion concerning lowering of relative alumina plus alkalis contents, and the role of water in magmas, is primarily applicable to the direct production of an immiscible-prone melt. However, differentiation characteristically enhances a residual magma in liquidus depressants such as iron and alkalis. Very high iron contents are especially necessary for successful immiscible splitting experiments in dry systems (e.g., Roedder and Weiblen, 1970; McBirney, 1975). Hence, where a tectonic environment does not allow direct enhancement of liquidus depressants in a primary magma, and that magma composition is not favorable to liquid immiscible splitting, it may still reach a two-liquid stage in its residual phases. We cannot yet distinguish with certainty which of these was responsible for the Archean variolites in the Abitibi belt, although their high iron contents removes the necessity of having wet tholeiitic magmas. Because, however, the Archean variolitic lava compositions suggest that immiscibility is restricted to the higher SiO₂ levels of tholeiitic magma evolution and because the tholeiite composite field overlaps the PMG only at higher SiO₂ levels, it is probable that some magmatic differentiation is required before a tholeiitic (or ancient, low-K calcalkaline) magma will split into two liquid fractions. This in turn favors Fe as a more important liquidus depressant than water in tholeiite magmas.

The evaluation presented here is not

complete. We are only now beginning to understand the secondary modification that pervades Archean volcanics, and as more and more data become available we may be able to extend or at least underline the conclusions here presented. At this stage, however, we can state that the recent abundance of liquid-immiscibility observations associated with tholeiitic magmatism is not in conflict with what is experimentally known about immiscibility. In fact, the reverse is true, and immiscibility considerations lead to a direct prediction that textural evidences of the phenomenon should be common in at least the more diversified members of the tholeiitic suites. Furthermore, there is evidence to indicate that such textural evidences will be more abundant in ancient rather than in modern terranes. Similar conclusions seem to apply to the distribution of peridotitic komatiites and ultramafic tuffs in time. Perhaps earth's mantle did leave a unique imprint at the Archean stage of continent evolution, an imprint which we are only now beginning to decipher.

References

- Anderson, A. T., and D. Gottfried, Contrasting behavior of P, Ti, and Nb in a differentiated high-alumina olivine-tholeiite and a calc-alkaline andesite suite, *Geol. Soc. Am. Bull.*, **82**, 1929–1942, 1971.
- Bowen, N. L., and J. F. Schairer, Crystallization equilibrium in nepheline-albite-silica mixtures with fayalite, *J. Geol.*, **46**, 397–411, 1938.
- Brooks, C., and S. R. Hart, On the significance of komatiite, *Geology*, **2**, 107–110, 1974.
- Cawthorn, R. G., and D. F. Strong, The petrogenesis of komatiites and related rocks as evidence for a layered upper mantle, *Earth Planet. Sci. Lett.*, **74**, 369–375, 1974.
- De, Aniruccha, Silicate liquid immiscibility in the Deccan Traps and its petrogenic significance, *Geol. Soc. Am. Bull.*, **85**, 471–474, 1974.
- Ferguson, J., and K. L. Currie, Silicate immiscibility in the ancient basalts of the Barberton Mountain land, Transvaal, *Nature Phys. Sci.*, **235**, 86–89, 1972.
- Grieg, J. W., Immiscibility in silicate melts, *Am. J. Sci.*, **13**, No. 73, 1–44, and **13**, No. 74, 133–154, 1927.
- Hart, S. R., C. Brooks, T. E. Krogh, and G. L. Davis, Ancient and modern volcanic rocks: a trace element model, *Earth Planet. Sci. Lett.*, **10**, 17–28, 1970.
- Holgate, N., The role of liquid immiscibility in igneous petrogenesis, *J. Geol.*, **62**, 439–480, 1954.
- Massion, P. J., and A. F. Koster Van Groos, Liquid immiscibility in silicates, *Nature, Phys. Sci.*, **245**, 60–63, 1973.
- McBirney, A., Differentiation of the Skaergaard intrusion, *Nature*, **253**, 691–694, 1975.
- Philpotts, A. R., Immiscibility between feldspathic and gabbroic magmas, *Nature, Phys. Sci.*, **229**, 107–109, 1971.
- Philpotts, A. R., and C. J. Hodgson, Role of liquid immiscibility in alkaline rock genesis, *Twenty-third Int. Geol. Congr.*, Vol. 2, pp. 175–188, 1968.
- Roedder, E., Low temperature liquid immiscibility in the system K_2O -FeO- Al_2O_3 - SiO_2 , *Am. Mineral.*, **36**, 282–286, 1951.
- Roedder, E., Liquid immiscibility in the system K_2O -FeO- Al_2O_3 - SiO_2 (abstr.), *Geol. Soc. Am. Bull.*, **64**, 1466, 1953.
- Roedder, E., The role of liquid immiscibility in igneous petrogenesis: A discussion, *J. Geol.*, **64**, 84–88, 1956.
- Roedder, E., and P. W. Weiblen, Silicate liquid immiscibility in lunar magmas, evidenced by melt inclusions in lunar rocks, *Science*, **167**, 641–644, 1970.
- Roedder, E., and P. W. Weiblen, Petrology of the silicate melt inclusions, Apollo 11 and Apollo 12 and terrestrial equivalents, *Proc. Second Lunar Sci. Conf.*, *Geochim. Cosmochim. Acta*, Suppl. 2, Vol. 1, MIT Press, 507–528, 1971.

Schairer, J. F., and N. L. Bowen, The system leucite-diopside-silica, *Am. J. Sci.*, 35A, 507-528, 1938.

Strong, D. F., and R. K. Stevens, Possible thermal explanation of contrasting Archean and proterozoic geological regimes, *Nature*, 249, 545-546, 1974.

Viljoen, J. J., and R. P. Viljoen, Evidence for the existence of a mobile extrusive peridotitic magma from Komati Formation of the Onverwacht Group, *Geol. Soc. S. Africa, Spec. Pub.* 2, pp. 87-112, 1969.

Watson, E. B., and J. S. Dickey, Jr., Silicate liquid immiscibility in alkaline mafic magmas: evidence in a White Mountain magma series dike, with a discussion of its origin, *Geochim. Cosmochim. Acta*, in press, 1975.

EARLY EVOLUTION OF THE CENTRAL ANDEAN VOLCANIC ARC

David E. James, Christopher Brooks,
and Arturo Cuyubamba

Introduction

We have reported previously (*Year Book 72* and *Year Book 73*) on our efforts to derive a model for the petrogenesis of the rocks of the earliest Andean volcanic arc. Our attention in these

studies has focused on two aspects of the initial phase of development of the Andean arc—the radiometric age and the Rb-Sr-K trace element geochemistry of the volcanic rocks. The radiometric age not only gives the time of inception of the Andean arc, but also provides information about plate motions in the Pacific during early Mesozoic time. The trace element geochemistry provides data on the depth to the Mesozoic subduction zone and on the chemical nature of the magmas of the primitive Andean arc relative to those of the more evolved arc of late Mesozoic and Cenozoic time.

The earliest volcanic rocks of the Andean arc are preserved in a narrow belt situated on the coast of southern Peru (see Fig. 68 for outcrop map and sample localities). The rocks show considerable evidence of deposition near sea level as witnessed by pillows and intercalated shallow-water marine sedimentary rocks. The volcanic rocks are considered to belong to the Chocolate Formation described by Jenks (1948), although the rock of the Chocolate type locality near Arequipa is not volcanic (as Jenks erroneously thought) but is instead a volcanic sedimentary rock. The only Chocolate volcanic rocks known to

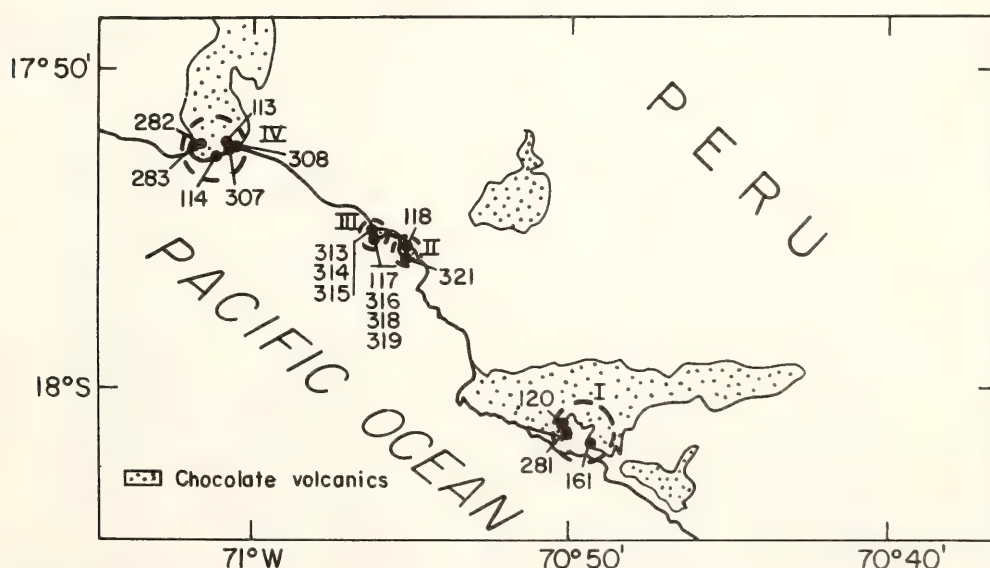


Fig. 68. Outcrop map showing the distribution of early Jurassic volcanic rocks of the Chocolate formation. Sample localities and sample numbers are shown and sample groupings are given by Roman numerals.

us occur along coastal Peru. They are primarily basalts and basic andesites (50%–57% SiO₂).

A major difficulty in untangling the origin and history of the Chocolate volcanics is the pervasive alteration that affects most of the samples. Rocks appearing fresh in hand specimen are commonly too altered to be of use geochemically. As a rule, we have achieved consistent results by first screening samples on the basis of H₂O and CO₂ contents. We have confined our discussion to those samples with H₂O < 2.0% and CO₂ < 0.2%. Our inability in previous years to obtain definitive results on the Chocolate volcanics stemmed principally from the paucity of samples that passed the screening criterion. For that reason we undertook during the past field season to obtain a substantially improved sample collection. We have succeeded in tripling our useful data with the addition of 13 samples that meet the H₂O-CO₂ screening criterion.

Analytical Results

The analytical data discussed here are summarized in Table 10. Analytical procedures have been described by us in

previous Reports. All strontium isotopic measurements have been normalized to an assumed E and A standard value of 0.70800.

Strontium isotopic composition. ⁸⁷Sr/⁸⁶Sr ratios are plotted versus Rb/Sr in Fig. 69. Regression analyses have been made on several subgroupings of samples and yield calculated ages ranging from 165 to 205 m.y. Our preferred age is 185 m.y., calculated for the group of samples with the least petrographic evidence of alteration. PE 120 appears fresh in thin section but is excluded because of its exceptionally high Rb/Sr ratio (2.1) and clear indication that its ⁸⁷Sr/⁸⁶Sr ratio has begun to “droop” on the isochron. This is not an uncommon characteristic of rocks with high Rb/Sr.

A histogram of initial ⁸⁷Sr/⁸⁶Sr ratios (excluding PE 120 and PE 316) is shown in Fig. 70. The mean (⁸⁷Sr/⁸⁶Sr) for an assumed age of 185 m.y. is 0.7038 and is identical to the average for normal island arcs. Initial ratios vary slightly with H₂O content, but the variation is not significant, suggesting that the ratios are little affected by alteration as measured by H₂O.

Rb-Sr variations. Rb and Rb/Sr ratios

TABLE 10. Analytical Data and Initial Sr-isotopic Ratios, Chocolate Volcanic Rocks of Southern Peru. Initial ⁸⁷Sr/⁸⁶Sr Ratios Calculated for *T* = 185 m.y.

Sample No.	Rb (ppm)	Sr (ppm)	Rb/Sr	⁸⁷ Sr/ ⁸⁶ Sr (present day)	⁸⁷ Sr/ ⁸⁶ Sr (initial)	H ₂ O(%)
PE 113	65	414	0.16	0.70501 ± 10	0.70383	0.90
114	77	381	0.20	0.70519 ± 17	0.70371	0.97
117	99	593	0.17	0.70491 ± 11	0.70365	1.03
118	20	468	0.04	0.70411 ± 6	0.70381	1.04
120	108	51	2.12	0.71748 ± 8	0.70179*	1.41
161	84	213	0.40	0.70751 ± 13	0.70455	1.48
281	17	296	0.056	0.70469 ± 5	0.70428	1.91
282	157	452	0.35	0.70620 ± 6	0.70361	0.97
283	55	390	0.14	0.70493 ± 5	0.70389	1.14
307	51	284	0.18	0.70585 ± 6	0.70452	1.08
308	73	445	0.16	0.70478 ± 7	0.70360	0.90
313	7	726	0.010	0.70457 ± 6	0.70450	0.65
314	140	584	0.24	0.70496 ± 8	0.70318	1.27
315	117	466	0.25	0.70556 ± 6	0.70371	1.24
316	177	281	0.63	0.70725 ± 7	0.70259*	1.25
318	149	608	0.25	0.70488 ± 5	0.70303	1.56

* Not included in calculating average ⁸⁷Sr/⁸⁶Sr initial ratio.

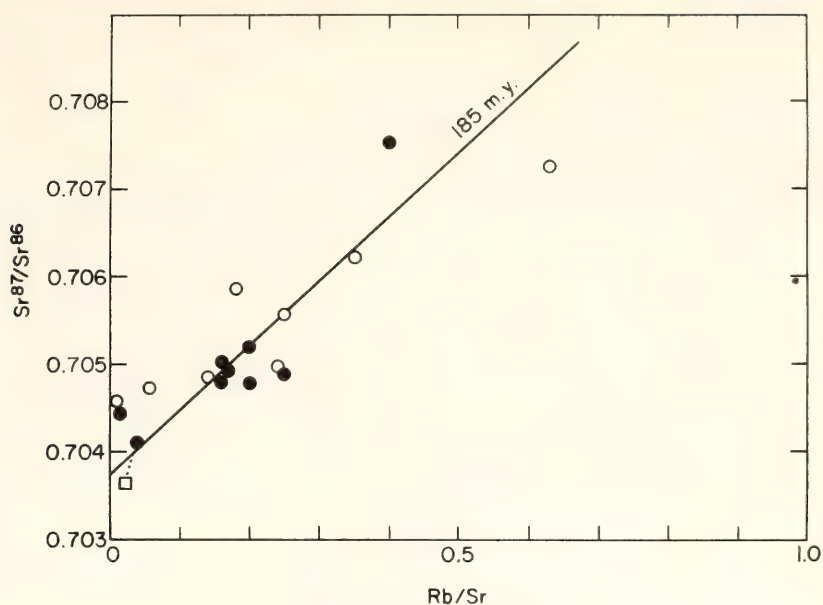


Fig. 69. $^{87}\text{Sr}/^{86}\text{Sr}$ ratios of Chocolate volcanics plotted versus Rb/Sr. Solid circles indicate data used for regression analysis; open circles and square are other data points.

of the Chocolate volcanics are abnormally high for normal volcanic arc basaltic rocks. The high Rb is apparently due to the addition of alkalis during late-stage alteration (possibly by sea water) of the rocks at the time of their formation. That the alteration was roughly contemporaneous with extrusion is indicated by the fact that the radiometric ages appear to be correct, being as great or greater than previous estimates based on stratigraphic correlations. In rocks with $\text{H}_2\text{O} < 2.0\%$, only minor alteration due to weathering appears to have occurred.

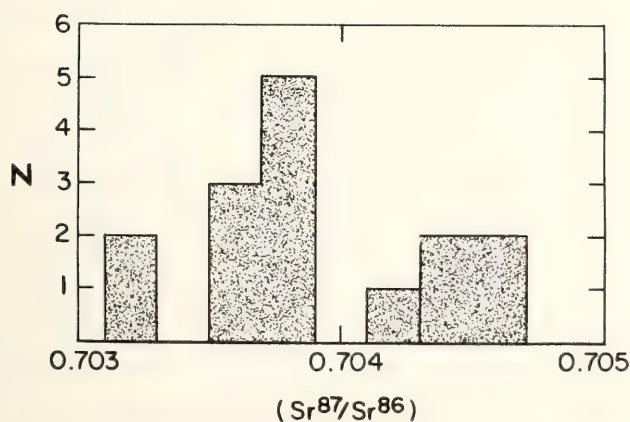


Fig. 70. Histogram of initial $^{87}\text{Sr}/^{86}\text{Sr}$ ratios of the Chocolate volcanics excluding PE 120 and PE 316. Initial ratios based on 185 m.y. age.

Sr concentrations in the Chocolate volcanics are comparatively normal (~ 250 – 700 ppm) for volcanic arc basalts. The fact that the $^{87}\text{Sr}/^{86}\text{Sr}$ initial ratios are low suggests that the alteration does not greatly involve Sr which is relatively highly buffered against sea water (Hart *et al.*, 1974).

A well-defined trend in the Rb-Sr data is obtained by plotting Rb/Sr vs. Rb as shown in Fig. 71. The good straight-line fit through the data could indicate that most of the change during alteration has been in Rb concentration, not in Sr. Only PE 161 and PE 316 lie significantly above the best-fit line through the data. Both of these samples have $^{87}\text{Sr}/^{86}\text{Sr}$ ratios that plot significantly off the isochron of Fig. 69.

Interpretation and Conclusions

The earliest volcanic rocks of the central Andean arc were extruded about 185 m.y. ago. They exhibit initial $^{87}\text{Sr}/^{86}\text{Sr}$ ratios that are identical to those measured in rocks of oceanic island arcs. Low initial ratios have been preserved despite pervasive alteration that has added alkalis (including Rb) to most of the samples. Sr concentrations appear to have been little affected by alteration, al-

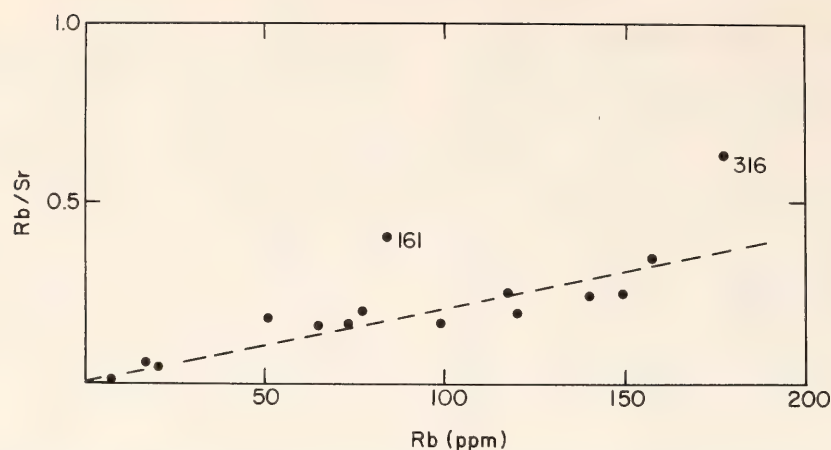


Fig. 71. Rb/Sr vs. Rb. Straight-line fit excludes PE 313 and PE 161.

though erroneous initial ratios may be more common in those samples with high Rb and other alkalis.

The Chocolate volcanics and other Mesozoic volcanic sequences that followed (see *Year Book 73*) are notable among Andean rocks for their low $^{87}\text{Sr}/^{86}\text{Sr}$ initial ratios. Late Cenozoic lavas of the same general region exhibit $^{87}\text{Sr}/^{86}\text{Sr}$ in the range 0.705–0.708. We have shown previously that the high ratios of the late Cenozoic assemblages cannot be due to crustal contamination of a parent magma with $^{87}\text{Sr}/^{86}\text{Sr}$ near 0.704. Hence, the difference in isotopic ratios between the Mesozoic and Cenozoic sequences must reflect a genuine change in the petrogenesis of the respective magmas. We suggest that the earliest magmas of the Andean arc were derived from the descending plate and overlying oceanic-type asthenosphere or young continental lithosphere at depths less than 100 km. The later Cenozoic magmas, generated at depths of 150–175 km in the Benioff zone, probably derive from melting of ancient continental lithosphere immediately overlying the descending slab and thus reflect the higher alkali abundance and aged isotopic character of that lithospheric mantle.

References

- Hart, S. R., A. J. Erlank, and E. J. D. Kable, Seafloor basalt alteration: Some chemical and Sr isotope effects,

Contrib. Mineral. Petrol., 44, 219, 1974.

Jenks, W. F., Geology of the Arequipa quadrangle, *Bol. Inst. Geol. Peru*, 9, 105, 1948.

STRONTIUM ISOTOPIC COMPOSITION OF LATE CENOZOIC CENTRAL ANDEAN VOLCANIC ROCKS: A DISEQUILIBRIUM MELTING MODEL

D. E. James

Introduction

The late Cenozoic Arequipa and Barroso andesitic-dacitic volcanic rocks of southern Peru (geologic map and sample localities shown in Fig. 72) form two geochemically distinct volcanic associations that have been described elsewhere (*Year Book 73*, pp. 983–997, 1974). A puzzling aspect of the Rb-Sr isotope data for these two volcanic units is that they define two internally consistent and parallel pseudochrons that yield an age of 400 m.y. (Fig. 73). The consistent variation of $^{87}\text{Sr}/^{86}\text{Sr}$ with Rb/Sr could be produced by at least three mechanisms: (a) crustal contamination, (b) small-scale inhomogeneity of the mantle source, and (c) disequilibrium melting of mantle material. The last two alternatives are not necessarily exclusive.

In the light of evidence presented previously (James *et al.*, 1974) crustal contamination is an unlikely cause of the observed strontium isotope variation.

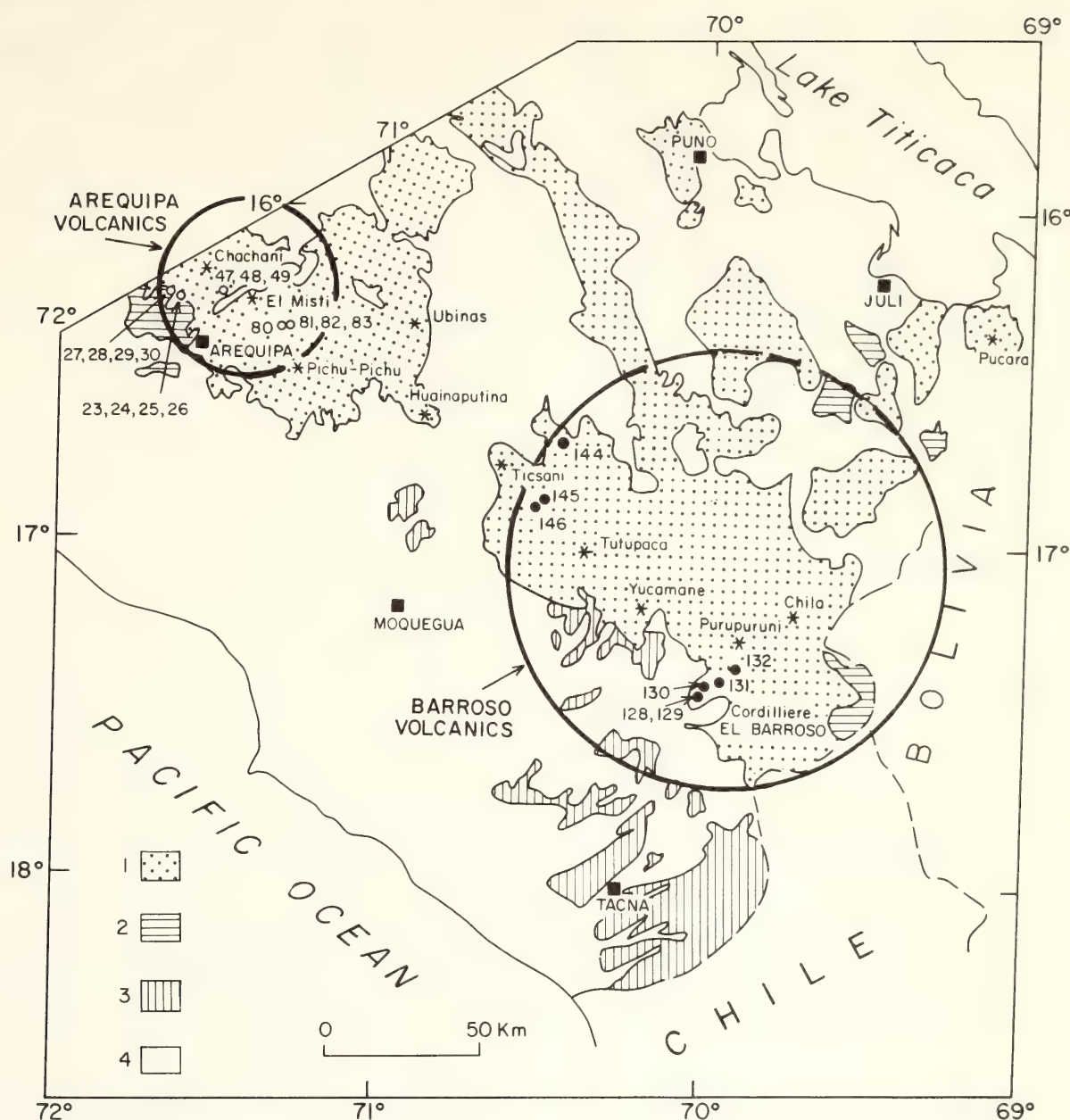


Fig. 72. Geologic sketch map showing principal late Cenozoic volcanic formations and sample localities: (1) Pliocene-Quaternary volcanic flows, mapped chiefly as belonging to the Barroso Group; (2) Pliocene-Quaternary rhyolitic ignimbrites of the Seneca formation; (3) Miocene-Pliocene rhyodacitic ignimbrites of the Huaylillas formation; (4) non-volcanic formations. Sample localities are indicated by closed circles for the Barroso volcanics and open circles for the Arequipa volcanics. Very approximate regional distributions of the Arequipa and Barroso units are delimited by circles. Asterisks mark sites of andesitic strato-volcanoes.

This conclusion is based chiefly on the large amounts of contaminant required and on the internal consistency of the isotopic variation within each of the two volcanic assemblages. Selective leaching of highly radiogenic phases from crystal rocks could greatly reduce the amount of contaminant required but could not plausibly account for the regionally independent internal consistency of the isotopic variation.

James *et al.* (1974) interpreted the Sr isotopic variation within the Arequipa and Barroso volcanics as due to either small-scale inhomogeneities in the mantle material at the source or disequilibrium melting of comparatively homogeneous source material. The latter process is usually described as melting of homogeneous mantle without isotopic equilibration between liquid and residual phases. Thus, as mineral phases with

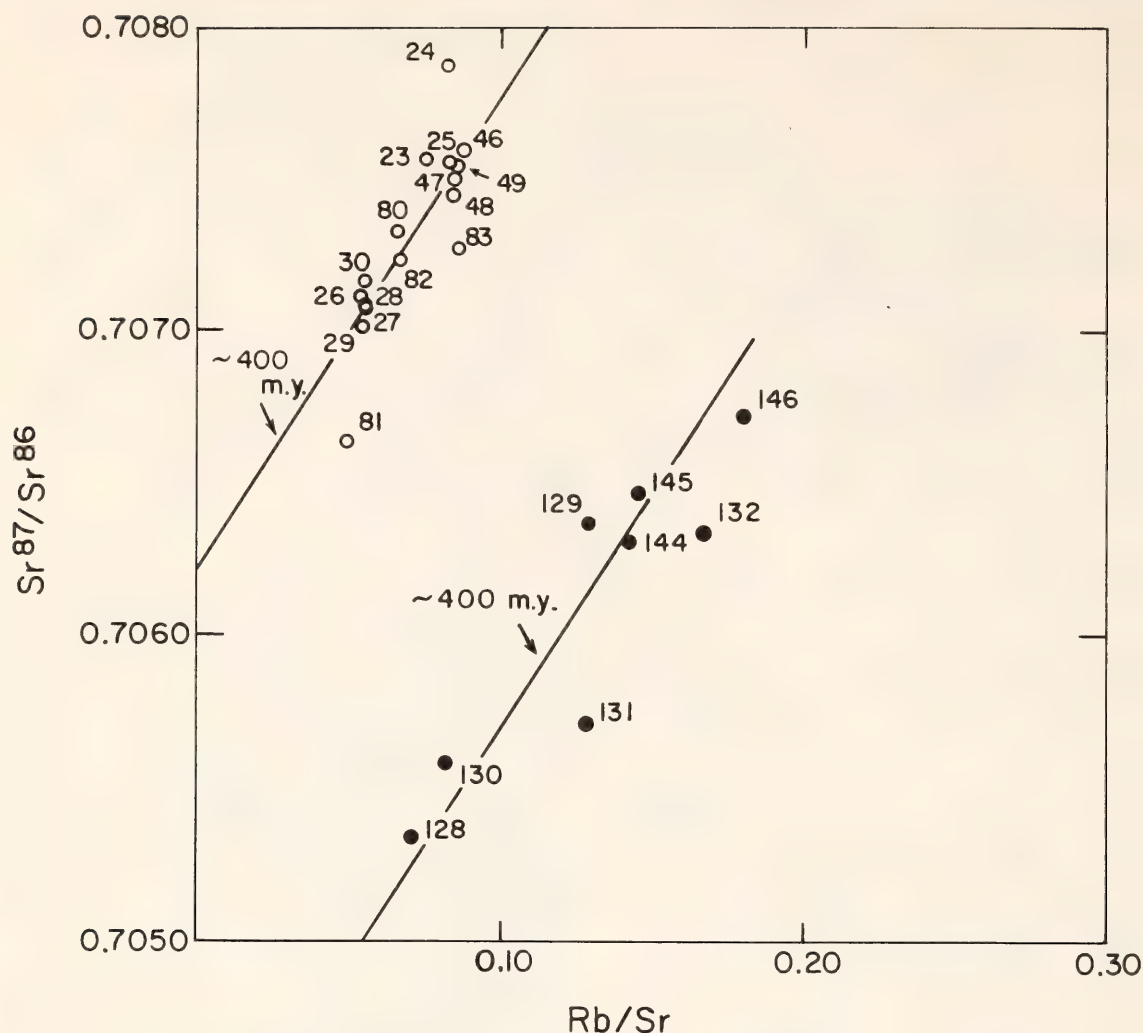


Fig. 73. Variation of $^{87}\text{Sr}/^{86}\text{Sr}$ vs. Rb/Sr for Arequipa and Barroso volcanics. Open circles denote Arequipa volcanics; closed circles, Barroso volcanics. Lines define 400 m.y. pseudo-isochrons through each group of samples.

greater or lesser abundances of Rb (and, hence, radiogenic Sr) enter the melt, the isotopic composition of the melt varies accordingly. A thorough discussion of disequilibrium melting models is given by Hofmann and Hart in this Report. James *et al.* (1974) hypothesized that the mantle source for the Arequipa and Barroso magmas is the continental lithosphere immediately overlying the descending oceanic plate and situated at a depth of 150 to 175 km. By this hypothesis, the isotopic differences between the Arequipa and Barroso volcanics are the result of gross inhomogeneity in the continental lithosphere at the site of magma generation. The isotopic discontinuity between the two volcanic units cannot be explained by normal disequilibrium melting. A disequilibrium melting model

can be applied only to explain the internal isotopic variation within each of the two volcanic assemblages.

Concepts and Assumptions

Numerous papers have been published recently on disequilibrium melting (see Hofmann and Hart in a companion report for a review of the literature and a complete list of references). The notion is both novel and attractive, albeit entirely unsubstantiated by laboratory experiments. The deficiencies of proposed disequilibrium melting models as applied to oceanic basalts are detailed by Hofmann and Hart and appear highly formidable. Nonetheless, if the Andean magmas are derived from solid continental lithosphere, the total absence of incipient melt prior to actual magma

formation should help significantly in maintaining long-term isotopic disequilibrium between phases. Data by Hofmann (this Report) support this assertion in that solid diffusion rates are found to be several orders of magnitude lower than those of partially molten rocks. I am encouraged, therefore, to apply the concepts of disequilibrium melting to an explanation of the 400 m.y. pseudoisochrons exhibited by young Andean volcanic rocks.

The virtual absence of ground rules on disequilibrium melting creates an immediate difficulty. It does seem clear, however, that advocacy of disequilibrium melting implies that at least certain trace elements are held selectively within single phases and that those trace elements enter the melt according to the degree to which their host phases participate in the melting process. Accordingly, and to limit an otherwise limitless range of combinations and permutations, I make the following assumptions:

1. All K and Rb in the mantle are contained in a single minor phase, phlogopite, for depths of 100 to 200 km (see Beswick, 1975). Radiogenic ^{87}Sr , produced by decay of ^{87}Rb in the phlogopite, is assumed bound to the phlogopite until the time of melting. By this assumption, excess ^{87}Sr in a melt is phlogopite controlled.

2. All additional Sr is contained in clinopyroxene at mantle depths greater than 100 km, where both plagioclase and hornblende are unstable.

3. The composition of the mantle from which the magma is derived is that of pyrolite or undepleted lherzolite (see Ringwood, 1966; Shimizu, 1973; Shimizu and Boyd, 1973) with $\text{K} \sim 0.1\%$ and $\text{K/Rb} \sim 200\text{--}300$. If all K is held in phlogopite, with 9.4% stoichiometric K, then phlogopite should constitute $\sim 1\%$ of the mantle. The actual K concentrations measured in phlogopite of ultramafic inclusions found in kimberlites and elsewhere average about 8% (Griffin and Murthy, 1969; Allsopp *et al.*,

1969). If this value is assumed and the amount of mantle phlogopite increased accordingly, the calculations summarized in this report will not be significantly altered.

Within the framework of these assumptions, I address the question of whether or not the observed variation in strontium isotope ratios can be produced by phlogopite-controlled disequilibrium melting of an appropriate mantle source. The objective is to compare calculated estimates of Sr isotope variation based upon the degree of partial melting of phlogopite with observed variations in the lavas exposed at the surface.

Model Calculations

Beswick (1975) lays the foundation for the calculations that follow and the reader is referred to his paper for details. His principal arguments may be summarized as follows:

1. If K is held in the mantle as a stoichiometric component of phlogopite, the K concentration in a given melt will be controlled solely by the degree to which phlogopite melts relative to other phases involved in the production of melt.

2. The K and Rb content of the melt can be equated with the mole fraction of phlogopite component in the melt if the distribution coefficient is known.

Beswick takes the distribution coefficient to be 3. Given this, the liquid fraction of phlogopite produced for a melt with a known concentration of K and known K/Rb ratio is given by

$$l = \frac{X_P^{\text{Rb}}/X_L^{\text{Rb}} + 2X_P^{\text{Rb}} - 3}{-2}$$

where X_P^{Rb} and X_L^{Rb} are the mole fractions of Rb in phlogopite (P) and liquid (L), respectively.

The total degree of melting at the source is obtained by multiplying the fraction of phlogopite liquid by that factor necessary to achieve the appropriate dilution of K in the final melt.

⁸⁷Sr/⁸⁶Sr enrichment. Initial ⁸⁷Sr/⁸⁶Sr ratios of the Arequipa and Barroso volcanics based upon a 400 m.y. pseudo-isochron are 0.7061 and 0.7044, respectively. Irrespective of the amount of disequilibrium melting and assuming all Rb is contained in phlogopite, the initial ratios must reflect the bulk Sr isotopic composition of the source region exclusive of phlogopite. Thus, in the discussion that follows, the ⁸⁷Sr/⁸⁶Sr ratios of all mineral phases except phlogopite are assumed equal to the initial ratio and all excess ⁸⁷Sr is assumed to come from phlogopite.

Pertinent analytical data on the Arequipa and Barroso volcanic rocks are summarized in Table 11, part A. The K contents and K/Rb ratios of these rocks (shown plotted in Fig. 74) are represented as two end-point pairs for each of the two volcanic assemblages. The end-point values are used to calculate the fractions of phlogopite melt and total melt given in Table 11, part B.

To calculate the amount of ⁸⁷Sr enrichment due to the melting of phlogopite, I assign a Rb-Sr age of 400 m.y. to the phlogopite and assume a present-day Rb/Sr ratio of 13.9 (Griffin and Murthy, 1969). (The choice of a particular Rb/Sr ratio does not affect the calculations because the ⁸⁷Sr/⁸⁶Sr ratio varies as a linear function of the Rb/Sr ratio. Thus phlogopite with greater or less Sr concentrations will have proportionately lower or higher present-day ⁸⁷Sr/⁸⁶Sr

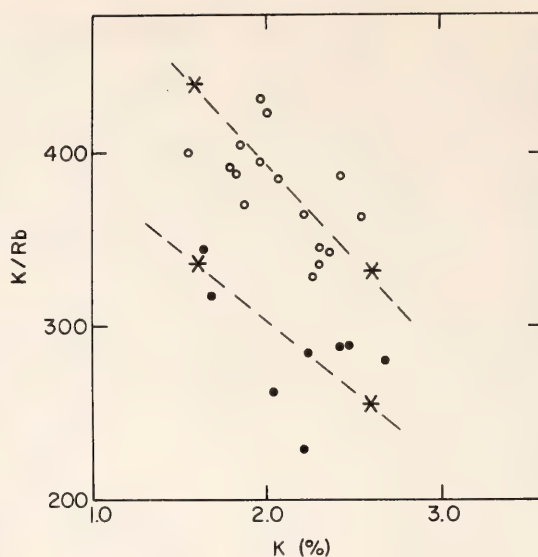


Fig. 74. Variation of K/Rb versus K for Arequipa and Barroso volcanics. Open circles denote Arequipa volcanics; closed circles, Barroso volcanics. Asterisks denote end-points used for calculations summarized in Table 11.

ratios.) Taking $1.39 \times 10^{-11}/\text{yr}$ to be the decay rate of ⁸⁷Rb and assuming an initial ⁸⁷Sr/⁸⁶Sr ratio of 0.706, the present-day ⁸⁷Sr/⁸⁶Sr ratio in the phlogopite will be 0.925.

Calculated values for ⁸⁷Sr/⁸⁶Sr based upon the assumptions already outlined are summarized in Table 11, part B. The ratios are obtained by assuming simple mixing between melted phlogopite and the remaining component of the melt and taking the bulk Sr concentration of the melt to be equal to the measured Sr concentrations given in Table 11, part A.

The first column of ⁸⁷Sr/⁸⁶Sr values is calculated assuming that *all* phlogopite-

TABLE 11A. Summary of K-Rb-Sr Analytical Data for Late Cenozoic Volcanic Rocks of the Central Andes*

	K (%)	Rb (ppm)	K/Rb	Sr (ppm)	⁸⁷ Sr/ ⁸⁶ Sr	(⁸⁷ Sr/ ⁸⁶ Sr) initial
Arequipa Volcanics						
a.	1.6	37	438	850	0.7071	0.7061
b.	2.6	75	348	760	0.7077	
Barroso Volcanics						
c.	1.6	48	336	680	0.7055	0.7044
d.	2.6	102	255	525	0.7067	

* a, b, c, and d are the end-members of the Arequipa and Barroso volcanics.

TABLE 11B. Compilation of Disequilibrium Melting Model Calculations for Late Cenozoic Volcanic Rocks of the Central Andes*

	Total melt (%)	Phlogopite melt (%)	$^{87}\text{Sr}/^{86}\text{Sr}\dagger$	$^{87}\text{Sr}/^{86}\text{Sr}\ddagger$	Sr _{cpx} (ppm)
Source I: Mantle = 1% phlogopite with K/Rb = 300					
a.	4.5	0.77	0.7070	0.7069	373
b.	3.3	0.92	0.7076	0.7075	258
c.	5.5	0.94	0.7055	0.7054	355
d.					
	cannot be obtained from source with K/Rb >255				...
Source II: Mantle = 1% phlogopite with K/Rb = 250					
a.	3.7	0.62	0.7073	0.7069	317
b.	2.9	0.80	0.7078	0.7075	233
c.	4.9	0.83	0.7056	0.7054	321
d.	3.6	0.99	0.7065	0.7065	191
Source III. Mantle = 1% phlogopite with K/Rb = 200					
a.	2.4	0.40	0.7080	0.7069	226
b.	2.3	0.63	0.7083	0.7075	195
c.	3.9	0.66	0.7059	0.7054	265
d.	3.1	0.86	0.7068	0.7065	170

* Assuming K_{phlog.} = 9.4%; (⁸⁷Sr/⁸⁶Sr)_{phlog.} = 0.925; (Rb/Sr)_{phlog.} = 13.9; and Sr_{phlog.} = 18 ppm (Griffin and Murthy, 1969). *a*, *b*, *c*, and *d* are the end-members of the Arequipa and Barroso volcanics.

† Ratios calculated assuming *all* phlogopite-held Sr enters the melt.
‡ Ratios calculated assuming phlogopite-held Sr enters the melt in proportion to the fraction of phlogopite melted.

held Sr enters the melt. This is roughly equivalent to assuming an extremely low Sr distribution coefficient between crystal and melt for phlogopite. For the Arequipa volcanics in this instance, the best agreement between observed and calculated ⁸⁷Sr/⁸⁶Sr ratios is obtained for source I (K/Rb = 300). For the Barroso volcanics, the best agreement is obtained for source II (K/Rb = 250).
The second column of ⁸⁷Sr/⁸⁶Sr values is calculated assuming that phlogopite-held Sr enters the melt in proportion to the amount of phlogopite melted. In this case, the calculated ⁸⁷Sr/⁸⁶Sr does not vary with K/Rb ratio and thus provides no constraint on the K/Rb of the source.
In both sets of calculations the agreement with observed ⁸⁷Sr/⁸⁶Sr ratios is good, but the agreement is somewhat better for that case when all phlogopite-held Sr enters the melt. In all instances there appears to be a rather small degree of partial melting, typically 3.5% to 5%. This may be near the lower limit

of melt fraction necessary for magma segregation.
The calculated ⁸⁷Sr/⁸⁶Sr ratios cannot be made to correspond more closely to the observed values by changing the assumption of a 400 m.y. age for the phlogopite. An assumed age of more than 400 m.y. will result in calculated ⁸⁷Sr/⁸⁶Sr ratios being too high; a lower age will further compress the already too small interval between calculated end-member isotopic ratios.
Sr variation. Both the Arequipa and Barroso volcanics exhibit high Sr concentrations, much higher than can be obtained by melting of pyrolite or undepleted lherzolite. The latter typically contains 10–15% clinopyroxene with 100 to 120 ppm of Sr (Shimizu, 1973). It seems necessary to postulate, therefore, that the Sr concentrations in the clinopyroxene of the source region are higher than those measured for clinopyroxene from lherzolite.
The requisite Sr concentrations of the

clinopyroxene can be calculated by the amount of clinopyroxene in the mantle, the fraction of total melt, and the distribution coefficient for Sr between solid and melt. For simplicity it is assumed that phases melt in proportion to the proportion in which they are present. Given 12% clinopyroxene in the mantle and a distribution coefficient, $K = 0.067$, the strontium concentration of clinopyroxene is given by:

$$C_{\text{cpx}} = C_{\text{melt}} (F + (x - f) K^{\text{cpx}}) / x$$

where C_{cpx} and C_{melt} are the concentrations in the clinopyroxene and melt, respectively; F is the fraction of melt; x is the fraction of clinopyroxene originally present; f is the fraction of clinopyroxene entering the melt, and K^{cpx} is the distribution coefficient.

The results of the calculations summarized in Table 11, part B, show the Sr concentrations to be about twice as high as those normally measured in clinopyroxenes of undepleted lherzolites. This conclusion is not significantly altered by assuming larger relative fractions of clinopyroxene entering the melt.

Summary of Conclusions

The pseudoisochrons observed in young andesitic-dacitic volcanic rocks of the central Andean arc can be explained by postulating disequilibrium melting of a 400 m.y. mantle source containing about 1% phlogopite. This conclusion, if correct, implies that excess radiogenic ^{87}Sr produced in phlogopite has not migrated from the lattice over the past 400 m.y. period. This seems possible only if the rock in which the phlogopite occurs has remained solid during that period of time (Hofmann and Hart, this Report). This requirement is consistent with the model presented by James *et al.* (1974) in which the Arequipa and Barroso magmas were derived from ancient continental lithosphere.

References

- Allsopp, H. L., L. O. Nicolaysen, and P. Hahn-Weinheimer, Rb/K ratios and Sr-isotopic compositions of minerals in eclogitic and peridotitic rocks, *Earth Planet. Sci. Lett.*, **5**, 231, 1969.
- Beswick, A. E., K and Rb relations in basalt and other mantle derived materials: Is phlogopite the key?, submitted to *Geochim. Cosmochim. Acta.*, 1975.
- Griffin, W. L., and V. Rama Murthy, Distribution of K, Rb, Sr, and Ba in some minerals relevant to basalt genesis, *Geochim. Cosmochim. Acta*, **33**, 1389, 1969.
- James, D. E., C. Brooks, and A. Cuyubamba, Andean Cenozoic volcanism: Magma genesis in the light of Sr-isotopic composition and trace element geochemistry, in *Carnegie Inst. Wash. Year Book 73*, p. 983, 1974.
- Ringwood, A. E., The chemical composition and origin of the earth, in *Advances in Earth Science*, P. M. Hurley, ed., p. 287, MIT Press, Cambridge, 1966.
- Shimizu, N., Geochemistry of ultramafic inclusions from Salt Lake Crater, Hawaii, in *Carnegie Inst. Wash. Year Book 72*, p. 262, 1973.
- Shimizu, N., and F. R. Boyd, Trace element contents of clinopyroxenes from garnet lherzolites in kimberlites, in *Carnegie Inst. Wash. Year Book 72*, p. 272, 1973.

ANOMALOUS ISLAND ARC ASTHENOSPHERE AND CONTINENTAL GROWTH

I. Selwyn Sacks

Introduction

Lithospheric plate motions are influenced by the rigidities and viscosities of those parts of the earth involved in the tectonic process, especially the crust and upper mantle. Viscosity in this region is difficult to determine directly but may be estimated from the anelasticity (Q^{-1}) by means of empirical relationships.

Anelasticity studies have shown that there are large regional variations in the thickness of the high-viscosity lithosphere. For example, the lithosphere beneath South America is more than 300 km thick, that beneath Japan only 70 km thick. The study described here may explain how new lithosphere is generated during the subduction process.

The anelasticity structure in island arc regions is shown in Fig. 75 (Sacks and Okada, 1974). The details of the structure in Fig. 75 are represented quantitatively by appropriate values of Q . It is known from observation that earthquakes occur only in high- Q regions. In the study by Sacks and Okada (1974), the shallower part of the asthenosphere to a depth of about 250 km

was modeled as laterally homogeneous with a Q_p of 400 (see Fig. 75). It was observed, however, that seismic rays which spent significant time near the apex of the wedge formed by the horizontal and subducting lithospheres (A in Fig. 75), had a higher apparent Q than predicted by this model. The study reported here was undertaken to determine the Q structure of this anomalous region in some detail, and to investigate the effect of this structure on the stress state of the subducting lithosphere. A model is presented for the evolution of continental lithosphere based upon the revised Q structure.

Data. The data analyzed in this study came from the large dynamic range, wide frequency band tape recording seismo-

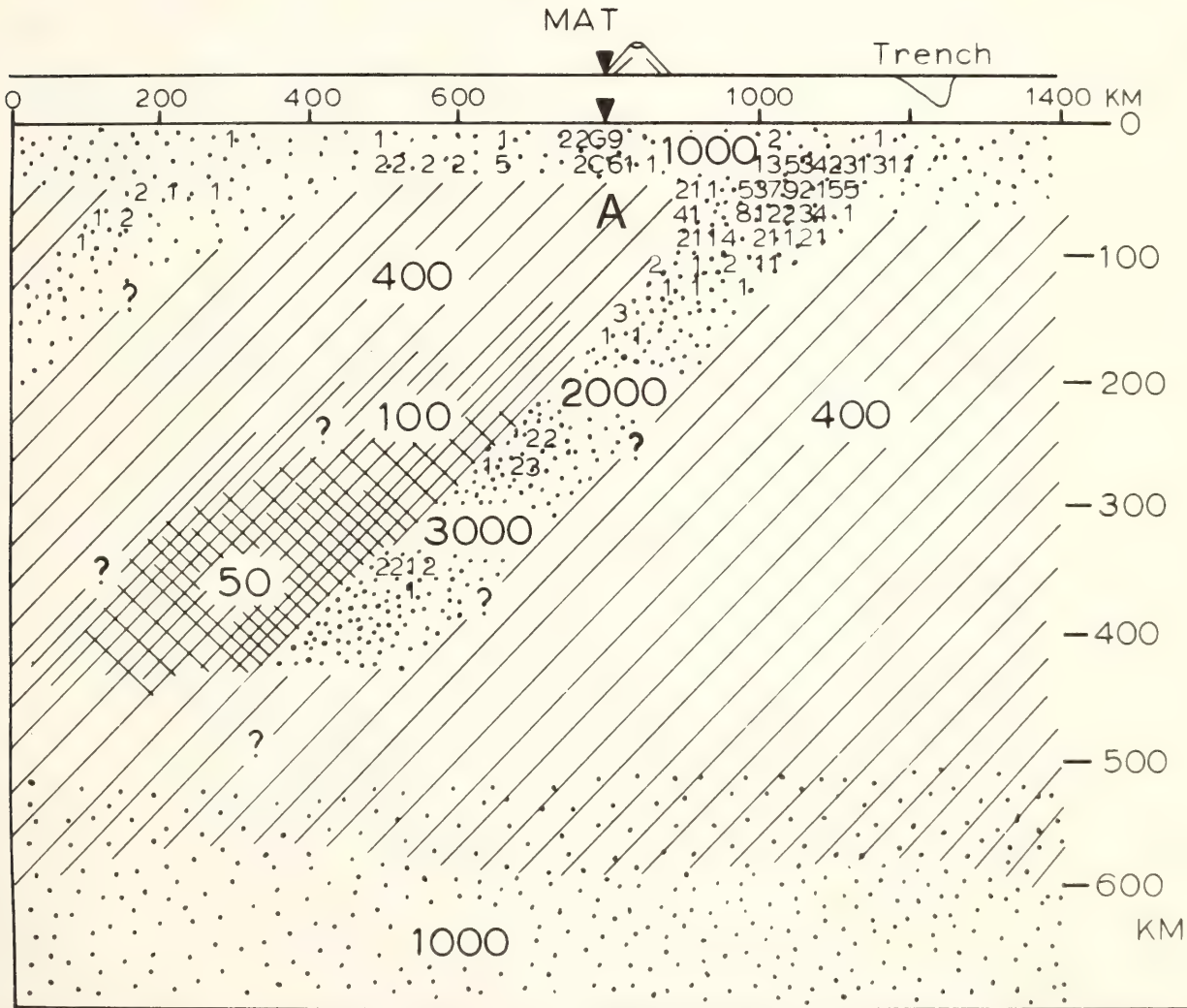


Fig. 75. Q_p beneath Japan determined by Sacks and Okada (1974). Dots indicate regions of high Q (1000–3000); slanted lines, intermediate Q (200–500); and hatching, low Q (50–100). It was observed that ray paths through region A had higher Q than predicted.

graphs (Sacks, 1966) operating near the Pacific coast of Hokkaido (KMU) and in central Honshu (MAT), Japan. The KMU instrument is located near the trench, and the MAT seismograph is near the volcanic front (see Fig. 79). The wide frequency range of the seismographs used (1/20 to 10 Hz) facilitated accurate determination of the spectral stops of the seismic arrivals. Spectral ratio techniques used here are independent of the earthquake's radiated spectrum (Sacks, 1968).

Q in the anomalous region. In general, seismic rays from an earthquake to a seismograph will traverse not only the region of interest (the near-trench section of the asthenosphere) but also other regions which will affect the spectrum of the seismic arrival. The Q values of a particular region are calculated from the overall, or apparent, Q value of the total path using the following identity:

$$T/Q = \sum_{i=1}^n t_i/q_i$$

where T is the total seismic travel time; Q is the apparent Q value for the total path; t_i is the travel time through the i th section of the path, e.g., through the asthenosphere; q_i is the apparent Q value of the i th section; and n is the number of sections considered.

Since all seismic waves have to traverse the lithosphere beneath Japan, the Q value and thickness of this region first had to be determined. The technique used is illustrated in Fig. 76. Seismograms recorded at MAT from earthquakes occurring in the subducting plate at depths ranging from 18 to 300 km were analyzed. The apparent Q values for these various paths were determined. For ray paths entirely within the (continental) lithosphere, Q values of about 1000 were obtained, nearly independent of the depth of the earthquake. However, for earthquakes at greater depths with ray paths lying partly in the asthenosphere, the apparent Q was significantly lower. Because the velocities in the asthenosphere are slightly lower

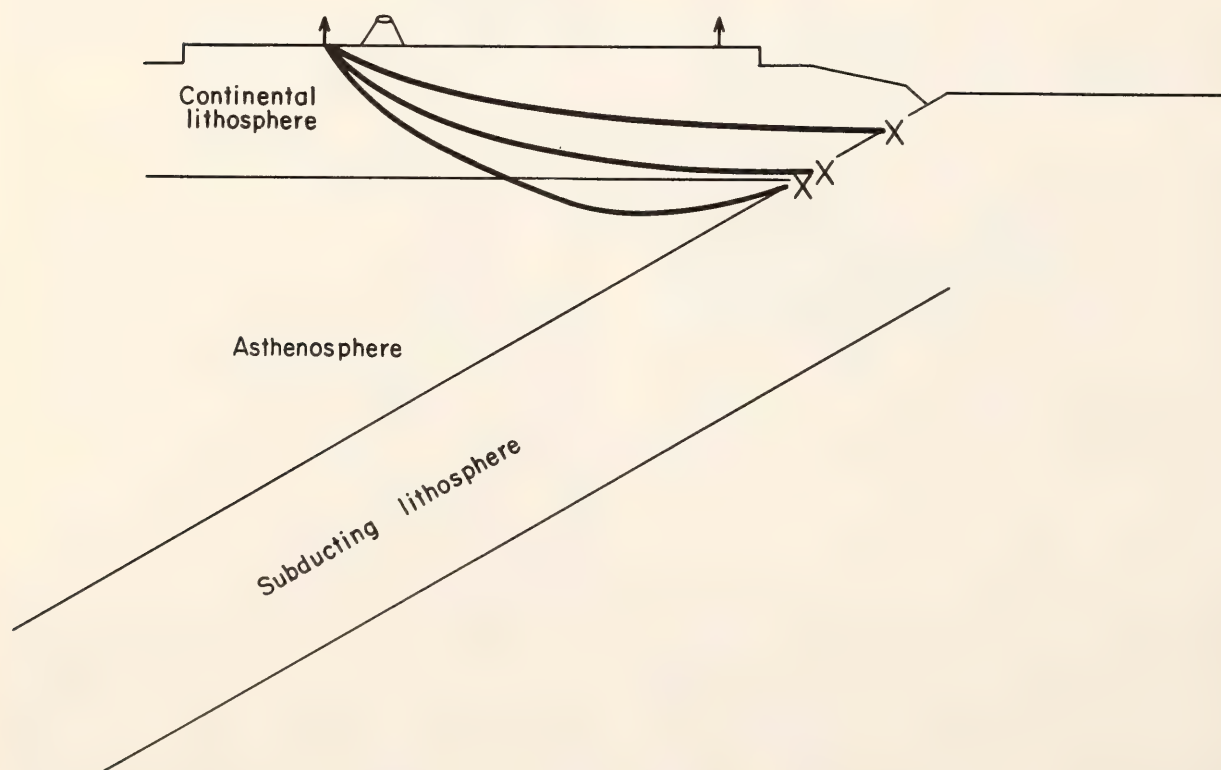


Fig. 76. Schematic of subduction zone showing ray paths studied to determine Q of the lithosphere. Crosses indicate earthquakes. There is a significant difference in the apparent Q between the two lower paths.

than those in the overlying lithosphere, ray paths tend to plunge fairly deeply into the asthenosphere once they enter it. Thus a substantial part of the path is in the lower Q medium even if the earthquake depth is only slightly greater than the thickness of the continental lithosphere (see Fig. 76). It was found that for earthquake depths less than 60 km the Q values were lithospheric, i.e., about 1000; but at depths greater than 77 km the apparent Q of the path had dropped significantly. The results from two earthquakes straddling the base of the lithosphere are given in Table 12. It can be seen that the earthquakes have similar epicenters (only the depth being dif-

ferent), and are of similar magnitude so that the same suite of seismograph stations would be used for the hypocenter location, assuring that their relative location is likely to be accurate. Based on results from these two earthquakes, the thickness of continental lithosphere was found to be 70 km, and it was found to have a Q value of 1000.

The Q structure of the asthenosphere was determined by studying the ray paths shown in Fig. 77. The apparent Q measurements for the paths shown in Fig. 77 are given in Table 13. Figure 78 illustrates the anelasticity structure found for the upper 280 km of the asthenosphere. The wedge-shaped section

TABLE 12. Hypocentral Data, Travel Times, and Anelasticity Results for Earthquakes Just Above and Below the Base of the Continental Lithosphere

Date	Distance	Azimuth	<i>P</i> time (sec)	<i>S</i> time (sec)	Depth (km)	<i>Q</i> _{<i>p</i>} apt
25 May 1969	1.74°	301°	29	50.2	60	1190
25 April 1971	1.80°	303°	29.6	50.4	77	315

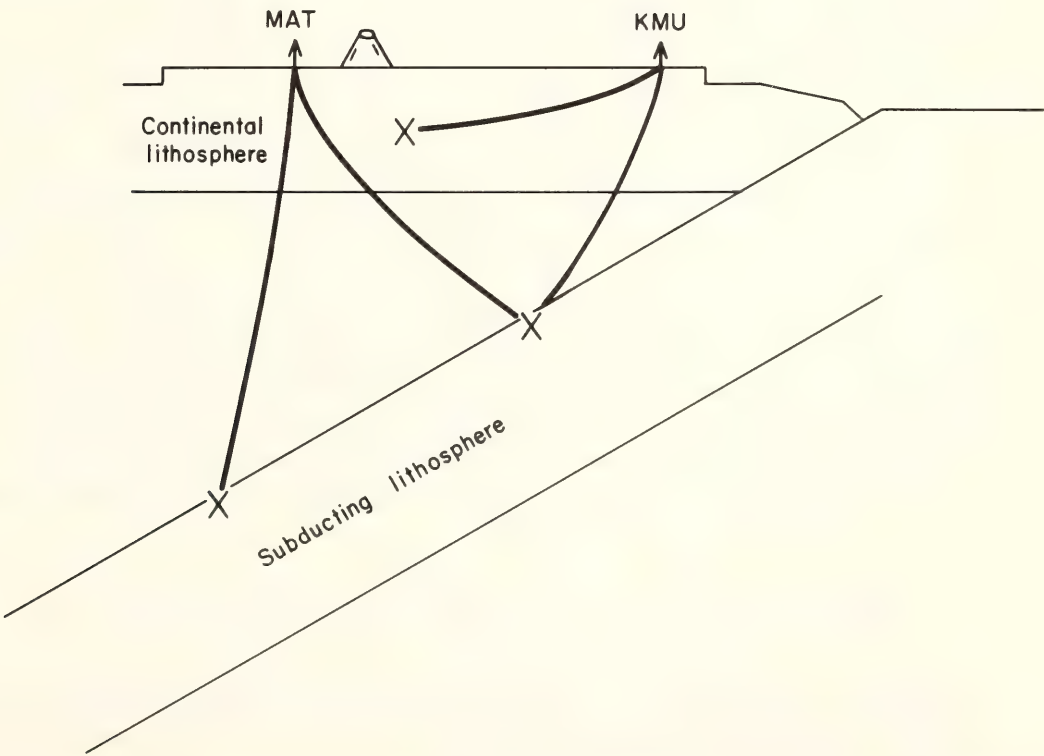


Fig. 77. Ray paths studied to determine Q structure of the asthenosphere. Crosses indicate earthquakes. The two paths from the shallower earthquake in the subducting plate gave higher Q to KMU than to MAT (after correcting for the effects of continental lithosphere). The deep event gave the same Q value to MAT as the shallower event did.

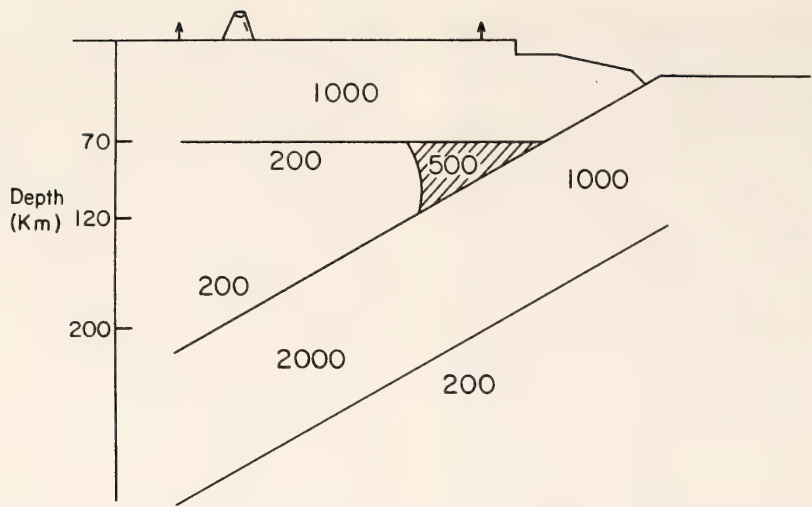


Fig. 78. Q model for the Japan region. The hatched region has an anomalously high Q for asthenosphere, $Q_p = 500$. Normal oceanic asthenosphere has $Q_p = 200$. In an earlier study, before the existence of the anomalous region was recognized, Sacks and Okada (1974) suggested a value of 400 for a homogeneous asthenosphere.

of asthenosphere bounded above by the continental lithosphere and below by the subducting lithosphere to a depth of about 110–120 km has a Q_p of about 500. The asthenosphere to the west of this wedge, to a depth of 300 km (the limit of this study), has a Q_p value of 200. The $Q = 200$ region appears to be fairly homogeneous, both laterally and vertically. The ray paths used for determining Q of the asthenosphere are shown in Fig. 76. Table 13 shows the Q calculated for the asthenosphere at various depths. Even for the shallowest earthquake still below the continental lithosphere, 77 km, a Q_p value of 190 was found. This value is less reliable than those from the deeper earthquakes, since the proportion of the total travel time spent in the asthenosphere is sensitive to the velocity structure, which is not well known.

It is important to know which of these two regions in the asthenosphere beneath Japan is most similar to the asthenosphere under the ocean. In an earlier study, Sacks and Okada (1974) compared the spectra observed at KMU and MAT from a distant deep earthquake (Fiji). The Q of the asthenospheric wedge beneath MAT is similar to that in the same depth range in the asthenosphere beneath the Japan trench, i.e., the $Q_p = 200$ region appears to be a typical sub-oceanic asthenosphere.

Seismicity. Higher Q values are commonly assumed to indicate higher viscosities and the presence of a high- Q zone sandwiched between the continental lithosphere and that of the descending plate should be detectable using other methods sensitive to the *state of stress* in the region. One obvious indicator of the state of stress is the seismicity.

TABLE 13. Asthenosphere Anelasticity Results for Paths Shown in Fig. 77

Station	Depth	Q_p Apparent	Q Asthenosphere
KMU	110	700	413
KMU	115	850	718
MAT	116	320	200
MAT	284		220

Figure 79 shows a map of the Japan region with the plans of the seismicity sections studied superimposed. Hypocenters determined from the Japan Meteorological Agency (JMA) network of seismographs (about 120 sites) were plotted for each section. Hypocenters determined from the JMA net are systematically displaced from those determined using teleseismic stations (Utsu, 1971). This effect presumably is related to high seismic velocities in the down-going plate. Nonetheless, because of the high density of local seismic stations, the relative hypocenter locations determined by the JMA network are reliable even if absolute locations are not. Figure

80 shows the earthquakes in one of the sections (10) under the continental region. It shows the normal pattern of island arc seismicity; i.e., in the subduction zone, some seismicity in the continental lithosphere, and an earthquake-free zone between these two regions. Figure 81 is a plot of the number of earthquakes occurring in the subduction zone as a function of depth of some continental sections. Most of the earthquakes occur in the zone of interaction between the subducting and continental lithospheres, i.e., in the upper 70 km or so, a value consistent with that determined by Q . The seismicity in the subducting plate below the continental

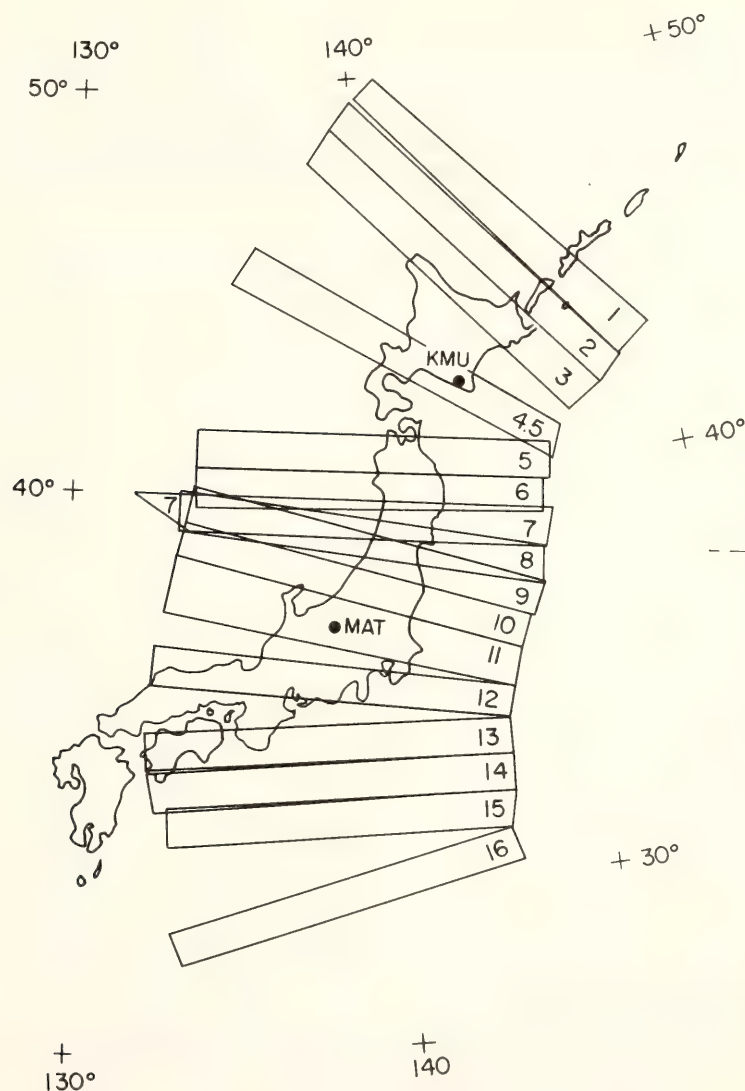


Fig. 79. Map of Japan showing plans of seismicity sections. The sections are normal to the ocean trenches. Sections 1, 2, 13, 14, 15, and 16 are considered oceanic; and sections 3, 4, 4.5, 5, 6, 7, 8, 9, 10, 11, and 12 are considered continental. The seismograph stations KMU and MAT are indicated.

lithosphere is generally much reduced. In this region the subducting plate is in contact with relatively low-viscosity asthenosphere. There appears to be a secondary region of high seismicity in the downgoing plate in the depth range 70–120 km. In this depth interval, the downgoing plate is adjacent to the anomalously high *Q* region of the asthenosphere. Seismicity sections outside the

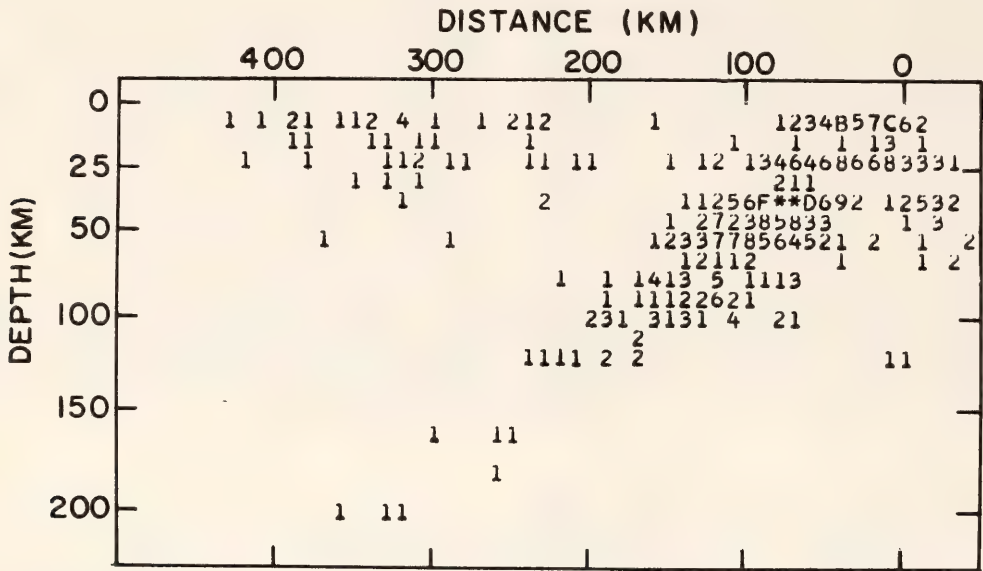


Fig. 80. Seismicity section 10, showing the dipping seismic plane, aseismic wedge, and earthquakes in the horizontal continental lithosphere. Only earthquakes in the upper 200 km are shown.

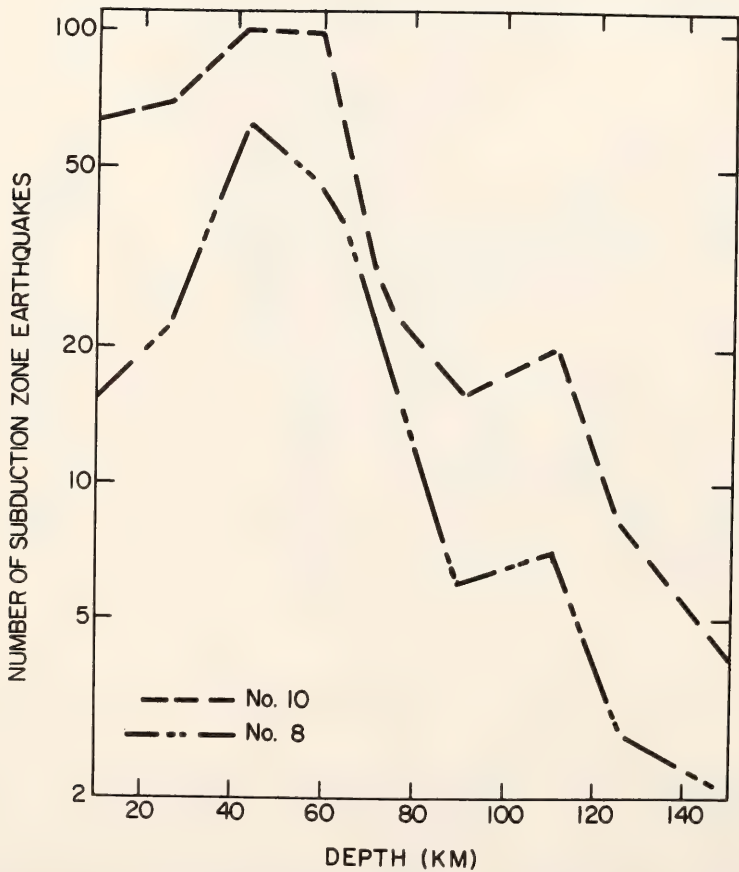


Fig. 81. Number of earthquakes in the subduction zone vs. depth for sections 8 and 10 (Fig. 78). The highest seismicity occurs in the upper 70 km where there is a lithosphere-lithosphere interaction, but there is a secondary peak in the 80–120 km depth range.

continental area, i.e., north of Hokkaido or in the Izu-Bonin arc, do not show this secondary zone of seismicity. Figure 82 compares the seismicity (in the subduction zone) beneath continental Japan with that of adjacent regions. The earthquake occurrence in these two regions is generally similar except in the depth range 80–120 km, in which there is significantly higher activity in the continental group.

Pressure axes. A further manifestation of the state of stress is the direction of the pressure axes of the force system causing the earthquakes. The pressure axes can be determined from observations of first-motion and shear-wave polarization from both local and teleseismic seismograms. Ichikawa (1971) studied the focal mechanisms of hundreds of earthquakes occurring in the Japan arcs. The nodal planes were picked by computer, which also assessed

the goodness of fit. Ichikawa's summary of the results is shown in Fig. 83. At depths where there is essentially a lithosphere-lithosphere interaction (less than 70 km), pressure axes are either horizontal or normal to the dipping plane. This holds true for all sections of the Japan arcs. It is found also that at depths greater than 120 km the pressure axes generally are in the direction of the dipping plane. However, beneath the continental areas, the pressure axis remains approximately horizontal and does not switch to the in-plate type of the deeper earthquake zone until a depth of about 120 km, which is well below the continental lithosphere.

Conclusions

There are indications from three independent techniques that there is a zone of asthenosphere with higher than nor-

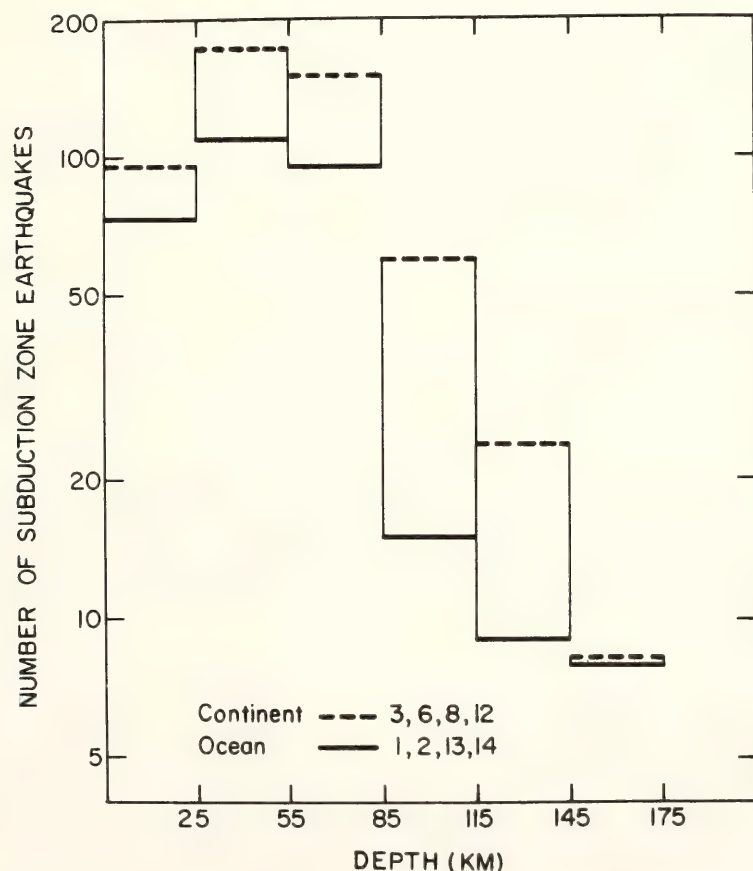


Fig. 82. Comparison of the number of earthquakes in the subduction zone beneath the continental areas 3, 6, 8, 12 (Fig. 78) and beneath oceanic areas adjacent to the continent, 1, 2, 13, 14 (Fig. 78). The seismicity is generally similar except for the depth interval, 100–130 km, in which there are more earthquakes in the continental region.

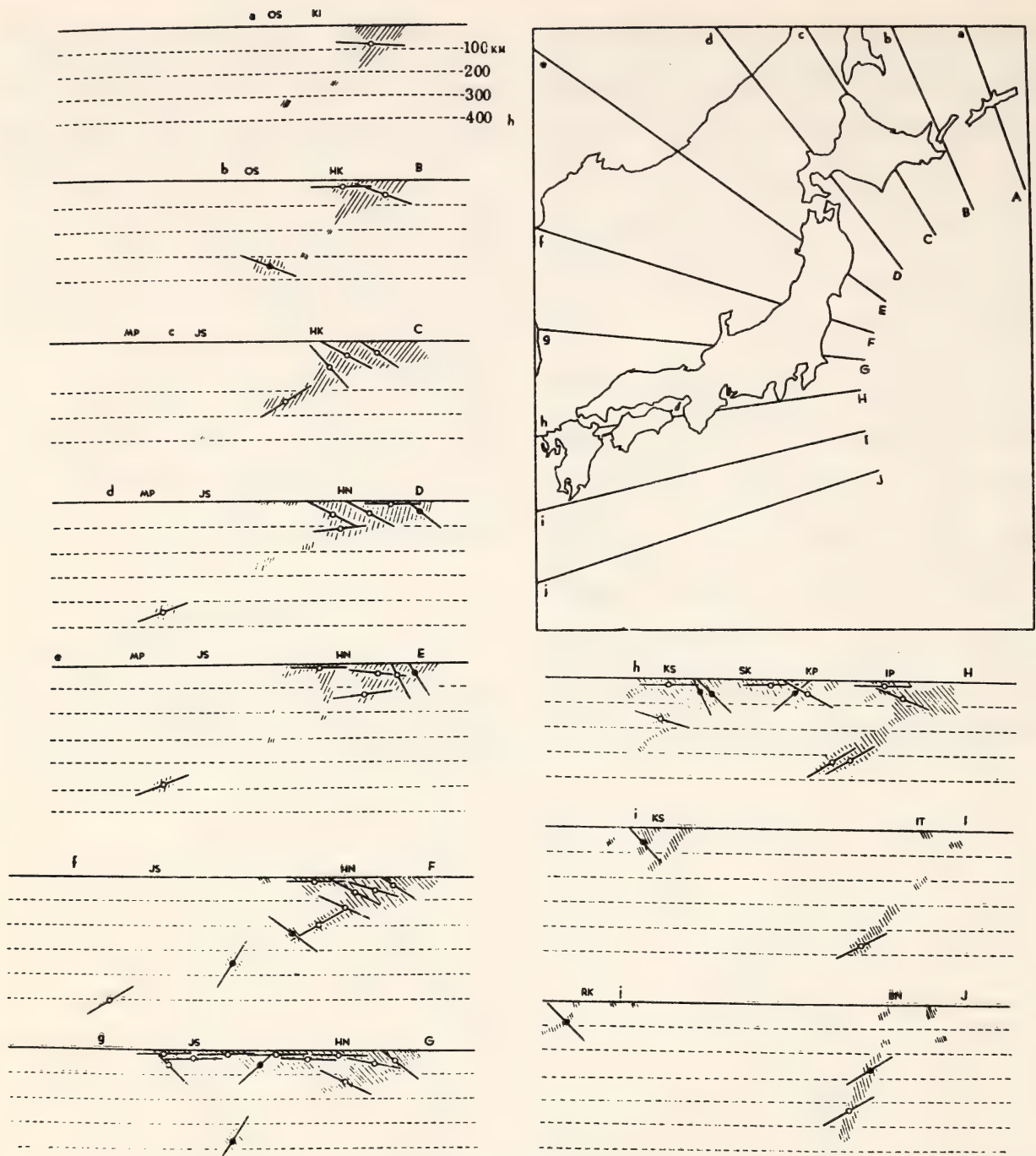


Fig. 83. Ichikawa's (1971) summary of the axes of maximum compression in the Japan arcs derived from focal mechanism studies. The subduction zone earthquakes at depths less than about 80 km all have pressure axes which are horizontal or normal to the dipping seismic plane. In the continental sections, *C*, *D*, *E*, *F*, *G*, this same pressure axis direction persists to a depth of about 120 km. Below this depth, the pressure axes lie in the seismic plane.

mal rigidity below the continental lithosphere near the trench. This zone appears to exist beneath continental-type regions only (based on seismicity considerations), and may not occur in ocean-ocean type arcs such as Izu-Bonin.

The higher *Q* and higher rigidity of the anomalous region of asthenosphere

may be due to a smaller degree of partial melting and hence lower temperatures than in normal asthenosphere. We conjecture that the cold subducting plate freezes out asthenosphere at the apex of the wedge (nearest the trench) where the circulation of asthenosphere material would be restricted. An evolutionary model for this process is shown in Fig.

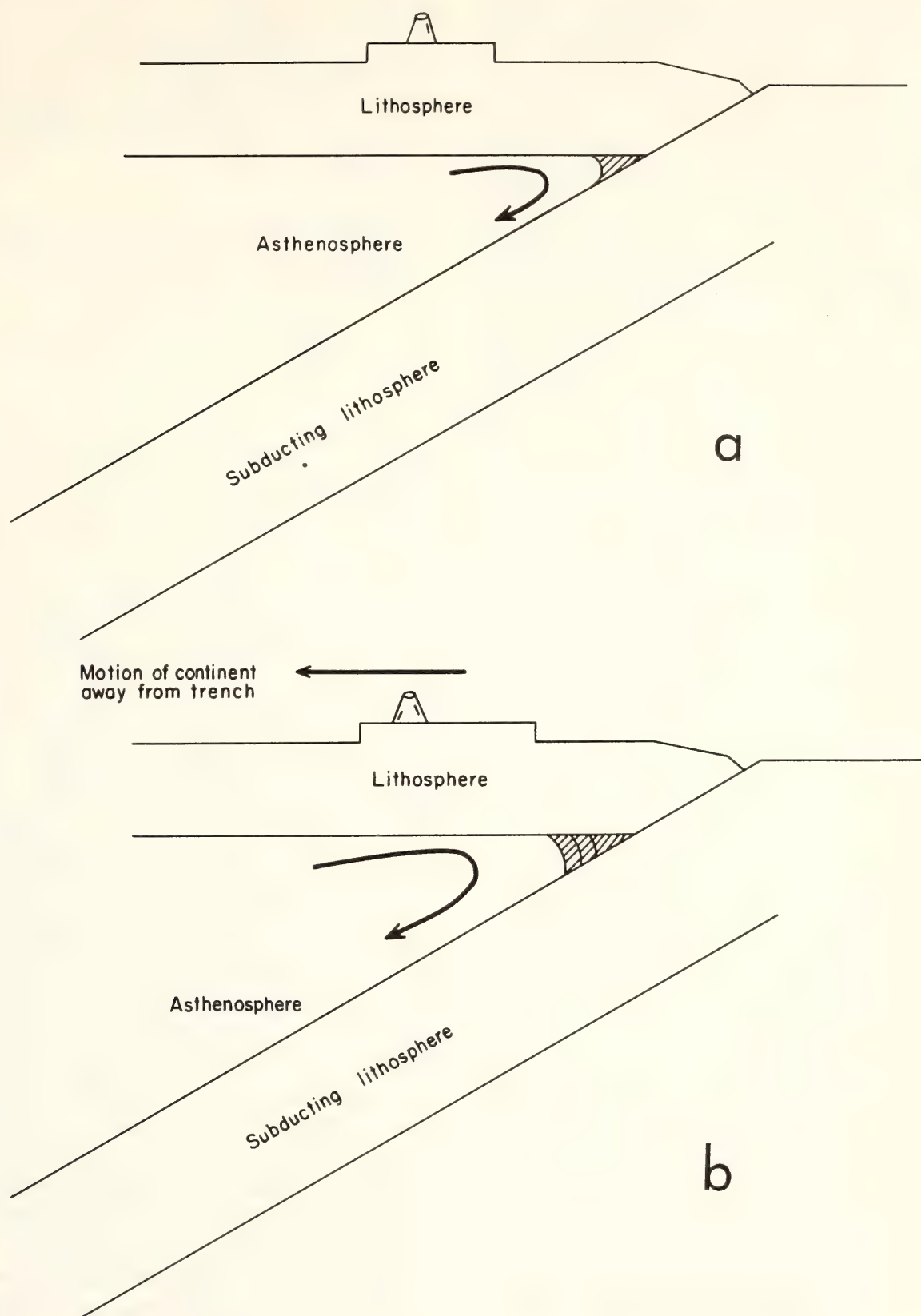


Fig. 84. Evolutionary model for a thick lithosphere under continents. The subducting plate is cold relative to the asthenosphere and freezes out a small segment, shown shaded (*a*). This segment will be eroded at that face (unbounded by lithosphere) by circulation of the adjacent (partially molten) asthenosphere. If there is any motion of the continental plate away from the trench, the higher rigidity wedge (shaded, *b*) will grow.

84. In the absence of motion other than subduction, a small wedge will be frozen out of the asthenosphere but will not grow because the side away from the trench will be eroded by the circulating asthenosphere. If there is motion of the continental side away from the trench for any reason, this higher wedge will grow, resulting in a thickening of continental lithosphere. Supporting evidence for this motion comes from Proverbio and Quesada (1974), who used astronomical observations from international latitude stations to determine that Japan and Europe are approaching one another at a relative velocity of 1 cm/year. It is possible that a mechanism such as this can be invoked to explain the thick lithospheres under the continents (e.g., Sacks and Okada, 1974). In this model, subduction at continental borders will cause an increase in the volume of continental lithosphere. Over the span of earth history, the total volume of lithosphere added to the continents will likely be large.

References

- Ichikawa, M., Re-analysis of mechanisms of earthquakes which occurred in and near Japan and statistical studies on the nodal plane solutions obtained, 1926–1968, *Geophys. Mag.*, **35**, 207–274, 1971.
- Proverbio, E., and V. Quesada, Secular variations in latitudes and longitudes and continental drift, *J. Geophys. Res.*, **79**, 4941–4943, 1974.
- Sacks, I. S., 1966. A broad-band large dynamic range seismograph. In: J. S. Steinhart and T. J. Smith (Editors), *The Earth Beneath the Continents*. Geophys. Monogr. 10, A.G.U., Washington, D.C., p. 543.
- Sacks, I. S., *Q* for *P* waves in the mantle, in *Carnegie Inst. Wash. Year Book* **66**, pp. 28–31, 1968.
- Sacks, I. S., and H. Okada, A comparison of the anelasticity structure beneath western South America and Japan, *Phys. Earth Planet. Interiors*, **9**, 211–219, 1974.
- Utsu, T., Seismological evidence for anomalous structure of island arcs with special reference to the Japanese region, *Rev. Geophys. Space Phys.*, **9**, 839–890, 1971.

DETERMINATION OF THE SUBDUCTING LITHOSPHERE BOUNDARY BY USE OF CONVERTED PHASES

J. Arthur Snoke and I. Selwyn Sacks

Introduction

The most commonly used technique to determine the upper boundary of an underthrusting plate in subduction zones is to correlate that boundary with a dipping plane of seismicity. Such a seismic plane is often well defined in island arcs, such as Japan, but is not well defined in cordilleran arcs, such as western South America. In the past few years two independent techniques have been developed to define the dipping interfaces of descending slabs. These techniques give results in good agreement with those obtained using seismicity and can therefore be used to define dipping interfaces in regions where the seismicity is either sparse or scattered. One technique employs the *ScSp* phase (Okada, 1971, 1973, 1974), and the other uses a class of anomalous high-frequency shear arrivals that has been described previously (Snoke *et al.*, 1973, 1974a, 1974b, 1974c; Isacks and Barazangi, 1973). In this report the two techniques are described briefly, and comparison is made of both their assumptions and their potential as determinators for the location of the upper boundary of subducting plates.

ScSp. An observed longitudinal-wave precursor to the *ScS* phase at Japanese and western South American stations has been identified as an *ScSp* phase; that is, a *P* phase converted from an *ScS* phase at a dipping interface (Okada, 1971, 1973, 1974). All observations appear to be consistent with this apparently unique interpretation (see Fig. 85).

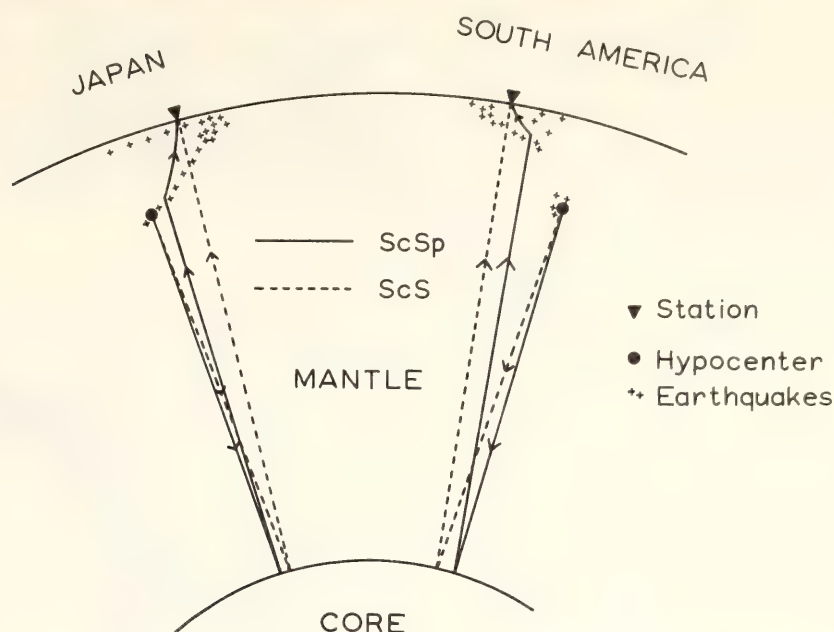


Fig. 85. A schematic model showing the paths of the *ScSp* phase (solid line) and the *ScS* phase (dashed line).

The phase is most clearly seen on short-period recordings of large, deep-focus earthquakes.

The time interval between the *ScS* and *ScSp* arrivals from an event produces a locus of possible *ScS*-to-*P* conversion points. The observed time difference, $\Delta T = T_{ScS} - T_{ScSp}$, is not sensitive to the details of the velocity contrast between the downgoing plate and the surrounding mantle. Within experimental error, ΔT is a constant for a given station. Amplitude studies by Okada (1973, 1975) indicate that the angle between the incident ray and the normal to the interface is near the critical angle.

Figures 86 and 87 show vertical seismicity cross sections taken perpendicular to the trench and passing through two stations at which *ScSp* has been observed, KMU in Hokkaido, Japan, and NNA in Peru, South America. Projections of surfaces on which $\Delta T = \text{constant}$ are drawn, and the projection corresponding to the observed ΔT is hatched. On each figure a circle shows the preferred conversion region predicted on the basis of amplitudes. In island arcs where a seismic plane is well defined (Fig. 85), the conversion region lies on or near that plane. Figure 87

shows a case where a seismic plane is not well defined. (See Okada, 1974, for further discussion.)

The part of the interface sampled is approximately on a line perpendicular to the trench and passing through the station. This follows from the fact that the *ScS* ray path is approximately along a radius vector of the earth ($\theta_s \sim 0$ in Fig. 88), and the scattering plane defined by an incident ray along a radius vector and the normal to the interface is the plane which intersects the interface along its maximum dip. To test the validity of this approximation we examine the ray path for the *ScSp* observed at NNA, Peru, from an earthquake on 5 March 1965. This event is atypical of those studied because of the large epicentral distance ($\Delta = 19.6^\circ$) and because α_1 , the angle between the back-azimuth and the horizontal projection of the maximum-dip direction (see Fig. 88), is about 80° (Fig. 89). The angle, α_2 , between the projected maximum-dip direction and the projection of the outgoing *P*, is given by

$$\sin \alpha_2 = \frac{v_P \sin \theta_s}{v_S \sin \theta_P} \sin \alpha_1 \quad (1)$$

where θ_s and θ_P are the angles with the

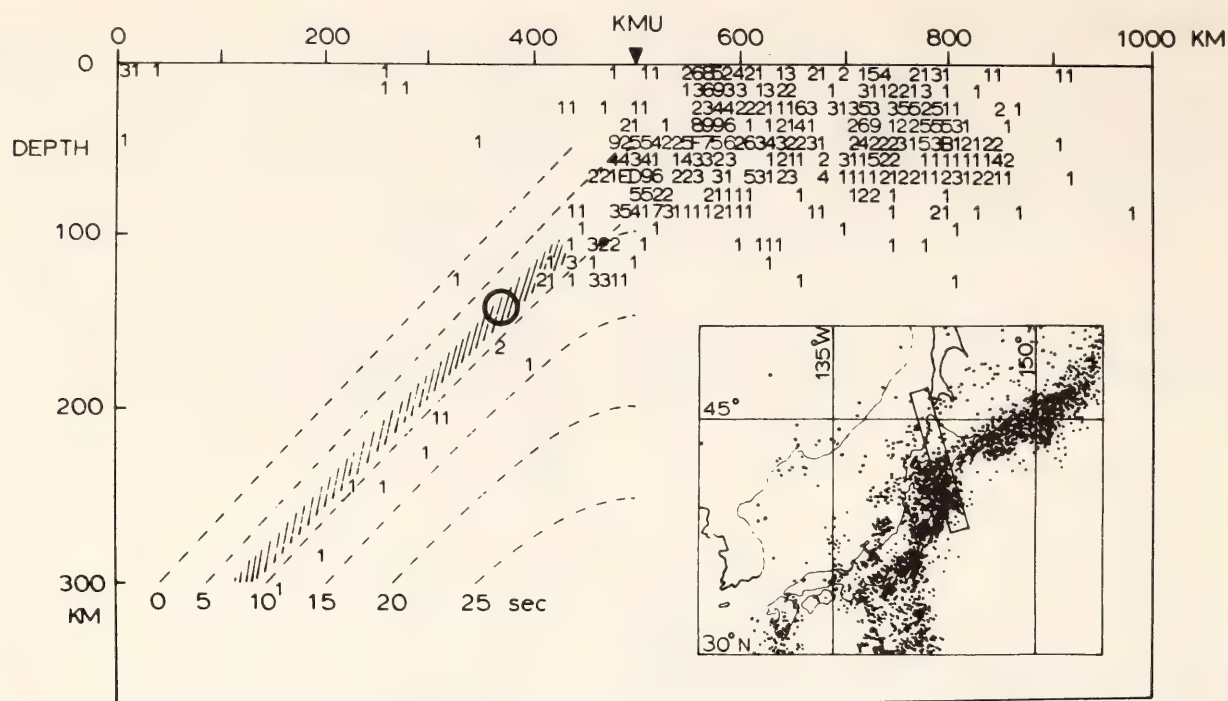


Fig. 86. Vertical cross section of the seismicity (U.S. Coast and Geodetic Survey and National Oceanographic and Atmospheric Administration, 1964–1971) for earthquakes inside the inset on the map. For the station KMU (Hokkaido, Japan) the ScS - $ScSp$ time using J - B travel times is indicated by the dashed lines, and the contour representing the observed time difference of eight seconds is hatched. The circle represents the preferred conversion region for ScS to $ScSp$ based on amplitude studies.

vertical of the incident S and the outgoing P , respectively (Fig. 88). For the 5 March 1965 event, θ_s is $\sim 8^\circ$. Taking $\alpha_1 \sim 80^\circ$, $\theta_P \sim 60^\circ$ (which is near grazing for a 30° dipping interface) and $v_P/v_S \sim 1.7$, we obtain a value for α_2 of $\sim 16^\circ$. Using the preferred conversion region (from Fig. 87), the approximate projected conversion region is at A in Fig. 89, and the projected region based on Equation 1 is at B . A and B are about 40 km apart. Hence, assuming that the interface is laterally homogeneous over such distances near the station, the approximation is a good one.

The anomalous high-frequency arrivals. Anomalous high-frequency arrivals have been observed at Peruvian and Chilean stations from deep-focus South American earthquakes (Isacks and Barazangi, 1973; Snoke *et al.*, 1973, 1974a, 1974b, 1974c). Similar arrivals have also been observed in Japan (Tsujiura, 1972) and Tonga (Oliver and Isacks, 1967; Barazangi *et al.*, 1972). These arrivals are shear waves with a greater

travel time, higher frequency content, longer duration, and lower apparent velocity than direct S . Examples of such arrivals (labeled AHFA) are shown in Fig. 90. Figure 89 shows the stations and location of events for which this arrival has been observed. The more northern (Peru-Brazil) events were observed at ANT, northern Chile, and the southern events (Argentina) at the other stations.

Two models have been proposed which can explain these arrivals: the waveguide model (Isacks and Barazangi, 1973) and the reflection model (Snoke *et al.*, 1973, 1974a, 1974b, 1974c). These models were compared in *Year Book 73* (Snoke *et al.*, 1974b), and it was concluded that although the reflection model may not be unique, it provides an adequate explanation for the arrivals, including the frequency content. It is preferred to the waveguide model because it makes fewer unverified assumptions, and it predicts the observed long-distance cut-off (see Fig. 117 in Snoke, 1974b). The following discussion per-

tains to the reflection model. Use of this phase to locate an interface is much less precise than the use of *ScSp*, because it is much more sensitive to the velocity-depth model used, the detailed structure of the dipping interface in the conver-

sion region, the location of the earthquake and the direction of the initial *S* or *P* phase.

The main tectonic implication of these arrivals is the existence of a dipping interface in the depth range 80–250 km

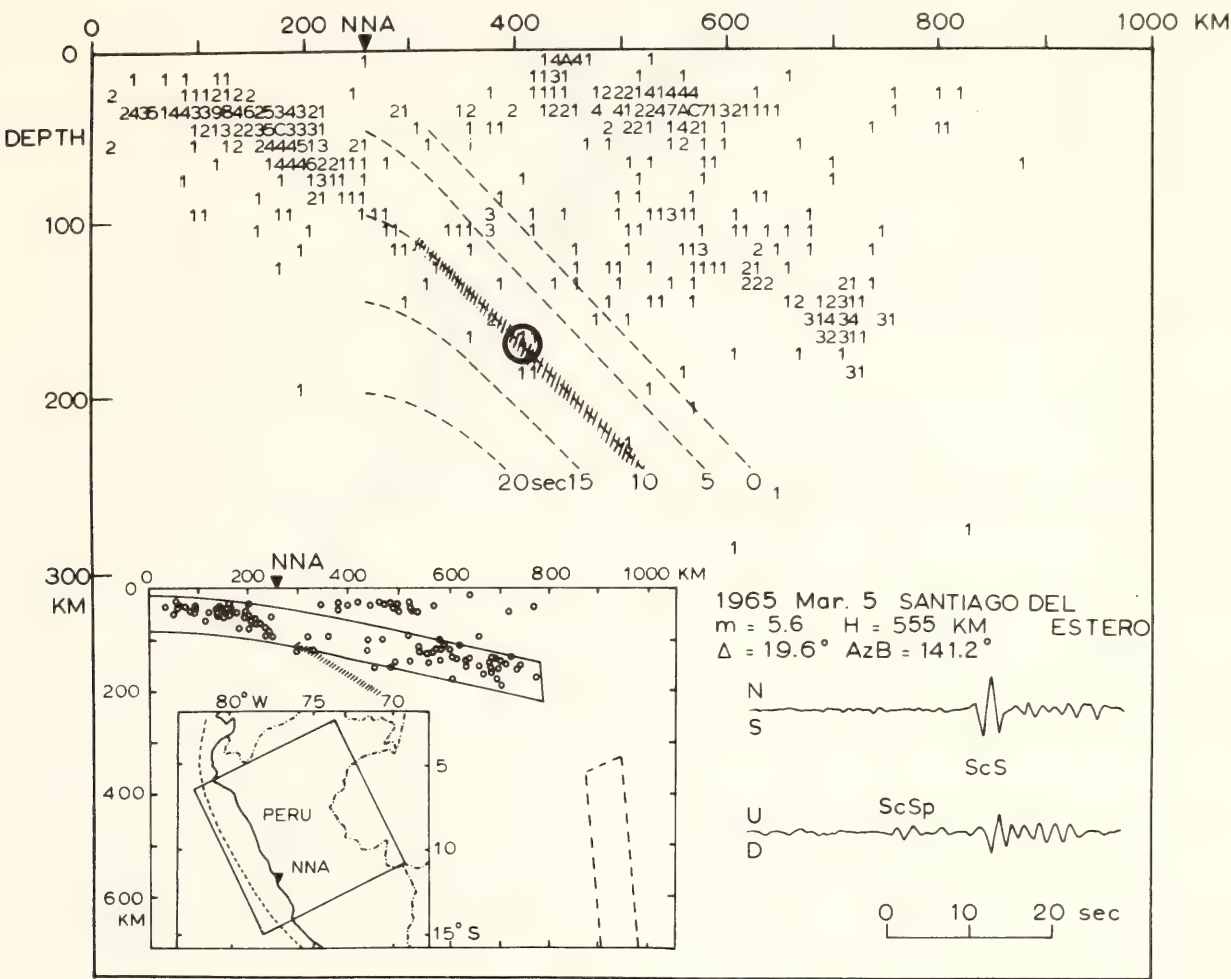


Fig. 87. Vertical seismicity cross section and traced seismograms of *ScS* and *ScSp* arrivals at NNA (central Peru); the circle represents preferred conversion region. Isacks and Molnar's (1971) gently dipping slab model is shown in the inset at the lower left. Their seismicity cross section is taken over the same region as the one above it, but they conclude only $M > 5$ (USCGS, 1961–1967).

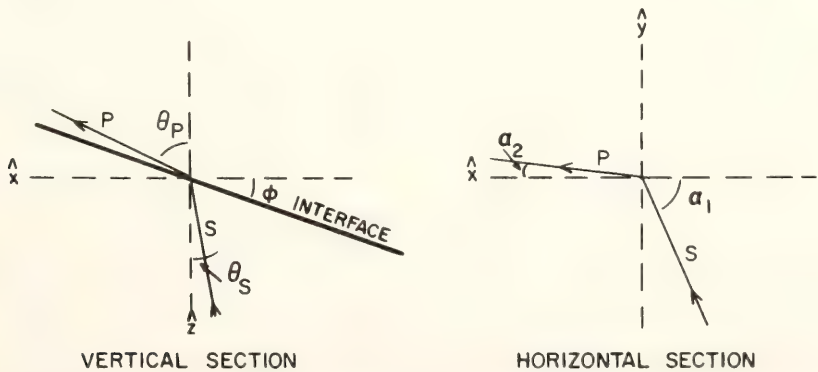


Fig. 88. Schematic showing two projects of the geometry for the *ScS*-to-*P* conversion at the dipping interface.

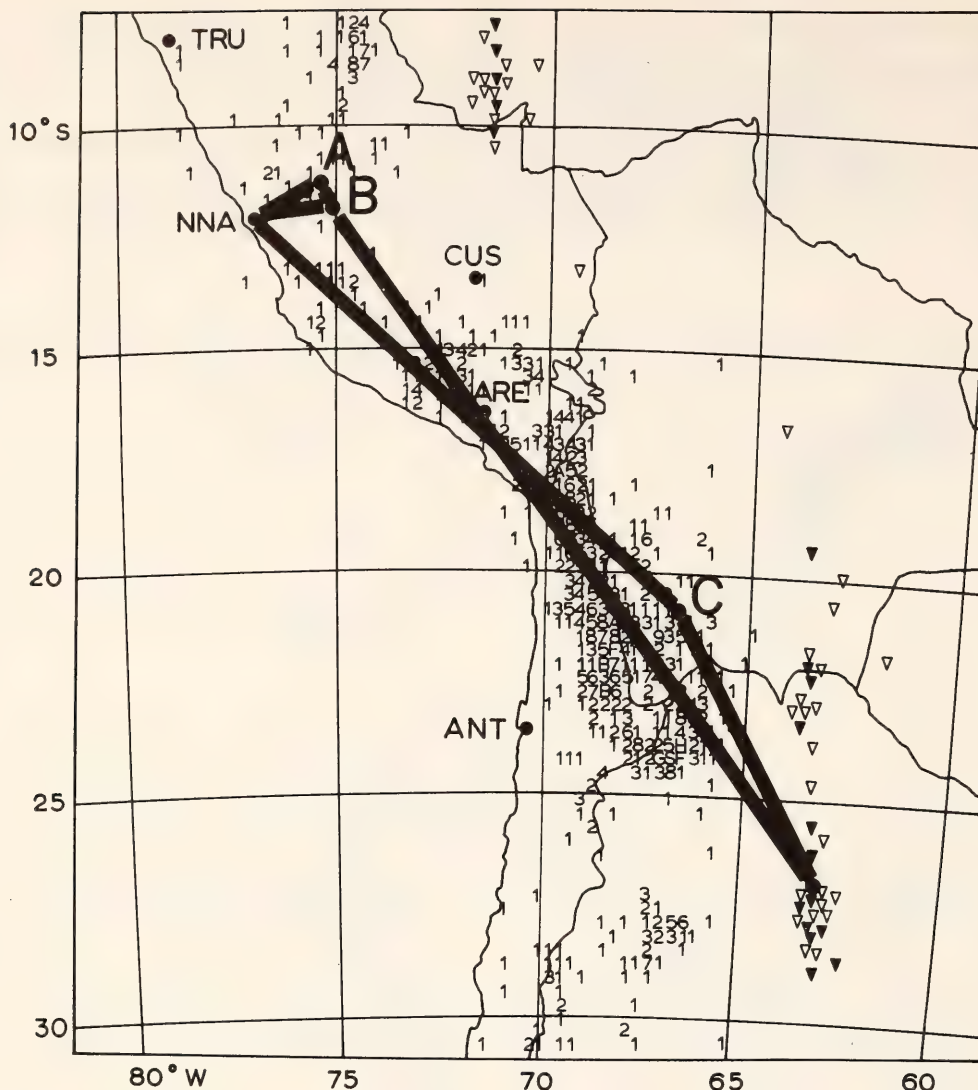


Fig. 89. Location map showing seismograph stations and epicenters (solid triangles) of earthquakes for which the anomalous high-frequency arrivals have been observed. Included are projections for the seismic activity for depths of 100–250 km (numbers) and depths greater than 500 km (open triangles). Also shown are ray paths for $ScSp$ and the anomalous high frequency arrival from the circled event.

which represents a sufficiently sharp velocity discontinuity to support efficient reflection of P or S phases incident from below. A schematic of the reflection model is shown in Fig. 91: The high-frequency anomalous arrivals result from an S -to- S or a P -to- S reflection at a dipping interface. The observed distances and arrival time onsets are consistent with the model calculations based on S -to- S reflections where the reflections can occur anywhere in a region between depths of 80 and 250 km and of similar lateral extent. If one assumes that the interface is the upper boundary of the subducting plate and that it must

therefore be correlated with the seismicity of $ScSp$, the possible location of conversion regions is decreased considerably. (The 10–20 second duration of the arrival indicates that the conversion occurs over a much larger region than does $ScSp$.) For all cases studied, the initial phase is necessarily an S phase.

An application of the two techniques for a single-station earthquake pair. Both an $ScSp$ and an anomalous high-frequency arrival were observed at NNA from a deep-focus event on 5 March 1965. The epicenter for this event is circled in Fig. 89. The projected path for the $ScSp$ arrival was discussed above,

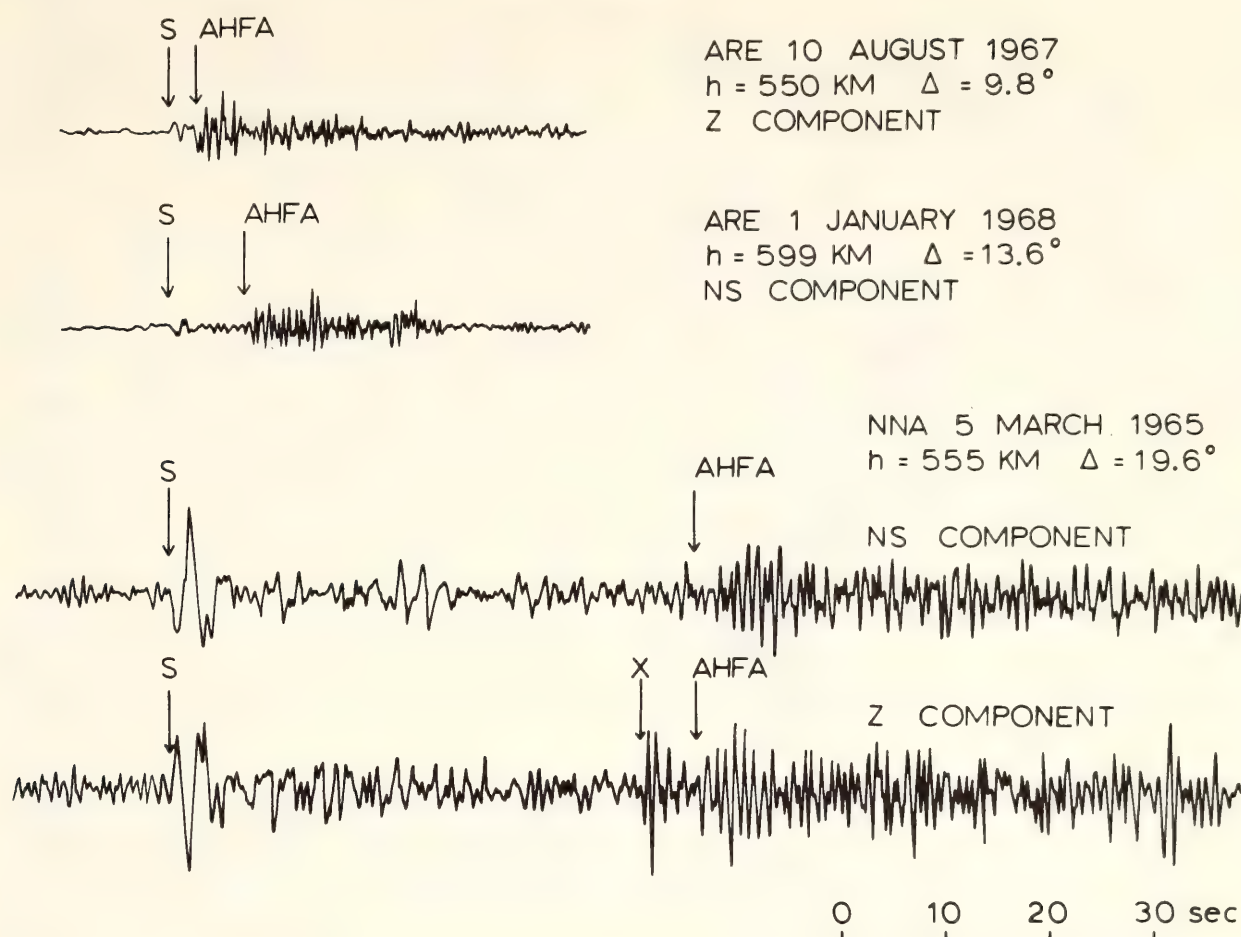


Fig. 90. Tracings of short-period records from ARE and NNA showing anomalous high-frequency arrivals (labeled AHFA) and the corresponding S arrivals for various epicentral distances. The arrival labeled X is interpreted as an AHFA-phase-to- P conversion at the Moho.

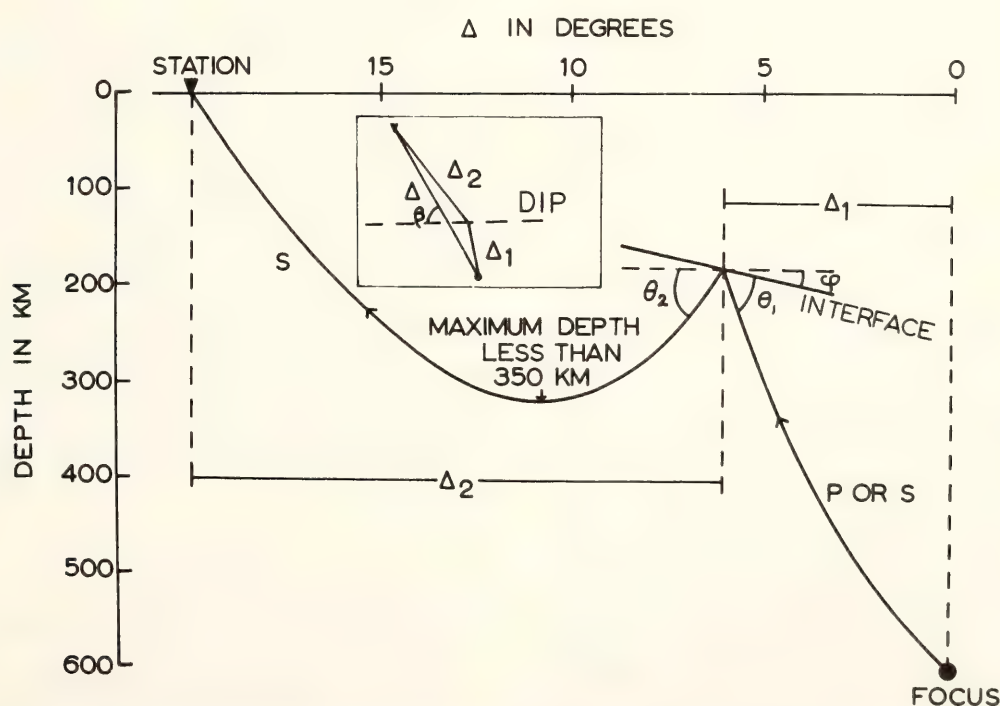


Fig. 91. A schematic of the reflection model. The actual path will be along Δ_1 and Δ_2 rather than the straight-line path Δ . Given Δ , velocity-depth model(s), a focal depth, and a conversion depth, and assuming Snell's Law at the conversion, one can calculate travel time, dip angle (ϕ), and strike angle (β) for each choice of phases 1 and 2.

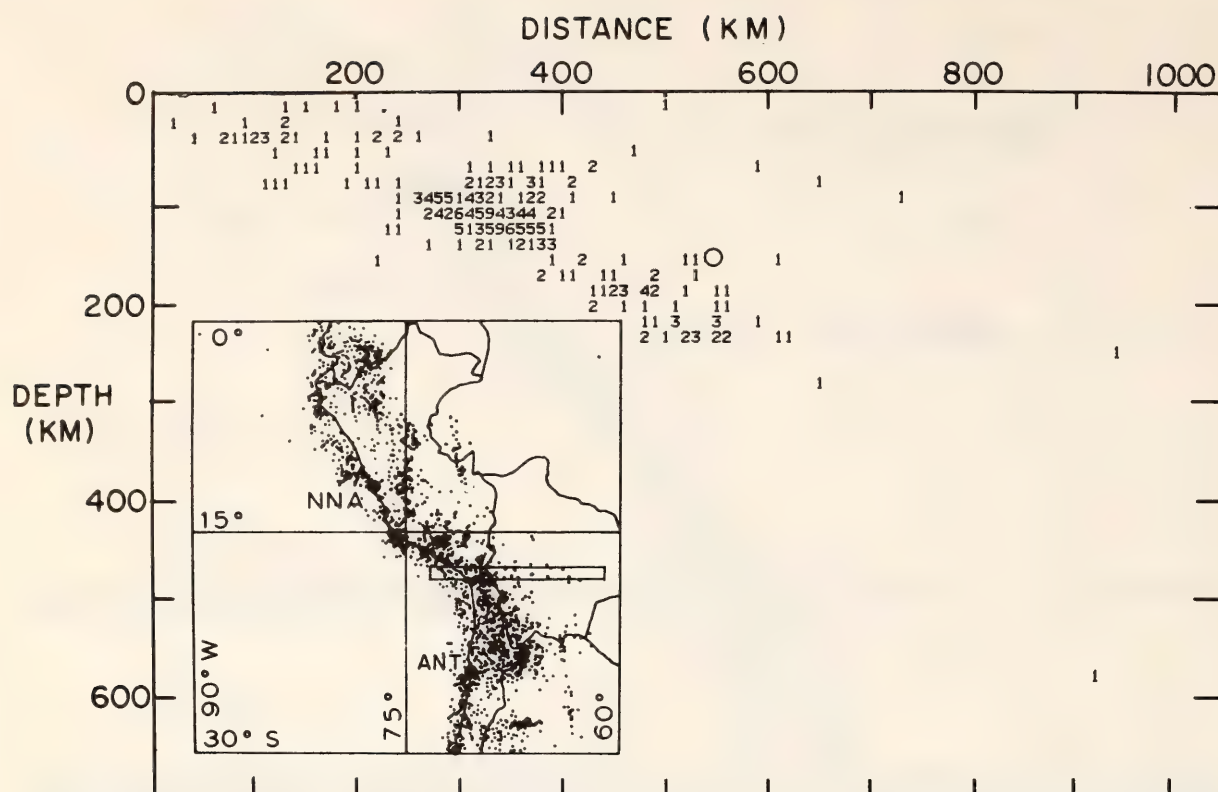


Fig. 92. Vertical seismicity cross section for events inside the inset. The circle indicates the conversion region for the *S*-to-*S* reflection leading to the observed anomalous high-frequency arrival at NNA from the event on 5 March 1965.

and a tracing of the seismic arrival is given in Fig. 87. Tracings of two components of the anomalous arrival are included in Fig. 90. Assuming a 4% higher velocity in the subducting plate than in the normal mantle at the same depth, one finds a possible path whose projections are shown in Figs. 89 and 92. The conversion region is denoted by *C* in Fig. 89 and a circle in Fig. 92.

One sees from Fig. 89 that although the *ScSp* and anomalous high-frequency phases sample the interface at roughly the same depth, the conversion points are about 1400 km apart. Hence, even though the earthquake and the station are the same, the two phases sample different parts of the plate boundary.

Concluding remarks. The conversion region for *ScSp* at a given station has a fixed location which, to a good approximation, is independent of the location of the earthquake sources. Hence, using *ScSp* observations at a single station provides information about the location of only a small part of the dipping inter-

face. To map large regions of a plate boundary using *ScSp* therefore requires a large number of appropriately located stations.

The conversion region giving rise to the high-frequency phases depends on the locations of the station and the earthquake relative to the interface, and its location is defined much less precisely than is the *ScSp* conversion region. These arrivals are useful in that their presence indicates the existence of a dipping interface, or, if the plate-boundary is already fairly well located by other means, it may provide information about the velocity contrasts which cannot be obtained from *ScSp* or seismicity.

References

- Barazangi, M., B. Isacks, and J. Oliver, Propagation of seismic waves through and beneath the lithosphere that descends under the Tonga island arc, *J. Geophys. Res.*, **77**, 952-958, 1972.
- Isacks, B. L., and M. Barazangi, High-frequency shear waves guided by a

- continuous lithosphere descending beneath South America, *Geophys. J. R. Astron. Soc.*, **33**, 129–139, 1973.
- Okada, H., Forerunners of ScS wave from nearby deep earthquakes and upper mantle structure in Hokkaido (in Japanese) *Jishin, Ser. 2*, **24**, 228–239, 1971.
- Okada, H., Converted *P* phase from the ScS phase at the inclined deep seismic zone, in *Carnegie Inst. Wash. Year Book 72*, pp. 238–245, 1973.
- Okada, H., Geophysical implications of the phase ScSp on the dipping lithosphere underthrusting western South America, in *Carnegie Inst. Wash. Year Book 73*, pp. 1032–1039, 1974.
- Okada, H., Ph.D. thesis, Hokkaido University, Sapporo, Japan, in preparation, 1975.
- Oliver, J., and B. Isacks, Deep earthquake zones, anomalous structure in the upper mantle and the lithosphere, *J. Geophys. Res.*, **72**, 4259–4275, 1967.
- Snoke, J. A., I. S. Sacks, and H. Okada, Empirical models for anomalous high-frequency arrivals from deep-focus earthquakes in South America, in *Carnegie Inst. Wash. Year Book 72*, pp. 233–238, 1973; *ibid.*, *Geophys. J. R. Astron. Soc.*, **37**, 133–139, 1974a.
- Snoke, J. A., I. S. Sacks, and H. Okada, A model not requiring continuous lithosphere for anomalous high-frequency arrivals from deep-focus South American earthquakes, in *Carnegie Inst. Wash. Year Book 73*, pp. 1039–1046, 1974b; *ibid.*, *Phys. Earth Planet. Interiors*, **9**, 199–206, 1974c.
- Tsujiura, M., Spectra of body waves and their dependence on source depth: 1. Japanese arc, *J. Phys. Earth*, **20**, 251–266, 1972.

SEISMIC SOURCE STUDIES

J. A. Snoke, A. T. Linde, and I. S. Sacks

General Introduction

Elastic strain, which is built up slowly in the earth due to various processes, can be released by earthquakes. Studies in

which the radiation and deformation from earthquakes are interpreted in terms of theoretical source models should enable one to estimate the earthquake's geometric parameters (fault length and orientation) and the physical parameters of the earthquake's environment (strength of rock and tectonic stress field).

For the past fifteen years the most commonly used source model has been the dislocation model, which assumes some specific time history for the displacement across the fault. Such an approach seemed to us to assume information that should more properly be derived from the model. Application of the dislocation model to date has involved highly simplified and unsatisfactory representations of an earthquake rupture. We therefore sought a more realistic earthquake source model. To that end, we investigated a version of a stress-relaxation model that Archambeau had introduced and solved. In this model certain details of the rupture process and the reaction of the medium are specified, and Archambeau's solution treated the problem as an initial-value problem. Archambeau's papers were quite controversial because his solution for the radiation-zone displacement amplitude had spectral peaks that did not exist in other solutions for apparently similar models. For the class of earthquakes we were studying, Archambeau's spectral structure was not inconsistent with the data. A closer examination of the underlying assumptions in Archambeau's approach has shown, however, that the stress-relaxation model is equivalent to a dislocation model and that Archambeau's spectral peaks resulted from physically inadmissible applications of his method of solution (see Snoke, Archambeau's elastodynamical source-model determination, this Report).

Hence, for a rupture process that occurs instantaneously, the stress-relaxation models and the dislocation models are equivalent. The source-model solutions for a finite rupture velocity are not

exact (see Snoke, The implications of moving boundaries in elastodynamics, this Report), but we believe that the radiation predicted by a model with a finite, smoothly varying rupture velocity will not differ significantly from that for the instantaneous-rupture models. There is some evidence that at least some earthquakes are multiple ruptures. A preliminary study (see Linde *et al.*, Multiple rupture earthquakes and the determination of source parameters, this Report) indicates that multiple ruptures produce spectra which, if interpreted in terms of a single-rupture model, lead to erroneous estimates for source parameters such as fault length and stress drop.

Our theoretical studies aimed at developing more realistic source models are continuing together with observational studies on selected suites of earthquakes.

ARCHAMBEAU'S ELASTODYNAMICAL SOURCE-MODEL SOLUTION

J. Arthur Snoke

Introduction

Earthquake source models provide a means by which the radiation and deformations due to earthquakes can be interpreted to provide information about the properties of the earth in the vicinity of the earthquake. In recent years there have been a number of different earthquake-rupture models proposed—none of them very realistic physically—and there have been an almost equal number of mathematical approaches introduced to solve these models. The most commonly used model at present is that of Brune (1970) which is the model derived by considering the effective stress available to accelerate the sides of the fault. Brune's solution is empirical, but its near-field and far-field displacements for *S*-wave radiation are in reasonable agreement with those derived from dislocation models (e.g., Haskell, 1964).

Another type of model is the stress-relaxation model whereby the rupture process consists of a phase change in a

prescribed region resulting in the release of a tectonic prestress. The instantaneous creation of a sphere has been solved exactly by Hirasawa and Sato (1963*a*, 1963*b*) for a spherical cavity and by Koyama *et al.* (1973) for a noncavity, zero-rigidity sphere. Archambeau (1968, 1972) has also treated this problem, but his solution in general is not exact because it neglects to take into account dynamical boundary conditions on the surface of the rupture shell. Randall (1966) has introduced a variant on this model in which the postrupture medium has no material boundaries. For this case, Archambeau's method for obtaining a solution is exact.

Although Archambeau's method of solution is not exact for most problems to which it has been applied, it is still potentially useful because it is much simpler analytically than the exact solution and because it is easily generalized to models for non-instantaneous ruptures. Before it can be applied in these cases, however, it is necessary to estimate the validity and closeness of the approximation.

Spectral Peaks

There has been considerable controversy regarding Archambeau's method of solution because two models employing it are the only earthquake source models at present which predict peaks in the long-period part of the far-field-displacement amplitude spectrum without explicitly assuming rebound or multiple ruptures along the fault plane. These models have generated interest because some long-period amplitude spectra of earthquakes seem to exhibit definite spectral peaks (Linde and Sacks, 1971; Rodriguez and Kisslinger, 1972; Archambeau, 1974), or, equivalently, there is some evidence for rebound in the time-domain displacement (Bollinger, 1970; Burdick and Helmberger, 1974).

In his early papers (Archambeau, 1968, 1972) Archambeau's displacement

amplitudes had pronounced low-frequency spectral peaks. Randall (1973; see also Snoke *et al.*, 1973) showed that these peaks were spurious. However, two recent applications of Archambeau's method of solution have led to spectral peaks: One model is Archambeau's earlier peak-producing model with a new interpretation (Minster, 1973; Archambeau and Minster, 1974; Archambeau, 1974), and the other is a different model (Snoke, 1974). Spectral peaks in these models have been interpreted as resulting from the assumption of a nonuniform prestress. There is general agreement that no long-period spectral peaks result if a uniform prestress is assumed.

Molnar *et al.* (1973) and Brune (1974, private communication) conjecture that the existence of the spectral peaks in

models using Archambeau's method of solution is a consequence of the assumption that the rupture-zone boundary becomes a free surface following the onset of rupture. Molnar *et al.* assume that for earthquakes, friction on the fault surface is sufficient to prevent rebound. If they are correct, a maximum in the amplitude spectrum should occur at zero frequency.

Brune argues that the radiation could not be affected by prestress nonuniformities if it results entirely from motion on the rupture-zone boundary. He notes that for the nonuniformity to affect the radiation, energy which leaves the fault surface at the onset of the rupture must have time to sample the nonuniform region and be reflected back to the fault surface before the fault locks. This is

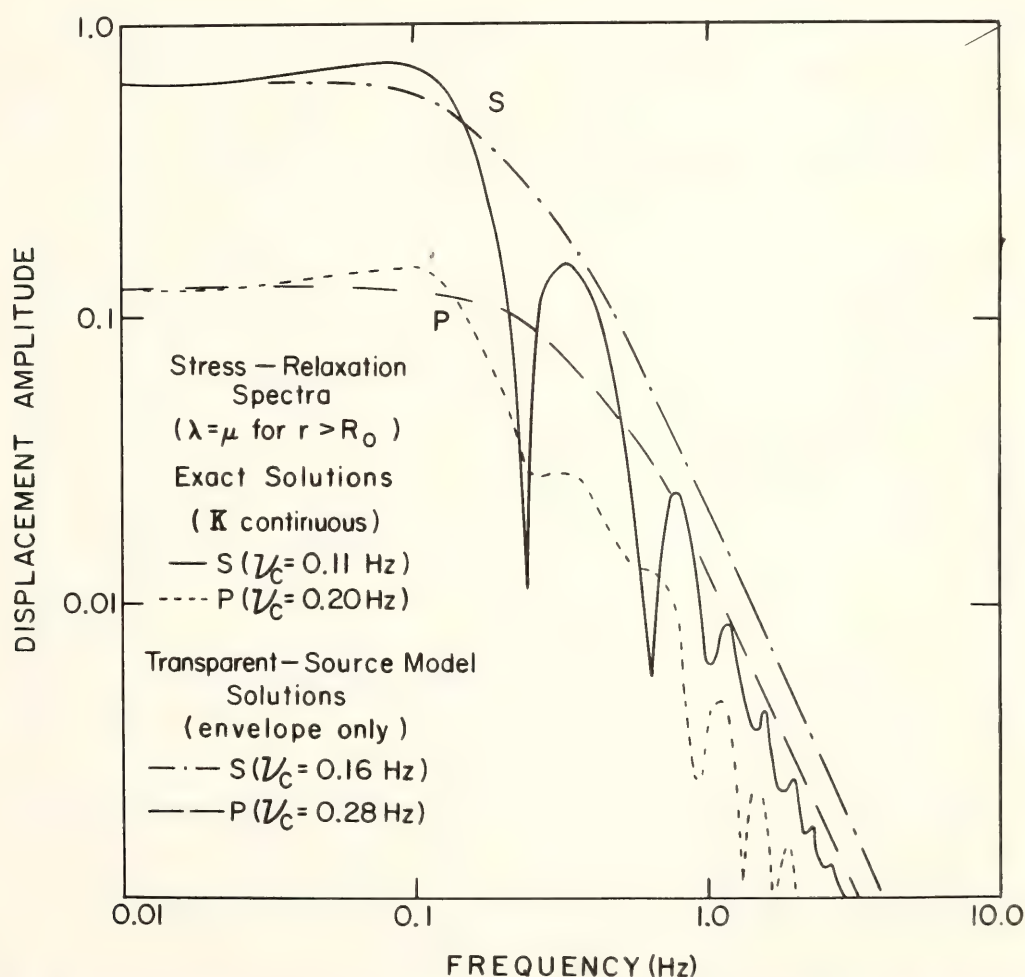


Fig. 93. Far-field displacement amplitude spectra for P and S radiation for the exact solutions and Archambeau's transparent-source model solutions of the stress-relaxation model. For all cases $\lambda = \mu$ outside the rupture zone, and for the exact solutions the compressibility is continuous across the rupture zone boundary. The radius of the rupture zone, R_0 is 10 km and $v_p = 10$ km/sec. Only the envelope for Archambeau's solutions is shown.

improbable because the prestress is taken to be uniform over a region that is large compared to the rupture zone. Brune speculates that spectral peaks might result from energy reflected from the boundary of the uniformly prestressed region, causing fault rebound along the still-free rupture zone. Calculations show, however, that the effects of reflected waves are an order of magnitude too small to account for the spectral structure predicted in Snoke's model (Snoke, 1974).

Results and Conclusions

This study was undertaken to resolve this dilemma and to determine the validity of the application of Archambeau's method when it does not lead to an exact solution. Given below is a summary of the conclusion of that study (see Snoke, 1975, for the more detailed account).

1. Contrary to a claim made by Ar-

chambeau (1972), there is no simple relationship between the ratio of P - and S -radiated energies and the ratio of the energy released from the hydrostatic and deviatoric parts of the prestress.

2. Archambeau's (or, equivalently, Randall's 1964) elastodynamical source-model solution for an instantaneous rupture is equivalent to an instantaneous stress pulse and/or dislocation on the rupture-zone boundary. (See also Minster, 1973.)

3. Figure 93 shows the frequency domain amplitude for Archambeau's solution and an exact solution for the P -wave and S -wave radiation resulting from the instantaneous creation of a zero-rigidity sphere in a uniformly (shear) prestressed, elastically homogeneous medium. Archambeau's solution is seen to be a good approximation to the exact solution for these cases: It has the same ω^{-2} high-frequency fall-off and zero-frequency limit in the frequency domain.

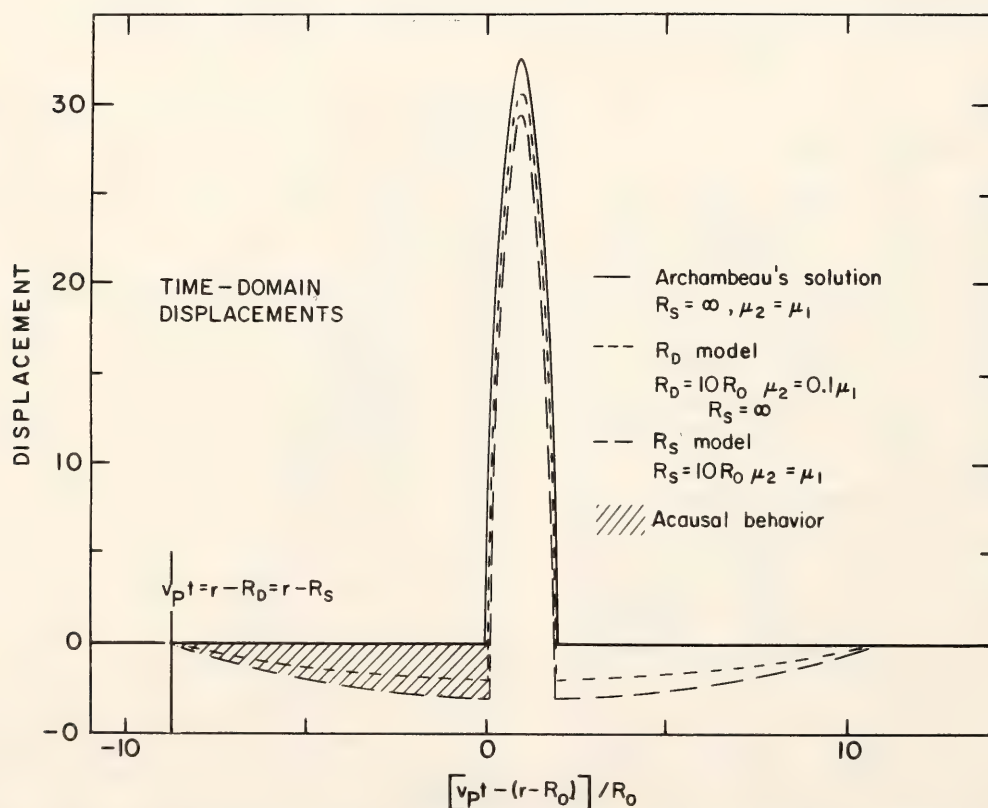


Fig. 94. Time-domain solutions for the P -wave far-field displacement in arbitrary units for the R_s model (Minster, 1973) with infinite and finite R_s and for Snoke's (1974) R_D model solved by Archambeau's method. (μ and μ_1 are the outside and inside rigidities, respectively, in the R_D model.) $R_0 = 10$ km and $v_p = 10$ km/sec in all cases. The acausal parts of the solutions are hatched.

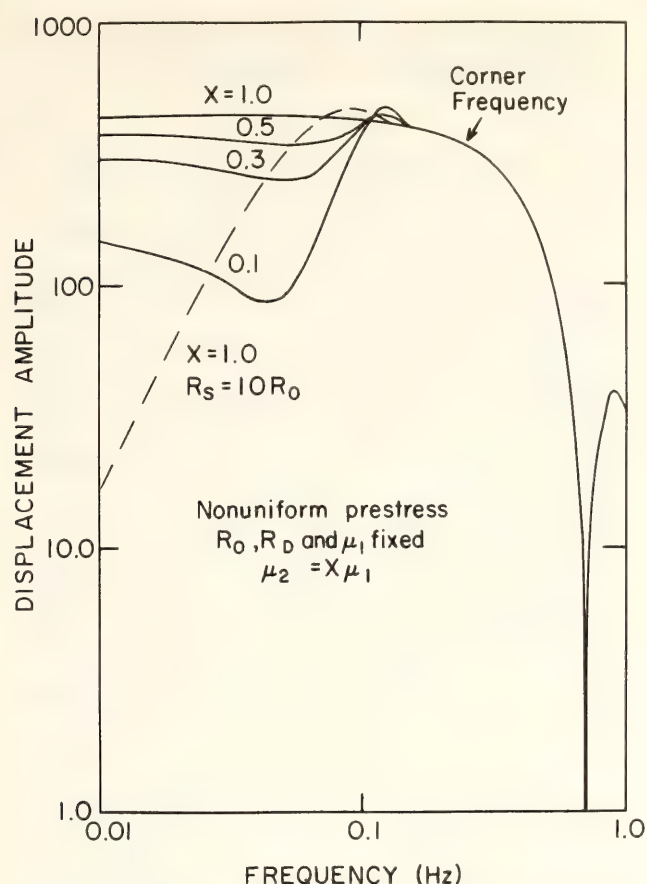


Fig. 95. P -wave far-field displacement amplitude spectra for the R_D model solved by Archambeau's method with $R_0 = 10$ km, $R_D = 100$ km, $v_p = 10$ km/sec and the inside rigidity μ_1 held constant while the outside rigidity μ is varied. The spectra for the (nonexact) causal solution for models are approximately equal to the non-discontinuity ($\mu_1 = \mu$) spectrum for all values of μ . The dashed line represents an R_s model spectrum with $R_s = 10 R_0 = 100$ km. The amplitude scale is in arbitrary units.

In the time domain, Archambeau's solution predicts a one-sided parabolic pulse which is quite similar in shape to the exact solution.

4. From the stress-pulse/dislocation-model representation for Archambeau's solution it follows that all discontinuity surfaces in the elastic medium radiate simultaneously for an instantaneous rupture. Physically, only the rupture zone would be a source of radiation, so that Archambeau's prescription for the solution cannot be applied directly when there are discontinuities in the medium other than that of the rupture-zone boundary. Two models, the R_s model (Minster, 1973) and the R_D model

(Snoke, 1974), have additional discontinuities: that direct application of Archambeau's prescription for the solution results in peaks in the long-period part of the far-field displacement amplitude spectrum is due only to assumptions that are physically impossible (see Figs. 94 and 95).

The controversy concerning the spectral peaks has therefore been resolved: all spectral peaks produced by models employing Archambeau's method of solution are spurious. Hence, observed spectral structure cannot be explained by any instantaneous rupture model using Archambeau's method of solution.

References

- Archambeau, C. B., General theory of elastodynamic source fields, *Rev. Geophys.*, 16, 241–288, 1968.
- Archambeau, C. B., The theory of stress wave radiation from explosions in prestressed media, *Geophys. J. R. Astron. Soc.*, 29, 329–366, 1972; Appendix, 31, 361–363, 1973.
- Archambeau, C. B., Investigations of tectonic stress, Semiannual Technical Report No. 1, Contract No. F19628-74-C-0087 ARPA/AFCRL, University of Colorado, 1974.
- Archambeau, C. B., and J. B. Minster, Elastodynamic representation theorem and the equivalence of various source theories, *Trans. Am. Geophys. Union*, 55, 683, 1974.
- Bollinger, G. A., Fault length and fracture velocity for the Kyushu, Japan earthquake of October 3, 1963, *J. Geophys. Res.*, 75, 955–964, 1970.
- Brune, J. N., Tectonic stress and the spectra of seismic shear waves from earthquakes, *J. Geophys. Res.*, 75, 4997–5009, 1970; erratum, 76, 5002, 1971.
- Burdick, L. J., and D. V. Helmberger, Time functions appropriate for deep earthquakes, *Bull. Seismol. Soc. Am.*, 64, 1419–1428, 1974.

- Haskell, N. A., Total energy and energy spectral density of elastic wave radiation from propagating faults, *Bull. Seismol. Soc. Am.*, 54, 1811–1841, 1964.
- Hirasawa, T., and R. Sato, Propagation of elastic waves from a spherical origin: Part 1 and Part 2 (in Japanese), *Zisin*, 16, 52–77, 1963a,b.
- Koyama, J., S. E. Horiuchi, and T. Hirasawa, Elastic waves generated from sudden vanishing of rigidity in a spherical region, *J. Phys. Earth*, 21, 213–226, 1973.
- Linde, A. T., and I. S. Sacks, Errors in the spectral analysis of long-period seismic body waves, *J. Geophys. Res.*, 76, 3326–3336, 1971.
- Minster, J. B., Elastodynamics of failure in a continuum, Ph.D. thesis, California Institute of Technology, 1973.
- Molnar, P., K. H. Jacob, and K. McCamy, Implications of Archambeau's earthquake source theory for slip on faults, *Bull. Seismol. Soc. Am.*, 63, 101–104, 1973.
- Randall, M. J., On the mechanism of earthquakes, *Bull. Seismol. Soc. Am.*, 54, 1283–1289, 1964.
- Randall, M. J., Seismic radiation from a sudden phase transition, *J. Geophys. Res.*, 71, 5297–5302, 1966.
- Randall, M. J., Spectral peaks and earthquake source dimensions, *J. Geophys. Res.*, 78, 2609–2611, 1973.
- Rodriguez, R., and C. Kisslinger, Spectral classification of New Madrid earthquakes, *Trans. Am. Geophys. Union*, 53, 450, 1972.
- Snoke, J. A., Earthquake radiation spectrum from models with concentrated prestress, in *Carnegie Inst. Wash. Year Book 73*, pp. 1048–1054, 1974.
- Snoke, J. A., Archambeau's elastodynamical source-model solution and low frequency spectral peaks in the far-field displacement amplitude, *Geophys. J. R. Astron. Soc.*, in press, 1975.
- Snoke, J. A., A. T. Linde, and I. S. Sacks, Source-spectral relations for earthquakes, in *Carnegie Inst. Wash. Year Book 72*, pp. 245–246, 1973.

THE IMPLICATIONS OF MOVING BOUNDARIES IN ELASTODYNAMICS

J. A. Snoke

Introduction

The preceding report (Snoke, 1975a; see also Snoke, 1975b) contains a comparison of Archambeau's (1968, 1972) solution with the exact solution for the radiation-zone displacement from the instantaneous creation of a zero-rigidity sphere of radius R_0 in a homogeneous medium with a uniform (shear) prestress. The creation of zero rigidity is brought about by a phase transition involving no external forces. Archambeau (1968, 1972) also treats the generalization of this model whereby the sphere grows with a finite (constant) rupture velocity V for the time interval $0 < t < T = R_0/V$. As for the instantaneous case, Archambeau's solution is not exact, but Burridge (1975) has derived what he claims to be an exact solution for this problem. In this report it is shown that Burridge's solution also is not exact because he has not taken into account the effect of the motion of the rupture-zone boundary on the boundary conditions.

Archambeau's Solution

For the instantaneous creation of a zero-rigidity sphere of radius R in a homogeneous, uniformly prestressed medium, the j th component of the displacement is taken to be given by $U_j(\vec{r}, t; R)$. Using superposition and convolution, Randall (1973) finds that the displacement $u_j(\vec{r}, t)$ for the finite-rupture-velocity case is given by

$$u_j(\vec{r}, t) = \int_0^T d\tau V \partial U_j[\vec{r}, t - \tau; R(\tau)] / \partial R \quad (1)$$

where $V = \partial R / \partial \tau$ for $0 < \tau < T$. One can derive Archambeau's (1968, 1972) form of the solution from Equation 1. (Randall also gives an expression for the frequency-domain displacement in his Equation 9, but this expression is incor-

rect because its derivation neglects the implicit dependence on U_j of τ through R).

For the u_j to be exact solutions, they and their spatial derivatives must satisfy certain boundary conditions at $r = R(t)$ for all times. For a given set of U_j , any boundary conditions to be satisfied by the u_j as defined by Equation 1 are determined through that equation. Archambeau's U_j are not exact because they satisfy the correct boundary conditions only in the infinite-time limit—they satisfy no dynamical boundary conditions. The u_j defined by Equation 1 are also not exact whether one uses Archambeau's U_j or the exact U_j (Snoke, 1975 b) in the right-hand side of the equation.

Burridge's Solution

Burridge's solution (1975) for the finite, constant rupture-velocity model uses an approach developed by Burridge and Alterman (1972) which is, in principle, exact. Archambeau's solution is independent of the compressibility or density for $r < R$, but Burridge's solution is for the specific case of zero compressibility and density—a cavity for $r < R$.

Burridge's solution is based on the boundary condition

$$\begin{aligned} \sigma_{ij}\hat{x}_j|_{r=R_+} = \\ -\sigma^{(0)}_{ij}\hat{x}_j|_{r=R_+} \quad t > 0 \end{aligned} \quad (2)$$

where the $\sigma^{(0)}_{ij}$ are the elements of the initial prestress tensor; the σ_{ij} are the elements of the stress tensor defined relative to the $\sigma^{(0)}_{ij}$; and repeated indices are summed from one to three.

Boundary Conditions for Moving Boundaries

Derivation. The equation of motion in elastodynamics is

$$\begin{aligned} \partial_j \sigma_{ij} = -F_i \\ + \partial(\rho \partial u_i / \partial t) / \partial t \end{aligned} \quad (3) \quad \text{where}$$

where \vec{F} is the body-force density, ρ the density, and $\partial_j A \equiv \partial A / \partial x_j$. Equation 3 is valid in an inertial frame, which we take to be the observer's frame of reference. The problem of interest is what Muskhelishvili (1963, p. 79) calls the "first fundamental problem;" namely, to find solutions to Equation 3 satisfying $\vec{F}(\vec{r}, t) \rightarrow \vec{f}(\vec{r}, t)$ on some surface S and having the initial conditions $\vec{u}(\vec{r}, 0) = \vec{u}^0(\vec{r})$ and $\partial \vec{u}(\vec{r}, t) / \partial t|_{t=0} = \vec{w}(\vec{r})$, where \vec{f} , \vec{u}^0 and \vec{w} are known.

In the problem of interest, the surface S —the surface of the rupture sphere—is moving for a period of time in the observer's frame of reference. The effects of moving boundaries on the boundary conditions satisfied by the variables of interest have been treated extensively in electrodynamics (e.g., the discussion of Faraday's law by Jackson, 1962, Ch. 6) and hydrodynamics (e.g., the discussion of Euler's equation by Landau and Lifshitz, 1959, Ch. 1). Minster (1973) considers moving boundaries in the context of Green's-function integral representations in elastodynamics.

The problem at hand is to reexpress the boundary conditions in terms of u_j and σ_{ij} defined at a given time in the observer's frame of reference. This can be done using Equation 3 after it has been transformed to a reference frame in which the surface S is at rest.

In a coordinate frame moving with respect to a fixed frame, the time derivative of a function $A(\vec{r}, t)$ in the moving frame must take into account the time dependence of \vec{r} . Designating the transformation velocity as $\vec{v} = \partial \vec{r} / \partial t$, one has

$$\begin{aligned} \partial A / \partial t|_{\text{moving frame}} &\equiv Da / Dt \\ &= \partial A / \partial t|_{\text{fixed frame}} + \vec{v} \cdot \vec{\nabla} A \end{aligned} \quad (4)$$

Using Equations 3 and 4, Equation 3 in the moving frame can be written:

$$\begin{aligned} \partial_j \sigma'_{ij} = -F'_i \\ + D(\rho D u_i / Dt) / Dt \end{aligned} \quad (5)$$

$$\begin{aligned}
& \sigma'_{ij} = \sigma_{ij} \\
& + D(\rho u_i v_j) / Dt \\
& + \rho v_j (Du_i / Dt \\
& - v_n \partial_n u_i \\
& + u_i \partial_n v_n)
\end{aligned} \quad (6)$$

are the elements of the stress tensor in the moving frame and

$$\begin{aligned}
& F'_i = F_i \\
& - D[u_i \partial_j (\rho v_j)] / Dt \\
& - \rho (\partial_n v_n) Du_i / Dt \\
& - u_i \partial_j (\rho v_j \partial_n v_n)
\end{aligned} \quad (7)$$

are the components of the body force in that frame.

The boundary condition can be derived from Equation 5 (e.g., Landau and Lifshitz, 1959, Ch. 1). The result is

$$[\sigma'_{ij} n_j] = -f'_i \quad (8)$$

where $\vec{n}(\vec{r})$ is the unit normal to the surface S at \vec{r} on S (defined so that $\vec{n} \cdot \vec{r} > 0$), $[A]$ represents the jump discontinuity in A across S and $-f'$ is the pressure on S resulting from any singular terms on the right-hand side of Equation 5 at \vec{r} and t on S .

Equations 5–8 differ from Minster's results (Minster, 1973, p. 54) because Minster has incorrectly transformed only one of the two time derivatives on the right-hand side of Equation 3 into the moving frame.

Applications. In the problem of interest, the non-instantaneous creation of a spherical cavity in a uniformly prestressed medium, the surface S is given by $r = R(t) = VtH(T - t)H(t)$, where H is the Heaviside function, so that the velocity \vec{v} is given by $\vec{v} = VH(T - t) \cdot H(t)\vec{r}$. The initial values are $\vec{u}^0 = \vec{w} = 0$, and $\vec{F} = \vec{f} = 0$ as well. Because the rupture sphere is taken to be a cavity, $\sigma_{ij} = -\sigma^{(0)}_{ij}$ for $r < R$. Using $\rho = \rho^0 H(r - R)$ one finds that $\vec{f}' = 0$, and Equation 8 takes the form:

$$\begin{aligned}
& \sigma_{ij} \hat{x}_j |_{r=R+} \\
& = [-\sigma^{(0)}_{ij} \hat{x}_j \\
& - \rho^0 V (2Du_i / Dt
\end{aligned}$$

$$\begin{aligned}
& -V\partial u_i / \partial R \\
& + 3Vu_i) H(T - t) H(t) |_{r=R+}
\end{aligned} \quad (9)$$

Hence, Burridge's boundary condition (Equation 2, above) is not correct for $0 < t < T$.

A commonly used model for an earthquake is a planar rupture zone (e.g., Brune, 1970). For a non-instantaneous rupture, \vec{n} is perpendicular to the plane while \vec{v} lies in the plane so that $\vec{v} \cdot \vec{n} = 0$. Hence, from Equation 6, $\sigma'_{ij} n_j = \sigma_{ij} n_j$ on each side of S so that the boundary conditions take the same form as for a stationary boundary.

Concluding Remarks

It has been shown that Burridge's solution (Burridge, 1975) is not exact for the problem of a growing spherical cavity in a uniformly prestressed medium because it assumes incorrect boundary conditions during the time the sphere is growing. The approach developed by Burridge and Alterman (1972) could in principle provide the exact solution for the problem if the correct boundary condition, Equation 9, were used. However, Burridge (1975) states that this approach for deriving exact solutions is limited in application to a class of closely related problems, and a preliminary investigation indicates that replacing Equation 2 by Equation 9 takes the problem of interest out of that class.

The lack of an exact solution for this problem makes it difficult to choose between Burridge's and Archambeau's (1972) solution as to relative correctness. Such a choice is only of academic interest because the two solutions produce quite similar far-field displacements in both the time and frequency domains, provided one uses the corrected form of Archambeau's solution (Randall, 1973; Snoke *et al.*, 1973; Snoke, 1975a, 1975b). Based on comparisons between the exact solution and Archambeau's solution for an instantaneous rupture (see the preceding paper and Snoke, 1975b), one

would anticipate that these solutions differ little from the exact solution.

References

- Archambeau, C. B., General theory of elastodynamic source fields, *Rev. Geophys.*, 16, 241–288, 1968.
- Archambeau, C. B., The theory of stress wave radiation from explosions in pre-stressed media, *Geophys. J. R. Astron. Soc.*, 29, 329–366, 1972; 31, 361–363, 1973.
- Brune, J. N., Tectonic stress and the spectra of seismic shear waves from earthquakes, *J. Geophys. Res.*, 75, 4997–5009, 1970; erratum, 76, 5002, 1971.
- Burridge, R., The pulse shape and spectra of elastic waves generated when a cavity expands in an initial shear field, *J. Geophys. Res.*, 80, 2606–2607, 1975.
- Burridge, R., and Z. Alterman, The elastic radiation from an expanding spherical cavity, *Geophys. J. R. Astron. Soc.*, 30, 451–477, 1972.
- Jackson, J. D., *Classical Electrodynamics*, John Wiley and Sons, 1962.
- Landau, L. D., and E. M. Lifshitz, *Fluid Mechanics*, Addison-Wesley, 1959.
- Minster, J. B., Elastodynamics of failure in a continuum, Ph.D. thesis, California Institute of Technology, 1973.
- Muskhelishvili, N. I., *Some Basic Problems of the Mathematical Theory of Elasticity*, P. Noordhoff Ltd., The Netherlands, 1963.
- Randall, M. J., Spectral peaks and earthquake source dimensions, *J. Geophys. Res.*, 78, 2609–2611, 1973.
- Snoke, J. A., Archambeau's elastodynamical source-model solution and low-frequency spectral peaks in the far-field displacement amplitude, *Geophys. J. R. Astron. Soc.*, in press, 1975.
- Snoke, J. A., A. T. Linde, and I. S. Sacks, Source-spectral relations for earthquakes, in *Carnegie Inst. Wash. Year Book* 72, pp. 245–246, 1973.

MULTIPLE RUPTURE EARTHQUAKES AND THE DETERMINATION OF SOURCE PARAMETERS

Alan T. Linde, I. Selwyn Sacks,
and J. Arthur Snoke

Introduction

A number of theoretical models for seismic sources (e.g., Ben-Menahem, 1962; Haskell, 1964; Aki, 1967; Brune, 1970; Archambeau, 1968) have yielded solutions for the radiation field. Snoke, in a companion paper (Archambeau's elastodynamical source-model solution, this Report) discusses certain of these models and concludes that in most important respects they do not differ fundamentally from one another. In all models which have been proposed (whether dislocation or initial value) the problem solved is that of stress release due to simple rupture in an infinite homogeneous medium subjected to a uniform shear field. Numerous studies have been reported in which the theoretical solutions have been used to infer earthquake source parameters (dimensions and stress release) from observed far-field spectra. California earthquakes have been extensively studied through this approach; Fig. 96, from Tucker and Brune (1973), is illustrative of the spread in results obtained. Spottiswoode and McGarr (1975) applied this method to tremors in a deep-level gold mine and obtained stress drops ranging from 5 to 50 bars. However, *in situ* observations indicate localized stress drops of about 2 kbar, which agree with laboratory tests.

Spottiswoode and McGarr also reported from studies of underground damage that many of the tremors are multiple events separated in space and time. Furthermore, there is an increasing body of evidence that large earthquakes are multiple events (Wyss and Brune, 1967; Trifunac and Brune, 1970; Gupta *et al.*, 1971) and, in a model study, Brune (1973) found multiple events were common.

Here we present a preliminary investi-

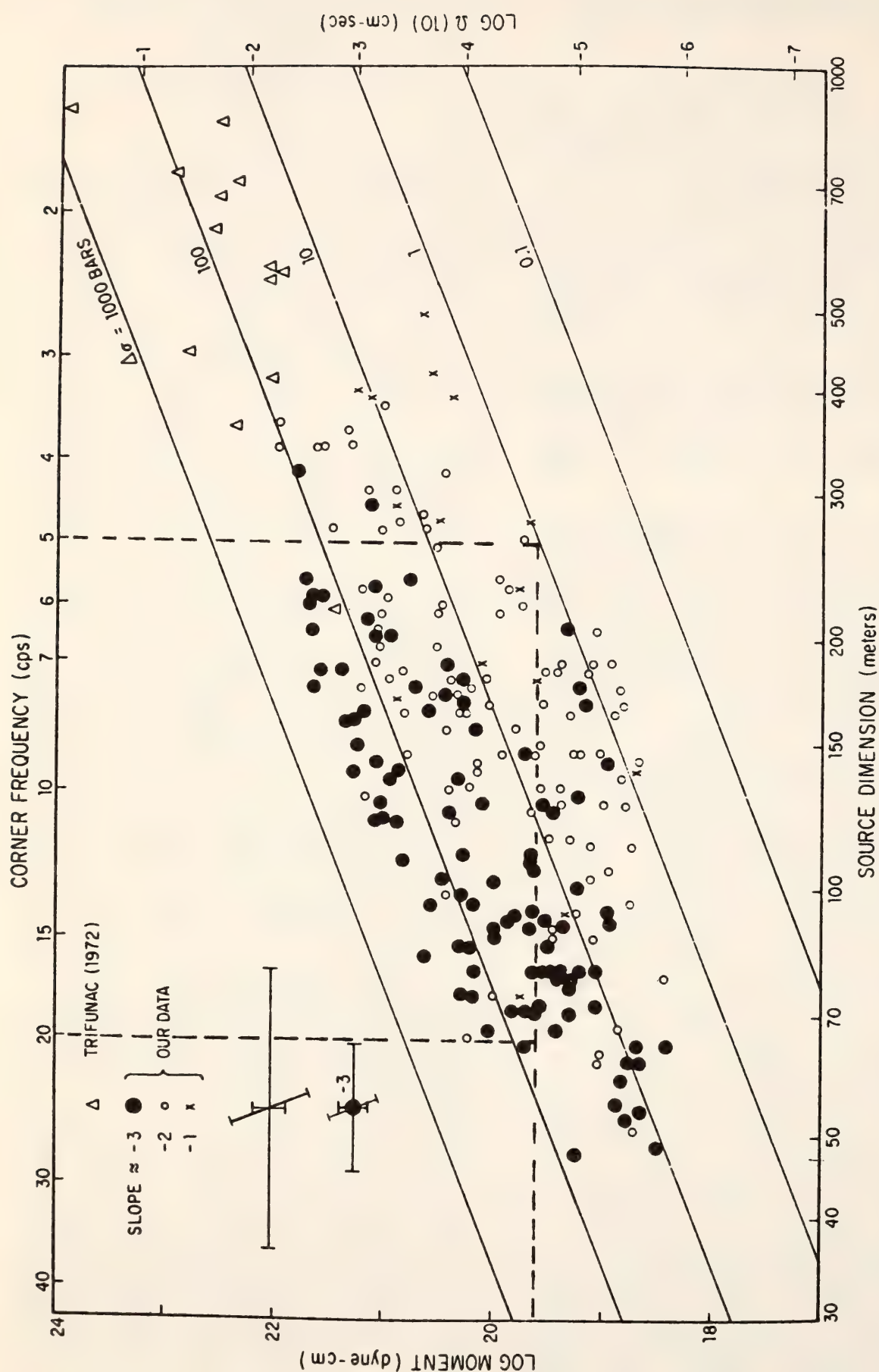


Fig. 96. From Tucker and Brune, 1973. Corner frequency amplitude reduced to 10 km source distance. Slopes of high frequency asymptotes are also shown. Source dimensions, seismic moments and stress drops are those calculated from Brune's (1970) model. Data from Trifunac (1972) are also included. The dashed lines indicate how different possible interpretations of spectra from a multiple rupture source yield a range in dimension and stress drop for a given seismic moment.

gation to determine whether or not some of the large variation in reported stress drops and the apparently (incorrect) low stress drops for the mine tremors may be the result of interpreting the radiation from a multiple source in terms of a single-event source model.

Source-spectral relationships. In the frequency domain, all the theories give amplitude spectra which are flat at frequencies lower than a corner frequency, f_0 , and decreases above f_0 as a power of frequency (often f^{-2}). The models relate the physical parameters of the source to the characteristics of the radiated spectrum. For an earthquake of fault area A with average slip \bar{d} in a medium of rigidity μ , the seismic moment M_0 is

$$M_0 = \mu A \bar{d} \quad (1)$$

and

$$M \propto \Omega_0 \quad (2)$$

where Ω_0 is the low frequency level of the far-field displacement amplitude spectrum. The corner frequency is related to the fault dimension by

$$f_0 \propto 1/L \quad (3)$$

If for simplicity we assume complete stress drop, then the stress drop is given by

$$\sigma \propto \mu \bar{d}/L \quad (4)$$

and hence

$$M_0 \propto \sigma AL \quad (5)$$

For a fault which grows symmetrically in two dimensions

$$\begin{aligned} \sigma &\propto M_0 f_0^3 \\ &\propto \Omega_0 f_0^3 \end{aligned} \quad (6)$$

Thus, in principle, determining Ω_0 and f_0 from the far-field spectrum allows an estimate of the stress release.

Numerical models of multiple rupture. We limit our discussion to double events (more complex sources show similar effects) and will assume that both sub-events have the same stress drop. In the time domain, we use a parabolic pulse

(see Snoke, Archambeau's elastodynamical source-model solution, this Report) as a reasonable approximation to the radiation from a single event and scale the height ratio of the pulses to reflect equal stress drops. We normalize our models by taking the seismic moment and total duration of rupture to be constant. If we assume constant rupture velocity, this is equivalent to taking the same-sized fault plane with the same average slip for all cases.

Figure 97 shows the spectrum of a parabolic pulse corresponding to a single rupture. The high-frequency asymptote of the envelope has a slope of f^{-2} , and the intersection of this asymptote with the low-frequency asymptote (zero slope) defines the corner frequency f_0 . Frequency scales for this and subsequent spectra are plotted in units of f_0 .

Equal duration sub-events. Two pairs of equal pulses are shown in Fig. 98. Interference effects at frequencies near f_0 introduce a change in the shape of the spectra from that of the single pulse. Depending on where f_0 lies within the pass-band of the seismograph, it is possible that different corner frequencies could be picked.

The high-frequency asymptote (slope of f^{-2}) gives a corner frequency $f_1 \approx 2f_0$, indicative of the sub-event size rather than of the total rupture dimension. If, however, f_0 is high in the seismograph pass-band, then it is conceivable that a lower slope, high-frequency asymptote would be chosen resulting in an estimate of $f_2 \approx 1/2f_0$. For a given seismic moment we see from Fig. 96, and Equation 6, that using these different values for corner frequency gives stress releases differing by a factor of about 60.

There exists a third possible interpretation of the double pulse spectrum: If f_0 is toward the low-frequency side of the pass-band, the wide interference hole in the amplitude spectrum could give the appearance of spectral peaks.

Nonequal-duration sub-events. For at least some large shallow earthquakes,

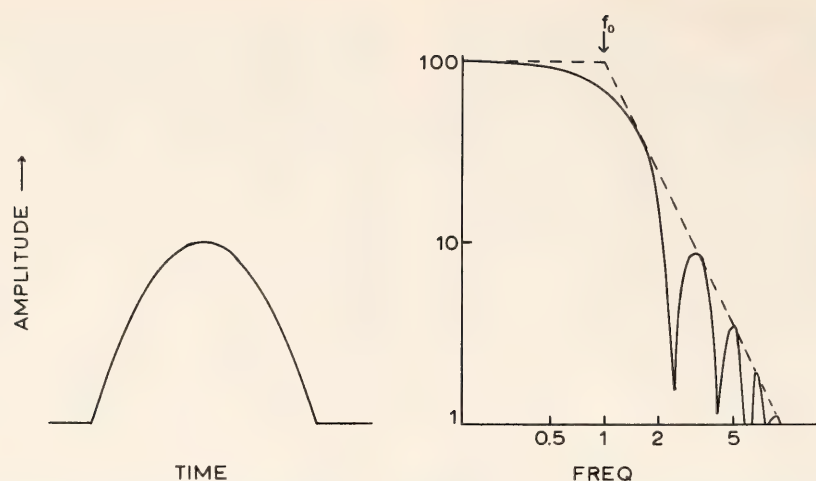


Fig. 97. A single parabolic pulse and its amplitude spectrum. The asymptotes (dashed line) define a corner frequency f_0 .

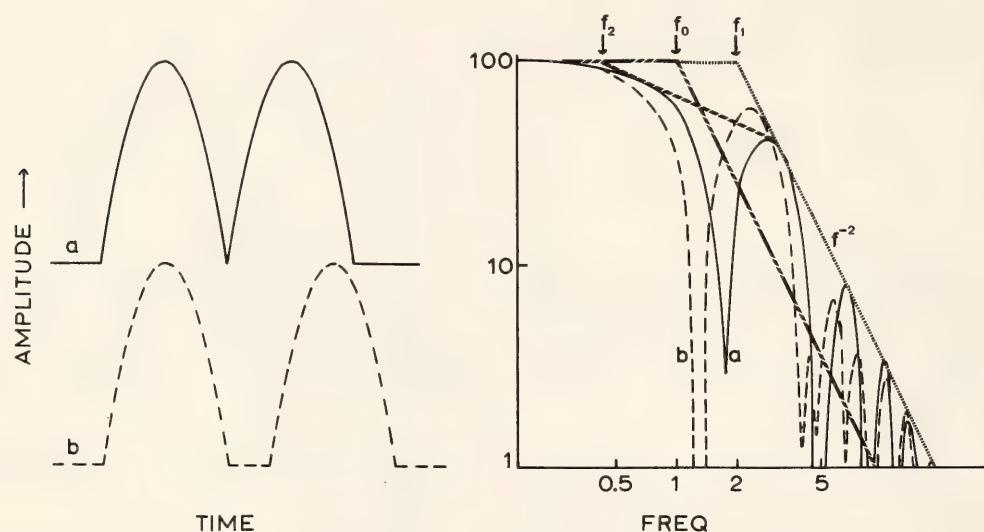


Fig. 98. Equal duration sub-events and their spectra. Asymptotes for the corresponding single pulse (see text) meet at f_0 . The high-frequency asymptote for the double-pulse spectra gives a corner frequency f_1 . The intermediate-slope asymptote defines a corner at f_2 .

later sub-events can be larger than the initial event (e.g., the Alaskan earthquake of 1964, see Wyss and Brune, 1967). In Fig. 99 we consider a simple example of this case. We compare two double ruptures of different duration. The pulse-height ratios for cases *a* and *b* in Fig. 99 reflect equal stress drops for the two sub-events for two different types of rupture growth. In case *a* the width of the two sub-event fault planes is the same, and the pulse height is proportional to the length (i.e., duration). In case *b* both length and width increase (e.g., a circular or elliptical fault), and the pulse height is proportional to the square of the dimension.

Over a wide frequency range, an intermediate slope of f^{-1} exists. Thus, depending on the value of f_0 and the pass-band of the seismograph, different interpretations of the double-event spectra could be made in terms of a simple rupture model. As in the previous example, the calculated stress drops for an earthquake of given seismic moment could therefore vary considerably.

Discussion

We have examined changes in spectral behavior as a result of varying the pulse lengths and heights and also of varying the time between pulses. The spectral effects of multiple events discussed above

hold for a wide range of these parameters but tend to become less obvious as one pulse is made much larger than the other. Similar effects occur if larger numbers of pulses are used to represent a more complex multiple rupture.

This simple numerical study indicates that the occurrence of multiple ruptures may be responsible for several observed effects:

1. The uncertainty and resultant scatter in calculated stress drops is a consequence of the fact that the corner frequency is not a stable indicator of rupture dimensions. This is in accord with the results presented by Tucker and Brune (1973) (see Fig. 96) in that calculations based on spectra with asymptotes of high slope yield high stress drops and vice versa.

2. Aki (1972) has argued that $M_s - M_b$ observations require a significant frequency interval with f^{-1} slope. For many of our numerical models, an intermediate slope of f^{-1} results. This is particularly marked for the models in which, for the sub-events, the length of the rupture increases but the width remains constant.

3. If the sub-events are about equal in size, then it is possible that the observed spectra could be interpreted as having a peak. Such observations have been made (Linde and Sacks, 1972;

Rodriguez and Kisslinger, 1972; Archambeau and Kisslinger, 1974; Bollinger, 1970; Burdick and Helmberger, 1974) but are not compatible with any of the current simple source models, unless rebound occurs on the fault (see Snoke, Archambeau's elastodynamical source-model solution, this Report).

Since the corner frequency-seismic moment method for determining stress drop may result in a wide scatter of results (both higher and lower than actual), we suggest that results should be checked independently by using relationships involving radiated energy. From Aki (1966) we have

$$\sigma \propto E_w / (\eta M_0)$$

where the seismic efficiency

$$\eta = E_w / E_s$$

the ratio of the seismic wave energy to elastic strain energy released. This approach is not a simple one, however. Elastic strain energy release is difficult to estimate for very shallow events, and for deep events the measurement is not feasible. Moreover, measurement of wave energy requires sensing of the radiated field over a wide range of frequencies, and little is known about seismic efficiency. Nevertheless, since efficiency has an upper bound of 1, it is possible to determine a lower limit to the stress

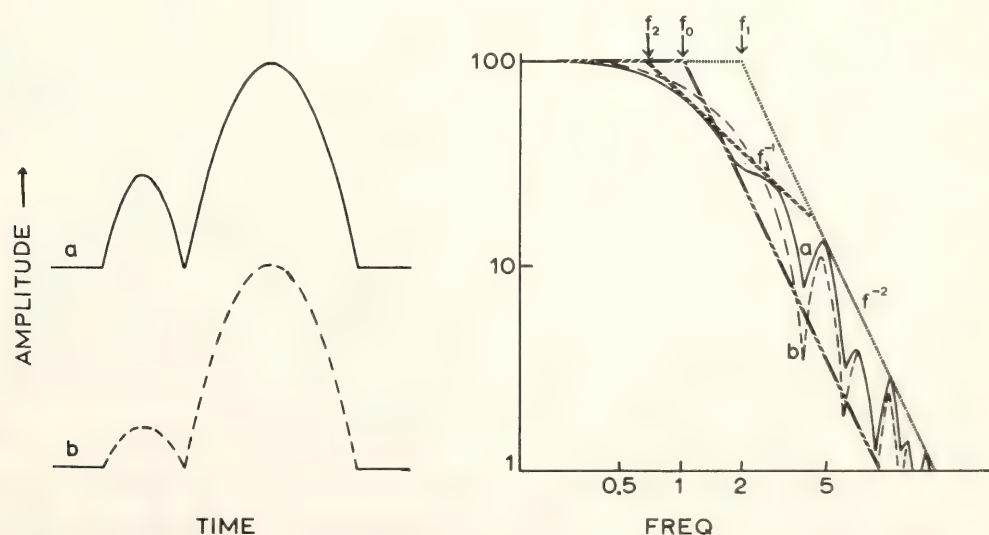


Fig. 99. Nonequal-duration sub-events and their spectra. As in Fig. 98, corners could be pulsed at f_1 and f_2 . The intermediate slope here is f^{-1} .

drop. (The observed corner frequency will depend also on seismic efficiency since efficiency is presumably frequency dependent. This added complication was ignored both in this study and in that of Tucker and Brune.)

The simple models discussed above do not appear to explain the large discrepancies between stress drops determined by spectral means and those calculated from measurements at the fault (Spottiswoode and McGarr, 1975). Nevertheless, the results do indicate that the multiple rupture model should be considered more seriously when attempting to interpret far-field spectral observations in terms of source parameters.

References

- Aki, K., Generation and propagation of G waves from the Niigata earthquake of June 16, 1964, 2, Estimation of earthquake moment, released energy, and stress-strain drop from the G wave spectrum, *Bull. Earthquake Res. Inst. Tokyo Univ.*, 44, 73–88, 1966.
- Aki, K., Scaling law of seismic spectrum, *J. Geophys. Res.*, 72, 1217, 1967.
- Aki, K., Scaling law of earthquake source time-function, *Geophys. J. R. Astron. Soc.*, 31, 3–25, 1972.
- Archambeau, C. B., General theory of elastodynamic source fields, *Rev. Geophys. Space Phys.*, 6, 241–288, 1968.
- Archambeau, C. B., and C. Kisslinger, Investigations of tectonic stress, Semi-annual Technical Report, ARPA Order No. 1795, University of Colorado, 1974.
- Ben-Menahem, A., Radiation of seismic body waves from a finite moving source in the earth, *J. Geophys. Res.*, 67, 345–350, 1962.
- Bollinger, G. A., Fault length and fracture velocity for the Kyushu, Japan earthquake of October 3, 1963, *J. Geophys. Res.*, 75, 955–964, 1970.
- Brune, J. N., Tectonic stress and the spectra of seismic shear waves from earthquakes, *J. Geophys. Res.*, 75, 4997–5009, 1970.
- Brune, J. N., Earthquake modelling by stick-slip along pre-cut surfaces in stressed foam rubber, *Bull. Seismol. Soc. Am.*, 63, 2105–2119, 1973.
- Burdick, L. J., and D. V. Helmberger, Time functions appropriate for deep earthquakes, *Bull. Seismol. Soc. Am.*, 64, 1419–1428, 1974.
- Gupta, H. K., B. K. Rastogi, and H. Narain, The Koyna earthquake of December 10, 1967: a multiple seismic event, *Bull. Seismol. Soc. Am.*, 61, 167–176, 1971.
- Haskell, N. A., Total energy and energy spectral density of elastic wave radiation from propagating faults, *Bull. Seismol. Soc. Am.*, 54, 1811–1841, 1964.
- Linde, A. T., and I. S. Sacks, Dimensions, energy, and stress release for South American deep earthquakes, *J. Geophys. Res.*, 77, 1439–1451, 1972.
- Rodriguez, R., and C. Kisslinger, Spectral classification of New Madrid earthquakes, *Trans. Am. Geophys. Union*, 53, 450, 1972.
- Spottiswoode, S. M., and A. McGarr, Source parameters of tremors in a deep-level gold mine, *Bull. Seismol. Soc. Am.*, 65, 93–112, 1975.
- Trifunac, M. D., Stress estimates for the San Fernando, California, earthquake of February 9, 1971: main event and thirteen aftershocks, *Bull. Seismol. Soc. Am.*, 62, 721–750, 1972.
- Trifunac, M. D., and J. N. Brune, Complexity of energy release during the Imperial Valley, California, earthquake of 1940, *Bull. Seismol. Soc. Am.*, 60, 137–160, 1970.
- Tucker, B. E., and J. N. Brune, Seismograms, S-wave spectra, and source parameters for aftershocks of San Fernando, California, earthquake of February 9, 1971. *Geological and Geophysical Studies*, Vol. III, pp. 69–121, U.S. Dept. of Commerce, 1973.
- Wyss, M., and J. N. Brune, The Alaskan earthquake of 28 March 1964; a complex multiple structure, *Bull. Seismol. Soc. Am.*, 57, 1017–1023, 1967.

BOREHOLE STRAINMETERS: LONG-TERM STABILITY AND SENSITIVITY TO DILATANCY

*I. S. Sacks, J. A. Snoke, Y. Yamagishi,
and S. Suyehiro*

Introduction

The performance of the borehole strainmeters that are operating in a seismically active region near Matsushiro, Japan, has been evaluated in a number of previous studies. The fidelity of the instrument when exposed to high acceleration such as might be expected from strong local earthquakes has been tested by Sacks *et al.* (1971a). The response of the strainmeter and its local environment to atmospheric pressure fluctuations has been studied by Sacks and Evertson (1970) and by Sacks *et al.* (1971b). The sensitivity of strainmeters to rainfall and pressure changes in the aquifer has been determined by Sacks (1974).

Long-Term Stability

In this report we consider the long-term stability of the borehole strain-

meter and the implications for detection of precursory dilatancy. There are three strain-measuring instruments operating at the Matsushiro Seismological Observatory. Two borehole volume strainmeters, 300 m apart, are situated about 250 m from a pair of 100-m-long quartz bar horizontal extensometers with N-S and E-W orientations. Figure 100 is a plan showing the locations of the various instruments.

The borehole strainmeters are dilatometers. Using the fact that the extensometers are installed at a free surface, the equivalent dilatant (volume) strain can be calculated from the data of the two horizontal extensometers. The result is $\theta_{\text{extensometers}} = [(1 - 2\sigma)/(1 - \sigma)] (\epsilon_{\text{NS}} + \epsilon_{\text{EW}})$ where ϵ_{NS} and ϵ_{EW} are the strains measured by the two horizontal extensometers and σ is Poisson's ratio. Poisson's ratio for the Matsushiro region is not known, but must lie in the usual range of 0.25 to 0.3. $(1 - 2\sigma)/(1 - \sigma)$ is then in the range 0.66 to 0.57.

Figure 101 shows the secular strain results from the two borehole strainmeters, and the extensometers calculated for Poisson's ratio = 0.25. The three

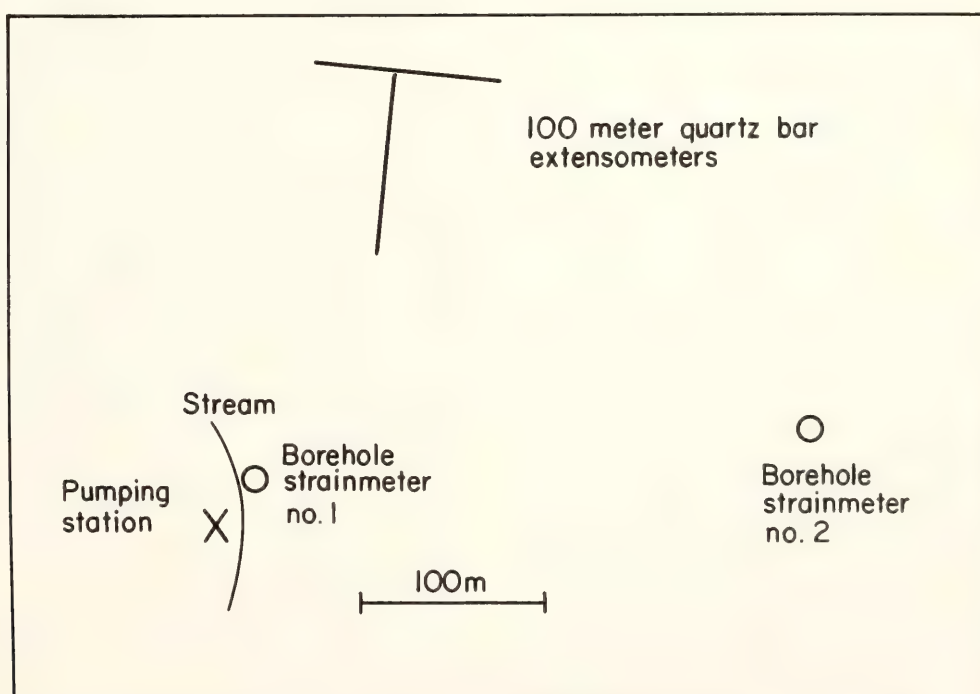


Fig. 100. Map of the Matsushiro Seismological Observatory area showing the location of the two borehole strainmeters and the 100-m quartz-bar extensometers.

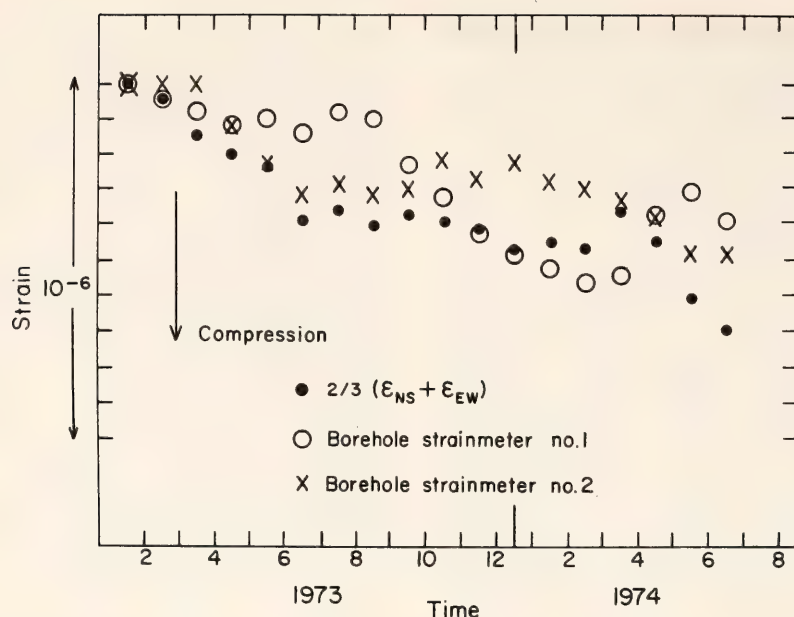


Fig. 101. Secular dilatant strain in the Matsushiro (swarm) region measured by three independent instruments located as shown in Fig. 100.

data sets agree moderately well and indicate a compressional volume strain rate of about $0.4 \times 10^{-7}/\text{year}$. The borehole instruments give values of about $0.36 \times 10^{-7}/\text{year}$ and the extensometers give $0.48 \times 10^{-7}/\text{year}$ ($\sigma = 0.25$) or $0.41 \times 10^{-7}/\text{year}$ ($\sigma = 0.3$). Based on the extensometer data, the mean dilatant strain rate since April 1968 has been 0.66×10^{-6} per year. This strain rate is consistent with geodetic observations which show that the horizontal strain in the region of the Matsushiro earthquake swarm reached 3.7×10^{-4} (extension) at the swarm's peak in October 1966 and has been decreasing since then (Kasahara *et al.*, 1967).

The intrinsic long-term noise of the strainmeters can be estimated from how well the instruments track. If one corrects for the differences in secular strain (Fig. 101), instrument 2 and the extensometers differ by less than 10^{-7} in the monthly readings with a mean difference of 0.5×10^{-7} . The mean difference between the monthly readings of borehole strainmeter 1 and the extensometers is 1.3×10^{-7} . Instrument 1 showed very much higher noise than 2 at periods of $1/2$ to 2 hours (Sacks, 1974), possibly due

to its proximity to an automatic pumping station. This noise was assumed to be due to fluctuations in the aquifer since that has been found to influence the local strain field very strongly.

Response to Dilatancy

According to the dilatancy model (see Nur, 1972), preceding an earthquake there is a change in volume in the region in which an earthquake will occur. It is of interest to know how the borehole strainmeters (which act as dilatometers) will react to such slow volume changes at some distance from the source region. We will approximate the dilatancy by assuming a point source of expansion which is constant in time. (The strainmeter is assumed to be outside the source region.) The solutions for both an infinite space and a half-space can be obtained from Cagniard (1962, Ch. 8).

For an infinite space the displacement due to a point source of expansion at $z = h$ and $\rho = 0$ (in cylindrical coordinates) is given by

$$\vec{u}^a = \frac{\delta V}{R^3} (\rho \hat{\rho} + (z - h) \hat{z}) \quad (1)$$

where $\rho^2 = x^2 + y^2$, $R^2 = \rho^2 + (z - h)^2$ and δV is the total volume change of any

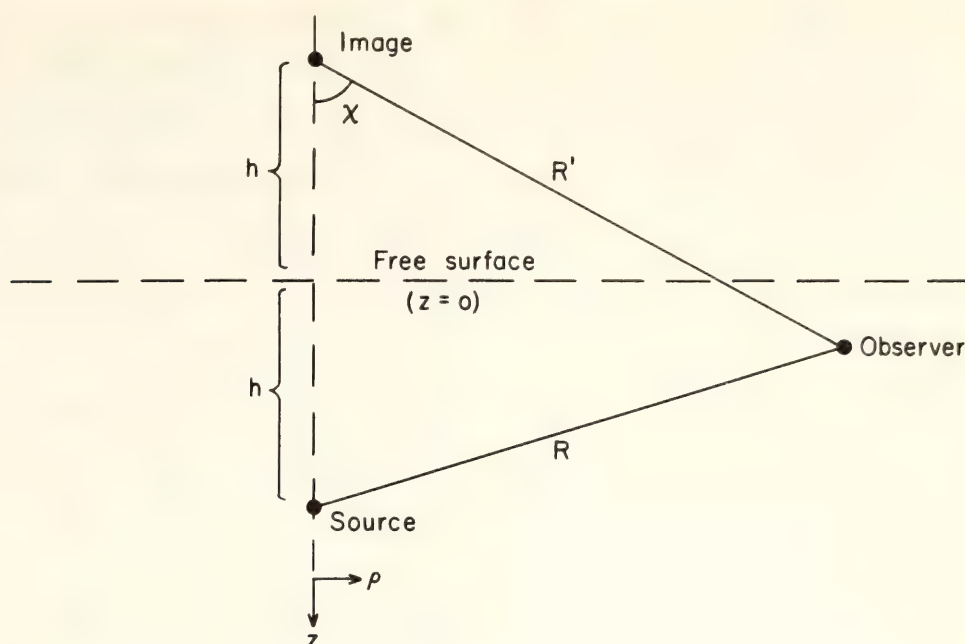


Fig. 102. Geometry for a dilatation point source in a half-space bounded by a free surface. The source is at $z = h$ and $\rho = 0$.

volume including the source point $R = 0$ (see Fig. 102). The dilatation $\theta = \vec{\nabla} \cdot \vec{u}$ is zero for $R \neq 0$. Hence, strainmeters outside the source region would not be affected by a dilatation source.

The strainmeters, however, are not imbedded in an infinite space but, to a good approximation, are at the free surface of a half-space. Although Cagniard has solved this problem, his solution is obtained by taking the static limit of a dynamic problem. We will outline here a more direct derivation.

The displacement \vec{u} can be written as $\vec{u} = \vec{u}^a + \vec{u}^b$ where \vec{u}^a is given above by Equation 1 and \vec{u}^b is the solution of the homogeneous Navier equation so that the normal stresses derived from \vec{u} are zero at $z = 0$. That is,

$$(\lambda + 2\mu)\vec{\nabla}(\vec{\nabla} \cdot \vec{u}^b) - \mu\vec{\nabla} \times (\vec{\nabla} \times \vec{u}^b) = 0 \quad z \geq 0 \quad (2)$$

and

$$\begin{aligned} 0 = \sigma_{zz} &= \lambda \vec{\nabla} \cdot \vec{u} + 2\mu \partial u_z / \partial z \\ 0 = \sigma_{z\rho} &= \mu (\partial u_z / \partial \rho + \partial u_\rho / \partial z) \end{aligned} \quad z = 0 \quad (3)$$

where λ and μ are the Lamé coefficients. A general representation of \vec{u}^b satisfying

Equation 2 is the Papkovitch-Neuber representation (see Sokolnikoff, 1956, Ch. 6)

$$\vec{u}^b = (\vec{\Phi} - \vec{\nabla}(\Phi_0 + \frac{1}{2}\alpha \vec{r} \cdot \vec{\Phi})) / \mu \quad (4)$$

where $\alpha = (\lambda + \mu) / (\lambda + 2\mu)$ and

$$\Delta^2 \Phi_\nu = 0 \quad \nu = 0, 1, 2, 3. \quad (5)$$

By symmetry the Φ_ν (and \vec{u}^b) can be thought of as resulting from a point force at the image source point $\rho = 0$, $z = -h$ (see Fig. 102). Hence a useful representation for the Φ_ν satisfying Equation 5 is

$$\Phi = \sum_{l=0}^{\infty} B_{\nu l} P_l(\cos \chi) / R'^{l+1} \quad (6)$$

where $R'^2 = \rho^2 + (z + h)^2$ and $\cos \chi = (z + h) / R'$. We have assumed that $\Phi_\nu \rightarrow 0$ as $R' \rightarrow \infty$. The solution is obtained by substituting Equation 6 into Equation 4 and applying the boundary conditions Equation 3. One finds, then, that

$$\Phi_0 = \frac{3\mu + \lambda}{\lambda + \mu} \frac{\mu \delta V}{4\pi R'}, \quad \vec{\Phi} = \frac{-\mu \delta V \cos \chi \hat{z}}{\pi \alpha R'^2} \quad (7)$$

which results in a dilatancy of

$$\begin{aligned}
 \theta &= \vec{\nabla} \cdot \mathbf{u} \\
 &= \vec{\nabla} \cdot \mathbf{u}^b \\
 &= \vec{\nabla} \cdot \vec{\Phi} / (\lambda + 2\mu) \\
 &= - \frac{\mu \delta V}{\lambda + \mu} \frac{1 - 3 \cos^2 \chi}{\pi R'^3} \quad (8)
 \end{aligned}$$

At the surface ($z = 0$) for $\lambda = \mu$ Equation 8 reduces to

$$\theta = \frac{\delta V}{2\pi[\rho^2 + h^2]^{3/2}} \{1 - 3h^2/(\rho^2 + h^2)\} \quad (9)$$

We assume that there is a spherical dilatant region enclosing the eventual fault such that the radius h is one-half the fault length, and that the dilatation is uniform, centered at $R = 0$ and of value 10^{-5} . This is equivalent to a point source dilatancy of strength $\delta V = 4/3 \pi h^3 \times 10^{-5}$. Equation 9 becomes

$$\begin{aligned}
 \theta &= - \frac{2}{3} \times 10^{-5} \\
 &\times [h/\sqrt{\rho^2 + h^2}]^3 \{1 - 3h^2/(\rho^2 + h^2)\}. \quad (10)
 \end{aligned}$$

Figure 103 gives the threshold strains

(θ) based on Equation 10 as functions of epicentral distance (ρ) and fault length ($2h$) of the earthquake for which the dilatancy was a precursor. Also included are the magnitudes corresponding to fault lengths. For magnitudes below 5 the relationship is the appropriate one for the Matsushiro region ($m = 3.47 + 1.90 \log_{10} 2h$) and the relationships for magnitudes above $6\frac{1}{2}$ are due to Iida (1965). (That relationships applicable to small and large earthquakes do not extrapolate into each other was pointed out by Chinnery, 1969.)

From Fig. 103 for a fault length of 20 km (nominally a magnitude 7 earthquake) a dilatancy of 10^{-5} can be detected at about 40 km from the center of dilatancy by a strainmeter array of the type described above for a detection threshold of 10^{-7} .

The precursory dilatation detection threshold is a function of the instrument noise level, the amount of dilatancy, and the size of the dilatant region. For the

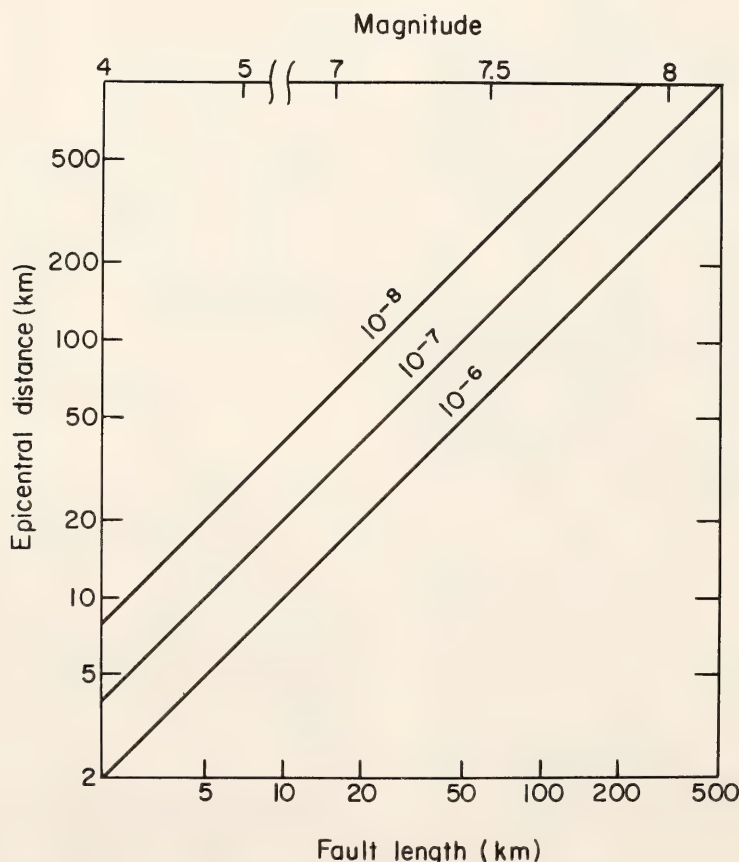


Fig. 103. The maximum distance at which a precursory dilatant strain of 10^{-5} would be detectable for noise thresholds of 10^{-6} , 10^{-7} , and 10^{-8} for various fault lengths and magnitudes.

instruments discussed, the threshold is about 10^{-7} . However, this threshold could probably be improved significantly by installing the strainmeters at greater depths and thus reducing aquifer effects. The amount of dilatancy is generally taken to be at least 10^{-5} . The dilatant region must be at least the size of the earthquake but the large deviations in V_P/V_S reported by various workers suggest an even larger dilatant region. The detection distances given in Fig. 103 therefore are probably minimum values.

References

- Cagniard, L., *Reflection and Refraction of Progressive Seismic Waves* (translated and revised by E. A. Flinn and C. H. Hewitt Dix), McGraw-Hill, New York, 1962.
- Chinnery, M. A., Earthquake magnitude and source parameters, *Bull. Seismol. Soc. Am.*, 59, no. 5, 1969–1982, 1969.
- Iida, K., Earthquake magnitude, earthquake fault, and source dimensions, *J. Earth Sci., Nagoya Univ.*, 13, 115–132, 1965.
- Kasahara, A., A. Okada, M. Shibano, K. Sasaki, and S. Matsumoto, Electro-optical measurement of horizontal strains accumulating in the swarm earthquake area (3), *Bull. Earthquake Res. Inst.*, 45, 159–288, 1967.
- Nur, A., Dilatancy, pore fluids, and premonitory variations of t_s/t_p travel times, *Bull. Seismol. Soc. Am.*, 62, 1217–1222, 1972.
- Sacks, I. S., Strainmeters: long period noise, in *Carnegie Inst. Wash. Year Book 73*, pp. 1058–1060, 1974.
- Sacks, I. S., and D. W. Evertson, A sensitive borehole strain-rate meter, in *Carnegie Inst. Wash. Year Book 68*, pp. 448–452, 1970.
- Sacks, I. S., S. Suyehiro, D. W. Evertson, and Y. Yamagishi, Sacks-Evertson strainmeter, its installation in Japan and some preliminary results concerning strain steps, *Pap. Meteorol. Geophys.*, 22, Nos. 3–4, 105–203, 1971a.
- Sacks, I. S., D. W. Evertson, and L. M. Dorman, Borehole strainmeters, in *Carnegie Inst. Wash. Year Book 69*, pp. 426–430, 1971b.
- Sokolnikoff, I. S., *Mathematical Theory of Elasticity*, 2nd ed., McGraw-Hill, 1956.

ELECTRICAL CONDUCTIVITY STUDIES IN SOUTH AMERICA

L. T. Aldrich and colleagues

Among the continuing geophysical studies of the interaction of the Nazca plate and the South American continent are those of the lateral variation in the radial structure of the electrical conductivity. These studies were initiated a dozen years ago under the direction of Dr. Ulrich Schmucker. With the collaboration of several South American colleagues, Schmucker showed (*Year Book 66*, p. 12) the evidence for a most unusual structure whose minimum depth followed the eastern Andean cordillera from northern Peru to central Bolivia. With continuing support from the National Science Foundation these collaborative studies have continued in Peru and Bolivia and in 1972 were extended to central Argentina and Chile. As this report is written a further extension of the observations into the region of Colombia, studied seismically in Project Nariño during 1973, has been arranged.

Argentina-central Chile with M. Casaverde, J. R. Bannister, and L. Beach. Last year's Report (*Year Book 73*, p. 1018) showed unusual areal distribution of the H - Z transfer functions (TFs) in this region. The long-period (one hour) TFs were small and uniform over the whole region for two night-time variations. The short-period (15 minute) TFs showed a pattern of areal variation parallel and adjacent to the coast line. Since the discontinuity of the oceanic conductivity is parallel to the direction of magnetic field variation for those events, the explanation for the pattern is not obvious. A third magnetic storm with a large component normal to the coast line now provides further in-

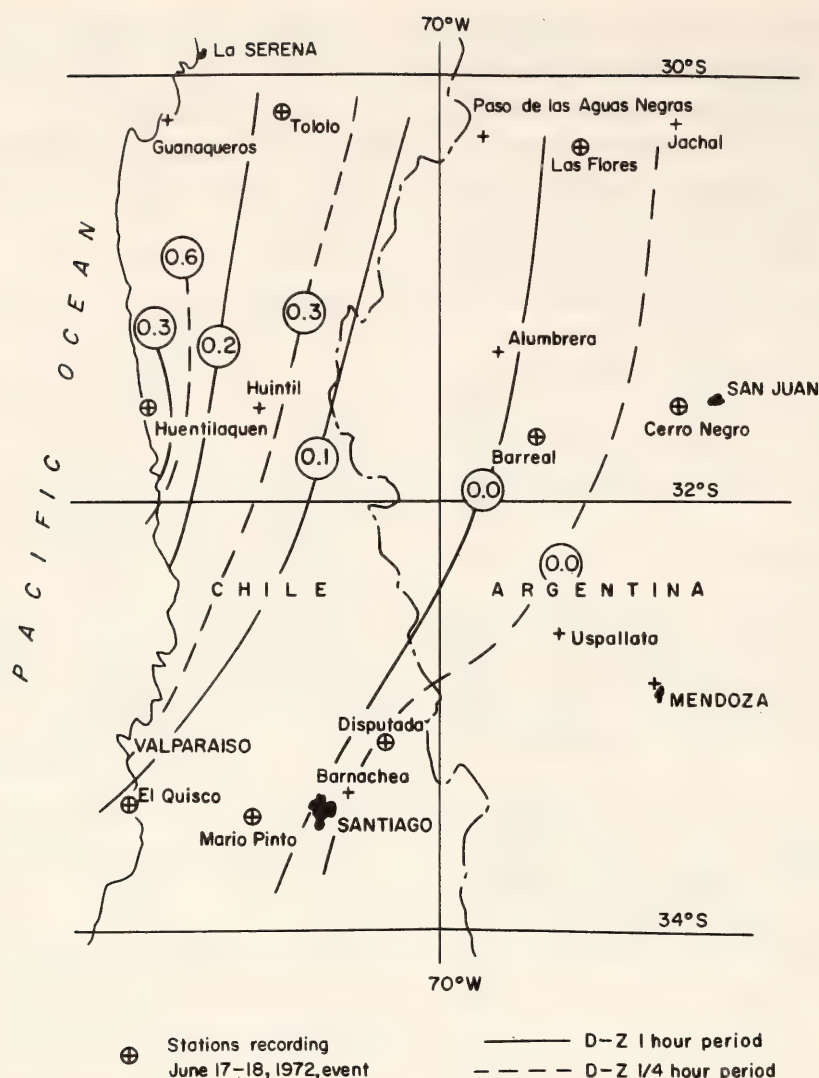


Fig. 104. Areal variation of the $D-Z$ transfer functions for a magnetic storm June 17-18, 1972. The patterns for periods of 15 minutes and one hour are the same, but the absolute magnitude differs by a factor of 2.

sight into the conductivity structure of the region. These results are shown in Fig. 104 with the contours for TFs of one-hour period nearly parallel to those of 15-minute period. These results indicate a conductivity anomaly with a N-S orientation in the ocean west of the array of stations. A similar result was obtained by Schmucker off the coast of southern California in 1960 (Schmucker, 1970). An uplift of the deep conductivity surface of the order of 100 km is implied by these results.

Chile-Bolivia with J. R. Bannister, S. del Pozo, R. Salgueiro, and L. Beach. Measurements completed in Chile and Bolivia in previous years have been combined to produce the profile shown in Fig. 105. This figure shows the geo-

graphic location of the stations studied and the profiles at both one-hour and one-quarter hour periods. There are only slight differences in the patterns, and the result implies a complex conductivity structure. There appears to be an uplift in the conductivity structure in the region of, and at some angle to, the western cordillera, and another east of Tarija. The angle is required since the cordillera is parallel to the magnetic field variation for the events studied. It is also possible that the complexity of the profile is due to the return current paths of the eddy currents generated in the anomaly present in southern Peru. In any case, there appears to be a profound difference in the results obtained from the stations in northern Chile and



Fig. 105. Profile showing variation of the H - Z transfer functions for periods of 15 minutes and one hour in the region of 22°S latitude. The pattern for the two periods is identical in form and magnitude.

those 1000 km to the south, and the need for further observations to clarify the structure of the electrical conductivity in these regions is demonstrated.

Several additional sites near the Cochabamba anomaly have been occupied, and others will be added during the coming field season to outline better this unusual structure.

Southern Peru with M. Casaverde, L. Tamayo, and A. Rodriguez. Data from six additional stations in southern Peru were obtained and, based on those data, additional sites in southern Peru will be occupied during the coming field season.

Reference

Schmucker, U., Anomalies of geomagnetic variations in the southwestern United States, *Bull. Scripps Inst. Oceanogr.*, 13, 1970.

LOCAL SEISMIC NET IN SOUTHERN PERU

A. Rodriguez and L. T. Aldrich

The seismic network in southern Peru is currently recording at all eight stations with revised systems which permit operation at reduced power. In addition to operation of the station network, the Geophysical Institute of San Agustín National University is completing the reading of the 1969 data. It is hoped that the data reduction will be up-to-date by the end of the period of operation of these stations. Because of previous commitments, Dr. Asada will be unable to install his ocean-bottom seismometers until April 1976. It is our hope that the Arequipa net supported by the A. L. Day Fund and those supported by the H. O. Wood Fund will be able to operate concurrently, thereby providing the same kind of total coverage described last year. The new data will provide information on earthquake distribution in both time and space over the last ten years.

COSMIC RAY RESEARCH

S. E. Forbush and L. Beach

Cosmic-ray diurnal anisotropy 1937-1974 and the reversals of the sun's poloidal magnetic field. The Annual Report for 1971-1972 (*Year Book 71*) contained a discussion of the variation, from 1937 to 1971, of the components of V and W of the cosmic-ray diurnal anisotropy obtained from Carnegie Institution of Washington ionization chambers at Huancayo (Peru), Cheltenham-Fredericksburg (U.S.A.), and Christchurch (New Zealand). Observations, first by Babcock (1959) and later by Howard (1972), at Mount Wilson Observatory since about 1953 show that the north polar magnetic field of the sun changed from positive to negative in 1958 and from negative to positive in 1971. These reversals coincided with the reversals in the component W of the cosmic-ray diurnal anisotropy in the asymptotic di-

rection 128° east of the sun. This reversal of W in 1971 now seems well established by the results, derived from observation through 1974, shown in Fig. 106. The yearly values of the component V (not shown), with maximum in the asymptotic direction 90° east of the sun, are correlated with $U_0(A)$ ($r = 0.75$) and exhibit a variation, analogous to that in sunspot numbers, with a range in each solar cycle of roughly 12%. $W_0(A)$ is the yearly mean value of the southward horizontal magnetic field at the geomagnetic equator. $U_0(A)$ is obtained quite simply from the empirical relation $U_0(A) = - [H(A - Q)_s - 0.68 H(D - Q)_s] / \cos \Phi$, in which the first term on the right is the difference in the horizontal magnetic component for all days and the five magnetically quiet days at station s , and the second is the difference, disturbed minus quiet days. Φ is the geomagnetic latitude of station s . The amplitude of W_s , about 0.07%, is only about one-tenth of the standard deviation of hourly values at one station, which indicates one reason why the reliable determination of W_s required data from three stations over several

decades. This reduces the standard deviation of the departures of open circles from the wave W_s in Fig. 106 to about 0.018%. That for the departures of the open squares from W_G (*re*, after 1966) is probably not much greater.

When the cosmic-ray program was initiated in the early 1930's by the Carnegie Institution of Washington Committee for Coordination of Cosmic Research, it was anticipated that by analysis of variations of cosmic-ray intensity from improved ionization chambers some evidence might be obtained to indicate the source of cosmic rays. From analyses of the data obtained in the program carried out at the Department of Terrestrial Magnetism, all the variations (except the troublesome ones due to meteorological causes) are due to solar mechanisms. The last of these variations to be reliably demonstrated is that discussed above and shown in Fig. 106. This could have been derived only from an observational program of several decades' duration at several stations. This variation must arise from some mechanism involving the long period variation (double the sunspot cycle

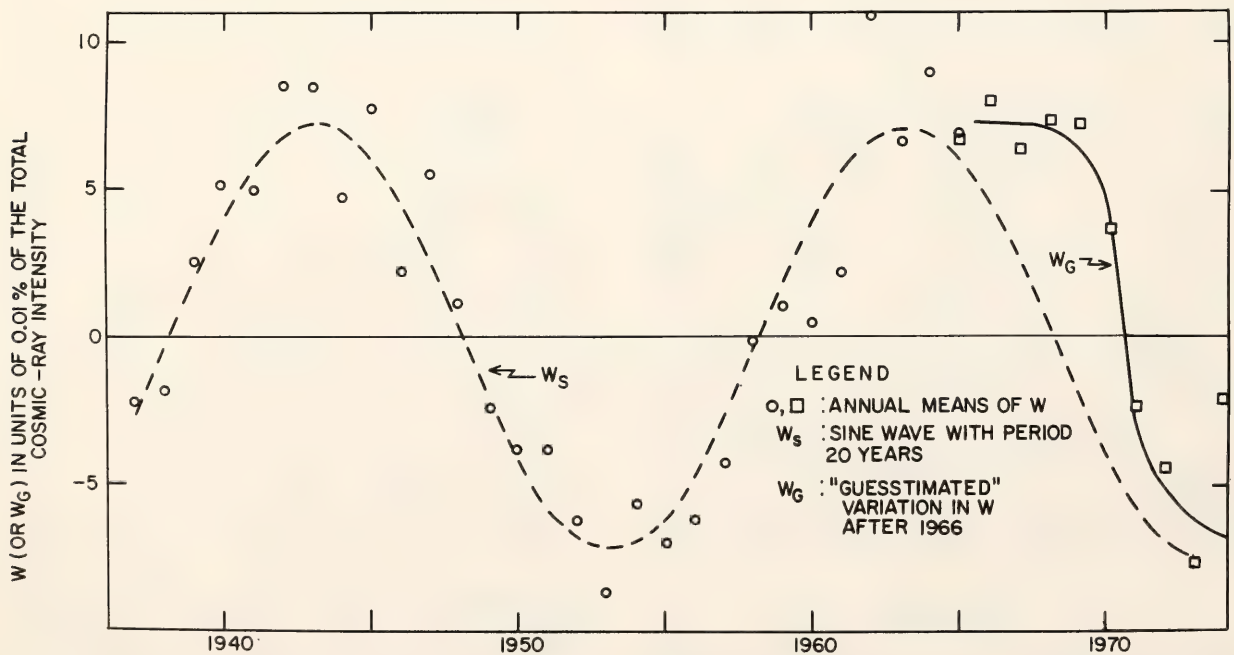


Fig. 106. Annual means of the diurnal anisotropy component in the asymptotic direction 128° east of the sun fitted by a sine wave W_s from 1937 to 1965 and by an estimated wave W_G from 1966 to 1974. Measurements at Mount Wilson of the sun's north polar magnetic field showed that it reversed in 1958 and in 1971, as did W_s and W_G .

variation) in the sun's general magnetic field, although the solar field is much too weak to effect a magnetic cutoff at the earth (analogous to the geomagnetic cutoff near the earth due to the earth's magnetic field).

Variability of cosmic-ray daily means over nearly four solar cycles. Figure 107 shows the values, 1937–1974, of the yearly pooled standard deviation of cosmic-ray daily means from monthly means at Huancayo, Peru. Values are also shown with the five magnetically disturbed days of each month omitted. These standard deviations are generally only slightly less than those for all days, even though most of the large decreases of cosmic-ray intensity (Forbush effects) occur only during magnetic storms. Figure 106 compares the variation of the yearly pooled standard deviations with that in yearly sunspot numbers. This shows the marked differences in different solar cycles of maximum sunspot numbers and of the standard deviations. Similar variability is well known in geomagnetic activity.

Observations and reduction of data. Cosmic-ray ionization chambers were operated throughout the report year at Huancayo, Peru; at Fredericksburg, Vir-

ginia, U.S.A.; and at Christchurch, New Zealand. Scalings and reduction of records have been maintained for these three stations. The reductions have been greatly facilitated by the use of the IBM 1130 computer.

Cooperation in operation of cosmic-ray meters. Appreciation is expressed to the U.S. Geological Survey and the U.S. Department of the Interior and its staff at the Fredericksburg Geomagnetic Center for efficient operation of the cosmic-ray meter there during the past report year, and to the Government of Peru and the Director and staff of the Instituto Geofísico del Peru for making cosmic-ray records from Huancayo available. Appreciation is also expressed to the Director and staff of the Geophysical Observatory at Christchurch, New Zealand, for the excellent maintenance of the equipment there and for the fine records obtained.

References

Babcock, H. W., The sun's polar magnetic field, *Astrophys. J.*, 130, 364, 1959.
Howard, R., Polar magnetic fields of the sun: 1960–1971, *Solar Phys.*, 25, 5, 1972.

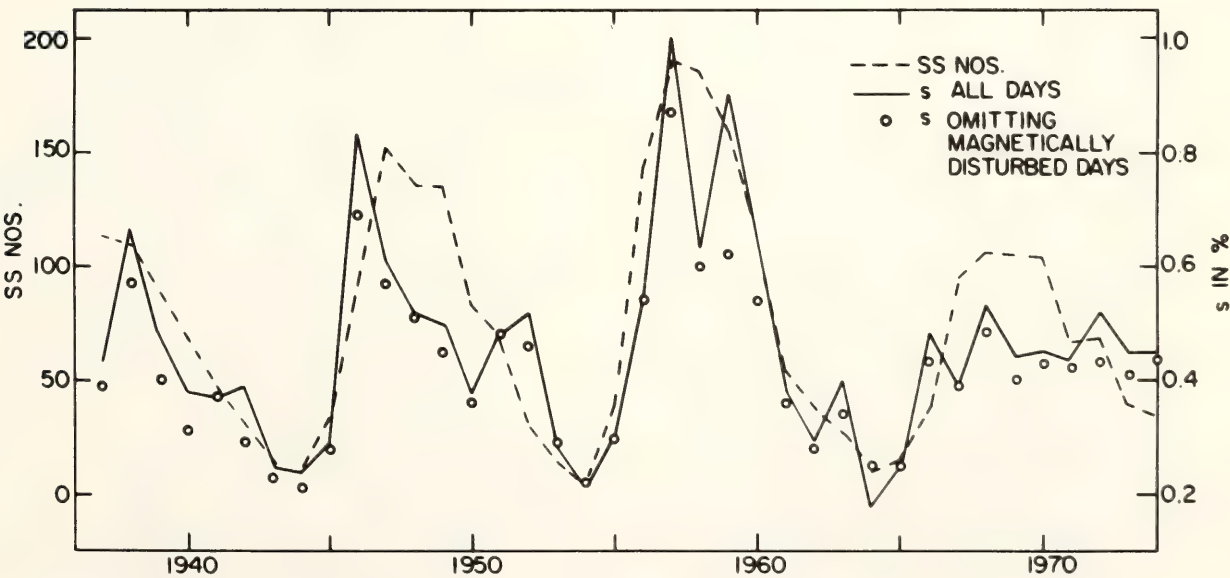


Fig. 107. Yearly pooled standard deviations of cosmic-ray daily means from monthly means at Huancayo, Peru.

BIBLIOGRAPHY

Publications listed below can be obtained at no charge from the Department of Terrestrial Magnetism, 5241 Broad Branch Rd., N.W., Washington, D.C. 20015. When ordering, please give reprint number(s). Titles marked with asterisks are out of print.

- *4361 Aldrich, L. T., Report of the Treasurer, *Trans. Am. Geophys. Union*, 56, 307, 1975.
- Andersen, C. A., *see* Hofmann, A. W.
- *4362 Arnold, L. G., R. G. Seyler, L. Brown, T. I. Bonner, and E. Steiner, 2⁺ threshold state in ⁸Be, *Phys. Rev. Lett.*, 32, 895–898, 1974.
- *4363 Arnold, L. G., R. G. Seyler, T. R. Donoghue, L. Brown, and U. Rohrer, Difference between polarization and analyzing power in the reaction ³H(p,n)³He, *Phys. Rev. Lett.*, 32, 310–313, 1974.
- Assousa, G. E., *see* Thonnard, N., and Warner, J. W.
- Balick, B., *see* Warner, J. W.
- Beach, L., *see* Sacks, I. S.
- Bonner, T. I., *see* Arnold, L. G.
- 4364 Brooks, C., and S. R. Hart, On the significance of komatiite, *Geology*, 2, 107–110, 1974.
- Brooks, C., *see* Hart, S. R., and James, D. E.
- 4365 Brown, L., and U. Rohrer, ³H(p,n)³He reaction with polarized protons from threshold to 2.9 MeV, *Nucl. Phys.*, A221, 325–332, 1974.
- *4366 Brown, L., N. Thonnard, and C. K. Kumar, The Z-dependence of vacancy production in asymmetric heavy ion collisions (abstr.), *Bull. Am. Phys. Soc.*, 20, 639, 1975.
- Brown, L., *see* Arnold, L. G., Rohrer, U., and Thonnard, N.
- Cohen, G. N., *see* Costrejean, J.-M.
- Comaford, D., *see* Hofmann, A. W.
- 4367 Costrejean, J.-M., N. Guiso, D. B. Cowie, G. N. Cohen, and P. Truffa-Bachi, The threonine-sensitive homoserine dehydrogenase and aspartokinase activities of *Escherichia coli* K 12, *Eur. J. Biochem.*, 50, 431–435, 1975.
- 4368 Cowie, D. B., Genetic interrelationships among the T-even bacteriophages, *J. Franklin Inst.*, 298, 4, 1974.
- Cowie, D. B., *see* Costrejean, J.-M.
- 4369 Cowley, A., R. Humphreys, B. Lynds, and V. Rubin, Report to the Council of the AAS from the Working Group on the Status of Women in Astronomy—1973, *Bull. Am. Astron. Soc.*, 6, 412–423, 1974.
- Craine, E. R., *see* Warner, J. W.
- Cuyubamba, A., *see* James, D. E.
- *4370 Dodson, M. H., Diffusion effects of a thermal pulse (abstr.), *Trans. Am. Geophys. Union*, 56, 472, 1975.
- Donoghue, T. R., *see* Arnold, L. G.
- Duggan, J. L., *see* McDaniel, F. D.
- Erlank, A. J., *see* Hart, S. R.
- 4371 Fletcher, R. C., Wavelength selection in the folding of a single layer with power-law rheology, *Am. J. Sci.*, 274, 1029–1043, 1974.
- 4372 Fletcher, R. C., and A. W. Hofmann, Simple models of diffusion and combined diffusion-infiltration metasomatism, in *Geochemical Transport and Kinetics*, A. W. Hofmann, B. J. Giletti, H. S. Yoder, Jr., and R. A. Yund, eds., *CIW Publ. 634*, pp. 243–259, 1974.
- 4373 Fletcher, R. C., and R. H. McCallister, Spinoidal decomposition as a possible mechanism in clinopyroxene exsolution (abstr.), *Trans. Am. Geophys. Union*, 55, 468, 1974.
- Gardner, R. K., *see* McDaniel, F. D.
- Giletti, B. J., *see* Hofmann, A. W.
- Gladwin, M. T., *see* Stacey, F. D.
- Goldich, S. S., *see* Hart, S. R.
- *4374 Grauert, B., Interpretation of Rb-Sr data of small whole-rock slabs and their minerals from the Manhattan schist, New York (abstr.), International Meeting for Geochronology. Cosmochemistry, and Isotope Geology, Paris, France, August 26–31, 1974.
- 4375 Grauert, B., U-Pb systematics in heterogeneous zircon populations from the Precambrian basement of the Maryland Piedmont, *Earth Planet. Sci. Lett.*, 23, 238–248, 1974.
- 4376 Grauert, B., M. G. Seitz, and G. Soptrajanova, Uranium and lead gain of detrital zircon studied by isotopic analyses and fission-track mapping, *Earth Planet. Sci. Lett.*, 21, 389–399, 1974.
- 4377 Grauert, B., and M. E. Wagner, Age of the granulite-facies metamorphism of the Wilmington Complex, Delaware-Pennsylvania Piedmont, *Am. J. Sci.*, 275, 683–691, 1975.
- Grauert, B., *see* Hännny, R.
- Gray, T. J., *see* McDaniel, F. D.
- Guiso, N., *see* Costrejean, J.-M.
- *4378 Hännny, R., B. Grauert, and G. Soptrajanova, Paleozoic migmatites in an area of high-grade Miocene metamorphism, Lepontinic gneiss complex, central Alps (abstr.), Interna-

- tional Meeting for Geochronology, Cosmochemistry, and Isotope Geology, Paris, France, August 26-31, 1974.
- *4379 Hart, S. R., LIL-element geochemistry, Leg 34 basalts (abstr.), *Geol. Soc. Am. Abstr. with Prog.*, 87th Annual Meeting, Miami Beach, Fla., p. 780, Nov. 18-20, 1974.
- 4380 Hart, S. R., and C. Brooks, Clinopyroxene-matrix partitioning of K, Rb, Cs, Sr, and Ba, *Geochim. Cosmochim. Acta*, 38, 1799-1806, 1974.
- *4381 Hart, S. R., A. J. Erlank, and E. J. D. Kable, Sea floor basalt alteration: some chemical and Sr isotopic effects, *Contrib. Mineral. Petrol.*, 44, 219-230, 1974.
- *4382 Hart, S. R., and S. S. Goldich, Most ancient known rocks may be found in all earth's Precambrian shields, *Geotimes*, 20, 22-24, 1975.
- Hart, S. R., see Brooks, C., and White, W. M.
- Hastie, L. M., see Stacey, F. D.
- Hinthorne, J. R., see Hofmann, A. W.
- *4383 Hofmann, A. W., Diffusion of Sr and Ca in basalt melt (abstr.), *Trans. Am. Geophys. Union*, 56, 472, 1975.
- 4384 Hofmann, A. W., B. J. Giletti, J. R. Hinthorne, C. A. Andersen, and D. Comaford, Ion microprobe analysis of a potassium self-diffusion experiment in biotite, *Earth Planet. Sci. Lett.*, 24, 48-52, 1974.
- 4385 Hofmann, A. W., J. W. Mahoney, Jr., and B. J. Giletti, K-Ar and Rb-Sr data on detrital and post-depositional history of Pennsylvanian clay from Ohio and Pennsylvania, *Geol. Soc. Am. Bull.*, 85, 639-644, 1974.
- Hofmann, A. W., see Fletcher, R. C.
- Humphreys, R., see Cowley, A.
- *4386 James, D. E., Initial $\text{Sr}^{87}/\text{Sr}^{86}$ ratios in Mesozoic volcanic rocks of the central Andes (abstract), *Trans. Am. Geophys. Union*, 55, 475, 1974.
- *4387 James, D. E., C. Brooks, and A. Cuyubamba, Petrogenesis of central Andean Cenozoic magmas (abstr.), *Trans. Am. Geophys. Union*, 56, 474, 1975.
- Kable, E. J. D., see Hart, S. R.
- Kumar, C. K., see Brown, L.
- Lear, R. D., see McDaniel, F. D.
- Light, G. M., see McDaniel, F. D.
- *4388 Linde, A. T., Differences in radiated energy from suites of South American earthquakes at depths of 200 km and 600 km (abstr.), *Trans. Am. Geophys. Union*, 56, 401, 1975.
- Linde, A. T., see Stacey, F. D.
- Lynds, B., see Cowley, A.
- McCallister, R. H., see Fletcher, R. C.
- *4389 McDaniel, F. D., T. J. Gray, R. K. Gardner, G. M. Light, J. L. Duggan, H. Van Rinsvelt, R. D. Lear, G. H. Pepper, and J. Nelson, K-shell X-ray production cross sections for ^7Li ions on selected elements Ti to Sb: 1.0 to 5.0 MeV/amu (abstr.), *Bull. Am. Phys. Soc.*, 20, 640, 1975.
- McKavanagh, B., see Stacey, F. D.
- Mahoney, Jr., J. W., see Hofmann, A. W.
- Nelson, J., see McDaniel, F. D.
- *4390 Okada, H., I. S. Sacks, and J. A. Snoke, Determination of the subducting lithosphere boundary by use of converted phases (abstr.), *Trans. Am. Geophys. Union*, 56, 394, 1975.
- Okada, H., see Sacks, I. S., and Snoke, J. A.
- Pepper, G. H., see McDaniel, F. D.
- *4391 Rohrer, U., and L. Brown, $^9\text{Be}(p,n)^9\text{B}$ reaction with polarized protons from 2.46 to 2.90 MeV (abstract), *Bull. Am. Phys. Soc.*, 20, 693, 1975.
- Rohrer, U., see Arnold, L. G., and Brown, L.
- 4392 Rubin, V. C., Two chains of interesting southern galaxies: NGC 7172-7173-7174-7176 and NGC 7201-7203-7204, *Astrophys. J.*, 191, 645-651, 1974.
- 4393 Rubin, V. C., D. Westpfahl, Jr., and M. A. Tuve, Second finding list of faint blue stars in the anticenter region of the galaxy, *Astron. J.*, 79, 1406-1409 and 1501-1505, 1974.
- Rubin, V. C., see Cowley, A., and Warner, J. W.
- *4394 Sacks, I. S., Anomalous island arc asthenosphere and continental growth (abstr.), *Trans. Am. Geophys. Union*, 56, 456, 1975.
- *4395 Sacks, I. S., and L. Beach, Lateral velocity variations at the base of the mantle and their correlation with gravity anomalies (abstr.), *Trans. Am. Geophys. Union*, 55, 350, 1974.
- 4396 Sacks, I. S., and H. Okada, A comparison of the anelasticity structure beneath western South America and Japan, *Phys. Earth Planet. Inter.*, 9, 211-219, 1975.
- Sacks, I. S., see Okada, H., Snoke, J. A., and Suyehiro, S.
- Schilling, J.-G., see White, W. M.
- Seitz, M. G., see Grauert, B.
- Seyler, R. G., see Arnold, L. G.
- 4397 Shimizu, N., An experimental study of the partitioning of K, Rb, Cs, Sr, and Ba between clinopyroxene and liquid at high pressures, *Geochim. Cosmochim. Acta*, 38, 1789-1798, 1974.
- *4398 Shimizu, N., Partitioning of K, Rb, Cs, Sr, and Ba between clinopyroxene

- and liquid at high pressures (abstr.), *Trans. Am. Geophys. Union*, 55, 473, 1974.
- 4399 Shimizu, N., Rare earth elements in garnets and clinopyroxenes from garnet lherzolite nodules in kimberlites, *Earth Planet. Sci. Lett.*, 25, 26-32, 1975.
- *4400 Snoke, J. A., Archambeau's elastodynamical source-model solution and low-frequency spectral peaks in the far field displacement amplitude from earthquakes or explosions (abstr.), *Trans. Am. Geophys. Union*, 56, 401, 1975.
- *4401 Snoke, J. A., Earthquake radiation from an inhomogeneous medium with concentrated prestress (abstract), *10th Symposium on Mathematical Geophysics*, Intern. Union Geod. Geophys., Cambridge, England, University of Cambridge, June 25-July 5, 1974.
- *4402 Snoke, J. A., Earthquake radiation spectrum from an inhomogeneous medium with concentrated prestress (abstr.), *Trans. Am. Geophys. Union*, 55, 352, 1974.
- 4403 Snoke, J. A., I. S. Sacks, and H. Okada, Empirical models for anomalous high-frequency arrivals from deep-focus earthquakes in South America, *Geophys. J. R. Astron. Soc.*, 37, 133-139, 1974.
- *4404 Snoke, J. A., I. S. Sacks, and H. Okada, A model not requiring continuous lithosphere for anomalous high-frequency arrivals from deep-focus South American earthquakes (abstr.), *10th Symposium on Mathematical Geophysics*, Intern. Union Geod. Geophys., Cambridge, England, University of Cambridge, June 25-July 5, 1974.
- 4405 Snoke, J. A., I. S. Sacks, and H. Okada, A model not requiring continuous lithosphere for anomalous high-frequency arrivals from deep-focus South American earthquakes, *Phys. Earth Planet. Interiors*, 9, 199-206, 1974.
- Snoke, J. A., see Okada, H.
- Soptrajanova, G., see Grauert, B., and Hanny, R.
- *4406 Stacey, F. D., M. T. Gladwin, B. McKavanagh, A. T. Linde, and L. M. Hastie, Linearity of anelastic damping: a conflict of evidence (abstr.), *Trans. Am. Geophys. Union*, 55, 1144-1145, 1974.
- Steiner, E., see Arnold, L. G.
- *4407 Suyehiro, S., and I. S. Sacks, Secular strain, strain steps and earthquake prediction criteria from observations in the Matsushiro region, central Honshu, Japan (abstr.), *Trans. Am. Geophys. Union*, 56, 400, 1975.
- *4408 Thonnard, N., L. Brown, G. E. Assousa, and H. A. Van Rinsvelt, Characteristic and continuum x-rays produced with potassium ions of a few MeV (abstr.), *Bull. Am. Phys. Soc.*, 20, 639, 1975.
- Thonnard, N., see Brown, L.
- Truffa-Bachi, P., see Costrejean, J.-M.
- 4409 Tuve, M. A., Early days of pulse radio at the Carnegie Institution, *J. Atmos. Terr. Phys.*, 36, 2079-2083, 1974.
- Tuve, M. A., see Rubin, V. C.
- Van Rinsvelt, H. A., see McDaniel, F. D., and Thonnard, N.
- Wagner, M. E., see Grauert, B.
- 4410 Warner, J. W., Narrow-band filter photography of IC 4406, *Publ. Astron. Soc. Pac.*, 86, 885-887, 1974.
- 4411 Warner, J. W., On the stellar content and reddening in the nucleus of NGC 5195, *Astrophys. J.*, 190, 19-26, 1974.
- 4412 Warner, J. W., G. E. Assousa, B. Balick, and E. R. Craine, Accurate positions and identifications for eleven Ohio survey sources, *Publ. Astron. Soc. Pac.*, 87, 103-106, 1975.
- 4413 Warner, J. W., and V. C. Rubin, Physical conditions and structures in NGC 7293, *Astrophys. J.*, 198, 593-603, 1975.
- Westpfahl, D., Jr., see Rubin, V. C.
- *4414 White, W. M., J.-G. Schilling, and S. R. Hart, Sr-isotope geochemistry of the Azores and the Mid-Atlantic Ridge: 29°N to 60°N (abstr.), *Trans. Am. Geophys. Union*, 56, 471, 1975.

PERSONNEL

Staff Members

L. Thomas Aldrich ¹	Bill H. Hoyer
George E. Assousa	David E. James
Manuel N. Bass ²	Alan T. Linde
Ellis T. Bolton ³	Nancy R. Rice
Louis Brown	Richard B. Roberts
Dean B. Cowie ⁴	Vera C. Rubin
W. Kent Ford, Jr.	I. Selwyn Sacks
Stanley R. Hart	Norbert Thonnard
Albrecht W. Hofmann	Kenneth C. Turner
	George W. Wetherill, <i>Director</i> ⁵

Distinguished Service Member of Carnegie Institution

Merle A. Tuve

Research Associates (Staff)

Tom I. Bonner ⁶	J. Arthur Snoke ⁸
Nobumichi Shimizu ⁷	Donald G. Wallace ⁹

Research Associates (Nonresident)

Mateo Casaverde, Instituto Geofísico del Peru, Lima, Peru	Leonidas Ocola, Instituto Geofísico del Peru, Lima, Peru
Cidambi K. Kumar, Howard University, Washington, D.C.	Hiromu Okada, Hokkaido University, Sapporo, Japan
Shigeji Suyehiro, Japan Meteorological Agency, Tokyo, Japan	

Carnegie Fellows (Postdoctoral)

Michael B. Davis ¹⁰	Charles J. Peterson ¹²
George H. Pepper ¹¹	J. Arthur Snoke ¹³
	John W. Warner III ¹⁴

Carnegie Fellows (Predoctoral)

John R. Bannister, University of Alberta, Edmonton, Canada	Arturo Cuyubamba, McGill University, Montreal, Canada
William M. White, University of Rhode Island, Kingston, Rhode Island ¹⁵	

¹ Acting Director September 23, 1974, through March 31, 1975.² Through March 15, 1975.³ Director, through September 23, 1974.⁴ Institut Pasteur, Paris, France, from January 20, 1975.⁵ From April 1, 1975.⁶ Supported by U.S. Public Health Service grant.⁷ Supported by National Science Foundation grant through August 31, 1974.⁸ Supported by National Science Foundation grant from April 1, 1975.⁹ Through March 31, 1975.¹⁰ Through July 31, 1974.¹¹ From September 1, 1974.¹² From September 1, 1974.¹³ Through March 31, 1975.¹⁴ Through September 30, 1974.¹⁵ From October 1, 1974, through February 28, 1975.

Visiting Investigators

Christopher Brooks, Université de Montreal, Montreal, Canada¹⁶ Martin H. Dodson, Leeds University, Leeds, England¹⁷
 Raymond C. Fletcher¹⁸

Trainee Fellows

Charles Doering¹⁹ Charles L. Bennett²⁰
 Antonio Flores²¹

Student Trainee

David Westpfahl, Jr.²²

Collaborators

- | | |
|---|--|
| C. Aguirre B., Universidad Mayor de San Andres, La Paz, Bolivia | J. B. Flexner, University of Pennsylvania, Philadelphia, Pennsylvania |
| E. Arnal, Instituto Argentino de Radioastronomía, Villa Elisa, Argentina | L. B. Flexner, University of Pennsylvania, Philadelphia, Pennsylvania |
| L. G. Arnold, Ohio State University, Columbus, Ohio | S. E. Forbush (retired), Department of Terrestrial Magnetism, Carnegie Institution of Washington, Washington, D.C. |
| E. Bajaja, Instituto Argentino de Radioastronomía, Villa Elisa, Argentina | C. Garavito, Planetario Destrital, Bogota, Colombia |
| B. Balick, Lick Observatory, Board of Studies in Astronomy and Astrophysics, University of California, Santa Cruz, California | L. Gélinas, Génie Mineral, Ecole Polytechnique, Montreal, Quebec, Canada |
| E. Berg, University of Hawaii, Honolulu, Hawaii | A. A. Giesecke, Instituto Geofísico del Peru, Lima, Peru |
| M. Bracamonte, Trujillo, Peru | M. Gil, Instituto Argentino de Radioastronomía, Villa Elisa, Argentina |
| R. Cabre, S.J., Observatorio San Calixto, La Paz, Bolivia | M. Gordon, Instituto Argentino de Radioastronomía, Villa Elisa, Argentina |
| G. N. Cohen, Institut Pasteur, Paris, France | J. A. Graham, Cerro Tololo Inter-American Observatory, La Serena, Chile |
| R. Colomb, Instituto Argentino de Radioastronomía, Villa Elisa, Argentina | C. Heiles, University of California, Berkeley, California |
| G. L. Davis, Geophysical Laboratory, Carnegie Institution of Washington, Washington, D.C. | C. E. Helsley, University of Texas, Dallas, Texas |
| S. del Pozo, Instituto Geofísico Boliviano, La Paz, Bolivia | D. Huaco, Instituto Geofísico del Peru, Lima, Peru |
| L. K. De Noyer, University of Illinois, Urbana, Illinois | T. Krogh, Geophysical Laboratory, Carnegie Institution of Washington, Washington, D.C. |
| J. W. Erkes, State University of New York, Albany, New York | I. Kushiro, Geophysical Laboratory, Carnegie Institution of Washington, Washington, D.C. |
| A. J. Erlank, University of Capetown, Rondebosch, South Africa | R. P. Meyer, University of Wisconsin, Madison, Wisconsin |
| D. W. Evertson, University of Texas at Austin, Austin, Texas | I. Mirabel, Instituto Argentino de Radioastronomía, Villa Elisa, Argentina |
| E. Filloy, Instituto Argentino de Radioastronomía, Villa Elisa, Argentina | |

¹⁶ From January 1, 1975.

¹⁷ From September 1, 1974.

¹⁸ Through August 31, 1974.

¹⁹ From January 1, 1975.

²⁰ From May 15, 1975.

²¹ From May 1, 1975.

²² Through September 30, 1974.

- R. Morras, Instituto Argentino de Radioastronomía, Villa Elisa, Argentina
 Y. Motoya, Kamikineusu Seismological Observatory of Hokkaido University, Sapporo, Japan
 G. Olafsson, Akureyri, Iceland
 E. Pimental, Cuzco University, Cuzco, Peru
 W. Pöppel, Instituto Argentino de Radioastronomía, Villa Elisa, Argentina
 J. E. Ramirez, S.J., Instituto Geofísico de los Andes Colombianos, Bogota, Colombia
 A. J. Ratkowski, New York University, New York, New York
 M. S. Roberts, National Radio Astronomy Observatory, Charlottesville, Virginia
 R. Rodriguez, Observatorio San Calixto, La Paz, Bolivia
 U. Rohrer, Swiss Institute for Nuclear Research, Villigen, Switzerland
 R. H. Sanders, National Radio Astronomy Observatory, Charlottesville, Virginia
 J. G. Schilling, Narragansett Marine Laboratory, University of Rhode Island, Kingston, Rhode Island
 R. G. Seyler, Ohio State University, Columbus, Ohio
 H. Sigtrygsson, Reykjavik, Iceland
 D. Simoni, Arequipa, Peru
 R. Stefansson, Reykjavik, Iceland
 L. Tamayo, Universidad Nacional de San Agustín, Arequipa, Peru
 J. L. Telleria, Planetario Destriral, Bogota, Colombia
 P. Truffa-Bachi, Institut Pasteur, Paris, France
 H. A. Van Rinsvelt, University of Florida, Gainesville, Florida
 F. Volponi, Universidad Nacional de Cuyo, San Juan, Argentina
 R. L. Walter, Duke University, Durham, North Carolina
 Y. Yamagishi, Matsushiro Seismological Observatory of Japan, Meteorological Agency, Matsushiro, Japan

Supporting Staff

- Liselotte Beach, Research Assistant
 Kenneth D. Burrhus, Computer Systems Engineer
 Wayne Corley, Laboratory Helper, temporary
 Dorothy B. Dillin, Stenographer-Librarian
 John B. Doak, Electronics Research Specialist
 Clayton B. Doak, Grounds Maintenance, temporary
 William N. Dove, Office Manager
 Everett T. Ecklund, Design Engineer
 Mark Feigensen, Laboratory Assistant, temporary
 Peter J. Fiekowsky, Laboratory Assistant, temporary
 Laura A. Gazze, Research Assistant²³
 Gustavo Gonzalez, Laboratory Helper, temporary
 Mark Goudy, Grounds Maintenance, temporary
 Leo J. Haber, Carpenter and Maintenance Foreman
 Bennie Harris, Caretaker
 E. Kathleen Hill, Secretary
 Willis Kilgore, Jr., Caretaker
 Charles A. Little, Electronics Research Specialist
 Eric J. Lynch, Laboratory Helper, temporary
 Lilly Niu, Laboratory Assistant, temporary
 Niels M. Pedersen, Fiscal Officer
 Glenn R. Poe, Electronics Research Specialist
 Elliot M. Quade, Assistant Maintenance Foreman
 Carl M. Rinehart, Instrument Maker
 Judith H. Rogers, Typist
 Michael Seemann, Design Engineer-Mechanical
 E. Lynn Smith, Typist, Fiscal Assistant
 James E. Spicer, Assistant Maintenance
 Milton T. Taylor, Instrument Maker
 Neltje W. van de Velde, Research Assistant
 John M. Wilson, Laboratory Helper, temporary

²³ Through April 30, 1975.

Hale Observatories

Operated by Carnegie Institution of Washington
and California Institute of Technology

Pasadena, California

Horace W. Babcock

Director

J. Beverley Oke

Associate Director

OBSERVATORY COMMITTEE

Horace W. Babcock, *Chairman*

J. Beverley Oke, *Vice-Chairman*

Jerome Kristian

Robert B. Leighton

Guido Münch

Leonard Searle

Arthur H. Vaughan, Jr.

Harold Zirin

Contents

Introduction	307	Supernovae	327
Observing Conditions	312	Supernova search	327
		Energy distribution and spectra	328
Physics of the Sun.	312	The Galaxy	328
The helium chromosphere	312	Luminosity function of halo stars	328
Solar flares.	314	Galactic structure	328
Synoptic observations	314	Galactic center	329
Large-scale solar magnetic fields.	314	The mass of the galaxy	331
Large-scale velocity fields	315	Galactic evolution	331
Systematics of solar magnetic field patterns	315	Galaxies	332
Solar System Studies.	316	Ionization structure of gaseous nebulae in galaxies	332
Infrared and <i>UV</i> observations of Venus	316	Compact galaxies	332
Infrared observations of Jupiter.	316	Seyfert galaxies	332
Satellites of Jupiter	316	Velocity dispersions	333
Saturn	316	Dynamics of elliptical galaxies	333
Uranus	317	Infrared photometry of galaxies	334
Titan	317	Metallicity of M31 and M32	334
Io	317	Globular clusters in M31	334
Stellar Spectroscopy	318	Further observations of BL Lacertae	334
Mercury stars.	318	Radio source of 3C130	335
Rotation of magnetic Ap stars	318	Velocity fields in spiral galaxies	335
Flare stars	319	Spiral structure in the old disks of galaxies	336
Stellar magnetism	319	Interacting galaxies	336
White dwarfs.	319	Large Magellanic Cloud	337
Studies of proper-motion stars	320	History of star formation in galaxies	338
AZ Cassiopeiae at the 1956-1957 eclipse	322	Formation of galaxies.	338
Stellar spectroscopy at 1 micron.	322	Clusters of Galaxies	339
Spectrophotometric standards	322	Redshifts and magnitudes	339
Eclipsing binary	323	Redshift-magnitude diagram for a complete sample of nearby high-latitude Abell clusters	339
Stellar Evolution	323	Determination of the background light in the Coma Cluster	339
Stellar Chromospheres	323	Collisions of members of clusters	340
Absolute magnitudes	323	Radio Sources	340
Chromospheric variations in main-sequence stars	324	Optical identification of radio sources.	340
Millimeter and Submillimeter		Radio sources near spirals	341
Photometry	324	Quasars and Quasi-Stellar Objects	342
Observations at 350 microns	324	Quasar surveys	342
1-mm observations of molecular clouds	325	Spectroscopic surveys.	342
Observations of extragalactic objects at 1 mm	325	Absorption lines.	342
Interstellar Matter and Gaseous		Energy distributions	343
Nebulae	325	Distribution of redshifts.	343
Orion Nebula	325	Variability	344
Orion Nebula at infrared wavelengths.	326	Observational Cosmology	344
Infrared sources in molecular clouds	326	Groups and clusters in the Southern Hemisphere	344
Planetary nebulae	327	Cluster redshifts	345
Crab Pulsar	327	Evolutionary effects	346

Instrumentation	346	Photographic Laboratory	365
PEPSIOS spectrometer	346	2.5-Meter du Pont Telescope	366
SIT-Vidicon system for photometry	346	Dome and building	367
Spectroscopy with the SIT-Vidicon	347	Optics	367
Wobbling secondary for infrared		Microprocessor control system	367
photometry	348	Auxiliary instruments	368
Big Bear Solar Observatory (BBSO)		Las Campanas Observatory	369
instrumental program	348	Construction by contractor	369
Las Campanas image-tube spectrographs	348	El Pino headquarters in La Serena	369
Astroelectronics Laboratory	349	Bibliography	370
Guest Investigators	349	Staff and Organization	375

INTRODUCTION

The study of galaxies—their structure, dynamics, clustering, and evolution—is certainly one of the most active areas of research in astronomy today. This kind of study requires large optical telescopes (to say nothing of radio telescopes) with their indispensable light-gathering power, large image scale, and excellent optical performance. The new generation of optical telescopes currently coming into use around the world is already accelerating research on galaxies to a very significant degree. Meanwhile, the productivity of the 5-meter Hale Telescope on Palomar Mountain is being enhanced by new image photometers and sky-subtraction spectrographs.

A review of research topics reported upon for the past year at the Hale Observatories shows that some twenty different projects or investigations related to galaxies are in progress or have just been completed. A few of these have been selected for comment in the following paragraphs, but it is appropriate first to refer to just two of many important milestones in the development of this subject. First was Hubble's 1936 classification of shapes according to a bifurcated scheme with a sequence of forms branching from ellipticals into normal spirals and barred spirals. Another milestone was the introduction in 1962 by Eggen, Lynden-Bell, and Sandage of the concept of galaxy formation by contraction and collapse of a primordial gas cloud to a plane, the difference in the formation history between elliptical and spiral galaxies depending on the relative rate of star formation in these systems. Of fundamental importance are the mutual viscosity of interacting parts of the gas cloud and the absence of strong interaction between stars and the cloud. It is clear that there is little evolutionary development along the sequence of forms.

J. Richard Gott III, of Caltech, and Thuan have further developed the con-

cept of galaxy formation and differentiation already mentioned. They analyzed the competing effects of dissipation and turbulent viscosity, using a model of cloud formation in the early protogalaxy. Numerical models, including both stars and gas, were used to simulate the collapse. The stars and gas collapsed together until they reached the plane, whereupon the gas formed a disk and the stars continued in elliptical orbits to form a spheroidal halo. Some oscillations of the disk are expected before equilibrium is reached. Models may be used to relate galaxial parameters to the original size and angular momentum of the cloud. In general, if star formation in the early protogalaxy is essentially complete by the time of maximum collapse, an elliptical galaxy is formed. If a significant amount of gas remains at this stage, it will dissipate its energy to form a disk-like spiral. Observed properties of ellipticals and spirals imply that ellipticals formed out of larger perturbations of the primordial gas cloud than did spirals, giving the ellipticals greater densities and shorter collapse times. If early star formation is rapid and dependent upon the square of the density, ellipticals are expected to complete their star formation by the time of maximum collapse, while spirals are not. Protogalaxies arising from larger initial density fluctuations cluster more readily, accounting for the preferential occurrence of ellipticals in large clusters.

Sargent collaborated with A. Boksenberg and K. Shortridge of University College, London, in obtaining spectrograms of ten elliptical galaxies with the 5-meter Hale Telescope and Image-Photon-Counting System. The purpose was to obtain the velocity dispersion for stars in each of these galaxies by analyzing Doppler broadening of lines. A typical result (for NGC 7626) is $\sigma = 285 \pm 26$ km s⁻¹.

C. P. Wilson also observed a group of

ellipticals, obtaining spectrograms to be used for the determination of velocity curves of galaxial rotation and for velocity dispersions. The SIT-Vidicon image photometer was used for part of this work, as well as for a study of the surface brightness in three colors.

Schweizer continued his photometric investigations of broad spiral structures in underlying old disks of spirals. This was done in the near infrared, with a 90-mm image tube, to show the enhanced surface-mass density in the old disk of M51, as contrasted to the narrower and younger spiral arms customarily observed in blue light. He also continued spectroscopic studies of tidally interacting galaxies to find their relation to "normal" galaxies.

The strong, variable radio source 3C120 was at one time thought to be a variable star in our Galaxy. Later, after it appeared that its spectrum is like that of a Seyfert galaxy and that its redshift is $10,000 \text{ km s}^{-1}$, the object was studied intensively because of its resemblance to a quasar. For some years there has been good evidence that some quasars occur in the nuclei of elliptical galaxies, so that when Arp reported in 1968 that there is a slight nebulous fringe around 3C120, this was regarded as consistent with the foregoing. New photographs by Arp with the 4-meter telescope of the Kitt Peak National Observatory show a much greater extent to this surrounding nebulosity, and resolution of features within it. With other evidence, this has led him to the conclusion that 3C120 is a spiral or disturbed spiral galaxy whose nucleus contains the active, compact, and variable source of energy.

The best hope for advancing knowledge of the chemical composition and chemical evolution of galaxies lies in the interpretation of the spectra of the regions of ionized interstellar gas within them. Searle has recently surveyed the strengths of emission lines that are probes of ionization structure in a number of H II regions in M31, M101, and M51. He has carried out a systematic

survey of the behavior of the infrared lines of [S III] and is collaborating with Dr. G. Shields of the University of Texas in the interpretation of the data. The observed behavior of the [S III] lines is not in accord with the predictions of the simple ionization-structure models that have so far been used to interpret the spectra of H II regions. Unexpectedly, large density fluctuations within the emitting regions are indicated. It is already clear that the low excitation that is characteristic of regions situated in the inner spiral arms of galaxies is not simply a consequence of an enhanced oxygen abundance, as had earlier seemed likely.

Zinn, collaborating with Dr. John Norris of the Mount Stromlo Observatory, has investigated the stellar populations of dwarf spheroidal galaxies. Color-magnitude diagrams for such galaxies and for globular clusters in our Galaxy long ago suggested similarities in star formation for the two groups. But variable stars in the dwarf spheroidal galaxies and in the globular clusters do not obey the same period-luminosity law. Norris and Zinn believe that the period-luminosity law, the evolutionary status of the variables, and the color-magnitude diagrams can be explained if there were two epochs of star formation in each of the dwarf galaxies, but with little enrichment of metal content in the intervening time. They suggest that either supernova explosions were unable to drive all the gas from these systems or that gas was accreted some time after the first epoch.

Infrared observations of galaxies in the 1- to 3-micron range were continued by Jay Frogel, E. Persson, and M. Aaronson of Harvard College Observatory in collaboration with Becklin, Neugebauer, and Matthews. They made use of the luminosity-sensitive CO index at 2.3 microns. Initial results showed that the radiation from the nuclei of elliptical galaxies is dominated by the light of giant stars.

Becklin and Neugebauer have made new high-resolution maps of the region

of the center of the Galaxy at wavelengths of 2.2, 10, and 20 microns. They conclude that over half of the 2.2-micron radiation from the central 2 parsecs of the Galaxy comes from discrete unresolved sources. These objects could be luminous individual late-type stars or very compact clusters of stars. At 10 microns, nine discrete sources of radiation were detected in the 2 parsec central region.

Observations bearing on the distribution of metallicity in the Andromeda Spiral, M31, were obtained by Dr. M. Schwarzschild of Princeton University in collaboration with Oke. They used the multichannel spectrometer on the Hale Telescope to obtain energy distributions at several locations in the central bulge of M31. The results can be interpreted as an increase of the heavy element abundance toward the nucleus of the spiral. Beyond a radius of 2', no further abundance changes were observed; but, at 7'.5 and 10' from the center of M31 along the major axis, there is evidence for young hot stars.

Van der Kruit reported on the reduction of spectrograms of three spiral galaxies he had obtained with the image-tube spectrograph of the Hale Telescope. Detailed velocity fields were constructed. Noncircular motions in NGC 4736 were of particular interest. An excellent correlation was found between the magnitude of such motions and the brightness of the radio continuum emission. In NGC 3310, a systematic pattern of strong noncircular motions was found associated with the bright spiral arms.

Gunn and B. M. Tinsley of Yale University are continuing their program to synthesize the stellar populations of elliptical galaxies in an effort to determine the evolutionary corrections to the Hubble diagram.

Sandage completed analysis of redshifts and photometry of selected groups and clusters of galaxies in the Southern Hemisphere. Two results of particular interest emerged. When the redshifts were plotted against magnitude to con-

struct the Hubble diagram for these groups, it was found that the residuals in absolute magnitude were only mildly correlated with population of the group. When aggregates of galaxies having populations in the range 20 to 300 are examined, it is found that the mean absolute magnitude of the first-ranked galaxy varies by only about 0.15 mag. This suggests that the absolute magnitude of the first-ranked galaxy is determined by some physical upper limit in the galaxy formation process that is independent of the statistics relating to other members of the cluster.

The new data from the Southern Hemisphere, when analyzed in terms of velocity differences and combined with existing northern data, failed to show any systematic velocity perturbation in the local velocity field. New and closer limits can be placed on the perturbation of the local Hubble rate H for galaxies having velocities smaller than 3000 km s⁻¹ toward or away from the Coma-Virgo complex. A lack of perturbation in the velocity field at this level, in the presence of the density contrast caused by the clumping of galaxies in the Virgo group, shows that the effect of gravity on the underlying linear velocity flow is small. This suggests that the kinetic energy in the expansion field is large compared to the gravitational potential energy of the density contrast, and hence that the deceleration parameter q_0 is very small, in agreement with the results reported last year.

Gunn and Oke have continued their separate program to discover faint clusters of galaxies and to measure the redshifts and absolute spectral-energy distributions of the brightest members of these clusters. The first aim is to produce a list of clusters found under well-controlled conditions within a definite limit of apparent magnitude. Hundreds of clusters were identified on plates obtained in the course of an initial survey with the 1.2-meter Schmidt telescope. Spectrophotometric observations of a few show that redshifts are typically

between 0.20 and 0.35. A deeper survey, conducted with a 90-mm image tube at the prime focus of the 5-meter telescope, has produced a sample of about 30 very faint clusters of galaxies that typically have redshifts larger than 0.40.

Halo stars of our own Galaxy have a roughly spherical distribution about the galactic center. Using a complete sample of stars of large proper motion with known trigonometric parallaxes, Schmidt derived the local luminosity function of high-velocity stars that belong to the halo. The luminosity function was deduced by using a kinematical criterion based on space velocities of metal-poor RR Lyrae variables. Schmidt found the local mass density of halo stars to be $1.7 \times 10^{-4} \mathfrak{M}_{\odot} \text{ pc}^{-3}$; he calculated that the halo contributes about 6% of the mass of the Galaxy interior to the location of the sun.

The foregoing brief reports constitute a sampling of galaxial research at the Observatories. References to some other fields of current interest are provided below.

The mode of excitation of helium in the sun's atmosphere has long been of interest. Because helium is difficult to excite, it was thought to be excited either by coronal ultraviolet radiation or by high chromospheric temperatures. Space observations showed that the resonance lines of He II showed minima in the regions known as coronal holes, where the corona is less dense. With the 65-cm vacuum telescope at Big Bear, Zirin found that the D3 helium emission line also disappears in regions of coronal holes and has a sharp lower limit about 1000 km above the photosphere. These two facts were combined to produce a model of the excitation of chromospheric helium by back-radiation from the corona. According to this model, the coronal radiation shortward of 500 Å ionizes helium to the depth of its penetration, producing the observed dark band below the region of optical depth unity. The helium lines seen are produced by recombination from the ionized state for both

neutral and ionized helium. Calculations based on this model gave good agreement with the intensities of D3 and other helium lines, including those in the ultraviolet. Two corollaries follow:

The solar helium abundance cannot be regarded as well determined because the helium intensity depends on the variable ultraviolet from above and not on the amount of helium. The observed helium-line absorption in late-type stars may also be attributed to coronal back-radiation.

Preston, Vaughan, and former Carnegie Fellow Richard E. White have completed their investigation of Hg isotope anomalies in the mercury stars. Wavelengths of Hg II λ 3984 in 30 stars are distributed rather uniformly from the value for the terrestrial mix of isotopes to a value that implies a preponderance of ^{204}Hg . The wavelengths are loosely correlated with effective temperature. Relative isotopic abundances derived from partially resolved profiles of λ 3984 in ι Coronae Borealis, χ Lupi, and HR 4072 suggest that simple mass-dependent fractionation has occurred in all three stars. This indicates that an isotope separation process rather than exotic nucleosynthesis is responsible for the isotope anomalies. Accordingly, a scheme has been devised whereby isotopic compositions can be inferred from a comparison of stellar wavelengths and equivalent widths of λ 3984 with those calculated for a family of fractionated isotopic mixes. For one star, 46 Aquilae, Preston reports a wavelength for the Hg II line that corresponds to pure ^{204}Hg .

Greenstein has continued the colorimetric search for white dwarfs, especially those with late-type spectra and colors, using the multichannel spectrophotometer on the Hale Telescope. The rarity of yellow and red degenerate stars continues to contradict the simple theory of cooling of the core of a degenerate object. Although numerous objects have been found cooler than 8000°K, none have been found cooler than about 4500°K (EG 202). A few have relatively

strong metallic lines, but at wavelengths longer than λ 5500 they prove to be relatively blue objects. The reasonable possibilities seem to be that (1) the cooling becomes rapid below effective temperature 5500°K and the stars disappear into the black dwarf stage, or (2) some physical mechanism delays cooling of old white dwarfs.

In cooperation with Dr. A. Boksenberg of University College, London, Greenstein used the image-photon-counting system in a study of spectra to show that all suspected late-type white dwarfs previously classified as DM are weak-lined subdwarf M stars, i.e., very metal poor. No degenerate star with TiO bands was found.

The magnetic degenerate stars provide the most unusual spectra; study of several such stars suspected of showing variable circular polarization demonstrated that the broad absorption features found and not yet identified do not move substantially; i.e., quadratic Zeeman effect does not grossly falsify their wavelength. The periodic variable G195-19, however, shows a trace of spectrum variability in its broad features, changing in location or intensity. The broad and somewhat wavelike distortion of these spectra approaches the limit of detectability. Magnetic fields of up to 10^8 gauss are suspected.

O. C. Wilson has completed his work on absolute magnitudes of stars obtained from measures of the width of chromospheric emission of the K-line of Ca II, and the material is being prepared for publication. The table of results contains useful information on luminosities for about 700 objects. These stars are of spectral types G, K, and M; subgiants and supergiants are included. One of the principal results is that the lower boundary of the color-magnitude diagram plotted from the tabular data conforms closely to the normal points found earlier by Sandage for NGC 188. This indicates that all of the nearby field stars listed are about the same age as the cluster. There is no real evidence for the presence

of an older population. The K-line data are very homogeneous, since they depend upon measures by one individual on spectrograms of the same dispersion. It is, therefore, of interest to compare them to the results from trigonometric parallaxes. This was done by plotting the published parallaxes against the moduli from the K-line measures to see how they fit the curve $m - M = -5 - 5 \log \pi$. Stars with galactic latitude $b > 25^\circ$ provide an excellent fit to the curve, but those with $b < 25^\circ$ are shifted in the sense that their trigonometric parallaxes are too small. Wilson concludes that there are most probably errors in the latter.

Sargent, with R. F. Carswell and A. Boksenberg of University College, London, applied Boksenberg's image-photon-counting system in observations of the 17th magnitude quasar PHL 957 at the coudé spectrograph of the Hale Telescope. This quasar has $z_{\text{em}} = 2.69$ and a very rich absorption spectrum. In all, 284 absorption lines were measured, and intensive effort was put into a search for redshifts, using computer techniques developed for the analysis of Pks 0237-23 last year. However, only one absorption redshift, $z_{\text{abs}} = 2.30$ is regarded as definite, and this accounts for only about 5% of the lines.

Westphal and Kristian have continued to refine and test the application of SIT television camera tubes for two-dimensional (image) photometry. The level of photometric precision obtained at the telescope is close to the 1% limit expected from laboratory tests of the system. Over a range of 10 magnitudes, from 12 to 22, it is possible with the SIT-Vidicon to reproduce with highly satisfactory precision a broad-band sequence established with photomultipliers. The limits are not intrinsic, but at magnitude 22 the signal is completely dominated by the sky. SIT measurements should be accurate to fainter levels, although fainter photoelectric standards are not available. In a 10-min exposure, stars are measurable fainter than $V = 24$ mag, with pro-

gressively lower precision attributable to photon statistics. Currently, the 1% limit for precision of the SIT system is due primarily to seemingly random variations of the order of 0.5% in the background.

The same SIT system used in image photometry has been employed by Westphal and Kristian for several programs of low- and high-resolution spectroscopy. When used with a small spectrograph, there are two important features of the SIT detector that make it particularly suitable for faint objects. The reproducibility of the transfer function allows accurate sky subtraction, while the two-dimensional format permits the spectra of the sky and object-plus-sky to be recorded simultaneously. The sky-subtraction process functions well and produces difference spectra that are limited essentially by photon noise. The SIT-Vidicon has also been applied successfully as a detector at the coude spectrograph of the Mount Wilson 2.5-meter

telescope, where it has been used by Brucato to study stellar line profiles and by C. P. Wilson to measure velocity dispersions and rotations of the central regions of galaxies. Cooling of the tube to -90°C makes possible exposure times of several hours.

An experimental grating spectrograph equipped with a cooled integrating SIT-Vidicon camera is nearing completion under Gunn's direction. The system is being interfaced with a PDP-11/40 mini-computer to give real time capability for addition, averaging, reduction, and display of spectra.

A new f/60 infrared photometer has been put into operation on the Mount Wilson 1.5-meter telescope. Signal modulation is obtained by wobbling the Cassegrain secondary of the telescope. The system provides a very satisfactory level of performance for the study of infrared radiation from molecular clouds, H II regions, and external galaxies.

OBSERVING CONDITIONS

The 2.5-meter Hooker telescope at Mount Wilson was used for observations on 240 complete nights and 36 partial nights for a total of 2579 hours. The telescope was out of service for six nights to permit replacement of main shaft bearings in the clock drive. The 1.5-meter telescope was used for 144 complete nights and 79 partial nights for a total of 1700 observing hours. The primary mirror was removed and taken to Palomar for realuminizing in July 1974. Rainfall for the year was near normal at 914 mm, and total snowfall was 1473 mm.

The 5-meter Hale Telescope at Palomar Mountain was used for a total of 3473.3 hours, of which 2892.8 were nighttime hours, as shown in Table 1. The difference represents twilight time that was used for infrared observations not requiring a dark sky. Total precipitation at Palomar was 730.5 mm, with 1366.5 mm of snow. The maximum temperature was 32.2°C in July; minimum was -8.3°C in December.

Public visitors at the Palomar Observatory numbered 140,000 for the year.

PHYSICS OF THE SUN

The Helium Chromosphere

For many years the mode of excitation of helium in the sun's atmosphere has been of great interest. Because helium is

difficult to excite under normal temperatures, it was considered that it was excited either by coronal ultraviolet radiation or by high chromospheric temperatures. With the advent of space

TABLE 1. 5-Meter Observations

Month	Complete Nights	Partial Nights	Zero Observation Nights	Total Hours Worked	Hours of Night-time Observing
July	27	2	2	292.5	227.0
August	31			306.1	269.9
September	28	2		308.9	286.7
October	24	1	6	338.5	264.3
November	26	2	2	353.9	298.0
December	21	5	5	302.5	251.9
January	25	4	2	339.6	317.1
February	19	4	5	281.6	224.9
March	15	6	10	209.0	165.2
April	12	7	11	180.7	147.8
May	28	3		322.5	226.5
June	26	1	3	237.5	213.5
Totals	282	37	46	3473.3	2892.8

observations, it was found that the resonance lines of He II showed minima in the regions of coronal holes, regions where the corona is less dense. Using the 65-cm vacuum telescope, Zirin found that the D3 helium emission line also disappears in regions of coronal holes and has a sharp lower limit, about 1000 km above the photosphere. These two facts were combined to produce a model of the excitation of chromospheric helium by coronal back-radiation. The idea is that the coronal radiation shortward of 500 Å ionized helium to the depth of its penetration, producing the observed dark band below the region of optical depth 1. The helium lines seen are produced by recombination from the ionized state, for both neutral and ionized helium. Calculations on this model gave good agreement with the observed intensities of D3 and other helium lines, as well as the ultraviolet lines. Where there is a coronal hole, the coronal ultraviolet radiation is weak and helium is not excited. This model produces two corollaries: the solar helium abundance cannot be regarded as well determined because the helium intensity depends on the variable ultraviolet flux from above and not on the amount of helium; and the observed helium-line absorption in late-

type stars may also be attributed to coronal back-radiation. This is discussed in a section on He λ 10830 stellar observations.

LaBonte has been working on the interpretation of the D3 helium emission from flares. Flares are seen in both absorption and emission in helium D3, but the new Big Bear photographs, as well as logic, show that the absorption is produced by any material raised above the surface by the flare, while the emission must occur at lower levels where density and excitation are sufficient to produce such emission. Therefore, the helium data provide a new key to the physics of flares.

At the recent low level of solar activity, coronal holes were noted principally at the two polar caps. Michalitsanos and Zirin, using the video magnetograph at Big Bear, were able to detect the polar magnetic field in two of these coronal holes. There appears to be a peaking of longitudinal field of one sign in a cap about 15° from the pole at these times, while at lower latitudes the field is of mixed sign. It has been conjectured that the presence of the coronal holes is connected with the existence of the poloidal field at the pole. The matter is under investigation.

Solar Flares

Moore, in collaboration with D. W. Datlowe of the University of California at San Diego has investigated the heating and cooling of the thermal x-ray plasma in solar flares. Characteristic times for heating and cooling of the plasma were estimated from the time profile of the thermal x-ray burst and from temperature, emission measure, and overall dimensions of the flare-heated plasma at thermal x-ray maximum. The heating was assumed to be due to magnetic field reconnection, and the cooling was assumed to be due to heat conduction and radiation. Temperatures and emission measures derived from U.C.S.D. OSO-7 x-ray flare observations were used, and length scales were obtained from Big Bear high-resolution ($\approx 1''$) $H\alpha$ filtergrams for 17 small (subflare to class 1) flares.

The empirical values obtained for the characteristic times and approximate proportionalities found between these times imply that (1) flares are in fact produced by magnetic field reconnection, (2) conduction cooling of the thermal x-ray plasma dominates radiative cooling, and (3) reconnection heating and conduction cooling of the thermal x-ray plasma are approximately in balance at thermal x-ray maximum. This model, in combination with the data, gives estimates for the electron number density ($10^{10} - 10^{11} \text{ cm}^{-3}$) and the magnetic field strength (10-100 gauss) in the thermal x-ray plasma and for the total thermal energy generated in a subflare ($\approx 10^{30}$ ergs for an $H\alpha$ area ≈ 1 square degree heliocentric). These estimates agree with previous observational and theoretical estimates obtained by others.

Synoptic Observations

Synoptic observations of the sun continue at Mount Wilson under the supervision of Howard. Solar observations were made on 325 days. Between June

1, 1974, and May 31, 1975, the following were obtained:

Direct photographs	302
$H\alpha$ spectroheliograms, 30-foot focus	554
K2 spectroheliograms, 30-foot focus	554
Full-disk magnetograms	374
Integrated-light magnetic-field measurements	315
Sunspot drawings	312
Sunspot magnetic-field polarity measurements	306

The computer-operated scanning and data system at the 150-foot tower telescope was put into operation during July 1974. This has made possible a flexibility in the observations and reductions that was unattainable before. Notwithstanding initial problems, the system now provides reliable data of high quality. It is now possible to obtain regular full-disk magnetograms with improved resolution. The standard aperture at the end of the report period was 12.5 arc sec square.

The daily magnetic plots are published monthly in the National Oceanic and Atmospheric Administration Bulletin *Solar Geophysical Data*. The magnetic synoptic charts are published in the *Quarterly Bulletin on Solar Activity* of the International Astronomical Union. Partial support for these observational programs comes from the National Aeronautics and Space Administration and the Office of Naval Research.

Large-Scale Solar Magnetic Fields

Howard has continued his studies of large-scale solar magnetic fields. Close to 95% of the total magnetic flux $|F^-| + |F^+|$ is found equatorward of 40° latitude. This fact implies that ephemeral regions, which are newly discovered, tiny, short-lived bipolar regions, cannot contribute significantly to the global magnetic-flux distribution. This follows from the strong equatorial concentration of the flux that Howard has found and from the fact that

the ephemeral regions are known to be distributed nearly uniformly in latitude. Thus, although ephemeral regions bring to the solar surface roughly as much magnetic flux as do the active regions, the contribution of this ephemeral-region flux to the large-scale flux distribution is negligible.

The large-scale inclination of magnetic-field lines has been studied by Howard. The total field is inclined so as to trail the rotation by a small amount at all latitudes. In the north at all latitudes and in the south equatorward of 40° latitude, the two polarities are, on the average, inclined toward each other by a small angle. Although the inclination of the total flux has shown only very little systematic variation with time, the individual polarities in the north have shown a systematic decrease at low latitudes in their inclination angles, starting at about 10° in early 1967 and decreasing to near 0° at the end of 1973. In the south the situation is less clear, but the effect is still present.

A cross-correlation analysis of the inclination angles of the separate polarities indicates a strong tendency for a negative correlation at latitudes above 40° and for a positive correlation below 40° . This means that, poleward of 40° , variations in inclination angle in one direction by fields of one polarity are likely to be accompanied by variations in the other direction by the other polarity. Equatorward of 40° , the two polarities tend to change their inclinations in the same direction. This may indicate a fundamental difference between the linkage of the field lines to the subsurface fields in the polar and equatorial regions.

Howard, in collaboration with Martin D. Altschuler, Dorothy E. Trotter, and Gordon Newkirk, Jr., of the High Altitude Observatory in Boulder, Colorado, has analyzed the large-scale surface magnetic field of the sun in terms of surface harmonics ($P_{m,n}^m(\theta) \cos m\varphi$ and $P_{m,n}^m(\theta) \sin m\varphi$) for the interval 1959

through 1972. The single harmonic that most often characterized the general solar magnetic field during this interval was a dipole in the plane of the equator ($n = m = 1$). This was particularly true during the active years of cycles 19 and 20. The north-south dipole ($n = 1, m = 0$) was prominent only during times of low activity. Contributions to the field from harmonics of principal index $4 \leq n \leq 9$ were generally rather small throughout the interval except for a period of a few months prior to the large flares of August 1972. The same authors published a microfilm tabulation of the harmonics of the surface-field distribution (*NCAR Technical Note/STR-85*, National Center for Atmospheric Research, Boulder, Colorado, July 1973).

Large-Scale Velocity Fields

Yoshimura and Howard have examined some of the accumulated solar-surface velocity-field data from the 150-foot tower telescope at Mount Wilson in order to study large-scale velocity patterns. Preliminary results indicate that significant variations from the smooth latitude dependence of differential rotation exist and change in latitude from time to time, that temporal variations in the rotation rate of the sun appear to occur over a broad range of latitude and longitude, that a large-scale (200,000 km) non-axisymmetric velocity field is seen in velocity synoptic charts, and that the large-scale meridional circulation is undetectably small ($<10 \text{ m s}^{-1}$).

Systematics of Solar Magnetic Field Patterns

Using the Mount Wilson magnetic-field-synoptic-chart data accumulated for 16 years, Yoshimura studied the slow changes of the latitudinal distribution of the poloidal field by averaging over longitude. The resultant pattern reflects the distribution of the magnetic flux in latitude, provided that proper corrections

can be made for the sunspot flux, which is not measured by the magnetograph. This pattern requires averaging over many solar rotations because of large noise. It shows that magnetic flux characteristic of leading spots migrates equatorward, while magnetic flux characteristic of the following parts of bipolar regions migrates toward higher latitudes.

Yoshimura studied the development of the toroidal field by subtracting the poloidal field from the original magnetic data to display the evolution of the latitudinal distribution of the absolute

value of the resultant field averaged over longitude. By averaging over many rotations, a diagram was obtained that is similar to the butterfly diagram of sunspots drawn by Howard, using Mount Wilson data for the same period. However, the evolution of this toroidal field, which relates to a relatively shallow region of the convection zone, differs from the butterfly diagram of sunspots in the sense that there is no conspicuous equatorial propagation of the wings or branches of the butterfly diagram of the toroidal field.

SOLAR SYSTEM STUDIES

Infrared and UV Observations of Venus

The mapping of Venus in the thermal *IR* described in *Year Book 73* (p. 130) has been continued by Westphal and D. Diner. Observations at several narrow-band wavelengths from 5 to 23 microns were collected with nearly simultaneous measurements in the *UV*. Diner is working with this material to correlate the *UV* and *IR* structure, and thereby to understand the nature of the "*UV* clouds" seen with Mariner 10. The use of the Gregorian secondary in a raster-scan mode has allowed very good *UV* pictures to be collected. This technique seems much better than the normal photographic *UV* photometry.

Infrared Observations of Jupiter

Westphal and Terrile recorded a large body of 5-micron data during this year's opposition. Terrile is now using these data to study the vertical cloud structure.

A number of 1"-resolution frames were also recorded at 8 to 14 microns. These data show smaller scale 10- μ structure than had previously been seen from ground-based measurements.

Satellites of Jupiter

At the suggestion of Dr. Dan Pascu of the U. S. Naval Observatory, Kowal

began a program of photographing the outer satellites of Jupiter with the 1.2-meter Schmidt telescope. The purpose of the project is to obtain improved ephemerides of the satellites. After experimenting with various methods of dimming the glare of Jupiter, it was decided to use an evaporated-Inconel neutral-density filter that allows Jupiter and the Galilean satellites to be photographed while leaving the outer satellites undimmed. The plates will be sent to Dr. Pascu for measuring.

During this project, Kowal decided to search for new satellites of Jupiter, using IIIa-J plates. As a result, he discovered Jupiter XIII on plates taken on September 11, 12, and 13, 1974. The new object is a member of the middle group of Jupiter's satellites, having an orbit similar to those of numbers VI, VII, and X. Its visual magnitude is approximately 20, and it is estimated to be less than 8 kilometers in diameter.

As a by-product of this program, Kowal discovered a rather distant asteroid (1974 UC) and an Apollo asteroid (1974 MA).

Saturn

The 6-inch aperture PEPSIOS spectrometer of the University of Wisconsin, installed at the coudé focus of the 5-

meter Hale Telescope, was used by F. Roesler and J. Trauger of the University of Wisconsin and Münch to search for the $\text{Pl}(4, 0)$ line of HD at λ 7467.5 Å in the spectrum of Saturn. The purpose of this search is to verify that the D/H ratio in Saturn is the same as found in Jupiter by Trauger, Roesler, Carleton, and Traub (*Astrophys. J. [Lett.]*, 184, L137, 1973) from the intensity ratio between the lines of HD $\text{Pl}(4, 0)$ and $\text{S1}(4, 0)$ of H_2 . The PEPSIOS spectrometer was used in an off-axis mode to compensate for the spread in wavelength introduced by the rotation of the planet. Under the same resolving power used for the Jupiter observations, a range of 1 Å around the expected position of the HD line was scanned in Saturn, and the photon flux in each of the 100 elements sampled was measured with an accuracy significant at the 1.0% continuum level. The spectrum obtained shows several weak lines, presumably due to CH_4 , not found in the Jupiter spectrum. In order to make a univocal measurement of the HD line in Saturn, it will be necessary to obtain a long-path CH_4 spectrum with equally high resolving power. The University of Wisconsin group of investigators is now preparing a laboratory experiment for this purpose.

Uranus

Attempts to verify the accepted value for the velocity of rotation of Uranus from the inclination of Fraunhofer lines in slit spectrograms made by Münch in the past years have led to inconclusive results. For this reason, a different approach was followed by Münch, Roesler, and Trauger in an experiment made with the University of Wisconsin PEPSIOS spectrometer installed at the coudé laboratory of the 5-meter telescope. Using an entrance aperture admitting the light from the entire planet, the profile of the Fraunhofer line $\text{Fe } \lambda$ 5263 was obtained with a resolving power of 250,000. In comparison with the same line in the lunar spectrum, an

equatorial velocity of $3.7 \pm 0.2 \text{ km s}^{-1}$ has been derived for Uranus on the basis of limb-darkening parameters fitted to the Stratoscope II observations. The comparison of the Uranus line profile with that of the moon has also shown that the amount of filling-in of the Uranus line that might be ascribed to Raman scattering is no more than 2% in units of the continuum.

A measurement of the profile of the $\text{S1}(4, 0)$ line of H_2 in the spectrum of Uranus was also made with the PEPSIOS instrument. The statistical accuracy of the profile is not high enough to obtain an independent determination of the equatorial velocity of rotation of Uranus, but it has provided an accurate measurement of the equivalent width of the line. The value found, $23 \pm 2 \text{ mÅ}$, is about 30% lower than previously published determinations. The value for the effective column of H_2 in the Uranus atmosphere should be correspondingly reduced to 400 km-Amagat.

Titan

Using the University of Wisconsin PEPSIOS spectrometer at the 5-meter telescope, the spectral region around the expected position of the $(3, 0)$ S1 line of H_2 in the spectrum of Titan has been scanned by Münch, Trauger, and Roesler. Under a resolving power of 150,000, no line could be detected. From the statistical accuracy of the profile obtained, it is estimated that the effective column of H_2 is not larger than 1.25 km-Amagat, about 25% of the upper limit established previously by Trafton (*Astrophys. J. [Lett.]*, 175, L285, 1972) from spectral scans with lower resolving power than those provided by the PEPSIOS experiment.

Io

The morphology and kinematics of the sodium emission apparently associated with Io have been studied by Münch in collaboration with J. Bergstrahl of

the Jet Propulsion Laboratory. A number of multislit spectrograms centered on Io, at times near its greatest elongation, have been obtained with the coudé spectrographs of the 1.5- and 2.5-meter Mount Wilson telescopes and of the 5-meter Palomar reflector. With the image intensifiers available and camera focal ratios around $f/5$, an exposure of about 4 hours is needed to record the Na-D lines out to a distance of 30" from the satellite in directions contained in its orbital plane. However, in directions normal to the orbital plane, the dimension of the emitting region is much smaller, probably no more than 3". This

is the limit set by seeing conditions during the long exposures required to obtain satisfactory spectra. The measured radial velocities of the Na-D lines have been found to agree with those of Io within $\pm 3 \text{ km s}^{-1}$, the uncertainty of the measurements. It thus appears that the sodium emission more properly manifests itself as a flat ring around Jupiter, approximately centered at Io, rather than a cloud around Io. In order to define more accurately the kinematics and form of the Jupiter ring at Io, interferometric observations with higher angular and spectral resolving powers are now being planned.

STELLAR SPECTROSCOPY

Mercury Stars

Preston, Vaughan, and former Carnegie Fellow Richard E. White have completed their investigation of Hg isotope anomalies in the mercury stars. Wavelengths of Hg II λ 3984 in 30 stars are distributed rather uniformly from the value for the terrestrial mix to a value that implies a preponderance of ^{204}Hg . The wavelengths are correlated loosely with effective temperature. Relative isotopic abundances derived from partially resolved profiles of λ 3984 in ι Coronae Borealis, χ Lupi, and HR 4072 suggest that simple mass-dependent fractionation has occurred in all three stars. This indicates that an isotope separation process rather than exotic nucleosynthesis is responsible for the isotope anomalies. Accordingly, a scheme has been devised whereby isotopic compositions can be inferred from a comparison of stellar wavelengths and equivalent widths of λ 3984 with those calculated for a family of fractionated isotopic mixes.

Preston is extending the initial Hg star survey with coudé observations of some twenty Hg stars with mild peculiarities that were missed in low-disper-

sion surveys. For one of these, 46 Aquilae, Preston reports a wavelength for the Hg II line that corresponds to pure ^{204}Hg (λ 3984.07).

Rotation of Magnetic Ap Stars

Preston has completed measurements of the projected rotational velocities of more than 200 magnetic Ap stars of the various SiSrCrEu species. If the stars are grouped in intervals of color temperature, the mean values of $v \sin i$ decline from $\sim 50 \text{ km s}^{-1}$ at $T_e \sim 15,000^\circ \text{K}$ to $\sim 20 \text{ km s}^{-1}$ at $T_e \sim 8500^\circ \text{K}$. At the cool end of the sequence, the modal velocity is less than 10 km s^{-1} . It is tempting to regard this correlation as an age effect produced by magnetic braking since main-sequence lifetimes vary by a factor ~ 10 in the effective temperature domain of the Ap stars. However, the presence of slowly rotating Ap stars in a few young clusters suggests that substantial loss of angular momentum may occur during premain-sequence evolution. Rotation measurements of a larger sample of demonstrably young Ap stars are needed to determine whether or not this is the case.

Flare Stars

The two-channel coudé scanner of the 2.5-meter telescope has been used by Preston to monitor the $H\gamma$ emission flux of the dMe flare stars AD Leonis and EV Lacertae. Sequential 20–30 sec integrations were made in 4-Å bands centered on $H\gamma$ and the continuum 10 Å longward for ~ 30 hours for each star. In both cases flares with peak $H\gamma$ fluxes ranging from 5 to 500% of the quiescent flux occur at a rate (~ 1 per hour) similar to those obtained for typical flare stars by broad-band photometry (Kunkel, *Astrophys. J. Suppl. Ser.*, 25, No. 213, 1973). However, the durations of the $H\gamma$ flares (5 to 50 min) are much greater than those obtained by U -band photometry. They correspond much more closely to the durations of solar flares that are observed in $H\alpha$ light.

Stellar Magnetism

Borra used the coudé polarimeter of the 2.5-meter Hooker telescope to search for longitudinal magnetic fields in Sirius. He found no convincing evidence that Sirius has longitudinal fields greater than the observational error (~ 20 gauss).

Borra has made a search for new magnetic stars in the southern hemisphere, using a Pockels-cell polarimeter (loaned by Dr. J. D. Landstreet of the University of Western Ontario) at the Cassegrain focus of the Las Campanas 1-meter telescope. Narrow-band (5 Å) interference filters permitted measurement of the circular polarization caused by the longitudinal Zeeman effect in the wings of $H\alpha$. Several known Ap stars were observed. HD 54118 was found to have a reversing magnetic field that varies between +1300 gauss and –900 gauss; its period of about 3.25 days is the shortest known for such stars. Other new magnetic variables that require further observation are α Circini (+400 to –400), HD 133880 (+2600 to –3250), HD 94600 (+2900).

Borra has used the coudé polarimeter

of the Hooker telescope to search for circular polarization in the wings of the He I line λ 6678 in the x-ray star candidates θ^2 Orionis, X Persei, the x-ray star HDE 226868 (Cygnus X-1), and the B2 Ib star HD 31327. These observations do not show evidence of longitudinal magnetic fields. The observations of HDE 226868 are especially interesting because of its well-established identification with Cyg X-1. Also, Bahcall *et al.* have proposed a mechanism for production of x rays. They predict a field of about 30,000 gauss for Cyg X-1. The observational errors were about 500 gauss (longitudinal field). The line width of He I λ 6678 in HDE 226868 also rules out surface fields of several thousands of gauss.

White Dwarfs

Greenstein has continued the colorimetric search for white dwarfs, especially those of late-type spectra and colors, using the multichannel spectrophotometer. The major results appeared in discovery lists (Papers VII and VIII). The rarity of yellow and red degenerate stars continues to contradict the simple theory of cooling of the core of a degenerate object. Although numerous objects have been found cooler than 8000°K, none have been found redder than EG 202, the companion to Ross 193 (about 4500°K). A few have relatively strong metallic lines, but at wavelengths longer than λ 5500 they prove to be relatively blue objects. The possibilities are (1) that the cooling becomes rapid below effective temperature 5500°K and the stars disappear into the black dwarf stage, or (2) that some physical mechanism delays cooling of old white dwarfs; and (3) the hypothesis that our Galaxy is not old enough to have produced cooler degenerate stars requires the mean atomic weight of the core not to exceed that of helium, which seems unreasonable.

In cooperation with Dr. A. Boksenberg of University College, London, almost all suspected late-type white dwarfs

previously classified as DM proved to be weak-lined subdwarf M stars, i.e., very metal-poor. No degenerate star with TiO bands was found.

The correlation between various multi-channel color indices and luminosity proves excellent; the scatter is only slightly larger than that determined from recent large and accurate parallax measures. The interpolation curves permit calibration of the luminosities of white dwarfs of various types, with the exception of the magnetic degenerate stars, with an accuracy of about ± 0.4 mag.

The magnetic degenerate stars provide the most unusual spectra; study of several cases suspected of showing variable circular polarization demonstrated that the broad absorption features found, and not yet identified, do not move substantially; i.e., quadratic Zeeman effect has not grossly falsified their wavelength. The periodic variable G195-19, however, shows a trace of spectrum variability in its broad features, changing in location, or disappearing and reappearing. However, their width is nearly one third of their wavelength, so that the broad and somewhat wavelike distortion of their spectra approaches the limit of detectability. Fields of up to 10^8 gauss are suspected.

From the evolutionary point of view, studies of the white dwarfs in galactic clusters indicate that stars of initial mass about $2.5 M_{\odot}$ in the Hyades have become white dwarfs without explosion. The white dwarf near the Pleiades seems, in fact, to be a member and to be single. Since the Pleiades turnoff mass is near $6 M_{\odot}$, stars over a considerable range of mass can reach the degenerate stage without violent collapse and explosion.

Studies of Proper-Motion Stars

The multichannel spectrophotometer has been used by Greenstein to observe about 375 stars, largely from the Lowell proper-motion lists. These were first selected for large proper motion at faint

apparent magnitude. It was hoped that this method would produce a large yield of cool degenerate stars, even among those objects for which the Lowell photographic color estimates were $+1$ or $+2$ mag. In fact, mostly metal-weak, very-high-velocity stars on or below the main sequence were found. The multichannel colors are sufficiently rich in information so as to provide many not previously known properties of the G, K, and M stars. Approximately 75 stars of known parallax and of various population types have been observed; unfortunately, few very-high-velocity stars are known with good parallaxes. The calibration of the absolute magnitudes by colors measured with the multichannel spectrophotometer proved quite successful. The parallax stars of known color provide an interpolation curve to obtain luminosities of all proper-motion stars so far observed. The most useful color from G to M seems to be that measured between λ 6900 and λ 4700. It is distorted by TiO bands; for the later dM stars an index between λ 6580 and λ 10,000 is used. The overall accuracy in luminosity is ± 0.4 mag; the systematic agreement between various color-magnitude systems seems excellent. A major program providing the energy distributions of the main-sequence and high-velocity stars has resulted in defining various color equivalents which measure strength of strong metallic lines, as well as luminosity. The high-velocity stars became almost indistinguishable from the low-velocity population in all colorimetric and line indices so far studied at about mid-M type. Another interesting property is shown in Fig. 1, which presents the spectrum of Wolf 629 and its faint companion, called Van Biesbrock 8 after its discoverer. This, at the moment, is the faintest star observed. The distortion of the entire spectrum below 1 micron is demonstrated by the increase of over 3 magnitudes in colors measured from 1μ to anywhere below 0.65μ . Few late-type high-velocity M dwarfs are yet known; the frequency of Population II stars of low mass is not

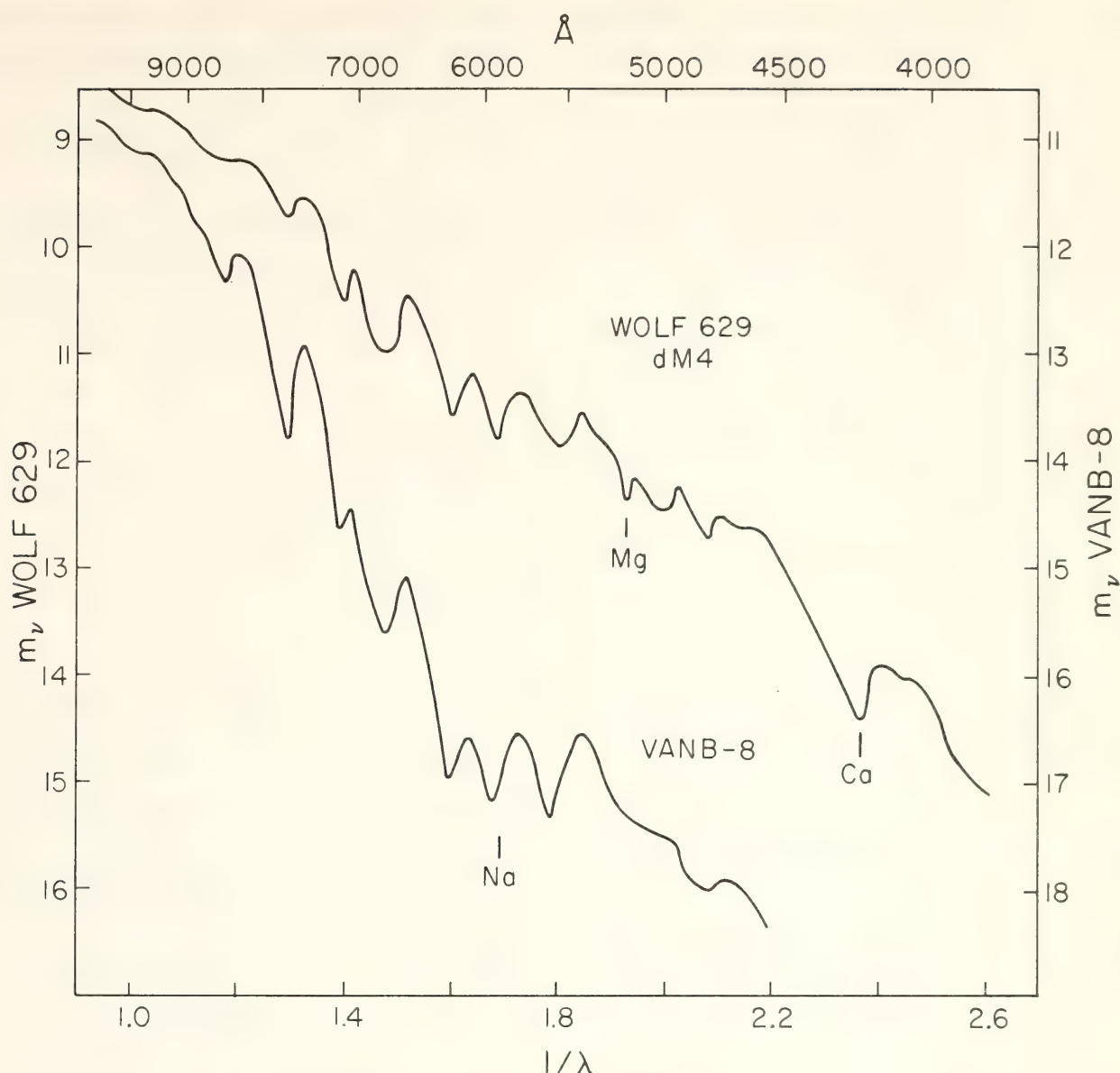


Fig. 1. Low-resolution multichannel spectroscopy by Greenstein shows two of the intrinsically faint M dwarfs of the Wolf 630 group. At least five M dwarfs move together through space at 41 km s^{-1} , separated by up to 1600 Å . The star known as Van Biesbroeck 8 is among the intrinsically faintest known, with a visual absolute magnitude of $+17.5$ ($M_{1.85}$ measured 5500 Å); its companion, Wolf 629, has $M_{1.85} = +12.5$ (i.e., 100 times brighter). However, at $10,000 \text{ Å}$, the $M_{1.00}$ are $+12.1$ and $+9.6$; i.e., Wolf 629 is only 10 times brighter. The ratio of total luminosities is even less. The difference in color arises from the greatly strengthened TiO bands and stronger atomic lines in the cooler, fainter star. Hertzsprung-Russell diagrams for stars are often based on these deceptive visual magnitudes and blue and yellow colors. The colors and brightnesses measured in red and infrared light will prove far more useful for theoretical interpretation of the mass-luminosity relation at the faint end of the main sequence. These faint M dwarfs, while largely unexplored, are, in fact, the most common type of star in the solar neighborhood. Their large mass-to-light ratios resemble those found from the integrated properties of other galaxies.

overwhelmingly high, although requiring further statistical studies. Knowledge of U , V , W space motions is largely lacking. Additional complete Lowell zones are being observed without prior selection for very large reduced proper motion. Approximately 20 stars have been found,

which, if on the main sequence, have space motions far too high to be found in our Galaxy. Numbers up to 1000 km s^{-1} are given from whichever color equivalent is used to calibrate luminosity. But, strangely, no one of these is found moving much faster than the sun in the

direction of galactic rotation, about to escape. Although the unknown radial velocity might alter these situations, a reasonable hypothesis is that, in fact, a number of stars are moving in retrograde orbits approaching the escape velocity backwards, with large motions toward and away from the galactic center. It seems almost necessary to say that stars exist as much as 1.5 magnitudes below the main sequence. This seems to be most common in spectral type G, but a few early M-type stars share this property. As Olin Eggen has conjectured for some years, there do apparently exist red subluminous stars. However, on purely kinematic evidence, it is unlikely that any stars are more than 1.5 mag below the normal color-luminosity diagram. This effect covers a wide range of spectral type and is unlikely to arise purely from differential line-blocking between normal and metal-poor stars.

AZ Cassiopeiae at the 1956-1957 Eclipse

Spectrograms of the VV Cephei-type star AZ Cas, obtained by Dr. J. Sahade with the Cassegrain spectrograph of the 1.5-meter Mount Wilson telescope and by Münch with the coudé spectrograph of the Hale reflector at the time of the 1956-1957 eclipse, have been studied by these two workers in collaboration with R. H. Méndez of the Instituto de Astronomía y Física del Espacio, Buenos Aires, Argentina. The system around the time of eclipse shows a combination spectrum of an F8 Ib star and a main-sequence B0-1 companion. The latter star is ejecting matter with nearly spherical symmetry at some 50-60 km s⁻¹, while the former has a very extended atmosphere. Previous determinations of the spectral type of the red companion have ranged from early-M, well before eclipse, to F8, in our material, with a luminosity class apparently constant. This range in spectral type has been interpreted as indicating variations in the optical thickness of the envelope surrounding the late-type

companion, either intrinsic (of Cassiopeiae episode) or related to the binary nature of the companion.

Stellar Spectroscopy at 1 Micron

Zirin has completed the reduction of spectra taken in the λ 10830 region since 1966 in continuation of the program started by Vaughan and Zirin. About 200 stars are included. There is a rough correlation between absolute magnitude or K-line intensity and the strength of helium absorption or emission. The line is found in emission in a number of stars, implying unusual physical conditions. The helium absorption or emission varies in most of the stars in which it is seen. In two or three stars it has been found to change from emission to absorption and back again. Helium emission has also been found in a few very-late-type variables such as R Aquarii, R Andromedae, and R Geminorum; it has also been found on the declining shelf of the light curve of the Cepheid η Aquilae, but spectra at other phases do not show it.

Because the helium excitation may be due to coronal back-radiation, one can develop a figure of merit for the possibility of detecting soft x rays from some of the stars in question. This is no more than the equivalent width of λ 10830 times the apparent stellar diameter. On this basis, Capella is an outstanding candidate, and, in fact, soft x-ray emission has been reported from that star by Acton and Catura.

Spectrophotometric Standards

It has long been known that spectrophotometric standards in common use are very poorly defined in the difficult region between the Balmer discontinuity and about 4100 Å, where early-type stars have heavy hydrogen absorption and later-type subdwarfs, even very metal-deficient ones, have complicated spectra. Gunn has used very hot O subdwarfs, primarily Feige 34 and 67 and

+28°4211, with model atmospheres and calibrated photographic spectra to interpolate in this region; the resulting fluxes for the four secondary faint Oke standards +17°4708, HD 140283, HD 19445, and HD 84937, should be accurate to better than 2%. In addition, observations tying +17°4708 directly to α Lyrae have been made with the multichannel spectrometer by Gunn and Oke.

Eclipsing Binary

Schmidt accidentally discovered an eclipsing binary through the integrating

television system of the 5-meter telescope. The star is PG 1413+01, an ultraviolet-intense star of the 17th magnitude found by Green in his Palomar 46-cm survey for bright quasars. The eclipse lasts 13 minutes, while the period is 8 hours 16 min. At minimum the object is fainter than 22 mag in *B* and *V*. Photometric, spectroscopic, and spectrophotometric work by Schmidt, Green, and Richstone suggests that the components are a hot white dwarf and a late M-type dwarf at a separation of about 2 solar radii. The object poses interesting questions concerning its prior evolution.

STELLAR EVOLUTION

Zinn and Dr. Pierre Demarque, Visiting Associate from Yale University, have investigated the two mixing mechanisms that have been proposed for the origin of the Population II carbon stars, the CH stars. Demarque and Zinn conclude that the chemical compositions of the CH stars are equally well explained by mixing at the two proposed times the helium-core flash at the tip of the giant branch and the helium-shell flashes on the as-

ymptotic giant branch. They find, however, that shell-flash mixing cannot produce CH stars fainter than about $M_v \sim -1.3$, which is brighter than many CH stars. It seems then that at least some of the CH stars must be produced by the core flash. Demarque and Zinn point out that if core-flash mixing is common among Population II stars, then the current picture of the horizontal branch may have to be revised.

STELLAR CHROMOSPHERES

Absolute Magnitudes

O. C. Wilson has completed his work on absolute magnitudes of stars obtained from measures of the width of the chromospheric emission of the K-line of Ca II, and the material is being prepared for publication. The table of results contains 761 stars; however, since some emission components are too weak or are affected by absorption on the violet edges, useful information on luminosities is available for about 700 objects. These stars are of spectral types G, K, and M; subgiants, giants, and supergiants are included. Principal results are as follows:

1. The lower boundary of the color-magnitude diagram plotted from the

tabular data is a very close fit to the normal points found earlier by Sandage for NGC 188. This indicates that the oldest of the nearby field stars are of about the same age as NGC 188. There is no real evidence for the presence of an older population.

2. The K-line data are very homogeneous since they depend upon measures by one individual on spectrograms of the same dispersion. It is therefore of interest to compare them to the results from trigonometric parallaxes. This was done by plotting the published parallaxes against the moduli from the K-line measures to see how they fit the curve $m - M = -5 - 5 \log \pi$. Only parallaxes of weights ≥ 20 were used. The stars were

divided into two groups with galactic latitudes $\geq 25^\circ$ and $< 25^\circ$. This also divides the usable stars into two equal groups of 198 each, with nearly the same mix of spectral types and luminosities. Nevertheless, the two groups do not fit the curve equally well. The stars with $b \geq 25^\circ$ provide an excellent fit to the curve; those with $b < 25^\circ$, however, are shifted obviously in the sense that their trigonometric parallaxes are systematically too small. Since there is no way to account for this difference by systematic errors in the moduli for the two groups, it is most probably due to the parallaxes themselves, and suggests that the correction from relative to absolute parallax is a function of galactic latitude.

3. The strength of $\lambda 4077$ Sr II, which is a luminosity criterion for the stars, was estimated on all spectrograms with respect to the nearby Fe I lines $\lambda\lambda 4045, 4063, 4071$. The logarithms of these eye-estimated intensities were plotted against the absolute magnitudes from the K-line, $M_v(K)$. For the majority of the stars the plotted points lie approximately along a straight line from the subgiants to the supergiants (there is, of course, considerable scatter). However, there is a sizable group of stars for which the strength of $\lambda 4077$ is too strong, in many cases by rather large amounts, so that they lie well above the line de-

finied by the majority. These stars appear to extend in luminosity from $M_v(K) \sim +1.5$ to ~ -3.5 (ξ Capricorni) and include representatives of spectral types G, K, and M. In fact, the fraction of M-type stars showing this anomaly appears to be higher than for types G and K. Some of the stars in this group are known to be Ba stars; hence it is likely that the Sr II anomaly is an abundance effect.

Chromospheric Variations in Main-Sequence Stars

With the coudé scanner of the 2.5 m telescope on Mount Wilson, observation of the fluxes at the centers of the H and K lines of Ca II is being continued by Wilson for a number of main-sequence stars. The most interesting result of this work is probably the discovery of what are almost certainly cyclical variations in the chromospheric emission from a number of these objects. Several have now virtually completed one cycle since the project was begun. It is hoped that one more season of observations will provide enough overlap with the early observations to confirm the cyclical nature of the variations beyond question and to provide reasonably accurate values of their periods.

MILLIMETER AND SUBMILLIMETER PHOTOMETRY

Observations at 350 Microns

During the past year, the first successful use of the 5-meter telescope for observations at 350μ was achieved by Werner, Becklin, Neugebauer, and Westbrook in collaboration with Rieke and Low of the University of Arizona. Observations in this atmospheric window are possible only under extremely dry conditions—less than 2 precipitable millimeters of H_2O to the zenith—which are expected to occur only rarely at Palomar Mountain. Thus the $350\text{-}\mu$ pro-

gram was designed to utilize the 5-meter telescope for specific observations requiring higher spatial resolution—a $25''$ beam was used—than could otherwise be attained at this wavelength. The $350\text{-}\mu$ system is incorporated directly into the instrumentation used every month for 1-mm twilight observations at the prime focus. Thus the system is readily accessible at the telescope for about one week of each winter month; this time coverage is necessary in view of the unlikely occurrence of suitable observing conditions. By implementing

this plan, it was possible to carry out observations at $350\ \mu$ on three days, two in February and one in March. The $350\text{-}\mu$ emission from the H II region-molecular cloud complexes in the Orion Nebula and in the source W51 was studied and was found to show interesting structure on a scale comparable with the $25''$ beam. In the case of the Orion source, the emission is peaked at the center of the molecular cloud. The $350\text{-}\mu$ flux density, $\sim 4000\text{ Jy}$, is about one half of what has been measured from this source with a $1'$ beam. The high signal-to-noise ratio of these initial observations indicates that the 5-meter telescope can be a powerful tool for work at this wavelength.

1-mm Observations of Molecular Clouds

The program of mapping the 1-mm emission from H II region-molecular cloud complexes has been continued by Werner, Neugebauer, Gezari, M. Hauser of the NASA Goddard Space Flight Center, and graduate students J. Elias and W. Westbrook at the 5-meter prime focus; this work is scientifically and instrumentally complementary to the $350\text{-}\mu$ work described above. One-arc-minute-resolution maps of 1-mm emission have been completed for five sources: W3, W49, DR21, Sgr B2, and Orion Molecular Cloud 1. The 1-mm radiation is produced largely by thermal emission from dust in the dense molecular clouds surrounding these H II regions. The results for W49 typify the general trends emerging from this work: the 1-mm emission is extended over a $3' \times 5'$

region and peaks very sharply at the location of a compact H II region that is associated with powerful H_2O and OH microwave masers. Near-infrared studies of W49 suggest that this particular compact source is located in an extremely dense dust cloud; a second compact source $2'$ to the southeast appears to involve less dust and also shows much less 1-mm emission.

Observations of Extragalactic Objects at 1 mm

A number of compact extragalactic objects have been studied at 1 mm by Werner, Neugebauer, Gezari, M. Hauser of the NASA Goddard Space Flight Center, and graduate students J. Elias and W. Westbrook, using a composite bolometer detector during twilight hours at the 5-meter prime focus. Five sources have been detected at 1 mm: 3C84, 3C120, 3C273, 3C279, and BL Lacertae. The 1-mm flux densities of these sources lie between 5 and 20 Jy. In no case is there evidence for an upturn in the spectrum at 1 mm over what would be expected from an extrapolation of the lower frequency microwave spectrum. The 1-mm flux from 3C273 has been monitored since December 1973. The mean 1-mm flux density is $\sim 15\text{ Jy}$, and no variations greater than those consistent with the overall calibration uncertainty of $\sim 40\%$ have been seen. In addition to the five sources listed above, 3σ upper limits in the 5 Jy range have been set on the 1-mm flux from other interesting sources, including M82, NGC 1068, NGC 4151, OJ 287, OH 471, and OQ 172.

INTERSTELLAR MATTER AND GASEOUS NEBULAE

Orion Nebula

With the double Fabry-Perot scanning monochromator of the 1.5-meter Palomar telescope, Münch and Taylor have attempted to detect in the Orion Nebula

the component of $\text{H}\alpha$ expected to arise from the cascade decay of resonantly scattered Lyman- β . It has earlier been found by Münch and Taylor (*Year Book* 74, p. 141) that the O I $\lambda\lambda$ 8446-8447 emission lines, also excited by resonant

Lyman- β , are redshifted by about 8 km s⁻¹ with respect to the lines arising in the H II region. Because the intrinsic width of recombination H α is larger than 8 km s⁻¹, however, it cannot be clearly separated from the resonant H α component. Nevertheless, Münch and Taylor have established that the H α line profiles, in regions where the emission in O I $\lambda\lambda$ 8446-8447 is strong in relation to H α , are systematically asymmetric and broader than those arising from regions with weak O I. The existence of an H α component with approximately the same velocity as that of O I $\lambda\lambda$ 8446-8447 has thus been verified in a statistical fashion. The existence of the H α resonance component, furthermore, reveals that the O I lines are indeed being excited by the Lyman- β fluorescence process.

Images of the Orion Nebula in H α radiation show in the neighborhood of θ^2 Orionis three distinct small-scale features brighter than their surroundings. Interferometric profiles of the H α and [N II] 6584 lines over areas including these features, obtained by Münch and Taylor, show components shifted to the blue of the main nebular emission by amounts ranging from 32 to 73 km s⁻¹. The radial velocities and distances of these features with respect to θ^2 Ori are consistent with the hypothesis that they were ejected from the vicinity of this star at one and the same epoch and speed. If the features have moved with a constant velocity since ejection, their lifetime would be only 1000 years. Possible mechanisms that might explain this phenomenon are now being studied theoretically.

Interferometric scans of the He I ($2^3P - 2^3S$) lines at $\lambda\lambda$ 10829-10830 emitted by the Orion Nebula have been obtained by Münch and Taylor with the 1.5-meter Palomar telescope. Under a spectral resolving power of 65,000 and an angular resolution of 50", line profiles over many areas in the central region of the nebula have been obtained with peak signal-to-noise ratios around 50. The strongest λ 10830.3 ($2^3P_{2,1} - 2^3S$) blended

line at most positions exhibits shifts of around +20 km s⁻¹ with respect to the bulk of the nebular emission, as measured, for example, by the O III lines. However, the line is in general complex, often displaying a weaker resolved component at around +10 km s⁻¹. In three cases this component has been observed to become the predominant feature. In contrast, the weaker line at λ 10829 ($2^3P_0 - 2^3S$) has a velocity coincident with the nebular standard of rest and shows no complex velocity structure at the signal levels obtained. The discrepant velocities derived from the $2^3P_{2,1} - 2^3S$ transition, together with its complex structure, indicate the existence of self-absorption effects in a region where velocity gradients prevail. A detailed interpretation of the line profiles is now being carried out in terms of models that take into consideration radiative transfer effects in a quasi-resonance line, and also extinction due to solid particles.

Orion Nebula at Infrared Wavelengths

Becklin, Neugebauer, Werner, and graduate students I. Gatley and S. Beckwith have studied the infrared radiation from the southern ionization front in the Orion Nebula. A 10- μ map of this region has been made showing that the area of highest infrared surface brightness is a narrow strip just outside the ionization front. The geometry suggests that the infrared radiation comes from dust heated by optical and ultraviolet radiation from the Trapezium stars. This requires that the dust be highly depleted within the ionized region. Outside the H II region a normal dust-to-gas ratio and a density of $\sim 10^4$ cm⁻³ will produce the observed strip of infrared radiation.

Infrared Sources in Molecular Clouds

A new region where star formation

may be taking place was discovered by Dr. Neal Evans of the California Institute of Technology and Steven Beckwith, a graduate student, using the new f/60 wobbling secondary at $10\ \mu$ on the Mount Wilson 1.5-meter telescope. The region, denoted Mon R2, closely resembles the BN/KL complex in Orion and contains four compact infrared sources as well as an extended source coincident with an H II region. The compact sources closely resemble the BN source in spectra, with one source ($L = 2700 L_{\odot}$) almost twice as luminous as BN. Another source ($L = 700 L_{\odot}$) is particularly important in that it appears to lie in front of the H II region and can be studied in absorption against it at very short wavelengths. This is the first time such an object has been seen against a more extended background source and offers the possibility of study of the structure in detail. The brightest source is at least $0.5''$ in size and its close resemblance to BN makes it extremely unlikely that the infrared radiation from these sources is reddened starlight.

Planetary Nebulae

The velocity field of planetary nebulae with large angular extent in radiation of the [O I], $H\alpha$, and [N II] lines is under study by Taylor. The double Fabry-Perot scanner of the 1.5-meter Palomar telescope is being used for this purpose. A general inference that can be made from the observations made to date is that many extended nebulae are not in a state of simple radial expansion, stratified only according to state of ionization. The classical work of O. C. Wilson showed that planetary nebulae compact enough to fit into multislit entrance arrays to coudé spectrographs indeed display such a simple kinematical state. But larger, presumably older, planetaries appear to have more complicated kinematics. Two outstanding examples may be mentioned: NGC 650-51 has a triple velocity structure of a nature never seen heretofore; and NGC 6720, the well-known Ring Nebula, exhibits in [O I] a $30\ \text{km s}^{-1}$ expansion (or contraction), not radially from the central star but around the axis of its "Ring," in the manner of an inflating (or deflating) tire.

C R A B P U L S A R

Kristian is continuing a series of measurements of the optical intensity of the pulsar to search for a possible secular change. In parallel with this program, a search was started for possible pulse-to-pulse variations. Raw photomultiplier counts in 2 ms integration times are recorded directly for periods of the order of 10 min. These strings of data are then folded into 100 bins, *modulo* the pulsar period, and the resulting distribution of counts in each bin is compared with the

distribution expected from Poisson photon statistics. The available data show no intrinsic pulse-to-pulse variations. In particular, there are no supergiant pulses or smaller amplitude variations similar to those seen in the radio pulses, and there are no factor-of-two variations, as have been suggested by the *Uhuru* x-ray data. These results confirm earlier studies of possible pulse-to-pulse variations by Kristian and are based on a larger sample of data.

S U P E R N O V A E

Supernova Search

Five supernovae were discovered at the Palomar Observatory in 1974. All

were found by Kowal under Sargent's supervision. The 46-cm Schmidt telescope was used to survey nearby Sc I galaxies for a fourth year. No supernovae were

found in this search. Graduate student John Huchra made a preliminary estimate that the supernova rate in Sc I galaxies is one every 30 years.

Energy Distribution and Spectra

Kirshner and Oke have made a careful study of absolute spectral energy distributions and slit spectra of the bright supernova 1972e in NGC 5253. The latest observation, made with the multichannel spectrometer on the 5-meter Hale telescope, was 700 days after maximum light, when the visual magnitude was fainter than 20. The observation confirms an exponential decay of the light in the *B* filter (most of the light) for this length of time. Based on the identification of a λ 6550 emission fea-

ture as $H\alpha$, a model is proposed that consists of a differentially expanding atmosphere in which the electron density ranges from 10^{10} cm^{-3} near maximum light to about 10^7 after an interval of 340 days. This atmosphere is illuminated by a photosphere with a temperature ranging from $10,000^\circ\text{K}$ down to 7000°K . For these conditions, previously suggested line identifications of Ca II λ 8600 and H and K, NaD lines, and the Mag I *b*-band are quite plausible. From 200 days after maximum, the spectrum is dominated by four features between λ 4200 and λ 5500. Three of these features match the predicted blend of over 100 [Fe II] lines. If correct, these identifications imply an Fe/H ratio about 20 times higher than the cosmic abundance.

THE GALAXY

Luminosity Function of Halo Stars

Schmidt has derived the local luminosity function of high-velocity stars on the basis of a complete sample of stars of large proper motion with trigonometric parallaxes. The function of these stars belonging to a roughly spherical galactic halo was deduced by using a kinematical criterion based on space velocities of metal-poor RR Lyrae variables. The local mass density of halo stars is found to be 1.7×10^{-4} solar masses per cubic parsec. The halo contributes about 6% of the galactic mass interior to the sun. The halo could carry a larger fraction of the mass if it contains unexpectedly many remnants of stellar evolution or stars of mass less than $0.1 M_\odot$.

Galactic Structure

A program was begun two years ago by Sandage to study the interstellar extinction and reddening by new methods. The ratio *R* of extinction to reddening depends on the nature of the inter-

stellar grains. The ratio is fundamental in many studies of galactic structure and extragalactic astronomy. Knowledge of *R* is almost always required to correct photometric data for the effects of the interstellar medium.

Study of the wavelength dependence of extinction (reddening) gives information on the grains that have diameters of the same order as the wavelength of the light they scatter. The presence of grains with appreciably larger diameters that would cause neutral absorption cannot be detected by the usual spectrophotometric color-difference method. A large percentage of neutral absorption could increase *R* significantly, with consequences for many problems, including the current mystery of the rapid change of galaxy counts as a function of galactic latitude in the absence of a steep change in the observed reddening with latitude. If *R* were large, perhaps due to neutral absorption, this particular problem could be understood.

In the past, several ingenious methods have been used to detect a neutral component to the interstellar extinction,

such as (1) Trumpler's classical study of the abnormal change of observed angular diameters of open star clusters with increasing photometric distance, (2) methods of star counts of dark nebulae in several colors, and (3) Joy's method, using Cepheids and OB stars whose true distance is known from the kinematic properties of galactic rotation and whose photometric distances are known from the period-luminosity relation or spectral type. None of these earlier methods indicated the presence of a neutral component. However, each of them has uncertainties, and the matter is generally considered to be still open.

A new method, using groups and clusters of galaxies, has become available. Studies reported in past issues of the Year Book have shown that the *absolute magnitude* of the first-ranked E galaxy in a group or cluster has a very small variation from group to group; further, the $B - V$ color is also remarkably stable at $(B - V)_0 = 0.98 \pm 0.04$ mag; and finally, that there is a remarkably tight relation between apparent magnitude and redshift (the Hubble diagram) for first-ranked cluster galaxies (in high galactic latitude). Hence, if a cluster of galaxies of known redshift were seen behind an absorbing screen, the total extinction A_v (mag) (both the neutral and the wavelength-dependent component) could be found by the derivation from the mean line in the Hubble diagram. The reddening also follows from the observed color excess, using the known $(B - V)_0$ intrinsic color.

To find such highly absorbed clusters, a search program was begun by Sandage several years ago in the galactic band ($|b| \lesssim 7^\circ$), using the Palomar Schmidt with red plates (098-02). A number of candidate clusters and groups have been located. Redshifts and photometry are required for the test. Generally, the more heavily obscured a cluster, the more powerful the method because percentage errors in A are reduced. However, the more heavily obscured clusters are fainter and very red, making redshifts

and photometric measurements more difficult.

The first results of this extended program became available this year with the redshift measurement by Spinrad at Lick Observatory of the radio galaxies 3C129 and 3C129.1, which are highly obscured at a galactic latitude of 0.4° . These radio sources had previously been identified with faint galaxies by Hill and Longaire at Cambridge. Inspection of the region showed that the galaxies are members of a group.

Sandage obtained BVR photometry of the two radio sources and of a third group member in March. Reduction of the photometry using Spinrad's redshift of 6400 km s^{-1} and the Hubble diagram for cluster and radio galaxies reported earlier (*Astrophys. J.*, 178, 1 and 25, 1972) gave $(A_v) \simeq 3.4$ mag (but variable across the group), and $\langle R \rangle \equiv A_v/E(B - V) = 3.7 \pm 0.3$ for the highly reddening galaxies. Correction for the broad bandwidth effects of the BV system gives $\langle R \rangle = 3.4 \pm 0.3(\sigma)$ for OB-type stars. This is close to the traditional value (variously given as between 3 and $3.5 \pm \sim 0.3$ from the spectrophotometric color-difference method). Hence, there is no evidence from the first application of this new method for a measurable neutral component. If the result is verified as the program continues, the explanation of the *apparently* large R ratio inferred from galaxy counts must lie elsewhere.

This result would put an upper limit of the order of 0.1 mag Kpc^{-1} for any neutral extinction that might be present in the average galactic field (i.e., at less than 0.1 of the value of 1 mag Kpc^{-1} for the selective absorption).

Galactic Center

Becklin and Neugebauer have made new high-angular-resolution ($2''$) maps of the galactic center region at 2.2, 10.0, and 20μ . The $2.2\text{-}\mu$ map is presented in Fig. 2. It shows the sur-

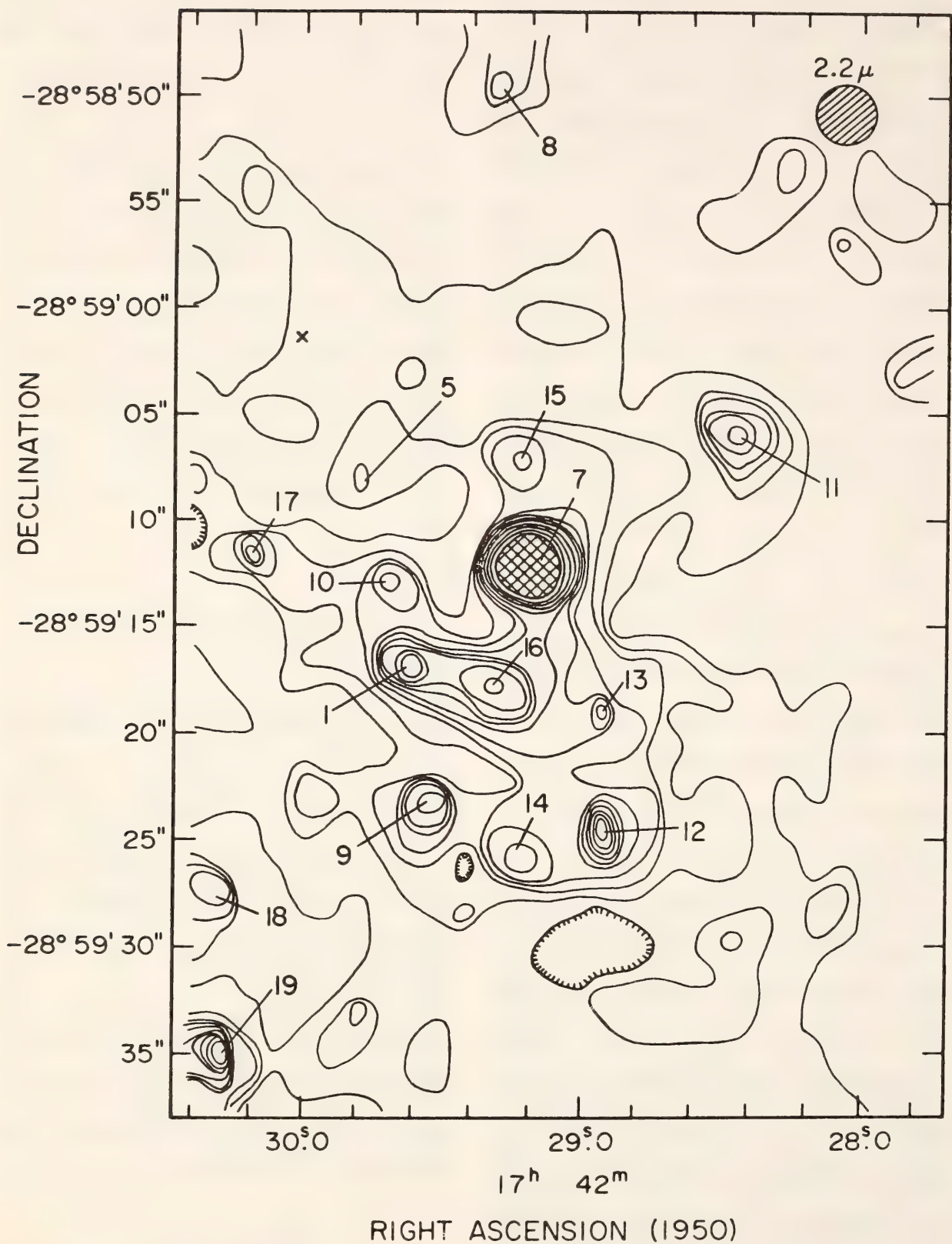


Fig. 2. Map of the central 1' of the galactic center at 2.2 μ made with a 2".5 circular aperture. The X denotes a visible field star. The contour levels each correspond to $2.5 \times 10^{-18} \text{ W m}^{-2} \text{ Hz}^{-1} \text{ ster}^{-1}$. The cross-hatching corresponds to 35 contour levels. The numbers refer to the source number. The angular resolution is shown by the circle in the upper right-hand corner.

prising result that over half of the $2.2\text{-}\mu$ radiation from the central 2 pc of the Galaxy comes from discrete unresolved sources. The absolute $2.2\text{-}\mu$ magnitude of these discrete sources is brighter than -8 mag; this is brighter than the brightest star in the globular cluster 47 Tucanae. These objects could be very luminous individual late-type stars or very compact clusters of stars. At $10\text{ }\mu$, nine discrete sources of radiation were detected in a 2-pc region. The nature of these sources is at present unclear, although some probably result from dust emission associated with regions of ionized hydrogen. In size and $10\text{-}\mu$ luminosity, several sources are similar to the planetary nebula NGC 7027.

S. Willner, a graduate student, has obtained $10\text{-}\mu$ spectra of five of the nine $10\text{-}\mu$ sources found by Becklin and Neugebauer and of one other source found by Rieke and Low. The spectra of the sources are similar, and all show a deep silicate absorption feature. All but one of the sources show an emission line due to Ne II; therefore, these sources must be associated with H II regions. The one source which does not show any Ne II emission has a deeper silicate absorption than the rest of the sources observed and may well be of a different nature.

The Mass of the Galaxy

Hartwick of the University of Victoria and Sargent began work to determine the radial velocities of outlying satellites of the Galaxy in order to determine its mass out to large radii. The project involves the measurement of accurate radial velocities of individual stars as faint as $B = 19.5$. Using R. Lynd's spectrograph on the Kitt Peak 4-meter Mayall Telescope, Sargent and Hartwick obtained widened spectrograms at a dispersion of $80\text{ }\text{\AA}\text{ mm}^{-1}$ of two K giant stars in each of the dwarf spheroidal galaxies Draco and Ursa Minor. Spectrograms were also obtained of the globular clusters Palomar 3 and 4 and the

Arp-van den Bergh cluster (Palomar 14). Preliminary results show all these systems to be exceedingly metal deficient—more so than M92 in some cases.

Galactic Evolution

Trinh X. Thuan, in collaboration with J. P. Ostriker of Princeton University Observatory, studied the chemical history of our Galaxy. They investigated models under certain restrictive assumptions: (1) the total mass in a cylindrical element (1 pc^2 cross section) perpendicular to the plane of the Galaxy is constant in time and initially gaseous and metal free; (2) the gaseous component is always well mixed; (3) the birthrates of various stellar types are declining (or increasing) exponential functions of time. *No satisfactory one-zone model could be constructed* when it was required that the calculated models, after ~ 12 billion years, match present conditions in the solar neighborhood. The models either produced far too many metal-poor, low-mass stars or had an increasing rate of low-mass star formation and were presently about to convert all the gas to low-mass stars, or they had both defects. No plausible variations of the input physics (stellar evolution theory) or boundary conditions (age of the Galaxy, etc.) could be found that would yield a satisfactory model.

After demonstrating the *failure* of the one-zone model, they suggest an alternative scheme involving a two-zone model in which material shed from dying halo stars accumulates in a smaller, more rapidly rotating disk. The two-zone models are both simpler and more successful than one-zone (pure disk) models in that (1) the observed absence of metal-poor low-mass dwarfs is expected, not anomalous, and (2) the relative birthrate function (IMF) need not be a strongly variable function of time, in agreement with recent interpretations of the observed stellar populations and neutral hydrogen in our own and other galaxies: even a simple "Salpeter" IMF for both

disk and halo will produce an acceptable model. The model with a halo Salpeter IMF, with $\sim 1/4$ of the mass of the disk secondary, and with $\geq 1/2$ of the metals made in the halo seems most compatible

with observations of metal abundance in low-mass stars, deuterium abundance, halo planetary nebulae and light from Population II stars, and with dynamical arguments on the stability of the disk.

GALAXIES

Ionization Structure of Gaseous Nebulae in Galaxies

The interpretation of the spectra of the regions of ionized interstellar gas in external galaxies offers the best hope for determining the chemical composition in those systems. The aim of such studies is to throw light on the origin of the chemical elements and the chemical evolution of galaxies.

Although some results from this type of analysis have been achieved (see, e.g., *Year Book* 69, p. 100, and *Year Book* 70, p. 423), and these have subsequently been amply confirmed, further progress requires that the ionization structure of these regions be better understood.

In this report year, Searle has surveyed the strengths of emission lines that are probes of ionization structure in a number of H II regions in M31, M101, and M51. In particular, a systematic survey of the behavior of the infrared lines of [S III] has been carried out. Searle is collaborating with G. Shields of the University of Texas in the interpretation of the data. The observed behavior of the [S III] lines is not in accord with the predictions of the simple ionization-structure models that have so far been used to interpret the spectra of H II regions. Unexpectedly large density fluctuations within the emitting regions are indicated. The analysis is continuing, but it is already clear that the low excitation that is characteristic of regions situated in the inner spiral arms of galaxies is not simply a consequence of an enhanced oxygen abundance, which hitherto had seemed to be the most likely hypothesis.

In a related program, Searle has collab-

orated with A. Boksenberg of University College, London. Using Boksenberg's image-photon-counting system to supplement the lower resolution spectra from the multichannel spectrometer, quantitative spectrophotometry has been carried out on a number of metal-poor nebulae. The extensive data on K 648, the planetary nebula in the globular cluster M15, and on the dwarf emission-line galaxies II Zw 40 and Markarian 116 are being analyzed by comparison with the predictions from model nebulae.

Compact Galaxies

An eighth list, giving positions and descriptions of some 500 compact galaxies identified in recent years by the late F. Zwicky, was prepared for publication by Sargent and Kowal.

Seyfert Galaxies

Sargent completed a program to obtain spectrum scans of all of the known Seyfert galaxies brighter than 16.5 mag at a resolution of 20 Å in the blue and 40 Å in the red. Observations are made of the nuclei of 64 galaxies through a 10" aperture with the multichannel spectrophotometer at the Cassegrain focus of the Hale Telescope. The intention is to make a uniform astrophysical study of these objects and to search for possible correlations between the observed continuum and emission-line properties. The survey has revealed a number of new "iron galaxies" similar to the archetype I Zw 1, in which there are strong permitted lines of Fe II and in which normal forbidden lines are absent or very weak. In several of these "iron" objects there

is an emission line at both λ 8600 in the rest frame of the source; this may be the Ca II triplet. Toward the end of the report year, higher-resolution scans were made of Markarian 231, in which this emission feature is most prominent, in order to measure its wavelength more accurately. The feature is particularly interesting because Kirshner, Oke, Penston, and Searle (*Astrophys. J.*, 185, 303, 1975) identified an emission band in supernovae of Type I with the Ca II triplet; other features in the visible part of the spectrum were identified with Fe II emission by these and other authors.

In parallel work, Sargent and Boksenberg used the latter's image-photon-counting system at the coude spectrograph of the Hale Telescope in order to obtain high-resolution emission-line profiles for a number of Seyfert galaxies. The regions around $H\alpha$, $H\beta$, $H\gamma$, and the [O III] lines were observed. An atlas of accurate line profiles, which can be compared with theoretical calculations, is being prepared for publication.

G. A. Shields of the Department of Astronomy of the University of Texas at Austin and Oke have made an analysis of the Seyfert galaxy NGC 1068, using absolute spectral energy distributions measured with the multichannel spectrometer on the 5-meter Hale Telescope. A reddening value $E_{B-V} = 0.4$ is obtained, in agreement with an earlier determination by Wampler. The line intensities indicate a filamentary geometry characterized by two electron densities, namely, $2 \times 10^5 \text{ cm}^{-3}$ and 800 cm^{-3} . Exponential and other extrapolations of the nonthermal continuum into the ultraviolet predict sufficient ionizing radiation for the emission-line region. Steady-state models can explain many of the observed line intensities, including [O I]. The observed strong [O II] and [S II] emission lines may result from time-dependent ionization due to continuum variability or shadowing effects of condensations. Assuming a solar oxygen abundance, the nitrogen abundance relative to hydrogen is larger than

the solar value, but similar to the high value found in the nuclei of normal galaxies.

Velocity Dispersions

Sargent collaborated with A. Boksenberg and K. Shortridge, University College, London, in making spectrograms of ten elliptical galaxies with the image-photon-counting system described in *Year Book* 73 (p. 154). Observations were made of NGC 584, 596, 720, 1052, 1172, 1395, 1426, 1439, 7507, and 7626 in the wavelength range $\lambda\lambda$ 4000–4300. Line widths were analyzed in conjunction with similar observations of four K-giant stars to obtain σ , the velocity dispersion for stars in each of these galaxies, by the Fourier transform method. Only one of these galaxies had been measured by other workers. R. Minkowski found $\sigma = 480 \text{ km s}^{-1}$ for NGC 7626; the new work leads to $\sigma = 285 \pm 36 \text{ km s}^{-1}$ for this object.

Dynamics of Elliptical Galaxies

C. P. Wilson has continued his study of elliptical galaxies described in *Year Book* 73 (p. 150). The aim of this program is to provide a set of data on early-type galaxies with different flattenings, ranging from E0 to S0, to serve as a basis for theoretical studies of these objects. The image-tube spectrograph on the Palomar 1.5-meter telescope has been used to obtain spectra for the determination of rotation curves of the following NGC galaxies: 221, 3115, 3379, 4473, 4697, 5322, and 7332. Also, the SIT-vidicon area photometer has been used to study the surface brightness in the *B*, *V*, and *R* passbands of these and other galaxies. Finally, high-dispersion spectra for the determination of velocity dispersions have been obtained with the SIT-vidicon at the 2.5-meter coude spectrograph on Mount Wilson. Reduction of these data is in progress.

Infrared Photometry of Galaxies

J. Frogel, E. Persson, and M. Aaronson of Harvard College Observatory in collaboration with Becklin, Neugebauer, and Matthews continued 1- to 3- μ observations of galaxies. The data consist of broad-band infrared colors, plus the luminosity-sensitive CO index at 2.3 μ . The initial results of this work showed that the 2- μ radiation from the nuclei of elliptical galaxies is dominated by the light of giant stars (*Astrophys. J. [Lett.]*, 195, L15, 1975). Current work involves extending the observations to more galaxies, determining the effective color temperatures of the radiation in the 1- to 3- μ region, and investigating the dependence of the broad-band and CO indices on position within the galaxies. These data are necessary for a proper evaluation of the evolutionary correction to q_0 via the CO index. Observations were made on the 61-cm and 2.5-meter telescopes on Mount Wilson, and the Palomar 5-meter telescope.

Metallicity of M31 and M32

Oke and Dr. M. Schwarzschild of Princeton University, using the multi-channel spectrometer on the 5-meter Hale Telescope, have obtained absolute spectral-energy distributions from $\lambda\lambda$ 3300 to 10,600 for a number of places in the bulge of M31 and for two places in M32. These energy distributions can be interpreted as an increase of the heavy element abundance toward the centers of both objects by a factor a little less than 2 and by an excess of heavy element in M31 compared with M32 by a factor probably greater than 2. These results are consistent with line-index data analyzed by other observers. Beyond a radius of 2' in M31, no further composition changes were observed. At 7'.5 and 10' from the center of M31, along the major axis, there is evidence for young hot stars.

On a night of excellent seeing, and with M31 almost at the zenith, Thuan

and Oke obtained similar observations of the well-defined nucleus of M31. These observations show that there is a smooth increase in metallicity as the center is approached; the nucleus is not strikingly different from the surrounding bulge.

Globular Clusters in M31

Sargent continued work with F. D. A. Hartwick of the University of Victoria on the globular clusters in M31. The goal is eventually to determine the mass of M31 out to large radii from a study of the virial motions of the clusters. In this season's work, a search was begun in collaboration with S. van den Bergh of the University of Toronto for new globular clusters in the outlying parts of M31. Two approaches were used. First, 29 plates were obtained on the Kitt Peak 4-meter telescope at the prime and Cassegrain foci. These plates reveal objects that are probably new globular clusters. Concurrently, tests were made with short-exposure unbaked IIIa-J plates at the 1.2-meter Schmidt telescope. It appears that an exposure of about 5 minutes is the optimal one for revealing the known M31 globular clusters with this combination; however, the large number of plate defects on IIIa-J emulsions make it necessary to use double exposures. A survey of the region around M31 is to be made using this technique in 1975-1976.

Further Observations of Bl Lacertae

Thuan, Oke, and Gunn have reobserved the nebulosity surrounding the peculiar object BL Lacertae. Spectrophotometric observations, using an entrance annulus to block out the nucleus, made a year ago by Oke and Gunn (*Astrophys. J. [Lett.]*, 189, L5, 1974), appeared to indicate that the nebulosity was essentially a normal elliptical galaxy. The observation was difficult and repetition under better conditions was obviously desirable. Such conditions were realized in 1975 with:

(1) excellent seeing, to minimize the amount of scattered light from the nucleus into the annulus; (2) higher resolution (40 Å in the blue and 80 Å in the red and near infrared); (3) use of a control star to actually measure the amount of light at each wavelength spilling over from the occulting disk into the annulus; and (4) observations very near the zenith, where atmospheric refraction effects would be almost eliminated. Four absorption features identified as the Mg I and MgH band, λ 4110 band, the G band, and H and K of Ca II were observed. The redshift is $z = 0.070 \pm 0.005$, in agreement with the previous results. When the effects of the radiation from the central bright source are removed, the residual spectral-energy distribution is found to be very similar to that of a standard giant elliptical galaxy redshifted by $z = 0.070$ and reddened corresponding to $E_{B-V} = 0.28$.

Radio Source 3C120

The strong variable radio source 3C120 was identified in early astronomical literature as a variable star in the Galaxy. Later, after it appeared that the object had an emission-line spectrum like a Seyfert galaxy and a redshift of 10,000 km s⁻¹, it was studied intensively because of its resemblance, in many respects, to a quasar. One suggestion that has been advanced for the explanation of quasars is that they are events taking place in the nuclei of elliptical (E) galaxies. Consequently, some astronomers have argued that the slight nebulous fringe reported by Arp (*Astrophys. J.*, 152, 1101, 1968) around 3C120 was evidence of a surrounding E galaxy.

New photographs by Arp at the f/2.7 prime focus of the 4-meter Kitt Peak National Observatory telescope show a much greater extent to this surrounding nebulosity and resolution of features within it. This evidence, together with several other lines of argument, has led Arp to the conclusion that 3C120 repre-

sents a spiral or disturbed spiral galaxy whose nucleus contains the active, compact, and variable source of energy.

Velocity Fields in Spiral Galaxies

Van der Kruit completed the reduction of the spectrograms he had taken of the spiral galaxies NGC 4736, 3310, and 2715 with the two-stage image-tube spectrograph at the Cassegrain focus of the Hale Telescope. Usually H α , [N II] $\lambda\lambda$ 6548, 6583, and [S II] $\lambda\lambda$ 6716, 6731 were measured. Extensive calibrations of the curvatures were carried out from various exposures of the comparison lines all the way along the slit, and distortions in the fiber optics were also investigated. It turned out that these could be treated as random, with a standard deviation of about 2.5 μ at each point. At the dispersion of ~ 40 Å mm⁻¹, this corresponds to about 4 km s⁻¹ and was the largest contributor to the final errors. Interspectrum comparisons of measurements at the same points in the galaxies gave a 1 σ error of about 7 km s⁻¹ in the final velocities.

From these measurements, detailed velocity fields were constructed. The consistency of adjacent position angles showed that shifts in the zero point in velocity between spectra were always smaller than 10 km s⁻¹, and in nearly all cases less than 5 km s⁻¹. For NGC 4736, 39 spectra were used (total exposure time 12.75 hours), giving velocities at 312 independent points in the inner ring of bright H II regions. For NGC 3310, there were 35 spectra (6.42 hours), giving velocities at 317 points, while 10 spectra (5.5 hours exposure) of NGC 2715 gave velocity information at 151 points.

The observations of NGC 4736 confirmed and extended the results obtained earlier (*Astrophys. J.*, 188, 3, 1974). The noncircular motions that were reported there for the directions near E-W were found to be isolated at the inner edge of the ring and somewhat smaller in magnitude. The formal solution for

the case of purely circular motion gives a dynamical line of nodes of $114^\circ \pm 2^\circ$, in agreement with the earlier value ($113^\circ \pm 2^\circ$), while the more extensive material also permitted solving for the inclination to the plane of the sky: $36^\circ \pm 6^\circ$. The solution of the "expanding ring," as proposed previously, indicates that in the N-S direction the expansions are small, increasing to 30 km s^{-1} on the minor axis and to about 60 km s^{-1} in the E-W direction before they became indeterminable on the line of nodes. This suggests an excellent correlation between the magnitude of the noncircular motions and the brightness of the radio continuum emission. Measurements of the H I velocity field done in Westerbork will be used to decide between the various models.

In NGC 3310 a systematic pattern of strong (50 to 100 km s^{-1}) noncircular motions was found associated with the bright spiral arms. The analysis is hampered by the lack of independent information on the position angle of the line of nodes, the inclination, and which side is the nearer. A program to determine the velocity field further from the center by obtaining measurements of the H I 21-cm line with the Westerbork radio telescope will be carried out to further elucidate the first two. A preliminary analysis indicates that gas is streaming inward along the spiral arms if the spiral structure is trailing, or streaming out if it is leading. The rotation center is displaced from the nucleus by about $1.5''$, as was earlier suggested by Chin-carini and Walker (*Astrophys. J.*, 147, 416, 1967).

NGC 2715 shows a velocity field that is consistent with a model having mainly circular rotational motions, although there are inward radial motions near the minor axis. High-dispersion spectra of the central part of NGC 4258 indicate that at distances less than $0.5'$ from the nucleus the lines of H α [N II] and [S II] are broad at most positions. Turbulent

but a quantitative reduction of these spectra is difficult.

Spiral Structure in the Old Disks of Galaxies

Schweizer continued the photometric investigation of spiral structures in galaxies, especially of the broad spiral patterns in the underlying old disks of Sb I and Sc I galaxies.

Near-infrared plates of M51, obtained with a 90-mm image tube, show directly the pattern in the underlying old disk. This pattern is significantly broader than the narrow arms usually seen on blue plates and is interpreted as a region of enhanced surface mass density in the old disk. The location of the dust lanes near the crest of this smooth pattern suggests that the maximum gas compression occurs near the potential minima of the disk, as predicted by the shock models of W. W. Roberts (*Astrophys. J.*, 158, 123, 1969).

A previous study indicated that M81 possesses a very pronounced spiral pattern in the underlying old disk. The amplitude of the azimuthal light variations increases outward and reaches ± 0.27 mag at 10 kpc radius, the observational cutoff. Since recently published spiral-density-wave models place corotation in M81 at 10–11 kpc radius, and since radio maps from Westerbork show that the surface brightness of H I arms drops sharply at $r \approx 10$ kpc, it should be interesting to know how the disk pattern behaves beyond $r = 10$ kpc. To answer this question, Schweizer obtained an extensive new set of ultraviolet, blue, and red plates of M81 with the 1.2-meter Schmidt camera. By digitizing and averaging the plates, it is hoped that an accurate light distribution may be obtained to a radius approaching 15 kpc.

Interacting Galaxies

Schweizer continued the spectroscopic

an attempt to find their relation to normal galaxies. Spectra of NGC 2535/6., 3718/29, and 7753/2 were obtained with the 5-meter Hale Telescope, and the reduction was started.

The pair of galaxies NGC 7753/2 forms a particularly interesting system. A disturbingly large velocity difference of -341 km s^{-1} between the two components was reported by Dr. F. Bertola and Dr. S. d'Odorico of the Osservatorio Astrofisico di Asiago, Italy. Such a large velocity difference implies a moderately hyperbolic passage of the companion, which is relatively inefficient at generating spiral structure, according to the tidal interaction models of Toomres (*Astrophys. J.*, 178, 623, 1972). However, NGC 7753 shows two very pronounced spiral arms, and the elliptical companion NGC 7752, which is located at the end of one of these arms, shows clear signs of recent tidal interaction: an integral-shaped deformation of the outer isophotes and a set of giant H II regions near the nucleus. From measurements of several pairs of spectra, Schweizer found a preliminary value of -274 km s^{-1} ($\sigma = \pm 7 \text{ km s}^{-1}$) for the velocity difference, the final value depending on the exact position of the nucleus in the companion. This supports the view that the orbit of the companion is hyperbolic and seems to indicate that spiral structure can be generated by tidal interactions under a wider range of conditions than hitherto assumed.

Large Magellanic Cloud

Ever since Baade (*Astrophys. J.*, 100, 137, 1944) first resolved the stellar content of M32 and NGC 205, the existence of an underlying population of red stars has been recognized as a common element of galaxies. The red giant population is found in all members of the Local Group, as discussed by Sandage (*Pontificiae Academiae Scientiarum Scripta Varia No. 35*, 601, 1971), and recent investigations have shown that it

exhibits a strong concentration toward the Bar in the Large Magellanic Cloud. With the aim of finding the metallicity distribution and the fraction of light represented by these red stars, Hardy started an observing program in 1973 at Las Campanas. By isolating areas in the LMC Bar free of bright ($M_V < -3$) Population I giants and supergiants, it is possible to observe the underlying population that forms the bulk of the system without the strong biasing in surface colors and magnitudes introduced by the patchy but very bright extreme Population I stars. Hardy observed more than a dozen areas photoelectrically in the DDO system at the 91-cm telescope at Cerro Tololo Inter-American Observatory, and in the *UBV* at the 1-meter telescope at Las Campanas Observatory. In addition, sets of *B* and *V* plates were obtained at the $f/7.5$ focus of the 1-meter telescope, covering a field 3° in diameter centered at $\alpha_{75} = 5^{\text{h}}18^{\text{m}}$, $\delta_{75} = -69^\circ20'$, and color-magnitude diagrams were constructed for four of the regions for which surface photometry was obtained. Tifft and Snell's (*Mon. Not. R. Astron. Soc.*, 151, 365, 1971) photoelectric sequence was extended photographically through the use of transfers. The plate limit was set at $V = 19.3$. A red giant branch similar to that of a globular cluster of intermediate to high metallicity is apparent, together with what has been tentatively identified as a horizontal branch at the plate limit ($M_V = 0.5 \text{ mag}$). In addition, a weak, young main sequence is present. Study of the surface colors indicates that, after the effect of the observed part of the young main sequence is removed, they closely resemble colors of globular clusters of intermediate-to-high metallicity, in agreement with the conclusions from the color-magnitude diagrams. The same conclusion is reached if the observed luminosity function is compared to that of globular clusters. Furthermore, if the count-brightness ratio technique of Baum and Schwarzschild (*Astron. J.*, 60, 247,

1955) is used to derive the ratio of light in Population II to that in Population I, a value between 60% and 75% is obtained, depending on the details of the normalization of the luminosity functions for globular clusters. The conclusions so far are consistent with the interpretation that the observed population is like that of globular clusters, but further work with plates of larger scale will help in reaching a definitive solution.

History of Star Formation in Galaxies

Zinn, in collaboration with Dr. John Norris of the Mt. Stromlo Observatory, has investigated the stellar populations of the dwarf spheroidal galaxies. The similarities between the color-magnitude diagrams for the Draco and Ursa Minor dwarf galaxies and those for the galactic globular clusters long ago suggested that the dwarf spheroidal galaxies and the globular clusters have had similar histories of star formation. It has been known for some time, however, that the variables in the dwarf spheroidal galaxies and the globular clusters do not obey the same period-luminosity law. Norris and Zinn have shown that the variables in the galaxies also do not fit the evolutionary scheme that successfully explains the globular cluster variables. These facts have led to a new picture of the history of star formation in these systems. According to Norris and Zinn, the period-luminosity law, the evolutionary status of the variables, and the color-magnitude diagrams can be explained if in each galaxy there were at least two epochs of star formation, one 8 to 10×10^9 years ago and one as recent as 1×10^9 years ago, but with very little enrichment in metal content from one generation of stars to the next. This picture of multiple stellar populations suggests that either supernova explosions during the first epoch of star formation were unable to drive all of the gas from these systems or gas was accreted some time

after the first epoch. Neither one of these events was expected to occur in galaxies of such small mass.

Formation of Galaxies

J. Richard Gott III, California Institute of Technology, and Thuan have proposed a simple scheme for the formation of spiral and elliptical galaxies. If star formation in the early protogalaxy is essentially completed by the point of maximum collapse, then an elliptical galaxy is formed. If a significant amount of gas is left over at this point, it will dissipate its energy to form a disk-like spiral galaxy. The competing effects of dissipation and turbulent viscosity are analyzed, using a model of cloud formation in the early protogalaxy. Numerical models including both stars and gas are used to follow the collapse. The gas and stars collapse together until they reach the plane, whereupon the gas forms a disk and the stars relax to form a spheroidal halo. The gas disk does not hit the plane at its equilibrium position, and both radial and nonaxisymmetric oscillations of the disk are expected before equilibrium is reached. "Zeroth" order Maclaurin spheroid models for equilibrium spiral and elliptical galaxies are presented, which relate many useful galactic parameters to the original size and angular momentum. Monte Carlo calculations suggest that the tidal interaction picture of Peebles is capable of explaining both the angular momentum of our Galaxy and the observed distribution of ellipticities among elliptical galaxies. Observed properties of ellipticals and spirals imply that ellipticals formed out of relatively larger perturbations at recombination than did spirals, giving the ellipticals greater densities and shorter collapse times. If early star formation is rapid and follows a ρ^2 dependence, ellipticals are expected to complete their star formation by the time of maximum collapse, while spirals

are not. Protogalaxies arising from larger initial density fluctuations cluster more

easily, thus explaining why ellipticals are found preferentially in large clusters.

CLUSTERS OF GALAXIES

Redshifts and Magnitudes

Westphal, Kristian, and Sandage have started a program to measure line redshifts of faint galaxy clusters, using a new prism spectrograph with an SIT-Vidicon detector at the Cassegrain focus of the Hale Telescope (see "Instrumentation"). Broad-band magnitudes and colors of the brighter clusters are being measured with an S20 photomultiplier and those of the fainter clusters with the SIT-Vidicon photometer.

The first stage of the program is concentrated on intermediate-redshift clusters ($z = 0.15$ to 0.3), especially the Abell clusters of richness class 3-5, supplemented by clusters of smaller richness and a range of Bautz-Morgan contrast type. There is a scarcity of data for clusters with $z > 0.2$, which is the cutoff for photographic spectra due to saturation by the night sky. The objectives of the program are to define better the Hubble diagram and to investigate the dependence of the brightest galaxy magnitude on richness and Bautz-Morgan type.

Redshifts have so far been measured for 40 clusters in the range $z = 0-0.4$, most of them in the interval $0.2-0.3$. New photometry is available for 16 of these.

Measurement of clusters with $z > 0.3$ requires particularly good seeing and will be pursued as observing conditions permit.

Redshift-Magnitude Diagram for a Complete Sample of Nearby High-Latitude Abell Clusters

Thuan and Gunn are engaged in an observational program to gather more data for the bright end of the redshift-

magnitude diagram. They are in the process of obtaining photometry and redshifts for the brightest member of a complete sample of high-latitude Abell clusters, chosen such that the Abell richness class is ≥ 1 , the Abell distance class is ≤ 4 , and the galactic latitude $\geq 30^\circ$. The color system is defined by four filters ranging from $\lambda\lambda$ 3300 to 7000, with a bandwidth from 400 Å in the blue to 1000 Å in the red. These observations, made with the Palomar 1.5-meter telescope, are designed to improve the precision in the determination of q_0 and to study better (1) the correlation found by Bautz and Morgan between the brightness of the brightest member and the contrast between the brightest member and the remainder of the cluster population, and (2) the possible dependence of M_v of the brightest cluster galaxy on the population of the parent cluster.

Determination of the Background Light in the Coma Cluster

Plates of the Coma Cluster in different colors (infrared to blue) have been obtained by Thuan and Kormendy at the 1.2-meter Schmidt in order to measure accurately the distribution of the background light (presumably due to intergalactic stars tidally stripped off in galaxy encounters) as a function of the distance from the center of the cluster. A preliminary reduction of the data for 5000 Å in a zone between 5' and 25' from the cluster center gives, for the diffuse light, $L = 3.6 \times 10^{11} L_\odot$ for $H = 100 \text{ km s}^{-1} \text{ Mpc}^{-1}$. This may be compared with the contribution from the galaxies in the same radius range of $7.1 \times 10^{11} L_\odot$. The background-light distribution follows closely that of the galaxies.

Collisions of Members of Clusters

In an extension of earlier work on the dynamics of galaxies in clusters, Richstone performed a crude analytic estimate of the extent and character of damage done to S0 galaxies during collisions with more massive galaxies. Numerical experiments to check the result are planned. These results suggest that the most elliptical-like S0's may be

thickened sufficiently to be identified as ellipticals. This phenomenon may account for the paucity of S0 galaxies relative to ellipticals in the densest clusters noted by Oemler; it lends additional theoretical support to the view that differences among rich clusters are due to initial density differences that make dynamical interactions more important in some cases than others.

RADIO SOURCES

Optical Identification of Radio Sources

In February, March, and April 1975, A. G. Willis and H. R. de Ruiter of the Leiden Observatory collaborated with Arp on the optical identification of radio sources discovered on a 21-cm survey with the Westerbork synthesis radio telescope in the Netherlands (see "Guest Investigators" section). The first 17 candidate identifications of radio sources with stellar objects in this study have been observed by Arp at the Cassegrain focus of the 5-meter telescope with the Oke multichannel spectrophotometer. A high success rate for identification is apparent, since preliminary analysis indicates all 17 to be confirmed as quasars. A number of probable redshifts have been estimated, including one slightly greater than $z = 3$.

One of the most interesting new quasars discovered is an object of neutral color associated with the compact radio source 0846+51W1. Between 15 January and 15 February, 1975, it increased in brightness dramatically from around $m \approx 19.5$ mag to $m \approx 15.8$ mag, a brightening of well over three magnitudes in less than one month (Fig. 3). The radio source was found to have the centimetric excess spectrum characteristic of variable compact sources. Sargent has cooperated with Arp in obtaining observations of this quasar as it decreased in brightness over the ensuing months. By May it was fainter than the

18th magnitude. The scans show the quasar has a power-law spectrum of about $\alpha = 1.8$; efforts are now in progress to determine its redshift. This quasar is situated within 10" of an interacting galaxy system.

Another interesting quasar discovered in this program lies about 5' north of the Seyfert galaxy NGC 4151. Arp has measured its energy distribution with the multichannel spectrophotometer and reports a magnitude $m_{4600\text{\AA}}$ of 20.7 and a probable redshift near $z = 1.84$.

Arp has also been cooperating with the radio astronomy group at Bologna and with M. H. Ulrich at the University of Texas in the identification of radio sources in the vicinity of galaxies. Deep plates around six radio E galaxies are being measured for identification purposes. The plates of one of these, NGC 5127 (B2 1321+31), show straight blue filaments emerging from the galaxy and a connected companion galaxy. In another instance, R. Ekers, R. Fanti, C. Lari, and M. H. Ulrich have demonstrated an alignment of compact and extended radio sources across a central radio E galaxy. One of the compact sources has been identified with a stellar object near apparent magnitude 21. Arp has obtained spectrum scans of this object and is analyzing them.

It is unusual for a dwarf galaxy to contain a radio source, but B2 2335+30 has been photographed by Arp with the 5-meter telescope and its dwarf morphol-

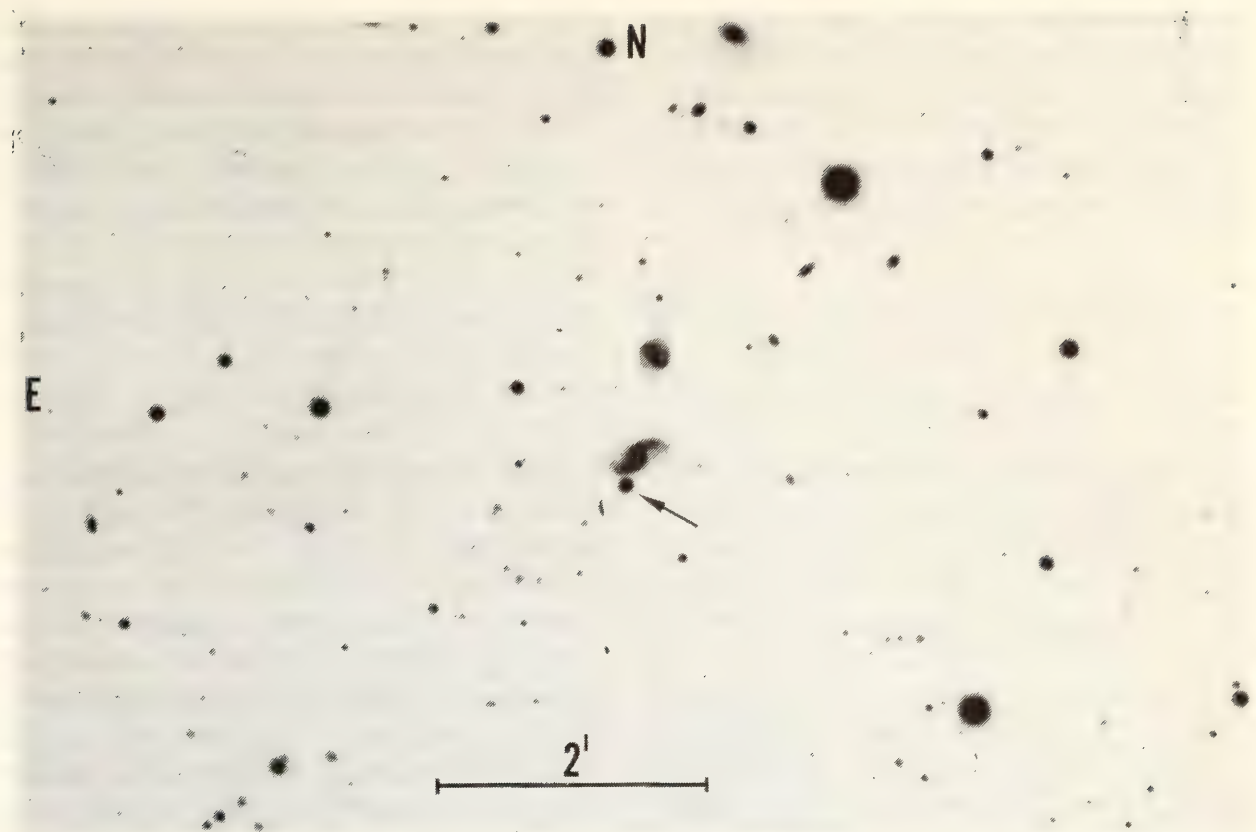


Fig. 3. Eruptive quasar 0848 + 51 W1. Discovered by Arp, Willis, and de Ruiter in February 1975. In less than one month it had brightened more than 3 mag to near the magnitude shown here. Exposure, 45 min on baked IIIa-J behind a GG 385 filter at the prime focus of the 4-meter Mayall reflector, Kitt Peak National Observatory.

ogy is confirmed. The exact location of the radio source within the galaxy is now being ascertained by the Bologna group. The dwarf system NGC 1569 has been investigated by Arp. The relationship of the extended radio halo, mapped by Westerbork observers, to the main galaxy is being studied. Arp also reports multichannel scans of the two bright stellar objects in the center of NGC 1569 which have featureless spectra. Preliminary analysis of the scans reveals straight featureless energy distributions closely approximating power-law spectra.

Radio Sources Near Spirals

It is well known that some elliptical galaxies have radio sources associated with them, usually strong radio sources paired across the central galaxy. It is not definitely established, however, that spiral galaxies similarly have radio

sources physically associated with them but lying outside their optical boundaries. S. Gulkis and M. Klein at the Jet Propulsion Laboratories, R. Carpenter at the California State University at Los Angeles, and Arp are collaborating on the study of this possibility. They have recently completed mapping of 4-square-degree areas around four separate spiral galaxies of magnitude brighter than 11.2. The measures were made with the 64-meter radio telescope at Goldstone, California. The galaxies were NGC 3521, 4030, 4565, and 4725. For these four galaxies the density of radio sources detected was not significantly greater than that expected from the general background-source density far from the galaxies. This general background density was accurately determined by the authors by careful analysis of four control fields in a fashion identical to the analysis of the areas around the galaxies.

Other studies, however, have indicated excess radio sources in the vicinity of some spiral galaxies. The largest one of these surveys is that by the Soviet astronomer, H. M. Tovmassian. The present authors check-measured a sample of 13

of Tovmassian's reported sources and confirmed each one of them. The results imply that Tovmassian's particular sample of spiral galaxies indeed have an excess of radio sources. The subject requires further investigation.

QUASARS AND QUASI-STELLAR OBJECTS

Quasar Surveys

Richard Green, a graduate student, has completed the Palomar 46-cm Schmidt survey designed to find bright quasars over a sky area of about 10,000 square degrees. Blue and ultraviolet exposures on the same film will be used to search for objects brighter than 16 or 17 mag with an ultraviolet excess. Green has inspected visually about 10% of the material and has found many ultraviolet-intense objects. Spectra have been obtained of more than 300 objects at the 1.5-meter telescope by Green and at the 5-meter telescope by Schmidt. Four new quasars of visual magnitudes between 14.7 and 16.5 and with redshifts between 8% and 16% have been found. In addition, at least 100 new white dwarfs and two compact N galaxies of small redshift have been isolated. Preparation is underway for scanning and processing the entire survey, using a PDS scanner, in cooperation with the Jet Propulsion Laboratory.

Spectroscopic Surveys

Schmidt is completing spectroscopic observations of quasi-stellar sources identified in part of the 6-cm National Radio Astronomy Observatory survey by D. Shaffer of the Department of Astronomy, Yale University. Optical flux densities of the confirmed quasars are measured with the multichannel spectrophotometer. This sample will allow a derivation of the space distribution of quasars with flat radio spectra, which make up more than half of the quasars identified at 6-cm wavelength.

Absorption Lines

Sargent and R. F. Carswell and A. Boksenberg of University College, London, continued work on high-resolution spectroscopy of absorption lines in quasars with Boksenberg's image-photon-counting system. The instrument was used for 10 nights at the coudé focus of the Hale Telescope. The main effort was put into obtaining observations of the 17 mag quasar PHL 957, which has $z_{\text{em}} = 2.69$ and a very rich absorption spectrum. Two independent sets of observations of the complete spectrum of this object were made in the wavelength range $\lambda\lambda$ 3400–5100 at a resolution of 0.7 Å. Two-hundred eighty-four absorption lines were found and measured, and intensive effort was put into a search for redshifts, using computer techniques developed for the analysis of Pks 0237–23 described in *Year Book* 73 (p. 154). At the end of the report year, only one absorption redshift, $z_{\text{abs}} = 2.30$, which accounts for only about 15 of the 284 lines, can be regarded as certain!

In related work, Sargent, Boksenberg, and Carswell observed other bright quasars with absorption lines: PHL 938, Markarian 132, and Pks 0735+178. These observations were made principally to investigate further the "magic" splitting of $\Delta z = 0.0012$ between adjacent redshifts found by Boksenberg and Sargent in Pks 0237–23 and described in *Year Book* 73 (p. 154). The new observations, taken in conjunction with earlier measurements by Dr. D. C. Morton and his associates at Princeton University Observatory, show that all the five absorption-line quasars observed at suffi-

ciently high resolution show at least one pair of redshifts split by about the above amount. However, the splitting is only a little larger than the spectral resolution of existing observations. Accordingly, Sargent and Boksenberg are planning a major effort to obtain even higher resolution than 0.7 \AA in observations to be made late in 1975. This will settle whether there is truly a characteristic splitting common to all absorption-line quasars or whether all merely begin to show structure at high resolution. If the first alternative is correct, it will be strong evidence that the absorbing clouds have been ejected by the quasars and that radiative pressure in lines plays some role in accelerating the clouds.

An interesting by-product of the foregoing observations is that two of the objects, PHL 938 and Pks 0735+187, show Mg I λ 2852 in absorption, as well as the Mg II doublet λ 2800 commonly found in absorption-line quasars. In PHL 938, the Mg I and Mg II lines are found in the absorption redshift $z_{\text{abs}} = 0.61$, which differs considerably from the emission-line redshift $z_{\text{em}} = 1.95$. The relative strength of Mg I and Mg II is similar to that revealed by ultraviolet observations of absorption lines arising in the interstellar medium of our own Galaxy. The possibility is suggested that the $z_{\text{abs}} = 0.61$ absorption system, which is one of uncommonly low degree of ionization, is produced in an intervening galaxy. A search for a cluster of galaxies at this redshift near PHL 938 on the plane of the sky should be undertaken. The other object, Pks 0735+187, is an object of the BL Lacertae type, with no emission lines. Its absorption redshift is $z_{\text{abs}} = 0.424$.

In connection with the work on the identification of quasar absorption spectra, Sargent and Caltech undergraduate Todd Boroson have devoted considerable attention to the phenomenon of "line locking." In a significant number of quasars, pairs of absorption-line redshifts are separated by an amount such as to cause the longer wavelength com-

ponent of a prominent doublet to coincide with the shorter wavelength component of the doublet in the other member of the pair. The C IV doublet $\lambda\lambda$ 1548, 1550 behaves in this manner in several objects. However, despite intensive efforts by Scargle and others, there is no plausible theory of the effect. Sargent and Boroson have used random number techniques to investigate the statistical probability of various coincidences between lines and doublets in different redshift systems in the same quasar. So far there is no evidence that any of the effects apart from the C IV line locking are real.

Energy Distributions

Richstone has begun an examination of Schmidt's low-resolution multichannel spectrophotometry of QSOs in the hope of developing a classification system and finding a possible "signature" of the physical process responsible for the continuum emission of the objects. Fairly uniform observational material exists for at least 50 objects. One preliminary result is that the broad depression in QSO spectra from 4000 to 4400 \AA (in the emitted frame) anticorrelates weakly with luminosity. The behavior of this feature is reproduced by a simple model in which the light comes from a bright galaxy, plus a smooth power law.

Distribution of Redshifts

Green and Richstone have reexamined the distribution of redshifts of QSOs and emission-line galaxies in an attempt to test the hypothesis that periodicities exist at wavelengths of 0.03 and 0.07 in z (Burbidge and O'Dell, *Astrophys. J.*, 178, 583, 1972, and references cited therein). An independent sample of QSOs and Markarian galaxies displays no significant periodicities. A series of random number experiments suggest that the significance of periodicities found in earlier work may have been overestimated.

Variability

On the basis of published observations, Borra has found some evidence that quasars that show absorption lines are less likely to vary than objects that have

only emission lines. A χ^2 test of the significance level (about 95%) of this difference between the two classes of objects is, however, not compelling. New observations are desired to improve the statistics.

OBSERVATIONAL COSMOLOGY

Groups and Clusters in the Southern Hemisphere

Sandage completed analysis of redshifts and photometry of selected groups and clusters of galaxies in the Southern Hemisphere. He had obtained the data in 1968-1969 and in 1971 at the Mount Stromlo and Siding Spring Observatories in Australia as part of the long-range redshift program (see *Year Book* 70, p. 417; *Year Book* 71, p. 689; *Year Book* 72, p. 131; and *Year Book* 73, p. 156). Analysis of the Hubble diagram for this subset of the complete material permits conclusions on a number of current problems.

1. The low-latitude groups permit a new solution for reddening as a function of $|b|$, similar to an earlier correlation for the northern E galaxies. As with these northern data, the color excess is a shallow function of latitude, consistent with a model where the galactic polar caps are reddening-free on the average, with reddening beginning at $|b| \lesssim 50^\circ$ at a rate of $E(B - V) \approx 0.033 (\cos b - 1)$ for $|b| \lesssim 50^\circ$. This slope is only about one half the traditional value.

2. The redshift-apparent magnitude plot (the Hubble diagram) is well populated between velocities $1500 \leq v \leq 4000$ km s⁻¹ with the southern groups, filling a gap in this interval caused by the lack of northern groups in this velocity range.

3. Residuals of the absolute magnitude about the mean Hubble line in the redshift-magnitude diagram for the first-ranked galaxies are correlated with population of the group, but only mildly. Figure 4 shows that for aggregates whose population is in the range $20 < N_c \lesssim 300$

(N_c is the number of cluster members in the first 2.5 mag intervals within a fixed linear radius, centered on the cluster), the mean absolute magnitude varies by only ~ 0.15 mag. This remarkably small dependence on population shows either that the luminosity function of cluster galaxies at the bright end is nearly vertical, or that the absolute magnitude of the first-ranked galaxy is determined by some upper limit in the galaxy formation process that is independent of the statistics relating to other members of the cluster. Work by Hardy and Sandage on the central density of the clusters in Fig. 4 as a function of N_c was begun by making counts on existing plates to advance the study of this remarkable property.

4. Analysis of the residuals, read as velocity differences of the new southern aggregates, combined with existing northern data, failed to show any systematic velocity perturbation in the *local* velocity field. The mapping of this field with the new data on E galaxies is better than a mapping that used Sc I systems, reported in *Year Book* 73 (p. 156), where again no perturbations were seen. The new material permits new limits of less than $\delta H/H = 0.08$ (σ) to be put on the perturbation of the local Hubble rate H for galaxies that have velocities smaller than 3000 km s⁻¹ toward and away from the Coma-Virgo complex.

5. A lack of perturbation in the velocity field at this level, in the presence of a density contrast of $\delta \rho/\rho \approx 3.4$ caused by the clumping of galaxies in the Virgo density maximum, shows that the effect of gravity on the underlying linear velocity flow is small. This suggests that the

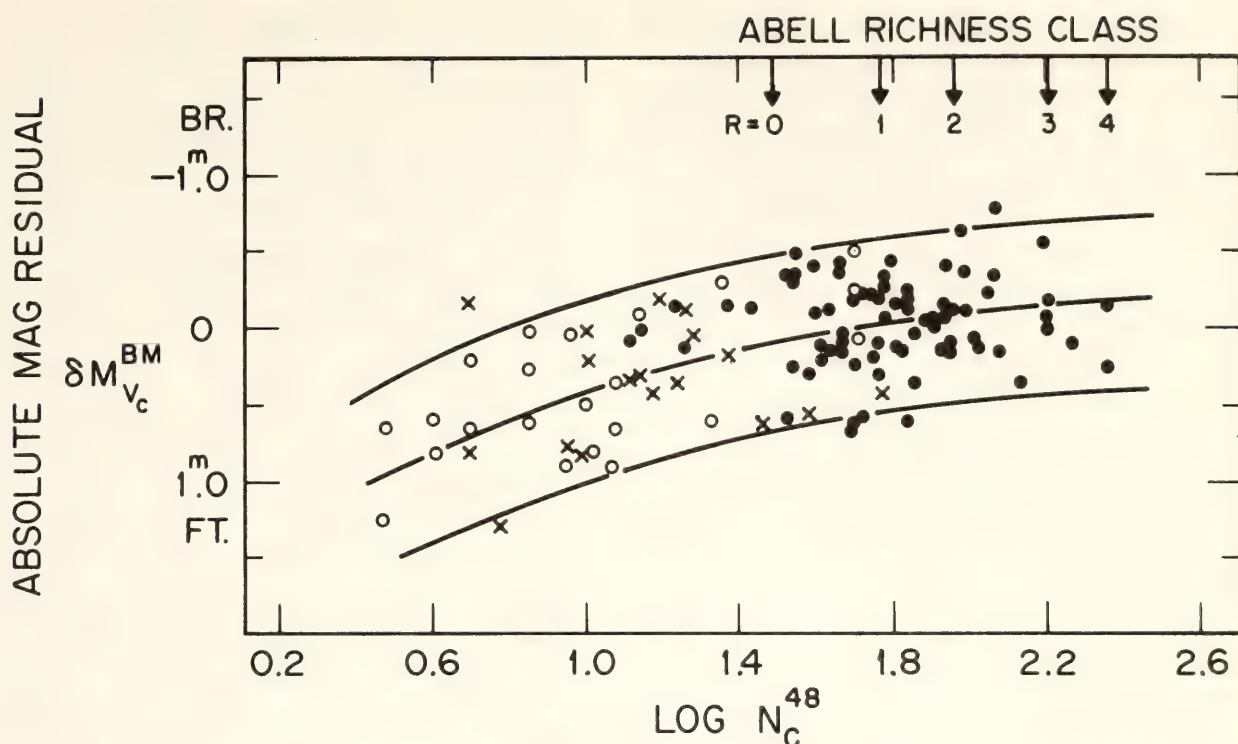


Fig. 4. Correlation of richness with the apparent-magnitude residuals δV_C^{BM} (corrected for aperture effect, K -dimming, galactic absorption, and Bautz-Morgan effect) from the linear $5 \log v_0$ line of the Hubble diagram. Crosses are from the re-reduced V_C^{BM} magnitudes for northern HMS groups; open circles are from V_C^{BM} magnitudes for the new Southern Groups; and closed circles are for the remaining clusters known from previous work. The mean Abell richness class, corresponding to $\log N_C^{48}$, is shown along the upper abscissa.

ratio of kinetic energy in the expansion field to the gravitational potential energy of the density contrast is large, and hence that the deceleration parameter q_0 is very small, in agreement with the results reported in *Year Book 73* (p. 156). A formal value, based on the limit to the velocity perturbation of $\delta H/H \leq 0.08$ (σ), using a calculation by Silk (*Astrophys. J.*, 193, 525, 1974), gives

$$q_0 = 0.02 \pm 0.02 (\sigma).$$

Taken at face value, these results suggest that (1) the deceleration is nearly negligible (the Milne model Universe with no matter; (2) the Universe is open; and (3) the expansion will not reverse.

Cluster Redshifts

Gunn and Oke have continued their program to discover faint clusters of

galaxies and to measure the redshifts and absolute spectral energy distributions of the brightest members of these clusters. The primary aim of the search program is to produce a list of clusters, found under well-controlled conditions, which go to a well-defined apparent magnitude limit. This search was carried out initially with the 1.2-meter Schmidt telescope using IIIa-J plates; in all, six $6^\circ \times 6^\circ$ fields were observed. This research produced hundreds of clusters; from the few spectrophotometric observations, the redshifts found are typically between $z = 0.20$ and 0.35 , with a few going to 0.38 . A deeper survey is now underway at the 5-meter prime focus with a 90-mm magnetically focused image tube and baked IIIa-J plates. The band pass is from $\lambda\lambda$ 6000–7000. The fields are arbitrarily chosen areas of the $6^\circ \times 6^\circ$ fields above. The current survey, about two-thirds complete, has produced a sample of about 30 very faint clusters

of galaxies; a few of them have been observed for redshift and energy distribution. They typically have $z > 0.40$.

Data obtained up to a year ago, for 20 clusters with $z > 0.20$ and over 40 nearer clusters, have been analyzed even though the samples are somewhat heterogeneous. Formal values of q_0 have been determined from several sets of assumptions. The radio source 3C295 appears to be abnormally luminous and probably should not be included in any sample because of the way it was discovered. During the last year, another 15 energy distributions and redshifts have been obtained; many of these redshifts have $z > 0.40$. One very faint object ($V = 22.5$) for which the redshift is still somewhat uncertain probably has $z = 0.61$. Dr. A. Wilkinson has begun work on the energy distributions to determine whether evolutionary effects are present in the data.

Evolutionary Effects

Gunn and B. M. Tinsley of Yale University have continued their program to synthesize the populations of elliptical galaxies in an effort to determine the evolutionary corrections to the Hubble diagram. The observations are almost complete, but the revision of the spectro-

photometric standards discussed elsewhere requires further attention. Work is meanwhile progressing on ancillary matters, such as the determination of the old-disk giant-luminosity function, along with those for several globular clusters. Rough syntheses have been done, using the new luminosity functions which match colors and the very sensitive infrared CO and Wing-Ford band strengths. The resulting models are inevitably strongly giant-dominated, and therefore evolve very quickly. The corrections, coupled with Gunn and Oke's data on distant clusters, imply a large negative value for q_0 , which in turn requires, if nothing else is wrong, a large positive cosmological constant if one wishes to make the smallest possible change in the General Theory. The result is, at this time, no more than suggestive, however, and several systematic effects have yet to be adequately ruled out or investigated thoroughly. The most intriguing possibilities for explaining the observations are significant intergalactic absorption (about $A_v = 0^m.2$ at $z = 0.5$), or significant evolution of the brightest cluster galaxies through dynamical friction and subsequent accretion of smaller systems. These effects will be investigated thoroughly in the coming year.

INSTRUMENTATION

PEPSIOS Spectrometer

On the basis of the experience gained in the design, construction, and operation of the double Fabry-Perot Cassegrain monochromator (*Year Book* 73, p. 159), a 3-etalon PEPSIOS-type spectrometer with 40-mm aperture is in the process of being finished by Münch and Taylor. The instrument will be permanently installed in the coudé laboratory of the Hale telescope and initially will be operated with a resolving power of 250,000 at $H\alpha$, thus allowing the use of circular entrance apertures up to 10" in dia-

meter. The primary use of the instrument will be the study of faint lines in the spectra of planets and the study of interstellar absorption lines. Funds for the construction of the PEPSIOS spectrometer have been provided by a grant from the National Aeronautics and Space Administration.

SIT-Vidicon System for Photometry

Westphal and Kristian have continued to investigate the use of SIT television camera tubes for two-dimensional photometry. Calibration and data reduction

techniques have been refined so that the level of photometric accuracy obtained at the telescope is close to the limit (1%) expected from laboratory tests of the system. It is possible to reproduce a broad-band sequence, established with photomultipliers, in the range $12^m < V < 22^m$, with scatter less than 2% at the bright end and about 5% at the faint end. The accuracy at the bright end is of the order of the accuracy of the photomultiplier measurements. At the faint end, the errors are a combination of statistical photon noise, accuracy of the photomultiplier measurements, and vidicon errors.

The brightness limits at 12^m and 22^m are not intrinsic to the system. Brighter stars cannot be measured at the 5-meter prime focus because the exposure times become too short to measure accurately with the mechanical shutter that is used. Photoelectric standards fainter than 22^m were not available, but the signal is completely dominated by the sky at this magnitude, and the SIT measurements should be accurate to fainter levels. In a 10-minute exposure, stars are measurable to fainter than $V = 24^m$, with progressively lower accuracy because of pixel-to-pixel noise, mostly from photon statistics.

The accuracy limit of 1% for the SIT system is primarily due to apparently random variations of the order of $\frac{1}{2}\%$ in the background. It is not yet known whether these are a property of the tubes or whether they are due to instabilities in the electronics.

Spectroscopy with the SIT-Vidicon

The same SIT system used in the photometry program has been employed by Westphal and Kristian as the detector for several programs of low- and high-resolution spectroscopy.

For redshift measurements of remote galaxy clusters, a small prism spectrograph has been built. The design parameters were matched to the SIT detector and optimized for the galaxy-redshift

program. A prism system was chosen to maximize the throughput for faint objects. Two important features of the SIT detector for faint objects are (1) the reproducibility of the transfer function, which allows accurate sky subtraction, and (2) the two-dimensional format, which gives a multiplexing advantage and allows the sky and the object to be measured simultaneously. The sky subtraction works well and produces difference spectra that are essentially photon-noise limited. The system and the first cluster redshifts are described in more detail in a paper by Westphal, Kristian, and Sandage (*Astrophys. J. [Lett.]*, 197, L95, 1975).

The SIT has also been adapted for use as the detector at the coudé spectrograph of the Mount Wilson 2.5-meter telescope. It is being used by Brucato to study stellar line profiles and by C. P. Wilson to measure velocity dispersions and rotations of the central parts of nearby galaxies.

To reduce the thermal background for the long coudé exposures, a dry-ice coldbox was modified for cooling to -90°C with liquid nitrogen. At this temperature, thermal buildup is barely detectable with exposure times of several hours.

For Wilson's program, a new Bausch and Lomb replica grating of 270 lines mm^{-1} has been installed. This gives dispersions as low as 22 \AA mm^{-1} in the blue and 45 \AA mm^{-1} in the red. The high quantum efficiency, linearity, sky-subtraction capability, and the full two-dimensional format of the SIT, combined with the new grating, permit the accurate study of faint objects such as galaxy nuclei even with the high background-light levels at Mount Wilson.

Under Gunn's direction, a project to equip an experimental digital spectrograph built last year with a cooled integrating SIT camera for general observatory use is nearing completion. A liquid-nitrogen gas-transfer system is used for cooling, giving controllable temperatures from 0 to -120°C , stable to better than

half a degree. The control electronics are similar in principle to those used by Westphal and Kristian, but the decision was made to interface the system with a PDP-11/40 minicomputer to give real-time capability for addition, averaging, reduction, and display of spectra. The interface electronics are being built and tested by Knapp.

Programming is being done in the FORTH language, which is a high-level language designed for small computers that interact with various devices. Programs have been written by Zimmerman and Oke to operate the SIT camera, align the camera, collect and store the output data, provide balance factors for every pixel used, obtain the absolute sensitivity of the instrument, display the field characteristics, and display the absolute flux versus wavelength. All these functions can be performed essentially in real time.

Wobbling Secondary for Infrared Photometry

A new f/60 wobbling Cassegrain mirror and a new f/60 infrared photometer have been installed on the Mount Wilson 1.5-meter telescope and put into operation. With this new system, the 1.5-meter telescope has become one of the best infrared telescopes currently in use. The system is used approximately one week per month by staff and students to study infrared radiation from molecular clouds, H II regions, and external galaxies.

Big Bear Solar Observatory (BBSO) Instrumental Program

The 65-cm vacuum reflector was put into operation in 1974 with only moderate success. The figure of the mirror was not good, and internal flexure produced image distortion. These problems have now been corrected, the mirror having been refigured to an accuracy of 0.03 wavelengths rms and the flexure corrected. The system is currently being

brought back into operation. Despite these problems, some excellent observations were made with the vacuum telescope, particularly with the universal birefringent filter, which permits observation in any wavelength of the spectrum. With this instrument, B. LaBonte, a graduate student, observed a number of flares in the helium line, and Zirin was able to study the structure of the helium chromosphere.

Flexibility has been added to the optical observational capabilities at BBSO with the development of a hardware interface and software to permit computer control of the universal birefringent filter and associated camera system. The filter, which is used with the 66-cm reflector, is capable of positioning a 0.1-0.25 Å bandpass anywhere in the range 4000-7000 Å. When fully operational, the system will permit successive registered frames at different wavelengths to be acquired in intervals as short as 1.5 seconds. It should prove to be a valuable observational tool for the study of dynamic solar phenomena, such as flares and oscillations.

Las Campanas Image-Tube Spectrographs

The Las Campanas 1-meter Cassegrain spectrograph was returned to Pasadena for modifications, including the installation of a new image intensifier, a new transfer lens, and a helium-discharge comparison source. Engineering tasks for this work were carried out by Kelderman and Ribbens. The new image intensifier, type RCA C33063, is a two-stage, magnetically focused tube; it represents an improvement over the previous type in that it operates at a high voltage (increased gain) and has a better resolution. To accommodate the new tube, the fixed focusing magnet was rebuilt to obtain a stronger, more uniform field. A new reimaging lens, giving improved resolution over the previous system, was also installed. These changes appear to have improved the resolution substantially. The comparison slit-

illumination system was redesigned to reduce scattered light in the instrument. At the same time, a helium discharge lamp was added as a comparison source.

Another major activity was in connection with the purchase from Boller and Chivens of the Cassegrain image-tube spectrograph for the Las Campanas 2.5-meter telescope. The instrument was delivered in April 1975. Specifications

were formulated for the remote-control system to be constructed by the Astroelectronics Laboratory, and a preliminary design for a remotely controlled plate holder was developed.

The two-channel television guider for the Las Campanas 2.5-meter telescope was delivered in June 1975 and is currently undergoing performance tests.

ASTROELECTRONICS LABORATORY

J. A. Westphal served as Staff Representative for the Laboratory, with Fridenberg in immediate charge of operations.

This year the Laboratory directed its major efforts toward the design and completion of the manual and automatic control systems for the 2.5-meter du Pont Telescope for Las Campanas. The design of the system, except for the section concerned with two-coordinate control of the coudé flat, has been completed, and construction has advanced on

schedule, with installation on the telescope slated for September 1975. A prototype of this system, which has been successfully installed as a back-up coordinate monitoring display on the Palomar 1.5-meter telescope, has proved to be satisfactory. A second Laboratory project has been the design and production of a digital scan converter. This is a portion of Gunn's digital spectrograph that is to be used at the Palomar 5-meter telescope.

GUEST INVESTIGATORS

Seventy-four observers from 50 different institutions were accommodated as guest investigators at Mount Wilson, Palomar Mountain, Big Bear, and Cerro Las Campanas during the year.

Dr. Saul J. Adelman of Boston University obtained additional coudé spectrograms with the 2.5-meter telescope at Mount Wilson and additional spectrophotometric scans with the 1.5-meter telescope at Palomar for his studies of sharp-lined magnetic Ap stars and suitable comparison main-sequence stars. Of the latter stars, particular emphasis is being given to τ Herculis, B5 IV, for which ultraviolet scans were obtained with the Princeton telescope on the Copernicus satellite. The three broad continuous absorption features found in many magnetic Ap stars are being studied with spectrophotometric scans

and by calculating the location of bound-free discontinuities of the apparently overabundant elements. The λ 4200 feature is most likely produced by Eu II.

Mr. G. Alcaino of the Catholic University of Chile, Santiago, continued to use the 1-meter telescope at Las Campanas to obtain *B* and *V* plates of selected globular clusters. Similar plates have been obtained for eight selected regions of the LMC and five for the SMC to study the clusters in the clouds.

Dr. J. R. P. Angel of the University of Arizona and Dr. J. D. Landstreet of the University of Western Ontario used the multichannel spectrophotometer with a polarization modulator on the 5-meter telescope to measure the wavelength dependence of circular and linear polarization in several newly discovered magnetic white dwarfs, including G227-35

(*Astrophys. J. [Lett.]*, 196, L27, 1975), and the wavelength dependence of linear polarization in several Mira variables, a Be star, a star polarized by interstellar dust, and some Seyfert galaxies. Previous multichannel spectrometer observations of Grw +70°8247 have led to a partially successful theoretical model of the polarization spectrum of that white dwarf (*Astrophys. J.*, 196, 819, 1975).

Dr. T. B. Austin and Mr. J. G. Godwin of Oxford University used the 1.2-meter Schmidt telescope in March 1975 to take plates in *U*, *B*, and *V* of the fields of rich clusters of galaxies. Because of poor observing conditions only one cluster, A1035, was obtained in *U*, *B*, and *V* and one cluster, A1367, in *B* and *V*. Plates of three other clusters, A754, A262, and A2065, were obtained in *B*, of which the latter two had been obtained previously in *V*. The plates were calibrated using a tube sensitometer, and the night sky intensity at the time of the plate exposure was monitored using the new night sky photometer. The *B* and *V* plates of A2065 have led to the production of a color-magnitude diagram to go with those already obtained for A1930, A1377, and A2199. Photometry of the other clusters is progressing well.

Drs. John Bahcall (Institute for Advanced Study), Neta Bahcall (Princeton University), and Stephen Murray (Center for Astrophysics) collaborated with Schmidt on an optical study of a representative sample of 10 unidentified high galactic latitude x-ray sources. A series of plates was taken with the Palomar 1.2-meter Schmidt telescope, including three-color (Haro-Luyten) plates as well as deep red and visual plates. One quasar, NAB 0137-01, with redshift 0.334, was found close to the error box of 3U 0138-01. X-ray observations are under way to determine if this is the correct identification. If it is correct, then NAB 0137-01 has a much higher x-ray-to-optical luminosity

than does 3C 273. A galaxy with a very ultraviolet nucleus, NGC 5506, was identified with the x-ray source 3U 1410-03. The spectrum of this galaxy resembles that of an H II region, or planetary nebula with strong [O III], [O II], and Balmer lines. The rich Abell cluster, A 2124, is suggested as the identification for 3U 1555+27. A 2142 would be the most distant x-ray cluster known if the identification is confirmed by an improved x-ray error box. The major negative conclusions of this study are that the unidentified high galactic latitude x-ray sources are mostly *not*: (1) quasi-stellar sources brighter than $17^m.5$; (2) rich Abell clusters of galaxies; or (3) bright galaxies ($15^m.7$). If the x-ray sources are galaxies then they must have an x-ray luminosity that is more than five times their optical luminosity; the corresponding ratio must be greater than 25 if the sources are faint quasars.

During September and October 1974, Drs. J. Bergstrahl of the Jet Propulsion Laboratory and Münch measured the two-dimensional brightness distribution of D-line emission from the extensive sodium cloud surrounding Jupiter's satellite Io. They used a multiple entrance slit on the Mount Wilson 1.5-meter telescope's coudé spectrograph to record D_1 and D_2 line emission from all parts of the cloud simultaneously. As expected, the observations revealed that the emitting region is highly flattened: it extends some 30 arc seconds along Io's orbital plane, but only a few arc seconds perpendicular to the plane. Results of these observations have been presented at several meetings, and will be published as a letter to *Publications of the Astronomical Society of the Pacific*.

During January 1975, Bergstrahl and Dr. G. Veeder of the Jet Propulsion Laboratory observed Titan and Eros photometrically at 0.5, 1.6, and 2.2 μ . They were successful in obtaining light curves of Eros through a full rotation of the asteroid on each of four nights.

Initial inspection of the raw photometric data seems to indicate color variation with rotational phase.

High spatial resolution time-lapse magnetograms taken with the Big Bear Solar Observatory's longitudinal video magnetograph by Michalitsanos and Dr. A. Bhatnagar of Vedhshala Astronomical Observatory show systematic motion of crescents and ridges of magnetic field at the outer penumbral boundary of a large complex sunspot group. These ridges and crescents were resolved into knots of typically 2" to 3" in extent and appear to move with velocities in the range of 0.2 to 0.3 km s⁻¹. In one case, three successive ridges were observed which emerged at the penumbral boundary and moved outward. The average lag time between the emergence of the ridges was about 3 hours, and it is suggested that large scale crescents and ridges of magnetic field emerge periodically at the penumbral boundary. Near simultaneous observations of a class II flare on September 13, 1974, were obtained in D₃ and H α and of the magnetic field, using the universal filter in conjunction with the 66-cm vacuum telescope for H α -filtergrams and video-magnetograms. Preliminary analysis of these observations indicate very conspicuous variation of D₃ absorption during the flare development. Spectrograms were also obtained during the post-flare period in the K-line, using the vacuum telescope and Littrow spectrograph of the Big Bear Solar Observatory. Work is in progress for a correlative study of all the data obtained during the flare.

From the magnetic flux and K-plage area measurements over bipolar regions observed on Mount Wilson, full-disk magnetograms and K-spectroheliograms, Howard and Bhatnagar attempted to detect and measure the inclination of the magnetic lines of force to the solar surface, over bipolar active regions. No definite conclusion was reached regarding the inclination of the flux tubes from this analysis.

To study the variation of line profile over sunspots, Bhatnagar and Liu obtained a large number of spectrograms in the H α D₁, D₂, and H β lines and in corresponding slit-jaw photographs using the 65-cm vacuum telescope and the spectrograph combination. Microphotometer scans have been obtained, using the fast scanning microphotometer of the Lockheed solar observatory, in collaboration with Dr. Schoolman.

Dr. K.-H. Böhm and Mr. W. A. Siegmund of the University of Washington, using the multichannel spectrometer of the 5-meter Hale Telescope, obtained spectra of Herbig-Haro objects Nos. 2G and 32A (designations according to Herbig's catalogue, *Lick Obs. Bull. No. 658*, 1974). The spectra will be used for the further study of models of individual condensations of Herbig-Haro objects as well as for an empirical determination of the degree of ionization, abundances, and filling factors. The spectra of Herbig-Haro No. 2G possibly will permit them to obtain further information about the time changes of the physical parameters in Herbig-Haro objects. They also obtained spectra of the white dwarfs G163-28 and G63-54, which will be used in connection with their theoretical studies of white dwarf atmospheres.

Dr. Pierre Connes of Centre National de la Recherche Scientifique has continued the near infrared spectroscopy program undertaken at the 5-meter Hale Telescope with a high-resolution Fourier spectrometer. In June 1974 a molecular oxygen emission at 1.27 μ was detected on Venus; this phenomenon is similar to (but much weaker than) the one found on Mars the previous year. This is the first evidence for molecular oxygen on Venus; of course, it concerns only the upper atmosphere. In November an attempt was made, in collaboration with Dr. Maillard, to observe Jupiter and Saturn with a new intrinsic germanium detector. Only a few hours of observing under poor conditions were ef-

fect; nevertheless, this was enough to show improved results compared to those given previously by PbS detectors in the 1 to 1.6 μ range. In May 1975 the same detector permitted a more detailed study of the oxygen emission on Mars and Venus; the line intensities and widths can now be measured, and it is feasible to look for day-to-day variations. At the same time, near infrared stellar spectra have been recorded for much fainter stars than previously, and over a more extended range of spectral types, e.g., β Lyrae (Be) and 61 Cyg A and B (K dwarf).

Dr. C. Coutts of the University of Toronto is carrying out a program to obtain *B* and *V* magnitudes of the RR Lyrae stars in the globular cluster IC 4499. IC 4499 is an interesting cluster because it appears that a significant fraction of the brightest stars are variables of the RR Lyrae type. The mean period of 28 ab types is 0.582 days (longer than most clusters of Oosterhoff type I). In March 1975, twenty *B* and twenty-six *V* plates of this cluster were obtained. The observations, on the whole, should be well distributed over all phases of the RR Lyrae cycles, and Coutts hopes to obtain good light curves. This research is being pursued in collaboration with Dr. R. J. Dickens and Miss Elizabeth Epps of the Royal Greenwich Observatory at Herstmonceux.

Dr. R. M. Crutcher of the University of Illinois used the Mount Wilson 2.5-meter telescope coude scanner to measure equivalent widths of interstellar Na I λ 3302 lines in 21 stars. The D-lines in all these stars are very saturated and cannot be used to derive column densities in the denser of the interstellar clouds, which can be studied using optical interstellar lines. Underestimates of column densities by an order of magnitude often result if the usual doublet-ratio method of analysis is applied to strongly saturated D-lines. Fortunately, the Na I λ 3302 lines are weaker by almost two orders of magnitude than the D-lines and allow accurate column

densities to be measured when the D-lines are saturated. Very little work has been done in working in the near ultraviolet, but the Mount Wilson coude scanner proved to be an efficient instrument for measuring these lines. One result of this study is that there seems to be no clear evidence for a variable sodium abundance (relative to hydrogen) over a wide range of densities. A constant sodium depletion factor of about 8 in the interstellar gas is consistent with observations. This suggests that models of interstellar clouds which call for a continuing depletion of their heavy elements on to the grain surfaces during the lifetimes of the clouds may not be correct. Further comparison of the Na I column densities which were measured in dense clouds with the very high resolution Na I D-line profiles measured by Hobbs and with other data is planned for the near future. Hopefully this will lead to a clearer understanding of processes which are important in interstellar clouds.

Amplitude interferometry observations have been conducted on the 5-meter Hale Telescope at Palomar Mountain and the 2.5-meter and 1.5-meter telescopes at Mount Wilson. These observations were conducted by Drs. D. G. Currie, K. M. Liewer, and R. Braunstein of the University of Maryland, and Dr. S. L. Knapp of the California Institute of Technology. The primary emphasis has been on stellar diameter measurements and observations were made on α Bootis, α Tauri, α Herculis, α Orionis, μ Geminorum, σ Ceti, γ Draconis, η Persei, α Scoti, δ Ophiuchi, R Lyrae, β Pegasi. These observations typically were conducted in two or three different wavelength regions (most with a width of about 100 Å), to explore both the general wavelength dependence of the limb darkening and the effects of molecular band structure. Most of these measurements have had an internal precision of between one and four milliarcseconds. This has been determined by comparing repeated observations

made on succeeding nights of the same star. This value for the internal precision is confirmed by comparing the value of the diameter measured during different years and on different telescopes. The practical limiting magnitude (for normal seeing conditions) of the instrument was improved to about 5.8. In addition, a new Koester Prism and an automatic guider system are now being tested on the telescope, and they should improve the practical magnitude limit by about two magnitudes. A new data recording system, using a NOVA 2/10 minicomputer, to permit the recording of a much more complete set of data, has been introduced. This will permit a reanalysis of the data at the University of Maryland if the parameters chosen for the real-time on-line data reduction were not optimal. A series of observations has been conducted on the apparent surface structure of α Ori. The objective is to determine the contrast of the convective features proposed by Schwarzschild. These data are now being analyzed primarily to determine if any systematic errors could produce an apparent high contrast.

In order to permit the observation of significantly fainter objects, a new instrument, the Multi-Aperture Amplitude Interferometer (MAAI), is being constructed and will be used late in 1975. In principle, this instrument consists of several thousand copies of the current Amplitude Interferometer operating simultaneously and in parallel. The greatly increased data rate (a factor of 8000) will increase sensitivity and permit the observation and precise analysis of objects such as the cores of Seyfert galaxies and the brightest quasars. In the current program for measuring diameters and surface structure of late spectral-type stars the MAAI will also yield much higher accuracy and precision in a reasonable observing time. Special data were taken in conjunction with the observations on the 2.5-meter and 5-meter telescopes in

order to evaluate certain atmospheric parameters. This information has already been used in the fabrication of an extended version of the Amplitude Interferometer, which uses two small heliostats and has a baseline of 20 to 800 meters. This interferometer is being constructed at the present time and is expected to be in operation within a year.

Dr. S. J. Czyzak of Ohio State University and Dr. L. H. Aller of the University of California at Los Angeles employed the Mount Wilson Cassegrain scanner on the 2.5-meter and 1.5-meter telescopes at Mount Wilson to observe the planetary nebulae BD+30°3639, IC4997, NGC 6741, NGC 7026, NGC 650, NGC 1501, NGC 6790, Merrill 2-2, VV5 and VV286. The following papers based on the observations secured at the Hale Observatories have been published: "Spectrophotometry of NGC 6003," S. J. Czyzak, P. Lee, L. H. Aller, and J. B. Kaler, *Astrophys. J.*, 192, 159, 1975; and "Spectrophotometry of IC 4593," E. Buerger, S. J. Czyzak, and L. H. Aller, *Astrophys. J.*, in press, 1975. Also submitted for publication were two papers: "Spectrophotometry of NGC 7027," J. B. Kaler, L. H. Aller, S. J. Czyzak, and H. Epps; and "Spectra of 21 planetary nebulae," J. B. Kaler, L. H. Aller, and S. J. Czyzak. Both of these investigations depend on the photoelectric calibrations obtained at the Hale Observatories.

Dr. John Danziger of the European Southern Observatory, Chile, has pursued a spectroscopic study of many supernova remnants (SNR) in the Galaxy and the Magellanic Clouds with the image-tube spectrograph on the 1-meter telescope at Las Campanas. N132 D in the Large Magellanic Cloud has been shown to contain high-velocity filaments characterized by strong emission lines of [O II], [O III], and [Ne III], for which the maximum observed range in radial velocities is 444 km s⁻¹.

Spectroscopy of a compact object 2' west of the SNR N11 L in the LMC

shows that it is an emission-line background galaxy with a redshift of $+7140 \text{ km s}^{-1}$. It had been previously suggested to be ejecta from N11 L.

Spectra of the two known SNRs in the Small Magellanic Cloud show that the [N II] lines are extremely weak relative to $H\alpha$. This empirical observation supports the accumulating evidence from stars, H II regions, and planetary nebulae that nitrogen is underabundant in the SMC.

Photometry of the integrated light of globular clusters in the LMC is now complete for 35 clusters. Metallicity parameters from the ten-color system show that there is no correlation between metal abundance and distance from the center of the LMC. This photometry provides a classification of clusters that might be studied in more detail by other techniques.

Dr. P. Demarque of Yale University, during a six-month stay as Visiting Associate at the Hale Observatories, continued his work on the evolution of stars of the halo and old disk populations with particular emphasis on the phases of evolution that follow the ignition of helium in the core. Making use of the extensive data on the color-magnitude arrays of the globular clusters 47 Tucanae, M3, M4, and M15 gathered over the last few years by Sandage and Katem and of some additional material, a detailed comparison of observed luminosity functions with the recent theoretical evolutionary tables of Sweigart, Gross, and Mengel was begun by Demarque and Sandage. Preliminary indications are that there exist significant differences among the luminosity functions of globular clusters which can be related to differences in their helium contents. Little is known about the nature of the blue stars in the galactic halo. Demarque searched deep plates of the globular cluster M13 for faint blue objects in order to investigate the population of the blue end of the horizontal branch. In M13, the luminosity function is found to extend to $V \sim 19$. However, the stellar

density appears to drop markedly below this luminosity level, which corresponds approximately to that of the helium main sequence.

Demarque and Zinn have investigated the two mixing mechanisms that have been proposed for the origin of the Population II carbon stars, the CH stars. They conclude that the chemical compositions of the CH stars are equally well explained by mixing at the two proposed times the helium core flash at the tip of the giant branch and the helium shell flashes on the asymptotic giant branch. They find, however, that shell-flash mixing cannot produce CH stars fainter than about $M_V \sim -1.3$, which is brighter than many CH stars. It seems then that at least some of the CH stars must be produced by the core flash. Demarque and Zinn point out that if core-flash mixing is common among Population II stars, then the current picture of the horizontal branch may have to be revised.

Dr. S. Demers of the Universidad de Chile has used the 1-meter telescope at Las Campanas to obtain plates of the Reticulum system near the LMC. The plates are being used to determine periods of the RR Lyrae variables in this globular cluster. The similarity of Reticulum, the Palomar clusters, and the dwarf elliptical galaxies led to the discovery of the Magellanic Plane. As seen from the galactic center, the LMC, SMC, Draco, Ursa Minor, Leo I, Leo II, Pal 3, and Pal 4 lie in a plane of 15° width. This plane probably coincides with the Magellanic Stream, although it is difficult to be sure since the distance to the Magellanic Stream is not well known. Plates have been taken of the globular cluster NGC 4833 to obtain light curves of the variables.

Dr. N. J. Evans of the California Institute of Technology has surveyed a number of molecular clouds at 10μ , searching for compact infrared objects at positions of peak molecular excitation. A cluster of strong 10μ sources has been discovered in Monoceros. Subsequent study

has revealed at least two and possibly more sources with infrared energy distributions like that of the Becklin-Neugebauer object, i.e., probable protostars. A source of extended $10\ \mu$ and $20\ \mu$ radiation coincides with a compact H II region. The region as a whole is very similar to the cluster of infrared sources in Orion and provides an opportunity for further study of such regions. In addition, several other sources with energy distributions like the Becklin-Neugebauer source have been found in other molecular clouds, including S140, NGC 2071, S235, and IC 2162. By adding to the number of such sources known, it is now possible to begin to develop the systematics of such objects and to take the first steps in developing an evolutionary scenario.

Dr. M. P. Fitzgerald of the University of Waterloo used the Carnegie Image-Tube Spectrograph on the 1-meter telescope at Las Campanas for five nights. After some trouble getting the instrument adjusted, very high quality spectra were obtained at $70\ \text{\AA}\ \text{mm}^{-1}$. Three to four spectra were obtained of the 14 brightest stars in NGC 2422, many of which may be spectroscopic binaries (Dworetzky, M. M., *Astron. J.*, 80, 131, 1975). Likely candidates appear to be HD 60941 and BD $-14^{\circ}2022$. The latter is possibly also eclipsing ($\Delta V \sim 0.5$). One blue and one red spectrum of the M23 nebula were obtained. Over 120 emission lines have been measured from 3700 to 7600 \AA . The lines of H α and [S II] are very strong.

Dr. K. J. Fricke of the University of Bonn and Dr. J. P. Kaufmann of the Technical University in Berlin used the coudé spectrograph of the 2.5-meter telescope at Mount Wilson to obtain 20 and $40\ \text{\AA}\ \text{mm}^{-1}$ spectra of helium-rich stars. Sufficient spectra of HD 128220, HD 113001, HD 160641, BD $+37^{\circ}1977$, BD $+48^{\circ}1777$, and BD $+13^{\circ}3224$ have been obtained to carry out fine analyses of their atmospheres. Spectra of the variables HD 33479, HD 37776, HD 184927, and R Coronae Borealis were obtained also.

Dr. Y. Fujita of the University of Tokyo is continuing his study of carbon stars. The identification of the spectral lines in the visual region from $\lambda 3700$ to $\lambda 4350$ in three typical very early carbon stars, HD 156074, HD 182040, and RU Camelopardalis, by measuring Mount Wilson and Palomar spectrograms, is being carried on. Though the general pattern of these spectra in the spectral region considered seems to be of solar type due to the dominant iron lines, it is interesting to note that the intensities of neutral and ionized atomic lines of various elements show quite large differences among those three stars. The wavelength identification table with eye-estimated intensities of each spectral line will be published. The spectra of some very early carbon stars were obtained in the spectral region from $\lambda 7700$ to $\lambda 8600$, using the 90-mm image tube and 182-cm camera in the coudé spectrograph of the 5-meter Hale Telescope. From the CN band analysis between $\lambda 7750$ and $\lambda 8200$, the $^{12}\text{C}/^{13}\text{C}$ ratio will be obtained using the iso-intensities method. (The details are described in Y. Fujita, T. Tsuji, and H. Maehara, *Proc. Jpn. Acad.*, 45, 484, 1969, and also in Y. Fujita, *Interpretation of Spectra and Atmospheric Structure in Cool Stars*, Toyko, 1970.) The determination of $^{12}\text{C}/^{13}\text{C}$ ratios is very interesting particularly in very early carbon stars such as HD 137613, HD 156074, and HD 182040.

Dr. P. Foukal of Harvard College Observatory has been using the magnetograph on the 46-meter tower telescope to study the rotation rate of the solar magnetic field relative to the photosphere. The $\lambda 5250$ line of Fe I, and a 5 arc sec aperture have been employed to do fine scans which resolve the magnetic network. It was found from the results of his first observing run last year that on the east limb of the sun, the Doppler shift of gas associated with magnetic fields stronger than about 50 gauss shows an approach velocity about 5% higher than the Doppler shift of

gas associated with lower field values. This effect is reversed on the west limb; that is, the gas associated with higher fields seems to be receding faster than the gas associated with lower fields. Since the plasma is probably well frozen to the field lines, it is concluded that the magnetic field is rotating about 5% faster than the photospheric gas. In a very recent observing run more data were taken in $\lambda 5250$ to check the reality of this interesting effect; $\lambda 5233$ was also used to obtain data in a line with a different g -value and temperature dependence. These latest results are presently undergoing computer processing.

Dr. T. Gehrels of the University of Arizona has obtained plates with the 1.2-meter Schmidt telescope to perform photometry of the faint outer satellites of Jupiter; these were sent to the Leiden Observatory for reduction and analysis. If these objects are collisional fragments of a larger original body, their shapes would be irregular and the rotation rate may be fast. These ideas are checked from light curves obtained with a set of many images on these plates.

Dr. R. F. Griffin of the Cambridge Observatories, England, and Gunn made radial-velocity observations with their photoelectric spectrometer at the coudé focus of the 5-meter telescope on nine nights, continuing their work on globular and galactic clusters. It now seems probable that the radial velocities will allow stars which have been considered possible members of the Hyades to be sorted into three groups. First, there is a set of stars having similar and constant velocities which, after correction for the perspective effect caused by the large angular size of the cluster, have dispersions well under 1 km s^{-1} ; such stars are almost certainly members. Second, there are stars having constant but discrepant velocities; it would seem that they tentatively must be rejected as Hyades members, notwithstanding that several of the Van Bueren stars fall into this category. There is, however, a possibility that some genuine Hyades presently assigned to

this group will prove to be spectroscopic binaries whose periods are much longer than the interval yet covered by the observations. Last, there are many stars whose velocities are not constant or whose radial-velocity traces indicate multiple spectra. In principle it will be possible to assign these objects as Hyades members or non-members, but only when their orbits are determined.

In an experimental observation, made during the dark time offered by the total lunar eclipse of May 25, 1975, Gunn and Griffin used the 90-mm image tube with the coudé spectrograph of the 5-meter telescope to obtain a 6.7 Å mm^{-1} spectrogram of a twelfth-magnitude star in M13.

Multichannel spectrometer scans were obtained of several giant stars in each of 12 globular clusters by Dr. F. D. A. Hartwick of the University of Victoria and Dr. R. D. McClure of Yale University. The clusters were chosen to be representative of different metal abundances and horizontal branch types. The physical parameters $\log g$, $\log T_{\text{eff}}$, M_{bol} , and $[\text{Fe}/\text{H}]$ were obtained and inter-compared. These data were also compared with similar results obtained in previous runs on the dwarf spheroidal galaxies Draco and Ursa Minor and on the outlying globular cluster Pal 5. Preliminary results are: (1) The metal-rich cluster giants within a given cluster appear to show a range in metal abundance and CN strengths. (2) The giants in all three of the outlying systems appear to have higher surface gravities than those in the inner system.

Mr. F. Holden of San Jose, California, used the 1-meter telescope at Las Campanas to measure visual double stars. A bifilar micrometer (on loan from Lick Observatory) was fitted at the Cassegrain focus of the telescope, and the optical system performed satisfactorily. Despite unusual weather patterns, which resulted in poor seeing, over 200 measures of some 100 pairs were obtained. Many of the pairs had separations less than one second of arc, and the measures repre-

sent a useful contribution to our knowledge of double stars in the southern hemisphere.

Dr. P. C. Keenan of the Perkins Observatory and O. C. Wilson have investigated the use of coudé spectrograms for the luminosity classification of giants and bright giants. On 9 \AA mm^{-1} Palomar spectrograms, it was possible to compare lines of such intersystem multiplets as Fe (2) and Fe (3) with excited lines of the same elements and thus to avoid the effects of abundance anomalies in the heavy elements Sr and Ba which distort the usual criteria on low-dispersion blue spectrograms. Several G-type stars, which had been classified as class II bright giants on the small-scale plates but which had K-line widths on Wilson's plates, suggesting class III or IIIb, were estimated in this way to be of class IIIa or II-III. In particular, ζ Cygni is now classified G8 III-IIIa. In the red region the coudé spectrograms at 13.5 \AA mm^{-1} have permitted the use of widths of the absorption lines to distinguish between supergiants of classes Ia, Ib, and O-Ia. Of special interest is Albers' star in the cluster Trumpler 27. Keenan and graduate student Cathy Imhoff find a luminosity class of O-Ia for this MO supergiant, which is so red that no satisfactory blue spectrograms have been taken.

Drs. D. E. Kleinmann and E. L. Wright of Harvard College Observatory and Smithsonian Astrophysical Observatory used their own and Massachusetts Institute of Technology infrared bolometers, etc., for several projects. They obtained total 10μ fluxes for each of ten H II regions given in the list of Frogel and Persson. Some of them show evidence for extended low-surface-brightness emission. Extensive maps of Orion A at 11.6 and 20μ were obtained, as were observations of Orion B, NGC 6357, and the galactic center. Upper limits were placed on the mid-infrared flux from ρ Ophiuchi and 30 Doradus. A new H II region, RCW 42, was discovered and mapped.

Dr. T. Kwast, visiting the University of California at Los Angeles from Poland,

has used the 1.2-meter Schmidt at Palomar to obtain photographs of the field at $\alpha = 14^{\text{h}}07^{\text{m}} \delta = 35^{\circ} 53'$. The field was chosen to be compared with the so-called Jagiellonian Field recently investigated by Dr. Rudnicki and his collaborators in Cracow. Both fields are located at the same declination and galactic latitude. The set of photographs contains 6 different exposures taken in blue, 6 in yellow, and 5 in red light and will be treated in the same way as the photographs of Jagiellonian Field (*Acta Cosmologica*, vol. 1, 1972). Additionally, photographs have been taken of 19 auxiliary fields surrounding both fields mentioned above. All plates are for use in the preparation of the Jagiellonian Field Catalogue extension.

Dr. A. Labeyrie of the Observatoire de Meudon and Dr. A. Boksenberg of University College, London, have observed QSOs, Seyfert nuclei, and x-ray sources down to $m_v = 18$, using two speckle interferometers installed, respectively, at the prime and Cassegrain foci of the 5-meter Hale Telescope. The prime-focus system was equipped with an all-electrostatic photon-counting television camera built at Observatoire de Paris. Hardware and software for computerized image processing have been developed and used for analyzing the brighter objects. Moonlight, poor seeing, and bad weather have, however, affected the reduction of the faint sources.

Landstreet used the coudé line-profile scanner of the 2.5-meter telescope at Mount Wilson with a polarization modulator to search for weak magnetic fields in main-sequence B0-F5 stars. Measurements of 22 stars with typical standard errors of 60 gauss have led to the discovery of no new fields. He also used the Palomar 1.5-meter telescope with his own Cassegrain polarimeter operated as an $H\beta$ stellar magnetograph to determine the photoelectric magnetic curves of several well-known magnetic Ap stars.

Drs. D. Matson, T. Johnson, and G. Veeder of the Jet Propulsion Laboratory

have continued their study of asteroids and satellites using 0.3 to 2.5 μ spectrophotometry. Asteroids Ceres and Pallas were found to have a carbonaceous-chondritic type surface composition, while the surface composition of Vesta is basaltic and looks much like lunar mare material (*Astrophys. J.*, 197, 527, 1975). As part of an internationally coordinated effort to obtain data on the important Apollo group asteroid Eros, they observed Eros in the visible and infrared using the Mount Wilson 1.5-meter and 2.5-meter telescopes. Preliminary results were presented at a workshop on Eros held at Tucson in May 1975. These results suggest that the spectrum of Eros has an absorption band in the 0.9–1.0 μ region, indicating the presence of iron-bearing minerals on its surface (pyroxene and/or olivine). Work on the Galilean satellites has continued in several directions. The nature of Io's surface has always been an enigma. Spectral reflectance data obtained by T. Johnson on Mount Wilson in 1969–1970 have now been successfully interpreted by F. Fanale, T. Johnson, and D. Matson (*Science*, 186, 922, 1974). They suggest that Io's surface is composed of evaporite minerals, much like those of certain desert lakes in the southwest United States. These salts originated when water evolved to the surface as Io differentiated due to internal heating. This work, in turn, led to an explanation of the sodium D-line emission from Io (Matson *et al.*, *Astrophys. J. [Lett.]*, 192, L43, 1975). During the last year, reduction of Galilean satellite mutual-event data obtained by Johnson and Matson has been completed (Duxbury, Johnson, and Matson, *Icarus*, in press). These observations enabled the ephemerides of Io to be corrected and led to the successful occultation of the Pioneer 10 spacecraft by Io.

Dr. Martin F. McCarthy of the Vatican Observatory experimented with different systems for detecting faint red objects. Pairs of plates (red and blue) were studied by blinking, and image pairs with red and blue filters on one plate were

photographed at Las Campanas and at Palomar. IN plates with GG13 and RG8 filters clearly revealed all of the red stars which had been selected for cluster membership in a 1964 objective-prism survey by Treanor and McCarthy, and many fainter red stars as well. With the 1-meter telescope at Las Campanas, and the Carnegie image-tube spectrograph, individual spectra were obtained in red and blue regions to check classification and color calibration.

Dr. T. B. McCord of the Massachusetts Institute of Technology employed the 1.5-meter telescope on Mount Wilson along with the Massachusetts Institute of Technology MK III silicon vidicon imaging system at the Cassegrain focus. The weather was generally good during all runs, but a dirty mirror prevented useful observing during the first run. Direct images were made at three wavelengths through interference filters of about 50% of the lunar surface and at 10 wavelengths, including methane absorption, of Jupiter. The lunar images were processed to produce color difference maps (0.40/0.56 μ and 0.95/0.56 μ) of the lunar surface to a resolution of about 2 km. Previous work on the optical properties of the moon and lunar samples had shown a relationship between these two optical properties and the mineralogical composition and exposure age of lunar soil. The extent of geologic units can be mapped by this technique. High-quality (<1%) maps of 50% of the lunar front side were obtained. One publication, using these images, is already in press. Several others are in preparation. The Jupiter images were processed similarly to produce maps of methane absorption and maps of scattering properties. The monitoring of cloud structure and the investigation of atmospheric dynamics is a major goal.

Dr. D. H. McNamara of Brigham Young University secured spectrograms of dwarf Cepheids and strong-lined RR Lyrae variables with the 2.5-meter telescope coude spectrograph in the red with the aid of the Varo image tube. The

purpose of the investigation was to test for the presence of the resonance lithium line. The line was identified in the spectra of a few of the longer period dwarf Cepheids. The presence of this line strongly suggests that the variables are in a post-main-sequence stage of stellar evolution rather than in a post-giant stage. Spectrograms of the two variables EH Librae and SZ Lyncis in the blue range of the spectrum were secured with the aid of the 20-cm camera in the coudé spectrograph. The spectrograms have been measured for radial velocity. These new data give much more precise information on the radial velocity variations of these two stars than obtained heretofore. Spectrograms of the A-F stars in the cluster NGC 2264 that are supposedly in a gravitational contraction stage of evolution have been secured to test for membership on the basis of radial velocity measurements. Many of these objects turn out to be spectroscopic binaries, but a few have constant radial velocities. Several of the constant radial-velocity stars are obviously not members of the cluster because their velocities differ significantly from the B-type stars that are members.

Dr. D. C. Morton of Princeton University Observatory used the Princeton SEC-Vidicon TV sensor with the coudé spectrograph of the Hale Telescope to study the central regions of the galaxies M31, M32, and NGC 1068. The two-dimensional detector provided spectra about 30" wide, including the nucleus in each case. Comparison of the nucleus of M32 with the KO III star 51 Orionis by Morton and Elmergreen from 4175 to 4375 Å gave a line-of-sight velocity dispersion σ between 40 and 65 km s⁻¹, in agreement with Richstone and Sargent. In the same wavelength region, fitting M32 or 51 Ori to the nucleus of M31 required σ between 105 and 140 km s⁻¹, consistent with the value obtained by Morton and Thuan, around 5100 Å. The spectrum of 51 Ori was a better match for the nucleus of M32 and the bulge of M31 than for the nucleus of

the latter galaxy. A weak spectrum of the H and K lines in M31 analyzed by Morton and Andereck showed that these lines increase in equivalent width between a region about 20" out in the bulge and the nucleus, implying that calcium may be approximately a factor 2 more abundant in the nucleus. Narrow interstellar K lines superposed on the broad stellar line in the nucleus of M31 were found at heliocentric velocities of -30, -290, -560, and -750 km s⁻¹. The first two probably represent normal absorbing clouds, respectively, in our Galaxy and in M31, which has a radial velocity of -300 km s⁻¹, while the last two could be due to gas ejected from the nucleus at velocities of 260 and 450 km s⁻¹. Richstone and Morton compared lines of Mn I and Fe I near 4050 Å in the nucleus of NGC 1068 with the KI III star δ Tauri and obtained $\sigma = 150 \pm 50$ km s⁻¹. H and K lines typical of a G or K star were clearly visible in the spectrum of both the nucleus and the fainter regions on each side.

Dr. J. Norris of Mount Stromlo Observatory and Zinn have investigated the stellar populations of the dwarf spheroidal galaxies. The similarities between the color-magnitude diagrams for the Draco and Ursa Minor dwarf galaxies and those for the galactic globular clusters have long led astronomers to conclude that the dwarf spheroidal galaxies and the globular clusters have had similar histories of star formation. It has been known for some time, however, that the variables in the dwarf spheroidal galaxies and the globular clusters do not obey the same period-luminosity law. Norris and Zinn have shown that the variables in the galaxies also do not fit the evolutionary scheme which successfully explains the globular cluster variables. These facts have led to a new picture of the history of star formation in these systems. According to Norris and Zinn, the period-luminosity law, the evolutionary status of the variables, and the color-magnitude diagrams can be explained if in each galaxy there were

at least two epochs of star formation, one $8-10 \times 10^9$ years ago and one as recent as 1×10^9 years ago, but with very little enrichment in metal content from one generation of stars to the next. This picture of multiple stellar populations suggests that either supernovae explosions during the first epoch of star formation were unable to drive all of the gas from these systems or gas was accreted some time after the first epoch. Neither one of these events was expected to occur in galaxies of such small mass.

Dr. V. Oinas of Queensborough Community College is working on a project concerned with a neutral-ion anomaly and a possible new source of continuous opacity in cool stars. High-dispersion spectra have been obtained for some of the program stars with the 2.5-meter telescope coude spectrograph.

Dr. J. Ostriker of Princeton University Observatory and Dr. H. Spinrad of the University of California at Berkeley obtained additional deep red and blue direct photographs of edge-on spiral and S0 galaxies with the 1.2-meter Schmidt. The program, a search for possible extended, faint halos, was badly hampered by bad weather. However, a few good, deep plates of NCG 4594 were obtained. The large halo around the "Sombrero" nebula shows a clear decrease in ellipticity with decreasing surface brightness and increasing radius. A considerable amount of work has been done to begin quantitative analysis of the photographs with the new Berkeley PDS microphotometer system. Photographs have been traced. Some effort has been made to remove plate faults and foreground stars in the PDS reduction. Then the data are smoothed and linearized, and elliptical isophotes are plotted from them. Integrations of the halo light, well beyond the easily visible images, have just begun.

Drs. E. Persson, J. Frogel, and M. Aaronson of Harvard College Observatory and Becklin, Neugebauer, and Keith Matthews of Caltech continued

their infrared observations of galaxies. The data consist of broad-band infrared colors, plus the luminosity-sensitive CO index at 2.3μ . The initial results of this work showed that the 2μ radiation from the nuclei of elliptical galaxies is dominated by the light of giant stars (*Astrophys. J. [Lett.]*, 195, L15, 1975). Current work involves extending the observations to more galaxies, determining the effective color temperatures of the radiation in the $1-2 \mu$ region, and investigating the dependence of the broad-band and CO indices on position within the galaxies. These data are necessary for a proper evaluation of the evolutionary correction to q_0 via the CO index. Observations were made on the 51-cm and 1.5-meter telescopes on Mount Wilson and on the 5-meter Hale Telescope. Persson, Frogel, and Aaronson continued their work on infrared photometry and mapping of newly found southern H II regions. The 1-meter telescope on Las Campanas was used for all the observations. Some results of this work appeared in *Astrophys. J.*, 192, 351, 1974, and *Astrophys. J.*, 197, 351, 1975. In a recent observing run, measurements of the silicate absorption feature at 10μ were completed for about 20 regions. The depth of the ice absorption band at 3.1μ was also determined for several of these objects. The sources display a considerable range in silicate optical depth. Correlations of the depth of this band with other nebular parameters should indicate directions for more detailed studies.

Dr. A. G. D. Philip of the State University of New York at Albany employed the 2.5-meter telescope on Mount Wilson to observe the symbiotic star MH α 328-116, which has been followed since 1967. It is now one of the bluest stars known. Field blue horizontal-branch and field A stars were measured in an area at $l = 76^\circ$, $b = 30^\circ$. The four-color and H β indices allow one to determine the color excess in the region accurately. When all the early-type stars in an area are

measured, one can determine absolute magnitudes and then the distribution of early-type stars of Populations I and II. Stellar spectra (some of which were obtained on the 2.5-meter telescope in 1969) of the field-horizontal-branch (FHB) stars allow kinematical studies to be made. Such investigations have confirmed that the stars identified as FHB stars from four-color photometry indeed are Population II stars. At five kiloparsecs from the galactic plane, the stellar density of FHB stars is about ten times that of RR Lyrae stars.

Several globular clusters were measured in integrated light. M31 was observed in order to calibrate the cluster measures. The objects were measured through diaphragms of radii 9", 20", 30", and 53"; skies were measured through each diaphragm in a dark-sky position well away from the galaxy or cluster. In agreement with Oke and Schwarzschild (*Astrophys. J.*, 198, 163, 1975), the $(b - y)$ and $(u - b)$ indices were redder at the center of M31 than at a position 2.4' away. An m_1 index can be calculated from the data in Table 3 of Oke and Schwarzschild. The index m_1 increases from a position 2.4' away from the center to the center. The four-color indices of M31, as measured with the 1.5-meter telescope, showed this same behavior. In the five globular clusters measured (M3, M5, M13, M15, M92) the $\delta(b - y)$'s from the center to 1' from the center were in the same sense as $\delta(b - y)$ for M31, but the magnitude of the change was about half as large. The changes in the m_1 were comparable to the change noted for M31.

Dr. H. B. Richer of the University of British Columbia used the 1.5-meter telescope at Mount Wilson for three nights to look for high-frequency optical variability in a number of white dwarfs. Two of the three nights were photometric. Six white dwarfs were observed. Within the detectable limits (about 0.1 magnitude) none were variable on time scales from 0.02 to about 1500 seconds. The rather high upper limit to

the amplitude of any variability was caused by the extreme brightness of the night sky.

Drs. G. Rieke and F. Low of the University of Arizona collaborated with Werner, Becklin, and Neugebauer of the Hale Observatories in an experiment to utilize the 5-meter Hale Telescope at $350\ \mu$ to obtain diffraction-limited resolution. It was expected that suitably dry atmospheric conditions would be rare. During the past year, data were obtained on one dry day. These observations are still being reduced, but they expect them to yield extremely interesting information about the compact structure of the far-infrared sources in the Orion Nebula and W51.

Dr. W. L. Sanders of New Mexico State University obtained four-color Stromgren photometry of approximately 300 Be stars with the Mount Wilson 1.5-meter telescope. The reductions are not yet complete, but the objective is to seek a luminosity criterion. Since that turns out to be impossible in the four-color system alone, a fifth color is presently being defined that should satisfy this purpose. These stars will then have to be reobserved in that fifth color.

Using the 1.2-meter Schmidt telescope, Dr. S. A. Sackett of the University of Michigan completed the collection of data on the outer regions of nearby spiral galaxies. Photographic surface photometry of the photoelectrically calibrated plates will be used to study the distribution of stars at the outskirts of these systems. Sackett also brought a new multi-stage image tube, photon-counting spectrograph to the Palomar 1.5-meter telescope. This prototype device detects photon events at the output of a six-stage image tube with a single 6 mm long row of self-scanned silicon diodes. A digital memory accumulates data simultaneously for 512 resolution elements along the array. The device was used to obtain velocity dispersions and metallic line strengths for supergiant (cD) galaxies and for Virgo cluster elliptical galaxies. In collaboration with Gunn, a radial-

velocity program was carried out to study the structure of the outer Coma cluster (beyond 4° angular radius). With Sargent, a survey of Seyfert galaxy emission-line widths and strengths was continued.

Dr. E. M. Shoemaker and Mrs. E. F. Helin of the California Institute of Technology continued their search for new Apollo-Amor asteroids using the 46-cm Schmidt at Palomar Mountain. One hundred ninety-three independent fields were photographed and scanned in 1974. Each field was photographed at least twice. This represents about 10,000 square degrees centered along the ecliptic. (Each Schmidt circular field is slightly more than 8° in diameter.) This sky coverage has led to the discovery of three new asteroids and to the rediscovery of an asteroid lost for more than 20 years. All of the objects discovered by Shoemaker and Helin in 1974 have high eccentricity, which is, in part, a consequence of the method of search. Two objects lie in a region of phase space occupied by a group of asteroids referred to as the Phocaea family by Brouwer, and the other two new objects are Mars-crossing asteroids. 1974 KA and 1974 QA (= 1952 RH), with very similar orbits, lie in the Phocaea region. Although the perihelia of these objects come close to the aphelion of Mars (1.667 AU), they are in apparently stable orbits that are separated from the Hungaria region on the one hand and from the mainbelt asteroids on the other by surfaces of strong resonance in a , e' , and $\sin i'$ space. Of particular significance is the independent rediscovery of 1952 RH after 22 years. Rediscoveries of this type help place statistical bounds on the population of objects in the Phocaea region.

During the past year, Dr. R. W. Shorthill, University of Utah, and Dr. T. B. Greene, the Boeing Aerospace Company and the University of Washington, concluded their observations of Jovian satellite eclipses with the multichannel spectrometer on the 5-meter Hale Telescope. The first phase of the

analysis, being performed jointly with Mr. Dale Smith of the University of Washington, is nearing completion. Their results include determination that the aerosol haze in Jupiter's atmosphere tails off to nothing above the thermal minimum and increases significantly with depth below the top side of the minimum. The next phase of the analysis will address the vertical distribution of NH_3 and CH_4 in Jupiter's atmosphere. Four satellites of Uranus and Triton were scanned with the multichannel spectrometer under excellent weather conditions. Preliminary reduction efforts, performed jointly with Mr. Paul Johnson of the University of Washington, indicate that Umbriel is especially blue, having a reflectivity at 0.45μ about twice that at 0.9μ . Triton's reflectivity is unusually flat from 0.35μ to 1.05μ . Ariel, Titania, and Oberon are progressively more red, in that order.

Dr. J.-P. Swings of the University of Liège used the multichannel spectrophotometer to obtain scans of a series of peculiar emission-line objects known to have prominent infrared excesses, in order not only to observe the emission lines present from the near UV to about 1.1μ , but also to detect the weak continuum of the objects and to measure the intensities of the Balmer and Paschen lines. Two nights were devoted to image-tube spectroscopy of those emission-line objects bright enough to be observed at the coudé focus; 30 \AA mm^{-1} (in the red) spectra were obtained for Bep stars such as MWC 342, MWC 349, MWC 623, MWC 645, which show striking similarities as far as their emission lines are concerned ([N II], [O I], [S II], [Fe II], for example).

In analogy to the Hertzsprung progression of Type I Cepheids, Type II Cepheids with periods between one and two days should have bumps on their light curves, according to R. F. Christy's pulsation theory. To check this, *UBV* light curves of some suitable Cepheids were observed by Dr. G. A. Tammann of the University of Basel with the

1.5-meter telescope on Mount Wilson. So far no clear correlation of the phase of any bumps with the period has been found. There is a rather stable feature at phase 0.78 for Cepheids with $P = 1.6$ – 1.7 days (e.g., VZ Aquilae).

During the course of an investigation of variable stars in the galaxy M33, Dr. S. van den Bergh of the David Dunlap Observatory discovered a 17th magnitude comet (1974g) on the morning of November 12 U.T. Subsequent calculations showed that this comet, which is now moving in a slightly hyperbolic orbit, passed perihelion on August 8, 1974. This is the first comet so far discovered that has a perihelion distance greater than 6 a.u.

Van den Bergh has used the 5-meter Hale Telescope to study the luminosity function of M92 down to $V \simeq 23.25$. The main-sequence luminosity function of the cluster is found to rise very steeply from $M_V = +4$ to $M_V = +6$. Between $M_V = +6$ and $M_V = +8$, the luminosity function appears to remain essentially constant. The observations are consistent with recent theoretical computations by Ostriker, Spitzer, and Chevalier, which predict that most low-mass stars will escape from globular clusters as a result of gravitational shocks that are produced when such clusters pass through the galactic plane.

Van den Bergh, Herbst, and Kowal have discovered 38 new variable stars in M33. These bright variables were found on plates obtained with the Palomar 1.2-meter Schmidt telescope during the period 1966–1974. Twelve of these objects are red semi-regular or irregular variables. These stars typically have light cycles of one to two years. The brightest red variable has $V(\text{max}) \simeq 17.0$ corresponding to $M_V(\text{max}) \simeq -7.6$. The red supergiant variables appear to favor the outer regions of M33. The Cepheids in M33 do *not* seem to be concentrated in the major associations that outline the spiral arms of this galaxy.

Van den Bergh's 5-meter telescope photometry of the globular clusters in

M31 has been combined with other published observations to derive the reddening of 97 globular clusters in M31. Comparison of these data with 21-cm observations by Guibert shows that the mean gas-to-dust ratio in M31 is similar to that observed near the sun. No evidence was found for a radial gradient in the gas-to-dust ratio within the disk of the Andromeda Nebula. M33 has a well-defined semi-stellar nucleus which has a diameter of ~ 1.5 arc sec. A widened spectrum of this nucleus has been obtained through a moonlight eliminator with the image-tube spectrograph at the Cassegrain focus of the 5-meter Hale Telescope. Comparison of this spectrogram with MK standards yields the following spectral types: Late A from $K/H + H\epsilon$; F2 to F4 from $4226/H\gamma$; F3 to F4 from $CH/H\gamma$. These observations suggest that the light from the semi-stellar nucleus of M33 is dominated by relatively young stars similar to those that contribute most of the light in the disk of the Triangulum Nebula. If this conclusion is correct then the nucleus of M33 must have been the site of relatively recent star formation. This observation suggests that the nucleus of M33 was probably not formed by the accumulation of globular clusters that, as a result of dynamical friction, spiraled into the center of M33. An additional argument against the assumption that the nuclei of galaxies are mainly formed from globular clusters is provided by an image tube spectrogram of the nucleus of M31, which shows that it has a spectrum that has *much* stronger lines than does the average globular cluster associated with the Andromeda Nebula. Of the 37 M31 globulars for which spectra have been obtained, only one cluster, No. 282, has a line strength that is comparable to that of the nucleus of M31. The *UBV* colors of this cluster are, however, still significantly bluer than are those of the nucleus of M31.

Van den Bergh has continued his long-term investigation of the changes in and expansion of the optical remnant

of Cassiopeia A with the Hale Telescope. A definitive proper-motion study of this object, involving plates covering the period 1951-1974, is currently being undertaken by Karl Kamper. Preliminary results indicate that the explosion of Cassiopeia A took place in A.D. 1665 ± 3 .

The Cepheid variable V367 Scuti in the cluster NGC 6649 has been studied photoelectrically by Madore from Chile and photographically from Palomar by van den Bergh. The cluster is found to have $(m - M)_V = 15.4 \pm 0.2$ and suffers a reddening $E_{B - V} = 1.37$. With these values, the Cepheid V367 Sct has $M_V = -3.8 \pm 0.2$, which is in excellent agreement with the value predicted from the period-luminosity relation of Sandage and Tammann. Madore and van den Bergh also find that the cluster contains a nonvariable star in the Cepheid instability strip and two red giants, one of which is variable.

Dr. M. F. Walker and Mr. D. Burstein of the University of California at Santa Cruz employed the 1.2-meter Schmidt to obtain long- and medium-exposure plates (103a-O emulsion + GG13 filter) of 16 fields, containing about 20 S0 galaxies. These plates will be combined with plates obtained with the Lick 90-cm Crossley for detailed two-dimensional surface photometry of these galaxies. These observations are part of a program to investigate the structure and composition of S0 galaxies.

Dr. G. Wallerstein of the University of Washington has completed his analysis of the radial velocities of photospheric and circumstellar features in long-period variables that show microwave maser emission. The data and a discussion will be published as an *Astrophysical Journal Supplement*. Wallerstein is continuing to work on microwave maser stars and is now concentrating on M supergiants such as PZ Cassiopeiae and S Persei. Wallerstein has completed his survey of interstellar lines in stars near the Monocerotis Loop. The data are being analyzed

to yield the velocities and column densities in the quiescent gas as well as the expanding supernova shell.

Dr. W. C. Wickes of Princeton University used the 1.5-meter telescope on Mount Wilson to study the performance of a new type of double-star interferometer (W. C. Wickes and R. H. Dicke, *Astron. J.*, 78, 757, 1973, and *Astron. J.*, 79, 1433, 1974) on a large-aperture telescope. It was found that there was no appreciable diminution of detected stellar interference fringe visibility compared with that measured on the Mount Wilson 61-cm telescope, which implies that the technique may be used on the largest telescopes for maximum angular resolution. The principal results of individual double-star measurements are as follows: (1) A previously undetected stellar companion of α Delphini was discovered. A small amount of orbital motion was found between the August and November observations. (2) A second measurement of the orbital positions of the astrometric Population II binary μ Cassiopeiae was obtained. (3) Precision measurements were made of the orbital positions of the Hyades binaries (ADS) 3210, 3475, and 3135 to test the computed orbits used in constructing the Hyades mass-luminosity diagram. A paper describing the observational results will appear in the August 1975 *Astronomical Journal*.

During February, March, and April 1975, Drs. A. G. Willis and H. R. de Ruiter of the Leiden Observatory worked in collaboration with Arp on optical identifications of radio sources discovered in a 21-cm wavelength survey with the Westerbork synthesis radio telescope (WSRT) in the Netherlands. In a typical WSRT 21-cm field one detects some 10 to 15 radio sources that usually appear to be unrelated to the object that motivated the observation. Willis, de Ruiter, and C. E. Oosterbaan have systematically classified those radio sources that were detected in fields surrounding bright nearby galaxies. In

previous 21-cm surveys with the WSRT about 22% of the detected radio sources could be identified on plates whose limiting magnitude was comparable to that of the *Palomar Sky Survey* ($m \sim 21$ in B). It was thus decided to search for optical identifications on deep IIIa-J plates of the fields surrounding the galaxies taken by Arp with the Palomar 1.2-meter Schmidt telescope. The limiting magnitude of these plates is about 22.5 after a 1-hour exposure with a WR 2 filter. Using the long-screw measuring engine of the Hale Observatories, Willis and de Ruiter determined accurate positions of optical candidates selected from the plates for some 750 radio sources. Because of the good positional accuracy of the radio sources (about $1''$ in right ascension by $1'' \cos \delta$ in declination for unresolved sources) final identifications could be made purely on the basis of radio-optical positional coincidence. In an initial analysis of the data, requiring positions to differ by no more than $3''$ in α and $3'' \cos \delta$ in δ , Willis and de Ruiter found optical counterparts for 182 radio sources, or an identification of 24%. After the extendedness of some of the remaining radio sources is taken into account, the identification percentage is expected to rise to $\sim 28\%$. Of the 182 identifications, about 55 were objects which would not have been seen on the *Palomar Sky Survey* or whose reality would have been questioned. The optical sample was found to consist of $\sim 43\%$ stellar objects, 48% galaxies, and 9% uncertain. This near equality in the

number of galaxies and stellar objects departs slightly from the distribution found in the first Westerbork survey, where only about 30% of the identifications had a stellar appearance. The distribution does agree, however, with the findings of the smaller second Westerbork survey and the optical identification content of Bologna radio sources determined by Grueff and Vigotti (who also used deep IIIa-J plates taken with the Palomar 1.2-meter Schmidt telescope).

Seven fields were further investigated by means of very deep IIIa-J plates taken by Arp with the Kitt Peak 4-meter telescope. The limiting magnitude of these plates is about 23.5. Optical counterparts were found for an additional 19 sources. Sixteen (84%) of these objects were classified as galaxies and 3 (16%) as stellar objects. The dramatic increase in the galaxy identification content at very faint magnitudes confirms the findings of the earlier, but smaller, study of Katgert-Merkelijn and Spinrad. Among interesting individual objects discovered from the identifications is the stellar object of neutral color associated with the compact radio source 0846+51W1. Between January 15 and February 15, 1975, it increased dramatically from $m = 19.5$ to $m = 15.8$. Since then it has slowly subsided in brightness. The radio source was found to have the centimeter excess spectrum characteristic of variable compact sources. It is situated within $10''$ of an interacting galaxy system.

PHOTOGRAPHIC LABORATORY

Miller performed extensive laboratory and telescope tests of experimental emulsions that showed promise for astronomical use. One outstanding example was the red-sensitive twin to the unique blue-sensitive IIIa-J emulsion, reported several years ago, which marked a significant breakthrough in the theory

and practice of increasing space penetration by improving photographic materials. The IIIa-J emulsion increased the limiting magnitude of any telescope by nearly 2 magnitudes beyond anything that could be done by even the best previous emulsions. The full potential of this significant improvement was

diminished, however, by the fact that the most distant objects within the theoretical range of the IIIa-J emulsion used in combination with the 5-meter Hale Telescope were so distant that the effects of redshift of their energy placed their images beyond the red-sensitivity limit of that emulsion. Hence, a red-sensitive twin was required.

As reported in *Year Book 73* (p. 172), Kodak produced such an emulsion, designated 127-02, used extensively until the middle of this year, when improvements suggested by Miller were made. The result, designated 127-04, has now passed laboratory and field tests with outstanding success and is in full production. It is faster than the original version, has more uniform spectral sensitivity, and responds excellently to hypersensitizing by baking in dry nitrogen for 3½ hours at 65°C.

Routine quality-control tests of all photographic plates received for use at Palomar, Mount Wilson, and Las Campanas have been continued throughout the year. The resultant data, providing emulsion speeds and chemical fog densities for all types of plates, have been posted on the appropriate mountains for the use of observers in establishing proper exposure times for their research plates.

The plate salvage program that was instituted several years ago to reclaim the large number of old plates in the Observatories' files that were exhibiting degenerative brown stain was continued

periodically when manpower was available. During this year a total of 2400 additional plates were salvaged, bringing the total number treated to date to 6500. This essentially completes the treatment of stained direct astronomical plates and historical photographs that record the history of the Mount Wilson Observatory from 1904 to the present. Spectrographic plates are next to be treated; a rough estimate of the number involved is between 6000 and 8000. It is hoped that this project can be completed within the next two years before plates suffer further deterioration.

Nitrogen-baking equipment and techniques have been standardized on Mount Wilson and Las Campanas for use by observers employing photographic plates. The majority of types currently in use show important gains in efficiency as a result of this hypersensitization, some showing gains as great as 300%-400%. Tests of hypersensitization by hydrogen soaking were discontinued because of the low gains resulting for most emulsions, as well as the hazards associated with the use of hydrogen gas in the laboratory.

Bedke has continued the production of photographic prints and slides for staff use in publications, research records, lectures, and colloquia. He also completed a series of tests of certain photographic solutions available commercially in ready-mix form to determine which are suitable for use in the Observatories' darkrooms.

2.5-METER DU PONT TELESCOPE

Good progress was made toward completion of the du Pont Telescope under the general direction of Rule as Project Officer. Final plant assembly trials and adjustments were finished in Los Angeles during July 1974. Parts and subassemblies were packed and shipped overseas to the Las Campanas site by October 1 for erection during the favorable summer in Chile.

The rotating dome structure was completed by September so that the observing floor area could be finished and sealed off sufficiently to start the telescope erection by November 18, 1974. Over a period of ten weeks, the 80-ton mechanical mount was completely assembled with drives and most service auxiliaries, but without optics. Operational trials were successfully made with all cables

installed by March 1975. Further tests will be conducted after installation of the control system console, microprocessor electronics, and cabling.

The 2.5-meter primary mirror in its special container was shipped by sea and trucked to the mountain from Coquimbo, arriving on Las Campanas on April 20, 1975.

Dome and Building

Adjustments are continuing on shutter-track alignment and windscreen track and drive controls. The central lift ram has been used, but the gate and other safety features remain to be completed. Although most of the building utilities and service equipment have been installed, much remains to be done in connection with plumbing, hardware, wiring, plastering, and similar items. With completion of major erection tasks and assembly work, the activities of the building contractor have been directed toward interior finishing and cleanup of outside areas.

Optics

In *Year Book 73* (p. 174), Vaughan reported that a final polishing run on the outermost edge of the du Pont 2.5-meter primary mirror was under consideration. This plan was carried out by Mr. Don Loomis, and acceptance tests were started in mid-July 1974, as it appeared that further optical work would be both unnecessary and inadvisable. For these tests the mirror was placed in its cell. Because of unusually hot weather in Tucson during this period, and other accidental factors, extraordinary measures were required to sustain good internal shop "seeing" for the final tests. Definitive results, consisting of Hartmann tests, knife-edge photographs, and unequal-path interferograms, were obtained, and on October 10, 1974, the Las Campanas Committee accepted the mirror as finished.

The final tests of the mirror in its

cell showed that the mirror-cell system would perform in such a way as to lead to no significant image degradation even under the best seeing conditions expected at Las Campanas. This conclusion is inferred in part from the fact that about 90% of all geometrical rays are contained by a circle $\frac{1}{2}$ " in diameter, and 50% in $\frac{1}{4}$ ". The geometrical design of the f/7.5 Cassegrain system is inherently aberration-limited at about $\frac{1}{4}$ " on axis, and $\frac{1}{3}$ " elsewhere in the 2.1° field. At optical wavelengths, the image quality will be relatively insensitive to geometrical effects of this size. It has been shown by means of an image test, using a null lens and helium-neon laser source, that for all practical purposes the primary mirror does perform as if it were diffraction-limited. Following installation at the site, a more extensive discussion of the fabrication and tested performance of this mirror is to be prepared by Vaughan for publication.

As of June 1975, the f/7.5 Cassegrain secondary mirror was nearing completion at Loomis Custom Optics in Tucson, delivering about 60% image concentration with a $\frac{1}{2}$ " circle. It is intended to aim for a final figure that is at least as good as that of the primary. During the past year, grinding of the aspheric Bowen-Gascoigne corrector was completed in Pasadena and final polishing started.

The vacuum tank for aluminizing, with associated pump equipment, was stored at the site for fourteen months prior to installation in the dome during March 1975. Aluminizing test runs by Rule and Fair in May showed excellent system performance with short pump-down time and the best low-pressure level of any known large tank—about 10^{-7} torr. The system was then used for aluminizing the primary mirror of the 1-meter telescope and the 61-cm primary of the University of Toronto telescope.

Microprocessor Control System

A microprocessor automatic control system has been developed by the Astro-

electronics Laboratory for control of the 2.5-meter telescope. The system is built in modular form on easily replaceable printed wiring boards. Data are transmitted serially between major subassemblies, using dedicated coaxial cables. The cables extend from the Cassegrain observing station by way of other stations to the data room; thus, data can be monitored or displayed at any of a number of locations on the telescope and in the dome. Special system functions, such as raster scans, can also be generated externally.

Basic telescope controls are built around four programmable microprocessors that are connected with the computation and display of telescope position, tracking rates, and control of the dome and wind-screen. The microprocessors are identical, although individually programmed for specific applications. The instructions are contained in several nonvolatile, integrated circuit memory chips that are easily field programmable.

Twenty-six coaxial cables are used to distribute all data and to synchronize signals throughout the system. Numerous break points are provided at appropriate intervals along the cable where a test display unit may be inserted for troubleshooting.

The telescope-hub interface unit is located on the tailpiece of the telescope. It accepts parallel input data from encoders and converts it into serial data for transmission to the rest of the system. The encoders give the positions of the secondary mirror, counterweights, Cassegrain corrector lens, and the rotating instrument ring. Provisions are being made in this assembly to add additional encoders if required later.

The declination interface unit is located in the telescope fork.

The telescope control cabinet contains all of the essential electronics involved in the control of the telescope.

The night assistant's console is located in the data room on the observing floor and is the central location for system monitoring and control, for manual

control functions, and for a redundant indicating system that employs synchros for use in the unlikely event that the encoders or microprocessors become inoperative.

Another section of the microprocessor control system, for governing the rotation of the coudé flat mirror in two coordinates, remains to be designed and constructed.

Auxiliary Instruments

Specific instruments for the du Pont Telescope are in various stages of construction, according to designs and specifications approved by the several instrument working groups. High priority has been given to the plate-holder system that will be ready first for adjustment and check-out at the telescope. The base structure is complete, including the two X-Y guider mechanical assemblies and the field-rotation drive. The handling dolly is finished. Four plate holders are being fabricated in three sizes: 51 × 51 cm, 35 × 35 cm, and 25 × 25 cm. Glass plates will be held to an accurate concave spherical radius of 9 meters by means of vacuum. A smaller size, 16 × 16 cm, is flat. Related items to be constructed include the optics for the two visual guiders and two TV guider-camera mounts, the plate-holder hoist, the vacuum system, and the handling-loading cart for the large plate holders.

An instrument-mounting base is being built to accommodate spectrographs, photometers, image tubes, etc. The associated offset guider and infrared-detector mounting base are also complete except for optics.

Design detail in progress includes a cable wrap-up for the Cassegrain instrument ring to carry the many leads from the telescope to the instrument without dangling cable loops. Power drive and remote position readout have been added to the instrument ring.

The Cassegrain spectrograph has been received from Boller and Chivens. It is designed for operation from a remote

station; a remotely operable multi-exposure plate holder, designed by Brucato, is under construction. The image-tube mount and transfer lens package is being constructed by Dr. Kent Ford of the Department of Terrestrial Magnetism.

Shop details are proceeding for the observer's Cassegrain chair platform. Several basic design changes became necessary to accommodate additional requirements of astronomers.

Word was received in June 1975 that the National Science Foundation would award a continuing grant covering about half of the cost of the construction of a coudé spectrograph for the du Pont Telescope in a four-year program under the supervision of Vaughan as principal investigator. The engineering group for this effort, including Kelderman, Friswold, and Snoddy, will begin its work during the summer of 1975.

LAS CAMPANAS OBSERVATORY

The 1-meter telescope was in operation on 206 nights, while the 61-cm telescope of the University of Toronto was used on 258 nights. One-hundred-thirty-nine visitors to the mountain were accommodated, and normal support was given to the University of Toronto under the agreement.

Observatory employees on Cerro Las Campanas accomplished many tasks of construction and maintenance under the supervision of Wagner and Papiç. The local dial telephone system was installed, with instruments at seven locations on the mountain. Communications with the gate and with the El Pino office continued to be maintained by radio. The kitchen and dining room at the Campamento were greatly improved. As many as 40 people can now be served. The second warehouse was completed. Like the first, its dimensions are 11 × 25 meters. An office and radio room were provided in warehouse No. 1. The equipment repair shop on Las Campanas was essentially completed. It is located in the plaza area near the warehouses and power house. The repair shop has two large pits for heavy trucks. A 120 KVA diesel generator was installed in the power house. Extensive repairs were made to the dome shutters of the 1-meter telescope.

In a joint project with the European Southern Observatory, the 10-kilometer common approach road in the valley was resurfaced with 5 cm of gravel.

The crew had total responsibility for trucking the components of the 2.5-meter telescope from the port of Coquimbo to Las Campanas. This was accomplished in one week in November 1974. The two large diesel trucks were indispensable. Similarly, the 2.5-meter mirror was trucked to the mountain in April 1975.

Construction by Contractor

Work progressed on the installation of various systems, including plumbing, electrical wiring for power and controls, chiller, air conditioner, central ram, and elevator. Several additional months will be required to complete interior plastering, as well as interior and exterior of the coudé room, exterior leach lines, and final painting.

At the lodge, the three principal dormitory buildings have been completed and furnished. Little progress has been made on the common building except for excavation and foundation forming.

The water system has been basically completed and in use since December 1974. Insulation on exposed pipe and fittings remains to be done, together with minor tasks on the pump houses.

El Pino Headquarters in La Serena

A steel structure with masonry walls and one large pit was constructed for the repair of cars and trucks. A short

access road to the shop was provided, with necessary culverts, ditches, and a retaining wall. A new entrance gate for the El Pino driveway was built, together with a 48-meter stone wall for the front property line. To meet municipal requirements, an electric substation of 100 KVA capacity was installed near the front gate

and associated distribution conduits and telephone lines were installed.

The working force was called on to repair considerable damage to walls and to older abode structures on the El Pino property that occurred as a result of a fairly severe earthquake on March 13, 1975.

BIBLIOGRAPHY

- Aaronson, M., *see* Frogel, J. A.
- Aksnes, K., *see* Kowal, C. T.
- Altschuler, Martin D., Dorothy E. Trotter, Gordon Newkirk, Jr., and Robert Howard, The large-scale solar magnetic field. *Sol. Phys.*, 39, 3-17, 1974.
- Andreasian, N. K., *see* Arp, Halton; Khachikian, E. Y.
- Arp, Halton, NGC 520 chain of quasars. *Astron. J.*, 79, 923-924, 1974.
- Arp, Halton, Distances of the quasars and evidence for nonvelocity redshifts, in *Astrophysics and Gravitation, Proceedings of XVIth Solvay Conference on Physics*, pp. 443-462, University of Brussels, 1974.
- Arp, Halton, Evidence for nonvelocity redshifts, in *Confrontation of Cosmological Theories with Observation, Int. Astron. Union Symp.*, 63, pp. 61-67, M. S. Longair, ed., D. Reidel Publishing Co., Dordrecht-Holland, 1974.
- Arp, Halton, Evidence for nonvelocity redshifts—new evidence and review, in *Formation and Dynamics of Galaxies, Int. Astron. Union Symp.*, 58, pp. 199-244, K. C. Freeman, ed., D. Reidel Publishing Co., Dordrecht-Holland, 1974.
- Arp, Halton, Lectures on QSOs, observations, and the redshift problem, in *High Energy Astrophysics and Its Relation to Elementary Particle Physics*, pp. 3-76, Kenneth Brecher and Giancarlo Setti, eds., The Massachusetts Institute of Technology Press, Cambridge, Massachusetts, 1974.
- Arp, Halton, Astronomy at the frontier. *Nat. Hist.*, 134, 90-92, 1975.
- Arp, Halton, and Robert W. O'Connell, Properties of two blue compact galaxies. *Astrophys. J.*, 197, 291-296, 1975.
- Arp, Halton, Jack A. Baldwin, and E. Joseph Wampler, Two new quasars near galaxies. *Astrophys. J. (Lett.)*, 198, L3-L5, 1975.
- Arp, Halton, A. G. Willis, and H. de Ruiter, Discovery announcement: 0846+51W1. *Int. Astron. Union Circ.*, 2750, February 25, 1975.
- Arp, Halton, W. L. W. Sargent, N. K. Andreasian, and E. Y. Khachikian, On the spectrum of the blue object near irregular galaxy NGC 520. *Astrofizika*, 10, 298-300, 1974.
- Baldwin, Jack A., *see* Arp, Halton.
- Becklin, E. E., Use of large optical telescopes at infrared wavelengths, in *Proceedings of Conference on Research Programmes for the New Large Telescope*, pp. 57-70, A. Reiz, ed., ESO-SRC-CERN, Geneva, Switzerland, July 1974.
- Becklin, E. E., and G. Neugebauer, Infrared observation of NGC 6334, in *H II Regions and the Galactic Centre, Proceedings of Eighth ESLAB Symposium*, pp. 39-42, A. F. M. Moorwood, European Research Organization, Frascati, Italy, 1974.
- Becklin, E. E., G. Neugebauer, and D. Early, Map of the galactic center region at 2.2 μ , in *H II Regions and the Galactic Centre, Proceedings of Eighth ESLAB Symposium*, pp. 227-228, A. F. M. Moorwood, ed., European Research Organization, Frascati, Italy, 1974.
- Becklin, E. E., J. A. Frogel, G. Neugebauer, S. E. Persson, and C. G. Wynn-Williams, Erratum: The H II region G333.6 - 0.2, a very powerful 1-20 μ source. *Astrophys. J. (Lett.)*, 193, L153, 1974 (*see Astrophys. J. (Lett.)*, 182, L125-L129, 1973).
- Becklin, E. E., F. J. Hawkins, K. O. Mason, K. Matthews, G. Neugebauer, D. Packman, P. W. Sanford, B. Schupler, A. Stark, and C. G. Wynn-Williams, Infrared, radio, and x-ray observations of Cygnus X-3. *Astrophys. J. (Lett.)*, 184, L119-L124, 1974.

- Becklin, E. E., *see also* Frogel, J. A.; Gatley, I.; Ney, E. P.; Penston, M. V.; Zappala, R. R.
- Boesgaard, Ann Merchant, Duncan Chesley, and George Preston, Magnetic field measurements in ξ Boo A. *Publ. Astron. Soc. Pac.*, 87, 353-355, 1975.
- Boksenberg, A., and W. L. W. Sargent, Doublet structure in the absorption redshifts in the spectrum of Pks 0237-23. *Astrophys. J.*, 198, 31-43, 1975.
- Borra, Ermanno F., Spectral changes induced by the Zeeman effect in oblique rotator models. *Astrophys. J.*, 193, 699-703, 1974.
- Borra, Ermanno F., A search for the Zeeman effect in the x-ray star candidates θ^2 Orionis and X Persei, the x-ray source Cygnus X-1, and the B2 Ib star HD 31327. *Astrophys. J. (Lett.)*, 196, L109-L111, 1975.
- Chase, S. C., Jr., E. D. Miner, D. Morrison, G. Münch, G. Neugebauer, and M. Schroeder, Preliminary infrared radiometry of the night side of Mercury from Mariner 10. *Science*, 185, 142-145, 1974.
- Chase, S. C., Jr., *see also* Ingersoll, A. P.
- Chesley, Duncan, *see* Boesgaard, Ann Merchant.
- Datlowe, Dayton W., *see* Roy, Jean-René.
- Deming, D., *see* Tovmassian, H. M.
- Deutsch, Armin J., *see* Keenan, Philip C.
- Diner, D. J., *see* Ingersoll, A. P.
- Dravins, Dainis, Magnetic field and electric current structure in the chromosphere. *Sol. Phys.*, 37, 323-324, 1974.
- Dworetzky, M. M., Spectroscopic study of the open cluster NGC 2422. *Astron. J.*, 80, 131-133, 1975.
- Early, D., *see* Becklin, E. E.
- Elias, Jonathan H., and Jesse L. Greenstein, Magnetic observations of white dwarfs. *Publ. Astron. Soc. Pac.*, 86, 957-959, 1974.
- Elias, Jonathan H., *see also* Werner, M. W.
- Fridenberg, J. T., J. A. Westphal, and Jerome Kristian, Microprocessors—A new alternative for automatic telescope control, in *Telescope Automation*, pp. 218-244, Maureen K. Huguenin and Thomas B. McCord, eds., Massachusetts Institute of Technology, Cambridge, Massachusetts, 1975.
- Frogel, J. A., S. E. Persson, M. Aaronson, E. E. Becklin, K. Matthews, and G. Neugebauer, Stellar content of the nuclei of elliptical galaxies determined from 2.3- μ CO band strengths. *Astrophys. J. (Lett.)*, 195, L15-L18, 1975.
- Frogel, J. A., *see also* Becklin, E. E.
- Garrison, Robert F., *see* Keenan, Philip C.
- Gatley, I., E. E. Becklin, G. Neugebauer, and M. W. Werner, Infrared observations of Comet Kohoutek (1973f). *Icarus*, 23, 561-565, 1974.
- Gatley, I., E. E. Becklin, K. Matthews, G. Neugebauer, M. V. Penston, and N. Scoville, A new infrared complex and molecular cloud in Orion. *Astrophys. J. (Lett.)*, 191, L121-L125, 1974.
- Gezari, D. Y., *see* Werner, M. W.
- Glackin, David L., Short-lived flarelike phenomena in the quiet chromosphere. *Sol. Phys.*, 41, 115-118, 1975.
- Gott, J. Richard III, James E. Gunn, David M. Schramm, and Beatrice M. Tinsley, An unbound universe? *Astrophys. J.*, 194, 543-553, 1974.
- Gott, J. Richard III, *see also* Turner, Edwin L.
- Green, R. F., Discovery announcement: Supernova in NGC 2207. *Int. Astron. Union Circ.*, 2743, February 10, 1975.
- Green, R. F., *see also* Tovmassian, H. M.
- Greenstein, Jesse L., Photometry of a Pleiades candidate and composite white dwarfs. *Astron. J.*, 79, 964-966, 1974.
- Greenstein, Jesse L., Spectrophotometry of magnetic degenerate stars. *Astrophys. J. (Lett.)*, 194, L51-L55, 1974.
- Greenstein, Jesse L., Large telescope astronomy, in *Proceedings of Conference on Research Programmes for the New Large Telescope*, pp. 11-25, A. Reiz, ed., ESO-SRC-CERN, Geneva, Switzerland, 1974.
- Greenstein, Jesse L., A further list of degenerate stars, VIII. *Astrophys. J. (Lett.)*, 196, L117-L120, 1975.
- Greenstein, Jesse L., *see also* Elias, Jonathan H.
- Griffin, Roger F., and James E. Gunn, The Palomar radial-velocity spectrometer. *Astrophys. J.*, 191, 545-556, 1974.
- Gunn, James E., A worm's-eye view of the mass density in the universe. *Comments Astrophys. Space Phys.*, 6, 7-14, 1974.
- Gunn, James E., and J. B. Oke, Spectrophotometry of faint cluster galaxies and the Hubble diagram: an approach to cosmology. *Astrophys. J.*, 195, 255-268, 1975.
- Gunn, James E., *see also* Gott, J. Richard III; Griffin, Roger F.

- Haro, G., *see* Tovmassian, H. M.
- Hawkins, F. J., *see* Becklin, E. E.
- Hickson, Paul, An automated sky photometer for the Palomar 48-inch Schmidt telescope. *Publ. Astron. Soc. Pac.*, 86, 1011-1013, 1974.
- Howard, Robert, The rotation of the Sun. *Sci. Am.*, 232, 106-114, 1975.
- Howard, Robert, Studies of solar magnetic fields, I, The average field strengths. *Sol. Phys.*, 38, 283-299, 1974.
- Howard, Robert, Studies of solar magnetic fields, II, The magnetic fluxes. *Sol. Phys.*, 38, 59-67, 1974.
- Howard, Robert, Studies of solar magnetic fields, III, The east-west orientation of field lines. *Sol. Phys.*, 39, 275-287, 1974.
- Howard, Robert, *see also* Altschuler, Martin D.
- Huchra, John P., Discovery announcement: Object Helin = 1952 RH. *Int. Astron. Union Circ.*, 2698, September 9, 1974.
- Huchra, John P., Discovery announcement: Suspected supernova. *Int. Astron. Union Circ.*, 2760, March 19, 1975.
- Huchra, John P., Normal redshifts in Markarian galaxies. A reply to Terrikorpi. *Nature*, 225, 430, 1975.
- Huchra, John P., *see also* Kowal, C. T.
- Ingersoll, A. P., G. Münch, G. Neugebauer, D. J. Diner, G. S. Orton, B. Schupler, M. Schroeder, S. C. Chase, R. D. Ruiz, and L. M. Trafton, Pioneer 11 infrared radiometer experiment: the global heat balance of Jupiter. *Science*, 188, 472-473, 1975.
- Johnson, Harold L., *see* Sandage, Allan.
- Katem, Basil, *see* Kristian, Jerome.
- Keenan, Philip C., Armin J. Deutsch, and Robert F. Garrison, Catalog of Mira variables. *Astrophys. J. Suppl. Ser.*, 28, no. 262, 271-308, 1974.
- Khachikian, E. Y., N. K., Andreasian, and W. L. W. Sargent, Determination of the redshift of irregular galaxy NGC 5360. *Astrofizika*, 10, 297-298, 1974.
- Khachikian, E. Y., *see also* Arp, Halton.
- Kirshner, Robert P., Spectrophotometry of the Crab Nebula. *Astrophys. J.*, 194, 323-327, 1974.
- Kirshner, Robert P., Spectrophotometry of supernovae, in *Highlights of Astronomy 1973*, pp. 533-544, G. Contopoulos, J. Kovalevsky, and Y. Fujita, eds., D. Reidel Publishing Co., Dordrecht-Holland, 1974.
- Kirshner, Robert P., and John Kwan, Distances to extragalactic supernovae. *Astrophys. J.*, 193, 27-36, 1974.
- Kirshner, Robert P., and John Kwan, The envelopes of Type II supernovae. *Astrophys. J.*, 197, 415-424, 1975.
- Kormendy, John, and Wallace L. W. Sargent, Tidal effects as criteria for membership in small groups of galaxies: application to VV 166. *Astrophys. J.*, 193, 19-25, 1974.
- Kowal, C. T., Discovery announcement: Object Kowal (1974 MA). *Int. Astron. Union Circ.*, 2683, July 8, 1974; 2687, July 22, 1974; 2688, July 26, 1974.
- Kowal, C. T., Discovery announcement: Probable new satellite of Jupiter (Jupiter XIII). *Int. Astron. Union Circ.*, 2702, September 20, 1974; 2711, October 24, 1974; 2742, January 31, 1975.
- Kowal, C. T., W. L. W. Sargent, and J. Huchra, The 1974 Palomar supernova search. *Publ. Astron. Soc. Pac.*, 87, 401-403, 1975.
- Kowal, C. T., K. Aksnes, B. G. Marsden, and E. Roemer, The thirteenth satellite of Jupiter. *Astron. J.*, 80, 460-464, 1975.
- Kowal, C. T., F. Zwicky, W. L. W. Sargent, and L. Searle, The 1973 Palomar supernova search. *Publ. Astron. Soc. Pac.*, 86, 516-525, 1974.
- Kristian, Jerome, Allan Sandage, and Basil Katem, The systematic optical identification of the remaining 3C radio sources, I, A search in 47 fields. *Astrophys. J.*, 191, 43-50, 1974.
- Kristian, Jerome, *see also* Fridenberg, J. T.; Westphal, James A.
- Kruit, P. C. van der, The velocity field of NGC 4258. *Astrophys. J.*, 192, 1-19, 1974.
- Kruit, P. C. van der, Rotation properties of the infrared spiral galaxy NGC 2675. *Astrophys. J.*, 193, 611-615, 1975.
- Kruit, P. C. van der, The motions in the central region of NGC 4736—Evidence for an expanding ring, in *Formation and Dynamics of Galaxies*, *Int. Astron. Union Symp.*, 58, pp. 431-437, K. C. Freeman, ed., D. Reidel Publishing Co., Dordrecht-Holland, 1974.
- Kwan, John, *see* Kirshner, Robert P.
- Lazareff, B., *see* Zirin, Harold.
- Liu, Sou-Yang, White light network in the solar photosphere. *Sol. Phys.*, 39, 297-300, 1974.
- Liu, Sou-Yang, and Andrew Skumanich, An empirical interpretation for the time evolution of the Ca K-line. *Sol. Phys.*, 38, 109-115, 1974.

- Marsden, B. G., *see* Kowal, C. T.
- Mason, K. O., *see* Becklin, E. E.
- Matthews, K., *see* Becklin, E. E.; Frogel, J. A.; Gatley, I.; Zappala, R. R.
- Melnick, J., and H. Quintana, Southern galaxy clusters identified with 3U x-ray sources. *Astrophys. J. (Lett.)*, 198, L97-L99, 1975.
- Méndez, Roberto H., Guido Münch, and Jorge Sahade, AZ Cassiopeiae at the 1956-57 eclipse. *Publ. Astron. Soc. Pac.*, 87, 305-310, 1975.
- Merrill, K. M., *see* Ney, E. P.
- Michalitsanos, Andrew G., The Sun's turbulent atmosphere. *Griffith Observer*, 39, 2-7, 1975.
- Miner, E. D., *see* Chase, S. C., Jr.
- Moore, R. L., and Frances Tang, Umbral oscillations and penumbral waves in H α . *Sol. Phys.*, 41, 81-88, 1975.
- Morrison, D., *see* Chase, S. C., Jr.
- Münch, Guido, Infrared sensing of atmospheric temperature clouds and motion, in *AIAA/AGU Space Science Conference: Exploration of the Outer Solar System*, Paper No. 73-561, American Institute of Aeronautics and Astronautics, New York, July 1973.
- Münch, Guido, and Keith Taylor, On the spectrum of neutral oxygen in the Orion Nebula. *Astrophys. J.*, 192, L93-L95, 1974.
- Münch, Guido, *see also* Chase, S. C., Jr.; Ingersoll, A. P.; Méndez, Roberto H.
- Neugebauer, Gerry, *see* Becklin, E. E.; Chase, S. C., Jr.; Frogel, J. A.; Gatley, I.; Ingersoll, A. P.; Ney, E. P.; Penston, M. V.; Zappala, R. R.
- Newkirk, Gordon, Jr., *see* Altschuler, Martin D.
- Ney, E. P., K. M. Merrill, E. E. Becklin, G. Neugebauer, and C. G. Wynn-Williams, Studies of the infrared source CRL 2688. *Astrophys. J. (Lett.)*, 198, L129-L134, 1975.
- O'Connell, Robert W., Jeffrey D. Scargle, and W. L. W. Sargent, The nature of Hoag's object. *Astrophys. J.*, 191, 61-62, 1974.
- O'Connell, Robert W., *see also* Arp, Halton.
- Oemler, Augustus, Jr., The systematic properties of clusters of galaxies, I, Photometry of fifteen clusters. *Astrophys. J.*, 194, 1-19, 1974.
- Oke, J. B., Current research programmes at the Hale Observatories, in *Proceedings of Conference on Research Programmes for the New Large Telescope*, pp. 29-34, A. Reiz, ed., ESO-SRC-CERN, Geneva, Switzerland, 4 July 1974.
- Oke, J. B., and M. Schwarzschild, Absolute spectrophotometry in M31 and M32. *Astrophys. J.*, 198, 63-70, 1975.
- Oke, J. B., and L. Searle, The spectra of supernovae, in *Annual Review of Astronomy and Astrophysics*, Vol. 12, pp. 315-329, G. R. Burbidge, D. Layzer, and J. G. Phillips, eds., Annual Reviews, Inc., Palo Alto, California, 1974.
- Oke, J. B., *see also* Gunn, James E.; Shields, G. A.
- Orton, G. S., *see* Ingersoll, A. P.
- Packman, D., *see* Becklin, E. E.
- Penston, M. J., *see* Penston, M. V.
- Penston, M. V., M. J. Penston, R. A. Selmes, E. E. Becklin, and G. Neugebauer, Broadband optical and infrared observations of Seyfert galaxies. *Mon. Not. R. Astron. Soc.*, 169, 357-393, 1974.
- Penston, M. V., *see* Gatley, I.
- Persson, S. E., *see* Becklin, E. E.; Frogel, J. A.
- Preston, George W., The chemically peculiar stars of the upper main sequence, in *Annual Review of Astronomy and Astrophysics*, Vol. 12, pp. 257-277, G. R. Burbidge, D. Layzer, and J. G. Phillips, eds., Annual Reviews, Inc., Palo Alto, California, 1974.
- Preston, George W., *see also* Boesgaard, Ann Merchant.
- Quintana, H., *see* Melnick, J.
- Roemer, E., *see* Kowal, C. T.
- Roy, Jean-René, and Dayton, W. Datlowe, X-ray bursts from solar flares behind the limb. *Sol. Phys.*, 40, 165-182, 1975.
- Ruiter, H. de, *see* Arp, Halton.
- Ruiz, J. D., *see* Ingersoll, A. P.
- Sahade, Jorge, *see* Méndez, Roberto H.
- Sandage, Allan, and Harold L. Johnson, A preliminary photoelectric sequence in the galaxy Messier 33 of the Local Group. *Astrophys. J.*, 191, 63-65, 1974.
- Sandage, Allan, and G. A. Tammann, Steps toward the Hubble constant, II, The brightest stars in late-type spiral galaxies. *Astrophys. J.*, 191, 603-621, 1974.
- Sandage, Allan, and G. A. Tammann, Steps toward the Hubble constant, III, The distance and stellar content of the M101 group of galaxies. *Astrophys. J.*, 194, 223-243, 1974.

- Sandage, Allan, and G. A. Tammann, Steps toward the Hubble constant, IV, Distance to 39 galaxies in the general field leading to a calibration of the galaxy luminosity classes and a first hint of the value of H_0 . *Astrophys. J.*, 194, 559-568, 1974.
- Sandage, Allan, and G. A. Tammann, Steps toward the Hubble constant, V, The regularity of the local velocity field and the Hubble constant from nearby galaxies. *Astrophys. J.*, 196, 313-328, 1975.
- Sandage, Allan, and G. A. Tammann, Steps toward the Hubble constant, VI, Redshifts and magnitudes of remote Sc I galaxies: the Hubble constant beyond the local velocity field and the value of q_0 . *Astrophys. J.*, 197, 265-280, 1975.
- Sandage, Allan, *see also* Kristian, Jerome; Westphal, James A.
- Sanford, P. W., *see* Becklin, E. E.
- Sargent, Wallace L. W., The redshifts of extragalactic objects, in *Formation and Dynamics of Galaxies*, *Int. Astron. Union Symp.*, 58, pp. 195-198, K. C. Freeman, ed., D. Reidel Publishing Co., Dordrecht-Holland, 1974.
- Sargent, Wallace L. W., and Beatrice Tinsley, On the correlation between M/L and color for spiral galaxies. *Mon. Not. R. Astron. Soc.*, 168, 19P-22P, 1974.
- Sargent, W. L. W., *see also* Arp, Halton; Boksenberg, A.; Khachikian, E. Y.; Kormendy, John; Kowal, C. T.; O'Connell, Robert W.; Turner, Edwin L.
- Scargle, Jeffrey D., *see* O'Connell, Robert W.
- Schmidt, Maarten, Optical spectra and redshifts of 4C quasi-stellar radio sources. *Astrophys. J.*, 193, 505-507, and 195, 253, 1975.
- Schmidt, Maarten, On the nature of faint blue objects in high galactic latitudes, III, A spectroscopic search for quasars in four survey fields. *Astrophys. J.*, 193, 509-512, 1974.
- Schmidt, Maarten, Distribution of quasars in the universe, in *Astrophysics and Gravitation, Proceedings of the XVIth Solvay Conference*, pp. 463-471, University of Brussels, 1974.
- Schmidt, Maarten, Discovery announcement: 1974 MA. *Int. Astron. Union Circ.*, 2696, August 28, 1974.
- Schmidt, Maarten, Quasars and the universe, in *The Nature of Scientific Discovery*, pp. 246-260, Owen Gingerich, ed., Smithsonian Institution Press, Washington, D.C., 1975.
- Schmidt, Maarten, Complete samples of 3CR and 4C quasars, in *Proceedings of Conference on Research Programmes for the New Large Telescope*, pp. 253-257, A. Reiz, ed., ESO-SRC-CERN, Geneva, Switzerland, 4 July 1974.
- Schramm, David M., *see* Gott, J. Richard III.
- Schroeder, M., *see* Chase, S. C., Jr.; Ingersoll, A. P.
- Schupler, B., *see* Becklin, E. E.; Ingersoll, A. P.
- Schwarzschild, M., *see* Oke, J. B.
- Schweizer, François, The spiral distribution of stars in galaxies, in *The Dynamics of Spiral Galaxies*, Centre National de la Recherche Scientifique, Paris, in press, 1975.
- Scoville, N., *see* Gatley, I.
- Searle, Leonard, *see* Kowal, C. T.; Oke, J. B.
- Selmes, R. A., *see* Penston, M. V.
- Shields, G. A., X-ray ionization and the helium abundance in 3C 120. *Astrophys. J.*, 191, 309-316, 1974.
- Shields, G. A., and J. B. Oke, The emission-line spectrum of NGC 1068. *Astrophys. J.*, 197, 5-16, 1975.
- Skumanich, Andrew, *see* Liu, Sou-Yang.
- Stark, A., *see* Becklin, E. E.
- Swenson, G. W., Jr., *see* Tovmassian, H. M.
- Swope, Henrietta, V2283 Sgr, an eclipsing star with a rotating apse. *Ric. Astron.*, 8, 481-490, 1974.
- Tammann, G. A., *see* Sandage, Allan.
- Tang, Frances, *see* Moore, R. L.
- Taylor, Keith, *see* Münch, Guido.
- Tinsley, Beatrice M., *see* Gott, J. Richard III; Sargent, Wallace, L. W.
- Tovmassian, H. M., G. Haro, J. C. Webber, G. W. Swenson, Jr., K. S. Yang, K. M. Yoss, D. Deming, and R. F. Green, Simultaneous optical and radio observations of flare stars in the Pleiades. *Astrofizika*, 10, 337-345, 1974.
- Trafton, L. M., *see* Ingersoll, A. P.
- Trotter, Dorothy E., *see* Altschuler, Martin D.
- Turner, Edwin L., and J. Richard Gott III, Evidence for a spatially homogeneous component of the universe: single galaxies. *Astrophys. J. (Lett.)*, 197, L89-L93, 1975.
- Turner, Edwin L., and Wallace L. W. Sargent, The nature of small groups of galaxies in the local supercluster. *Astrophys. J.*, 186, 587-592, 1974.

- Turnrose, Barry E., Absolute spectral energy distribution of the night sky at Palomar and Mount Wilson Observatories. *Publ. Astron. Soc. Pac.*, 86, 545-551, 1974.
- Veeder, Glenn J., Luminosities and temperatures of M dwarf stars from infrared photometry. *Astron. J.*, 79, 1056-1072, 1974.
- Veeder, Glenn J., The local mass density. *Astrophys. J. (Lett.)*, 191, L57-L58, 1974.
- Visvanathan, Natarajan, Comparison of the optical spectrum of the filaments with the spectrum of the central region of M82. *Astrophys. J.*, 192, 319-324, 1974.
- Visvanathan, Natarajan, Extragalactic optical polarimetry, in *Planets, Stars, and Nebulae Studied with Photopolarimetry*, *Int. Astron. Union Colloq.*, 23, pp. 1059-1083, T. Gehrels, ed., The University of Arizona Press, Tucson, Arizona, 1974.
- Wampler, E. Joseph, *see* Arp, Halton.
- Webber, J. C., *see* Tovmassian, H. M.
- Werner, M. W., J. H. Elias, D. Y. Gezari, and W. E. Westbrook, 1-mm continuum radiation from Orion molecular Cloud 2. *Astrophys. J. (Lett.)*, 192, L31-L32, 1974.
- Werner, M. W., *see also* Gatley, I.
- Westbrook, W. E., *see* Werner, M. W.
- Westphal, James A., Jerome Kristian, and Allan Sandage, Absorption-line redshifts of galaxies in remote clusters obtained with a sky-subtraction spectrograph using an SIT television detector. *Astrophys. J. (Lett.)*, 197, L95-L98, 1975.
- Westphal, James A., *see also* Fridenberg, J. T.
- Willis, A. G., *see* Arp, Halton.
- Wynn-Williams, C. G., *see* Becklin, E. E.; Ney, E. P.
- Yang, K. S., *see* Tovmassian, H. M.
- Yoss, K. M., *see* Tovmassian, H. M.
- Zappala, R. R., E. E. Becklin, K. Matthews, and G. Neugebauer, Angular diameter of IRC +10011 at 2.2, 10, and 20 μ . *Astrophys. J.*, 192, 109-112, 1974.
- Zirin, Harold, Spicules are bright and dark, in *Chromospheric Fine Structure*, *Int. Astron. Union Symp.*, 56, pp. 49-50, R. G. Athay, ed., D. Reidel Publishing Co., Dordrecht-Holland, 1974.
- Zirin, Harold, The magnetic structure of plages, in *Chromospheric Fine Structure*, *Int. Astron. Union Symp.*, 56, pp. 161-175, R. Grant Athay, ed., D. Reidel Publishing Co., Dordrecht-Holland, 1974.
- Zirin, Harold, Studies of K-line filtergrams. *Sol. Phys.*, 38, 91-108, 1974.
- Zirin, Harold, and B. Lazareff, Sunspot motion, flares, and Type III bursts in McMath 11482. *Sol. Phys.*, 41, 425-438, 1975.
- Zwicky, Fritz, *see* Kowal, C. T.

STAFF AND ORGANIZATION

Olin C. Wilson retired after a long association with the Hale Observatories. He was a Research Assistant at the Mount Wilson Observatory from 1931 to 1936, at which time he became a Staff Member. In 1934, he received the first Ph.D. degree in astronomy awarded by the California Institute of Technology. Wilson's professional work has been devoted to various phases of spectroscopy, including the stellar radial velocity program, various investigations of stellar atmospheres and interstellar material, Wolf-Rayet stars, planetary nebulae, and stellar chromospheres. He plans to continue part-time work on his current interest—the study of cyclic chromospheric activity in main-sequence stars.

The retirement of William C. Miller on June 30 marks the end of a twenty-six year association, during which he has been head of the Photographic Research Laboratory. His departure entails the end of the research aspects of the Laboratory's operations. Miller hopes to continue experimental work on an unofficial basis in order to complete for publication a number of investigations related to the improvement of photographic techniques and materials.

George W. Preston was appointed Astronomer-in-Charge, Mount Wilson.

Arthur H. Vaughan, Jr., was appointed Astronomer-in-Charge, du Pont Telescope.

Dr. Pierre Demarque, Chairman of the Department of Astronomy, Yale

University, was in residence in Pasadena from January to June as Visiting Associate of the Hale Observatories.

Dr. S. Eric Persson was appointed a Staff Member of the Hale Observatories, effective August 1, 1975.

Dr. Stephen A. Sackett was appointed a Staff Member of the Hale Observatories, effective June 1, 1975.

William E. Westbrook died on June 4, 1975, at the age of 26. A graduate student at the California Institute of Technology, he was a member of the group conducting 1-mm photometry at the 5-meter telescope. His outstanding work at the Observatories contributed significantly to the development and success of the millimeter program.

Research Division

Staff Members

Halton C. Arp
 Horace W. Babcock, *Director*
 Edwin W. Dennison
 Jesse L. Greenstein¹
 James E. Gunn²
 Robert F. Howard
 Jerome Kristian
 Robert B. Leighton³
 Guido Münch²
 Gerry Neugebauer⁴
 J. Beverley Oke, *Associate Director*²
 George W. Preston
 Bruce H. Rule, *Chief Engineer*
 Allan R. Sandage
 Wallace L. W. Sargent²
 Maarten Schmidt⁵
 Leonard Searle
 Stephen A. Sackett
 Arthur H. Vaughan, Jr.
 James A. Westphal⁶
 Harold Zirin⁷

¹Lee A. DuBridge Professor of Astrophysics, California Institute of Technology.

²Professor of Astronomy, California Institute of Technology.

³Professor of Physics; Chairman of the Division of Physics, Mathematics, and Astronomy, California Institute of Technology.

⁴Professor of Physics, California Institute of Technology.

⁵Professor of Astronomy; Executive Officer for Astronomy, California Institute of Technology.

⁶Associate Professor of Planetary Science, California Institute of Technology.

Members Engaged in Post-Retirement Studies

Alexander Pogo
 Henrietta H. Swope
 Olin C. Wilson

Visiting Associates

Pierre Demarque
 N. Visvanathan

Staff Associates

Eric E. Becklin⁸
 Robert J. Brucato
 Michael W. Werner⁹

Senior Research Fellow

Ronald Moore

Carnegie Fellows

Ermanno F. Borra¹⁰
 Michael H. Hart¹¹
 François Schweizer
 Pieter C. van der Kruit¹²
 Christopher P. Wilson
 Hirokazu Yoshimura
 Robert J. Zinn

Research Fellows

William M. Adams
 Daniel Y. Gezari
 Gordon J. Hurford
 Stephen L. Knapp
 Sou-Yang Liu¹³
 Andrew G. Michalitsanos¹⁴
 Douglas O. Richstone
 Jean-René Roy¹⁵
 Keith Taylor
 Trinh X. Thuan
 Althea Wilkinson

Carnegie-Chilean Fellows

Eduardo Hardy
 Maria Teresa Ruiz

⁷Chief Astronomer of Big Bear Solar Observatory; Professor of Astrophysics, California Institute of Technology.

⁸Senior Research Fellow in Physics, California Institute of Technology.

⁹Assistant Professor of Physics, California Institute of Technology.

¹⁰Resigned December 15, 1974.

¹¹Resigned August 15, 1974.

¹²Resigned November 15, 1974.

¹³Resigned October 31, 1974.

¹⁴Resigned November 30, 1974.

¹⁵Resigned June 21, 1974.

Librarians

Heleen Z. Knudsen
Nan W. Schow

Senior Research Assistants

Grace V. Knox
A. Louise Lowen

Research Assistants

John M. Adkins
John E. Boyden
Ken D. Clardy
Thomas A. Cragg
Thomas S. Gregory
Basil N. Katem
Margaret Katz
Charles Kowal
Peter N. Kupferman
Frances Y. C. Tang

Student Observers

Jill Bechtold
Steven V. W. Beckwith
France Cordova
Jonathan H. Elias
Richard F. Green
Paul Hickson
John G. Hoessel
John P. Huchra
John Kormendy
Philip Massey
Jorge Melnick
William C. Friedhorsky
Douglas M. Rabin
Anneila I. Sargent
William L. Sebok
Edwin L. Turner
Barry E. Turnrose
William E. Westbrook¹⁶
Theodore B. Williams
Steven P. Willner

Photographic Department

John R. Bedke, Photographer
William C. Miller, Research Photographer¹⁷

Instrument Design and Construction

David A. Bell, Electronics Engineering Aide
Lawrence E. Blakée, Supervisor, Electronic Services
Robert E. Cadman, Electronics Technician

Maynard K. Clark, Electronics Operations Manager

John P. Cowley, Engineering Assistant

Barbara L. Dailey, Draftswoman

Martin A. Danihel, Associate Computing Analyst¹⁸

Juan D. Diez, Electronics Engineer¹⁹

Stephen Doro, Machinist

Raymond Dreiling, Machinist²⁰

Earle B. Emery, Research Engineer

Eugene B. Fair, Head Optician

Hannah Fox, Computing Analyst

Jerry T. Fridenberg, Head, Astroelectronics Laboratory; Chief Electronics Engineer

Robert D. Georgen, Machinist

Richard M. Goeden, Engineer

Simon Groesz, Electronics Specialist

Donn M. Hall, Chief Computing Analyst²¹

Fred H. Harris, Junior Electronics Technician

Melvin W. Johnson, Optician

Herman F. Kelderman, Research Engineer

Leroy M. Kimoto, Senior Electronics Specialist

Erich R. Koch, Senior Electronics Engineer

Wilfred H. Leckie, Senior Draftsman

John Nick Lee, Senior Electronics Specialist²²

Steve A. Macenka, Senior Engineer²³

William H. McLellan, Senior Engineer

Martin J. Olsiewski, Electronics Specialist

Frederick G. O'Neil, Shop Foreman

Richard A. Prout, Senior Engineer

Rudolf E. Ribbens, Design and Shop Superintendent

Orval A. Smith, Electronics Specialist

Robert G. Stiles, Optician

Merle R. Sweet, Supervisor, Electronics Construction

David F. Thompson, Technical Assistant

Walter Uchiyama, Junior Photographic Laboratory Technician²⁴

Virgil Z. Vaughan, Supervisor, Stockroom

Felice Woodworth, Draftswoman

*Maintenance and Operation**Mount Wilson Observatory and Offices*

Fern V. Borgen, Typist-Telephone Operator

Clyde B. Bornhurst, Mountain Superintendent

¹⁸ Resigned October 11, 1974.

¹⁹ Resigned April 28, 1975.

²⁰ Terminated June 30, 1975.

²¹ Resigned September 26, 1974.

²² Resigned August 20, 1974.

²³ Resigned May 9, 1975.

²⁴ Resigned May 23, 1975.

¹⁶ Died June 4, 1975.

¹⁷ Retired June 30, 1975.

Herman E. Carpentier, Carpenter
 Linda Chaffee, Clerk-Typist
 Hugh T. Couch, Superintendent, Buildings
 and Grounds
 Helen S. Czaplicki, Typist-Editor
 Sue H. DeWitt, Secretary
 James E. Dittmar, Night Assistant²⁵
 Raquel E. Ferrer, Secretary
 James Frazer, Night Assistant
 Hazel M. Fulton, Head Stewardess
 Eugene L. Hancock, Night Assistant
 Mary Hark, Stewardess
 Jeannie M. Knight, Bookkeeper
 Howard H. Lanning, Night Assistant
 Jose Lopez-Tiana, Purchasing Clerk
 Ernest O. Lorenz, Assistant Mountain
 Superintendent
 Michael Marcario, Night Assistant²⁶
 Ethel Marszalek, Stewardess
 Peter Mastrosimone, Custodian-Mechanic²⁶
 Glen Sanger, Senior Custodian
 Clair E. Sharp, Accountant²⁷
 William D. St. John, Chauffeur
 Frank Trylko, Custodian
 Frederick P. Woodson, Assistant to the
 Director

*Palomar Observatory and Robinson
 Laboratory*

Ranney G. Adams, Night Assistant
 Albert R. Andrews, Maintenance Mechanic
 Bradley N. Bailey, Relief Night Assistant
 and Junior Instrument Technician
 Ray L. Ballard, Senior Administrative
 Assistant
 Stephen A. Barry, Maintenance Mechanic
 and Junior Night Assistant
 Donald C. Bates, Assistant Mountain
 Superintendent
 Jan Adriaan Bruinsma, Painter and
 General Maintenance
 Maria J. Bruinsma, Housekeeping Aide
 Juan R. Carrasco, Night Assistant and
 General Mechanic
 Lily D. Carrasco, Housekeeping Aide
 Philip E. Fain, Custodian
 Liselotte M. Hauck, Secretary
 Helen Holloway, Secretary

²⁵ Terminated August 31, 1974.

²⁶ Resigned June 30, 1975.

²⁷ Terminated February 28, 1975.

Dorothy J. Howard, Administrative
 Secretary
 Taras Kiceniuk, Mountain Superintendent
 J. Luz Lara, Maintenance Mechanic
 Carl D. Palm, Night Assistant²⁸
 Marilynne J. Rice, Secretary
 Sharon L. Soltesz, Accounting Clerk
 Elsa-Brita Titchenell, Secretary
 Gary M. Tuton, Senior Night Assistant
 Paul Van Ligten, Electrician
 Marion Warren, Secretary
 Ruth E. Weaver, Secretary
 David K. Williams, Relief Night Assistant
 and Maintenance Mechanic
 Dorothy Williams, Cook

Big Bear Solar Observatory

Alberta R. Altman, Clerk-Typist
 Luella M. Goetz, Housekeeping Aide²⁹
 Jack R. Klemroth, Solar Observing As-
 sistant
 Eugene H. Longbrake, Superintendent
 Charles F. Mason, General Machinist
 Walter M. Nagao, Junior Mechanic

Las Campanas Observatory

Bruce Adkison, Associate for Administra-
 tion, *Pasadena*²⁰
 Wilma J. Berkebile, Executive Secretary
 S. Thomas Couch, Shipping and Receiving
 Clerk
 Ljubomir Papic, Mountain Superintendent,
Las Campanas
 Manfred Wagner, Project Supervisor, *La
 Serena*

Irénée du Pont Telescope Project

Louis E. Beidler, Engineer
 Oscar D. Dubón, Field Engineer, *Las
 Campanas*³⁰
 C. L. Friswold, Instrument Designer
 Roger L. Minnix, Engineer
 June A. Rains, Secretary
 Bruce H. Rule, Chief Engineer and Project
 Officer
 Edward H. Snoddy, Engineer

²⁸ Died December 26, 1974.

²⁹ Resigned September 12, 1974.

³⁰ Terminated December 31, 1974.

Geophysical Laboratory

Washington, District of Columbia

Hatten S. Yoder, Jr.

Director

Contents

Director's Commentary and Review	383	Solubility of volatiles in silicate melts at high pressure and temperature: the role of carbon dioxide and water in feldspar, pyroxene, and feldspathoid melts (Mysen)	454
New Techniques and Equipment	399	Peridotite-carbonate relations in the system $\text{CaO-MgO-SiO}_2\text{-CO}_2$ (Eggler)	468
Laser optical system for heating experiments and pressure calibration of the diamond-windowed, high-pressure cell (Bell and Mao)	399	Solution of H_2O and CO_2 in diopside melt (Rosenhauer and Eggler) . .	474
Design of a diamond-windowed, high-pressure cell for hydrostatic pressures in the range 1 bar to 0.5 Mbar (Mao and Bell)	402	Melt-vapor relations on the join $\text{NaAlSi}_3\text{O}_8\text{-H}_2\text{O-CO}_2$ (Kadik and Eggler)	479
Mössbauer studies at high pressure using the diamond-anvil cell (Hug-gins, Mao, and Virgo)	405	Properties of Magmas	484
Solubility measurement by differential thermal analysis (Rosenhauer) . . .	410	The silica immiscibility effect in magmas (Irvine)	484
Studies on the high-pressure polymorphism of analcite by powder x-ray diffraction and differential thermal analysis methods (Rosenhauer and Mao)	413	Olivine-pyroxene-plagioclase relations in the system $\text{Mg}_2\text{SiO}_4\text{-CaAl}_2\text{-Si}_2\text{O}_8\text{-KAlSi}_3\text{O}_8\text{-SiO}_2$ and their bearing on the differentiation of stratiform intrusions (Irvine) . .	492
Separation and analysis of carbamyl amino acids and their corresponding hydantoins by ion exchange and gas chromatography (Cronin)	415	Partitioning of trace and minor elements between coexisting silicate liquids (Watson)	500
The production and preparation of ^{205}Pb for use as a tracer for isotope dilution analyses (Krogh and Davis)	416	Phase relations in the system $\text{Mg}_2\text{SiO}_4\text{-iron oxide-CaAl}_2\text{Si}_2\text{O}_8\text{-SiO}_2$ at 10 kbar and their bearing on the origin of andesite (Osborn and Arculus)	504
Metasomatism and Metamorphism	417	Phase relations in the system $\text{MgO-iron oxide-Cr}_2\text{O}_3\text{-SiO}_2$ (Arculus and Osborn)	507
Bimetasomatism resulting from intergranular diffusion: multiminerale zone sequences (Frantz and Mao)	417	Melting behavior of two basanites in the range 10 to 35 kbar and the effect of TiO_2 on the olivine-diopside reactions at high pressures (Arculus)	512
A finite-difference model for diffusion and combined diffusion-infiltration metasomatism in a multicomponent system (Fletcher and Vidale)	424	Heat of melting of simple systems related to basalts and eclogites (Yoder)	515
Equilibria in the system plagioclase-muscovite-phlogopite-sanidine-quartz-aqueous chloride solution (Vidale)	428	Ultramafic Rocks and Minerals	519
Kinetics and microstructure of pyroxene exsolution (McCallister and Yund)	433	Homogeneity of minerals in mantle rocks from Lesotho (Boyd and Finger)	519
Oxygen isotope geochemistry of the Clough Formation, Black Mountain, New Hampshire (Rumble, Muehlenbachs, and Hoering)	436	Stress-heating and compositional variations in enstatites from sheared lherzolites (Boyd)	525
Determination of a pelite petrogenetic grid for the eastern Scottish Dalradian (Harte)	438	Ore mineral and phlogopite mineralization within ultramafic nodules from the Matsoku kimberlite pipe, Lesotho (Harte and Gurney)	528
Uvarovite stability in the $\text{CaSiO}_3\text{-Cr}_2\text{O}_3$ join up to 10 kbar (Huckenholz)	446	An experimentally produced clinopyroxene-ilmenite intergrowth (Wyatt, McCallister, Boyd, and Ohashi)	536
Igneous Petrology: Experimental and Field	454		
Volatiles in Ultrabasic and Derivative Rock Systems	454		

The equilibrium cation distribution in ca-rich clinopyroxenes (McCallister, Finger, and Ohashi)	539	O ₁₂ (Huggins, Virgo, Hölzl, and Huckenholz)	579
Statistical Petrology (Chayes)	542	Cation distributions in some compounds with the pseudobrookite structure (Virgo and Huggins)	585
Distribution of major oxides in Ceno- zoic volcanics: SiO ₂	542	Lunar Petrology	590
The names of Cenozoic volcanic rocks	545	Study of the microfeatures of lunar agglutinate particles (Mao, Bell, and Adams)	590
On distinguishing alkaline from other basalts	546	Trivalent titanium in Apollo 17 samples (Bell, Mao, and Haggerty)	593
Average compositions of the commoner Cenozoic volcanic rocks	547	Analysis of type-B lunar symplectites: garnet composition (Bell and Mao)	595
A world data base for igneous petrology	549	Biogeochemistry	598
NTRM, a major revision of RKNFSYS	550	The biogeochemistry of the stable hy- drogen isotopes (Hoering)	598
Mineralogy	551	The association of organic molecules with clay minerals in aqueous solu- tions (Hedges)	604
The effect of pressure on the covalency of Fe ²⁺ -oxygen bonds (Huggins) ..	551	Simulation of natural hydrolysis of pro- teins in fossils (Hare, Miller, and Tuross)	609
High-pressure transformation in mag- nesioferrite (MgFe ₂ O ₄) (Mao and Bell)	555	Use of amino acid reactions in some Arctic marine fossils as strati- graphic and geochronological indi- cators (Miller and Hare)	612
Preliminary evidence of disproportiona- tion of ferrous iron in silicates at high pressures and temperatures (Bell and Mao)	557	Amino acids and their derivatives in carbonaceous chondrites (Cronin)	617
Contribution of anionic complexes to charge-transfer and associated op- tical, electrical, and thermal effects at high pressure (Mao and Bell) ..	559	Geochronology	
Pyroxenoids: a variation in chemistry of natural rhodonites and pyrox- mangites (Ohashi, Kato, and Mat- subara)	561	Alteration in zircons and differential dissolution of altered and metamict zircon (Krogh and Davis)	619
Pyroxenoids: a comparison of refined structures of rhodonite and pyrox- mangite (Ohashi and Finger)	564	Isotopic ages in the eastern Lac Seul region of the English River gneiss belt (Krogh, Davis, Harris, and Ermanovics)	623
An effect of temperature on the feld- spar structure: crystal structure of sanidine at 800°C (Ohashi and Finger)	569	Staff Activities	625
Least-squares refinement of the rigid- body motion parameters of CO ₃ in calcite and magnesite and correla- tion with lattice vibrations (Finger)	572	Mass Transport Conferences	625
A neutron-diffraction and ⁵⁷ Fe Möss- bauer study of a synthetic Ti-rich garnet (Weber, Virgo, and Huggins)	575	Petrologists' Club	627
Distribution of Al, Fe ³⁺ , and Ti ⁴⁺ be- tween the octahedral and tetra- hedral sites in garnets between Ca ₃ Al ₂ Si ₃ O ₁₂ and Ca ₃ Fe ₂ Ti _{1.416} Si _{1.584}		Washington Crystal Colloquium	628
		Seminar Series	628
		Field Studies	629
		Exhibits	630
		Lectures	630
		Bibliography	633
		References Cited	635
		Personnel	648

DIRECTOR'S COMMENTARY AND REVIEW

The great rush to solve today's societal problems has deflected attention from the continuing critical need for broad understanding of the interrelated basic sciences. Despite the warnings of the National Academy of Sciences, new Federal agencies are created or old agencies reorganized to deal only with specific programmatic problems with little or no provision for extension of fundamental knowledge to be used tomorrow. Much of the best scientific talent of the country is channeled by these agencies into the study of applied problems and given no opportunity to generate a body of principles to solve the complex earth science problems that investigators confront. Successful solutions will depend to a great extent on future discovery, not on the existing body of fact.

The Geophysical Laboratory has held to its tradition of investigating basic earth science problems. Its principal goals remain the discovery of new knowledge and the training of new talent. Its staff members, not confined to applied research, are free to pursue the broad principles of their mixed disciplines. Those investigators in training at the Laboratory enjoy the same freedoms and receive, as well, the help of seasoned colleagues. The impetus and direction to earth science provided by the Geophysical Laboratory result from its focus on principles rather than ephemeral problems. It is not sufficient to expand the limits of capability alone, but it is necessary in addition to develop those insights that lead to wise choices of direction. Within the constraints of today's economy it is not possible to pursue all prospective avenues. The wisdom of the choices made below may be tested sooner than we think.

The expansions of capability are listed first because they open the way to new opportunities, and the thoughtful choices of research direction follow. The year's

work represents the consensus of a small group of exceptional investigators on what are the most highly significant contemporary areas of research within our telescopic view of earth science.

New Techniques and Equipment

A major advance in the capability of investigating experimentally the physical chemistry of the mantle was achieved. Temperatures in excess of 2000°C at pressures close to 500 kbar can now be sustained in a device developed by *Mao and Bell*. Heating of a diamond-anvil, high-pressure cell is obtained with a neodymium-doped YAG (yttrium aluminum garnet—first synthesized at this Laboratory) continuous laser beam. The diamond is transparent to the chosen wavelength of laser radiation, and therefore only the sample to be investigated is heated. The specimen can be viewed during the experiment, and its temperature measured with an optical pyrometer. Pressure is achieved with a simple screw-lever device and measured with the shift of a fluorescence line of ruby excited with an He-Cd laser. The pressure is also calibrated with the B1-B2 transition in NaCl at 300 kbar. The first observations in the device indicate that major reactions and transitions predicted to occur in the earth's mantle may proceed rapidly. For example, the olivine-spinel transition was observed visually. New data on the disproportionation of ferrous iron were obtained, and a new high-pressure phase in the magnesioferrite system was discovered. The simplicity of the device and the advantage of visual observation open up a great region in the earth to experimentation.

The diamond-anvil cell is a most versatile device and is now adapted for Mössbauer experiments on iron minerals under high pressure. Knowledge of the iron-containing phases in the mantle is important because iron is a major ele-

ment and its properties strongly influence the melting behavior, heat transfer, seismic response, electrical and magnetic fields, and oxidation state of the stable phases. It was found by *Huggins, Mao, and Virgo* that a combination of a screw-driver-tip design for the Mössbauer γ -ray source and careful collimation of the flux through the diamond cell produces excellent spectra on less than 10 μg of material. One obvious advantage of such Mössbauer experiments is that they can be directly correlated with x-ray, optical, spectroscopic, and visual investigations of the same sample under identical high-pressure conditions in the diamond cell. By using a suitable gasket to contain the sample in a liquid, the Mössbauer experiments can be performed hydrostatically to pressures up to at least 80 kbar.

Another high-pressure technique, involving differential thermal analysis (DTA), has been improved and adapted to volatile-containing silicate systems by *Rosenhauer*. He applied DTA to the study of melting in the presence of volatile components and has analyzed the changes in the H_2O content of the melt and the nature of the DTA signal. His procedure can be applied to systems that are difficult or impossible to quench, and it provides an alternative method for measurements of solubility at high pressures and temperatures.

By combining the DTA technique with x-ray methods it was possible for *Rosenhauer and Mao* to study high-pressure phase changes in the hydrous mineral analcite. The high-pressure DTA confirmed the reported value for a transition pressure at 25°C within experimental error and extended the results to other temperatures. Using the measured change of the inversion temperature with pressure and the known change of volume, they calculated the heat of transformation. The small value of the heat of transformation (207 cal/mol) suggests a displacive transition, in agreement with the small thermal hysteresis

effect observed. A powder x-ray diffraction pattern of the high-pressure phase taken in the diamond-anvil cell at 20 kbar and room temperature displayed a structure different from that of cubic analcite. It had great similarity to the structure of an anomalous noncubic natural analcite that may be a metastable high-pressure phase.

A major effort in organic geochemistry is in characterizing the compounds in the various fractions isolated from sediments, fossils, and meteorites. A large fraction (70%) of the amino acid precursors extracted by water from the Murchison carbonaceous chondrite are acidic compounds, and it is possible that their conversion to free amino acids by hydrolytic conditions involves the release of some groups bonded to the amino function through a carbonyl group. Of the various amino acid derivatives of this type, *N*-carbamyl amino acids or their dehydration products, 5-substituted hydantoins, or both, seem particularly favored because they can be formed readily from amino acids and cyanate ion, a species identified in interstellar molecular clouds and in comets.

A procedure has been developed by *Cronin* for the isolation of these compounds from the meteorite aqueous extract and their subsequent separation and identification by gas chromatography. In brief, the procedure involves (1) removal of free amino acids from the meteorite extract by cation-exchange column chromatography, (2) separation of carbamyl amino acids and their corresponding hydantoins from each other and from interfering substances by anion-exchange chromatography, (3) formation of their trimethylsilyl derivatives, and (4) separation of the trimethylsilyl-carbamyl amino acids and the trimethylsilyl-hydantoins by gas chromatography.

A major breakthrough in lead-uranium geochronology and geochemistry was achieved by *Krogh and Davis* as a result of the production and availability of

^{205}Pb . Now for the first time both lead and uranium can be determined in the same solution so that errors due to aliquotting solutions are eliminated. The chemical processing is reduced and simplified; weighing errors are eliminated; and the lead concentration can be determined from one rather than two mass spectrometric analyses.

Several unrelated factors were essential to the development of the ^{205}Pb tracer. The project was initiated by inquiring at the Holifield National Laboratory (Oak Ridge) about cyclotron production of ^{203}Pb or ^{205}Pb . By coincidence, Dr. Larry Brown in the Oak Ridge group had just completed the production and isolation of ^{206}Bi for cancer research, and his process could equally well be used to make ^{205}Bi , which decays to ^{205}Pb . A final stage of purification of ^{205}Bi was added using an ion-exchange technique and ultrapure reagents, both developed by Krogh. In addition to improving U-Pb dating of zircons, the ^{205}Pb tracer can be used to analyze many minerals (e.g., rutile, sphene) that, although soluble in high-pressure vessels at 220°C , generally form precipitates at room temperature. A few tests are still necessary, but the feasibility of using the ^{205}Pb tracer has been demonstrated. Plans are now being laid to obtain sufficient ^{205}Pb of adequate purity for general distribution to other geochronology laboratories.

Metasomatism and Metamorphism

Chemical alteration of rocks by aqueous solutions plays an important role in many processes such as ore deposition, contact metamorphism, and hydrothermal alteration. Models for developing quantitative insight into these metasomatic processes must be sufficiently flexible to accommodate such features as multicomponent chemistry, variable permeabilities, diffusion constants, and infiltration rates, or the partial attainment of local equilibrium between solid phases and pore fluid. Two new models were devised using different approaches

in developing the mechanisms and direction of transport in natural rock systems. One team used an analytical approach involving continuous functions to describe changes in both space and time, whereas another team preferred a finite-difference approach considering changes within elements of space and time.

Frantz and Mao, using the analytical approach, developed a mathematical model to predict quantitatively the thicknesses and mineralogy of zones in metasomatic sequences that occur by intergranular diffusion, infiltration, or both. Their calculations have shown that the modal analysis of minerals across a multimineralic reaction zone varies according to the transport mechanism. They have also shown that the relative directions of zone boundary movements can, in many cases, be deduced when only the mineralogy of the reaction zones is known. Both results should be quite useful in determining the mechanisms and direction of transport in ore deposits.

The *Fletcher and Vidale* model, based on a finite-difference scheme, applies at present to one-dimensional transport by diffusion or combined diffusion-infiltration, complete local equilibrium between solid phases of fixed composition, and a binary pore fluid. The model has been applied to obtain quantitative results for transport from a reservoir into the initially invariant assemblage quartz (excess)–potassium feldspar–anorthite–muscovite–pore fluid (KCl , CaCl_2 , HCl in H_2O solvent), and for bimetasomatic reaction between univariant assemblages in this compositional system. The results place constraints on the transport mechanism (diffusion or infiltration), the composition of the reacting fluid, the time required for transport, and the ordering of the mineral zoning. The method is readily expanded to include the array of chemical components in natural assemblages.

The application of the above model was dependent on obtaining the experimentally determined equilibrium con-

stants in the invariant system involving anorthite, potassium feldspar, muscovite, quartz, and pore fluid. In addition, it was necessary to know whether the pore solution was ideal. An experimental study carried out by *Vidale* demonstrated that at high temperature (550°–600°C) the aqueous solution is nearly ideal from 2 to 20 *N* chloride concentration, and simple equilibrium expressions of its composition can be formulated for use in transport models. The amount of material that a pore solution will transport through a rock increases with increasing salinity of the solution. It was important, therefore, to know whether chemical equilibria between solid and solution could be determined for solutions of high salinity. The results obtained may be of considerable significance in ore genesis, where recent oxygen-isotope studies suggest that large cells of convecting aqueous pore solution have concentrated ore components by a process of leaching, transport, and redeposition.

Transport of material by volume diffusion alone, without the aid of infiltration, is well displayed by crystal exsolution, the solid-state unmixing of a homogeneous phase into two structurally distinct phases. *McCallister and Yund* examined by electron microscopy crushed grain mounts of annealed material having compositions on the important pyroxene join $\text{CaMgSi}_2\text{O}_6$ – $\text{Mg}_2\text{Si}_2\text{O}_6$ to observe the microstructure of and the orientation between the host and guest phases. Although the exsolved pigeonite shares a common plane (001) with the host diopside, two different microstructures are developed that depend on composition.

In bulk compositions yielding large amounts of the guest phase, the exsolved lamellae appeared to be perfectly coherent and irregular. However, in bulk compositions yielding small amounts of the guest phase the rate of exsolution was considerably slower, and the lamellae, when developed, were straight and continuous. They suggest that the rapid

exsolution that produces the irregular lamellae occurs by spinodal decomposition; the much slower exsolution that produces regular lamellae is interpreted to be due to nucleation and growth.

These interpretations are most informative when the laboratory observations are compared with textures seen in natural rocks. The irregular lamellar microstructure is very similar to that observed in pyroxenes from quickly cooled rocks, and the straight lamellae are similar to those found in slowly cooled pyroxenes. Because of the high temperature of the miscibility gap, slow cooling of natural pyroxenes can result in nucleation and growth before the coherent spinodal is reached. In rapidly cooled pyroxenes, or those that enter the miscibility gap at lower temperature, no exsolution texture is developed until the coherent spinodal is crossed.

The relative proportions of the isotopes of oxygen (^{16}O and ^{18}O) in minerals depend on the temperature of mineral formation and the composition of the fluid in the rock. In many cases metamorphic rocks appear to have equilibrated with a fluid of uniform isotopic composition. In contrast to this conclusion, however, *Rumble, Muehlenbachs, and Hoering* have demonstrated that the rocks of Black Mountain, New Hampshire, could not have been in chemical equilibrium with a fluid of uniform isotopic composition. Such a conclusion is supported by a previous chemical petrologic study of these rocks which showed that the rocks did not achieve equilibrium with a fluid having uniform chemical composition.

Although oxygen isotopes may have difficulty in attaining equilibrium, hydrogen is known to diffuse readily and equilibrium is to be expected. It is this property of hydrogen isotopes, in fact, that is relied upon to achieve chemical equilibrium between buffers and reactant charges in hydrothermal experiments. *Rumble* has described the osmotic equilibrium of hydrogen in the rocks of Black

Mountain, New Hampshire, using algebraic methods. Two cases of osmotic equilibrium are distinguished: (1) isobaric osmotic equilibrium, as in the experiments of Eugster (1957), and (2) polybaric osmotic equilibrium, as in the classic study of J. W. Gibbs (1878). The first type of osmotic equilibrium was not achieved by the Black Mountain rocks because isobaric gradients in the chemical potential of hydrogen between adjacent rock layers are recorded by the mineral assemblages. If the second type of osmotic equilibrium was achieved, then it would require pressure differences of the order of 1 kbar between adjacent rock layers. Polybaric osmotic equilibrium of hydrogen thus would require that the rocks retain appreciable strength even under the conditions of middle-grade regional metamorphism. States of stress of that magnitude are possible within the crust but unlikely to persist for an appreciable interval of geologic time.

The studies of oxygen and hydrogen isotopic equilibrium deal mainly with the influence of strongly localized controls on metamorphic assemblages, but it is equally important to interpret the broader patterns of metamorphic parageneses. These patterns provide a basis for establishing the nature and variations of P - T conditions on a regional scale and thus determine the thermal structure and tectonic relations in orogenesis. *Harte* has shown that the common pelitic mineral assemblages and their distribution in the classic Barrovian-Buchan terrain of the eastern Scottish Dalradian can be interpreted in terms of a single petrogenetic grid for assemblages on which H_2O is an unbuffered component. It is remarkable indeed that the sequences of metamorphic zonal assemblages are coordinated for the first time in an orderly array with the facies determined experimentally. The result is a quantitative P - T grid that can be applied to the entire region! It is now possible to reconstruct the P - T

conditions and gradients developed during the Caledonian orogenesis. *Harte* has demonstrated that the region has been affected by at least one essentially unified regional metamorphic event. Furthermore, he established the value of using metamorphic mineral assemblages as a tool in determining regional thermal structure. A basis for unraveling the tectonic structure is at hand.

Garnet is one of the key minerals in estimating grade of metamorphism. Its compositional complexity makes it most useful in recording a variety of intensive parameters. *Huckenholz* conducted experiments on the stability of uvarovite, $Ca_3Cr^{3+}_2Si_3O_{12}$, a comparatively minor garnet end-member but thermally the most stable of the rock-forming garnet end-members. The maximum temperature of uvarovite formation exceeds those temperatures encountered within the upper mantle, at least in its upper portion, and garnets from ultramafic nodules brought up with kimberlites contain considerable amounts of the uvarovite components. Crustal occurrences of uvarovite, on the other hand, are confined to host rocks rich in Ca and Cr. Such bulk chemistry is approached only in ultramafites associated with chromite ores and in skarn rocks.

Igneous Petrology: Experimental and Field

Volatiles in ultrabasic and derivative rock systems. New data on the solubility of CO_2 , H_2O , and CO_2 and H_2O together in silicate liquids have generated some exciting new ideas on partial melting and fractional crystallization in the upper mantle. Emphasis in the past has been on the dramatic role H_2O plays in lowering melting temperatures, suppressing high-temperature polymorphs, enriching magmas in silica, and acting as the chief propellant in explosive volcanism. New effects are now being observed because of the small but greatly influential amounts of CO_2 that dissolve in melts. *Mysen* obtained infrared spec-

tra on quenched CO_2 -saturated liquids and demonstrated that CO_2 enters these liquids both as discrete CO_2 molecules and as the carbonate anion. Increasing temperature increases the proportion of the carbonate anion, as does increasing basicity of the silicate melt. Highly polymerized (acid) melts such as the melt of albite composition dissolve the least CO_2 (1–2 wt %) according to Mysen, and at temperatures near the albite- CO_2 liquidus the only carbon dioxide species in the melt is molecular CO_2 . Less polymerized silicate melts such as the melt of diopside composition display a large CO_2^{2-} absorption band under all conditions investigated. Increasing basicity, temperature, and pressure also result in increasing CO_2 solubility in all compositions studied ($\text{CaMgSi}_2\text{O}_6$, $\text{NaAlSi}_3\text{O}_8$, $\text{NaAlSi}_2\text{O}_6$, NaAlSiO_4 , natural olivine nephelinite).

The effect of H_2O on CO_2 solubility was studied by Mysen in the system $\text{Na}_2\text{O}-\text{Al}_2\text{O}_3-\text{SiO}_2-\text{H}_2\text{O}-\text{CO}_2$ using albite, jadeite, and nepheline compositions. In all compositions, the CO_2 solubility passes through a maximum at some condition of $\text{CO}_2/(\text{CO}_2 + \text{H}_2\text{O}) < 1.0$. The $\text{CO}_2/(\text{CO}_2 + \text{H}_2\text{O})$ corresponding to the maximum CO_2 solubility is insensitive to temperature and silicate chemistry, but the ratio shifts to lower CO_2 values as the total pressure is increased. Infrared measurements indicate that the CO_2^{2-} ion is more important in hydrous than in H_2O -free silicate melts.

The β -track method used in measurements of CO_2 solubility has also been applied by Mysen to measure the H_2O contents of $(\text{CO}_2 + \text{H}_2\text{O})$ -saturated silicate melts. Hydrogen-3 was used as a source of β particles. He has shown that the β -track mapping technique is applicable to solubility studies of both H_2O and CO_2 occurring together in a silicate melt. (Isotopes can also be used to measure the contents of Cl, S, and P.)

On the basis of his present studies, Mysen places emphasis on the low solubility of CO_2 compared with that of

H_2O and also on how strong the dependence of CO_2 solubility is on temperature, pressure, and silicate chemistry. These results together with phase equilibrium data on model mantle CO_2 - H_2O systems can aid in understanding the fractionation of tholeiitic magmas to compositions containing normative nepheline and larnite. It is proposed by Mysen that CO_2 -rich vapors can evolve from silicate magmas during ascent in the upper mantle. The development of such a vapor presents a means of generating nephelinitic magmas by partial melting of a peridotite upper mantle, where previous models have lacked the mechanism to generate the vapor itself.

The origin of kimberlite, containing the three principal minerals olivine, calcite, and phlogopite, depends greatly on the role of CO_2 and H_2O . In the course of studying the system $\text{CaO}-\text{MgO}-\text{SiO}_2-\text{CO}_2$, Eggler discovered another invariant point that bears directly on the generation of kimberlite. The invariant point is formed by the intersection of the decarbonation reaction dolomite + enstatite = forsterite + diopside + CO_2 with the melting curve of the assemblage diopside + forsterite + carbonate at a pressure between 25 and 30 kbar. Because of these relationships the subsolidus phase assemblage of a simple peridotite composition at 30 kbar is not diopside + forsterite + orthopyroxene + CO_2 but forsterite + orthopyroxene + dolomite (at lower temperature, orthopyroxene + dolomite + magnesite). The latter assemblage melts to a carbonate-rich liquid at a temperature hundreds of degrees below the solidus of volatile-free peridotite. Pressure release by tectonic processes could, therefore, trigger melting that yields kimberlitic liquids at relatively low temperature. It had previously been thought that such melts could form only by fractionation of more silica-rich partial melts. Eggler also proposes, on the basis of these phase equilibria, a new concept of the low-velocity zone beneath the oceans where

partial melting results from the presence of small amounts of CO_2 rather than H_2O .

New phenomena bearing on the melting, ascent, and evolution of vapor from other volatile-bearing basic magmas were discovered by *Rosenhauer and Eggler*. They examined the solubility of H_2O in diopside ($\text{CaMgSi}_2\text{O}_6$) melt by a combination of quenching and differential thermal analysis methods. Changes in slope of melting and solubility curves at H_2O contents between 5 and 10 wt % were found, and they interpret these as breaks between entry into melt of 1 mole (7.7 wt %) of H_2O and of additional H_2O . One mole can separate double chains of silica tetrahedra into single chains, in the process forming OH ions. Additional H_2O may separate these chains into smaller units and may enter as H_2O molecules.

In a related study of melting on the join $\text{CaMgSi}_2\text{O}_6\text{-H}_2\text{O-CO}_2$, *Rosenhauer and Eggler* have found previously unsuspected temperature minima at about 5 kbar pressure in melting curves of equal $\text{CO}_2/(\text{CO}_2 + \text{H}_2\text{O})$ mole ratio, analogous to minima on the join $\text{NaAlSi}_3\text{O}_8\text{-H}_2\text{O-CO}_2$ discovered by *Kadik and Eggler*, and maxima at about 30 kbar pressure. The comprehensive study of melting and vapor solubility on $\text{NaAlSi}_3\text{O}_8\text{-H}_2\text{O-CO}_2$ resulted in a pattern of melting curves that have several important implications. Melts apparently originating in the upper mantle or crust could rise without freezing or extensive crystallization into the upper crust, and vapor evolved during the ascent would be relatively CO_2 -rich until the upper crust was reached, whereupon H_2O -rich vapor would be distilled out. This postulated process has application to ore deposition and to the evolution of a crust stratified with respect to volatile composition.

Properties of magmas. The extensive studies on layered intrusions give the impression that there is little left to be done, yet *Irvine* has brought a fresh view

to the origin of layered intrusions that will give new impetus to their study. Following on his work of a year ago in which he proposed a mechanism by which chromitite layers may be precipitated in stratiform ultramafic-gabbroic intrusions by contamination of the basic magma of the intrusion with granitic liquid melted from salic roof rocks, *Irvine* has studied the effects of mixing haplobasaltic and haplogranitic liquids in the system forsterite-anorthite-orthoclase-silica. He has found that although the liquids are completely miscible in the compositional region investigated, the mixing is distinctly nonideal, as evidenced by a strong silica immiscibility effect in the liquidus relations.

With respect to the origin of chromitite layers, the data indicate that salic contamination of basaltic liquid should enhance the crystallization of orthopyroxene relative to both olivine and plagioclase, a feature that accords with the abundant development of orthopyroxene cumulates in association with chromitite in the Muskox, Stillwater, Bushveld, and Great Dyke complexes. Also, the liquidus relations show that, because of the silica immiscibility effect, it is possible to produce melts with only anorthite on the liquidus by mixing "contaminated" basic liquid that has crystallized enough pyroxene to differentiate to the pyroxene-anorthite cotectic with relatively fresh liquid on the olivine-anorthite cotectic. *Irvine* proposes that this type of mixing is in principle the mechanism of origin of the anorthositic layers in intrusions such as the Muskox, Stillwater, Bushveld, and Rhum complexes.

Interest in liquid immiscibility in silicate systems has been renewed mainly because of its discovery in low-temperature melts of high FeO/MgO in lunar rocks and certain terrestrial igneous rocks. It is emphasized by *Irvine*, however, that such immiscibility has significance in magmas extending far beyond the thermal and compositional regions

in which it can actually occur. The basis of his argument is the important observation that at 1 atm silica melt has miscibility gaps with the melts of all the stable end-members of the common mafic silicate and oxide minerals that have been investigated, but it is completely (indeed almost ideally) miscible with the melts of the feldspar end-members. Through thermodynamic considerations, he has shown that the non-ideality relating to the immiscibility should tend to cause liquidus boundaries—and particularly the cotectic boundaries between plagioclase and the mafic and oxide minerals—to be deflected or shifted away from the regions of immiscibility. This feature, which he terms the “silica immiscibility effect,” is apparent in numerous ternary synthetic systems, and Irvine has demonstrated that it can be identified in the chemical trends of tholeiitic, calcalkaline, and even alkaline magmatic series. The effect would appear to play a major role in determining certain fundamental similarities and differences of these series.

In an isothermal series of 1 atm doping experiments, *Watson* examined the fractionation of trace and minor elements between immiscible liquids in the system $K_2O-Al_2O_3-FeO-SiO_2$. The study was designed principally to evaluate the effects of charge, size, and bond type of a cation upon the relative preference that it shows for a basic versus an acidic melt. These experiments have provided new insight into solid-liquid partitioning because they measure directly the degree to which a solid-liquid partition coefficient must be a function of liquid composition. Of the elements investigated to date, Ba and Sr are least fractionated between basic and acidic liquid, and La is most strongly fractionated (into the basic liquid). Thus, the assumption of constant $D_{solid/liquid}$ often made in fractional crystallization modeling and geothermometry is probably most valid for Ba and Sr. If observed in contemporaneous mafic and felsic mag-

mas, the trends of trace element distribution established in this study may prove diagnostic of occurrences of magma unmixing in nature.

Studies of phase relations in the system Mg_2SiO_4 -iron oxide- $CaAl_2Si_2O_8-SiO_2$ reported by *Roeder and Osborn* (1966) for 1 atm total pressure were extended to 10 kbar by *Osborn and Arculus*. The objective was an understanding of the changes in crystallization trends of tholeiitic and calcalkalic magmas as they move from a depth of about 35 km to the surface. Preliminary data indicate that the contraction of the phase volume of anorthite and fractionation of orthopyroxene and spinel produce a liquid of high Al_2O_3 content. If that Al_2O_3 -rich liquid moves to lower pressure, anorthite will be the liquidus phase and possibly spinel will be in reaction relationship with the liquid. An explanation of the temperature-composition-phase relations of many Cascade and other calcalkalic series may lie in their being formed principally at lower crustal levels by fractional crystallization of parent olivine basalt magma.

Arculus and Osborn have continued their study of phase relations among olivine, pyroxene, “silica,” and spinel in the system Mg_2SiO_4 -iron oxide- $SiO_2-Cr_2O_3$ at 1 atm. Equilibria in air and at lower oxygen fugacities have been examined. Some revisions to the Cr_2O_3 -free join and preliminary results obtained previously in the system have been made. The spinels show continuous solid solution in the join picrochromite-magnesioferrite-magnetite and approach magnetite at low temperatures and reduced f_{O_2} . No evidence of pyroxene-spinel reactions has been discovered.

One of the major gaps in our knowledge of the response of basalts to high pressures is that of the nepheline-normative types. For this reason *Arculus* has examined the melting behavior of two basanite compositions in the pressure range 10 to 35 kbar. Some independent geochemical evidence supports the view

that these lavas are derived by partial melting of a garnet-bearing peridotite. However, olivine is the primary liquidus phase only up to 20 kbar, and under dry conditions the appropriate phase relations for direct derivation of the basanites from a garnet-peridotite were not observed. Volatiles such as CO_2 and H_2O are known to affect the phase relations considerably. The presence of relatively high concentrations of polyvalent cations such as Ti and P in basanites may also affect olivine-pyroxene reactions. For example, the addition of TiO_2 in proportions designed to simulate a natural basanite has been found to modify the phase relations deduced by Yoder and Kushiro last year on the join diopside-pyrope (*Year Book* 73, pp. 266-269). The stability of olivine on the liquidus is reduced by 2-3 kbar in comparison with the TiO_2 -free condition. Nevertheless, the major observation remains that basanite does not yield olivine at pressures where it is believed to be derived from an olivine-bearing parent.

Melting is involved in most of these experiments, and knowledge of the heat requirements is vital to understanding magma generation. On the basis of new as well as published calorimetric measurements, Yoder obtained estimates for the heat of melting of basalt, eclogite, and garnet peridotite. In addition, he calculated the pressure effect on the heat of melting and found it to be exceptionally large. Assuming the entire internal radioactive heat production is used to melt 5% of a rock at 130 km, Yoder found that roughly 45 m.y. is required. It was concluded, therefore, that the episodic character of volcanism is dependent on factors affecting a shallow subsidiary magma chamber rather than those operating at the site of magma generation. In another calculation it was shown that in the event melting is achieved by adiabatic rise of an eclogite, it would be necessary to initiate the ascent at depths at least as great as 160

km to achieve complete melting by the time the magma arrives at the surface.

Ultramafic rocks and minerals. The controversy on the interpretation of data from nodules believed to be from the mantle has stimulated new efforts in the study of ultramafic rocks and minerals. Knowledge of the homogeneity of minerals in garnet peridotites from the mantle is required for consideration of the hypothesis that these rocks have equilibrated under ambient conditions of temperature and pressure at depth in the earth. *Boyd and Finger* have devised a statistical test for homogeneity, using electron microprobe data on all primary phases in four garnet lherzolites from kimberlite pipes in Lesotho. Variation in the Cr_2O_3 content of garnets and diopsides is the only major inhomogeneity found, although there are significant minor inhomogeneities in distribution of other elements. Uncertainties in estimation of temperatures and pressures of equilibration due to inhomogeneities are shown to be small in comparison with the large systematic differences in these parameters exhibited by the garnet peridotites from the mantle beneath southern Africa.

The intensely deformed lherzolite nodules found in many kimberlites may have been stress-heated, and evidence for such a process has been sought by *Boyd* in compositional variations between enstatite in the finely granulated groundmass and that occurring as coarse porphyroclasts. One lherzolite with a fluidal mosaic texture from Lesotho showed no effect, but in two specimens from Kimberley the enstatite in the groundmass is richer in Ca, Al, and Cr than the enstatite porphyroclasts. These relations could be due to a reequilibration with garnet and diopside in a heating event associated with eruption.

Little information is available on the occurrence of oxides (other than spinels), sulfides, and, to a lesser extent, phlogopite, in mantle peridotites and pyroxenites, even though these minerals may

add significantly to knowledge of mantle environments and play an important role in geochemical models. A study has been made by *Harte and Gurney* of veins as well as more evenly dispersed associations of ilmenite and rutile (both commonly showing exsolution lamellae of Al_2O_3 - and Cr_2O_3 -rich spinels), together with sulfide intergrowths (pyrrhotite, pentlandite, and chalcopyrite) and phlogopite in xenoliths from the Matsoku kimberlite pipe. The mineral compositions fall within restricted ranges. Ilmenite compositions are distinct from those of both lamellar intergrowths with clinopyroxene and many discrete nodules. Phlogopite compositions show similarities to those of xenocrysts and megacrysts in kimberlite. A close approach to equilibration with the host rock silicates (with the partial exception of garnet) is indicated, and the ore minerals and phlogopite are believed to have formed as a result of the infiltration of a TiO_2 - and K_2O -rich hydrous fluid under P - T conditions similar to those of Matsoku garnet peridotite xenoliths lacking ore minerals and phlogopite.

For the first time it has been possible to duplicate experimentally the clinopyroxene-ilmenite intergrowths that are found in kimberlites. The intergrowth was obtained by slowly cooling (20°C/hr) and quenching, from above the liquidus at 38 kbar, a melt whose composition can be represented by a weight ratio of ilmenite/clinopyroxene of 29/71. According to *Wyatt, McCallister, Boyd, and Ohashi*, the similarity in chemistry, texture, and crystallography between the experimentally produced and the natural intergrowths suggest that the latter probably form by eutectic crystallization from magmas under mantle conditions.

The crystal chemistry of clinopyroxenes comprising a discrete nodule in kimberlite from the Thaba Putsoa pipe, Lesotho, and a megacryst and eclogite clinopyroxene from the Kakanui nephelinite breccia have been examined by

McCallister, Finger, and Ohashi by means of crystal-structure refinements. Both untreated crystals and those annealed in evacuated silica glass tubes containing iron were refined to obtain the distribution coefficient (K_d) for Fe^{2+} and Mg between the M1 and M2 sites. The composition of the discrete nodule, when projected into the CaSiO_3 - MgSiO_3 - FeSiO_3 system, corresponds to $\text{Wo}_{27.7}\text{-En}_{64.3}\text{Fs}_{8.0}$, the other impurities consisting primarily of approximately 12% jadeite plus aegirine. The data obtained from the annealing experiments and the K_d of the untreated material yield a value of 0.068 ± 0.013 , indicating an equilibrium temperature of $530^\circ \pm 50^\circ\text{C}$. This temperature is consistent with *McFadden's* (1973) results, in which he obtains an emplacement temperature of 550° - 620°C for the kimberlite pipes at the DeBeers Mine.

A second set of annealing experiments was carried out by the same team on portions of a megacryst from the Kakanui nephelinite breccia. The projected composition of this material corresponds to $\text{Wo}_{38.4}\text{En}_{53.4}\text{Fs}_{8.2}$, the major impurities being approximately 9.5% jadeite plus aegirine. The results of the annealing experiments and site-occupancy refinements from the crystal structure correspond to a temperature of $1367^\circ \pm 120^\circ\text{C}$ for the untreated material. Although the uncertainty is large, the lower temperature range lies within the estimated megacryst crystallization temperature of 1200° - 1300°C of *Merrill and Wyllie* (1975). Using the same calibration curve for the clinopyroxene from the eclogite ($\text{Wo}_{40.0}\text{En}_{45.6}\text{Fs}_{14.4}$) the equilibration temperature was found to be $710^\circ \pm 50^\circ\text{C}$. This result is also consistent with those of *Merrill and Wyllie* (1975), who suggest that the eclogites cooled subsolidus to 700° - 800°C prior to eruption.

Statistical Petrology

Chayes has now shown that the frequency distribution of SiO_2 in published

analyses of Cenozoic volcanic rocks is characterized by a strong positive skew with the median of all available analyses at 52.5% SiO_2 and the mean at 54.0% SiO_2 . His data base, in which inclusion of an analysis depends on neither rock name nor announced chemical composition, contains approximately seven analyses of basalt and four of andesite for each one of rhyolite. From data in the base he has prepared new estimates of the average chemical compositions of the common Cenozoic volcanic rocks. He has now begun active development of an information system for igneous petrology along lines suggested in *Year Book 73*. The data base of the new system is to contain analyses of igneous rocks of all kinds and ages, as well as much qualitative geological, mineralogical, and petrographic information about each analyzed specimen. During the long compilation period Chayes plans to improve and continue exploiting the existing system, which contains only published chemical analyses and names of Cenozoic volcanic rocks.

Mineralogy

The field of mineralogy has been greatly stimulated by the large number of new tools made available through solid-state physics. The entire spectral array from neutrons to microwaves is being applied in concert to solve complex mineralogical problems. The Geophysical Laboratory has been especially productive in this area because of the cooperative efforts of the staff in exploiting their individual specialties.

Minerals containing ferrous iron are especially important in the mantle because these phases are responsible for the majority of electronic phenomena in the earth. Such phenomena can be expected to be sensitive to changes in the nature of the Fe^{2+} -oxygen bond, caused by increasing pressure. By combining optical and Mössbauer spectroscopic data, further understanding has been gained of the manner in which Fe^{2+} -

oxygen bonds undergo compression. The increase in covalency of the bonding and the related changes in spectroscopic parameters caused by increasing pressure can be best explained, according to *Huggins*, in terms of increased overlap between ferrous and anion orbitals rather than in terms of expansion of the 3d orbitals of the cation. This covalency change with pressure is also consistent with the large increase in electrical conductivity and charge-transfer phenomena observed for ferrous minerals with increasing pressure.

Magnesioferrite, a dense oxide mineral of magnesium and ferric iron, is thought to occur at great depths in the earth, where close-packed structures tend to be stabilized by high gravitational pressures. *Mao and Bell* studied magnesioferrite, using the newly designed high-pressure cell and the new laser heating technique to determine its properties and its stability at high pressure and temperature.

At approximately 200 kbar, 1500°C, a new phase was formed from pure magnesioferrite. X-ray diffraction data obtained on the new phase under high pressure show that it has the high-pressure magnetite structure (with two extra x-ray diffraction lines). Inversion back to magnesioferrite (spinel structure) was accomplished upon release of pressure and lowering of the temperature to 25°C. This new phase will probably play an important role in mineralogical models of the earth's interior.

In the search for additional evidence of the disproportionation of ferrous iron in silicates at high pressures and temperatures, *Bell and Mao* studied a synthetic "basalt" glass composition in the system $\text{FeO-MgO-CaO-Al}_2\text{O}_3\text{-SiO}_2$ at 200 kbar. The glass was green, owing to crystal-field absorption of Fe^{2+} , until it was heated at pressure to approximately 1300°C, when it changed to brown. Scanning electron microscope images of the product show that the glass reacted to form two phases—one, spherical me-

tallic grains; the other, a fine intergrowth of a crystalline phase. Nondispersive x-ray analysis and x-ray diffraction study showed that the metallic spheres were pure Fe and the crystalline intergrowth was a garnet-like phase.

Disproportionation of Fe^{2+} to $\text{Fe}^{3+} + \text{Fe}^0$ may have occurred in these experiments. Although this type of reaction is well known in metallurgy, this is the first observation of the stabilization of $\text{Fe}^{3+} + \text{Fe}^0$ by high pressure. If this interpretation is correct, it would be a confirmation of the theoretical model for the earth proposed by Mao (*Year Book* 73, p. 510) in which iron disproportionation plays a major role.

Because of the important bearing of charge-transfer effects at high pressures on the temperature distribution and magnetic field of the earth, *Mao and Bell* studied the charge-transfer spectra in the visible range of several molybdates, chromates, and a copper chloride. Although these substances probably do not exist as major components in the mantle, they contain Mo, Cr, and Cu and are therefore useful to illustrate the principle of charge transfer for these elements at pressures near 100 kbar. The effects observed at low pressures are small, but are intensified by orders of magnitude at high pressure. Charge transfer was found to be very strong in PbCrO_4 and PbMoO_4 ; strong in $(\text{NH}_4)_2\text{CrO}_4$, $\text{K}_2\text{Cr}_2\text{O}_7$, $\text{CuCl} \cdot 2\text{H}_2\text{O}$, and $(\text{NH}_4)\text{MoO}_4$; but weak in K_2CrO_4 and Na_2MoO_4 . New models of the earth will have to take into account the thermal barriers that are implied if the absorption is as great as predicted from these new data.

Many mineralogical problems require complete knowledge of the crystal structure before progress can be made in understanding physical properties or chemical variations. The pyroxenoid group of minerals affords an opportunity to relate cation variations to the several structural variants that the group displays. Various phases with tetrahedral repeats

of 2, 3, 5, 7, and 9 are known in single chain silicates. *Ohashi, Kato, and Matsubara* have examined natural rhodonites and pyroxmangites from various localities in an attempt to characterize compositional ranges of these two minerals. They observed a compositional limit with respect to $\text{Ca}/(\text{Mg} + \text{Fe})$ in natural samples. By comparing the results with experimentally determined phase relations, they attributed this compositional limit to a relatively restricted range of physical conditions in nature. In a related study of these pyroxenoids, *Ohashi and Finger* refined the crystal structures of rhodonite (5 tetrahedra repeat) and pyroxmangite (7 tetrahedra repeat), using samples with approximately equal Mn concentration. They found a close similarity between rhodonite and a portion of the pyroxmangite structure, although the cation band arrangements are different in the two minerals. The results are especially interesting because large cations, such as Ca, and smaller ones, such as Fe or Mg, play an important role in controlling the pyroxene structure. Manganese, an intermediate-sized ion, on the other hand, enhances the stability of chain silicates with longer tetrahedral repeats as in the pyroxenoids.

As the temperature of a crystal changes, the mean positions of the atoms move to new equilibrium positions that correspond to the minimum free energy. Analysis of these complicated changes in atomic positions is needed for better understanding of the effect of temperature on the crystal structure. *Ohashi and Finger* utilized tetrahedral tiltings as a measure of the tetrahedral framework changes in the structural study of sanidine up to 800°C . Although feldspars consist of a tetrahedral framework linked in three dimensions, the lattice thermal expansion is quite anisotropic, and this anisotropy can be explained by a combination of changes in the alkali polyhedron and tetrahedral tilting.

Thermal motion in crystals can be de-

scribed either on the basis of individual atomic vibrations or by treating segments of the structure as units that vibrate. *Finger* has applied the technique of direct refinement to calcite and magnesite, assuming the CO_3^{2-} group acts as a rigid body. He finds that the quality of the description of the structure is not diminished in spite of the decrease in the number of parameters used to describe the thermal motion. He also notes that the refined parameters may be correlated with lattice mode vibrations and these are in agreement with certain absorption frequencies in the far-infrared spectrum.

The freedom with which atoms move at high temperatures leads to complications where an ion can change sites as well. Some ions, such as Fe^{3+} and Ti^{4+} , are evidently able to exchange between octahedrally and tetrahedrally coordinated sites as in the garnet solid solutions along the join andradite–Ti-andradite. To confirm the Ti^{4+} tetrahedral occupancy, a long contested issue, *Weber, Virgo, and Huggins* have refined the crystal structure of the garnet $\text{Ca}_3\text{Fe}_2\text{Si}_{1.59}\text{Ti}_{1.41}\text{O}_{12}$ by powder neutron diffractometry, using the profile refinement method. The cell dimension $a_0 = 12.241 \text{ \AA}$ is in agreement with that determined by x-ray diffractometry. The refinement indicates that 24% Ti^{4+} shares the tetrahedral sites with Fe^{3+} and Si. This result compares with a value of $\sim 17\%$ determined by ^{57}Fe Mössbauer spectroscopy. Systematic errors in the least-squares fitting of the partially resolved absorption spectra of Ti-garnets have been evaluated by statistical methods in terms of the number of fitted peaks and relative errors in the computed peak areas due to peak overlap. The discrepancy in the site occupancies determined by neutron diffractometry and Mössbauer spectroscopy has not been resolved, and other factors such as the differential Fe^{3+} recoil-free fractions for the two distinct sites involved in the exchange process are being considered.

In spite of the difficulties of assigning Ti^{4+} to its structural position, a Mössbauer study by *Huggins, Virgo, Hölzl, and Huckenholz* of a suite of garnets between grossular and titanandradite was carried out. The interpretation of the Mössbauer data for Fe^{3+} in garnets along the join by means of an ideal solid solution model led to the determination of the complete tetrahedral and octahedral site-occupancy data for the three cations Al^{3+} , Fe^{3+} , and Ti^{4+} . The results show that the relative site preferences for these cations are dependent on composition. For low Ti contents the site preferences are close to random, but for Ti-rich samples the tetrahedral site preference is $\text{Fe} = \text{Al} > \text{Ti}$. The cation distribution in natural Ti-rich garnets may reflect, within the framework of these findings, conditions of crystallization.

Further studies on site population problems involving Fe^{3+} and Ti^{4+} were carried out by *Virgo and Huggins* on synthetic armalcolite, a phase found on the moon. Previous attempts to determine the site occupancies in pseudobrookite, ferropseudobrookite, and armalcolite from x-ray structure refinements have failed because of the similar scattering factors for Fe and Ti. The ^{57}Fe Mössbauer studies of these compounds have shown conclusively that Fe_2TiO_5 has an approximately inverse configuration at 1300°C , $(\text{Fe}^{3+}) (\text{Fe}^{3+} + \text{Ti}^{4+})\text{O}_5$, and that FeTi_2O_5 and $\text{Fe}_{0.5}\text{Mg}_{0.5}\text{Ti}_2\text{O}_5$ have disordered cation configurations at 1300° and 1100°C , respectively, derived from a low-temperature normal structure. The high-temperature stability of these compounds with the pseudobrookite-type crystal structure can now be explained by a balance of endothermic enthalpies of formation and significant positive entropies of formation arising from cation disordering between the distinct octahedral sites.

Lunar Petrology

The lunar rocks continue to capture the attention of the staff as vast amounts

of new information are synthesized and principal questions are put into focus. Major efforts are being made to characterize the conditions of formation of the soil components and ultrabasic rocks.

In a study by *Mao, Bell, and Adams* of fine particles of soil from the moon's surface, a number of features related to composition and chemical processes have been observed in minute (100–200 μm diameter) grains made of crystals and glass. These particles, called agglutinates, form a portion of the lunar soil significant enough in amount to affect the optical properties and therefore to affect interpretations of the bulk composition of the moon's surface. The main feature in the glassy portions is the presence of numerous bubbles, metallic spherules, and zones of brown glass. These features are interpreted to be evidence of oxidation (by the disproportionation of ferrous iron) and reduction (both by disproportionation reactions and by the thermal release of implanted solar wind hydrogen).

The presence of Ti^{3+} (the reduced form of titanium) in lunar rocks can be used as an indicator of the chemical environment in which the rocks formed, according to *Bell, Mao, and Haggerty*. Calibrations relating the ratio $\text{Ti}^{3+}/\text{Ti}^{4+}$ to temperature and oxygen fugacity that were successful in the study of Ti^{3+} in minerals from the Allende meteorite have proved essential in a similar study of lunar samples. The Ti^{3+} ion usually causes a single-crystal field absorption that produces a purple color. Purple glass was identified in Apollo 17 sample 70019. The associated absorption band in the purple glass was more intense than the band observed in synthetic glass made at an oxygen fugacity of $10^{-11.6}$ atm. Intensification may be due in part to internal reflection or to electronic coupling effects, but it nevertheless suggests that the purple glass in sample 70019 formed at a fugacity lower than the lowest experimental value. This study provides evidence that sample

70019 is the most chemically reduced lunar sample yet studied.

As part of a larger study (with E. Roedder and P. Weiblen) on the general problem of symplectic intergrowths in lunar rocks, it has been discovered by *Bell and Mao* that the dunite sample (72415) collected at the Apollo 17 landing site contains numerous symplectic intergrowths of garnet composition. Electron microprobe and scanning electron microscope data confirm the garnet composition, although no unreacted garnet has been found. If these symplectites were garnet, the composition would be useful in determining the depth of formation of the Apollo 17 dunite, the oldest rock yet found on the moon.

Biogeochemistry

Stable isotope ratios in the organic matter of living organisms and in sediments are useful tracers for identifying sources and following the fate of material in the geochemical cycles of some elements. *Hoering* has made a survey of the deuterium-hydrogen ratios in classes of compounds in plants from several environments and also measured isotope ratios in crude oils and in organic matter from recent sediments. He finds that the deuterium concentration in plant material is always lower than that of the water available to the plant as it grew. The lipid fraction has less deuterium than the carbohydrates and proteins. There is a wide range of deuterium concentration among the lipid fractions, the nonsaponifiable material having much lower values than the fatty acids. Hydrocarbons and fatty acids from the same plant have similar isotope ratios. Several crude oils have a deuterium concentration similar to that of plant fatty acids and may therefore retain some record of the source organic matter that was transformed into petroleum.

The organic matter in sediments is associated with clay minerals, and it is important to learn the cause of this association. Toward this end *Hedges* in-

vestigated the association of L-valine, D-glucose, and stearic acid with kaolinite and montmorillonite clay minerals in model systems similar to natural bodies of water. The percentage of organic matter removed from freshwater and seawater solutions depended upon the concentrations and chemical properties of the organic substances and upon the clay minerals with which they were equilibrated. He found that glucose was not removed from solution by either clay mineral under any experimental conditions. At initial concentrations of 10^{-2} to 10^{-8} M, from 1% to 9% of the dissolved valine was removed from both seawater and distilled water suspensions of kaolinite and montmorillonite. Up to 40% of the initial stearic acid was extracted by the clays from distilled water solutions over a concentration range of 1.0 to 0.01 mg/l. More stearic acid was lost from the corresponding seawater suspensions, but experimental evidence suggests that the acid was not in true solution. The relative abilities of the two clays to extract dissolved organic molecules were not directly related to either their surface area or their cation-exchange capacity. The clay-organic associations that were measured indicate preferential removal of simple organic molecules from natural bodies of water, but are orders of magnitude too small to explain the high concentrations of total organic matter occurring in fine-grained sediments.

Proteins in fossil shells, bones, and teeth found in sediments are hydrolyzed slowly by H_2O to peptides and free amino acids. The ratio of free amino acids (before acid hydrolysis) to total amino acids (after acid hydrolysis) increases with the age of fossil shells and teeth. In contrast, fossil bone generally does not have any significant concentration of free amino acids. Because of the porous nature of bone, free amino acids are readily leached out, according to *Hare, Miller, and Tuross*. Experiments with bone heated in water at tempera-

tures of 110° to $160^{\circ}C$ show that significant leaching does not occur until the collagen in the bone is solubilized. Because a number of fossils ranging in age up to 100,000 years still contain intact insoluble collagen without appreciable racemization, the use of amino acid racemization for age determination may lead to ages in bone that are probably grossly in error. Shell and teeth provide a closer approximation to a closed system and yield more consistent results.

The organic compounds in sediments can be most useful for correlation purposes in the view of *Miller and Hare*. The diagenesis of amino acids in arctic marine mollusks from Quaternary deposits, for example, has been studied to determine the suitability of the various reactions for possible use in geochronology. Shell samples were collected along the east coast of Baffin Island, Canada, where extensive wave-cut cliffs expose a complex sequence of interbedded marine, glaciomarine, and glacial sediments. Shells from the marine unit overlying the youngest glaciogene sediments are beyond the useful range of radiocarbon dating, suggesting that the underlying sediments are of considerable antiquity and may contain some of the oldest known direct evidence for early fluctuations of the Laurentide Ice Sheet.

New analyses show that both the extent of natural hydrolysis of protein in the molluscan shell structure and the racemization of the various amino acids are directly related to the time elapsed since burial. Shells collected from individual sections, where their relative ages are fixed stratigraphically, show a consistent increase down section in the proportion of free to peptide-bound amino acids and in the degree of racemization in both the hydrolyzed and free fractions. Additionally, a comparison of these reactions in several valves of *Hiatella arctica* from a single collection and between collections made along the same stratigraphic horizon produced consistent results for all valves. Interspecies

variations may be considerable, however, and species identification is necessary for accurate relative age assignment. An independently calibrated absolute time scale for the various amino acid reactions is being constructed, based on the results of high-temperature laboratory simulation of age. These studies have provided the first technique by which it may be possible to decipher the rich but complex Quaternary glacial and marine record of the eastern Canadian Arctic.

Organic compounds are also found in carbonaceous chondrites, especially in the C1 (3.5% carbon) and C2 (1.8%–2.6% carbon) types. About 30% of this material is of low molecular weight and is readily extracted from the meteorite, and the remaining 70% is an insoluble, unsaturated, kerogen-like material. Many of the organic molecules in carbonaceous chondrites are the same as, or similar to, those found in the contemporary biosphere, and this fact provides the best evidence found in nature to date in support of the Oparin-Haldane abiotic theory of chemical evolution preceding the first organisms. This similarity, which makes the carbonaceous chondrites so interesting on the one hand, poses, on the other, the serious risk of mistaken identification of terrestrial contaminants as constituent materials. The ease of contamination was not fully appreciated in much of the early analytical work, and many of these results are now either discredited or of questionable validity. This appreciation, along with the availability of relatively uncontaminated samples from recent falls (Murchison and Allende meteorites) and a clearer understanding of the contamination pitfalls, has led to renewed study of the organic analysis of meteorites.

Within the Murchison and Murray C2 chondrites is found a diverse suite of racemic amino acids that includes the common amino acids found in protein as well as many that are biologically rare. Their racemic nature offers strong

evidence against terrestrial contamination, and the seemingly all-inclusive structural diversity suggests abiotic synthesis. *Cronin* has found that the C2 chondrites also contain compounds that are converted to amino acids under hydrolytic conditions. The nature of these compounds is of interest: If they are amino acids combined in peptide linkage, this finding would provide the first evidence in nature for the second (polymerization) stage of chemical evolution; if they prove to be monomeric species, their characterization suggests a mechanism (of which many have been proposed) for pre-biotic amino acid synthesis. The work done to date has shown that (1) these precursors are not highly polymerized forms, but are small molecules of roughly the size of amino acids; (2) they are not, for the most part, small peptides; (3) they are acidic species lacking the accompanying basicity characteristic of amino acids.

Geochronology

Metamict zircons used for age determination give discordant ages, indicating that the uranium-lead relationship has been disturbed. *Krogh and Davis* believe that alteration of the metamict parts of the zircon is the major contributing factor of the discordance. After removal of the altered material by differential solution techniques they were able to demonstrate concordant uranium-lead relationships. It is no longer necessary to postulate loss of lead by diffusion to explain the major part of the discordance of zircon ages.

Much of the success of the geochronology program can be attributed to the careful collection of specimens well documented in the field. The close cooperation of field geologists with geochemists is essential to the establishment of meaningful ages of rocks and their constituent minerals. A major geological question in the Canadian Shield has been the age relationships of the large east-west trending belts of acidic and basic rocks.

Previous U-Pb isotopic age determinations on volcanic rocks from these belts indicate that the belts become progressively younger to the south. *Krogh, Davis, Harris, Goodwin, and Ermanovics* have studied the eastern Lac Seul region of the English River gneiss belt to provide dates on the associated intrusives and metamorphic rocks. Isotopic results indicate that the tonalitic gneiss has a minimum age of 3008 ± 12 m.y. and is the oldest rock in the region. Zircon from pegmatites provide an age of the anatexis during regional metamorphism of 2688 ± 26 m.y. Late dikes cutting the tonalitic gneiss were found to have an age of 2568 ± 40 m.y. These

ages conform to the pattern found earlier, namely that the ages become younger to the south. Remnants of old basement have been found in spite of the development of younger volcanism, intrusion, and metamorphism. The progression of plutonic-metamorphic cycles supports the concept of continental accretion.

Further details of the various investigations just described are presented in this Report, and complete documentation of the work presented as well as many other studies incomplete or awaiting confirmation will eventually be found in the regular journals devoted to each field.

NEW TECHNIQUES AND EQUIPMENT

LASER OPTICAL SYSTEM FOR HEATING EXPERIMENTS AND PRESSURE CALIBRATION OF THE DIAMOND-WINDOWED, HIGH-PRESSURE CELL

P. M. Bell and H. K. Mao

The diamond-windowed, high-pressure cell can now reach pressures of approximately 500 kbar, corresponding to a depth of 1000 km in the earth (Mao and Bell, this Report). The appropriate temperature range for this depth is 2000° – 2500° C. Design considerations for the high-pressure cell made it necessary to avoid excessive heating of the diamonds and supporting blocks, so application of a high-power laser system (Ming and Bassett, 1974) was employed that heated the sample alone.

A second laser system was designed for pressure calibration of the cell. This technique uses the pressure shift of the R_1 strong-line ruby fluorescence spectrum, which is related to a pressure transition in NaCl (Piermarini and Block, 1975). A combination of the two laser systems with the improved pressure cell makes this apparatus a powerful tool in geochemical and geophysical experiments at calibrated static pressures and temperatures corresponding to greater depths

in the earth than have been achieved before.

Laser Heating System

The heating system employs an Nd-YAG (yttrium aluminum garnet single crystal doped with Nd) laser that continuously emits a coherent beam at $1.064 \mu\text{m}$ with 60 W power. The system, shown diagrammatically in Fig. 1, includes a dichroic-multilayered reflecting filter. The dichroic filter (Schott Optical Co. No. 116) reflects 95% of the laser beam and transmits 95% of the visible light, thus causing the laser beam to be reflected through the objective lens and focused onto the pressurized sample. The filter scatters wavelengths of the laser beam reflected back from the sample and transmits 95% of the visible thermal emission of the heated sample to the eyepiece and optical pyrometer. The laser beam can be focused to a diameter of approximately $20 \mu\text{m}$ for selective heating.

The laser is optically pumped with two 2.5 kW krypton-arc lamps and can be designed to emit a beam of various wavelengths (depending on the dopant). The Nd-YAG laser emits in a region that is particularly suitable for geochemical

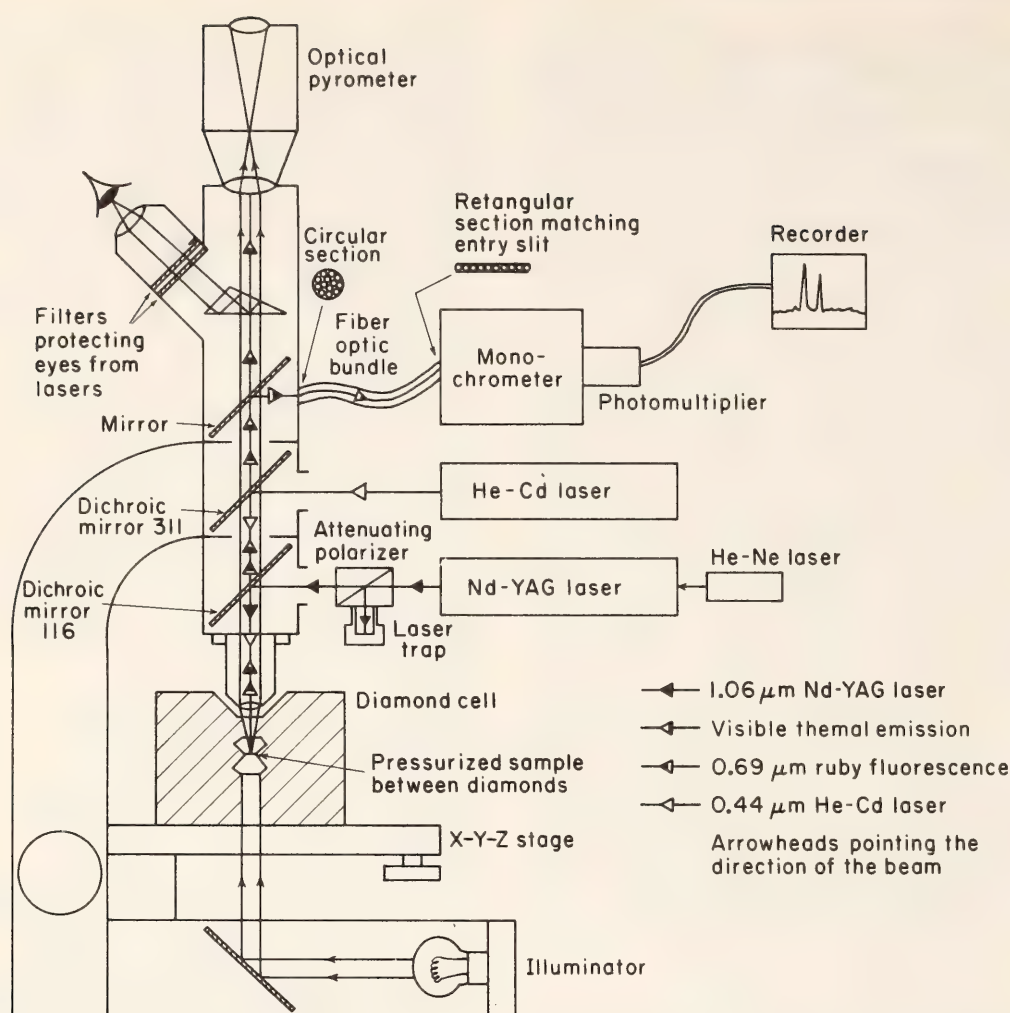


Fig. 1. Block diagram of laser optical system for heating experiments and pressure calibrations of the diamond-windowed high-pressure cell. The dichroic mirror 116 reflects 95% of the Nd-YAG laser at $1.06\ \mu\text{m}$ and transmits 95% of the He-Cd laser at $0.44\ \mu\text{m}$, the ruby fluorescence at $0.69\ \mu\text{m}$, and the visible thermal emission of the heated sample. The dichroic mirror 311 reflects 90% of the He-Cd laser and transmits 90% of the ruby fluorescence. Each mirror can be switched in and out separately to optimize heating or pressure calibration experiments.

and geophysical work. It is an energy region where heat is transferred efficiently in the earth by radiation (above 1000°C) where iron-bearing minerals with Fe^{2+} bonded in an octahedral site absorb heat (caused by a crystal-field transition in Fe^{2+}), and where diamond is totally transparent and does not absorb heat. The laser beam is focused onto the sample, heating it but not the diamonds or other parts of the apparatus. A small temperature rise occurs from secondary heat lost from the heated sample, but the amount is minor (less than 100°C at the outer surface of the diamond).

Alignment of the optical system is made using a second, He-Ne, gas laser.

This laser is a low-energy type (0.001 W, continuous output), that can be focused and centered visually (emission, $0.6328\ \mu\text{m}$) through the optical system to the temperature-sensing aperture.

Temperature is measured in the system by an optical pyrometer, whose accuracy is a function of the thermal emissivity of the sample at high pressure and the transparency of a thin film of cool material that usually forms adjacent to the pressurized surface of the diamond. Calibration of the pyrometer by thermocouple is essential in these experiments.

The sample can be viewed under both high-pressure and high-temperature con-

ditions with a filter system and an ocular lens system. Figure 2 is a photomicrograph through the diamond window of an experiment ranging over the olivine-spinel transition. The starting material was olivine (fayalite) that was first raised to a pressure above 50 kbar. The dark central region was heated to 1000°C and converted to spinel. The pressure

was then lowered to less than 50 kbar, causing the spinel phase to be quenched. Subsequently, the laser beam was focused to approximately 20 μm diameter and then tracked across the spinel, converting it back to olivine (lighter tone in Fig. 2) along the track. In the past, the olivine-spinel transition had been very difficult to accomplish, but Fig. 2 illus-



Fig. 2. Photomicrograph of Fe_2SiO_4 under high pressure and high temperature in a diamond cell. The bright spot in the middle is the incandescence of the sample being heated by the Nd-YAG laser.

trates the relative ease of observing the reversible reaction.

Laser System for Pressure Calibration

The design of a pressure calibration system (Fig. 1) using the pressure shift of two ruby fluorescent emission lines (wavelength 0.6928 and 0.6942 μm) was made on the basis of a system used at the National Bureau of Standards (G. Piermarini, personal communication, 1975). In this design a gas-diffusion, He-Cd laser emits at 0.4416 μm continuously at approximately 0.015 W and excites fluorescence in a small crystal of ruby (20–40 μm diameter) located in or adjacent to the sample in the high-pressure cell.

A dichroic reflecting filter (Schott Optical Co. No. 311) reflects 90% of the laser beam and transmits 90% of the fluorescent emission of the ruby crystal. The fluorescent emission line is transmitted to a spectrometer via a fiber-optic bundle. The wavelength of the line is recorded and related to a pressure scale (Barnett, Block, and Piermarini, 1973). The primary calibration is based on fixed points, such as transition in NaCl at 300 kbar and 25°C.

Experimental Range

This new design has worked routinely up to a pressure of approximately 500 kbar at 2500°C. The projected precision of the pressure measurement is ± 2 kbar throughout the range. The absolute accuracy above the NaCl transition is not known, but can be determined in all probability using the volume equation of state of MgO, based on x-ray diffraction.

Temperature in the pressurized sample is controlled by adjusting the power input to the laser and by alternating the laser beam (a Glanlaser polarizer, shown in Fig. 1, is used for this purpose). At present the temperature is no better than $\pm 25^\circ\text{C}$ throughout the heating range.

With the new design one can experiment routinely at conditions equivalent to greater depths in the earth than ever

before. It should be possible for the first time to measure some critical physical properties of materials that exist in the mantle. It should also be possible to experiment with the chemical stability and compositions of the minerals that comprise the greater portion of the earth.

DESIGN OF A DIAMOND-WINDOWED, HIGH-PRESSURE CELL FOR HYDROSTATIC PRESSURES IN THE RANGE 1 BAR TO 0.5 MBAR

H. K. Mao and P. M. Bell

The diamond-windowed, high-pressure cell originated from a design made by the National Bureau of Standards in 1959 (Weir *et al.*, 1959). Variations of that design have been used successfully since then to obtain maximum pressures of approximately 300 kbar. For hydrostatic conditions the pressure was, by necessity, limited to approximately 80 kbar, and in the range 80–300 kbar there was a strong stress gradient across the sample. This report describes an improved design of the diamond-windowed, high-pressure cell whereby a sample of larger volume (an increase of a factor of 10) can be pressurized hydrostatically (or nearly so) to 500 kbar. The modifications in design in no way limit the versatility of the cell, and the hydrostatic conditions greatly improve the quality of data on physical properties of minerals in the upper pressure range. It is now possible to make routine experimental observations at pressures and temperatures equivalent to those at depths of 1000 km in the earth.

Design of the Diamond-Windowed Pressure Cell

Both the original and modified designs of the diamond-windowed, high-pressure cell are displayed in Fig. 3. Both designs employ a lever advanced by a spring-loaded screw. In the old design the supporting block was rectangular, and the load movement was approximately 40°

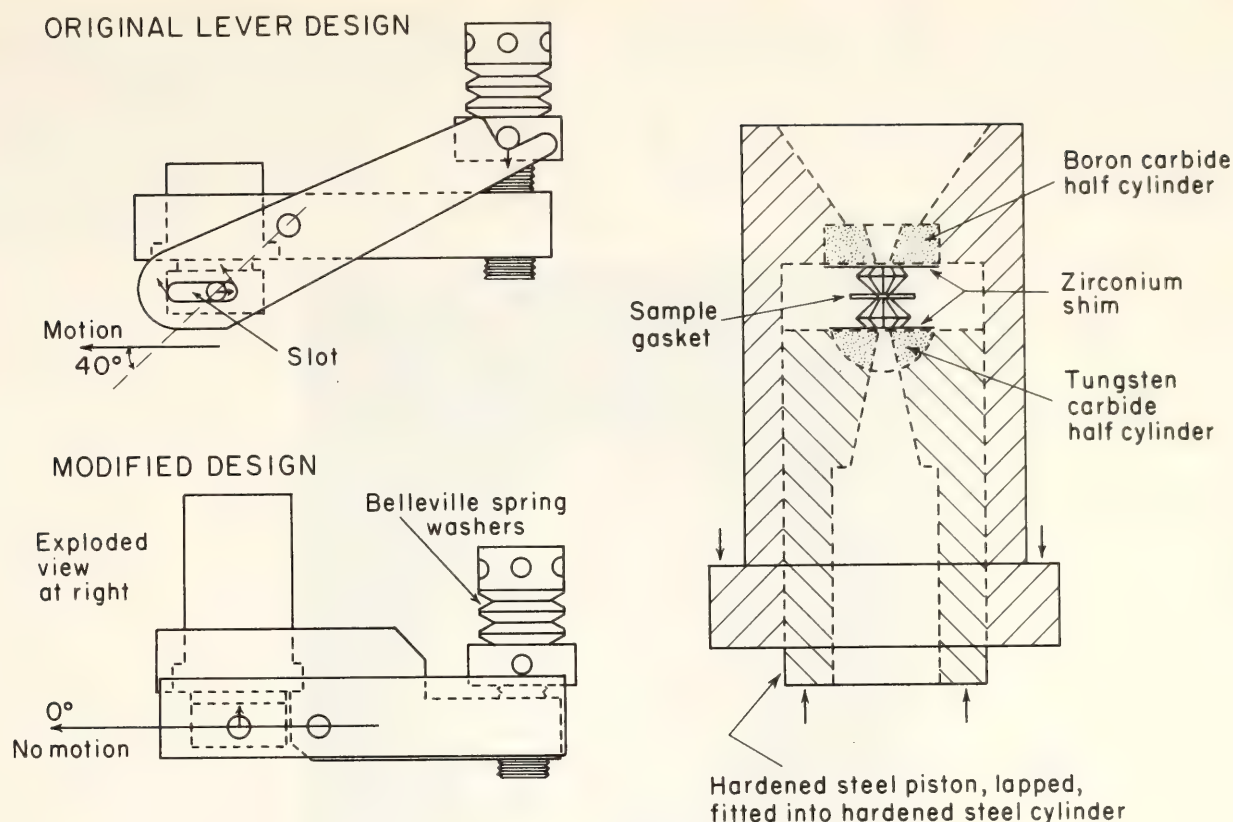


Fig. 3. Original and modified designs of the diamond-windowed high-pressure cell.

to the direction of loading, causing horizontal displacement torque and a tendency to misalign the diamonds.

The new design overcomes these problems in two ways. First, the supporting plate is stepped for positioning of the lever fulcrum, thus avoiding horizontal displacement. The resulting movement acts in the same direction as the applied force. A second refinement is the addition of a long cylindrical travel to preserve linear stability. (An increase in linear stability is also a feature of a recent design by the National Bureau of Standards; A. Piermarini, personal communication, 1975, and Piermarini and Block, 1975). The increased stability and the pure linear displacement of the diamonds make it feasible to use larger forces and thereby obtain larger volumes.

Previously the diamonds used were approximately 0.1 carat (pressure surface diameter = 0.3 mm) and therefore small enough to keep the forces moderate (less than 250 kg). In the modified design, 0.3–0.4 carat (pressure surface diameter = 0.6 mm) diamonds are used

for larger sample volume, and the forces are significantly high. A pressure of 500 kbar in the cell corresponds to an applied force of approximately 700 kg. This force is supported by using carbide thrust blocks and by using a ring gasket to act as the cylindrical walls supporting the sample.

The carbide thrust blocks play an important role in providing a strong, flat surface. The blocks are half-cylinder “rockers,” opposed 90° (see Bassett, Takashi, and Stook, 1967, for detailed description), made of boron carbide. This material is relatively transparent to x rays and stronger than tungsten carbide. A shim of thin (0.03 mm) zirconium is placed between the diamond and carbide surfaces to act as an intermediate support. Zirconium also acts as a β filter for Mo x rays that are used in x-ray diffraction.

The sample gasket is made of a special alloy called René 41, manufactured by the Teledyne Corporation. This alloy has high-temperature strength, is ductile, and contains less than 0.3 wt % iron. The

gasket is ideal for high-temperature experiments and for ^{57}Fe Mössbauer experiments. Appropriate ports through all pieces provide an adequate pathway for viewing the interior of the cell under pressure.

Pressure Calibration

The modified pressure cell is calibrated against known fixed points. The highest such point is the $B1 \rightleftharpoons B2$ transition in NaCl. This transition, which occurs at 300 ± 10 kbar, 25°C (Piermarini and

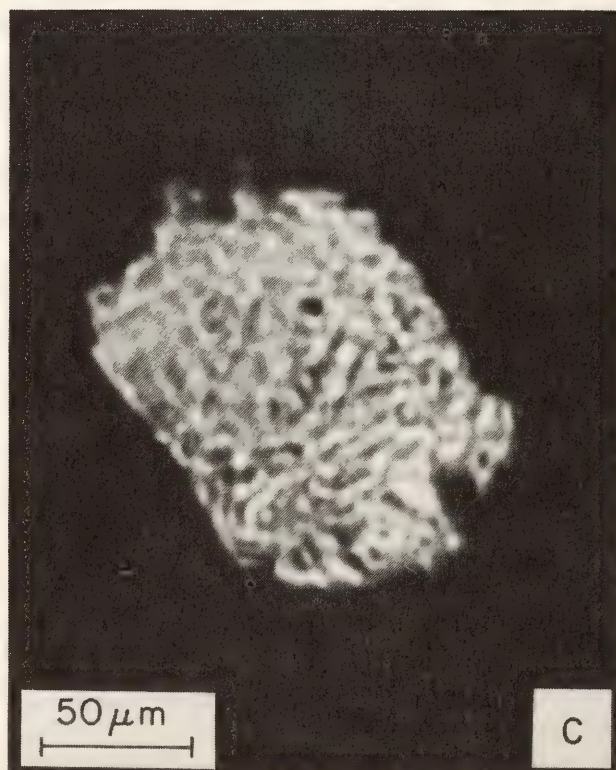
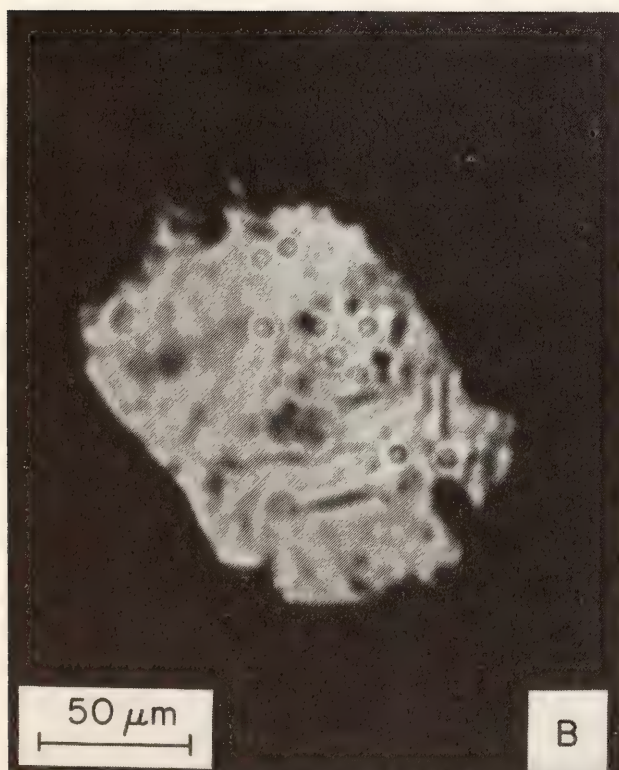
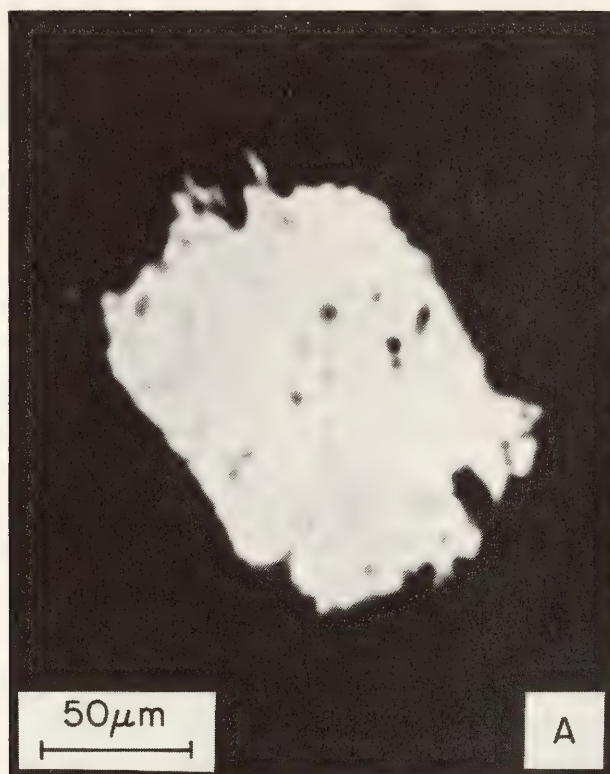


Fig. 4. Photomicrograph of sodium chloride in the diamond cell: (A) below 300 kbar; (B) 300 kbar, onset of growth of B2 phase; (C) 300 kbar, substantial growth of B2 phase.

Block, 1975), is a structural phase change from the sodium chloride type to the cesium chloride type. Figure 4 shows a photomicrograph of sodium chloride slightly below the transition, at the transition, and slightly above the transition in pressure. Extension of the pressure range to 500 kbar is approximate, estimated from a linear application of force that is corrected for loss in the system. Eventually, it will be possible to calibrate absolute pressures above 300 kbar by measuring the volume equation of the state of sodium chloride (this requires approximately 240 hours of x-ray diffraction exposure).

It is possible to obtain nearly hydrostatic conditions at these high pressures because of the property of certain liquids that do not freeze but remain quasi-hydrostatic at pressures above their glass point. A useful liquid for this purpose is a 4:1 methanol:ethanol mixture (Piermarini and Block, 1975), but many organic liquids behave in a similar way.

The new cell design opens a yet unexplored pressure region for static geochemical and geophysical experiments. It should be possible to test critically compositions, reactions, and phase assemblages for their suitability for the earth's mantle to a depth of 1000 km. Simultaneously, it should be possible to measure physical properties, such as electrical and thermal conductivity, of materials that exist at these depths in the earth.

MÖSSBAUER STUDIES AT HIGH PRESSURE USING THE DIAMOND-ANVIL CELL

F. E. Huggins, H. K. Mao, and D. Virgo

The high-pressure diamond-anvil cell is proving to be a most versatile and useful apparatus for working at pressures of hundreds of kilobars and temperatures in excess of 1000°C. For earth-science studies, use of the diamond-anvil cell makes it possible to investigate minerals under conditions equivalent to those at depths of 500–1000 km, providing infor-

mation on phenomena occurring in the transition zone of the mantle.

One of the most important elements to relate to phenomena in the deep earth is iron because it is the only transition element of major abundance. Thus, iron can be expected to give rise to most, if not all, of the complications associated with crystal-field and charge-transfer phenomena, variable valence and spin states, and the electrical and magnetic properties of cations in minerals likely to be found in the mantle. For this reason, Mössbauer studies of minerals containing iron under the pressures and temperatures of the mantle are expected to be especially informative. Mössbauer data as a function of pressure can be related to pressure-induced changes in the crystal chemistry, and magnetic, spin, and valence properties of iron in minerals, on which may be based interpretations of pressure-induced phenomena within the earth.

The feasibility of carrying out Mössbauer experiments in the diamond cell (specifically, the one designed by Mao and Bell, this Report) was therefore investigated for the following reasons. First, the range of pressure and temperature conditions obtainable in the diamond cell is much greater than in other apparatus used for high-pressure Mössbauer experiments. Second, hydrostatic experiments may be performed to very high pressures in the diamond cell, using the gasketing technique and the appropriate liquid as a pressure medium (Mao and Bell, this Report). Third, other experimental and optical absorption spectroscopies, and visual examination, may be performed on the sample under the same conditions, and the results can be related directly to those from Mössbauer experiments. In this report, the modifications necessary for observing the Mössbauer effect through the diamond-anvil cell are described, and the potential of the technique is illustrated by preliminary experimental results on the spinel modifi-

cation of Fe_2SiO_4 and on the gillespite $\text{I} \rightarrow \text{II}$ transition at about 25 kbar.

The critical factors in the design of high-pressure Mössbauer experiments are regulating the strength and collimation of the γ -ray flux so that the most concentrated and strongest possible flux interacts with the sample. These factors are especially restrictive for work with the diamond-anvil cell because the size of the sample is very small. The area of the typical diamond-anvil cell sample is only about 10^{-4} cm^2 (cf. between 1 and 5 cm^2 in 1 bar Mössbauer experimentation). With this small area, however, it is possible to move the γ -ray source much closer to the sample, increasing the γ -ray flux, until the dimensions of the source extend at an angle of about 10° with respect to the sample (Fig. 5). For this reason and because of cost considerations, a source of small dimensions and high activity was required. The source of the γ -ray flux was ^{57}Co , which was diffused into the flat end of the tip of a screwdriver-shaped rod of palladium metal by New England Nuclear, Boston, Massachusetts. The dimensions of the flat end were $0.05 \times 0.1 \text{ cm}$. It contained about 10 mCi of ^{57}Co , yielding an activity of 2000 mCi/cm² (cf. $\sim 100 \text{ mCi/cm}^2$ in experimentation at 1 bar). On the basis of these dimensions, the source can be placed within 0.3 cm of the sample (cf. greater than 6 cm in experimentation at 1 bar) with-

out giving rise to a significant $\cos \theta$ broadening effect (Bancroft, 1974). Hence the γ -ray flux experienced by the sample in the high-pressure cell compares favorably with that in experiments at 1 bar.

The γ -ray beam was directed through the diamonds (Fig. 5) because in this direction in the diamond cell designed by Bell and Mao (this Report) the conical shape of the apertures in the WC seats collimates the flux to a diameter of about $5 \times 10^{-2} \text{ cm}$. Some further collimation is provided by the gasket, which is used to contain the sample and the liquid medium, while ensuring hydrostaticity. The thickness of the gasket, however, is only about $2 \times 10^{-2} \text{ cm}$ before compression between the diamonds. Therefore a large portion of the γ -ray flux passes through the gasket without interacting with the sample. Because the sample is contained in a central hole of diameter 10^{-2} cm in the gasket, probably only about 20% of the flux coming through the apertures in the WC seats interacts with the sample.

Compression of the gasket by the diamonds can thin the gasket to a thickness of about $5 \times 10^{-3} \text{ cm}$, so that at high pressure the volume of the sample chamber is approximately $4 \times 10^{-7} \text{ cm}^3$. Hence the mass of sample in the cell is usually less than $1 \mu\text{g}$. For an absorber such as Fe_2SiO_4 , this mass of sample corresponds to an iron absorber density

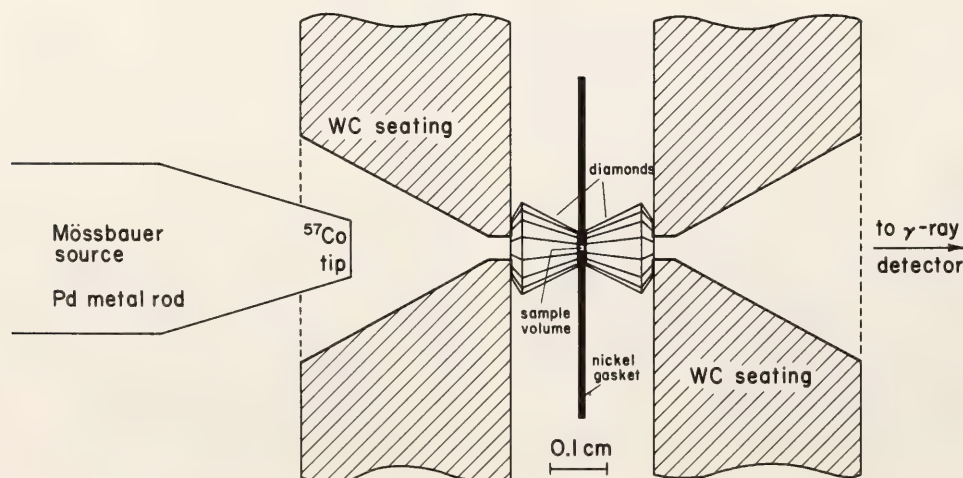


Fig. 5. Schematic detail of the diamond cell and Mössbauer source.

of about 10 mg/cm², which is more than adequate (cf. 3–5 mg/cm² in experimentation at 1 bar). The spectrum of Fe₂SiO₄ spinel is shown in Fig. 6. The 2% absorption effect is much lower than would be expected from an absorber density of 10 mg/cm² and confirms that the collimation may not be completely effective.

The Mössbauer spectrum of Fe₂SiO₄ spinel is similar to that of fayalite; the most significant difference is the smaller quadrupole splitting for the spinel (Table 1). No tetrahedral Fe²⁺ is apparent in the spectrum; hence the spinel is pre-

dominantly normal. Owing to the low absorption effect, however, the quality of the data is insufficient to test the suggestion that $2.3 \pm 1.0\%$ of the Fe²⁺ cations are in tetrahedral coordination (Yagi, Marumo, and Akimoto, 1974). In order to improve the quality of the data, it is necessary either to improve the collimation of the γ -ray beam still further or to enrich the phase in ⁵⁷Fe, the isotope of iron exhibiting the Mössbauer effect.

More than adequate absorption can be obtained with enriched samples, as

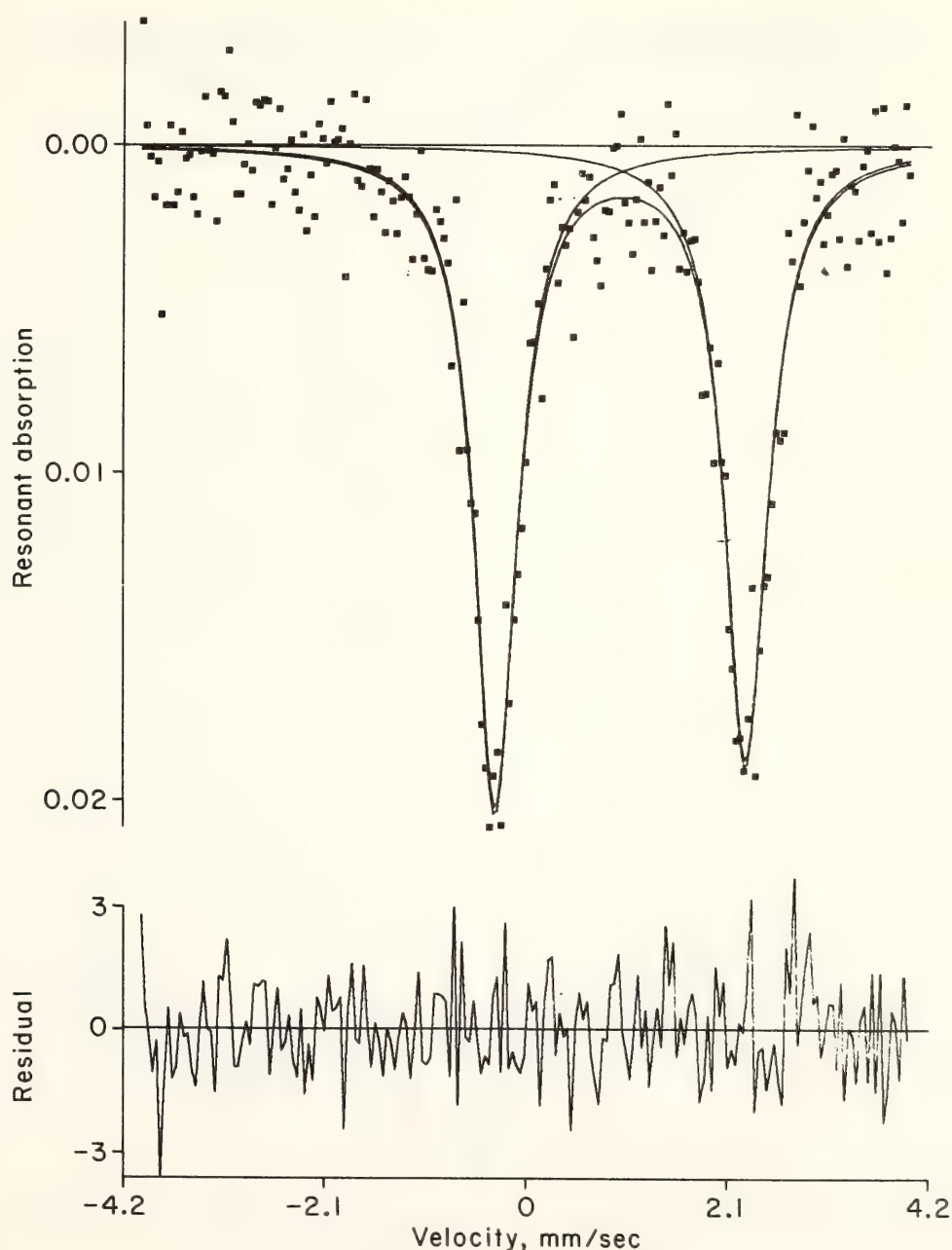


Fig. 6. Mössbauer spectrum of Fe₂SiO₄ spinel, in the diamond cell at 1 bar.

TABLE 1. Mössbauer Data for Fe₂SiO₄ (Spinel) and BaFeSi₄O₁₀

Phase	IS (mm/sec)	QS (mm/sec)
Fe ₂ SiO ₄ , spinel, at 1 bar	1.16	2.61*
BaFeSi ₄ O ₁₀ , at 1 bar on Be disk	0.77	0.56
BaFeSi ₄ O ₁₀ , above transition		
large doublet (89%)	0.85	0.61
small doublet (11%)	1.16	2.16

* Cf. fayalite: IS, 1.15 mm/sec; QS, 2.78 mm/sec.

indicated in Fig. 7B. The mineral gillespite, BaFeSi₄O₁₀, synthesized hydrothermally at 800°C and 1 kbar using enriched ⁵⁷Fe₂O₃ (D. J. Vaughan, personal communication), gave a 20% absorption effect in the diamond cell, so that within 2 days, even at the relatively slow count rate of 7.5 × 10⁴ counts/channel/day, a high-quality spectrum was obtained on applying the criteria of spectral quality proposed by Dollase (1975).

Preliminary Mössbauer studies of the gillespite transition at high pressure in

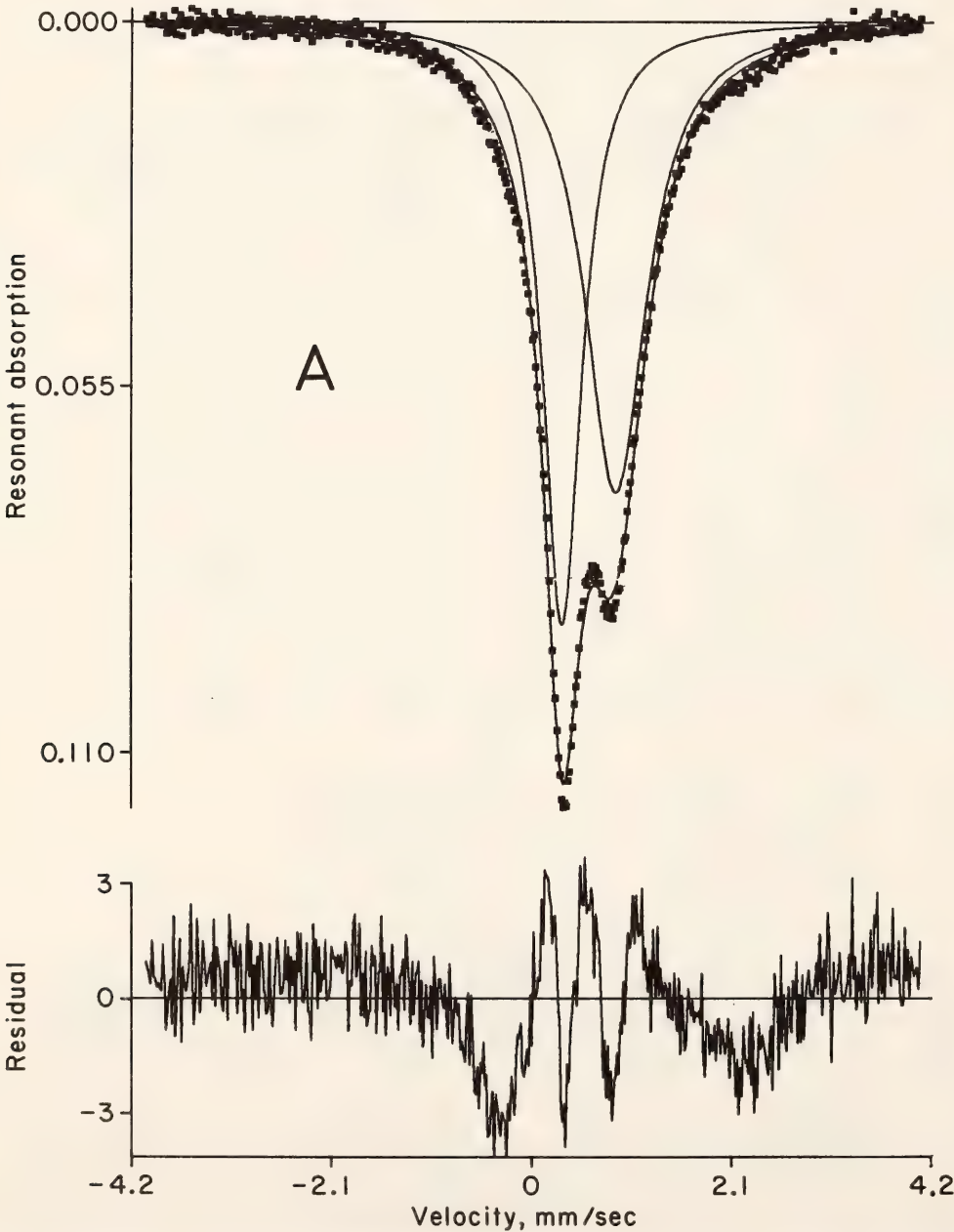


Fig. 7. Mössbauer spectrum of gillespite, Ba⁵⁷FeSi₄O₁₀: (A), on beryllium disk.

the diamond-anvil cell agree in principle with the unpublished results of D. J. Vaughan and J. A. Tossell on gillespite in a pressure cell similar in design to that described by Debrunner *et al.* (1966). These earlier data are also briefly discussed by Abu-Eid, Mao, and Burns (*Year Book* 72, pp. 564–567). Both sets of experiments show the presence of four peaks in the high-pressure Mössbauer spectra, and because the present study was carried out hydrostatically, it appears unlikely that the coexistence of ferrous cations in two distinct sites in

gillespite at high pressure can be explained by pressure gradients or by shear in the experiment. These possibilities were raised in the interpretation of the earlier Mössbauer experiment, which was not performed hydrostatically. It was suggested, on the basis of results from other experimental techniques using the hydrostatic diamond cell and single-crystal flakes of natural gillespite, that the transition is abrupt, signifying a phase change or first-order transition. Originally, because of the striking color change, the transition was reported as a

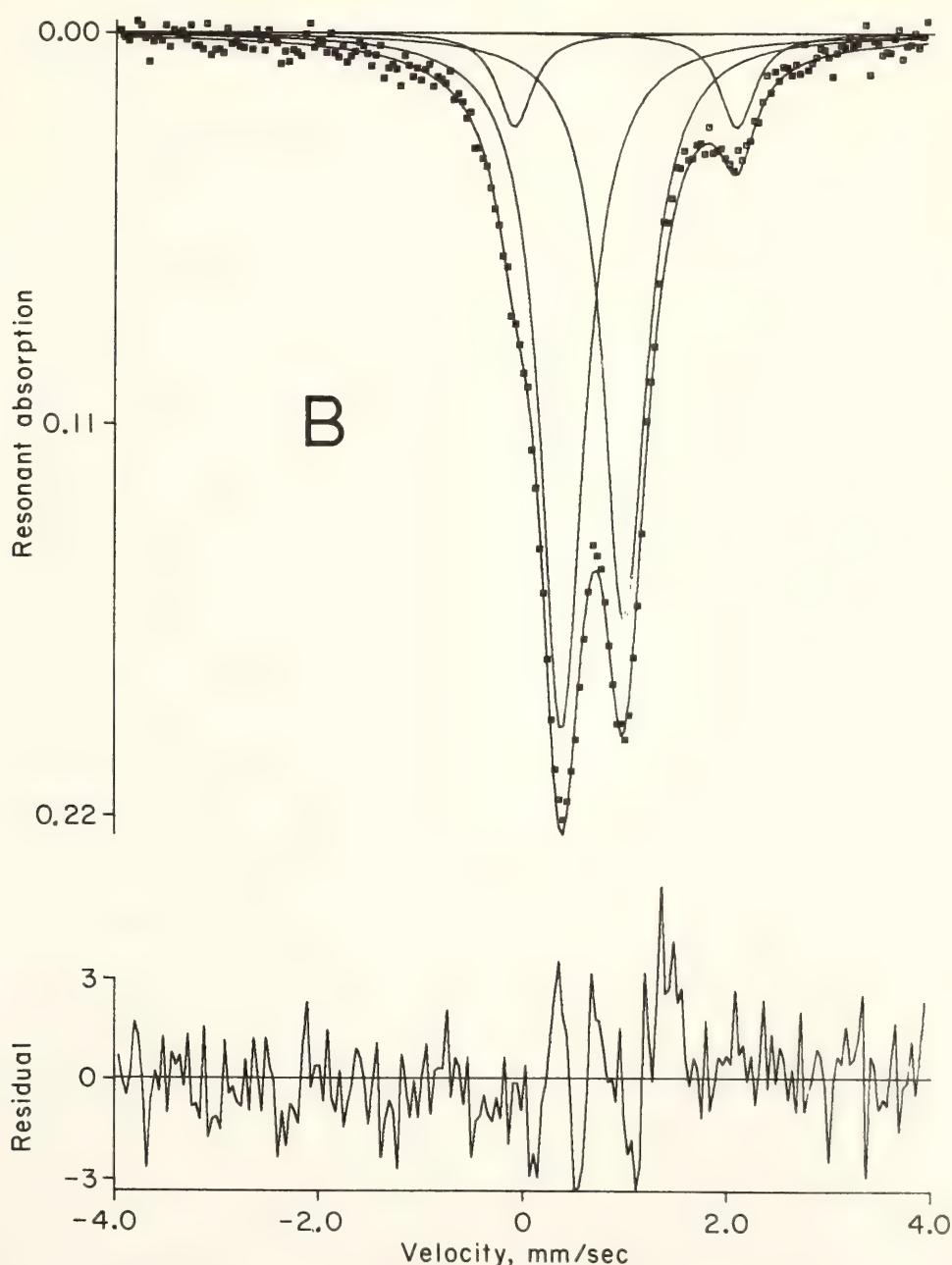


Fig. 7B. In high-pressure cell, above I \rightarrow II transition.

spin-state change (Strens, 1969), but a subsequent study (Abu-Eid, Mao, and Burns, *Year Book* 72) showed that the color change was consistent with a displacive structural phase change involving a change in the symmetry of the square planar ferrous site. Further studies using single-crystal x-ray techniques (Hazen and Burnham, 1974) confirmed that the transition was primarily a structural change but indicated that it was not a simple displacive transition. More recently, Abu-Eid (1975) has reported that the transition may show hysteresis effects with pressure, pointing to further complications.

The Mössbauer experiments on polycrystalline samples in the diamond-anvil cell differ from previous studies by indicating that the transition may be gradual rather than abrupt with respect to pressure, owing to the coexistence of two distinct ferrous species (the Mössbauer parameters of one species are consistent with either a regular or a distorted square planar configuration, those of the other, with an octahedral configuration, Table 1). In this connection, it is interesting to note that the spectrum of gillespite at 1 bar (Fig. 7A) deviates considerably from a two-peak fit in the region where the high-pressure peaks occur. Similar deviations can also be noted in the Mössbauer spectrum of natural gillespite reported by Clark, Bancroft, and Stone (1967).

In conclusion, the experiments reported here, even though preliminary, have shown that Mössbauer studies with the high-pressure diamond-anvil cell are feasible and should be most useful for interpreting phenomena in iron-containing minerals within the earth.

SOLUBILITY MEASUREMENT BY DIFFERENTIAL THERMAL ANALYSIS

M. Rosenhauer

Differential thermal analysis (DTA) is a convenient method for studying reversible, nonquenchable thermal effects.

It has been widely used in studying phase relationships in one-component and multicomponent systems, recently reviewed by Gutt and Majumdar (1972). Application to silicate systems has been rare because of notoriously slow reaction rates. Nevertheless, some of the major rock-forming minerals exhibit either nonquenchable polymorphism, for example low Ca-pyroxenes (Schwab and Jablonski, 1973; Smyth, 1974a), or rapid nucleation rates, as evidenced by the inability to quench forsterite melts or diopside melts in the presence of volatiles to glass. Because of the wide field of potential application of DTA to rock-forming minerals, interpretation of DTA signals in binary systems is reviewed, and a method for tracing isopleths and estimating solubilities is developed.

General explanations of cooling curves in binary systems have been given by Ricci (1951) and Rhines (1956). Etter (1963) has discussed the interpretation of DTA curves obtained on heating. His results have been directly applied to a model binary system, A - H_2O (Fig. 8), with a refractory component A , to illustrate how the differential signal changes with the composition of the sample when it is linearly heated in a DTA apparatus. In the pure substance A , a single endothermic effect is observed on melting. For compositions between A and x_E , DTA signals are characterized by the appearance of a broad melting peak with a clearly distinguished first maximum and a flat, less pronounced second maximum. The apparent two extrema on the DTA curve reflect the variable amounts of melt produced between the solidus and the liquidus temperature. This relationship (between percentage of melt and temperature) is shown diagrammatically for a number of compositions in the model system A - H_2O (Fig. 8). Comparison of these curves with schematic DTA signals (Fig. 8) makes it evident that the first maximum on the melting peak originates at the eutectic. The associated latent heat is linearly related to the

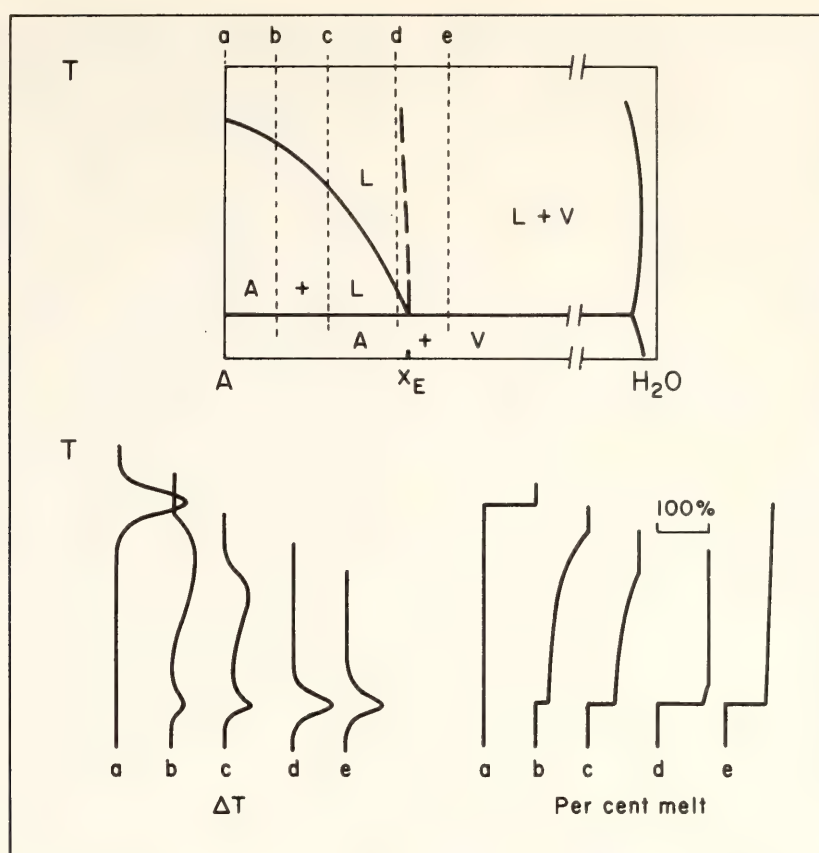


Fig. 8. Model system A-H₂O with schematic traces of DTA signals and percentage of melt for different chemical compositions (partly after Etter, 1963).

composition, assuming ideal mixing, with a maximum value at the eutectic point. Melting behavior in the divariant field $A + L$, where the remaining crystalline phase A melts continuously over the whole temperature interval, is different, the amount of melting being dependent upon the geometry of the liquidus. For DTA measurement this field of the phase diagram is accessible only if the heat consumed by melting exceeds that dissipated into the sample through the surroundings. In a number of cases the amount of melting in this field can be increased by increasing the heating rate to such an extent that the latent heat in the sample accumulates until the liquidus is reached. The resultant DTA signal shows a steady rise with a very distinct break after melting is completed. In practice, however, the shape of the DTA signal is also significantly influenced by temperature gradients and the overall cell arrangement. Definition of temperatures on the DTA curve can be

arbitrary because there is no unequivocal relationship *a priori* between those temperatures defined on the DTA curve and a physicochemical parameter such as the melting temperature. Such relations can be established only by experiment. In order to provide a common basis for relating independently obtained data, the International Confederation for Thermo Analysis has recommended definition of the onset temperature, T_o , and the peak temperature, T_P , on single-phase DTA curves. Their construction is shown in Fig. 9A. Inasmuch as there are no similar recommendations for two-component systems available at present, the onset temperature T_o , and the end temperature T_E , have been defined to characterize the width of the DTA peak; T_{P1} and T_{P2} refer to the two maxima on the DTA signal (Fig. 9B).

Phase studies in binary systems can be performed with DTA either changing the chemical composition isobarically or varying the pressure isochemically. In

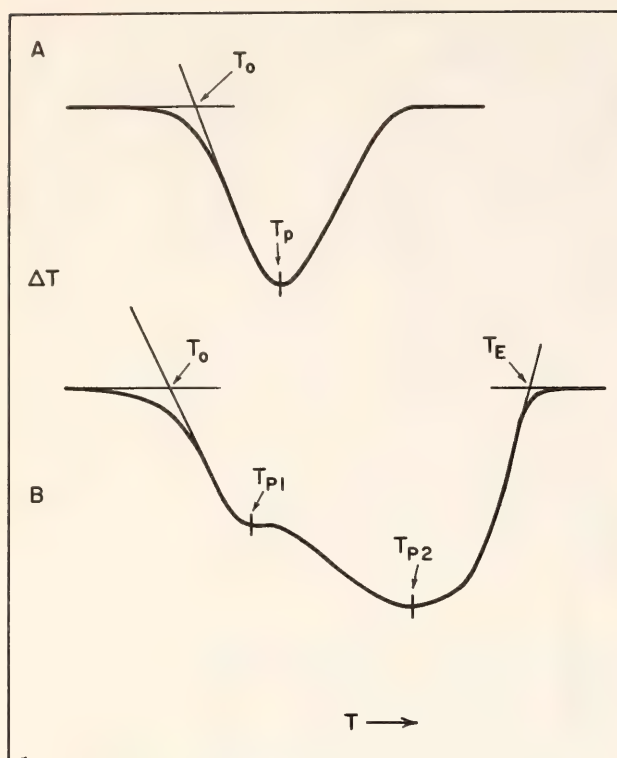


Fig. 9. (A) Definition of temperatures on DTA curves in one-component systems according to the International Confederation for Thermo Analysis. T_o , extrapolated onset temperature; T_p , peak temperature (after McAdie, 1972). (B) Definition of temperatures as used in the present study of the binary system diopside- H_2O .

the latter case, which will be the only one considered here, experience shows that commonly the extrapolated onset temperature T_o and T_{P1} can be chosen consistently, but T_{P2} cannot be located precisely in most experiments. However, a rough estimate of T_{P2} is helpful together with T_E to define an interval for the liquidus temperature. On the DTA signal, T_E represents a point at which temperature equilibrium between sample and reference is reestablished and therefore gives an upper limit for the liquidus temperature. The plot of T_{P1} as a function of pressure and temperature gives agreement with the peak temperatures in H_2O -saturated runs, which are interpreted as solidus temperatures (Rosenhauer and Eggler, this Report). The maxima T_{P2} and T_E , on the other hand, contour the lower and upper temperature limits for the liquidus isopleth. Therefore,

the intersections of the solidus with the lines through T_{P2} and T_E bracket the saturation pressure, which can be related, by means of the known chemical composition of the sample, to the solubility of the volatile phase in the melt.

The experimentally determined values of T_{P1} , T_{P2} , and T_E for 4 wt % H_2O in diopside melt are presented in Fig. 10. The value obtained for the saturation pressure is 1.35 ± 0.45 kbar. The indicated uncertainty is taken from the uncertainty of the liquidus isopleth, assuming that this introduces the largest error into the measurement. Other solubilities of H_2O in the system diopside- H_2O have been obtained in this way and are discussed by Rosenhauer and Eggler (this Report). Extension to more complex mixtures of volatiles and other non-quenchable silicate melts, such as Mg_2SiO_4 and Ca_2SiO_4 , is possible.

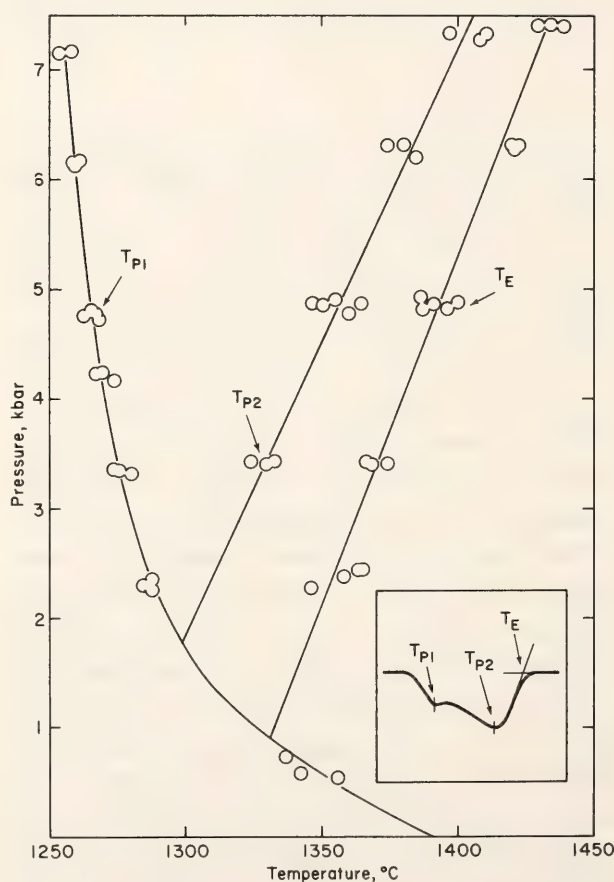


Fig. 10. Experimental results for 4 wt % H_2O in diopside melt. Represented temperatures are defined in the inset. Saturation pressure is given by the intersection of lines through T_{P2} and T_E with the solidus curve.

STUDIES ON THE HIGH-PRESSURE
POLYMORPHISM OF ANALCITE BY POWDER
X-RAY DIFFRACTION AND DIFFERENTIAL
THERMAL ANALYSIS METHODS

M. Rosenhauer and H. K. Mao

Analcite is a common mineral in rocks in association with other zeolites. The crystal structure, based on cubic space group $Ia3d$, was determined by Taylor (1930) and confirmed by Ferraris, Jones, and Yerkess (1972). Several conflicting observations on analcite have been reported, however, that are not compatible with a cubic symmetry, such as birefringency and the appearance of some weak reflections (200, 411, 300) violating the $Ia3d$ space group. It has been suggested that the birefringency is associated with internal lattice strain (Stewart, 1941) or the ordering of the silicon and aluminum atoms, which are usually assumed to be randomly distributed (Taylor, 1930). An additional complication was introduced when Yoder and Weir (1960) found in their compressibility measurements a reversible, non-quenchable phase transition at 8.4 kbar and room temperature for a very pure natural analcite from Golden, Colorado. Although this sample showed birefringency after the transition, the powder x-ray diffraction pattern was unchanged. Unfortunately, attempts to establish the identity of the high-pressure phase by powder x-ray diffraction, using a beryllium high-pressure vessel, were unsuccessful, and the relation of this transition to other observed deviations from ideal analcite remained to be studied.

Experiments reported here were undertaken to test whether a change in the powder x-ray diffraction pattern of analcite above and below the transition point is detectable and whether the high-pressure phase has some relationship to a noncubic analcite from Låven, Norway, which has been described as having only traces of K and Ca (Coombs, 1955, p. 701). For this purpose an analcite from Golden, Colorado, kindly provided

by H. S. Yoder, Jr., has been examined at room temperature by the powder x-ray diffraction method, using a diamond-anvil, high-pressure cell (Bassett, Takahashi, and Stook, 1967) with monochromatic Mo radiation. No internal standard was used in the present study, to avoid possible interference with the unknown high-pressure phase. X-ray diffraction lines were recorded on a cylindrical film of 50 mm radius; exposure time was 230 hours. In order to establish nearly hydrostatic conditions, H_2O was used as a pressure transmitting medium. One powder pattern was obtained under approximately 10 kbar pressure, and a second, at 1 atm after the pressure was released without the sample being changed. The d values of both powder x-ray diffraction patterns are given in Table 2. The 1-atm values have been indexed on the basis of a cubic unit cell and show no significant deviation from cubic analcite. The high-pressure phase of analcite is clearly distinguished by the presence of splitting and the appearance of new lines. Comparison of the high-pressure pattern with the powder pattern of analcite from Låven (Coombs, 1955), also presented in Table 2, shows considerable similarity. Two new lines correspond to reflections 420 and (411, 300); the latter are forbidden in space group $Ia3d$ for cubic analcite. Two other lines probably originate from splitting of 332 and 431, also observed in the Låven analcite. Coombs (1955) suggested that in the Låven analcite, a cubic cell was distorted into trigonal or nearly trigonal symmetry where the $h00$ planes become rhombohedral. Whether the same distortion occurred in the high-pressure phase cannot be stated at present because only two split reflections are observable. However, it appears reasonable to assume that the cubic symmetry of the Golden analcite has been reduced under pressure to lower symmetry rather than changing into another cubic space group. It is also possible that some reflection

TABLE 2. *d* Values for Analcite

<i>hkl</i> †	Golden, Colorado				Låven, Norway (Coombs, 1955)	
	1 atm*		10 kbar		Int	<i>d</i> (Å)
	Int‡	<i>d</i> (Å)	Int‡	<i>d</i> (Å)		
(200)					2	6.88
211	8	5.60	8	5.56	8	5.61
220	4	4.85	3	4.82	4B§	4.85
321	2		3	3.64	3B	3.64–3.67
400	10	3.43	10	3.38	10	3.43
(411, 330)			1	3.21	<1	3.24
420			3	3.05	2	3.08
					<1	3.06
332	6	2.92	5	2.91	7	2.929
			2	2.85	3	2.896
422					2	2.804
					1	2.779
431 (510)	2	2.69	2	2.69	4	2.696
			2	2.59	2	2.673
521	3	2.50	4	2.49	5	2.506
440	2	2.42			2	2.434
					2	2.412
(530, 433)					<1B	2.36
(600, 442)					1	2.290
611, 532	2	2.23	2	2.21	3B	2.217–2.229

* After pressure was released.
† Indices in parentheses are for cubic analcite reflections forbidden in the space group *Ia3d*.
‡ Relative intensities estimated by eye.
§ B, broad reflection.

may have been obscured by the presence of ice-VI, and this possibility must be checked in subsequent runs.

In order to establish the pressure dependence and the transformation enthalpy of the transition, high-pressure DTA experiments have been performed in the pressure range 8–10.5 kbar. The DTA apparatus is similar to that described by Yoder (1950) but has been updated in some respects (Rosenhauer and Eggler, this Report). In three successful high-pressure runs more than 50 measurements of the inversion temperature were obtained. Values for the peak temperature on heating (heating rate, 20°C/min) are plotted together with the estimated uncertainty in Fig. 11. The present data confirm the high-pressure transition reported by Yoder and Weir (1960) and are in agreement, within the limits of error, with their value at 25°C. Because the slope of the transition curve

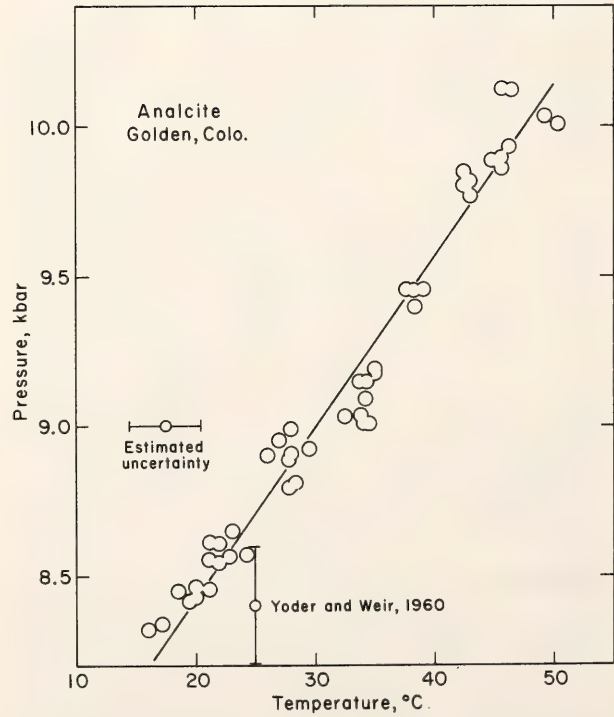


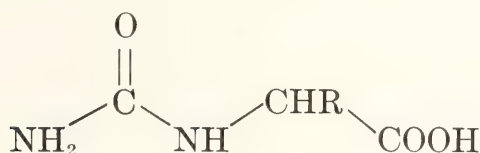
Fig. 11. Polymorphic phase transition for analcite from Golden, Colorado, into high-pressure form. Points indicate peak temperatures on heating.

is 17.4°C/kbar and the observed volume change is 0.5 cc/mol (Yoder and Weir, 1960), a transformation enthalpy of 180 cal/mol is obtained by calculation. This small enthalpy suggests that the transition is displacive, a conclusion in agreement with the observed small thermal hysteresis and the x-ray diffraction results.

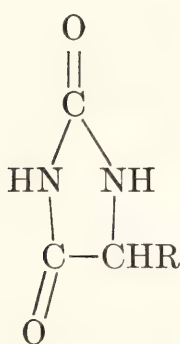
SEPARATION AND ANALYSIS OF CARBAMYL AMINO ACIDS AND THEIR CORRESPONDING HYDANTOINS BY ION-EXCHANGE AND GAS CHROMATOGRAPHY

J. R. Cronin

N-Carbamyl amino acids (I) and their dehydration products, 5-substituted hydantoins (II), may be present in extracts of carbonaceous chondrites (Cronin, this Report):



I



II

A method was needed by which these two classes of compounds could be separated from interfering substances and from each other, preliminary to their definitive analysis by gas chromatography-mass spectrometry.

These compounds can be readily separated from free amino acids by adjusting the mixture to approximately pH 2 and applying it to a 1.1 × 5.0 cm column packed with the cation-exchange resin, AG50W-X4 (Bio-Rad Laboratories, —400

mesh, H⁺ form). The carbamyl amino acids and amino acid hydantoins are eluted from the column with water, while the amino acids are quantitatively retained. The carbamyl amino acids and amino acid hydantoins can be partially separated from each other and further purified by chromatography on an anion-exchange resin. The AG50W water eluate is concentrated, made alkaline, and applied to a 1.1 × 5.0 cm column of AG 1-X8 (200–400 mesh, acetate form). The column is eluted and the carbamyl amino acids and hydantoins fractionated as shown in Table 3. A complete separation of these two groups of amino acid derivatives could not be achieved with this column by any of several different elution procedures tried. However, because the carbamyl derivatives of the acidic amino acids are completely separated from their corresponding hydantoins, the separation is unambiguous.

After drying, the trimethylsilyl derivatives of these fractions are prepared for gas chromatographic separation. A variety of silylating reagents and reaction conditions were evaluated with the *N*-carbamyl derivatives of glycine, alanine, aspartic acid, and glutamic acid. The best results were achieved with the carbamyl derivatives when the silylation was carried out in a 1:1 by volume mixture of dry acetonitrile and bis (trimethylsilyl) trifluoroacetamide (BSTFA) containing 1% trimethylchlorosilane. The reaction mixture was briefly immersed in the ultrasonic generator to promote solution of the carbamyl derivatives and promptly injected into the gas chromatograph. Optimal results were obtained with the amino acid hydantoins employing a 1:1 by volume mixture of dry acetonitrile and BSTFA and reaction at room temperature. The silylated products obtained under these conditions were analyzed by GC mass spectrometry and found to be disilyl derivatives of glycine and alanine hydantoins and trisilyl derivatives of aspartic and glutamic acid hydantoins.

TABLE 3. Separation of Carbamyl Amino Acids and Hydantoins by Anion Exchange Chromatography

Eluant	Volume (ml)	Content
(1) 0.1 <i>M</i> pyridine	25	Extraneous neutral materials
(2) 0.1 <i>M</i> pyridine-acetate, <i>pH</i> 5.5	50	Hydantoins of the neutral amino acids
(3) 1.0 <i>M</i> acetic acid	100	Hydantoins of the acidic amino acids (aspartic and glutamic acids) and carbamyl derivatives of the neutral amino acids.
(4) 0.5 <i>M</i> HCl	25	Carbamyl derivatives of the acidic amino acids

Various columns, supports, and stationary phases were evaluated using these trimethylsilyl (TMS) derivatives. The best results were obtained for the TMS-*N*-carbamyl amino acids using a 1/8 in \times 10 ft glass column packed with 3% SE-30 (methylsilicone substrate). The TMS-*N*-carbamyl amino acids were found to be subject to decomposition when their gas chromatographic separation was attempted on several other systems. The TMS-hydantoins of glycine, alanine, aspartic and glutamic acids were run on the SE-30 column; however, this procedure failed to resolve TMS-hydantoins of glycine and alanine. Excellent resolution of all four TMS-hydantoins was achieved with a 1/4 in \times 6 ft glass column packed with 3% OV-17 (methylphenylsilicone substrate). The TMS-hydantoins were more stable than the TMS-*N*-carbamyl amino acids.

This analytical scheme will be useful to search for carbamyl amino acids and 5-substituted hydantoins in aqueous extracts of carbonaceous chondrites (e.g., Murchison).

THE PRODUCTION AND PREPARATION OF ^{205}Pb FOR USE AS A TRACER FOR ISOTOPE DILUTION ANALYSES

T. E. Krogh and G. L. Davis

In the usual isotope dilution analysis for lead and uranium in a mineral it is necessary to decompose the mineral, convert the product to a soluble form,

add uranium tracer, and aliquot the solution into two portions. One portion is used to determine the isotopic composition of the lead; the other portion is equilibrated with a known amount of lead tracer and analyzed to provide the concentrations of the isotopes of lead. Errors arise if the solution is not perfect, for example, when it contains a trace of precipitate. The aliquotted portions then would not be representative of the whole, and the parent-daughter ratios would be in error.

The use of a tracer of ^{205}Pb , an isotope not found in natural materials and having a relatively long half-life of 1.4×10^7 years, eliminates the need for aliquotting the solution. The determination of both the isotopic composition and the concentration of lead can then be accomplished with a single analysis. If a mixed tracer of ^{205}Pb and ^{235}U is added to the sample before dissolution, the tracer will equilibrate with the sample during decomposition. If a precipitate appears later, the relationship of the tracer to the sample would not change. Ages determined in this way are all referred to the ratio of uranium to lead in the tracer solution and are not affected by weighing errors or changes due to evaporation of the tracer during storage.

Only recently has the use of ^{205}Pb as a tracer become practicable. Isotopic analysis of nanogram, rather than microgram, quantities is now routine so that the amount of tracer required, and consequently the cost per determination, has

been reduced by a factor of 1000. Furthermore, ^{205}Pb has not until now been produced with a sufficiently low contamination by ^{204}Pb . For example, the best ^{205}Pb tracer currently available (Holifield National Laboratory) contains 30% ^{204}Pb . The new tracer described here, produced in conjunction with the Holifield National Laboratory, has a content of less than 0.001% ^{204}Pb . This low content will not mask the amount of ^{204}Pb in the samples.

Production and purification. A target of ^{206}Pb was exposed to a 22 MeV proton beam. Some ^{205}Bi is formed by a p , $2n$ reaction and decays to ^{205}Pb with a 15-day half-life. The procedure used was identical with that described by Brown and Callahan (1975), who made carrier-free ^{206}Bi for medical applications using a ^{207}Pb target. A final purification step was added using a 0.5 ml, 2.5 cm Teflon anion-exchange column containing AG 1-X8 resin, 200–400 mesh, in the chloride form (Bio-Rad Laboratories). Tests using ^{210}Pb - ^{210}Bi tracer with approximately 50 μg of lead and bismuth as carrier, showed that all the lead could be removed from the column in the first 4 ml of wash and that a total of 15 ml of 6.2 HCl did not cause breakthrough of bismuth. The column was precleaned in

a laminar-flow air hood, using about 20 ml of ultraclean water and 6.2 HCl. A total volume of 2 ml of 6.2 HCl was added during the loading of the column in a hot cell at Holifield National Laboratory. Three successive washes (3, 3, and 2 ml) were then added to remove the small amounts of background and target lead remaining with the ^{205}Bi . A check for activity in the final drop of each wash indicated no detectable breakthrough. Isotope dilution analysis of the loading solution combined with the first wash indicated 4 μg of ^{205}Pb , 0.65 μg of ^{208}Pb , and 2.3 μg of ^{206}Pb , the last two from contamination and target. The ratio of ^{205}Pb to ^{204}Pb in the wash was 250 and the ratio of ^{205}Pb to ^{206}Pb was estimated at 20 from the activity of an aliquot of the starting material. The lead on the column after decay of the ^{205}Bi will have a ratio of ^{205}Pb to ^{204}Pb of about one million if the expected yield and column blank are achieved. Considering contamination from the bottle and reagents during preparation of the final tracer solution, a value for this ratio between 10^4 and 10^5 is expected. A recent measurement here of a 60 ng portion of the ^{205}Pb indicates a ratio of ^{205}Pb to ^{204}Pb in excess of 200,000 and a yield of 8.8 μg ($\pm 15\%$) of ^{205}Pb .

METASOMATISM AND METAMORPHISM

BIMETASOMATISM RESULTING FROM INTERGRANULAR DIFFUSION: MULTIMINERALIC ZONE SEQUENCES

J. D. Frantz and H. K. Mao

A mathematical model suitable for describing sequences of monomineralic reaction zones occurring by the diffusion of two aqueous solutes through an intergranular fluid was discussed by Frantz and Mao (*Year Book* 73, pp. 384–392). Many natural bimetasomatic columns, however, result from transport of more than two solutes and may involve both diffusion and infiltration. Such systems

commonly consist of a combination of both multimineraleic and monomineralic zones and because of the diversity of possible zone sequences, offer great opportunities for evaluating the importance of the various transport mechanisms and the relative magnitudes of their controlling parameters.

Consider reaction columns that can be represented by the system $\text{CaO-MgO-SiO}_2\text{-H}_2\text{O-CO}_2$. Metasomatism of chert nodules in dolomitic limestone is one example. Schematic solution compositions (experimental mineral-solution data are not yet available for this sys-



Fig. 12. Triangular diagram showing solution compositions in equilibrium with quartz, talc, tremolite, forsterite, magnesite, dolomite, calcite, diopside, and wollastonite in the system $\text{CaO-MgO-SiO}_2\text{-H}_2\text{O-CO}_2$. The invariant points, univariant curves, and divariant fields are projections of the saturated solution surface projected through the H_2O apex with constant CO_2 . See text for additional details.

tem) projected from H_2O onto the CaO-MgO-SiO_2 plane with X_{CO_2} externally controlled are shown in Fig. 12. The diagram shows the topology for the system at 650°C , 2 kbar, with the mole fraction of CO_2 equaling 0.5. Using Fig. 12, a variety of possible reaction-zone sequences can be deduced between the stability fields of quartz and dolomite. These can be entirely bimineralic sequences such as path *a*, entirely monomineralic as shown by path *b*, or a mixture of bimineralic and monomineralic zones as seen in path *c*. The sequence and mineralogy of the reaction zones are fixed by the controlling transport mechanism and its accompanying parameters. In this report, the authors describe a method for predicting such reaction se-

quences, which occur by intergranular diffusion, infiltration, or both.

Theory

Consider the following equation describing the flux of component *i* (J_i) resulting from both diffusion (2nd term) and infiltration (3rd term) of material in an intergranular fluid:

$$J_i = -\beta\tau D_i^* \nabla c_i + \beta V c_i, \quad (1)$$

where D_i^* , β , τ , V , and c_i are the diffusion coefficient, the porosity, the tortuosity factor, the mean velocity of the fluid, and the concentration of the *i*th fluid component, respectively. The growth or loss of a solid phase resulting from material transport can be related to changes

in the fluxes of the fluid components within the intergranular film. Frantz and Mao (*Year Book* 73, pp. 384-392) demonstrated that the fluxes of the aqueous species change both within the reaction zones and at boundaries between the zones. Within a reaction zone where p phases coexist, the changes in the fluxes in infinitely small volumes are continuous and can be related to solid changes by a set of n mass-balance equations of the following form (n equals number of aqueous species):

$$\nabla J_i = -D_i \nabla^2 c_i + v \nabla c_i = \partial c_i / \partial t + \sum_{j=1}^p a_{ij} N_j, \quad (2)$$

where a_{ij} is the stoichiometric coefficient of the i th component in the j th phase, N_j is the rate of growth of phase j per unit volume, and t is time. The term v (volume flux) is equal to βV and $D_i = \beta \tau D_i^*$ as seen with reference to Equation 1. With the assumption of steady-state solution concentration profiles, Equation 2 can be reduced to the following:

$$-D_i \nabla^2 c_i + v \nabla c_i = \sum_{j=1}^p a_{ij} N_j. \quad (3)$$

At zone boundaries, the gradients in concentrations are discontinuous and the changes in fluxes must be considered across a plane normal to the direction of transport:

$$\Delta J_i = -\Delta(D_i \nabla c_i) + \Delta(v c_i) = \sum_{j=1}^p a_{ij} N_j^*, \quad (4)$$

where N_j^* is the rate of production of j th phase per unit area and Δ denotes the difference of the quantity across the boundary. It can be shown that the concentration profiles cannot be discontinuous at zone boundaries because the diffusion flux would be infinite. Therefore, $\Delta(v c_i) = 0$ and equations of the form of (4) reduce to the following:

$$-\Delta(D_i \nabla c_i) = \sum_{j=1}^p a_{ij} N_j. \quad (5)$$

In addition to n equations of the form of (3) or (5), the assumption of local equilibrium provides p additional mass-action equations of the following form (p equals the number of phases present at any point x):

$$\prod_{i=1}^n c_i^{a_{ij}} = K_j, \quad (6)$$

where K_j is the solubility constant of the j th phase.

Assuming that the porosity, tortuosity, diffusion coefficients, volume flux, stoichiometric coefficients, and solubility constants are known, there are $n + p$ equations of the form of (3) and (6) or (5) and (6) and $n + p$ unknowns ($c_1, c_2, \dots, c_n; N_1, N_2, \dots, N_p$). Thus, sufficient equations exist to evaluate production or loss of the solid phases at every point in the reaction column. These sets of equations are solved by first calculating the concentration profiles, using a set of $n - p$ mass balance equations in which the solid-phase production rates (N_j) were eliminated (derived from equations of the form of Equation 3) with a set of p mass-action expressions of the form of (6). The concentration profiles are then related to the solid growth rates using equations of the form of (3) and (5). These sets of equations and the proposed scheme of solution are sufficient for the determination of zone sequences, their mineralogies, modes, and thicknesses in systems with any number of components and phases.

Qualitative Aspects of Boundary Growth

As seen by inspection of Fig. 12, there are numerous possible reaction paths in multicomponent bimetasomatic systems. It is possible, however, to eliminate some of these, using theories derived from the equations of the last section. Consider a boundary between two reaction zones with p coexisting phases. In the zone where the j th phase is stable, the product

of the concentrations raised to the powers of their stoichiometric coefficients (w_j) is equal to the solubility constant:

$$w_j = \prod_{i=1}^n c_i^{a_{ij}} = K_j. \quad (7)$$

In a zone where the j th phase is not stable, however,

$$w_j = \prod_{i=1}^n c_i^{a_{ij}} < K_j. \quad (8)$$

Calculating the gradient of w_j in the zone in which the j th phase is not stable,

$$\nabla w_j = \sum_{i=1}^n (a_{ij}/c_i) \nabla c_i, \quad (9)$$

where $\nabla w_j > 0$ when the boundary is approached from smaller x and $\nabla w_j < 0$ when it is approached from larger x . Two types of phases exist at zone boundaries—common phases and singular phases. A common phase is stable on both sides of the boundary, but a singular phase is stable on only one side. Considering Equation 9 at the zone boundary,

$$\Delta \nabla w_j = \sum_{i=1}^n (a_{ij}/c_i) \Delta \nabla c_i, \quad (10)$$

where $(\Delta \nabla w_j) < 0$ if the j th phase is singular and $(\Delta \nabla w_j) = 0$ if it is common. Combining equations of the form of (10) with mass-balance equations of the form of (5), one finds that at the boundary, if all diffusion coefficients are positive,

$$\sum_{j=1}^p (\Delta \nabla w_j) N_j^* > 0. \quad (11)$$

Considering the acceptable values for $(\Delta \nabla w_j)$ for both singular and common phases, the following conclusion is reached. a. *At least one of the singular phases disappears at a zone boundary.* Also derivable from Equations 5 and 10 is the following: b. *If all stoichiometric coefficients of the boundary phases are positive and common phases exist, the*

growth rate of one of the phases (common or singular) must be positive.

It is unlikely that more than one singular phase will disappear on one side of any single boundary. For this to happen, their rates of loss would have to be exactly equal to the modal abundances of phases in the disappearing zone. Normally such a boundary would not be stable and would split into additional boundaries and zones. c. *Any stable boundary should have only one singular phase in at least one of the neighboring zones. The boundary will always move toward the zone with only one singular phase.*

The application of these rules can best be seen by examining several examples. Consider first a boundary with one common phase (A) and one singular phase (B): $\overrightarrow{A|AB}$.

As a consequence of the above rules, one knows that the boundary may be stable and can move only toward the right. An example in the ternary system depicted in Fig. 12 might be a boundary in which a tremolite zone grew at the expense of a tremolite + diopside zone. Next, assume that a boundary has one common phase (C) and two singular phases (AB). The following combinations exist: $AC|BC$ $ABC|C$.

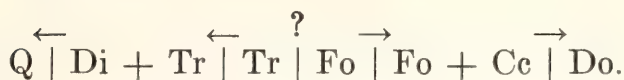
The first combination may exist; however, because both sides have only one common phase the direction of boundary movement cannot be determined. The second combination violates the third rule and is likely to split into additional zones and boundaries, e.g. $ABC|BC|C$ or $ABC|AC|C$. The boundary between the tremolite-diopside and tremolite-calcite zones in the above ternary example is of the first type. Lastly, consider that the boundary has one common phase (E) and four singular phases (ABCD). The following types of combinations exist:

$$ABCE|\overrightarrow{DE} \quad ABE|CDE \quad ABCDE|E.$$

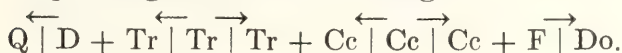
The first combination is possible and

grows to the right. The last two violate the above rules and are not stable.

Determination of the relative direction of boundary movements in multi-zone columns can be quite useful in understanding the history of a metasomatic event. Consider, for example, path *c* on the ternary diagram in Fig. 12:



By analyzing the relative movements of each boundary, one can determine within limits that the position of the original quartz-dolomite boundary is within or between the tremolite and forsterite zones. The thicknesses of the reaction zones on either side of the original boundary may give estimates of the relative magnitudes of the fluxes in either direction. When infiltration is the dominant mechanism, one would expect to see quite thin zones on the side of the boundary from which the flow originated. A profile with two or more apparent original boundaries indicates a change in the temperature-pressure conditions or a change in the transport mechanism during its evolution. An example might be the following:



The actual original boundary exists within or between the tremolite and the calcite zones. Given sufficient time, the tremolite + calcite zone will probably disappear owing to the direction of boundary movements.

An Example: a Bimineralic Zone between Two Monomineralic Zones

To illustrate the use of the equations described in the previous section, consider a system with three aqueous solutes having a single bimineralic reaction zone growing between two monomineralic zones. As described in the above section, the method employed at present is first to eliminate the solid-growth-rate variables from the mass-balance equations, and then using the mass-action

equations, to calculate solution concentration profiles for the aqueous species. Letting 2 and 3 be the phases in the bimineralic zone and 1 and 4 be the phases in the left and right monomineralic boundary zones, the growth-rate variables (N_2, N_3) are eliminated from the set of mass-balance equations. Consider the following equations represented by Equation 3:

$$-D_1 \nabla^2 c_1 + v \nabla c_1 = a_{12} N_2 + a_{13} N_3,$$

$$-D_2 \nabla^2 c_2 + v \nabla c_2 = a_{22} N_2 + a_{23} N_3,$$

$$-D_3 \nabla^2 c_3 + v \nabla c_3 = a_{32} N_2 + a_{33} N_3.$$

Elimination of the two variables N_2 and N_3 provides the following single expression relating the derivatives of the concentrations:

$$(D_1 A_1 \nabla^2 c_1 + D_2 A_2 \nabla^2 c_2 + D_3 A_3 \nabla^2 c_3) = v (\nabla c_1 + \nabla c_2 + \nabla c_3), \quad (12)$$

where A_1, A_2, A_3 are defined as follows:

$$A_1 = (a_{22} a_{33} - a_{23} a_{32}),$$

$$A_2 = (a_{13} a_{32} - a_{12} a_{33}),$$

$$A_3 = (a_{12} a_{23} - a_{13} a_{22}).$$

For systems with insignificant infiltration ($v = 0$), the integrated form of Equation 12 is

$$D_1 A_1 c_1 + D_2 A_2 c_2 + D_3 A_3 c_3 = M_1 X + M_2, \quad (13)$$

where M_1 and M_2 are integration constants. For systems with equal diffusion coefficients and significant infiltration,

$$D_1 A_1 c_1 + D_2 A_2 c_2 + D_3 A_3 c_3 = M_1 e^{vx} + M_2. \quad (14)$$

Numerical integration is required when the diffusion coefficients are unequal and infiltration is significant. Using Equation 13 or 14 together with two solubility-constant equations for phases 2 and 3, the concentration profiles of the three aqueous species can be computed. All that must be known are the diffusion coefficients, stoichiometric coefficients, volume flux, and solubility constants.

These calculations were performed for

a calcite-forsterite reaction zone between thick monomineralic zones of dolomite and tremolite, using the hypothetical data upon which Fig. 12 is based. The concentration profiles of silicon, calcium, and magnesium in solution are shown in Fig. 13A for equal diffusion coefficients and no infiltration. The profile of calcium is flat owing to the presence of the single-component phase calcite (CO_2 is assumed to be externally buffered). The profiles of magnesium and silicon show some curvature, indicating the presence of internal production of forsterite. The flat gradients in the dolomite and tremolite zones result from the assumption that they are much thicker than the bimineralic reaction zone. In Fig. 13B, profiles are drawn for equal diffusion coefficients and significant infiltration. Note that the change in the concentration profiles enhances the discontinuities in the gradients of the right boundary while reducing them at the left.

After the concentration profiles have been calculated, the thickness of the reaction zone and its mineralogical mode can be determined at any time t . The growth rates of the solids at each boundary can be calculated from the set of relations of the form of Equation 5. Consider the first boundary:

$$\Delta(-D_1 \nabla c_1) = a_{11}N_1^* + a_{12}N_2^* + a_{13}N_3^*,$$

$$\begin{aligned} \Delta(-D_2 \nabla c_2) &= a_{21}N_1^* + a_{22}N_2^* + a_{23}N_3^*, \\ \Delta(-D_3 \nabla c_3) &= a_{31}N_1^* + a_{32}N_2^* + a_{33}N_3^*. \end{aligned} \quad (15)$$

By obtaining the derivatives of the solution concentrations at the zone boundaries, N_1^* , N_2^* , N_3^* can be evaluated. A similar set of equations exists for the second boundary. To evaluate growth rates within zones, the following set of equations (similar to Equation 3) are used:

$$\begin{aligned} -D_1 \nabla^2 c_1 + v \nabla c_1 &= a_{12}N_2 + a_{13}N_3, \\ -D_2 \nabla^2 c_2 + v \nabla c_2 &= a_{22}N_2 + a_{23}N_3. \end{aligned} \quad (16)$$

Again, by using solution profile data, the production or loss of phases at every point within the bimineralic zone can be evaluated. With the knowledge of these growth rates, changes in the thickness of the bimineralic reaction zone and its mineralogical modes can be calculated as functions of time.

On the basis of the concentration profiles shown in Fig. 13A and 13B, the mineralogical modes of the calcite-forsterite bimineralic reaction zone were calculated. Figure 14 shows the calculations for systems with no significant infiltration. The solid line represents the volume mode of forsterite when $D_{\text{Si}} \ll D_{\text{Ca}} = D_{\text{Mg}}$; the long-dashed line, when

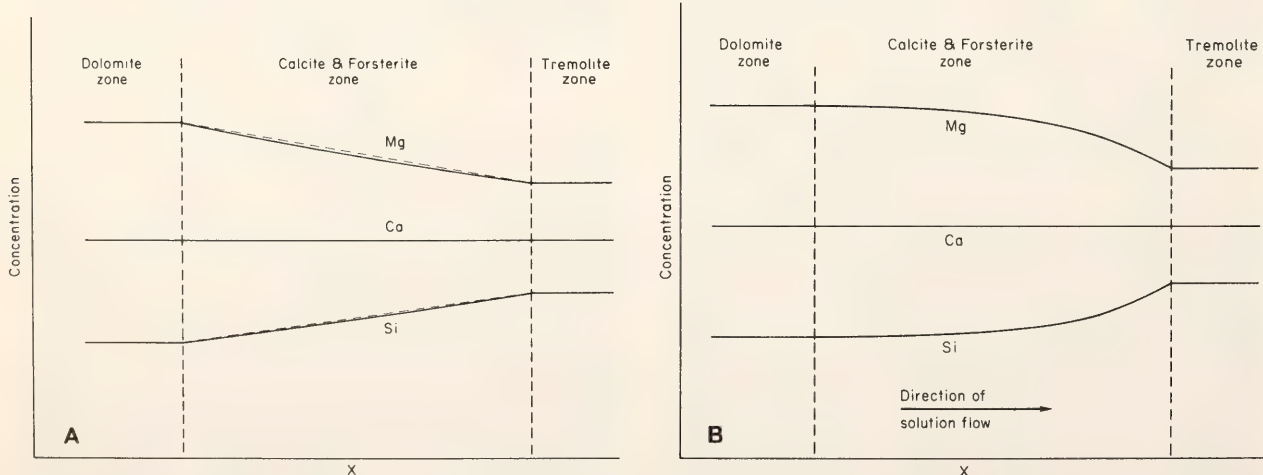


Fig. 13. Solution concentration profiles for Dol | Cc + F | Tr: (A) no infiltration; (B) significant infiltration. Dashed line present to emphasize curvature.

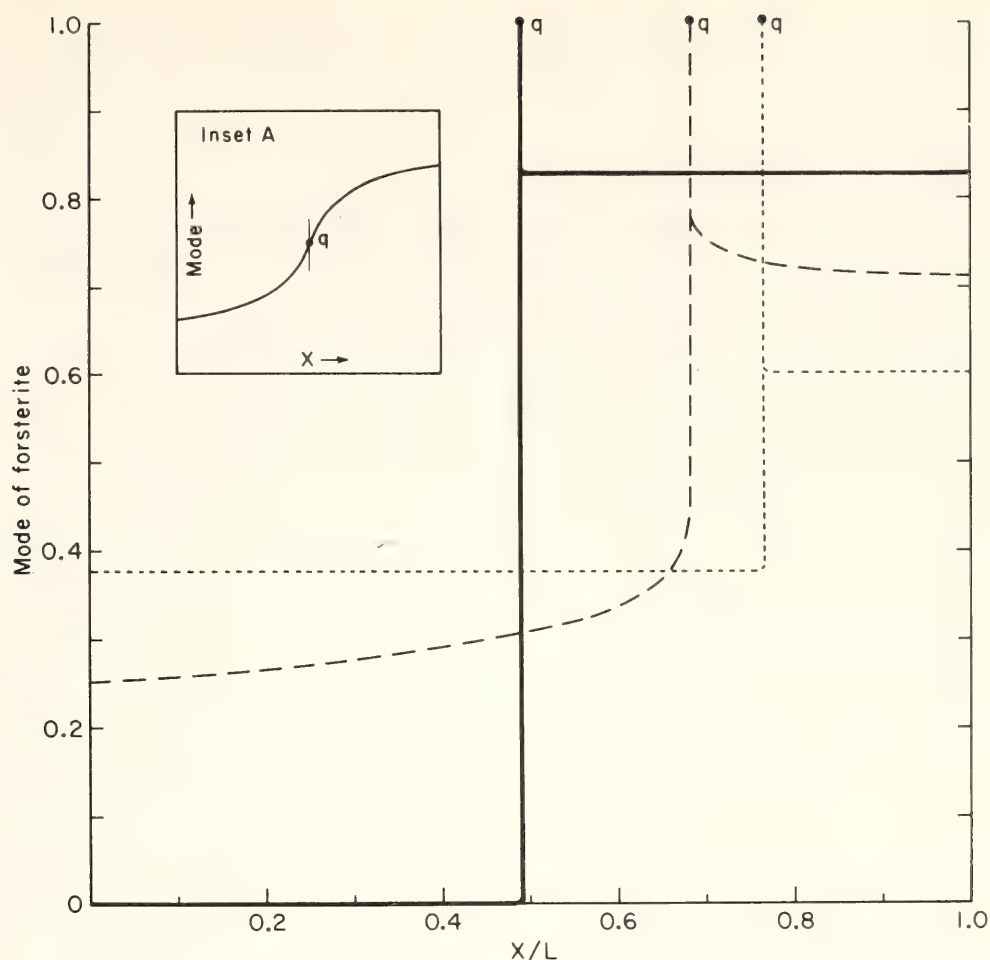


Fig. 14. Volume mode of forsterite for different values of D_{Mg} , D_{Si} in calcite-forsterite bimineralic zone. See text for details.

$D_{Si} = D_{Ca} = D_{Mg}$; and the short-dashed line, when $D_{Si} = D_{Ca} \gg D_{Mg}$. The break in the mode gradients represents the original dolomite-tremolite boundary at $t = 0$. Note that when the D_i 's are very different, the interior modes reflect the growth rates of the two minerals at the boundaries. For equal diffusion coefficients, however, the modes that resulted from boundary growth are significantly altered by internal production of forsterite. In all cases the mode profiles on either side of the original boundary vary continuously, meeting with a mode that is equal to the ratio of internal production of forsterite and calcite at the original boundary (points q in Fig. 14). Because the calcite in this case does not precipitate internally, the ratio is unity, thus explaining the spiked appearance. When the two reaction minerals have equal internal precipitation, the mode of either mineral might have

the form shown in Fig. 14A. Note that the relative position of the original boundary varies as a function of the ratio of the magnesium and silicon diffusion coefficients as do the boundary and internal modes. Figure 15 demonstrates the effect on the volume when infiltration is significant. Plotted are the volume modes of forsterite for different intervals of elapsed time with $D_{Si} = D_{Ca} = D_{Mg}$ and $D/\mu = 1.0$. To aid in comparison, all thicknesses were normalized to 1.0. At short times, concentration gradients are large and the growth occurs mainly by diffusion (a). As the reaction zone thickens, the gradients decrease and the importance of the volume flux increases (b, c). With increased infiltration, one can see that the first boundary moves out more slowly than the second and the original contact moves toward the left. The limiting case (d) of a relatively flat mode with no

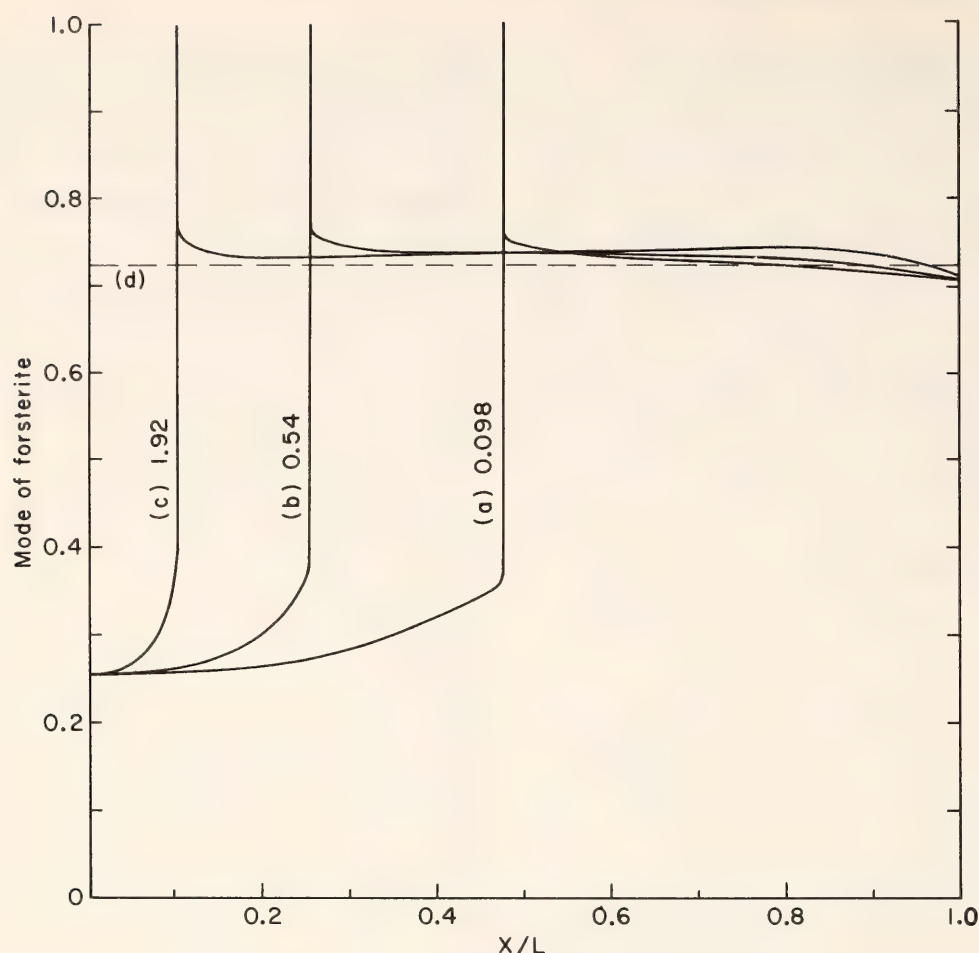


Fig. 15. Variation of volume modes of forsterite in calcite-forsterite zone as a function of time when infiltration is significant and diffusion coefficients are equal. Numbers labeled *a*, *b*, and *c* indicate relative elapsed times. See text for details.

apparent break is approached as the zone gets quite thick. Even in the limiting case, however, the boundary does move outward, still obeying rule *c* in the foregoing section.

Conclusions

Complicated metasomatic systems involving many phases and components require theoretical models if one is to be able to understand fully their evaluation. A general theory has been developed by which multicomponent systems occurring by diffusion, infiltration, or both, can be modeled. Using the equations upon which this model is based, qualitative rules concerning the relative directions of boundary movements have been derived. The importance of the internal production principle, introduced by Frantz and Mao (*Year Book* 73, p. 386), in the calculation of the modal abundances of solids has been shown.

With further accumulation of data on diffusion coefficients and solubility constants, geologists should be able to evaluate the parameters controlling the paragenesis of these types of natural systems.

A FINITE-DIFFERENCE MODEL FOR DIFFUSION AND COMBINED DIFFUSION-INFILTRATION METASOMATISM IN A MULTICOMPONENT SYSTEM

R. C. Fletcher and R. J. Vidale

A model for developing quantitative insight into metasomatic processes such as ore deposition and hydrothermal alteration must couple transport and local chemical reaction. At the same time, it must be sufficiently flexible to accommodate such features as multicomponent chemistry, variable transport parameters, and the partial attainment of local equilibrium between solid phases and pore

fluid. A finite-difference model that fulfills these conditions is illustrated here.

The complete description of the metasomatic process is obtained in the finite-difference scheme by the iterative application of the solution to a much simpler subproblem, the computation of a small increment of advance in the evolution of each of a sequence of effectively uniform volumes of rock. A finite-difference model applicable to one-component transport has been described by Fletcher and Hofmann (1974). The key to a convenient computational scheme for multiple-component transport is a formal separation of an increment of advance of the metasomatic process into two parts: a transport step and a step establishing a new local state of chemical equilibrium. This division of the entire initial and boundary value problem for a metasomatic process into tractable subproblems removes many of the restrictions on complexity of the transport and chemical process that are imposed by a more analytical approach.

The method is illustrated by modeling a simple case of one-dimensional transport, by diffusion or by combined diffusion-infiltration, with complete local equilibrium between solid phases of fixed composition and a multicomponent pore fluid. Quantitative results are obtained for transport from a reservoir (such as a fluid-filled fissure) into the assemblage muscovite-anorthite-sanidine-quartz (excess)-pore fluid (KCl, CaCl₂, HCl, in H₂O solvent), which is invariant at fixed temperature (600°C), total pressure (2000 bars), partial pressure of H₂O (approximately 2000 bars), and total chloride concentration (2 *N*). As transport progresses, zones of higher variance form and grow between the reservoir and the invariant assemblage.

In the finite-difference scheme, the concentration profiles in a slab are represented by discrete sets of values at equally spaced planes, $x_n = n\Delta x$, $n = 0, 1, \dots, N$. It is helpful to imagine that each interior plane in this set is centered

in a lamina of thickness Δx within which the concentrations may be thought of as uniform. For metasomatic transport between a reservoir of fixed composition and a uniform rock, the fluid concentrations at the surface $x = 0$ are the specified reservoir composition, and the process can be followed until the rock at x_{N-1} begins to react. The evolution of each lamina is treated in the computation. First, the total mass increments of the components transported into the lamina in a small time interval Δt are calculated. Second, the state of local equilibrium is established by treating the lamina as a closed system.

In the transport step, the total concentrations of the two independent moving components at an interior plane change by amounts $\Delta\rho_k$ in a small interval of time Δt according to the transport equation

$$\Delta\rho_k = \left[\sum_{j=1}^2 D_{kj} \frac{\partial^2 c_j}{\partial x^2} - \bar{v} \frac{\partial c_k}{\partial x} \right]_{x_n, t} \Delta t. \quad (1)$$

Here uniform and constant diffusivities, D_{kj} , and mean fluid velocity, \bar{v} , are treated. The term in brackets is evaluated from the present values of the fluid concentrations (moles per unit volume rock), $c_k(x_n, t)$, using the familiar finite-difference approximations for the partial derivatives,

$$\left(\frac{\partial c_k}{\partial x} \right)_{x_n, t} \cong [c_k(x_{n+1}, t) - c_k(x_{n-1}, t)] / 2\Delta x, \quad (2)$$

and

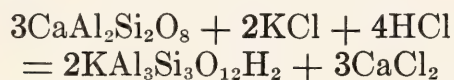
$$\left(\frac{\partial^2 c_j}{\partial x^2} \right)_{x_n, t} \cong [c_j(x_{n+1}, t) - 2c_j(x_n, t) + c_j(x_{n-1}, t)] / (\Delta x)^2. \quad (3)$$

The state of equilibrium that is consistent with the new total concentrations of components present is then calculated. As a typical chemical equilibration step for reaction in the system treated, con-

sider that the plane is part of a zone containing the univariant assemblage muscovite-anorthite-quartz-aqueous chloride solution. The increments in the concentrations of K and Ca added in the transport step are denoted $\Delta\rho_1$ and $\Delta\rho_2$ (moles per unit volume of rock). Let the fluid concentrations of these components at time t (before the transport step) be denoted by c_1^* and c_2^* ; and the concentrations of the phases quartz, anorthite, and muscovite, in moles per unit volume of rock, be denoted by s_1^* , s_3^* , and s_4^* , respectively, with s_2^* (sanidine) = 0. To obtain the new equilibrium concentrations, denoted by the same symbols with the asterisks removed, the old concentrations must be incremented by the amounts Δc_1 , Δc_2 , Δs_3 , and Δs_4 . The five increments are determined by the conditions describing the conservation of mass of the components K, Ca, Al, and Si:

$$\begin{aligned}\Delta c_1 + \Delta s_4 &= \Delta\rho_1, \\ \Delta c_2 + \Delta s_3 &= \Delta\rho_2, \\ 2\Delta s_3 + 3\Delta s_4 &= 0, \\ \Delta s_1 + 2\Delta s_3 + 3\Delta s_4 &= 0, \quad (4)\end{aligned}$$

and the requirement that the equilibrium condition for the reaction



be satisfied. The equilibrium condition for this reaction may be written in the form

$$c_2^3 - (K_2/\beta^3)c_1^2c_3^4 = 0, \quad (5)$$

where $c_k = c_k^* + \Delta c_k$, β is the porosity, K_2 is the equilibrium constant for the reaction, and salt activities at 600°C are approximated by concentrations (Vidale, this Report). This concentration of c_3 (HCl) is obtained from the condition of constant and uniform chloride normality, N_{Cl} ,

$$c_1 + 2c_2 + c_3 = \beta N_{\text{Cl}} = \beta(2). \quad (6)$$

If Δt is chosen so that $\Delta c_k \ll 1$, only linear terms in the Δc_k need be retained in Equation 5, yielding

$$\begin{aligned}3c_2^{*2}\Delta c_2 - (K_2/\beta^3)(2c_1^*c_3^{*4}\Delta c_1 \\ + 4c_1^{*2}c_3^{*3}\Delta c_3) \cong 0, \quad (7)\end{aligned}$$

where the fact that the c_k^* alone satisfy Equation 5 has been used. This, together with the four equations (4) determines the five increments. In practice, it is more convenient to expand Equation 5 to second order in the Δc_k so that a larger value of Δt may be used. The equilibration part of this model is analogous to the procedure described by Helgeson (1968).

Fluid concentration paths for pure diffusional exchange between reservoirs of different composition and a rock, R_1 , consisting of 40% (modal percent) quartz, and 20% each of sanidine, anorthite, and muscovite, are shown in Fig. 16. The fluid composition proceeds along such a path in each lamina as reaction progresses. (Each fluid composition propagates into the rock at a rate proportional to $1/\sqrt{t}$.) The sequence of compositions proceeds from the point representing the fluid phase of the invariant assemblage, along a univariant line, and across a divariant field to the reservoir composition. This sequence is independent of time for pure diffusion.

Two interesting features may be noted in Fig. 16: (1) The univariant assem-

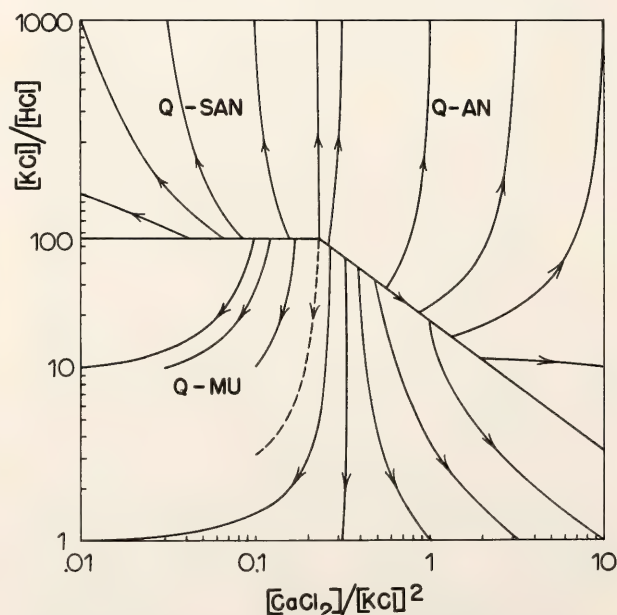


Fig. 16. Fluid concentration paths for pure diffusional transport and rock composition R_1 .

blage quartz-sanidine-anorthite is absent from the metasomatic zones for all but the special case of a reservoir with a composition of this univariant line. The same result is obtained when R_1 is replaced by a rock consisting of 55% quartz, 20% sanidine, 20% anorthite, and 5% muscovite, or when the transport mechanism is combined diffusion and infiltration. (2) The dashed path separates reservoir compositions that yield the univariant zone quartz-sanidine-muscovite and those that yield quartz-anorthite-muscovite, and marks the fluid path in a sequence in which the invariant assemblage quartz-muscovite-sanidine-anorthite is succeeded directly by the divariant assemblage quartz-muscovite.

Figure 17A shows fluid concentration profiles for pure diffusion ($D_{11} = D_{22}$, $D_{ij} = 0$, $i \neq j$, $\bar{v} = 0$), and Fig. 17B shows combined diffusion infiltration

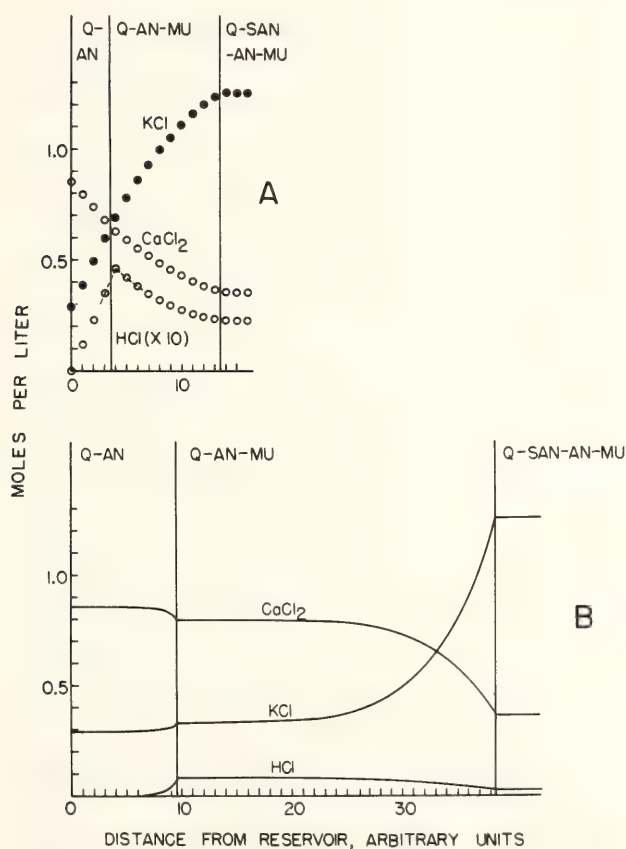


Fig. 17. Fluid concentration (moles/liter fluid) profiles for metasomatic exchange between R_1 and a reservoir with $(\text{KCl})/(\text{HCl}) = 1000$ and $(\text{CaCl}_2)/(\text{KCl})^2 = 10$ for (A) pure diffusion and (B) combined infiltration and diffusion, both after the same duration of exchange.

transport from a reservoir with $(\text{KCl})/(\text{HCl}) = 1000$ and $(\text{CaCl}_2)/(\text{KCl})^2 = 10$ into the rock R_1 after the same duration of transport. The points give the computed values of the concentrations. Because only discrete points in x are considered, the interfaces between the zones containing divariant, univariant, and invariant assemblages cannot move continuously. These increase, instead, by an amount Δx whenever a solid phase is used up in the next lamina. The solid concentrations in this lamina change continuously in time from a value characteristic of the zone to the left to values characteristic of the zone to the right of the interface. The solid concentrations at this and the adjacent laminae can be used to infer the correct position of the interface. The broad plateaus shown in Fig. 17B are characteristic of infiltration transport. Combined infiltration and diffusion leads to steady-state diffusion-damped fronts that propagate at a constant rate after an initial transient period.

The variation in modal composition across the solid zones is shown for diffusion in Fig. 18A and for diffusion-infiltration in Fig. 18B. The case including infiltration affects a broader region of the rock, but modal compositions in the zones are nearly the same. In both cases there is reaction within the univariant zone. This effect was noted by Frantz and Mao (*Year Book* 73, p. 384). The amount of reaction within the zone, as indicated by the difference in modal composition across the zone, is small relative to the amount of reaction at the zone interfaces. It leads to an increase in the amount of muscovite by 1%–2% toward the divariant-univariant interface where this solid phase disappears, and to a complementary decrease in the amount of anorthite. These variations, better shown in Fig. 19, are diagnostic of the transport mechanism. They result from diffusion of material toward and away from reactions at the zone boundary. In the idealized case of pure infiltra-

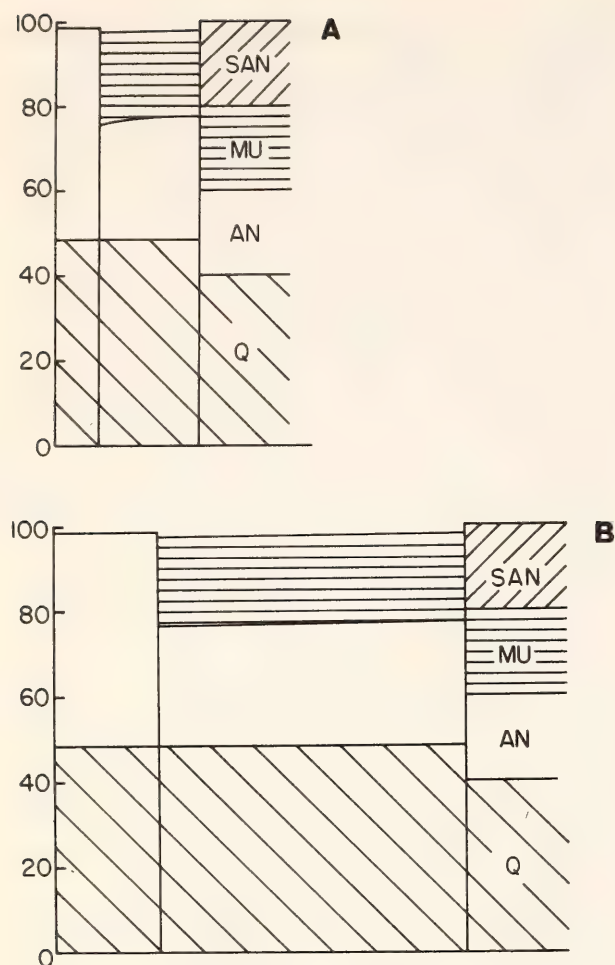


Fig. 18. Modal composition profiles for the solid phases for the same cases as in Fig. 17: (A) diffusion and (B) diffusion-infiltration.

tion transport, the solid concentrations would be uniform across the univariant zone. The solid concentration profiles, which can be observed directly in natural examples, thus contain significant information on both the composition of the reservoir fluid and the mechanism of transport.

In summary, a method has been presented for treating combined transport and reaction under conditions of complete local equilibrium. It has been illustrated by a simple example consisting of exchange between a reservoir and an adjacent rock. The transport step is sufficiently general to handle different diffusivities for the moving species, coupled diffusion, variable permeabilities, and changing infiltration rates. The chemical system can be expanded to include more components by adding equations analogous to (4), (5), and (6).

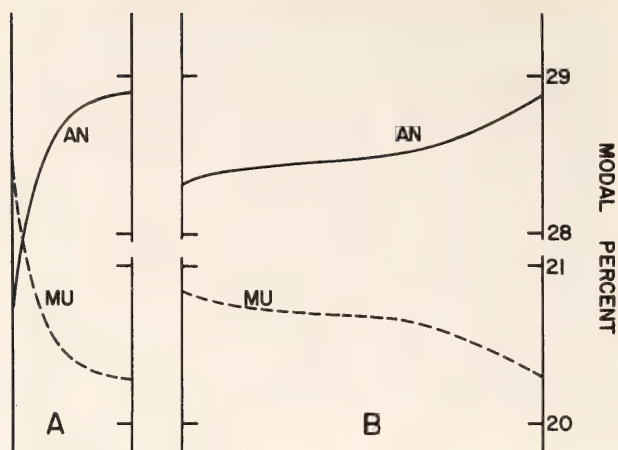


Fig. 19. Modal concentration profiles on an expanded scale for anorthite (An) and muscovite (Mu) within the univariant zones for the cases illustrated in Figs. 17 and 18.

Studies currently under way involve transport and reaction between adjacent incompatible assemblages with more components. Partial equilibration may be treated by introducing chemical reaction rates in the equilibration step.

The present version of the model applies to metasomatism in a region of constant temperature and pressure and can be used to describe a wide variety of reactions between fluid-filled fissures and country rock and between incompatible rock assemblages.

EQUILIBRIA IN THE SYSTEM PLAGIOCLASE-MUSCOVITE-PHLOGOPITE-SANIDINE-QUARTZ-AQUEOUS CHLORIDE SOLUTION

Rosemary Vidale

Recent oxygen isotope studies have suggested the existence of large cells of convecting pore solution in the earth's crust (e.g., Taylor, 1974). The solution leaches and redeposits chemical constituents as it infiltrates the rock. Any transport model that describes movement of material by such a solution requires formulation of the relevant reactions between aqueous solution and solid phase assemblages. The study presented here demonstrates the feasibility of determining and formulating equilibrium expressions for multicomponent assemblages at high

temperatures and pressures over a wide range of salinity.

The mineral assemblages chosen for this study were hypothetical Fe-free two-mica schists in the chemical system K_2O - MgO - Al_2O_3 - SiO_2 - H_2O - KCl with and without Na_2O and CaO , consisting of plagioclase, muscovite, phlogopite, sanidine, quartz, and aqueous chloride solution. Such assemblages have a wide temperature and pressure stability range and are close analogues of common igneous and metamorphic rocks. Relatively high temperatures were chosen (550° – $600^\circ C$) to accelerate reaction and to minimize ionization of solution species (Franck, 1961; Marshall, 1972); it was hoped that, because most species are molecular, aqueous solution behavior would be nearly ideal. High enough pressures were chosen (2 and 4 kbar) to favor a single solution phase (Sourirajan and Kennedy, 1962; Keevil, 1942). Chloride concentration was varied over a wide range (2 to 20 equivalents of chloride per 1000 g H_2O) to determine the extent of hydration of solution species.

The experimental procedure consisted of (1) combining 200 mg of well-mixed synthetic minerals, salts, and 100 μl of water, in a 4×40 mm platinum capsule; (2) holding the minerals and aqueous solution at pressure and temperature, usually for 28 days; (3) rapid quenching using tipping-bombs; and (4) analyzing the solution and solids. The solutions were analyzed by atomic absorption (K^+ , Na^+ , Ca^{2+} , Mg^{2+}), spectrophotometer (Al^{3+} , Si^{4+}), and titration

(Cl^-). The solids were analyzed by powder x-ray diffraction before and after equilibration to ensure that no phases were exhausted. The polyphase run products were too fine-grained for analysis of individual phase compositions by electron microprobe.

Experimental equilibria were reversed in the sense that they were approached from at least two directions with respect to solution composition. For example, one run might start with K^+/Ca^{2+} higher than the final value and another with K^+/Ca^{2+} lower than the final value. The point of convergence of all runs was considered the equilibrium solution composition. The final solution composition was approached only from the Ca^{2+}/Na^+ -rich side for assemblages including plagioclase of intermediate An content. Equilibration was too slow from the Ca^{2+}/Na^+ -poor side, as was also reported by Orville (1972).

Four independent reaction equations combined with conservation of total chloride normality were sufficient to describe the solution composition (Na^+ , K^+ , Ca^{2+} , H^+) for the assemblage plagioclase–muscovite–phlogopite–sanidine–quartz–aqueous chloride solution. This assemblage is invariant at constant temperature, total pressure, bulk chemistry, and activity of water, in the presence of excess quartz and of the two coexisting feldspar phases. One set of independent reaction equations is shown in Table 4A (these may be combined to represent different reactions) and the corresponding equilibrium constants are

TABLE 4A. Independent Reaction Equations for the System Plagioclase–Muscovite–Phlogopite–Sanidine–Quartz–Aqueous Chloride Solution

-
- | | |
|-----|---|
| (1) | $NaAlSi_3O_8 + KCl \cdot bH_2O = KAlSi_3O_8 + NaCl \cdot cH_2O + (b-c)H_2O$ |
| (2) | $10/3 KAlSi_3O_8 + MgCl_2 \cdot dH_2O = KAl_3Si_3O_{10}(OH)_2$
$+ 1/3 KMg_3AlSi_3O_{10}(OH)_2 + 6SiO_2$
$+ 2KCl \cdot bH_2O + (d-2b-4/3)H_2O$ |
| (3) | $2KAlSi_3O_8 + CaCl_2 \cdot eH_2O = CaAl_2Si_2O_8 + 2KCl \cdot bH_2O + 4SiO_2 + (e-2b)H_2O$ |
| (4) | $3/2 KAlSi_3O_8 + HCl \cdot fH_2O = 1/2 KAlSi_3O_{10}(OH)_2 + KCl \cdot bH_2O + 3SiO_2$
$+ (f-b-1/2)H_2O$ |
-

given in Table 4B. The assemblage albite-muscovite-phlogopite-sanidine-quartz-aqueous chloride solution is described by the three independent reaction equations and equilibrium constants 1, 2, and 4, and the assemblage anorthite-muscovite-phlogopite-sanidine-quartz-aqueous chloride solution by 2, 3, and 4. These assemblages are invariant at constant temperature, total pressure, and activity of water, in the presence of excess quartz and of the two coexisting feldspar phases.

Calculated products that are partial equilibrium constants are shown in Tables 5A and 5B for the albite- and anorthite-bearing assemblages, respectively. Salt concentrations have been substituted for salt activities and the mole fraction of water has been substituted for activity of water on the assumption that solution behavior is ideal. The calculated products given in the tables should be constant for these

TABLE 5A. Partial Constants from the Solution Data for the Assemblage Albite-Muscovite-Phlogopite-Sanidine-Quartz-Aqueous Chloride Solution

Temperature (°C)	Pressure (kbar)	$\frac{[\text{NaCl}]}{[\text{KCl}]}$	$\frac{[\text{KCl}]^2(X_{\text{H}_2\text{O}})^{4.67}}{[\text{MgCl}_2 \cdot 6\text{H}_2\text{O}]}$
550	2	3.5 ± 0.2	16 ± 4
550	4	3.6 ± 0.3	19 ± 6
600	2	3.0 ± 0.3	9 ± 2
600	4	3.2 ± 0.2	14 ± 4

two assemblages because the remainder of the total constants of Table 4B, the activities of solid solution components, are fixed.

The ratio $[\text{NaCl}]/[\text{KCl}]$ remains constant at the values shown in Table 5A for the albite-bearing assemblage over the range of chloride concentration from 2 to 20 equivalents per 1000 g H_2O . Therefore $(b-c)$ in K_1 of Table 4B is equal to zero. The calculated product including MgCl_2 remains constant, with changing salinity for the albite-bearing assemblage of Table 5A and the anorthite-bearing assemblage of Table 5B when the MgCl_2 -bearing solution species is formulated as $\text{MgCl}_2 \cdot 6\text{H}_2\text{O}$. (The numerical value of the product for the two assemblages differs because the solid-solution components have different activities.) The factor $(d - 2b - 4/3)$ of K_2 is thus equal to 4.67. All six water molecules have been assigned to MgCl_2 because the nexahydrate of MgCl_2 is the stable hydrate at atmospheric conditions and because it is probably also observed

TABLE 4B. Corresponding Equilibrium Constants

$$(1) \ K_1 = \left(\frac{a_{\text{NaCl} \cdot c\text{H}_2\text{O}}}{a_{\text{KCl} \cdot b\text{H}_2\text{O}}} \right) \left(\frac{a_{S_1}}{a_{S_6}} \right) (a_{\text{H}_2\text{O}}^{(b-c)})$$
$$(2) \ K_2 = \left(\frac{a_{\text{KCl} \cdot b\text{H}_2\text{O}}^2}{a_{\text{MgCl}_2 \cdot d\text{H}_2\text{O}}} \right) \left(\frac{a_{S_4} a_{S_5}^{1/3}}{a_{S_1}^{10/3}} \right) (a_{\text{H}_2\text{O}}^{(d-2b-4/3)})$$
$$(3) \ K_3 = \left(\frac{a_{\text{KCl} \cdot b\text{H}_2\text{O}}^2}{a_{\text{CaCl}_2 \cdot e\text{H}_2\text{O}}} \right) \left(\frac{a_{S_2}}{a_{S_1}^2} \right) (a_{\text{H}_2\text{O}}^{(e-2b)})$$
$$(4) \ K_4 = \left(\frac{a_{\text{KCl} \cdot b\text{H}_2\text{O}}}{a_{\text{HCl} \cdot f\text{H}_2\text{O}}} \right) \left(\frac{a_{S_4}^{1/2}}{a_{S_1}^{3/2}} \right) (a_{\text{H}_2\text{O}}^{(f-b-1/2)})$$

S_1 , KAlSi_3O_8 ; S_2 , $\text{CaAl}_2\text{Si}_2\text{O}_8$; S_3 , SiO_2 ; S_4 , $\text{KAl}_3\text{Si}_3\text{O}_{10}(\text{OH})_2$; S_5 , $\text{KMg}_3\text{AlSi}_3\text{O}_{10}(\text{OH})_2$; S_6 , $\text{NaAlSi}_3\text{O}_8$.

TABLE 5B. Partial Constants from the Solution Data for the Assemblage Anorthite-Muscovite-Phlogopite-Sanidine-Quartz-Aqueous Chloride Solution

Temperature (°C)	Pressure (kbar)	$\frac{[\text{KCl}]^2(X_{\text{H}_2\text{O}})^{4.67}}{[\text{MgCl}_2 \cdot 6\text{H}_2\text{O}]}$	$\frac{[\text{KCl}]^2(X_{\text{H}_2\text{O}})^4}{[\text{CaCl}_2 \cdot 4\text{H}_2\text{O}]}$
550	2	45 ± 3	1.72 ± 0.13
550	4	51 ± 3	1.34 ± 0.04
600	2	34 ± 10	3.26 ± 0.90
600	4	53 ± 4	2.22 ± 0.34

at higher pressures (H. K. Mao, personal communication).

The CaCl_2 -bearing solution species is formulated as $\text{CaCl}_2 \cdot 4\text{H}_2\text{O}$ to give a nearly constant value with changing salinity to the calculated product shown in Table 5B. The factor $(e - 2b)$ of K_3 is therefore 4.

Table 6 gives formulations for the complete reaction constants as shown in Table 4B. The value of K_1 has been determined from the solution data from the albite-bearing assemblages combined with activities of albite and sanidine calculated from the solvus-derived data of Thompson and Waldbaum (1969). The ΔH and ΔV of reaction have been calculated (each on the basis of two points only) for the reactions as written and are

$$\Delta H_{2 \text{ kbar}} = -5400 \text{ cal/mol} \\ (550^\circ\text{--}600^\circ\text{C}),$$

$$\Delta H_{4 \text{ kbar}} = -5000 \text{ cal/mol} \\ (550^\circ\text{--}600^\circ\text{C}),$$

$$\Delta V_{550^\circ\text{C}} = -6.6 \times 10^{-5} \text{ cal/bar-mol} \\ (2000\text{--}4000 \text{ bars}),$$

$$\Delta V_{600^\circ\text{C}} = -8.0 \times 10^{-5} \text{ cal/bar-mol} \\ (2000\text{--}4000 \text{ bars}).$$

The value of K_2 has been determined from the data on the An-bearing assemblage, assuming the activities of the solid solution components S_1 , S_4 , and S_5 to be 1. The value of K_3 has been determined from the data on the An-bearing assemblage, assuming the activities of the solid solution components S_1 and S_2

to be 1. Because of these approximate activities of the solid solution components no ΔH 's or ΔV 's have been calculated. The value of K_4 was determined at 2 kbar and $577^\circ\text{--}677^\circ\text{C}$ by Gunter, Frantz, and Eugster (1973).

The $[\text{KCl}]^2 (X_{\text{H}_2\text{O}})^{4.67}/[\text{MgCl}_2 \cdot 6\text{H}_2\text{O}]$ part of K_2 has been calculated from the data on both the albite- and the anorthite-bearing assemblages (Tables 5A and 5B). The value of K_2 must be the same for both. The numerical differences are differences in the remaining factors in the complete constant (Table 4B), that is, in $a_{S_4}a_{S_5}^{1/2}/a_{S_1}^{10/3}$. A difference would be expected because more Na^+ than Ca^{2+} enters muscovite, phlogopite, and sanidine.

The solid component activities may be compared by setting the complete constant K_2 for the two systems equal, substituting the numerical values for the part given in Tables 5A and 5B, and solving for the ratio of the activity products. The resulting ratio, given in the third column of Table 7, suggests that there is little change in solid activity with pressure but significant change with temperature as compositions move up the various solvi. This derivation of solid activity ratios illustrates a method for the evaluation of activities of solids in solid solution.

In the fourth column of Table 7, the activity of S_1 in the albite-bearing system has been calculated from the solvus-derived data of Thompson and Waldbaum (1973), substituted into the ratios of column 3, and a new ratio calculated. The activities of S_1 , S_4 , and S_5 in the anorthite-bearing assemblage might be set equal to 1 as an approximation since little Ca^{2+} enters these phases. This substitution, however, leads to the conclusion that the activity of S_4 or S_5 or both in the albite-bearing system is significantly greater than 1. Another possible conclusion is that the value for the activity of sanidine calculated from the monoclinic solvus may be too high.

TABLE 6. Complete Equilibrium Constants, $550^\circ\text{--}600^\circ\text{C}$, 2–4 kbar, T in $^\circ\text{K}$, P in bars

(1) $\log K_1 = \frac{1150}{T} + 1.6 \times 10^{-5}P - 0.97$
(2) $\log K_2 = \frac{1740}{T} + 2.8 \times 10^{-5}P - 0.52$
(3) $\log K_3 = \frac{-3150}{T} - 5.4 \times 10^{-5}P + 4.17$

TABLE 7. Activity Ratios for Solid Solution Components

Temperature (°C)	Pressure (kbar)	$\left[\frac{a_{S_1}^{10/3}}{a_{S_4}a_{S_5}^{1/3}}\right]$ Ab-bearing system	$\left[\frac{1}{a_{S_4}a_{S_5}^{1/3}}\right]$ Ab-bearing system
		$\left[\frac{a_{S_1}^{10/3}}{a_{S_4}a_{S_5}^{1/3}}\right]$ An-bearing system	$\left[\frac{a_{S_1}^{10/3}}{a_{S_4}a_{S_5}^{1/3}}\right]$ An-bearing system
550	2	0.36	0.80
550	4	0.37	0.75
600	2	0.26	0.73
600	4	0.26	0.64

S₁, KAlSi₃O₈; S₄, KAl₃Si₃O₁₀(OH)₂; S₅, KMg₃AlSi₃O₁₀(OH)₂

The complete constants, in combination with the appropriate solid solution activities, should give aqueous solution compositions for assemblages with plagioclase of intermediate An content that is in a fairly disordered structural state. A series of runs were made at 600°C and 2 kbar with 2 equivalents of chloride per 1000 g H₂O and plagioclase compositions ranging from An₂₇ to An₈₄. Equilibrium was approached only from the Ca-rich aqueous solution side. The final plagioclase composition was calculated from the bulk composition and final solution composition, assuming all Na and Ca in the solid to be in plagioclase. The solution data are summarized in Table 8. No attempt is made to evaluate complete constants because of lack of good data on phase composition and on activities of solid solution components.

Equilibrium constants of the type determined in this study are an essential part of transport models that include chemical reaction (e.g., see Frantz and

Mao, Fletcher and Vidale, this Report). A complete description of transport by aqueous fluid through a rock includes two parts: (1) the appropriate transport equations (for diffusion or for infiltration combined with diffusion) and (2) equations describing local chemical reaction. The chemical reaction includes mass balance equations, reaction rate equations, and equilibrium constant equations. Equilibrium constant equations were the object of this study.

The equilibrium constants from this work are being applied to a geologic system in which a convecting aqueous solution moves within a homogeneous rock through a succession of temperature and pressure environments. As the solution passes through each element of the rock, it leaches some mineral phases and deposits others. This model illustrates a process by which rock components can be segregated. Such a segregation process can concentrate appropriate rock components into economic ore deposits.

TABLE 8. Partial Constants from the Solution Data for the Assemblage Plagioclase–Muscovite–Phlogopite–Sanidine–Quartz–Aqueous Chloride Solution at 600°C, 2 kbar, for the Plagioclase Composition Range An₂₇ to An₈₄

$\frac{[\text{NaCl}]}{[\text{KCl}](X_{\text{Ab}})}$	$\frac{[\text{KCl}]^2(X_{\text{H}_2\text{O}})^{4.67}}{[\text{MgCl}_2 \cdot 6\text{H}_2\text{O}]}$	$\frac{[\text{KCl}]^4(X_{\text{H}_2\text{O}})^4(X_{\text{An}})}{[\text{CaCl}_2 \cdot 4\text{H}_2\text{O}]}$
1.8 ± 0.1	20 ± 6	2.6 ± 1.2

KINETICS AND MICROSTRUCTURE OF
PYROXENE EXSOLUTION

R. H. McCallister and R. A. Yund*

The need for kinetic and microstructural information for pyroxenes as a basis for interpreting cooling histories of igneous and metamorphic rocks has been emphasized by Nord *et al.* (1975). Recent studies have been made on the exsolution microstructure observed in natural pyroxenes, but few studies have been made of samples annealed under known conditions. McCallister (1974, and *Year Book 73*, pp. 392–396) has investigated the kinetics of exsolution in iron-free pyroxenes, and in this report the authors describe the microstructure in these and additional samples that were annealed below the solvus.

*Department of Geological Sciences, Brown University.

The bulk compositions of all samples lie on the $\text{Mg}_2\text{Si}_2\text{O}_6$ - $\text{CaMgSi}_2\text{O}_6$ join, and compositions are given in mol percent diopside ($\text{Di}_{54.1}$, etc.). The bulk compositions, annealing temperatures, and annealing times are shown in Fig. 20. McCallister's (1974) original compositions are shown by open squares, and annealing times were as long as 3000 hours. Compositions crystallized from glasses prepared by melting oxide mixes or gels and then annealed below the solvus are shown in Fig. 20 by solid circles, open circles, and crosses.

Crushed grain mounts of these samples have been examined by transmission electron microscopy, using either a JEM-200A operating at 200 kV (Monash University) or a JEM-7A at 100 kV (Brown University). The microstructure in samples represented by solid circles in Fig. 20 consists of irregular lamellae parallel

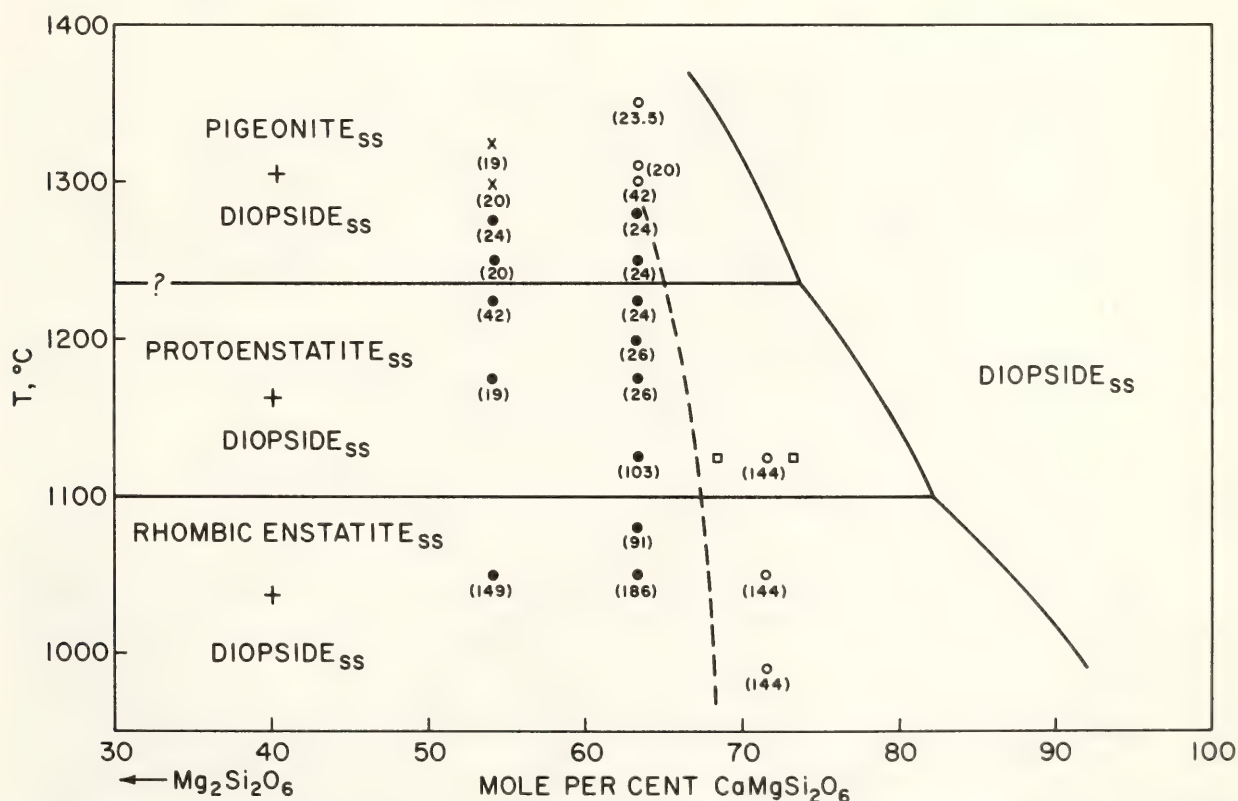


Fig. 20. Conditions of annealing experiments on the $\text{Mg}_2\text{Si}_2\text{O}_6$ - $\text{CaMgSi}_2\text{O}_6$ join. Annealing times (hours) are shown in parentheses. Irregular lamellar microstructure was observed in samples shown by solid circles; no lamellae or straight, widely spaced lamellae, in samples shown by open circles and squares. See text for discussion of samples shown by crosses. All symbols refer to initial bulk compositions. The position of the coherent spinodal is shown by the dashed line, and the phase fields are those given by Kushiro (1972b). Note that Yang (1973) showed the reaction $\text{pigeonite}_{ss} + \text{diopside}_{ss} \rightleftharpoons \text{protoenstatite}_{ss} + \text{diopside}_{ss}$ occurring at 1270°C .

to (001). A typical example of this texture is shown in Fig. 21A of sample $\text{Di}_{54.1}$ annealed at 1250°C for 20 hours. This microstructure was observed in all properly oriented fragments and is developed uniformly throughout a fragment. These lamellae appear to be perfectly coherent because all reflections on the ($hk0$) net are sharp, whereas (001) reflections show streaking or doubling. Fainter ($h + k$) odd reflections that violate the $C2/c$ symmetry are due to the inversion of the iron-free, high pigeonite lamellae during cooling. This relation is observed for samples annealed at all temperatures, indicating that the Mg-rich phase at all annealing temperatures is a high pigeonite, although the stable, strain-free, Mg-rich phase should be rhombic enstatite or protoenstatite, as illustrated in Fig. 20.

In samples represented by open circles, exsolution lamellae are either absent or rare. Lamellae are more common in many of McCallister's (1974) original samples for which the annealing times were longer. In all these samples the lamellae are also parallel to (001), but they are straight and more continuous, and their spacing appears to be related to the supersaturation. Figure 21B shows the lamellae in $\text{Di}_{68.4}$ annealed at 1125°C for 696.5 hours.

The change in the microstructure from irregular, coherent lamellae to the straight, more continuous type correlates with the kinetics of exsolution. It is suggested that the rapid exsolution that produces the irregular lamellae (Fig. 21A) occurs by a spinodal mechanism. The much slower exsolution that produces regular lamellae (Fig. 21B) is interpreted as due to nucleation and growth. Because these lamellae also appear to be coherent, the bulk compositions must lie within the coherent solvus. The solvus shown in Fig. 20 is from Kushiro (1972b) and represents a revision of the original phase equilibria given by Boyd and Schairer (1964). It probably represents the strain-free solvus for the most part; however, a careful

study to distinguish between the coherent solvus and the strain-free solvus in this system is needed. The dashed line in Fig. 20 gives the approximate location of the coherent spinodal based on the results presented here.

The position of the coherent spinodal at high temperature is problematical. Sample $\text{Di}_{54.1}$ annealed at 1300° and 1325°C (represented by crosses in Fig. 20) has a microstructure similar to that shown in Fig. 21A, except that the lamellae appear somewhat more regular. This change could be due to either coarsening of an initially irregular spinodal microstructure (Yund, McLaren, and Hobbs, 1974) or homogeneous nucleation at this high temperature and supersaturation. McCallister (*Year Book 73*, pp. 392–396) has described the contrasting behavior of the x-ray powder diffraction data for these two samples compared with the same bulk composition annealed at lower temperatures. It is also noted that the predicted temperature of the coherent spinodal (Fletcher and McCallister, *Year Book 73*, pp. 396–399) for this composition is near 1300°C . Additional samples must be examined, however, to determine accurately the position of the coherent spinodal above 1275°C .

The irregular lamellar microstructure is very similar to that observed in pyroxenes from quickly cooled rocks. The straight lamellae are similar to those in natural pyroxenes that are believed to have cooled more slowly (see, for example, Champness and Lorimer, 1971). Because of the high temperature of the miscibility gap in the Ca-rich pyroxenes, slow cooling can result in nucleation and growth before the coherent spinodal is reached. Only rapidly cooled pyroxenes, or perhaps those which enter the miscibility gap at much lower temperatures, remain homogeneous until they reach the coherent spinodal. An important objective will be to determine the extension of the coherent spinodal surface into the pyroxene quadrilateral. Also, it will be

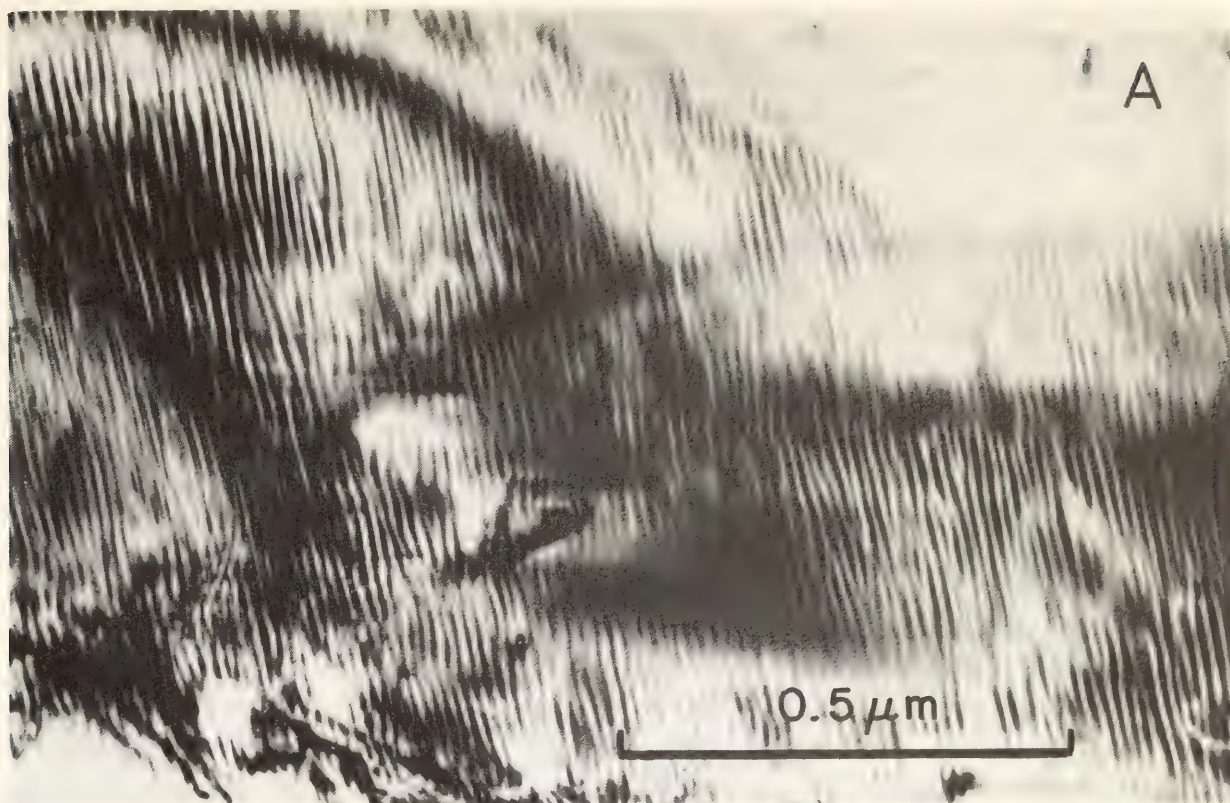


Fig. 21. Bright field micrographs of pyroxene lamellae approximately normal to crystal fragment. Taken at 200 kV. (A) Irregular lamellae in $\text{Di}_{54.1}$ annealed at 1250°C for 20 hours.

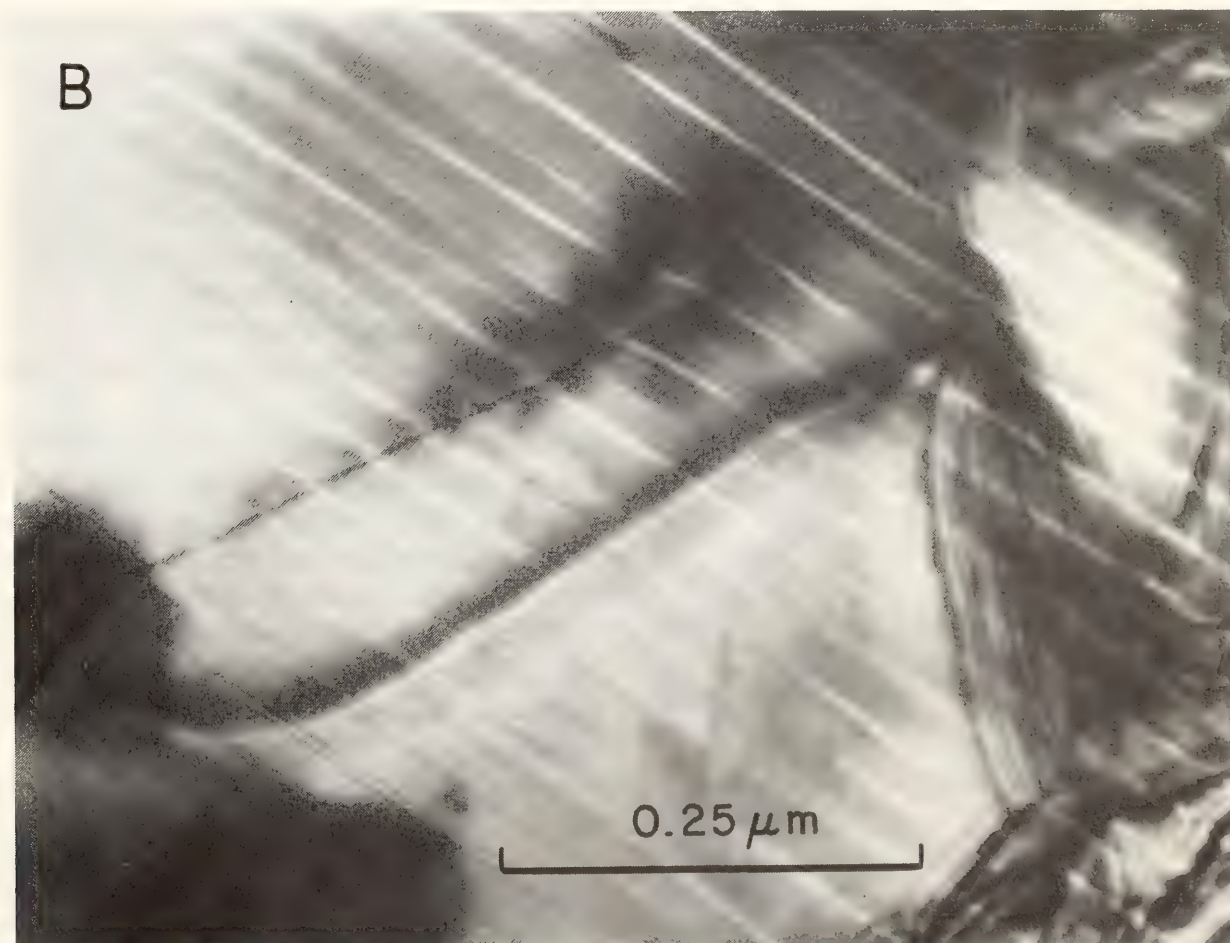


Fig. 21 B. Regular, widely spaced lamellae in $\text{Di}_{68.4}$ annealed at 1125°C for 696.5 hours.

necessary to determine whether the coherent spinodal for lamellae parallel to (100) in iron-bearing pyroxenes approximates that for (001) exsolution.

OXYGEN ISOTOPE GEOCHEMISTRY OF THE CLOUGH FORMATION, BLACK MOUNTAIN, NEW HAMPSHIRE

Douglas Rumble III, Karlis Muehlenbachs, and T. C. Hoering

The mineral assemblages of the quartzites and quartz-mica schists of the Clough Formation exposed at Black Mountain, western New Hampshire, record gradients in the chemical potentials of the volatile components H_2O , H_2 , and O_2 between adjacent sedimentary beds (Rumble, *Year Book 73*, pp. 371–380). There could not have been a pervasive fluid of uniform composition in equilibrium simultaneously with all the different mineral assemblages. If diffusion or infiltration of fluid or fluid components occurred between rock layers, it did not occur in sufficient quantity to exhaust the inherent buffer capacity of the different mineral assemblages.

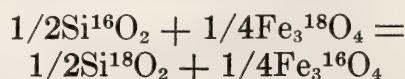
Measurement of the isotopic composition of the minerals of Black Mountain offers the opportunity to test the hypothesis of control of fluid composition by local mineral assemblages. The isotopic composition of the oxygen in minerals depends not only on temperature but also on the bulk isotopic composition of the rock and its fluid. Oxygen isotope analyses can be used to check the validity of the assumption of uniform temperature made in the paragenetic analysis (Rumble, *Year Book 73*, pp. 371–380) and to determine whether or not the different mineral assemblages could have been in equilibrium with a fluid of uniform isotopic composition.

Isotope analyses of minerals were made using the BrF_5 technique of Clayton and Mayeda (1963). Results are expressed in terms of the per mil difference in the $^{18}O/^{16}O$ ratio between the mineral and Standard Mean Ocean Water,

$$\delta^{18}O = \left(\frac{(^{18}O/^{16}O)_x}{(^{18}O/^{16}O)_s} - 1 \right) \times 1000,$$

where the subscript x refers to the unknown and the subscript s refers to the standard. The precision of the measurements is 0.2‰ for quartz and 0.3‰ for magnetite, based on duplicate or triplicate extractions. Standardization of the ^{18}O scale was made by the analysis of three oxygen-containing materials that have been measured in a number of other laboratories. These materials are (1) a synthetic quartz prepared by J. D. Frantz by quantitatively reacting a sample of Standard Mean Ocean Water (International Atomic Energy Agency, Vienna, Austria) with an excess of metallic silicon at 650°C in a sealed platinum tube under 2 kbar confining pressure of argon; (2) an aliquot of National Bureau of Standards (NBS) isotope reference material No. 28, glass sand; and (3) an aliquot of the St. Peter's sandstone, kindly supplied by H. Ohmoto. The NBS No. 28 material measured $+10.2 \pm 0.2\text{‰}$ relative to the synthetic quartz; the St. Peter's sandstone measured $+10.9 \pm 0.2\text{‰}$ relative to the same standard. These values may be compared with published analyses, which give $+10.0 \pm 0.1\text{‰}$ for NBS No. 28 (Friedman and Gleason, 1973) and $+11.02 \pm 0.2\text{‰}$ for the St. Peter's sandstone (Clayton and Mayeda, 1963, p. 48, Table 1).

The results of the isotopic analyses are presented in Fig. 22. The basis of the diagram is the ternary-reciprocal phase diagram used to display isothermal-isobaric, ion-exchange equilibria (Ricci, 1951, pp. 371–389; Orville, 1963, p. 214, Fig. 2). Its use to portray isotopic measurements is justified by the condition of isotopic exchange equilibrium,



(Urey, 1947, p. 563), which is analogous to the condition of equilibrium for ion exchange between two binary solutions in a ternary system. Tie lines join ana-

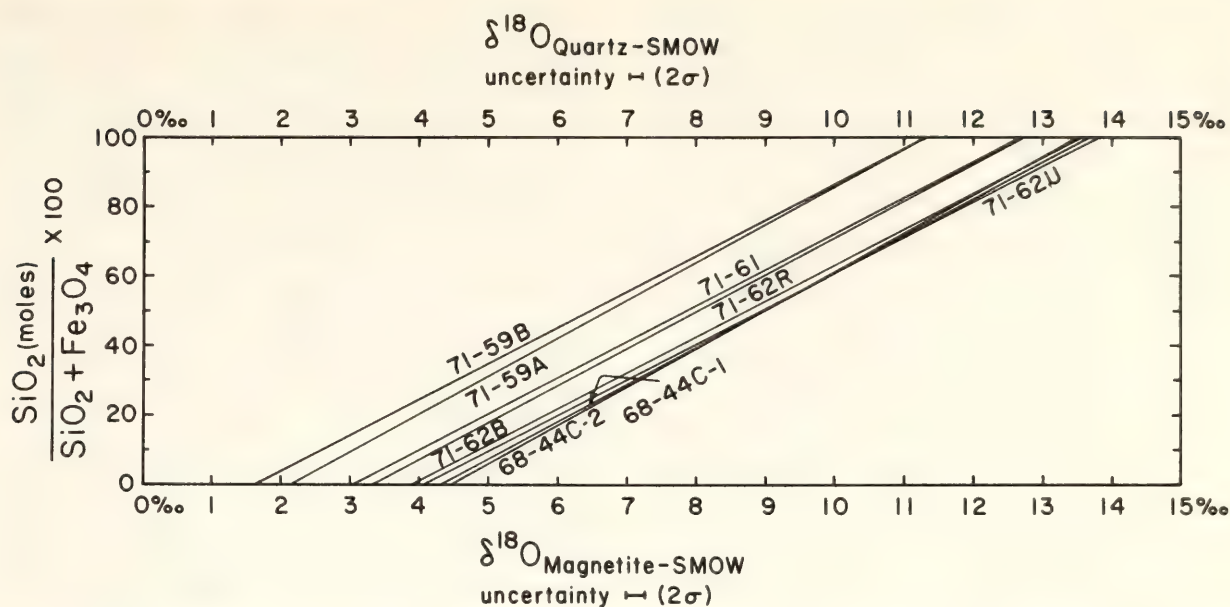


Fig. 22. Exchange equilibrium diagram showing isotopic composition of oxygen in quartz and magnetite. Horizontal axis gives $\delta^{18}\text{O}_{\text{SMOW}}$ for quartz and magnetite. Vertical axis gives mol percentage of $\text{SiO}_2/(\text{SiO}_2 + \text{Fe}_3\text{O}_4)$.

lyzed quartz and magnetite from the same mineral assemblage. The diagram has the advantage that it simultaneously displays information on the temperature of equilibration of the mineral pair and on the bulk isotopic composition of the rock. The slope of the tie lines is dependent on temperature as it is equal to $\Delta^{18}\text{O}_{\text{quartz-magnetite}}$. The relative position of the tie lines is dependent on the bulk isotopic composition of the rock. The diagram also provides graphic evidence of the attainment of isotopic equilibrium or lack thereof. Crossing tie lines indicate failure to attain equilibrium, polythermal equilibration, or both. Mutually parallel tie lines are consistent with the attainment of isotopic equilibrium under uniform temperature conditions between mineral pairs from rocks of different bulk isotopic composition. The analyses plotted in Fig. 22 show mutually parallel tie lines within the limits of error of measurement and are consistent with the attainment of isothermal isotopic equilibrium between mineral pairs of different bulk isotopic composition.

The average fractionation of ^{18}O and ^{16}O between nine quartz-magnetite pairs is equal to 9.45 ± 0.3 ($1000 \ln \alpha$). This

value corresponds to a temperature of $495^\circ \pm 10^\circ\text{C}$ according to the calibration of Bottinga and Javoy (1973, p. 257, Table 5). The uncertainty in the value of $1000 \ln \alpha$ is comparable to the analytical uncertainty; thus the assumption of uniform temperature for the Black Mountain rocks is confirmed within the limits of error of the isotopic compositions. The validity of the temperature estimate based on oxygen isotopic fractionation may be judged by comparison with mineral geothermometers. The compositions of coexisting muscovite ($\text{K}_{0.66}\text{Na}_{0.27}\text{Ba}_{0.01}\text{Fe}_{0.08}\text{Mg}_{0.01}\text{Al}_{2.91}\text{Si}_{3.03}\text{O}_{10}(\text{OH})_2$) and paragonite ($\text{Na}_{0.72}\text{K}_{0.14}\text{Ca}_{0.06}\text{Al}_{3.06}\text{Si}_{2.94}\text{O}_{10}(\text{OH})_2$) from Black Mountain give a temperature estimate of $650^\circ \pm 50^\circ\text{C}$ based on the solvus of Eugster *et al.* (1972, p. 170, Fig. 9); however, such an estimate takes into account neither the appreciable substitution of Ca in the natural paragonite nor the substitution of Fe and Mg in the muscovite. The compositions of coexisting magnetite and ilmenite are consistent with the 550° and 600°C tie lines of Buddington and Lindsley (1964), but accurate geothermometry is impossible because of the uncertainty in location of the experimental tie lines at low tem-

perature and the Mn substitution in natural ilmenite (cf. Rumble, 1973a, p. 191). The Black Mountain rocks contain kyanite and lie within 3 miles of the trace of the isobar of the Al_2SiO_5 invariant point (Rumble, 1973b, p. 2425, Fig. 1). The oxygen isotopic temperature estimates are consistent with the P - T coordinates of the Al_2SiO_5 invariant point measured experimentally by Holdaway (1971, p. 115, Fig. 5), and the muscovite-paragonite temperature estimate is consistent with the invariant point of Richardson, Gilbert, and Bell (1969, p. 266, Fig. 2).

The quartz-water fractionation curves of Bottinga and Javoy (1973) may be used to estimate the isotopic composition of the water in equilibrium with the minerals. For an equilibration temperature of 495°C the oxygen isotopic composition of water in equilibrium with the analyzed quartz samples would range in value from $+8.0\text{‰}$ for the quartz samples lowest in ^{18}O content to $+10.5\text{‰}$ for the quartz samples highest in ^{18}O content. These values lie within the field of metamorphic H_2O as described by Taylor (1974, p. 852, Fig. 9).

The results of this study of the oxygen isotopic composition of quartz and magnetite from Black Mountain are (1) the rocks retain a record of isotopic equilibration at a uniform temperature and (2) the various mineral assemblages could not have been in equilibrium with a pervasive fluid of uniform isotopic composition. Thus both paragenetic analysis and isotopic analysis lead to the same conclusion: the rocks of Black Mountain were not metamorphosed in the presence of a fluid of uniform chemical or isotopic composition.

DETERMINATION OF A PELITE PETROGENETIC GRID FOR THE EASTERN SCOTTISH DALRADIAN

Ben Harte

The geographic distribution of different mineral assemblages in regional

metamorphic rocks having a restricted range of bulk composition has long been recognized as an important guide to the nature and variation of P - T conditions during orogenesis, and therefore to the geophysical processes involved in the evolution of the earth's crust. The regional metamorphic terrain of the eastern Scottish Dalradian contains a wide diversity of pelitic mineral assemblages; it has been divided into a Barrovian area, characterized by the development of kyanite- and garnet-bearing assemblages, and a Buchan area, characterized by andalusite- and cordierite-bearing assemblages. Chinner (1966) made a valuable contribution to establishing the qualitative variation of pressure and temperature within this terrain by using the dP/dT of three isograd reactions to delineate relative isotherms and isobars. In the present study a basis for quantitatively determining P - T conditions and elucidating thermal structure is provided by constructing and fixing in P - T space a petrogenetic grid in which the whole variety of sequences of pelitic mineral zones mapped in the field are modeled.

In attempting to model regional patterns of mineral assemblages in a petrogenetic grid, certain general assumptions and interpretations have to be made and their limitations estimated. In turn, the degree to which the natural relations are accurately represented in the model tests these assumptions. The principal initial assumptions and interpretations of the present model are briefly discussed below.

The contemporaneity of metamorphic mineral growth in the Barrovian and Buchan areas has been noted by Johnson (1963), and the disposition of metamorphic mineral zones in the eastern Scottish Dalradian is further assumed to reflect an event of regional metamorphism in which temperatures increased progressively, though not necessarily uniformly, to a maximum (the climax of metamorphism) and then declined (Harte and Johnson, 1969). During this

event some overprinting of earlier (lower grade) by later (higher grade) mineral assemblages occurred, and the distribution of metamorphic zones seen at present is considered to relate to the climax of metamorphism, which corresponds to the time of the sillimanite overprint in the high-grade area (Chinner, 1966; Harte and Johnson, 1969).

The pelitic mineral assemblages are believed to represent largely stable equilibrium assemblages, which may be reasonably projected into the system Al_2O_3 - K_2O - FeO - MgO - SiO_2 - H_2O (Thompson, 1957). However, some pelites contain more phases than are permissible in equilibrium in this system at arbitrary P , T , $\mu_{\text{H}_2\text{O}}$. Garnet, in particular, commonly appears to be an extra phase in higher grade assemblages (Chinner, 1965; Harte, 1966; Hudson, 1975). The presence of such garnet is believed to be caused by the presence of the additional components, MnO and CaO (Chinner, 1965; Hudson, 1975), or the refractory (nonreactive) nature of garnet (Hollister, 1969, p. 2489; Atherton and Brotherton, 1972), or both. Such garnet has been ignored in the present paragenetic analysis. Refractory nature during progressive metamorphism may be a property of other porphyroblastic minerals and is believed to be responsible for the common occurrence of kyanite and andalusite in sillimanite-grade rocks. The distribution of the overprinted Al_2SiO_5 polymorphs is a useful guide to pressure conditions during metamorphism (Chinner, 1966).

The model is based on mineral assemblages in the common hematite-free pelites, which usually contain ilmenite with or without either rutile or magnetite and which may also contain graphite. This restriction has been made in order to minimize complications introduced by the presence of Fe_2O_3 and by variation in oxygen fugacity (Chinner, 1960; Harte, 1966, 1975).

The assumption is made that mineral assemblages at given P and T have

formed at some fixed chemical potential of H_2O (Thompson, 1957). Because local assemblages seem to have the potential to buffer their associated gas phase (Chinner, 1960; Harte, 1966, 1975; Rumble, *Year Book* 73, pp. 371-380, and this Report), this assumption may not be true in detail; it is nonetheless considered to be a reasonable general approximation for the critical parageneses considered and is specifically tested by the model presented (see also Chinner, 1966, p. 177).

Metamorphic Zones and Sequences

The disposition of pelitic metamorphic zones in the eastern Scottish Dalradian is shown in Fig. 23, and mineral assemblages occurring adjacent to the low-grade boundary of each zone of higher grade than the biotite zones are presented in Table 9.

The mineral assemblages occurring along the coast north of Stonehaven are commonly grouped with the Barrovian sequence, but they contain andalusite and sillimanite, without kyanite, and have been given separate status in Table 9, under the heading of Stonehavian. This region also contains distinctive chloritoid-bearing assemblages adjacent to the boundary between the garnet and staurolite zones (Chinner, 1967), and the assemblage Ct-G-B^* has been given separate zonal status in Table 9, though its outcrop is too narrow to depict on Fig. 23 (this zone forms only the high-grade margin of the area of chloritoid localities shown on Fig. 23).

Two principal subdivisions are also recognized for the area of Buchan metamorphism. The commoner sequence is that labeled D (Fig. 23 and Table 9), which appears to apply to the region south and east of the Buchan biotite zone. The Buchan section E , to the west of the biotite zone, shows the extensive development of the assemblage And-S-B

* Abbreviations of mineral names given in the text are the same as those of Table 9 and Fig. 24.

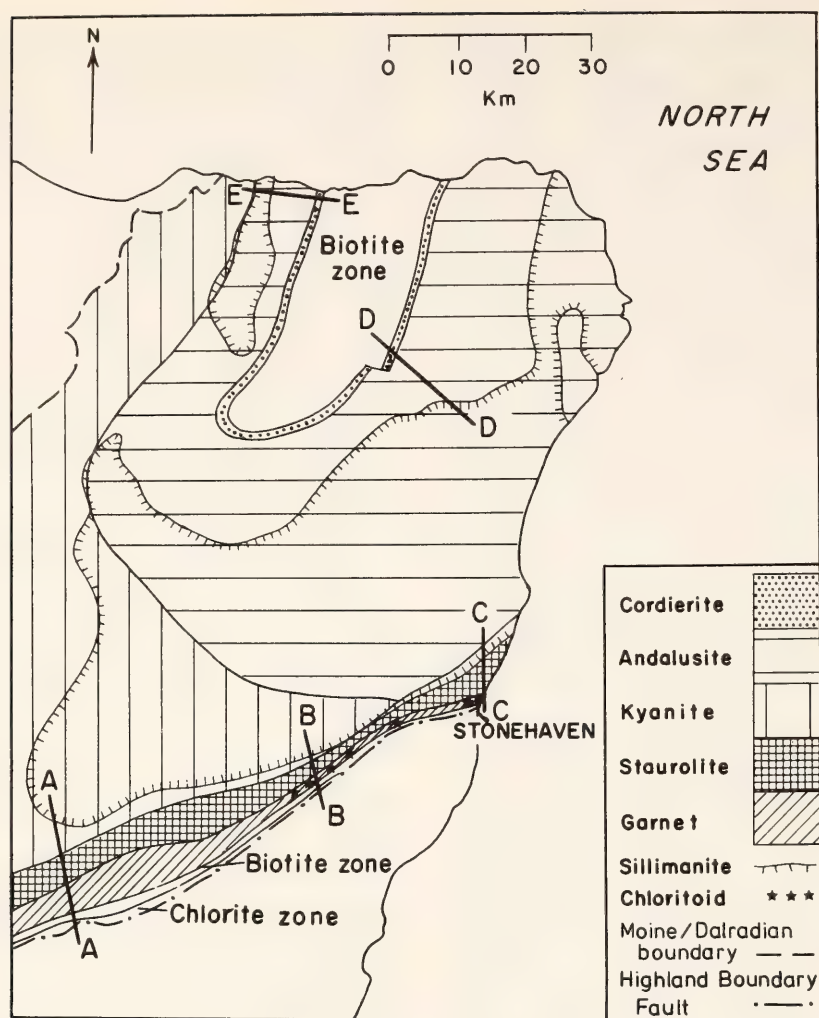


Fig. 23. Distribution of pelitic metamorphic zones in the eastern Scottish Dalradian. Based on Barrow (1912), Read (1923, sheets 86 and 96), Tilley (1925), Chinner (1966, 1967), Harte (1966), Porteous (1973), Hudson (1975). Areas on the hatched side of the sillimanite boundary belong to the sillimanite zone, within which kyanite and andalusite occur as indicated. The isolated sillimanite zone area crossed by *E-E* may be wholly of contact metamorphic origin (Ashworth, 1975). Only principal localities for chloritoid are shown (after Chinner, 1967).

(Hudson, 1975). Assuming, in accordance with Ashworth (1975), that high-grade sillimanite-potash feldspar assemblages that developed adjacent to the boundary between andalusite- and kyanite-bearing assemblages in section *E* are of contact metamorphic origin, then Buchan sequence *E* may also pass upgrade into the equivalent of the Barrovian kyanite zone.

Isograd Reactions

Table 10 lists isograd reactions determined for the zonal sequences of Table 9. The reactions are based on detailed studies by Chinner (1961, 1965, 1967), Harte (1966), Atherton (1968), and Hudson (1975), together with the data

on mineral assemblages in Table 9 and data on bulk rock chemical compositions. An extensive collation of Dalradian pelite bulk compositions has been made by Atherton and Brotherton (1972, 1973, 1974), who noted that the majority of bulk compositions are less aluminous than the muscovite-chlorite join in AK(FM) projection, and that the range of FeO:MgO is also restricted (the average value of mol MgO/(MgO + FeO) is quoted as 0.437 with a standard deviation of 0.100). Because of the relatively low Al₂O₃ content of the rocks, aluminous minerals (cordierite, chloritoid, staurolite, Al₂SiO₅ polymorphs) are not expected to occur without the breakdown of white mica-chlorite tie lines

TABLE 9. Zonal Assemblages and Sequences above Biotite Zone for Sections of the Eastern Scottish Dalradian Shown in Fig. 23

	<i>garnet</i>	<i>staurolite</i>	<i>kyanite</i>	<i>sillimanite</i>
Barrovian (A)	G-Chl-B	S-G-B	S-G-B Ky-S-B	Sill-S-B (S-G-B)
	<i>garnet</i>	<i>chloritoid- biotite</i>	<i>staurolite</i>	<i>sillimanite</i>
Stonehavian (C)	G-Chl-B Ct-Chl-G	Ct-G-B Ct-Chl-B (S-Ct-Chl)	S-G-B S-Chl-B	Sill-S-B
	<i>cordierite</i>	<i>andalusite</i>	<i>sillimanite</i>	<i>sillimanite-K feldspar</i>
Buchan (D)	C-Chl-B	And-C-B	Sill-C-B	Sill-C-B Sill-K feldspar
	<i>cordierite</i>	<i>andalusite</i>	<i>staurolite</i>	<i>kyanite</i>
Buchan (E)	C-Chl-B	And-C-B	And-S-B (And-C-B)	Ky-S-B S-G-B

Zones corresponding to Fig. 23 in italics (the precise distribution of the Buchan *D* sillimanite-K feldspar zone is uncertain and is omitted from Fig. 23). Assemblages refer principally to the low-grade part of each zone. All assemblages + muscovite + quartz. Based on data from Chinner (1960, 1965, 1966, 1967), Harte (1966), Atherton (1968), Hudson (1975). The Barrovian sequence given corresponds to the most commonly observed assemblages, and is possibly modified by the replacement of S by Sill-G-B at high grade in the western part of Fig. 23. Also, Chinner (1973) has noted the unusual occurrence of chloritoid within garnet and in muscovite aggregates, which may imply, though not necessarily, that the Barrovian largely belongs to facies series *B* rather than *A* in Fig. 26. Sillimanite has been omitted from the Buchan (*E*) sequence; see Fig. 23 and text. Abbreviations: And, andalusite; Ky, kyanite; Sill, sillimanite; S, staurolite; Ct, chloritoid; C, cordierite; G, garnet; Chl, chlorite; B, biotite.

consequent to the restriction of the Fe/Mg solid solution field of chlorite (see Albee, 1972, pp. 3260–3261, for further discussion). In accordance with this compositional restriction, the more aluminous minerals, except chloritoid and very rarely staurolite, first appear in biotite-bearing assemblages (Table 9). Chloritoid does occur with chlorite (+ muscovite + quartz) and with or without garnet in a restricted low-grade area by and to the west of Stonehaven (Fig. 23). Atherton and Brotherton (1974) demonstrated the unusually high Al_2O_3 ratios of the pelites from this area. In the same area, the aluminous assemblage S-Ct-Chl, which is very rare in the Dalradian, is recorded also (Chinner, 1967).

Derivation of the Petrogenetic Grid

A *P-T* net of invariant points and univariant reactions for assemblages of

chlorite, biotite, garnet, chloritoid, cordierite, staurolite, and Al_2SiO_5 polymorph in the subsystem Al_2O_3 -FeO-MgO may be constructed by following the method of Schreinermakers (1915–1925). The relative Fe/Mg contents of the phases have been taken as garnet > staurolite > chloritoid > biotite > cordierite > chlorite, the less well-known Fe/Mg relationship of staurolite and chloritoid being taken from Albee (1972) and Rumble (1974) and that of cordierite and chlorite being taken from Hudson (1975).^{*} The relative disposition of univariant reactions about an invariant point has essentially been inferred from the expectation that H_2O

^{*} Guidotti, Cheney, and Conatore (1975) showed a different relationship within the C-Chl-B assemblage in higher grade rocks than those from Buchan. Modification for their findings does not substantially alter the grid presented.

TABLE 10. Isograd Reactions for Diagnostic Minerals in Pelitic Zonal Sequences in the Eastern Scottish Dalradian

Barrovian (A)	
Garnet Isograd	chlorite \rightarrow garnet + biotite
Continuous; G-Chl-B moves to progressively more Mg-rich compositions	
Staurolite Isograd	garnet + chlorite \rightarrow staurolite + biotite
Discontinuous	
Kyanite Isograd	staurolite \rightarrow kyanite + biotite
Continuous; Ky-S-B moves to progressively more Fe-rich compositions	
Sillimanite Isograd	kyanite \rightarrow sillimanite
Discontinuous	
Stonehavian (C)	
Garnet Isograd	chlorite \rightarrow garnet + biotite
Continuous; G-Chl-B moves to progressively more Mg-rich compositions	
Chloritoid-Biotite Isograd	garnet + chlorite \rightarrow chloritoid + biotite
Discontinuous	
Staurolite Isograd	chloritoid + chlorite \rightarrow staurolite + biotite
Discontinuous	
Sillimanite Isograd	staurolite \rightarrow biotite + sillimanite
Continuous; Sill-S-B moves to progressively more Fe-rich compositions	
Buchan (D)	
Cordierite Isograd	chlorite \rightarrow cordierite + biotite
Continuous; C-Chl-B moves to progressively more Mg-rich compositions	
Andalusite Isograd	cordierite \rightarrow andalusite + biotite
Continuous; And-C-B moves to progressively more Mg-rich compositions	
Sillimanite Isograd	andalusite \rightarrow sillimanite
Discontinuous	
Buchan (E)	
Cordierite Isograd	chlorite \rightarrow cordierite + biotite
Continuous; C-Chl-B moves to progressively more Mg-rich compositions	
Andalusite Isograd	cordierite \rightarrow andalusite + biotite
Continuous; And-C-B moves to progressively more Mg-rich compositions	
Staurolite Isograd	andalusite + biotite \rightarrow staurolite
Continuous; And-S-B moves to progressively more Mg-rich compositions	
Kyanite Isograd†	andalusite \rightarrow kyanite
Discontinuous	

* The exact position of this reaction, or of a zone with the critical assemblage S-Ct-B and without S-G-B or Ct-Chl-B, is uncertain and may be impossible to locate considering the refractory nature of garnet. Mineral compositions assumed in this reaction are based on Albee (1972) and Rumble (1974).

† A narrow sillimanite zone may be present between andalusite- and kyanite-bearing assemblages (Fig. 23).

The mineral reactions are given only for AFM projection (i.e. without quartz, muscovite, H₂O) and are classified as continuous or discontinuous in accordance with Thompson (1957). Only the overall net reaction is given for the continuous reactions—each one involves a series of reactions of the type: Fe-chlorite + Fe-biotite \rightarrow Mg-chlorite + Mg-biotite + garnet.

will be liberated on the high-temperature, high-entropy side of a reaction and that cordierite will occur on the low-pressure, high-molar volume side of a reaction.

For the Buchan area, Hudson (1975) showed that the sequence of metamorphic zones is compatible with reactions occurring about a [Ct, G]* invariant point. Examination of the Stonehavian and Barrovian zonal sequences shows that they may be modeled using the invariant points [A, C] and [Ct, C]. Assuming the stability of these three invariant points and placing them in relative P - T space according to the known changes with grade and expected pressure variation, $P_{\text{Barrovian}} > P_{\text{Stonehavian}} > P_{\text{Buchan}}$, the whole of the net of Schreinemakers bundles may be delineated (Korzhinskii, 1959, pp. 128–129).

The resultant Schreinemakers net is illustrated in Fig. 24. Except for the removal of mineral composition collinearities and consequent degeneracies, the net of Fig. 24 is the same as that of Albee (1965, Fig. 6) for the condition $P_{\text{H}_2\text{O}} \approx P_{\text{solid}}$ —a feature of particular interest in itself, which adds support to the initial assumption of restricted variation in $\mu_{\text{H}_2\text{O}}$. The net has been fixed in P - T space using experimental data for $P_{\text{H}_2\text{O}} = P_{\text{solid}}$ and for oxygen fugacities corresponding approximately to the QFM buffer, in conjunction with the constraints of the Schreinemakers geometry (see legend of Fig. 24). The principal experimental data used and the adopted positions for stable invariant points of the Schreinemakers net are shown in Fig. 25. The P - T constraints are quite restrictive, especially with regard to temperature. Pressure coordinates are more arbitrary, particularly for the invariant points [A, C], [Ct, C], and [B, C].

* In accordance with normal practice, invariant points and univariant reactions are identified by the phases absent from them. Invariant points are placed in brackets, and univariant reactions, in parentheses.

P-T Relations of Dalradian Pelite Zones

Using the data of Figs. 24 and 25, the possible P - T conditions of the zonal mineral assemblages of Table 9 have been plotted in Fig. 26. The position of the transition from biotite to cordierite zones is based on the experimental work of Seifert (1970) and Hirschberg and Winkler (1968), with emphasis upon the former because of its compatibility with the experimental data of Fig. 25. The position of the garnet isograd in Fig. 26 is much more arbitrary. Hirschberg and Winkler (1968) indicated the formation of garnet, rather than cordierite, from muscovite + chlorite assemblages above 4–5 kbar, but the relationships are complicated by the common presence of appreciable MnO and CaO in natural garnet (Atherton, 1968), which increases garnet stability with respect to chlorite and cordierite (Hsu, 1968; Hirschberg and Winkler, 1968). For this reason and in order to permit full representation of the mineral zones, the garnet isograd has been offset by 40°C with respect to the cordierite isograd.

The locations of the continuous isograds are dependent upon the solid solution equilibria involving divariant assemblages, but they must lie within the stability fields of the critical zonal assemblages shown in Fig. 26 (subject to some displacement of univariant curves also as a function of changing mineral compositions). Although the relative arrangement of zonal assemblages in Fig. 26 is unlikely to be affected, it must be emphasized that the boundaries of zones marked by continuous isograd reactions are not rigid, and will be displaced within the maximum stability fields of critical mineral assemblages, as a function of chemical compositions.

Facies series corresponding to the Barrovian, Stonehavian, and Buchan zonal sequences of Table 9 are also shown in Fig. 26, and show an orderly progression consistent with the field relations (Fig. 23). A facies series involving garnet and kyanite (and therefore essentially Bar-

gneisses (with and without sillimanite or K feldspar) delineated by Chinner (1966, Fig. 5).

Figure 26 also demonstrates that the Barrovian, Stonehavian, and Buchan *D* facies series may have similar *P-T* gradients with values of approximately 100°–

125°C/kbar and therefore higher than the geothermal gradients expected from average heat-flow values (Richardson, 1970). The Buchan *E* sequence has a markedly steeper *P-T* gradient, at least at higher grade. This difference of Buchan *E* with respect to the other se-

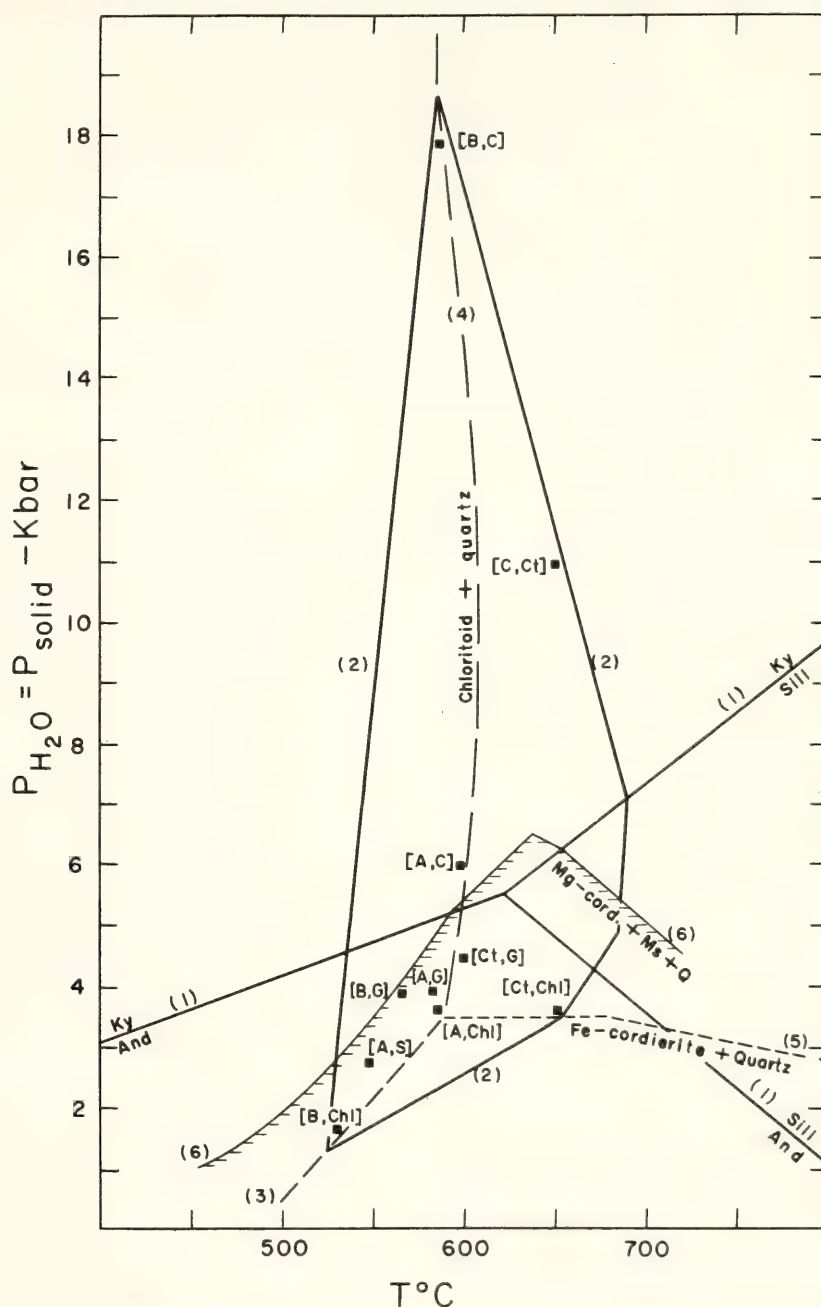


Fig. 25. Experimentally determined stability limits for (1) Al_2SiO_5 polymorphs (Richardson, Gilbert, and Bell, 1969); (2) staurolite + quartz (Richardson, 1968; Ganguly, 1972; Grieve and Fawcett, 1974); (3)–(4) chloritoid + quartz; (3)–(5) Fe-cordierite + quartz (Schreyer, 1965; Richardson, 1968; Grieve and Fawcett, 1974); (6) Mg-cordierite \pm muscovite + quartz (Seifert and Schreyer, 1970; Seifert, 1970; Bird and Fawcett, 1973). Note that the upper temperature limit of stability of chloritoid + quartz is put in schematically above 4 kbar and that several reactions (undetermined experimentally) are involved. Fe-system reactions for approximate conditions of QFM buffer. The adopted positions of the invariant points of the Schreinemakers net (Fig. 24) are also shown.

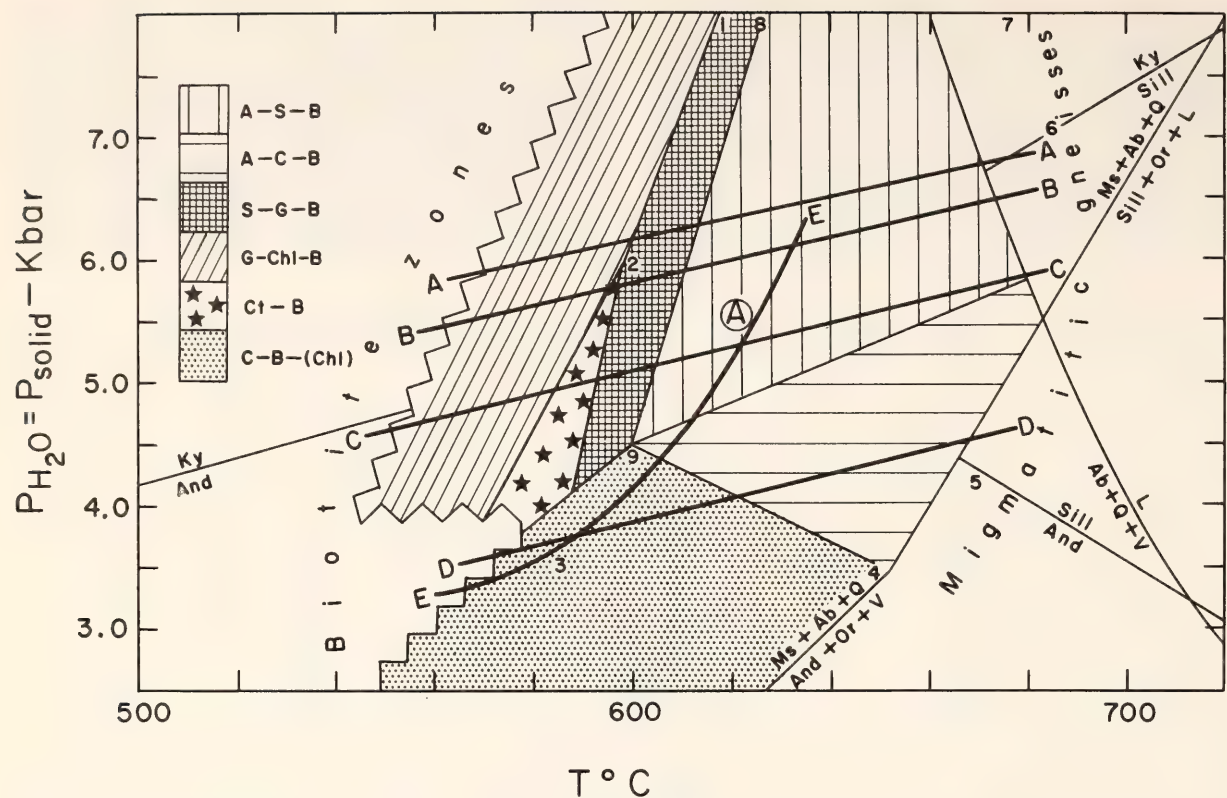


Fig. 26. *P-T* fields and facies series for critical mineral assemblages in pelites from the eastern Scottish Dalradian. The shaded regions shown for the stability fields C-B-(Chl), A-C-B, S-G-B, and A-S-B are the parts extending from their lowest temperatures of stability up to the lowest possible temperatures for the next higher grade (temperature) assemblage. Maximum stability fields are larger; in particular, C-B-(Chl) extends across the shaded field of A-C-B, while the full stability fields of S-G-B and A-S-B lie within boundaries indicated by 1-2-3-4-5-6-7 and 8-9-4-5-6-7, respectively. Univariant reaction lines for the Al_2SiO_5 polymorphs are from Richardson, Gilbert, and Bell (1969), with point A (encircled) corresponding to the triple point. Curves for muscovite (Ms) + albite (Ab) + quartz (Q) = Al_2SiO_5 + K feldspar (Or) + H_2O (V) and $\text{Ms} + \text{Ab} + \text{Q} = \text{Al}_2\text{SiO}_5 + \text{Or} + \text{liquid}$ (L) and $\text{Ab} + \text{Q} + \text{V} = \text{L}$ are from Thompson (1974), and the last two curves are taken as a guide to melting temperatures and the formation of migmatitic gneisses (cf. Chinner, 1966). The reaction $\text{A} + \text{Chl} + \text{B} = \text{C}$ of Fig. 24, which separates the shaded portions of the A-S-B and A-C-B stability fields, probably terminates at temperatures below those of $\text{Ab} + \text{Q} + \text{V} = \text{L}$ because chlorite and cordierite become unstable with quartz and muscovite; the diagram has been simplified in this respect because the terminal reactions do not occur within the range of natural compositions. Facies series A, B, C, D, E are for zonal sequences (upgrade of the biotite zones) at the locations correspondingly lettered in Fig. 23.

quences corresponds with the orientation of its direction of increasing grade away from rather than toward the major central area of sillimanite occurrence (Fig. 23), which is also the site of the thermal anticline of Chinner (1966). The location of this zone of relatively high heat flow is similar to that of the hinge zone of the Tay-Banff Nappe (B. Harte and D. J. Fettes, in preparation) and may indicate a tectonic contribution to heat transport during orogenesis in the eastern Scottish Dalradian.

UVAROVITE STABILITY IN THE
 $\text{CaSiO}_3\text{-Cr}_2\text{O}_3$ JOIN UP TO 10 KBAR

H. G. Huckenholz

Uvarovite, $\text{Ca}_3\text{Cr}_2\text{Si}_3\text{O}_{12}$, is one of the less abundant garnet end-members but is found as nearly pure $\text{Ca}_3\text{Cr}_2\text{Si}_3\text{O}_{12}$ in chemically restricted mineral assemblages of ultrabasic rocks that have undergone metamorphism at low temperature and pressure within the lower crust of the earth. Uvarovite is omnipresent as a component in complex pyrope solid

solutions brought up with kimberlites (Nixon and Hornung, 1968; Hornung and Nixon, 1973; Sobolev *et al.*, 1973; Gurney and Switzer, 1973) and as inclusions in diamonds (Meyer and Boyd, 1972; Sobolev *et al.*, 1969). These occurrences indicate a deep-seated origin at a rather high pressure and temperature of formation within the upper mantle. However, uvarovite has a very high thermal stability limit at low pressures and the highest breakdown temperature for a pure end-member garnet. Uvarovite decomposes to pseudowollastonite (CaSiO_3) and eskolaite (Cr_2O_3) at $1385^\circ \pm 10^\circ\text{C}$ and 1 atm total pressure (Huckenholz and Knittel, 1975).

The purpose of this study was to investigate the thermal behavior of pure uvarovite up to 10 kbar with and without H_2O . Related studies on compositions in the joins $\text{CaSiO}_3\text{-Cr}_2\text{O}_3$ and $\text{CaSiO}_3\text{-Cr}_2\text{O}_3\text{-H}_2\text{O}$, in which uvarovite, pseudowollastonite, eskolaite, liquid, and vapor are phases, give information about the phase relationships involved in the univariant and invariant equilibria.

Previous Syntheses of Uvarovite

The join $\text{CaSiO}_3\text{-Cr}_2\text{O}_3$ was studied by Glasser and Osborn (1958) at a total pressure of 1 atm of air. Attempts to synthesize uvarovite from various kinds of starting materials were reported by Hummel (1950), Geller and Miller (1959), Swanson *et al.* (1960), Gentile and Roy (1960), Isaaks (1966), and Arnould, Kabbani, and Kien (1969). Huckenholz and Knittel (1975) recently obtained new data on the stability of uvarovite between 1050° and 1550°C at 1 atm as a result of studying the join grossularite-uvarovite. The maximum thermal stability limit of uvarovite was found to be $1385^\circ \pm 10^\circ\text{C}$, in general accord with the results obtained by Glasser and Osborn (1958). Hummel (1950) and Geller and Miller (1959), however, reported the formation of uvarovite from appropriate oxide mixtures even at 1400°

C in runs of short duration (of the order of 1 hour).

The uvarovite breakdown products, pseudowollastonite + eskolaite, melt at 1420°C . Pseudowollastonite and eskolaite coexist with liquid over a temperature range of 80°C before pseudowollastonite disappears at 1500°C ; eskolaite remains in the liquid. These observations are not in accord with the results obtained by Glasser and Osborn (1958) on the join $\text{CaSiO}_3\text{-Cr}_2\text{O}_3$. The coexistence of 2 solids + liquid over a temperature interval at a fixed pressure displays ternary behavior. Two phases of the pseudowollastonite + eskolaite + liquid assemblage refer to compositions in the $\text{CaO-Cr}_2\text{O}_3\text{-SiO}_2$ system in particular. Presumably, eskolaite will incorporate CaO (as CaCr_2O_4) in small amounts, as indicated by a shift of the (116) reflection of eskolaite toward lower interplanar spacing. The coexisting liquid must have a composition within the $\text{CaSiO}_3\text{-Cr}_2\text{O}_3\text{-SiO}_2$ subsystem and probably reflects its minimum melting at 1418°C (Glasser and Osborn, 1958). Thus, the Alkemade line pseudowollastonite-eskolaite has shifted slightly toward pseudowollastonite-eskolaite_{ss} (toward CaCr_2O_4), and a narrow three-phase field of pseudowollastonite + eskolaite + liquid is created for bulk compositions close to uvarovite at temperatures between 1420° and 1500°C . Pseudowollastonite disappears when the composition of the liquid, eskolaite_{ss}, and the uvarovite bulk composition lie on a line (restricted singularity for $\text{Ca}_3\text{Cr}_2\text{-Si}_3\text{O}_{12}$ composition). The reaction yielding liquid at 1420°C within the $\text{CaSiO}_3\text{-Cr}_2\text{O}_3\text{-SiO}_2$ subsystem is pseudowollastonite + eskolaite + tridymite = liquid. Tridymite, however, was not encountered in runs between 1385° and 1420°C , and failure to observe it is probably due to the location of the uvarovite bulk composition very close to the join $\text{CaSiO}_3\text{-(Cr}_2\text{O}_3\text{)}_{\text{ss}}$, where a small percentage of tridymite cannot be seen. One option that explains the possible phase re-

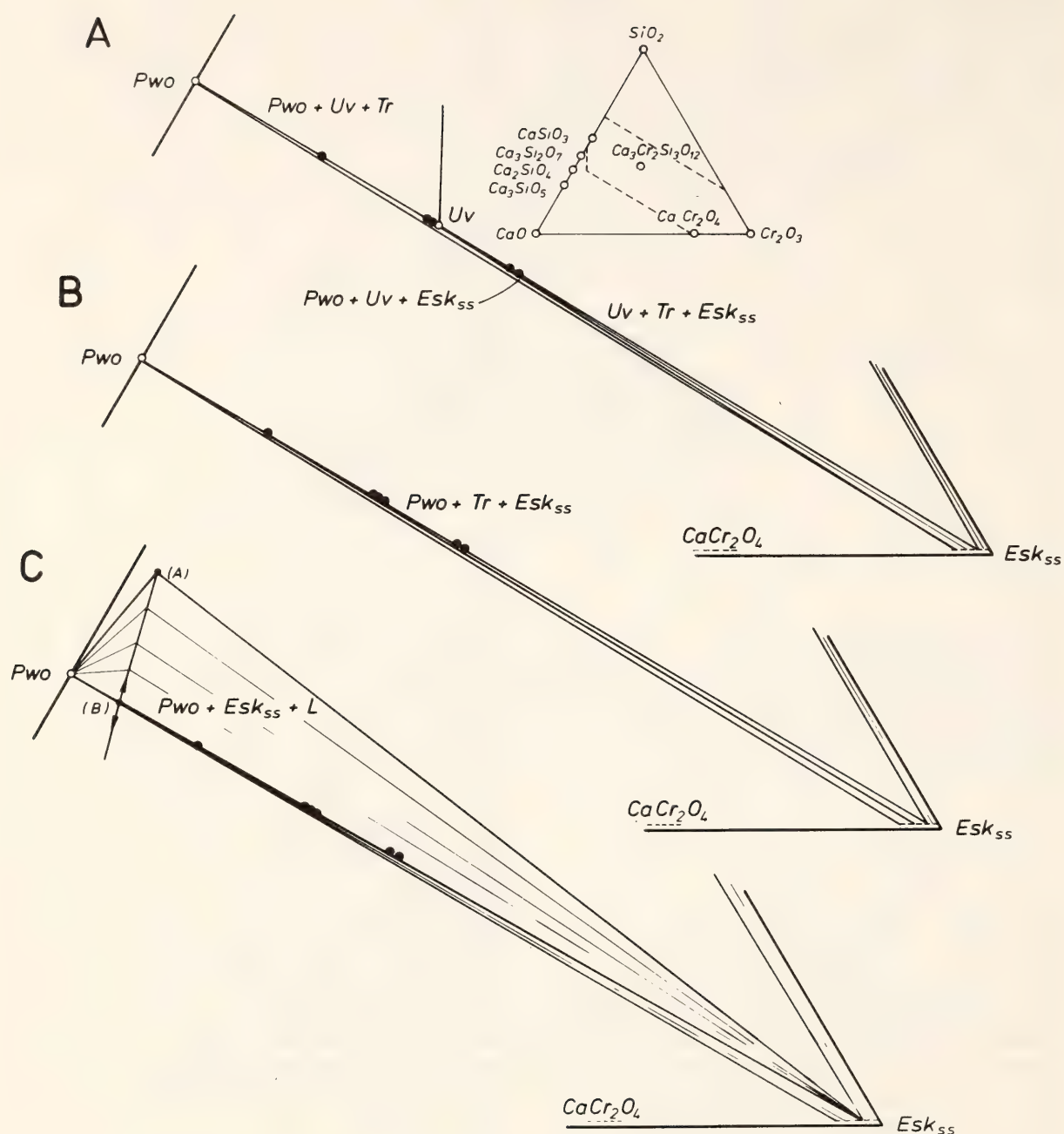


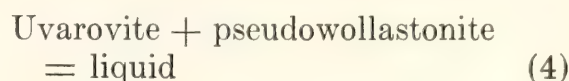
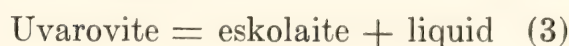
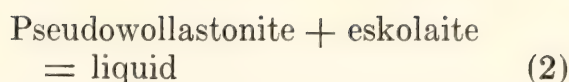
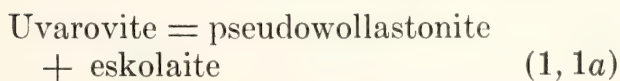
Fig. 27. Representation of phase relations for compositions along $\text{CaSiO}_3\text{-Cr}_2\text{O}_3$ in the join $\text{CaSiO}_3\text{-Cr}_2\text{O}_3\text{-SiO}_2$. (A) Phase relations on the low-temperature side of reactions 1 and 1a, uvarovite = pseudowollastonite + eskolaite (for comparison see Fig. 28). (B) Phase relations on the low-temperature side of reaction 2a, pseudowollastonite + eskolaite + tridymite (?) = liquid. (C) Phase relations between reaction 2a, pseudowollastonite + eskolaite + tridymite (?) = liquid, and reaction 2b, pseudowollastonite + eskolaite = liquid, at 1 atm and for total pressures up to S'_1 . The eutectics A and B refer to the ternary join $\text{CaSiO}_3\text{-Cr}_2\text{O}_3$ and its binary bounding join $\text{CaSiO}_3\text{-Cr}_2\text{O}_3$, respectively. At 1 atm total pressure, A has a temperature of $1420^\circ \pm 10^\circ\text{C}$; B, $1500^\circ \pm 10^\circ\text{C}$ (Glasser and Osborn, 1958). Abbreviations: Pwo, pseudowollastonite (CaSiO_3); Wo, wollastonite (CaSiO_3); Esk, eskolaite (Cr_2O_3); Uv, uvarovite ($\text{Ca}_3\text{Cr}_2\text{Si}_3\text{O}_{12}$); Tr, tridymite (SiO_2); L, liquid.

relationships in $\text{CaSiO}_3\text{-Cr}_2\text{O}_3\text{-SiO}_3\text{(-H}_2\text{O)}$ is depicted in Fig. 27. The unit-cell parameter and refractive index of uvarovite grown at 1 atm are 11.996(2) Å and 1.865(3),* respectively (Huckenholz and Knittel, 1975).

Stability Relations of Uvarovite in the Join $\text{CaSiO}_3\text{-Cr}_2\text{O}_3$ from 1 atm up to 6.5 kbar Total Pressure

The nature of the stability field of uvarovite in the join $\text{CaSiO}_3\text{-Cr}_2\text{O}_3$ can be deduced from chemographic principles established by Schreinemakers (1925) and Morey and Williamson (1918). At a total pressure of 1 atm the sequence of participating phases within the strictly binary system $\text{CaSiO}_3\text{-Cr}_2\text{O}_3$ has to be pseudowollastonite, liquid, uvarovite, and eskolaite. For this analysis their compositions are assumed to lie on a line (Fig. 27). Uvarovite decomposes to pseudowollastonite + eskolaite at $1385^\circ \pm 10^\circ\text{C}$. Tridymite was not found in the breakdown assemblage. The assemblage begins to melt at 1420°C , yielding pseudowollastonite + eskolaite + liquid; pseudowollastonite disappears in favor of eskolaite + liquid at 1500°C . The (ternary) three-phase assemblage pseudowollastonite + eskolaite + liquid changes between 4 and 4.5 kbar at 1503°C to eskolaite and liquid, indicating that the Alkemade line pseudowollastonite-eskolaite_{ss} of the $\text{CaO-Cr}_2\text{O}_3\text{-SiO}_2$ system at 1 atm has shifted to pseudowollastonite-eskolaite on the $\text{CaSiO}_3\text{-Cr}_2\text{O}_3$ (binary) system with increasing pressure, as depicted in Fig. 28 for S'_1 (restricted singularity).

On the basis of the binary system $\text{CaSiO}_3\text{-Cr}_2\text{O}_3$, only one possible set of chemical relationships results in the following univariant reactions about an invariant point at some elevated pressure (read in a counterclockwise direction):



The subsolidus stability of uvarovite, which is represented by reactions 1 and 1a, uvarovite = pseudowollastonite + eskolaite, increases from $1385^\circ \pm 10^\circ\text{C}$ at 1 atm to 1493°C at a total pressure of 5 kbar (Fig. 28). Reaction 1 was bracketed at 0.75, 1.5, 2.5, 4.5, and 5 kbar in paired and duplicated runs. The slope of reactions 1 and 1a can be expressed by the equation

$$T = 1385 + 21.8P,$$

where T is in degrees centigrade and P in kilobars. The increase in temperature of the beginning of melting (binary) of the uvarovite breakdown products, pseudowollastonite + eskolaite, is negligible when pressure is applied. Above 4 kbar the breakdown products melt at about 1505°C . Thus, reaction 2, pseudowollastonite + eskolaite = liquid (valid above the restricted singularity S'_1 for the uvarovite bulk composition at about 4 kbar), intersects the uvarovite breakdown curve, represented by reactions 1 and 1a at $1505^\circ \pm 10^\circ\text{C}$ and 5.5 ± 0.25 kbar, creating a (binary) invariant point (Iu_1) in the P - T diagram (Fig. 28) with pseudowollastonite, liquid, uvarovite, and eskolaite in equilibrium.

The foregoing chemographic relationships dictate the presence of reactions 3 and 4, which will emanate from invariant point Iu_1 . Reaction 3, uvarovite = eskolaite + liquid, could be bracketed only at 1505°C and 6.5 kbar. The slope of reaction 3, however, is further determined by its metastable extension, which must lie on the low-temperature side of reaction 2, and by invariant point Iu_1 itself. Thus, a reasonably accurate extrapolation of reaction 3 to higher pressure is possible if an increase of about 4°C per kilobar is taken into considera-

* Plus-minus errors are given in parentheses.

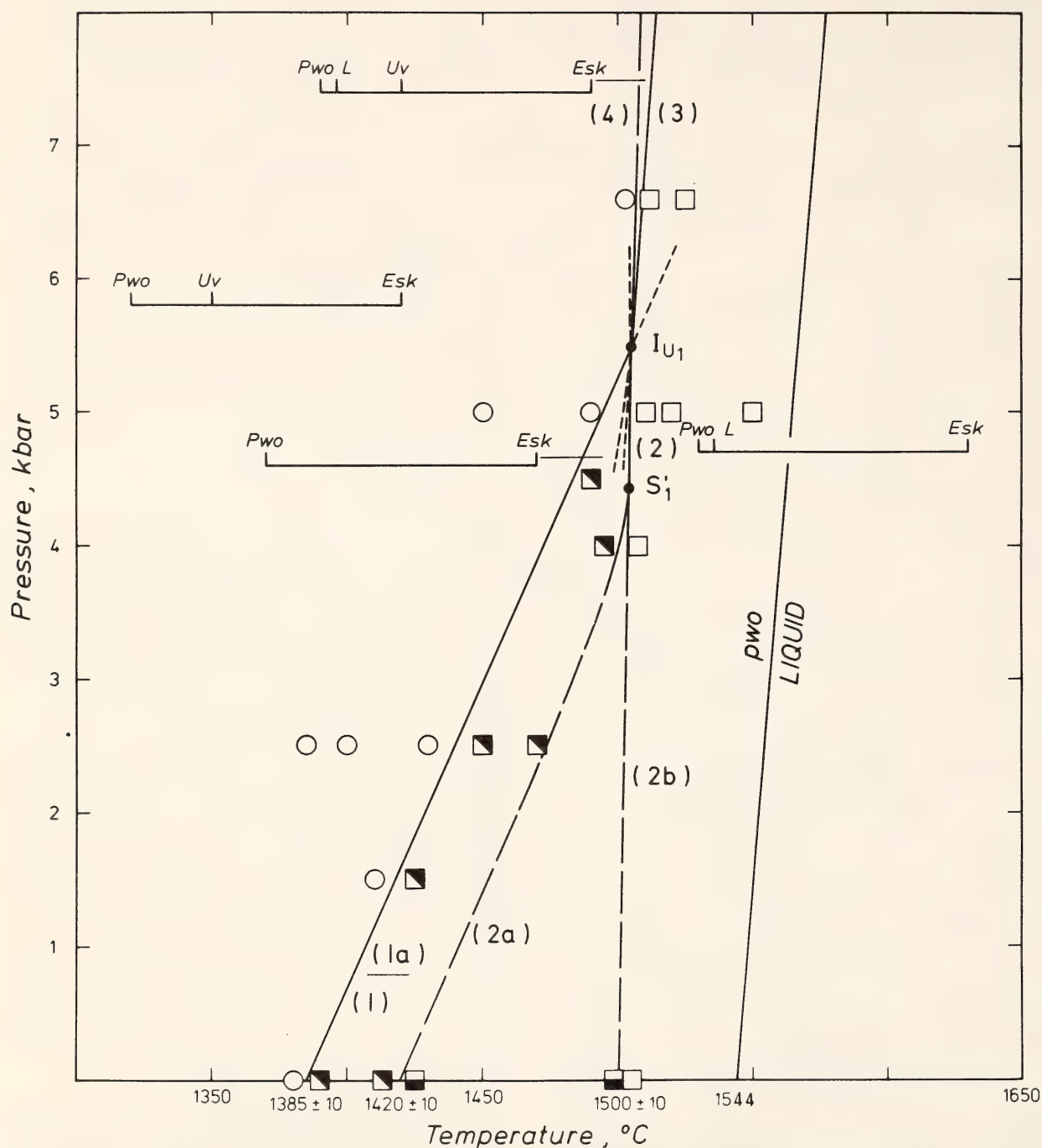


Fig. 28. Pressure-temperature diagram for compositions in the join $\text{CaSiO}_3\text{-Cr}_2\text{O}_3$ at a total pressure up to 6.5 kbar. I_{U1} , invariant point; S'_1 , singular point restricted to a $\text{Ca}_3\text{Cr}_2\text{Si}_3\text{O}_{12}$ bulk composition. Reactions are (1, 1a) uvarovite = pseudowollastonite + eskolaite, (2a) pseudowollastonite + eskolaite + tridymite (?) = liquid, (2, 2b) pseudowollastonite + eskolaite = liquid, (3) uvarovite = eskolaite + liquid, (4) pseudowollastonite + uvarovite = liquid. Anhydrous melting of pseudowollastonite from Kushiro (*Year Book 63*, pp. 83-84). Abbreviations as in Fig. 27. Symbols: open circles, uvarovite or uvarovite + eskolaite; diagonally shaded squares, pseudowollastonite + eskolaite; half shaded squares, pseudowollastonite + eskolaite + liquid; open squares, eskolaite + liquid.

tion. It can be further assumed that eskolaite will still be the liquidus phase at pressures above 6.5 kbar for the uvarovite bulk composition. Within the $\text{CaO-Cr}_2\text{O}_3\text{-SiO}_2$ system, eskolaite is very refractory and disappears from the join only above 2000°C (Glasser and Osborn, 1958).

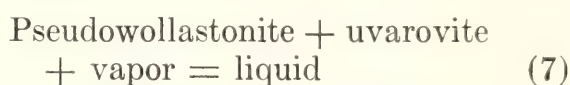
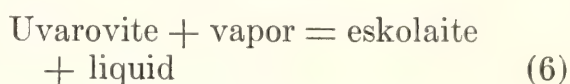
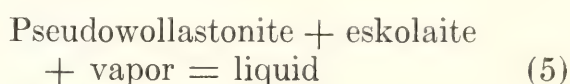
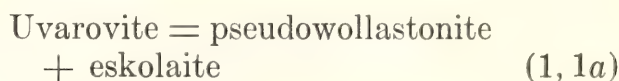
The geometric arrangement of the univariant reactions 1, 2, and 3 about Iu_1 locates reaction 4, pseudowollastonite + uvarovite = liquid, on the low-temperature side of reaction 2. The metastable extension of reaction 4 and invariant point Iu_1 determines the slope of reaction 4, which was not investigated experimentally. The close sequence of reactions 3 and 4 is caused by the very small difference in the temperatures at which the two liquids involved in the univariant equilibria of these reactions are generated on the (binary) join $\text{CaSiO}_3\text{-Cr}_2\text{O}_3$. The unit-cell parameter and refractive index of uvarovite crystallizing in mono- and polyphase assemblages of the $\text{CaSiO}_3\text{-Cr}_2\text{O}_3$ join at pressures between 0.75 and 6.5 kbar are $11.999(2)$ Å and $1.866(2)$, respectively (Huckenholz, Masch, and Hölzl, 1975).

Stability Relations of Uvarovite in the $\text{CaSiO}_3\text{-Cr}_2\text{O}_3\text{-H}_2\text{O}$ Join up to 10 kbar

The maximum stability limit of uvarovite is drastically reduced in the presence of a hydrous vapor phase. Univariant reaction 5, pseudowollastonite + eskolaite + vapor = liquid (if the system is taken as strictly ternary), intersects the uvarovite breakdown curves 1 and 1a, uvarovite = pseudowollastonite + eskolaite, at $1400^\circ \pm 10^\circ\text{C}$ and 0.9 ± 0.2 kbar (Iu_2), having pseudowollastonite + eskolaite + uvarovite + liquid + vapor as an invariant equilibrium assemblage (Fig. 29). From the absence of tridymite in the hydrous experiments, it is inferred that the bulk composition of the uvarovite breakdown product is too close to the conjugation line (= Alkemade line) pseudowollas-

tonite-eskolaite_{ss}-vapor, and tridymite cannot be detected in the reactants.

As under anhydrous run conditions, a restricted singularity (S'_2) must have occurred between 1 atm and 0.75 kbar, changing the quaternary phase assemblage of pseudowollastonite + eskolaite + liquid + vapor to eskolaite + liquid + vapor. Thus ternary invariant phase relations occur at invariant point Iu_2 . Five univariant reaction curves radiate from Iu_2 , consistent with experimental observations and chemographic relations (Fig. 30):



Univariant reaction 6, uvarovite + vapor = eskolaite + liquid, exhibits the incongruent melting of uvarovite in the presence of a hydrous vapor phase; reaction 7, pseudowollastonite + uvarovite + vapor = liquid, exhibits the minimum melting within the $\text{CaSiO}_3\text{-Cr}_2\text{O}_3\text{-H}_2\text{O}$ system. The chromatite quenched from the vapor phase and the yellow (condensed) fluid, however, indicates that hydrous experiments must be referred to the $\text{CaSiO}_3\text{-CrO}_x\text{-H}_2\text{O}$ - (or Ca-Cr-Si-H-O) system in general. Further information is required to evaluate the stability of uvarovite under a fixed f_{O_2} . Preliminary experiments on the minimum melting of the $\text{CaSiO}_3\text{-Cr}_2\text{O}_3\text{-H}_2\text{O}$ system buffered with Ni/NiO lack chromatite and yellow (condensed) fluid but reveal a melting behavior almost identical with that under unbuffered run conditions. These experiments, however, are restricted to temperatures below the melting point of Ni, which is 1453°C under a pressure of 1 atm and increases by

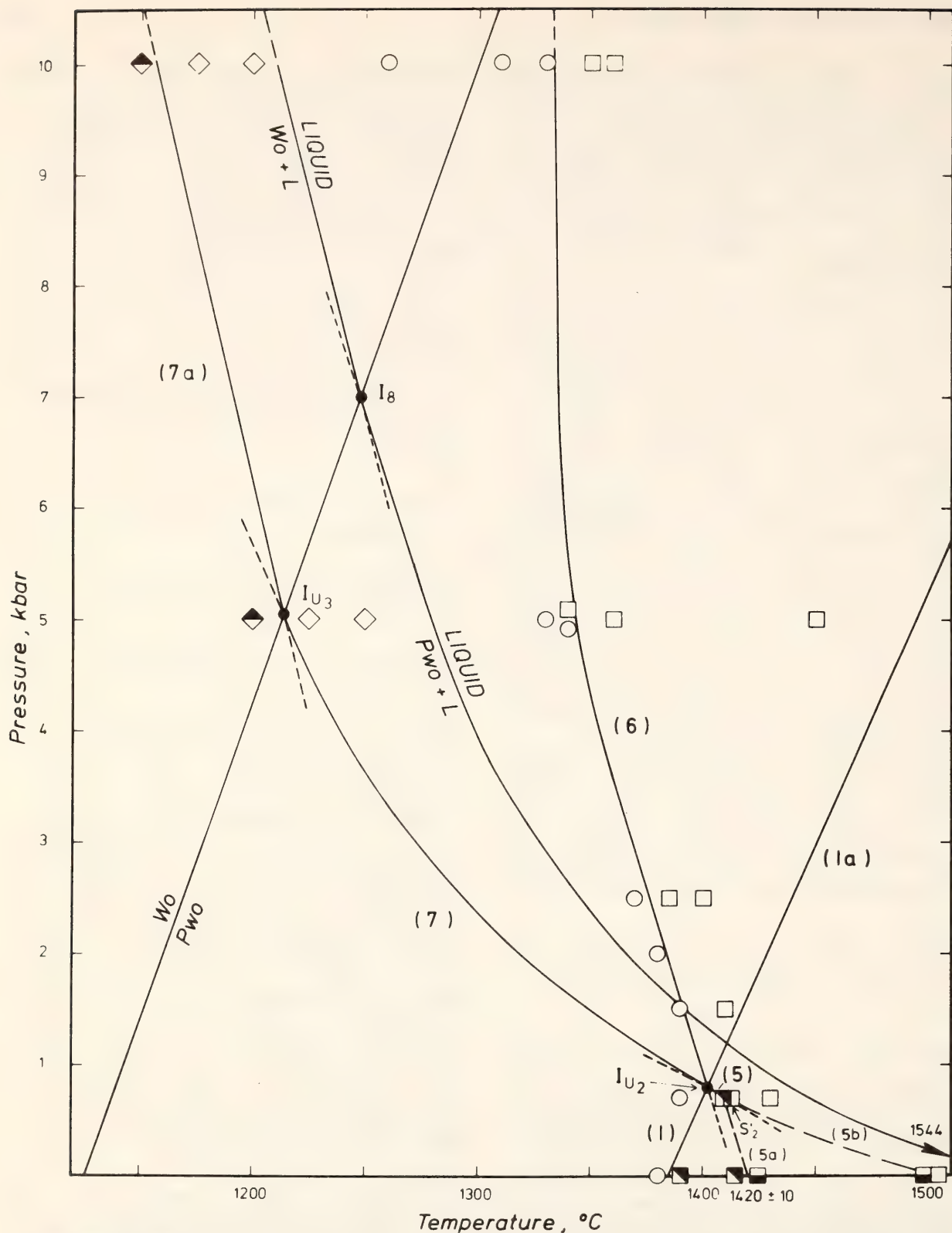


Fig. 29. Pressure-temperature diagram for compositions in the $\text{CaSiO}_3\text{-Cr}_2\text{O}_3\text{-H}_2\text{O}$ join at a total pressure up to 10 kbar. I_{u2} , I_{u3} , and I_s , invariant points; S'_2 , singular point restricted to $\text{Ca}_3\text{Cr}_2\text{Si}_3\text{O}_{12}\text{-H}_2\text{O}$ compositions. Univariant reactions are (1, 1a) uvarovite = pseudowollastonite + eskolaite, (5a) pseudowollastonite + eskolaite + tridymite (?) + vapor = liquid, (5, 5b) pseudowollastonite + eskolaite + vapor = liquid, (6) uvarovite + vapor = eskolaite + liquid, (7) uvarovite + pseudowollastonite + vapor = liquid, (7a) uvarovite + wollastonite + vapor = liquid. The hydrous melting of the CaSiO_3 polymorphs, the pseudowollastonite = wollastonite transformation, and invariant point I_s are from Huckenholz and Yoder (*Year Book* 73, pp. 440-443) and Huckenholz (*Year Book* 73, p. 425). Abbreviations as in Fig. 27. Symbols: open circles, uvarovite + vapor or uvarovite + eskolaite + vapor; diagonally shaded squares, pseudowollastonite + eskolaite + vapor; half shaded squares, pseudowollastonite + eskolaite + liquid + vapor; open squares, eskolaite + liquid + vapor; open diamonds, uvarovite + liquid + vapor; half shaded diamonds, uvarovite + pseudowollastonite/wollastonite + vapor.

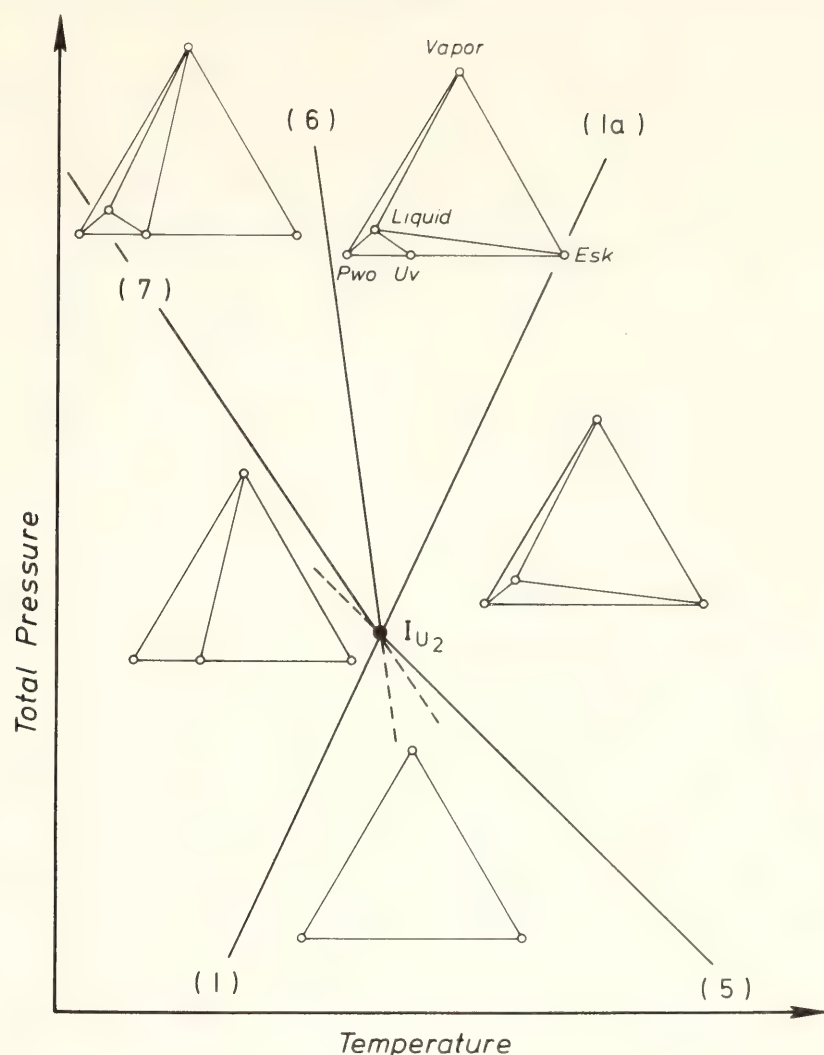


Fig. 30. Theoretical pressure-temperature diagram around the invariant point Iu_2 under hydrous conditions. Numbers of reactions as in Fig. 29; abbreviations as in Fig. 27.

about 4°C per kilobar (Kennedy and Newton, 1963).

The minimum melting curve, pseudowollastonite + uvarovite + vapor = liquid, intersects the pseudowollastonite = wollastonite transformation curve (Huckenholz and Yoder, *Year Book* 73, pp. 440–443; Kushiro, *Year Book* 63, pp. 83–84) at $1215^\circ \pm 10^\circ\text{C}$ and 5.1 ± 0.3 kbar, generating the invariancy at (Iu_3) with pseudowollastonite + wollastonite + uvarovite + vapor + liquid in equilibrium. Thus, the pseudowollastonite-bearing assemblage of reaction 7 will change to a wollastonite-bearing assemblage (7a) above the invariant point Iu_3 . The wollastonite = pseudo-

wollastonite transformation curve is intersected by the hydrous melting of the CaSiO_3 polymorphs at I_8 (Huckenholz and Yoder, *Year Book* 73, pp. 440–443; Huckenholz, *Year Book* 73, p. 425). Either pseudowollastonite + vapor or wollastonite + vapor will disappear in favor of a hydrous liquid in CaSiO_3 -bearing assemblages on the high-temperature side of the melting curve. The unit-cell parameter and refractive index of uvarovite crystallizing in mono- and polyphase assemblages of the CaSiO_3 - Cr_2O_3 - H_2O join between 0.75 and 10.0 kbar are $12.000(2)$ Å and $1.866(2)$, respectively (Huckenholz, Masch, and Hölzl, 1975).

IGNEOUS PETROLOGY: EXPERIMENTAL AND FIELD

VOLATILES IN ULTRABASIC AND
DERIVATIVE ROCK SYSTEMSSOLUBILITY OF VOLATILES IN SILICATE
MELTS AT HIGH PRESSURE AND
TEMPERATURE: THE ROLE OF CARBON
DIOXIDE AND WATER IN FELDSPAR,
PYROXENE, AND FELDSPATHOID MELTS*Bjørn O. Mysen*

The presence of volatiles (H_2 , H_2O , CO_2 , CO , F , Cl , SO_2 , etc.) during the formation and evolution of igneous rocks is well documented (e.g., Oxburgh, 1964; Roedder, 1965; Nordlie, 1971; Sigvaldsson and Elisson, 1968; Dawson and Powell, 1969; McGetchin and Besancon, 1973; Killingley and Muenow, 1974). Phase equilibrium studies relating to the origin of magmas in the upper mantle in the presence of volatiles have been chiefly concerned with equilibria in the presence of H_2O , CO_2 , and various proportions of the two (Eggler, 1972; *Year Book 72*, pp. 457–467; *Year Book 73*, pp. 215–224; this Report; Mysen, *Year Book 72*, pp. 467–478; Hill and Boettcher, 1970; Holloway and Burnham, 1972; Mysen and Boettcher, 1975a, b). These studies have shown that carbon dioxide affects phase relations in model mantle systems at high pressure; however, an understanding of the mode of solution of the volatiles into silicate melt structures is necessary for evaluating their role during partial melting in the upper mantle.

Preliminary experiments have shown that carbon dioxide solubility (ΣCO_2^*) depends on physical parameters such as pressure (P), temperature (T), and the bulk composition of the silicate melt (X), and on the presence of H_2O in the silicate. Data on carbon dioxide solubility have therefore been collected for a series of carefully selected compositions

* ΣCO_2 refers to total carbon dioxide content of silicate glass. CO_2 and CO^{2-} refer to actual contents of these two species in the silicate glass.

in an attempt to evaluate these factors. In addition, data by Mysen (1975) have indicated that carbon dioxide enters silicate melts both as discrete CO_2 molecules and in the form of the carbonate. Selected experimental charges were therefore analyzed for carbon species with infrared spectrometric techniques. The compositions are those of albite (Ab), jadeite (Jd), and nepheline (Ne). In addition, a natural olivine melilite nephelinite composition, W47 (Winchell, 1947), was chosen to demonstrate how the principles developed for simple silicate systems also apply to more complex natural silicate rocks.

One composition, $NaAlSi_3O_8 + H_2O + CO_2$, was chosen for a study of the solubilities of both ΣCO_2 and H_2O because in the presence of multicomponent volatiles, the solubility of each component in the silicate melt depends on the other volatile species, which do not necessarily form ideal mixtures, and because volatiles can affect the silicate melt structure (Burnham, 1975; Burnham and Davis, 1971, 1974). Direct measurements of the solubilities of the individual volatile components of a multicomponent vapor are therefore desirable.

Experimental Technique

Starting materials were finely ground mixtures of various oxides and carbonates, with carbonate as the source of CO_2 . A known activity of carbon-14 in the form of $BaCO_3$ was added to the samples for measurements of ΣCO_2 solubility. The BaO impurity thus introduced is less than 0.2 wt % (see Mysen, Seitz, and Frantz, *Year Book 73*, pp. 224–226, for details of experimental techniques). The compositions of the starting materials (excluding Ab, Ne, and Jd compositions) are listed in Table 11. The W47 composition (Winchell, 1947) was made with $MgO = MgO + FeO$ (total Fe as FeO) + MnO (wt %) to alleviate redox problems. Because iron-

TABLE 11. Volatile-Free Compositions of Starting Materials

	Or	C	CM	W47
SiO ₂	64.78	69.56	70.63	37.78
TiO ₂	2.53
Al ₂ O ₃	18.31	19.65	19.93	12.98
MgO	3.95	25.76*
CaO	...	10.79	5.49	14.32
Na ₂ O	4.91
K ₂ O	16.91	0.91
P ₂ O ₅	1.41
Totals	100.00	100.00	100.00	100.00
CO ₂ , wt%	7.9	7.8	7.9	12.2
Mol weight, O = 8	278	259	255	249
Specific activity of starting material, mCi/mg	7.23×10^{-4}	2.49×10^{-7}	1.30×10^{-5}	1.37×10^{-4}

* MgO = MgO + FeO (total Fe as FeO) + MnO (wt %). Original composition contains 6.2 Fe₂O₃, 7.6 FeO, and 0.1 MnO (wt %).

free olivine melilite nephelinite melts at temperatures in excess of 1400°C, Pt sample containers are required. However, iron loss to the Pt capsule would be significant at such temperatures (Merrill and Wyllie, 1973). This iron loss would alter the rock composition, particularly Mg/(Mg + Fe), and the Mg/(Mg + Fe) ratio is required in corrections for electron penetration in the sample (Mysen and Seitz, 1975). The use of magnesium instead of Fe + Mg slightly increases the basicity of the melt (Mg is less electronegative than Fe), but this effect is negligible and is therefore ignored in this report.

All experiments were accomplished by heating oxide + carbonate mixtures (thoroughly dried prior to the experiment) to super-liquidus temperatures at $P = 10$ – 30 kbar in solid-media, high-pressure apparatus (Boyd and England, 1960) using Pt capsules as sample containers. Experiments were performed using the piston-out technique with no correction for friction. Temperatures were measured with Pt/Pt90Rh10 thermocouples.

Run durations were 15, 10, and 5 minutes at 1450°C, 1525°C, and 1625°C, respectively. Mysen and Seitz (1975)

demonstrated that these run durations are sufficient to attain experimental equilibrium. Relatively short run durations were used to minimize errors in temperature due to thermocouple contamination (Presnall, Brenner, and O'Donnell, 1973).

Carbon dioxide and water solubilities have been determined by the β -track mapping technique described by Mysen, Seitz, and Frantz (*Year Book* 73, pp. 224–226) and Mysen and Seitz (1975). The method has already been successfully used to determine carbon contents of silicate liquids and crystals (Eggler, Mysen, and Seitz, *Year Book* 73, pp. 226–228; Mysen and Seitz, 1975). Fortunately, tritium decays by emission of β particles with half-life ($t_{1/2}$) = 12 years and decay energy (ϵ) = 18.1 keV, thus facilitating measurements of the solubility of H₂O and CO₂ in silicates coexisting with a (CO₂ + H₂O)-rich vapor. These β particles can be registered in nuclear emulsions similar to those used for carbon-14. The only modification is the use of K-2 emulsions (supplied by Ilford Company, England) instead of the more sensitive K-5 type used for the carbon-14 studies. For studies of other vapor systems, a list of iso-

topes that may be used is supplied in Table 11.

In a ($\text{H}_2\text{O} + \text{CO}_2$)-bearing system, tritium of known activity is added to H_2O . Carbon dioxide can be added to the system either in gaseous form (Muehlenbachs and Mysen, *Year Book* 73, pp. 605–606) or as a solid (carbonate or oxalate) that releases CO_2 at moderate temperatures. In the present experiments Na_2CO_3 , KHCO_3 (heated to 220°C before use), CaCO_3 , and $\text{CaMg}(\text{CO}_3)_2$ were the sources of CO_2 . For measurement of the H_2O content, the carbonate contains no carbon-14. Conversely, the ΣCO_2 content of the liquid is measured by repeating the experiment with a known activity of carbon-14 added to the sample. The latter method is identical with that described by Mysen, Seitz, and Frantz (*Year Book* 73, pp. 224–226).

The standard for carbon dioxide measurements was the same calcite prepared and used by Eggler, Mysen, and Seitz last year (*Year Book* 73, pp. 226–228). Albite glass with 3.5 wt % H_2O , quenched from 1450°C and 20 kbar, was chosen as the standard for the H_2O measurements. Burnham (1975) has shown that albite glass containing less than 5 wt % water will not exsolve any vapor during the quench so the standard was prepared with a H_2O content within this limit. Although no vapor bubbles indicative of H_2O exsolution during the quench were observed and β -track maps of tritium from this standard are homogeneous within the uncertainty of the counting statistics (4%–5%, Mysen and Seitz, 1975), it is recognized that H_2O tends to escape from silicate glasses even after the quench, making experiments of this nature somewhat more uncertain.

All data on ΣCO_2 and H_2O solubility are recalculated to mol fraction ($X^{\text{m}_{\text{CO}_2}}$) based on $\text{O} = 8$ in the chemical formulae in accord with the principles developed by Burnham (1975).

Nine samples of known total carbon contents were studied by infrared tech-

niques using a double-focusing spectrometer. The samples, crushed to $<1\ \mu\text{m}$ grain size, were mixed with KBr (weight ratio: 99 KBr/1 sample) and pelletized at 180 bars pressure. Carbon dioxide-free glasses and various carbonate mixtures were run to separate absorption bands related to the silicate matrix from those of carbon species.

Samples for infrared spectrometry were run in duplicate; one sample was stored (after crushing) at atmospheric conditions and the other at 110°C until analysis (more than 48 hours). This procedure was carried out to determine whether the infrared spectrometer picked up molecular CO_2 gas absorbed on the surfaces of the materials during experiments with liquids in equilibrium with CO_2 vapor.

Solubility of Carbon Dioxide in the System $\text{Na}_2\text{O}-\text{Al}_2\text{O}_3-\text{SiO}_2-\text{CO}_2$

Data reported previously (Eggler, *Year Book* 72, pp. 457–467; Eggler, Mysen, and Seitz, *Year Book* 73, pp. 226–228) indicated that the ΣCO_2 solubility in silicate melts depends on bulk composition as well as on pressure and temperature. The dependence of solubility on these parameters has now been studied in greater detail.

The ΣCO_2 solubility isotherms shown in Fig. 31 display positive pressure dependence, as was also reported for the diopside composition (Eggler, Mysen, and Seitz, *Year Book* 73, pp. 226–228) and for a natural olivine nephelinite (see below). Furthermore, the solubility (at constant P and T) increases systematically with increasing basicity of the silicate (basicity = number of moles of basic oxides/number of moles of acidic oxides; Pearce, 1964). Qualitatively, it seems that the relation between basicity of the silicate melt and CO_2 solubility proposed last year (Eggler, Mysen, and Seitz, *Year Book* 73, pp. 226–228) also holds true for these compositions. In contrast to CO_2 solubility, H_2O solubility does not depend on the

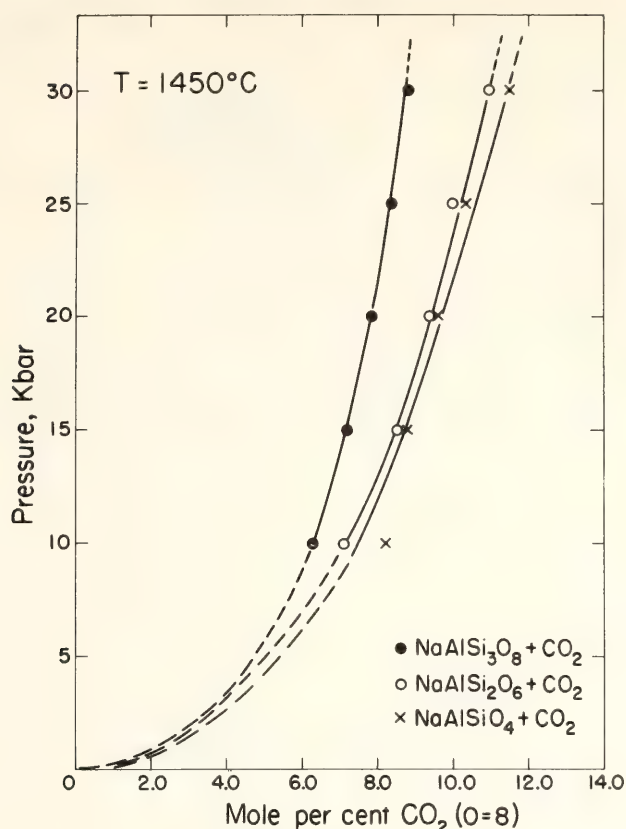


Fig. 31. Solubility isotherms of ΣCO_2 in albite, $(X^{\text{m}_{\text{CO}_2}})^{\text{Ab}_T}$, jadeite, $(X^{\text{m}_{\text{CO}_2}})^{\text{Jd}_T}$, and nepheline, $(X^{\text{m}_{\text{CO}_2}})^{\text{Ne}_T}$ compositions at 1450°C ($O = 8$ in all three chemical formulae; mol % $\text{CO}_2 = 100 \times X^{\text{m}_{\text{CO}_2}}$).

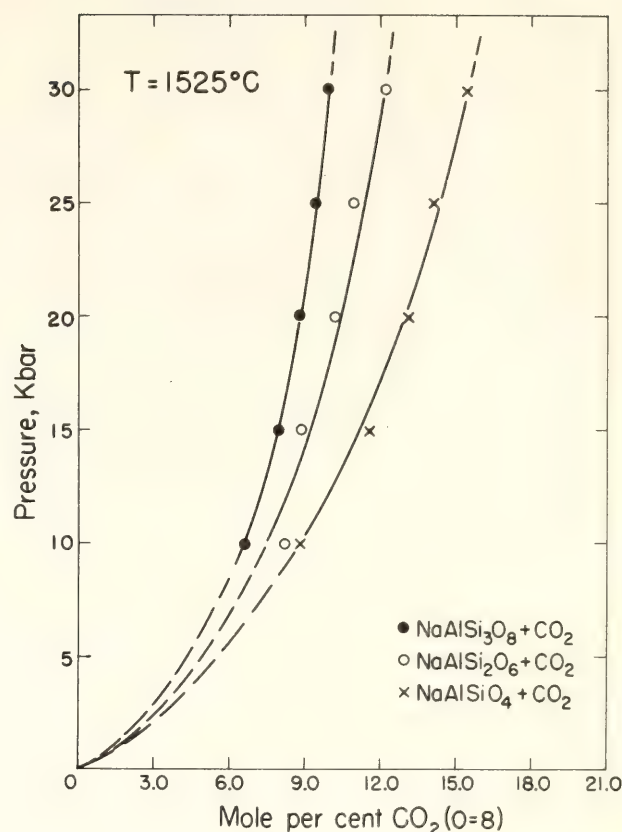


Fig. 32. Solubility isotherms. As in Fig. 31, but with $T = 1525^\circ\text{C}$.

bulk composition when compared on an equal anion basis (Burnham and Davis, 1971, 1974), thus indicating different solubility mechanisms for these two important volatiles.

The differential solubility of ΣCO_2 in Ab, Jd, and Ne melt compositions increases with increasing temperature (Figs. 32 and 33). The slope of the solubility isotherms approaches a constant value as the temperature increases (Fig. 33). In addition, there is a positive temperature dependence of the ΣCO_2 solubility in this system (Fig. 34), as was also suggested by Eggler, Mysen, and Seitz (*Year Book* 73, pp. 226–228) for the diopside composition. The data in Fig. 34 show two additional features: (1) In general, the rate of increase is in the direction $X^{\text{m}_{\text{Ab}}} < X^{\text{m}_{\text{Jd}}} < X^{\text{m}_{\text{Ne}}}$.

* Mole fraction of ΣCO_2 in Ab, Jd, and Ne melts (calculated with $O = 8$).

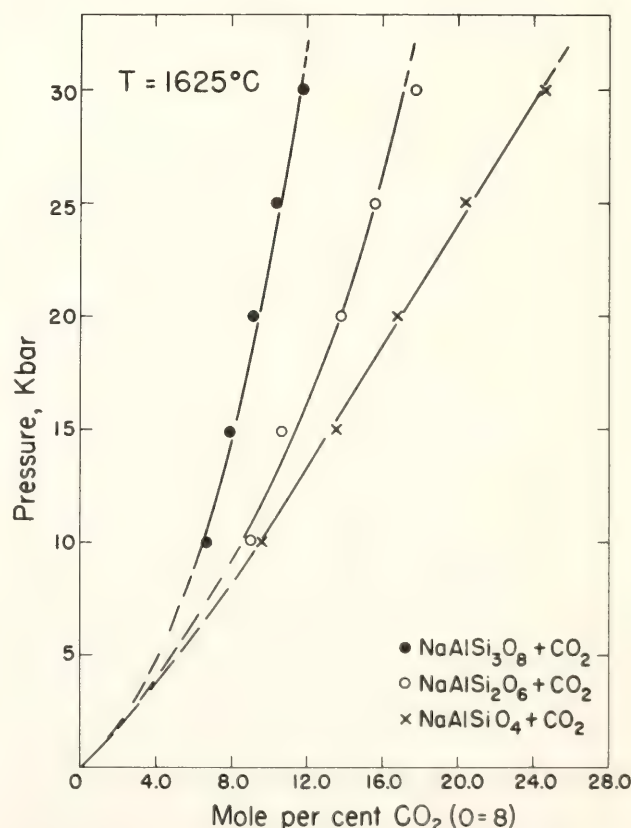


Fig. 33. Solubility isotherms. As in Fig. 31, but with $T = 1625^\circ\text{C}$.

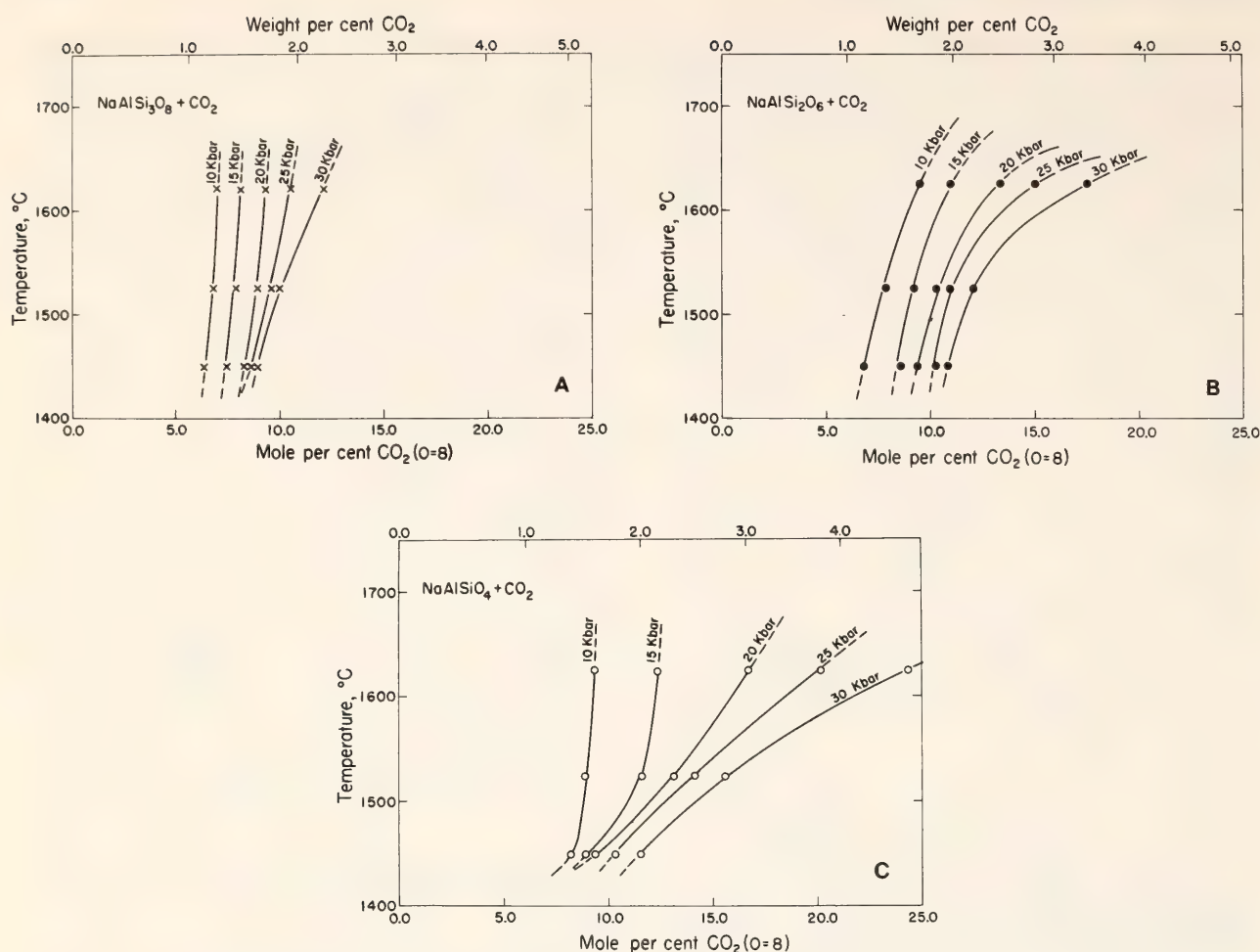


Fig. 34. Solubility isobars of CO₂ in albite, jadeite, and nepheline compositions. (A) Albite compositions, $(X^m_{\text{CO}_2})^{\text{Ab}}P_{\text{CO}_2} = 10\text{--}30$ kbar. CO₂ = ΣCO_2 . (B) Jadeite compositions, $(X^m_{\text{CO}_2})^{\text{Jd}}P_{\text{CO}_2} = 10\text{--}30$ kbar. (C) Nepheline composition, $(X^m_{\text{CO}_2})^{\text{Ne}}P_{\text{CO}_2} = 10\text{--}30$ kbar. O = 8 in all three chemical formulae. CO₂ = ΣCO_2 .

(2) The slopes of the solubility isotherms of nepheline and albite change from convex to concave toward the solubility axis at $P_{\text{CO}_2} = 20\text{--}25$ kbar. This effect is not observed for the jadeite composition, where the concavity is retained down to at least 10 kbar.

The data obtained for the H₂O-free Ab, Jd, and Ne compositions show that the behavior of the ΣCO_2 solubility contrasts sharply with that of H₂O. Compared with H₂O on a molar basis, the ΣCO_2 solubility is only about 10%–20% of the amount of H₂O (in the presence of excess H₂O) that dissolves. Also, the dependence of $X^m_{\text{CO}_2}$ on parameters such as bulk composition and temperature indicates a different solubility mechanism for ΣCO_2 than for H₂O. This conclusion is supported by the contrast in phase re-

lations of silicate-H₂O systems compared with silicate-CO₂ systems such as Di-Fo-SiO₂-H₂O (Kushiro, 1969) and Di-Fo-SiO₂-CO₂ (Eggler, *Year Book* 72, pp. 457–467). These differences have important implications for the thermodynamics and petrology of CO₂-bearing natural silicate systems. Unfortunately, the thermodynamic properties of carbon dioxide at high pressure and temperature are poorly known. It seems, however, that ΣCO_2 solubility can best be discussed in terms of carbonate formation in the melt, solution of discrete CO₂ molecules, or both. Solubility measurements alone cannot determine uniquely whether the solubility mechanism is that of CO₃²⁻ or CO₂ formation because physical processes such as varying degree of polymerization of the silicon-

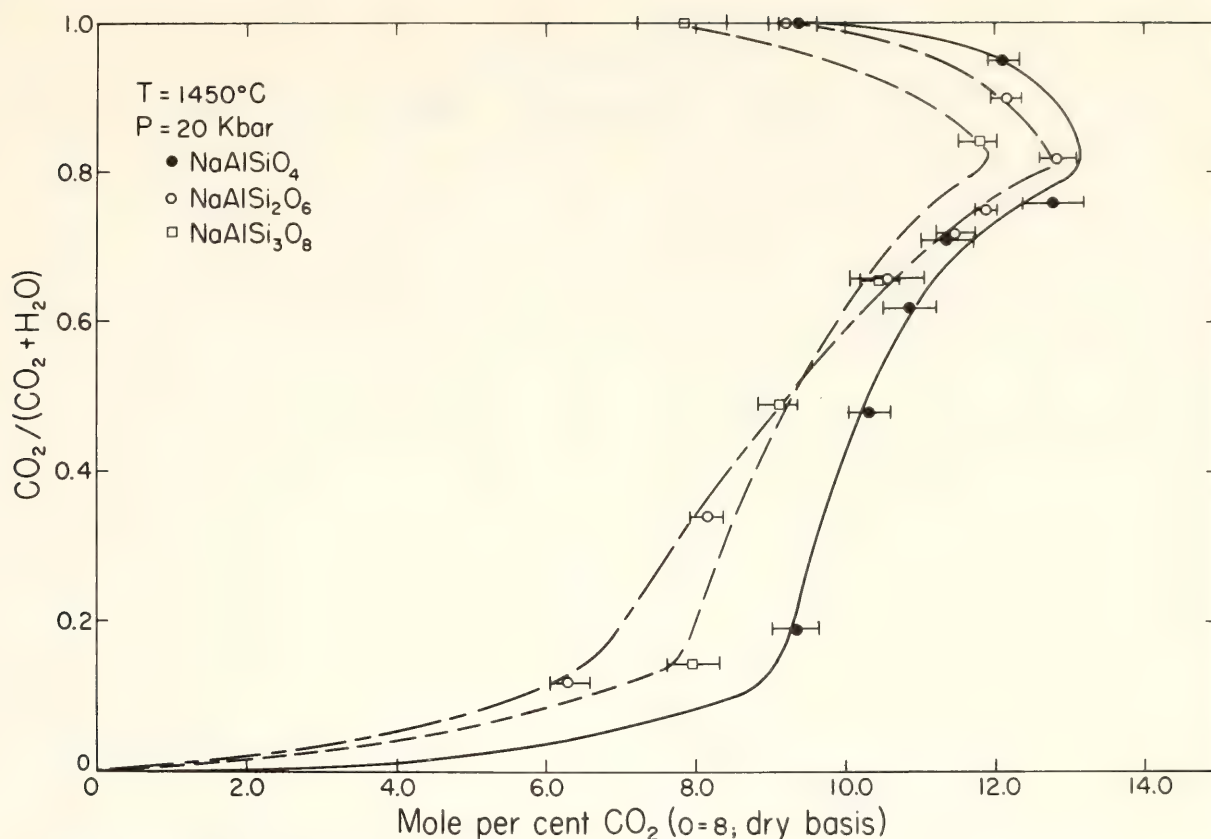


Fig. 35. Solubility of ΣCO_2 in hydrous Ab, Jd, and Ne melts in equilibrium with $(\text{H}_2\text{O} + \text{CO}_2)$ vapor. $\text{CO}_2/(\text{CO}_2 + \text{H}_2\text{O})$ ratio reflects the $\text{CO}_2/(\text{CO}_2 + \text{H}_2\text{O})$ of the entire system. $\text{CO}_2 = \Sigma\text{CO}_2$.

oxygen network qualitatively have similar influence on carbon dioxide solubility whether CO_2^{2-} or CO_2 is the mode of solution.

Relations between $\text{CO}_2/(\text{CO}_2 + \text{H}_2\text{O})$ and $X_{\text{CO}_2}^m$ in the System $\text{Na}_2\text{O}-\text{Al}_2\text{O}_3-\text{SiO}_2-\text{CO}_2-\text{H}_2\text{O}$

Data on the solubility of ΣCO_2 from Ab, Jd, and Ne melt compositions at 1450°C and 20 kbar are given in Fig. 35. The data in Fig. 35 show maximum ΣCO_2 solubility at $X_{\text{CO}_2}^* < 1.0$, in agreement with Eggler (*Year Book 72*, pp. 457–467) and Holloway and Reese (1974). Note that the maxima for all compositions occur at the same X_{CO_2} (~ 0.84). As also observed in the H_2O -free part of these systems (Figs. 31–33), the geometry of the Ab and Ne curves is similar to but somewhat different from the solubility curve for Jd composition. In fact,

* $X_{\text{CO}_2} = \text{CO}_2/(\text{CO}_2 + \text{H}_2\text{O})$ of the volatile fraction (mol) of the entire system.

at X_{CO_2} less than about 0.5, more ΣCO_2 enters melt of albite composition than of jadeite composition (Fig. 35).

Nepheline composition was selected for studies of pressure and temperature dependence of ΣCO_2 solubility because more carbon dioxide enters Ne than Jd and Ab. Any variations, therefore, are likely to be larger and more easily defined.

The data at 20 kbar (Fig. 36) show the positive temperature dependence of CO_2 solubility, $(dX_{\Sigma\text{CO}_2}^m/dT)_P$, in hydrous Ne melt, which is also observed in various H_2O -free systems including nepheline melt (see Fig. 34 and Eggler, Mysen, and Seitz, *Year Book 73*, pp. 226–228). The temperature dependence tends to decrease with decreasing X_{CO_2} . The solubility maxima (Fig. 35) also occur at 1525° and 1625°C (Fig. 36), but the X_{CO_2} corresponding to these maxima remains at about 0.84 (Fig. 36). The $(dX_{\Sigma\text{CO}_2}^m/dT)_{P,X_{\text{CO}_2}}$ increases with

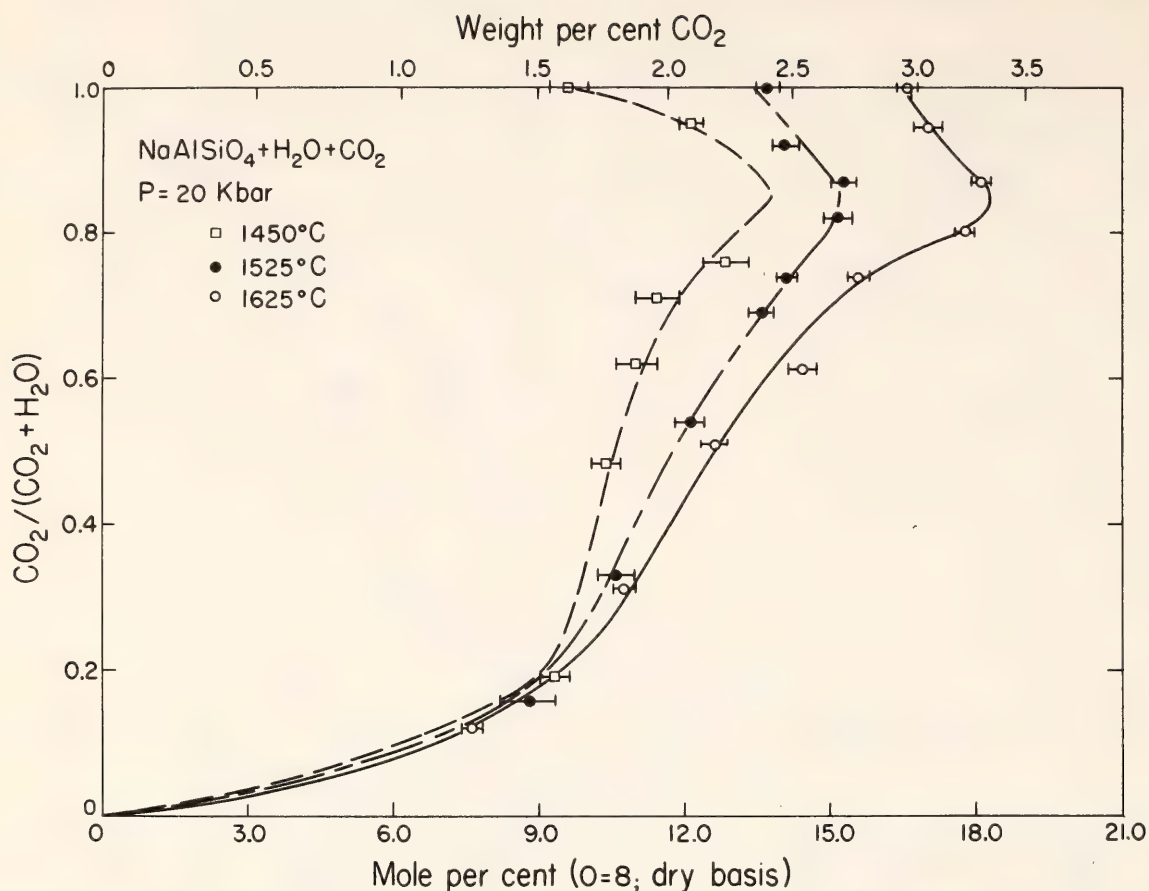


Fig. 36. Temperature dependence of ΣCO_2 solubility in Ne + H₂O + CO₂ melt at 20 kbar pressure. $\text{CO}_2 = \Sigma\text{CO}_2$.

increasing temperature (Fig. 37). The ΣCO_2 solubility in hydrous Ne melt increases with increasing pressure (Fig. 38). The solubility maxima shift to lower values of X_{CO_2} with increasing pressure (Fig. 39).

The most notable features of ΣCO_2 solubility in hydrous Ab, Jd, and Ne melts are the distinct maxima at $X_{\text{CO}_2} < 1.0$ (Figs. 35, 36, and 38). As with the solubility of H₂O in silicate melts, the value of $\text{CO}_2/(\text{CO}_2 + \text{H}_2\text{O})$ at the ΣCO_2 solubility maxima is significantly dependent on total pressure, whereas the silicate chemistry and temperature do not affect X_{CO_2} , suggesting that its P - T - X coordinates relate to the solubilities of H₂O in these melts. Burnham (1975) and Burnham and Davis (1971, 1974) concluded that solution of H₂O in silicate melts in effect increases the basicity of the melt. If so, the ΣCO_2 solubility in such a melt would increase with increasing solution of H₂O. Addition of H₂O to

the system also decreases f_{CO_2} , however, thus tending to reduce $X^m_{\text{CO}_2}$, and it appears that the solubility maxima represent the points where these two effects balance each other. Evidently, this balance is shifted to lower activity of CO₂ as the total pressure (and thus H₂O solubility) increases.

*Carbon Dioxide (ΣCO_2) and Water
Solubilities in Albite Melt at
20 kbar Pressure and 1450°C*

Solubility data for H₂O and ΣCO_2 appear in Table 12 accompanied by calculated mol fractions of NaAlSi₃O₈ (X^m_{Ab}), CO₂ ($X^m_{\text{CO}_2}$), and H₂O ($X^m_{\text{H}_2\text{O}}$) in the melt. Knowledge of the total amounts of H₂O and ΣCO_2 in the experimental charge may then be used to calculate the composition of vapor coexisting with such liquid. These data are useful in assessing activities of H₂O and CO₂ in the system. Unfortunately, several percent silicate dissolves in (H₂O +

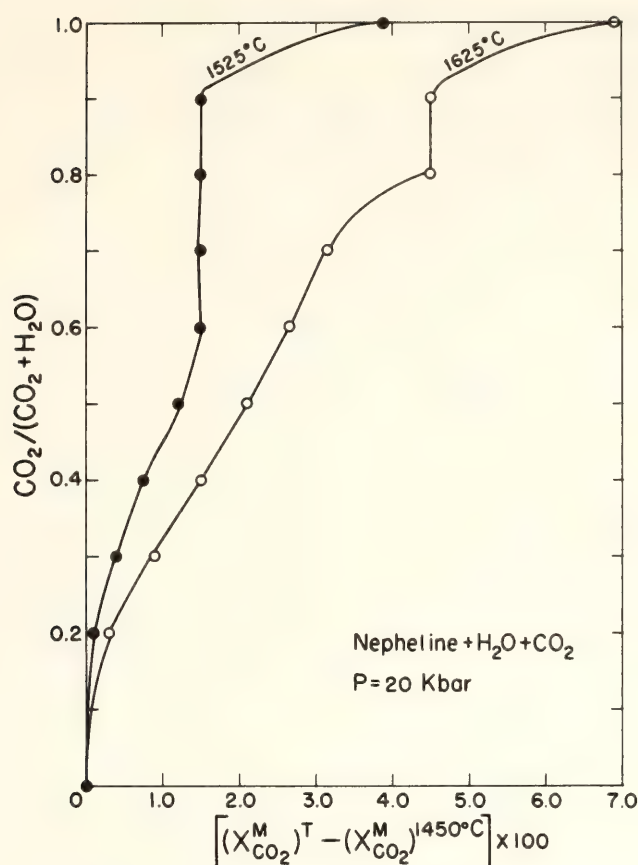


Fig. 37. Relative temperature dependence of ΣCO_2 solubility, $(X^m_{\text{CO}_2})^T - (X^m_{\text{CO}_2})^{1450^\circ\text{C}}$; in Ne + H_2O + CO_2 as a function of $\text{CO}_2/(\text{CO}_2 + \text{H}_2\text{O})$ at $P_{\text{total}} = 20$ kbar.

CO_2)-rich vapors at high pressures and temperatures (Eggler, *Year Book* 72, pp. 457–467; Kadik and Eggler, this Report) making the quality of such data questionable.

Data on ΣCO_2 and H_2O solubility in albite melt are plotted in Fig. 40. The solubility curves are obtained by graphical interpolation and extrapolation of the weight percentage data in Table 12. The $X^m_{\text{H}_2\text{O}}$ end point for pure H_2O vapor is that of Boettcher and Wyllie (1969).

The data in Fig. 40 illustrate the large solubility difference between H_2O and ΣCO_2 in silicate melt. On a molar basis $X^m_{\text{CO}_2} > X^m_{\text{H}_2\text{O}}$ only for $\text{CO}_2/(\text{CO}_2 + \text{H}_2\text{O}) > 0.97$. Petrologically, these data are best discussed together with phase equilibrium data for silicate- H_2O - CO_2 systems (Eggler, *Year Book* 72, pp. 457–467; *Year Book* 73, pp. 215–224; this Report; Mysen, *Year Book* 72, pp. 467–478; Mysen and Boettcher, 1975a, b). It

will only be pointed out here that the contrasting solubilities of ΣCO_2 and H_2O under upper mantle conditions present a possibility for generating a separate CO_2 -rich vapor phase during ascent (cooling and decompression) of an H_2O - and ΣCO_2 -bearing magma where the magma is likely to be close to ΣCO_2 saturation owing to the small solubility of ΣCO_2 .

In more general terms, the experimental method described here is directly applicable to solubility studies of multi-component vapors including hydrogen, chlorine, phosphorous, sulfur, and carbon in any system of interest because the only requirement is the availability of suitable β -emitting isotopes. Such isotopes are available for these elements (Table 13) and can be routinely employed for studies not previously possible.

Solubility Models for CO_2 in Silicate Melts

Experimentally determined carbon dioxide solubilities (ΣCO_2) of a few additional samples used in this study are given in Table 14. These data are plotted in Fig. 41 together with those for Ab, Jd, and Ne compositions and diopside (Eggler, Mysen and Seitz, *Year Book* 73, pp. 226–228).

The data in Fig. 41 show that $X^m_{\text{CO}_2}$ depends on the silicate melt composition. Notably, the solubilities in the two pyroxene compositions, Jd and Di, are very different (35%–44% more ΣCO_2 in Di than in Jd). Also, 27%–29% more ΣCO_2 dissolves in sample W47 than in Ne (Fig. 41). Sample W47 contains mainly normative olivine + larnite + nepheline. The olivine and larnite compositions therefore must dissolve in excess of 10 wt % ΣCO_2 at high pressure (20–30 kbar). Unfortunately, ΣCO_2 solubilities in these two compositions could not be analyzed because Mg_2SiO_4 and Ca_2SiO_4 melts do not quench to a clear glass free of quench minerals.

Previous investigators of ΣCO_2 solu-

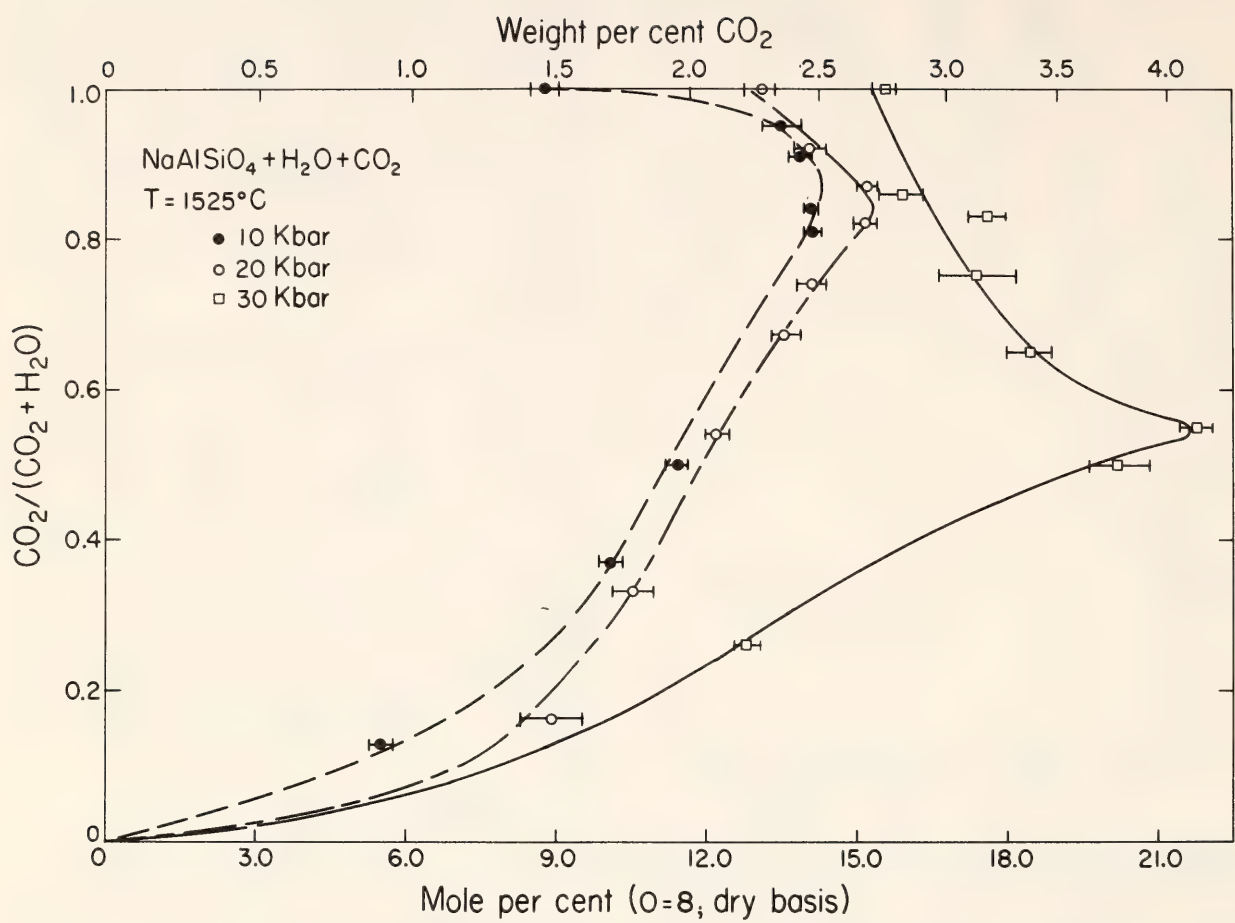


Fig. 38. Pressure dependence of ΣCO_2 solubility in Ne + H₂O + CO₂ melt at 1525°C. CO₂ = ΣCO_2 .

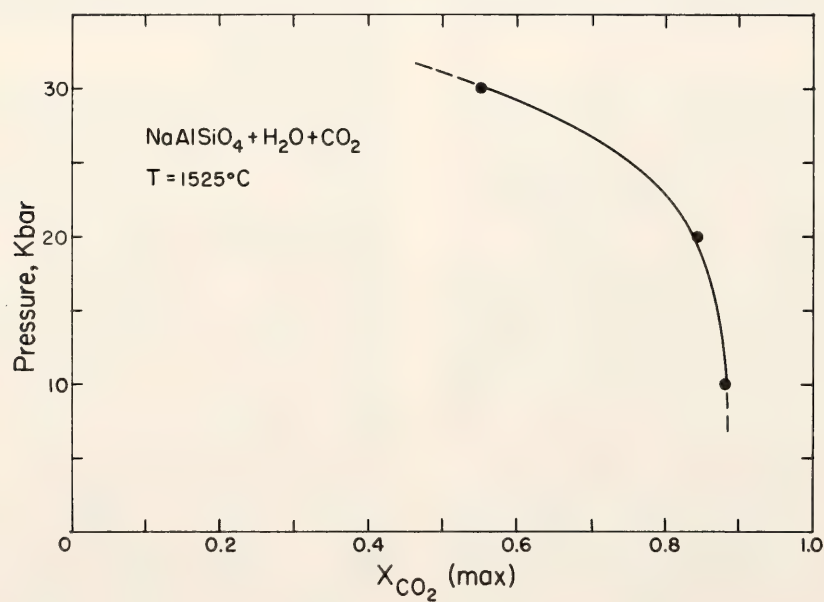


Fig. 39. CO₂/(CO₂ + H₂O) ($X^{\text{max}}_{\text{CO}_2}$) in the system Ne + H₂O + CO₂ corresponding to the maximum CO₂ solubility as a function of pressure at 1525°C.

TABLE 12. Solubility of H₂O and ΣCO₂ in NaAlSi₃O₈ Melt at 1450°C and 20 kbar

CO ₂ /(CO ₂ + H ₂ O)	H ₂ O (wt %)	CO ₂ (wt %)	X ^m _{H₂O}	X ^m _{CO₂}	X ^m _{Ab}
1.00	...	1.43	...	0.080	0.92
0.84	3.13	2.20	0.297	0.085	0.617
0.66	6.20	1.67	0.462	0.051	0.487
0.48	13.1	1.41	0.669	0.029	0.301
0.26	23.8*	1.15*	0.809	0.016	0.175
0.00	36.0†	...	0.891	...	0.109

* No optical evidence of exsolved vapor during quenching. Uncertainty in H₂O and CO₂ data about 5%.

† From Boettcher and Wyllie (1969).

bility in silicate melts have either implicitly assumed CO²⁻₃ to be the carbon species in the silicate melt (e.g., Pearce, 1964) or interpreted the data as consistent with CO²⁻₃ being the carbon spe-

cies (Morey and Fleischer, 1940; Wyllie and Tuttle, 1959; Eggler, Mysen, and Seitz, *Year Book* 73, pp. 226–228).

The data in Fig. 42 suggest a way to relate the basicity of the silicate melt, *B*, to ΣCO₂ solubility. The percentage of basic oxides is positively correlated with X^m_{CO₂}. However, melts of basic oxides of predominantly divalent cations (Mg²⁺

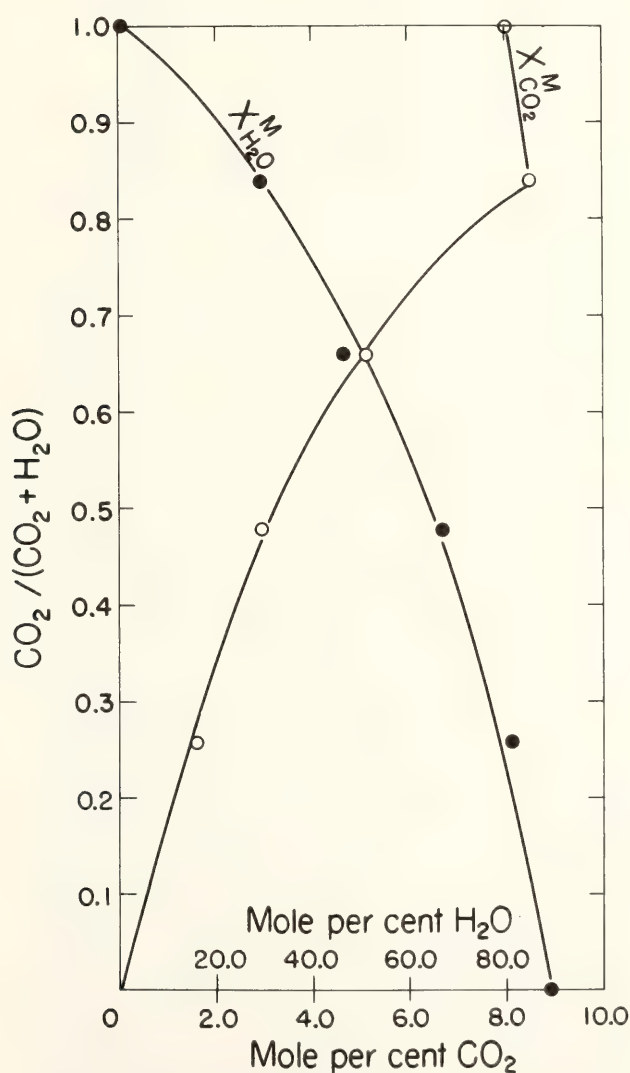


Fig. 40. Solubility of H₂O (X^m_{H₂O} × 100) and ΣCO₂ (X^m_{CO₂} × 100) in NaAlSi₃O₈ melt coexisting with (H₂O + CO₂) vapor. P_{total} = 20 kbar; T = 1450°C.

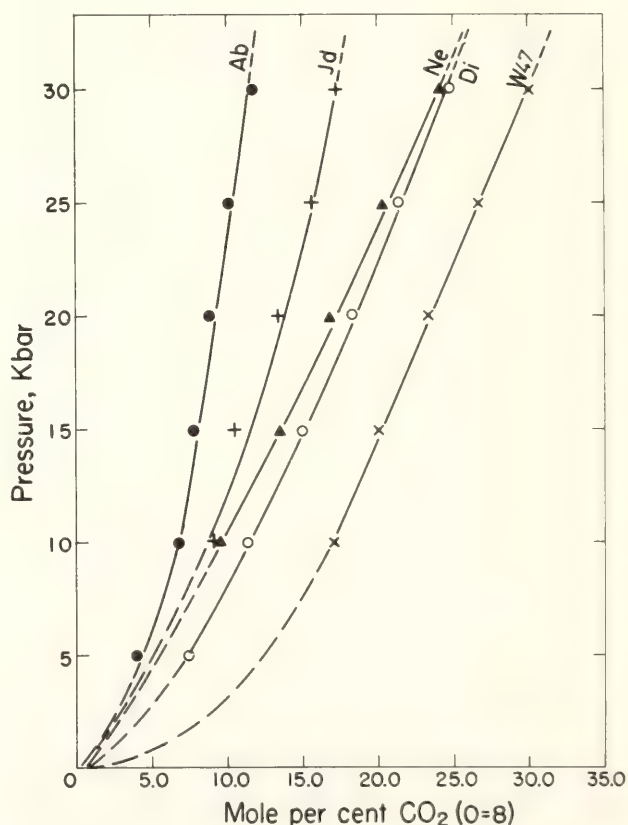


Fig. 41. Solubility isotherms for Ab, Jd, Ne, Di, and W47 compositions at T = 1625°C. Ab, NaAlSi₃O₈ + CO₂; Jd, Na_{4/3}Al_{4/3}Si_{8/3}O₈ + CO₂; Ne, Na₂Al₂Si₂O₈ + CO₂; Di, Ca_{4/3}Mg_{4/3}Si_{8/3} + O₈ + CO₂; W47, natural olivine melilite nephelinite (Winchell, 1947) + CO₂. CO₂ = ΣCO₂.

TABLE 13. Isotopes Suitable for Use in Solubility Studies of Volatile Components

Element	Isotope	$t_{1/2}$ *	ϵ^* (keV)	Sensitivity (ppm)†
Hydrogen	$^1\text{H}^3$	12.26 y	18.1	1.4×10^{-3}
Carbon	$^{12}\text{C}^{14}$	5770 y	156	1.65×10^{-1}
Phosphorous	$^{31}\text{P}^{33}$	25.0 d	250	1.5×10^{-6}
Sulfur	$^{32}\text{S}^{35}$	86.7 d	168	6.5×10^{-6}
Chlorine	$^{35}\text{Cl}^{36}$	3×10^5 y	710	4.72

* Half-lives ($t_{1/2}$) and decay energies (ϵ) from *Table of Isotopes* (compiled by Heath, 1966).
† Calculated according to Mysen and Seitz (1975) assuming perfect, carrier-free isotopes, silica-matrix, and exposure time of 2 months.
Abbreviations: d, days; y, years.

TABLE 14. Measured ΣCO_2 Contents of Silicate Liquids*

Pressure (kbar)	T (°C)	Run Duration (min)	Starting Material	CO_2 (wt %)	$X^{m*}_{\text{CO}_2}$ (O = 8)
20	1625	5	Or	1.48 ± 0.07	0.087
20	1625	5	C	1.49 ± 0.07	0.082
20	1625	5	CM	1.61 ± 0.06	0.087
10	1625	5	W47	3.5 ± 0.2	0.170
20	1625	5	W47	5.1 ± 0.3	0.233
30	1625	5	W47	7.0 ± 0.3	0.299

* Mole fraction of ΣCO_2 in melt.

and Ca^{2+}) appear to dissolve more than those of monovalent cations. This behavior is consistent with cation-carbonate complexing in the melt because the stabilities of carbonates such as CaCO_3 and MgCO_3 in the melt are most likely higher than those of monovalent cations (e.g., Na_2CO_3). However, the similar solubility of ΣCO_2 in feldspar-type melts with Na^+ exchanged with K^+ , Ca^{2+} , and $(\text{Ca,Mg})^{2+}$ (Table 14) does not support this hypothesis.

In an attempt to resolve the inconsistency, selected ΣCO_2 -saturated, quenched silicate liquids were studied with infrared spectrometric techniques. The resulting spectra are reproduced in Fig. 43, which shows that ΣCO_2 can enter silicate liquids both as CO_2 and as CO_3^{2-} . All samples show an absorption band at $4.3\text{ }\mu\text{m}$, which corresponds to molecular CO_2 . In addition, Di and W47 glasses quenched from 1600°C have a clear absorption at $7.0\text{ }\mu\text{m}$, which corresponds to

asymmetric stretching of a planar CO_3^{2-} anion. Absorption at longer wavelengths is obliterated by absorption related to the silicate matrix. Spectra *G*, *H*, and *I* (Fig. 43) also show a $7.0\text{ }\mu\text{m}$ absorption band corresponding to CO_3^{2-} . The absorption band in dry albite melt (spectra *H* and *I*) is small, suggesting only minor CO_3^{2-} ; however, the spectra have not been calibrated. Albite melt quenched from 1600°C and 20 kbar with 38% (mol) of vapor as H_2O shows a larger absorption at $7.0\text{ }\mu\text{m}$. These results indicate that the breakup of the silicate structure by adding H_2O promotes stabilization of CO_3^{2-} probably because of the higher $a^m_{\text{O}_2-}$ in hydrous than in volatile-free albite melt. Spectra *E* and *F* (Fig. 43) exhibit a peak at $7.4\text{ }\mu\text{m}$. This peak is tentatively ascribed to HCO_3^- but is somewhat enigmatic because the charge corresponding to spectrum *E* ($\text{Ab} + \text{CO}_2$ quenched from 1450°C and 20 kbar) contains no H_2O .

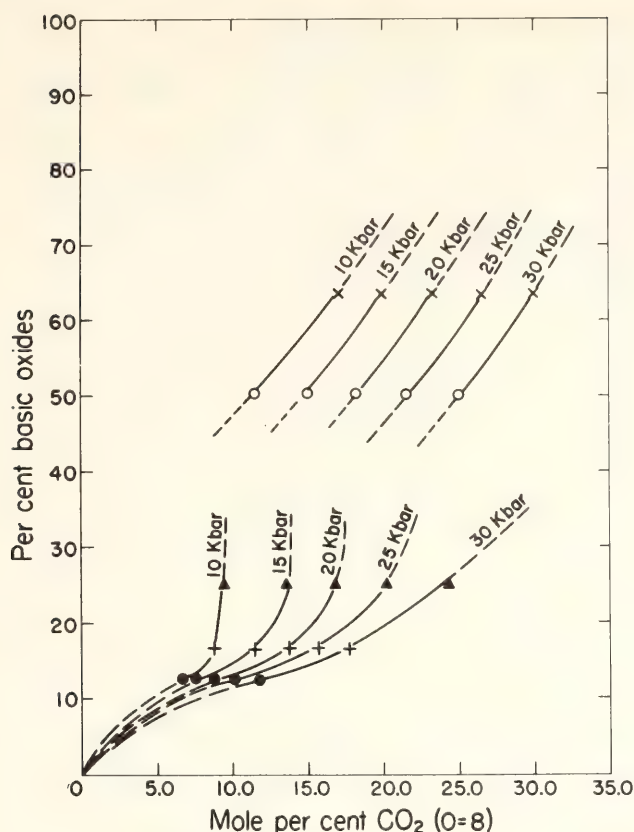


Fig. 42. Percentage of basic oxides of compositions vs. mol percentage of CO_2 in melt ($\text{O} = 8$) with $T = 1625^\circ\text{C}$. $\text{CO}_2 = \Sigma\text{CO}_2$. Symbols: solid circles, albite melt; plus signs, jadeite melt; solid triangles, nepheline melt; open circles, diopside melt; crosses, W47 (nephelinite) melt. Basic oxides: Na_2O , K_2O , CaO , MgO .

Also, the absorption is approximately as strong as the $7.4\ \mu\text{m}$ band of $\text{Ab} + \text{H}_2\text{O} + \text{CO}_2$ (at 1450°C and 20 kbar) even though the activity of H_2O ($a_{\text{H}_2\text{O}}$), and thus supposedly the activity of bicarbonate anion ($a_{\text{HCO}_3^-}$), would be much higher in $\text{Ab} + \text{H}_2\text{O} + \text{CO}_2$ (spectrum *F*) than in $\text{Ab} + \text{CO}_2$ (spectrum *E*). It is therefore doubtful that the $7.4\ \mu\text{m}$ peak corresponds to HCO_3^- , but it could be related to CO_3^{2-} . If this is the case, the vibrational energy of C-O bonds of the carbonate molecule in Ab melts quenched from 1450°C is slightly lower than in Ab, W47, and Di melts quenched from 1600°C . This possibility should not be excluded; in general, however, it seems that ΣCO_2 enters Ab melt predominantly as discrete CO_2 molecules and that a CO_3^{2-} component might become more important as the temperature

increases. The carbonate anion is generally present in less polymerized melts such as those of Di and W47. It is not clear whether the appearance of CO_3^{2-} is due to stabilization of cation-carbonate complexes by virtue of high Ca^{2+} and Mg^{2+} activities or due to higher activity of the oxygen anion in Di and W47 than in Ab melts (Di and W47 are less polymerized, thus the activity of the oxygen anion in the melt, $a_{\text{O}^{2-}}^m$, is higher). The appearance of CO_3^{2-} in Ab melt as the temperature increases indicates that increased $a_{\text{O}^{2-}}^m$ is the cause, since increasing temperature would tend to increase $a_{\text{O}^{2-}}^m$ (depolymerization by increased thermal agitation). Also, the absence of a cation effect on the ΣCO_2 solubility in feldspar melts at 1600°C (Table 14) suggests that $a_{\text{O}^{2-}}^m$ governs the extent of CO_3^{2-} formation in silicate melts.

The data obtained thus far suggest that the compositional dependence of CO_2 solubility in silicate melts relates to whether or not $a_{\text{O}^{2-}}^m$ at a given temperature and carbon dioxide activity is sufficiently high to stabilize CO_3^{2-} . In natural silicate melts, the small but compositionally dependent ΣCO_2 solubility has important implications because change in liquid composition due to fractional crystallization can affect the level of the ΣCO_2 -saturation surface considerably.

Petrological Implications of Contrasting Solubilities of Carbon Dioxide and Water during Partial Melting and Crystal Fractionation in the Upper Mantle

The relatively small solubility of ΣCO_2 in silicate melts as compared with H_2O provides a means of generating a separate vapor phase during magmatic evolution in the upper mantle. For example, 0.2 wt % ΣCO_2 in the source region of a basaltic melt at 15–20 kbar can saturate 10% of partial melt. Even if the initial melt is CO_2 -undersaturated,

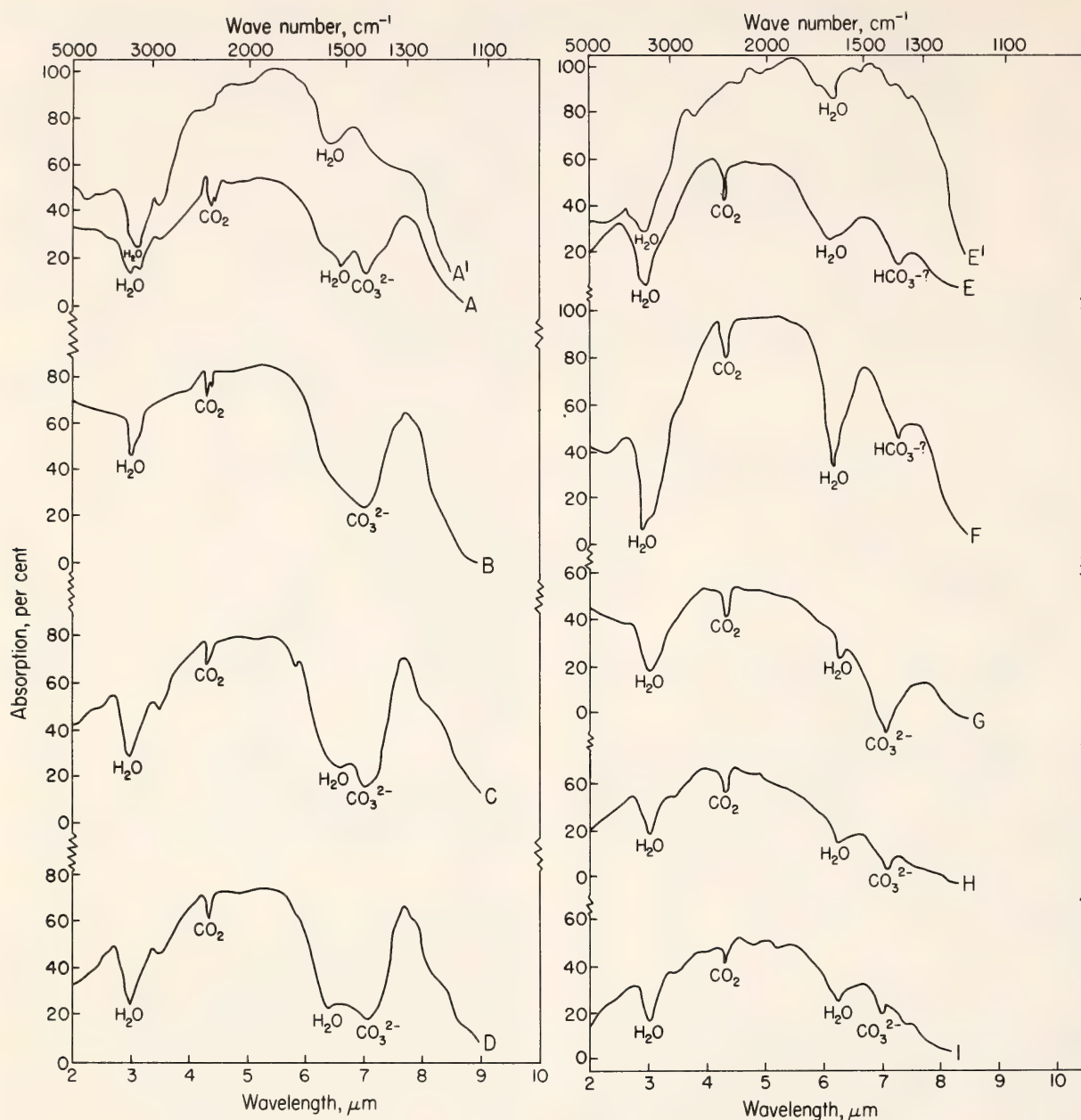


Fig. 43. Infrared spectra of ΣCO_2 - and $(\Sigma\text{CO}_2 + \text{H}_2\text{O})$ -saturated, quenched silicate liquids. Experimental details are given in Table 15.

the strong positive pressure and temperature dependence of the ΣCO_2 solubility (Figs. 34 and 36) may lead to saturation during cooling or decompression of the magma, or both. Experimental work on peridotite- H_2O - CO_2 systems at 10–30 kbar pressure (Mysen, *Year Book 72*, pp. 467–478; Eggler, *Year Book 73*, pp. 215–224; Boettcher, Mysen, and Modreski, 1975; Mysen and Boettcher, 1975a, 1975b) has demonstrated that the composition of a $(\text{H}_2\text{O} + \text{CO}_2)$ vapor phase can determine whether the liquid is quartz + orthopyroxene normative (andesite), orthopyroxene + olivine nor-

mative (tholeiite), or nepheline + olivine normative (nephelinite). Under conditions of very high ΣCO_2 activity, the liquids may even become larnite-normative. It is thus possible to fractionate even a quartz-normative liquid to one that contains olivine + nephelinite + larnite, provided the liquid is in equilibrium with a peridotite mineral assemblage and the $\text{CO}_2/\text{H}_2\text{O}$ ratio of the system increases during fractionation. The solubility data presented above can thus be combined with phase equilibrium data (Eggler, *Year Book 73*, pp. 215–224; Eggler, this Report; Mysen,

TABLE 15. Experimental Details of Infrared Spectrometry

Spectrum	Composition	<i>T</i> (°C)	<i>P</i> (kbar)	Scanning Speed (μm/min)	Wt Ratio (KBr/sample)
A'	Di glass	1400	0.001	1	99.03/0.97
A	Di + CO ₂ 3.17 ± 0.11 wt % CO ₂ (wet*)	1600	20	3	98.89/1.11
B	Di + CO ₂ 3.06 ± 0.11 wt % CO ₂ (dried*)	1600	20	3	99.02/0.98
C	W47 + CO ₂ 4.43 ± 0.12 wt % CO ₂ (wet)	1600	20	3	99.24/0.76
D	W47 + CO ₂ 4.44 ± 0.08 wt % CO ₂ (dried)	1600	20	3	99.10/0.90
E'	Ab glass	1600	20	3	99.00/1.00
E	Ab + CO ₂ 1.43 ± 0.09 wt % CO ₂ (wet)	1450	20	1	99.00/1.00
F	Ab + CO ₂ + H ₂ O 1.43 ± 0.03 wt % CO ₂ (dried) <i>X</i> _{co₂} = 0.52	1450	20	1	99.00/1.00
G	Ab + H ₂ O + CO ₂ 3.22 ± 0.14 wt % CO ₂ (dried) <i>X</i> ^v _{co₂} = 0.62	1600	20	3	99.00/1.00
H	Ab + CO ₂ 2.73 ± 0.18 wt % CO ₂ (wet)	1600	20	3	99.00/1.00
I	Ab + CO ₂ 2.73 ± 0.1 wt % CO ₂ (dried)	1600	20	3	99.00/1.00

* "Wet" and "dried" denote whether sample was kept at 110°C until analysis (at least 48 hours).

Year Book 72, pp. 467–478) to analyze the compositional variations to be expected in a magma in equilibrium with surrounding peridotite during ascent to the surface, provided the magma initially contained a small amount of CO₂. The nephelinite lavas of Hawaii, which contain websterite and peridotite nodules, serve as an example for this model. Olivine and pyroxene in these nodules are rich in CO₂-dominated fluid inclusions (Roedder, 1965; Green, 1972; Killingley and Muenow, 1974), supporting the contention that a CO₂-rich phase

may have played a role during the formation of the nephelinite magma. It is hypothesized that partial melting of garnet peridotite in the presence of perhaps a few tenths of a percent ΣCO₂ (and some H₂O) to yield ΣCO₂- and H₂O-undersaturated liquid of tholeiite affinity occurred at depths of 60–100 km beneath the Hawaiian Islands. Most of this magma may have risen rapidly to shallow depth before it differentiated (see Wright and Fiske, 1971). It is likely, however, that some of the primary magma remained at depth (~60

km?) where it slowly cooled. Because tholeiite-like magma can dissolve only about 3–4 wt % ΣCO_2 at the depth of its formation (corresponding to 20–30 kbar pressure), 10%–20% melting results in a magma close to ΣCO_2 saturation; and because the temperature dependence of the ΣCO_2 solubility (Fig. 34) is very strong at this pressure, the ΣCO_2 solubility decreases rapidly ($a^m_{\text{CO}_2}$ increases) as the magma cools. Also, precipitation of cumulate phases such as clinopyroxene, and perhaps some garnet, decreases the amount of melt and thus increases the proportion of ΣCO_2 in the residual magma. In fact, if the rare earth element data of Schilling and Winchester (1969) are applied to the problem, only about 10% of the initial tholeiite magma volume can become nephelinite. At the high a_{CO_2} conditions thus established, the magma, in equilibrium with peridotite, must be nephelinitic or perhaps even melilite nephelinite (Mysen, *Year Book* 72, pp. 467–478; Eggler, *Year Book* 73, pp. 215–224; Mysen and Boettcher, 1975b). The high vapor pressure also acts as a propellant for a rapid ascent of the magma, carrying with it ultramafic and pyroxenite nodules. This model is consistent with both field and trace element data as well as phase equilibrium data.

Exsolution of a CO_2 -rich vapor during cooling or decompression of an ($\text{H}_2\text{O} + \text{CO}_2$)-bearing magma, or both, may also produce a separate CO_2 -rich phase, which could be left behind in the form of a carbonate phase (Eggler, this Report) or as vapor after the magma ascends. During subsequent melting of peridotite mantle this CO_2 -rich vapor phase is instrumental in determining the composition of the initial melt. Mysen and Boettcher (1975b) ascribed the occurrence of highly alkaline, silica-undersaturated magmas associated with carbonatite in southwest Africa (e.g., Dawson, Powell and Reid, 1970) and in Siberia (e.g., Ukhonov, 1965; Egorov, 1970) to melting of peridotite under such conditions.

Eggler (this Report) demonstrates how the formation of carbonatite and silicate melts is related. However, the models of Mysen and Boettcher (1975b) and Eggler (this Report) lack a mechanism for generating the high a_{CO_2} conditions. The data on CO_2 solubility presented here may be the key to this problem, inasmuch as they provide a means of generating a CO_2 -rich vapor phase that may be stored either in the form of a vapor or, as suggested by Eggler (this Report), in the form of carbonate mineral(s).

PERIDOTITE-CARBONATE RELATIONS IN THE SYSTEM $\text{CaO-MgO-SiO}_2\text{-CO}_2$

David H. Eggler

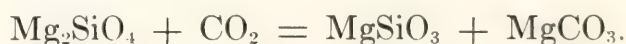
Interest in the role of CO_2 in the derivation of magmas has been stimulated in a number of ways. These include the recognition of CO_2 fluid inclusions in mantle-derived minerals (Roedder, 1965; Green, 1972), the discovery that CO_2 is significantly soluble in silicate melts (Eggler, *Year Book* 72, pp. 457–467), and the discovery that CO_2 has a significant effect on liquidus relations of systems involving olivine and pyroxene (Eggler, *Year Book* 73, pp. 215–224; Mysen and Boettcher, 1975b; Brey and Green, 1975). In addition there has been continuing investigation of silicate-carbonate relations in the system $\text{CaO-MgO-SiO}_2\text{-CO}_2$ (Irving and Wyllie, 1973, 1975; Huang and Wyllie, 1974, 1975; Newton and Sharp, 1975; Kushiro, Satake, and Akimoto, 1975). Eggler (*Year Book* 73, pp. 215–224) has also investigated the system $\text{CaO-MgO-SiO}_2\text{-CO}_2$, particularly the phase relations involving peridotite minerals—olivine, orthopyroxene, and clinopyroxene. A critical join involving a model peridotite, carbonate, and melt is $\text{CaMgSi}_2\text{O}_6\text{-Mg}_2\text{SiO}_4\text{-CO}_2$. Phase relations on this join define the presence or absence of carbonate in the subsolidus phase assemblage of peridotite compositions and the degree of silica saturation of partial

melts derived from peridotite compositions. Eggler (*Year Book* 73, pp. 215–224) discovered that orthopyroxene was a liquidus phase on this join at 30 kbar pressure. It has now been found that orthopyroxene has a stability field extending well toward carbonate compositions, with the result that peridotite composition will melt at a relatively low temperature to a very silica-undersaturated liquid, which may be related to melilitite and kimberlite. Because of the abrupt shift in the solidus temperature at about 28 kbar pressure, a geotherm may cross the solidus. In a mantle containing a CO₂-rich vapor, such a crossing would lead to a small degree of melting that would explain seismic properties of the low-velocity zone.

Runs have been made in sealed platinum capsules in solid-media, high-pressure apparatus and are unbuffered for H₂ pressure. However, the pressure assembly itself buffers P_{H_2} at a level low enough that CO₂ in the capsules remains essentially as CO₂ during the experiment (Eggler, Mysen, and Hoering, *Year Book* 73, pp. 228–232). The piston-out technique was used with an initial excess pressurization of about 2 kbar. Starting materials included glasses or mixtures of glass + crystals (Kushiro and Schairer, *Year Book* 62, p. 96); mechanical mixtures of silica, calcite, dolomite, and MgO; and a mixture of crystalline enstatite and dolomite. To all these materials Ag₂C₂O₄ was added in all the capsules to ensure that there was an excess of CO₂ vapor. Quenched charges have been studied by a combination of optical microscopy, x-ray diffraction, and electron microprobe analysis. The interpretation of run products is seldom unambiguous, because few of the phases attain a size in excess of a few micrometers and because of extensive quench crystallization of the melts. Some of the quench crystals assume a typical dendritic pattern but most of them appear as granular aggregates of crystals 1–2 μ m in size. These crystals are some-

times difficult to distinguish from stable crystals that, although euhedral, are also small. Granular, clear stable carbonate crystals can be distinguished from turbid quench crystals (see Irving and Wyllie, 1975). Quench minerals include clinopyroxene, olivine, and carbonate. Enstatite is not found as a quench mineral, probably because it is not a stable phase of the low-pressure, low-temperature assemblage in the compositional volume CaMgSi₂O₆-Mg₂SiO₄-MgO-CaO-CO₂ within which the melts lie. The composition of carbonate, whether stable or quenched from liquid, has been determined for most runs by measurement of the 211 peak (Goldsmith and Graf, 1958). These measurements were useful in understanding compositional relations and detecting melting. Enstatite compositions were determined in two runs by electron microprobe analysis and were found to be MgSiO₃ with a very small CaMgSi₂O₆ component. Olivine compositions were analyzed from two near-liquidus runs on the join Ca₂SiO₄ (La)-Mg₂SiO₄ (Fo)-CO₂ at bulk (volatile-free) compositions La₅₀Fo₅₀ and La₃₃Fo₆₇ and were found to be Fo_{97.5–99.3}La_{2.5–0.7}. All olivines are therefore assumed to be essentially CaO free.

There are three subsolidus phase assemblages on the join CaMgSi₂O₆-Mg₂SiO₄-CO₂ at 30 kbar pressure (Fig. 44): diopside (Di) + enstatite (En) + dolomite (Dol) + CO₂ vapor (V), En + Dol + magnesite (Mag) + V, and forsterite (Fo) + En + Dol + V. Phase boundaries have been determined in part by measurement of carbonate compositions and in part by use of data on the Di-En solvus (Davis and Boyd, 1966) and the Dol-Mag solvus (Irving and Wyllie, 1975). The assemblage En + Dol + Mag + V changes to the higher temperature assemblage Fo + En + Dol + V at 1210° ± 20°C by the reaction



Newton and Sharp (1975) also studied

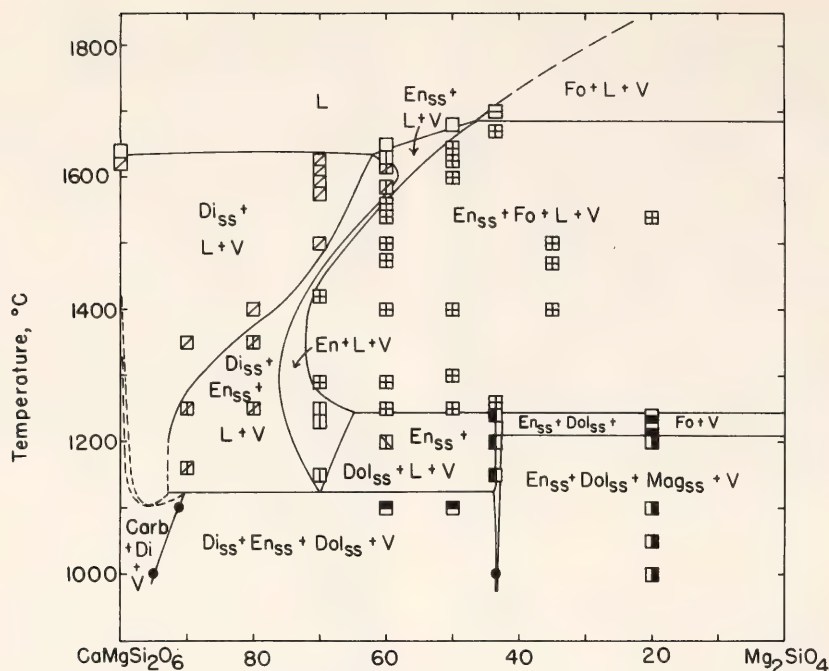
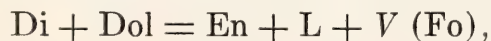


Fig. 44. Phase relations on the join $\text{CaMgSi}_2\text{O}_6$ - Mg_2SiO_4 in the presence of an excess of CO_2 (more than about 20 wt %). Solid circles indicate phase boundaries determined by measurement of phase compositions.

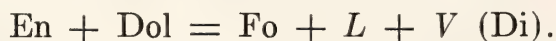
this reaction and found the transition at 1240°C at 30 kbar. The experimental difference may be explained by an effect of small amounts of CaO in phases in the present study. According to Kushiro, Satake, and Akimoto (1975), the assemblage $\text{En} + \text{Di} + \text{Dol}$ reacts to $\text{Mag} + \text{En} + \text{Di}$ at a temperature of about 550°C at 30 kbar. No experiments were made under these conditions in this study. A small stability field for $\text{Di} + \text{Mag}$ at a pressure less than 22 kbar was deduced from Schreinemaker's principles (Fig. 46).

Melting occurs on the join (Fig. 44) by two reactions. The assemblage $\text{En} + \text{Di} + \text{Dol} + \text{V}$ melts at $1125^\circ \pm 20^\circ\text{C}$ to the assemblages $\text{Di} + \text{En} + \text{L} + \text{V}$ and $\text{En} + \text{Dol} + \text{L} + \text{V}$ (Fig. 44). Detection of the melting reaction,



was based on the presence of stable euhedral Di and monitoring of carbonate composition. While only Dol is present at subsolidus temperatures, carbonate quenched from melt is more calcite-rich. The phase assemblage $\text{En} + \text{Fo} + \text{Dol} + \text{V}$ melts at a temperature of 1245°

$\pm 15^\circ\text{C}$ to $\text{En} + \text{Fo} + \text{L} + \text{V}$ (Fig. 44) by the second reaction,



This reaction was detected primarily by the first appearance of olivine as a phase in runs on the bulk composition $\text{Di}_{43.5}\text{-Fo}_{56.5}$, which was prepared as a mechanical mixture of pure enstatite and pure analyzed dolomite. A temperature of 1245°C also marks the melting of the assemblage $\text{En} + \text{Dol} + \text{L} + \text{V}$ to $\text{En} + \text{Fo} + \text{L} + \text{V}$ (Fig. 44), detected by the appearance of Fo and disappearance of stable Dol.

At supersolidus temperatures, the join (Fig. 44) is characterized by a melting interval of over 300°C involving Fo, En, and Di. Liquidus relations on the join have been presented previously (Eggler, *Year Book* 73, pp. 215-224) and are notable for the small primary phase field of En and the extended phase field of Fo.

The phase relations in Fig. 44 have been used to draw isothermal projections of the tetrahedron $\text{CaO-MgO-SiO}_2\text{-CO}_2$ at 30 kbar pressure (Fig. 45). These projections are in part inferred but are also based on unpublished phase relations

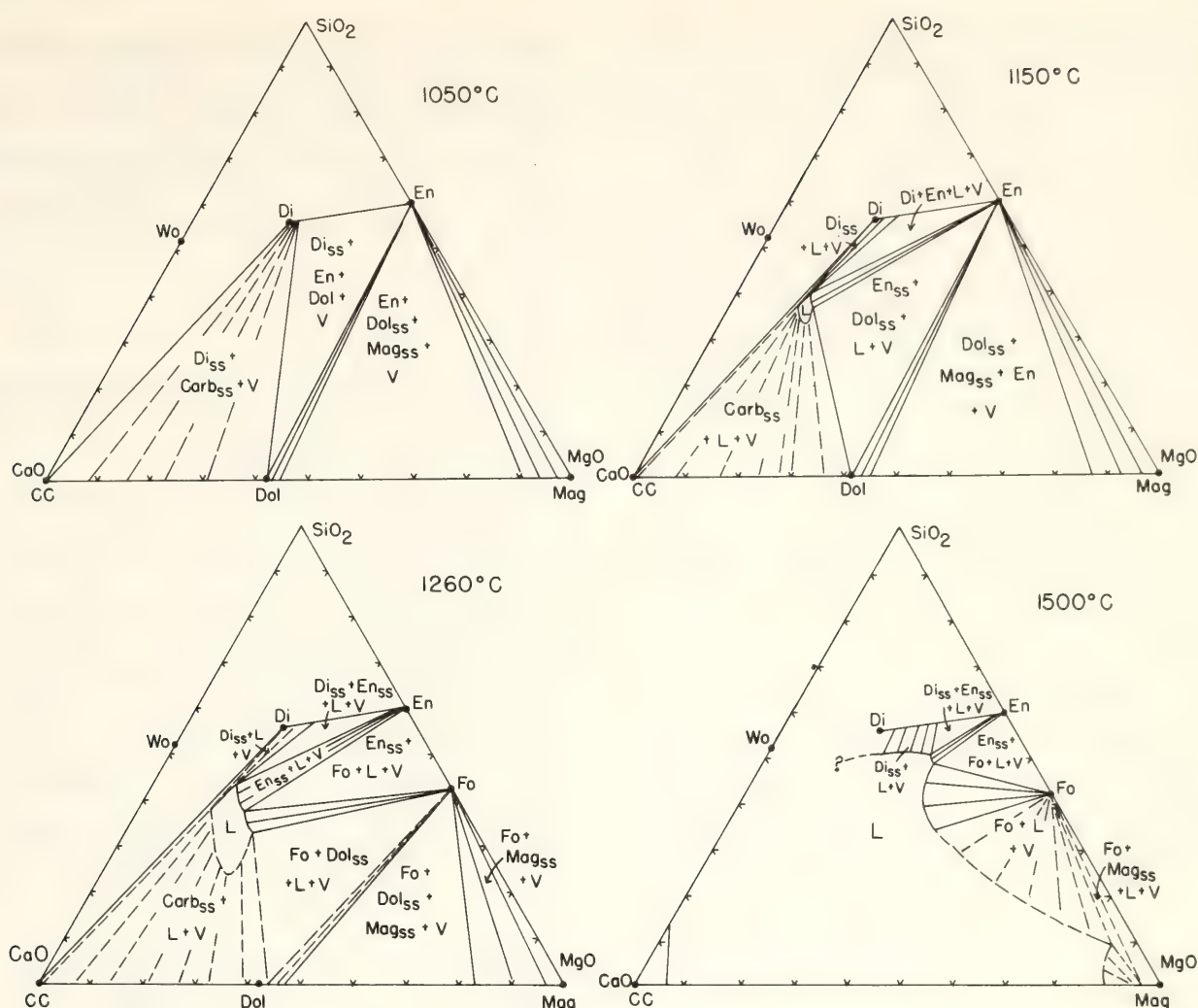
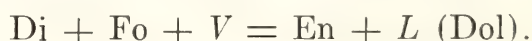


Fig. 45. Isothermal projections, at 30 kbar pressure, of phase relations of interest with respect to peridotite assemblages in the system $\text{CaO-MgO-SiO}_2\text{-CO}_2$. Compositions are projected onto the plane CaO-MgO-SiO_2 . All fields contain vapor. Boundaries are dashed where not well known. Phase relations of carbonates are based on measured carbonate compositions and data of Irving and Wyllie (1975).

determined on the join Ca_2SiO_4 (La)– Mg_2SiO_4 (Fo)– CO_2 . In particular it should be noted that the melt in equilibrium with $\text{En} + \text{Fo}$ at 1260°C has a SiO_2 content of less than 37%. Because En was found as a liquidus phase for the composition $\text{La}_{65}\text{Fo}_{35}$, melt coexisting with $\text{En} + \text{Fo}$ must lie on the SiO_2 -poor side of the join Fo-La (in projection).

The reactions discussed previously are two of five univariant reactions emanating from an invariant point of relevance to an understanding of peridotite-carbonate relations. This point and the reaction sequence, deduced by Schreinemakers' rules, appear in Fig. 46b. The position of three of these reactions can

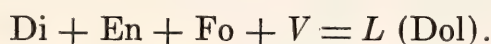
be determined from runs on the $\text{En} + \text{Dol}$ composition, which are shown in Fig. 46a. The pressure of the invariant point can be closely fixed by the reaction



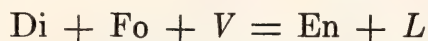
The reaction has a very flat slope and limits the invariant point to a pressure between 27.5 and 30 kbar.

In the model system $\text{CaO-MgO-SiO}_2\text{-CO}_2$, peridotite compositions lie in the compositional triangle $\text{CaMgSi}_2\text{O}_6\text{-MgSiO}_3\text{-Mg}_2\text{SiO}_4$. The subsolidus phase assemblage will be $\text{Di} + \text{Fo} + \text{En} + \text{V}$ only for a relatively low-pressure (less than 27.5 kbar), high-temperature (more than 1000°C) regime. At higher pressures or lower temperatures the phase assem-

blage will be $\text{En} + \text{Fo} + \text{Dol} + \text{V}$ (in the absence of vapor, $\text{En} + \text{Di} + \text{Fo} + \text{Dol}$) or $\text{En} + \text{Mag} + \text{Dol} + \text{V}$ (in the absence of vapor, $\text{Mag} + \text{Dol} + \text{Fo} + \text{En}$ or when even less CO_2 is present relative to refractory components, $\text{Dol} + \text{En} + \text{Fo} + \text{Di}$). The phase assemblage that *melts*, however, is $\text{Di} + \text{Fo} + \text{En} + \text{V}$ at pressures less than about 27.5 kbar, and melting takes place at elevated temperature ($1400^\circ\text{--}1550^\circ\text{C}$) by the reaction

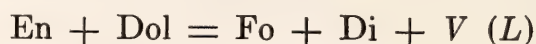


At a pressure of about 27 kbar a singular point S_1 occurs at which the reaction changes to



This point marks the appearance of En on the liquidus on the join $\text{CaMgSi}_2\text{O}_6\text{--Mg}_2\text{SiO}_4\text{--CO}_2$, as discussed by Eggler (*Year Book 73*, pp. 214–224). Brey and

Green (1975) have found a similar effect in a natural melilitite composition. Between 27 and 30 kbar the solidus temperature falls rapidly to the invariant point I_1 , which marks the intersection of the solidus with the decarbonation reaction



At higher pressure the solidus reaction ($\text{En} + \text{Dol} = \text{Fo} + \text{L} + \text{V}$) probably assumes a positive slope.

Possible oceanic and shield geotherms are also shown in Fig. 46 (Clark and Ringwood, 1964; Ringwood, 1966). The oceanic geotherm crosses the kinked solidus of the model peridotite at about 29 kbar (90 km depth). At greater depth, the mantle would consist of peridotite containing pockets of melilititic magma. A similar model has been proposed for a H_2O -bearing mantle (Lambert and Wyllie, 1968). In that model, melting

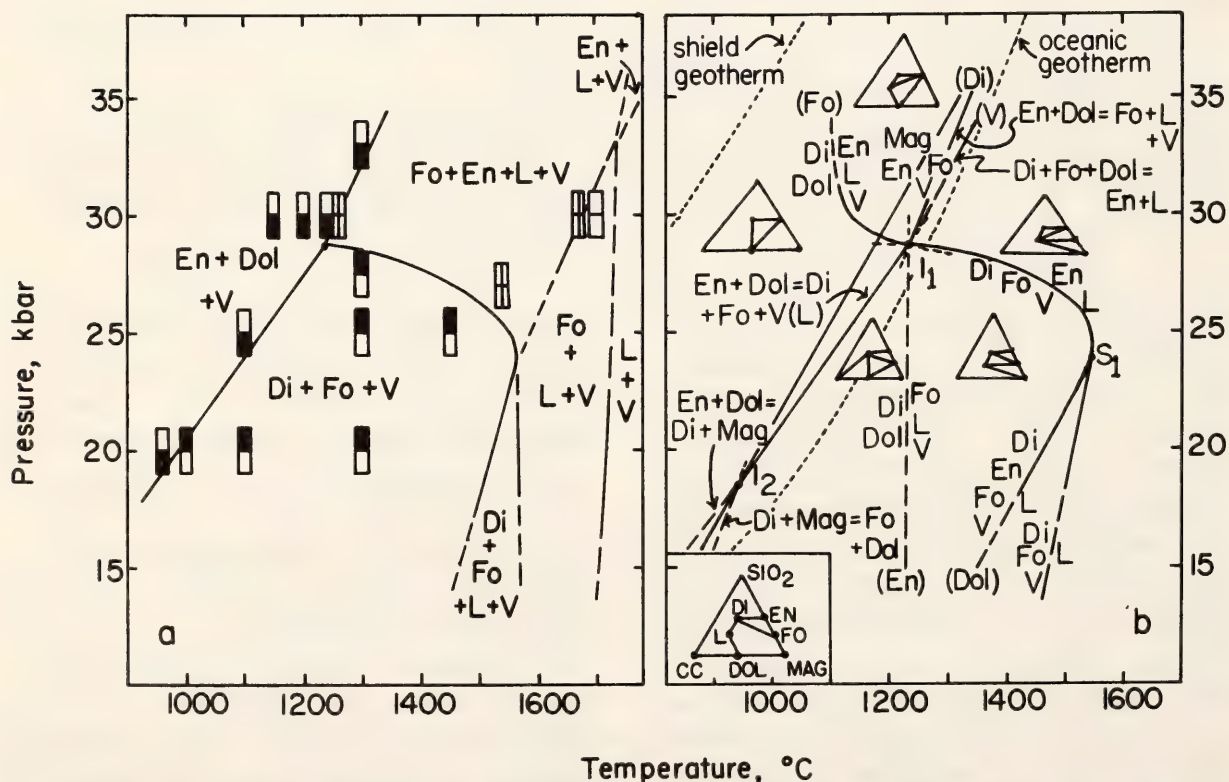


Fig. 46. (a) Phase relations of the composition $\text{En}_{68.5}\text{Dol}_{31.5}$ (equivalent to $\text{Di}_{43.5}\text{Fo}_{56.5} + \text{CO}_2$) with an excess of CO_2 vapor based on runs shown and data of Eggler (*Year Book 73*, pp. 215–224). Dashed lines indicate that relations were not determined. (b) Phase relations involving forsterite, enstatite, diopside, and carbonates in the system $\text{CaO-MgO-SiO}_2\text{-CO}_2$, as deduced from experiment and analysis by Schreinemaker's rules. Reaction $\text{Mag} + \text{En} = \text{Fo} + \text{V}$ is taken from Newton and Sharp (1975), corrected by +1.5 kbar to be compatible with the present data. Geotherms are taken from Clark and Ringwood (1964) and Ringwood (1966).

below a depth of about 100 km occurs because of instability of amphibole. In either model, pockets of melt can explain seismic properties of the low-velocity zone. However, in a mantle with a bulk composition including CO_2 (or a CO_2 -rich mixture of $\text{CO}_2 + \text{H}_2\text{O}$), residual melts will be melilititic. Melts produced in the presence of H_2O may be alkaline or tholeiitic but will certainly be more silica-saturated (Kushiro, 1972a; Eggler, *Year Book* 73, pp. 215–224). Melting of a typical peridotite composition ($\text{Fo}_{75}\text{-En}_{15}\text{Di}_{10}$) in the vapor-saturated simple system at temperature $5^\circ\text{--}20^\circ\text{C}$ above the solidus will produce only about 4% melt (Fig. 45); vapor-absent melting will produce less. Thus a natural melt would be rich in incompatible elements. Addition of highly alkalic melt rich in incompatible elements can explain trace element characteristics of depleted peridotite nodules (Frey and Green, 1974), and subtraction of such melt from parental peridotite can explain trace element characteristics of oceanic basalts (Gast, 1968).

At high pressure, the subsolidus phase assemblage of peridotite contains the carbonate minerals dolomite and magnesite. This hypothesis has been suggested by Irving and Wyllie (1973), and appropriate reactions have been studied by Newton and Sharp (1975) and Kushiro, Satake, and Akimoto (1975), and in the present work. Carbonates form by various reactions at the expense of diopside and olivine. The exact pressure at which carbonates form depends upon the bulk composition, including amounts of CO_2 and H_2O , and the geotherm. Because it is unlikely that sufficient CO_2 is present in the mantle to completely react out appropriate silicate minerals, free vapor will not be present. For this reason CO_2 fluid inclusions in mantle-derived minerals must form at relatively shallow depths, perhaps by decomposition of carbonates. Carbonates react rapidly with silicates and are unlikely to reach the surface. Indeed, car-

bonate inclusions in peridotite minerals are rare (McGetchin and Besancon, 1973). Of course, even if no vapor is present, carbonate stabilities remain as depicted in Fig. 46b, because at temperatures exceeding carbonate stabilities, CO_2 pressure equals total pressure. If H_2O is also present, however, CO_2 fugacity is lowered and carbonates are less stable.

Clinopyroxene is a rare phase in peridotite inclusion suites in diamonds (Meyer and Boyd, 1972). One interpretation of this observation is that in the environment in which diamonds form, CO_2 was sufficiently abundant to completely react out clinopyroxene by the reaction $\text{Di} + \text{Fo} + \text{V} = \text{En} + \text{Dol}$, the dolomite concurrently melting to form kimberlite liquid. However, CO_2 was not sufficiently abundant to react out olivine to enstatite + magnesite, because olivine is a common phase in diamonds (Meyer and Boyd, 1972).

Although kimberlite magmas are believed to originate at pressures considerably in excess of the 30 kbar at which experiments have been conducted, it can now be demonstrated that peridotite assemblages that include carbonate melt at temperatures much lower than dry peridotite (1245°C at 30 kbar compared with over 1600°C). The presence of H_2O would lower these temperatures further, although H_2O fugacity cannot be high. If there were a significant $f_{\text{H}_2\text{O}}$, and hence reduced f_{CO_2} , the stability fields of carbonates would be reduced. Moreover, partial melts formed in the presence of $\text{H}_2\text{O} + \text{CO}_2$, rather than CO_2 alone, would be more silica-rich than kimberlite composition (Eggler, *Year Book* 73, pp. 215–224; Mysen and Boettcher, 1975b).

It has been thought that fractionation is necessary to produce extremely silica-poor liquids from a peridotite parent (Huang and Wyllie, 1974). It now appears probable that liquids with low SiO_2 content (36 wt % SiO_2 , 16% MgO , 48% CaO on a volatile-free basis, at 30

kbar) can be produced by direct partial melting. This SiO_2 content is comparable to that of kimberlites and melilitites, but the ratio of CaO/MgO is far larger than that of natural rocks. Partial melt compositions will change with the addition of other components and at higher pressures. Alternatively, natural kimberlite compositions, which are variable, may represent mixtures of melt and residual peridotite or mixtures of two or more melts. It should also be recognized that an increased degree of partial melting considerably decreases the CaO/MgO ratio of melt, and although SiO_2 content increases, melts are still larnite-normative (see 1500°C projection, Fig. 45).

Yoder (*Year Book* 72, pp. 449–457) has demonstrated that akermanite composition in the presence of CO_2 melts to a homogeneous glass. Although glasses were not found as quench products in this study, there was no textural evidence of immiscibility. Thus in the system $\text{CaO-MgO-SiO}_2\text{-CO}_2$ immiscibility plays no role in the derivation of highly silica-undersaturated melts. The presence of alkalis may increase the compositional region in which immiscible carbonate and silicate liquids separate (Koster van Groos and Wyllie, 1973; Koster van Groos, 1975).

SOLUTION OF H_2O AND CO_2 IN DIOPSIDE MELT

M. Rosenhauer and David H. Eggler

Volatile species play important roles in melting, elemental partitioning, and material transport in the earth's upper mantle and crust. The two most abundant volatile species in natural rocks and gases are H_2O and CO_2 . To increase the understanding of the behavior of these volatiles in melts of basic chemical character, melting and solubility studies have been conducted on the $\text{CaMgSi}_2\text{O}_6$ (diopside) composition.

Melting curves were determined to extend known melting relations and to test the applicability of differential ther-

mal analysis (DTA) methods. The DTA measurements were conducted in an internally heated, gas-pressure apparatus (Yoder, 1950). The DTA equipment is a modification of that used by Yoder (1951). The principal improvements are preamplification of temperature and differential temperature signals and registration on a two-pen recorder having sensitivities of 0.1 mV/inch and $6\ \mu\text{V/inch}$ of chart. High-pressure DTA experiments on volatile components were first attempted by Harker (1964) in sealed platinum capsules. Unlike his method, in this study only one capsule, 4 mm in diameter and 20 mm long, was required because the reference thermocouple could be placed in grain Alundum, which served as space filler in the furnace assembly. For increased sensitivity the Pt-Pt10%Rh thermocouple wires were spotwelded into a sleeve on the bottom of the capsule. The heating rate was usually $8^\circ\text{--}10^\circ\text{C/min}$, but when melting occurred over a large temperature interval, heating rates up to 30°C/min were required. Starting materials for the DTA experiments were an exceptionally pure natural diopside from Twin Lakes, California, kindly provided by H. S. Yoder, Jr., and diopside synthesized by Eggler. For experiments with CO_2 , a mechanical mixture of oxides and carbonate prepared by Eggler (*Year Book* 72, pp. 457–467) was employed. For each run, approximately 100 mg of sample was loaded into Pt capsules, which were welded shut without loss of volatiles. Thirty-one experiments have been carried out, in the course of which over 200 determinations of melting temperature were made. Some of these results are plotted in Fig. 47.

In order to correlate melting temperature and DTA signal, diopside was melted at 1 atm. In three independent experiments it was found that the melting temperature of diopside at 1 atm, 1391.5°C , agreed within $\pm 3^\circ\text{C}$ with the peak temperature of the DTA signal. Therefore, all melting temperatures

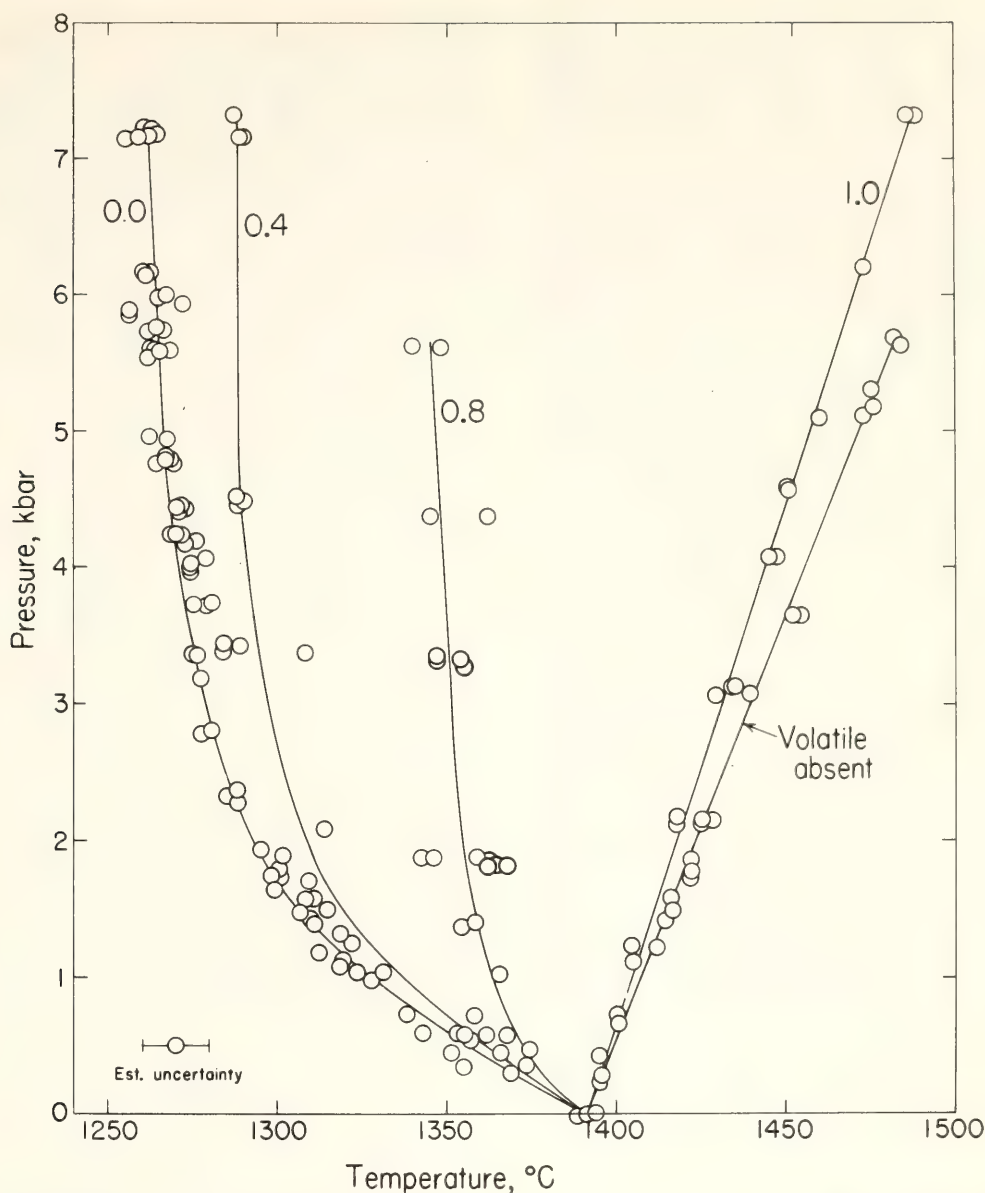


Fig. 47. Melting of diopside in the presence of CO_2 and H_2O vapor and in the absence of volatiles. Numbers indicate $\text{CO}_2/(\text{CO}_2 + \text{H}_2\text{O})$ of vapor. Each circle represents one DTA measurement; peak temperatures have been recorded.

measured by DTA refer to peak temperatures unless otherwise stated. The same correlation between the melting temperature and the maximum of the DTA signal was used by Yoder (1951).

The melting curve with no volatiles present was determined by runs in sealed Pt capsules and is consistent with results of Boyd and England (1963) at higher pressure. Yoder (1951) reported results about 15°C lower at 5 kbar pressure. His runs, however, were made in capsules open to argon. One DTA run in which the capsule was believed to have been accidentally open to argon gave results consistent with those of Yoder

(1951). These experiments are interpreted to indicate a small freezing-point depression by argon. It is significant that Yoder's (1951) results are very close to the CO_2 -saturated melting curve determined by DTA (Fig. 47). Because argon certainly enters the silicate melt as a molecular species, CO_2 , although a somewhat larger molecule than argon, probably also dissolves as a molecular species at low pressure. At pressures greater than 10 kbar, infrared spectra of quenched CO_2 -bearing diopside glass indicate the presence of the carbonate ion (B. O. Mysen, D. H. Eggler, M. G. Seitz, and J. R. Holloway, in preparation); and the

melting curve, determined by quenching runs in solid-media apparatus (Fig. 48), deviates considerably from the volatile-absent melting curve.

The H_2O -saturated melting curve of diopside (Fig. 47) was determined by DTA methods on samples containing excess H_2O and also on samples containing insufficient H_2O to saturate the sample when completely melted. In the latter experiments the DTA signal is characterized by a broad peak having two maxima (Rosenhauer, this Report). In both types of experiments the sample first melts to a H_2O -saturated liquid, and thus the peak temperature of the DTA signal in experiments with excess H_2O and the temperature of the first maximum on broad peaks in experiments containing insufficient H_2O to saturate the completely melted sample agree within experimental uncertainties. The curve fitted through measured melting points extrapolates smoothly to fit melting points determined by quenching runs in solid-media, high-pressure apparatus

at 20 kbar pressure by Eggler (*Year Book 73*, pp. 459–467) and at 30 kbar (Fig. 49). The interpolated value of 10 kbar, $1252^\circ \pm 10^\circ\text{C}$, agrees within experimental uncertainty with the value $1265^\circ \pm 5^\circ\text{C}$ determined by Yoder (*Year Book 64*, pp. 82–89). Hodges (*Year Book 73*, pp. 251–255) determined a melting temperature of $1265^\circ \pm 10^\circ\text{C}$ at 30 kbar, indicating a change in the slope of the melting curve from negative to positive on a P - T projection. The $\text{CaMgSi}_2\text{O}_6$ - H_2O join was redetermined at 30 kbar (Fig. 49), and a solidus temperature of $1240^\circ \pm 10^\circ\text{C}$ was obtained. Because in vapor-saturated regions the solidus temperature is also the liquidus temperature, the solidus is taken at the disappearance of crystals in vapor-present runs. The criterion of first appearance of melt may be ambiguous because diopside has been found to melt incongruently at 1 atm pressure, producing traces of melt below the nominal melting curve (Kushiro, *Year Book 72*, pp. 708–710; Biggar and O'Hara, 1969).

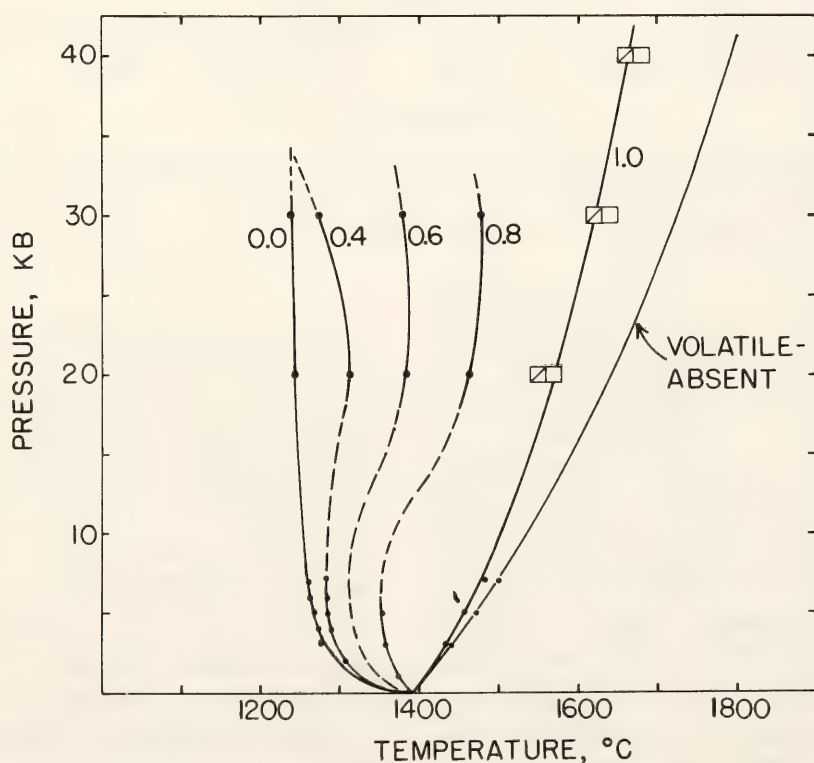


Fig. 48. Melting of diopside in the presence of CO_2 and H_2O vapor and in the absence of volatiles. Numbers indicate $\text{CO}_2/(\text{CO}_2 + \text{H}_2\text{O})$ of vapor. Points have been determined by DTA methods at pressures less than 10 kbar and by quenching methods at other pressures. For CO_2 -saturated melting, actual runs at 20–30 kbar are shown.

This behavior may continue to high pressure. Indeed, runs at temperatures as low as 1215°C at 30 kbar (Fig. 49) contained traces (<0.2%) of quench crystals. The disappearance of crystals occurs between 1240°C, where a run contained equal amounts of crystals and quench

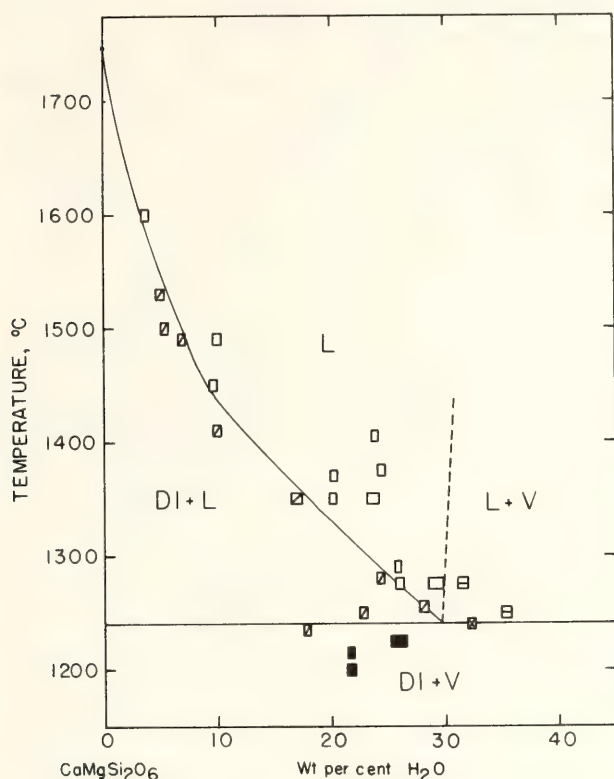


Fig. 49. Phase relations on the join $\text{CaMgSi}_2\text{O}_6$ - H_2O at 30 kbar pressure.

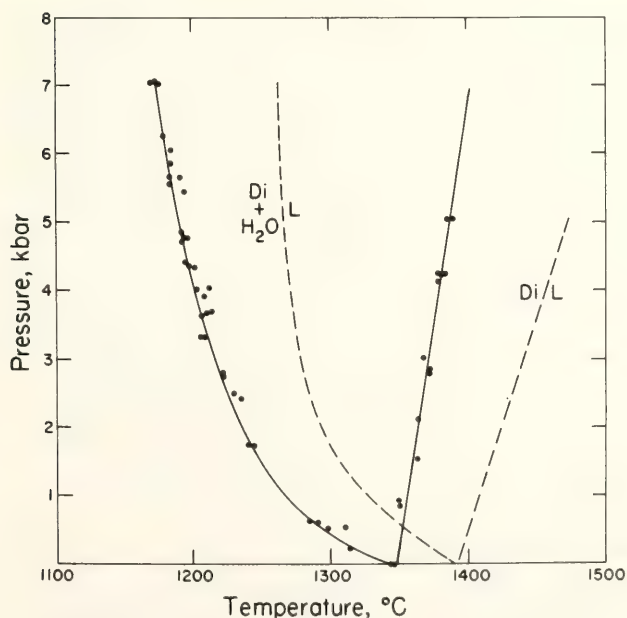


Fig. 50. A nonquenchable heat effect observed in DTA experiments on diopside with H_2O and on diopside without H_2O .

crystals, and 1250°C, where a run contained all quench crystals. Because a small thermal gradient exists over the capsule length, the 1240°C run is interpreted to have bracketed the melting reaction.

A small endothermic DTA signal has been observed at subsolidus temperatures in both volatile-absent and volatile-present experiments. Pressure dependence of this peak is given for volatile-absent and for H_2O -saturated conditions in Fig. 50. The thermal effect is reversible and nonquenchable and has a hysteresis of approximately 40°–50°C on heating relative to cooling. Comparison of the peak area with that of the melting peak yields for the 1 atm experiments a latent heat of the order of 700 cal/mol of diopside. Because the position of the DTA signal is affected by volatiles, both H_2O and CO_2 , this heat effect is not believed to reflect a subsolidus phase transition in diopside. The peaks might reflect incongruent melting of diopside, referred to above. However, optical examination of quenched runs at temperatures above and below the peak boundary revealed no quench crystals. Rather, crystalline diopside was observed in all runs.

Solidus temperatures have been determined for diopside melting in the presence of two volatiles, H_2O and CO_2 . Univariant CO_2 -saturated and H_2O -saturated melting reactions generate sharp DTA peaks. Because melting in the presence of two volatiles is divariant, temperature intervals between solidus and liquidus develop, and a broad peak is detected. For melting in the presence of vapor of mol ratio $\text{CO}_2/(\text{CO}_2 + \text{H}_2\text{O}) = 0.4$, the first maximum on the broad peak (T_{P1}) was taken as the solidus temperature. This case is analogous to melting in the presence of H_2O alone but with insufficient H_2O to saturate all melt present (see above). For $\text{CO}_2/(\text{CO}_2 + \text{H}_2\text{O}) = 0.8$ the T_{P1} peak was not clearly defined, and the onset temperature T_0 (Rosenhauer, this Report) was recorded, usually 10°–15°C below T_{P1} . Solidus

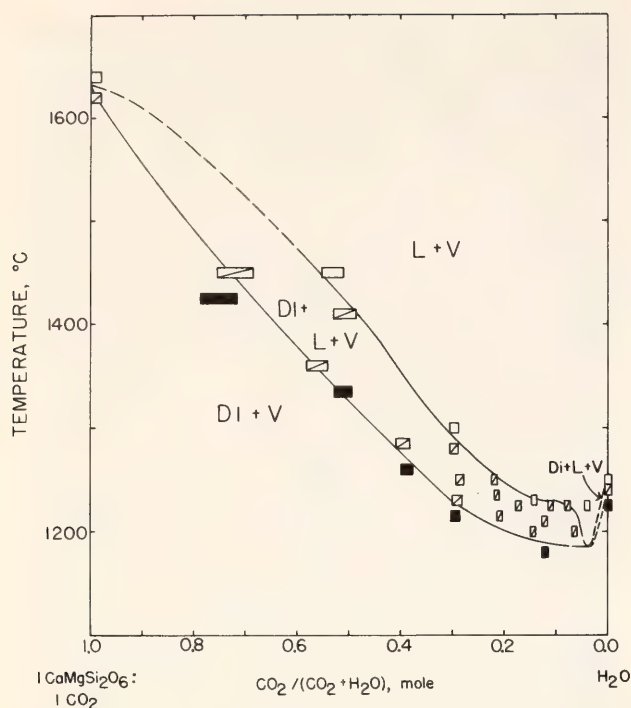


Fig. 51. Phase relations on the join $1\text{CaMgSi}_2\text{O}_6:1\text{CO}_2\text{-H}_2\text{O}$ at 30 kbar pressure. Abscissa indicates molar $\text{CO}_2/(\text{CO}_2 + \text{H}_2\text{O})$ content of the volatile portion of the bulk composition.

temperatures at 20 kbar pressure have been determined (Eggler, *Year Book* 72, pp. 457–467). Data at 30 kbar are presented here (Fig. 51). The solidus curve in Fig. 51 is taken at the appearance of at least 1% (estimated) distinct quench crystals; the actual amount of melt is probably larger because of the difficulty of seeing intergranular films of melt quenched to crystals. In this diagram a previously unknown feature can be seen—a temperature minimum in a divariant melting field involving H_2O and CO_2 , the minimum occurring at a mol ratio of $\text{CO}_2/(\text{CO}_2 + \text{H}_2\text{O}) = 0.04$. There can be no doubt of the existence of this minimum because a run at 1225°C containing H_2O and a small amount of CO_2 melted completely, but a run containing only H_2O was subsolidus (see above).

Melting (solidus) points have been joined by smooth curves in Fig. 48, and a curve for $\text{CO}_2/(\text{CO}_2 + \text{H}_2\text{O}) = 0.6$ has been drawn by interpolation. These curves indicate that the divariant melting surface, which represents composi-

tions of vapor in equilibrium with crystals and liquid, is characterized by temperature minima at about 5 kbar and maxima at 30 kbar (reflecting the temperature minimum on the isobaric section, Fig. 51). The maxima indicate the possibility that at high pressures, vapor may have lower $\text{CO}_2/(\text{CO}_2 + \text{H}_2\text{O})$ than coexisting melt. At the minimum in Fig. 51 vapor and melt have the same $\text{CO}_2/(\text{CO}_2 + \text{H}_2\text{O})$ composition because the $\text{Di} + \text{V}$ and $\text{Di} + \text{L}$ tie lines merge. For more H_2O -rich compositions, vapor has lower $\text{CO}_2/(\text{CO}_2 + \text{H}_2\text{O})$ than melt. For more CO_2 -rich compositions, and all compositions at lower pressures, vapor has higher $\text{CO}_2/(\text{CO}_2 + \text{H}_2\text{O})$ than melt. The minimum trough at about 5 kbar (Fig. 48) is similar to that found on the join $\text{NaAlSi}_3\text{O}_8\text{-H}_2\text{O-CO}_2$ by Kadik and Eggler (this Report). This figure has application to evolution of vapor from ascending basic magmas because the curves indicate compositions of vapor in equilibrium with melt and crystals. If a magma ascends isothermally and vapor (if present) is continuously distilled off, vapor compositions follow an appropriate isotherm across the vapor composition curves. For melts ascending from about 30 to 5 kbar pressure, vapor will change composition very little or will become more CO_2 -rich, depending on bulk composition. At about 5 kbar, patterns change dramatically and H_2O -rich vapor is evolved. These processes are discussed more fully by Kadik and Eggler (this Report). For *bulk* compositions falling on one of these curves (crystal mushes with small amounts of melt), the curves indicate that such mushes could ascend, probably with some increase in the melt-crystal ratio, until the bulk composition curve was again intercepted. Of course, if the melt were separated from the mush, it would not freeze until a curve was intersected with $\text{CO}_2/(\text{CO}_2 + \text{H}_2\text{O})$ of the separated melt.

The solubility of H_2O in diopside melt at the solidus was determined by Eggler at 20 kbar pressure by quenching experi-

ments (*Year Book 72*, pp. 457–467) and has been determined here at 30 kbar pressure. Solubilities at pressures less than 10 kbar have been measured by the DTA method described by Rosenhauer (this Report). These values are plotted in Fig. 52 (inset) together with a value determined by Yoder (*Year Book 64*, pp. 82–89) at 10 kbar.

Inspired by the elegant treatment of H_2O solubility in albite melt by Burnham and Davis (1974), the authors have attempted to analyze the solubility of H_2O in diopside melt. On Fig. 52 a distinct change in slope of the solubility curve is seen between 5 and 10 wt % H_2O . A change is likewise seen in the liquidus surface at 30 kbar pressure between 5 and 10 wt % H_2O (Fig. 49). Because a value of 7.7 wt % H_2O corresponds to 50 mol %, it is reasonable to write the reaction

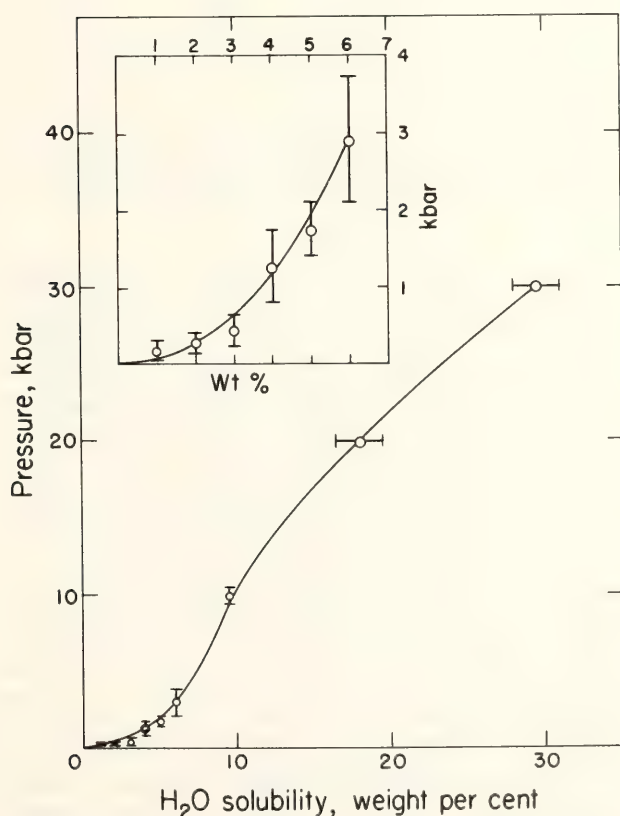
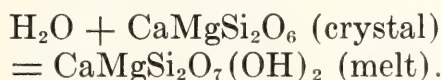


Fig. 52. Solubility of H_2O in $CaMgSi_2O_6$ melt at solidus temperatures. Values at pressures to 4 kbar, determined by DTA methods, are expanded in the inset. Value at 10 kbar was determined by Yoder (*Year Book 64*).

This reaction corresponds to the splitting of double chains of silica tetrahedra into single chains by reaction of H_2O with nonbridging oxygens linked to M_2 (Ca) cations, where one resultant hydroxyl ion is associated with the M_2 ion and the other with the chain. Any additional H_2O must enter the melt by a different mechanism, probably by breaking single chains into smaller polymeric units and as molecular H_2O .

MELT-VAPOR RELATIONS ON THE JOIN $NaAlSi_3O_8-H_2O-CO_2$

A. A. Kadik and David H. Eggler

Since the work of Goranson (1938) at this Laboratory, $NaAlSi_3O_8$ (albite) has been recognized as a useful synthetic composition for modeling of thermodynamic properties of silicate melts, in particular, melts of granitic compositions. Phase-equilibrium and thermodynamic data on the join $NaAlSi_3O_8-H_2O$ by Goranson (1938) and Burnham and Davis (1971, 1974) have been extended to the join $NaAlSi_3O_8-H_2O-CO_2$ in preliminary studies by Millhollen, Wyllie, and Burnham (1971) and Eggler (*Year Book 72*, pp. 457–464). Sufficient data have now been gathered to characterize melting and solubility on the join $NaAlSi_3O_8-H_2O-CO_2$ to a pressure of 20 kbar. These data have important implications with regard to the evolution of fluids in the crust during magmatism and metamorphism.

Eight isobaric, isothermal sections at pressures of 3–20 kbar and temperatures of 850°–1050°C have been determined from 133 runs. Three sections are shown as examples in Fig. 53. Two compositions were used in these experiments: the same sample of Varuträsk albite (Ab 98.7, Or 0.7, An 0.6 mol %) used by Kracek and Neuvonen (1952); and a mechanical mixture of Al_2O_3 , SiO_2 (cristobalite), and Na_2CO_3 , a portion of which is ^{14}C . H_2O and $Ag_2C_2O_4$ were added to these compositions in the needed proportions. Phases in the run products were identi-

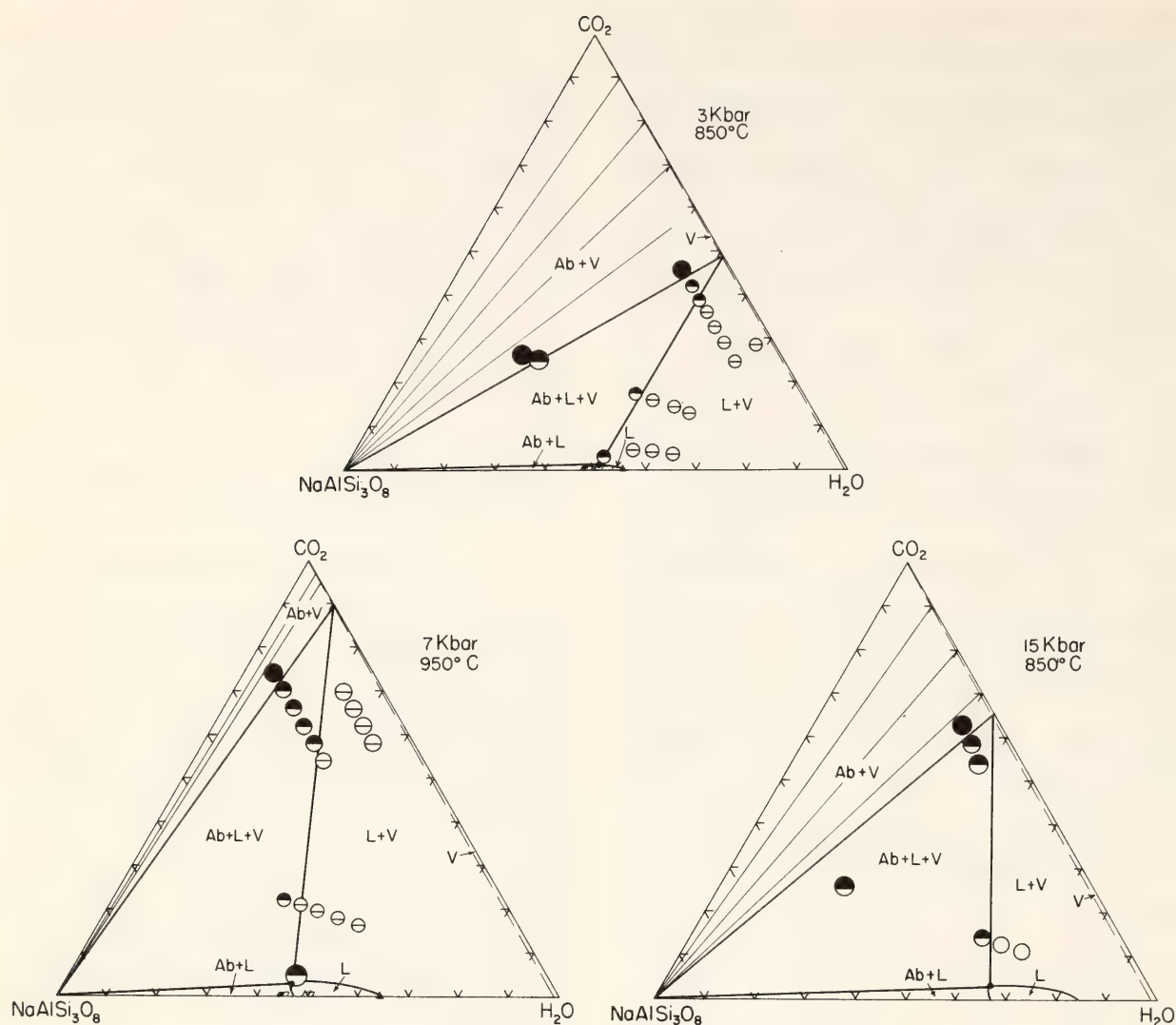


Fig. 53. Three isobaric, isothermal sections of the join $\text{NaAlSi}_3\text{O}_8\text{-H}_2\text{O-CO}_2$. Compositions are in mol %. Solid triangles indicate solubilities determined by Burnham and Davis (1974).

fied by optical examination. Experiments at pressures in excess of 10 kbar were made in solid-media, high-pressure apparatus in sealed platinum capsules unbuffered for H_2 . The fugacity of H_2 in these capsules is approximately that of the hematite-magnetite- H_2O buffer (Eggler, Mysen, and Hoering, *Year Book 73*, pp. 228–232). Quenching was sufficiently rapid that liquid quenched unambiguously to glass; and vapor quenched to low-birefringence material, to glass of different refractive index, or, in some experiments, to material that included carbonate. In some experiments at pressures less than 10 kbar, which were made in an internally heated, gas-media pressure vessel, the melt quenched to glass and crystals of albite, which from their

anhedral form and irregular extinction have been interpreted as quench crystals.

Determination of phase boundaries between vapor-present and vapor-absent fields is difficult because of problems in identifying quenched vapor. These difficulties have been overcome in this study by use of a new technique. The $\text{Ab} + \text{L}$ side of the three-phase triangle $\text{Ab} + \text{L} + \text{V}$ was located precisely by determining the CO_2 content of the melt in runs quenched from the $\text{Ab} + \text{L} + \text{V}$ field by counting of β -tracks emitted by ^{14}C in the quenched glass (Mysen, Seitz, and Frantz, *Year Book 73*, pp. 224–226). Because this tie line is approximately parallel to the $\text{Ab-H}_2\text{O}$ sideline, and because the tie line $\text{L} + \text{V}$ is located precisely by runs (presence or absence

of albite crystals), the composition of L is readily determined without recourse to interpretation of the presence or absence of vapor. Other studies (Eggler, Mysen, and Seitz, *Year Book* 73, pp. 226–228; Mysen and Seitz, 1975) have shown that equilibrium concentrations of CO_2 can be quenched into glass. This conclusion was checked for albite- H_2O - CO_2 by determining the CO_2 content of glass quenched from the $\text{Ab} + L + V$ field at 20 kbar and 950°C . Eggler (*Year Book* 72, p. 461), from careful observa-

tion of vapor bubbles, had previously determined that the melt contained 5 ± 3 mol % CO_2 , equivalent to 2.0 wt % CO_2 . A run was made with the albite mix and H_2O , which contained vapor, melt, and a trace of crystals. Analysis of the glass showed 2.23 ± 0.06 wt % CO_2 , or 6 mol %, well within the error of Eggler's (*Year Book* 72) determination. As a further precaution during routine analysis of glass, only glasses with small amounts of crystals and no quench crystals were selected.

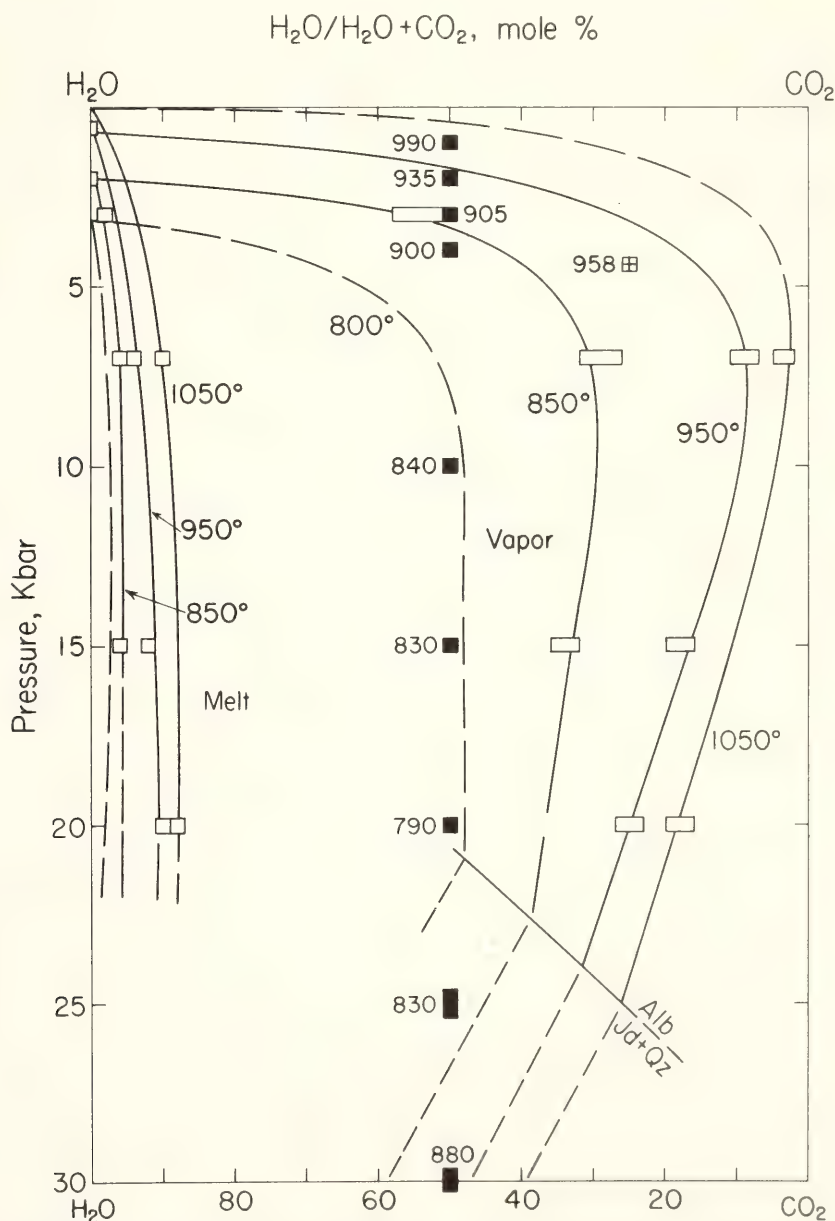


Fig. 54. Compositions, in mol %, of volatile content of vapor and melt in equilibrium with albite. Points denoted by open boxes have been determined in isothermal, isobaric sections. Points denoted by closed boxes were determined by Millhollen, Wyllie, and Burnham (1971) at the temperatures indicated. Point denoted by cross in box was determined by Kesson and Holloway (1974).

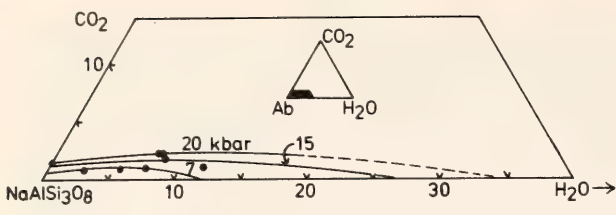


Fig. 55. Isobaric, polythermal vapor saturation curves of melt in equilibrium with vapor and albite. CO₂-saturated data points are from B. O. Mysen, D. H. Eggler, M. G. Seitz, and J. R. Holloway (in preparation); H₂O-saturated data points, from Burnham and Davis (1974).

Each three-phase triangle is, in effect, one determination of the composition of co-existing liquid and vapor and, simultaneously, of one P - T - X_{CO_2} point on the melting (solidus) surface of albite, where $X_{\text{CO}_2} = \text{CO}_2/(\text{CO}_2 + \text{H}_2\text{O})$ (mol). The data have been combined in three diagrams. Figure 54 shows the compositions

of coexisting vapor and melt, in terms of X_{CO_2} , in equilibrium with albite. The vapor compositions are also solidus curves in P - X section. The eight P - T - X determinations are shown as open boxes. Results of other workers are also shown and are in general agreement. The same melt compositions, which define isobaric, polythermal saturation surfaces, are shown in weight percentages in Fig. 55. Finally, the smoothed curves in Fig. 54 have been used to plot solidus curves in P - T projection in Fig. 56. Also shown in Fig. 56 are runs used to bracket the melting curve of albite in the presence of CO₂. If the CO₂ were pure, albite would melt completely at one temperature. The CO₂ is not pure, however, containing about 1 mol % CO and 1 mol % H₂O produced by H₂ diffusion from the

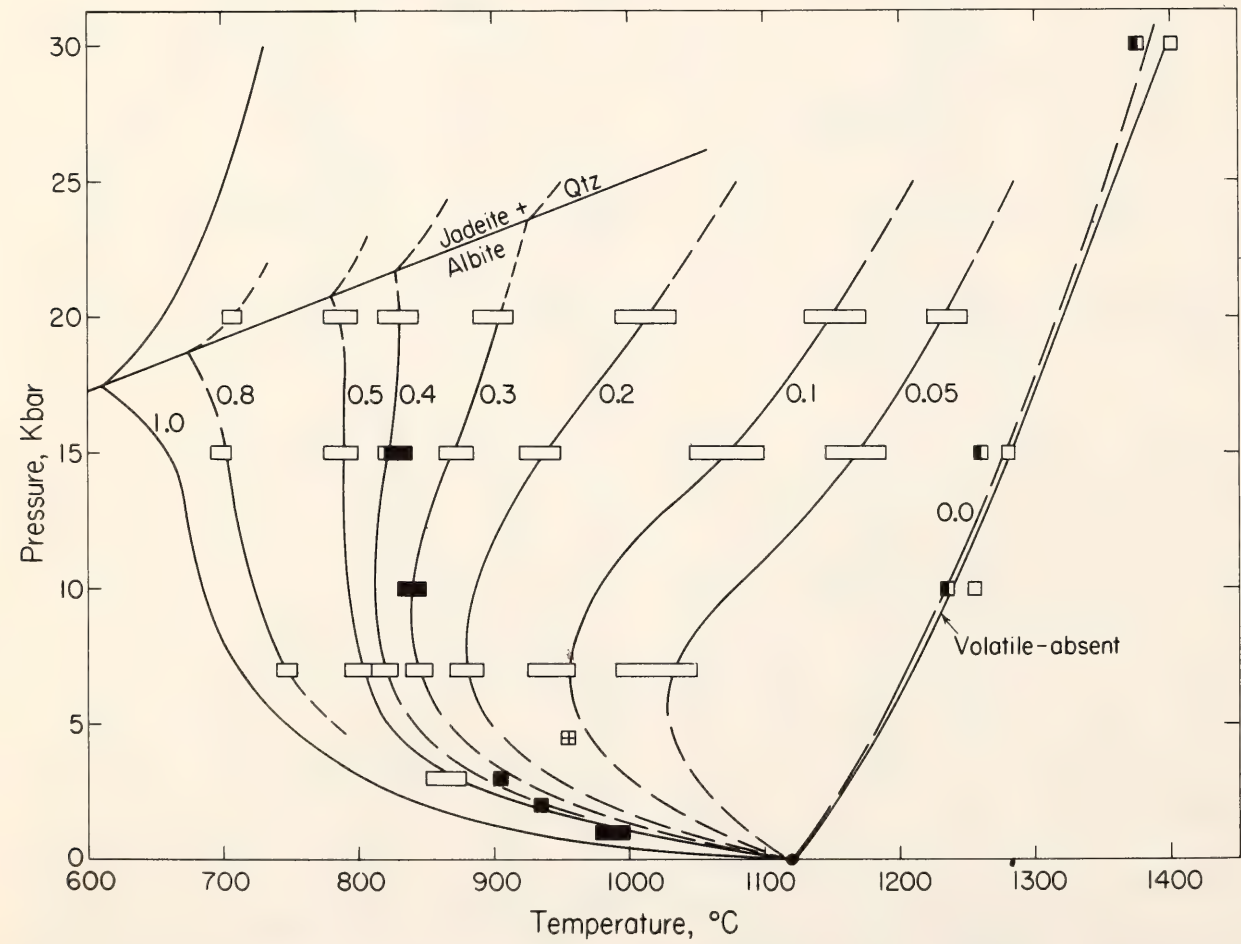


Fig. 56. Melting (solidus) curves of albite as a function of vapor composition, $\text{H}_2\text{O}/(\text{H}_2\text{O} + \text{CO}_2)$. Open boxes are data of this report, taken by interpolation. Closed boxes are data from Millhollen, Wyllie, and Burnham (1971), $\text{H}_2\text{O}/(\text{H}_2\text{O} + \text{CO}_2) = 0.5$; cross in box, from Kesson and Holloway (1974), $\text{H}_2\text{O}/(\text{H}_2\text{O} + \text{CO}_2) = 0.25$. Volatile-absent melting curve is from Boyd and England (1963). Run symbols delimit CO₂-saturated melting curve. Albite — jadeite + quartz transition is from Boettcher and Wyllie (1968).

assembly (Eggler, Mysen, and Hoering, *Year Book* 73, pp. 228–232). Because of these impurities in the vapor phase, a divariant melting interval is developed between solidus and liquidus. This interval was found to be 100°C or more. The experimentally determined solidus temperature for this vapor composition of $X_{\text{CO}_2} \approx 0.98$ is of little interest. However, Eggler (*Year Book* 72, pp. 457–467) deduced that for diopside the liquidus temperature for $X_{\text{CO}_2} \approx 0.98$ was within 10°C of the liquidus (hence solidus) temperature for $X_{\text{CO}_2} = 1.0$. The analogous liquidus curve for albite is seen to lie very close to the volatile-absent melting curve, as determined by Boyd and England (1963). The volatile-absent curve was checked by melting synthetic albite at 10 kbar pressure and was found to agree within 10°C with determinations by Boyd and England (1963). The very small freezing-point depression is further evidence of the low solubility of CO_2 in albite melt.

The principal findings of this study are that CO_2 is slightly soluble in albite melt, confirming the preliminary results of Eggler (*Year Book* 72, p. 464), and that there is a temperature minimum trough on the $\text{CO}_2/\text{H}_2\text{O}$ divariant melting surface at a pressure of approximately 5 kbar. These findings have important implications with regard to the melting and crystallization of granitic magmas in the upper mantle and lower crust. One implication is that source rocks containing vapor more CO_2 -rich than $\text{CO}_2/(\text{CO}_2 + \text{H}_2\text{O}) = 0.5$ at pressures in excess of 5 kbar would melt along curves with positive (dP/dT) slope. Thus diapiric sources could melt by rising within the mantle or crust. After the source rock melts, derivative melts may or may not have freezing curves with positive slope.

Another implication is that granitic melts will in general evolve vapor during ascent. Albite melt dissolves a maximum of 2.2 wt % CO_2 at pressures less than 20 kbar (Fig. 55), and therefore

melts need not contain large quantities of volatiles to be saturated if one volatile is CO_2 . If melts are not saturated, vapor will be evolved during ascent, because the solubilities of H_2O and CO_2 are lower at lower pressures.

Vapor evolved during ascent changes in a systematic manner, becoming more H_2O -rich at shallower depths. An example is instructive. A magma produced by partial melting at 20 kbar pressure and 950°C in equilibrium with vapor of $\text{CO}_2/(\text{CO}_2 + \text{H}_2\text{O}) = 0.75$ contains volatiles in the ratio $\text{CO}_2/(\text{CO}_2 + \text{H}_2\text{O}) = 0.10$ (Fig. 54). (Any bulk composition with $\text{CO}_2/(\text{CO}_2 + \text{H}_2\text{O})$ in excess of 0.10 but less than 0.75 will melt at this pressure and temperature to a vapor-saturated liquid.) If the melt is separated from the source and rises isothermally, vapor will be evolved. If the vapor distills off continuously into country rocks, its composition follows the 950°C vapor curve (Fig. 54) because this curve marks the composition of vapor in equilibrium with melt (and with crystals—the magma cannot be superheated). Vapor evolved becomes more CO_2 -rich until a pressure of about 5 kbar is reached and then changes markedly, becoming very H_2O -rich with further pressure decrease. If vapor is not distilled off and the magma rises as a closed system with entrapped vapor, proportions of melt, crystals, and vapor will change, and the melt will crystallize completely at about 2 kbar pressure when the composition of co-existing vapor has $\text{CO}_2/(\text{CO}_2 + \text{H}_2\text{O}) = 0.10$. (Although $\text{CO}_2/(\text{CO}_2 + \text{H}_2\text{O})$ in the source region was 0.75, the ratio of the ascending melt is 0.10. This melt crystallizes at a considerably lower temperature than the solidus curve of the source.) Many other situations can be imagined, but one general conclusion can be reached: Magmas containing two volatiles will evolve relatively CO_2 -rich vapor at pressures in excess of 5 kbar and relatively H_2O -rich vapor at lower pressures. Furthermore, significant fractionation of evolved vapor in terms of

CO₂ and H₂O content occurs only at pressures less than 5 kbar. This conclusion is very important with regard to country rock alteration and to ore deposition because H₂O and CO₂ vapor have different elemental solubilities. For example, vapor containing CO₂ and H₂O in equilibrium with granite dissolves less alkalis, relative to Si and Al, than H₂O vapor (Burnham, 1967).

Kadik and Lukanin (1973) and Khitarov and Kadik (1973) have noted that compositions of fluid inclusions in minerals of rocks of the granulite facies are rich in CO₂ (Sobolev, Dobnetsov, and Khlestov, 1966). Kadik and his co-workers hypothesized that this pattern reflects a continental crust rich in CO₂ in its lower portions and rich in H₂O above, and that this pattern evolved through igneous processes. The new data in this report support this hypothesis. One contributory process is depletion of upper mantle or lower crust by partial melting, selectively removing H₂O relative to CO₂. Separation of melt and vapor compositions is especially great at pressures in excess of 5 kbar because melts dissolve much more H₂O (see Fig. 54). A second process is that discussed above—volatile-bearing magmas ascending through the crust lose CO₂-rich vapor in the lower crust ($P > 5$ kbar) and H₂O-rich vapor in the upper crust.

PROPERTIES OF MAGMAS

THE SILICA IMMISCIBILITY EFFECT IN MAGMAS

T. N. Irvine

Liquid immiscibility between silica and oxides such as CaO, MgO, FeO, MnO, NiO, Fe₂O₃, Cr₂O₃, and TiO₂ is one of the familiar features of 1-atm liquidus diagrams of silicate systems. After classic early studies by Greig (1927) and Bowen (1928), however, this feature has not received much attention in petrology because it characteristically occurs only at very high temperatures in compositions not encountered in magmas. In

1951, Roedder described low-temperature immiscibility between melts resembling pyroxenite and potassic granite in the join $\text{KAlSi}_2\text{O}_6\text{-Fe}_2\text{SiO}_4\text{-SiO}_2$, and in recent years petrologists have taken considerable interest in this type of immiscibility, owing to its discovery in lunar rocks and in certain terrestrial rocks (e.g., Roedder and Weiblen, 1970, 1971, 1972). But these liquids are exotic too, compared with common magmas, in that they typically have extremely high FeO/MgO ratios.

Liquid immiscibility in silicate melts is, however, a reflection of the chemical structure or polymerization characteristics of the melts and, considered in this context, has broader implications. This report draws attention to certain liquidus relations in silicate systems that indicate that the factors responsible for silica immiscibility have influence extending far beyond the temperature and compositional regions in which the immiscibility is stable, and it is suggested that these factors have major significance in magmas. The basis of this thesis is the observation that silica melt is completely miscible at liquidus temperature with the melts of the feldspar end-members but shows a miscibility gap with every stable end-member of the common mafic silicate and oxide minerals that has been investigated. From simple thermodynamic considerations it may be inferred that the nonideality in the melts surrounding these miscibility gaps should tend to shift or deflect liquidus temperature contours and phase boundaries—and in particular, the cotectic boundaries between the mafic and oxide minerals and plagioclase—away from the gaps. This feature, which is termed “the silica immiscibility effect,” is well displayed in numerous phase diagrams of silicate systems, and evidence will be presented showing that it can be identified in the chemical trends of tholeiitic, calcalkaline, and even alkaline magma series. The effect appears to be a principal determining control on such funda-

mental petrographic features of igneous rocks as the relationship between color index and plagioclase composition, and it is believed to underlie many of the reactions induced by salic contamination of basic magmas.

Theory

Figure 57 summarizes available data on 1-atm liquidus relations between silica and the principal end-members of the major (stable) rock-forming mafic silicate, oxide, and feldspar minerals. It serves to illustrate the contrast in liquid miscibility mentioned above.* Silica also shows liquid immiscibility with other less abundant components of the mafic and oxide minerals, such as Mn_2SiO_4 , Ni_2SiO_4 , CaSiO_3 , and Fe_2O_3 , as well as

* In Fig. 57, the abundance of silica is represented as normative quartz (Q), plotted in "cation-unit percent," according to the method of the cation norm. Cation units are oxide units containing a single cation, such as SiO_2 , $\text{AlO}_{1.5}$, MgO , and $\text{Na}_{0.5}\text{O}$, and the percentage of a normative component is the percentage of the total number of these units that is allotted to the component. The method is of interest because it provides a definitive expression of composition in terms of the number of ions or atoms present, with none of the ambiguity associated with the definition of moles or species in nonmolecular systems. Also, it creates none of the graphical inconsistencies that plague certain mole percentage plots. (Compare, for example, the relationships of forsterite, enstatite, and quartz in mole percentage plots of MgO vs. SiO_2 and Mg_2SiO_4 vs. SiO_2 .) On the other hand, in cases where mole percentage is traditionally considered important, as in defining the composition of mineral solid solutions, the cation-unit percentage values are identical. A minor facet of some practical interest is that compositions and graphs based on cation-unit percentage are generally very similar to their weight percentage counterparts, and so the conversion is seldom distracting. In the present context, it is noted that cation-unit percentage plots provide a useful graphical framework in which to examine the thermodynamics of liquid-solid phase relations in silicate systems. The corresponding calorimetric unit would be calories per gram formula weight divided by the number of cations in the formula and might be termed "calories per gram cation unit (cal gcu^{-1})."

with the principal components of certain dark accessory minerals such as CaTiSiO_5 (sphene) and $\text{Ca}_3(\text{PO}_4)_3$ (whitlockite). Immiscibility no doubt also exists with certain important compositions not yet investigated, such as FeTiO_3 (ilmenite) and $\text{Ca}_5\text{F}(\text{PO}_4)_3$ (apatite). The immiscibility with these end-member components obviously relates closely to that with the simple oxides listed in the introduction, and one may similarly infer that the complete miscibility between silica and the feldspar melts is related to the complete miscibility between silica melt and the melts of Al_2O_3 , Na_2O , and K_2O . Reference to the end-member components, however, has greater thermodynamic and petrologic relevance.

Another feature of fundamental importance indicated in Fig. 57A is that the miscibility gaps are so large that they may be expected to have large metastable extensions into the subsolidus. No direct evidence of this feature is known for the systems in Fig. 57A, but metastable liquid immiscibility is a well-known phenomenon of major importance in the glass industry, and the stable low-temperature immiscibility in the join KAlSi_2O_6 - Fe_2SiO_4 - SiO_2 (Roedder, 1951) can readily be interpreted as representing the reemergence of the high-temperature solvus on the join Fe_2SiO_4 - SiO_2 from an intervening region of metastability in which it was submerged beneath the liquidus fields of cristobalite and tridymite. Given the principles outlined below, one can find almost countless other indications of similar metastability in the published ternary phase diagrams of silicate systems.

Whether metastable solvi exist for the feldspar-silica melts at igneous temperatures is unknown, but certainly there is no strong indication of them in the liquidus profiles in Fig. 57B. The literature records several attempts to calculate these liquidus profiles (cf. Carmichael, Turner, and Verhoogen, 1974), and the results suggest some nonideality in the melt solutions, but the calculations are

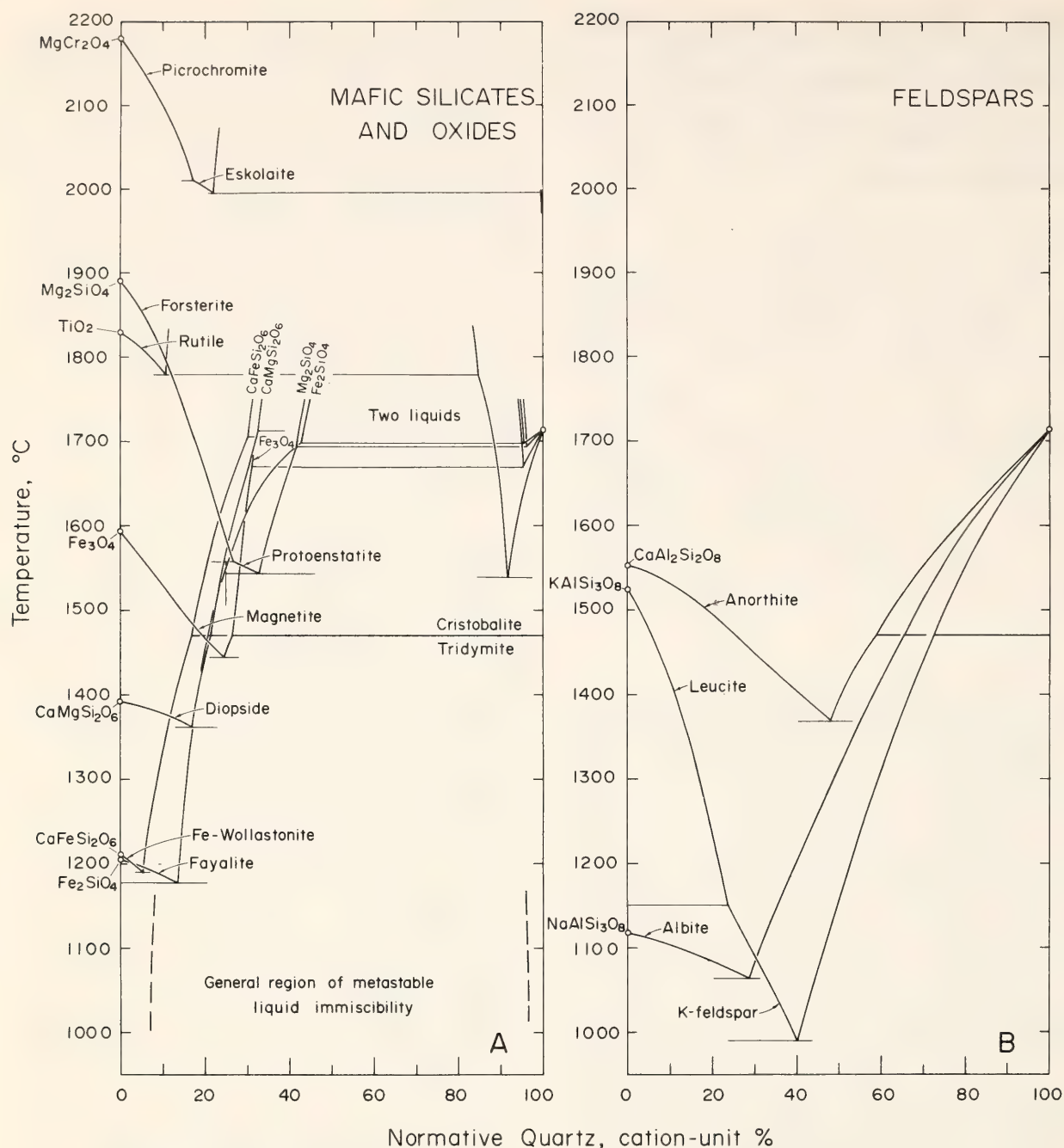


Fig. 57. Plots of the 1-atm liquidus relations between silica and the end-members of the important rock-forming mafic silicate, oxide, and feldspar minerals. Note that silica melt shows immiscibility with all the mafic silicate and oxide melts but complete miscibility with the feldspar melts. Data from sources cited in *Phase Diagrams for Ceramists* (Levin, Robbins, and McMurdie, 1964, Figs. 80, 82, 113, 266, 412, 508, 586, 599, 715, and 957).

fraught with uncertainties relating to the choice of solution model, the definition of molar quantities, and the quality of the requisite data on heats of fusion. From the profiles of the silica minerals in Fig. 57B, one might argue that, if the melt species are the same for all three feldspar end-members, then the $\text{KAlSi}_3\text{O}_8\text{-SiO}_2$ melts are the most nearly

ideal,* and the $\text{CaAl}_2\text{Si}_2\text{O}_8\text{-SiO}_2$ melts, the least ideal. This interpretation ac-

* An interesting alternative possibility is that the $\text{KAlSi}_3\text{O}_8\text{-SiO}_2$ melts might have a negative excess Gibbs free energy of mixing related to complexing. This possibility is suggested by the low temperature of the eutectic point on the join and by the very high viscosity of the eutectic melt (cf. Schairer and Bowen, 1955).

cords with the observations that SiO_2 appears to form a more nearly ideal solution with K_2O than with Na_2O , whereas the solutions with CaO are so nonideal as to show a miscibility gap (cf. Kracek, *Year Book* 32, pp. 62–65).

The essential principle underlying the concept of a silica immiscibility effect is that the nonideality relating to the immiscibility will generally extend well beyond the compositional limits of the solvus. Consequently, liquids in the vicinity of miscibility gaps of the type in Fig. 57A (stable or metastable) should have higher Gibbs molar free energies and, therefore, higher liquidus temperatures than they would if they were ideal solutions. (In other words, the nonideality in the liquid tends to shift the liquid-solid equilibrium in favor of the solid and so raises the melting temperature.) Thus the liquidus temperature contours and any liquidus boundaries in the vicinity of a solvus will tend to be shifted or deflected away from it. As applied to igneous systems, this principle is particularly important with respect to the relations between the mafic and oxide minerals and anorthite. The consequences with respect to the alkali feldspars are different owing to their tendency to concentrate in low-temperature residual liquids.

Figure 58 is a graphical illustration of the silica immiscibility effect for a hypothetical system of anorthite, a mafic silicate or oxide mineral, and a component X consisting of either SiO_2 or SiO_2 plus some definite proportion of KAlSi_3O_8 .* The diagrams are largely explained in the caption, but particular attention should be given to 58C and D. Diagram C, in which X consists only of SiO_2 , is well represented among published phase diagrams. Four examples are shown in Fig. 59; another is the system Mg_2SiO_4 - $\text{CaAl}_2\text{Si}_2\text{O}_8$ - SiO_2 in Fig.

61A in the next section of this Report. The configuration of boundaries in Fig. 59D is, however, considerably more important geologically. The introduction of the alkali feldspar component results in marked expansion of the liquidus fields of the mafic mineral and anorthite toward X , which is now representative of "petrogeny's residua system," and the relations may be compared with those of basaltic and granitic liquids. The system Mg_2SiO_4 - $\text{CaAl}_2\text{Si}_2\text{O}_8$ - KAlSi_3O_8 - SiO_2 , explored in the next section of this Report, exhibits this type of configuration.

Petrologic Applications

Evidence that the silica immiscibility effect is significant in magmas is given in Fig. 60. The projection used in the plots is like Fig. 59D. Plot A, of the immiscible lunar melts, shows that, as viewed in this perspective, the field of actual immiscibility in magmas can be very large. As noted in the caption, the immiscibility through part of the field may be metastable, depending on the FeO/MgO ratio and other compositional characteristics of the liquids.

The immiscibility fields and liquidus boundaries indicated in Fig. 59B, C, and D are essentially schematic but serve to illustrate that the arcuate chemical trends of the magma series in this projection can be attributed to the tendency of the phase boundaries between plagioclase and the mafic and oxide minerals to skirt a probable region of immiscibility. The considerations to follow indicate that the factors suggested as being critical in determining the size of the immiscibility fields are in general accord with the chemical characteristics of the magmas.

As a rule, the size of a field of stable liquid immiscibility in silicate systems represents a balance between the tendency of the various components of the system to promote or suppress the immiscibility and their tendency to depress liquidus temperatures (see also Watson and Dickey, 1975). In systems approxi-

* Component X could also include $\text{NaAlSi}_3\text{O}_8$, but this possibility has been excluded in Fig. 58 in order to avoid the complications of solid solution with anorthite.

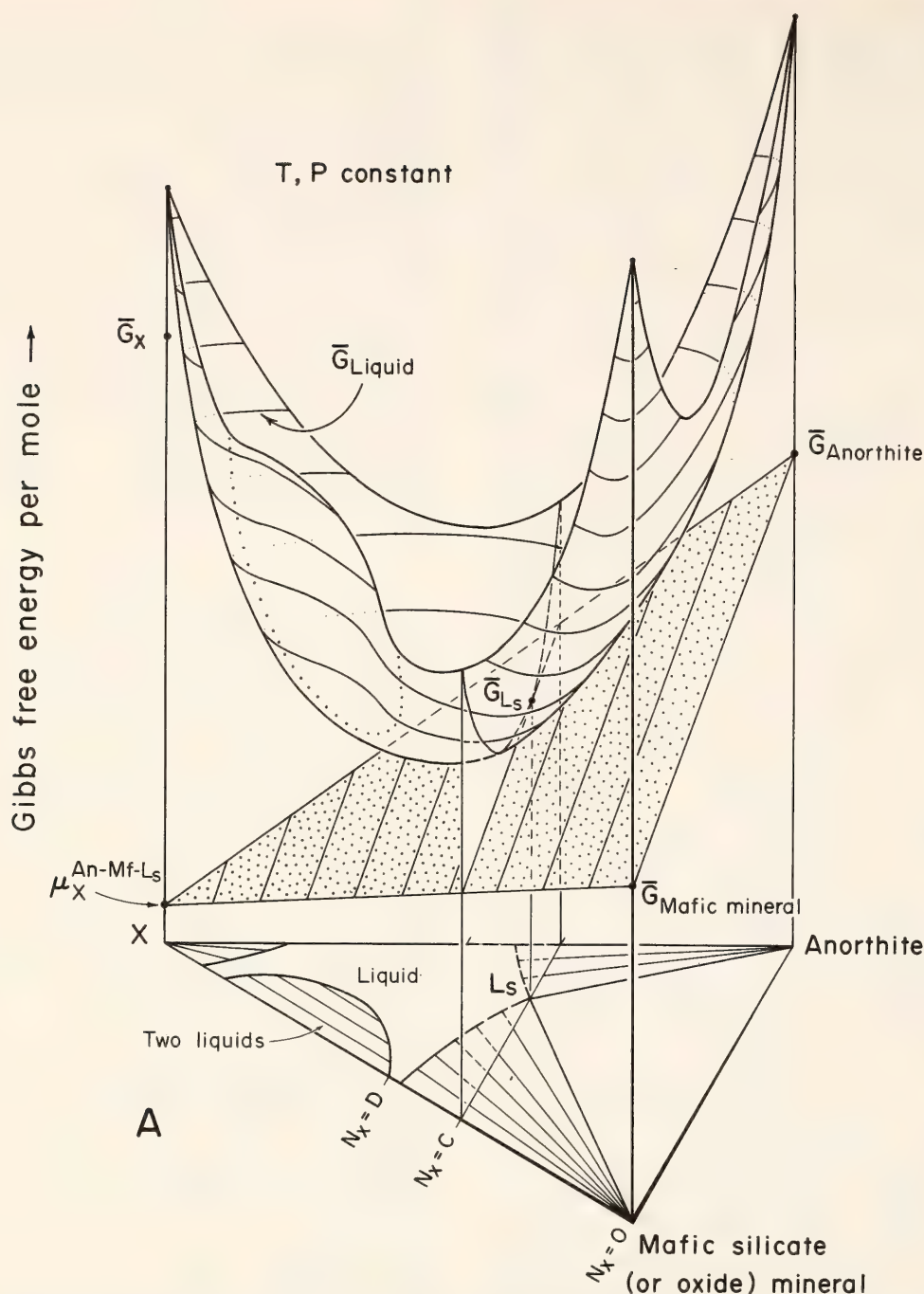


Fig. 58A. Schematic illustration of the silica immiscibility effect in a hypothetical system of anorthite, a mafic (or oxide) mineral, and a component X , representing either SiO_2 or a combination of SiO_2 and KAlSi_3O_8 . 58A illustrates the relationship between the phase relations and the molar Gibbs free energies of the liquid and solid phases: \bar{G}_α = the free energy of α ; $\mu_X^{\text{An-Mf-L}_s}$ = the chemical potential or molar free energy of X in an assemblage of anorthite, the mafic mineral, and the cotectic liquid, L_s ; N_X = the mole (or cation-unit) fraction of X . The composition of L_s is determined by the point of tangency of the stippled planar surface with the curved, \bar{G}_{liquid} surface. The indentation in the \bar{G}_{liquid} surface represents the departure from ideality in the liquid solution that gives rise to the two-liquid field.

mating magmas it may be expected to depend especially on the depression of the liquidus of the mafic and oxide minerals relative to the liquidus of plagioclase. For example, MgO shows immiscibility with SiO_2 , but systems of high

MgO/FeO ratio generally have very high liquidus temperatures, so their stable immiscibility fields tend to be small. By contrast, high concentrations of CaO , FeO and Fe_2O_3 may be expected to favor stable immiscibility because

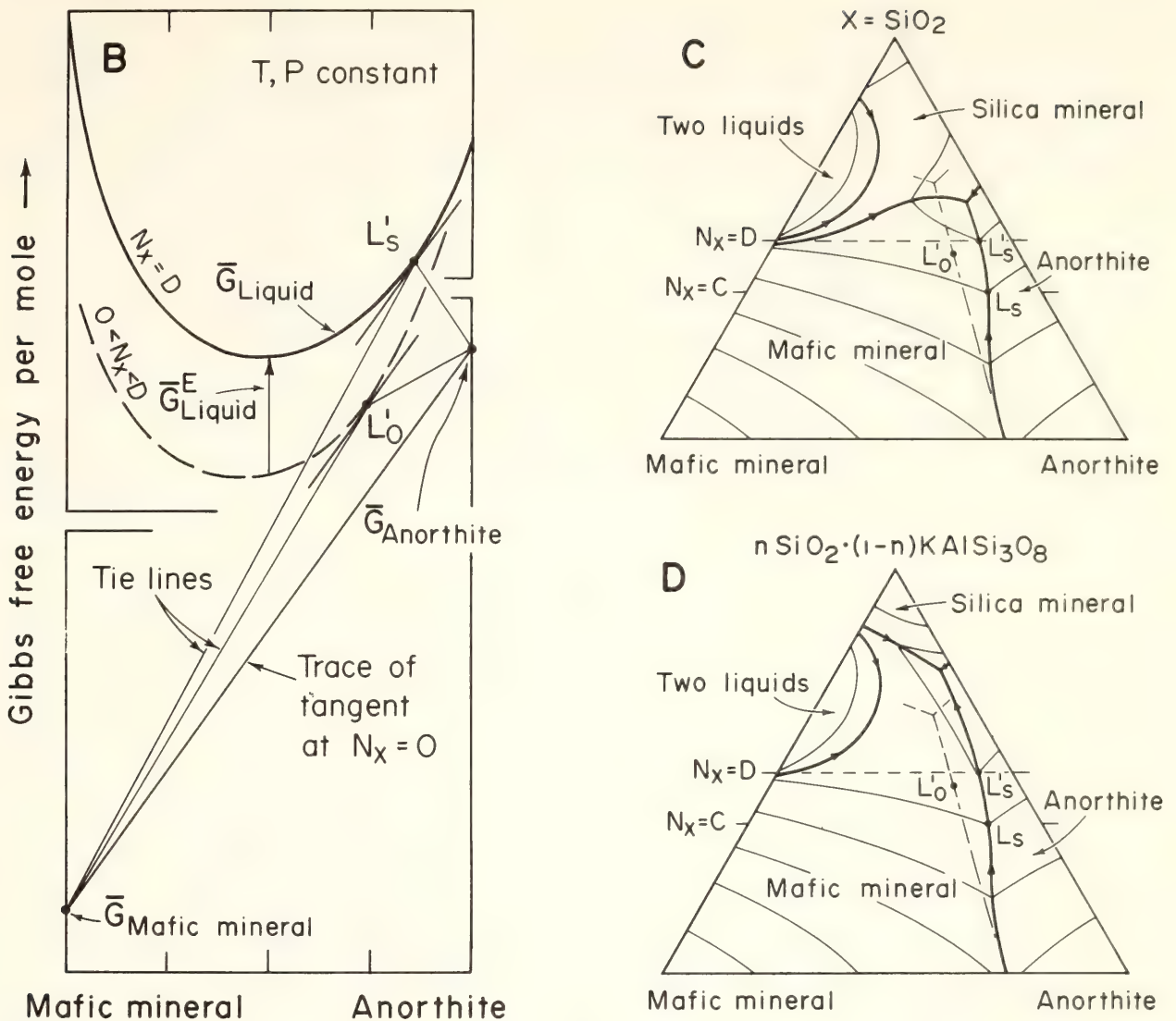


Fig. 58B is a combination of projections of 58A, showing that the cotectic liquid should be closer to the anorthite- X join than it would be if the liquid were ideal. The nonideality is represented by the positive excess free energy, $\bar{G}_{\text{Liquid}}^E$, which is assumed to increase monotonically toward the region of immiscibility. L'_S is the stable cotectic liquid in the section $N_X = D$; L'_O would be the liquid in equilibrium with the same solid phases at the same temperature and pressure if the liquid solution were ideal. (Note that L'_O will generally lie at a value of N_X different from D .) 58C and D are two possible manifestations of the complete liquidus relations. Examples of 58C are shown in Fig. 59. The relations in 58D have not been identified in any experimentally investigated system in which the liquid immiscibility is stable, but they can probably be expected if the mafic mineral is picrochromite or rutile (cf. Fig. 57), and they are apparently representative of many systems in which the immiscibility is metastable (see Fig. 63, below).

these oxides are not only immiscible with SiO_2 but also relatively effective in lowering the liquidus temperatures of the mafic and oxide minerals (see Fig. 57A), especially in combination at eutectic points or cotectic boundaries. The combination of high CaO , FeO , and Fe_2O_3 is probably the principal factor behind the immiscibility shown by the Skaergaard intercumulus melts (cf. McBirney and

Nakamura, *Year Book* 73, Table 27). The alkalis, which are not themselves immiscible with silica melt, would not be expected to promote immiscibility, but they are exceptionally effective in lowering liquidus temperatures (of both the mafic and oxide minerals and plagioclase), and this feature is clearly essential to the low-temperature immiscibility in the join KAlSi_2O_6 - Fe_2SiO_4 - SiO_2 and in

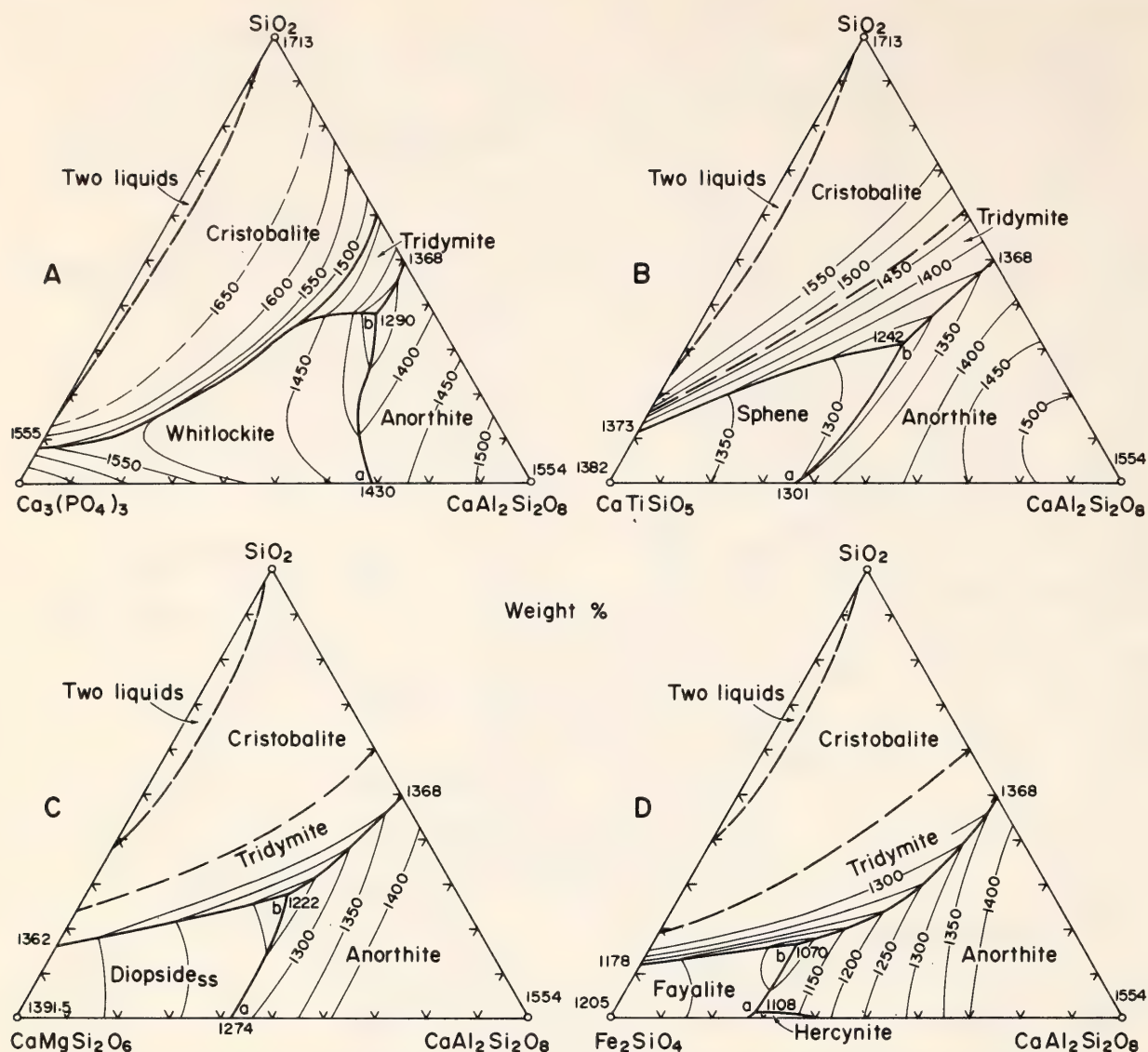


Fig. 59. Four systems involving anorthite in which the silica immiscibility effect is apparent. Consider in particular the trends of the cotectic boundaries denoted *ab* between anorthite and the "mafic" phase. In (A) the immiscibility effect along *ab* becomes prominent only below 1400°C. In the other diagrams, even *a* is far below 1400°C; hence the entire boundary is probably affected. The implied nonideality along the diopside-anorthite cotectic in (C) could be a major factor behind the dramatic projected shift of this boundary from *a* toward anorthite with the addition of H₂O (cf. Yoder, *Year Book* 64, pp. 82–89). Data sources: (A) St. Pierre (1956); (B) Agamawi and White (1954); (C) Clark, Schairer, and de Neufville (*Year Book* 61); (D) Levin, Robbins, and McMurdie (1964, Fig. 870), after Schairer (1942).

the lunar melts (Roedder and Weiblen, 1971). The role of H₂O is presumably similar because it generally affects silicate liquidus relations in much the same way as the alkalis. Alumina, on the other hand, neither promotes immiscibility nor is, by itself, particularly effective as a flux, and these features are apparently reflected in the fact that the immiscibility in Fig. 60 is restricted to compositions low in normative anorthite.

These same factors may be expected

to determine the petrologic importance of the silica immiscibility effect. Thus it may be inferred that the comparatively small effect apparent in tholeiitic magmas (Fig. 60B) is a function of their relatively low content of alkalis and H₂O, and that the effect becomes pronounced or actual immiscibility is observed only in the rare situations (as in the Skaergaard intrusion) that high FeO/MgO and CaO/Al₂O₃ ratios are developed. Similarly, the large silica

immiscibility effect suggested by the trend of the calcalkaline series may be attributed to the typically high content of alkalis and H_2O in this type of magma, while the lesser effect apparent

in the alkali basalt series probably results because the effect of the alkalis has been offset by low silica activity. High concentrations of TiO_2 and P_2O_5 may also contribute significantly to the

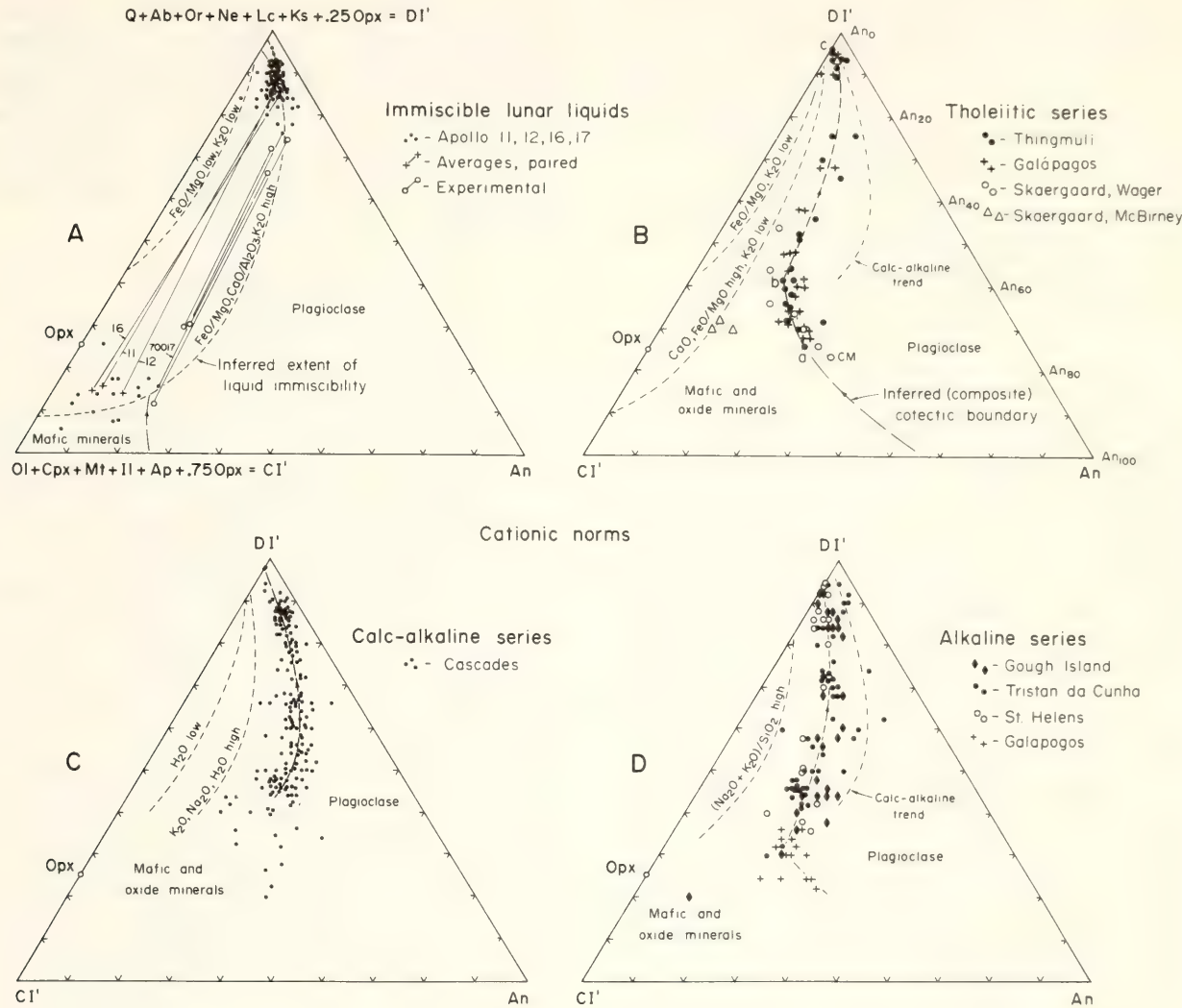


Fig. 60. Plots showing by a comparison of data on immiscible lunar melts with data on tholeiitic, calcalkaline, and alkaline magma series that the silica immiscibility effect is apparent in the trends of the magmatic series. The variable DI' , which may be compared with X in Fig. 58, is approximately the Differentiation Index of Thornton and Tuttle (1960). In graphical terms, it represents a joint projection along the $Ks-Q$ and $Ne-Q$ normative joins. The variable CI' is essentially the normative color index of the rock and comprises components that probably all show liquid immiscibility with silica melts. The projected position of Opx corresponds to that of enstatite ($MgSiO_3$) in Fig. 57. In 60B the compositional distribution of the plagioclase series is shown for reference in considering the effect of plagioclase fractionation on the magmatic trends: CM , Skaergaard chilled margin; abc , Thingmuli trend. The inferred field of liquid immiscibility in 60A is probably about the maximum size to be expected in magmatic systems; the smaller field denoted "FeO/MgO low, K_2O low" is typical of high-temperature immiscibility in experimental systems such as those in Fig. 59. Between these curves, the immiscibility may be partly submerged beneath the liquidus (metastable) as, for example, in the join $Fe_2SiO_4-KAlSi_2O_6-SiO_2$ (Roedder, 1951). The indicated fields of immiscibility in B, C, and D are schematic only, except that in B the An-poor Skaergaard intercumulus melts investigated by McBirney do show stable immiscibility. Lunar data are from Roedder and Weiblen (1970, 1971, 1972) and Rutherford, Hess, and Daniel (1974); Galápagos data, from McBirney and Williams (1969); and Skaergaard data, from Wager (1960) and McBirney and Nakamura (*Year Book* 73, p. 350). Other data are from sources cited by Irvine and Baragar (1971).

silica immiscibility effect, especially in the alkali basalt series.

The importance of the silica immiscibility effect in determining the color index of igneous rocks is evident in Fig. 60. The following report illustrates its role in salic contamination of basic magmas.

OLIVINE-PYROXENE-PLAGIOCLASE
RELATIONS IN THE SYSTEM
 Mg_2SiO_4 - $\text{CaAl}_2\text{Si}_2\text{O}_8$ - KAlSi_3O_8 - SiO_2
AND THEIR BEARING ON THE
DIFFERENTIATION OF STRATIFORM
INTRUSIONS

T. N. Irvine

A mechanism of origin for chromitite layers in stratiform intrusions has been proposed (Irvine, *Year Book* 73, pp. 300-316) whereby the chromite is precipitated when the basic magma of the intrusion is suddenly extensively contaminated with granitic liquid melted from salic roof rocks. The purpose of the present study was to investigate in more detail the effects of mixing basaltic and granitic liquids, using a relatively simple system in which the phase relations are amenable to analysis by graphical methods. The approach has been to examine relations along lines between haplobasaltic compositions in the system Mg_2SiO_4 (Fo)- $\text{CaAl}_2\text{Si}_2\text{O}_8$ (An)- SiO_2 (Q) and a haplogranitic composition on the join KAlSi_3O_8 (Or)- SiO_2 (Q). The results show that, in the compositional region investigated, the liquids are completely miscible, but the liquidus relations exhibit a strong, apparent silica immiscibility effect (see Irvine, this Report), implying that the mixing is nonideal. The phase relations indicate that salic contamination of subalkaline basaltic magma should tend to enhance the crystallization of Ca-poor pyroxene relative to both olivine and plagioclase, a feature that accords with the abundant development of orthopyroxene cumulates in association with chromitite in the Muskox, Stillwater, Bushveld, and Great

Dyke intrusions. The relations also show that it is possible to produce melts with only anorthite on the liquidus by mixing "contaminated" basic liquid that has crystallized enough pyroxene to differentiate to the pyroxene-anorthite cotectic, with "relatively fresh" liquid on the olivine-anorthite cotectic. Fractional crystallization of the intermediate liquid would then yield plagioclase precipitates comparable to anorthositic layers in the Muskox, Bushveld, Stillwater, and Rhum intrusions.

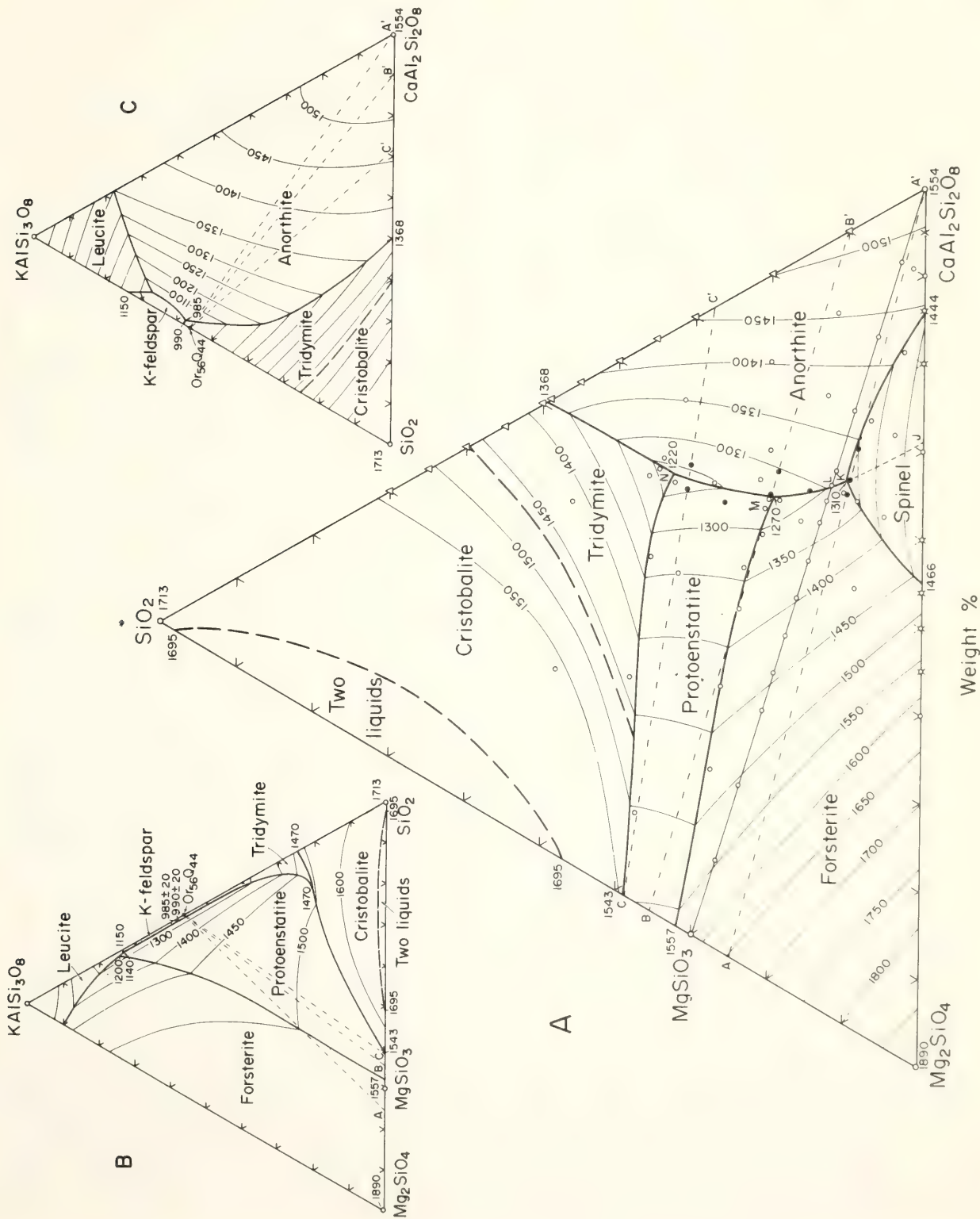
Experimental Methods

The available data on the bounding joins of the system Fo-An-Or-Q are shown in Fig. 61. The present investigation was primarily concerned with compositions between points near the forsterite-anorthite and protoenstatite-anorthite cotectics along lines AA', BB', and CC' in Fig. 61A and the composition $\text{Or}_{56}\text{Q}_{44}$ (wt %) near the K-feldspar-tridymite eutectic in Fig. 61B and C. Some work was also done on the Fo-An-Q liquidus boundaries.

The experimental charges consisted of precrystallized mixes on the Fo-An-Q join combined in various proportions with an $\text{Or}_{56}\text{Q}_{44}$ glass prepared by Schairer and Bowen (1955) in their study of the system $\text{K}_2\text{O}-\text{Al}_2\text{O}_3-\text{SiO}_2$.*

* The $\text{Or}_{56}\text{Q}_{44}$ composition, which was checked by electron microprobe analysis, is not exactly the K-feldspar-tridymite eutectic composition, which was estimated by Schairer and Bowen (1955, p. 718) to be $\text{Or}_{58.2}\text{Q}_{41.8}$, but the difference was not considered critical. In retrospect, it is evident that the ideal haplogranitic composition to have used would be the composition of the quaternary eutectic point between enstatite, anorthite, K-feldspar, and tridymite. The next best would be a composition near this point on the pyroxene-anorthite cotectic. As best one can estimate, however, the mixing lines between $\text{Or}_{56}\text{Q}_{44}$ and the investigated haplobasaltic compositions pass within less than 1 wt % of the salic end of the cotectic in quaternary space, almost within the uncertainty of its location, and any possible deficiencies arising from this difference relate less to the excess Q in the glass than to a lack of about 0.5 wt % An (cf. Fig. 63).

Fig. 61. Liquidus relations for three of the bounding joins of the system Mg_2SiO_4 (Fo)- $\text{CaAl}_2\text{Si}_2\text{O}_8$ (An)- KAlSi_3O_8 (Or)- SiO_2 (Q): (A) Fo-An-Q, modified from Andersen (1915); (B) Fo-Or-Q, redrawn from Schairer (1954, Fig. 5); (C) An-Or-Q, redrawn from Schairer and Bowen (1947, Fig. 4). In (A) the small open circles are compositions studied by Andersen; solid circles are compositions investigated in the present study. Crosses along the Fo-An join are compositions investigated by Osborn and Tait (1952), and triangles on the An-Q join are compositions studied by Schairer and Bowen (1947). Phase relations in the planes from AA', BB', and CC' to $\text{Or}_{56}\text{Q}_{44}$ are shown in Figs. 62 and 63.



The precrystallized compositions were prepared from weighed amounts of dried MgO , CaCO_3 , SiO_2 (cristobalite), and Al_2O_3 . These were mixed and calcined, and then were fused at about 1500°C and quenched to glasses that were crushed and re-fused two to four more times to ensure homogeneity. The final glasses were pulverized and crystallized for a day at temperatures $50^\circ\text{--}100^\circ\text{C}$ below their solidi. The crystallized material, which consisted of plagioclase, pyroxene, and either olivine or tridymite, was then reground and dried. The mixtures with $\text{Or}_{56}\text{Q}_{44}$ were made by grinding in an agate mortar for about 45 minutes to a maximum grain size of no more than $1\text{--}2\ \mu\text{m}$.

Phase relations were established by melting experiments, using standard 1-atm quenching methods. In the original study of the system Fo-An-Q, Andersen (1915) found that equilibrium could be established at liquidus temperatures in runs of only $1/2\text{--}2$ hours duration, but in the present study much longer times were used, especially for runs on compositions rich in Or at relatively low temperatures. Most runs were 4–24 hours long, and some were more than 100 hours. Temperatures are believed generally to be accurate to $\pm 5^\circ\text{C}$.

Phases were identified optically. The forsterite, pyroxene, and anorthite were relatively easy to distinguish, except that it was difficult to discern the first appearance of anorthite after pyroxene in compositions rich in $\text{Or}_{56}\text{Q}_{44}$. In the diagrams, the pyroxene has been called protoenstatite in accord with earlier work, but this identification is provisional pending further study. Both pigeonite and orthoenstatite are possible alternatives.

Experimental Results

The data obtained for the system Fo-An-Q are generally compatible with those of Andersen (see Fig. 61A) but require slight revisions of the phase boundary lines drawn by him. The spinel

field extends slightly farther toward Q than he indicated, the tip of the field at K now being located at $\text{Fo}_{28.2}\text{An}_{61.8}\text{Q}_{10}$ and 1310°C rather than $\text{Fo}_{29.5}\text{An}_{61}\text{Q}_{9.5}$ and 1320°C . The present results also suggest that the temperature of point M is about 10°C higher than the 1260°C value reported by Andersen. The most significant discovery, however, is that the forsterite-anorthite cotectic, KLM, is slightly curved. As revised, this boundary now projects to the point (J) on the Fo-An join suggested by Osborn and Tait (1952) for its location beneath the spinel liquidus field, but more important, the curvature is in the appropriate direction to be ascribed to the silica immiscibility effect and therefore probably implies that the liquid solution is nonideal.

Most of the data that have been obtained in the system Fo-An-Or-Q are presented in Fig. 62, and the results for the sections from AA' and BB' to $\text{Or}_{56}\text{Q}_{44}$ are interpreted in Fig. 63. Figure 64 shows two projections of the liquidus boundaries between Or_0 and Or_{20} that are particularly useful for petrological considerations, and Fig. 65 shows additional data for the mixing line 20-16 in Fig. 64. Perhaps the most remarkable feature in Fig. 62 is the presence of maxima in the protoenstatite liquidus profiles. As shown in Fig. 63, the maxima arise because the protoenstatite liquidus (including its cotectic junction with the anorthite liquidus) is bulged toward the An-Or-Q join. This feature is also symptomatic of the silica immiscibility effect and thus suggests the presence of the metastable solvus shown beneath the liquidus. The maxima would seem to reflect the shape of such a solvus.

Implications with Respect to Salic Contamination of Basaltic Magmas

The following observations deriving from the experimental results appear significant with respect to contamination of basaltic magma by granitic liquid.

1. The subalkaline, magnesian haplo-basaltic melts of the system Fo-An-Q

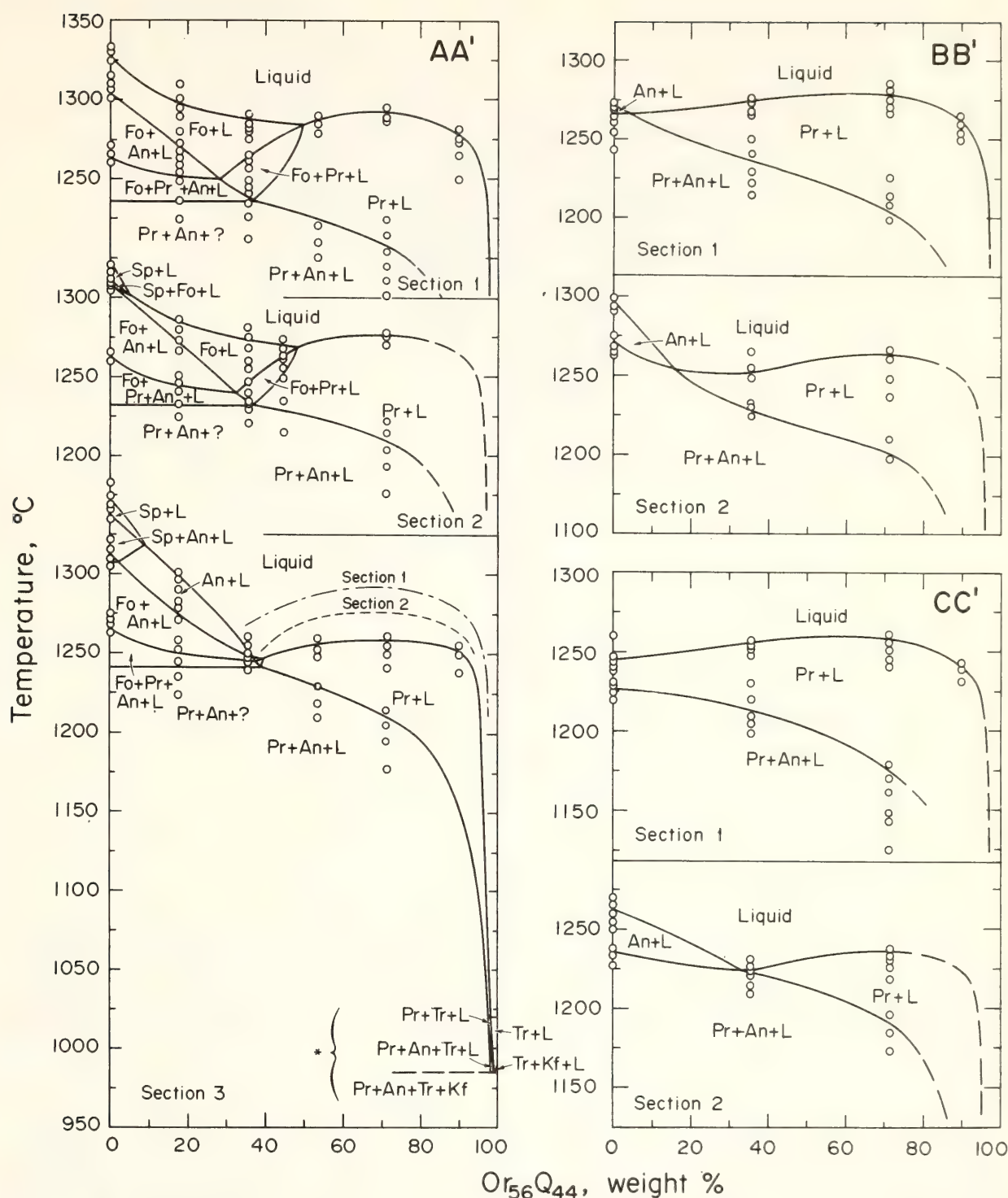


Fig. 62. Experimental data for temperature-composition sections between haplobasaltic compositions on lines AA' , BB' , and CC' in Fig. 61A and the haplogranitic composition, $Or_{56}Q_{44}$. Abbreviations: Fo, forsterite; Pr, protoenstatite (provisional identification); An, anorthite; Kf, K-feldspar; Tr, tridymite; L, liquid. The phase denoted by a question mark in AA' is only minor and may be either leucite or K-feldspar, or both. The investigated compositions are at 0, 10, 20, 25, 30, 40, and 50 wt % Or. Relations in the vicinity of the asterisk are inferred from Fig. 61 B and C; the field composition widths are exaggerated for clarity but are expected to be typical of all sections. Note the temperature maxima on the protoenstatite liquidus. Interpretations of the data from AA' and BB' appear in Fig. 63.

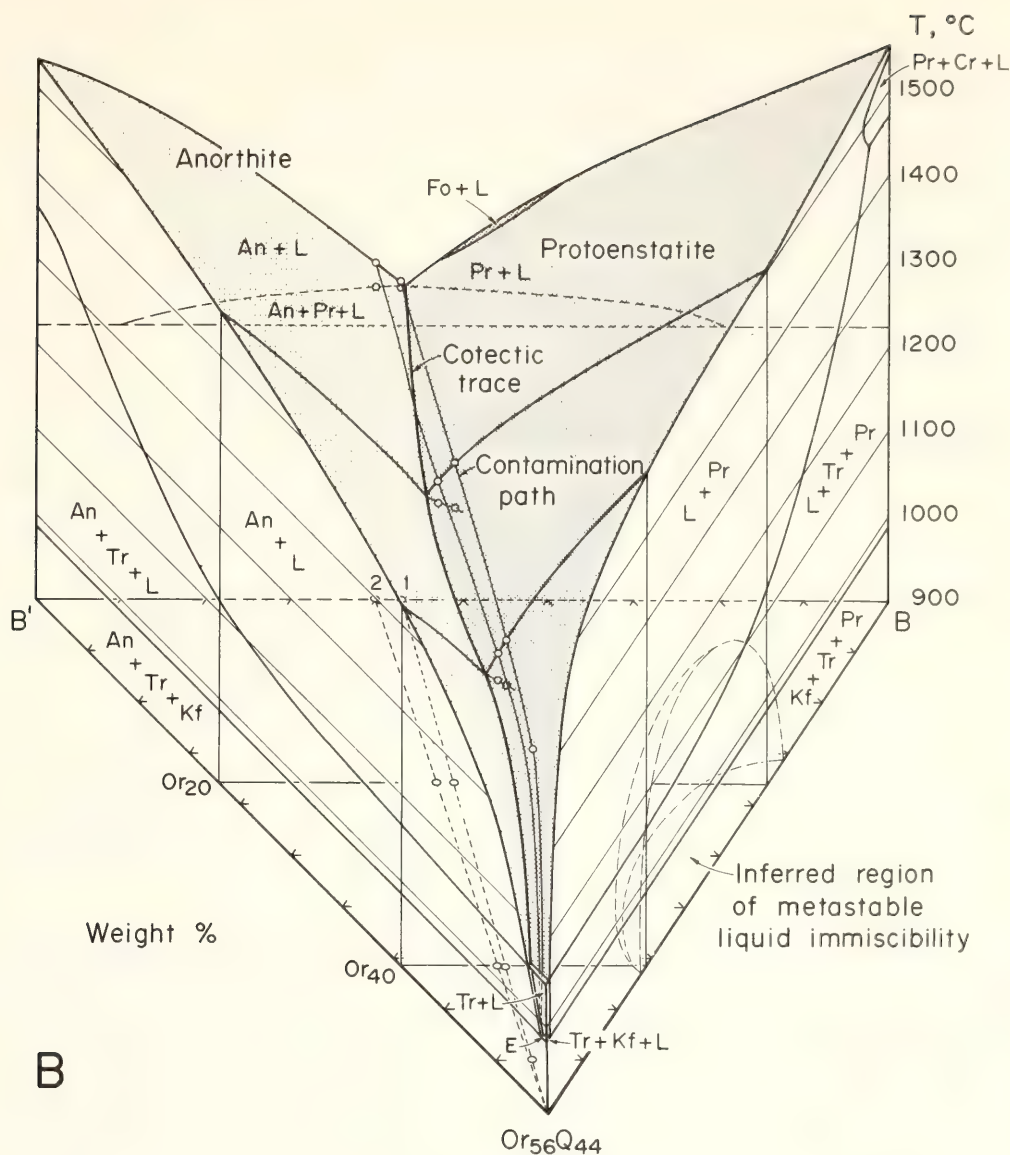


Fig. 63 B.

also suppresses aluminous spinel (Fig. 63A), but as shown in *Year Book 73* (pp. 300–316) it may be expected to favor chromium-rich spinel over forsteritic olivine. As noted above, the enhancement of the pyroxene crystallization is a line of support for the origin of chromitite layers by salic contamination in that it accords with the abundant development of orthopyroxene cumulates with chromitite in the Muskox, Stillwater, Bushveld, and Great Dyke intrusions.

4. Basic liquids near the olivine-anorthite cotectic can undergo remarkably large degrees of salic contamination before olivine ceases to be the liquidus

phase. For example, the investigated liquids along AA' in Fig. 61A show only 6–7 wt % normative olivine but still have olivine on the liquidus after 40%–45% contamination (Fig. 62). Moreover, because of the curvature of the olivine-anorthite cotectic, the amount of olivine precipitate that can be derived from a melt with olivine on the liquidus is not much reduced by salic contamination until pyroxene becomes the second phase (compare paths Aa and Bb in Fig. 66, below). Thus the presence of large amounts of cumulus olivine in a layered intrusion does not rule out the possibility that the parental magma was extensively contaminated with siliceous material.

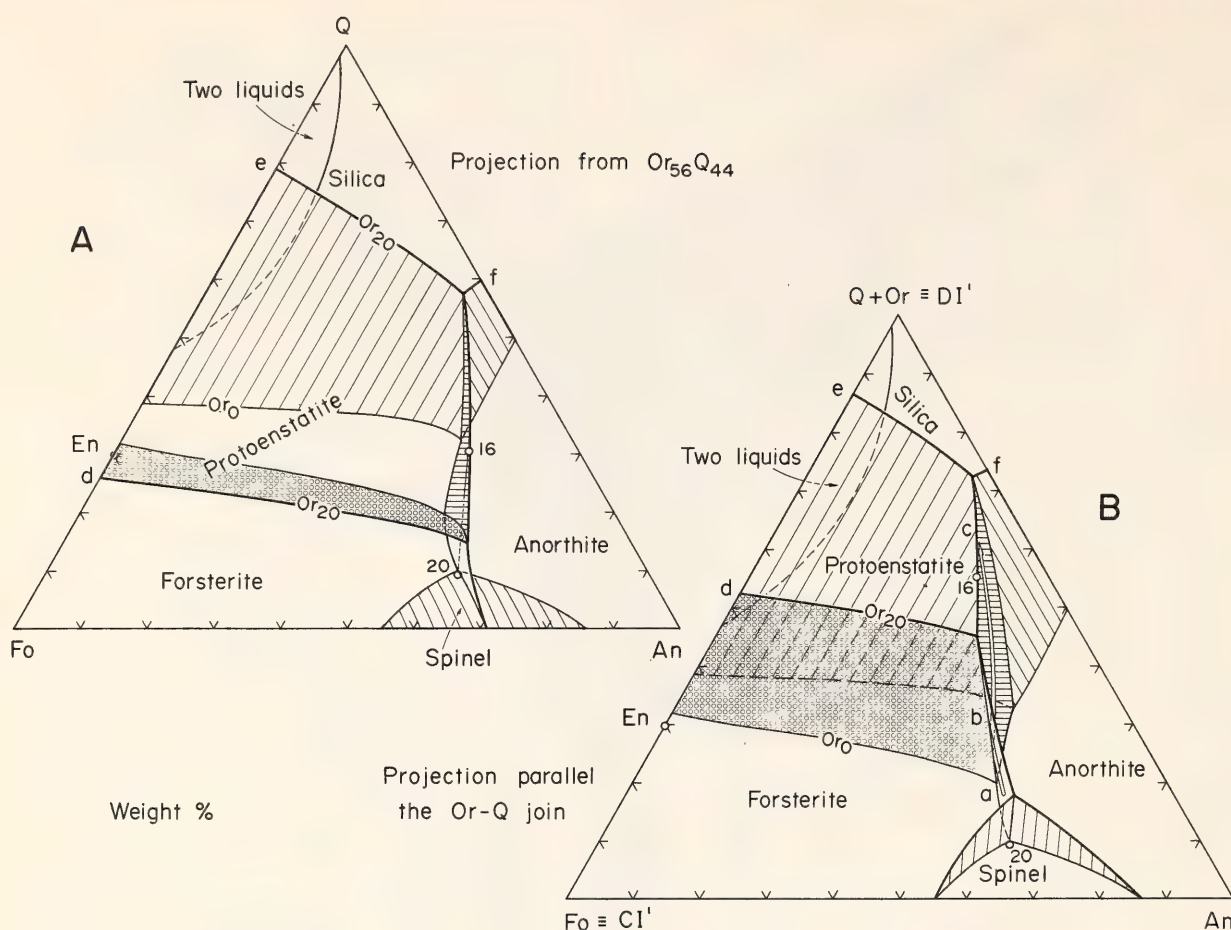


Fig. 64. Two projections of the system Fo-An-Or-Q showing the liquid boundaries between Or₀ and Or₂₀. Note how different the relations appear, depending on how they are viewed, even though the plane of projection is the same. Points *d* and *e* are from Fig. 61B; *f* is from Fig. 61C. The forsterite-anorthite and protoenstatite-anorthite boundaries are based on Figs. 62 and 63; the relations along line 20-16 are shown in Fig. 65. The spinel volume is assumed to taper out at Or₂₀, and other parts of the boundary surfaces are interpolated. Figure 64A illustrates directly the effects of contamination of melts on the Fo-An-Q join with Or₅₆Q₄₄; Fig. 64B is analogous to the diagram used in Fig. 60, and the fractionation path *abc* may be compared with the Thingmuli trend line *abc* in Fig. 60B.

Origin of Anorthositic Layers in Stratiform Intrusions

The suggested origin for anorthosite layers in stratiform intrusions could have been inferred directly from the Andersen (1915) version of the system Fo-An-Q, but the explanation has been strengthened by the results of the present work and by the realization that the necessary configuration of phase boundaries is probably due in large degree to the silica immiscibility effect. The essential argument is that, because of the relations of the forsterite-anorthite and protoenstatite-anorthite cotectic boundaries in the interval *KLM* in Fig. 61A, it is possible by mixing liquids from *KM* with those

from *MN* to obtain intermediate melts with only anorthite on the liquidus. Fractional crystallization of the intermediate melts would then yield the anorthositic precipitates. The data in Fig. 65 show that this possibility extends to the system Fo-An-Or-Q and thereby provide a basis for combining it with the silic contamination mechanism in stratiform intrusions (Fig. 66). By this combination, the liquid on the pyroxene-plagioclase cotectic is produced by fractionation of pyroxene from contaminated magma that had originally been in the olivine field; the liquid on the olivine-plagioclase cotectic is relatively uncontaminated magma from which the "ex-

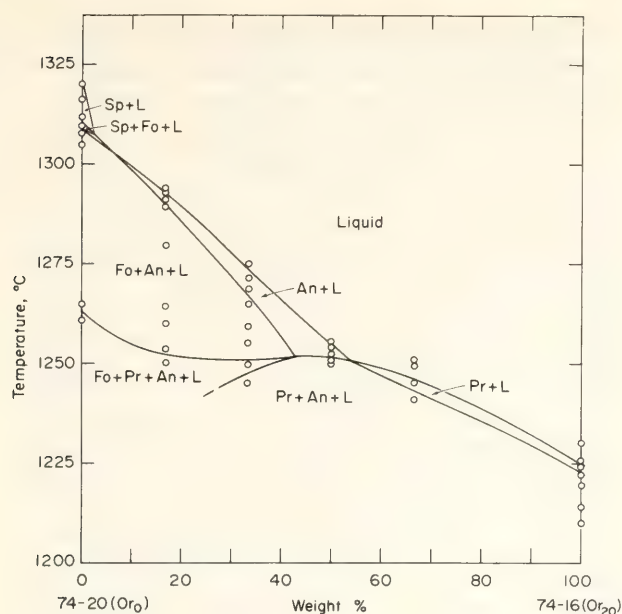


Fig. 65. Phase relations for the line 20-16 in Fig. 64. Abbreviations as in Fig. 62. It is seen that melts with anorthite on the liquidus can be produced by mixing melts having spinel and forsterite on the liquidus with melts having protoenstatite on the liquidus. (In the experimental runs, spinel appeared only in trace amounts; hence composition 74-20 essentially has forsterite on the liquidus.) Note that there is no inhibiting heat effect associated with the mixing in the sense that no crystallization is apparently required if the end-member melts are combined while at their respective liquidus temperatures.

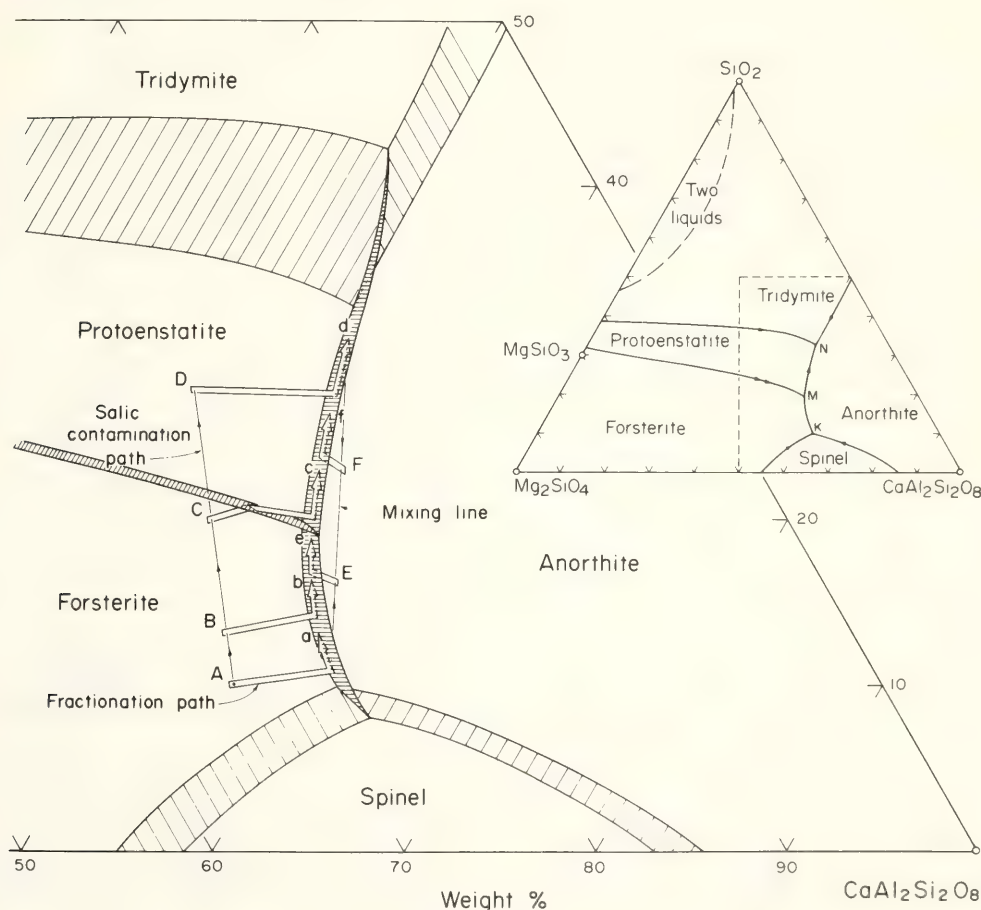


Fig. 66. Liquidus diagram of part of the system Fo-An-Or-Q, showing the crystallization orders that can be developed from a haplobasaltic liquid at A by the combined effects of salic contamination, fractional crystallization, and magma mixing. The diagram is not quantitative in detail but may be regarded as a projection from about Or₈₀Q₂₀. The extent of contamination and mixing has been exaggerated for purposes of illustration. If the various precipitates are equated with rock types (e.g., forsterite with peridotite, protoenstatite with orthopyroxenite, anorthite with anorthosite), the indicated fractionation paths give the following sequences of rock layers: Aa and Bb, peridotite, troctolite (and, eventually, norite); Cc, peridotite, orthopyroxenite, norite; Dd, orthopyroxenite, norite; Ee, anorthosite, troctolite (and, eventually, norite); Ff, anorthosite, norite. Note that a given path length in the anorthite field yields much more crystalline material than an equivalent path length in the olivine or pyroxene field.

cess" olivine has been precipitated. The two types of magma might be derived from different parts of the magma chamber; or the uncontaminated liquid might represent an infusion of fresh magma, an event that has been shown commonly to occur in some stratiform intrusions (Irvine and Smith, 1967). From the different possibilities outlined in Fig. 66, the anorthosite layers would be expected to be associated with layers of orthopyroxenite, norite, troctolite, and peridotite, and this association is in fact well developed. The anorthositic layers through the Critical Zone of the Bushveld Complex are generally interstratified with orthopyroxenite and norite (e.g., Cameron, 1963), and those associated with the important platiniferous Merensky Reef are accompanied as well by layers of troctolite and harzburgite (e.g., Van Zyl, 1970). In the Stillwater Complex, the anorthositic zones occur stratigraphically above thick zones of orthopyroxenite and norite and contain thin interlayers of troctolite (Hess, 1960). The Muskox intrusion contains only one relatively thin anorthositic layer (which is more accurately described as anorthositic olivine gabbro), but the layer occurs immediately above a cyclic unit of peridotite, orthopyroxenite, and websterite that is believed to have differentiated from contaminated magma (Irvine, 1970), and just beneath the peridotite layer of a later cyclic unit, presumably formed after an influx of fresh magma.

Finally, it is noted that because of the curvature of the forsterite-anorthite cotectic (Fig. 66), melts with only anorthite on the liquidus can also be produced by mixing liquids from different points along this boundary alone, without involving pyroxene. This possibility might be applicable to the origin of the anorthositic, allivalite layers of the Rhum intrusion, a body in which peridotite and olivine gabbro are dominant rock types and orthopyroxene is rare (cf. Wager and Brown, 1968).

PARTITIONING OF TRACE AND MINOR ELEMENTS BETWEEN COEXISTING SILICATE LIQUIDS

*E. Bruce Watson**

The behavior of trace and minor elements in geological systems has been of major concern to geochemists in recent years. Theoretical, experimental, and analytical investigations of element fractionation between coexisting phases have established a basis for temperature and pressure measurement in the earth, and for quantitative modeling of melting and crystallization processes in magmatic systems. Crystal-liquid partitioning studies on numerous elements have contributed to a qualitative understanding of the relative preference of different trace cations for crystalline compounds coexisting with silicate liquid. Cation size, valence, and bond type, as well as crystal-field stabilization effects, have been shown to be important (Burns and Fyfe, 1967; Whittaker, 1967). However, the development of quantitative predictive models of crystal-liquid partitioning has been hampered by lack of knowledge of short-range structure and site availability in complex silicate melts. Direct analysis of melt structure is difficult: even the supercooled equivalent (glass) does not yield to many of the structural analysis methods applicable to crystalline compounds. For this reason, estimation of the relative abundance in petrologically important liquids of sites† favorable for occupation by different cations has not been attempted.

A silicate system containing a two-liquid field provides the opportunity to examine indirectly the relative site availability in two complex melts by

* Work carried out under a cooperative predoctoral fellowship program between the Geophysical Laboratory and Massachusetts Institute of Technology.

† The term "site" is used here in a very general way, in reference to an *average* position relative to oxygen and other cations in the melt.

equilibrating them with respect to trace or minor constituents. To this end, an isothermal series of 1 atm doping experiments, involving systematic addition of trace and minor elements to immiscible $\text{K}_2\text{O}-\text{Al}_2\text{O}_3-\text{FeO}-\text{SiO}_2$ liquids, has been undertaken. The primary objectives are (1) to examine the relative ability of acidic and basic liquids to accommodate cations of variable size, charge, and bonding characteristics; (2) to determine the compositional range over which Henry's law is valid in silicate melts for various elements of geological interest; and, ultimately, (3) to investigate possible cation interaction effects by doping the melts with more than one element at a time.

Method

Bulk compositions on the two-liquid boundary of the system $\text{K}_2\text{O}-\text{Al}_2\text{O}_3-\text{FeO}-\text{SiO}_2$ (Roedder, 1951) were selected for study (see Fig. 67 and Table 16).

This system affords stable, low-temperature immiscibility between liquids that are relatively simple yet broadly analogous to natural melts. The two liquids contain all the major cation types present in magmas: Si^{4+} (glass-former), Al^{3+} , divalent cation (Fe^{2+}), and alkali (K^+). When compared on a molar basis, the melt compositions differ appreciably from magmatic liquids only in their lesser alumina content (Table 16).

Experiments were performed in 1 atm vertical furnaces. Charges of 20–40 mg were contained in pure iron capsules sealed in evacuated silica glass tubes. Runs were quenched in 4–5 seconds by dropping the tubes into water.

Starting materials consisted of mechanical mixtures of silica glass and synthetic leucite and fayalite (prepared from spectroscopic grade chemicals). In preliminary experiments, compositions within the two-liquid field were found to melt completely and undergo phase sep-

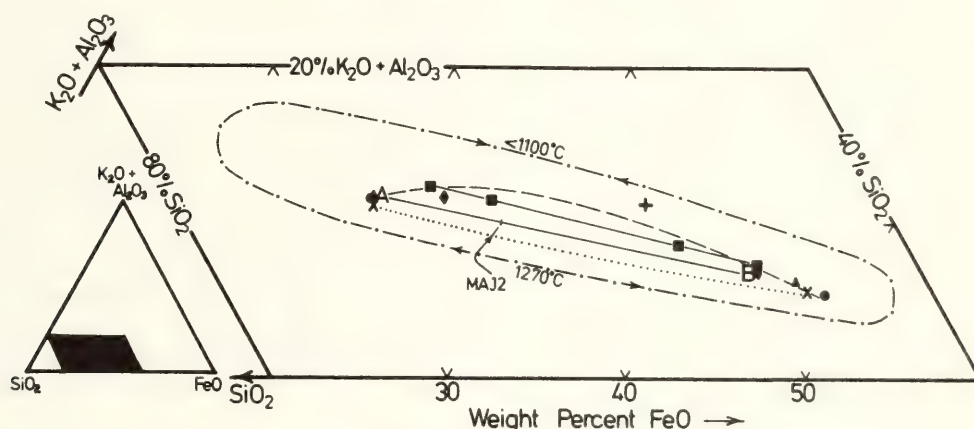


Fig. 67. Coexisting liquid compositions at 1180°C in the system $\text{K}_2\text{O}-\text{Al}_2\text{O}_3-\text{FeO}-\text{SiO}_2$. The molar ratio of total K_2O :total Al_2O_3 in all experiments is 1:1. However, immiscible liquids differentially partition these components, thus upsetting the 1:1 ratio in both liquids and necessitating the use of the sum ($\text{K}_2\text{O} + \text{Al}_2\text{O}_3$) to plot the diagram (see Table 16 for mole percentage of oxides in an immiscible liquid pair). Symbols: triangles, circles, and diamonds represent immiscible liquid pairs after 14 hours at temperature, starting as a $\text{Lc} + \text{Fa} + \text{SiO}_2$ mechanical mixture of intermediate composition; crosses, immiscible liquids resulting from 2-day equilibration of fragments of two glasses whose compositions lie outside the immiscibility volume; squares, immiscible liquid compositions after 4-1/2 hours (inner pair) and 14 hours (outer pair), starting as an intermediate mechanical mixture of Lc , Fa , and SiO_2 glass; A and B, conjugate liquids A and B used for partitioning studies, obtained by melting MAJ2 mechanical mixture (run times up to 108 hours); plus sign, composition melting to a single liquid at 1180°C . Dashed line is the intersection of the 1180°C isotherm with the two-liquid volume; dotted line is the approximate position of the tridymite liquidus at 1180°C . Dot-dash line is the (nonisothermal) intersection of the immiscibility volume with the liquidus surface of the $\text{Lc}-\text{Fa}-\text{SiO}_2$ system (modified from Roedder, 1951). Most tie lines are omitted for the sake of clarity.

TABLE 16. Mole Percentage of Oxides in Immiscible Si-Rich (A) and Fe-Rich (B) Liquids* Compared with Some Common Igneous Rocks

	Liquid A (Si-rich)	Average Dacite†	Liquid B (Fe-rich)	Average Abyssal Tholeiite‡	Average Basalt‡
SiO ₂	74.0	69.6	55.8	52.1	55.2
Al ₂ O ₃	3.6	10.8	2.3	9.9	9.0
Oxides of divalent cations§	18.4	14.4	40.1	35.0	32.9
Alkali oxides	4.0	5.2	1.8	2.9	2.9

* See Fig. 67 and text.
† From Nockolds (1954).
‡ From Cann (1971).
§ All Fe expressed as FeO. For natural rocks, this is summed with MgO and CaO.
|| Only K₂O is present in liquids A and B.

aration in about 4 hours at 1180°C. However, the compositions of the initial immiscible liquids were less extreme (Fig. 67) than the equilibrium compositions obtained by maintaining temperature for an additional 8–10 hours. After 14 hours, globules of the two liquids, each including the other, were as large as 200 μm in diameter.

For two-liquid partitioning studies, a bulk composition (MAJ2; see Fig. 67) was selected that would yield an Si-rich liquid (liquid A) and an Fe-rich liquid (liquid B) in the ratio of 7:3 at 1180°C (see Fig. 67 and Table 16). A mechanical mixture of MAJ2 composition was doped with the minor element of interest in amounts ranging from 0.1 to 1 wt %. The minor element was added in oxide form and thoroughly premixed with the starting material by grinding in an agate mortar. Although 2-day run times were found sufficient to equilibrate the immiscible liquids at all concentrations of the elements examined, the usual run time was 4 days. The quenched two-glass charges were analyzed by electron microprobe for both major and trace or minor constituents. Operating conditions varied depending on the trace or minor element being analyzed. Counting times for analysis at low concentrations ranged from 50 to 300 seconds per analysis spot (most were 100 or 200 seconds).

Results

The results of doping experiments on Ba, Sr, Ca, Mg, La, and Zr are presented in Fig. 68. Hess and Rutherford (1974) predicted that cations able to replace Si⁴⁺ in melts (e.g., Al³⁺) and cations required for local charge balance (alkalies, Ba²⁺) would be enriched in the more acidic of two coexisting liquids, and that all other cations would favor the basic melt. To the extent that they were tested, the predictions of these authors are generally confirmed by the present data, except that barium behaves more like the other alkaline earth elements than like potassium. For alkaline earth elements, the two-liquid partition coefficient (hereafter referred to as

$$D_{B/A} = \frac{\text{concentration in Basic (Fe-rich) liquid}}{\text{concentration in Acidic (Si-rich) liquid}} \quad (\text{hereafter referred to as } D_{B/A})$$

shows no straightforward dependence on ionic radius. In fact, Ba²⁺ (ionic radius ≈ 1.34 Å for 6-fold coordination with oxygen) is partitioned in exactly the same way as the smaller Sr²⁺ ion (although more Sr data are required). The weak partitioning of both these ions suggests that neither occupies the same structural position in the melt as Fe²⁺. However, more than one type of site

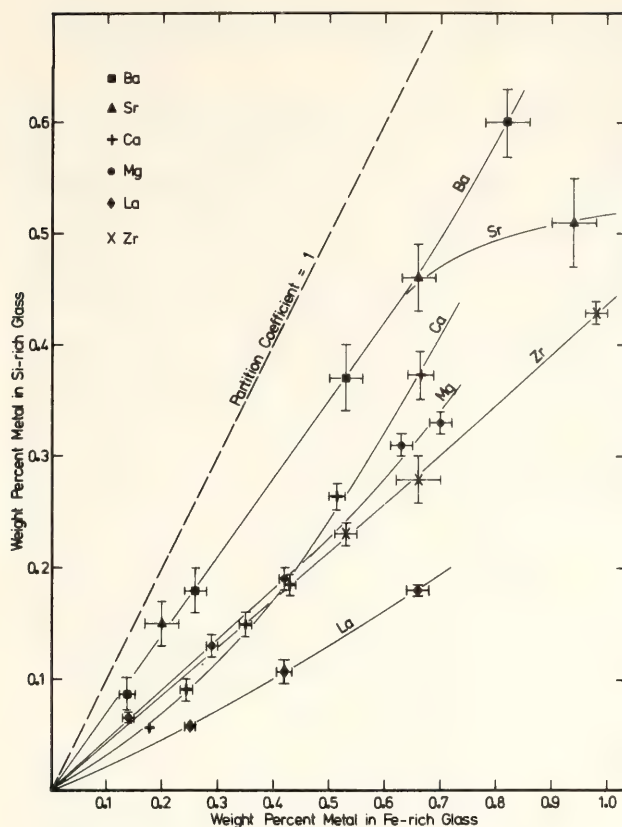


Fig. 68. Graphical illustration of trace and minor element partitioning between liquids *A* and *B*. Error bars are 2σ counting precision for ten separate analysis spots. Counting error is probably better than 7% for all points except the lowest Ba concentration, which is about 15%. No data are reported on charges doped above about 1% because additions above this level affect the composition of equilibrium phases. The addition of small amounts of di- and trivalent cations shifts the tridymite liquidus into the two-liquid volume. As a result, most charges represented in this figure contain minor amounts of tridymite. The major components of liquids *A* and *B* in doped charges vary from the values in undoped experiments by no more than 6% of the amount present.

may be involved (e.g. both K^{+} - and Fe^{2+} -type sites). Magnesium and calcium are partitioned into the Fe-rich liquid, a result to be expected because of the similarity in charge and general similarity in size of Mg^{2+} and Ca^{2+} to Fe^{2+} . The distribution of trace amounts of Mg between the two liquids is identical with the distribution of Fe, a major component of the system ($D_{B/A}$ for Mg and Fe = 2.1–2.2). The Mg/Fe in the two liquids is therefore the same, indi-

cating that the energy change for the substitution $Mg^{2+} \rightleftharpoons Fe^{2+}$ is equivalent in the two liquids (and perhaps generally independent of liquid composition). At the *trace element* level, Ca^{2+} shows more enrichment in the basic melt than Mg^{2+} , suggesting that Ca^{2+} does not so readily replace Fe^{2+} in the acidic melt.

The distribution of lanthanum between Fe-rich and Si-rich melts contrasts sharply with aluminum partitioning, indicating that cation charge alone does not determine substitution behavior in melts. Lanthanum is strongly depleted in the silicic glass, probably because La^{3+} is too large to replace Si^{4+} as a glass-forming cation in the manner of Al^{3+} (Day and Rindone, 1962). Zirconium shows greater solubility than La in the silicic melt, suggesting that Zr^{4+} might substitute to some degree for Si^{4+} in network-forming units.

In addition to two-liquid partition coefficients, the data presented in Fig. 68 establish approximate limits of applicability of Henry's law for oxides dissolved in complex silicate melts. The limit for a given element corresponds to the point where the plot begins to deviate from linearity (above which $D_{B/A}$ is no longer constant with increased concentration). At greater concentrations, Henry's law is no longer obeyed in one or both of the liquids (it is not possible to say in which). Table 17 summarizes approximate limits of Henry's law for Ba, Sr, Ca, Mg, La, and Zr in the (liquid *A* + liquid *B*) system. Because of the compositional similarity of liquids *A* and *B* to natural melts (Table 16), it is believed that these limits can be used semi-quantitatively to distinguish trace from minor elements in magmas. Compared on a molar basis, Mg^{2+} has by far the highest limit, probably because of its similarity in charge and radius to Fe^{2+} .

Application of Data

It is often assumed in measuring and applying solid-liquid partitioning data that a trace element distribution coeffi-

TABLE 17. Approximate Limits of Applicability of Henry's Law for Elements Dissolved in the Liquid A + Liquid B System*

Ele- ment	Wt % Metal	Atomic Wt	Mole % Relative to Mg
Mg	0.50	24.3	1
Ca	0.15	40.1	0.20
Sr	0.65	87.6	0.35
Ba	0.70	137.3	0.25
La	0.15	138.9	0.05
Zr	0.75	91.2	0.40

* For the purpose of making this table, the limit is considered to be the maximum concentration in Liquid B (Fe-rich) for which $D_{B/A}$ can be considered constant (see Fig. 68).

cient is constant with changing liquid composition. Burns and Fyfe (1964), Banno and Matsui (1973), and Irvine (*Year Book* 73, pp. 300–316), among others, have recognized the fallacy of this assumption. The present two-liquid partitioning data can be directly applied to this problem in a qualitative way. For example, Ba and Sr are only weakly partitioned into the basic liquid ($D_{B/A} = 1.4$) at 1180°C, indicating that sites suitable for these ions are nearly as abundant in the silicic melt as in the less structured (Hess, 1971) basic melt. By analogy, it is likely that natural intermediate to felsic liquids are almost as accommodating to the large alkaline earth ions as are basaltic liquids. Consequently, the distribution coefficients for Ba and Sr between a given solid phase and magmatic liquid should remain nearly constant with changing liquid composition (ignoring temperature dependence). Barium and strontium, then, are acceptable elements to use in trace element modeling of fractional crystallization processes, and for possible applications to temperature measurement. From the data shown in Fig. 68, it is clear that other elements (e.g., La) are not so suitable for these purposes. This conclusion is supported by the analytical data of Nagasawa and Schnetzler (1971), who found larger rare earth ele-

ment phenocryst-matrix partition coefficients in dacites than in more basic rocks.

Roedder and Weiblen (1971) suggested that fractionation of elements between immiscible silicate liquids could be an important process in the evolution of the lunar crust, noting in particular the potential significance of enrichment of incompatible elements in the more basic of two coexisting liquids. Such a pattern is the opposite of that expected for contrasting magmas resulting from fractional crystallization processes, and if found in rocks, might be evidence for the occurrence of liquid immiscibility. The data in Fig. 68 indeed indicate that the operation of liquid immiscibility in nature would produce unusual trace element distributions (the rare earth elements, for example, would be enriched in the more basic of two immiscible liquids). These data are therefore useful as evaluative tools for possible instances of magma unmixing. Two-liquid partition coefficients might, for example, help to constrain speculation on the origin of mafic-felsic associations such as basalt and rhyolite. The data must, however, be applied qualitatively and with caution, considering especially the possible coexistence of one or more crystalline phases with the two liquids.

PHASE RELATIONS IN THE SYSTEM
 Mg_2SiO_4 –IRON OXIDE– $CaAl_2Si_2O_8$ – SiO_2
AT 10 KBAR AND THEIR BEARING ON
THE ORIGIN OF ANDESITE

E. F. Osborn and R. J. Arculus

The system Mg_2SiO_4 –iron oxide– $CaAl_2Si_2O_8$ – SiO_2 (Fo–M–An– SiO_2) is a useful model for understanding the phase relations of common tholeiitic and calc-alkaline rocks, as shown by Roeder and Osborn (1966). Their studies were carried out at a series of partial pressures of oxygen (P_{O_2}), at a total pressure of 1 atm. Phase relations in the system Fo–M–An– SiO_2 can be expected to change significantly with increasing pressure, as

judged from the studies of Clark, Schairer, and de Neufville (*Year Book 61*, pp. 59–68) and Kushiro (*Year Book 71*, pp. 357–362) for the iron-free systems, Di-An-SiO₂ and Fo-An-SiO₂. To extend knowledge of the system Fo-M-An-SiO₂, a study was therefore begun of phase equilibria at higher pressures, and preliminary data obtained at 10 kbar are reported here. The objective is an understanding of the change in phase relations to a depth of about 35 km. The data should give information applicable to courses of crystallization of a magma as it moves from the upper mantle to the surface, and to the composition of liquids derived by partial melting of peridotite in the upper mantle.

The original mixtures of Roeder and

Osborn were used along with some that have been newly prepared. Solid-media, high-pressure apparatus, Pt and Pt₉₅Au₅ capsules, and run times of 10 to 20 minutes were employed at a pressure of 10 ± 2 kbar. The magnetite-hematite (M-H) buffer was used to provide oxygen partial pressures similar to that of air in the temperature range of these studies, about 1320° to 1420°C. Run products were analyzed on the electron microprobe.

The preliminary sketch in Fig. 69 compares phase relations at approximately 10 kbar, using the M-H buffer, with those at 1 atm in air. Results of quenching experiments for three of the mixtures studied are summarized in Table 18. In changing the pressure from

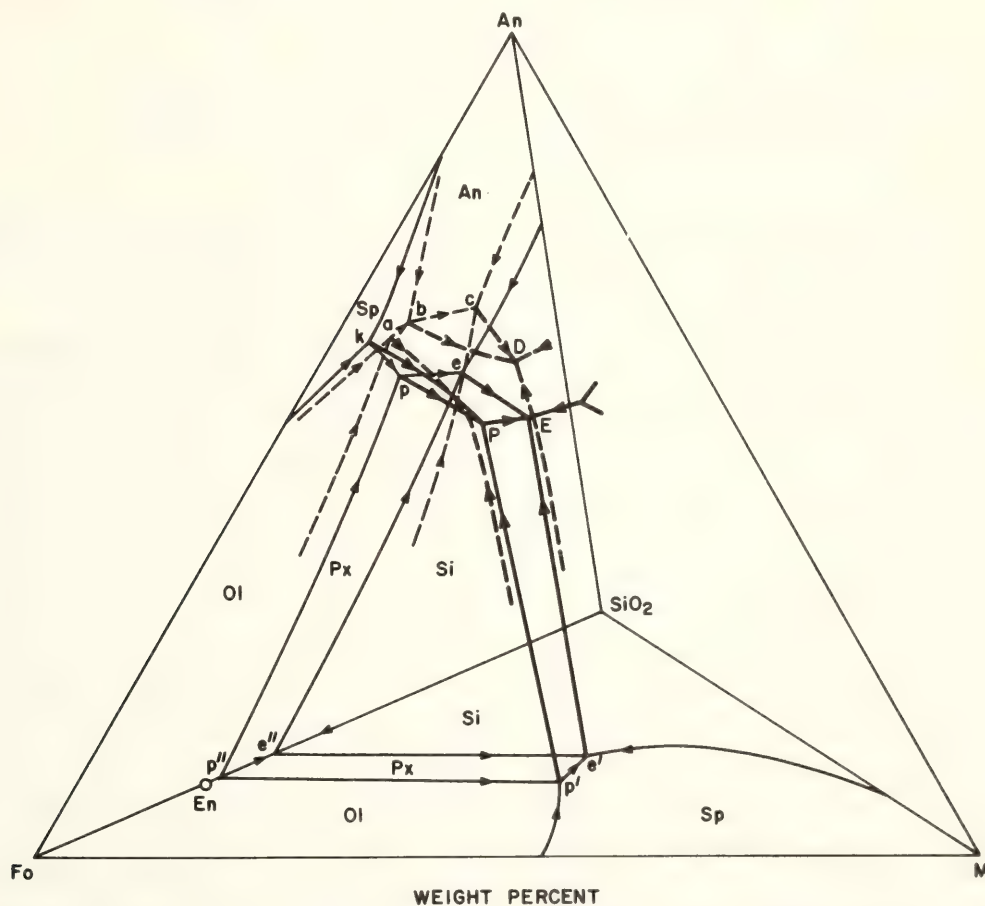


Fig. 69. Tetrahedron representing the system Fo-M-An-SiO₂. Solid lines are boundary curves at 1 atm total pressure in air. Solid lines on the left face are from Andersen (1915), on the base from Muan and Osborn (1956), and within the tetrahedron from Roeder and Osborn (1966). Dashed lines are estimated positions of boundary curves at 10 kbar total pressure, using a magnetite-hematite buffer for mixtures containing iron oxide. Dashed lines on the left face are from Kushiro (*Year Book 71*, pp. 357–362), and those within the tetrahedron are from the present study. Abbreviations: Fo, Mg₂SiO₄; M, Fe₃O₄; An, CaAl₂Si₂O₈; En, MgSiO₃; Px, orthopyroxene; Ol, olivine; Sp, spinel; Si, tridymite or cristobalite.

TABLE 18. Results of Quenching Experiments for Three Mixtures at 1 atm in Air and at 10 kbar Using the M-H Buffer

	Composition of Mixture (wt %)				Pres- sure	Temper- ature (°C)	Phases Present*
	Fo	M	An	SiO ₂			
No. 154	26	8	50	16	1 atm	1272†	<i>L</i>
						1260	<i>Ol+Sp+L</i>
						1254†	<i>Ol+Sp+An+L</i>
						1240	<i>Px+Sp+An+L</i>
						10 kbar	<i>Px+Sp+L</i> (<i>Px</i> =12.6 Al ₂ O ₃ , 2.6 CaO, 6.7 FeO)
No. 84	17.5	10.0	50.0	22.5	1 atm	1250†	<i>L</i>
						1241†	<i>An+L</i>
						1232†	<i>An+Sp+L</i>
						10 kbar	<i>Px+L</i> (<i>Px</i> =10.0 Al ₂ O ₃ , 1.4 CaO, 8.3 FeO)
No. 101	18	4	60	18	1 atm	1270	<i>An+L</i>
						1250	<i>An+L</i>
						1235	<i>Px+An+L</i>
						1220	All <i>xln</i>
						10 kbar	<i>Px+An+L</i> (<i>Px</i> =13.6 Al ₂ O ₃ , 1.6 CaO, 4.0 FeO)
						1340	<i>Px+An+L</i>
						1320	All <i>xln</i>

* Abbreviations: *L*, liquid; *xln*, crystalline. For others see caption, Fig. 69.

† Data from Roeder and Osborn (1966).

1 atm in air to 10 kbar with the M-H buffer, the following major changes in phase relations are suggested: (1) The *Px-An** surface, *p-e-P-E*, moves to the higher *An* level of *b-c-D*, increasing from a region of about 50% *An* to one of about 60% *An*. (2) The size of the primary phase volumes of *Px* and *Sp* increases and that of *An* decreases. (3) The Al₂O₃ content of the *Px* increases to about 12% (see Table 18). (4) The peritectic, *P*, and eutectic, *E*, are replaced by the single eutectic, *D*, at which a high-alumina orthopyroxene, *An*, *Sp*, and tridymite coexist with liquid and gas. (5) The *Sp-An-Ol-L* curve, *k-P*, and the *Sp-Ol-Px-L* curve, *P-p'* are replaced by the single *Sp-Ol-Px-L* curve entering the tetrahedron from point *a*; the single curve is a consequence of the incompatibility of *Ol* and *An* in this system at 10

kbar total pressure. (6) Temperatures of various melting reactions are increased about 100°C.

The differences in boundary-curve configuration between 1 atm and 10 kbar lead to important differences in paths of crystallization. At 1 atm, fractional crystallization at constant *P*_{O₂} (0.21 atm) of a haplolivine basalt will move the liquid to the *Px-An* surface (*p-e-P-E*) at about 18% Al₂O₃, while at 10 kbar and about the same *P*_{O₂}, the liquid will move to and then along the *Sp-Px* surface toward the curve, *bD*, at a much higher Al₂O₃ level. Fractional crystallization at 10 kbar thus will produce a high-alumina haplobasalt or haploandesite liquid in equilibrium with *Px* and *Sp* and having a composition that at low pressure lies within the primary phase volume of anorthite. Therefore, if the pressure should drop rapidly, as by a magma moving from a depth of 35 km to near surface in a short time compared with the rate of precipitation of crystals, *Px* and *Sp* may cease crystallizing as *An*

* For explanation of abbreviations for phases, see caption of Fig. 69 and footnote of Table 18. The only pyroxene identified in the runs is an orthopyroxene having a composition illustrated by three examples in Table 18.

precipitates, thereby causing the liquid composition to move down toward the Px-An surface, *p-e-P-E*. A mechanism therefore exists whereby a high-alumina calcalkaline liquid formed at lower crustal depths by separation of Ol, Px, and Sp may, by moving to shallow depths, have plagioclase as the liquidus phase, Px or possibly Ol followed by Px as the secondary phase, and spinel (magnetite) as a still lower temperature phase. Laboratory studies of calcalkaline volcanic rocks at 1 atm total pressure (Fudali, 1965; Brown and Schairer, *Year Book 66*, pp. 460–467) have shown that plagioclase is commonly the primary phase and that the accompanying liquidus temperatures are high and variable. The reason for this anomalous appearance of plagioclase as the primary phase at atmospheric pressure may be that these calcalkaline liquids inherited compositions developed during fractional crystallization at a much higher pressure, as outlined above.

The phase relations as sketched in Fig. 69 indicate an additional situation that will cause spinel to cease crystallization. The curve, *bD*, from considerations of compositions of the phases, is very likely a spinel reaction curve along its entire length. In other words, as the liquid moves along *bD* during crystallization, An and Px crystallize while Sp dissolves. With fractional crystallization, precipitation of Sp will therefore cease when the composition of a liquid precipitating Px and Sp reaches this curve. Px, joined by An, continues to precipitate, and if the liquid should reach the point *D* as it continues to crystallize, Sp (magnetite) will again crystallize. These relations serve to emphasize the importance of depth (pressure) during fractional crystallization. An olivine basalt fractionally crystallizing at shallow depths will develop the calcalkaline trend when magnetite begins to crystallize, and magnetite will then continue as a liquidus phase. This crystallization sequence is suggested by the study both of model

systems (Muan and Osborn, 1956; Osborn, 1959; Roeder and Osborn, 1966), and of certain basalt-andesite-dacite series (Carmichael, 1964; Nicholls, 1971; Katsui, Ando and Inaba, 1975). On the other hand, if the fractional crystallization takes place at lower crustal levels, an andesitic liquid may then reach the surface having plagioclase as the liquidus phase, and Px as a secondary phase, magnetite appearing only at a lower temperature if at all. If, then, fractional crystallization continues under near-surface conditions, some iron enrichment may occur in the later (higher silica) liquids until magnetite is again a precipitating phase. The absence of phenocryst magnetite in the Cascade andesites, as emphasized by Carmichael and Nicholls (1967) and by Eggler and Burnham (1973), may be explained if a large part of the fractional crystallization occurred at deep levels in the crust. The reactions outlined above may account for the lack of magnetite after movement of the liquid to the surface. In all these reactions the P_{O_2} is maintained at a higher level than would be the case in a closed system, as a small amount of O_2 is added to the system (see Osborn, 1959 and 1969).

PHASE RELATIONS IN THE SYSTEM MgO-IRON OXIDE-CR₂O₃-SiO₂

R. J. Arculus and E. F. Osborn

The compositional variation of spinels coexisting with olivine, pyroxenes, and plagioclase may provide useful information concerning the changes in intensive variables during the crystallization of basaltic magmas (Irvine, 1965). Spinel present in basaltic lavas and basic intrusions are complex solid solutions primarily of the oxides of Mg, Fe²⁺, Fe³⁺, Al, Cr, and Ti. In an attempt to model phase relations among olivine, pyroxene, and spinel, the experimental studies reported by Arculus, Gillberg, and Osborn (*Year Book 73*, pp. 317–322) have been continued. Data have been obtained in

the system MgO –iron oxide– Cr_2O_3 – SiO_2 at 1 atm in air ($P_{\text{O}_2} = 0.21$ atm) and at lower P_{O_2} 's.

The components Al_2O_3 , TiO_2 , and CaO are not present in the system studied; consequently clinopyroxene and plagioclase do not appear and the range of solid solution in the spinel is limited. Nevertheless the results obtained may be compared with the behavior of natural systems in that the extensive $\text{Cr}^{3+} \rightleftharpoons \text{Fe}^{3+}$ exchange in spinels in the model system is analogous to the compositional variation of spinels in natural lavas (Arculus, *Year Book 73*, pp. 322–327).

The preliminary diagram for equilibria in air presented previously (*Year Book 73*, Figs. 65–66) has been corrected on the basis of additional data and is re-

drawn as Fig. 70. All phase compositions are plotted with iron oxide calculated as Fe_3O_4 . The liquidus relations shown are those of the lower surface of the primary phase volume of spinel (surface discussed in *Year Book 73*, pp. 317–322). The electron microprobe has been used to determine the compositions of the condensed phases. Liquids along the pyroxene-spinel surface contain only small amounts of Cr_2O_3 , increasing regularly from 0% at *E* and *P* to 1.4% at *H* and *I*. Liquid, pyroxene, and olivine compositions are projected onto the base by recalculating MgO , Fe_3O_4 , and SiO_2 to 100%. Pyroxene and olivine in equilibrium with these liquids contain even less Cr_2O_3 , a maximum of about 0.3%. Spinel compositions in equilibrium with (1)

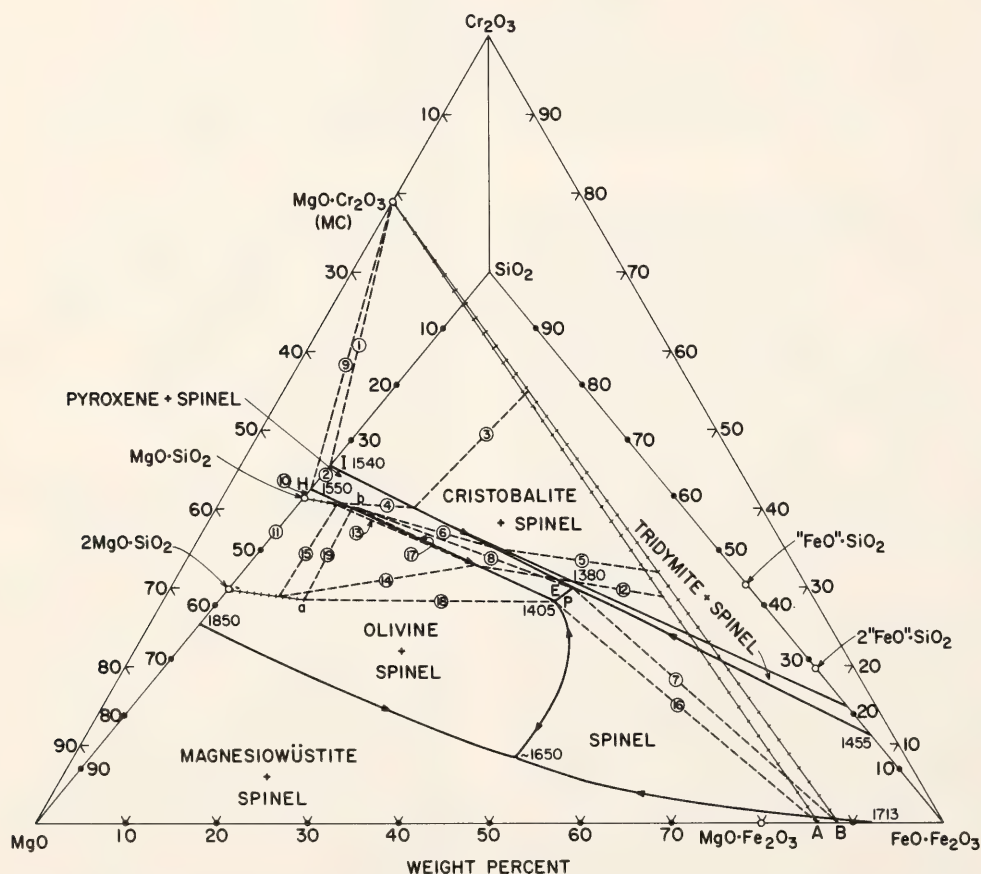


Fig. 70. Tetrahedron representing liquidus phase relations in the olivine-pyroxene-tridymite region of the MgO –iron oxide– Cr_2O_3 – SiO_2 system in air at a total pressure of 1 atm. Iron oxide is calculated and plotted as Fe_3O_4 for all phases. Solid lines are boundary curves on the spinel surface; dashed lines are representative tie lines joining the composition points of phases coexisting in equilibrium at a single temperature; and hatched lines represent composition joins for olivine, pyroxene, and spinel. *H* and *I* are ternary invariant points at approximately 1.4% Cr_2O_3 , occurring on the left face of the tetrahedron but projected to the base by subtracting Cr_2O_3 . *P* and *E* are isobaric invariant points in the system MgO –iron oxide– SiO_2 , projected onto the basal plane.

pyroxene, olivine, and liquid and (2) pyroxene, tridymite (or cristobalite), and liquid are shown by points on the hatched lines *MC-A* and *MC-B* extending across the front face of the tetrahedron. The spinel analyses invariably show approximately 0.4% SiO_2 . This component may be due to the presence of included silicates though none are visible in reflected light. In general, natural spinels contain $< 0.4\%$ SiO_2 . The spinel compositions are projected onto the front face by recalculating MgO , Fe_3O_4 , and Cr_2O_3 to 100%.

The liquidus boundary surfaces of the pyroxene volume have all been found to be essentially planar. The previously reported curvature of the olivine-pyroxene and pyroxene-tridymite surface (*Year Book 73*, Figs. 65–66) was found to be related to a few tenths percent of Na_2O in mixtures made from gels. Using mixtures made from pure oxides, no curvature can be detected. The effectiveness of a small amount of Na_2O in causing a large shift in the pyroxene-tridymite-spinel boundary curve to higher SiO_2 compositions is noteworthy.

The equilibrium relations of coexisting phases are shown in Fig. 70 by sets of representative tie lines (numbered, dashed lines). One tie line set (1-2 and 3-4) indicates the relations of spinel, liquid, and pyroxene with cristobalite; another (5-6 and 7-8), their relations with tridymite. The tie line sets 9-10-11, 12-13-14-15, and 16-17-18-19 indicate the compositional relation of coexisting spinel, liquid, pyroxene, and olivine.

Spinel compositions in equilibrium with olivine, pyroxene, and liquid lie along *MC-A*, whereas spinels in equilibrium with pyroxene, cristobalite or tridymite, and liquid have compositions along *MC-B*. Spinel compositions in equilibrium with only pyroxene and liquid have compositions lying within the zone *MC-A-B*. The compositions of points *A* and *B* were determined as 13.7 wt % MgO , 86.3 wt % Fe_3O_4 and 11.7 wt % MgO , 88.3 wt % Fe_3O_4 , respectively, in agreement

with the previous estimates of Muan and Osborn (1956) and of Speidel and Osborn (1967). Point *a* (9 ± 1 wt % Fe as Fe_3O_4) and point *b* (6.5 ± 1 wt % Fe as Fe_3O_4), respectively, represent olivine and pyroxene of maximum iron content in air. Their compositions are in agreement with the earlier study (Muan and Osborn, 1956).

The compositions and temperatures of the two invariant points on the basal plane were redetermined using the original mixtures of Muan and Osborn (1956) supplemented by several new mixtures made from oxides. The new locations, along with those of Muan and Osborn shown in parentheses, are as follows (wt %):

	T (°C)	MgO	Fe_3O_4	SiO_2
Peritectic:	1405 (1374)	22.3 (19)	36.7 (41)	41.0 (40)
Eutectic:	1380 (1367)	19.5 17	37.5 (39)	43.0 (44)

A preliminary diagram of the phase relations for the $\text{CO}_2:\text{CO}$ ratio of 40:1 is shown in Fig. 71. Relations on the base at a $\text{CO}_2:\text{H}_2$ ratio of 40:1 are from Muan and Osborn (1956). Compositions of spinels in equilibrium with pyroxene and liquid are shifted to lower MgO contents as compared with those in Fig. 70, lying along *MC-F* on the front face of the tetrahedron. The zone of spinel compositions, *MC-F*, comes to a point at both ends. The reason is that at the *MC* end a spinel of constant MgCr_2O_4 composition is presumed for the system $\text{MgO}-\text{Cr}_2\text{O}_3-\text{SiO}_2$. At the *F* end, the single magnesioferrite composition is that in equilibrium only with olivine, tridymite, and liquid *E*. As in Fig. 70, representative tie lines have been drawn indicating compositions of coexisting phases. For example, the tie line sets 1-2 and 3-4 represent the compositions of spinel, pyroxene, and liquid coexisting with cristobalite; set 5-6 represents their composition in equilibrium with tridymite. The tie line sets 7-8-9, 10-11-12, 13-14-15 relate the compositions of co-

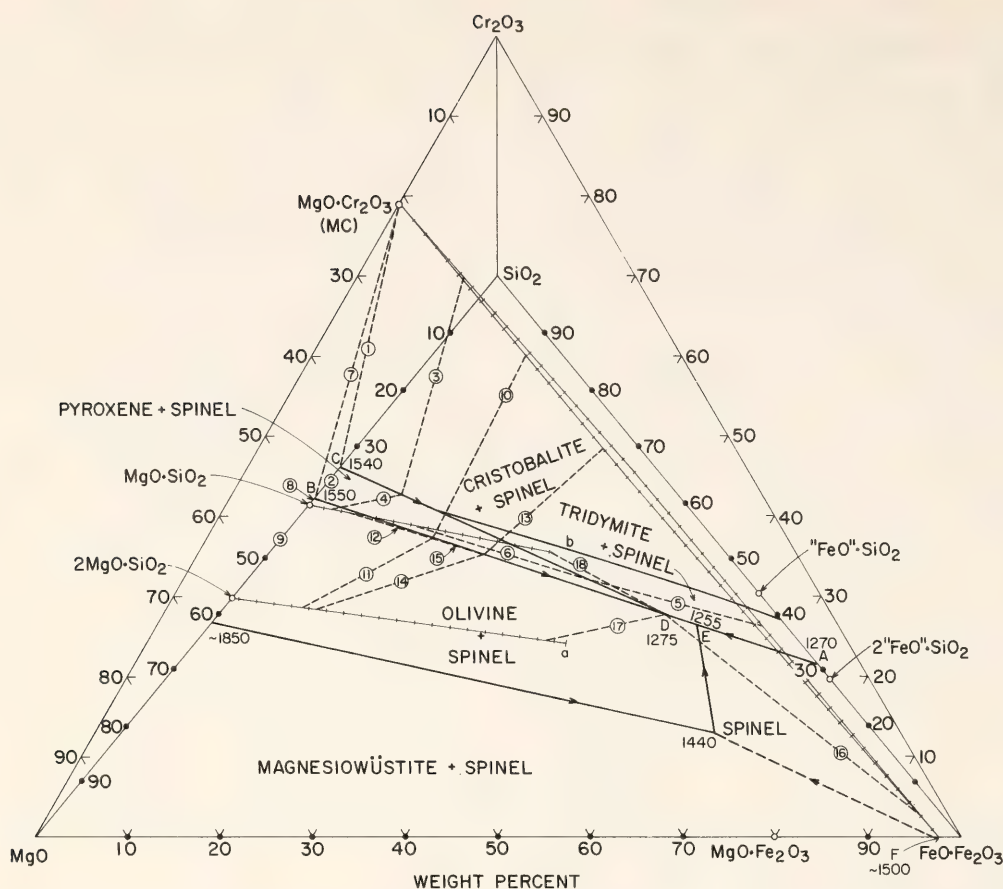


Fig. 71. Tetrahedron representing liquidus phase relations in the olivine-pyroxene-tridymite region of the MgO-iron oxide- Cr_2O_3 - SiO_2 system at 1 atm in equilibrium with a CO_2 :CO mixture in 40:1 proportions; iron oxide is calculated and plotted as Fe_3O_4 for all phases. Notation as in Fig. 70; B and C are equivalent to H and I of Fig. 70.

existing spinel, liquid, pyroxene, and olivine. The tie line set 16-17-18 indicates coexisting spinel, olivine, tridymite, liquid, and pyroxene. The olivine at point *a* contains approximately 40 ± 1 wt % Fe as Fe_3O_4 , a value in agreement with the study of Muan and Osborn (1956). The pyroxene at *b* is estimated to contain approximately 28 ± 1.0 wt % Fe as Fe_3O_4 , on the basis of the data of Muan and Osborn (1956). The indicated temperatures for points A and E are from Muan and Osborn (1956). On the basis of the new determination of the composition of D (11.2 wt % MgO, 48.6 wt % Fe_3O_4 , 0.10 wt % Cr_2O_3 , 40.7 wt % SiO_2), the composition of point E is estimated to be 10.2 wt % MgO, 52 wt % Fe_3O_4 , 37.8 wt % SiO_2 . Muan and Osborn (1956) estimated the composition of the same point to be 7 wt % MgO, 55 wt % Fe_3O_4 , 38 wt % SiO_2 .

Liquid E on the base is in equilibrium with spinel F (2.5 wt % MgO, 97.5 wt % Fe_3O_4), olivine *a*, and tridymite.

The relation between the projected compositions of the spinels in Figs. 70 and 71 and their compositions as calculated according to the spinel stoichiometric ratio, $A^{2+}:B^{3+} = 1:2$, is shown in Fig. 72. The points MF' , *a'*, and *b'* correspond to MF , B, and F of Figs. 70 and 71. These same points, if the ratio $A^{2+}:B^{3+}$ is 1:2, have the locations MF , *a*, and *b*. The lengths of the dashed lines are an indication of the difference in O_2 content between the points on MF -M and their projected location on MgO-M. The ratio $\text{Fe}^{2+}:\text{Fe}^{3+}$ of spinels along the join MC-*a* increases from 0.23 at *a* to almost 0.5 at MC. The same ratio for the spinels along MC-*b* increases from 0.43 at *b* to almost 0.5 near MC and thus more nearly approaches the ideal Fe^{2+} :

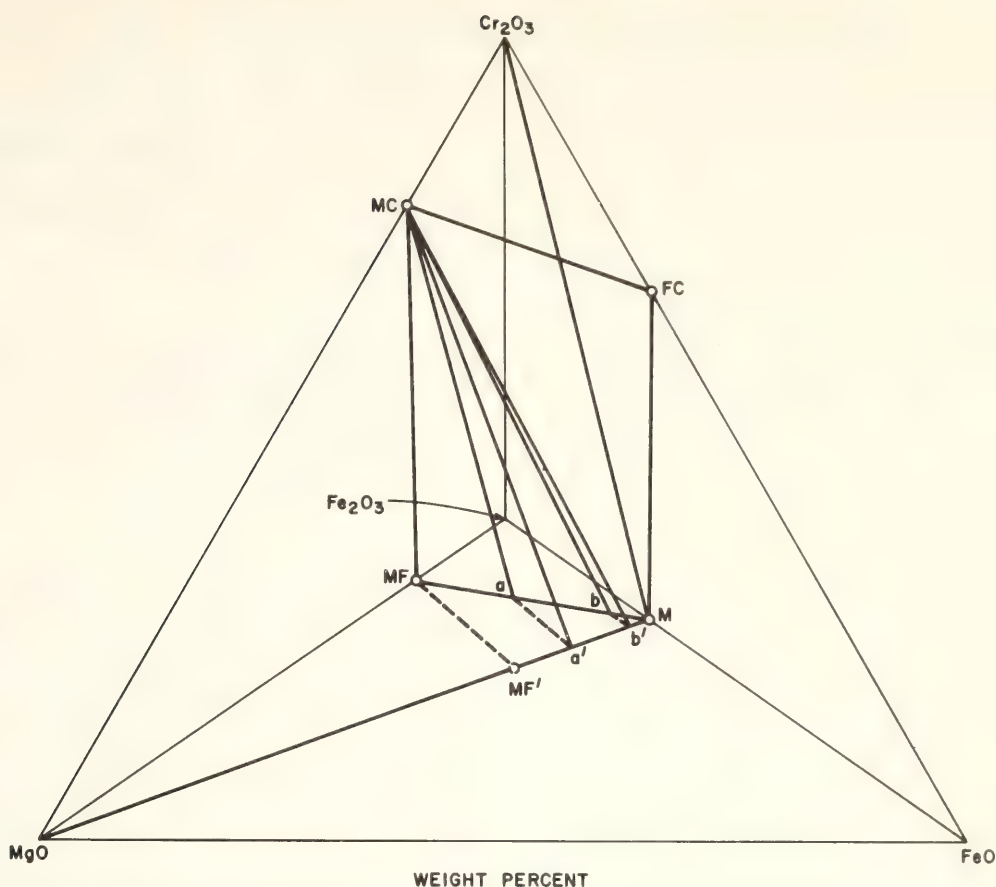


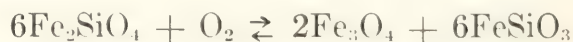
Fig. 72. Tetrahedron illustrating the nature of spinel composition projections used in Figs. 70 and 71. The lines $MC-a$ and $MC-b$ represent spinel compositions calculated assuming $A^{2+}:B^{3+}$ of 1:2 in air ($MC-a$) and at 40:1 of $CO_2:CO$ ($MC-b$). These lines are projected to the plane $MgO-M-Cr_2O_3$ by calculating Fe as Fe_3O_4 . Abbreviations: MC , $MgCr_2O_4$; FC , $FeCr_2O_4$; MF , $MgFe_2O_4$; M , Fe_3O_4 .

Fe^{3+} ratio (0.5) of the projection plane $MgO-Fe_3O_4-Cr_2O_3$ of Figs. 70 and 71.

The spinel compositions are also shown in Fig. 73, where atomic proportions are used rather than weight percentages as in Fig. 72. Figure 73 represents the Al_2O_3 -free join of the spinel compositional prism (Irvine, 1965) and may be used to depict the compositions of spinels in equilibrium with olivine and pyroxene at variable P_{O_2} 's. The variations in spinel composition in the basalts of Grenada, Lesser Antilles (Arculus, *Year Book 73*, pp. 322–327), Kilauea (Evans and Wright, 1972), and Snake River (Thompson, 1973) are also shown in Fig. 73. On theoretical grounds, Irvine (1965) has shown that the natural Al_2O_3 -bearing spinels are in equilibrium with olivine and orthopyroxene of a given Mg:Fe ratio at lower P_{O_2} 's than is ap-

parent when projected onto the Al_2O_3 -free join. Similarly, the presence of clinopyroxene rather than orthopyroxene in equilibrium with olivine and spinel in the Grenada lavas (Arculus, *Year Book 73*, pp. 322–327) implies equilibration at a lower P_{O_2} than is suggested in Fig. 73.

The experimental results may be used to calculate apparent equilibrium constants (K^* 's, assuming ideal solid solution) for the reactions involved in the system studied. For example, for the reaction



at $1300^\circ C$ and P_{O_2} of $10^{-6.5}$, the value of K^* is approximately 5.0×10^7 . In comparison, thermodynamic data suggest a value for K^* of 1.57×10^5 (Irvine, 1965). The higher value obtained

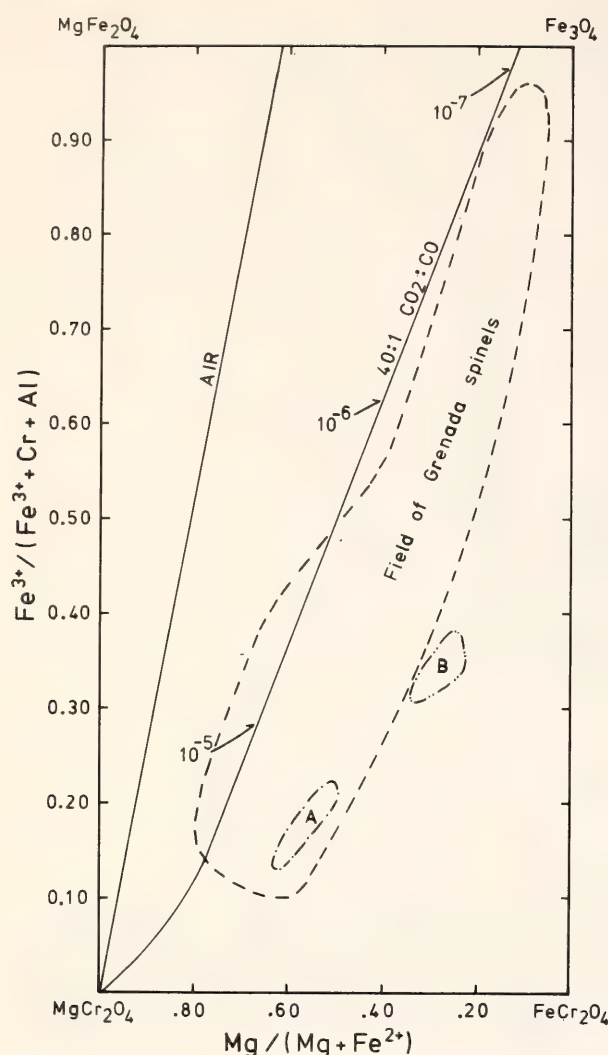


Fig. 73. Spinel compositions in equilibrium with olivine and orthopyroxene in air and at lower P_{O_2} 's. The numbers alongside the 40:1 $CO_2:CO$ curve correspond to the approximate P_{O_2} at which the spinel composition indicated is in equilibrium with olivine and orthopyroxene. The ordinate includes Al since natural spinel compositions are included in the projection. Fields A and B refer to the Kilauea and Snake River spinels, respectively.

experimentally suggests that either the spinel or silicate solid solutions or both are nonideal. The data obtained so far suggest the following:

1. Spinel solid solutions are continuous in the plane $MgCr_2O_4$ - $FeCr_2O_4$ - $MgFe_2O_4$ - Fe_3O_4 in equilibrium with olivine, orthopyroxene, and liquid or orthopyroxene, cristobalite (or tridymite), and liquid.

2. There is no evidence of a pyroxene-spinel reaction relationship at 1 atm (cf. Irvine, 1967).

3. The $Fe^{3+}:Fe^{2+}$ ratio of the spinel increases with declining temperature and the $Mg/(Mg + Fe^{2+})$ ratio decreases with decreasing P_{O_2} .

4. The compositional relations of natural spinels coexisting with olivine and pyroxene suggest equilibration at P_{O_2} 's lower than 10^{-5} to 10^{-7} .

MELTING BEHAVIOR OF TWO BASANITES IN THE RANGE 10–35 KBAR AND THE EFFECT OF TiO_2 ON THE OLIVINE-DIOPSIDE REACTIONS AT HIGH PRESSURES

R. J. Arculus

A useful model for the generation of basalt magmas by partial melting of garnet peridotite has been developed by O'Hara and Yoder (1967) and Kushiro and Yoder (*Year Book 73*, pp. 263–269) based on phase relations in the system CaO - MgO - Al_2O_3 - SiO_2 . Melts on the join diopside-pyroxene display appropriate olivine and orthopyroxene reaction relationships leading to eclogite fractionation at pressures at least up to 26 kbar.

Analogous liquidus boundary configurations have not so far been observed in natural compositions studied at similar pressures. O'Hara (1965) proposed that predominant olivine fractionation and approach to low-pressure equilibrium and cotectic olivine, pyroxene, and plagioclase crystallization would account for the absence of the appropriate reaction relationships in the basalts studied.

Natural samples selected for investigation at high pressures should therefore be those in which petrologic or geochemical evidence is indicative of the sample derivation directly from an upper mantle peridotite source. For example, lavas bearing peridotite nodules must have ascended from regions in the upper mantle at rates that exceed the rates of crystal setting in the magma. Basanites are comparatively rare alkalic lavas that commonly contain peridotite nodules and are possible examples of melts derived directly from an upper mantle source without modification by exten-

sive fractional crystallization. The experiments reported here constitute an attempt to determine whether isobaric fractional crystallization in natural basanite melts could involve olivine and orthopyroxene reaction relations leading to eclogite fractionation.

Two basanites crushed to $\leq 10\text{ }\mu\text{m}$ grain size were used as starting materials. One sample studied was a basanite from Victoria, Australia, donated by A. J. Irving. This basanite occurs together with spinel lherzolites, megacryst assemblages, and rare garnet-bearing peridotites (Irving, 1974). The other basanite studied was a sample analyzed for rare earth elements by Arculus and Shimizu (*Year Book 73*, pp. 553–560). Derivation of these compositions from depths at which garnet is stable in the upper mantle is suggested by Irving (1974) and Shimizu and Arculus (1975). Bulk analyses of the samples are given in Table 19.

Graphite capsules were used as sample containers in order to prevent iron loss from the samples. Sample and furnace parts were dried for 45 seconds with a gas torch immediately prior to an experimental run. Access to the charges by

water upon dehydration of the talc liners was prevented by using glass sleeves in place of boron nitride (Cohen, Ito, and Kennedy, 1967). Run times varied from 15 minutes to 6 hours in solid-media, high pressure apparatus.

Preliminary *P-T* diagrams of the melt region of the basanites in the range 10 to 35 kbar are presented in Fig. 74A and B. The most important feature is that olivine is the primary liquidus phase up to only 18–20 kbar and orthopyroxene is not a near-liquidus phase. In the model system $\text{CaO-MgO-Al}_2\text{O}_3\text{-SiO}_2$ (Kushiro and Yoder, *Year Book 73*, pp. 263–269), olivine is the liquidus phase to 26–27 kbar, and orthopyroxene is the liquidus phase up to at least 30 kbar. In the basanites, calcic augite is the liquidus phase from 18–20 kbar to the highest pressure studied (30–35 kbar). Thus under dry conditions, the only possibility of isobaric crystallization involving olivine, orthopyroxene, and garnet is the situation where the composition of the melt might be shifted into an olivine or orthopyroxene stability field as the result of clinopyroxene or garnet fractionation. In any case, it does not seem likely that the basanites studied can be

TABLE 19. Analyses of Basanites Studied at High Pressure

Oxide (wt %)	AJI2164	G531	Normative (Cationic) Compositions		
				AJI2164	G531
SiO ₂	44.19	44.78	Or	12.07	5.38
TiO ₂	2.75	1.02	Ab	13.79	8.32
Al ₂ O ₃	13.26	15.95	An	13.70	30.17
Cr ₂ O ₃	0.03	0.03	Ne	11.92	7.84
Fe ₂ O ₃	2.82	2.59	Cpx	19.08	26.80
FeO	8.79	6.80	Ol	20.53	18.58
MnO	0.18	0.18	Mt	2.98	2.71
MgO	10.30	10.71	Il	3.87	1.42
CaO	8.77	12.81	Ap	2.05	0.78
Na ₂ O	3.71	2.38			
K ₂ O	2.02	0.91			
P ₂ O ₅	0.97	0.37			
H ₂ O ⁺	0.86	0.64			
H ₂ O ⁻	0.26	0.15			
CO ₂	0.19	...			
Totals	99.10	99.32			

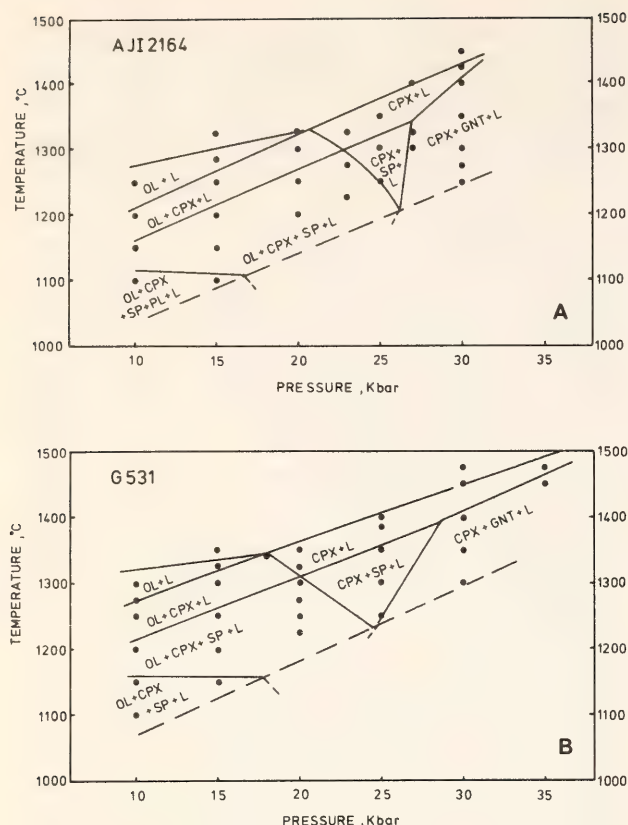


Fig. 74. (A) P - T diagram for basanite Aji2164 (Mt. Shadwell, Victoria, Australia). The dashed line represents the estimated solidus. (B) P - T diagram for basanitoid G531 (South East Mountain, Grenada, Lesser Antilles). Abbreviations: Ol, olivine; Cpx, clinopyroxene; Sp, spinel; Pl, plagioclase; GNT, garnet; L, liquid.

derived directly from a dry garnet peridotite source.

In the presence of water the olivine liquidus is shifted to higher pressure; also, Egger (Year Book 73, pp. 215-224) has shown that orthopyroxene is stable on the join forsterite-diopside in the presence of CO_2 at 30 kbar. In addition, Kushiro (1975) has demonstrated that in the presence of oxides of polyvalent cations (TiO_2 , P_2O_5), more polymerized silicates are stabilized relative to less polymerized ones. Both TiO_2 and P_2O_5 are concentrated in strongly undersaturated alkalic lavas, and it is possible that clinopyroxene is stabilized relative to olivine at high pressure in the presence of polyvalent cations. In order to test this possibility a composition on the join diopside-pyroxene with olivine on the liquidus to at least 26 kbar (Kushiro

and Yoder, Year Book 73, pp. 266-269) has been studied with the addition of 3 wt % TiO_2 (Di 35.6, Py 61.4, TiO_2 3.0). Sealed platinum capsules and solid-media, high-pressure apparatus were used. A preliminary P - T diagram is presented in Fig. 75. The results suggest that the stability of olivine is reduced 2-3 kbar relative to the TiO_2 -free join; however, the olivine reaction relationship described by Kushiro and Yoder (Year Book 73, pp. 263-269) persists. Preliminary results with 1 wt % P_2O_5 added to $\text{Di}_{36.7}\text{Py}_{63.3}$ (added as $\text{Ca}_3(\text{PO}_4)_2$) indicate at least as extensive a shift in phase boundaries and an apparent expansion of the phase volume of clinopyroxene. Thus the presence of small concentrations of the oxides of polyvalent cations may affect the phase relations elucidated for model systems such as $\text{CaO-MgO-Al}_2\text{O}_3\text{-SiO}_2$ (cf. Bultitude and Green, 1971). However, the effects can be analyzed only by independently varying the amounts of the polyvalent cations present in the systems studied.

There are at least three factors, therefore, that have to be considered in the interpretation of the melting behavior of natural systems at high pressures and

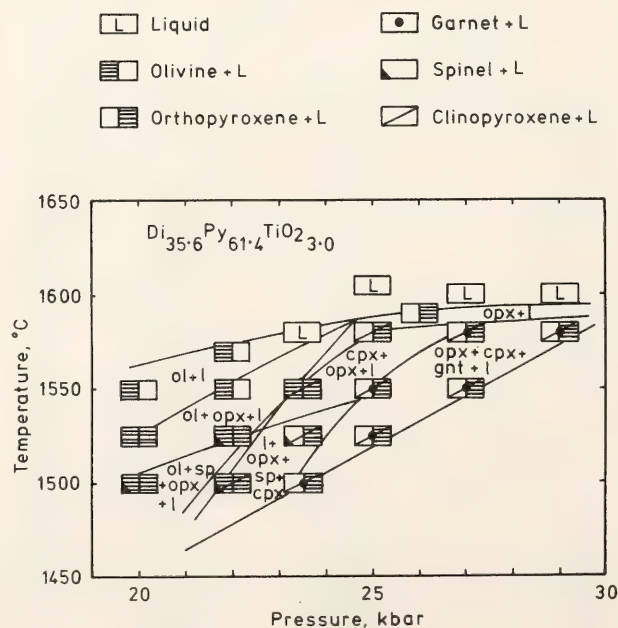


Fig. 75. P - T diagram for the composition Di 35.6, Py 61.4, TiO_2 3.0.

the possibility that these melts are derived directly from an upper mantle source. Two of these factors, olivine fractionation and the presence of polyvalent cations, will tend to eliminate olivine relative to pyroxene at high pressure and preclude the possibility of isobaric fractionation involving olivine and eclogite assemblages. In the Grenada sample, the absence of included peridotite nodules does not rule out the possibility that some olivine fractionation has taken place. Any olivine fractionation in the Victoria basanite, however, must have occurred prior to the inclusion of the peridotite nodules.

The presence of the oxides of polyvalent cations such as TiO_2 and P_2O_5 is the second factor that may tend to eliminate olivine relative to pyroxene under dry conditions at high pressure. It is probable that the presence of the volatiles CO_2 and H_2O is essential in the genesis of basanite lavas if the phase relations deduced for model systems are applicable to the genesis of these melts in the upper mantle. The stabilization of olivine relative to pyroxene in the presence of H_2O and orthopyroxene relative to olivine and diopside in the presence of CO_2 may be interpreted as indicating that the presence of these volatiles is essential for the models discussed by O'Hara and Yoder (1967) and Kushiro and Yoder (*Year Book* 73, pp. 263–269) to be applicable to natural systems.

HEAT OF MELTING OF SIMPLE SYSTEMS RELATED TO BASALTS AND ECLOGITES

H. S. Yoder, Jr.

The heat of melting of basalt or gabbro, eclogite, garnet peridotite, and related rocks is needed for calculations of the depth and time required for generation of the most common magma, basalt. Early measures of the heat of melting, ΔH_f , were made, for example, by Barus (1893), who obtained a value of 24 cal/g (1200°C) for a diabase, using the cooling-curve method. Vogt (1904, p. 55)

considered this value to be too low because the diabase did not crystallize completely on cooling. He preferred a value of 90–100 cal/g based on the heat of melting of minerals such as diopside, anorthite, akermanite, and fayalite. Bowen (1928, pp. 314–315) assumed the value 100 cal/g to be roughly that of basalt, presumably relying on the values for diopside and anorthite obtained from freezing-point depression calculations as well as measured values for the constituent minerals (e.g., White, 1909, p. 486). The value 100 cal/g has been used in many present-day calculations of the thermal factors involved in the generation of basaltic magma.

Although it is not yet possible to deal effectively with iron-bearing natural rocks in high-temperature calorimeters because of oxidation and crystallization problems, estimates of the heat of melting can be made using the data on the constituent end-member minerals. The newly determined heat of melting of two critical end-member minerals, pyrope and anorthite, along with published values and estimates for other pertinent end-member minerals are given in Table 20. The new calorimetric measurements were kindly made for the writer by O. J. Kleppa and T. V. Charlú by solution of the minerals and compositionally

TABLE 20. Enthalpy of Melting*

	ΔH_m (kcal/mol)	Formula Weight	ΔH_m (cal/g)
Forsterite	29.3† (est)	140.70	208.2
Fayalite	22.0 ₃	203.78	108.1
Clinoenstatite	14.7	100.38	146.4
Diopside	18.5‡	216.52	85.4
Pyrope§	33.2‡	403.08	82.4
Anorthite§	18.7	278.14	67.2
High albite	13.5 ₆	262.15	51.7
High sanidine	14.7	278.24	52.8

* From Robie and Waldbaum (1968) unless otherwise noted.

† Bradley (1962).

‡ ΔH_m at 700°C.

§ O. J. Kleppa and T. V. Charlú (unpublished data, 1975).

equivalent glasses in $2\text{PbO} \cdot \text{B}_2\text{O}_3$ melt at 700°C . The pyrope glass had been prepared by J. F. Schairer; and the pyrope crystals were made in six batches at 1400°C and 30 kbar in a solid-media, high-pressure apparatus, using furnace assemblies of $3/4$ inch diameter and runs of $1/2$ hour duration, by Bjørn Mysen from a glass previously made by G. Chinner. The glass and crystals of anorthite were made by E. F. Osborn. The anorthite was crystallized at 1000°C and had been used for redetermination of the melting point (Osborn, 1942). In addition, Dr. Osborn prepared new batches of both glass and crystals of the piercing-point composition of the system diopside-anorthite-forsterite (Osborn and Tait, 1952). Each sample was sieved to +325, -150 mesh for use in the calorimeter. Optical verification of the state of each sample was made, and powder x-ray diffraction patterns were made of the crystalline preparations. In order to be sure that the glass did not crystallize in the calorimeter before the sample achieved thermal equilibrium, Dr. Osborn held a small portion of each glass sample at 700°C for 2 hours. The glass samples showed no optical evidence of crystallization.

The calculated heat of melting for the eutectic composition, $\text{Di}_{58}\text{An}_{42}$ (wt %), of the system diopside-anorthite (Osborn and Tait, 1952, p. 419, Fig. 5), neglecting solid solution, phase changes, and heat of mixing, is 77.8 cal/g (or 18.57 kcal/mol for an average formula weight of 238.73 g). Using values for the heat content of the end-member phases from Robie and Waldbaum (1968, pp. 221 and 226), the heat requirements to melt compositions in the diopside-anorthite system can be displayed in a plot of $H_T - H_{298}$ versus composition (Fig. 76). Such a diagram can be used as a model for some aspects of the melting of basalt.

The data in Fig. 76 illustrate how small ΔH_f is relative to the total heat required to bring the assemblage to the

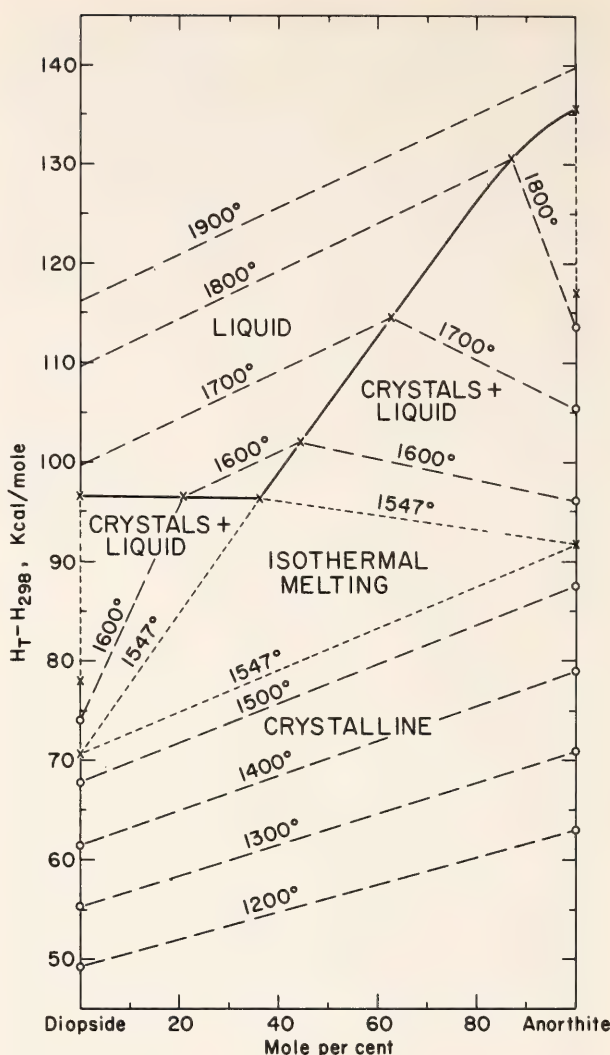


Fig. 76. Plot of $H_T - H_{298}$ vs. composition in the diopside-anorthite system, neglecting solid solutions, phase changes, heat of mixing, and pressure effects. Temperature in $^\circ\text{K}$. The value of ΔH_m for diopside measured at 973°K was used and not corrected to the melting temperature.

temperature of the beginning of melting. The figure also indicates how the heat requirements change as a function of composition in the isothermal region and through the crystal + liquid regions. Although basalts are eutectic-like at the liquidus because all major phases appear within a small temperature interval (Yoder and Tilley, 1962), these phases continue to crystallize together over a more extended range of temperature owing to solid solution. The temperature range is also a function of the degree of fractionation of crystals and liquid. It is instructive, therefore, to examine melting in a system involving a solid

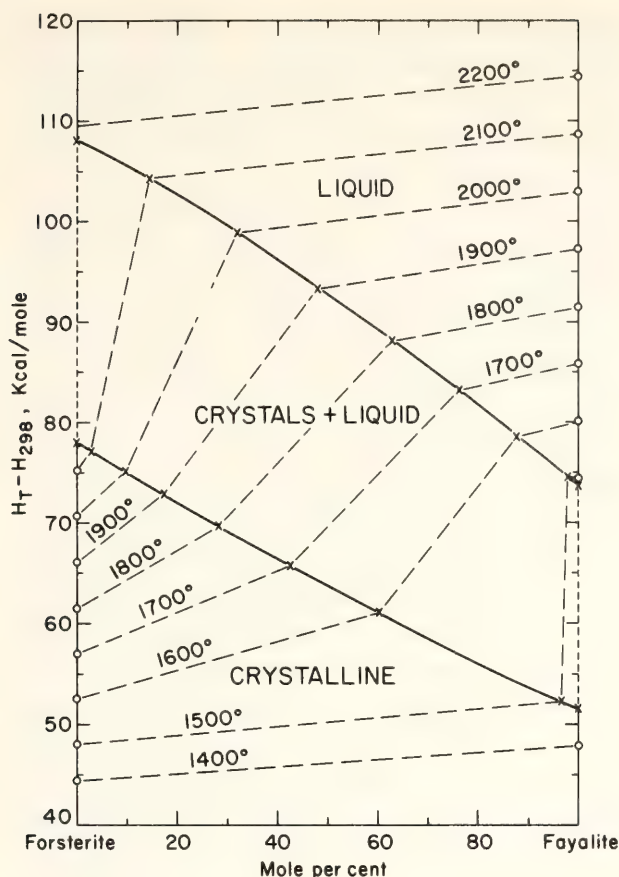


Fig. 77. Plot of $H_T - H_{298}$ vs. composition in the forsterite-fayalite system, neglecting heat of mixing, incongruent melting, and pressure effects. Temperature in $^{\circ}\text{K}$.

solution series such as forsterite-fayalite. Figure 77 was constructed for the most part from the thermodynamic data given by Robie and Waldbaum (1968) and the phase equilibrium data of Bowen and Schairer (1935).^{*} It is seen that, with melting, heat is consumed at a greatly increased rate but without a thermal arrest.

The model system for basalt can be improved by choosing the piercing-point composition at 1 atm, $\text{Di}_{49.0}\text{An}_{43.5}\text{Fo}_{7.5}$ (wt %), in the diopside-anorthite-forsterite system studied by Osborn and

^{*} It should be recalled that the forsterite-fayalite system has been determined experimentally up to only 1500°C in the presence of iron. The incongruent melting of fayalite to iron + liquid is rarely illustrated in the olivine diagrams, nor is mention made of the fact that the liquids do not lie on the join because they contain measurable amounts of Fe_2O_3 . Estimates of the heat of melting are not compensated for the effects of these factors.

Tait (1952). The heat of melting can be calculated from the end-member minerals, assuming no solid solution or heat of mixing. The contribution of the requisite portion of forsterite toward the heat of melting is estimated from the calculated value of Bradley (1962) because all techniques tried have failed to produce a glass of forsterite composition for calorimetric measurement. The calculation yielded a value of 85.6 cal/g for the piercing-point composition. To determine the order of magnitude of the heat of mixing, the heat of melting of the piercing-point composition was measured in the high-temperature calorimeter at 700°C by Kleppa and Charlu. They obtained a value for the heat of melting of 18.25 ± 0.14 kcal/mol based on an average molecular weight of 229.38, or 79.6 cal/g. If the estimate for the heat of melting of forsterite is acceptable and the effects of solid solution can be neglected, the heat of mixing, obtained by difference, is about -6.0 cal/g or about -1.4 kcal/mol.

For a model basalt with a more appropriate feldspar composition, the piercing point of the system diopside-forsterite-anorthite₅₀-albite₅₀ (Yoder and Tilley, 1962, p. 396) may be taken. The composition of this point is $\text{Di}_{28.5}\text{Fo}_{4.5}\text{An}_{33.5}\text{Ab}_{33.5}$ (wt %) and has a ΔH_f at 1 atm of 73.5 cal/g. The addition of iron to the system would tend to lower the heat of melting but by an unknown amount.

In a similar way the heat of melting for the eutectic composition of the system diopside-pyroxene (O'Hara and Yoder, 1967, p. 74, Fig. 3) can be calculated, neglecting solid solution, heat of mixing, and the presence of orthopyroxene. For this composition, $\text{Di}_{34}\text{Py}_{66}$ (wt %), the heat of melting calculated for 1 atm is 83.4 cal/g (or 26.0 kcal/mol using an average formula weight of 311.76 g). To obtain the heat of melting at 30 kbar it is necessary to use the relationship

$$\left. \frac{\partial \Delta H}{\partial P} \right|_T = \Delta V_f (1 - \Delta \alpha T),$$

where ΔV_f is the volume change on fusion and $\Delta\alpha$ is the difference between the coefficients of thermal expansion of the solid and liquid phases (see Maaløe, 1973, p. 111). Because of the small value of the coefficients of thermal expansion ($\sim 10^{-4}$ deg $^{-1}$), the last term may be neglected. For a ΔV_f of about 0.049 cc,* the change of heat of melting resulting from a pressure increase of 30 kbar is about 35.1 cal/g (or 11.9 kcal/mol), a substantial increase! The value for the heat of melting of $\text{Di}_{34}\text{Py}_{66}$ at 30 kbar is therefore about 118.5 cal/g (or 37.9 kcal/mol). The melting of the diopside-pyroxene system may be used as a model for some aspects of the melting of eclogite.

Garnet peridotite is the most likely parent of basaltic magma, and therefore an estimate of its heat of melting is useful. The piercing point of the system diopside-forsterite-pyroxene at 40 kbar (Davis and Schairer, *Year Book 64*, 1965, p. 124, Fig. 35) has the composition $\text{Di}_{47}\text{Fo}_6\text{Py}_{47}$ (wt %), and the estimated ΔH_f at 1 atm is 91.4 cal/g. Davis and Schairer (*Year Book 64*, 1965, p. 125) also estimated the composition of the invariant point for the diopside-enstatite-forsterite-pyroxene system to be $\text{Di}_{47}\text{En}_3\text{Fo}_3\text{Py}_{47}$ (wt %) at 40 kbar. The ΔH_f at 1 atm for that reaction point, estimated from the end-member phases, is 89.5 cal/g. The composition of the invariant point is suitable for the formation of a basaltic liquid: Its norm is $\text{Di}_{22}\text{Fo}_{20}\text{An}_{32}\text{En}_{26}$ (wt %). The ΔH_f values, when corrected for pressure, are $\sim 25\%$ higher than the 100 cal/g value

* Based on the following densities measured at 1 atm and not corrected for pressure or temperature:

Pyroxene:

$\rho_{\text{glass}} = 3.031$ g cm $^{-3}$ (B. Mysen, unpublished data, 1975)

$\rho_{\text{crystal}} = 3.582$ g cm $^{-3}$ (Skinner, 1956, p. 428)

Diopside:

$\rho_{\text{glass}} = 2.846$ g cm $^{-3}$ (Larsen, 1909, p. 271)

$\rho_{\text{crystal}} = 3.275$ g cm $^{-3}$ (Allen and White, 1909, p. 14)

used by Bowen for basalts. On the other hand, the pressure effect may be counterbalanced by the presence of water, which would be expected to reduce the ΔH_f greatly.

If the entire radioactive heat production ($\sim 10^{-14}$ cal/cm 3 sec; Clark and Ringwood, 1964) within an undepleted garnet peridotite is used to melt the rock at 130 km (≈ 40 kbar), assuming the rock is already at the temperature of the beginning of melting, then the time required for melting can be calculated. A 5% melt, requiring about 4.5 cal/g, would be achieved in roughly 45 m.y. The resulting perturbation in surface heat flow would be negligible if a layer of only a few kilometers is affected. It would appear, on the basis of this length of time for magma generation, that the periodicity of volcanism is dependent on factors affecting a shallow subsidiary magma chamber rather than those operating at the site of magma generation.

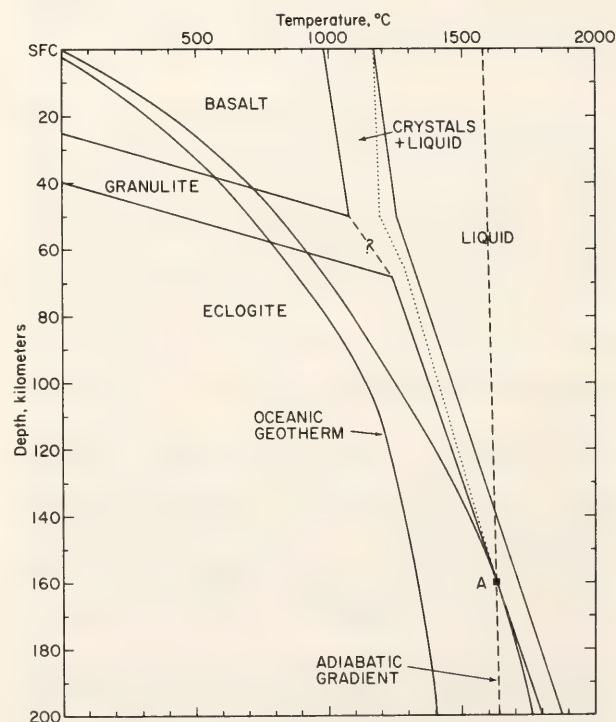


Fig. 78. Path of eclogite undergoing melting as a result of adiabatic rise. Phase-equilibrium data from Yoder and Tilley (1962, p. 498, Fig. 43). The average adiabat is 0.3°C/km; the slope of the eclogite liquidus is 3.8°C/km; the slope of the basalt liquidus is 1.9°C/km; the heat capacity is taken as 0.2 cal/g deg.

In the event that the heat of melting is obtained by adiabatic rise (e.g., by convection) of eclogite, it would be necessary to initiate the ascent at a depth at least as great as 160 km to achieve complete melting by the time the magma arrives at the surface. Figure 78 displays the path of such a magma through the crystal + liquid region. The simple model is not wholly realistic because it does not consider heat losses, crystal settling, or other factors affecting the rise of magma. It is assumed that essentially no heat of reaction is required as the magma passes from its association with eclogitic minerals to an equilibrium relation with basaltic minerals. For example, if a clinopyroxene is on the liquidus of the eclogite, it could be converted into clinopyroxene of a different composition suitable for basalt with only a small endothermic heat effect.

It is interesting to note that the heat of reaction for the conversion of eclogite to basalt is endothermic and has a value of about 10.7 cal/g based on a $dT/dP = 145^{\circ}\text{C}/\text{kbar}$ (Yoder and Tilley, 1962), $\Delta V = 0.051 \text{ cm}^3/\text{g}$ ($\rho_{\text{basalt}} = 2.85$; $\rho_{\text{eclogite}} = 3.33$), $T = 1275^{\circ}\text{C}$.

ULTRAMAFIC ROCKS AND MINERALS

HOMOGENEITY OF MINERALS IN MANTLE ROCKS FROM LESOTHO

F. R. Boyd and L. W. Finger

The use of mineral compositions in ultramafic xenoliths erupted in kimberlites to provide estimates of ambient conditions of temperature and pressure in the upper mantle should be considered only if it can be shown that the minerals comprising these rocks are reasonably homogeneous. The degree of homogeneity need not be perfect, but it must be sufficient to ensure that meaningful estimates of the temperature and pressure of equilibration can be made. Homogeneity is in no sense proof of equilibration under ambient conditions at depth, but it is a fundamental requirement.

Electron microprobe studies thus far carried out on nodules from kimberlites have been primarily aimed at characterizing average mineral compositions rather than revealing significant inhomogeneities. Because some inhomogeneities have been noted in nodules from kimberlites (e.g., Boyd, *Year Book* 73, Table 19) and because of the large inhomogeneities discovered in nodules from basalts (Wilshire and Jackson, 1975), it is clearly desirable to examine a selection of garnet peridotite nodules from kimberlites with the specific aim of discovering and evaluating such inhomogeneities that may exist in mineral composition.

Four rocks were chosen for intensive probe study from among the group of garnet lherzolites described by Nixon and Boyd (1973). These were selected to reflect a wide range in texture and in equilibration temperature (estimated from the diopside solvus). Sample PHN 1569 is a typical granular garnet lherzolite and has a relatively low equilibration* temperature (965°C). Sample PHN 1591 shows minimal effects of shearing; its texture is tabular, verging on porphyroclastic, and it has an equilibration temperature of 1260°C . Sample FRB 1 is more deformed and has a well-developed porphyroclastic texture and an equilibration temperature of 1180°C . Sample PHN 1611 is intensely sheared and foliated; it has a fluidal mosaic texture and a relatively high equilibration temperature of 1385°C .

Electron probe analyses were carried out on standard rectangular thin sections, measuring $2.7 \times 4.6 \text{ cm}$. These dimensions are small in relation to the size of some nodules from kimberlites, but they are comparable with the size of the probe mounts of ultramafic nodules from basalts in which Wilshire and Jackson (1975) found major inhomogeneities. Previous experience had sug-

* See footnote in paper by Boyd (this Report).

gested that larger inhomogeneities would be found between grains than within grains, so that only one analysis was made per grain. A total of 15 grains of each mineral in each section was analyzed except where fewer than 15 grains of a mineral could be found in a section; in such sections all the grains of the mineral that could be located were analyzed. Wherever possible, analyses were spaced on grids covering the whole area of each thin section.

Results presented in Tables 21–24 show averages obtained for a total of 220 grains. These results are in satisfactory agreement with mineral compositions previously published for these rocks (Nixon and Boyd, 1973, for PHN samples 1569, 1591, and 1611; Boyd and Nixon, 1975, for FRB 1), except for a few cases in which significant inhomogeneities have caused discrepancies. Values for the standard deviations (σ_o) observed for these analyses show

TABLE 21. Composition and Homogeneity of Minerals in Garnet Lherzolite Nodule PHN 1569, Granular Texture, Thaba Putsoa, Lesotho

	Garnet (10 grains)				Olivine (15 grains)			
	Wt %	σ_o Rel. %	σ_o/σ_e	No. Cations O = 12,000	Wt %	σ_o Rel. %	σ_o/σ_e	No. Cations O = 4000
SiO ₂	42.3	0.9	1.2	3008	41.0	0.5	0.7	989
TiO ₂	<0.03	0	<0.03	0
Al ₂ O ₃	19.9	2.7	3.5	1669	0.03	1
Cr ₂ O ₃	5.45	14	7.3	304	0.03	1
FeO*	6.60	0.8	0.7	392	7.08	4.6	4.3	143
MnO	0.44	25	0.10	2
MgO	20.2	1.9	2.4	2138	51.9	1.0	1.3	1866
CaO	6.09	5.1	6.2	463	<0.03	0
Na ₂ O	0.03	4	n.d.†
NiO	n.d.	0.48	9
Totals	101.0			8003	100.6			3011

	Diopside (13 grains)				Enstatite (15 grains)			
	Wt %	σ_o Rel. %	σ_o/σ_e	No. Cations O = 6000	Wt %	σ_o Rel. %	σ_o/σ_e	No. Cations O = 6000
SiO ₂	54.8	0.9	1.1	1972	57.3	0.7	0.8	1963
TiO ₂	<0.03	0	<0.03	0
Al ₂ O ₃	2.12	17(3.3)‡	15(3.1)‡	89	0.95	4.2	2.6	38
Cr ₂ O ₃	1.60	8.8	3.5	45	0.38	10
FeO*	1.57	12(1.9)‡	6.5(1.3)‡	46	4.21	1.2	0.9	121
MnO	0.08	2	0.11	3
MgO	17.2	1.6	2.0	922	36.5	0.6	0.8	1863
CaO	21.5	3.5(1.9)‡	4.3(2.4)‡	828	0.34	5.9	4.2	12
Na ₂ O	1.38	5.1	2.0	96	0.04	2
Totals	100.3			4000	99.8			4012
Ca/(Ca + Mg)				0.473				0.006
σ_o				0.011(0.003)‡				0.0004

* Total Fe as FeO.
† Not determined.
‡ Values in parentheses obtained with one aberrant analysis deleted.
 σ_o is the observed value of the standard deviation. σ_e is the standard deviation expected from the counting statistics.

that the largest inhomogeneities are present in PHN 1569 (Table 21) and PHN 1611 (Table 24), which have, respectively, the lowest and the highest equilibration temperatures. Values of σ_o for PHN 1591 (Table 22) and FRB 1 (Table 23), which have intermediate equilibration temperatures and intermediate textural relations, show that these two rocks are remarkably homogeneous.

The principal inhomogeneity found is

for Cr_2O_3 in the garnets and diopsides, where the standard deviation for Cr_2O_3 ranges up to 25 relative % (diopside, Table 24). The other constituents of these minerals are considerably more homogeneous. A second kind of inhomogeneity occurs in PHN 1569, in which a single diopside crystal of aberrant composition was found in a total population of 13 grains. The aberrant crystal is appreciably richer in Fe, Na, Al, and Ti than the other 12 grains. Presumably its

TABLE 22. Composition and Homogeneity of Minerals in Garnet Lherzolite Nodule PHN 1591, Texture Transitional between Tabular and Porphyroclastic, Thaba Putsoa, Lesotho

	Garnet (13 grains)				Olivine (15 grains)			
	Wt %	σ_o Rel. %	σ_o/σ_e	No. Cations O = 12,000	Wt %	σ_o Rel. %	σ_o/σ_e	No. Cations O = 4000
SiO_2	41.6	0.8	0.9	3014	40.6	0.7	0.9	990
TiO_2	0.04	0	<0.03	0
Al_2O_3	17.9	1.3	1.6	1530	0.04	0
Cr_2O_3	6.71	2.7	1.6	382	0.07	0
FeO^*	6.06	1.3	1.2	365	7.91	1.1	1.1	161
MnO	0.25	15	0.12	2
MgO	21.1	0.9	1.1	2276	50.5	0.9	1.1	1838
CaO	5.64	3.6	4.3	438	0.09	2
Na_2O	<0.03	n.d.†
NiO	n.d.	0.36	6
Totals	99.3			8020	99.7			2999

	Diopside (5 grains)				Enstatite (15 grains)			
	Wt %	σ_o Rel. %	σ_o/σ_e	No. Cations O = 6000	Wt %	σ_o Rel. %	σ_o/σ_e	No. Cations O = 6000
SiO_2	54.9	0.3	0.4	1978	57.0	1.0	1.2	1966
TiO_2	<0.03	0	<0.03	0
Al_2O_3	1.32	1.7	1.3	56	1.00	1.4	1.0	41
Cr_2O_3	0.95	3.1	3.0	26	0.42	11
FeO^*	3.04	0.7	0.5	91	4.72	1.4	1.2	136
MnO	0.13	3	0.15	4
MgO	20.8	0.4	0.5	1115	34.8	0.7	0.8	1790
CaO	17.5	1.3	1.6	674	1.40	2.7	2.9	52
Na_2O	0.82	0.6	0.2	57	0.13	9
NiO	n.d.	0.10	3
Totals	99.5			4000	99.7			4012
$\text{Ca}/(\text{Ca} + \text{Mg})$				0.377				0.028
σ_o				0.003				0.0006

* Total Fe as FeO .

† Not determined.

σ_o is the observed value of the standard deviation. σ_e is the standard deviation expected from the counting statistics.

composition has been affected by late-stage alteration. Including the analysis for the aberrant crystal with the data for the other grains has little effect on the mean composition but has a large effect on values of σ_o for these elements (Table 21).

Lherzolite nodule FRB 1 has numerous coarse porphyroclasts of olivine in a mesostasis of fine-grained recrystallized olivine. A difference in composition between the two generations of olivine was

specifically sought but not found. Both generations are included in the average analysis in Table 23.

Although the standard deviations in most of the analyses in Tables 21–24 are small, it is of interest to calculate a parameter indicating the degree of homogeneity. The size of the standard deviation obtained for an analysis is influenced by the counting statistics as well as by the degree of inhomogeneity. To evaluate the significance of a par-

TABLE 23. Composition and Homogeneity of Minerals in Garnet Lherzolite Nodule FRB 1, Porphyroclastic Texture, Monastery Mine, South Africa

Garnet (15 grains)					Olivine (15 grains)				
Wt %	σ_o		No. Cations O = 12,000		Wt %	σ_o		No. Cations O = 4000	
	Rel. %	σ_o/σ_e				Rel. %	σ_o/σ_e		
SiO ₂	41.8	0.7	0.8	2987	40.0	0.7	0.8	982	
TiO ₂	0.42	4.8	3.4	21	<0.03	0	
Al ₂ O ₃	20.6	0.7	0.9	1738	<0.03	0	
Cr ₂ O ₃	3.05	3.5	1.8	172	0.04	0	
FeO*	6.89	0.7	0.6	411	8.64	0.6	0.6	177	
MnO	0.32	19	0.12	2	
MgO	21.6	0.8	1.0	2295	50.3	1.0	1.3	1843	
CaO	4.91	1.2	1.5	375	0.07	1	
Na ₂ O	0.07	8	n.d.†	
NiO	n.d.	0.35	6	
Totals	99.7			8026	99.5			3011	

Diopside (15 grains)					Enstatite (15 grains)				
Wt %	σ_o		No. Cations O = 6000		Wt %	σ_o		No. Cations O = 6000	
	Rel. %	σ_o/σ_e				Rel. %	σ_o/σ_e		
SiO ₂	55.3	0.5	0.6	1977	57.1	0.6	0.7	1966	
TiO ₂	0.15	3	0.08	2	
Al ₂ O ₃	2.08	1.1	0.7	87	0.93	0.8	0.6	37	
Cr ₂ O ₃	0.89	2.0	0.7	25	0.24	6	
FeO*	3.14	0.8	0.6	93	5.20	1.0	0.8	149	
MnO	0.12	3	0.13	3	
MgO	19.1	0.6	0.8	1018	34.9	0.9	1.2	1793	
CaO	18.2	0.8	1.0	695	1.06	3.6	3.4	38	
Na ₂ O	1.48	2.1	0.9	102	0.21	14	
NiO	n.d.	0.09	2	
Totals	100.5			4003	99.9			4010	
Ca/(Ca + Mg)				0.406				0.021	
σ_o				0.002				0.0009	

* Total Fe as FeO.
† Not determined.

σ_o is the observed value of the standard deviation. σ_e is the standard deviation expected from the counting statistics.

ticular inhomogeneity it is first necessary to predict the standard deviation to be expected from the counting statistics for that particular element analysis.

Given a dependence of the sort where $y = f(x_1, x_2 \dots x_n)$, the general form of the error propagation equation, if covariances are assumed to be zero, is:

$$\sigma_y^2 \cong \sum_{i=1}^n \left(\frac{\partial f}{\partial x_i} \right)^2 \sigma_{x_i}^2 \quad (1)$$

In the present problem it is desired to estimate σ for the concentration of an element in an unknown phase. If matrix effects and the contributions to σ of variations in background are neglected,

$$c \cong \frac{nTC}{Nt}, \quad (2)$$

where c and C are, respectively, the concentrations of the element in unknown and standard; n and N are the numbers

TABLE 24. Composition and Homogeneity of Minerals in Garnet Lherzolite Nodule PHN 1611, Fluidal Mosaic Texture, Thaba Putsoa, Lesotho

Garnet (15 grains)					Olivine (15 grains)				
	Wt %	σ_o Rel. %	σ_o/σ_e	No. Cations O = 12,000		Wt %	σ_o Rel. %	σ_o/σ_e	No. Cations O = 4000
SiO ₂	42.6	0.5	0.6	3029		39.8	0.9	1.1	986
TiO ₂	0.85	12	10	43		0.03	0
Al ₂ O ₃	20.3	1.6	2.3	1703		0.07	1
Cr ₂ O ₃	2.07	21	9	115		0.03	0
FeO*	8.50	3.8	3.7	505		11.7	4.7	4.7	243
MnO	0.27	14		0.14	2
MgO	21.2	1.1	1.3	2248		47.9	1.6	2.0	1769
CaO	4.51	2.3	2.7	342		0.14	2
Na ₂ O	0.07	8		n.d.†
NiO	n.d.		0.34	6
Totals	100.4			8007		100.2			3009

Diopside (15 grains)					Enstatite (14 grains)				
	Wt %	σ_o Rel. %	σ_o/σ_e	No. Cations O = 6000		Wt %	σ_o Rel. %	σ_o/σ_e	No. Cations O = 6000
SiO ₂	54.8	0.5	0.7	1974		55.9	0.9	1.2	1950
TiO ₂	0.34	2.1	0.6	8		0.22	5
Al ₂ O ₃	2.60	0.9	0.9	110		1.36	1.5	0.8	55
Cr ₂ O ₃	0.45	25	7.1	12		0.20	5
FeO*	5.22	4.8	4.1	156		6.67	5.1	4.5	194
MnO	0.14	4		0.13	3
MgO	21.0	1.0	1.2	1125		33.2	0.9	1.2	1726
CaO	13.3	2.3	2.8	513		1.58	1.9	2.0	58
Na ₂ O	1.47	2.9	1.2	102		0.31	20
NiO									
Totals	99.3			4004		99.6			4016
Ca/(Ca + Mg)				0.313					0.033
σ_o				0.005					0.0009

* Total Fe as FeO.

† Not determined.

σ_o is the observed value of the standard deviation. σ_e is the standard deviation expected from the counting statistics.

of counts obtained; and t and T are the counting times.

Equation 1 may be written for this problem as

$$\sigma_o^2 = \left(\frac{\partial c}{\partial n} \right)^2 \sigma_n^2 + \left(\frac{\partial c}{\partial N} \right)^2 \sigma_N^2. \quad (3)$$

Differentiating Equation 2 and substituting in Equation 3 gives

$$\sigma_c^2 = \left(\frac{TC}{Nt} \right)^2 \sigma_n^2 + \left(-\frac{nTC}{N^2t} \right)^2 \sigma_N^2. \quad (4)$$

From counting statistics, $\sigma_n^2 = n$. Substituting and simplifying, where the counting rates on the standard (R) and unknown (r) are related to the counting times by $r = n/t$ and $R = N/T$,

$$\sigma_c = \frac{C}{R} \left[\frac{Rc}{Ct} + \frac{Rc^2}{TC^2} \right]^{1/2} \quad (5)$$

Values of the standard deviations to be expected from the counting statistics (σ_e) have been calculated for the analyses in Tables 21–24 and are shown in the form of the ratio σ_o/σ_e . Neglecting the contribution of background effects in calculating σ_e results in its being too low in analyses where the counting rate on peak approaches the background. In such cases the sigma ratio is overestimated. Nevertheless a value for this ratio of the order of 1 or less definitely suggests homogeneity. Thus, SiO_2 appears homogeneous in all the analyses given, and MgO is homogeneous in most of them (Tables 21–24).

A value of the sigma ratio in excess of 2–3 for a major element is highly suggestive of the presence of an inhomogeneity, but for a minor element where background effects may become significant the sigma ratio must be in excess of about 4–5 before the presence of an inhomogeneity is established. No attempt was made to calculate σ_e for analyses in which the absolute oxide concentrations are less than 0.3–0.5 wt % (de-

pending on the element) because in such analyses the contribution of background effects becomes very large.

Inspection of the values given in Tables 21–24 for the sigma ratio reveals a number of minor inhomogeneities in addition to those previously identified. In particular, Fe appears to be definitely inhomogeneous in all the minerals in PHN 1611 (Table 24); Ti is inhomogeneous in the garnet in this rock, but appears homogeneous in the diopside; Ca is inhomogeneous in the garnet in PHN 1569 and probably also in PHN 1591. Only one of the four specimens studied in detail (FRB 1, Table 23) appears to be free of significant inhomogeneities in any of its constituent minerals.

The analytical data that are of primary concern in estimation of temperatures and pressures of equilibration are Ca and Mg in diopside and Al in enstatite. If corrections such as those devised by Wood and Banno (1974) are made, the analytical data for Fe, Cr, Na, etc., may also be used. Uncertainties in the latter elements nevertheless will normally have a negligible effect on the uncertainties in estimated pressure and temperature.

The data in Tables 21–24 show that σ_o for $\text{Ca}/(\text{Ca} + \text{Mg})$ in diopside is equal to or less than 2 relative % for all four rocks. Values of σ_o for Al_2O_3 in enstatite are less than 2 relative % in three rocks, but σ_o is about 4 relative % in PHN 1569. In applying the diopside solvus, uncertainty in the estimated equilibration temperature is obviously greater for high values of $\text{Ca}/(\text{Ca} + \text{Mg})$ where the solvus steepens. This uncertainty in temperature makes a larger contribution to the uncertainty in estimated pressure or depth than does the uncertainty in Al_2O_3 in the enstatite.

Estimates of temperatures and depths of equilibration for the four rocks studied, based on the analytical data in Tables 21–24, are shown in Fig. 79. Error bars show the uncertainties that

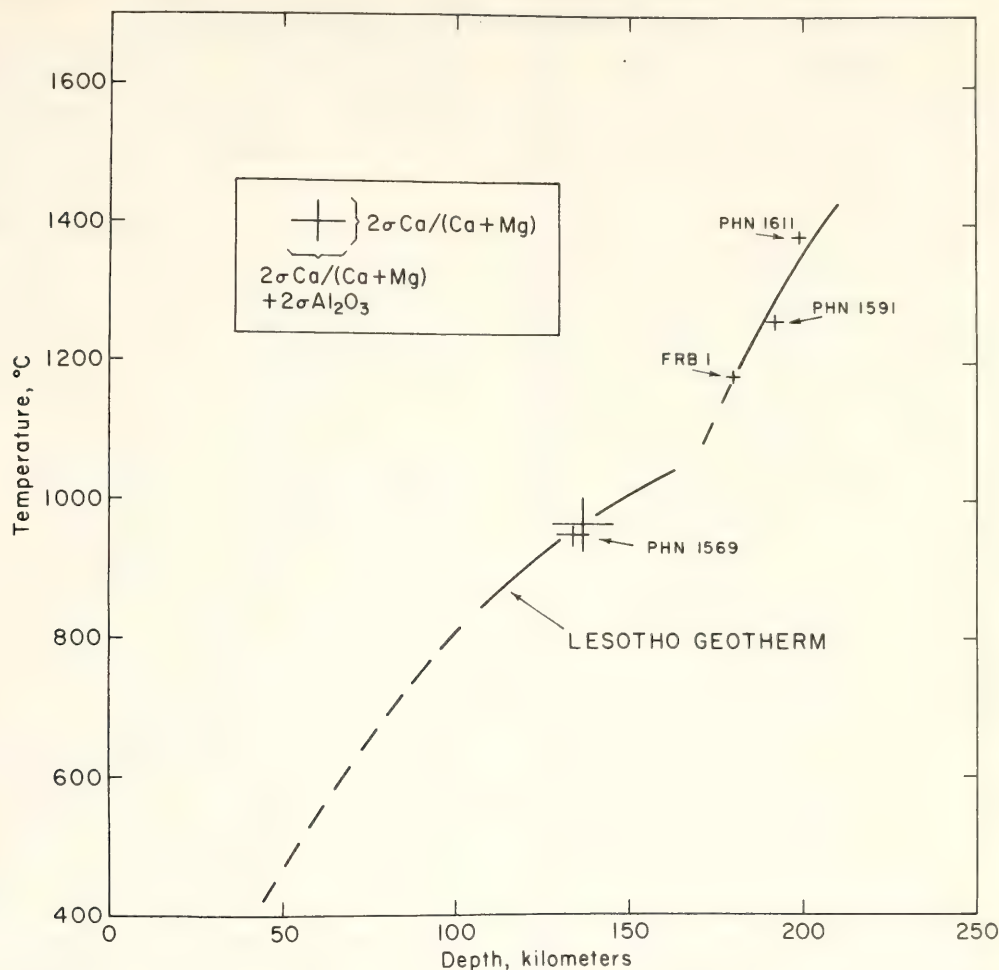


Fig. 79. Estimated temperatures and depths of equilibration for four Lesotho garnet lherzolites, calculated from the analytical data in Tables 21–24. Error bars show the uncertainties that derive from the analytical data. The uncertainty in temperature is obtained directly from the uncertainty in $\text{Ca}/(\text{Ca} + \text{Mg})$. The uncertainty in depth comes partly from analytical uncertainty for Al_2O_3 in the enstatite and partly from the uncertainty in the temperature estimate; these effects are summed. The Lesotho geotherm, which is given for comparison, is the “raw Al_2O_3 ” plot taken from Boyd (1973, Fig. 7A). Two points are shown for PHN 1569: the point with the larger error bars is calculated for all 13 grains whose analyses are averaged in Table 21; the point with the smaller error bars is calculated with one analysis for a grain of aberrant composition deleted from the average.

arise from the electron probe analyses and from such inhomogeneities as are present. Inclusion of the analysis for the aberrant diopside crystal in PHN 1569 causes a substantial increase in the error bars for this point but does not appreciably shift the position of the point. Thus the differences in equilibration temperature and depth calculated for these rocks are very much larger than the uncertainties that derive from the analytical data. It is concluded, therefore, that these differences in equilibration conditions are clearly significant.

STRESS-HEATING AND COMPOSITIONAL VARIATIONS IN ENSTATITES FROM SHEARED LHERZOLITES

F. R. Boyd

Many garnet lherzolite nodules from kimberlites are intensely deformed, and these nodules generally have higher equilibration temperatures (estimated from the diopside solvus) than those with coarse granular or tabular textures. Boyd and Nixon (*Year Book 72*) suggested that the sheared lherzolites might have been deformed and stress-heated in

the Low Velocity Zone (LVZ). Mercier and Carter (1975) have considered the conditions of viscosity and strain rate that would be appropriate for creep in the LVZ, and they have asserted that stress-heating under such conditions would be negligible.

Goetze (1975) has concluded that the dislocation densities for olivine porphyroclasts in sheared lherzolite nodules from Lesotho indicate that they were deformed under differential stresses of at least 2–3 kbar and that the deformation took place in “a matter of minutes or days.” Conceivably such a stress pulse could have been associated with kimberlite eruption, and under such rapid deformation, stress-heating is a possibility (Goetze, 1975). It seems unlikely that the coarse-grained porphyroclasts in these rocks could have achieved a state of chemical equilibration in such a short period of time. However, the possibility that the deformation textures may have been imposed on a preexisting mineralogy (as revealed by the chemistry of the porphyroclasts) warrants careful consideration.

Some insights into these problems might be gained by electron microprobe study of grains in the fine-grained, recrystallized groundmass of the sheared rocks. Olivine, which comprises most of the groundmass in a typical sheared lherzolite, is not very useful in this regard because it does not exhibit solid solutions involving major elements that are sensitive to temperature and pressure. Enstatite is present in the groundmass of some sheared lherzolites, however, and its solid solutions with diopside and garnet are temperature and pressure sensitive.

Mercier and Carter (1975) reported compositional differences between enstatite in the groundmass and enstatite porphyroclasts for a number of sheared lherzolites from Hawaii and Newfoundland and for a single specimen (PHN 1611) from the Thaba Putsoa kimberlite in Lesotho. They attributed these differ-

ences to reequilibration under conditions of cooling, decrease of pressure, or both.

Some of the enstatite porphyroclasts in lherzolite PHN 1611 are partially or wholly disaggregated into lenticles and bands of fine-grained enstatite, which is mixed with recrystallized olivine. The rock has a fluidal mosaic texture with a pronounced foliation (*Year Book* 72, p. 436, Fig. 2B). The equilibration* temperature (1385°C) determined from the porphyroclasts in this rock is near the maximum thus far found for lherzolite xenoliths in kimberlite. Analyses for the fine-grained enstatite in the groundmass (Table 25) were carried out on grains 10–30 μm in diameter, and their composition is identical with that of the enstatite that comprises the porphyroclasts (Table 25). These results, therefore, do not confirm the data of Mercier and Carter (1975) on PHN 1611.

Nevertheless, significant differences in enstatite composition have been found in two sheared lherzolites from the Bultfontein Floors (Kimberley, South Africa). The sheared lherzolites from Bultfontein differ from most of those found in Lesotho in that the enstatite is commonly disaggregated and some of the garnets are broken apart. Equilibration temperatures for the Bultfontein sheared rocks are in the range 1000°–1050°C (Davis and Boyd, 1966), which is considerably below temperatures estimated for deformed nodules with porphyroclastic-mosaic textures from Lesotho. An additional difference is that in some of the Bultfontein sheared rocks, the groundmass contains phlogopite that

* The diopside solvus of Davis and Boyd (1966) was used to estimate equilibration temperatures. Three recent determinations of this solvus (Nehru and Wyllie, 1974; Howells and O'Hara, 1975; Mori and Green, 1975) show substantial differences from one another and from the Davis and Boyd curve. Nevertheless the recent determinations agree in showing less solid solution at temperatures above 1200°C than the Davis and Boyd curve; hence, the equilibration temperatures reported here may be low by as much as 100°C.

TABLE 25. Compositions of Pyroxene Porphyroclasts and Groundmass Pyroxenes in Sheared Lherzolite Nodules from Kimberlites, wt %

	PHN 1611* Enstatite		PHN 2766/8† Enstatite	
	Porphyroclast	Groundmass	Porphyroclast	Groundmass
No. Grains Averaged :	(14)	(8)	(7)	(4)
SiO ₂	55.9	56.3	57.7	56.8
TiO ₂	0.22	0.23	<0.03	0.13
Al ₂ O ₃	1.36	1.35	0.78	1.54
Cr ₂ O ₃	0.20	0.21	0.48	0.73
FeO‡	6.67	6.87	4.17	4.27
MnO	0.13	0.14	0.12	0.11
MgO	33.2	32.9	36.3	35.5
CaO	1.58	1.61	0.52	0.75
Na ₂ O	0.31	0.33	0.14	0.18
Totals	99.6	99.9	100.2	100.0

	FRB 351† Enstatite		FRB 351† Diopside	
	Porphyroclast	Groundmass	Porphyroclast	Groundmass
No. Grains Averaged :	(3)	(1)	(3)	(1)
SiO ₂	57.0	56.8	54.8	53.0
TiO ₂	<0.03	<0.03	<0.03	1.00
Al ₂ O ₃	0.71	1.11	1.54	1.55
Cr ₂ O ₃	0.31	0.38	1.46	0.66
FeO‡	4.48	4.48	1.93	2.86
MnO	0.14	0.13	0.07	0.10
MgO	36.6	35.3	17.5	17.6
CaO	0.45	0.59	21.2	20.3
Na ₂ O	0.04	0.13	1.39	1.28
Totals	99.7	98.9	99.9	98.4

* Thaba Putsoa, Lesotho.
† Bultfontein Floors, Kimberley, South Africa.
‡ Total Fe as FeO.

has been sheared and is partly recrystallized (A. M. Boullier, personal communication).
Results for the two sheared nodules from Bultfontein (Table 1, PHN 2766/8 and FRB 351) are similar in that the groundmass entatite is erratically but markedly enriched in CaO, Al₂O₃, and Cr₂O₃ relative to the enstatite porphyroclasts. In PHN 2766/8 the groundmass enstatite also is richer in TiO₂. One grain of diopside was found in the groundmass in FRB 351, and it shows much more TiO₂ and less Cr₂O₃ and CaO than the diopside porphyroclasts.

These analytical results were obtained

for groundmass grains of enstatites and diopside that are 10–30 μm in diameter. However, not all grains of enstatite in this size range showed the same composition. Many of them have compositions identical with those of the porphyroclasts; others have intermediate compositions. Some enstatite in the groundmass is richer in Al₂O₃ than the porphyroclasts but has the same CaO content. This last observation suggests that, if reequilibration is responsible for these differences, the rate of the reaction of enstatite with garnet was faster than with diopside. In PHN 2766/8 the margins of some porphyroclasts are also affected in a zone

10–30 μm in width, and in one porphyroclast the interior of the grain adjacent to a crack was also changed.

The increases in TiO_2 shown by some of these pyroxenes suggest alteration by reaction with kimberlite or with a vapor phase because these Bultfontein rocks are extremely depleted in TiO_2 . Sample PHN 2766/8 contains sparse phlogopite that mantles the garnet and appears to have been introduced after the deformation. On the other hand, the changes in CaO and Al_2O_3 in the groundmass enstatites could well reflect reequilibration with garnet and diopside during a heating event combined with a decrease in pressure. Perhaps both alteration and reequilibration are involved.

If reequilibration has taken place during eruption, it is unlikely that the compositions of the groundmass enstatites reflect true P - T points because the rates of reaction of the enstatite with diopside and garnet would probably differ. At face value, however, the magnitude of the changes shown by the enstatite in the groundmass of PHN 2766/8 suggests a heating of the order of 100°C and a decrease in depth of about 20 km. Such heating could have happened in response to inclusion of the rocks in kimberlite magma, or it might reflect short-term stress-heating as proposed by Goetze (1975).

ORE MINERAL AND PHLOGOPITE MINERALIZATION WITHIN ULTRAMAFIC NODULES FROM THE MATSOKU KIMBERLITE PIPE, LESOTHO

*Ben Harte and John J. Gurney**

The compositions and mode of formation of minor mineral phases in the ultramafic nodules found in kimberlite pipes are important with respect to (a) determination of physico-chemical environments within the upper mantle, (b) the geochemistry of mantle and igneous rocks, (c) the origin of xenocrysts and

megacrysts within kimberlite. Data are presented on the occurrence and nature of phlogopite, ilmenite, rutile, and sulfides within garnet-peridotite and pyroxenite nodules from the Matsoku kimberlite pipe, Lesotho.

Harte, Cox, and Gurney (1973, 1975) reported petrographic data on a group of Matsoku garnet-peridotite facies xenoliths and noted the occurrence of an apparently metasomatically introduced suite of the minerals referred to above. Textural relations were considered to indicate equilibration of this suite of minerals with the host rock silicates (olivine, orthopyroxene, clinopyroxene, garnet), and the suite was referred to as "primary-metasomatic" in distinction to "late-secondary" ore minerals and phlogopite associated with kelyphite and serpentine. Examination of an extended collection of Matsoku xenoliths has supported this distinction, although the chemical compositions of late-secondary minerals indicate that they probably have a variety of modes and conditions of formation. Only the primary-metasomatic suite of minerals is considered in detail in this paper. The occurrence of these minerals is confined to discrete veins in some ultramafic xenoliths, but in other xenoliths they are widely distributed. The major silicate minerals in the xenoliths may or may not show changes in grain size and evidence of recrystallization where associated with primary-metasomatic minerals.

The Primary-Metasomatic Minerals

The relative proportions of phlogopite, ilmenite, rutile, and sulfide(s) differ considerably from xenolith to xenolith. Sulfide is the most constant member of the association, although usually present only in subordinate amounts. Ilmenite or rutile may be the dominant primary-metasomatic ore mineral in any given xenolith; in some cases (e.g., LMB-101*)

* Department of Geochemistry, University of Cape Town.

* Numbers prefixed by "LBM" refer to specimen numbers in the University of Cape Town catalogue.

both minerals are common, but in others either rutile (e.g., LBM-22, LBM-110, LBM-114) or ilmenite (e.g., LBM-38B, LBM-108, LBM-129) occurs to the virtual exclusion of the other. Phlogopite occurs in approximately 70% of the xenoliths examined. Electron microprobe analyses have been made of primary-metasomatic minerals in 14 Matsoku xenoliths; representative analyses are given in Tables 26 and 27, and the ranges of mineral compositions, in Table 28.

Phlogopite. Analytical data for TiO_2 , Cr_2O_3 , and total Fe as FeO in Matsoku phlogopites are plotted in Fig. 80 together with phlogopite data from the literature. The primary-metasomatic phlogopite analyses have a restricted compositional range, which partly overlaps that of mica compositions from kimberlite megacrysts and glimmerites and is adjacent to the compositions of primary phlogopite in peridotite nodules from other localities. Late-secondary phlogopite grains mantling garnets in Matsoku xenoliths have high Cr_2O_3 values consistent with those of secondary phlogopite analyses from other localities (Fig. 80).^{*} These secondary phlogopites also show lower SiO_2 , MgO , and possibly K_2O , and higher Al_2O_3 and Na_2O than the other types of phlogopite.

The spread of primary-metasomatic phlogopite compositions (Fig. 80) across the field of megacryst phlogopites does not support the distinction between "peridotite" and "nonperidotite" micas proposed by Dawson and Smith (1975). For further comparison, xenocrysts of phlogopite within the Matsoku kimberlite (in section PHN 1678) were examined. The xenocrysts commonly show a sharp contact between pale and darker phlogopites that are in optical continuity. The compositions of the pale and dark

varieties are reasonably consistent from xenocryst to xenocryst and are similar to those of the primary-metasomatic and late-secondary phlogopites (Fig. 80).

Ilmenite. The primary-metasomatic ilmenite is rich in MgO and low in Fe_2O_3 (calculated from the structural formula; see Finger, *Year Book* 71, pp. 600–603). In polished section, ilmenite grains commonly show parallel, short, narrow (usually $<2.0\ \mu\text{m}$) exsolution lamellae of low reflectivity. Even the broadest lamellae are too narrow for quantitative electron microprobe analysis, but qualitative analyses made by centering the electron microprobe on the broadest lamellae show much higher Al_2O_3 and Cr_2O_3 , and lower TiO_2 than host ilmenite lacking visible lamellae, thus indicating that the lamellae are Al_2O_3 - and Cr_2O_3 -rich spinel. Exsolution of Al_2O_3 - and Cr_2O_3 -bearing spinel from picroilmenite has previously been reported by Danchin and D'Orey (1972). The large standard deviations in the weight percentage of Al_2O_3 and Cr_2O_3 in ilmenite in Tables 26 and 27 result from the presence of the exsolution lamellae.

Figure 81 shows $\text{Fe}^{2+}/(\text{Fe}^{2+} + \text{Mg})$ and $\text{Cr}/(\text{Cr} + \text{Al})$ for the analyzed ilmenites, together with data from the literature. The primary-metasomatic Matsoku ilmenite analyses (together with two analyses of primary ilmenites in garnet lherzolites; Boyd and Nixon, 1973, p. 256) plot in a moderately small compositional field. Most ilmenite analyses from lamellar intergrowths with clinopyroxene and from "discrete" nodules in kimberlite occupy closely defined and distinct composition fields in Fig. 80 and also show higher Fe_2O_3 . The low Cr_2O_3 content of lamellar ilmenites has previously been noted by Boyd and Nixon (1973, p. 260). Ilmenites occurring as xenocrysts or megacrysts (not also described as "discrete" nodules) in kimberlite and in kimberlite autoliths show a wide spread of compositions in Fig. 81 (see also Mitchell, 1973, p. 306), and appear to be heterogeneous in origin.

^{*} More than one variety of late-secondary phlogopite occurs in Matsoku xenoliths. In contrast to the phlogopite mantling garnet, phlogopite occurring in serpentine veins shows $<0.05\ \text{wt}\ \% \text{Cr}_2\text{O}_3$. Discussion has been limited to the variety described in the text.

TABLE 26. Compositions of Minerals Occurring Inside and Outside of a Vein Containing Primary-Metasomatic Minerals in Xenolith LBM-101, wt %

	Average Compositions Outside Vein				Average Compositions Inside Vein						
	Olivine	Opx	Cpx	Garnet*	Olivine	Opx	Cpx	Phlogopite	Ilmenite†	Rutile‡	Spinel§
SiO ₂	41.0 (2)	57.5 (1)	54.2 (2)	41.8 (2)	41.3 (1)	57.4 (1)	54.0 (3)	41.5 (6)	0.21 (2)	0.09 (1)	0.23
TiO ₂	<0.05	0.16 (1)	0.35 (1)	0.45 (2)	<0.05	0.13 (1)	0.35 (2)	1.59 (4)	56.1 (5)	97.8 (4)	5.2 (4)
Al ₂ O ₃	<0.05	0.83 (1)	2.58 (4)	20.0 (2)	<0.05	0.85 (5)	2.66 (3)	12.9 (3)	0.79 (30)	<0.05	42.3 (7)
Cr ₂ O ₃	<0.05	0.20 (4)	1.31 (7)	4.65 (43)	<0.05	0.12 (1)	0.45 (6)	0.31 (3)	1.70 (31)	1.05 (7)	18.4 (8)
FeO	8.49 (12)	5.23 (10)	2.56 (6)	7.54 (2)	8.61 (8)	5.16 (8)	2.71 (5)	3.49 (14)	22.9 (6)	0.08 (5)	19.4 (3)
NiO	0.26 (7)	0.10 (4)	0.06 (4)	<0.05	0.31 (5)	0.10 (4)	0.06 (2)	0.16 (9)	0.17 (3)	<0.05	0.13
MnO	0.12 (2)	0.12 (5)	0.09 (3)	0.36 (2)	0.12 (7)	0.14 (4)	0.17 (9)	<0.05	0.30 (5)	<0.05	0.16
MgO	51.7 (4)	36.0 (1)	17.1 (1)	20.6 (3)	51.9 (4)	36.0 (1)	17.3 (1)	25.5 (2)	17.2 (2)	<0.05	15.1 (2)
CaO	<0.05	0.52 (2)	19.1 (2)	5.29 (2)	<0.05	0.52 (1)	19.2 (1)	<0.05	<0.05	<0.05	<0.05
Na ₂ O	<0.05	0.14 (5)	2.16 (9)	<0.05	<0.05	0.05 (3)	2.11 (7)	0.28 (17)	n.d.	n.d.	n.d.
K ₂ O	<0.05	<0.05	<0.05	<0.05	<0.05	<0.05	<0.05	9.56 (36)	n.d.	n.d.	n.d.
Totals	101.57	100.80	99.51	100.69	102.24	100.45	99.04	95.29	99.37	99.52	100.92

Standard deviations of the last figure quoted are given in parentheses.
* Average core and margin composition of a single garnet occurring in polished section; see first footnote of Table 27.
† Weight percentages of FeO and Fe₂O₃ calculated from structural formula are 19.6 and 3.70, respectively.
‡ Analysis includes (wt %): 0.20 Nb₂O₅, 0.30 ZrO₂, <0.05 Ta₂O₅.
§ Broad lamella in rutile, average of two analyses (for Ti, Al, Cr, Fe, Mg) executed on different days.
|| Total iron calculated as ferrous.

TABLE 27. Compositions of Minerals from Different Petrographic Environments in Xenolith LBM-108, wt %

	Olivine-A	Olivine-C	Opx-A	Opx-C	Cpx-A	Cpx-B	Cpx-D
SiO ₂	40.2 (1)	40.2 (1)	56.9 (2)	57.2 (1)	54.3 (4)	54.1 (10)	53.7 (2)
TiO ₂	<0.05	<0.05	0.16 (1)	0.16 (1)	0.37 (2)	0.39 (2)	0.39 (1)
Al ₂ O ₃	<0.05	<0.05	0.82 (1)	0.83 (3)	2.86 (3)	2.87 (4)	2.95 (11)
Cr ₂ O ₃	<0.05	<0.05	0.24 (2)	0.20 (2)	1.36 (7)	1.27 (11)	1.34 (3)
FeO§	9.64 (8)	9.73 (20)	5.84 (6)	5.82 (6)	2.98 (5)	3.00 (5)	3.09 (4)
NiO	0.35 (3)	0.35 (3)	0.09 (2)	0.07 (3)	n.d.	n.d.	n.d.
MnO	0.12 (1)	0.13 (2)	0.13 (2)	0.15 (2)	0.11 (2)	0.11 (2)	0.11 (2)
MgO	49.6 (2)	49.4 (3)	34.8 (1)	34.8 (2)	16.4 (1)	16.3 (1)	16.3 (1)
CaO	<0.05	<0.05	0.52 (1)	0.52 (1)	18.5 (5)	18.8 (2)	17.9 (5)
Na ₂ O	<0.05	<0.05	0.14 (2)	0.13 (2)	2.33 (6)	2.28 (7)	2.26 (5)
K ₂ O	n.d.	n.d.	n.d.	n.d.	n.d.	n.d.	n.d.
Totals	99.91	99.81	99.64	99.88	99.19	99.12	98.04
	Garnet-A*	Garnet-D	Phlog-D	Ilm-B(b)†	Ilm-B(a)†	Ilm-D(a)†	Rutile-B‡
SiO ₂	41.3 (3)	42.0 (4)	42.4 (10)	0.16 (9)	0.14 (4)	0.17 (3)	0.21 (1)
TiO ₂	0.35 (12)	0.37 (1)	1.56 (4)	54.4 (15)	54.6 (15)	53.1 (25)	97.8 (6)
Al ₂ O ₃	20.3 (6)	21.7 (3)	13.2 (2)	0.70 (66)	1.03 (77)	1.16 (105)	0.09 (1)
Cr ₂ O ₃	4.00 (79)	2.09 (5)	0.46 (3)	2.66 (96)	2.17 (76)	2.83 (157)	1.01 (4)
FeO§	8.30 (36)	8.27 (15)	3.88 (18)	26.1 (6)	27.3 (10)	27.8 (5)	0.46 (2)
NiO	n.d.	n.d.	0.21 (2)	0.17 (5)	0.19 (9)	0.12 (2)	<0.05
MnO	0.41 (4)	0.41 (3)	0.05 (1)	0.30 (8)	0.30 (3)	0.43 (5)	<0.05
MgO	20.2 (4)	21.0 (1)	24.7 (3)	15.0 (4)	14.1 (9)	13.5 (1)	0.20 (2)
CaO	5.10 (24)	4.44 (7)	<0.05	<0.05	<0.05	<0.05	<0.05
Na ₂ O	0.06 (4)	0.05 (3)	0.20 (2)	n.d.	n.d.	n.d.	n.d.
K ₂ O	n.d.	n.d.	9.61 (0)	n.d.	n.d.	n.d.	n.d.
Totals	100.02	100.33	96.27	99.49	99.83	99.11	100.46

Standard deviations of the last figure quoted are given in parentheses.

A, average composition outside the zone of primary-metasomatic mineralization.

B, average composition inside the zone of primary-metasomatic mineralization (excludes inclusions in other minerals).

C, average composition of small recrystallized grains occurring inside the zone of primary-metasomatic mineralization.

D, average composition of poikiloblastic garnets and inclusions within poikiloblastic garnets. (a) and (b) distinguish different thin sections.

* Garnets outside the zone of primary-metasomatic mineralization show more Cr₂O₃-rich core regions, following the pattern described by Cox, Gurney, and Harte (1973, pp. 88–89).

† Weight percentages of FeO and Fe₂O₃ calculated from structural formulae are B(b), 21.9, 4.71; B(a), 23.6, 4.11; D(a), 23.3, 5.00.

‡ Analysis includes (wt %): 0.35 Nb₂O₅, 0.27 ZrO₂, and 0.07 Ta₂O₅.

§ Total iron calculated as ferrous.

Rutile. Primary-metasomatic rutile analyses are notable for their relatively high Cr₂O₃, ZrO₂, and Nb₂O₅ contents. Exsolution lamellae, usually <3.0 μm thick and of low reflectivity, are common in the rutile grains. An exceptionally broad (8.0 μm) lamella was found that yielded consistent electron microprobe analyses, and its composition (Table 26)

is that of a (Fe, Mg)O: (Cr, Al)₂O₃ spinel with few magnetite or ulvospinel molecules. Composite analyses of other lamellae and host rutile consistently indicate high FeO, MgO, Cr₂O₃, and Al₂O₃, but have widely varying Cr₂O₃/Al₂O₃. The possible occurrence of picrochromite lamellae in rutile has been indicated by Dawson and Smith (1973).

TABLE 28. Ranges in Mineral Compositions and Parameters

(A) Primary-Metasomatic Minerals, wt %

	Phlogopite (8)*	Ilmenite (10)*	Rutile (6)*
SiO ₂	41.0–42.7	0.11–0.30	0.09–0.21
TiO ₂	1.07–1.59	52.0–56.1	94.2–97.8
Al ₂ O ₃	11.7–13.2	0.13–1.01	<0.05–0.14
Cr ₂ O ₃	0.19–0.81	1.70–3.96	1.01–3.18
FeO†	2.72–4.57	22.9–32.1	0.08–0.46
NiO	0.16–0.24	0.05–0.19	<0.05
MnO	<0.05–0.05	0.25–0.48	<0.05
MgO	23.9–25.5	11.9–17.2	<0.05–0.20
CaO	<0.05	<0.05	<0.05
Na ₂ O	0.17–0.43	n.d.	n.d.
K ₂ O	9.27–9.97	n.d.	n.d.
Nb ₂ O ₅	n.d.	<0.05‡	0.20–1.11
ZrO ₂	n.d.	<0.05–0.05‡	0.27–0.72
Ta ₂ O ₅	n.d.	<0.05‡	<0.05–0.07

(B) Pyroxenes

Rock Group	Ca/(Ca+Mg) in Clino- pyroxene	Al ₂ O ₃ Orthopy- roxene, wt %
Garnet lherzolites with primary-metasomatic minerals	44.4–45.3	0.81–0.87
Garnet lherzolites without primary-metasomatic minerals	44.4–45.3	0.73–0.81

* Number of rocks in which mineral was analyzed.

† Total Fe as FeO.

‡ Analyzed in two rocks only.

Sulfides. Grains of primary-metasomatic sulfide typically appear heterogeneous under reflected light. They consist principally of flame-like exsolution intergrowths of pyrrhotite and pentlandite (cf. Ramdohr, 1969, Fig. 362), and around their margins variable amounts of chalcopyrite (containing minute orientated intergrowths) commonly occur and show smoothly curving boundaries against the pyrrhotite-pentlandite intergrowths. These relationships possibly indicate unmixing of a single, high-temperature, Fe-Ni-Cu sulfide phase.

Olivine, Orthopyroxene, Clinopyroxene, and Garnet Mineral Compositions

The ranges of the chemical parameters, Ca/(Ca + Mg) in clinopyroxenes, and weight percentage of Al₂O₃ in orthopyroxenes relevant to temperature and pressure estimation (Boyd, 1973) are summarized in Table 28. The *P-T* conditions of formation of rocks bearing primary-metasomatic minerals are inferred to be closely similar to those of other Matsoku mantle xenoliths. Studies of the homogeneity of mineral composition have been made on two specimens (LBM-101 and LBM-108) in order to test the degree to which the primary-metasomatic minerals have equilibrated with the other minerals and to assess further their petrogenesis.

In LBM-101, primary-metasomatic minerals (rutile, phlogopite, ilmenite, sulfide) are confined to a vein (Fig. 82) within which olivine, clinopyroxene, and orthopyroxene show finer grain size than in the main body of the rock. Chemical analyses, with standard deviations, of mineral grains from within and without the vein are given in Table 26. The only compositional difference (outside the limit of likely analytical uncertainty) for those two petrographic units is that Cr₂O₃ is lower in the vein clinopyroxene.

In LBM 108, primary-metasomatic minerals (ilmenite, minor sulfide, and rare phlogopite and rutile) occur in a zone up to 3.0 cm thick within which their distribution varies from one of wide dispersal to one of concentration in discontinuous veinlets (Fig. 83). Where ilmenite is abundant and well dispersed, olivine and pyroxenes are recrystallized and fine grained (0.1–0.3 mm); elsewhere the silicates are coarser grained and show textures similar to those of regions outside the zone (Fig. 83). Garnet is common and within the mineralized zone shows indications of slight disruption together with partial development of poikiloblastic texture (see Harte, Cox, and Gurney, 1975, p. 495). The inclusions

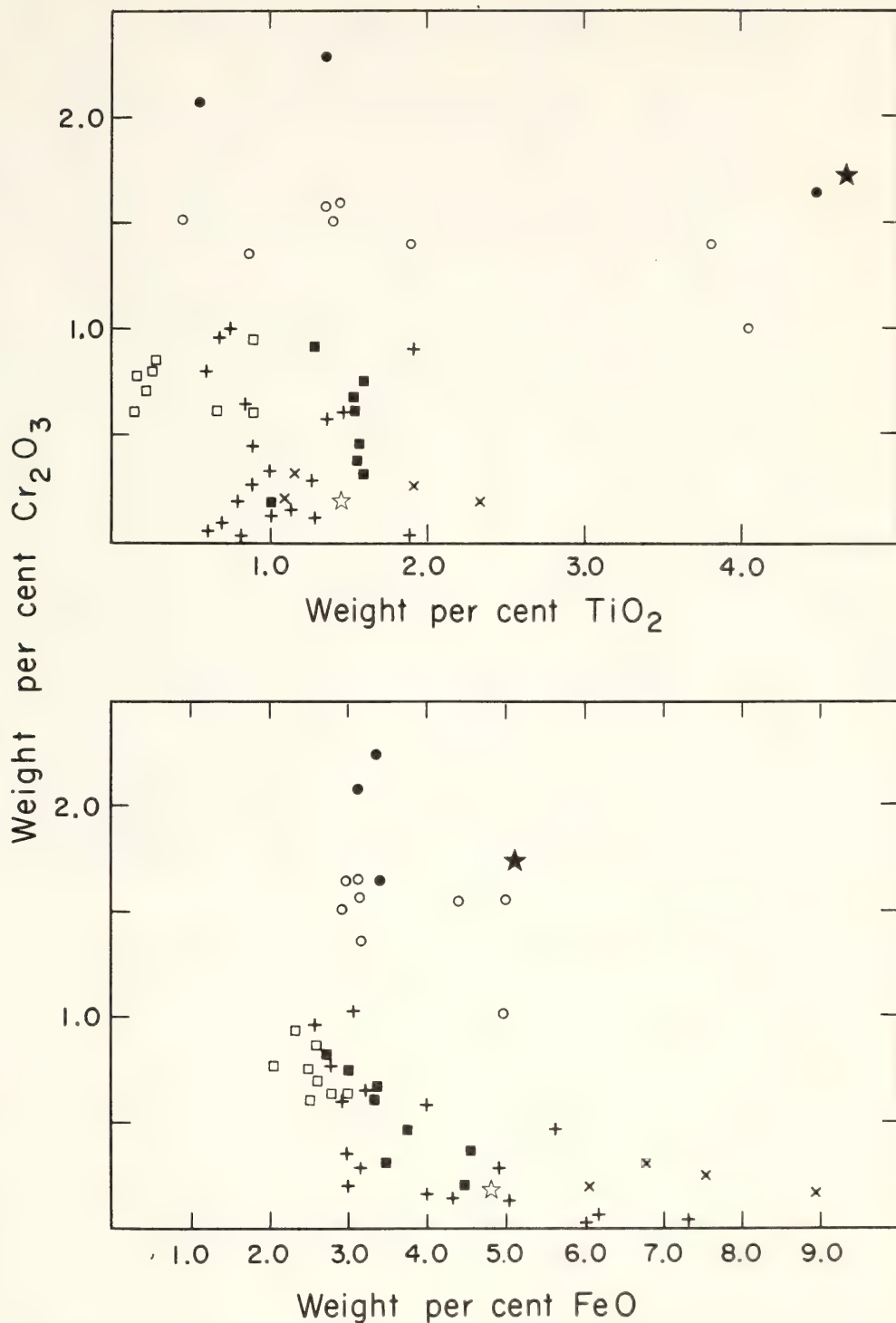


Fig. 80. Cr_2O_3 vs. TiO_2 and total Fe as FeO in weight percent for micas from Matsoku and other localities, plotted after the manner of Dawson and Smith (1975). Symbols: solid squares, Matsoku primary-metasomatic phlogopite; open squares, primary phlogopite in peridotite from other localities; solid circles, Matsoku late-secondary phlogopite mantling garnet; open circles, secondary phlogopites in peridotite from other localities; solid star, dark phlogopite in xenocrysts in Matsoku kimberlite; open star, pale phlogopite in xenocrysts in Matsoku kimberlite; plus signs, phlogopite megacrysts/xenocrysts in kimberlite from other localities; crosses, phlogopite in glimmerite nodules from other localities. Data for other localities from Boyd and Nixon (1973, p. 257 and Table 60), Carswell (1973), Dawson and Smith (1975).

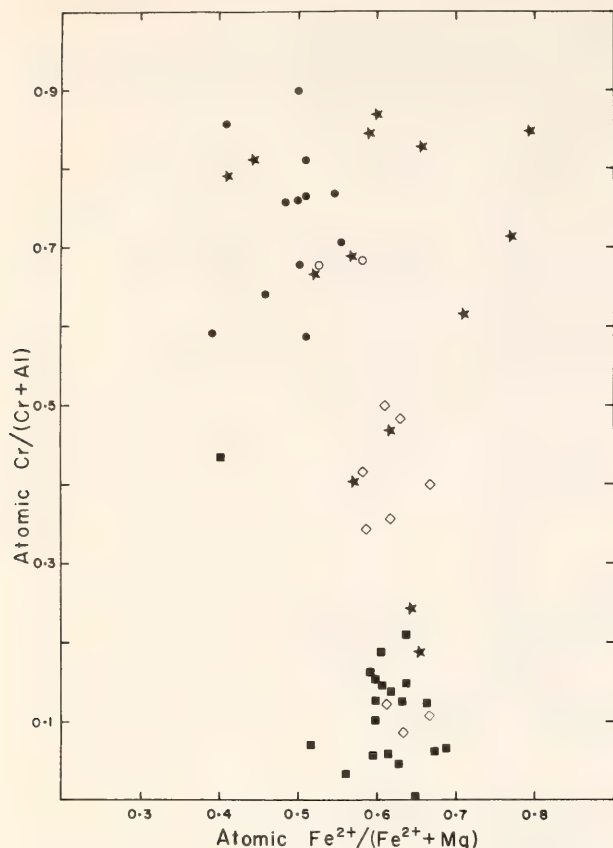


Fig. 81. Atomic Cr/(Cr + Al) against $\text{Fe}^{2+}/(\text{Fe}^{2+} + \text{Mg})$ for ilmenites: Solid circles, primary-metasomatic ilmenite from Matsoku; open circles, primary ilmenite in garnet peridotites (Boyd and Nixon, 1973); diamonds, ilmenite discrete nodules; solid squares, ilmenite in lamellar intergrowths with clinopyroxene; stars, ilmenite occurring in kimberlite as a primary phase, as megacrysts, or within autoliths. Data for last three categories from Boyd (in Nixon, 1973, Tables 17, 20, 23, 36, 44, 51, 60, 74); Ferguson, Danchin, and Nixon (1973); Gurney, Fesq, and Kable (1973); Haggerty (1973); Mitchell, Carswell, and Brunfelt (1973). Fe^{2+} and Fe^{3+} calculated from structural formula.

within such poikiloblastic garnet are largely ilmenite and clinopyroxene.

A detailed electron microprobe study of mineral compositions (for a total of 247 point analyses) inside and outside the LBM-108 mineralized zone is summarized in the chemical analyses of Table 27, which shows average compositions with standard deviations for grains in various petrographic environments in two thin sections, taken from different areas of the xenolith. For the major part, the analyses show the absence of compositional variation beyond the limits

of analytical uncertainty. There is probably a small significant variation of FeO/MgO in ilmenite, but the clearest departure from compositional homogeneity is seen in the garnet analyses, which show lower $\text{Cr}_2\text{O}_3/\text{Al}_2\text{O}_3$ and CaO/MgO in the poikiloblastic garnet. The extent of these differences has been found to correlate approximately with both the number of inclusions and the extent of disruption of the garnet, and it therefore appears that the garnet is refractory (Hollister, 1969, p. 2489) unless affected by these physical changes. In general, the chemical compositions of olivine, orthopyroxene, clinopyroxene, and garnet associated with the primary-metasomatic minerals are closely similar to compositions found in Matsoku garnet-peridotite nodules lacking primary-metasomatic minerals (Cox, Gurney, and Harte, 1973).

Discussion and Conclusions

1. The data presented on mineral chemistry show that the primary-metasomatic minerals cannot have been derived solely by reaction among the major peridotite silicates (olivine, orthopyroxene, clinopyroxene, garnet). In conjunction with the textural and structural relationships previously discussed (Harte, Cox, and Gurney, 1975) the mineral compositions indicate the formation of the primary-metasomatic minerals as a consequence of infiltration by a hydrous fluid especially enriched in Ti and K, but also containing S and probably Fe and minor elements (Ni, Cu, Nb, Zr).

2. On the basis of the low $\text{Fe}^{3+}/\text{Fe}^{2+}$ of ilmenite, the fluid is suggested to have had a relatively low oxygen fugacity.

3. Infiltration of the metasomatic fluid occurred at depth within the mantle, under P - T conditions similar to those of common Matsoku garnet-peridotite xenoliths, and extensive chemical equilibrium with the host-rock silicates was attained.

4. The localized occurrence of phlogopite, ilmenite, rutile, sulfides, and possibly the fluid from which they are derived,

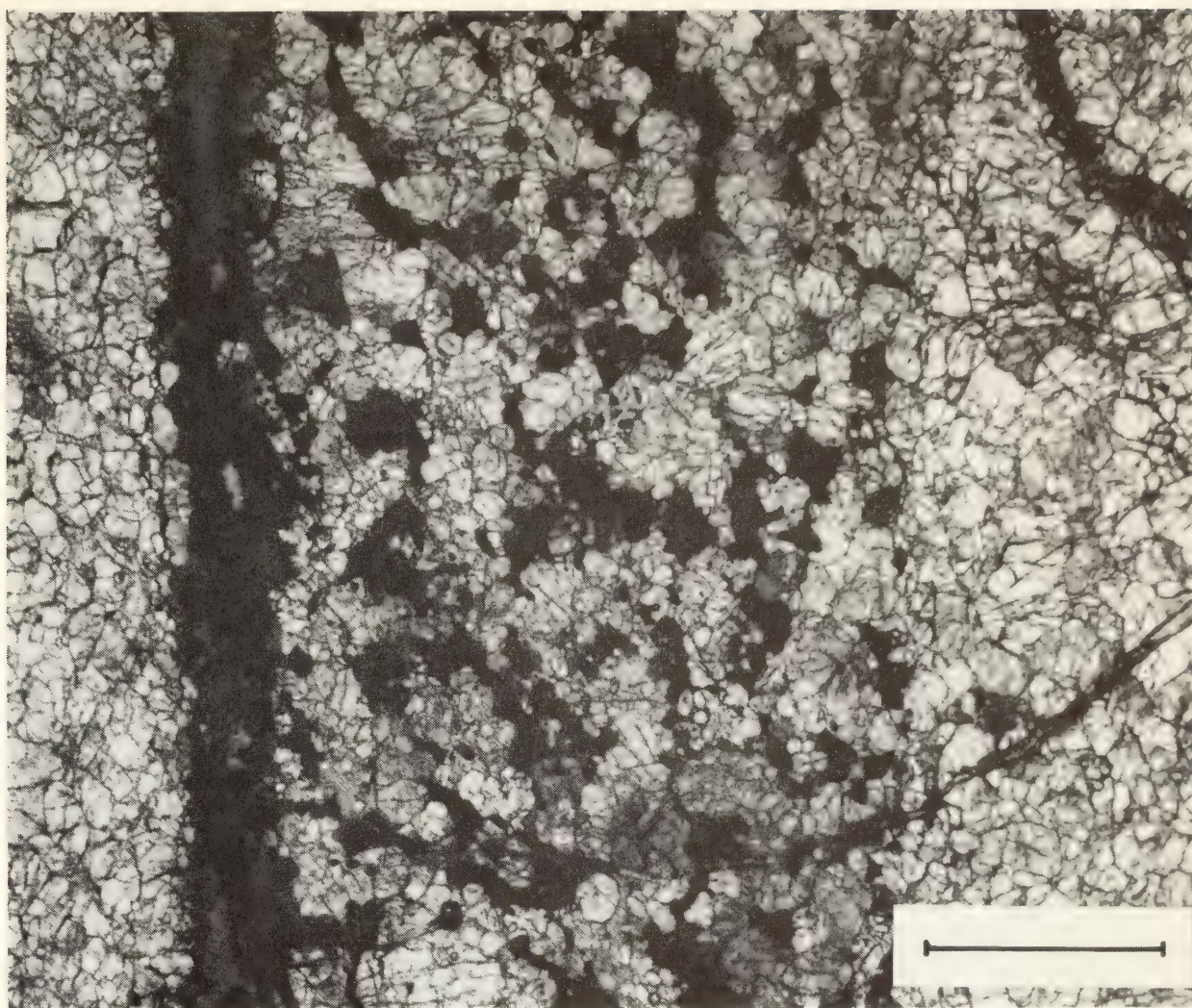


Fig. 82. Photomicrograph of 1.0 cm wide vein containing primary-metasomatic minerals in xenolith LBM-101. Narrow late-secondary veins rich in serpentine occur in the host peridotite to the right and along the left margin of the primary-metasomatic vein. Scale bar, 3.0 mm.

provides evidence of the existence of mantle heterogeneities that may be relevant to the genesis of basaltic and other magmas with varying isotope and minor- and trace-element geochemistry (see, for example, O'Nions and Pankhurst, 1974). Such fluids also provide a means of fractionation within the upper mantle, but their mobility does not support the existence of isolated heterogeneities over extended periods of geologic time.

5. Nevertheless, the metasomatic fluid itself may have been derived from magma. Kimberlite magma prior to eruption or the crystal-mush, low-velocity zone magmas of Boyd and Nixon (1973) are the more obvious possible magma sources for the fluid. The

tentative evidence of a relatively late stage of development of the primary-metasomatic minerals (Harte, Cox, and Gurney, 1975) favors the former of these two possibilities.

6. The similarity of primary-metasomatic phlogopite compositions to those of xenocrysts-megacrysts in kimberlite and those of glimmerite nodules indicates the possibility that some of both the last two types may also be formed in metasomatic (pneumatolytic?) events.

7. Primary metasomatic ilmenites are distinct in composition from those of lamellar intergrowths with clinopyroxene and those of certain discrete nodules, both of which show a higher weight percentage of Fe_2O_3 and lower Cr_2O_3 . The

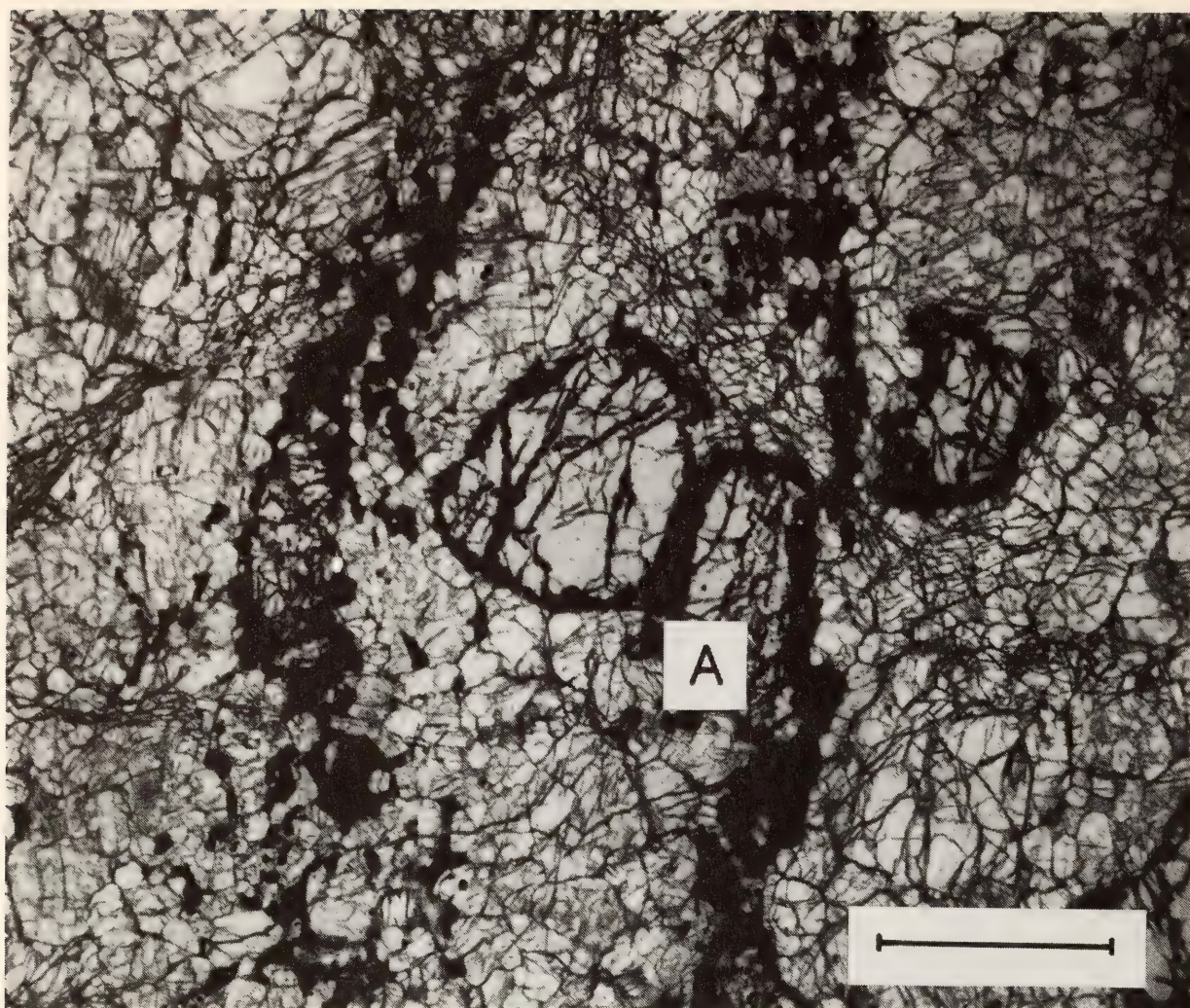


Fig. 83. Photomicrograph of LBM-108 showing two principal veinlets of primary-metasomatic ilmenite within garnet peridotite. Note that the garnet *A* has numerous inclusions and cracks only within the side adjacent to the ilmenite veinlet. Scale bar, 3.0 mm.

latter may be tentatively correlated with the suggested formation of both lamellar intergrowths (Wyatt *et al.*, this Report) and ilmenite discrete nodules (Boyd and Nixon, 1973) in near-solidus magmas.

AN EXPERIMENTALLY PRODUCED CLINOPYROXENE-ILMENITE INTERGROWTH

*B. Wyatt, R. H. McCallister, F. R. Boyd,
and Y. Ohashi*

Nodules of ilmenite and pyroxene exhibiting distinctive lamellar and micrographic intergrowths have been found in many kimberlites. They were originally described by Harger (1906), and their origin has been the subject of considerable interest, especially during the past five years because it is believed that they

record the special conditions under which kimberlite formed. Three possible mechanisms of formation that have been suggested are (1) eutectoid breakdown of a Ti-rich garnet, (2) exsolution from a Ti-rich clinopyroxene by the discontinuous mode, and (3) eutectic crystallization.

The first of these mechanisms was suggested by Ringwood and Lovering (1970), who succeeded in synthesizing garnet from a fused portion of a clinopyroxene-ilmenite intergrowth at 1000°C and 105 kbar. At lower pressures the same glass crystallized to an ilmenite-clinopyroxene assemblage. The fact that garnet was never produced directly from the intergrowth and the implication that the nodules would have to be derived from depths of approximately 300 km

are debatable points of this interpretation.

Dawson and Reid (1970) suggested that exsolution of ilmenite from a clinopyroxene-ilmenite solid solution might occur at lower pressure and temperature. An intergrowth consisting of lamellae of ilmenite and clinopyroxene is consistent with an exsolution texture that is commonly observed in metal systems and is referred to as discontinuous precipitation (see Yund and McCallister, 1970). The work of Akella and Boyd (*Year Book* 72, pp. 523–526), however, indicates that the solubility of TiO_2 in clinopyroxenes at 31 kbar and 1350°C is only about 2–3 wt % and thus is insufficient to account for the commonly observed weight ratio of 20%–40% ilmenite/80%–60% clinopyroxene.

The third mechanism, eutectic crystallization, was originally suggested by Williams (1932), who observed that the intergrowths were somewhat similar to quartz-feldspar symplectites. Support for this mechanism has come from the experimental work of MacGregor and Wittkop (1970) on the diopside-geikielite join at 20 kbar and 1150°C . They obtained a minimum melt composition of $50 \pm 10\%$ geikielite/ $50 \pm 10\%$ diopside; however, a coexisting assemblage of these phases was never obtained. Further evidence for the eutectic crystallization mechanism is provided by the geochemical data of Gurney, Fesq, and Kable (1973). Also, Boyd and Nixon (1973), on the basis of the mineral chemistry of ilmenite-bearing nodules from kimberlite, suggested that the intergrowths have been produced by crystallization from a magma in the upper part of the low-velocity zone.

In an attempt to test the eutectic crystallization hypothesis, a number of melting experiments were carried out at 38 kbar in a solid-media, high-pressure apparatus (Boyd and England, 1960). The starting materials for these runs were separated from a natural intergrowth from Monastery Mine in eastern

Orange Free State, South Africa, and recombined with a weight ratio of ilmenite to clinopyroxene of 29:71. The mixture was ground to approximately $5\text{--}10\ \mu\text{m}$ and dried over nitrogen for a minimum of $1\frac{1}{2}$ hours at 1100°C . Compositions of the ilmenite and clinopyroxene starting materials and results obtained for a run are presented in Table 29.

Figure 84A illustrates the texture produced by cooling the melt at a rate of 20°C/hr from 1570°C , which is approximately 50°C above the liquidus to 1200°C , approximately 200°C below the solidus. The same texture was also produced in an experiment in which the run was terminated slightly above the solidus at a temperature of 1404°C . Traces of glass in the latter run prove that the formation of the intergrowth is associated with a crystal-liquid interaction. On the basis of these results, therefore, it is suggested that the large clinopyroxene crystals in Fig. 84A represent the liquidus phase and that the intergrowth is the result of eutectic crystallization at lower temperatures within the melting interval. Microprobe analyses (Table 29) illustrate the close similarities of the experimental run products to the natural samples with the possible exception that the run products crystallized under more reducing conditions to ilmenite. Also, comparison of Fig. 84A produce a lower hematite content in the and Fig. 84B shows the similarity between the experimentally produced intergrowth and a natural sample (BD 1374) studied by Dawson and Reid (1970). Note in particular the 60° and 120° intersections between sets of ilmenite lamellae. In the Dawson and Reid sample it was observed on precession photographs that the thin ilmenite set is oriented so that the plates are parallel to $(0001)_{\text{ilm}}$ and $(100)_{\text{cpx}}$ with $[100]_{\text{ilm}}$ parallel to $[010]_{\text{cpx}}$. This orientation corresponds to a matching of the close-packed oxygen layers in each of the structures and has also been observed in

TABLE 29. Electron Microprobe Analyses of Starting Materials and Run CI/104*

	Starting Materials		CI/104	
	Il	Cpx	Il	Cpx
SiO ₂	n.d.†	54.66	0.25	53.89
TiO ₂	49.15	0.3	51.56	1.82
Al ₂ O ₃	0.72	2.41	0.80	1.55
Cr ₂ O ₃	0.02	0.01	0.06	0.02
Fe ₂ O ₃	14.59‡	n.d.	6.59‡	n.d.
FeO	25.99	6.19§	31.11	7.03§
MnO	0.23	0.13	0.22	0.08
MgO	10.08	17.29	8.60	18.31
NiO	n.d.	n.d.	n.d.	n.d.
CaO	n.d.	16.94	n.d.	15.53
Na ₂ O	n.d.	1.76	n.d.	0.74
K ₂ O	n.d.	0.02	n.d.	n.d.
Totals	100.78	99.77	99.19	98.97
FeO§	39.12		37.04	
Fe ₂ O ₃ /FeO	0.56		0.21	
MgO/(MgO + FeO)§	0.20	0.74	0.19	0.72
Ilmenite	51.4		63.0	
Geikielite	35.6		31.0	
Hematite	13.0		6.0	

* Cooled from 1570° to 1200°C at 20°C/hr and 38 kbar.
† Not determined.
‡ Calculated from the mineral formula.
§ Total iron as FeO.
Abbreviations: Il, ilmenite; Cpx, clinopyroxene.

an enstatite-ilmenite intergrowth (McCallister, Meyer, and Brookins, 1975). The crystal-chemical significance of the other common planes between the ilmenite and clinopyroxene single crystals is being investigated.

Unfortunately, because of the complexity of the experimentally produced intergrowth texture and its fine grain size, it has not been possible to determine the crystallographic relationship of the two phases. However, intergrowths were also produced as quench products in runs that were rapidly cooled from temperatures above the solidus. Only one set of lamellae appears in the runs (see Fig. 84C). In one case it was possible by x-ray single-crystal techniques to show that the quench intergrowth has the orientation of (0001)_{ilm} parallel to

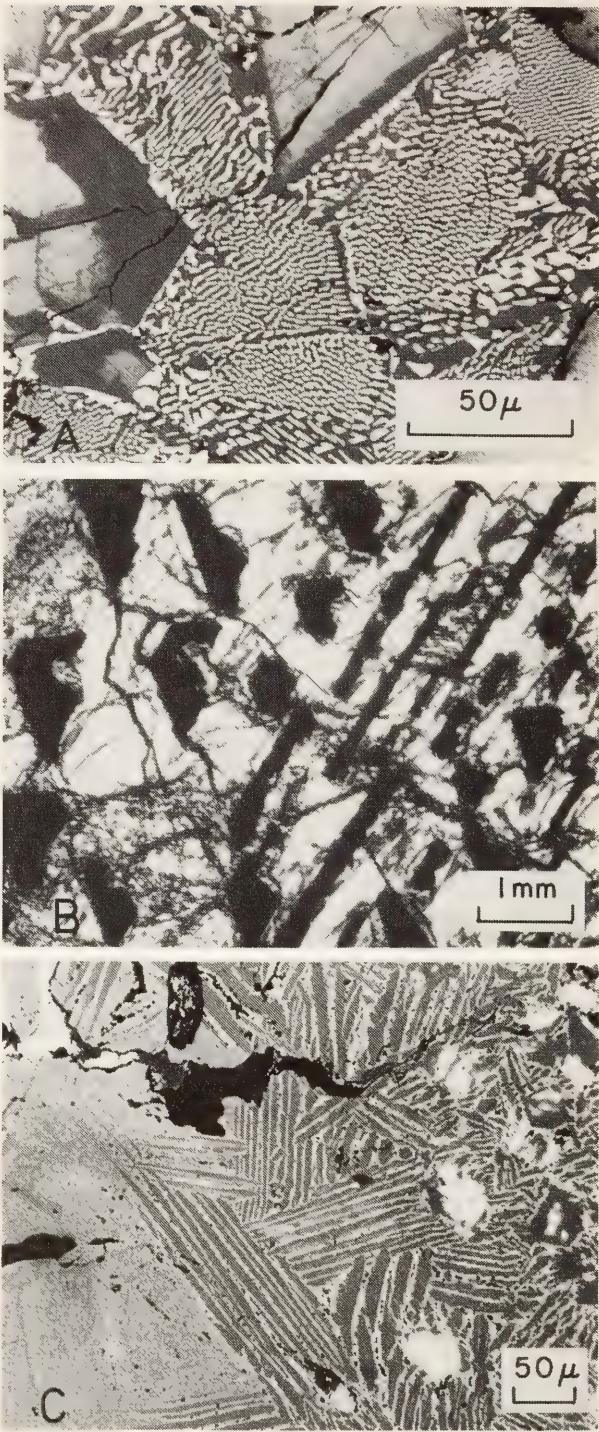


Fig. 84. (A) Reflected light photomicrograph of intergrowth developed at 38 kbar and cooled from 1570° to 1200°C at the rate of 20°C/hr. The large gray crystals are clinopyroxene. (B) Transmitted light photomicrograph of clinopyroxene-ilmenite intergrowth from Monastery Mine, South Africa. This specimen (BD 1374) was kindly supplied by J. B. Dawson. (C) Reflected light photomicrograph of intergrowth developed by quenching from above the solidus at 38 kbar.

(100)_{cpx}. This is the same relationship commonly observed in the natural intergrowths.

Comparison of the experimental and natural clinopyroxene-ilmenite intergrowths shows them to be similar in the following respects: (1) the compositions of clinopyroxene and ilmenite, (2) texture, and (3) crystallographic orientation. Thus, it appears probable that the natural clinopyroxene-ilmenite intergrowths formed by eutectic crystallization from magmas under mantle conditions.

THE EQUILIBRIUM CATION DISTRIBUTION IN CA-RICH CLINOPYROXENES

R. H. McCallister, L. W. Finger, and Y. Ohashi

An experimental study of the equilibrium distribution of Mg^{2+} and Fe^{2+} between the M1 and M2 sites of clinopyroxene as a function of temperature has been undertaken as a means of acquiring a better understanding of the thermal history of this mineral during its formation and subsolidus cooling in igneous environments. Natural pyroxenes have been used in this study, including samples from a discrete clinopyroxene nodule from the Thaba Putsoa kimberlite pipe, Lesotho (supplied by F. R. Boyd), from a megacryst in the Kakanui nephelinite breccia (supplied by B. Mason), and from an eclogite xenolith, also from Kakanui (supplied by J. Dickey). The method of investigation included annealing portions of the discrete nodule and megacryst in evacuated silica-glass tubes. The charge was contained in a $Ag_{70}Pd_{30}$ capsule and surrounded with iron. Also, two experiments were carried out with the megacryst at 20 kbar and 1350° and 1250°C, respectively. A solid-media, high-pressure apparatus was used for this purpose, and the sample was held in a graphite container. After the sample was annealed, a complete crystal structure refinement was carried out on a crystal from each run, and from the refined site occupancies a distribution

coefficient $K_d = [Fe^{2+}(M1)/Mg(M1)]/[Fe^{2+}(M2)/Mg(M2)]$, was calculated. These results were used to establish calibration curves of $\ln K_d$ vs. $1/T^\circ K$, from which the equilibrium temperature of the untreated material could be estimated.

X-ray intensity data were obtained by using an automated Picker four-circle diffractometer (Finger, Hadidiacos, and Ohashi, *Year Book* 72, pp. 694–699) and Nb-filtered Mo $K\alpha$ radiation. The observed intensities were corrected for absorption, background, and Lorentz and polarization effects. The least-squares program RFINE 2 (Finger and Prince, 1975) was used for all cycles of refinement, and the secondary extinction factor (Zachariasen, 1967) was calculated during the later stages of refinement. The atomic scattering factors used in the computations were those of neutral atoms as given by Cromer and Mann (1968); the anomalous scattering factors and mass absorption coefficients were those of Cromer and Liberman (1970).

For all crystals the least-squares refinement was initiated using the atomic coordinates of diopside given by Finger and Ohashi (1975). Approximately 700 reflections were measured for each sample, and on the average, 70 were rejected because their intensity was less than 2 standard deviations of the observed intensity or $|F_o - F_c| > 10$. The latter rejection criterion was applied only during the final cycle of anisotropic refinement. In all cycles of refinement the scale factor, isotropic extinction parameter, atomic coordinates, temperature factors, and occupancies were refined. The chemistry used in the refinements was constrained to the composition determined by electron microprobe analysis of the Kakanui samples; the bulk analysis of the discrete nodule was modified, however, owing to the presence of exsolved pigeonite. In the site assignments, Ti, Cr, and octahedral Al were placed in M1; and Na, Ca, and Mn, in M2. For the pyroxene from the discrete nodule it was assumed that $Fe' = Fe^{2+} +$

$\text{Fe}^{3+} + \text{Ti} + \text{Cr} + \text{Mn}$; but in the Kakanui samples, Ti was considered separately in the refinement, hence $\text{Fe}' = \text{Fe}^{2+} + \text{Fe}^{3+} + \text{Cr} + \text{Mn}$. The uncertainty resulting from the site occupancy refinements is approximately 0.004.

The details of the crystal structure of the discrete clinopyroxene nodule were described by McCallister, Finger, and Ohashi (*Year Book 73*): Its bulk composition was corrected for the presence of approximately 10% exsolved pigeonite, giving a host composition that, in terms of the $\text{CaSiO}_3\text{-MgSiO}_3\text{-FeSiO}_3$ system, corresponded to $\text{Wo}_{27.7}\text{En}_{64.3}\text{Fs}_{8.0}$. The major components outside the pyroxene quadrilateral consist of approximately 12% jadeite plus aegirine. The Fe^{3+} concentration was estimated by assuming stoichiometry (Finger, *Year Book 71*, pp. 600–603). Since that time, annealing experiments and crystal structure refinements have been carried out on crystals of the nodule, and the data are presented in Table 30 and Fig. 85.

The K_d determined for the untreated material is 0.068 ± 0.013 . This low value, implying a high degree of order, corresponds to a temperature of $530^\circ \pm 50^\circ\text{C}$. The low temperature, determined from the experimental study, is in accord with temperature estimates made by other investigators for kimberlites from other localities. For example, Brookins and Meyer (1974) have suggested that the emplacement temperature of kimberlite in Riley County, Kansas, was about 200°C , and McFadden (1973), on

TABLE 30. Equilibrium Distribution Coefficients as a Function of Temperature for the Discrete Clinopyroxene Nodule from the Thaba Putsoa Pipe, Lesotho

$T(^{\circ}\text{C})$	Time (hrs)	K_d
625	739.0	0.082 ± 0.011
675	158.5	0.108 ± 0.019
675*	168.0	0.108 ± 0.019
802	141.5	0.123 ± 0.014
927	42.0	0.175 ± 0.022

* Initially disordered at 927°C for 42 hours.

DISCRETE NODULE

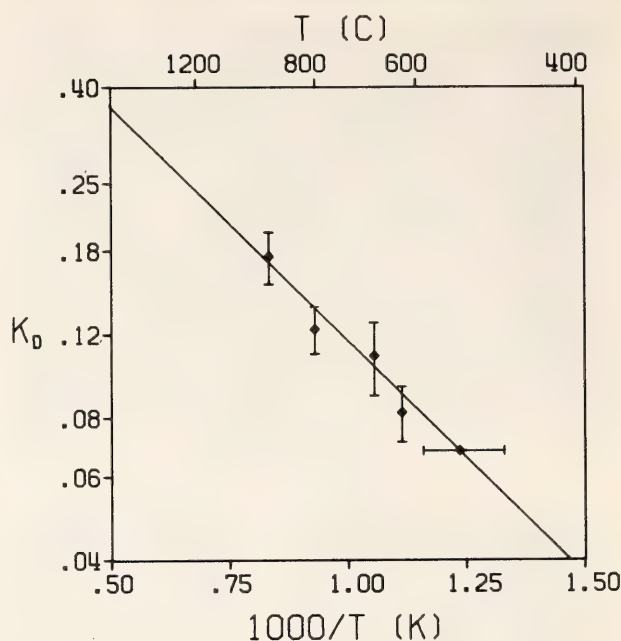


Fig. 85. $\ln K_d$ vs. $1/T^{\circ}\text{K} \times 1000$ for the discrete clinopyroxene nodule from the Thaba Putsoa kimberlite pipe, Lesotho. Error bars represent 1σ .

the basis of thermal demagnetization experiments on samples of the Ventersdorp Lava and heat flow calculations, estimated an emplacement temperature for the kimberlite at the DeBeers Mine of 550° to 620°C .

A second set of annealing experiments was made on portions of the Kakanui clinopyroxene megacryst. Representative crystallographic and chemical data are presented in Table 31. The nominal composition of this material is $\text{Wo}_{38.4}\text{En}_{53.4}\text{Fs}_{8.2}$; the main additional normative constituents are approximately 9.5 jadeite plus aegirine. The results of the site occupancy refinements on single crystals from each annealing run are presented in Table 32 and Fig. 86.

Unlike the discrete clinopyroxene nodule, which was found to be ordered, the megacryst from Kakanui is significantly disordered, having a K_d of 0.289 ± 0.042 . On the basis of a weighted least-squares fit of the data in Table 32, this K_d corresponds to a temperature of $1367^\circ \pm 120^\circ\text{C}$. The uncertainty in this number is large, but the lower temperature limit

TABLE 31. Chemical and Crystallographic Data for the Kakanui Clinopyroxenes

	Megacryst*	Eclogite
Cations per 6 Oxygen Atoms		
Na	0.093	0.198
Mg	0.885	0.677
Al	0.350	0.316
Si	1.822	1.854
Ca	0.634	0.594
Ti	0.023	0.024
Cr	0.004	0.004
Mn	0.005	0.007
Fe ²⁺	0.134	0.213
Fe ³⁺	0.048	0.114
Cell Dimensions†		
a, Å	9.684(2)	9.683(3)
b, Å	8.840(3)	8.846(3)
c, Å	5.266(1)	5.264(1)
β, deg.	106.89(3)	106.83(2)
V, Å ³	431.3(2)	431.6(2)
Calculated Density (g/cm ³)		
	3.35	3.39
Size of Crystal (mm)		
	0.070 × 0.140 × 0.210	0.042 × 0.019 × 0.168
Linear Absorption Coefficient (cm ⁻¹) for Mo Kα		
	21.9	25.6

* Data are representative and were taken from the untreated sample.
† Cell dimensions were obtained from four-circle diffractometer.

TABLE 32. Equilibrium Distribution Coefficients as a Function of Temperature for the Clinopyroxene Megacryst from Kakanui, New Zealand

T(°C)	Time (hrs)	K _d
1350*	3.75	0.250 ± 0.024
1250*	7.0	0.253 ± 0.024
927	152.25	0.162 ± 0.022
927	152.25	0.139 ± 0.022
802	89.25	0.096 ± 0.015
802†	96.0	0.123 ± 0.020
675	302.5	0.066 ± 0.013

* 20 kbar, graphite container.
† Disordered from 675°C.

KAKANUI AUGITE

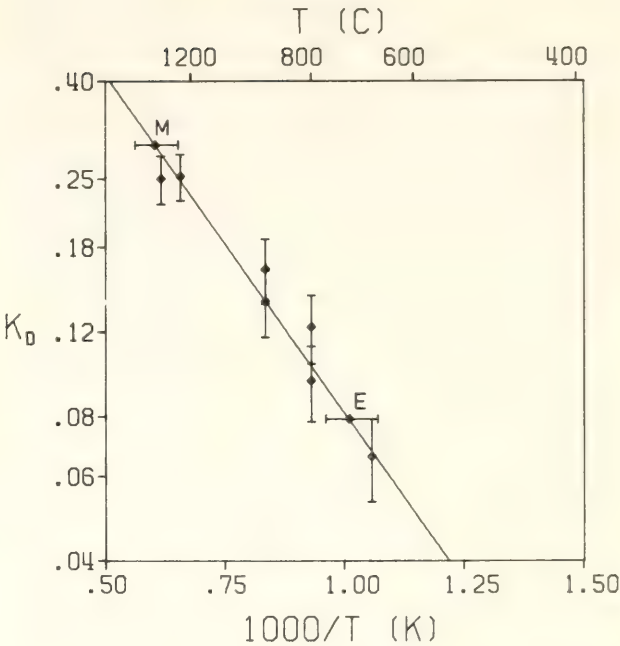


Fig. 86. $\ln K_d$ vs. $1/T^\circ\text{K} \times 1000$ for the clinopyroxene samples from Kakanui, New Zealand. Solid diamonds are the results of annealing experiments at 20 kbar and 1350° and 1250°C; open diamonds represent runs performed in evacuated SiO glass tubes. The diamonds labeled M and E are the data for the untreated megacryst and eclogite clinopyroxenes, respectively. Error bars are 1σ .

lies within the estimated temperature of 1200°–1300°C given by Merrill and Wyllie (1975) for the megacryst crystallization. Also, if it is assumed that the garnet megacrysts present at Kakanui were in equilibrium with the clinopyroxene megacrysts, a $K_D[(\text{Mg}/\text{Fe}^{2+})_{\text{garnet}}/(\text{Mg}/\text{Fe}^{2+})_{\text{clinopyroxene}}]$ of 0.482 is obtained. This value, when compared with the experimental K_D values determined by Akella and Boyd (*Year Book* 73, pp. 269–273) and Hensen (*Year Book* 72, pp. 527–534), indicates an equilibration temperature of approximately 1325°C. Thus, both inter- and intracrystalline equilibrium constants yield the same temperature. One final point worth mentioning is that at 1250° and 1350°C the $\text{Wo}_{38.4}$ (mol %) composition is outside the two-pyroxene miscibility gap at 20 kbar. Because the experiments were carried out using graphite containers,

however, the samples were reduced to the point of having no ferric iron, as indicated by the ideal pyroxene stoichiometry shown by the electron microprobe analysis. Accordingly, no Fe^{3+} contribution to the total iron in M1 was subtracted; whereas in all other runs 27% of the total iron was considered to be Fe^{3+} , and consequently was subtracted from the refined M1 iron occupancy.

In order to obtain a more complete understanding of the clinopyroxenes from Kakanui, a sample from a kaersutite-bearing eclogite was also studied. The chemistry and crystallographic data of the sample that was refined are presented in Table 31. The normative composition of this material is $\text{Wo}_{40.0}\text{En}_{45.6}\text{Fs}_{14.4}$, and because the Wo content is similar to that of the megacryst ($\text{Wo}_{38.4}$) the K_d has been referred to the megacryst calibration curve. The observed K_d of 0.077 ± 0.021 yields a temperature of $710^\circ \pm 50^\circ\text{C}$. This result is also consistent with the experimental study of Merrill and Wyllie (1975), who suggest that the Kakanui eclogites cooled in the subsolidus to $700^\circ\text{--}800^\circ\text{C}$ prior to eruption.

It is obvious from the above examples that studies of intracrystalline distribution of Fe^{2+} and Mg in clinopyroxenes can contribute to the understanding of geologic processes associated with their crystallization and subsolidus cooling.

However, it will be necessary to understand the kinetics of order and disorder in Ca-rich clinopyroxenes and to develop a solution model appropriate to the equilibrium data before detailed thermal histories may be inferred. Because of the uncertainty in interpreting Mössbauer spectra of clinopyroxenes (cf. Virgo, *Year Book* 72, pp. 540–544; Dowty and Lindsley, 1973), complete x-ray crystal-structure analyses have been performed on single crystals. Although this technique is considerably more time-consuming than Mössbauer resonance spectroscopy, at present it provides the only reasonable alternative. Correlation between Mössbauer results and x-ray studies on a wide variety of clinopyroxene compositions may lead to a procedure to correct for the problems associated with interpreting the Mössbauer data on the basis of a simple two-doublet fit.

STATISTICAL PETROLOGY

F. Chayes

It has been shown (*Year Book* 73, pp. 480–488) that an electronic data base for igneous petrology characterized by much broader coverage and deeper information content than in those currently available is now feasible, and it has been argued (Chayes, 1975) that such a base is imperative if conventional scholarly standards are to be maintained without further crippling fragmentation of the science. The inception and current status of a project whose objective is the construction of a new and more satisfactory world data base for igneous petrology are briefly noted in a later section of this report. One of the immediate consequences of the decision to begin design of the new data base has been cessation of further systematic expansion of the

base developed and used in this Laboratory. It seems appropriate at this time, therefore, to review progress on a few of the continuing major synoptic reductions of data drawn from that base, which now contains complete essential oxide analyses of nearly 12,000 specimens of Cenozoic volcanic rocks.

Distribution of Major Oxides in Cenozoic Volcanics: SiO_2

More than a half century ago Daly (1914) concluded that most volcanic rocks are of basaltic or andesitic composition, and that most plutonic rocks are granitic or granodioritic. Although apparently carried out contemporaneously with preparation of his widely used set of average values noted below,

the study leading to this dictum was based not on relative frequencies of analyses but on quantitative and semi-quantitative planimetric measurements of areas occupied by various petrographically defined symbols on geological maps.

In 1922 Richardson and Sneesby published their well-known plot of the distribution of SiO_2 in the analyses contained in what proved to be the final edition of Washington's (1917) compendium of *Chemical Analyses of Igneous Rocks*. The Richardson-Sneesby diagram shows a broad, centrally located minimum. There is considerable scatter of the data points in this region, so that neither the shape of the curve nor the position of the minimum can be precisely fixed. But it is clear from the diagram that the table contains far fewer analyses of intermediate content than of either basaltic or granitic SiO_2 content. Richardson and Sneesby concluded "it will be evident that we have arrived at the same result as Daly," but although their diagram is often reproduced, their suggestion of its potential importance is usually—there are conspicuous exceptions—accepted with strong reservations or simply ignored.

Indeed, their announcement was premature; their result is surely compatible with Daly's position, but the relation between mode of occurrence and chemical composition proposed by Daly is only one of many ways in which the bimodality of SiO_2 shown in their diagram might have been generated. It would be possible, for instance, for the low-silica peak of the Richardson-Sneesby diagram to include the mean value for basalt and yet contain as many analyses of gabbro as of basalt; similarly, the high-silica peak might include the mean value for granite and yet contain as many analyses of rhyolite as of granite. Clearly the distribution of SiO_2 in either volcanic or plutonic rocks separately must be available for comparison with the overall diagram before one can decide whether Richardson and Sneesby did confirm

Daly's result by an independent method; generations of petrologists must have been aware of this, but despite the obvious interest of the matter no one seems to have had the patience and courage to extract complete data for either class from Washington's table, in which analyses are sequenced without regard to mode of occurrence.

The distribution of SiO_2 in the analyses of nonplutonic rocks* contained in the data base of system RKNFSYS, shown in Fig. 87A, strongly suggests that Richardson and Sneesby did indeed make the right guess. This sample distribution exhibits a pronounced positive skew from a maximum that includes the averages of both alkaline and subalkaline basalt; the skew persists, and the position of the maximum remains virtually unchanged, if excessively oxidized or hydrous materials are eliminated from the tally.

For the purpose of this study, excessive hydration and oxidation—features considered indicative of possible post-emplacement alteration, whether hydrothermal or surficial—were arbitrarily defined as total H_2O in excess of 2%, and Fe^{3+} ions in excess of Fe^{2+} ions. As shown in Fig. 87B, however, these criteria reach maximum effectiveness in quite different parts of the silica range. For a given range of SiO_2 content the number of analyses in which $\text{H}_2\text{O} > 2\%$ is roughly proportional to the number of analyses available, as if H_2O were simply a diluent of the rock as a whole. The distribution of SiO_2 in the 3183 rocks containing more than 2% H_2O is thus very like that in the initial collection. The oxidation criterion, on the other hand, reaches maximum effect in the intermediate silica range, eliminat-

* Of the 11,978 specimens whose analyses are stored in the base, 270 are unnamed in the source references; 296 may or may not be named in the source references but are unnamed in the base; and another 542 bear names, e.g., syenite, harzburgite, generally not indicative of volcanic origin. All three categories are excluded from the work reported in this section.

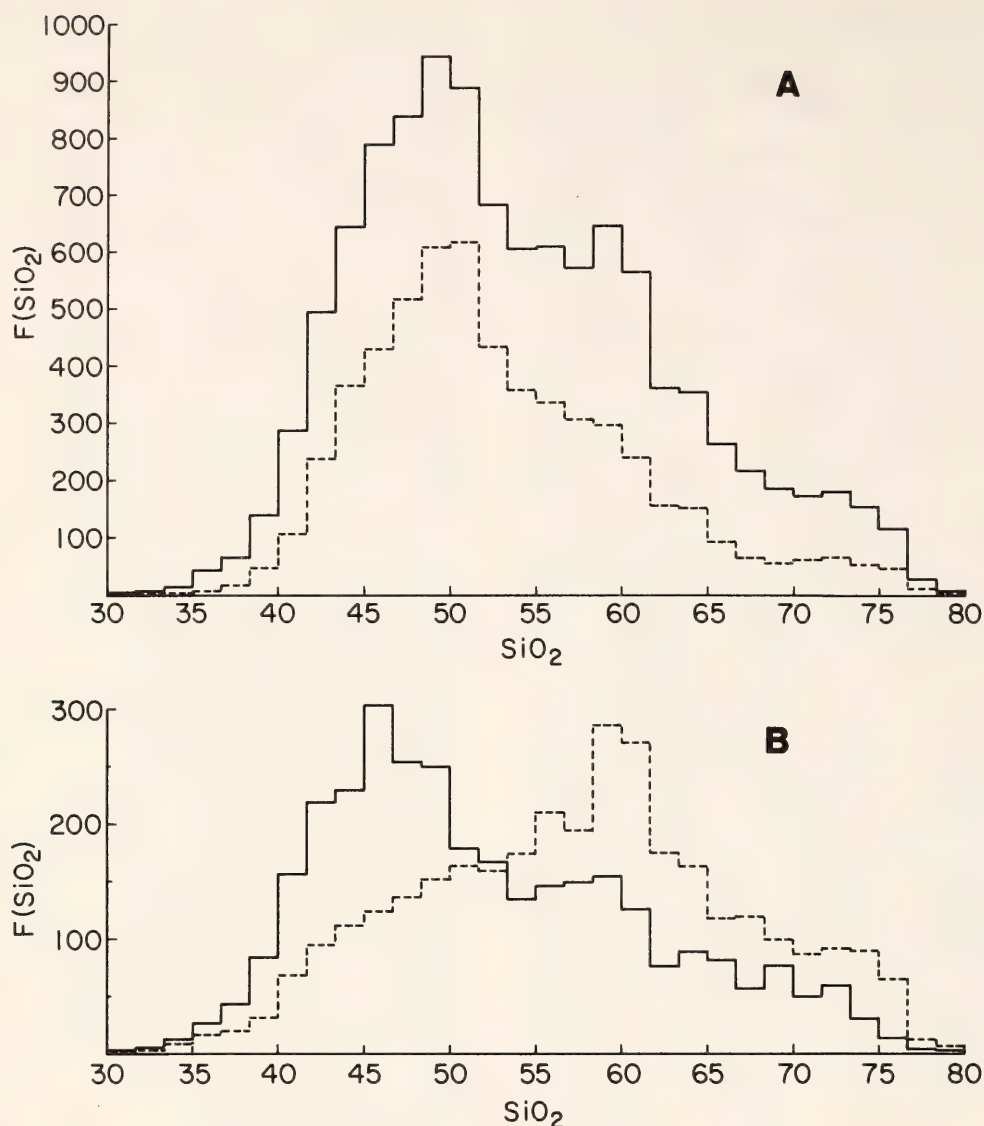


Fig. 87. Distribution of SiO₂ in 10,870 analyses of Cenozoic volcanic rocks. (A) Solid line, all data; dashed line, 5697 analyses with H₂O < 2 and Fe³⁺/Fe²⁺ < 1. (B) Solid line, 3183 analyses with H₂O ≥ 2; dashed line, 3253 analyses with Fe³⁺/Fe²⁺ ≥ 1.

ing many andesites, very large numbers of trachytes and rhyolites, and most of the phonolites, latites, and trachyandesites from the tally. This strongly localized effect is rather unexpected, and it is clear that the Fe³⁺/Fe²⁺ ratio deserves much more careful study and consideration than it has received. It evidently varies directly, but not simply, with SiO₂ content, H₂O content, and alkali content. It may also be subject to geographic (geotectonic?) influence; a very large proportion of the analyses in which Fe³⁺ > Fe²⁺ are of European specimens.

Figure 87B scarcely suggests a direct

variation of oxidation ratio with H₂O content, but it is nevertheless true that the number of specimens qualifying for either rejection or acceptance on both scores is significantly larger than would be expected if these properties were independent. Specifically, of 10,870 specimens, H₂O > 2% in 3183 and Fe³⁺/Fe²⁺ > 1 in 3253. On the hypothesis of independence, therefore, the expected number qualifying for rejection on both counts is $(3183)(3253)/10,870 = 953$, whereas the number actually found is 1263; similarly, the expected number of acceptable specimens is 5387, and the observed number is 5697. As regards the

association of high oxidation ratio with alkaline affinity, it is perhaps worth noting that a similar tendency has been detected (Chayes, *Year Book* 72, pp. 671–673) even among basalts that project in the *di-ol-hy* ternary.

All of this discussion, however, is incidental to the main issue, which is simply that, in a sample so large it can hardly be misleading, the distribution of SiO_2 in published analyses of Cenozoic volcanic rocks shows a strong positive skew. This is as clear from the solid line of Fig. 87A as it is from the dashed one. Because neither gabbro nor rhyolite is rare, or even, in an absolute sense, uncommon, Daly's relation implies that the distribution of SiO_2 is positively skewed in volcanic rocks and negatively skewed in plutonic ones. The appropriate skew is surely established now for published information about Cenozoic volcanic rocks and from data most of which were unavailable both to Daly and to Sneesby and Richardson. Whether the appropriately opposed skew is characteristic of Cenozoic plutonics, and whether similar relations hold for pre-Cenozoic rocks, are questions that obviously can not be resolved by data reductions obtained from a base confined to the products of Cenozoic volcanism. They certainly could be examined if a suitably comprehensive base of the kind suggested below were available.

If the gross relation between chemical composition and mode of occurrence announced so long ago by Daly is still not, as Sneesby and Richardson aver "a fact of the first order of importance of which any general theory of petrogenesis must take cognizance," it is assuredly one of the major descriptive hypotheses awaiting definitive test by contemporary petrographers.

The Names of Cenozoic Volcanic Rocks

Prompted by the commission on Systematics in Petrology of the International Union of Geological Sciences, there is

currently considerable discussion of rock nomenclature and taxonomy, subjects that would hardly receive much attention if they did not seriously need it. Most of the commoner names of volcanic rocks have been in general use for a very long time, so decisions about how they ought to be used must be strongly conditioned by how in fact they have been and are used. Unless a prescribed redefinition coincides fairly well with established usage it will create endless confusion, for the student of the subject encounters the commoner names of rocks much more frequently in their past than in their present incarnations. This, of course, is not to say either that no restrictions should be imposed on future usage of existing names or that no new names should be proposed. Nevertheless, the first business of the systematist who contemplates prescribing future usage of the commoner rock names is clearly to discover in the published *corpus* of the subject the shared properties of the objects they denote. In the widely scattered, multilingual technical literature of petrology this is a formidable task, and the ways in which a sophisticated electronic information system could be of assistance in it are obvious. In designing the work reviewed in the next two sections of this report, for instance, some notion of the incidence of the commoner rock names was essential. This kind of information is readily obtained from the existing data base, which contains, with exceptions noted above, the name by which each specimen is denoted in the reference from which its analysis was drawn.

It is of course no secret that most students of volcanic rocks actually use rather few of the plethora of available rock names, but the paucity of working names for these objects is far more extreme than is usually supposed. Some 226 words appear as nouns in the 10,870 rock names stored in the existing base. The primary petrological connotation of

TABLE 33. Frequency of Occurrence of 203 Principal Nouns in the Names of 10,870 Cenozoic Volcanic Rocks

Names	Frequency of Occurrence of Each Name in Existing Data Base
Andesite, basalt	>2000
Basanite, dacite, phonolite; rhyolite, trachyandesite, trachybasalt, trachyte	200-1999
Ankaratrite, ankaramite, comendite, diabase, dolerite, latite, leucitite, limburgite, mugearite, nephelinite, oceanite, plagiliparite, rhyodacite, tephrite, tholeiite	56-199
Doreite, labradorite, ordanchite, pantellerite, shoshonite, tahitite, trachydolerite, verite, vicoite	20-55
All others (170)	<20

203 of these nouns is compositional,* so their average incidence in the file is approximately 56. Actually, only 24—less than an eighth—occur that often; 9 are used more than 200 times and 2 more than 2000 times each. The frequency of occurrence of compositional nouns (and leading compositional nominal adjectives modifying noncompositional nouns) in the base is summarized in Table 33.

Nearly half the analyses in the collection are of rocks denoted in the source references by one of just two principal nouns—andesite or basalt—and another quarter require less than 4% of the available stock of rock names. It is to be remembered that neither the broad characterizations sometimes unavoidable in areal geology nor the casual identifications based on hand-specimen examination are at issue, but only the incidence of names applied to individual specimens

* There are in all 23 (e.g., pumice, breccia, porphyry) with noncompositional connotation; in practice each is often, but by no means always, preceded by a compositional nominal adjective.

for which full chemical analyses and, in most cases, rather extensive petrographic descriptions are available. Further, most of the analyses and descriptions are fairly recent; only 17% were published prior to 1940 and 63% bear publication dates later than 1960. Surely this tally reflects a strong and rather general indisposition on the part of the informed public to apply the rich nomenclatures offered by systematists. It also indicates where effort should be concentrated in an attempt to characterize the chemical composition and variation of the commoner Cenozoic volcanic rocks, and that is the principal reason for its discussion here.

On Distinguishing Alkaline from Other Basalts

The equation of the field boundary separating Hawaiian alkali and tholeiitic basalts in the well-known diagram of Macdonald and Katsura (1964) is approximately

$$D_m = 0.374 \text{ SiO}_2 - \text{Na}_2\text{O} - \text{K}_2\text{O} - 14.63.*$$

The projection of a specimen will fall in the tholeiitic or alkali-basalt field of their diagram depending on whether or not $D_m > 0$. The graphical location of the field boundary (and hence the equation of the function) is based on detailed petrographic examination of the same specimens for which complete chemical analyses were available, and the check between the *a priori* mineralogical and *a posteriori* chemical discriminations is nearly letter perfect. These authors believed that similar classification might be equally effective for basaltic suites from other areas but thought that the position of the field boundary might differ considerably from suite to suite.

The writer (Chayes, 1966) later suggested a twofold subdivision of Cenozoic

* Normative rationalizations of this field boundary have been proposed by Yoder (see Macdonald and Katsura, 1964, p. 86) and McBirney and Williams (1969, pp. 129-130).

basalts in which ($ne + q = 0$) into those with which nonbasaltic alkaline extrusives are or are not closely associated. Considerably more than two thirds of the basalt analyses in question are either ne - or q -normative. Their *a posteriori* chemical classification presents no problem; the former are alkaline, the latter subalkaline. With classification of the remainder by linear or quadratic discriminants calculated from any two of the ternary ratios $ol:di:hy$, the numerical classification into alkaline and subalkaline basalts recaptures with 95% consistency the *a priori* partition based on association with nonbasaltic alkaline extrusives. The linear discriminant generated from noncontinental materials for this purpose is

$$D_c = hy' + 0.134\ ol' - 26.942,$$

where $hy' = 100\ hy/(ol + di + hy)$, $ol' = 100\ ol/(ol + di + hy)$, and a specimen is classified as subalkaline if $D_c > 0$, alkaline if $D_c < 0$.

Until recently a comparison of the performance of the two discriminants would have required custom programming or an excessive amount of hand calculation. It can now be performed as a matter of routine. For 627 Hawaiian analyses now contained in the data base of the information system RKNFSYS the results are as shown in Table 34; 87% of the analyses are consistently classified by the two discriminants, and it is quite possible that inconsistencies arise more from compositional peculiarities of Hawaiian lavas than from inadequacies of the hy' - ol' discriminant.

In the work reviewed in the next section, partition of basalts into alkaline and subalkaline variants is necessary. As the kind of mineralogical information required for proper application of the Macdonald-Katsura procedure is not contained in the existing data base, and is in fact lacking in a great many of the source references, the partition has been effected by means of the linear hy' - ol' discriminant.

TABLE 34. Consistency of Partition of 627 Analyses of Hawaiian Lavas by Means of the ol' - hy' Linear Discriminant (D)_c and the Numerical Equivalent of the Macdonald-Katsura Procedure (D)_m*

D_m	D_c		
	>0	<0	
>0	400	42	442
<0	39	146	185
Totals	439	188	627

* Row totals are the numbers of tholeiitic and alkaline basalts indicated by D_m ; column totals, the number of subalkaline and alkaline basalts yielded by D_c .

Average Compositions of the Commoner Cenozoic Volcanic Rocks

The chemical compositions of the commoner igneous rocks, perhaps of special concern to petrologists and geochemists, are of major interest to all who speculate or argue about the properties and history of the lithosphere. This information usually takes the form of averages based on literature surveys varying in coverage and selectivity. The best-known set of such averages, and perhaps even now the most widely used, is that published in 1910, and reissued with revisions in 1914 and 1933, by Daly. The only other comparably comprehensive collection is by Nockolds (1954).

It is obvious that the existing data base of system RKNFSYS can be used to generate a similar set of averages for Cenozoic volcanic rocks, and a comparison of these with the stratigraphically more inclusive sets of Daly and Nockolds would be of considerable interest. Further, less than 1% of the analyses in the base were available to Daly in 1910, and Nockolds could have had access to little more than 25% of them in 1954. On this ground alone close comparison of the three sets is in order. Such a comparison is under way and will be presented elsewhere; here only summary results of the current compilation are

TABLE 35. Average Values for the Compositions of the More Common Cenozoic Rocks*

	Rhyo- lite	Dacite	Andesite	Subalkaline Basalt	Alkaline Basalt	Basa- nite	Trachy- basalt	Trachy- andesite	Phono- lite	Trachyte with $Q=0$	Trachyte with $Q>0$
A. All Analyses in Base											
No. of analyses:	547	495	2177	1366	1698	338	229	231	446	264	332
SiO ₂	71.56	65.33	58.19	50.48	45.56	43.74	48.54	57.72	56.70	58.28	63.02
Al ₂ O ₃	13.58	15.58	17.22	16.19	14.61	14.31	16.56	16.96	19.06	18.28	16.48
Fe ₂ O ₃	1.58	2.37	3.09	3.68	4.27	4.47	3.65	3.22	2.71	2.93	2.92
FeO	1.10	2.33	4.05	6.84	7.38	7.25	6.24	3.30	1.70	2.00	1.84
MgO	0.47	1.62	3.22	6.23	8.45	8.64	5.81	2.29	1.04	1.20	0.75
CaO	1.41	4.31	6.81	9.40	10.23	10.59	8.28	5.18	2.62	3.05	1.95
Na ₂ O	3.80	3.72	3.29	2.66	3.20	3.54	3.95	4.37	7.55	6.63	5.47
K ₂ O	4.19	2.27	1.68	0.91	1.40	1.76	2.29	3.20	5.17	4.82	4.75
TiO ₂	0.32	0.62	0.82	1.63	2.55	2.81	2.25	1.22	0.84	0.86	0.70
P ₂ O ₅	0.12	0.18	0.23	0.31	0.59	0.68	0.67	0.48	0.22	0.25	0.19
MnO	0.07	0.12	0.15	0.17	0.18	0.18	0.18	0.15	0.21	0.19	0.15
ΣH ₂ O	1.96	1.54	1.33	1.43	1.56	1.88	1.55	1.88	1.99	1.47	1.63
B. Screened Sample											
No. of analyses:	389	274	1059	890	961	193	144	89	88	76	74
SiO ₂	72.54	65.26	58.69	51.03	45.68	44.32	48.66	57.16	57.32	58.53	63.29
Al ₂ O ₃	13.47	15.76	17.02	16.45	14.68	14.33	16.79	17.25	18.99	18.35	15.99
Fe ₂ O ₃	0.92	1.80	2.55	3.06	3.58	3.88	3.11	2.61	1.83	2.09	1.93
FeO	1.82	3.11	4.61	7.42	8.14	7.97	6.93	4.39	2.83	3.23	3.47
MgO	0.53	1.77	3.31	6.25	8.92	8.69	5.82	2.52	1.15	1.09	0.81
CaO	1.47	4.60	6.70	9.76	10.44	10.65	8.41	5.26	2.68	3.00	2.38
Na ₂ O	4.05	3.84	3.54	2.57	3.11	3.58	4.03	4.74	7.88	6.34	5.58
K ₂ O	4.06	2.12	1.62	0.80	1.30	1.84	2.25	3.09	4.81	4.99	4.28
TiO ₂	0.31	0.65	0.86	1.53	2.58	2.89	2.29	1.40	0.96	0.82	0.75
P ₂ O ₅	0.12	0.17	0.25	0.24	0.52	0.67	0.67	0.50	0.28	0.25	0.21
MnO	0.08	0.13	0.14	0.17	0.17	0.18	0.18	0.18	0.23	0.19	0.16
ΣH ₂ O	0.75	0.80	0.80	0.69	0.87	0.92	0.85	0.86	0.93	1.11	0.90

* For definitions of groups see text.
A, All analyses in data base of RKNFSYS.
B, All analyses in which H₂O < 2% and Fe³⁺/Fe²⁺ < 1.

briefly reviewed. Specifically, Table 35 contains averages for all rocks whose names, shown in the first two categories of Table 33, are attached to at least 200 of the 11,978 specimens whose analyses comprise the base.

In the initial sampling, results of which are shown in Part A of Table 35, the test battery was minimal. No analysis was included in any group unless the noun in the name of the group was the noun (or leading nominal adjective modifying a noncompositional noun) in the name attached to the specimen in the source reference. Thus, specimens that perhaps should have been so denoted in the source references, but in fact were not, are omitted; and rocks that perhaps should not have been so denoted in the source references, but in fact were, are included. The overriding objective was to obtain in each case an average composition for rocks that had actually been described under some particular common name in the references from which the analyses were drawn.

For results given in Part A of Table 35 no other criteria were imposed in the selection of basanite, phonolite, trachyandesite, trachybasalt, or rhyolite. For reasons described at length elsewhere (Chayes, 1969) *ol*-normative analyses were filtered out of the andesite sample. Trachytes whose analyses are *ol*-normative were separated from those whose analyses are not *ol*-normative. Finally, basalts were split into alkaline and subalkaline groups by means of the *ol'*-*hy'* discriminant described above.*

In the sampling leading to results shown in Part B of Table 35 further selection criteria were imposed. Analyses in which $H_2O > 2\%$ or the molar ratio $2Fe_2O_3/FeO > 1$ were excluded from

all groups. Further, andesites in which the *an* content of normative plagioclase is greater than the average value for basalt (58.5) were eliminated, as were basalts (alkaline or subalkaline) in which the *an* content of normative plagioclase is less than the average value for andesite (48). Although these restrictions do not seem harsh, they are nevertheless sufficient to approximately halve the size of the basalt and andesite samples, and their effect on certain other varieties is devastating. The use of oxidation state as a rejection criterion of course has the expected effect on Fe_2O_3 and FeO values, but it is notable that in other respects the differences between analogous entries in the two parts of Table 35 are for the most part rather slight, even when screening eliminates much of the data.

A World Data Base for Igneous Petrology

Material scattered through technical publications in many different countries and languages would be better collected by an international group than by an individual or national organization. The extraction of chemical analyses from petrographic publications is a case in point, but while the data base was restricted to quantitative data the organization of such a group seemed premature and unwise, for it seemed obvious that whatever work it did would soon have to be redone. From work reported in *Year Book 73* (pp. 480–488) it is clear that qualitative mineralogical, petrographic, and geological data concerning the analyzed specimens could readily be incorporated in and selectively retrieved from a properly designed base. There is thus no further reason to delay beginning construction of a world data base for igneous petrology, and at the writer's request, the International Mineralogical Association has created a working group to advise on and guide this work.

The first problem facing the group was design of a data form (a) that could be

* One of the unexpected consequences of this selection procedure is that alkali basalt is in many respects more "basanitic" in composition than basanite! As with andesite and dacite (Chayes, *Year Book 68*, p. 177), most petrologists call basalt what some petrologists call basanite.

completed with little clerical work by petrologists who volunteered to scan particular publications, (b) that could be used directly as copy by a keypunch operator working with a minimum of professional supervision, and (c) in which the information was so structured as to permit its ready incorporation in and utilization by a system designed to place major stress on selection and reduction rather than retrieval.

At first it was supposed that the work of system development could proceed more or less independently of what seemed the not particularly interesting business of designing the data form, but it soon turned out that this would be extremely impractical if not impossible. A provisional form, based upon the record structure proposed in *Year Book 73* and providing for mineralogical and petrographic "vocabularies" of 32 words each, was circulated for criticism. A vocabulary of 32 terms can be referenced on the bits of a single computer word, and it was considered safe to allot three words of each analysis record to the storage of qualitative, attribute-type data—one for phenocryst minerals, one for groundmass minerals, and one for petrographic descriptors. As the correspondents of the group submitted their comments and suggestions, the mineralogical and petrographic vocabularies increased in size. By the time the review was complete and a trial form satisfactory to most correspondents had been developed, there were 95 words in the mineralogical vocabulary and 88 in the petrographic vocabulary. (Copies of the form are available to interested readers.)

Whether word lists of this length are referenced better by key bits or key numbers is a purely practical problem, but the choice between these alternatives strongly influences design of the basic elements of the system, the programs

that build, edit, and scan the data base. To choose intelligently between them one must know not only the number of words in each list but also, with fair precision, the average number that will be used in a single observation record. An experiment intended only to provide information about nonelectronic aspects of the construction of the new data base thus turns out to be of crucial and immediate importance in the design of the system.

NTRM, a Major Revision of RKNFSYS

Even with generous collaboration by interested petrologists and adequate financial support, considerable time will elapse before the new data base discussed in the preceding section is large enough to be of general utility to the profession. In the meantime, if support is available, service will be maintained under NTRM, an extensive revision and improvement of RKNFSYS developed during the report year. NTRM reads a restructured version of the existing data base that uses about a third less storage space than was previously required. From the user's point of view the major distinction between NTRM and its predecessors is in relaxation and standardization of input format. Under the new format the user references all variables by name rather than number, introduces specification lists in almost any order that seems reasonable to him, and both sequences and spaces items in any list in almost any way he chooses. Designed to facilitate development of a version that would permit conversational communication between the system and users establishing contact with it via remote terminal, the new format also greatly simplifies preparation of card copy for ordinary batch mode operation. A user's manual for version NTRM is available for distribution to interested readers.

MINERALOGY

THE EFFECT OF PRESSURE ON THE
COVALENCY OF Fe^{2+} -OXYGEN BONDS*Frank E. Huggins*

The changes that chemical bonds undergo upon compression have many possible implications for studies of the earth's interior. Among the ions of major abundance in the earth, however, only ferrous cations give rise to parameters that provide a qualitative understanding of the effect of pressure on the covalency of cation-oxygen bonds. Such parameters include the isomer shift and quadrupole splitting from Mössbauer spectra and the energies of spin-forbidden bands in optical spectra of ferrous phase. In this report, data on the effect of pressure on these parameters are used to indicate the manner in which Fe^{2+} -oxygen bonds undergo compression.

The spectral parameters referred to above may be used as measures of the changes in covalency between the ferrous orbitals and their neighboring anions. Specifically, the $3d$ electrons are primarily involved in the bonding and determine the spectral parameters. Energy-level schemes for the five $3d$ orbitals in various regular and distorted coordinations are shown in Fig. 88. For ferrous

cations, the isomer shift is determined by all six $3d$ electrons over the five $3d$ orbitals and thus may be used as a measure of the overall covalency; whereas the quadrupole splitting, according to the model of Ingalls (1964), is a measure of the covalency of only the set of two or three $3d$ orbitals at lower energy. The energies of spin-forbidden bands can be related to the Racah parameter, which is determined by the interelectronic repulsions of the cation. Since such repulsions depend on the interactions between anion and cation, Racah parameters and hence the energies of spin-forbidden bands are also measures of bond covalency.

The behavior of Racah parameters reflects two possible types of covalency (Jørgensen, 1962), central-field and symmetry-restricted. The former describes expansion of the cation orbitals owing to the presence of the anions, reducing the effective nuclear charge of the cation, and the latter describes effects arising from specific screening interactions between cation and anion electrons (π or σ bonding effects). Changes in central-field covalency have been shown to be the dominant factor accounting for the variation of covalency of Fe^{2+} -ligand bonds as a function of the coordinating ligand (Hazony, 1971). It has generally been assumed that this factor will predominate also in changes of bond covalency caused by increasing pressure (Drickamer and Frank, 1973). This assumption has not been confirmed, however, as the observed decreases in Racah parameter with increasing pressure (Drickamer, 1965; Abu-Eid, 1975) could result from changes in either symmetry-restricted or central-field covalency. For ferrous phases, the pressure-induced shifts of spin-forbidden bands could also arise from changes in either type of covalency. In the present study, however, by considering evidence from both Mössbauer and optical spectra as a function of pressure, a more defini-

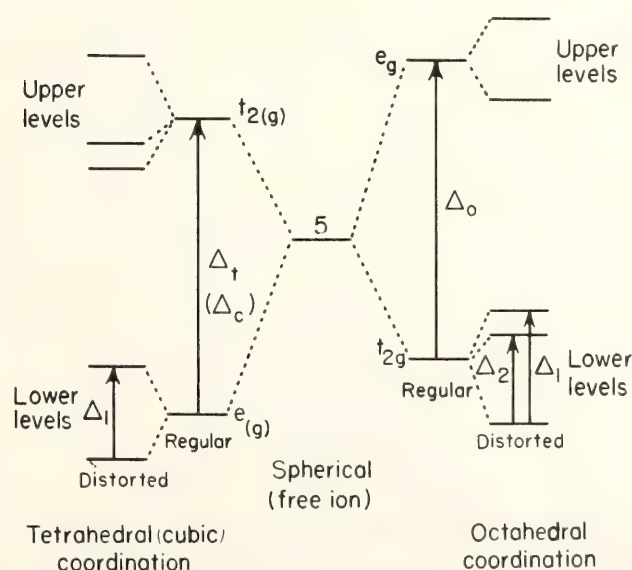


Fig. 88. The $3d$ energy levels of ferrous iron in various regular and distorted coordinations.

tive understanding of the interrelationship between bond covalency and bond compression for Fe^{2+} -oxygen bonds is obtained.

Figure 89 shows the changes in the Mössbauer parameters of ferrous cations in fluorine and oxygen environments resulting from pressures of up to 200 kbar. Two general trends with increasing pressure are immediately apparent: first, all isomer-shift trends decrease; second, the majority of quadrupole-splitting trends increase. The ubiquitous decrease in isomer shift reflects the fact that this parameter is independent of the crystal structure and depends only on the immediate interactions between ferrous cations and the ligands. Because decreasing values of isomer shift reflect increasing s electron density at the nucleus, it can be concluded that some or all of the $3d$ electrons interact less with their own s electrons with increasing pressure, as

a result of which the s electrons spend more time at the nucleus. This decrease in isomer shift indicates that some or all of the ferrous $3d$ electrons become delocalized with increasing pressure.

The ferrous quadrupole splitting, on the other hand, does depend on the geometry of site and is expected to be sensitive to changes in the distortion of the surrounding anion framework. The quadrupole splitting, QS , may be represented parametrically in the form (Ingalls, 1964)

$$QS = (QS_0)\alpha^2 F_{\text{val}}(\Delta_1, \Delta_2, T) + F_{\text{lat}},$$

where (QS_0) is the quadrupole splitting of a hypothetical, completely ionic ferrous species at 0°K ; α^2 is the covalency parameter; F_{val} is the valence contribution arising from the sixth $3d$ electron, which depends on temperature, T , and the distortion of the site from a regular cubic symmetry as measured by Δ_1 and

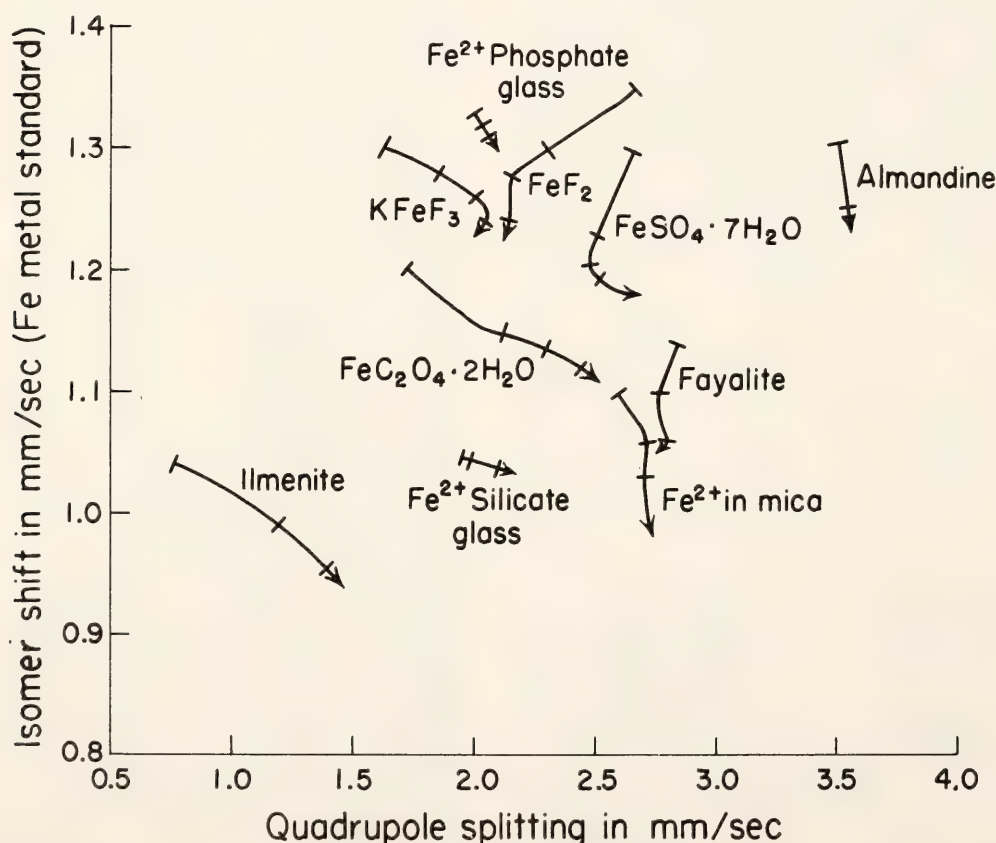


Fig. 89. The effect of pressure on the Mössbauer parameters of ionic ferrous phases. The tail of each arrow represents 0 kbar data; the gradations along each arrow represent 50 kbar intervals.

Δ_2 , the splittings of the lower set of $3d$ orbitals (Fig. 88); and F_{lat} is the lattice contribution arising from charges on the surrounding ions. The covalency parameter, α^2 , is given by

$$\alpha^2 = \langle r^{-3} \rangle / \langle r^{-3} \rangle_0$$

where $\langle r^{-3} \rangle$ is a measure of the charge density of the ferrous $3d$ orbital containing the sixth $3d$ electron in the phase and $\langle r^{-3} \rangle_0$ is the same for the hypothetical, completely ionic phase. Hence, $\langle r^{-3} \rangle$ is a measure of the covalency of the orbital. In theory, then, the changes in quadrupole splitting at constant temperature are brought about by changes in $\langle r^{-3} \rangle$ and also in Δ_1 and Δ_2 . The quadrupole splitting is determined by the sum of the valence and lattice contributions, which are generally of opposite sign, and takes the form shown in Fig. 90 as a function of site distortion. It may be concluded that actual values of the maxima in such diagrams are

determined only by the normalization factor, $(QS_0)\alpha^2$, and hence by $\langle r^{-3} \rangle$ or the orbital covalency. Of the ten phases shown in Fig. 89, it is possible to place limits on the change in $\langle r^{-3} \rangle$ with pressure for only almandine and ilmenite, as only these phases give information relating to possible changes in the values of the maxima in the quadrupole-splitting curves.

On the basis of the observed temperature dependence of the quadrupole splitting in almandine, Δ_1 can be estimated to be about $1100 \pm 50 \text{ cm}^{-1}$ for the eight coordinated ferrous cations (Lyubutin and Dodokin, 1971; Huggins, 1975). Thus, at 1 bar the site distortion is found to be slightly larger than that which gives rise to the maximum possible quadrupole-splitting value (Fig. 90A). Specifically, the quadrupole-splitting value for almandine at 1 kbar is about 0.10 mm/sec less than the maximum. As pressure is increased, the quadrupole

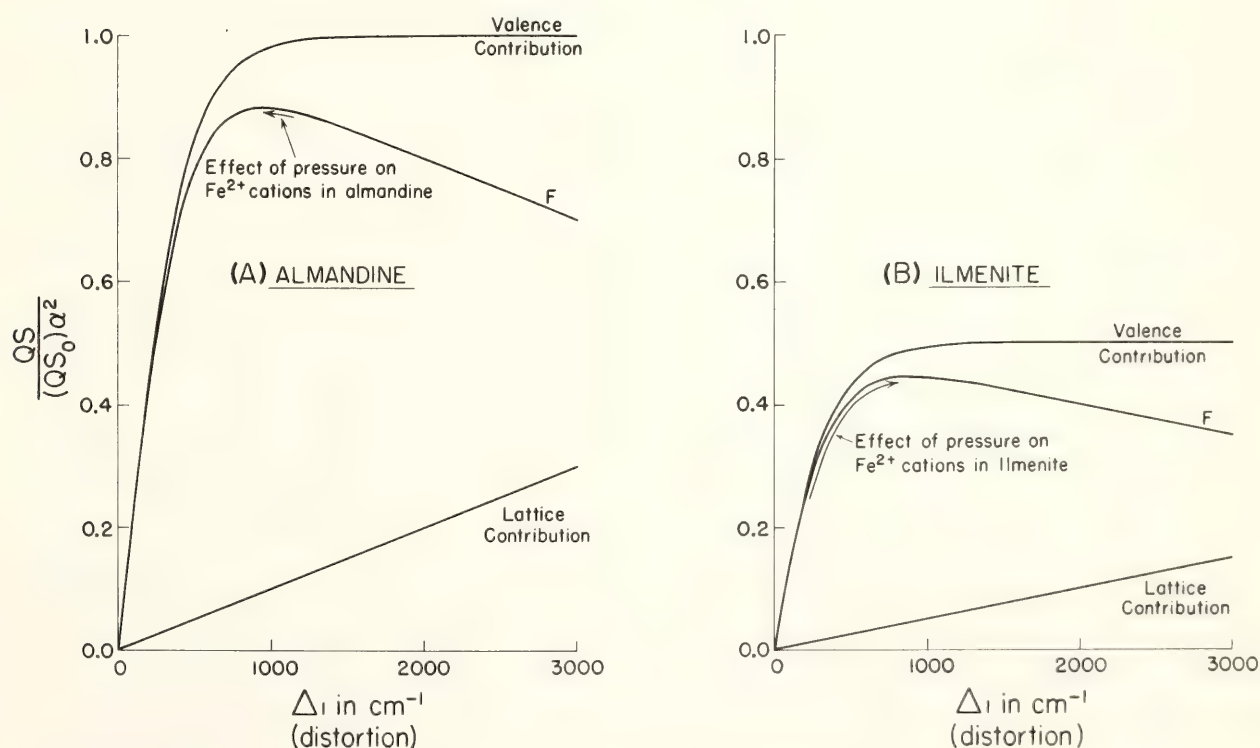


Fig. 90. Model for high-spin ferrous quadrupole splittings as a function of distortion at constant temperature. The quadrupole splitting is proportional to F , which is the difference between the valence and the lattice contributions. The lattice contribution is shown only schematically because it is not very important in determining the position of the maxima. A, model used for almandine; B, model for ilmenite.

splitting of almandine increases by 0.05 mm/sec over 150 kbar, indicating that the site distortion decreases with pressure. Hence, it is concluded that the largest possible decrease of the value of the maximum in the quadrupole splitting is 0.05 mm/sec, requiring less than a 2% change in α^2 . The data therefore eliminate the possibility of a large decrease in α^2 with pressure but do not rule out the possibility of α^2 remaining constant or increasing.

A similar explanation can also be advanced for ilmenite. Bashkirov *et al.* (1967) found that ilmenite has the following lower $3d$ splittings: $\Delta_1 = 200 \text{ cm}^{-1}$, $\Delta_2 = 0 \text{ cm}^{-1}$. Thus, in order to explain the large increase in quadrupole splitting with pressure (Fig. 89), it is inferred that the site distortion must increase rapidly and, as indicated in Fig. 90B, must cause the quadrupole splitting to reach the maximum value. Again it is found that any possible decrease in α^2 must be small.

Based on these two phases and also the fact that the majority of the quadrupole splitting trends increase with pressure, it appears that the expected pressure-induced increase in covalency is not reflected by a significant decrease in α^2 or, equivalently, by expansion of the $3d$ orbitals.

Additional evidence concerning the effect of pressure on the covalency of Fe^{2+} -oxygen bonds comes from optical absorption spectroscopy. It has been found in studies of ferrous oxides and silicates (Shankland, Duba, and Woronow, 1974; Abu-Eid, 1975) that certain ferrous spin-forbidden bands, which can be related to the Racah parameter, B , do not shift appreciably with increasing pressure. As the crystal-field parameter definitely does increase with pressure, it can be concluded with the aid of the Tanabe-Sugano diagram for d^6 (Figgis, 1966; Mao and Bell, *Year Book* 73, p. 336) that B remains constant or possibly increases with increasing pressure. As B is approximately inversely proportional

to $\langle r \rangle$ (Jørgensen, 1962), it is inferred from the behavior of the spin-forbidden bands that the ferrous $3d$ orbitals do not expand with increasing pressure. The interpretation of this behavior is consistent with the Mössbauer data, and it is concluded, on the basis of data from both techniques, that the increase in covalency of Fe^{2+} -oxygen bonds with pressure results primarily from increased symmetry-restricted covalency rather than from central-field covalency. This increase in symmetry-restricted covalency most likely comes about from an increase in overlap between the anion orbitals and the upper set of $3d$ orbitals.

The interrelationship between bond compression and bond covalency is of considerable importance for understanding pressure-induced phenomena in oxides and silicates that are likely to occur in the earth. For ferrous iron, the present study indicates that bond compression alters bond covalency by changes principally in symmetry-restricted covalency, in contrast to the changes produced by varying the ligand, in which changes in central-field covalency predominate (Hazony, 1971). Further evidence that the interaction between ferrous and oxygen orbitals increases with pressure is provided by the pressure-induced increases in the electrical conductivity and intensity of charge-transfer bands in the optical spectra of Fe^{2+} -oxygen phases (Mao, *Year Book* 72, pp. 552-557). The alternative hypothesis of increasing central-field covalency does not require these changes related to orbital overlap, but instead requires that the cation orbitals expand with pressure. This requirement may be construed as contradictory because the volume of the bulk phase generally decreases with pressure.

The present study implies that the ionic model becomes less appropriate for oxides and silicates with increasing pressure. However, properties such as electrical conductivity and metal-oxygen charge-transfer phenomena are most sensitive to the degree of overlap be-

tween cation and anion orbitals; whereas other properties, such as the systematic relationships between volume and elastic properties, which do not depend critically on the interactions between ions, may not be appreciably affected by moderate pressures. These systematics have been successfully rationalized on the basis of the ionic model (Anderson and Anderson, 1970; Shankland, 1972) even though they encompass a wide range of bond covalency in oxides. Hence, changes in covalency induced by pressures up to at least 200 kbar could probably be encompassed in such a rationalization as well.

Another property of ferrous cations in minerals which is likely to be affected by changes in covalency induced by pressure is spin-pairing of the 3d electrons. Because ferrous iron is the principal transition metal ion in the earth, it is the most likely cation to give rise to spin-pairing transitions that might be observed as seismic discontinuities in the lower mantle. Predicting the pressures at which such transitions occur, however, requires a knowledge of the behavior of the Racah parameter, B , as a function of pressure. The present study has indicated that for Fe^{2+} -oxygen bonds, the value of B is likely to remain constant or even increase with pressure because increases in symmetry-restricted covalency dominate the change in covalency with pressure. Thus the assumption of a value of B that is independent of pressure in such calculations will give minimum pressures and depths at which spin-pairing will occur.

HIGH-PRESSURE TRANSFORMATION IN MAGNESIOFERRITE (MgFe_2O_4)

H. K. Mao and P. M. Bell

The possible existence of significant quantities of ferric iron in the earth's mantle was suggested, in a theoretical model involving disproportionation of ferrous iron (Mao, *Year Book* 73, pp.

510–518). In this model, the ferric magnesioferrite (MgFe_2O_4) would be a potentially important constituent of the mantle, but its stability range under conditions other than those at the earth's surface is unknown. As part of a study of the geochemistry of the deep mantle, utilizing the modified diamond-windowed, high-pressure cell and the laser heating system (Mao and Bell, and Bell and Mao, this Report) magnesioferrite was subjected to experimental conditions equivalent to a depth in the earth of approximately 600 km.

Synthetic magnesioferrite spinel made at 1 atm (Virgo and Ulmer, *Year Book* 72, pp. 564–567) was raised to a pressure of approximately 200 kbar in the high-pressure cell and heated to approximately 1500°C for 15 minutes with a laser beam. Figure 91 shows the view through the diamond-windowed pressure cell of an experimental run in which the central portion of the sample has been heated. Note the dark zone where the laser beam has been focused. The lighter portion at the edges was not heated.

After heating, the sample, still under pressure, was placed on a high-intensity, x-ray generator using monochromatized $\text{MoK}\alpha$ radiation, and a 500-hour x-ray exposure was taken. The interplanar spacings listed in Table 36 are consistent with the hypothesis that magnesioferrite has undergone a phase transformation to a high-pressure form much like the high-pressure form of magnetite (Mao *et al.*, 1974). Although the space group of the high-pressure magnetite phase is unknown, the symmetry change is thought to be displacive from cubic (spinel) to monoclinic. This new phase of MgFe_2O_4 is probably monoclinic as well. All diffraction lines can be indexed with the monoclinic Fe_3O_4 cell, although the intensities are different.

On the release of pressure, the high-pressure magnesioferrite phase inverted to the low-pressure spinel phase. The nonquenchable characteristic was also

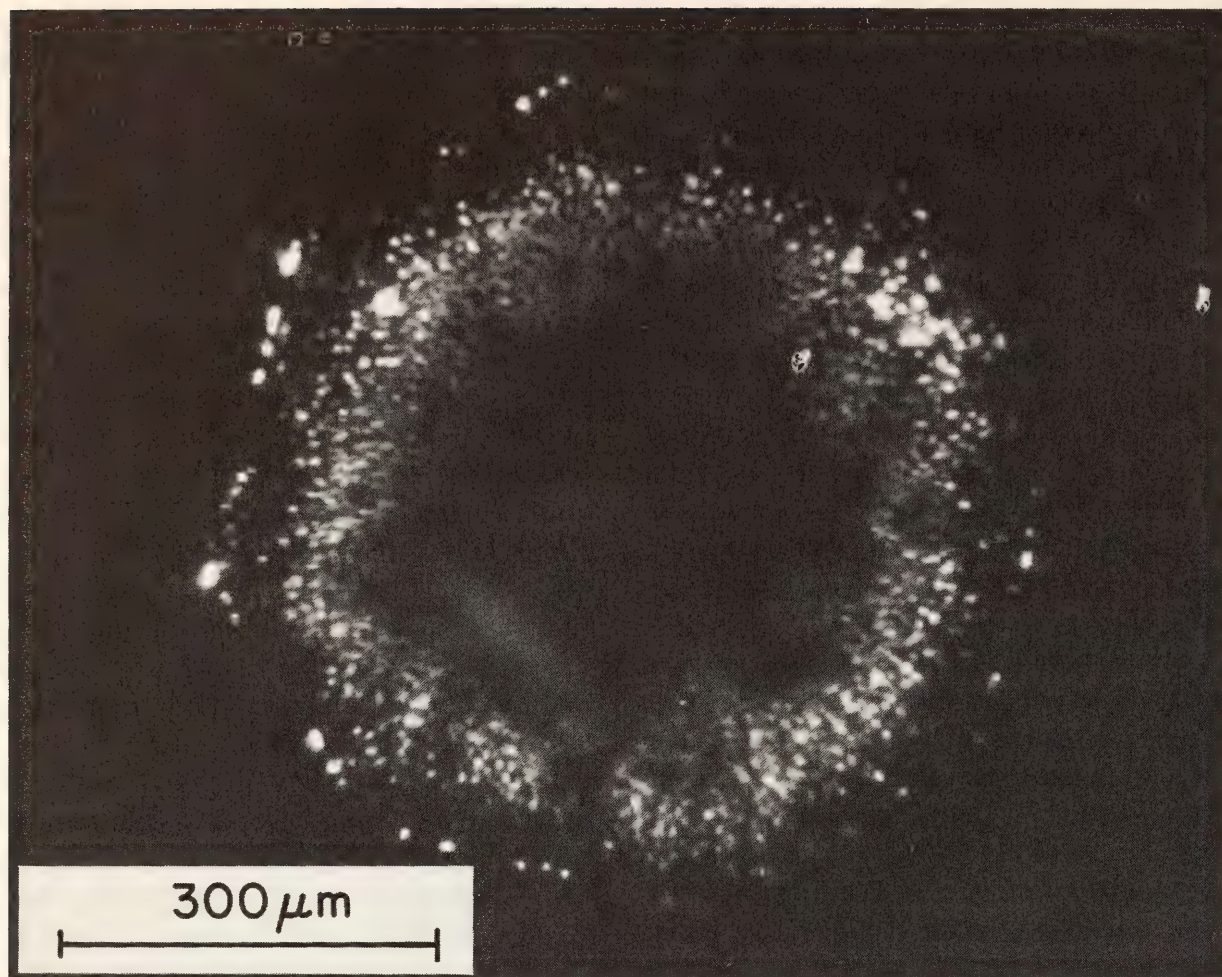


Fig. 91. MgFe_2O_4 in a diamond cell. The pressure at the center of the cell is 200 kbar. The dark area at the center has been heated to 1500°C .

observed in magnetite (the transition occurs at approximately 250 kbar at 25°C).

The disproportionation of ferrous iron at high pressures depends on the molar volume of the related phases. Mao (*Year Book 73*, pp. 510–518) has demonstrated that the high-pressure phase transformation in magnetite reduces the volume of Fe_3O_4 sufficiently to favor the disproportionation of wüstite to $h\text{Fe}_3\text{O}_4$ and metallic iron. In this report, a phase transition and volume reduction similar to those observed in magnetite were discovered in magnesioferrite. By analogy, magnesiowüstite, the suggested predominant constituent in the lower mantle where silicates break down to oxides, is expected to disproportionate to the

high-pressure form of magnesioferrite and iron in the lower mantle. The results support the model that the segregation of the earth's core is formed by disproportionation of ferrous iron.

Mao (*Year Book 73*, p. 515) discussed the implications of ferric iron minerals in the earth's mantle. The physical, electrical, and magnetic properties of the mantle would be much different than was previously thought if high-pressure magnetite and magnesioferrite actually exist in the earth. The properties of high-pressure magnesioferrite are yet unknown, although the occurrence of strong darkening is probably related to the optical and electrical effects noted in other compounds at high pressure (Bell and Mao, this Report).

TABLE 36. The X-Ray Diffraction Pattern of MgFe_2O_4 at 200 kbar and 25°C

Low-Pressure $\text{MgFe}_2\text{O}_4^*$			High-Pressure $\text{MgFe}_2\text{O}_4^\dagger$		High-Pressure $\text{Fe}_3\text{O}_4^\ddagger$		
I/I_{10}^\S	(hkl)	$d, \text{\AA} $	I/I_{10}^\S	$d, \text{\AA} $	I/I_{10}^\S	(hkl)	$d, \text{\AA} $
>1	111	4.69					
4	220	2.868	3	2.88	...	101	2.88
			10	2.60	10	102	2.60
			2	2.54	...	111	2.54
10	311	2.447	8	2.45	1	021	2.42
>1	222	2.343	4	2.33	3	112	2.35
			10	2.07	1	201	2.10
3	400	2.029	8	2.02	4	200	2.03
			8	1.90	4	202,210	1.90
			5	1.76	2	003,212	1.79
1	422	1.656	2	1.64	...	130,131	1.65,1.63
3	511,333	1.56	7	1.55	4	222	1.55
4	440	1.43	5	1.44	...	202,113	1.44
			8	1.39	5	104,301	1.40

* The low-pressure magnesioferrite pattern at 200 kbar, measured from a photograph taken under room conditions.
† The x-ray diffraction pattern of MgFe_2O_4 at 200 kbar.
‡ The x-ray diffraction pattern of Fe_3O_4 at 250 kbar (Mao *et al.*, 1974).
§ Observed intensities.
|| Calculated d values on the basis of a monoclinic cell with $a = 4.22\text{\AA}$, $b = 5.43\text{\AA}$, $c = 5.60\text{\AA}$, and $\beta = 106^\circ$.

PRELIMINARY EVIDENCE OF
DISPROPORTIONATION OF FERROUS IRON
IN SILICATES AT HIGH PRESSURES
AND TEMPERATURES
P. M. Bell and H. K. Mao

Disproportionation of ferrous iron (Fe^{2+}) to ferric iron (Fe^{3+}) plus metallic iron (FeO) is a process favored thermodynamically at high pressure because it yields a lower specific volume. Mao (*Year Book 73*, pp. 510–518) considered the geochemical consequences of an Fe^{3+} - FeO mixture in the earth's interior at pressures above 100 kbar. It remains to be demonstrated experimentally that ferrous iron in silicates, stable in the earth's upper mantle, will disproportionate at the high pressures and temperatures of the deep mantle. In this study, the first preliminary data in support of the disproportionation hypotheses are presented.

In a series of experimental runs, a synthetic basaltic glass (Bell and Mao, *Year Book 73*, p. 496, Table 59) was

melted at high pressure and temperature utilizing the laser-heated, diamond-windowed, high-pressure cell (Bell and Mao, this Report). In each experiment the pressure was first raised to 150 kbar, and the sample was then heated to approximately 2000°C for 10 minutes by scanning of the laser beam. Figure 92A and B shows scanning electron microscope (SEM) photographs of two heated zones after quenching and removal from the pressure cell. The bright, dendritic structure has the composition of a spinel. Semiquantitative analysis of the structure by nondispersive x-ray detection gives a composition enriched in Fe, Mg, and Al, with a surrounding matrix of a Ca-rich silicate, probably pyroxene. Figure 92C and D shows SEM photographs at high magnification. The bright spherical objects are pure metallic iron.

The assumption in the experiments is that the chemical system is isolated and inert and that no net oxidation or reduction has occurred. For this reason the results cannot be interpreted as incon-

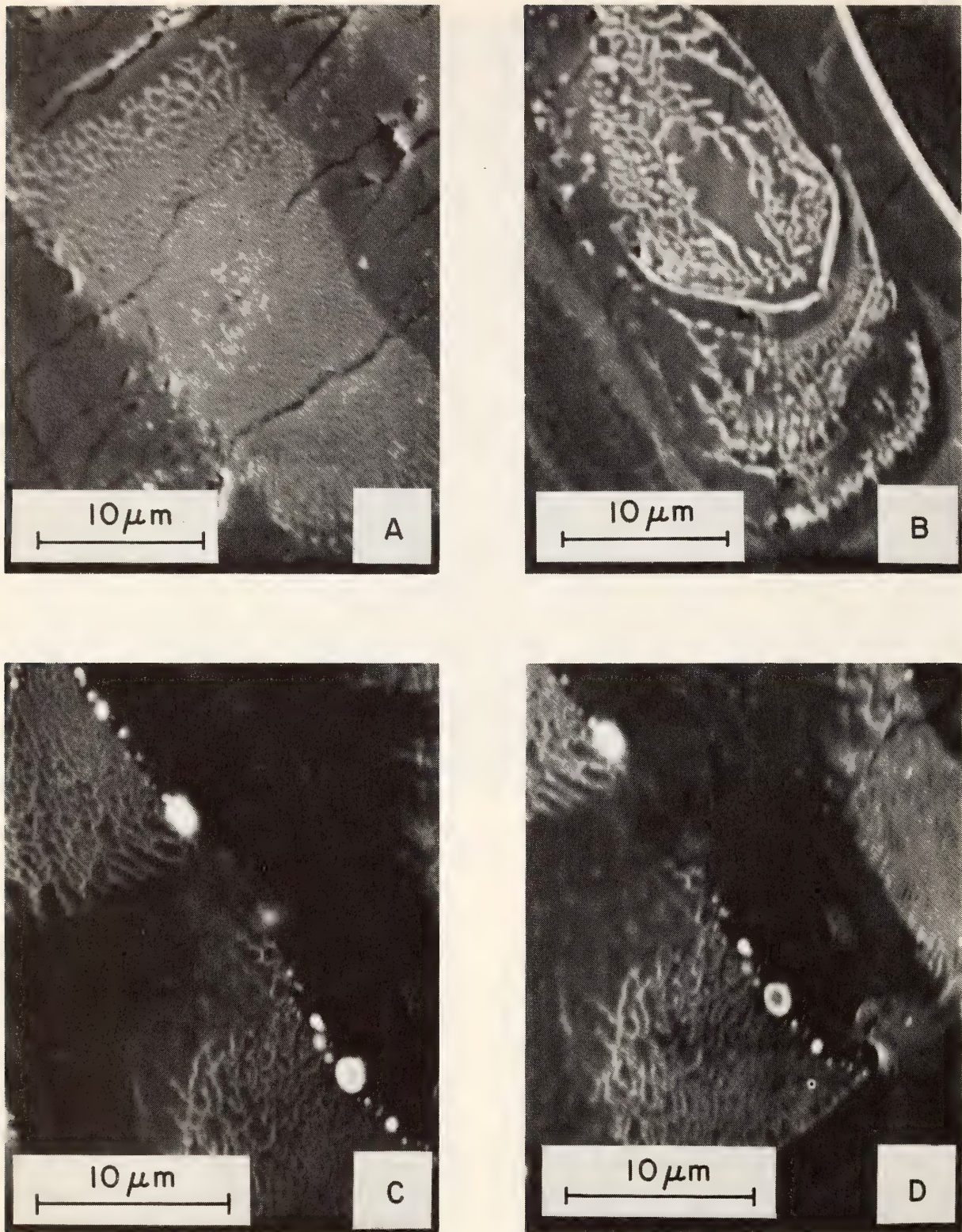


Fig. 92. Scanning electron microscope photographs of a basaltic glass quenched from 150 kbar and 2000°C.

gruent melting. These data are preliminary because the valence state of iron in the oxide phase has not been determined; however, the experiments on the precipitation of metallic iron are reproducible, suggesting that disproportionation has

occurred. Proof of the coexistence of ferric iron will be required to dispel the notion of possible chemical reduction of the sample, although such reduction is considered unlikely in these experiments. Inspection of the diamonds in the high-

pressure cell after the experiment shows no sign of reaction between the sample and the diamonds.

If the interpretation of these preliminary results is correct, disproportionation processes of ferrous iron have far-reaching implications in any system where the pressure is sufficiently high. For example, meteorite and micrometeorite impact processes may result in the formation of metallic and ferric iron on the moon's surface. Possibly such a process has caused the high magnetic anomalies on the moon's surface. (The moon has no magnetic field, and the origin of the anomalies is currently being debated.) In the earth and in other planetary interiors the existence of ferric iron will also have an effect on the magnetic properties. Furthermore, if a mixture of ferric iron and metallic iron is stable at high pressures, as the present experiments suggest, the disproportionation model of the earth's core formation may be correct. This model is unlike other models of planetary evolution, which are based on the gravitational separation of metallic iron from an accreted mass whose oxygen balance was unchanged during the process.

CONTRIBUTION OF ANIONIC COMPLEXES
TO CHARGE-TRANSFER AND ASSOCIATED
OPTICAL, ELECTRICAL, AND THERMAL
EFFECTS AT HIGH PRESSURE

H. K. Mao and P. M. Bell

A series of high-pressure experiments with iron-bearing minerals showed that the optical, electrical, and thermal properties change greatly at pressures above 100 kbar (Mao and Bell, *Year Book* 71, pp. 520–524). Subsequently, a similar but more pronounced optical effect was observed in the charge-transfer spectra of the minerals vivianite, $\text{Fe}_3(\text{PO}_4)_2 \cdot 8\text{H}_2\text{O}$, and wulfenite, PbMoO_4 (Bell and Mao, *Year Book* 73, pp. 507–510). In these two minerals the optical effect was an increase in the intensity of the absorption band caused by charge-transfer

processes. If the observed effect is indeed an increase in the probability of charge-transfer, it means that charge-transfer will dominate in most processes in the earth.

In the present study charge-transfer was systematically tested for several anionic complexes as part of an effort to characterize the processes at high pressure. It had been thought that the effects were caused by transitions in iron, on the basis of the first results with olivine and spinel, but it was later proved that iron-free minerals and compounds show the effect as well, given a known charge-transfer process (Bell and Mao, *Year Book* 73, p. 508). In wulfenite the process was thought to be caused by charge-transfer in Mo, although it was pointed out that wulfenite usually contains impurity chromate ions that could be responsible for the observed effects (G. Rossman, personal communication). This study was made on a series of reagent-grade compounds to test these possibilities.

The results, obtained in the range 1 bar–300 kbar, are given in Table 37, on the basis of overall absorption in the visible region. Potassium dichromate showed a strong effect, but potassium chromate did not. However, an effect stronger than that in either potassium compound was observed in lead chromate and in ammonium chromate, demonstrating that the response of a given anionic complex is variable and is probably related to the crystallographic structure.

Wulfenite was not the only molybdate to show a strong absorption. Ammonium molybdate showed a similar effect, as did sodium molybdate, although the effect in the latter was weak. These results show that the effect is caused by no single complex and support the contention that the effect is a property of transition elements, varying from structure to structure. The strong effect noted in hydrated copper chloride supports this view.

The data on the pressure effect on charge-transfer were obtained in the

TABLE 37. Pressure Effect on Charge-Transfer Processes Deduced from Optical Absorption in the Visible Region*

Substance	Relative Intensity of Induced Absorption (Relative Absorbance at 0.5 μm)
$\text{K}_2\text{Cr}_2\text{O}_7$	45
K_2CrO_4	10
PbCrO_4	100
$(\text{NH}_4)_2\text{CrO}_4$	50
PbMoO_4 (wulfenite)	100
$(\text{NH}_4)\text{MoO}_4$	45
NaMoO_4	10

* The effects are observed as a continuous increase of absorption in the pressure range 1 bar–300 kbar.

diamond-windowed, high-pressure cell, but the pressure was not hydrostatic in most of these experiments. It was necessary to use nonhydrostatic pressure to maintain a moderate mean pressure and avoid failure of the cell. The new design of the high-pressure cell (Mao and Bell, this Report) extends the pressure range, although the pressure is nearly hydro-

static. Figure 93 shows a crystal of wulfenite at 150 kbar and 1 bar in a pressure medium of methanol mixed with ethanol in a 4:1 ratio by volume. Wulfenite shows the same enhanced charge-transfer absorption at these hydrostatic pressures as it did under nonhydrostatic conditions, thus demonstrating that the effect was not related to high shear stress but was caused by high pressure alone.

The demonstration that high pressure causes greatly enhanced charge-transfer in transition metal complexes in general has important consequences with regard to the temperature distribution in geochemical and geophysical theories of the earth. It is essential to consider the optical effects in transition metal-bearing minerals in the earth and the electrical and thermal effects that accompany them because they affect the temperature distribution and the magnetic field. The effects are a high pressure coefficient of electrical conductivity and high thermal absorption. Models of the earth should take into account the effects of high con-

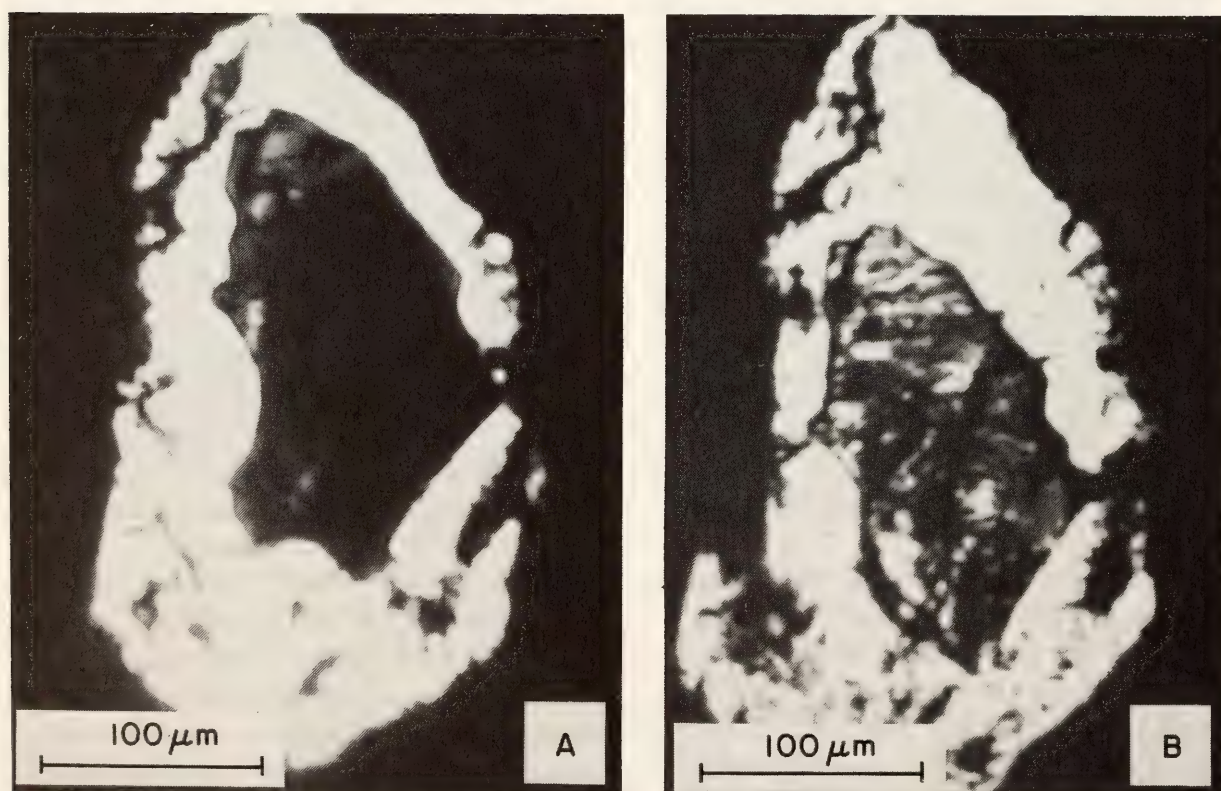


Fig. 93. Single crystal of wulfenite in a diamond cell. The pressure medium is a 4:1 methanol-ethanol mixture. The photographs were taken at (A) 150 kbar and (B) 1 bar.

duction and low radiative transfer in zones that are enriched in iron or other transition metals. New models will have thermal barriers and rising temperatures whenever the absorption is as great as predicted from the present data.

PYROXENOIDS: A VARIATION IN
CHEMISTRY OF NATURAL RHODONITES
AND PYROXMANGITES

Y. Ohashi, A. Kato, and S. Matsubara**

The relation between cations and SiO_4 tetrahedral configuration is one of the interesting problems in the crystal chemistry of silicates. In pyroxenes, for example, the ionic size of the cations plays an important role in controlling chain configuration (Papike *et al.*, 1973; Ohashi and Finger, *Year Book* 73, pp. 522–525). Conversely the chain configuration places some restrictions on the size of the cations that can occupy a particular site in the structure. The idea that some structural sites can accommodate only certain kinds of cations has been accepted as a crystal-chemical explanation for compositional limits often observed in minerals. Pyroxenes and pyroxenoids provide critical examples for the study of this cation-chain structure relationship.

The chain repeat is two tetrahedra in pyroxenes and longer in pyroxenoids; three in wollastonite, bustamite, and pectolite; five in rhodonite, babingtonite (Araki and Zoltai, 1972), and nambulite (Narita, Kato, and Morimoto, 1975); seven in pyroxmangite and pyroxferroite (Burnham, 1971); nine in ferrosilite III (Burnham, 1966) (for general discussions, see Liebau, 1960, 1962; Prewitt and Peacor, 1964).

As part of a study on the relationships of Mn-bearing chain silicates, natural rhodonites and pyroxmangites from various mines in Japan have been examined by means of the single-crystal x-ray diffraction method and the electron microprobe. The purpose of this study is (a)

to characterize the chemistry of natural rhodonites and pyroxmangites and (b) to elucidate their occurrence in the light of experimentally determined phase relations. Results of refinements of crystal structures of the minerals are reported elsewhere (Ohashi and Finger, this Report).

Electron microprobe analyses of Japanese rhodonites and pyroxmangites are given in Table 38. Because a distinction between these two minerals in the literature is not always clear and many so-called pyroxmangites are found to have the rhodonite structure (Chao *et al.*, 1970), each sample was examined using the single-crystal x-ray diffraction method to check the length of the unit translation of the silicate chains (~ 12 Å for rhodonite and ~ 17 Å for pyroxmangite).

The chemical analyses showed that the minerals can be well represented in the quaternary system CaSiO_3 - MnSiO_3 - FeSiO_3 - MgSiO_3 . To display graphically the chemical variations in this system, projections of this tetrahedron along the Ca-Mn, Mn-Fe, and Fe-Mg edges have been prepared and are shown in Fig. 94. In each such diagram, cations with similar ionic radii are combined in the projection.

Sundius (1931), in his investigation of "triclinic pyroxenes" (rhodonite and pyroxmangite), used a diagram similar to Fig. 94A to show a compositional difference among chain silicates. The present study, however, shows that the field for pyroxmangite is extended toward the MnSiO_3 corner along the join MnSiO_3 -(Fe, Mg) SiO_3 . The minimum Ca content in rhodonites and the maximum Ca content in pyroxmangites seem to depend linearly on the Mn concentration (Fig. 94A), and the boundary is approximately the line of $\text{Ca}/(\text{Fe} + \text{Mg}) = 1:3$.

Because the Ca content does not exceed $1/5$ in rhodonite and $1/7$ in pyroxmangite (or the Fe-rich member pyroxferroite), this compositional limit of Ca had been interpreted to mean that the

* National Science Museum, Japan.

TABLE 38. Electron Microprobe Analyses of Rhodonites and Pyroxmangites from Japan

	Rhodonites†						
	AK18R	AK20	AK13	AK5	AK8	AK2	AK3
SiO ₂	46.29	46.26	45.45	46.76	46.66	46.59	46.58
Al ₂ O ₃	0.00	0.19	0.03	0.00	0.04	0.07	0.41
FeO*	0.48	0.20	0.39	1.79	3.93	4.36	4.02
MnO	51.18	50.34	49.43	48.30	44.89	43.33	40.55
MgO	1.29	0.82	0.95	0.42	1.99	1.94	1.37
CaO	1.19	2.40	1.37	2.72	2.14	3.12	6.36
Totals	100.43	100.21	97.62	99.99	99.65	99.41	99.29
Number of Cations for 3 Oxygens							
Si	1.00	0.99	1.00	1.00	1.00	1.00	0.99
Al	0.00	0.00	0.00	0.00	0.00	0.00	0.01
Fe	0.01	0.00	0.01	0.03	0.07	0.08	0.07
Mn	0.93	0.92	0.92	0.88	0.81	0.79	0.73
Mg	0.04	0.03	0.03	0.01	0.06	0.06	0.04
Ca	0.03	0.05	0.03	0.06	0.05	0.07	0.15
Totals	2.01	1.99	1.99	1.98	1.99	2.00	1.99
	Pyroxmangites†						
	AK15	AK18P	AK4	AK19	AK6	AK14	AK9
SiO ₂	44.83	46.44	45.95	46.89	46.60	46.65	47.11
Al ₂ O ₃	0.03	0.02	0.20	0.00	0.04	0.02	0.09
FeO*	0.24	0.65	3.91	0.16	3.95	6.17	14.56
MnO	51.05	51.27	47.50	46.70	45.10	39.52	30.17
MgO	0.32	1.90	1.26	4.50	2.81	4.35	3.89
CaO	0.78	0.36	0.45	0.09	0.75	1.14	2.21
Totals	97.25	100.64	99.27	98.34	99.25	97.85	98.03
Number of Cations for 3 Oxygens							
Si	1.00	0.99	1.00	1.00	1.00	1.00	1.01
Al	0.00	0.00	0.01	0.00	0.00	0.00	0.00
Fe	0.00	0.01	0.07	0.00	0.07	0.11	0.26
Mn	0.96	0.93	0.87	0.85	0.82	0.72	0.55
Mg	0.01	0.06	0.04	0.14	0.09	0.14	0.12
Ca	0.02	0.01	0.01	0.00	0.02	0.03	0.05
Totals	1.99	2.00	2.00	1.99	2.00	2.00	1.99

* All iron as FeO.
† AK2, Nagasawa, Ibaragi; AK3, Ohbori, Shiga; AK4, Yaei, Shiga; AK5, Rito, Gumma; AK6, AK8, Taguchi, Aichi; AK9, Kamiotomo, Iwate; AK13, Ichinoki, Fukushima; AK14, Kaso, Tochigi; AK15, Minazawa, Tochigi; AK18R, AK18P, Watsuka, Kyoto; AK19, Osotari, Miyazaki; AK20, Okutama, Tokyo.

Ca atom can occupy only one of five cation sites in rhodonite and one of seven in pyroxmangite (Lindsley and Burnham, 1970; Chao *et al.*, 1970). Burnham (1971), however, concluded from site occupancies, bond distances, and apparent temperature factors obtained from x-ray refinement that the Ca atom is distrib-

uted over three different sites, and thus a crystal-chemical explanation for the compositional limit of Ca is still a subject for future study.

The concentration of Mg in most of the rhodonites is in the region of Mg < Ca (Fig. 94C), whereas the Mg/Ca ratio in the pyroxmangites is consid-

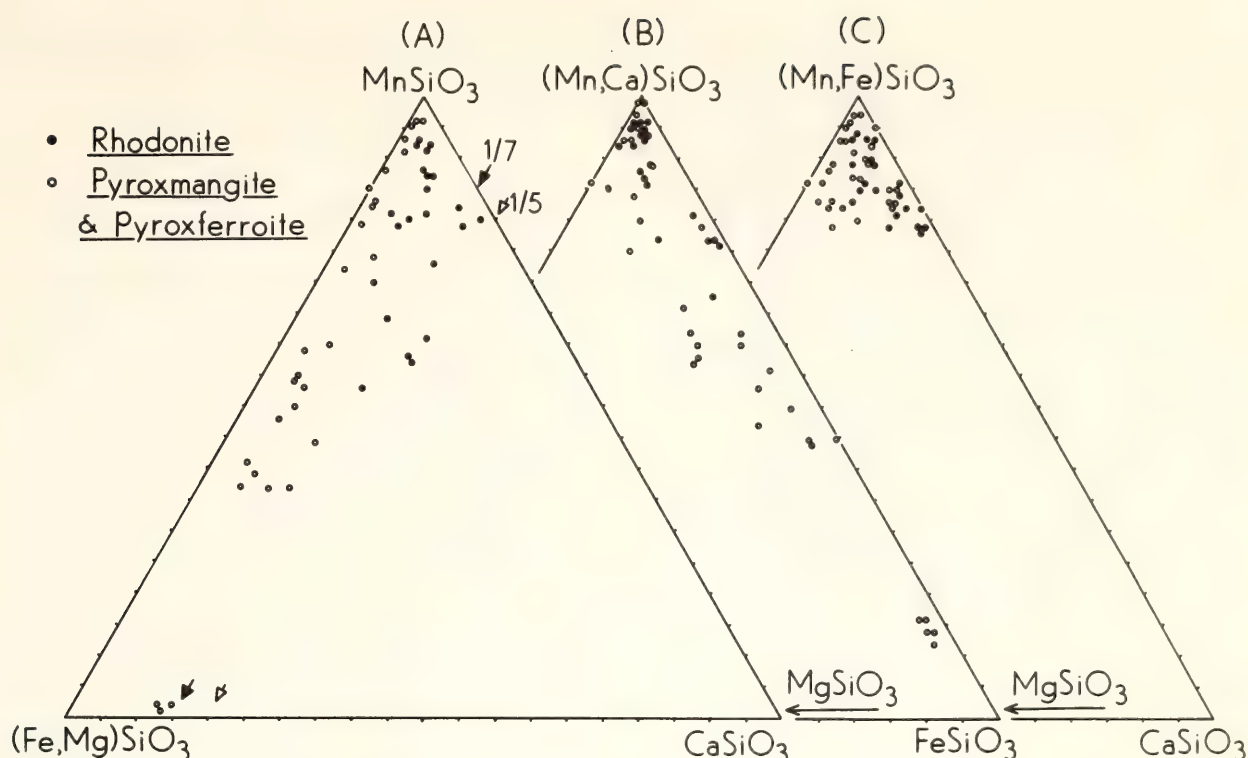


Fig. 94. Compositions (mol %) of natural rhodonites and pyroxmangites plotted in the MnSiO_3 - CaSiO_3 - FeSiO_3 - MgSiO_3 system. Sources of data: this study (Table 38); Chao *et al.* (1970); Deer, Howie, and Zussman (1963); Dickson (1975); Klein (1966).

erably scattered. It is also interesting to note that the concentration of Mg, like that of Ca, in natural pyroxmangites is less than 1/7 of the total cations, a fact that might suggest a single site for Mg. Ito (1972a), however, synthesized very Mg-rich pyroxmangites ranging between $\text{Mn}_{0.5}\text{Mg}_{0.5}\text{SiO}_3$ and $\text{Mn}_{0.1}\text{Mg}_{0.9}\text{SiO}_3$ at temperatures above 1100°C.

Phase relations in the Mn-rich portion of the $(\text{Mn,Ca,Fe,Mg})\text{SiO}_3$ tetrahedron were studied by Ito (1972b) in the presence of water (shown schematically in Fig. 95A). He showed that the stability field of pyroxmangite is shifted away from the MnSiO_3 apex as temperature increases and that the rhodonite field is more Ca-rich at lower temperature. The Mn-rich portion of the binary join MnSiO_3 - CaSiO_3 (Momoi, 1968) is also shown in Fig. 95B. For the end-member composition MnSiO_3 , pyroxmangite has been synthesized at lower temperature and higher pressure than rhodonite (Akimoto and Syono, 1972; Momoi, 1974).

A comparison of natural rhodonites

and pyroxmangites (Fig. 94) with experimentally determined phase relations (Fig. 95) requires a five-dimensional space, three independent compositional variables plus temperature (T) and pressure (P). Because the P - T conditions for natural samples may vary, the compositional diagrams in Fig. 94 are also *projections* in terms of the pressure and temperature axes, whereas the synthesis diagrams in Fig. 95A are *sections* at fixed P and T . The fact that the two fields in Fig. 94A do not overlap suggests that the compositional limit on $\text{Ca}/(\text{Fe} + \text{Mg})$ observed for natural samples is related either to a limited range of temperature-pressure conditions in nature or to the existence of a third phase that controls the compositional limits of rhodonite and pyroxmangite over a relatively wide range of P and T conditions. In the latter respect, bustamite, for example, may be important (cf. Fig. 95B).

A more complete analysis of the pyroxenoid phase relations obviously requires a careful examination not only of

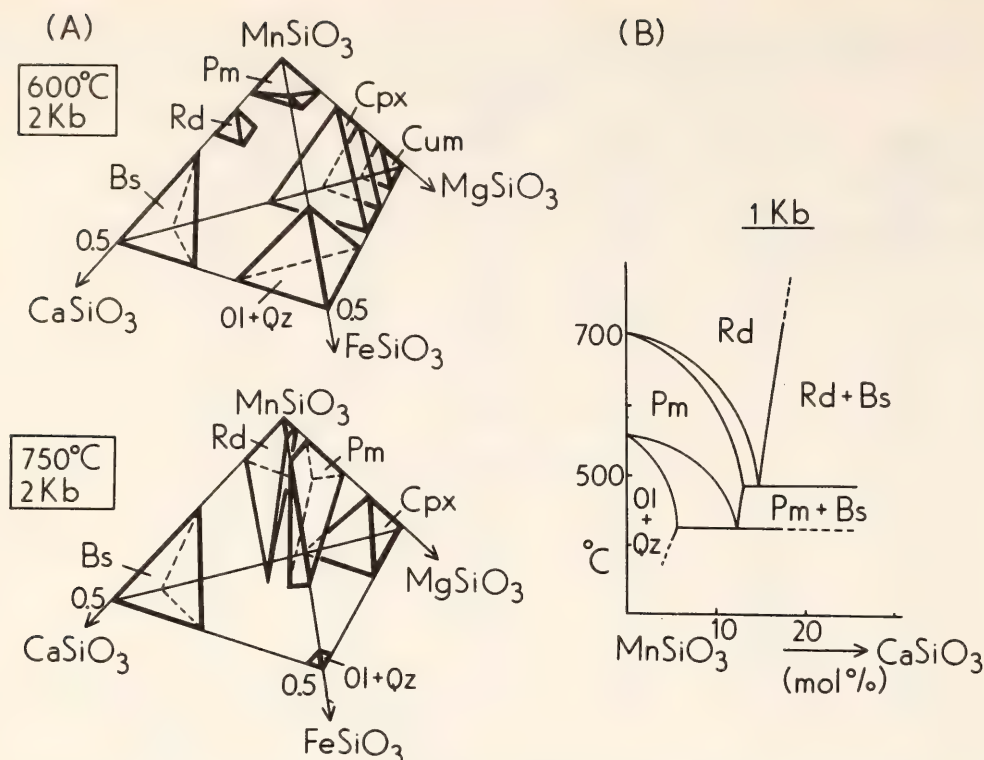


Fig. 95. Synthesis diagrams: (A) in the system MnSiO_3 - $\text{Ca}_{0.5}\text{Mn}_{0.5}\text{SiO}_3$ - $\text{Fe}_{0.5}\text{Mn}_{0.5}\text{SiO}_3$ - $\text{Mg}_{0.5}\text{Mn}_{0.5}\text{SiO}_3$ (Ito, 1972b); and (B) on the join MnSiO_3 - CaSiO_3 (Momoi, 1968). Abbreviations: Bs, bustamite; Cpx, clinopyroxene; Cum, cummingtonite; Ol, olivine; Pm, pyroxmangite; Qz, quartz; Rd, rhodonite.

rhodonite and pyroxmangite but also of other coexisting phases such as bustamite, johannsenite, tephroite, quartz, amphiboles, and rhodochrosite, a mineral assemblage that introduces the additional components H_2O and CO_2 into the system.

PYROXENOIDS: A COMPARISON OF REFINED STRUCTURES OF RHODONITE AND PYROXMANGITE

Y. Ohashi and L. W. Finger

The existence of a variety of chain silicates can probably be attributed to a delicate structural adjustment of the silicate tetrahedra and the cation polyhedra. The ratio of a tetrahedral edge to an octahedral edge is not quite either 1:1 or $\sqrt{3}$:2, from which idealized structures can be derived (Thompson, 1970; Papike *et al.*, 1973). Thus the cation in the octahedral sites is one of the important factors controlling the pyroxenoid structure. If there is a substantial amount of Mn, which is intermediate

in size between Ca and Fe, the stable pyroxene-pyroxenoid phases include johannsenite (Mn pyroxene), bustamite, rhodonite, and pyroxmangite. All these minerals can be represented by the formula MSiO_3 , where M denotes such cations as Mn, Ca, Fe, and Mg.

To analyze the details of the structural relationship among Mn-bearing chain silicates, the structures of rhodonite and pyroxmangite have been refined. The crystals used in this study were kindly supplied by Dr. A. Kato, and the results of the electron microprobe analyses are given elsewhere (see samples AK6 and AK8 in Ohashi, Kato, and Matsubara, this Report). Specimens of rhodonite and pyroxmangite, both from the Taguchi Mine (a regionally metamorphosed manganese ore deposit), Aichi, Japan, were selected for crystal structural study mainly because of their similarity in chemistry. $\text{Mn}_{0.81}\text{Fe}_{0.07}\text{Mg}_{0.06}\text{Ca}_{0.05}\text{SiO}_3$ (rhodonite) and $\text{Mn}_{0.82}\text{Fe}_{0.07}\text{Mg}_{0.09}\text{Ca}_{0.02}\text{SiO}_3$ (pyroxmangite). These compositions, when plotted in the MnSiO_3 -

CaSiO_3 -(Fe,Mg) SiO_3 system, lie close to the rhodonite-pyroxmangite boundary found for natural samples (Ohashi, Kato and Matsubara, this Report).

Because of their triclinic symmetry, the unit cells for rhodonite and pyroxmangite are not uniquely defined, and several different unit-cell settings have been used. In this study, however, the C -centered unit cell is used for both minerals with the chain direction chosen as the c axis and the oxygen closest-packing layer parallel to (100). The major consideration in selecting this setting is the ease of comparison among the various pyroxenes and pyroxenoids. The same setting has been used by Narita (1973; quoted by Morimoto, 1974). The origin of the unit cell is chosen at the inversion center between the two adjacent M1 octahedra, and thus in some cases a shift of the origin may be required for transforming atomic coordinates between the $C\bar{1}$ and other settings. The unit-cell parameters given in Table 39 are those for the $C\bar{1}$ setting, obtained from least-squares refinement of 12 re-

flections centered on the four-circle diffractometer.

Crystals approximately $0.16 \times 0.16 \times 0.09$ mm (rhodonite) and $0.30 \times 0.17 \times 0.14$ mm (pyroxmangite) in size were selected for intensity measurements on the automated four-circle diffractometer with Nb-filtered $\text{MoK}\alpha$ radiation (Finger, Hadidiacos, and Ohashi, *Year Book* 72, pp. 694–699). Corrections were made for Lorentz and polarization effects and absorption ($\mu_l = 56.3 \text{ cm}^{-1}$ for rhodonite and 56.9 cm^{-1} for pyroxmangite). Reflections having an intensity greater than two standard deviations and 2θ less than 55° were used in the subsequent structural analysis. Least-squares refinement of the structure has been initiated using computer program RFINE2 (Finger and Prince, 1975) and the atomic coordinates of rhodonite and pyroxferroite determined by Peacor and Niizeki (1963) and Burnham (1971), respectively. The refined atomic coordinates and isotropic temperature factors are given in Table 40. The final weighted residual factor, R , is 4.7% for 2353 reflections (rhodonite) and 4.4% for 2793 reflections (pyroxmangite).

TABLE 39. Unit Cell Data for Rhodonite and Pyroxmangite from Taguchi Mine, Japan

	Rhodonite			Pyroxmangite		
a , Å	9.758(1)			9.690(2)		
b , Å	10.499(1)			10.505(3)		
c , Å	12.205(1)			17.391(3)		
α , degrees	108.58(1)			112.17(2)		
β , degrees	102.92(1)			102.85(1)		
γ , degrees	82.52(1)			82.93(2)		
V , Å ³	1152.9(2)			1596.7(6)		
Space group	$C\bar{1}$			$C\bar{1}$		
Z based on MSiO_3	20			28		
Transformation matrix T^*	$-1/2$	$-1/2$	0	$1/2$	$-1/2$	0
	$1/2$	$1/2$	1	$1/2$	$1/2$	0
	$-1/2$	$1/2$	0	0	0	1

* In the form of $A' = TA$, where A is the base vector set for the $C\bar{1}$ cell; and A' for the $P\bar{1}$ cell used by Peacor and Niizeki (1963) and Burnham (1971).

Crystal Structure

The rhodonite and pyroxmangite structures are compared in Fig. 96. In addition to the tetrahedral chain repeat distance, the cation band arrangement is different in these two structures. Because the inversion centers in both structures are not the same relative to the cation polyhedra, there is one polyhedral sequence M(5-4-3-2-1-1-2-3-4-5) in rhodonite (point indicates a center of inversion), whereas in pyroxmangite there are two, M(7-6-4-3-3-4-6-7) and M-(5-2-1-1-2-5). Note that the inversion center on the O-O edge shared by the two M2 polyhedra in rhodonite is not part of a separate sequence, but relates one band of octahedra to an equivalent unit.

When the M-O distances and O-M-O angles are compared, a close similarity

TABLE 40. Final Positional Parameters* and Isotropic Temperature Factors (\AA^2) for Rhodonite and Pyroxmangite

	Rhodonite				Pyroxmangite			
	<i>x</i>	<i>y</i>	<i>z</i>	<i>B</i>	<i>x</i>	<i>y</i>	<i>z</i>	<i>B</i>
M1(M1)†	0.0001	0.0291	0.1478	0.64	−0.0004	0.0419	0.1052	0.72
M2(M2)	0.0011	0.1281	0.4454	0.69	−0.0011	0.1686	0.3122	0.59
M3(M3)	0.0163	0.2034	0.7306	0.67	0.0013	0.0679	0.6055	0.53
M4(M4)	0.0580	0.2648	0.0263	0.92	0.0143	0.1767	0.8066	0.66
M5(M5)	−0.0053	0.3455	0.2991	1.04	0.0040	0.2703	0.5098	0.69
M6					0.0604	0.2639	0.0176	1.03
M7					−0.0075	0.3707	0.2096	0.82
Si1(Si4)	0.2045	0.4498	0.9118	0.69	0.2024	0.4426	0.9355	0.63
Si2(Si5)	0.2123	0.3649	0.6548	0.65	0.2106	0.3319	0.7516	0.54
Si3(Si2)	0.2153	0.5779	0.5317	0.68	0.2115	0.5321	0.6626	0.57
Si4(Si3)	0.2123	0.5069	0.2637	0.66	0.2077	0.4253	0.4692	0.54
Si5(Si1)	0.2056	0.7006	0.1251	0.64	0.2101	0.6318	0.3805	0.57
Si6					0.2087	0.5291	0.1891	0.56
Si7					0.2039	0.7104	0.0892	0.61
OA1(O11)	0.1272	0.0706	0.0397	0.81	0.1281	0.0729	0.0282	0.82
OA2(O1)	0.1182	0.1588	0.3208	0.84	0.1186	0.1880	0.2266	0.79
OA3(O4)	0.1155	0.9209	0.4357	0.87	0.1174	0.9629	0.3108	0.83
OA4(O2)	0.1211	0.0135	0.7319		0.1225	0.0898	0.5197	0.86
OA5(O8)	0.1290	0.7910	0.8545	0.80	0.1195	0.8708	0.6057	0.79
OA6(O6)	0.0999	0.8330	0.1316	0.81	0.1218	0.9879	0.8067	0.74
OA7					0.1288	0.7790	0.8979	0.85
OA8					0.0997	0.8435	0.0936	0.78
OB1(O5)	0.1290	0.3222	0.9050	1.19	0.1292	0.3111	0.9301	0.98
OB2(O3)	0.1246	0.2337	0.6114	1.01	0.1258	0.1963	0.7234	0.92
OB3(O10)	0.1249	0.7073	0.5950	1.21	0.1230	0.6643	0.7130	1.05
OB4(O7)	0.1216	0.3800	0.1885	1.32	0.1223	0.2867	0.4264	0.97
OB5					0.1294	0.7756	0.4219	1.06
OB6					0.1205	0.3957	0.1323	1.03
OC1(O15)	0.1704	0.4671	0.7782	0.94	0.1674	0.4495	0.8393	0.86
OC2(O14)	0.1620	0.4526	0.5617	1.32	0.1610	0.4024	0.6799	0.95
OC3(O13)	0.1640	0.5428	0.3897	1.13	0.1604	0.4982	0.5614	1.02
OC4(O12)	0.1578	0.6410	0.2195	0.85	0.1513	0.5313	0.4177	0.97
OC5(O9)	0.1468	0.5938	0.9956	0.86	0.1534	0.5667	0.2772	0.91
OC6					0.1567	0.6614	0.1590	0.84
OC7					0.1435	0.5907	0.9965	0.86
Estimated Standard Errors								
M	0.0001	0.0001	0.0001	0.02	0.0001	0.0001	0.0001	0.03
Si	0.0001	0.0001	0.0001	0.02	0.0002	0.0002	0.0001	0.03
O	0.0004	0.0004	0.0004	0.06	0.0005	0.0005	0.0003	0.07

* Based on $C\bar{1}$ setting. Coordinates (x' , y' , z') for $P\bar{1}$ cells used by Peacor and Niizeki (1963) and Burnham (1971) are $x' = -x - y + z$, $y' = z$, $z' = -x + y$ for rhodonite and $x' = x - y$, $y' = x + y - 1/2$, $z' = z - 1/2$ for pyroxmangite.
† Site nomenclature in parentheses is that of Peacor and Niizeki (1963).

is found between certain cation polyhedra in rhodonite and pyroxmangite. The following octahedra are very similar in shape: M1_R-M1_P, M3_R-M4_P, M4_R-M6_P, M5_R-M7_P, and to a lesser extent, M2_R-M2_P. The subscripts R and P refer to the rhodonite and pyroxmangite structures, respectively. Therefore, to a first approximation, the pyroxmangite structure can be regarded as the rhodonite

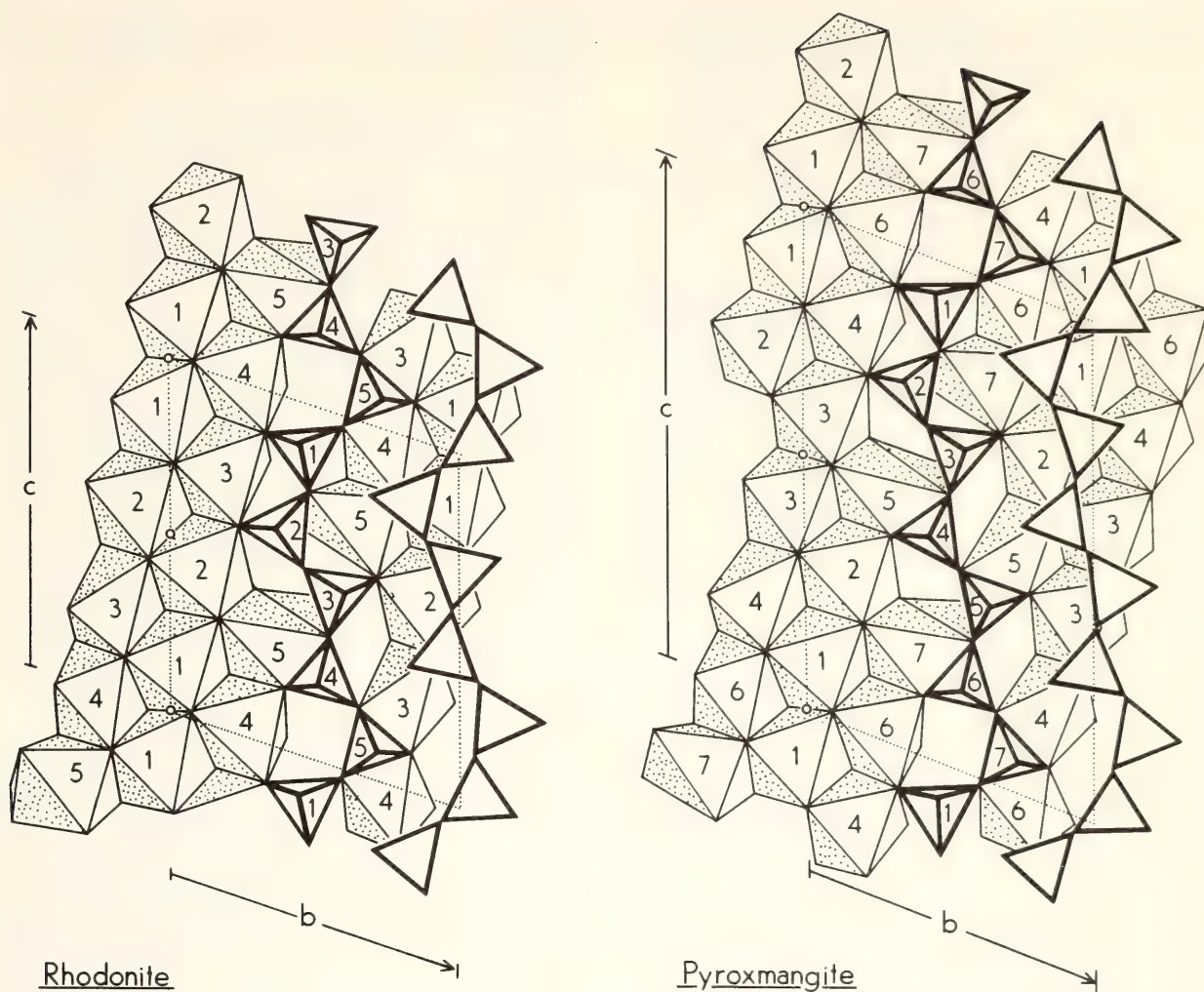


Fig. 96. Portions of the rhodonite and pyroxmangite structures projected onto the plane parallel to the oxygen closest-packed layer.

structure plus the band consisting of M3, M5, Si4, and Si5 (see Fig. 96).

Cation Distribution

Although the unique solutions of cation site occupancies cannot be determined, the electron density at each cation site can be obtained from refinement of x-ray diffraction data. The apparent site occupancies that give the best fit of the electron density have been refined using the linear combination of the scattering factors for Mn^{2+} and Mg^{2+} without any constraint on chemistry. The physical meaning of this procedure is that the total number of electrons in a certain site is to be approximated by the combination of the cations with 23 electrons (Mn^{2+}) and 10 electrons (Mg^{2+}). The refined values given in Table 41 yield an average number of electrons per site of

21.4 for rhodonite and 21.3 for pyroxmangite. These values are in agreement with the value 21.8 expected from the bulk chemistry.

In this electron-density refinement for cation sites the Ca^{2+} ion, which has 18 electrons, effectively increases the apparent " Mg^{2+} " occupancy factor. Alternatively these two ions are quite different in size and possibly distinguishable on the basis of the polyhedral size (Table 42). Both the occupancy and the polyhedral size indicate that the M1, M2, and M3 sites in rhodonite are essentially occupied by manganese. When compared with a more Ca-rich rhodonite (Peacor and Niizeki, 1963) these three sites are similar in size, but the average M-O distance for M5, the site that is partially occupied by the Ca atom, is longer in Ca-rich rhodonite than that of

TABLE 41. Cation Site Occupancies*
Obtained from Unconstrained Refinement of
the Linear Combination of Mn²⁺ and Mg²⁺

	Rhodonite		Pyroxmangite	
	"Mn ²⁺ "	"Mg ²⁺ "	"Mn ²⁺ "	"Mg ²⁺ "
M1	0.93(1)	0.07(1)	0.97(1)	0.03(1)
M2	0.93(1)	0.07(1)	0.81(1)	0.19(1)
M3	0.91(1)	0.09(1)	0.83(1)	0.17(1)
M4	0.78(1)	0.22(1)	0.89(1)	0.11(1)
M5	0.83(1)	0.17(1)	0.88(1)	0.12(1)
M6			0.81(1)	0.19(1)
M7			0.91(1)	0.09(1)

* The Fe²⁺ ion can be treated as Mn²⁺, and Ca²⁺ effectively increases the apparent Mg²⁺ occupancy factor (see text).

this study. The M4 polyhedron, which is also slightly larger in Ca-rich rhodonite, is very distorted and possibly can accommodate Ca as well as Fe and Mg. The Mössbauer study indicates that the Fe atom prefers the M4 site to the other sites (Dickson, 1975).

A comparison of pyroxmangite and pyroxferroite (Burnham, 1971) shows some differences in cation polyhedral size. The sites of M1 through M4 in

pyroxmangite are larger, reflecting the difference between Mn and Fe; and M5 and M7 are smaller in pyroxmangite, probably resulting from the difference in the Ca concentration. The mean M-O distance for M6 is shorter in pyroxferroite if five distances are used in average, but the sixth distance is 2.761 Å for pyroxmangite and 2.864 Å for pyroxferroite. The observations on M5 and M7 support the idea that the Ca atom is not restricted to one site but is distributed over both sites (Burnham, 1971). If the Ca were restricted to one particular site, such as M7 in pyroxferroite, the comparison of pyroxmangite and pyroxferroite would show the primary difference in polyhedral size only for M7, not for M5, because the Ca concentration in pyroxmangite is low.

The M6 site, which shows the relatively high "Mg²⁺" occupancy factor and the short mean M-O distance, is considered to include an appreciable amount of Mg in addition to Ca. This interpretation is also consistent with the fact that the shortest M-O distance in all octahedral cation sites is 1.958 Å in M6

TABLE 42. Mean M-O Distances (Å) in Rhodonite, Pyroxmangite, and Pyroxferroite

		Rhodonite, This Study	Rhodonite,* Peacor and Niizeki (1963)	Pyroxman- gite, This Study	Pyrox- ferroite,† Burnham (1971)
M1-O	[6]‡	2.213	2.219	2.207	2.185
M2-O	[6]	2.228	2.215	2.192	2.159
M3-O	[6]	2.217	2.228	2.199	2.162
M4-O	[5]	2.139	2.150		
	[6]	2.248	(2.272)§	2.199	2.180
M5-O	[6]	2.331	2.382	2.300	2.316
	[7]	2.395	2.418	(2.387)§	(2.390)§
M6-O	[5]			2.132	2.118
	[6]			2.237	(2.249)§
M7-O	[6]			2.272	2.289
	[7]			(2.377)§	(2.371)§
Standard errors		0.004		0.004	0.006-0.007

* Mn_{0.80}Fe_{0.03}Mg_{0.03}Ca_{0.16}SiO₃.
† Mn_{0.02}Fe_{0.83}Mg_{0.02}Ca_{0.13}SiO₃.
‡ Number of M-O distances used in average.
§ The longest interatomic distance included in average is greater than 2.8Å.
|| Standard deviations quoted are representative of the uncertainties in the individual distances.

for pyroxmangite and 1.922 Å in M4 for pyroxferroite.

Polymorphism

Although the compositional ranges of rhodonite and pyroxmangite are different (Ohashi, Kato, and Matsubara, this Report), these minerals have a polymorphic relationship in the manganese-rich compositions, pyroxmangite being stable at lower temperature and higher pressure than rhodonite (Akimoto and Syono, 1972; Momoi, 1974). Because a close correspondence in the individual cation polyhedra has been found between the minerals, the principal factor controlling the phase stability must be the structural difference associated with the change in the *horizontal offset* (Burnham, 1966) of the tetrahedra. The polymorphic relations found in other pyroxene-pyroxenoids include rhodonite [$n = 5$]-wollastonite [3] (Dent Glasser and Glasser, 1961), johannsenite [∞]-bustamite [3] (Morimoto, Koto and Shinohara, 1966), clinopyroxene [∞]-pyroxferroite [7] (Lindsley and Burnham, 1970) and clinopyroxene-pyroxmangite (Ito, 1972a), where the number n given in brackets is the frequency of occurrence of tetrahedral horizontal offset. In pyroxene-pyroxenoid polymorphic relationships, the phase with larger n seems to be the more stable at lower temperature and higher pressure.

In conclusion, there is a close correspondence in the cation polyhedral shape in rhodonite and pyroxmangite when the chemical compositions of the two minerals are similar. A comparison of the present results with more Ca-rich rhodonite and pyroxferroite indicates that Ca is not restricted to one site but is distributed over more than one position. Thus the compositional limit on the Ca concentration in the chain silicates cannot be explained, as previously suggested, by the hypothesis that only one crystallographic site is capable of accommodating the Ca atom. When polymorphic relations exist in pyroxene-pyroxenoids,

the phase with a larger n is a lower temperature and higher pressure phase.

AN EFFECT OF TEMPERATURE ON THE FELDSPAR STRUCTURE: CRYSTAL STRUCTURE OF SANIDINE AT 800°C

Y. Ohashi and L. W. Finger

The effect of temperature on a crystal can be observed in changes in unit-cell parameters and atomic coordinates. Because of the constraints of symmetry, simple compounds such as alkali halides show homogeneous structural expansion but no change in *fractional* atomic coordinates. In such relatively complex structures as silicates, however, one part of the structure can show a larger change than the rest of the structure. This inhomogeneous structural change is one of the characteristic features found in high-temperature studies of silicates (e.g., Bloss and Papike, 1973). The SiO_4 tetrahedral unit is found to be rigid compared with the cation polyhedra. As it is assumed that the tetrahedron itself is rigid but that it can rotate with respect to the other tetrahedra, structural changes in silicates can be analyzed by examining (1) changes in relative orientation of tetrahedra linked together by the bridging oxygen, (2) changes in the cation polyhedral shape, and (3) correlation between (1) and (2). In pyroxenes the parameters used for (1) are chain rotation angle and out-of-plane tilting (Thompson, 1970; Papike *et al.*, 1973; Cameron *et al.*, 1973; Ohashi and Finger, *Year Book 73*, pp. 522–525). In feldspars, however, all four corners of the tetrahedron are linked to other tetrahedra, and thus more parameters are necessary to analyze the relative orientation of tetrahedra.

The results of a refinement of the crystal structure of sanidine from Laacher See, Germany, at 20° and 400°C were previously reported (Ohashi and Finger, *Year Book 73*, pp. 539–544), and the results at 800°C are summarized in Tables 43 and 44. The lattice parameters

TABLE 43. Atomic Coordinates and Equivalent Isotropic Temperature Factors (\AA^2) for Laacher See Sanidine at 800°C

	<i>x</i>	<i>y</i>	<i>z</i>	<i>B</i> (eq)
K,Na	0.2924(4)	0	0.1426(5)	7.29(7)
T1	0.0108(2)	0.1867(1)	0.2245(2)	2.49(3)
T2	0.7156(2)	0.1185(1)	0.3462(2)	2.45(3)
OA1	0	0.1489(5)	0	4.06(12)
OA2	0.6503(7)	0	0.2895(8)	3.97(11)
OB	0.8326(6)	0.1503(4)	0.2314(6)	4.88(10)
OC	0.0427(5)	0.3114(3)	0.2615(6)	4.12(9)
OD	0.1755(5)	0.1261(3)	0.4056(5)	4.34(9)

at 800°C are $a = 8.682(3) \text{ \AA}$, $b = 13.013(3) \text{ \AA}$, $c = 7.184(2) \text{ \AA}$, and $\beta = 115.71(1)^\circ$; and the space group is $C2/m$. The maximum expansion direction between 20°C and 800°C was found to be approximately normal to the (100) plane with an expansion coefficient of $2 \times 10^{-5}/^\circ\text{C}$. This value is comparable to the maximum principal coefficient for low albite but is smaller than that for high albite (Ohashi and Finger, *Year Book 72*, pp. 569–573). The other two principal axes of the strain ellipsoid show essentially no or only slightly negative expansion. This anisotropy of lattice expansion is a general feature of feldspar lattice expansion, although orientation varies depending on composition (Ohashi and Finger, *Year Book 72*, pp. 569–573; Willaime, Brown, and Perucaud, 1974; Grundy and Brown, 1974).

One of the more useful ways of describing the tetrahedral framework structure in feldspars is to take a four-membered ring of tetrahedra as a unit of the network. The choice of such a ring is not unique because of its three-dimensional nature, and in this study the one

discussed by Megaw (1974a), which is parallel to (010), is regarded as a basic unit (Fig. 97A). The four-tilt parameters of Megaw (1974b) are used in the following analysis of temperature effect on the feldspar structure. An angle between two adjacent rings is also considered. These angles are shown in Fig. 97A.

The first hinge tilt, ϕ_1 , is a rotation of the T1 tetrahedron in (100). In sanidine there is essentially no change in this parameter as temperature changes (Table 45). The second hinge tilt, ϕ_2 , which describes a rotation of the T2 tetrahedron in the plane normal to [001], increases by heating such that in the b projection the OC oxygen atom moves farther out and O2A comes closer to the center of the ring (cf. Fig. 97A). The third measure is a wrinkling tilt, ϕ_3 , which is a rotation of the T1 tetrahedron about the c axis. Because two oxygen atoms in the diagonal positions in the ring are related by the two-fold axis passing through the center of the ring parallel to b , an increase in ϕ_3 results in wrinkling of the ring. When sanidine is heated this tilt increases. The shearing tilt, ϕ_4 , is a distortion of the parallelogram of the ring. Sanidine does not show significant change in this tilt on heating.

In a discussion of changes in the framework structure, not only changes within the ring but also the relative change of two adjacent rings is one of the important parameters. Although the individual distances and angles between tetrahedral sites do not change very much, the vector connecting two sites in adjacent rings rotates about the c axis (Fig. 97A). When an angle Ψ with the

TABLE 44. Interatomic Distances* (\AA) for Laacher See Sanidine at 800°C

T1-OA1	1.650(2)	T2-OA2	1.633(2)	(K,Na)-OA1 [$\times 2$]	2.999(4)
T1-OB	1.639(4)	T2-OB	1.616(4)	(K,Na)-OA2 [$\times 1$]	2.815(7)
T1-OC	1.649(4)	T2-OC	1.631(4)	(K,Na)-OB [$\times 2$]	3.114(5)
T1-OD	1.657(4)	T2-OD	1.619(4)	(K,Na)-OC [$\times 2$]	3.141(4)
Mean	1.649	Mean	1.625	Mean	3.034

* With no thermal correction.

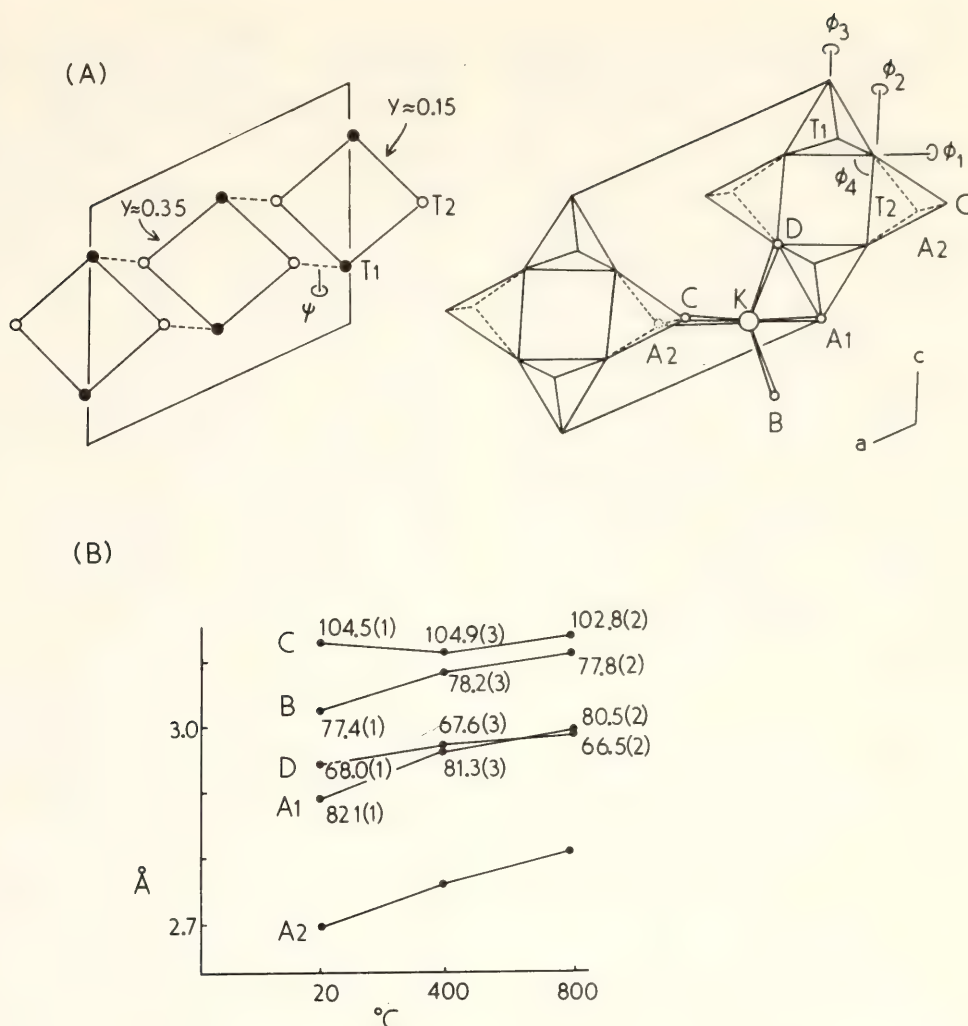


Fig. 97. (A) Arrangement of the tetrahedral rings in sanidine and definitions of the angles ϕ_n ($n = 1, 2, 3, 4$) and Ψ in Table 45. (B) Variations of the K-O distances and the O-K-O angles in sanidine as a function of temperature. The numbers associated with each data point are the O-K-O angles for oxygens related by the mirror plane. Both K and O42 are on the mirror planes. See (A) for the oxygen coordination around the alkali atom.

(010) plane is used as a measure of this rotation, it decreases on heating in such a way that two rings become more distant in the (010) projection and the

difference in height along the projection axis b decreases.

The changes in the alkali polyhedron are shown in Fig. 97B. Both the alkali atom and the oxygen O42 in sanidine are on the mirror plane at $y = 0$. Because the other oxygens are not on the mirror plane, each has two equivalent positions, one above and one below the mirror plane. In total, nine oxygen atoms are less than or about 3.2 Å from the alkali position. With increasing temperature the K-OA2 distance increases by about 0.1 Å between 20°C and 800°C, whereas K-OC is essentially unchanged. These changes in the alkali polyhedron correspond to a rotation of T2 about c , or the second-hinge tilt.

It is obvious that not only the K-O

TABLE 45. Variations of Four Tetrahedral Tilts* and an Angle Ψ * with Temperature for Laacher See Sanidine

	20°C	400°C	800°C
ϕ_1	3.3†	3.4	3.5
ϕ_2	16.2	17.3	17.4
ϕ_3	5.2	6.2	6.7
ϕ_4	1.2	1.7	1.1
Ψ	59.4	58.5	57.7

* See Fig. 97 for definition of these angles.

† Although a standard error has not been computed for each angle quoted here, it is estimated as 0.1 to 0.2 from the uncertainty in the O-O-O and T-T-T angles.

distances but also the O-K-O angles across the mirror plane will change. Such angles for O41 and O \bar{D} decrease with an increase in temperature (Fig. 97). The decrease in the O41-K-O41 angle and the expansions of the K-O41 and K-O42 distances result in an elongation of the alkali polyhedron along the reciprocal a^* axis, the direction normal to (100), and relative flattening along the b axis.

In conclusion, the major structural changes in sanidine are the second-hinge tilt and the wrinkling tilt of the tetrahedra and the elongation of the alkali polyhedron along a^* . These changes in the structure yield the maximum lattice expansion in the direction approximately normal to (100).

LEAST-SQUARES REFINEMENT OF THE RIGID-BODY MOTION PARAMETERS OF CO₃ IN CALCITE AND MAGNESITE AND CORRELATION WITH LATTICE VIBRATIONS

L. W. Finger

In the least-squares refinement of a crystal structure, the parameters to be determined include terms that describe the delocalization of point scatterers. Because the major source of such dispersion is usually the effects of thermal vibrations, the quantities are called temperature factors; however, many other factors may be of importance in determining the size, shape, and orientation of the ellipsoid enclosing surfaces of equal probability density. These factors may include the effects of uncorrected physical factors such as absorption and extinction (both primary and secondary) as well as errors in the model. The effects due to positional disorder caused by (a) defects in the structure such as found in mullite (Burnham, *Year Book* 63, pp. 223–228) and (b) positional disorder in solid-solution minerals such as pyroxenes on the hedenbergite-ferrosilite join (Ohashi, Burnham, and Finger, 1975) are well known to many mineralogists.

One implicit assumption in the model

of thermal motion for an ordinary refinement of a crystal structure is that the atoms vibrate independently. Obviously this assumption is poor for materials such as certain organic compounds that have crystal structures composed of discrete molecules. Several workers, including Cruikshank (1956) and Schomaker and Trueblood (1968), have developed techniques for extracting information about the motion of such molecules from the refined anisotropic temperature factor coefficients by assuming that the molecule acts as a rigid body. An alternative approach (Pawley, 1963, 1964; Johnson, 1970; and Prince and Finger, 1973) uses the least-squares process to directly estimate the parameters of the molecular motion. This approach has the desirable effect of constraining the structure to eliminate variations that have no physical meaning.

The direct refinement of molecular motion parameters has not been widely used because it has been necessary to prepare special subprograms for each structure, a time-consuming procedure. With the completion of the least-squares program RFINE4 (Finger and Prince, 1975), however, the constraint equations may be applied without any reprogramming in a fashion similar to that for the constraints on occupancies (Finger, *Year Book* 67, pp. 216–217) used in earlier versions of the program. Although few, if any, minerals may be described as having a molecular structure, there are several instances in which portions of the structure are relatively rigid. The SiO₄ tetrahedra in silicates and the CO₃ triangle in carbonates are examples of segments of a nonmolecular structure that are coherent. In the present study, the initial results of the refinement of rigid-body parameters for the carbonate groups in magnesite and calcite are presented and compared with the ordinary refinement and the far-infrared spectrum.

The rigid-body motions may be analyzed in terms of translations, librations, and screw motions that may be repre-

sented by three tensors **T**, **L**, and **S** of rank 3 (Schomaker and Trueblood, 1968). In the general case, **T** and **L**, which are symmetric, each have six unique terms, and **S**, which is nonsymmetric, has eight unique terms.* However, as in the case of anisotropic temperature factors, the presence of symmetry reduces the number of independent values.

In the calcite-type structure, the CO_3^{2-} ion is in a site with symmetry $\bar{3}2$. Using the symmetry constraints tabulated by Schomaker and Trueblood (1968), there are five independent coefficients, two each in **T** and **L** and one in **S**. The physical interpretation of the rigid-body parameters is as follows: T_{11} (which is equal to T_{22}) describes translations in the plane normal to c ; T_{33} is the coefficient for translations parallel to c ; L_{33} describes librations about the 3-fold axis; L_{11} (equal to L_{22}) is for librations about axes normal to c ; and S_{11} describes screw or coupled libration and translation motion. By comparison, the usual, free-atom thermal model has six variable coefficients.

Oh *et al.* (1973) reported the crystal structure of magnesite with structure factor data that were suitable for rigid-body refinement. The recent study of calcite by Chessin, Hamilton, and Post (1965), however, did not include any diffraction peaks that had scattering contributions from either calcium or carbon. As a result, these data could not be used in the present study, and it was necessary to measure a complete set of intensities. A cleavage fragment of calcite from the Linden Mine, Iowa County, Wisconsin (U.S. National Museum No. 49122) was selected, and standard data collection and reduction techniques (including an absorption correction) were applied. In a partial chemical analysis performed with the electron microprobe,

the Fe, Mn, and Mg values for this material are less than 0.05 wt %.

Each structure was first refined using conventional anisotropic thermal parameters; the refinement was then repeated applying the rigid-body constraints. The final values for the various structure quantities are presented in Table 46. The differences in the thermal ellipsoids, C-O bond distances, and residuals between the rigid-body and ordinary refinements are insignificant. As shown above, the transformation from conventional to rigid-body refinement eliminates one independent parameter that accounts for the internal modes of the carbonate group (E. Prince, personal communication), which should not be important in this study since the frequencies of these vibrations, $700\text{--}1400\text{ cm}^{-1}$ (Oh *et al.*, 1973; White, 1974), involve energies much greater than the thermal energy at room temperature.

Not only do the rigid-body parameters describe the scattering without introducing extraneous coefficients, but the eigen values of **T** and **L** may be used to calculate expected frequencies for lattice-mode vibrations in these crystals. Prince, Schroeder, and Rush (1973) relate the eigen values of **L** to frequencies by

$$\theta^2 = \frac{h}{8\pi^2 \omega c I} \coth \left(\frac{hc\omega}{2kT} \right)$$

where θ^2 is the mean-square amplitude in radians; ω is the frequency in cm^{-1} ; I is the molecular moment of inertia; and the other quantities have the usual meaning. The equation may be extended to translations by substituting the mean-square amplitude of linear motion for θ^2 and the mass of the molecule for its moment of inertia. A comparison of the frequencies of the infrared modes with the computed value from the x-ray data is presented in Table 47. The agreement between the spectroscopic and x-ray values is excellent for vibrations about the 3-fold axis of the carbonate group. Correlation of the other librations with the infrared spectrum is somewhat more

* There are nine coefficients in **S**; however, the trace of **S** must be a constant (usually chosen as zero), thereby reducing the number of independent parameters to eight.

TABLE 46. A Comparison of the Unconstrained and Rigid-Body Refinements for Calcite and Magnesite

		Calcite		Magnesite	
		Unconstrained	Rigid-Body	Unconstrained	Rigid-Body
Thermal Ellipsoids					
Ca	$r_1 (c), \text{\AA}$	0.095(2)	0.095(2)	0.085(4)	0.084(4)
or Mg	$r_2 (c)$	0.099(2)	0.099(2)	0.074(4)	0.076(4)
C	$r_1 (c)$	0.099(5)	0.102(5)	0.078(8)	0.085(8)
	$r_2 (c)$	0.096(5)	0.092(5)	0.077(8)	0.067(8)
O	$r_1 (a_1)$	0.089(2)	0.092(2)	0.064(7)	0.067(7)
	$r_2 (a_1)$	0.112(2)	0.113(2)	0.085(5)	0.087(5)
	$r_3 (a_1)$	0.171(2)	0.169(2)	0.100(3)	0.097(3)
	$\alpha,^* \text{ deg.}$	50(2)	50(2)	19(5)	15(5)
Other Parameters					
C-O distance, \AA		1.284(1)	1.282(1)	1.283(1)	1.283(1)
$T_{11}, \text{\AA}^2$			0.0084(3)		0.0046(3)
$T_{33}, \text{\AA}^2$			0.0103(5)		0.0070(6)
L_{11}, rad^2			0.0054(4)		0.0015(4)
L_{33}, rad^2			0.0083(4)		0.0017(3)
S_{11}, rad^2			0.0020(1)		0.0002(1)
Wtd $R, \dagger \%$		3.2	3.3	3.9	4.0
$R, \ddagger \%$		3.0	3.1	3.7	3.8

* α is the angle between axis r_3 and c .
† Wtd $R = (\sum W (|F_o| - |F_c|)^2 / \sum W F_o^2)^{1/2}$.
‡ $R = \sum (|F_o| - |F_c|) / \sum |F_o|$.

TABLE 47. Single-Crystal Vibrational Frequencies (cm^{-1}) for Calcite and Magnesite

		Frequencies, cm^{-1}						
		Calcite			Magnesite			
Mode	Symmetry	Rigid-Body Parameter	ν_t^*	ν_l^*	Rigid-Body	ν_t^*	ν_l^*	Rigid-Body
ν_7^\dagger	A_{2u}	L_{33}	92	136	104(2)	230	281	240(22)
ν_{11}	$E_g \ddagger$	T_{33}	107(3)	131(6)
ν_{10}	E_u	T_{11}	102	123	119(2)	225	241	163(5)
ν_9	E_u	L_{11}	223	239	186(7)	301	315	387(10)

* ν_t and ν_l from infrared reflectance spectra by Hellwege *et al.* (1970).
† Mode notation from White (1974).
‡ This mode is inactive in both infrared and Raman spectra.

difficult. The coefficient T_{33} probably corresponds to a mode having symmetry E_g , which is inactive in both the infrared and Raman spectra; an inelastic neutron-scattering experiment would be required to measure this frequency. The frequencies corresponding to T_{11} and L_{11} do not match the values from Hellwege *et al.* (1970) as quoted by White (1974). If the assignment is reversed, however—a possibility because the symmetry of each of these modes is E_u and the modes cannot be distinguished in the infrared spectrum (W. B. White, personal communi-

cation)—the agreement is considerably improved. The calculated frequencies are higher in magnesite than in calcite. This difference is in agreement with the Mg-O bond being shorter and stronger than Ca-O; therefore, lattice vibrations will involve higher energies in magnesite.

The results of this initial study strongly indicate that rigid-body coefficients determined for minerals may be directly converted into lattice motions that correlate with spectroscopic data. In addition, in the present study it has also been possible to resolve ambiguities in the spectral assignments and to determine the frequencies of vibrations that are inactive in the infrared spectrum. It will be necessary to extend these calculations to a wider range of compounds to determine whether systematic features of chemical bonding and lattice dynamics may be derived from single-crystal intensities.

A NEUTRON-DIFFRACTION AND ^{57}Fe MÖSSBAUER STUDY OF A SYNTHETIC Ti-RICH GARNET

H. P. Weber, D. Virgo, and F. E. Huggins*

Neutron-Diffractometry

The difficulty of growing single crystals of mineral solid solutions suitable for detailed three-dimensional x-ray refinement has often hampered progress in petrologic crystal chemistry. Although some nuclear spectroscopic techniques (e.g., nuclear magnetic resonance and Mössbauer effect) offer the necessary quantification that other spectroscopic methods lack in the determination of cation substitutional trends in powdered samples, it is often desirable to confirm an unexpected finding by another quantitative method. Until recently, powder diffractometric techniques employing x-rays were used only to identify and to determine their lattice metrics; complete

structural refinements usually faltered because of the presence of overlapping reflections that either were not included in the refinement or were treated as an unresolved group. In both these cases, significant detail in the line profiles was lost. X-ray lines commonly assume an analytically complex shape, while neutron-diffraction lines can generally be approximated by curves of Gaussian shape. Consequently, powder neutron-diffraction profiles have recently been fitted in a way similar to Mössbauer spectra (Rietveld, 1969); the structure factors provide the constraints in the neutron diffraction, in contrast to the Mössbauer spectra in which the parameters of related absorption peaks are constrained. Neutron diffraction as compared with x-ray diffraction offers a few more advantages. First, often the scattering lengths of neighboring atoms in the Periodic Table are dissimilar. For example, the ratio of the neutron scattering lengths $b(\text{Ti})/b(\text{Fe})$ is equal to -0.36 , whereas for x-rays $f(\text{Ti}^{3+})/f(\text{Fe}^{2+})$ is equal to 0.79 at $2\theta = 0^\circ$. In addition, nuclei scatter neutrons isotropically, but x-ray scattering from electron shells decreases with increasing 2θ angles; in other words, the high-angle diffraction region still contains appreciable intensity in the neutron case. Both the above factors proved very beneficial in the present study of Ti-andradite by powder neutron diffraction.

Powder patterns of Ti-andradite ($\text{Ca}_{3-}\text{Fe}_2\text{Si}_{1.58}\text{Ti}_{1.42}\text{O}_{12}$) were collected at the HFBR reactor of Brookhaven National Laboratory using neutrons monochromatized to $\lambda = 1.36 \text{ \AA}$. The diffracted intensities were recorded in steps of 0.05° over the range $15.20^\circ < 2\theta < 90^\circ$ from $\sim 3\text{g}$ of sample contained in a thin-walled quartz can. The pattern is shown as Fig. 98. Refinement of the data proceeded in several steps, using a version of Rietveld's profile refinement program as modified by Hewat (personal communication). In all refinement trials, the initial guess was that all Ti was located

* Lamont-Doherty Geological Observatory, Columbia University, Palisades, New York.

on the octahedrally coordinated sites. To avoid any correlation between site occupancies and temperature factors, the temperatures were held constant at the following values: $B(\text{Ca}) = 0.6 \text{ \AA}^2$, $B(\text{octahedral}) = 0.3 \text{ \AA}^2$, $B(\text{tetrahedral}) = 0.2 \text{ \AA}^2$, $B(\text{oxygen}) = 0.4 \text{ \AA}^2$. These

are the average values determined for garnets of different composition from single-crystal structure refinements published in the last five years (Prandl, 1966; Novak and Gibbs, 1971). The sites were assumed to be fully occupied, and the scattering lengths were constrained

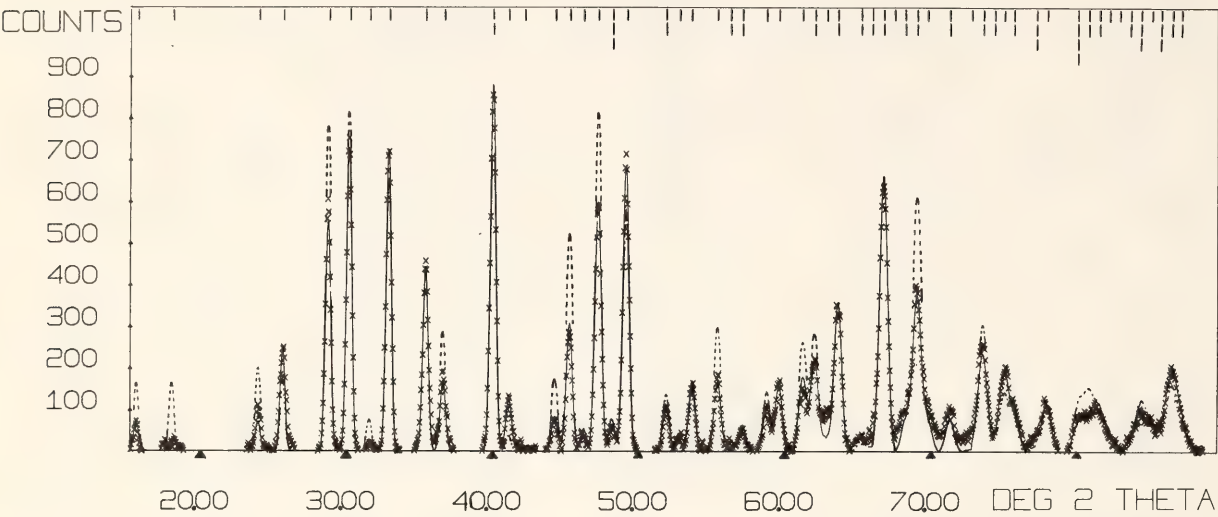


Fig. 98. Powder neutron-diffraction profile of Ti-garnet ($\text{Ca}_3\text{Fe}_2\text{Si}_{1.58}\text{Ti}_{1.42}\text{O}_{12}$). The observed pattern is indicated by crosses; the calculated pattern is shown by the solid line. The position of each reflection is indicated by a vertical bar.

TABLE 48. Refinement Data for Ti-Garnet ($\text{Ca}_3\text{Fe}_2\text{Si}_{1.58}\text{Ti}_{1.42}\text{O}_{12}$)

Cell edge:			
a_0	12.2399(13) Å		
x	0.03524(22) Å		
y	0.04892(20) Å		
z	0.65078(24) Å		
Site occupancies:			
Octahedral	0.481(5) Fe,	0.519 Ti	
Tetrahedral	0.346(3) Fe,	0.127 Ti,	0.527 Si
$R_{\text{profile}}(\text{weighted})^*$	19.45%		
$R_{\text{profile}}(\text{expected})^\dagger$	12.88%		
$R_{\text{nuclear}}^\ddagger$	10.60%		

The total number of observed reflections is 90 and the number of overlapping reflections is 86.

$*R_{\text{profile}}(\text{weighted})$

$$= 100 \sqrt{\Sigma W(Y_o - \frac{1}{C} Y_c)^2 / \Sigma W Y_o^2}$$

$^\dagger R_{\text{profile}}(\text{expected})$

$$= 100 \sqrt{N - P + C} / \Sigma W Y_o^2$$

$^\ddagger R_{\text{nuclear}}$

$$= 100 \Sigma |F_o|^2 - \frac{1}{C} F_c^2 / \Sigma F_o^2$$

$$W = 1/Y_o$$

Y_o , observed count minus background; Y_c , calculated count; N , number of observables; P , number of variables; C , number of linear constraint equations.

to give the correct chemical composition. Preliminary findings are summarized in Table 48. The lattice constant is in agreement with that reported by Virgo and Huckenholz (*Year Book 73*, pp. 426–433) using x-ray diffractometer data, viz. $a_0 = 12.239 \text{ \AA}$. This result was expected because the profile refinement of even a mediocre pattern results in acceptable lattice parameters. The interatomic distances between Ca and oxygen (2.38 \AA , 2.52 \AA) and between the octahedral cations and oxygen (1.99 \AA) are similar to the values found in other garnets; the distance between tetrahedral cations and oxygen (1.74 \AA) lies between the values for an unsubstituted Si-garnet (1.64 \AA) and the rare earth garnets containing only iron in tetrahedral coordination (1.87 \AA). The refinement suggests that 27% of the available Ti shares the tetrahedral site with Si and Fe. In view of the preliminary stage of the refinement, this result is in reasonable agreement with the site occupancy of 17% determined from Mössbauer effect analysis, (Virgo and Huckenholz, *Year Book 73*). However, drastic changes in the site-occupancy refinement are not to be expected as the pattern is further refined. The strong asymmetry of the line shape, the half-width parameters, and isotropic as well as anisotropic thermal motion still remain to be considered as variables in the refinement. The counting statistics are acceptable but could be improved with more material.

Analysis of ^{57}Fe Mössbauer Spectra of Synthetic Ti-Garnets

For a comparison of site-occupancy data determined from Mössbauer spectra and the neutron-diffraction refinement discussed above, the least-squares fitting of Mössbauer data of Ti-garnets has been evaluated in terms of the number of fitted peaks and the uncertainty in the spectral parameters resulting from the counting statistics and peak overlap. It is particularly relevant to evaluate

the systematic errors in the intensity ratios determined from the Mössbauer spectra because the Ti^{4+} occupancies for garnet compositions along the join andradite–Ti-andradite are determined solely by difference on the assumption that both the tetrahedrally and octahedrally coordinated sites are fully occupied. In this study, two new methods for statistically evaluating the least-squares fitting of Mössbauer data are used. The statistical criteria are those of Ruby (1973) and Dollase (1975).

The absorption spectra of garnets along the join andradite–Ti-andradite consist of two overlapping doublets due to Fe^{3+} in the octahedrally and tetrahedrally coordinated sites (*Year Book 73*, Fig. 145). Implicit in the model proposed by Virgo and Huckenholz (*Year Book 73*, pp. 426–433) and Huggins, Virgo, Hölzl, and Huckenholz (this Report) is that the spectral data can be least-squares fitted to only three absorption lines of Lorentzian shape. This model was used because of the nearly complete overlap of the two Fe^{3+} doublets at positive velocities. However, it is important to compare this fit of the Ti-garnet spectra to a fit based on four peaks (Fig. 99). It is noted that four-line fits to the spectral data converge only by constraining the areas of the component peaks of each doublet to be equal. For garnet solid solutions between andradite and Ti-andradite (Virgo and Huckenholz, *Year Book 73*), the four-peak fit results in a reduction of χ^2 from values in the range 1600–850 to 1400–800; the significantly higher values of χ^2 are found for samples containing $\leq 20 \text{ wt } \%$ Ti-andradite. For comparison, the statistical criterion proposed by Ruby (1973), MISFIT, varies from ~ 0.15 to 0.30% with an uncertainty of $\sim \pm 0.02$. It is instructive that the absolute value of MISFIT is not systematically related to the bulk composition, nor is it significantly different from the model assuming only three Lorentzian lines. These results suggest that all samples are fitted equally well by either of

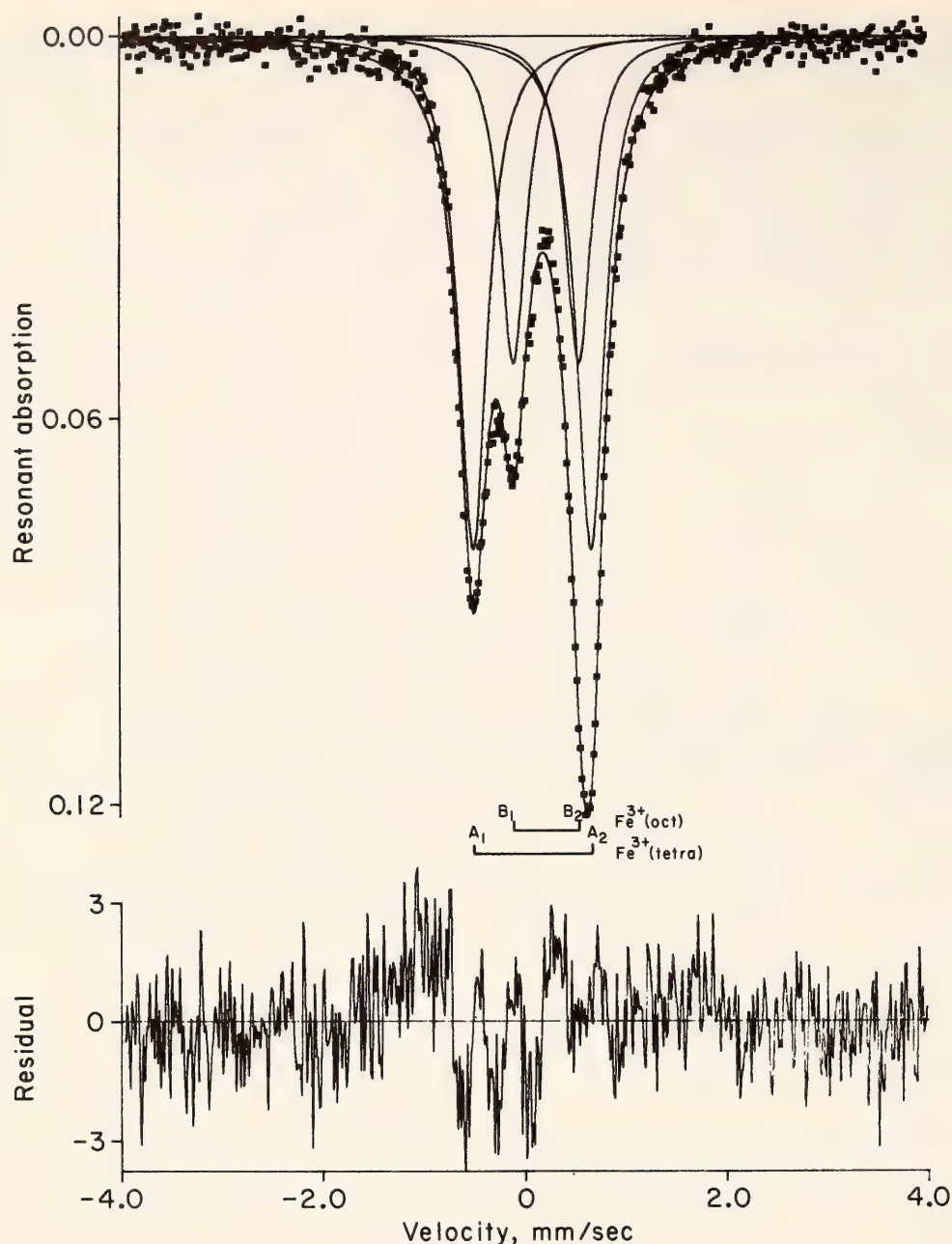


Fig. 99. ^{57}Fe Mössbauer spectra of Ti-garnet ($\text{Ca}_3\text{Fe}_2\text{Si}_{1.58}\text{Ti}_{1.42}\text{O}_{12}$) measured at 298°K . The solid line is a least-squares fit to four Lorentzian lines (eight peak variables, one background variable), the areas $A_1 = A_2$ and $B_1 = B_2$ being constrained.

these models. However, the smaller value for the uncertainty of MISFIT compared with MISFIT itself is significant (cf. Ruby, 1973) and suggests that although the quality of the counting data is sufficient to test either model (three or four absorption lines), the absolute value of MISFIT might suggest that a further alternative model would be appropriate.

In this connection, Dowty (1971) suggested that a second Fe^{3+} octahedral doublet with a slightly larger quadrupole splitting could be fitted under the ab-

sorption envelopes of natural Ti-garnets. Although Dowty did not invoke two distinct octahedral sites in garnets, which would be contrary to crystal-structure refinements, he suggested that the split of the octahedral ferric absorption is due to short-range ordering. As pointed out by Burns (1972), however, this aspect of Dowty's fitting procedure can be rejected for the following reason. A consequence of Dowty's least-squares fitting procedure is that the doublet due to tetrahedrally coordinated Fe^{3+} has an

isomer shift in the range 0.04–0.14 mm/sec (Dowty, 1971, Table 3), which is low for Fe^{3+} in an oxygen environment. A case in point is the isomer shift for Fe^{3+} in kimzeyite (0.19 mm/sec). For comparison, the isomer shift for tetrahedrally coordinated Fe^{3+} in the andradite–Ti-andradite solid-solution series (calculated from the four-line fits) is constant at ~ 0.20 – 0.21 mm/sec.

To evaluate further the probable errors resulting from the degree of overlap of the Ti-garnet spectra, the statistical uncertainty of the spectral data has been calculated by the method of Dollase (1975). In this approach, simulated two-peak spectra were generated on a computer and as a function of peak separation and different relative intensity ratios, and the spectra were then fitted by the usual least-squares technique. Dollase defined a statistical quality Ξ of any peak in a given spectrum in terms of background counts, velocity increment, and width and fractional absorption of a peak. Importantly, he demonstrated that the statistical uncertainty with which each peak parameter may be determined from a given spectrum is an inverse linear function of the peak Ξ value. For example, a plot of $\Xi \epsilon_A$, where ϵ_A is the relative error in the computed area, asymptotically varies as a function of peak separation. It is shown that below a critical separation of about 0.6Γ , where Γ is the peak width, the probable error in determining the area of a given peak rapidly increases toward infinity (Dollase, 1975, Fig. 4).

Generally, the value of the product $\Xi \epsilon_A$ for each peak in a three-line fit of the Ti-garnet spectra is ~ 2 – 5 for values of peak separation, which are always $> 1.0 \Gamma$. The statistical parameter Ξ is in the range 200–400, which gives relative errors, ϵ_A , of 0.5%–2.0% for a given peak parameter. Admittedly, the relative error is significantly larger for garnets with a small Ti-andradite component. For example, Ξ for the low-velocity tetrahedral peak in the sample containing 10 wt %

Ti-andradite is ~ 50 , which gives a relative error of $\sim 14\%$ in the calculated area. Nevertheless, regardless of bulk composition, the relative deviation of the ratio $\text{Fe}/\Sigma\text{Fe}$ is only $\sim 1\%$ – 2% . This degree of precision is also found for the four-line constrained fits of Ti-garnets even though the relative errors of the unresolved positive velocity lines (Fig. 99) are significantly large ($\sim 20\%$).

In summary then, the above evaluation of determining site occupancies in the synthetic Ti-garnets from Mössbauer spectroscopy indicates that the sample ($\text{Ca}_3\text{Fe}_2\text{Si}_{1.58}\text{Ti}_{1.42}\text{O}_{12}$) has an average value of the ratio $\text{Fe}_{\text{VI}}/\Sigma\text{Fe}$ equal to $0.413 (\pm 0.005)$ and is to be compared with the neutron-diffraction result of 0.481 (Table 48). The apparent discrepancy in site occupancies determined by the two techniques cannot be accounted for at this time. In particular, least-squares fitting of the Mössbauer absorption data by either the three- or the four-line model does not reveal any systematic errors in the Fe^{3+} intensity ratios, and furthermore the precision of the intensity ratios is only 1%–2% despite the strong degree of peak overlap. There still remains the problem of correlating the experimentally determined cation substitution in synthetic Ti-garnets to their natural analogues. The results from this study contradict past prejudices regarding Ti^{4+} substituting in tetrahedrally coordinated crystal sites in the garnet structure.

DISTRIBUTION OF AL, Fe^{3+} , AND Ti^{4+}
BETWEEN THE OCTAHEDRAL AND
TETRAHEDRAL SITES IN GARNETS BETWEEN
 $\text{Ca}_3\text{Al}_2\text{Si}_3\text{O}_{12}$ AND
 $\text{Ca}_3\text{Fe}_2\text{Ti}_{1.416}\text{Si}_{1.584}\text{O}_{12}$

F. E. Huggins, D. Virgo, E. Hölzl,
and H. G. Huckenholz**

Natural titanium-containing garnets are commonly Si-deficient and contain Al, Fe^{3+} , Ti^{4+} , and possibly Ti^{3+} , which

* University of Munich.

can be located on the remaining tetrahedral sites. Hence the crystal chemistry of these garnets with respect to the distribution of cations between the octahedral and tetrahedral sites in garnets is complex. Most previous investigations of these garnets have been carried out on natural samples and lack systematic compositional control and knowledge of the conditions of formation. Such investigations lack correlation between samples and are hampered by the presence of more variables than can be adequately monitored. The most comprehensive attempts to study natural samples (Dowty, 1971; Burns, 1972; Moore and White, 1971) have indicated complications related to the oxidation state of iron, titanium, or both, and have shown that some if not all Ti^{4+} must be located on the octahedral sites, but ferric iron, aluminum, or both go onto the tetrahedral sites. Synthetic phase studies relating to the substitution of Ti^{4+} in garnets have indicated that Ti^{4+} can enter tetrahedral coordination (Ito and Frondel, 1967) but do not provide specific site-occupancy data for garnets of compositions close to those of natural garnets. Virgo and Huckenholz (*Year Book 73*, p. 426), by means of the Mössbauer effect, systematically studied a garnet solid solution between andradite and titanandradite, $\text{Ca}_3\text{Fe}_2\text{Ti}_{1.416}\text{Si}_{1.584}\text{O}_{12}$, a garnet of composition close to the limit of the solubility of Ti-andradite in andradite (Huckenholz, 1969). Their study effectively showed that the tetrahedral sites of these garnets contained both ferric iron and titanium. This result for the Ti-rich garnet of the composition given above has also been confirmed by neutron diffraction (Weber, Virgo, and Huggins, this Report). In order to extend such systematic studies to include other end-members important in natural garnets, synthetic garnets along the join grossular-titanandradite were studied by the Mössbauer effect and are reported here.

Garnets with compositions between

$\text{Ca}_3\text{Al}_2\text{Si}_3\text{O}_{12}$ and $\text{Ca}_3\text{Fe}_2\text{Ti}_{1.416}\text{Si}_{1.584}\text{O}_{12}$ were synthesized at the University of Munich in the course of an investigation into the phase relations along that join. The garnets, which have the formula $\text{Ca}_3\text{Al}_{2-2x}\text{Fe}_{2x}\text{Ti}_{1.416x}\text{Si}_{3-1.416x}\text{O}_{12}$, were crystallized from glasses in air at temperatures of 1050°C over a period of months or in hydrothermal runs at 800°C and 1 kbar over a period of weeks and buffered by the breakdown of PtO_2 . No sample showed the presence of ferrous iron in its Mössbauer spectrum. Compositions and synthesis conditions are listed in Table 49. Experimental details relating to synthesis of these samples will be discussed elsewhere (Huckenholz and Hölzl, in preparation).

Mössbauer spectra were taken at room temperature and fitted to three Lorentzian lines by means of a least-squares fitting procedure. As discussed elsewhere (Weber, Virgo, and Huggins, this Report), these garnet spectra in theory should be fitted to four lines, but the difference in four-line vs. three-line fits, as indicated by the statistical procedure MISFIT (Ruby, 1973) and the semi-empirical scheme of Dollase (1975), is not significant. Thus, the data listed in Table 50 refer to three peak fits to the data. Although the trends in the Mössbauer parameters vary systematically with composition and require explanation, this report will concentrate only on the systematic trend shown by the area ratio, $\text{Fe}_{\text{VI}}/(\text{Fe}_{\text{VI}} + \text{Fe}_{\text{IV}})$, as this quantity refers directly to site occupancy of iron (and indirectly to Al^{3+} and Ti^{4+}) in these garnets.

The data on the area ratio are shown in Fig. 100, plotted against various equations defined by the extreme order or disorder schemes listed in Table 51. It is immediately apparent that the data do not follow any one of these schemes, although for Al-rich garnets ($x < 0.558$) the data do plot close to the most disordered scheme. Hence the possibility that any one of the three cations—Al, Fe^{3+} , or Ti—has an overriding tendency

TABLE 49. Compositions and Synthesis Conditions of Garnets between Grossular and Titanandradite

Gross (wt %)	Titan (wt %)	Gross (Mol %)	Titan (Mol %)	Synthe- sis Time (days)	Crystalli- zation Tem- perature (°C)	Al (pfu)†	Si (pfu)	Fe (pfu)	Ti (pfu)
100	0	100	0	2.000	3.000	0.000	0.000
80	20	82.64	17.36	17	800	1.653	2.754	0.347	0.246
70	30	73.53	26.47	18	800	1.471	2.625	0.529	0.375
60	40	64.10	35.90	8	800	1.282	2.492	0.718	0.508
50	50	54.35	45.65	20	800	1.087	2.354	0.913	0.646
40	60	44.25	55.75	{ (a)14 (b)75 }	{ 800 1050 }	0.885	2.211	1.115	0.789
30	70	33.78	66.22	120	1050	0.676	2.062	1.324	0.938
20	80	22.94	77.06	120	1050	0.459	1.909	1.541	1.091
10	90	11.68	88.32	75	1050	0.234	1.749	1.766	1.251
0	100‡	0	100	30	1050	0.000	1.584	2.000	1.416

* Samples synthesized at 800°C were under 1 kbar pressure; samples synthesized at 1050°C were in air.

† Per formula unit.

‡ Virgo and Huckenholz (*Year Book* 73).

for one site and constrains the other two cations to the other site is effectively eliminated by the Mössbauer data.

The data were then examined with the aid of an ideal solid-solution model. Because of the following compositional and site-occupancy constraints:

$$\text{Al} + \text{Fe} + \text{Ti} = 2 + 1.416x; \quad (1)$$

$$\text{Al}_{\text{VI}} + \text{Fe}_{\text{VI}} + \text{Ti}_{\text{VI}} = 2; \quad (2)$$

$$\text{Al}_{\text{IV}} + \text{Fe}_{\text{IV}} + \text{Ti}_{\text{IV}} = 1.416x; \quad (3)$$

$$\text{Al}_{\text{IV}} + \text{Al}_{\text{VI}} = \text{Al} = 2 - 2x; \quad (4)$$

$$\text{Fe}_{\text{IV}} + \text{Fe}_{\text{VI}} = \text{Fe} = 2x; \quad (5)$$

$$\text{Ti}_{\text{IV}} + \text{Ti}_{\text{VI}} = \text{Ti} = 1.416x; \quad (6)$$

only two site occupancies (for different elements) need be obtained for complete knowledge of the cation distributions. Unfortunately, the Mössbauer effect provides information only about the distribution of Fe. However, K_1 and K_2 , the distribution coefficients for Al-Fe and Ti-Fe exchange, can be defined as follows:

$$K_1 = \frac{[\text{Al}_{\text{IV}}][\text{Fe}_{\text{VI}}]}{[\text{Al}_{\text{VI}}][\text{Fe}_{\text{IV}}]}; \quad (7)$$

$$K_2 = \frac{[\text{Ti}_{\text{IV}}][\text{Fe}_{\text{VI}}]}{[\text{Ti}_{\text{VI}}][\text{Fe}_{\text{IV}}]}. \quad (8)$$

By manipulation of Equations 4–8, the octahedral occupancies may be expressed in terms of K_1 , K_2 , and R_{Fe} , the ratio $\text{Fe}_{\text{IV}}/\text{Fe}_{\text{VI}}$, as follows:

$$\text{Al}_{\text{VI}} = \frac{2 - 2x}{K_1 R_{\text{Fe}} + 1}; \quad (9)$$

$$\text{Ti}_{\text{VI}} = \frac{1.416x}{K_2 R_{\text{Fe}} + 1}; \quad (10)$$

$$\text{Fe}_{\text{VI}} = \frac{2x}{R_{\text{Fe}} + 1}. \quad (11)$$

By substituting these values in Equation 2, an expression involving only K_1 , K_2 , x , and R_{Fe} is obtained,

$$2 = \frac{2 - 2x}{K_1 R_{\text{Fe}} + 1} + \frac{1.416x}{K_2 R_{\text{Fe}} + 1} + \frac{2x}{R_{\text{Fe}} + 1}. \quad (12)$$

Thus at a given value of x , a measured value of R_{Fe} defines a relationship between K_1 and K_2 . If the solid solutions are ideal, the values of K_1 and K_2 should

TABLE 50. Mössbauer Data* for Garnets between Grossular and Titanandradite

Mol Frac- tion Titan, <i>x</i>	Crys- talli- zation Temper- ature (°C)	IS6† (mm/sec)	QS6† (mm/sec)	Γ6 (mm/sec)	IS4† (mm/sec)	QS4† (mm/sec)	Γ4 (mm/sec)	ΓC‡ (mm/sec)	Area Ratio Fe _{IV} +Fe _{VI} Fe _C	χ ²	Base Line ×10 ⁻⁵	Area Ratio Fe _{VI} Fe _{IV} +Fe _{VI}
0.174	800	0.40	0.66	0.36	0.11	1.26	0.48	0.39	0.98	693	8.1	0.86
0.265	800	0.40	0.68	0.34	0.11	1.25	0.43	0.37	0.99	890	14.8	0.82
0.359	800	0.40	0.71	0.34	0.13	1.24	0.40	0.38	0.99	1182	12.5	0.77
0.457	800	0.40	0.71	0.34	0.14	1.23	0.39	0.36	1.01	882	8.2	0.74
0.558	800	0.40	0.72	0.34	0.15	1.22	0.37	0.35	1.01	879	11.2	0.70
0.558	1050	0.40	0.73	0.34	0.16	1.21	0.34	0.37	1.00	1161	5.9	0.70
0.662	1050	0.40	0.74	0.35	0.17	1.21	0.35	0.36	1.02	1093	8.4	0.63
0.771	1050	0.40	0.74	0.36	0.18	1.18	0.35	0.37	1.02	1526	6.5	0.55
0.883	1050	0.40	0.74	0.35	0.19	1.17	0.33	0.36	0.99	834	9.4	0.48
1.000§	1050	0.39	0.73	0.34	0.19	1.13	0.32	0.36	1.01	850	2.8	0.41

* Mössbauer data reported are averages for the two sides of mirror-image spectra fitted to three Lorentzian peaks.

† Based on the position of the composite peak at high velocity and hence liable to a large systematic error.

‡ Composite peak formed by the superposition of the high-velocity peaks of the two doublets.

§ From Virgo and Huckenholz (*Year Book* 73).

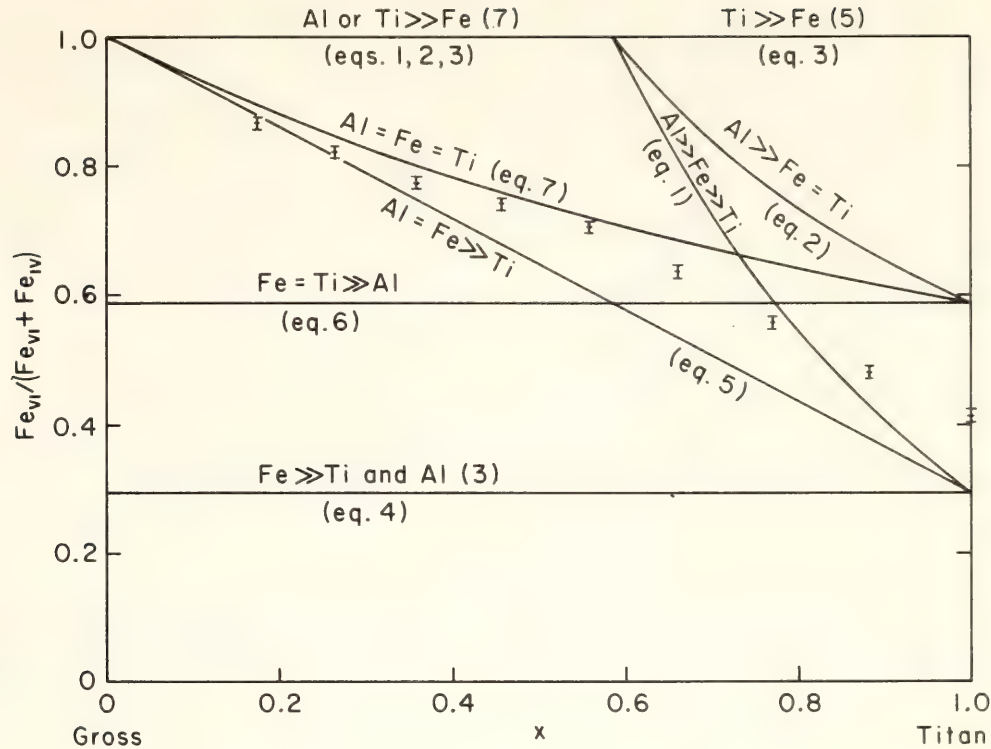


Fig. 100. Mössbauer area ratio, $Fe_{VI}/(Fe_{VI} + Fe_{IV})$, as a function of composition across the join grossular-titanandradite. The lines representing ordering schemes were obtained using the equations listed in Table 51. Numbers in parentheses refer to the number of schemes following the same line.

TABLE 51. Ordering Schemes Considered for Garnets across the Grossular-Titanandradite Join

No.	Ordering Scheme*	Equation for R^\dagger		
1	Al >> Fe >> Ti	$R = 1.00$	$(0.0 \leq x \leq 0.58548)$	(1)
		$R = (2-1.416x)/2x$	$(0.58548 \leq x \leq 1.0)$	
1A	Al >> Fe = Ti	$R = 1.00$	$(0.0 \leq x \leq 0.58548)$	(2)
		$R = 0.58548/x$	$(0.58548 \leq x \leq 1.0)$	
2	Al >> Ti >> Fe	$R = 1.00$	$(0.0 \leq x \leq 1.0)$	(3)
2A	Al = Ti >> Fe	(3)		
3	Fe >> Al >> Ti	$R = 0.292$		(4)
3A	Fe = Al >> Ti	$R = 1-0.708x$		(5)
4	Fe >> Ti >> Al	(4)		
4A	Fe >> Ti = Al	(4)		
5	Ti >> Al >> Fe	(3)		
5A	Ti >> Al = Fe	(3)		
6	Ti >> Fe >> Al	(3)		
6A	Ti = Fe >> Al	$R = 0.58548$		(6)
7	Al = Fe = Ti	$R = 2/(2+1.416x)$		(7)

* In terms of preference for tetrahedral sites $x \gg y$ means completely ordered, all x in tetrahedral site before any y ; $x = y$ means completely disordered, x and y in tetrahedral sites in accord with bulk ratio.
 $^\dagger R = Fe_{VI}/(Fe_{VI} + Fe_{IV})$.

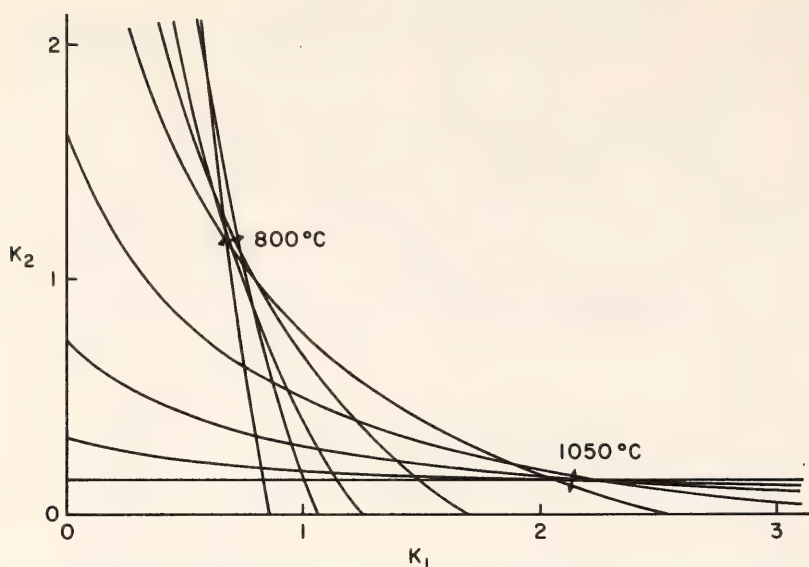


Fig. 101. Plot of the relationship between the two distribution coefficients, K_1 and K_2 , defined by the Mössbauer ratio, $\text{Fe}_{\text{IV}}/\text{Fe}_{\text{VI}}$, at a given composition using Equation 12. The approximate points of intersection at the different temperatures define the most appropriate values: 800°C , $K_1 = 0.71$, $K_2 = 1.12$; 1050°C , $K_1 = 2.15$, $K_2 = 0.143$.

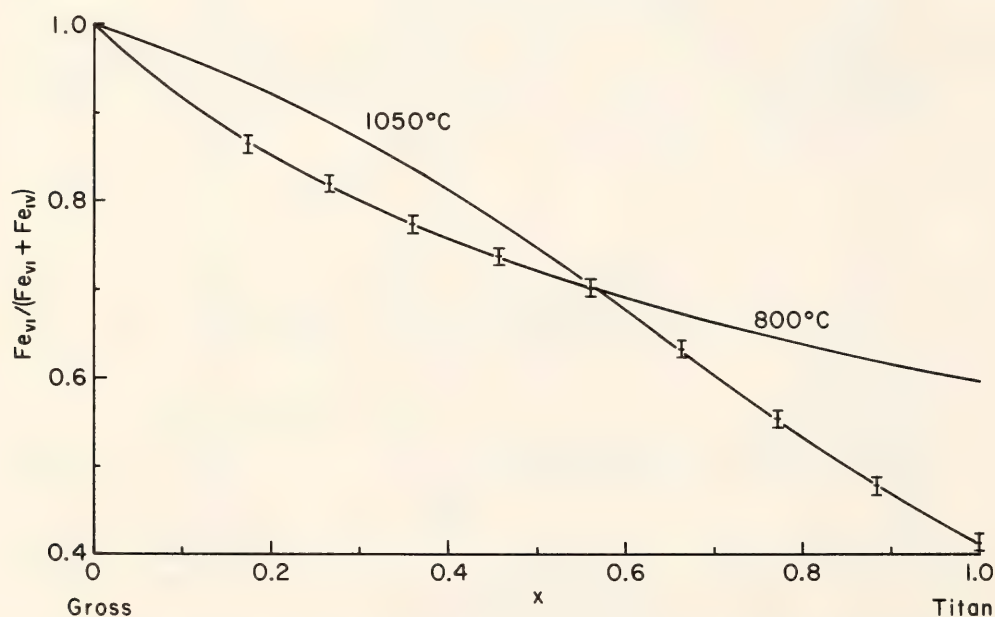


Fig. 102. Mössbauer area ratio, $\text{Fe}_{\text{VI}}/(\text{Fe}_{\text{VI}} + \text{Fe}_{\text{IV}})$, as a function of composition across the join grossular-titanandradite. The curves are calculated isotherms for the ratio as a function of composition, based on the most appropriate values of K_1 and K_2 obtained in Fig. 101.

be independent of x at any given temperature; therefore, curves relating K_1 and K_2 for each value of x should intersect at a unique point, reflecting the most appropriate values of K_1 and K_2 at that temperature. If the measured R_{Fe} values are substituted into Equation 12, the curves shown in Fig. 101 result, and the assumption of ideal solid-solution

behavior appears to be satisfied because a unique point is obtained for each temperature. The data not only seem to provide a test of the ideality of the solid solution but also give the values of K_1 and K_2 at the two temperatures and *complete* site-occupancy data. Calculated isotherms based on these values of K_1 and K_2 and the Mössbauer data are

shown in Fig. 102. Unfortunately, at the present time attempts to interrelate the two sets of data have not been successful; for instance, when one of the Ti-rich samples ($x = 0.883$), originally crystallized at 1050°C , was heated at 800°C (dry, 1 atm) for 12 days the Mössbauer ratio changed only slightly toward the 800°C curve. The kinetics for exchange may be extremely sluggish, or perhaps there is additional complexity in this subsolidus region of the phase diagram; the interpretation based on an ideal solid-solution model is therefore regarded as tentative.

CATION DISTRIBUTIONS IN SOME COMPOUNDS WITH THE PSEUDOBROOKITE STRUCTURE

D. Virgo and F. E. Huggins

Compounds with the pseudobrookite structure, $\text{Fe}^{3+}_2\text{TiO}_5$, $\text{Fe}^{2+}\text{Ti}_2\text{O}_5$, $\text{Mg-Ti}_2\text{O}_5$, and solid solutions of these end-members are mineral components of some lunar and terrestrial volcanic rocks. Recently Navrotsky (1975) has suggested that the high-temperature stability of these compounds is related to a balance between the endothermic enthalpies of formation (from binary oxides for the $A^{3+}_2B^{4+}_2\text{O}_5$ pseudobrookites or from assemblages of ilmenite and rutile structures for the $A^{2+}B^{4+}_2\text{O}_5$ type) and substantial positive entropies of formation. It is inferred that the configurational entropy plays an important role in their phase stability.

However, recent crystal-structure refinements (Lind and Housley, 1972; Smyth, 1974b; Wechsler, Prewitt, and Papike, 1975) in which determination of site occupancies was attempted are not wholly unambiguous because the x-ray scattering powers of Fe and Ti are similar. Thus quantitative data pertaining to the oxidation state and location of Fe and Ti in these compounds are still lacking. Of principal concern in this report are the compounds $\text{Fe}^{3+}_2\text{Ti}^{4+}\text{O}_5$, $\text{Fe}^{2+}\text{-Ti}^{4+}_2\text{O}_5$, and $\text{Fe}^{2+}_{0.5}\text{Mg}_{0.5}\text{Ti}^{4+}_2\text{O}_5$.

Generally the orthorhombic pseudobrookite crystal structure consists of bands of distorted edge-sharing octahedra that are aligned parallel to b . Of importance in this study is that there are two crystallographically distinct octahedral sites: one with a site multiplicity of 4 (Wyckoff notation 4c) and the other with a multiplicity of 8 (Wyckoff notation 8f).

Fe_2TiO_5 . The crystal structure of pseudobrookite was first refined by Pauling (1930), who determined the cation distribution to be $(\text{Ti})^{4c}[\text{Fe}_2]^{8f}\text{O}_5$. However, Muranaka *et al.* (1971) suggested that the broad line widths in the Mössbauer spectrum of Fe_2TiO_5 measured at 4°K result from two overlapping Zeeman patterns due to Fe^{3+} in both the 4c and 8f sites.

The paramagnetic absorption spectrum at 298°K of Fe_2TiO_5 prepared in air from an oxide mix at 1220°C , 29 days (A. Muan, personal communication), shows a single absorption doublet (Fig. 103A). The hyperfine parameters listed in Table 52 characterize the iron as entirely in the trivalent state, and these values are comparable to the values reported by Gibb, Greenwood, and Twist (1969); quadrupole splitting = 0.75 mm/sec , and isomer shift = 0.27 mm/sec . However, the residuals to the fit and the statistic parameters ($\chi^2 \sim 1000$; MISFIT = $0.37 \pm 0.037\%$) suggest that the model of a single Fe^{3+} doublet may not be satisfactory (Fig. 103A). An improved model to the data is achieved by using a two-doublet fit and constraining the areas of the component peaks of each doublet to be equal (Fig. 103B; $\chi^2 \sim 580$; MISFIT = $0.06 \pm 0.02\%$). Undoubtedly Fe_2TiO_5 has a cation configuration between inverse and random. The calculated cation distribution at 1220°C in pseudobrookite is $(\text{Fe}_{0.88}\text{Ti}_{0.12})^{4c}[\text{Fe}_{0.56}\text{Ti}_{0.44}]^{8f}\text{O}_5$. Using the approach of Dollase (1975), discussed by Weber, Virgo, and Huggins (this Report), the relative error in each

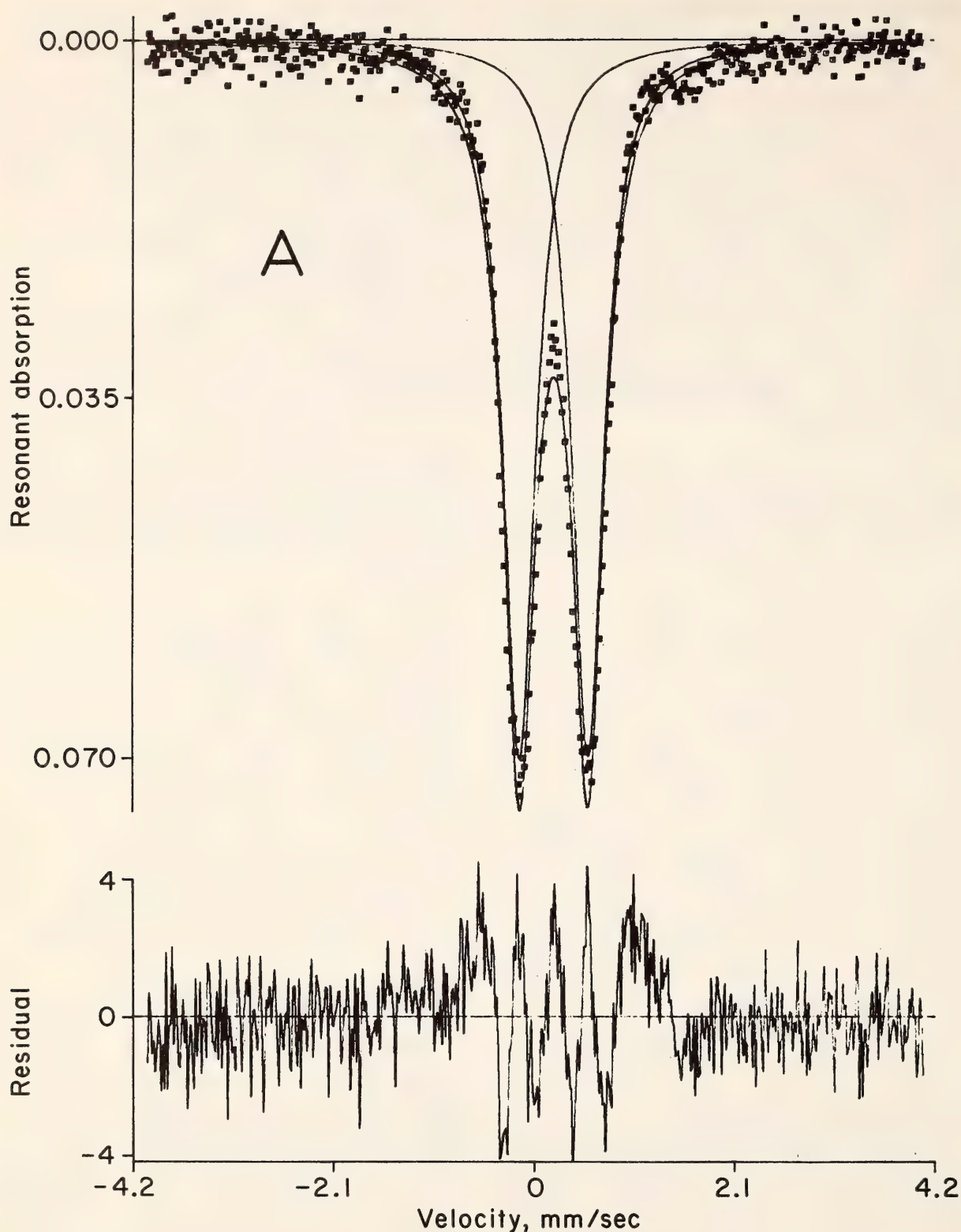


Fig. 103. ^{57}Fe Mössbauer spectrum of Fe_2TiO_5 at 298°K . (A) Solid line is a least-squares fit assuming two Lorentzians (six peak variables, one background variable).

of the calculated peak areas is $\sim 12\%$. This result translates to an error in the fraction of Fe^{3+} in the $8f$ site (equal to 0.56) of about 9%.

FeTi_2O_5 . The absorption spectrum at 298°K of ferropseudobrookite synthe-

sized at 1300°C , $f_{\text{O}_2} = 10^{-9.8}$ atm (A. Muan, personal communication), is plotted in Fig. 104 and shows the presence of a sharp, more intense outer doublet together with an inner doublet having broader line widths. The hyper-

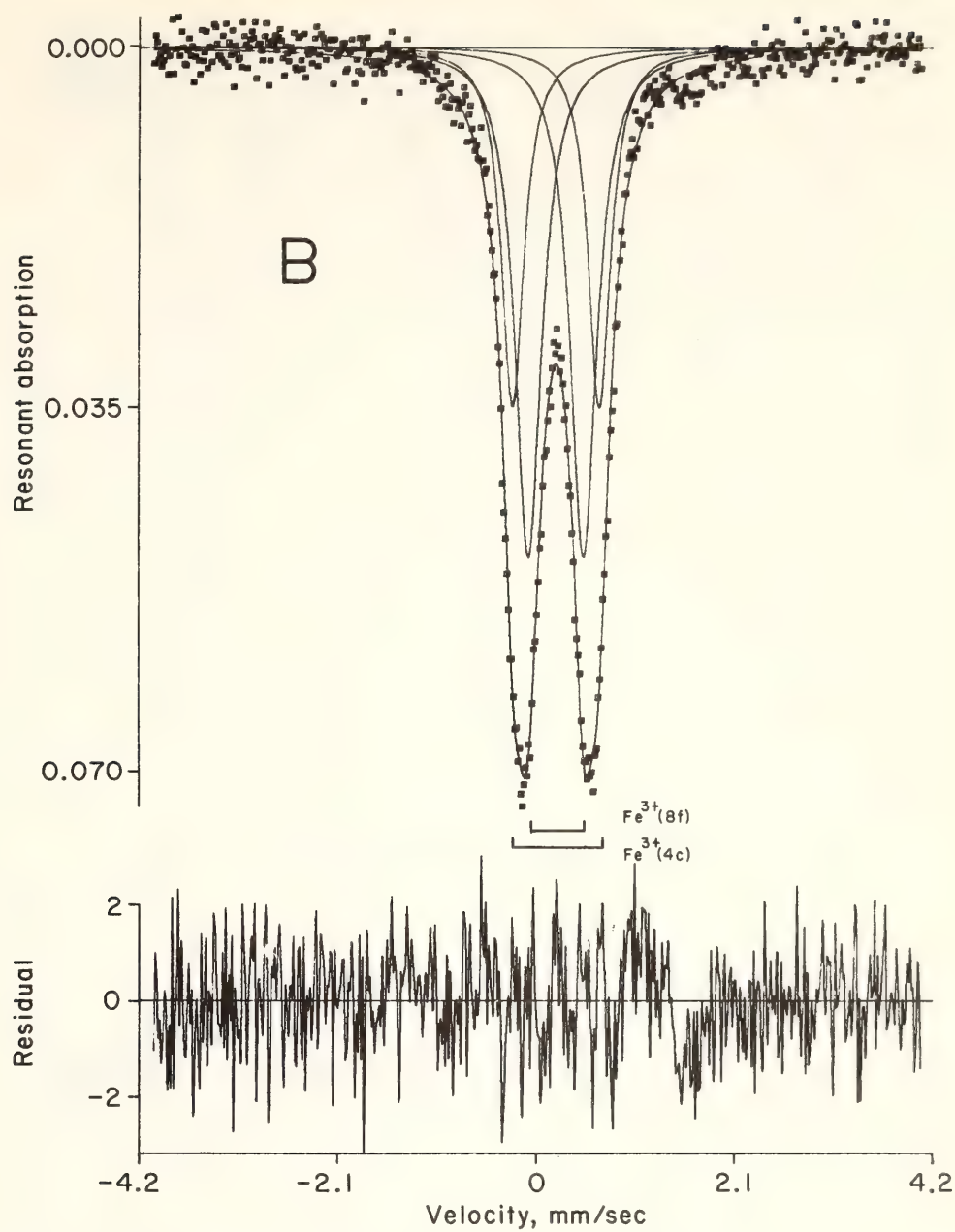


Fig. 103 (B). Solid line is a least-squares fit assuming four Lorentzians with area constraints (eight line variables, one background variable).

TABLE 52. Mössbauer Parameters for Synthetic Pseudobrookite, Ferropseudobrookite, and Armalcolite

Sample	Absorber Temper- ature (°K)	4c Site			8f Site		
		Isomer Shift* (mm/sec)	Quad- rupole Splitting (mm/sec)	Γ^\dagger (mm/sec)	Isomer Shift* (mm/sec)	Quad- rupole Splitting (mm/sec)	Γ^\dagger (mm/sec)
$\text{Fe}^{3+}_2\text{TiO}_5$	298	0.38	0.90	0.29	0.38	0.56	0.32
$\text{Fe}^{2+}\text{Ti}_2\text{O}_5$	298	1.05	3.20	0.28	1.02	2.18	0.64
$\text{Fe}^{2+}_{0.5}\text{Mg}_{0.5}\text{Ti}_2\text{O}_5$	298	1.05	3.15	0.30	1.03	2.01	0.58

* Referred to metallic iron at 298°K.
† Half width at half peak height.

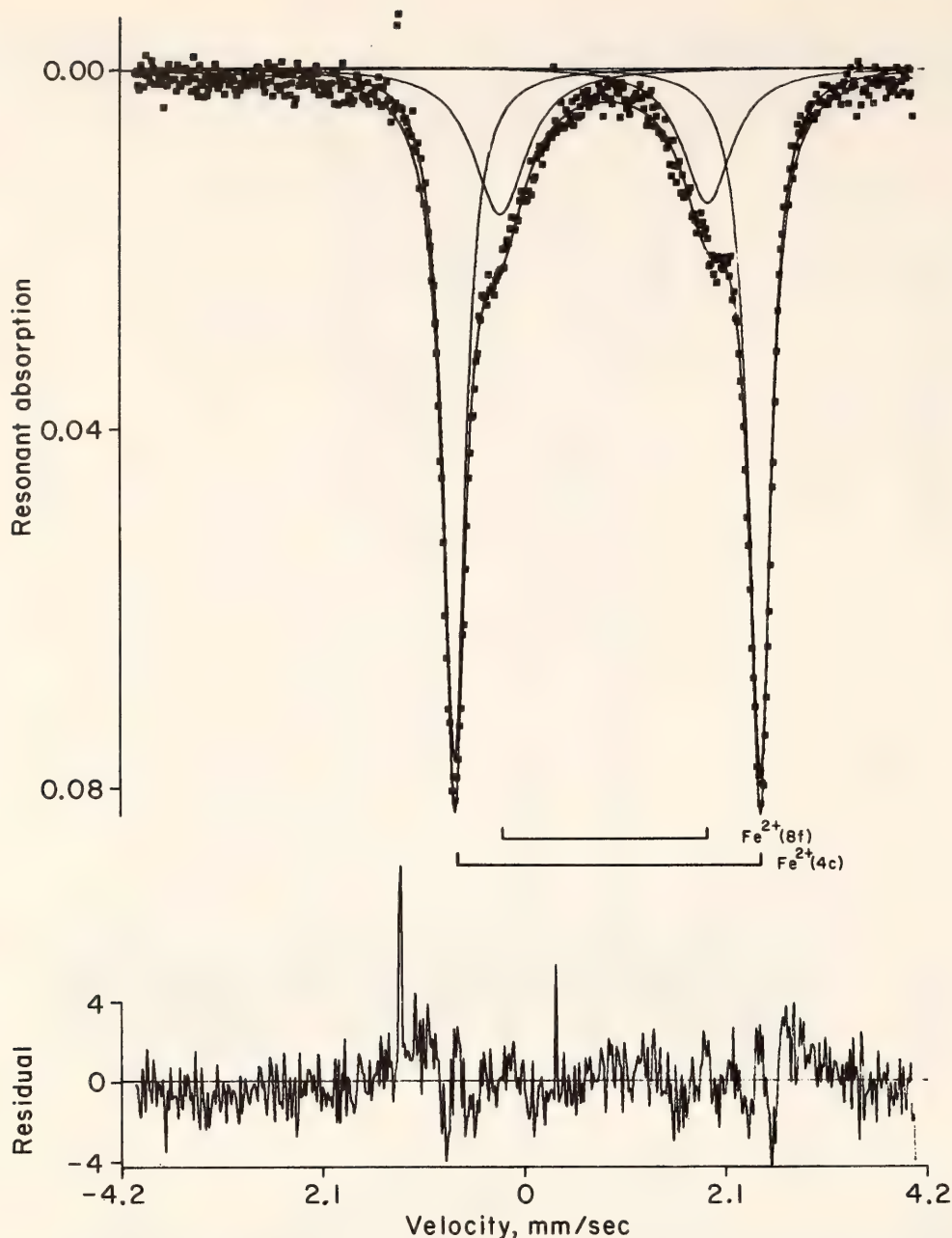


Fig. 104. ^{57}Fe Mössbauer spectrum of FeTi_2O_5 at 298°K . Solid line is a least-squares fit, assuming four Lorentzians (12 peak variables, one background variable).

fine data listed in Table 52 are in agreement with values reported by Grey and Ward (1973), although the sample reported by these authors contains ilmenite. Both sets of hyperfine data are entirely consistent with iron in the divalent state. The assignment of the absorption peaks to the crystal sites is based on a neutron diffraction study of FeTi_2O_5 and on the fact that the inner doublet (cf. Fig. 104) is observed to split into two doublets for monoclinic phases close in composition to Ti_3O_5 (Grey and Ward, 1973). This splitting corresponds to the

8-fold site degenerating into two 4-fold sites as in Ti_3O_5 (Åsbrink and Magnéli, 1959). The distribution of Fe^{2+} in the 8f sites is 31.2%, corresponding to the cation distribution $(\text{Fe}_{0.68}\text{Ti}_{0.32})^{4c}[\text{Fe}_{0.16}\text{Ti}_{0.84}]_2^{8f}\text{O}_5$.

$(\text{Fe}_{0.5}\text{Mg}_{0.5})(\text{Ti}_2)\text{O}_5$. Armalcolite was synthesized from an oxide mix at 1100°C , 80 hours, with an intermediate grinding to remove metastable ilmenite. The Mössbauer spectrum at 298°K is shown in Fig. 105. The spectrum is similar to that for ferropseudobrookite consisting of two overlapping Fe^{2+} doublets. From

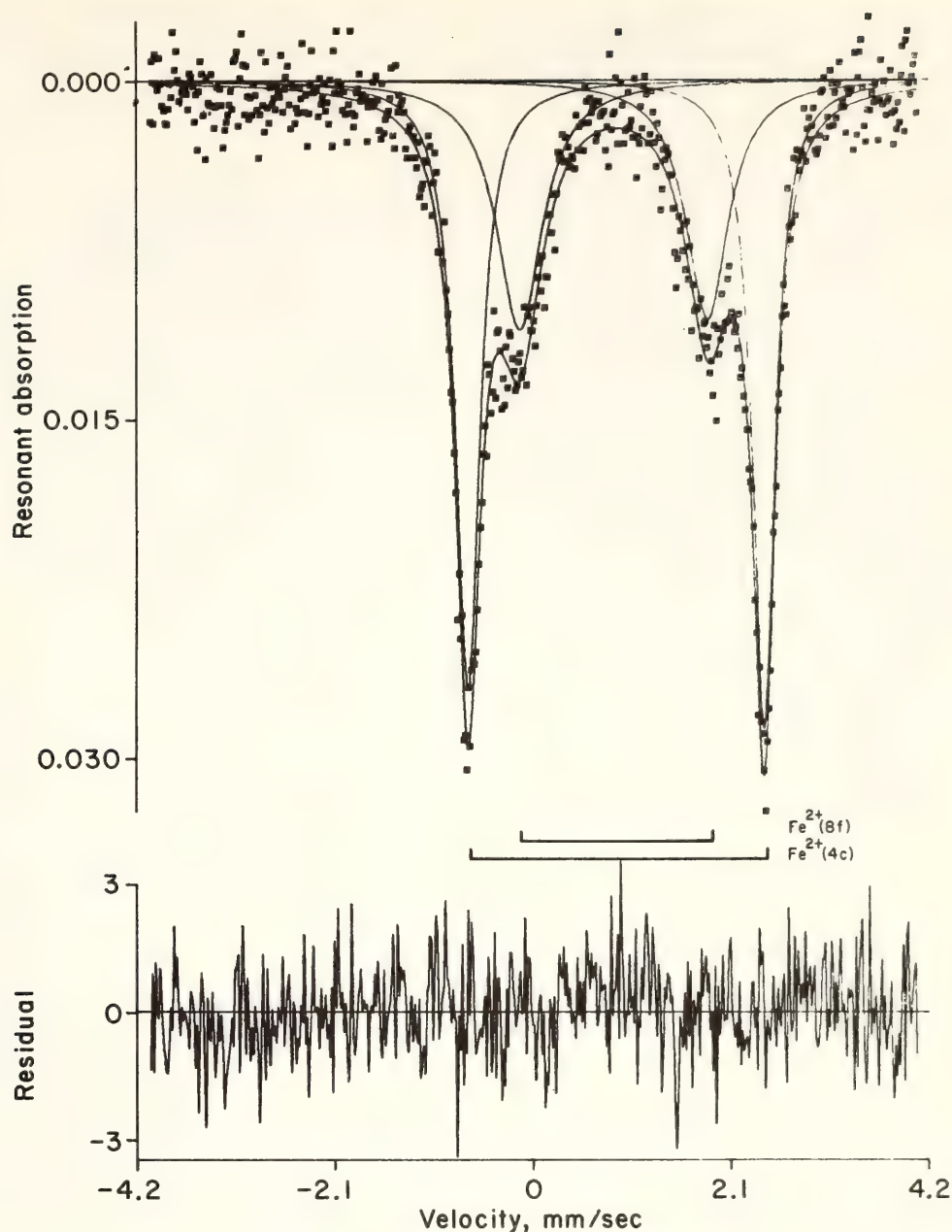


Fig. 105. ^{57}Fe Mössbauer spectrum of $\text{Fe}_{0.5}\text{Mg}_{0.5}\text{Ti}_2\text{O}_5$ at 298°K . Solid line is a least-squares fit, assuming four Lorentzians (12 peak variables, one background variable).

the least-squares fitting of the absorption data, there is $\sim 42.3\%$ Fe^{2+} in the $8f$ sites. This is the first quantitative determination of the distribution of Fe^{2+} in armalcolite and contrasts with previous studies. Lind and Housley (1972) synthesized armalcolite crystals from an appropriate glass composition on the heating stage of an x-ray diffractometer. Refinement of the x-ray diffraction intensity data for armalcolite crystals at $\sim 1000^\circ\text{C}$ suggested that essentially all the Ti^{4+} ions are in the $8f$ sites and that the $4c$ sites contain Fe^{2+}

and Mg within error limits of $\sim \pm 15\%$. In the same study, refinement of data for karrooite synthesized at 1500°C in air indicated that the $8f$ sites are $84.2 \pm 0.6\%$ occupied by Ti^{4+} and $15.8 \pm 0.6\%$ by Mg^{2+} ions, whereas the $4c$ sites contain $68.4 \pm 1.2\%$ Mg^{2+} and $31.6 \pm 1.2\%$ Ti^{4+} ions. The preference for an ordered configuration of cations in armalcolite (Lind and Housley, 1972) stems from the significantly lower limits of error in the refinement of karrooite compared with armalcolite and from the fact that the karrooite sample was syn-

thesized at a considerably higher temperature than the armalcolite. Furthermore, the Mössbauer spectrum of the quenched glass containing armalcolite crystals shows the presence of Fe^{2+} in the glass in addition to a single sharp Fe^{2+} doublet due to Fe^{2+} in the 4c site. It is reasonable to suggest that the contamination of their armalcolite sample by the glass prohibited quantitative determination of the disorder in armalcolite.

Wechsler, Prewitt, and Papike (1975) have refined the crystal structure of a synthetic armalcolite $[(\text{Fe}, \text{Mg})\text{Ti}_2\text{O}_5]$ by using the mean M-O distances to in-

fer the site populations. In this approach, a site-occupancy model which most closely approximates the mean M-O distances gives $\sim 33\%$ Fe^{2+} in the 8f site. However, this model also gives the same refinement (weighted R factor, 0.022) as a model in which Ti^{4+} exclusively occupies the 8f sites.

The results of this study support the contention that compounds with the pseudobrookite-type structure are indeed entropy-stabilized phases at high temperatures and have demonstrated the applicability of the Mössbauer technique to the study of the order-disorder phenomenon in these compounds.

LUNAR PETROLOGY

STUDY OF THE MICROFEATURES OF LUNAR AGGLUTINATE PARTICLES

H. K. Mao, P. M. Bell, and J. Adams

Portions of the lunar surface covered with layers of unconsolidated soil or regolith material have characteristic absorption "signatures" in the spectral region sampled by earth-based telescope (Charette *et al.*, 1974). These signatures are spectral features related to electronic transitions in the mineral and glass particles of the lunar soil. Their study is essential to interpretations of broadly based telescope surveys of the moon's surface that are currently under way and that will be made in the forthcoming lunar polar orbiter (LPO) mission planned for 1978.

Agglutinate particles in lunar soils are aggregates of mineral and rock fragments welded by glass. In the present study it has been determined that a major portion of these particles are not simply volcanic in origin but are products of shock processes of meteorite and micrometeorite impacts. The physical and chemical character of the agglutinates contributes significantly to the soil spectrum (Rhodes *et al.*, 1975), and it is essential to determine their properties in

detail. The present study is an examination of the fine structure (to micrometers) of agglutinate mineral, glass, and matrix components in order to assess the following factors: (1) the physical structure of agglutinates; (2) the chemistry of agglutinates; (3) the spectral properties of agglutinates (in transmission) in terms of their contribution to the spectral properties of the lunar surface; and (4) the state of iron in agglutinates insofar as it may relate to the process of agglutinate formation and to magnetic properties.

Agglutinate fragments were selected after concentration by magnetic separation of lunar soil samples 10084, 66081, and 67701. A typical agglutinate from 67701 is shown in Fig. 106. Anorthite-rich zones that are relatively fresh grade into brown-colored glassy zones. One of the brown glassy zones is shown in Fig. 106B. Note various size bubbles, which formed from trapped gas, most likely of solar wind origin. The release of solar wind gas, mainly hydrogen, would cause localized chemical reduction.

Figure 107A shows a polished mount of an agglutinate grain from 67701. The light areas are unaffected anorthosite; the darker areas grade into brown glass

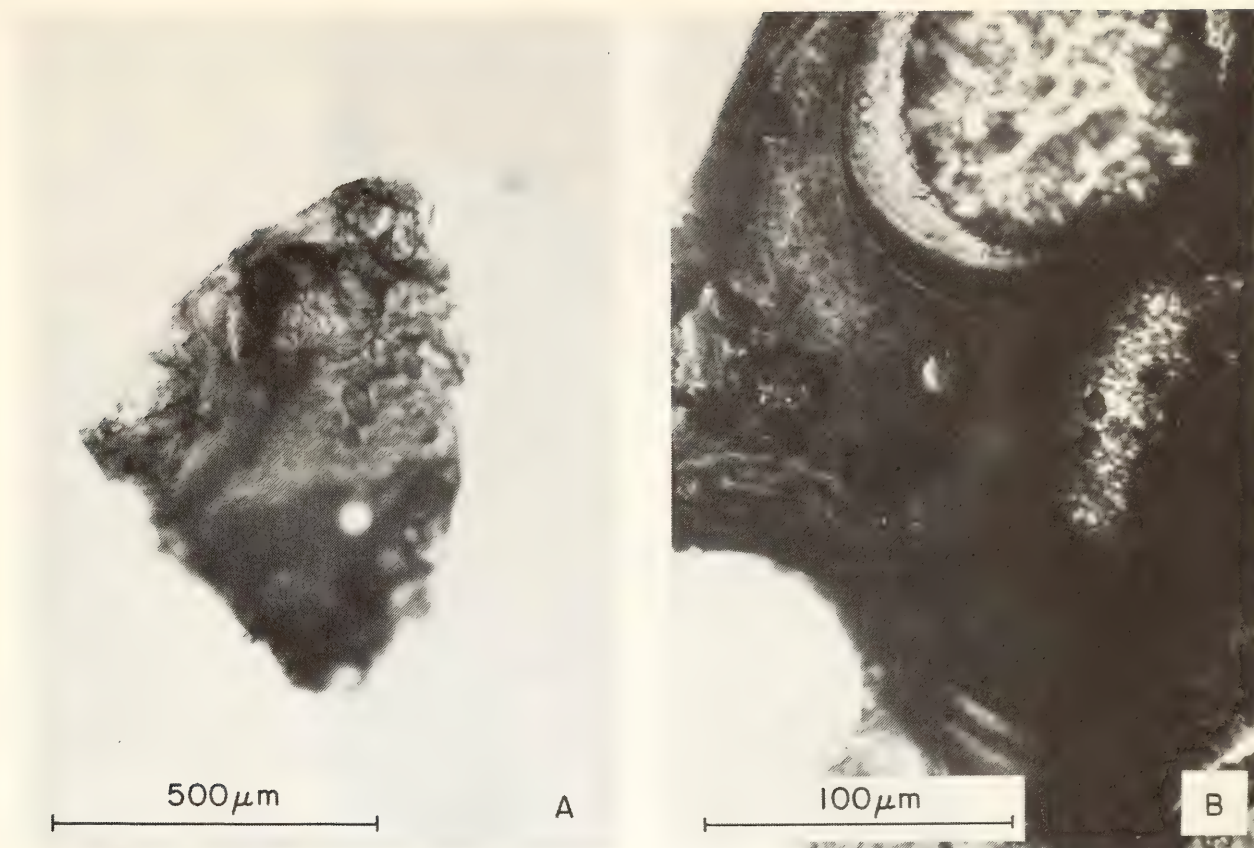


Fig. 106. Photomicrograph of 67701,38,1d agglutinate; transmitted light. (A) Whole grain, unpolished. (B) Polished thin section. Area on left, anorthosite; dark central zone, brown glass; zone on right, glass plus metal, shown in detail in Fig. 107.

zones. The brown glass zones contain minute metallic spheres, apparently quenched in the glass from the molten state. The metallic spheres are concentrated in glassy swirls and in what appear to be cracks or veins in Fig. 107B. Figure 107C shows another grain in which metallic spheres are concentrated in a glassy "rind" that grades into unmelted anorthite. The largest of the metallic spheres is approximately $100\text{ }\mu\text{m}$ in diameter, ranging down to a size of a few hundred angstroms (or less, depending on the limit of resolution of the scanning electron microscope).

Composition

Table 53 gives electron microprobe analyses of three agglutinate particles from 67701. Anorthositic and clear glass zones are nearly pure anorthite; the light, average tone and dark brown glass are very similar to each other in composition, but contain considerably

more iron and magnesium than anorthosite.

The metallic spheres are either pure iron or iron-nickel alloys where $\text{Fe/Ni} = 10.8/1$ (wt %, measured by nondispersive x-ray analysis). This analysis suggests that the metallic spheres are of lunar origin and were produced by shock melting or disproportionation of iron-bearing minerals or perhaps are of meteoritic origin. Significantly, the metallic iron spheres are observed only in brown glass.

Absorption Spectra

Spectral features are observed in the brown glass portions of the agglutinate grains as a broad shoulder steeply rising into the near ultraviolet region. This type of spectral shoulder and the brown color are often caused by small amounts of ferric iron (Bell and Mao, *Year Book* 73, pp. 496–497). Possibly disproportionation of ferrous iron to metallic iron

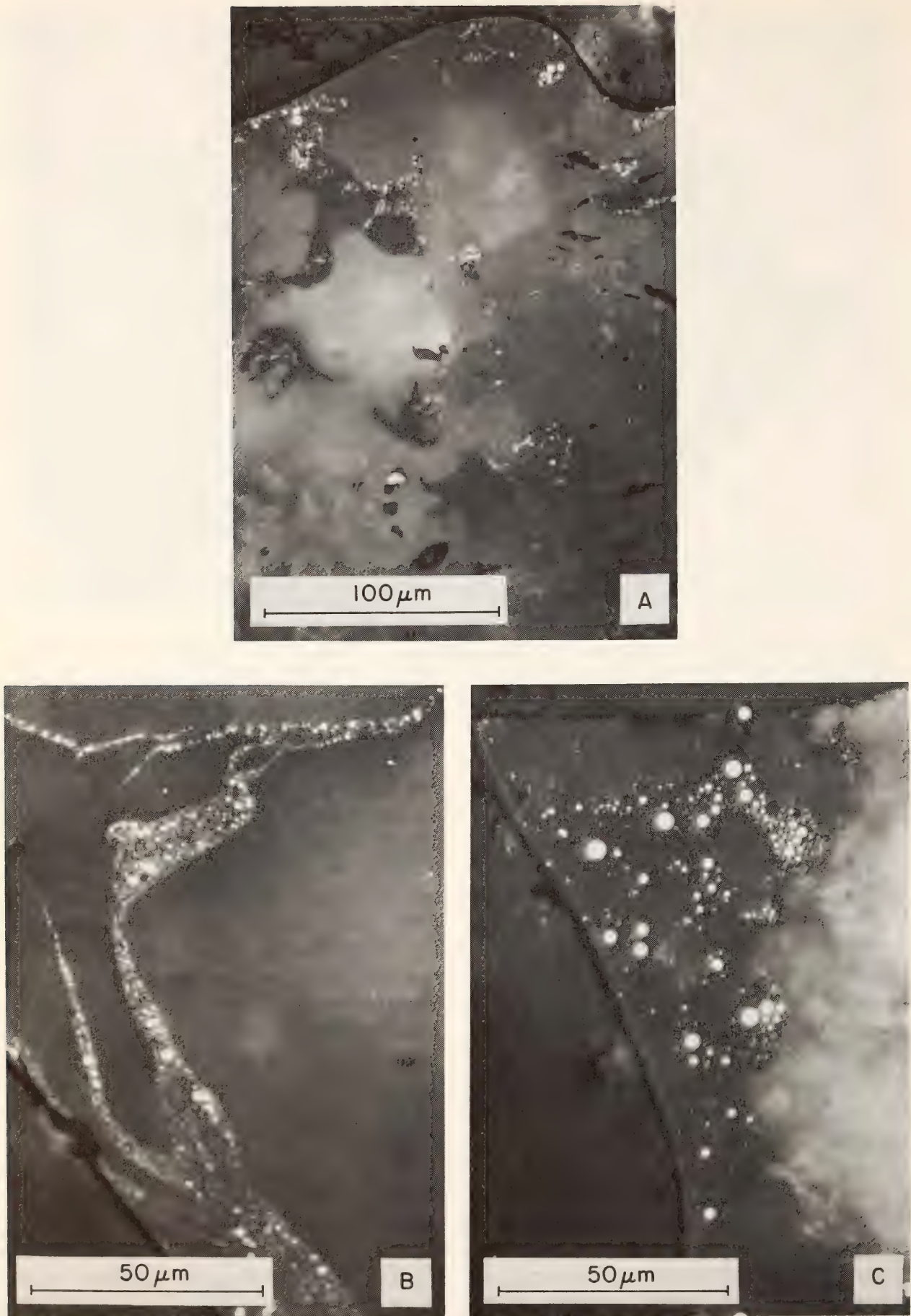


Fig. 107. Photomicrograph of 67701,38,2 agglutinate; reflected light. (A, B, C) Selected views of metal plus glass portions.

TABLE 53. Electron Microprobe Analyses of Agglutinate Particles from Soil Sample 67701

	Glass			Anorthosite 67701,38,2		
	67701,38,1c Average Brown	67701,38,1d		Plagio- class Glass	Plagio- class (Anorth.)	Ilmen- ite
		Light Brown	Dark Brown			
SiO ₂	43.39	43.25	43.77	44.74	44.34	0.35
TiO ₂	0.68	0.44	0.46	0.00	0.05	49.64
Al ₂ O ₃	28.31	28.63	28.93	36.05	36.04	0.31
Cr ₂ O ₃	0.11	0.15	0.14	0.00	0.00	0.18
MnO	0.06	0.07	0.05	0.00	0.00	0.68
FeO	5.04	4.48	4.51	0.00	0.10	44.71
NiO	0.09	0.08	0.12	...	0.00	...
MgO	6.26	5.53	4.77	0.05	0.05	1.57
CaO	15.95	16.84	16.88	19.89	19.29	0.74
Na ₂ O	0.48	0.53	0.60	0.30	0.15	0.00
K ₂ O	0.04	0.05	0.05	0.00	0.00	0.02
Totals	100.40	100.05	100.28	101.03	100.04	98.20

plus ferric iron has occurred during the impact process (Mao, *Year Book 73*, pp. 510–518). This argument is strengthened by the low intensity of absorption bands at 1.0 μ m usually seen if an appreciable amount of ferrous iron is present.

It would appear that the most significant spectral features are those of the brown glass (with minor contributions from ilmenite and anorthite yet unresolved). Brown glass is unlike most lunar glasses in composition and structure (Bell *et al.*, *Year Book 73*, pp. 464–467), and if formed by disproportionation may strongly affect the magnetic properties of lunar soils.

In summary, the physical structure of agglutinate includes minute bubbles, melted zones, and a metallic iron phase. Chemically, the host rock is unaffected by melting in heated zones. The optical properties of the glassy portions are typical of most lunar brown glasses and may be related to the existence of a ferric iron-bearing phase. Such a phase could be ferromagnetic and therefore could contribute to the magnetic properties of the lunar surface where the samples were collected.

TRIVALENT TITANIUM IN APOLLO 17
SAMPLES

*P. M. Bell, H. K. Mao, and S. Haggerty**

The chemically reduced character of lunar rocks is a key factor in their mode of origin. If detected in lunar samples, oxidation states such as the trivalent state of titanium could provide an essential index to the reduction process that affected lunar rocks. Data on the crystal-field spectra and electron paramagnetic resonance spectra of trivalent titanium in synthetic “basalt” glass (iron-free for these experiments) under controlled oxygen fugacities were reported last year (Bell, Mao, and Weeks, *Year Book 73*, pp. 492–496). These data were obtained in order to interpret the oxidation state of titanium in meteorite and terrestrial basalts and to provide a basis for the possible identification of trivalent titanium in lunar samples. Glasses were chosen because they are easily recognized by their purple color when they contain trivalent titanium and thus

* Department of Geology, University of Massachusetts.

should aid in the study of lunar samples, most of which contain abundant amounts of glass. The present study is a report of the first discovery of purple trivalent titanium-bearing lunar glass, based on the above calibrations. Many lunar samples may contain measurable amounts of trivalent titanium, but the amount required to cause a purple color is sufficient to suggest reducing conditions of formation far below those of most lunar samples. An origin for the lunar breccia sample 70019 that contains the trivalent titanium-bearing glass is described in this report.

Chemical Analysis

Electron microprobe analyses of three grains of purple glass in 70019 are given in Table 54. Chemically the purple glasses are not greatly different from large (1 mm diameter) and small (10 μ m diameter) orange glass spheres in the same sample. Brown glass filled with bubble structures also occurs in the same sample and, curiously, contains much less iron and more aluminum than either the purple or orange glass.

Color and Optical Spectra

The color difference in these glasses is caused by the oxidation states of iron and titanium. The absorption spectra

for both synthetic and lunar glasses are identical to those assigned in studies by Mao, Virgo, and Bell (1973); Bell, Mao, and Weeks (*Year Book 73*, p. 492); and Bell and Mao (*Year Book 73*, p. 496). The color, spectral bands, and electronic processes are related as shown in Table 55.

Origin of the Oxidation States of the Glasses in 70019

The coexistence of three glasses of very similar composition in the same sample suggests that chemical reduction has been local and that sharp boundaries of the permeation of a reducing gas have been quenched. This range of disequilibrium state is another example of a fugacity quench (Mao, El Goresy, and Bell, *Year Book 73*, p. 467) in lunar samples. Apparently the gas was hydrogen-rich, probably of solar wind origin. As the melted parts of the breccia quenched to a glass, the chemical reduction process was rapidly halted, and the gas escaped or was trapped as shown by the bubble structure in the brown glass. On the basis of these data and previous petrographic and analytical data (Mao, El Goresy, and Bell, *Year Book 73*, pp. 467-473), it is concluded that sample 70019 is the most chemically reduced sample yet studied from the Apollo mis-

TABLE 54. Electron Microprobe Analysis of Glasses in 70019,93 Breccia

	Purple Glass 1	Purple Glass 2	Purple Glass 3	Large Orange Glass Sphere	Small Orange Glass 1	Small Orange Glass 2	Brown Bubble Glass
SiO ₂	39.21	39.09	38.84	37.72	38.68	38.29	45.63
TiO ₂	8.78	9.23	9.26	10.89	8.92	8.97	1.91
Al ₂ O ₃	5.85	6.30	6.29	11.97	5.73	5.78	17.73
Cr ₂ O ₃	0.73	1.01	1.02	0.39	0.75	0.64	0.38
MnO	0.32	0.29	0.27	0.28	0.29	0.31	0.25
FeO	21.23	19.46	19.27	16.83	21.15	21.20	11.20
NiO	0.00	0.00	0.00	0.00	0.00	0.00	0.04
MgO	16.29	15.89	14.99	10.67	15.39	14.49	10.05
CaO	6.21	6.70	7.11	11.09	6.77	7.02	11.08
Na ₂ O	0.06	0.13	0.04	0.05	0.33	0.34	0.41
K ₂ O	0.00	0.00	0.00	0.00	0.04	0.04	0.10
Totals	98.67	98.09	97.10	99.89	98.05	97.09	98.80

TABLE 55. Correlation of Color to Absorption Spectra in Lunar Basaltic Glass

Color	Spectral Bands	Electronic Process
Orange	Shoulder at 400–550 nm	Fe ²⁺ -Ti ⁴⁺ charge transfer
	Fe ²⁺ crystal-field band at 1000 nm	Fe ²⁺ crystal-field transition (<i>d</i> ⁶)
	Window: high-transmission zone bordered by absorption shoulders at 600 and 700 nm	Interaction between Fe ²⁺ -Ti ⁴⁺ and Fe ²⁺
Brown	Same as above with shift of window to red	
Purple	Crystal-field band at 500 nm	Ti ³⁺ crystal-field transition (<i>d</i> ¹)
	Crystal-field band at 1000 nm	Fe ²⁺ crystal-field transition (<i>d</i> ⁶)
	“White” radiation and shoulder at 400 nm (approx.)	Metal-metal interaction of FeO clusters

sions. Such major chemical reduction may have been highly important as a lunar regolith process.

Permeation and release of hydrogen implanted from the solar wind on heating in the lunar regolith probably has affected the character of most or all of the lunar samples returned from the Apollo missions. It would, therefore, be incorrect to assume a value for the partial pressure of oxygen of the moon’s surface or interior based on observations of Apollo samples without accounting for the important effects of hydrogen gas released by the heat from meteorite impact or by the heat of volcanic lavas.

ANALYSIS OF TYPE-B LUNAR
SYMPLECTITES: GARNET COMPOSITION
P. M. Bell and H. K. Mao

Type-B lunar symplectites (intimate intergrowths of spinel and pyroxene, nomenclature of Bell *et al.*, 1975) in Apollo 17 dunite rock 72415 were discovered to be of an overall garnet composition (Bell and Mao, 1975). Rock 72415, sampled by Astronaut H. H. Schmidt, Jr., was a dunite “clast” from a polymict breccia boulder. If the symplectites are breakdown products of garnet, the dunite may have been formed at depth in the moon. In order to determine whether the Apollo 17 dunite is a

sample of the moon’s interior, the present study was initiated to analyze the composition of type-B symplectite inclusions (Bell *et al.*, 1975) and to establish whether they are all of bulk garnet composition. This report is confined to the study of symplectites in rock 72415; however, the study was recently expanded to include several other symplectite-bearing rocks (Bell *et al.*, 1975). The mode of symplectite origin is still unknown, but the observations make lunar dunite a potentially significant rock for use in interpreting the history of the moon.

Figure 108 shows a secondary electron image of a typical type-B symplectite inclusion in olivine in rock 72415. The evidence that the symplectites were originally garnet is inferred from the chemical analyses determined by electron microprobe (Table 56). These analyses show that garnet has reacted with olivine according to the equilibrium relation

$$\begin{array}{c} \text{R}^{2+}_3\text{R}^{3+}_2\text{R}^{4+}_3\text{O}_{12} \\ \text{Garnet} \\ + \text{R}^{2+}_2\text{R}^{4+}\text{O}_4 \rightleftharpoons 4\text{R}^{2+}\text{R}^{4+}\text{O}_3 \\ \text{Olivine} \qquad \qquad \text{Pyroxene} \\ + \text{R}^{2+}\text{R}^{3+}_2\text{O}_4 \\ \text{Spinel} \end{array}$$

as proved experimentally in the simple system MgO-Al₂O₃-SiO₂ by MacGregor



Fig. 108. Secondary electron image of a type-B symplectite in 72415. The bright phase is a spinel. The gray bands between the spinel rods consist of two pyroxenes. The gray background region is the host olivine.

TABLE 56. Electron Microprobe Analyses of Symplectites in 72415, wt %*

	1	2	8	9	10	12	13	Host Olivine
Na ₂ O	0.16	0.01	0.00	0.00	0.05	0.01	0.00	0.00
MgO	16.06	24.72	24.30	19.07	17.80	17.95	21.68	47.52
FeO	8.17	9.83	9.32	8.29	7.84	8.10	8.21	11.48
NiO	0.00	0.00	0.00	0.02	0.04	0.04	0.03	0.00
CaO	14.75	5.36	6.90	12.91	14.55	12.22	12.61	0.12
MnO	0.21	0.11	0.12	0.13	0.09	0.11	0.04	0.12
Cr ₂ O ₃	18.02	15.95	15.48	15.90	16.12	17.04	14.23	0.08
Al ₂ O ₃	4.61	3.97	4.16	4.48	4.13	5.36	3.80	0.00
SiO ₂	37.13	39.59	39.39	38.12	38.05	38.45	38.39	40.71
TiO ₂	0.46	0.30	0.41	0.34	0.32	0.22	0.17	0.01
Arithmetic totals	99.58	99.83	100.09	99.26	98.99	99.50	99.14	100.04

* Each analysis is the average of four or five separate analyses made within a single symplectite (average symplectite diameter, 30 μm).

(*Year Book 63*, pp. 156–157). Because both reaction phases, olivine and garnet, have an R^{4+} -to-oxygen ratio of 1:4, and because neither of the product phases, pyroxene and spinel, has such a ratio, the ratio is a critical test for the garnet hypothesis. In Table 57 the totals for R^{2+} , R^{3+} , and R^{4+} oxides have been normalized to 16 oxygen atoms involved in the reaction. The crucial $\Sigma R^{4+}O_2$ is 4 within analytical error. The $\Sigma R^{2+}O$ is higher than the theoretical value 5, and the $\Sigma R^{3+}O_{3/2}$ is lower than 2, reflecting the amount of olivine unavoidably included during the microprobe analysis.

It is useful to examine in detail two cases where $\Sigma R^{3+}O_{3/2}$ is low (compared with a value of 2) and compare the average for rock 72415 in order to determine the relative proportions of garnet and olivine in the bulk symplectite composition. It is assumed that garnet was stoichiometric $R^{2+}_3R^{3+}_2R^{4+}_3O_{12}$, and all R^{3+} is assigned to it. In Table 58 olivine has been subtracted, leaving garnet (Bell and Mao, 1975), which is then normalized to 12 oxygens as follows:

(a) Symplectite 2 (Table 57): $1/2 (\Sigma R^{2+} - 3/2 \Sigma R^{3+}) = 1.275$ (olivine, Table 58, column 1; garnet is given in

TABLE 57. Average Compositions of Symplectites in Atoms per 16 Oxygens

	1	2	8	9	10	12	13	Host Olivine
MgO	2.532	3.762	3.698	2.974	2.795	2.786	3.371	1.746
FeO	0.720	0.839	0.794	0.725	0.689	0.702	0.716	0.236
CaO	1.669	0.584	0.755	1.447	1.642	1.362	1.408	0.003
MnO	0.019	0.009	0.009	0.009	0.006	0.009	0.003	...
$\Sigma R^{2+}O$	4.94	5.194	5.256	5.155	5.132	4.859	5.498	...
$CrO_{3/2}$	1.505	1.286	1.250	1.314	1.342	1.402	1.172	0.001
$AlO_{3/2}$	0.574	0.477	0.500	0.550	0.513	0.656	0.465	...
$\Sigma R^{3+}O_{3/2}$	2.079	1.763	1.750	1.864	1.855	2.058	1.637	1.0035
SiO_2	3.925	4.044	4.021	3.991	4.007	4.001	4.004	...
TiO_2	0.034	0.021	0.030	0.024	0.024	0.015	0.012	...
$\Sigma R^{4+}O_2$	3.959	4.065	4.051	4.015	4.031	4.016	4.016	...
Totals	10.978	11.021	11.057	11.034	11.018	10.933	11.151	...

TABLE 58. Olivine Subtraction and Normalization of Type-A and Type-B Symplectite Analyses to Garnet*

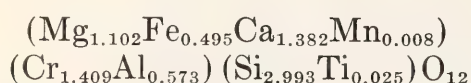
	1	2	3	4	5	6	7	8	9	10
MgO	2.226	1.536	1.691	2.656	0.715	0.865	3.079	2.038	1.041	1.102
FeO	0.301	0.538	0.692	0.359	0.357	0.432	0.742	0.275	0.467	0.495
CaO	0.004	0.580	0.638	0.005	1.403	1.698	1.307	0.004	1.303	1.382
MnO	0.003	0.006	0.007	0.003	0.010	0.002	0.008	0.008
$\Sigma R^{2+}O$...	2.66	2.928	...	2.475	2.995	5.139	2.987
$CrO_{3/2}$...	1.286	1.416	...	1.172	1.418	1.324	...	1.329	1.409
$AlO_{3/2}$...	0.477	0.525	...	0.465	0.582	0.541	...	0.541	0.573
$\Sigma R^{3+}O_{3/2}$...	1.763	1.941	...	1.631	1.981	1.870	...	1.870	1.982
SiO_2	1.279	2.765	3.044	1.527	2.477	2.998	3.992	1.171	2.821	2.993
TiO_2	...	0.021	0.023	...	0.012	0.014	0.024	...	0.024	0.025
$\Sigma R^{4+}O_2$...	2.786	3.067	...	2.489	3.012	4.017	3.018

* Column 1, 1.275 moles of host olivine; 2, analysis 3, Table 57, minus 1.275 moles of host olivine; 3, column 2 normalized to 12 oxygens; 4, 1.521 moles of host olivine; 5, analysis 13, Table 57, minus 1.521 moles of host olivine; 6, column 5 normalized to 12 oxygens; 7, average of symplectite compositions in Table 57; 8, 1.167 moles of host olivine; 9, column 7 minus column 8; 10, column 9 normalized to 12 oxygens.

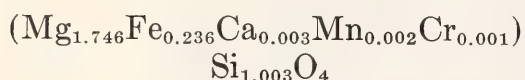
column 2, normalized to 12 oxygens in column 3).

(b) Symplectite 13 (Table 57): $1/2(\Sigma R^{2+} - 3/2 \Sigma R^{3+}) = 1.521$ (olivine, Table 58, column 4; garnet is given in column 5, normalized to 12 oxygens in column 6).

Using the same procedure for the average (Table 58, column 7), $1/2(\Sigma R^{2+} - 3/2 \Sigma R^{3+}) = 1.167$ (olivine, Table 58, column 8; garnet is given in column 9, normalized to 12 oxygens in column 10). The resulting average symplectite formula (including some host olivine) is 1 garnet:



+1.236 olivine:



where 1 of the 1.236 olivine has reacted with the garnet to form the pyroxene + spinel symplectite, and the remaining 0.236 olivine is the host olivine sampled by the microprobe beam.

The garnet composition is complicated, but less so than those of similar rare garnets in terrestrial rocks (Meyer, 1968). It belongs in the system pyrope-grossularite-knorringite-uvarovite studied experimentally by Malinovsky and Doroshev (1974) and Malinovsky, Doroshev, and Godoikov (1975). This garnet has less knorringite component and

more uvarovite component than terrestrial garnet (found as inclusions in diamond), suggesting that it formed at lower pressure than the stability field of diamond but at higher pressure than the lunar surface.

The basis for making the above calculations is simply the subtraction of the garnet composition leaving one or more moles of host olivine composition (depending on the amount of host olivine sampled by penetration of the electron microprobe beam compared with the amount of olivine reacted with garnet). This procedure is the only valid method of calculating garnet composition.

The actual stability field of the garnet so deduced is impractical to predict without experimental data because a minimum of six components is required to characterize the thermodynamic system. The data presented in this report confirm the finding that all symplectites studied are of garnet bulk composition. The effect of solid solutions would probably reduce significantly the pressure of formation compared with that of garnets found in diamond, but if the garnet of the composition given above coexisted in the dunite, an equilibrium pressure higher than that at the moon's surface was probably involved. Therefore, lunar dunite sample 72415 may indeed be a sample of the moon's interior although it is not possible to specify the depth of formation.

BIOGEOCHEMISTRY

THE BIOGEOCHEMISTRY OF THE STABLE HYDROGEN ISOTOPES

Thomas C. Hoering

Relatively few studies have been published on the hydrogen-isotope composition of naturally occurring organic substances, and in general the work was done on unfractionated material or material that was only partially separated. Experience with carbon isotopes has

shown that valuable biochemical and geochemical information is obtained from the examination of closely fractionated material. Previous work in this laboratory on the hydrogen-isotope ratios in sedimentary organic matter indicated a need for research on isotope fractionation by plants. Therefore, work this year was focused on the development and application of suitable techniques for separating compound classes

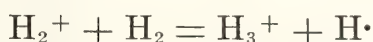
from plants and for routinely measuring their isotopic compositions on the mass spectrometer.

Isotope geochemical studies measure variations in the deuterium-hydrogen ratios of samples as compared with a standard substance. Results are reported in parts per thousand differences in the ratio

$$\delta D = \frac{(D/H)_x - (D/H)_s}{(D/H)_s} \times 1000,$$

where the subscript x refers to the unknown and the subscript s refers to the standard (Standard Mean Ocean Water, distributed by the International Atomic Energy Agency).

Special problems are encountered in the measurement of small differences in hydrogen-isotope ratios by mass spectrometry. New solutions to two of these problems were developed. The first dealt with the calibration and standardization of the instrument with hydrogen gas of known isotopic composition. When hydrogen gas is ionized in the mass spectrometer, H_2^+ and HD^+ ions are formed. In addition, the hydrogen ion undergoes an ion-molecule reaction:



The triatomic hydrogen ion has a molecular weight of 3 and is not resolved from the isotopic ion HD^+ . Measurements of the HD^+/H_2^+ ratio must be corrected for a 10%–20% contribution by the H_3^+ ion. This correction was accomplished by constructing an empirical calibration curve derived from the analysis of a series of water samples of known isotopic compositions.

A series of secondary standards was prepared by quantitatively diluting distilled water having an isotopic composition near that of Standard Mean Ocean Water with water that was nearly free of deuterium. Mr. William Thurston, of the Atomic Energy of Canada, Ltd., Chalk River, Ontario, donated water that had been synthetically depleted to 3.5 ± 1.0 ppm deuterium. It was mixed

with water with 155.5 ppm to give samples having a range of δD that spanned the naturally occurring variations. Because the synthetic water was so nearly deuterium-free, the values calculated for the secondary standards are not sensitive to errors in the measurement of hydrogen isotopes in the diluent. The calculated values depend only on the chemical purity of the waters and the precision of weighing their relative proportions. Errors due to differences in oxygen-isotope composition of the waters and differences in their densities are negligible.

The waters were quantitatively converted to H_2 , and the apparent δD was measured from the observed ion currents at mass 3 ($H_3^+ + HD^+$) and at mass 2 (H_2^+). A plot of the apparent δD versus the δD calculated from the dilutions was a straight line having a correlation coefficient greater than +0.9998. The slope of the line varied from 1.10 to 1.20, depending on operating conditions of the mass spectrometer, but remained constant when conditions were constant. The slope of the line is a measure of the contribution of the H_3^+ ion plus other correction factors normally applied to hydrogen isotope analyses.

Thus, an empirical calibration curve can be determined quickly and precisely. Samples of the hydrogen-isotope secondary standards NBS-1 and NBS-1a, distributed by the International Atomic Energy Agency, were analyzed and found to have δD of -47.0 and -182.2 , respectively. The results are in agreement with the averages of -47.1 ± 0.36 (1σ) and -183.0 ± 1.08 (1σ) calculated from results by 14 other laboratories.

The second problem in isotope ratio measurements is generation of large quantities of hydrogen gas of precisely known isotopic composition for routine operation instead of frequently generating standard gases from water. Commercial cylinders of compressed hydrogen have a deuterium content that is far too low to be useful. Appropriate samples

were produced by an Elhygen Hydrogen Generator manufactured by the Milton Roy Company, St. Petersburg, Florida. This device electrolyzes water and produces very pure hydrogen by diffusing it through a heated palladium metal membrane. The instrument gives a large positive isotope effect, but by adding water with excess deuterium to the electrolyte, large volumes of hydrogen gas were produced that had isotopic compositions covering the range of values found in nature. The gases were carefully compared with the isotope secondary standards described above and were stored in 2-liter steel cylinders at 80 psig. They have been stable for 6 months and have greatly facilitated the routine measurement of hydrogen-isotope ratios.

The third major experimental problem that was studied dealt with appropriate methods for separating compound classes from plants. There are several stringent requirements for such separations. Pure materials must be isolated without introducing isotope fractionation because of incomplete yields. Mild methods must be used in the separations to avoid exchanging reactive hydrogens in the molecules with solvents. The examination of the lipid fraction of plants by column chromatography is one logical way to start the survey. Lipids have most of their hydrogens stably bonded to a carbon atom and are not easily exchanged. Column chromatographic separations do not require high temperatures or strong chemical conditions, and quantitative recovery of most fractions is possible. In contrast, carbohydrates and proteins have a large number of hydrogens that exchange readily with water. The separation and fractionation of these components without introducing large uncertainties may be difficult.

The results described here were obtained on the chloroform-methanol extract of freeze-dried plant material. The extract was saponified by refluxing with 3% potassium hydroxide in methanol. During this reaction, triglycerides,

waxes, sterol esters, and other compounds were converted to their corresponding acids and alcohols. The mixture was greatly simplified and could then be adequately separated by chromatography on silicic acid using gradient elution (Hirsch and Ahrens, 1958). Some hydrogens were necessarily exchanged in the process, but control samples of palmitic and oleic acids that were saponified and separated had a δD that was within 5‰ of the starting compound.

Identification of the separated classes of compounds was facilitated by adding ^{14}C -tagged tracers to the mixture applied to the chromatography column. The fatty acids and saturated hydrocarbons eluted exactly with their radioactive counterparts. Identification was verified by analysis with gas chromatography and mass spectrometry. The phytol and sterol fractions eluted with radioactively labeled *n*-octadecanol and cholesterol, respectively. The carotene fraction eluted as a sharp red band at the expected time. These tentative identifications were verified by gas chromatography and mass spectrometry.

Several experiments were done on lipid extracts without the preliminary saponification step to determine whether the uncertainties caused by this step could be avoided. The hydrogen-isotope analyses were not reproducible. The unsaponified lipids from plants are a very complex mixture, and a suitable separation could not be accomplished with a reasonable chromatographic procedure.

The crude petroleums were dried over anhydrous calcium sulfate and separated by column chromatography on activated silica gel. Three fractions were isolated by successive elution with hexane, benzene, and methanol. Samples of the total crude oil and the three compound classes were analyzed for carbon- and hydrogen-isotope content.

A fourth experimental problem has been only partially resolved. Organic matter was combusted to carbon dioxide and water for isotopic analysis. The wa-

ter was converted to hydrogen for introduction into the mass spectrometer. An analysis for both carbon and hydrogen isotopes was made for each sample. The combustion system worked well for carbon, but water was strongly absorbed on the glassware and the copper-oxide packing. This water was difficult to remove, and consequently there was a sizable water blank. Fifteen to 20 mg of organic matter were combusted to give an amount of water that was much greater than the blank. The combustion system was evacuated by a diffusion pump, and adequate time between samples was taken to exhaust traces of water from the previous samples in order to avoid a "memory" effect.

Preliminary results indicate that the precision of measurement is adequate for current purposes. The mass spec-

trometer is capable of detecting differences in δD of 0.5‰. Repeated analyses of two water samples gave results with a standard deviation of 1.1‰. Two different samples of pure organic compounds were combusted; the water was converted to hydrogen and analyzed. A series of combustions gave results with a standard deviation of 3‰. The largest source of error in the present experiments is probably the saponification and separation steps.

The data for the plants, given in Table 59, are consistent with published results and show several new facts. Both a carbon-isotope and a hydrogen-isotope effect occur during fixation of carbon dioxide and water to organic matter during photosynthesis. Plants have a lower abundance of the heavy isotopes of hydrogen and carbon than the water and

TABLE 59. Carbon and Hydrogen Isotopic Composition of Fractions from Plants

	PAJ-2		PAJ-1		LGL		DEL-6	
	$\delta^{13}C$	δD	$\delta^{13}C$	δD	$\delta^{13}C$	δD	$\delta^{13}C$	δD
Water	...	-7.5	...	-7.5	...	-20.0*	...	-6.0
Extracted plant	-13.42	-112.7	-13.24	-156.1	-27.74	-101.9	-10.54	- 82.5
Total saponified lipid	-19.21	-155.0	-20.67	-110.4	-33.39	-140.7	-18.89	-134.7
Total nonsaponified lipid	-19.15	-271.0	n.d.†	n.d.	-28.67	-192.07	-16.21	-178.9
Saturated fatty acids	-18.81	-129.9	-22.42	-114.5	-32.84	-131.3	-19.63	-127.7
Unsaturated fatty acids	-18.63	-146.3	-21.81	-126.1	-34.61	-143.1	-18.83	-118.7
Saturated hydrocarbons	-20.94	-141.3	-24.52	-131.7	-32.73	-146.1	-20.86	-158.1
Carotene pigments	-19.85	-267.6	n.d.	n.d.	n.d.	n.d.	-16.23	-177.3
Phytol	-21.67	-309.8	-19.82	-337.6	-29.44	-207.2	-16.78	-211.1
Sterols	n.d.	n.d.	n.d.	n.d.	-30.83	-233.2	-14.48	-209.6

* Water distilled from freshly harvested leaves. Ground waters measure $\delta D = -39.0$.
† Not determined.
PAJ-2: Red alga, *Hypnea cornuta*, Gulf of Mexico, Port Aransas, Texas.
PAJ-1: Green alga, *Ulva fasciata*, Gulf of Mexico, Port Aransas, Texas.
LGL: Honey locust, *Gleditsia triacanthus*, Geophysical Laboratory grounds, Washington, D.C.
DEL-6: Marsh grass, *Spartina patens*, The Great Marsh, Lewes, Delaware.

$$\delta^{13}C = \frac{(^{13}C/^{12}C)_x - (^{13}C/^{12}C)_s}{(^{13}C/^{12}C)_s} \times 1000$$

The standard material for carbon isotope analysis is NBS-20, Limestone, Isotope Reference Material. On this scale, NBS-22, Petroleum, Isotope Reference Material, is -28.33 . The PDB reference material would measure $+1.08$.

carbon dioxide that surround them. With one exception, lipids have less of the heavy isotope than the protein and carbohydrate of the extracted plant. These results are in partial agreement with the observations of Smith and Epstein (1970).

The difference in the δD of the saponifiable and nonsaponifiable lipids is large and consistent. When these materials are separated into compound classes and analyzed, the lipids fall into two groups having greatly different deuterium contents. The first contains the fatty acids and saturated hydrocarbons; the second has the phytol, sterols, and carotenes. It is significant that the first group has a common biosynthetic pathway involving synthesis from two carbon fragments, while the second group is synthesized via the five-carbon isoprenoid pathway. Plants have an isotopic marker for the different classes of compounds. This marker has potential use for studying sources and fates of organic matter in sedimentary rocks.

The carbon-isotope measurements agree with the published distributions for plants. For example, the tree (LGL), which uses atmospheric carbon dioxide for its carbon source, has less ^{13}C than the algae (PAJ-1 and PAJ-2), which use the bicarbonate ion of sea water. The marsh grass (DEL-6) uses the C_4 pathway for photosynthesis, and the others use the C_3 pathway. This fact is reflected in the higher ^{13}C content of the marsh grass. The hydrogen-isotope ratios, however, do not seem to show any such differences among the plants.

In last year's Report, the hypothesis was made that the hydrogen-isotope ratio of sedimentary organic matter may reflect the geographical location of its source because fresh water has a lower deuterium concentration than sea water. The new data show that this hypothesis may not be true. The algae PAJ-1 and PAJ-2 grew a few feet from each other in water, yet there are large differences in δD between the two that obscure the

isotopic composition of the water. A factor that governs the deuterium concentration of some plants is shown by the tree (LGL). The ground waters, streams, and springs located within a mile of the tree have an average δD of -39‰ . The water distilled from freshly harvested leaves of the tree has a δD of -20‰ . There is an isotope effect during transpiration of water through the tree, H_2O being transpired more readily than HDO (Wershaw *et al.*, 1970).

The deuterium concentrations of the first seven petroleum shown in Table 60 fall in the same range as those of plant lipids. Because the hydrocarbons of petroleum are probably formed from lipids, the deuterium content of petroleum may reflect the original source material. However, the extent to which organic hydrogen in sediments exchanges with formation waters is not known. The stability of carbon-to-hydrogen bonds under geochemical conditions must be studied if hydrogen isotopes are to be used to investigate ancient organic matter. Previous work in this laboratory (Hoering, *Year Book* 67, pp. 199–201) showed that when saturated hydrocarbons were produced by the mild thermal treatment of kerogen in sediments that had been exposed to pure D_2O , there was an appreciable amount of deuterium in the hydrocarbons. A number of carbon-to-hydrogen bonds were apparently ruptured and reformed during the process.

The δD of the petroleum of Precambrian age shown in Table 60 is strikingly different from the δD of its younger counterparts. There is not enough evidence at present to determine whether this difference is due to a difference in the isotopic composition of the waters at the time of formation or to diagenetic changes that may have occurred since then.

In summary, work this year has shown that there are systematic differences in the hydrogen-isotope ratios among classes of compounds in plants. Some of these differences have potential uses as

TABLE 60. Carbon and Hydrogen Isotopic Composition of Petroleum Fractions

Sample No.	Total Crude Oil		Hexane Eluate		Benzene Eluate		Methanol Eluate		Field	Location	Age of Reservoir
	$\delta^{13}\text{C}^*$	δD^*	$\delta^{13}\text{C}$	δD	$\delta^{13}\text{C}$	δD	$\delta^{13}\text{C}$	δD			
798	-20.96	-153.3	-21.59	-165.0	-20.69	-159.4	-20.24	-159.0	Midway-Sunset	California	Upper Pliocene
801	-20.97	-142.5	-21.42	-147.4	-20.11	-132.7	-20.34	-148.5	Midway-Sunset	California	Lower Miocene
799	-22.33	-150.5	-22.00	-163.7	-21.46	-151.0	-20.56	-158.5	Midway-Sunset	California	Upper Miocene
4159	-21.13	-121.1	-20.91	-128.0	-20.21	-113.2	-19.34	-121.2	Sante-Fe Springs	California	Upper Miocene
3944	-22.72	-105.9	-22.59	-109.5	-22.78	-89.5	-22.47	-112.6	Lab-E-Safid	Iran	Miocene
4190	-28.95	-109.4	-28.55	-112.1	-28.58	-112.5	-28.65	-103.9	Deep River	Michigan	Devonian
White Pine	-29.66	-69.2	-29.75	-68.8	-30.17	-64.7	-30.55	-65.0	Seep in White Pine Copper Mine	Michigan	Precambrian (ca. 1100 m.y.)

* Defined in the text and in the footnote of Table 59.

an isotopic tracer for the study of the geochemistry of organic matter. The measurements of the hydrogen-isotope composition of petroleum point to further experiments that may be valuable for understanding the pathways of transformations of lipids in sedimentary rocks.

THE ASSOCIATION OF ORGANIC MOLECULES WITH CLAY MINERALS IN AQUEOUS SOLUTIONS

John Hedges

Sediments composed primarily of clay minerals usually contain higher concentrations of organic matter than deposits formed from sands or carbonate debris. Mineralogists have demonstrated that organic ions can occupy ion-exchange sites on clay crystals and that polar organic molecules can be adsorbed on clay mineral surfaces (Weiss, 1969). These studies suggest that the occurrence of organic material in fine-grained sediments may result in part from the uptake of dissolved organic molecules by clay minerals suspended in natural water bodies. In this way organic substances having an affinity for clay mineral surfaces would be preferentially removed from solution and transported to the underlying sediment by the settling particles. A series of model experiments is described here that test the feasibility of this method of transport.

The laboratory experiments were designed to simulate interactions of simple organic molecules with clay minerals suspended in lakes and oceans. Stearic acid, D-glucose, and L-valine were chosen as model organic substances because they exhibit a wide range of chemical properties and represent the three most abundant classes of biochemicals occurring in aquatic organisms: the lipids, sugars, and amino acids. Simple organic molecules similar to the model compounds occur in natural waters (Duursma, 1965) and may be important precursors of the brown acidic polymers (fulvic acid or

gelbstoff) that account for much of the organic material in solution (Stevenson and Butler, 1969).

Kaolinite and montmorillonite were used in the model experiments because they represent two chemically dissimilar families of clay minerals that are abundant in many depositional environments (Milot, 1970). Kaolinite crystals are composed of one silica and one alumina sheet. Montmorillonite crystals are formed from an octahedral alumina sheet sandwiched between two layers of silica. The surface area and cation-exchange capacity of kaolinite are relatively small in comparison with those of montmorillonite (Grim, 1968).

A number of previous studies concerning clay-organic associations in aqueous solutions have included organic molecules and clay minerals similar to those treated here (Jepson and Williams, 1972; Meyers and Quinn, 1973; Bader, Hood, and Smith, 1960). Most of these investigators were specialized, involving one family of organic compounds or one variety of clay mineral. The experimental results that have been reported are not easily compared owing to differences in sample preparation and analytical methods. As a result the literature dealing with this topic is incomplete, and few unifying principles have emerged.

Experimental

Tritium and ^{14}C -labeled tracers were used to measure the quantities of model compounds present in concentrated and extremely dilute solutions. The radioactive purity of the tracers was greater than 98%. All nonradioactive organic materials were at least 99% pure.

The clay minerals were purchased from Ward's Natural Science Establishment, Inc. The minerals were collected from the same sites as the original samples described in American Petroleum Institute (API) Clay Mineral Standard Project No. 49 (American Petroleum Institute, 1951). The montmorillonite and kaolinite clays used in this study corre-

spond to API standard clays Nos. 5 and 27, respectively.

The commercial clays were reacted with 3% H_2O_2 to remove organic matter. They were dispersed in distilled water (montmorillonite) or 0.005 M NaOH (kaolinite) with ultrasonic vibration until an unflocculated suspension was formed. Particles smaller than approximately $0.5\ \mu\text{m}$ were separated by centrifugation and freeze-dried. This size fraction was used in all experiments.

Analytical data for sized fractions of the two model clays are given in Table 61. Powder x-ray diffraction measurements were made with $\text{Cu K}\alpha$ radiation. Samples were analyzed in untreated form and after exposure to ethylene glycol vapors.

Weight percentages of carbon were determined manometrically after a known weight of clay was combusted to produce CO_2 (Calder and Parker, 1973). Calculated values include contributions from both organic and inorganic forms of carbon. Surface areas were determined from the weight of glycerol retained by the clays after 48 hours of heating at 110°C (Diamond and Kinter, 1958).

Cation-exchange capacities were measured using a 1.00 M solution of CaCl_2 that was spiked with ^{45}Ca . The clay was repeatedly equilibrated with aliquots of the calcium solution and then washed with distilled water until the wash solution contained no radioactivity above background. Portions of freeze-dried

clay were weighed into scintillation vials and dispersed in a 10% solution of distilled water in a commercial scintillator preparation (Handifluor, Mallinkrodt Chemical Works). Clay suspensions and control solution containing no clay were analyzed in a liquid scintillation counter, spiked with a known volume of the CaCl_2 solution, and recounted. The measured radioactivities were corrected for background contributions and for slight differences (3%) in the counting efficiency of the spike in clay suspension and control mixtures. Cation-exchange capacities (CEC) were calculated using the formula

$$\text{CEC, meq/100 g clay} = \text{meq (spike)} \times \frac{\text{counts (clay)}}{\text{counts (spike)}} \times \frac{100}{\text{g of clay}}. \quad (1)$$

Duplicate determinations agreed within $\pm 2\%$ and were within the range of exchange capacities published for the corresponding API standard clays.

Seawater was collected at an offshore site in the Gulf of Mexico. Dissolved organic matter was removed using a photo-oxidation procedure similar to that described by Armstrong, Williams, and Strickland (1966).

A 200 mg sample of sized clay was dispersed with ultrasonic vibration in 10.0 ml of distilled water (or seawater). A control solution containing no clay was also prepared. A solution (10.0 ml) of radioactively tagged organic material

TABLE 61. Properties of Model Clay Minerals*

Clay	Total Surface Area (m^2/g)	Cation Exchange Capacity (meq/100 g)	Exchangeable Cations	Carbon (wt %)	Mineral Purity
Kaolinite	36	3.3	Na	0.07	95%+
Montmorillonite	500†	91	Na, 86%‡ Ca, 16%‡	0.06	95%+

* Less than $0.5\ \mu\text{m}$ size fraction.

† Assumed 1.6% glycerol retention after heating to 600°C failed to collapse clay (Diamond and Kinter, 1958).

‡ API Research Project No. 49.

was added to the clay suspension and control solution. The reaction vials were stoppered and transferred to a constant temperature bath (25°C), which was mounted on a platform shaker.

Aliquots were removed at intervals from the control and suspension vials and centrifuged. One ml of supernatant was added to 19 ml of scintillator preparation (Handifluor) and assayed to a total of approximately 40,000 counts. Corrections for background radioactivity and differences in counting efficiency were made. The percentage of the original organic material that was removed from solution by the suspended clay was calculated from the relative difference between the radioactive concentrations of the control and suspension solutions:

Percentage removed =
$$\left[1 - \frac{\text{counts (supension)}}{\text{counts (control)}} \right] \times 100. \quad (2)$$

This difference measures only organic material that is preferentially removed from solution and is not affected if unpartitioned solvent is physically trapped between clay crystals. All suspensions except stearic acid in seawater came to steady state within 48 hours.

Results

The percentages of dissolved valine that were preferentially removed from distilled water and seawater solutions by kaolinite and montmorillonite are given in Table 62. Valine concentrations were studied over a range that extended from near the solubility limit of the amino acid down to levels similar to those in natural waters.

No more than 10% of the initial concentration of valine was removed under any experimental condition. In general, percentages of removal increased as amino acid concentrations were decreased. The dissolved salts in seawater decreased the capacity of kaolinite to extract valine but increased the capacity of montmorillonite.

Association measurements for glucose were made at the same concentrations and experimental conditions that were used in the study of valine. Neither kaolinite nor montmorillonite extracted more than 1% of the total glucose that was initially present in freshwater or seawater suspensions.

Stearic acid was extracted from distilled water solutions by the suspended clays much more efficiently than the other two model compounds (Table 63). This affinity for clay mineral surfaces probably results from the limited solubility of the fatty acid in distilled water (3 mg/l at 20°C). Kaolinite adsorbed approximately twice the quantity of stearic acid that was removed by montmorillonite under the same conditions. In both clay systems the quantity of stearic acid taken up by 100 mg of clay varied nearly linearly with the concentration of stearic acid in solution at steady state (Fig. 109).

Stearic acid-clay associations in sea-

TABLE 62. Percentage of Total Valine Removed in Distilled Water and Seawater Suspensions

Concen- tration (molar)	Percentage of Removal			
	Distilled Water		Seawater	
	Kaolin- ite	Mont- moril- lonite	Kaolin- ite	Mont- moril- lonite
10 ⁻¹	0	0	0	0
10 ⁻²	3	0	0	0
10 ⁻³	3	0	1	3
10 ⁻⁴	4	0	2	5
10 ⁻⁵	9	2	3	4

TABLE 63. Percentage of Total Stearic Acid Removed from Distilled Water Suspensions

Concen- tration (mg/1)	Kaolin- ite	Montmoril- lonite
1.0	23	13
0.1	40	18
0.01	46	14

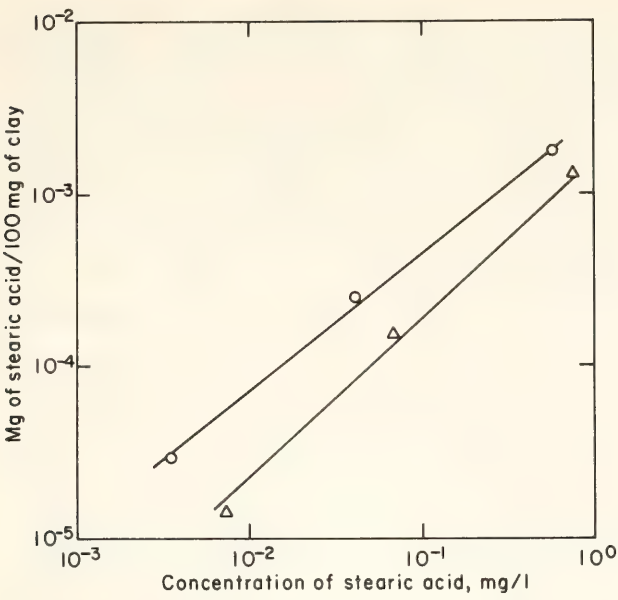


Fig. 109. Plot of the weight of stearic acid (mg) associated with 100 mg of clay against the concentration of stearic acid in distilled water. Circles, montmorillonite data points; triangles, kaolinite data points.

water suspensions were different in magnitude and in mechanism from those occurring in the distilled water suspensions. This difference resulted from a decrease in the solubility of the fatty acid in seawater. At initial concentrations as low as 0.01 mg/l, over 30% of the stearic acid was lost from control solutions during centrifugation. At an initial concentration of 0.1 mg/l, the quantities of stearic acid lost during centrifugation (15%–30%) were similar for a seawater solution and for 3% solutions of NaCl, KCl, CaCl₂, and MgCl₂. Under the same conditions only 2% of the initial stearic acid was removed from a distilled water solution. These results suggest that stearic acid is salted out of the saline solutions and not precipitated as a salt of a specific metal ion.

When montmorillonite or kaolinite was present in the seawater solutions, approximately 60% of the initial quantity of stearic acid was lost from the liquid phase (representative data in Table 64). Direct measurements of stearic acid on the equilibrated clays indicated that the clays contained approximately ¾ of the stearic acid that was lost from solution. The quantities of

TABLE 64. Representative Data from Stearic Acid–Seawater Suspensions

	Kaolinite in Suspension (mg)		
	200	20	2
Stearic acid lost during centrifugation (%)	64	64	64
Lost acid recovered on clay (%)	73	62	...

acid that were extracted, however, were largely independent of the type or quantity of clay that was present in the suspensions (Table 63).

At a given equilibrium concentration, the weight of acid removed from solution should be proportional to the weight of clay in suspension if the stearic acid is in true solution and is reversibly partitioned between clay and liquid. The experimental evidence, however, indicates that constant partitioning does not occur and that the seawater “solutions” are saturated with stearic acid over the range 1.0 to 0.01 mg/l. Apparently, most of the stearic acid that was lost from solution and recovered in the clay sediments simply precipitated from solution. The clays may have enhanced precipitation losses by providing nucleation centers and a relatively dense vehicle for sedimentation.

Discussion

The extent to which clay-organic association occurred in the model experiments was determined primarily by the nature of the organic compounds. The order of increasing reactivity toward both clay minerals was glucose, valine, stearic acid. The effect of clay mineral variation upon the degree of association was secondary. The percentages of organic material removed from solution were not directly related to either the cation-exchange capacity or the total surface area of the suspended clay minerals.

The geochemical implications of the

model experiments can be viewed from two perspectives, (1) the selective transport of individual species by clay association and (2) the relative contributions made by clay-bound organic materials to the total organic matter in natural sediments.

The potential exists for selective removal of simple organic molecules from natural water bodies by suspended clays. Hydrophobic compounds such as stearic acid should be scavenged from solution more efficiently than more soluble substances such as simple sugars and neutral amino acids. The selective removal of hydrophobic compounds may be enhanced in saline solutions.

The absolute amounts of model organic compounds that were removed from solution in the laboratory simulations were small. At organic concentrations near 1 mg/l, approximately 0%, 5%, and 30% of the total amounts of glucose, valine, and stearic acid, respectively, were extracted by the suspended clays. These values correspond to approximately zero mg of glucose, 5×10^{-4} mg of valine, and 5×10^{-3} mg of stearic acid (Fig. 109) removed from solution per 100 mg of clay. The amount of organic material on the model clays, therefore, did not exceed 0.005 wt % at organic concentrations near 1 mg/l.

The results of the laboratory experiments can be compared to distributions of organic materials in the western Gulf of Mexico, which is a well-studied depositional environment. The concentration of dissolved organic matter in seawaters from this region is approximately 1 mg/l (Calder, 1969). The outer continental shelf is covered with Recent sediments, which are composed primarily of montmorillonite along with smaller amounts of illite, chlorite, and kaolinite (Pinsak and Murray, 1960). The amount of organic matter in the surface sediments is approximately 2 wt % (Hedges, 1975). This concentration is orders of magnitude greater than the weight percentages of simple organic molecules that

were associated with the model clays in the laboratory experiments. Clay-organic associations of the magnitude obtained in the model experiments cannot, therefore, directly produce the concentrations of total organic matter that commonly occur in fine-grained sediments from the Gulf of Mexico.

There are several possible explanations for the higher concentrations of organic material in natural sediments: (1) Minerals such as illite or chlorite may have a greater affinity for dissolved organic material than kaolinite or montmorillonite. The model experiments, however, suggest that differences in at least the clay mineralogy are of secondary importance in association reactions and probably do not account for the observed differences between laboratory and natural systems. (2) The dissolved organic material in natural waters is predominantly in the form of acidic polymers (gelbstoff). These polymers may be more efficiently extracted from solution by suspended clay minerals than are the simple molecules that were used in the model study. (3) Alternatively, clay organic associations in natural water bodies may not contribute significantly to the transport of organic materials to sedimentary deposits. An extension of last year's research on lignin compounds in marine sediments indicated that much of the land-derived organic matter in surface sediments from the Gulf of Mexico is introduced as small particles and not in chemical forms that could easily be dissolved in water or bound to clay minerals (Hedges, 1975).

It is likely that a large proportion of marine-derived organic material is also transported to the ocean floor in particulate form. The preferential concentration of these particles in clay-rich sediments may result from a similarity in the hydrodynamic properties of clay minerals and organic debris and from the preservation of organic remains by fine-grained sediments that restrict the flow

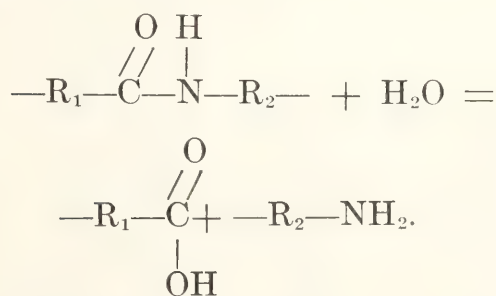
of oxygen and nutrients to benthic organisms. These possibilities are being further explored in model experiments that simulate the formation of organic polymers from simple molecules in the presence of clay minerals and in direct observations of organic particles in natural sediments using a scanning electron microscope.

SIMULATION OF NATURAL HYDROLYSIS OF PROTEINS IN FOSSILS

P. E. Hare, G. H. Miller, and N. C. Tuross

The extent of naturally occurring hydrolysis of proteins in fossil materials is a useful indicator of their relative ages. Proteins in shells, bones, and teeth undergo hydrolysis in the natural environment under mild conditions of temperature and *pH*. Few experimental data are available on peptide-bond stability under these conditions. This report describes an experimental approach for the determination of relative peptide-bond stabilities and presents data on the relative rate of hydrolysis of various peptide bonds in fossil shells and bone.

The primary structure of proteins consists of a sequence of amino acids in peptide linkage. The α -amino group (R_2-NH_2) of one amino acid is bound to the α -carboxyl group (R_1-COOH) of the adjacent amino acid with the elimination of a molecule of H_2O . In the hydrolysis of a peptide bond, water is added to re-form the free amino and carboxyl groups:



The stability of the various peptide bonds in proteins is determined largely by the kinds of amino acids forming the peptide bond. The peptide bonds adja-

cent to aspartic acid, serine, and glycine residues are among the most labile, while the peptide bonds involving valine and isoleucine are among the most stable. The differences in peptide-bond stabilities may be at least two orders of magnitude.

Temperature and *pH* are important factors in the rate of hydrolysis of bonds. Strong acids (6 *N* HCl) and strong bases (4 *N* NaOH) catalyze the hydrolysis. Under these conditions most peptide bonds are hydrolyzed within 24 hours at 110°C, but some are completely hydrolyzed only after 72 hours at 110°C.

Strong acids, in contrast to strong bases, cause relatively little racemization of the amino acids during hydrolysis and for this reason are generally used in the hydrolysis of a protein for amino acid analysis. Extensive data are available in the literature on the hydrolysis of proteins by strong acid. By using sample aliquots hydrolyzed for various time periods, it is possible to make corrections for the destruction of some amino acid residues (particularly threonine and serine) and the slow hydrolysis of peptide bonds involving amino acids such as valine and isoleucine.

During the hydrolysis of a protein, free amino acids are released. The proportion of free amino acids to the total amino acids (bound plus free) is a measure of the extent of hydrolysis. Because the various amino acids form peptide bonds of varying stability, it is instructive to consider each amino acid separately during the hydrolysis of a protein. For example, glycine forms labile peptide bonds, and the free glycine compared with the total glycine in the sample is a measure of the proportion of glycine peptide bonds hydrolyzed.

Experimental Procedures

The determination of the ratio of free to total amino acid involves two measurements. First, a sample aliquot is dissolved in cold 6 *N* HCl under conditions that will not hydrolyze peptide bonds.

This is done in a few minutes in the vacuum centrifuge, resulting in a temperature near 0°C. The excess acid is removed in a rotary evaporator, and the sample is dissolved in a buffer of pH2, and analyzed directly. Proteins and peptides seldom interfere, and the quantity of each amino acid can be readily determined.

The second measurement is made on a second sample aliquot that has been dissolved in 6 N HCl and hydrolyzed at 157°C for 20 minutes. This hydrolyzes essentially all the peptide bonds in the sample. Again the excess acid is removed on the rotary evaporator, the sample dissolved in a buffer of pH2, and the quantity of each amino acid determined. In this sample the total of the free and peptide-bound amino acids is analyzed. If

P_1 = the total concentration of a particular amino acid (free and bound),

X_1 = the concentration of the free amino acid,

and

$\frac{dX_1}{dt}$ = rate of appearance of free amino acid or by definition the rate of hydrolysis,

then

$P_1 - X_1$ = concentration of the amino acid still in peptide linkage,

and

$\frac{P_1 - X_1}{P_1}$ = fraction of amino acids still in peptide linkage.

Therefore,

$$\frac{dX_1}{dt} = k_1 \left(\frac{P_1 - X_1}{P_1} \right) \text{ or}$$

$$\ln \left(\frac{P_1 - X_1}{P_1} \right) = k_1 t$$

is the expression for a first-order reaction and has been found to fit the data.

Water is obviously necessary for hydrolysis and must be present as vapor or liquid even though it does not appear in the rate equation. To determine if significant leaching takes place, some samples were placed in liquid water and the results compared with those on samples heated only in water vapor. Experiments were performed at temperatures of 157°, 110°, and 75°C to make it possible to determine activation energies for the hydrolysis reactions of several kinds of peptide bonds. Shells were *Hiatella arctica*, and bone samples were bovine.

Results

Although the rates are several orders of magnitude slower than with strong acid, the hydrolysis of proteins in water shows a number of similarities: (1) Threonine and serine are partially destroyed. (2) Alanine, serine, and glycine are released relatively rapidly. (3) Valine and isoleucine peptide bonds have the slowest rates of hydrolysis.

In Fig. 110 the results are plotted for seven amino acids. The rates for threonine, serine, and glycine do not follow the predicted rate equation for longer time periods. This behavior may be due to side reactions that may be obscuring the hydrolysis reaction. Valine and isoleucine follow the predicted equation far better than do the other amino acids.

Leaching is a problem in both shell and bone (Fig. 111). Owing to the porosity of bone, the free amino acids are leached out almost as soon as they are formed by hydrolysis. Little free amino acid material is found in naturally occurring fossil bones, indicating that extensive leaching has occurred.

Although leaching in shell also occurs, abundant free amino acids remain, showing that the rate of transport of free amino acids out of shell is relatively slow. It should be possible to account for the leaching effects by comparing the total amino acid content of a fossil with that of an equivalent modern shell structure.

Discussion

The data from these experiments, together with data from a series of fossils (see Miller and Hare, this Report), indicate that this approach may provide a

sensitive method for detecting the first steps in the diagenesis of proteins in fossils. The procedures normally used determine only the total amino acid concentration and the degree of racemiza-

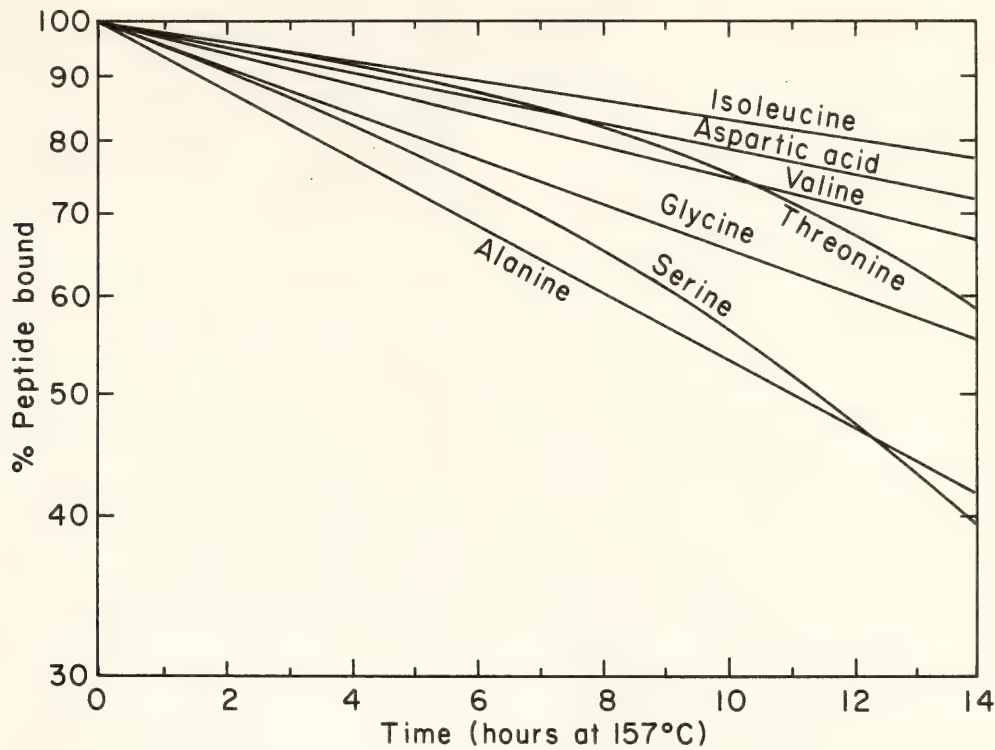


Fig. 110. Relative rates of release of various amino acids during hydrolysis in *Hiatella* shells at 157°C.

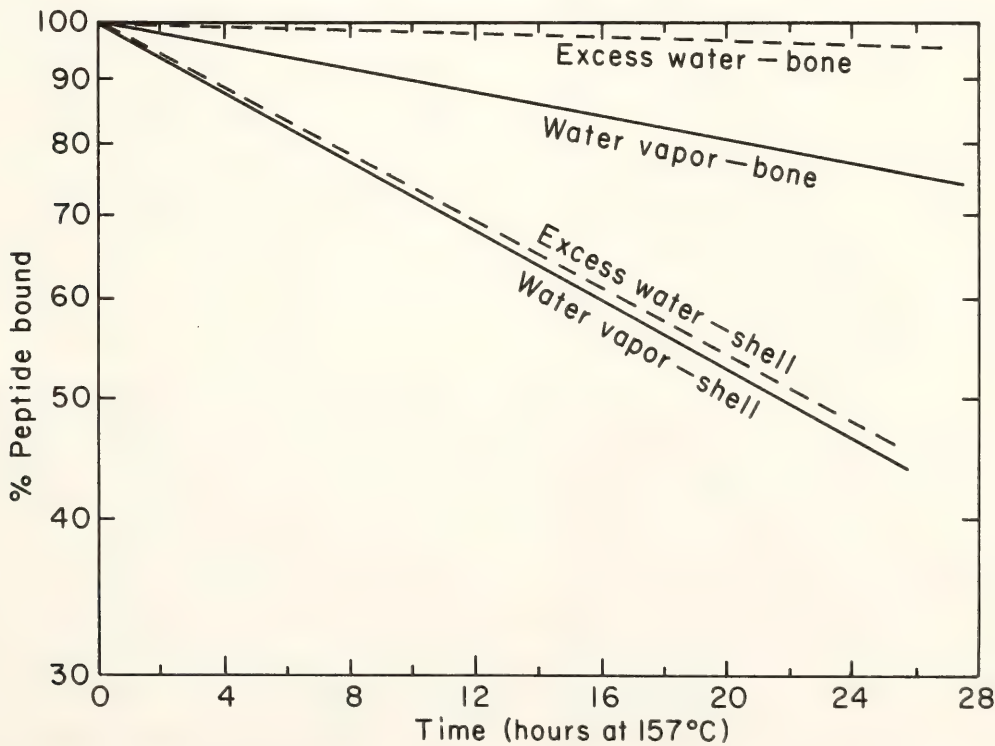


Fig. 111. Relative rates of hydrolysis of proteins in *Hiatella* shell and bovine bone at 157°C. Dashed lines show results from samples in excess water with extensive leaching.

tion. Without determining the free amino acid proportion one often cannot easily distinguish a young fossil or a fossil from the Arctic, for example, from a modern shell. By means of the method outlined in this report it is possible to distinguish fossil shells only a few years old. A series of *Rangia* shells from museum collections made in 1974, 1958, 1930, and 1890 showed progressively increased free amino acids proportional to the time since their collection. The total amino acid patterns and extent of racemization were indistinguishable.

USE OF AMINO ACID REACTIONS IN SOME ARCTIC MARINE FOSSILS AS STRATIGRAPHIC AND GEOCHRONOLOGICAL INDICATORS

G. H. Miller and P. E. Hare

During its many past expansions, the northeastern margin of the former Laurentide Ice Sheet terminated along the coastal lowlands of eastern Baffin Island, Northwest Territories, Canada. Because this area was seldom inundated by actively eroding continental ice, glaciogene and associated marine sediments are preserved along much of eastern Baffin Island. The most extensive sections are exposed in wave-cut cliffs north of Clyde River which extend uninterrupted for 35 km and vary from 5 to 35 m in height. These cliffs expose a complex set of tills, separated by sediments of marine and glacio-fluvial origin, including terrestrial soils, peats, and accumulations of organic matter. Many of the marine units are fossiliferous, containing both molluscan and foraminiferal remains. In some sections glacial tills deposited during at least four distinct glaciations are preserved. Mollusks from the marine unit overlying the uppermost (youngest) till are beyond the range of radiocarbon dating ($>40,000$ years), suggesting that these cliffs contain some of the oldest known direct evidence for early fluctuations of the Laurentide Ice Sheet.

The cliffs were first described by

Løken (1966), who distinguished two pre-classical Wisconsin glaciations, and in more detail by Feyling-Hanssen (1967 and in preparation), who analyzed the variations in foraminiferal faunal assemblages throughout the cliff sections. Both studies are, however, hampered by a lack of any absolute age control. It is with the intention of providing a correlative, and eventually an independently calibrated absolute dating method, that the diagenesis of amino acids in mollusk valves from these cliffs has been studied. Of the many reactions involved in the diagenesis of amino acids in fossil organic matter, the natural hydrolysis of proteins and the related racemization of the constituent amino acids were used. Both of these reactions appear to be directly related to the time elapsed since death of an organism.

In the preceding article, Hare, Miller, and Tuross have shown the strong dependence of the rate of hydrolysis on temperature. Because Baffin Island samples have had a low thermal history (present mean annual temperatures are -10° to -12°C), the rate of hydrolysis (and racemization) is slow. Consequently, the release of free amino acids is a useful chronologic indicator for a longer time than in samples from lower latitude. Additionally, many of the arctic samples have only recently been eroded from permanently frozen ground, so leaching of the shells has been minimal.

Method of Analysis

Over 200 mollusk collections from fossiliferous units on eastern Baffin Island are available for analysis. Prior to analysis of a valve, it was identified as to species, and a fragment weighing 300–400 mg was cleaned of possible surface contamination by dissolving in sufficient 2 N HCl to remove one-third of the shell weight. The cleaned fragments were then fractured, two chips weighing about 20 mg each were separated, and the remainder was stored. Most of the analy-

ses were of the common pelecypods *Hiatella arctica* and its close relative, *Mya truncata*.

The free amino acids were extracted by simply dissolving one chip in HCl, and the total amino acid population was obtained through acid hydrolysis of the second chip in 6 N HCl for 25 minutes at 157°C. The constituent amino acids of each fraction were then resolved on an ion exchange column using *o*-phthalaldehyde fluorescence for detection (Benson and Hare, 1975).

Results

To provide a broad framework for the range of amino acid diagenesis in Arctic Quaternary shells, valves having known ages of modern, 8000, *ca.* 60,000, *ca.* 120,000 and >120,000 years BP were analyzed.* The extent to which natural hydrolysis has occurred in each of these samples is listed in Table 65. The amino acids valine, isoleucine, leucine, and arginine gave the most consistent age relationships. In modern valves, essentially all the amino acids are peptide-bound in the protein structure, but after 8000 years of diagenesis, a measurable proportion of free amino acids has been released. The proportion of free to bound amino acids continues to increase in progressively older shells, although each amino acid is released at a different rate.

The extent of racemization in *H. arctica* from the same collections is listed in Table 66, including the epimerization of

* The age of the 8000 BP sample is based on radiocarbon analysis; the 60,000 BP sample is correlated by molluscan and foraminiferal assemblages with a unit U-series (²³⁰Th and ²³¹Pa) dated at 59,000 ± 10,000 BP (¹⁴C ≅ 40,000 BP); the next older sample is tentatively correlated on stratigraphic position with a unit having a U-series age of 137,000 ± 12,000 BP (Pheasant and Andrews, 1973); and the oldest sample is stratigraphically below shells correlated with the 137,000-year-old unit. Although the absolute ages of the older units are probably not precise, their relative stratigraphic positions are considered correct.

TABLE 65. The Extent of Natural Hydrolysis in *Hiatella arctica* from Deposits of Known Age in the Eastern Canadian Arctic*

Age (years BP)	Valine	Isoleu- cine	Leu- cine	Argi- nine
Modern	0	0	0	0
8,000	2	2	3	3
<i>ca.</i> 60,000	11	7	17	12
<i>ca.</i> 120,000	21	14	20	16
>120,000	33	21	37	...

* Proportion of free to bound + free amino acids × 100 (rounded to the nearest whole number).

L-isoleucine to D-alloisoleucine.† For those amino acids having an asymmetric center, only the L isomer is present in modern shells. However, as the peptide bonds are broken these L isomers begin to racemize to the D form. A similar progression of increasing diagenesis, in this case racemization, with increasing sample age is apparent. The rate of racemization varies considerably between the various amino acids. Proline, aspartic acid, and glutamic acid form detectable quantities of free D isomers in 8000 years, but detectable levels of the slower racemizing amino acids are formed only after 60,000 years of diagenesis.

It was found that the rates of hydrolysis and racemization vary in different shell species but are consistent within a given species. Three species from BSh63 (Fig. 112) were analyzed, and the allo/iso ratios of the hydrolyzed fractions gave markedly different results: *Hiatella arctica*, 0.21; *Clinocardium ciliatum*, 0.11; *Astarte* sp., 0.09. It

† The D/L ratios were determined by gas chromatography, and the allo/iso ratios were determined by ion-exchange liquid chromatography. The apparent racemization in the total fraction of the 8000-year-old sample is largely the result of laboratory-induced racemization during hydrolysis. Shells of this age from Baffin Island are not readily differentiable from modern shells on the basis of racemization in the hydrolyzed fraction. D/L ratios formed during hydrolysis of modern valves of *Mercenaria* are given in Hare and Hoering (*Year Book* 72, p. 694, Table 61).

TABLE 66. Racemization of Amino Acids in *Hiatella arctica* Valves from Deposits of Known Age in the Eastern Canadian Arctic

	D/L							
Age	val	ala	leu	pro	asp	phe	glu	allo/ iso
Total Fraction								
8,000	...	0.07	0.04	0.09	0.13	0.08	0.09	0.015
ca. 60,000	0.06	0.15	0.11	0.14	0.26	0.21	0.18	0.06
ca. 120,000	0.16	0.20	0.34	0.28	0.20	0.12
>120,000	0.24	0.44	0.26	0.29	0.42	0.40	0.37	0.23
Free Fraction								
Modern
8,000	0.36	0.31	...	0.18	...
ca. 60,000	0.35	0.39	0.26	0.57	0.53	0.29	...	0.30
ca. 120,000	0.81	0.58	0.44	0.72	0.68	0.68	0.34	0.60
>120,000	0.84	0.77	0.68	0.90	0.81	0.88	0.70	0.80

Abbreviations: val, valine; ala, alanine; leu, leucine; pro, proline; asp, aspartic acid; phe, phenylalanine; glu, glutamic acid; allo, alloisoleucine; iso, isoleucine.

is apparent that the species identification of each shell analyzed is important. An analysis of the extent of racemization in several valves of *H. arctica* from a single collection and between collections made along the same stratigraphic horizon produced comparable results for all valves, indicating that intraspecies variation in the rate of amino acid diagenesis is not appreciable.

Application to Arctic Quaternary Stratigraphy

During field studies along eastern Baffin Island, sections were located containing interbedded fossiliferous units of several depositional episodes. In these sections, the relative ages of the various units are fixed stratigraphically, and they provide an independent check on the results of the amino acid analyses.

One such section located between Clyde Inlet and Eglington Fiord was originally described by Feyling-Hanssen (1967, Profile IV). The general stratigraphy of the section, based on field studies in 1974, is shown in Fig. 112. Fossil shells were collected at sites BSh60-63, and a buried soil was sampled for pollen analysis at BO29. For simplicity, the

amino acid diagenesis is indicated by the epimerization of isoleucine to alloisoleucine (allo/iso ratio); the D/L ratios and extent of natural hydrolysis give parallel results. The allo/iso ratios in the four shell collections from this section, in keeping with their stratigraphic positions, show increasing diagenesis down section.

Shells from the uppermost unit at this section (BSh60) are correlated with a unit for which the radiocarbon age is 40,000 ± 1740 BP (GSC-796), and although this is probably a minimum age, the unit is most likely of Wisconsin age. A palynological analysis of the buried soil underlying this unit (BO29) revealed a high proportion of birch pollen (S. Short, personal communication), indicating that the soil developed under interglacial conditions (the nearest occurrence of birch at present is over 500 km southwest of the locality). Thus the till enclosing BSh61 is of pre-Wisconsin age, and the basal glaciogene units are considerably older, on the basis of the greater degree of racemization of the associated molluscan shells (BSh62 and 63).

Other sections from which several fos-

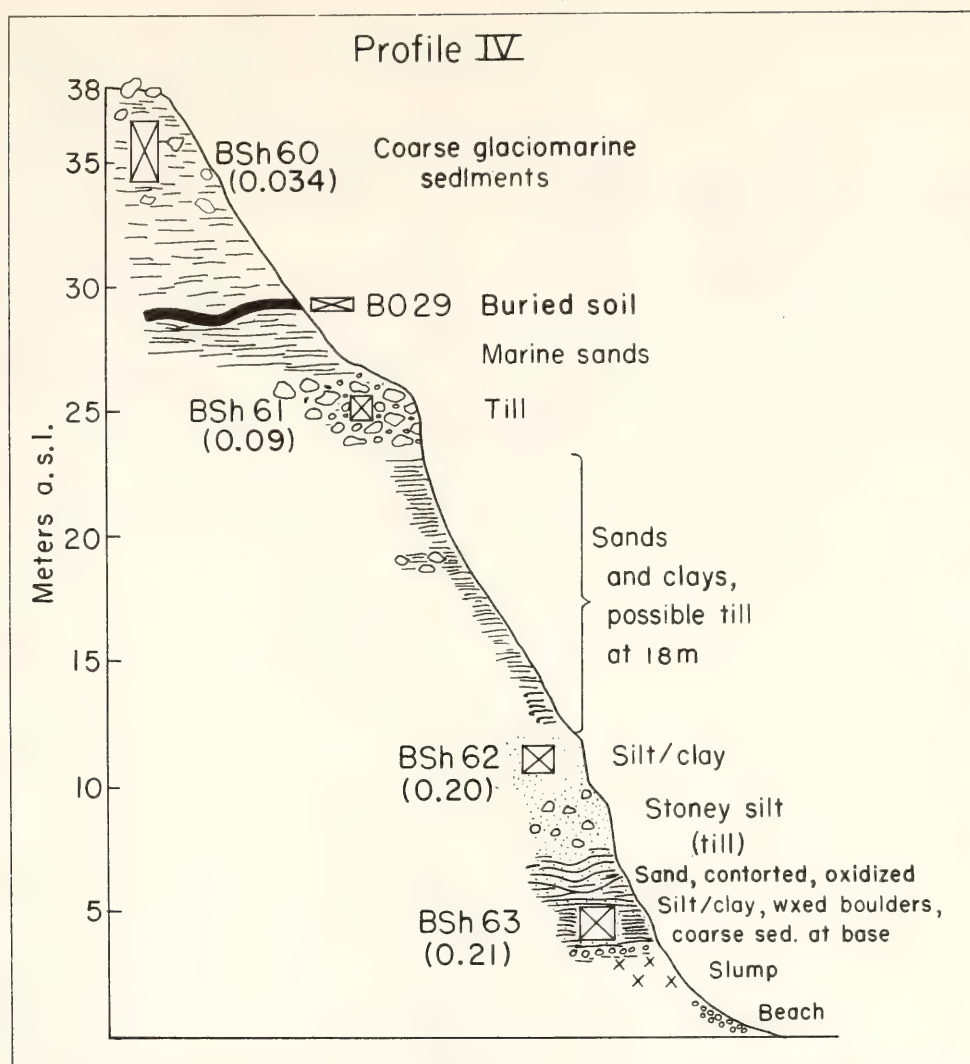


Fig. 112. General stratigraphy at Profile IV of Feyling-Hanssen (1967) on the surficial cliff section north of Clyde Inlet, eastern Baffin Island. The allo/iso ratios in the total amino acid population are indicated below each shell locality. Species identification was not possible for shell fragments at BSh60 or 61; BSh62 and 63 contained *H. arctica*.

siliferous units were collected and for which the relative ages of the units are fixed stratigraphically yielded similar results, with increasing diagenesis for samples of increasingly older relative age.

Amino acid diagenesis can also be readily used as a correlation tool. Figure 113 illustrates the general stratigraphy of two sections less than 4 km apart, between which lateral correlation of the individual units is hampered by a major river outlet. Both profiles have a glaciogene unit at or near the surface that is associated with shell-bearing sediments. Shells were collected at BSh64–69. Lacking any relative age data, an initial correlation attempt would likely suggest

that the upper glaciogene unit in each profile was deposited during the same depositional interval. Such correlations based on similar stratigraphic position are common. However, the results of amino acid analyses on *H. arctica* valves from the various units indicate that such a correlation is not correct. All four fossiliferous units in Profile XXII are of roughly the same age and are most likely the result of a single glaciation: isostatic depression of the land as a continental ice sheet develops and normal marine sedimentation (BSh68, 69); coarser sediment deposited as the fiord glacier approaches the site (BSh67); outwash or till, or both, emplaced as the glacier reaches the site; followed by

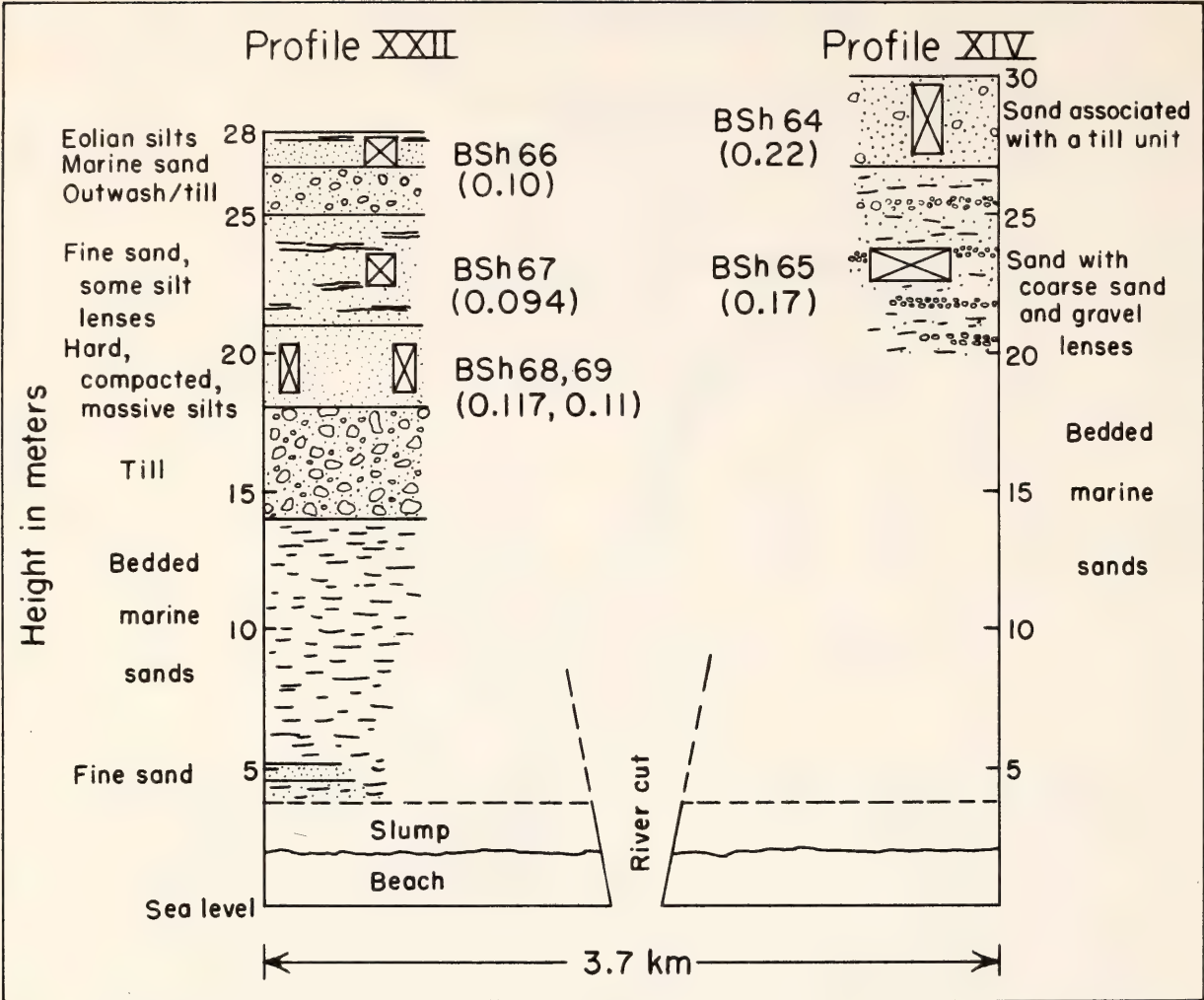


Fig. 113. General stratigraphy at Profiles XXII and XIV (Feyling-Hanssen, 1967). The units cannot be correlated laterally owing to the intervening river valley. Allo/iso ratios in the total amino acid population are indicated. All values analyzed were of *H. arctica*. The apparent stratigraphic reversal in the ratios of BSh64 and 65 is not readily explained but may be due to local shell transportation in these units.

deposition of marine sands (BSh66) as the glacier recedes and before the land emerges from the sea during isostatic readjustment. In contrast, the two upper fossiliferous units in Profile XIV exhibit considerably more advanced diagenesis and clearly relate to a glaciation that substantially predates the glacier advance represented in the upper portion of Profile XXII. Such information is invaluable in any attempt to decipher the Quaternary history of an area and is necessary for understanding the east Baffin coastal cliffs where lateral correlation of the units is often obscured by slumps and rapid facies change.

The use of amino acid diagenesis as a correlative tool has also been demon-

strated by analyzing shells from deposits that are independently correlated on the basis of diagnostic warm-water molluscan and foraminiferal faunal assemblages. Radiocarbon ages of shells from these deposits are all $\geq 35,000$ BP. *Hiatella arctica* valves collected from deposits of this warm marine episode along 500 km of eastern Baffin Island show a similar degree of racemization and hydrolysis.

Conclusions

The consistent results of the amino acid analyses and the agreement between the extent of diagenesis and other absolute and relative age-dating methods substantiate the use of these amino acid

reactions as geochronologic and stratigraphic indicators. The application of the amino acid dating method to Arctic Quaternary deposits beyond the range of ^{14}C capabilities provides the potential for resolving the rich but complex glacial and marine record of the eastern Canadian Arctic that has heretofore been largely ignored. A series of high-temperature laboratory experiments simulating time should lead to the eventual construction of an independently calibrated absolute time scale for the various amino acid reactions.

AMINO ACIDS AND THEIR DERIVATIVES IN CARBONACEOUS CHONDRITES

J. R. Cronin

Beginning with the work of Kvenvolden *et al.* (1970), the period 1970–1975 has seen renewed interest in the analysis of carbonaceous chondrites for amino acids and other organic compounds. Carbonaceous chondrites had been examined for the presence of amino acids beginning twenty years earlier; however, serious doubt was cast on these early analyses when it was recognized that there were striking similarities between the results and the amino acid content of potential contaminants such as fingerprints and laboratory dust (Hayes, 1967). In late 1969, specimens from two recent carbonaceous chondrite falls became widely available. Several laboratories were by then equipped for high-sensitivity amino acid analysis in preparation for returned lunar samples. Their analytical capability included separate determination of the amino acid optical isomers by gas chromatography. This capability provided a new and powerful tool for evaluating the extent of terrestrial contamination. Using this approach extensive amino acid analyses have now been done on representatives of the various types of carbonaceous chondrites (Lawless *et al.* 1971, 1972; Lawless, 1973). A diverse suite of amino acids has been found in the Murchison

and Murray meteorites, type II carbonaceous chondrites (Kvenvolden, Lawless, and Ponnamperna, 1971; Lawless *et al.* (1971)). These amino acids include some that are found in all terrestrial organisms and several that are rarely, if ever, found in living things. The amino acids have been found to be racemic, or nearly so, in all cases in which the optical isomers could be analyzed individually (Kvenvolden *et al.* 1970; Oró *et al.* 1971). These facts strongly suggest that in these studies, unlike much of the pre-1970 work, terrestrial contamination is not an important factor in the results. The amino acids are generally believed to have been produced by an abiotic process. If this is true, the carbonaceous chondrites offer evidence in support of the Oparin-Haldane theory of chemical evolution. This theory proposes that the origin of life is preceded by a period of abiotic synthesis and accumulation of the chemical components of the first organisms (Kenyon and Steinman, 1969). The products of such a process or a residue thereof might be expected to be found in ancient sedimentary rocks and in some extraterrestrial samples.

Cronin and Moore (1971) reported that water extracts of the Murchison and Murray chondrites have only about one half the overall amino acid content before acid hydrolysis that is found after such treatment. The extent of increase varies among the amino acids. Aspartic and glutamic acids increase six- to sevenfold, while sarcosine and β -alanine increase by only $\sim 50\%$. Glycine, the predominant amino acid in these samples, doubles. Thus, these meteorite water extracts seem to contain acid-labile amino acid precursors as well as free amino acids. These precursors are of interest, for they may yield clues to the mechanism of synthesis or further chemical evolution of the meteorite amino acids.

Some general properties of these acid-labile amino acid precursors have been ascertained by various chromatographic

experiments. Cronin (unpublished results) has found that the precursors can be fractionated on a cation-exchange column. The precursors were analyzed as amino acids after hydrolysis. Approximately 70 mol % of the precursors pass through the column from acidic solution and are obtained in the initial water eluate. Thus a large fraction of these precursors do not share the basicity characteristic of the amino acids and behave as neutral or acidic compounds. In order to distinguish between these two possibilities a sample of the Murchison water extract was made alkaline and applied to a column packed with the anion-exchange resin, AG2-X8 (Bio-Rad Laboratories, 200–400 mesh, hydroxide ion form). The column was eluted first with 10 ml water and then with 15 ml 2 *N* acetic acid. The results are shown in Table 67. The water eluate contains only small amounts of amino acids, both before and after hydrolysis. The acetic acid eluate contains nearly

the full complement of the free amino acids of the Murchison extract (90% recovery). However, the increase in amino acids on acid hydrolysis of this eluate accounts for less than 40% of the total precursor content of the extract. The remainder of the precursors were presumably still bound to the column. The precursors thus behave as acidic species on an anion exchanger.

A sample of the Murchison extract was dissolved in 0.1 *M* NaCl and applied to a 1.1 × 13.4 cm column packed with the polyacrylamide gel filtration material, Bio-Gel P-2 (Bio-Rad Laboratories, —400 mesh). The column was eluted with 0.1 *M* NaCl, and fractions were collected and analyzed for amino acids both before and after acid hydrolysis. The fractions containing amino acids before acid hydrolysis showed proportional increases after acid hydrolysis; i.e., the amino acid precursors were not separated from the amino acids on this column. Because Bio-Gel

TABLE 67. Anion-Exchange Chromatography of Amino Acids and Amino Acid Precursors of the Murchison Meteorite*

	Water Eluate		Acetic Acid Eluate	
		Hydro-lyzed		Hydro-lyzed
Aspartic acid	0.3	0.3	1.1	5.1
Threonine	0.1	0.2	0.9	3.3
Serine	0.3	0.2	1.5	3.4
Sarcosine	0	0	5.3	3.4
Proline	0	0	3.1	8.0
Glutamic acid	0.2	0.3	1.6	6.2
Glycine	0.6	1.1	20.6	29.8
Alanine	0.3	0.7	12.6	17.2
α-Aminoisobutyric acid	0	0	14.1	14.9
α-Amino- <i>n</i> -butyric acid	0	0	4.8	5.0
Valine/isovaline	0	0	3.7	6.5
Norvaline	0	0	0.7	1.0
Isoleucine	0	0.5	0.7	2.7
Leucine	0	0.4	0.7	3.9
β-Alanine	0	0	5.2	6.3
β-Aminoisobutyric acid	0	0	1.4	4.4
γ-Aminobutyric acid	0	0	1.6	4.9
Totals	1.8	3.7	79.6	126.0

* Nanomoles per gram meteorite.

P-2 has a discriminating range for peptides of about 300–1800 daltons, this result indicates that the precursors are not greatly different from the amino acids in molecular dimensions.

Taken together, these results indicate that most of the acid-labile amino acid precursors of the Murchison extract are acidic compounds of approximately the same molecular size as amino acids. These facts, along with the susceptibility to acid hydrolysis, are accounted for if amino acids exist in the meteorite (or form during the extraction process) as compounds in which a carbonyl group is bonded to the amino group nitrogen atom. Such derivatives could not be basic but would retain their acidic character. They would be readily converted to amino acids by acid hydrolysis. Of the various compounds of this type that conceivably could be present in the meteorite extract, the carbamyl amino acids and their dehydration products,

the 5-substituted hydantoins (2, 4-imidazolidinediones), will be initially sought. These compounds are readily formed from free amino acids and cyanate ion or urea under mild reaction conditions. Although neither cyanate ion nor urea has been identified in carbonaceous chondrites, they are simple molecules and might well have been produced by the same process that led to amino acid synthesis. For example, Miller (1957) has found that urea is produced in experiments simulating a primitive atmosphere. Amino acids are synthesized in these experiments in an array quite similar to that found in the Murchison and Murray carbonaceous chondrites (Wolman, Haverland, and Miller, 1972). A method has been worked out for the analysis of carbamyl amino acids and their corresponding hydantoins at the level of their potential occurrence in the Murchison extract (Cronin, this Report).

GEOCHRONOLOGY

ALTERATION IN ZIRCONS AND DIFFERENTIAL DISSOLUTION OF ALTERED AND METAMICT ZIRCON

T. E. Krogh and G. L. Davis

Metamict zircons, when used for age determinations, give discordant ages indicating that the uranium-lead relationship has been disturbed. Many of these zircons have been found to contain altered material (*Year Book 73*, pp. 560–567). Recent tests as well as earlier deductions indicate that this alteration is a contributing factor if not the major cause of discordance. As described last year and shown in Fig. 114 (A, B, C) this alteration occurs primarily along grain boundaries and along cracks in metamict zones within crystals or in wholly metamict crystals. In unzoned crystals the alteration has a spherical or botryoidal form, but in zoned crystals an entire growth layer may be so altered that the form is not visible. When pol-

ished sections of grains are exposed for 10 to 20 seconds in the vapor over 36% HF, altered regions are attacked to reveal complex internal zonation, as shown in Fig. 114A and C. In every case, however, a highly soluble frontal zone is present in the altered material at its interface with the unattacked mineral. In certain cases when 48% HF is used, minute crystal-like forms appear on the more reactive surfaces. These forms, referred to in *Year Book 73* as apparent crystallites, have been shown to be simply an artifact of the etching process. During exposure to the vapor small crystal-like forms appear on the surface and protect local areas that are left standing in relief.

Previous qualitative analyses (*Year Book 73*, p. 565) had shown a decrease in Si and Zr suggestive of hydration and an increase in Fe in altered zones. The exact chemical changes associated with the alteration process are under investi-

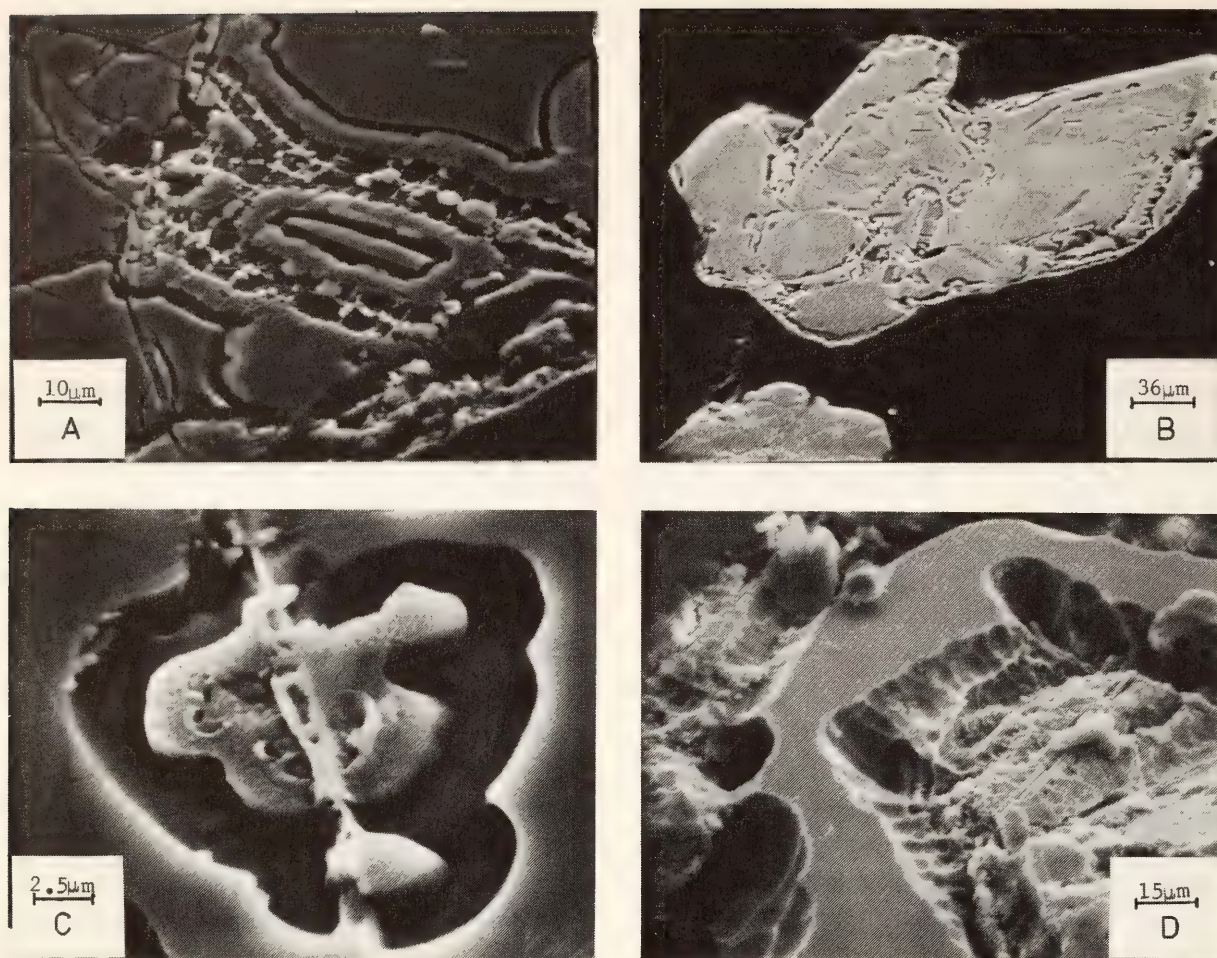


Fig. 114. Scanning electron photomicrographs of etched zircon grains: (A) zircon from Sudbury felsic norite showing complex internal zonation in altered regions after exposure to vapor of 36% HF; (B) composite grain from a paragneiss showing a complex pattern of alteration along internal cracks, growth layers, and outer margins after vapor etching; (C) local region of (B) showing alteration along a fracture and the development of a highly soluble zone next to unaltered material; (D) grain from a pegmatite after treatment with liquid 48% HF.

gation by Drs. O. Medenbach and A. El Goresy at the Max-Planck-Institut für Kernphysik in Heidelberg, Germany, using an electron microprobe. They have found that the sum of the oxides in altered zones is low by 5% to 12%, implying that water is present in approximately this amount. They have also established that calcium and aluminum as well as iron are enriched in the altered zones compared with the unaltered host. The concentrations of these oxides found in several altered zones in one sample are FeO, 0.5% to 1.8%; CaO, 1.1% to 2.8%; and Al_2O_3 , 0.9% to 1.9%. The occurrence of Fe in altered zircon is especially significant because it may account at least in part for the correla-

tion of increased discordance with the increase in magnetic susceptibility noted by Silver (1963) and observed in most zircon populations.

Recent results have now confirmed that alteration is of fundamental importance to the phenomenon of discordant uranium-lead relationships in zircons. In an earlier test reported in *Year Book 73* (pp. 565–567) a concordant residue was produced from a discordant population, but because both metamict and altered zircon had been removed it was not possible to specify which was responsible for the discordance. A more specific test has been completed on a population of relatively homogeneous high-uranium magnetic zircons that con-

tained only two components, a metamict host and regions of alteration. These zircon grains dissolve completely in 48% HF in less than 1 hour at room temperature. Tests on polished grain mounts indicated that most of the altered parts could be removed from this sample in 10 minutes in 5% HF. From a sample treated in this way, clear grains with numerous spherical indentations, similar to those shown in Fig. 114D but containing no partially attacked material, were selected for analysis. The U-Pb isotopic results indicate a point on a concordia diagram that lies within experimental error on the line defined by the data for eight other fractions of zircon from this intrusion (data point labeled "Residue," Fig. 115). A parallel

line through the data point has an age on concordia only 1 m.y. less than that for the eight samples.

The residue contained about 1400 ppm U, yet the data are more concordant than for most of the previously analyzed samples. The lower intercept of about 500 m.y. is critical to this test because laboratory leaching of the residue would displace the data point along a line through the origin. Thus the close fit of the data for the residue confirms both that the alteration was responsible for generating the lead-loss trajectory and that the residue remained a closed system during the acid treatment. A late low-temperature alteration stage rather than a continuous loss of lead by diffusion is therefore responsible for the ob-

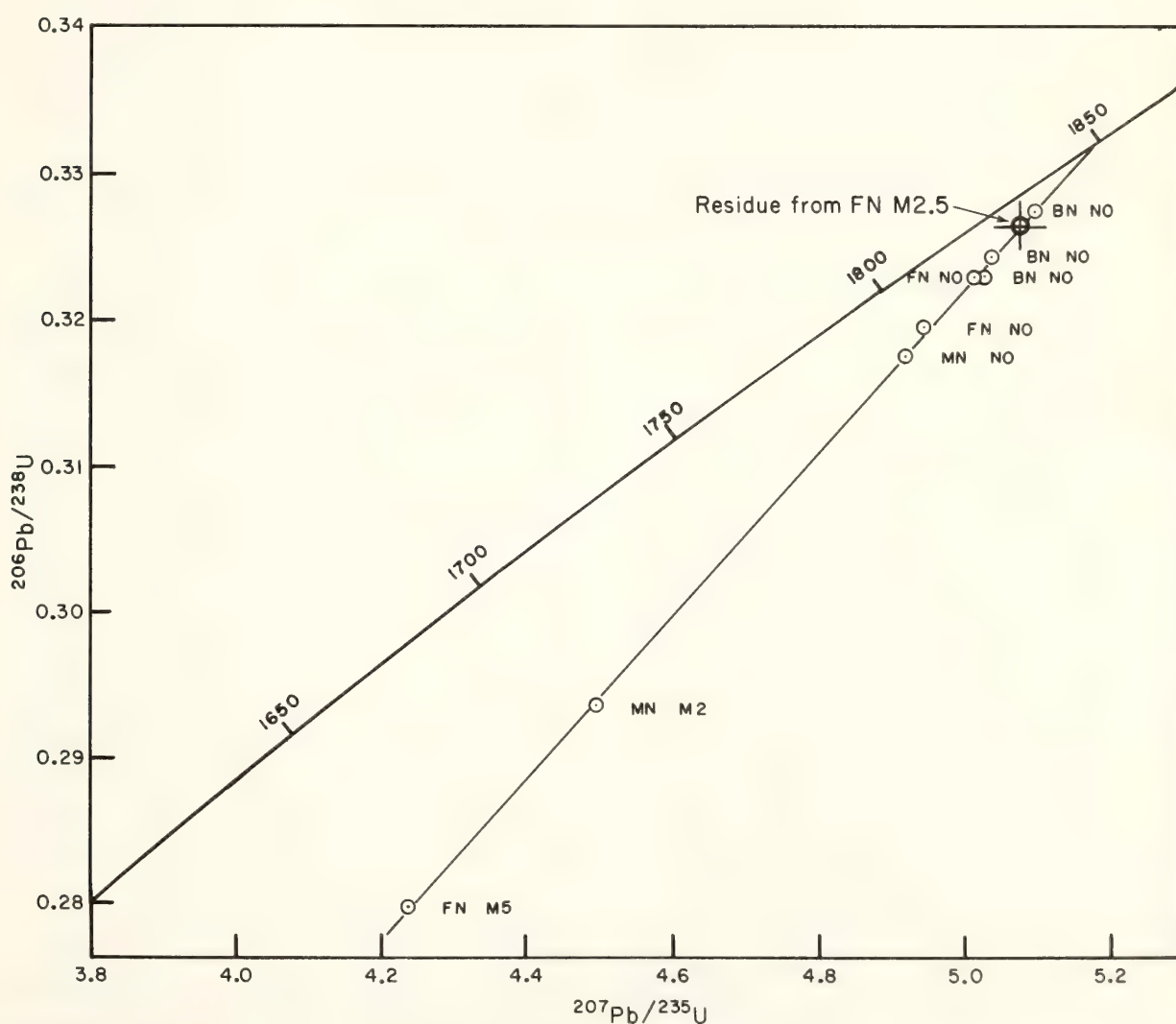


Fig. 115. Concordia diagram for zircons from the Sudbury norite, Sudbury, Ontario. The point labeled "Residue" is from the analysis of a sample of magnetic zircon that has had altered portions removed by treatment with hydrofluoric acid.

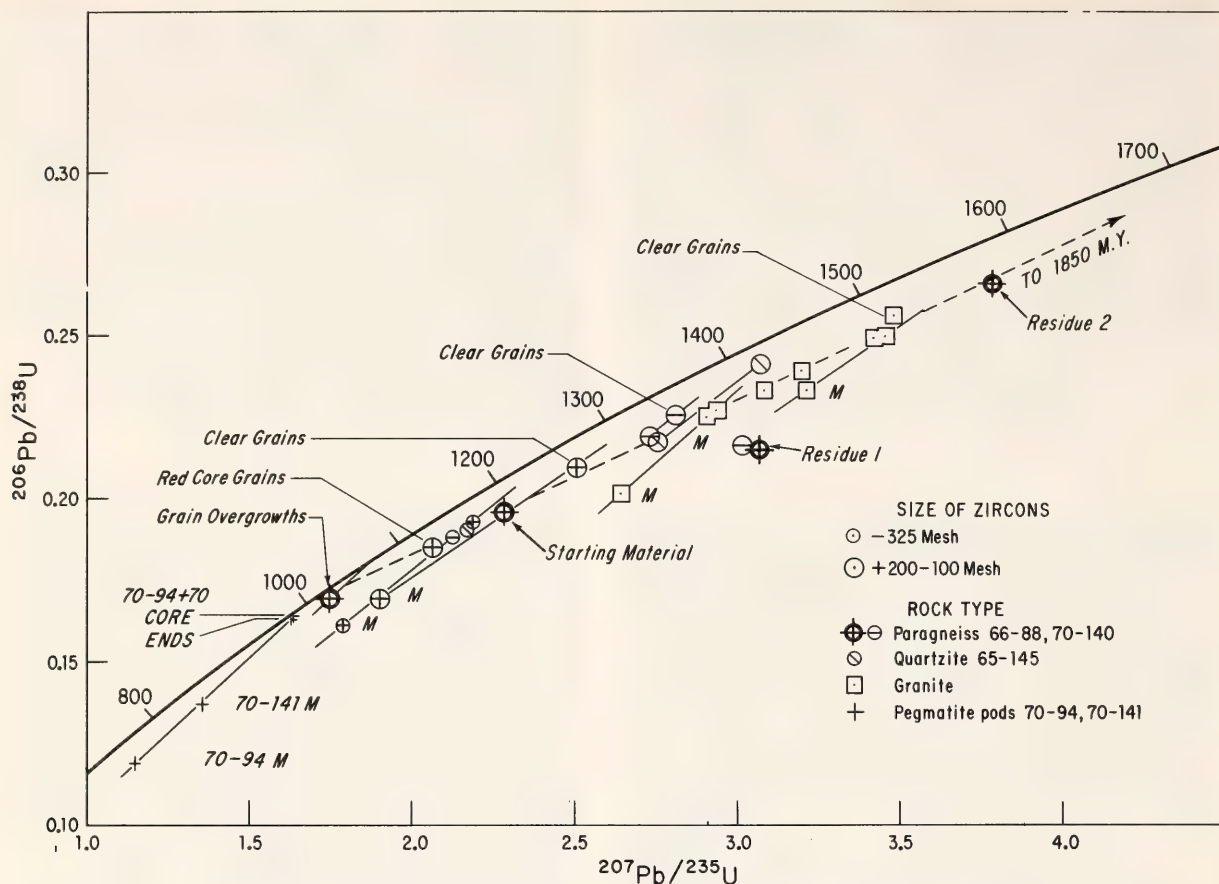


Fig. 116. Concordia diagram from *Year Book 72* (p. 603). The points labeled "Residue 1" and "Residue 2" illustrate the effect of the removal of metamict overgrowths by treatment of "Starting material" in cold hydrofluoric acid.

served discordance of the magnetic zircons from this rock.

The possibility of leaching U or Pb from the residual fraction required further testing. For this test a population of zircons known to have uranium-rich overgrowths on much older cores was selected (*Year Book 72*, pp. 601-605). In this case any disturbance of the U-Pb system in the residue would displace the data point from a mixing line between 1000 and 1850 m.y. as defined by the other samples (Fig. 116). The isotopic data for the residue data point ("Residue 2" on Fig. 116) demonstrate that the residual fraction has remained a closed system during the acid treatment.

An earlier test on the same sample gave a residue ("Residue 1," Fig. 116) that lay below this line (*Year Book 73*, p. 567). The acid treatment used to produce this residue was 1.5 hours in duration in 48% HF at room temperature,

while in the earlier test, a 0.5-hour leach in 1% HF was used. From this observation and from visual examination it is probable that some partially attacked material was present in Residue 1. This material may undergo differential removal of uranium or lead or may resorb some of these elements from the solution. The fact that the two residues have the same ^{207}Pb - ^{206}Pb age (1682.8 and 1682.1 m.y. for residues 1 and 2, respectively) implies that the ^{207}Pb - ^{206}Pb ratio is the true ratio for the residue, and that the displacement of this age from the 1850 m.y. age results from lead loss by diffusion during the amphibolite facies metamorphism 1000 m.y. ago.

In general, this work shows that zircons or parts of zircons that have become metamict are susceptible to attack by solutions that can cause alteration. Calcium, aluminum, iron, and water are introduced. Lead is lost, disturbing the

uranium-lead system upon which age determinations are based, with the result that the measured ages are discordant and difficult to interpret. When the altered regions are removed by treatment with hydrofluoric acid, analysis of the residue gives results that are much less discordant. It is not necessary to postulate loss of lead by continuous diffusion to explain the major part of the discordance of zircon ages.

ISOTOPIC AGES IN THE EASTERN LAC SEUL REGION OF THE ENGLISH RIVER GNEISS BELT

T. E. Krogh, G. L. Davis, N. B. W. Harris,
and I. F. Ermanovics†*

Previous U-Pb isotopic age determinations on volcanic rocks in the western part of the Canadian shield indicated that the east-west trending belts are progressively younger toward the south (*Year Book 70*, pp. 241-242). Ages of intrusive rocks that comprise the major part of one region, the Berens batholithic belt east of Lake Winnipeg, indicated an extensive period of intrusion and metamorphism coeval with and as much as 50 m.y. younger than the volcanic rocks (*Year Book 73*, pp. 573-575). In this study ages have been determined for metamorphism and intrusion in the Lac Seul region of the English River gneiss belt adjoining the Berens block on the south. A comparison of the age of metamorphism in the two regions is now possible.

The area studied was mapped and sampled in the summer of 1974 by N. B. W. Harris with the guidance of A. M. Goodwin of the University of Toronto; Harris also participated in the age determinations.

Because there had been no previous uranium-lead isotopic ages determined in this region, the investigation was designed to provide a limited amount of

age information for as many rock types as possible. Twelve zircon fractions from six rock types were analyzed. Where a complex metamorphic history was indicated, tests were made to determine if the U-Pb systems of the zircons had been modified. In two cases disturbed systems were detected so that a somewhat qualitative interpretation of the data is necessary. Two lead-loss trajectories were projected to concordia from lower intersections at 1000 and 0 m.y. to give a maximum and a minimum age for a single point. This procedure is realistic because cogenetic suites of zircons of this age have always given a lower intersection with concordia between 0 and 1000 m.y.

The eastern Lac Seul region of the English River gneiss belt is underlain by east-west trending biotite garnet paragneiss in the north and by a weakly foliated, massive tonalitic gneiss with associated north-west trending, biotite-rich and feldspar-rich gneisses to the south. Granite sills and local pegmatite lenses occur in the paragneiss, but numerous small granitic intrusions and cross-cutting dikes are common in the tonalite.

Isotopic results indicate that the tonalitic gneiss has a minimum age of 3008 ± 12 m.y. and is the oldest rock in the region (samples 74-115, Fig. 117). The data define an area on the concordia diagram indicating that the U-Pb systems of these zircons have been modified by a later metamorphism (*Year Book 72*, pp. 601-605). In this case, an empirical lead-loss trajectory through the data is invalid, and assumed trajectories for the oldest point, as noted earlier, give a more reliable result. This assumption yields a probable age of 3043 ± 35 m.y. for these zircons. Considering that the system has been modified by metamorphism, a true age in excess of this value is probable for this rock.

Zircons from a local pegmatite lens (samples 74-76, Fig. 117) within the paragneiss provide an estimate of the

* University of Toronto.

† Geological Survey of Canada.

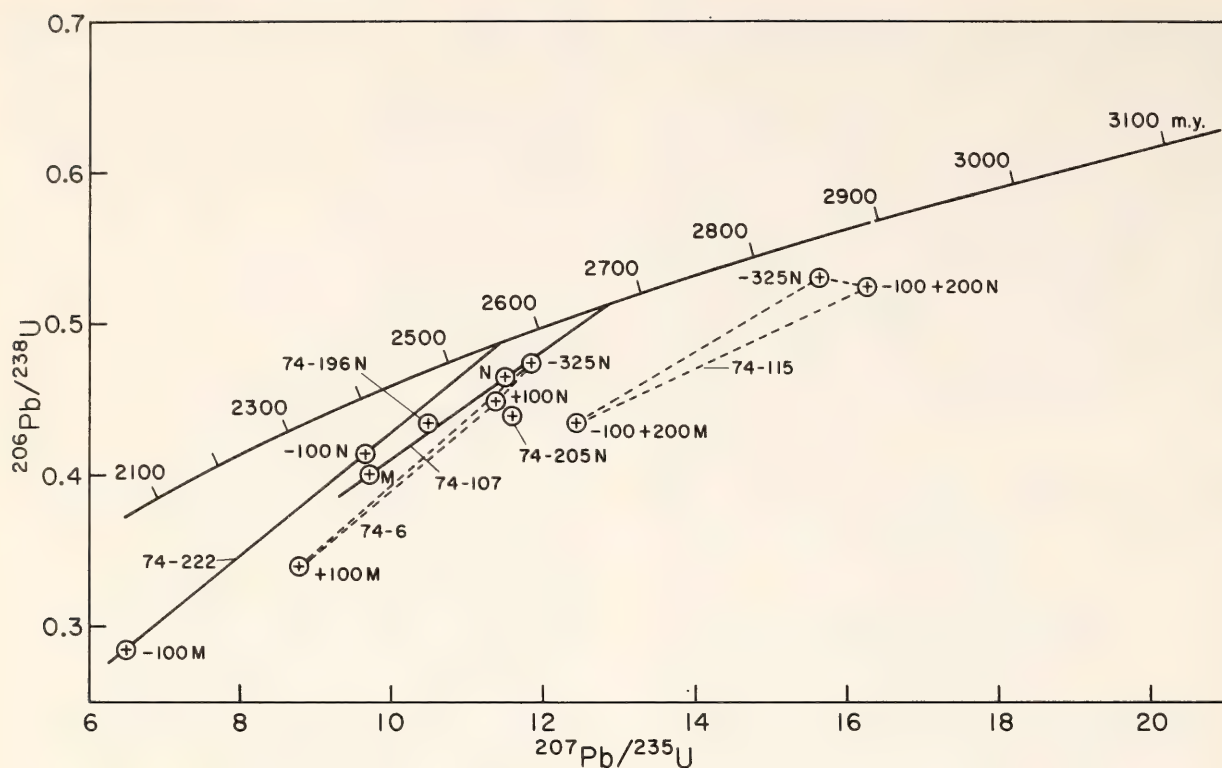


Fig. 117. Concordia diagram for zircons from the eastern Lac Seul region of the English River gneiss belt, near Sioux Lookout, Ontario. Solid lines mark empirical lead-loss trajectories. Broken lines join points for zircon fractions from the same rock having different sizes and magnetic properties (*M*, magnetic; *N*, nonmagnetic).

time of anatexis during regional metamorphism. The isotopic data for these coarse-grained fractions imply that an inherited older component is present; for example, the lower projection on concordia passes to the right of the origin (*Year Book* 72, pp. 601–605). Because the fine-grained fraction is relatively free of cores, an interpreted age using assumed trajectories is realistic. This interpreted age yields a maximum age for the metamorphism of 2688 ± 26 m.y. The occurrence of older cores within the pegmatite zircons is compatible with the presence of older zircons within the host paragneiss (sample 205, Fig. 117). These zircons are probably composed of material formed both during metamorphism and at the time of formation of the source region of the sediments so that no information relative to the age of sedimentation is provided. Zircons from a post-orogenic granite (sample 107, Fig. 117) give a minimum age for the time of metamorphism of 2669 ± 20

m.y. Data for a single sample of zircon from a granite sill in the paragneiss (sample 196, Fig. 117) yield a less precise but compatible age of 2662 ± 52 m.y. using assumed lead-loss trajectories. The youngest age in the region, 2568 ± 40 m.y., was determined on zircons from a late pegmatitic granite dike (sample 74-222, Fig. 117) that occurs in the tonalitic gneiss. The lower intercept at 200 m.y. is relatively low for rocks of this age, indicating that this age may be too young.

It is now possible to compare the histories of these adjacent areas to determine whether they conform to the pattern found earlier, namely that the ages become younger toward the south. Previous as well as recent determinations in the Berens batholithic block indicate that although small patches of older gneiss formed about 3 b.y. ago are widespread, the major intrusives that underlie most of the region were emplaced between 2770 and 2715 m.y. ago. Quartz

diorites are typically the earliest intrusives, and quartz monzonite and granites are the youngest. Regional metamorphism occurred more than 2715 m.y. ago because granites of this age are not deformed. In the Lac Seul region to the south, older basement at least 3 b.y. old has again been discovered. The sample dated is representative of the largest mappable unit in the area. The unit is massive rather than layered as were the older rocks found in the Berens block. Although both areas have similar ages for the older basement, the age of metamorphism and intrusion is younger in the Lac Seul area. The regional meta-

morphism occurred more than 2715 m.y. ago in the Berens block and less than 2688 m.y. ago in the English River gneiss belt. The late granitic intrusives were emplaced more than 2715 m.y. ago to the north and 2669 and 2568 m.y. ago in the English River gneiss belt to the south.

Taken together these data support the conclusion that at least a small amount of older basement was present prior to volcanism, intrusion, and metamorphism in both regions and that the plutonic-metamorphic cycle in the Berens block preceded that in the English River gneiss belt to the south.

STAFF ACTIVITIES

Mass Transport Conferences

Research efforts of several staff members have been directed toward the understanding of the role of geochemical mass transport in the evolution of metamorphic rock systems (Fletcher, Frantz, Mao, McCallister, and Vidale, this Report). To further developments in the field of mass transport, the Geophysical Laboratory held three conferences in the fall of 1974 and the spring of 1975 on (1) transport models, (2) application of models to zoned skarns, and (3) application of models to ore deposits. In each conference the participants were chosen to represent a variety of backgrounds and viewpoints. The size of the conferences was kept small (about 20) in order to promote informal discussion.

The conferees considered the meetings successful in prompting interaction between theoreticians and field and laboratory workers. The meetings provided each participant with the opportunity to discuss with other investigators the exact details of his approach to geochemical kinetics and the assumptions on which his approach is based. Subtle aspects of an approach (particularly subtle differences between two approaches) are com-

monly glossed over in papers, and face-to-face discussions were effective in settling outstanding questions.

Transport models. The first conference, concerning the theoretical approaches to transport along intergranular boundaries, was held on November 4 and 5, 1974, at the Robert Morris Lodge in Oxford, Maryland. The principal speakers were Dr. John Weare ("Diffusion metasomatism in mineral reaction zones") and Dr. Larry Cathles ("Ground water convection around plutons"). Discussants (G. W. Fisher, J. D. Frantz, H. Helgeson, A. W. Hofmann, T. N. Irvine, H. K. Mao, and H. Ohmoto) presented critical comments and alternative approaches. Other participants included H. P. Eugster, R. C. Fletcher, R. H. McCallister, D. Rumble, R. Vidale, H. S. Yoder, Jr., and E. Zen.

Weare introduced the general framework of irreversible thermodynamics necessary to describe the time-dependence of geologic systems, assuming local equilibrium. An example of binary diffusion and multiple reaction zones was presented by Frantz and Mao, illustrated by the system $\text{MgO-SiO}_2\text{-H}_2\text{O-HCl}$. Hofmann and Fletcher discussed their work on coupling of diffusion with

infiltration and showed a number of numerical solutions illustrating the dependence on the activity profiles of the isotherm and development of self-sharpening fronts during infiltration metasomatism. Helgeson talked about "path calc" and suggested how his procedure could be incorporated into a more encompassing scheme for treating metasomatic reaction. Fisher showed how simple arguments involving chemical potential gradients could be used to arrive at relative fluxes of material and hence the stoichiometry of the reactions responsible for segregations. Cathles presented a hydrodynamic model of circulation of aqueous solutions around a pluton and the decay of that circulation with cooling. Ohmoto discussed the isotopic data on which the model of circulation during porphyry copper deposition is based. He cautioned against taking literally the conventional water/rock ratio calculated in isotopic studies because the model does not include recirculation of fluid.

Applications of transport models to zoned skarns. The second conference, focusing on the application of theoretical transport models to zoned skarns, was held January 27 and 28, 1975, at Airlie House, Warrenton, Virginia. Two aspects of mass transport were discussed: (1) small-scale mass transport, such as that between rock layers of contrasting chemical composition; and (2) large-scale mass transport, such as occurs along the contacts between intrusive granitic rocks and limestones. Carnegie Institution participants included R. C. Fletcher, J. D. Frantz, A. W. Hofmann, H. K. Mao, R. H. McCallister, D. Rumble, R. Vidale, and H. S. Yoder, Jr. Participants from other institutions were J. B. Brady (Harvard), D. M. Burt (Yale), G. W. Fisher (Johns Hopkins), D. Hewitt (Virginia Polytechnic Institute and State University), R. Joesten (University of Connecticut), D. Kerrick (Pennsylvania State University), G. Kullerud (Purdue), B. Morgan (U. S.

Geological Survey), and A. B. Thompson (Harvard).

Hewitt opened the conference with a discussion of metasomatism resulting from the transport of volatiles such as CO_2 and H_2O . Vidale described her experiments on the growth of metasomatic columns resulting from transport of aqueous solutes through a pore solution. Fletcher and Vidale presented a finite-difference method for modeling aqueous transport coupled with chemical reactions. Joesten continued with a report on calcsilicate nodules from a contact aureole in the Christmas Mountains, Texas. Fisher, using Joesten's example, demonstrated his technique for determining phenomenological coefficients from natural rock systems. Burt presented a general description of skarn deposits and demonstrated the usefulness of chemical potential diagrams in understanding their paragenesis. Thompson, discussing calcsilicate zonations in a roof pendant in northern Vermont, demonstrated that the observed zonal sequence of four distinct reaction zones is close to that predicted by a simple model of cation diffusion. Kerrick, however, argued that in the Sierra Nevada the formation of skarns results mainly from infiltration of carbonate wall rocks by fluids derived from a cooling magma. Morgan discussed the mineralogy and petrography of skarns within the Mount Morrison pendant of the Sierra Nevada, California. He suggested that the variations in skarn deposits can be related to the pluton-wall rock interface geometry.

Applications of transport models to ore deposits. The third conference on Ore Deposits met at Airlie House on April 7 and 8, 1975. Its general purpose was to consider four types of ore deposits from the standpoint of how to model the derivation, transport, and deposition of ore components. The deposits, presented in order of increasing complexity, were the White Pine copper deposit (Michigan), the Kuroko stratiform deposit

(Japan), the Creede vein deposit (Colorado), and porphyry copper deposits.

Carnegie Institution participants included R. C. Fletcher, J. D. Frantz, A. W. Hofmann, H. K. Mao, R. H. McCallister, D. Rumble, R. Vidale, and H. S. Yoder, Jr. Participants from other institutions were H. L. Barnes (Pennsylvania State University), P. Barton (U. S. Geological Survey), J. Brady (Harvard), W. Burnham (Pennsylvania State University), D. Burt (Yale), L. Cathles (Kennecott), J. Ferry (Harvard), J. Hass (U. S. Geological Survey), J. Hemley (U. S. Geological Survey), G. Kullerud (Purdue), D. Norton (University of Arizona), and H. Ohmoto (Pennsylvania State University).

Hass began the first session with a discussion of the White Pine copper deposit and its sequence of Cu-Fe sulfides. He presented a model suggesting that a low-temperature aqueous fluid flowed under a hydraulic head from underlying metamorphosing lavas up through the carbonaceous Copper Harbor conglomerate where the copper leached from the volcanic rocks was reduced and deposited.

Ohmoto described the Kuroko stratiform sulfide deposits, one of the youngest and least metamorphosed occurrences of this type. He suggested that convective circulation of seawater, heated by intrusives at depth, leached ore components from the intrusive and volcanic pile and precipitated them as the yellow ores at about 200°–300°C at depth and as the black ores at about 150°–250°C at the seawater interface as temperature and chemical environment changed.

Barton discussed the Creede Pb-Zn vein deposit, describing the zonation and stratigraphy observed in sphalerite and the corresponding fluid inclusion evolution. He believes convecting fluid to have scavenged the mineralizing components from the underlying Precambrian basement, and he has estimated upward flow velocities from the local settling rate of hematite.

Barnes led a group discussion of the relative importance of chloride- and sulfide-bearing solution species in transport of ore components. He concluded that bisulfide complexes are especially important at lower temperatures (for example, under conditions of deposits of the Mississippi Valley type) and that chloride complexes become increasingly significant at higher temperatures. Burnham gave an overview of transport and deposition processes associated with porphyry copper deposits, emphasizing the importance of magmatic fluids and the fact that these deposits are highly fractured. He proposed a hydromagma-fract process caused by crystallization of solid phases from a magma already saturated with water, resulting in release of water and a large concurrent volume increase.

Hemley described the time sequence of vein assemblages observed at the El Salvador porphyry deposit, the corresponding alteration sequence, and the main body zonation. He related these to magmatic intrusion, concentration by a convective system, and ultimate supergene enrichment. Norton and Cathles described solution flow and reaction in various segments of a large convecting system, leading to observed copper porphyry zonation. Burnham concluded the conference with a summary of the proceedings.

Petrologists' Club

Seven meetings were held during the sixty-fourth year of the Petrologists' Club. The lectures presented were:

"Repeated opening and closing of the Atlantic Ocean basin: evidence from the southern Appalachian Mountains," by D. W. Rankin (U. S. Geological Survey), October 1, 1974.

"Our mineral resource problem and what we can do about it," by E. F. Osborn (Carnegie Institution of Washington), October 29, 1974.

"The first deep penetration of oceanic crustal layer 2," by Fabrizio Aumento

(Dalhousie University), December 18, 1974.

"Water and magmas: a mixing model," by C. Wayne Burnham (The Pennsylvania State University), January 14, 1975.

"Metamorphic zones and isograds in the Scottish Dalradian," by Ben Harte (Geophysical Laboratory), February 18, 1975.

"Kinetics and microstructure of coherent exsolution in alkali feldspar," by R. A. Yund (Brown University), March 18, 1975.

"Studies in volcanology at the U. S. Geological Survey Hawaiian Volcanological Observatory," by R. S. Fiske and T. L. Wright (U. S. Geological Survey), April 29, 1975.

Washington Crystal Colloquium

The Washington Crystal Colloquium, an informal organization of crystallographers from the Washington area, met six times during the report year. The following lectures were presented;

"Low resolution structure of deoxygenated sickle cell hemoglobin," by Barry Wishner (Johns Hopkins University), October 18, 1974.

"On the simple relationship of bonding and crystal structure to the Fermi surface in reciprocal space," by Forrest L. Carter (Naval Research Laboratory), November 22, 1974.

"Application of constrained refinement to studies of group thermal motions," by E. Prince (National Bureau of Standards), December 13, 1974.

"Cooling history of rocks from crystal structures of pyroxenes," by Larry W. Finger and Robert H. McCallister (Geophysical Laboratory), January 31, 1975.

"X-rays from unusual sources for diffraction and other uses," by D. J. Nagel (Naval Research Laboratory), February 28, 1975.

"What x-ray interferometry can do for you," by Richard Deslattes (National Bureau of Standards), April 11, 1975.

Seminar Series

The seminar series met 26 times during the report year. In addition, Professor G. Tunell of the University of California, Santa Barbara, delivered eight lectures about basic chemical thermodynamics, and Dr. H. S. Yoder, Jr., presented five seminars on magma generation. The Seminar Series included lectures by resident scientists at the Geophysical Laboratory with emphasis on significant new ideas and advances in specific fields. The following lectures were presented:

"The use of the digital plotter," by L. W. Finger (Geophysical Laboratory), October 3, 1974.

"Deep submersible observations of the mid-Atlantic Ridge," by W. B. Bryan (Woods Hole Oceanographic Institution), October 15, 1974.

"Role of CO₂ in the evolution of magmas—new concepts," by D. Eggler, (Geophysical Laboratory), October 25, 1974.

"Alkaline rocks in island arcs," by R. Arculus (Geophysical Laboratory), November 15, 1974.

"Experimental *in situ* determination of trace element partitioning with beta-track mapping," by B. Mysen (Geophysical Laboratory), November 25, 1974.

"Crystal-field band assignments," by P. M. Bell (Geophysical Laboratory), December 6, 1974.

"Spatial and temporal variation in the volcanic rocks of the Canary Islands," by Jose M. Fuster (University of Madrid), December 11, 1974.

"Volcanic eruption of Teneguia, Canary Islands" (motion picture), by Jose M. Fuster (University of Madrid), December 12, 1974.

"A new model for the kinetics of the Fe²⁺, Mg order-disorder phenomenon in chain silicates," by D. Virgo (Geophysical Laboratory), December 19, 1974.

"Phase transitions and mechanical properties in the lower mantle," by W.

A. Bassett (University of Rochester), January 8, 1975.

"Transport of organic matter from continents to adjacent ocean basins," by J. Hedges (Geophysical Laboratory), January 17, 1975.

"Speculation on the chemical equilibrium of crystal surfaces," by Y. Nakamura (Geophysical Laboratory), January 30, 1975.

"Crystal-field effects in the mantle," by H. K. Mao (Geophysical Laboratory), February 7, 1975.

"1974 Skaergaard field trip," by N. Irvine (Geophysical Laboratory), February 14, 1975.

"Basic chemical thermodynamics," by George Tunell (University of California), February 24–March 5, 1975.

"Effect of deformations accompanying transformations in crystals and rocks," by R. Fletcher (Geophysical Laboratory), March 7, 1975.

"Crystals at high temperature: 1. Macroscopic lattice expansion, 2. Atomic thermal vibrations," by Y. Ohashi (Geophysical Laboratory), March 14, 1975.

"The geochemistry of the stable isotopes of hydrogen," by T. Hoering (Geophysical Laboratory), March 21, 1975.

"Dynamics of Benioff Zone magmatism," by Bruce Marsh (Johns Hopkins University), March 27, 1975.

"Kinetic geothermometry," by Martin Dodson (University of Leeds), April 24, 1975.

"Pore solution compositions in pelitic assemblages," by R. Vidale (Geophysical Laboratory), April 25, 1975.

"*Si tibi sit dubium, discerne residuum*—Marcus Aurelius," by A. McBirney (University of Oregon), May 2, 1975.

"Deconvolution of thermal expansion: a simple method of obtaining lattice frequency information from structurally complex solids," by R. R. Reeber (Fritz-Haber Institute, Berlin), June 9, 1975.

"Some quantitative aspects of orogenic volcanism," by A. R. McBirney (University of Oregon), June 10, 1975.

"Magma generation," by H. S. Yoder,

Jr. (Geophysical Laboratory), June 23–27, 1975.

"The rocks of the Nyiragongo volcano (Zaire)," by Th. G. Sahama (University of Helsinki), June 30, 1975.

Field Studies

P. E. Hare examined the early man site at Murray Springs, Arizona, and collected geochemical samples together with C. V. Haynes of the University of Arizona. On another excursion, he studied and collected fossil material from a series of marine terraces north of Santa Cruz, California, and he studied an early man site at Sunnyvale, California, with K. Lajoie of the U. S. Geological Survey at Menlo Park.

T. C. Hoering took part in a short cruise on the RV *Lorene* from the Marine Science Institute of the University of Texas, Port Aransas, to collect marine plants from the Gulf of Mexico. He later accompanied members of the Marine Laboratory of the University of Delaware to the Great Marsh at Lewes, Delaware, to make further plant collections. Preliminary results from a hydrogen isotopic study of the plants are presented in this Report.

T. N. Irvine participated in an expedition to the Skaergaard intrusion, Kangerdlugssuag Fiord, East Greenland, in August 1974. The expedition was organized by Professor A. R. McBirney of the University of Oregon (also Research Associate of the Carnegie Institution of Washington) and included 13 participants from the United States, Canada, and South Africa. The Skaergaard intrusion, long considered a standard of comparison in igneous petrology, has been undergoing an extensive reexamination since 1971, principally by Professor McBirney and his students.

T. E. Krogh worked in the Noranda District of Quebec with E. Dimroth of the Quebec Department of Mines, principally to examine primary textures and sedimentation structures in Archean pyroclastic rocks. He then went to the

Sudbury District in Ontario to collect material from pegmatitic segregations in the Nipissing diabase for U-Pb zircon dating.

Bjørn Mysen visited Taal volcano in the Philippines and collected lava samples representative of the 1965 eruption and subsequent eruptions.

Douglas Rumble continued his field studies in New Hampshire, collecting additional samples for petrographic and isotopic studies and investigating various regional geological problems. He led field trips designed to collect material for research work on behalf of C. V. Guidotti of the University of Wisconsin, L. Mutti of Harvard University, and G. Oertel of The University of California, Los Angeles.

R. Vidale, J. Frantz, and D. Rumble participated in the North Atlantic Treaty Organization Advanced Study Institute on "Volatiles in Metamorphism." The Institute included a two-week field trip in the French, Italian, and Swiss Alps for the purpose of studying examples of fluid-mineral interaction.

Exhibits

The Geophysical Laboratory from its inception has emphasized the integration of laboratory experimental work and geological field studies. Both approaches are essential to an understanding of the geologic history of the earth's crust and mantle. Nowhere are the results of this approach better illustrated than in the Laboratory's petrology program. Through the years investigators have brought specific field-observed problems to the Laboratory. In recognition of their contributions to mineralogy and petrology, nearly 30 individuals associated with the Geophysical Laboratory have had minerals named after them. An exhibit in the Main Hall of the Laboratory, prepared by R. H. McCallister, displays many of these minerals. Specimens of eskolaite, fleischerite, joesmithite, merwinite, rankinite, ringwoodite, roedderite, tombarthite, yagiite, don-

ayite, and gaidonnayite are being sought for the exhibit.

T. N. Irvine also prepared an exhibit illustrating the contributions made by both laboratory experimental work and field work. It shows photographs of the classic Skaergaard intrusion in East Greenland as a natural example of crystallization differentiation, a concept attributed to the late N. L. Bowen (1915) at the Geophysical Laboratory. The Skaergaard intrusion resembles a large crucible in which gabbroic magma has solidified, partly by crystallization whereby crystals were carried downward by convection currents and deposited by sedimentary processes into layers of progressively changing composition.

Lectures

During the report year Staff Members and Fellows presented lectures and participated in symposia and other extracurricular activities as follows:

R. J. Arculus gave lectures at the Seventh Caribbean Geological Conference in Guadeloupe, West Indies; the Geology Department of the State University of New York at Albany; the Department of Geosciences, Pennsylvania State University; the Department of Geology, Rice University; and the Department of Geosciences, University of Arizona at Tucson.

P. M. Bell lectured at the Physics Division, National Bureau of Standards; the chemistry departments of the University of Maryland and Arizona State University; the Lunar Science Institute at Houston; and the Department of Geology, Brooklyn College. He was a member of the National Aeronautics and Space Administration (NASA) Lunar Sample Analysis Planning Team and the NASA Advisory Panel, as well as Editor of the U. S. National Report on Geophysics for the American Geophysical Union. Dr. Bell received the NASA Lunar Sample Research and Skylab Mission High Achievement Awards and the NASA Apollo Medal.

F. R. Boyd, Jr., delivered lectures on "Speculations on the origin of kimberlite" at the Geological Society of Canada, and "Discrete nodules and the origin of kimberlite" at Pennsylvania State University.

As chairman of a newly formed Working Group on Electronic Data Processing in Petrology, F. Chayes organized and conducted an open panel discussion of plans for construction of a world data base for igneous petrology, at the Berlin meeting of the International Mineralogical Association in September. He then attended the Regensburg meetings of the Deutsche Mineralogische Gesellschaft that immediately followed and in Regensburg was an observer at the session of Working Group 5 of the Geodynamics Project. He was also an observer at meetings of CODATA's advisory panels on Earth and Biological Sciences in London, April 27-28, 1975. During the report year he lectured in the geology departments of Syracuse University, Virginia Polytechnic Institute and State University, Purdue University, and the University of Reading.

J. Cronin addressed the Biology Department faculty of St. Francis College on "Meteorites and chemical evolution."

D. H. Eggler presented an invited talk on "Origin of the calcalkaline rocks" at the Granite-Rhyolite Workshop of the U. S. Geological Survey in Denver, Colorado. He also lectured on Wyoming kimberlites to the Department of Earth and Planetary Science at the Johns Hopkins University.

L. W. Finger lectured to the Geochemistry Section of the Department of Chemistry at the University of Maryland, and the U. S. Geological Survey at Reston, Virginia.

R. C. Fletcher gave two invited talks to the Department of Geology at Stanford University.

J. D. Frantz lectured on "Mass transport in metamorphic rocks" at the North Atlantic Treaty Organization Confer-

ence on Volatiles in Metamorphism at Nancy, France.

P. E. Hare addressed a seminar on High Sensitivity Amino Acid Analysis at the National Institutes of Health; delivered lectures at the Andrews University (Michigan) Centennial Conference on Life, the joint meeting of the Biochemical and Analytical Divisions of the Delaware Section of the American Chemical Society, and the Alfred I. du Pont Institute at Delaware. He also gave invited papers at the Symposium on Archaeometry, Society for American Archaeology at Dallas, Texas; the First International Conference on Solid-Phase Methods in Protein Sequence Analysis at Boston, Massachusetts; and the Penrose Conference on Plio-Pleistocene Geochronology at Mammoth Lakes, California.

B. Harte gave an invited lecture on "The Ban-Tây Nappe (and below) in the eastern Scottish Dalradian" to the Geological Society of Washington.

T. C. Hoering lectured on "Humic materials in marine sediments" at the Gordon Research Conference on Organic Geochemistry at Holderness School, Plymouth, New Hampshire. He served for the second year as Chairman of the Goldschmidt Medal Award Committee of the Geochemical Society.

T. N. Irvine presented a lecture on chromite deposits in stratiform intrusions to the Department of Geology and Geophysics at Yale University. He gave an invited paper on the Polaris and Axelgold intrusive complexes in north central British Columbia at the western annual meeting of the Geological Association of Canada, and he spoke on the Polaris complex to the Geological Society of Washington.

A. R. McBirney gave invited lectures on "Geological constraints on models for generation of orogenic magmas by wet melting" at a Symposium on the Role of Water in Magma Generation at Waterloo, Ontario; on "Orogenic igneous rocks" and "Differentiation of the Skaer-

gaard intrusion" at Ohio State University; and on "Relations of volcanism to the structure of orogenic systems" at the Lamont-Doherty Geological Laboratory, Columbia University.

R. H. McCallister addressed the Department of Geology at the University of Pennsylvania on "Kinetics and mechanisms of pyroxene exsolution."

B. O. Mysen presented an invited lecture at Yale University on "Melting in a volatile rich upper mantle. The influence of $a_{\text{H}_2\text{O}}$, a_{CO_2} , and a_{O_2} as independent variables between 7.5 and 40 kbar pressure."

Y. Ohashi participated in the International Union of Crystallography Symposium on "Intra- and Intermolecular Forces" at Pennsylvania State University, and gave an invited lecture at the Department of Geosciences, Purdue University.

E. F. Osborn presented the first Edward H. Kraus Memorial Lecture at the University of Michigan and delivered a lecture to the geology faculty and students at the University of Michigan on the origin of volcanic rocks. He spoke at the University of Washington on "Our mineral resources problem and what we can do about it," as part of the program on "Social Management of Technology," and also lectured to the faculty and students of the Ceramic Engineering Department on phase equilibrium research on silicate systems applied to steel plant refractories and slag problems and to origin of igneous rocks. Osborn presented the John P. Buwalda Memorial Lecture at the California Institute of Technology and delivered a lecture to geology faculty and students on the origin of andesite. He also lectured to the Engineering College faculty and students at Old Dominion University on "Problems and prospects in the expansion of coal utilization"; presented two lectures to faculty and students of the Chemistry and Geology Departments, College of William and Mary, on mineral resources and on high temperature-

pressure research on the origin of igneous rocks; delivered a lecture on mineral resources availability to the Sparrows Point, Maryland, Engineer's Club; and presented a paper entitled "Government action to increase coal use" at the Energy Symposium held at the annual meeting in New York of the American Association for the Advancement of Science. Dr. Osborn chaired meetings of the Board on Mineral Resources of the National Research Council; attended meetings of the *Ad Hoc* Committee on Materials Policy of the Office of Technology Assessment of the Congress of the United States; the Commission on Natural Resources and the Committee on Mineral Resources and the Environment of the National Research Council; the Panel on Sulfur Oxide Control Technology of the U. S. Department of Commerce Technical Advisory Board; the Geosciences Advisory Panel, Los Alamos National Laboratory, Energy Research and Development Administration; the Pennsylvania Science and Engineering Foundation Board (Commonwealth of Pennsylvania, Harrisburg); the Pennsylvania Research Corporation Board of Directors (Pennsylvania State University); the Geisinger Medical Center Board of Directors, Danville, Pennsylvania; the Board of Directors of the Institute for Medical Education and Research at Geisinger Medical Center; and the Consultants to the Science and Technology Policy Office of the National Science Foundation. He also served as a member of the U. S. National Committee on Geology; as a member of the College of Engineering Advisory Board at the University of California at Berkeley; participated in the National Materials Advisory Board Workshop at Airlie House, Warrenton, Virginia, on the role of materials research in "Project Independence"; and participated in a Workshop on Deep Continental Drilling sponsored by the Carnegie Institution of Washington at Ghost Ranch, New Mexico.

M. Rosenhauer presented an invited

lecture on "Phase studies at high pressures and high temperatures with differential thermal analysis" to the Department of Geology and the Graduate Geologists' Association of the University of Pennsylvania.

D. Rumble III gave an invited lecture to the Mineralogical Society of America Symposium on Modern Concepts in Metamorphism in Miami, Florida, on "Use of mineral solid solutions to measure gradients in the chemical potentials of volatile components in regionally metamorphosed rocks." He also participated in the NATO Conference on Volatiles in Metamorphism at Nancy, France.

Rosemary Vidale lectured on "Experimental pore solution compositions" at the NATO Conference on Volatiles in Metamorphism at Nancy, France. She also gave invited lectures at the University of Pennsylvania, the Geological Society of Washington, Cornell University, the University of Arizona, Virginia Polytechnic Institute and State University, and the Los Alamos Scientific Laboratory.

D. Virgo lectured on the kinetics of the order-disorder phenomenon in chain silicates and the calculation of quantitative cooling rates in rocks at the Chemistry Department, University of Maryland; Department of Geology, Brooklyn College, New York; and the U. S. Geological Survey, Reston, Virginia.

H. S. Yoder, Jr., presented five lectures on Magma Generation at Dartmouth College on May 5-9, 1975. They were (1) "Magma generation models and constraints on parental material," (2) "Depth of melting and melting processes," (3) "Heat requirements and sources," (4) "Physicochemical constraints on melting," and (5) "Tectonophysics of melting." The lecture series was sponsored by the National Academy of Sciences under the terms of the Arthur L. Day Prize and Lectureship. He also addressed the Department of Geological Sciences, University of Texas at Austin. Dr. Yoder served on the Geosciences Advisory Panel for the Los Alamos Scientific Laboratory and as a member of the Geological Sciences Visiting Committee of Brown University. He was active in the work of the National Academy of Sciences, serving as Chairman of the Section of Geology; on the Executive Committee of the Assembly of Mathematical and Physical Sciences; the Advisory Committee to the Office of Earth Sciences, National Research Council; the U. S. Geodynamics Committee of the Geophysics Research Board; the Auditing Committee; the Report Review Committee; and the Class Membership Committee. He is a member of both the U. S. National Committees for Geology and for Geochemistry.

BIBLIOGRAPHY

- Bell, P. M., A. El Goresy, and H. K. Mao, A study of iron-rich particles on the surfaces of orange glass spheres from 74220, *Proc. Fifth Lunar Sci. Conf., Geochim. Cosmochim. Acta*, Suppl. 5, Vol. 1, Pergamon Press, New York, pp. 187-191, 1974 (G. L. Paper 1643).
- Bell, P. M., H. K. Mao, and G. R. Rossman, Absorption spectroscopy of ionic and molecular units in crystals and glasses, in *Infrared and Raman Spectroscopy of Lunar and Terrestrial Minerals*, Academic Press, Inc., New York, pp. 1-38, 1975 (G. L. Paper 1667).
- Bell, P. M. *see also* Mao, H. K.; Taylor, L. A.
- Benson, J. R., and P. E. Hare, *o*-Phthalaldehyde: fluorogenic detection of primary amines in the picomole range; comparison with fluorescamine and ninhydrin, *Proc. Nat. Acad. Sci. USA*, 72, 619-622, 1975 (G. L. Paper 1654).
- Bryan, W. B., and G. Kullerud, Mineralogy and chemistry of the Ashmore chondrite, *Meteoritics*, 10, 41-50, 1975 (G. L. Paper 1665).
- Burnham, C. W., *see* Ohashi, Y.
- Charles, Robert W., The phase equilibria of richterite and ferrichterite, *Am. Mineral.*, 60, 367-374, 1975 (G. L. Paper 1661).
- El Goresy, A., *see* Bell, P. M.; Mao, H. K.
- Finger, L. W., and E. Prince, A system of Fortran IV computer programs for crystal structure computations, *Nat. Bur. Stand.*

- (U.S.), *Tech. Note*, 854, 133 pp., 1975 (obtainable from Superintendent of Documents, U.S. Government Printing Office, Washington, D.C., \$2.00) (G. L. Paper 1651).
- Finger, L. W., *see also* Ohashi, Y.
- Frantz, J. D., and A. Weisbrod, Infiltration metasomatism in the system $K_2O-SiO_2-Al_2O_3-H_2O-HCl$, in *Geochemical Transport and Kinetics*, A. W. Hofmann, B. J. Giletti, H. S. Yoder, Jr., and R. A. Yund, eds., *Carnegie Inst. Washington Publ.* 634, pp. 261-271, 1974 (obtainable from Academic Press, Inc., New York) (G. L. Paper 1653).
- Hare, P. E., *see* Benson, J. R.
- Hodges, F. N., and I. Kushiro, Apollo 17 petrology and experimental determination of differentiation sequences in model moon compositions, *Proc. Fifth Lunar Sci. Conf., Geochim. Cosmochim. Acta*, Suppl. 5, Vol. 1, Pergamon Press, New York, pp. 505-520, 1974 (G. L. Paper 1644).
- Irvine, T. N., Crystallization sequences in the Muskox intrusion and other layered intrusions—II. Origin of chromitite layers and similar deposits of other magmatic ores, *Geochim. Cosmochim. Acta*, 39, 991-1020, 1975 (G. L. Paper 1658).
- Kullerud, G., *see* Bryan, W. B.
- Kushiro, I., Melting of hydrous upper mantle and possible generation of andesitic magma: an approach from synthetic systems, *Earth Planet. Sci. Lett.*, 22, 294-299, 1974 (G. L. Paper 1640).
- Kushiro, I., On the nature of silicate melt and its significance in magma genesis: regularities in the shift of the liquidus boundaries involving olivine, pyroxene, and silica minerals, *Am. J. Sci.*, 275, 411-431, 1975 (G. L. Paper 1650).
- Kushiro, I., *see also* Hodges, F. N.
- Mao, H. K., and P. M. Bell, Crystal-field effects in spinel: oxidation states of iron and chromium, *Geochim. Cosmochim. Acta*, 39, 865-874, 1975 (G. L. Paper 1656).
- Mao, H. K., A. El Goresy, and P. M. Bell, Evidence of extensive chemical reduction in lunar regolith samples from the Apollo 17 site, *Proc. Fifth Lunar Sci. Conf., Geochim. Cosmochim. Acta*, Suppl. 5, Vol. 1, Pergamon Press, New York, pp. 673-683, 1974 (G. L. Paper 1647).
- Mao, H. K., *see also* Bell, P. M.; Taylor, L. A.
- Mattinson, J. M., Early Paleozoic ophiolite complexes of Newfoundland: isotopic ages of zircons, *Geology*, 3, 181-183, 1975 (G. L. Paper 1663).
- Mysen, B. O., and M. G. Seitz, Trace element partitioning determined by beta track mapping: an experimental study using carbon and samarium as examples, *J. Geophys. Res.*, 80, 2627-2635, 1975 (G. L. Paper 1662).
- Ohashi, Y., C. W. Burnham, and L. W. Finger, The effect of Ca-Fe substitution on the clinopyroxene crystal structure, *Am. Mineral.*, 60, 423-434, 1975 (G. L. Paper 1660).
- Osborn, E. F., Coal and the present energy situation, *Science*, 183, 477-481, 1974 (G. L. Paper 1649).
- Osborn, E. F., Our mineral resource problem and what we can do about it, *Edward H. Kraus Memorial Lecture*, The University of Michigan, Ann Arbor, Michigan, 17 pp., 1974 (G. L. Paper 1652).
- Prince, E., *see* Finger, L. W.
- Rossmann, G. R., *see* Bell, P. M.
- Rumble, D., III, Gibbs phase rule and its application in geochemistry, *J. Wash. Acad. Sci.*, 64, 199-208, 1974 (G. L. Paper 1645).
- Schwerer, F. C., *see* Wasilewski, P.
- Seifert, F. A., and D. Virgo, Kinetics of the Fe^{2+} -Mg, order-disorder reaction in anthophyllites: quantitative cooling rates, *Science*, 188, 1107-1109, 1975 (G. L. Paper 1664).
- Seitz, M. G., and R. E. Taylor, Uranium variations in a dated fossil bone series from Olduvai gorge, Tanzania, *Archaeometry*, 16, 129-135, 1974 (G. L. Paper 1639).
- Seitz, M. G., *see also* Mysen, B. O.
- Taylor, L. A., H. K. Mao, and P. M. Bell, β -FeOOH, akaganéite, in lunar rocks, *Proc. Fifth Lunar Sci. Conf., Geochim. Cosmochim. Acta*, Suppl. 5, Vol. 1, Pergamon Press, New York, pp. 743-748, 1974 (G. L. Paper 1646).
- Taylor, L. A., H. K. Mao, and P. M. Bell, Identification of the hydrated iron oxide mineral akaganéite in Apollo 16 lunar rocks, *Geology*, 2, 429-432, 1974 (G. L. Paper 1659).
- Taylor, R. E., *see* Seitz, M. G.
- Ulmer, G. C., *see* Wasilewski, P.
- Virgo, D., *see* Seifert, F. A.; Wasilewski, P.
- Wasilewski, P., D. Virgo, G. C. Ulmer, and F. C. Schwerer, Magnetochemical characterization of $Fe(Fe_xCr_{2-x})O_4$ spinels, *Geochim. Cosmochim. Acta*, 39, 889-902, 1975 (G. L. Paper 1657).
- Weisbrod, A., *see* Frantz, J. D.

REFERENCES CITED

- Abu-Eid, R. M., Absorption spectra and phase transformation of minerals at pressures up to 200 kilobars, Ph.D. thesis, Massachusetts Institute of Technology, 1975.
- Agamawi, Y. M., and J. White, The quaternary system $\text{CaO-Al}_2\text{O}_3\text{-TiO}_2\text{-SiO}_2$, Part III, The quaternary system calcium metasilicate-anorthite-sphene-silica, *Trans. Brit. Ceram. Soc.*, **53**, 23-38, 1954.
- Akimoto, S., and Y. Syono, High pressure transformations in MnSiO_3 , *Am. Mineral.*, **57**, 76-84, 1972.
- Albee, A. L., A petrogenetic grid for the Fe-Mg silicates of pelitic schists, *Am. J. Sci.*, **263**, 512-536, 1965.
- Albee, A. L., Metamorphism of pelitic schists: reaction relations of chloritoid and staurolite, *Geol. Soc. Am. Bull.*, **83**, 3249-3268, 1972.
- Allen, E. T., and W. P. White, Diopside and its relations to calcium and magnesium metasilicates, *Am. J. Sci.*, **27**, 1-47, 1909.
- American Petroleum Institute, *American Petroleum Institute Research Project No. 49 (Clay Mineral Standards)*, Columbia University, New York, 1951.
- Andersen, O., The system anorthite-forsterite-silica, *Am. J. Sci.*, **39**, 407-454, 1915.
- Anderson, D. L., and O. L. Anderson, The bulk modulus-volume relationship for oxides, *J. Geophys. Res.*, **75**, 3494-3500, 1970.
- Araki, T., and T. Zoltai, Crystal structure of babingtonite, *Z. Kristallogr.*, **135**, 355-373, 1972.
- Armstrong, F., P. M. Williams, and J. D. Strickland, Photo-oxidation of organic matter in sea water by ultra-violet radiation, analytical and other applications, *Nature*, **211**, 481-483, 1966.
- Arnould, M., M. Kabbani, and D. P. H. Kien, Nouvelle synthèse de l'uvarovite obtenu par frittage d'un mélange de wollastonite artificielle et d'oxide de chrome, *C. R. Acad. Sci. (Paris)*, *Ser. D*, **269**, 4-5, 1969.
- Åsbrink, S., and A. Magnéli, Crystal structure studies on Trititanium pentoxide, Ti_3O_5 , *Acta Crystallogr.*, **12**, 575-581, 1959.
- Ashworth, J. G., The sillimanite zones of the Huntly-Portsoy area in the north-east Dalradian, Scotland, *Geol. Mag.*, **112**, 113-224, 1975.
- Atherton, M. P., The variation in garnet, biotite and chlorite composition in medium grade pelitic rocks from the Dalradian, Scotland, with particular reference to the zonation in garnet, *Contrib. Mineral. Petrol.*, **18**, 347-371, 1968.
- Atherton, M. P., and M. S. Brotherton, The composition of some kyanite-bearing regionally metamorphosed rocks from the Dalradian, *Scot. J. Geol.*, **8**, 203-213, 1972.
- Atherton, M. P., and M. S. Brotherton, The composition of some kyanite-bearing regionally metamorphosed rocks from the Dalradian, *Scot. J. Geol.*, **9**, 244-248, 1973.
- Atherton, M. P., and M. S. Brotherton, Metamorphic index minerals in the eastern Dalradian, *Scot. J. Geol.*, **10**, 321-324, 1974.
- Bader, R. G., D. W. Hood, and J. B. Smith, Recovery of dissolved organic matter in seawater and organic sorption by particulate material, *Geochim. Cosmochim. Acta*, **19**, 236-243, 1960.
- Bancroft, G. M., *Mössbauer Spectroscopy: An Introduction for Inorganic Chemists and Geochemists*, John Wiley and Sons, Inc., New York, 1973.
- Banno, S., and Y. Matsui, On the formulation of partition coefficients for trace elements distribution between minerals and magma, *Chem. Geol.*, **11**, 1-16, 1973.
- Barnett, J. D., S. Block, and G. J. Piermarini, An optical fluorescence system for quantitative pressure measurement in the diamond-anvil cell, *Rev. Sci. Instrum.*, **44**, 1-9, 1973.
- Barrow, G., On the geology of lower Deeside and the southern Highland Border, *Proc. Geol. Assoc. (London)*, **23**, 268-273, 1912.
- Barus, C., The fusion constants of igneous rock, *Phil. Mag.*, *Ser. 5*, **35**, 1893.
- Bashkirov, Sh. Sh., G. D. Kurbatov, R. A. Maropov, I. N. Penkov, E. K. Sadykov, and V. A. Chistiakov, Ilmenite (FeTiO_3) examined with the aid of the nuclear gamma-resonance method, *Dokl. Acad. Sci. USSR, Earth Sci. Sect.*, **173**, 89-91, 1967.
- Bassett, W. A., T. Takahashi, and P. W. Stook, X-ray diffraction and optical observations on crystalline solids up to 300 kbar, *Rev. Sci. Instrum.*, **38**, 37-42, 1967.
- Bell, P. M., and H. K. Mao, Cataclastic plutonites: possible keys to the evolutionary history of the early moon (abstr.), in *Lunar Science VI*, Lunar Science Institute, Houston, pp. 34-35, 1975.
- Bell, P. M., H. K. Mao, E. Roedder, and P. W. Weiblen, The problem of the origin of symplectites in olivine-bearing lunar rocks, *Proc. Sixth Lunar Sci. Conf.*, *Geochim. Cosmochim. Acta*, Suppl. 6, Pergamon Press, New York, in press, 1975.
- Benson, J. R., and P. E. Hare, *o*-Phthalaldehyde: fluorogenic detection of primary amines in the picomole range. Comparison with fluorecamine and ninhydrin, *Proc. Nat. Acad. Sci. USA*, **72**, 619-622, 1975.
- Biggar, G. M., and M. J. O'Hara, Solid solutions at atmospheric pressure in the system CaO-MgO-SiO_2 with special reference to the instabilities of diopside, akermanite, and moniticellite, *Progress in Experimental Petrology*,

- Natural Environment Research Council, Manchester-Edinburgh, First Report, pp. 86-96, 1969.
- Bird, G. W., and J. J. Fawcett, Stability relations of Mg-chlorite-muscovite and quartz between 5 and 10 kb water pressure, *J. Petrol.*, **14**, 415-428, 1973.
- Bloss, F. D., and J. J. Papike, eds., High temperature crystal chemistry, *Am. Mineral.*, **58**, 577-704, 1973.
- Boettcher, A. L., B. O. Mysen, and P. J. Modreski, Phase relationships in natural and synthetic peridotite-H₂O and peridotite-H₂O-CO₂ systems at high pressure, *Phys. Chem. Earth*, in press, 1975.
- Boettcher, A. L., and P. J. Wyllie, Jadeite stability measured in the presence of silicate liquids in the system NaAlSiO₄-SiO₂-H₂O, *Geochim. Cosmochim. Acta*, **32**, 999-1012, 1968.
- Boettcher, A. L., and P. J. Wyllie, Phase relationships in the system NaAlSiO₄-SiO₂-H₂O to 35 kilobars pressure, *Am. J. Sci.*, **267**, 875-909, 1969.
- Bottinga, Y., and M. Javoy, Comments on oxygen isotope geothermometry, *Earth Planet. Sci. Lett.*, **20**, 250-265, 1973.
- Bowen, N. L., Crystallization differentiation in silicate liquids, *Am. J. Sci.*, **39**, 175-191, 1915.
- Bowen, N. L., *The Evolution of the Igneous Rocks*, Princeton University Press, Princeton, N.J., 1928.
- Bowen, N. L., and J. F. Schairer, The system MgO-FeO-SiO₂, *Am. J. Sci.*, **29**, 151-217, 1935.
- Boyd, F. R., A pyroxene geotherm, *Geochim. Cosmochim. Acta*, **37**, 2533-2546, 1973.
- Boyd, F. R., and J. L. England, Apparatus for phase-equilibrium measurements at pressures up to 50 kb and temperatures up to 1750°C, *J. Geophys. Res.*, **65**, 741-748, 1960.
- Boyd, F. R., and J. L. England, Effect of pressure on the melting of diopside, CaMgSi₂O₆, and albite, NaAlSi₃O₈, in the range up to 50 kbar, *J. Geophys. Res.*, **68**, 311-323, 1963.
- Boyd, F. R., and P. H. Nixon, Origin of the ilmenite-silicate nodules in kimberlites from Lesotho and South Africa, in *Lesotho Kimberlites*, P. H. Nixon, ed., Lesotho National Development Corporation, Maseru, Lesotho, pp. 254-268, 1973.
- Boyd, F. R., and P. H. Nixon, Origins of the ultramafic nodules from some kimberlites of northern Lesotho and the Monastery Mine, South Africa, "Proceedings of the International Kimberlite Conference," *Phys. Chem. Earth*, **9**, in press, 1975.
- Boyd, F. R., and J. F. Schairer, The system MgSiO₃-CaMgSi₂O₆, *J. Petrol.*, **5**, 275-309, 1964.
- Bradley, R. S., Thermodynamic calculations on phase equilibria involving fused salts, II, Solid solutions and application to the olivines, *Am. J. Sci.*, **260**, 550-554, 1962.
- Brey, G., and D. H. Green, The role of CO₂ in the genesis of olivine melilitite, *Contrib. Mineral. Petrol.*, **49**, 93-103, 1975.
- Brookins, D. G., and H. O. A. Meyer, Crustal and upper mantle stratigraphy beneath eastern Kansas, *Geophys. Res. Lett.*, **1**, 269-272, 1974.
- Brown, L. C., and A. P. Callahan, The large-scale production of carrier-free ²⁰⁶Bi for medical application, *Int. J. Appl. Radiat. Isot.*, **26**, 213-217, 1975.
- Buddington, A. F., and D. H. Lindsley, Iron-titanium oxide minerals and synthetic equivalents, *J. Petrol.*, **5**, 310-357, 1964.
- Bultitude, R. J., and D. H. Green, Experimental study of crystal-liquid relationships at high pressures in olivine nephelinite and basanite compositions, *J. Petrol.*, **12**, 121-147, 1971.
- Burnham, C. W., Ferrosilite III: a triclinic pyroxenoid-type polymorph of ferrous metasilicate, *Science*, **154**, 513-516, 1966.
- Burnham, C. W., Hydrothermal fluids at the magmatic stage, in *Geochemistry of Hydrothermal Ore Deposits*, H. L. Barnes, ed., Holt, Rinehart, and Winston, New York, pp. 34-76, 1967.
- Burnham, C. W., The crystal structure of pyroxferroite from Mare Tranquillitatis, *Proc. Second Lunar Sci. Conf.*, *Geochim. Cosmochim. Acta*, Suppl. 2, Vol. 1, MIT Press, Cambridge, pp. 47-57, 1971.
- Burnham, C. W., Thermodynamics of melting in experimental silicate-volatile systems, *Geochim. Cosmochim. Acta*, in press, 1975.
- Burnham, C. W., and N. F. Davis, The role of H₂O in silicate melts, I, *P-V-T* relations in the system NaAlSi₃O₈-H₂O to 10 kilobars and 1000°C, *Am. J. Sci.*, **270**, 54-79, 1971.
- Burnham, C. W., and N. F. Davis, The role of H₂O in silicate melts, II, Thermodynamic and phase relations in the system NaAlSi₃O₈-H₂O to 10 kilobars, 700° to 1100°C, *Am. J. Sci.*, **274**, 902-940, 1974.
- Burns, R. G., Mixed valencies and site occupancies of iron in silicate minerals from Mössbauer spectroscopy, *Can. Spectrosc.*, **17**, 51-59, 1972.
- Burns, R. G., and W. S. Fyfe, Site of preference energy and selective uptake of transition-metal ions from a magma, *Science*, **144**, 1001-1003, 1964.
- Burns, R. G., and W. S. Fyfe, Trace element distribution rules and their significance, *Chem. Geol.*, **2**, 89-104, 1967.
- Calder, J. A., Carbon isotope effects in biochemical and geochemical systems, Ph.D. thesis, University of Texas at Austin, 1969.
- Calder, J. A., and P. L. Parker, Geochemical implication of induced changes of C¹³ frac-

- tionation by blue-green algae, *Geochim. Cosmochim. Acta*, 37, 133-140, 1973.
- Cameron, E. N., Structure and rock sequences of the Critical Zone of the eastern Bushveld Complex, *Mineral. Soc. Amer. Spec. Pap.*, 1, 93-107, 1963.
- Cameron, M., S. Sueno, C. T. Prewitt, and J. J. Papike, High-temperature crystal chemistry of aegirine, diopside, hedenbergite, jadeite, spodumene and ureyite, *Am. Mineral.*, 58, 594-618, 1973.
- Cann, J. R., Major element variations in ocean-floor basalts, *Philos. Trans. R. Soc. London, Ser. A*, 268, 495-505, 1971.
- Carmichael, I. S. E., The petrology of Thingmuli, a Tertiary volcano in eastern Iceland, *J. Petrol.*, 5, 435-460, 1964.
- Carmichael, I. S. E., and J. Nicholls, Iron-titanium oxides and oxygen fugacities in volcanic rocks, *J. Geophys. Res.*, 72, 4665-4687, 1967.
- Carmichael, I. S. E., F. J. Turner, and J. Verhoogen, *Igneous Petrology*, McGraw-Hill Book Company, New York, 1974.
- Carswell, D. A., Primary and secondary phlogopites and clinopyroxenes in garnet lherzolite xenoliths, *International Conference on Kimberlites, Extended Abstracts*, University of Cape Town, Rondebosch, South Africa.
- Champness, P. E., and G. W. Lorimer, An electron microscopic study of a lunar pyroxene, *Contrib. Mineral. Petrol.*, 33, 171-183, 1971.
- Chao, E. T. C., J. A. Minkin, C. Frondel, C. Klein, Jr., J. C. Drake, L. Fuchs, B. Tani, J. V. Smith, A. T. Anderson, P. B. Moore, G. R. Zechman, Jr., R. J. Traill, A. G. Plant, J. A. V. Douglas, and M. R. Dence, Pyroxferroite, a new calcium-bearing iron silicate from Tranquillity Base, *Proc. Apollo 11 Lunar Sci. Conf., Geochim. Cosmochim. Acta*, Suppl. 1, Vol. 1, Pergamon Press, New York, pp. 65-79, 1970.
- Charette, M. P., T. B. McCord, C. Pieters, and J. B. Adams, Application of remote spectral reflectance measurements to lunar geology; classification and determination of titanium content of lunar soils, *J. Geophys. Res.*, 79, 1605-1613, 1974.
- Chayes, F., Alkaline and subalkaline basalts, *Am. J. Sci.*, 264, 128-145, 1966.
- Chayes, F., The chemical composition of Cenozoic andesite, *Oreg. Dep. Geol. Miner. Ind. Bull.*, 65, 1-11, 1969.
- Chayes, F., On the need, design and prospects for an electronic information system serving igneous petrology, *J. Int. Assoc. Math. Geol.*, in press, 1975.
- Chessin, H., W. C. Hamilton, and B. Post, Position and thermal parameters in calcite, *Acta Crystallogr.*, 18, 689-693, 1965.
- Chinner, G. A., Pelitic gneisses with varying ferrous/ferric ratios from Glen Clova, Angus, Scotland, *J. Petrol.*, 1, 178-217, 1960.
- Chinner, G. A., The origin of sillimanite in Glen Clova, Angus, *J. Petrol.*, 2, 312-323, 1961.
- Chinner, G. A., The kyanite isograd in Glen Clova, Angus, *Mineral. Mag.*, 34, 132-143, 1965.
- Chinner, G. A., The distribution of pressure and temperature during Dalradian metamorphism, *Quart. J. Geol. Soc. London*, 122, 158-186, 1966.
- Chinner, G. A., Chloritoid, and the isochemical character of Barrow's zones, *J. Petrol.*, 8, 268-282, 1967.
- Chinner, G. A., Metamorphic index minerals in the eastern Dalradian, *Scot. J. Geol.*, 9, 248-249, 1973.
- Clark, M. G., G. M. Bancroft, and A. J. Stone, Mössbauer spectrum of Fe²⁺ in a square planar environment, *J. Chem. Phys.*, 47, 4250-4261, 1967.
- Clark, S. P., Jr., and A. E. Ringwood, Density distribution and constitution of the mantle, *Rev. Geophys.*, 2, 35-88, 1964.
- Clayton, R. N., and T. K. Mayeda, The use of bromine pentafluoride in the extraction of oxygen from oxides and silicates for isotopic analysis, *Geochim. Cosmochim. Acta*, 27, 43-52, 1963.
- Cohen, L. H., K. Ito, and G. C. Kennedy, Melting and phase relations in an anhydrous basalt to 40 kilobars, *Am. J. Sci.*, 265, 519-538, 1967.
- Coombs, D. S., X-ray observations on wairakite and non-cubic analcime, *Mineral. Mag.*, 30, 699-708, 1955.
- Cox, K. G., J. J. Gurney, and B. Harte, Xenoliths from the Matsoku pipe, in *Lesotho Kimberlites*, P. H. Nixon, ed., Lesotho National Development Corporation, Maseru, Lesotho; pp. 76-100, 1973.
- Cromer, D. T., and David Liberman, Relativistic calculation of anomalous scattering factors for x-rays, *J. Chem. Phys.*, 53, 1891-1898, 1970.
- Cromer, D. T., and J. B. Mann, X-ray scattering factors computed from numerical Hartree-Fock wave functions, *Acta Crystallogr., Sect. A*, 24, 321-324, 1968.
- Cronin, J., and C. B. Moore, Amino acid analyses of the Murchison, Murray, and Allende carbonaceous chondrites, *Science*, 172, 1327-1329, 1971.
- Cruikshank, D. W. J., The analysis of the anisotropic thermal motion of molecules in crystals, *Acta Crystallogr.*, 9, 754-756, 1956.
- Daly, R. A., Average chemical compositions of igneous-rock types, *Proc. Am. Acad. Arts Sci.*, 45, 211-240, 1910.
- Daly, R. A., *Igneous Rocks and Their Origins*,

- McGraw-Hill Book Company, New York, 1914.
- Daly, R. A., *Igneous Rocks and the Depths of the Earth*, McGraw-Hill Book Company, New York, 1933.
- Danchin, R. V., and F. D'Orey, Chromian spinel exsolution in ilmenite from the Premier Mine, Transvaal, South Africa, *Contrib. Mineral. Petrol.*, **35**, 43-49, 1972.
- Davis, B. T. C., and F. R. Boyd, The join $\text{Mg}_2\text{Si}_2\text{O}_6\text{-CaMgSi}_2\text{O}_6$ at 30 kbar pressure and its application to pyroxenes from kimberlites, *J. Geophys. Res.*, **71**, 3567-3576, 1966.
- Dawson, J. B., and D. G. Powell, Mica in the upper mantle, *Contrib. Mineral. Petrol.*, **22**, 233-237, 1969.
- Dawson, J. B., D. G. Powell, and A. M. Reid, Ultrabasic xenoliths from the Lashaine volcano, Northern Tanzania, *J. Petrol.*, **11**, 519-545, 1970.
- Dawson, J. B., and A. M. Reid, A pyroxene-ilmenite intergrowth from the Monastery Mine, South Africa, *Contrib. Mineral. Petrol.*, **26**, 296-301, 1970.
- Dawson, J. B., and J. V. Smith, Chemistry of opaque minerals from peridotite and eclogite xenoliths, *International Conference on Kimberlites, Extended Abstracts*, University of Cape Town, Rondebosch, South Africa, p. 83, 1973.
- Dawson, J. B., and J. V. Smith, Chemistry and origin of phlogopite megacrysts in kimberlite, *Nature*, **253**, 336-338, 1975.
- Day, D. E., and G. E. Rindone, Properties of soda aluminosilicate glasses, III, Coordination of aluminum ions, *J. Am. Ceram. Soc.*, **45**, 579-581, 1962.
- Debrunner, P., R. W. Vaughan, A. R. Champion, J. Cohen, J. Moyzis, and H. G. Drickamer, Versatile high pressure Mössbauer apparatus, *Rev. Sci. Instrum.*, **37**, 1310-1315, 1966.
- Deer, W. A., R. A. Howie, and J. Zussman, *Rock-Forming Minerals*, Vol. 2, John Wiley and Sons, Inc., New York, 1963.
- Dent Glasser, L. S., and F. P. Glasser, Silicate transformations: rhodonite-wollastonite, *Acta Crystallogr.*, **14**, 818-822, 1961.
- Diamond, S., and E. B. Kinter, Surface areas of clay minerals as derived from measurements of glycerol retention, in *Clays and Clay Minerals*, A. Swinford, ed., *National Academy of Sciences Publ.* 556, Washington, D.C., pp. 334-475, 1958.
- Dickson, B. L., The iron distribution in rhodonite, *Am. Mineral.*, **60**, 98-104, 1975.
- Dollase, W. A., Statistical limitations of Mössbauer spectral fitting, *Am. Mineral.*, **60**, 257-264, 1975.
- Dowty, E., Crystal chemistry of titanian and zirconian garnet, I, Review and spectral studies, *Am. Mineral.*, **56**, 1983-2009, 1971.
- Dowty, E., and D. H. Lindsley, Mössbauer spectra of synthetic hedenbergite-ferrosilite pyroxene, *Am. Mineral.*, **58**, 850-868, 1973.
- Drickamer, H. G., The effects of high pressure on the electronic structure of solids, *Solid State Phys.*, **17**, 1-133, 1965.
- Drickamer, H. G., and C. W. Frank, *Electronic Transitions and the High Pressure Chemistry and Physics of Solids*, Chapman and Hall, Ltd., London, 1973.
- Duursma, E. K., The dissolved organic constituents of seawater, in *Chemical Oceanography*, Vol. 1, J. P. Riley and G. Skirrow, eds., Academic Press, New York, pp. 433-475, 1965.
- Eggler, D. H., and C. W. Burnham, Crystallization and fractionation trends in the system andesite- H_2O - CO_2 - O_2 at pressures to 10 kb, *Geol. Soc. Am. Bull.*, **84**, 2517-2532, 1973.
- Egorov, L. S., Carbonatites and ultrabasic-alkaline rocks of the Maimecha-Kotui region, N. Siberia, *Lithos*, **3**, 341-359, 1970.
- Etter, D. E., Application of differential thermal analysis to the study of phase equilibria, in "Symposium on Research at Mound Laboratory, June 6-7, 1963," R. A. Benson, ed., *Rep. Mound Lab. No. MLM-1163*, Monsanto Research Corp., Mound Laboratory, Miamisburg, Ohio, pp. J1-J14, 1963.
- Eugster, H. P., Heterogeneous reactions involving oxidation and reduction at high pressures and temperatures, *J. Chem. Phys.*, **26**, 1760-1761, 1957.
- Eugster, H. P., A. L. Albee, A. E. Bence, J. B. Thompson, Jr., and D. R. Waldbaum, The two-phase region and excess mixing properties of paragonite-muscovite crystalline solutions, *J. Petrol.*, **13**, 147-179, 1972.
- Evans, B. W., and T. L. Wright, Composition of liquidus chromite from the 1959 (Kilauea Iki) and 1965 (Makaopuhi) eruptions of Kilauea volcano, Hawaii, *Am. Mineral.*, **57**, 217-230, 1972.
- Ferguson, J., R. V. Danchin, and P. H. Nixon, Petrochemistry of kimberlite autoliths, in *Lesotho Kimberlites*, P. H. Nixon, ed., Lesotho National Development Corporation, Maseru, Lesotho, pp. 285-293, 1973.
- Ferraris, G., D. W. Jones, and J. Yerkess, A neutron-diffraction study of the crystal structure of analcime, $\text{NaAlSi}_2\text{O}_6\cdot\text{H}_2\text{O}$, *Z. Kristallogr.*, **135**, 240-252, 1972.
- Feyling-Hanssen, R. W., The Clyde foreland, in *Field Report, North-Central Baffin Island*, O. H. Løken, ed., Department of Energy, Mines, and Resources, Ottawa (mimeographed report), pp. 35-55, 1967.
- Figgis, B. N., *Introduction to Ligand Fields*, Interscience Publishers, New York, 1966.
- Finger, L. W., and Y. Ohashi, The thermal expansion of diopside to 800°C and a refine-

- ment of the crystal structure at 700°C, *Am. Mineral.*, in press, 1975.
- Finger, L. W., and E. Prince, A system of Fortran IV computer programs for crystal structure computations, *Nat. Bur. Stand. (U.S.) Tech. Note*, 854, 133 pp., 1975.
- Fletcher, R. C., and A. W. Hofmann, Simple models of diffusion and combined diffusion-infiltration metasomatism, in *Geochemical Transport and Kinetics*, A. W. Hofmann, B. J. Giletti, H. S. Yoder, Jr., and R. A. Yund, eds., Carnegie Inst. Wash., Publ. 634, Washington, D.C., pp. 243-259, 1974.
- Franck, E. U., Überkritisches Wasser als elektrolytisches Lösungsmittel, *Angew. Chem.*, 73, 309-322, 1961.
- Frey, F. A., and D. H. Green, The mineralogy, geochemistry, and origin of lherzolite inclusions in Victorian basanites, *Geochim. Cosmochim. Acta*, 38, 1023-1060, 1974.
- Friedman, I., and J. D. Gleason, A new silicate intercomparison standard for ^{18}O analysis, *Earth Planet. Sci. Lett.*, 18, 124, 1973.
- Fudali, R. F., Oxygen fugacities of basaltic and andesitic magmas, *Geochim. Cosmochim. Acta*, 29, 1063-1075, 1965.
- Ganguly, J., Staurolite stability and related parageneses: theory, experiments, and applications, *J. Petrol.*, 13, 335-365, 1972.
- Gast, P. W., Trace element fractionation and the origin of tholeiitic and alkaline magma types, *Geochim. Cosmochim. Acta*, 32, 1057-1086, 1968.
- Geller, S., and C. E. Miller, The synthesis of uvarovite, *Am. Mineral.*, 44, 445-446, 1959.
- Gentile, A. L., and R. Roy, Isomorphism and crystalline solubility in the garnet family, *Am. Mineral.*, 45, 701-711, 1960.
- Gibb, T. C., N. N. Greenwood, and W. Twist, The Mössbauer spectra of natural ilmenites, *J. Inorg. Nucl. Chem.*, 31, 947-954, 1969.
- Gibbs, J. W., On the equilibrium of heterogeneous substances, *Trans. Conn. Acad.*, 3, 108-248, 343-524, 1876-1878 (reprinted as *The Scientific Papers of J. Willard Gibbs*, Vol. 1, Dover Publications, New York, pp. 55-371, 1961).
- Glasser, F. P., and E. F. Osborn, Phase equilibrium studies in the system $\text{CaO-Cr}_2\text{O}_3\text{-SiO}_2$, *J. Am. Ceram. Soc.*, 41, 358-367, 1958.
- Goetze, C., Sheared lherzolites: from the point of view of rock mechanics, *Geology*, 3, 172-173, 1975.
- Goldsmith, J. R., and D. L. Graf, Relation between lattice constants and composition of the Ca-Mg carbonates, *Am. Mineral.*, 43, 84-101, 1958.
- Goranson, R. W., Silicate-water systems: phase equilibria in the $\text{NaAlSi}_3\text{O}_8\text{-H}_2\text{O}$ and $\text{KAlSi}_3\text{O}_8\text{-H}_2\text{O}$ systems at high temperatures and pressures, *Am. J. Sci.*, Day Volume, 35A, 71-91, 1938.
- Green, H. W., II, A CO_2 -charged asthenosphere, *Nature*, 238, 2-5, 1972.
- Greig, J. W., Immiscibility in silicate melts, *Am. J. Sci.*, 13, 1-44, 133-154, 1927.
- Grey, I. E., and J. Ward, An x-ray and Mössbauer study of the $\text{FeTi}_2\text{O}_5\text{-Ti}_2\text{O}_3$ system, *J. Solid State Chem.*, 7, 300-307, 1973.
- Grieve, R. A. F., and J. J. Fawcett, The stability of chloritoid below 10 kb $P_{\text{H}_2\text{O}}$, *J. Petrology*, 15, 113-139, 1974.
- Grim, R. E., *Clay Mineralogy*, McGraw-Hill Book Company, New York, 1968.
- Grundy, H. D., and W. L. Brown, A high-temperature x-ray study of low and high plagioclase feldspars, in *The Feldspars*, W. S. MacKenzie and J. Zussman, eds., Manchester University Press, Manchester, pp. 162-173, 1974.
- Guidotti, C. V., J. T. Cheney, and P. D. Conatore, Coexisting cordierite + biotite + chlorite from the Rumford quadrangle, Maine, *Geology*, 3, 147-148, 1975.
- Gunter, W. D., J. D. Frantz, and H. P. Eugster, Mineral solution equilibria in the system $\text{K}_2\text{O-MgO-Al}_2\text{O}_3\text{-SiO}_2\text{-H}_2\text{O-HCl}$ (abstr.), *Eos, Trans. Am. Geophys. Union*, 54, 487, 1973.
- Gurney, J. J., H. W. Fesq, and E. J. D. Kable, Clinopyroxene-ilmenite intergrowths from kimberlite: a reappraisal, in *Lesotho Kimberlites*, P. H. Nixon, ed., Lesotho National Development Corporation, Maseru, Lesotho, pp. 238-253, 1973.
- Gurney, J. J., and G. S. Switzer, The discovery of garnets closely related to diamonds in the Finsch pipe, South Africa, *Contrib. Mineral. Petrol.*, 39, 103-116, 1973.
- Gutt, W., and A. J. Majumdar, Phase studies, in *Differential Thermal Analysis*, R. C. MacKenzie, ed., Academic Press, New York, pp. 79-117, 1972.
- Haggerty, S. E., Spinels of unique composition associated with ilmenite reactions in the Lihobong kimberlite pipe, Lesotho, In *Lesotho Kimberlites*, P. H. Nixon, ed., Lesotho National Development Corporation, Maseru, Lesotho, pp. 149-158, 1973.
- Harger, H. S., The diamond pipes and fissures of South Africa, *Trans. Geol. Soc. S. Afr.*, 8, 110-134, 1906.
- Harker, R. I., Differential thermal analysis in closed systems at high hydrostatic pressures, *Am. Mineral.*, 49, 1741-1747, 1964.
- Harte, B., Stratigraphy, structure and metamorphism in the south-eastern Grampian Highlands of Scotland, unpublished Ph.D. thesis, University of Cambridge, 1966.
- Harte, B., Displacement of the kyanite "isograd" by local variations of oxygen fugacity within pelitic schists, in Glen Lethnot, Angus, Scotland (abstr.), *Eos, Trans. Am. Geophys. Union*, 56, 466, 1975.
- Harte, B., K. G. Cox, and J. J. Gurney,

- Petrography and geological history of upper mantle xenoliths from the Matsoku kimberlite, *International Conference on Kimberlites, Extended Abstracts*, University of Cape Town, Rondebosch, South Africa, pp. 155-158, 1973.
- Harte, B., K. G. Cox, and J. J. Gurney, Petrography and geological history of upper mantle xenoliths from the Matsoku kimberlite pipe, in "Proceedings of the International Kimberlite Conference," *Phys. Chem. Earth*, 9, in press, 1975.
- Harte, B., and M. R. W. Johnson, Metamorphic history of Dalradian rocks in Glens Clova, Esk, and Lethnot, Angus, Scotland, *Scot. J. Geol.*, 5, 54-80, 1969.
- Hayes, J. M., Organic constituents of meteorites—a review, *Geochim. Cosmochim. Acta*, 31, 1395-1440, 1967.
- Hazen, R. M., and C. W. Burnham, The crystal structure of gillespite I and II: a structure determination at high pressure, *Am. Mineral.*, 59, 1166-1176, 1974.
- Hazony, Y., H_c -QS-IS correlations in octahedral iron compounds, *Mössbauer Effect Methodology*, 7, 147-166, 1971.
- Heath, R. L., Table of the isotopes, in *Handbook of Chemistry and Physics*, R. C. Weast, ed., Chemical Rubber Co., Cleveland, Ohio, pp. B4-B96, 1966.
- Hedges, J. I., Lignin compounds as indicators of terrestrial organic matter in marine sediments, Ph.D. thesis, University of Texas at Austin, 1975.
- Helgeson, H. C., Evaluation of irreversible reactions in geochemical processes involving minerals and aqueous solutions, I, Thermodynamic relations, *Geochim. Cosmochim. Acta*, 32, 853-877, 1968.
- Hellwege, K. H., W. Lesch, M. Plihal, and G. Schaak, Zweiphononen-Absorptionsspektren und Dispersion der Schwingungszweige in Kristallen der Kalkspatstruktur, *Z. Physik*, 232, 61-86, 1970.
- Hess, H. H., Stillwater igneous complex, Montana, a quantitative mineralogical study, *Geol. Soc. Am. Mem.*, 80, 1960.
- Hess, P. C., Polymer model of silicate melts, *Geochim. Cosmochim. Acta*, 35, 289-306, 1971.
- Hess, P. C., and M. J. Rutherford, Element fractionation between immiscible melts (abstr.), in *Lunar Science V*, Lunar Science Institute, Houston, pp. 328-329, 1974.
- Hill, R. E. T., and A. L. Boettcher, Water in the earth's mantle: melting curves of basalt-water and basalt-water-carbon dioxide, *Science*, 167, 980-982, 1970.
- Hirsch, J., and E. H. Ahrens, The separation of complex lipid mixtures by the use of silicic acid chromatography, *J. Biol. Chem.*, 233, 311-320, 1958.
- Hirschberg, A., and H. G. F. Winkler, Stabilitätsbeziehungen zwischen chlorit, cordierit und almandin bei der metamorphose, *Contrib. Mineral. Petrol.*, 18, 17-42, 1968.
- Holdaway, M. J., Stability of andalusite and the aluminum silicate phase diagram, *Am. J. Sci.*, 271, 97-131, 1971.
- Hollister, L. S., Contact metamorphism in the Kwoiek area of British Columbia: an end-member of the metamorphic process, *Geol. Soc. Am. Bull.*, 80, 2465-2494, 1969.
- Holloway, J. R., and C. W. Burnham, Melting relations of basalt with equilibrium water pressure less than total pressure, *J. Petrol.*, 13, 1-29, 1972.
- Holloway, J. R., and R. L. Reese, The generation of N_2 - CO_2 - H_2O fluids for use in hydrothermal experimentation, I, Experimental method and equilibrium calculations in the C-O-H-N system, *Am. Mineral.*, 59, 587-597, 1974.
- Hornung, G., and P. H. Nixon, Chemical variations in the knorringite-rich garnets, in *Lesotho Kimberlites*, P. H. Nixon, ed., Lesotho National Development Corporation, Maseru, Lesotho, pp. 122-127, 1973.
- Howells, S., and M. J. O'Hara, Palaeogeotherms and the diopside-enstatite solvus, *Nature (London)*, 254, 406-408, 1975.
- Hsu, L. C., Selected phase relationships in the system Al-Mn-Fe-Si-O-H: a model for garnet equilibria, *J. Petrol.*, 9, 40-83, 1968.
- Huang, W. L., and P. J. Wyllie, Eutectic between wollastonite II and calcite contrasted with thermal barrier in MgO - SiO_2 - CO_2 at 30 kilobars, with applications to kimberlite-carbonatite petrogenesis, *Earth Planet. Sci. Lett.*, 24, 305-310, 1974.
- Huang, W. L., and P. J. Wyllie, Melting relationships in the systems CaO - CO_2 and MgO - CO_2 to 33 kilobars, *Geochim. Cosmochim. Acta*, in press, 1975.
- Huckenholz, H. G., Synthesis and stability of Ti-andradite, *Am. J. Sci.*, Schairer Vol. 267A, 209-232, 1969.
- Huckenholz, H. G., and D. Knittel, Stability of grossularite-uvarovite solid solutions, *Contrib. Mineral. Petrol.*, 49, 211-232, 1975.
- Huckenholz, H. G., L. Masch, and E. Hölzl, Physical properties of ugrandite garnets, *Neues Jahrb. Mineral., Monatsh.*, in press, 1975.
- Hudson, N. F. C., Mineral facies in pelitic rocks with particular reference to the Buchan type metamorphism of north-eastern Scotland, unpublished Ph.D. thesis, University of Edinburgh, 1975.
- Huggins, F. E., The 3d levels of ferrous ions in silicate garnets, *Am. Mineral.*, 60, 316-319, 1975.
- Hummel, F. A., Synthesis of uvarovite, *Am. Mineral.*, 35, 324-325, 1950.
- Ingalls, R., Electric-field gradient tensor in

- ferrous compounds, *Phys. Rev., A*, 133, 787-795, 1964.
- Irvine, T. N., Chromian spinel as a petrogenetic indicator, Part 1, Theory, *Can. J. Earth Sci.*, 2, 668-672, 1965.
- Irvine, T. N., Crystallization sequences in the Muskox intrusion and other layered intrusions, I, Olivine-pyroxene-plagioclase relations, *Geol. Soc. S. Afr., Spec. Publ.*, 1, 441-476, 1970.
- Irvine, T. N., and W. R. A. Barager, A guide to the chemical classification of the common volcanic rocks, *Can. J. Earth Sci.*, 8, 523-548, 1971.
- Irvine, T. N., and C. H. Smith, The ultramafic rocks of the Muskox intrusion, Northwest Territories, in *Ultramafic and Related Rocks*, P. J. Wyllie, ed., John Wiley and Sons, Inc., New York, pp. 38-49, 1967.
- Irving, A. J., Pyroxene-rich ultramafic xenoliths in the Newer Basalts of Victoria, Australia, *Neues Jahrb. Mineral., Abh.*, 120, 147-167, 1974.
- Irving, A. J., and P. J. Wyllie, Melting relationships in CaO-CO₂ and MgO-CO₂ to 36 kilobars with comments on CO₂ in the mantle, *Earth Planet. Sci. Lett.*, 20, 220-225, 1973.
- Irving, A. J., and P. J. Wyllie, Subsolidus and melting relationships for calcite, magnesite and the join CaCO₃-MgCO₃ to 36 kb, *Geochim. Cosmochim. Acta*, 39, 35-53, 1975.
- Isaaks, Th., A study of uvarovite, *Mineral. Mag.*, 35, 38-43, 1966.
- Ito, J., Rhodonite-pyroxmangite peritectic along the join MnSiO₃-MgSiO₃ in air, *Am. Mineral.*, 57, 865-876, 1972a.
- Ito, J., Synthesis and crystal chemistry of Li-hydro-pyroxenoids, *Mineral. J.*, 7, 45-65, 1972b.
- Ito, J., and C. Frondel, Synthetic zirconium and titanium garnets, *Am. Mineral.*, 52, 773-781, 1967.
- Jepson, W. B., and J. F. Williams, The adsorption of water by clays, *Clay Miner.*, 9, 275-279, 1972.
- Johnson, C. K., An introduction to thermal-motion analysis, in *Crystallographic Computing*, F. R. Ahmed, ed., Munksgaard, Copenhagen, pp. 207-219, 1970.
- Johnson, M. R. W., Some time relations of movement and metamorphism in the Scottish Highlands, *Geol. Mijnbouw*, 42, 121-142, 1963.
- Jørgensen, C. K., The nephelinitic series, *Prog. Inorg. Chem.*, 4, 73-124, 1962.
- Kadik, A. A., and O. A. Lukanin, The solubility-dependent behavior of water and carbon dioxide in magmatic processes, *Geochem. Int.*, 10, 115-129, 1973.
- Katsui, Y., S. Ando, and K. Inaba, Formation and magmatic evolution of Mashu volcano, East Hokkaido, Japan, *J. Fac. Sci., Hokkaido Univ., Ser. 4*, 16, 533-552, 1975.
- Keovil, N. B., Vapor pressures of aqueous solutions at high temperatures, *J. Am. Chem. Soc.*, 64, 841-850, 1942.
- Kennedy, G. C., and R. C. Newton, Solid-liquid and solid-solid phase transitions in some pure metals at high temperatures and pressures, in *Solids under Pressure*, W. Paul and D. M. Warschauer, eds., McGraw-Hill Book Company, New York, pp. 163-178, 1963.
- Kenyon, D. H., and G. Steinman, *Biochemical Predestination*, McGraw-Hill Book Company, New York, 1969.
- Kesson, S. E., and J. R. Holloway, The generation of N₂-CO₂-H₂O fluids for use in hydrothermal experimentation, II, Melting of albite in a multispecies fluid, *Am. Mineral.*, 59, 598-603, 1974.
- Khitarov, N. I., and A. A. Kadik, Water and carbon dioxide in magmatic melts and peculiarities of the melting process, *Contrib. Mineral. Petrol.*, 41, 205-215, 1973.
- Killingley, J. S., and D. W. Muenow, A mass spectrometric method for the determination of the size distribution of CO₂ inclusions in olivine, *Am. Mineral.*, 59, 863-867, 1974.
- Klein, C. K., Jr., Mineralogy and petrology of the metamorphosed Wabush Iron Formation, southwestern Labrador, *J. Petrol.*, 7, 246-305, 1966.
- Korzhinskii, D. S., *Physicochemical Basis of the Analysis of the Paragenesis of Minerals*, Consultants Bureau, New York, 1959.
- Koster van Groos, A. F., The effect of high CO₂ pressures on alkalic rocks and its bearing on the formation of alkalic ultrabasic rocks and the associated carbonatites, *Am. J. Sci.*, 275, 163-185, 1975.
- Koster van Groos, A. F., and P. J. Wyllie, Liquid immiscibility in the join NaAlSi₃O₈-CaAl₂Si₂O₈-Na₂CO₃-H₂O, *Am. J. Sci.*, 273, 465-487, 1973.
- Kracek, F. C., and K. J. Neuvonen, Thermochemistry of plagioclase and alkali feldspars, *Am. J. Sci., Bowen Vol.*, 293-318, 1952.
- Kushiro, I., The system forsterite-diopside-silica with and without water at high pressures, *Am. J. Sci., Schairer Vol.*, 267A, 269-294, 1969.
- Kushiro, I., Effect of water on the composition of magmas formed at high pressures, *J. Petrol.*, 13, 311-334, 1972a.
- Kushiro, I., Determination of the liquidus relations in synthetic silicate systems with electron probe analysis: the system forsterite-diopside-silica at 1 atmosphere, *Am. Mineral.*, 57, 1260-1271, 1972b.
- Kushiro, I., On the nature of silicate melt and its significance in magma genesis: regularities in the shift of the liquidus boundaries in-

- volving olivine, pyroxene, and silica minerals, *Am. J. Sci.*, **275**, 411-431, 1975.
- Kushiro, I., H. Satake, and S. Akimoto, Carbonate-silicate reactions at high pressure and possible presence of dolomite and magnesite in the upper mantle, *Earth Planet Sci. Lett.*, in press, 1975.
- Kvenvolden, K., J. Lawless, K. Pering, E. Peterson, J. Flores, C. Ponnampertuma, I. Kaplan, and C. Moore, Evidence for extraterrestrial amino-acids and hydrocarbons in the Murchison meteorite, *Nature*, **228**, 923-926, 1970.
- Kvenvolden, K. A., J. G. Lawless, and C. Ponnampertuma, Nonprotein amino acids in the Murchison meteorite, *Proc. Nat. Acad. Sci. USA*, **68**, 486-490, 1971.
- Lambert, I. B., and P. J. Wyllie, Stability of hornblende and a model for the low-velocity zone, *Nature*, **219**, 1240-1241, 1968.
- Larsen, E. S., Relation between the refractive index and the density of some crystallized silicates, *Am. J. Sci.*, **28**, 263-274, 1909.
- Lawless, J. G., Amino acids in the Murchison meteorite, *Geochim. Cosmochim. Acta*, **37**, 2207-2212, 1973.
- Lawless, J. G., K. A. Kvenvolden, E. Peterson, C. Ponnampertuma, and E. Jarosewich, Evidence for amino-acids of extraterrestrial origin in the Orgueil meteorite, *Nature*, **236**, 66-67, 1972.
- Lawless, J. G., K. A. Kvenvolden, E. Peterson, C. Ponnampertuma, and C. Moore, Amino acids indigenous to the Murray meteorite, *Science*, **173**, 626-627, 1971.
- Levin, E. M., C. R. Robbins, and H. F. McMurdie, *Phase Diagrams for Ceramists*, The American Ceramic Society, Inc., Columbus, Ohio, 1964.
- Liebau, F., Zur Kristallchemie der Silikate, Germanate und Fluoberyllate des Formeltyps ABX_3 , *Neues Jahrb. Mineral., Abh.*, **94**, 1209-1222, 1960.
- Liebau, F., Die Systematik der Silikate, *Naturwissenschaften*, **49**, 481-491, 1962.
- Lind, M. D., and R. M. Housley, Crystallization studies of lunar igneous rocks: crystal structure of synthetic armalcolite, *Science*, **175**, 521-523, 1972.
- Lindsley, D. H., and C. W. Burnham, Pyroxferroite: stability and x-ray crystallography of synthetic $Ca_{0.15}Fe_{0.85}SiO_3$ pyroxenoid, *Science*, **168**, 364-367, 1970.
- Løken, O. H., Baffin Island refugia older than 54,000 years, *Science*, **153**, 1378-1380, 1966.
- Lyubutin, I. S., and A. P. Dodokin, Temperature dependence of the Mössbauer effect for Fe^{2+} in dodecahedral coordination in garnet, *Sov. Phys. Crystallogr.*, **15**, 1091-1092, 1971.
- Maaløe, S., The significance of the melting interval of basaltic magmas at various pressures, *Geol. Mag.*, **110**, 103-112, 1973.
- Macdonald, G. A., and T. Katsura, Chemical composition of Hawaiian lavas, *J. Petrol.*, **5**, 82-133, 1964.
- MacGregor, I. D., and R. W. Wittkop, Diopside-ilmenite xenoliths from the Monastery Mine, Orange Free State, South Africa (abstr.), *Abstr. with Programs (Geol. Soc. Am.)*, **2**, 113, 1970.
- Malinovsky, I. G., and A. M. Doroshev, Stability of the garnet series uvarovite-knorringite, and grossularite-uvarovite at 1200°C and 30 kbar, *Akad. Nauk SSSR, Siberian Branch, Experimental Investigations to Mineralogy* [in Russian], pp. 70-72, 1974.
- Malinovsky, I. G., A. M. Doroshev, and A. A. Godoikov, Stability of the series pyrope-grossularite-knorringite-uvarovite at 1200°C and 30 kbar, *Akad. Nauk SSSR, Siberian Branch, Experimental Investigations to Mineralogy* [in Russian], pp. 73-77, 1974.
- Mao, H. K., T. Takahashi, W. A. Bassett, G. L. Kinsland, and L. Merrill, Isothermal compression of magnetite to 320 kbar and pressure-induced phase transformation, *J. Geophys. Res.*, **79**, 1165-1170, 1974.
- Mao, H. K., D. Virgo, and P. M. Bell, Analytical and experimental study of iron and titanium in orange glass from Apollo 17 soil sample 74220, *Proc. Fourth Lunar Sci. Conf., Geochim. Cosmochim. Acta*, Suppl. **4**, Vol. 1, Pergamon Press, New York, pp. 397-412, 1973.
- Marshall, W. L., Predictions of the geochemical behavior of aqueous electrolytes at high temperatures and pressures, *Chem. Geol.*, **10**, 59-68, 1972.
- McAdie, H. G., Requirements and realization of thermal analysis standards, temperature standards for DTA, in *Proc. Third Int. Conf. Thermal Analysis*, H. G. Wiedemann, ed., Birkhäuser Verlag, Basel, pp. 591-608, 1972.
- McBirney, A. R., and H. Williams, Geology and petrology of the Galápagos Islands, *Geol. Soc. Am. Mem.*, **118**, 1969.
- McCallister, R. H., Kinetics of enstatite exsolution from supersaturated diopsides, in *Geochemical Transport and Kinetics*, A. W. Hofmann, B. J. Giletti, H. S. Yoder, Jr., and R. A. Yund, eds., Carnegie Inst. Wash., Publ. **634**, Washington, D.C., pp. 195-203, 1974.
- McCallister, R. H., H. O. A. Meyer, and D. G. Brookins, "Pyroxene"-ilmenite xenoliths from the Stockdale pipe, Kansas; chemistry, crystallography, and origin, *Phys. Chem. Earth*, in press, 1975.
- McFadden, P. L., A paleomagnetic study of the DeBeers diamond mine, in *International Conference on Kimberlites: Extended Abstracts*, University of Cape Town, Rondebosch, South Africa, pp. 221-223, 1973.
- McGetchin, T. R., and J. R. Besancon, Car-

- bonate inclusions in mantle-derived pyropes, *Earth Planet. Sci. Lett.*, **18**, 408–410, 1973.
- Megaw, H. D., The architecture of the feldspars, in *The Feldspars*, W. S. MacKenzie and J. Zussman, eds., Manchester University Press, Manchester, pp. 2–24, 1974a.
- Megaw, H. D., Tilts and tetrahedra in feldspars, in *The Feldspars*, W. S. MacKenzie and J. Zussman, eds., Manchester University Press, Manchester, pp. 87–113, 1974b.
- Mercier, J. C., and N. L. Carter, Pyroxene geotherms, *J. Geophys. Res.*, in press, 1975.
- Merrill, R. B., and P. J. Wyllie, Absorption of iron by platinum capsules in high-pressure rock-melting experiments, *Am. Mineral.*, **58**, 16–20, 1973.
- Merrill, R. B., and P. J. Wyllie, Kaersutite and kaersutite eclogite from Kakanui, New Zealand—water-excess and water-deficient melting to 30 kilobars, *Geol. Soc. Am. Bull.*, **86**, 555–570, 1975.
- Meyer, H. O. A., Chrome pyrope: an inclusion in natural diamond, *Science*, **160**, 1446–1447, 1968.
- Meyer, H. O. A., and F. R. Boyd, Composition and origin of crystalline inclusions in natural diamonds, *Geochim. Cosmochim. Acta*, **36**, 1255–1273, 1972.
- Meyers, P. A., and J. G. Quinn, Factors affecting the association of fatty acids with mineral particles in seawater, *Geochim. Cosmochim. Acta*, **37**, 1745–1759, 1973.
- Miller, S. L., The mechanism of synthesis of amino acids by electric discharges, *Biochim. Biophys. Acta*, **23**, 480–489, 1957.
- Millhollen, G. L., P. J. Wyllie, and C. W. Burnham, Melting relations of $\text{NaAlSi}_3\text{O}_8$ to 30 kb in the presence of $\text{H}_2\text{O}:\text{CO}_2 = 50:50$ vapor, *Am. J. Sci.*, **271**, 473–480, 1971.
- Millot, G., *Geology of Clays*, Springer Verlag, New York, 1970.
- Ming, L., and W. A. Bassett, Laser heating in the diamond anvil press up to 2000°C sustained and 3000°C pulsed at pressure up to 260 kilobars, *Rev. Sci. Instrum.*, **45**, 1115–1118, 1974.
- Mitchell, R. H., Magnesian ilmenite and its role in kimberlite petrogenesis, *J. Geol.*, **81**, 301–311, 1973.
- Mitchell, R. H., D. A. Carswell, and A. O. Brunfelt, Ilmenite association trace element studies, Part I, in *Lesotho Kimberlites*, P. H. Nixon, ed., Lesotho National Development Corporation, Maseru, Lesotho, pp. 224–229, 1973.
- Momoi, H., Some manganese pyroxenoids [in Japanese], *J. Mineral. Soc. Jpn.*, **8**, Spec. Issue 2, 1–5, 1968.
- Momoi, H., Hydrothermal crystallization of MnSiO_3 polymorphs, *Mineral. J.*, **7**, 359–373, 1974.
- Moore, R. K., and W. B. White, Intervalence electron transfer effects in the spectra of the melanite garnets, *Am. Mineral.*, **56**, 826–840, 1971.
- Morey, G. W., and M. Fleischer, Equilibrium between vapor and liquid phases in the system $\text{CO}_2\text{--H}_2\text{O--K}_2\text{O--SiO}_2$, *Geol. Soc. Am. Bull.*, **51**, 1035–1058, 1940.
- Morey, G. W., and E. D. Williamson, Pressure-temperature curves in univariant systems, *J. Am. Chem. Soc.*, **40**, 59–84, 1918.
- Mori, T., and D. H. Green, Pyroxenes in the system $\text{Mg}_2\text{Si}_2\text{O}_6\text{--CaMgSi}_2\text{O}_6$ at high pressure, *Earth Planet. Sci. Lett.*, in press, 1975.
- Morimoto, N., Problems on the crystal structures of pyroxenes [in Japanese], *Chishitsugaku Ronshu*, **11**, 303–321, 1974.
- Morimoto, N., K. Koto, and T. Shinohara, Oriented transformation of johannsenite to bustamite, *Mineral. J.*, **5**, 44–64, 1966.
- Muan, A., and E. F. Osborn, Phase equilibria at liquidus temperatures in the system $\text{MgO--FeO--Fe}_2\text{O}_3\text{--SiO}_2$, *J. Am. Ceram. Soc.*, **39**, 121–140, 1956.
- Muranaka, S., T. Shinjo, Y. Bando, and T. Takada, Mössbauer study of Fe_2TiO_5 and FeTi_2O_5 , *J. Phys. Soc. Jpn.*, **30**, 890, 1971.
- Mysen, B. O., Solubility of CO_2 in the system $\text{Na}_2\text{O--Al}_2\text{O}_3\text{--SiO}_2\text{--H}_2\text{O--CO}_2$ to 30 kbar (abstr.), *Eos, Trans. Am. Geophys. Union*, **56**, 469, 1975.
- Mysen, B. O., and A. L. Boettcher, Melting of a hydrous mantle, I, Phase relations of natural peridotite at high pressures and temperatures with controlled activities of water, carbon dioxide and hydrogen, *J. Petrol.*, in press, 1975a.
- Mysen, B. O., and A. L. Boettcher, Melting of a hydrous mantle, II, Geochemistry of crystals and liquids formed by anatexis of mantle peridotite at high pressures and high temperatures as a function of controlled activities of water, hydrogen and carbon dioxide, *J. Petrol.*, in press, 1975b.
- Mysen, B. O., and M. G. Seitz, Trace-element partitioning determined by beta-track mapping; an experimental study using carbon and samarium as examples, *J. Geophys. Res.*, in press, 1975.
- Nagasawa, H., and C. C. Schnetzler, Partitioning of rare earth, alkali and alkaline earth elements between phenocrysts and acid igneous magma, *Geochim. Cosmochim. Acta*, **35**, 953–968, 1971.
- Narita, H., Crystal chemistry of pyroxene and pyroxenoid polymorphs of MnSiO_3 , Ph.D. thesis, Osaka University, 1973.
- Narita, H., K. Koto, and N. Morimoto, Nambulite $(\text{Li,Na})\text{Mn}_4\text{Si}_5\text{O}_{14}(\text{OH})$: a new fünferkettens structure (abstract), *Acta Cryst.*, **A31**, S75, 1975.
- Navrotsky, A., Thermodynamics of formation of some compounds with the pseudobrookite

- structure and of the $\text{FeTi}_2\text{O}_5\text{-Ti}_3\text{O}_5$ solid solution series, *Am. Mineral.*, **60**, 249-256, 1975.
- Nehru, C. E., and P. J. Wyllie, Electron microprobe measurement of pyroxenes coexisting with H_2O -undersaturated liquid in the join $\text{CaMgSi}_2\text{O}_6\text{-Mg}_2\text{Si}_2\text{O}_6\text{-H}_2\text{O}$ at 30 kilobars with applications to geothermometry, *Contrib. Mineral. Petrol.*, **48**, 221-228, 1974.
- Newton, R. C., and W. E. Sharp, Stability of forsterite + CO_2 and its bearing on the role of CO_2 in the mantle, *Earth Planet. Sci. Lett.*, in press, 1975.
- Nicholls, I. A., Petrology of Santorini volcano, Cyclades, Greece, *J. Petrol.*, **12**, 67-119, 1971.
- Nixon, P. H., ed., *Lesotho Kimberlites*, Lesotho National Development Corporation, Maseru, Lesotho, 1973.
- Nixon, P. H., and F. R. Boyd, Petrogenesis of the granular and sheared ultrabasic nodule suite in kimberlites, in *Lesotho Kimberlites*, P. H. Nixon, ed., Lesotho National Development Corporation, Maseru, Lesotho, pp. 48-56, 1973.
- Nixon, P. H., and G. Hornung, A new chromium garnet end-member, knorringite from kimberlite, *Am. Mineral.*, **53**, 1833-1840, 1968.
- Nockolds, S. R., Average chemical compositions of some igneous rocks, *Geol. Soc. Am. Bull.*, **65**, 1007-1032, 1954.
- Nord, G. L., A. H. Heuer, J. S. Lally, and J. M. Christie, Substructures in lunar clinopyroxenes as petrologic indicators (abstr.), in *Lunar Science VI*, Lunar Science Institute, Houston, pp. 601-603, 1975.
- Nordlie, B. E., The composition of the magmatic gas of Kilauea and its behavior in the near surface environment, *Am. J. Sci.*, **271**, 417-463, 1971.
- Novak, G. A., and G. V. Gibbs, The crystal chemistry of the silicate garnets, *Am. Mineral.*, **56**, 791-825, 1971.
- Oh, K. D., H. Morikawa, S. Iwai, and H. Aoki, The crystal structure of magnesite, *Am. Mineral.*, **58**, 1029-1033, 1973.
- O'Hara, M. J., Primary magmas and origin of basalts, *Scot. J. Geol.*, **1**, 19-40, 1965.
- O'Hara, M. J., and H. S. Yoder, Jr., Formation and fractionation of basic magmas at high pressures, *Scot. J. Geol.*, **3**, 67-117, 1967.
- Ohashi, Y., C. W. Burnham, and L. W. Finger, The effect of Ca-Fe substitution on the clinopyroxene crystal structure, *Am. Mineral.*, **60**, 423-434, 1975.
- O'Nions, R. K., and R. J. Pankhurst, Petrogenetic significance of isotope and trace element variations in volcanic rocks from the Mid-Atlantic, *J. Petrol.*, **15**, 603-634, 1974.
- Oró, J., J. Gibert, H. Lichtenstein, S. Wikstrom, and D. A. Flory, Amino-acids, aliphatic and aromatic hydrocarbons in the Murchison meteorite, *Nature*, **230**, 105-106, 1971.
- Orville, P. M., Alkali ion exchange between vapor and feldspar phases, *Am. J. Sci.*, **261**, 201-237, 1963.
- Orville, P. M., Plagioclase cation exchange equilibria with aqueous chloride solution: results at 700°C and 2000 bars in the presence of quartz, *Am. J. Sci.*, **272**, 234-272, 1972.
- Osborn, E. F., The system $\text{CaSiO}_3\text{-diopside-anorthite}$, *Am. J. Sci.*, **240**, 751-788, 1942.
- Osborn, E. F., Role of oxygen pressure in the crystallization and differentiation of basaltic magma, *Am. J. Sci.*, **257**, 609-647, 1959.
- Osborn, E. F., The complementariness of orogenic andesite and alpine peridotite, *Geochim. Cosmochim. Acta*, **33**, 307-324, 1969.
- Osborn, E. F., and D. B. Tait, The system diopside-forsterite-anorthite, *Am. J. Sci.*, *Bowen Vol.*, 413-433, 1952.
- Oxburgh, E. R., Petrological evidence for the presence of amphibole in the upper mantle and its petrogenetic and geophysical implications, *Geol. Mag.*, **101**, 1-19, 1964.
- Papike, J. J., C. T. Prewitt, S. Sueno, and M. Cameron, Pyroxenes: comparison of real and ideal structural topologies, *Z. Kristallogr.*, **138**, 254-274, 1973.
- Pauling, L., The crystal structure of pseudobrookite, *Z. Kristallogr.*, **73**, 97-112, 1930.
- Pawley, G. S., On the least-squares analysis of the rigid body vibrations of non-centrosymmetrical molecules, *Acta Crystallogr.*, **16**, 1204-1208, 1963.
- Pawley, G. S., Least-squares structure assuming molecular rigidity, *Acta Crystallogr.*, **17**, 457-458, 1964.
- Peacor, D. R., and N. Niizeki, The determination and refinement of the crystal structure of rhodonite, $(\text{Mn,Ca})\text{SiO}_3$, *Z. Kristallogr.*, **119**, 98-116, 1963.
- Pearce, M. L., Solubility of carbon dioxide and variation of oxygen ion activity in soda-silica melts, *J. Am. Ceram. Soc.*, **47**, 342-347, 1964.
- Pheasant, D. R., and J. T. Andrews, Wisconsin glacial chronology and relative sea-level movements, Narpaing Fiord-Broughton Island area, eastern Baffin Island, N.W.T., *Can. J. Earth Sci.*, **10**, 1621-1641, 1973.
- Piermarini, G. J., and S. Block, An ultra high pressure diamond-anvil cell and several semiconductor phase transition pressures in relation to the fixed point pressure scale, *Rev. Sci. Instrum.*, in press, 1975.
- Pinsak, A. P., and H. H. Murray, Regional clay mineral patterns in the Gulf of Mexico, *Clays Clay Miner.*, **5**, 162-177, 1960.
- Porteous, W. G., Metamorphic index minerals in the eastern Dalradian, *Scot. J. Geol.*, **9**, 29-43, 1973.
- Prandl, W., Vereinerung der Kristallstruktur des Grossulars mit Neutronen und Röntgenstrahlbeugung, *Z. Kristallogr.*, **123**, 87-116, 1966.
- Presnall, D. C., N. L. Brenner, and T. H.

- O'Donnell, Drift of Pt/Pt90Rh10 and W3Re/W25Re25 thermocouples in single-stage piston-cylinder apparatus, *Am. Mineral.*, 58, 771-777, 1973.
- Prewitt, C. T., and D. R. Peacor, Crystal chemistry of the pyroxenes and pyroxenoids, *Am. Mineral.*, 49, 1527-1542, 1964.
- Prince, E., and L. W. Finger, Use of constraints on thermal motion in structure refinement of molecules with librating side groups, *Acta Crystallogr., Sect. B*, 29, 179-183, 1973.
- Prince, E., L. W. Schroeder, and J. J. Rush, A constrained refinement of the structure of durene, *Acta Crystallogr., Sect. B*, 29, 184-191, 1973.
- Ramdohr, P., *The Ore Minerals and Their Intergrowths*, Pergamon Press, Oxford, 1969.
- Read, H. H., The geology of the country around Banff, Huntly, and Turriff, *Mem. Geol. Surv. Scotland*, 1923.
- Rhines, F. N., *Phase Diagrams in Metallurgy, Their Development and Application*, McGraw-Hill Book Company, New York, 1956.
- Rhodes, J. M., J. B. Adams, M. B. Charette, and K. V. Rodgers, The chemistry of agglutinate fractions in lunar soils (abstr.), in *Lunar Science VI*, Lunar Science Institute, Houston, pp. 665-667, 1975.
- Ricci, J. E., *The Phase Rule and Heterogeneous Equilibrium*, D. Van Nostrand Company, Inc., Princeton, N.J., 1951.
- Richardson, S. W., Staurolite stability in part of the system Fe-Al-Si-O-H, *J. Petrol.*, 9, 467-488, 1968.
- Richardson, S. W., The relation between a petrogenetic grid, facies series, and the geothermal gradient in metamorphism, *Fortschr. Mineral.*, 47, 65-76, 1970.
- Richardson, S. W., M. C. Gilbert, and P. M. Bell, Experimental determination of kyanite-andalusite and andalusite-sillimanite equilibria; the aluminum silicate triple point, *Am. J. Sci.*, 267, 259-272, 1969.
- Richardson, W. A., and G. Sneesby, The frequency-distribution of igneous rocks, I. Frequency-distribution of the major oxides in analyses of igneous rocks, *Mineral. Mag.*, 19, 303-313, 1922.
- Rietveld, H. M., A profile refinement method for nuclear and magnetic structures, *J. Appl. Crystallogr.*, 2, 65-71, 1969.
- Ringwood, A. E., Chemical evolution of the terrestrial planets, *Geochim. Cosmochim. Acta*, 30, 41-104, 1966.
- Ringwood, A. E., and J. F. Lovering, Significance of pyroxene-ilmenite intergrowths among kimberlite xenoliths, *Earth Planet. Sci. Lett.*, 7, 371-375, 1970.
- Robie, R. A., and D. R. Waldbaum, Thermodynamic properties of minerals and related substances at 298.15°K (25.0°C) and one atmosphere (1.013 bars) pressure and at higher temperatures, *U.S. Geol. Surv. Bull.*, 1259, 1968.
- Roedder, E., Low-temperature liquid immiscibility in the system K₂O-FeO-Al₂O₃-SiO₂, *Am. Mineral.*, 36, 282-286, 1951.
- Roedder, E., Liquid CO₂ inclusions in olivine-bearing nodules and phenocrysts from basalts, *Am. Mineral.*, 50, 1746-1782, 1965.
- Roedder, E., and P. W. Weiblen, Lunar petrology of silicate melt inclusions, Apollo 11 rocks, *Proc. Apollo 11 Lunar Sci. Conf., Geochim. Cosmochim. Acta*, Suppl. 1, Vol. 1, Pergamon Press, New York, pp. 801-837, 1970.
- Roedder, E., and P. W. Weiblen, Petrology of silicate melt inclusions, Apollo 11 and Apollo 12 and terrestrial equivalents, *Proc. Second Lunar Sci. Conf., Geochim. Cosmochim. Acta*, Suppl. 2, Vol. 1, MIT Press, Cambridge, pp. 507-528, 1971.
- Roedder, E., and P. W. Weiblen, Petrographic features and petrologic significance of melt inclusions in Apollo 14 and 15 rocks, *Proc. Third Lunar Sci. Conf., Geochim. Cosmochim. Acta*, Suppl. 3, Vol. 1, MIT Press, Cambridge, pp. 251-259, 1972.
- Roeder, P. L., and E. F. Osborn, Experimental data for the system MgO-FeO-Fe₂O₃-CaAl₂Si₂O₇-SiO₂ and their petrologic implications, *Am. J. Sci.*, 264, 428-480, 1966.
- Ruby, S., Why Misfit when you already have X²?, *Mössbauer Effect Methodology*, 8, 263-276, 1973.
- Rumble, D., III, Fe-Ti oxide minerals from regionally metamorphosed quartzites of western New Hampshire, *Contrib. Mineral. Petrol.*, 42, 181-195, 1973a.
- Rumble, D., III, Andalusite, kyanite, and sillimanite from the Mt. Moosilauke region, New Hampshire, *Geol. Soc. Am. Bull.*, 84, 2423-2430, 1973b.
- Rumble, D., III, Silicate, sulfide, and oxide mineral parageneses of the Clough Formation, Black Mountain, New Hampshire (abstr.), *Eos, Trans. Am. Geophys. Union*, 55, 449, 1974.
- Rutherford, M. J., P. C. Hess, and G. H. Daniel, Experimental liquid line of descent and liquid immiscibility for basalt 70017, *Proc. Fifth Lunar Sci. Conf., Geochim. Cosmochim. Acta*, Suppl. 5, Vol. 1, Pergamon Press, New York, pp. 569-583, 1974.
- St. Pierre, P. D. S., Constitution of bone china: III, High-temperature phase equilibrium studies in the system tricalcium phosphate-anorthite-silica, *J. Am. Ceram. Soc.*, 39, 147-150, 1956.
- Schairer, J. F., The system CaO-FeO-Al₂O₃-SiO₂: I, Results of quenching experiments on five joins, *J. Am. Ceram. Soc.*, 25, 241-274, 1942.
- Schairer, J. F., The system K₂O-MgO-Al₂O₃-

- SiO₂: 1, Results of quenching experiments on four joins in the tetrahedron cordierite-forsterite-leucite-silica and on the join cordierite-mullite-potash feldspar, *J. Am. Ceram. Soc.*, **37**, 501-533, 1954.
- Schairer, J. F., and N. L. Bowen, The system anorthite-leucite-silica, *Bull. Soc. Geol. Finl.*, **20**, 67-87, 1947.
- Schairer, J. F., and N. L. Bowen, The system K₂O-Al₂O₃-SiO₂, *Am. J. Sci.*, **253**, 681-746, 1955.
- Schilling, J.-G., and J. W. Winchester, Rare earth contribution to the origin of Hawaiian lavas, *Contrib. Mineral. Petrol.*, **23**, 27-37, 1969.
- Schomaker, V., and K. N. Trueblood, On the rigid-body motion of molecules in crystals, *Acta Crystallogr., Sect. B*, **24**, 63-76, 1968.
- Schreinemakers, F. A. H., In-, mono-, and divariant equilibria, *Proc. K. Ned. Akad. Wet.*, **18-28**, 1915-1925.
- Schreyer, W., Zur stabilität des Ferrocordierits, *Beitr. Mineral. Petrol.*, **11**, 297-322, 1965.
- Schwab, R. G., and K. H. Jablonski, Der Polymorphismus der Pigeonite, *Fortschr. Mineral.*, **50**, 223-263, 1973.
- Seifert, F., Low-temperature compatibility relations of cordierite in haploplites of the system K₂O-MgO-Al₂O₃-SiO₂-H₂O, *J. Petrol.*, **11**, 73-99, 1970.
- Seifert, F., and W. Schreyer, Lower temperature stability limit of Mg cordierite in the range 1-7 kb water pressure: a redetermination, *Contrib. Mineral. Petrol.*, **27**, 225-238, 1970.
- Shankland, T. J., Velocity-density systematics: derivation from Debye theory and the effect of ionic size, *J. Geophys. Res.*, **77**, 3750-3758, 1972.
- Shankland, T. J., A. G. Duba, and A. Woronow, Pressure shifts of optical absorption bands in iron-bearing garnet, spinel, olivine, pyroxene and periclase, *J. Geophys. Res.*, **79**, 3273-3282, 1974.
- Shimizu, N., and R. J. Arculus, Rare earth element concentrations in a suite of basanitoids and alkali olivine basalts from Grenada, Lesser Antilles, *Contrib. Mineral. Petrol.*, in press, 1975.
- Sigvaldasson, G. E., and G. Elisson, Collection and analysis of volcanic gases at Surtsey, Iceland, *Geochim. Cosmochim. Acta*, **32**, 797-805, 1968.
- Silver, L. T., The relation between radioactivity and discordance in zircons, *NAS-NRC Publ.* **1075**, 34-42, 1963.
- Skinner, B. J., Physical properties of end-members of the garnet group, *Am. Mineral.*, **41**, 428-436, 1956.
- Smith, B. N., and S. Epstein, Biogeochemistry of the stable isotopes of hydrogen and carbon in salt marsh biota, *Plant Physiol.*, **46**, 738-742, 1970.
- Smyth, J. R., The high temperature crystal chemistry of clinohypersthene, *Am. Mineral.*, **59**, 1069-1082, 1974a.
- Smyth, J. R., The crystal structure of armalcolites from Apollo 17, *Earth Planet. Sci. Lett.*, **24**, 262-270, 1974b.
- Sobolev, N. V., Y. G. Lavrent'yev, L. I. Pospelova, and V. S. Sobolev, Chrome pyrope in diamonds from Yakutia, *Dokl. Akad. Nauk SSSR*, **189**, 162-165, 1969.
- Sobolev, N. V., Y. G. Lavrent'yev, N. P. Pokhilenko, and L. V. Usova, Chrome-rich garnets from the kimberlites of Yakutia and their parageneses, *Contrib. Mineral. Petrol.*, **40**, 39-53, 1973.
- Sobolev, V. S., I. L. Dobnetsov, and V. V. Khlestov, H₂O and CO₂ in progressive regional metamorphism, *Dokl. Akad. Nauk SSSR*, **166**, no. 2, 1966.
- Sourirajan, S., and G. C. Kennedy, The system H₂O-NaCl at elevated temperatures and pressures, *Am. J. Sci.*, **260**, 115-141, 1962.
- Speidel, D. H., and E. F. Osborn, Element distribution among coexisting phases in the system MgO-FeO-Fe₂O₃-SiO₂ as a function of temperature and oxygen fugacity, *Am. Mineral.*, **52**, 1139-1152, 1967.
- Stevenson, F. J., and J. H. A. Butler, Chemistry of humic acids and related pigments, in *Organic Geochemistry*, G. E. Eglinton and M. T. J. Murphy, eds., Springer Verlag, New York, pp. 534-556, 1969.
- Stewart, F. H., On sulphatic cancrinite and analcime (eudnophite) from Loch Borolan, Assynt, *Mineral. Mag.*, **26**, 1-8, 1941.
- Strens, R. G. J., The nature and geophysical importance of spin-pairing in minerals of iron (II), in *The Application of Modern Physics to the Earth and Planetary Interiors*, S. K. Runcorn, ed., John Wiley and Sons, Inc., New York, pp. 213-220, 1969.
- Sundius, N., On the triclinic manganiferous pyroxenes, *Am. Mineral.*, **16**, 411-429, 488-518, 1931.
- Swanson, H. E., Th. Isaak, M. I. Cook, E. H. Evans, and J. de Groot, Standard x-ray diffraction patterns, *Nat. Bur. Stand. (US) Circ.*, **539**, Vol. 10, 17, 1960.
- Taylor, H. P., The application of oxygen and hydrogen isotope studies to problems of hydrothermal alteration and ore deposition, *Econ. Geol.*, **69**, 843-883, 1974.
- Taylor, W. H., The structure of analcite (NaAlSi₂O₆·H₂O), *Z. Kristallogr.*, **74**, 1-19, 1930.
- Thompson, A. B., Calculations of muscovite-paragonite-alkali feldspar phase relations, *Contrib. Mineral. Petrol.*, **44**, 173-194, 1974.
- Thompson, J. B., Jr., The graphical analysis of

- mineral assemblages in pelitic schists, *Am. Mineral.*, **42**, 842-858, 1957.
- Thompson, J. B., Jr., Geometrical possibilities for amphibole structures: model biopyriboles, *Am. Mineral.*, **55**, 292-293, 1970.
- Thompson, J. B., Jr., and D. R. Waldbaum, Mixing properties of sanidine crystalline solutions: III, Calculations based on two-phase data, *Am. Mineral.*, **54**, 811-838, 1969.
- Thompson, R. N., Titanian chromite and chromian titanomagnetite from a Snake River Plain basalt, a terrestrial analogue to lunar spinels, *Am. Mineral.*, **58**, 826-830, 1973.
- Thornton, C. P., and O. F. Tuttle, Chemistry of igneous rocks: Part I, Differentiation index, *Am. J. Sci.*, **258**, 644-684, 1960.
- Tilley, C. E., A preliminary study of metamorphic zones in the southern Highlands of Scotland, *Quart. J. Geol. Soc. London*, **71**, 100-112, 1925.
- Ukhanov, V. V., Olivine melilite from the diamond-bearing diatremes on Anabar, *Dokl. Akad. Sci. USSR, Earth Sci. Sect.*, **153**, 176-178, 1965.
- Urey, H. C., The thermodynamic properties of isotopic substances, *J. Chem. Soc. London*, 562-581, 1947.
- Van Zyl, J. P., The petrology of the Merensky Reef and the associated rocks on Swartklip 988, Rustenburg District, *Geol. Soc. S. Afr. Spec. Publ.*, **1**, 80-107, 1970.
- Virgo, D., and S. S. Hafner, Fe^{2+} , Mg order-disorder in heated orthopyroxenes, *Mineral. Soc. Am. Spec. Pap.*, **2**, 67-81, 1969.
- Vogt, J. H. L., Die Silikatschmelzlösungen: II, Über die Schmelzpunkt-Erniedrigung der Silikatschmelzlösungen, *Videnskabs-Selskabets Skrifter I, Math.-Naturv. Klasse (Christiania)*, No. 1, 1904.
- Wager, L. R., The major element variation of the layered series of the Skaergaard intrusion and a re-estimation of the average composition of the hidden layered series and the successive residual magmas, *J. Petrol.*, **1**, 364-398, 1960.
- Wager, L. R., and G. M. Brown, *Layered Igneous Rocks*, Oliver and Boyd, Ltd., Edinburgh, 1968.
- Washington, H. S., Chemical analyses of igneous rocks, *US Geol. Surv. Prof. Pap.*, **99**, 1917.
- Watson, B. G., and J. S. Dickey, Jr., Silicate liquid immiscibility in alkaline mafic magmas: evidences in a White Mountain magma series dike, with a discussion of its origin, *Geochim. Cosmochim. Acta*, in press, 1975.
- Wechsler, B. A., C. T. Prewitt, and J. J. Papike, Structure and chemistry of lunar and synthetic armalcolite (abstr.), *Abstracts, Sixth Lunar Science Conference*, 860-862, 1975.
- Weir, C. E., E. R. Lippincott, A. Van Valkenburg, and E. N. Bunting, Infrared studies in the 1- to 15-micron region to 30,000 atmospheres, *J. Res. Nat. Bur. Stand., Sect. A*, **63**, 55-62, 1959.
- Weiss, A., Organic derivatives of clay minerals, zeolites, and related minerals, in *Organic Geochemistry*, G. E. Eglinton and M. T. J. Murphy, eds., Springer Verlag, New York, pp. 737-781, 1969.
- Wershaw, R. L., I. Friedman, S. J. Heller, and P. A. Frank, Hydrogen isotope fractionation of water passing through trees, in *Advances in Organic Geochemistry*, G. D. Hobson and G. C. Speers, eds., Pergamon Press, New York, pp. 56-67, 1970.
- White, W. B., The carbonate minerals, in *The Infrared Spectra of Minerals*, V. C. Farmer, ed., Mineralogical Society, London, pp. 227-284, 1974.
- White, W. P., Specific heats of silicates and platinum, *Am. J. Sci.*, **28**, 334-346, 1909.
- Whittaker, E. J. W., Factors affecting element ratios in the crystallization of minerals, *Geochim. Cosmochim. Acta*, **31**, 2275-2288, 1967.
- Willaime, C., W. L. Brown, and M. C. Perucaud, On the orientation of the thermal and compositional strain ellipsoids in feldspars, *Am. Mineral.*, **59**, 457-464, 1974.
- Williams, A. F., *The Genesis of the Diamond*, 2 Vols., E. Benn Ltd., London, 1932.
- Wilshire, H. G., and E. D. Jackson, Problems in determining mantle geotherms from pyroxene compositions of ultramafic rocks, *J. Geol.*, **83**, 313-329, 1975.
- Winchell, H., The Honolulu series, Oahu, Hawaii, *Geol. Soc. Am. Bull.*, **58**, 1-48, 1947.
- Wolman, Y., W. J. Haverland, and S. L. Miller, Nonprotein amino acids from spark discharges and their comparison with the Murchison meteorite amino acids, *Proc. Nat. Acad. Sci. USA*, **69**, 809-811, 1972.
- Wood, B. J., and S. Banno, Garnet-orthopyroxene and orthopyroxene-clinopyroxene relationships in simple and complex systems, *Contrib. Mineral. Petrol.*, **42**, 109-124, 1973.
- Wright, T. L., and R. S. Fiske, Origin of the differentiated and hybrid lavas of the Kilauea volcano, Hawaii, *J. Petrol.*, **12**, 1-65, 1971.
- Wyllie, P. J., and O. F. Tuttle, Effect of carbon dioxide on the melting of granite and feldspars, *Am. J. Sci.*, **257**, 648-655, 1959.
- Yagi, T., F. Marumo, and S. Akimoto, Crystal structures of spinel polymorphs of Fe_2SiO_4 and Ni_2SiO_4 , *Am. Mineral.*, **59**, 486-490, 1974.
- Yang, H.-Y., Crystallization of iron-free pigeonite in the system anorthite-diopside-enstatite-silica at atmospheric pressure, *Am. J. Sci.*, **273**, 488-497, 1973.
- Yoder, H. S., Jr., High-low quartz inversion up to 10,000 bars, *Trans. Am. Geophys. Union*, **31**, 827-835, 1950.
- Yoder, H. S., Jr., Change of melting point of

- diopside with pressure, *J. Geol.*, 60, 364-374, 1951.
- Yoder, H. S., Jr., and C. E. Tilley, Origin of basalt magmas: an experimental study of natural and synthetic rock systems, *J. Petrol.*, 3, 342-532, 1962.
- Yoder, H. S., Jr., and C. E. Weir, High-pressure form of analcite and free energy change with pressure of analcite reactions, *Am. J. Sci., Bradley Vol.*, 258A, 420-433, 1960.

- Yund, R. A., and R. H. McCallister, The kinetics and mechanisms of exsolution, *Chem. Geol.*, 6, 5-30, 1970.
- Yund, R. A., A. C. McLaren, and B. E. Hobbs, Coarsening kinetics of the exsolution microstructure in alkali feldspar, *Contrib. Mineral. Petrol.*, 48, 45-55, 1974.
- Zachariasen, W. H., A general theory of x-ray diffraction in crystals, *Acta Crystallogr.*, 23, 558-564, 1967.

PERSONNEL

Scientific Staff

- Director*: H. S. Yoder, Jr., *Petrologist*
- Emeritus Research Associate*: E. G. Zies, *Chemist*
- Distinguished Professor, CIW*: E. F. Osborn, *Petrologist*
- Research Associate*: A. R. McBirney¹
- Systematic Petrologist*: F. Chayes
- Petrologists*: F. R. Boyd, Jr.; D. H. Eggler; T. N. Irvine; I. Kushiro;² D. Rumble III
- Physical Chemists*: J. D. Frantz,³ T. C. Hoering
- Geophysicists*: P. M. Bell, H. K. Mao
- Organic Geochemists*: J. R. Cronin,⁴ P. E. Hare
- Crystallographer*: L. W. Finger
- Isotope Geochemists*: G. L. Davis, T. E. Krogh
- Solid-State Geochemist*: D. Virgo
- Postdoctoral Fellows*: J. Akella, University of California at Los Angeles;⁵ R. J. Arculus, Durham University, England; J. I. Hedges, Marine Science Institute, University of Texas at Port Aransas;⁶ F. N. Hodges, University of Texas at Austin;⁷ F. E. Huggins, Massachusetts Institute of

- Technology;⁸ R. H. McCallister, Purdue University;⁹ G. H. Miller, University of Colorado;¹⁰ K. Muehlenbachs, University of Chicago;¹⁰ B. O. Mysen, Pennsylvania State University;³ Y. Nakamura, University of Tokyo, Japan;¹¹ Y. Ohashi, Harvard University;¹² M. G. Seitz, Washington University;¹³ Rosemary J. Vidale, State University of New York at Binghamton⁶
- Predocctoral Fellows*: J. I. Hedges, Marine Science Institute, University of Texas at Port Aransas;¹⁴ B. R. Lipin, Pennsylvania State University;¹⁵ H. R. Naslund, University of Oregon;¹⁶ E. B. Watson, Massachusetts Institute of Technology¹⁷
- Guest Investigators*: J. B. Adams, West Indies Laboratory, Fairleigh Dickinson University; J. Akella, National Aeronautics and Space Administration Johnson Space

¹ Appointment from March 1, 1975, terminated June 30, 1975, to return to position as Professor, Center for Volcanology, University of Oregon.

² On leave of absence at University of Tokyo, Japan, from September 1, 1974.

³ Appointment from July 1, 1974.

⁴ Temporary appointment from September 16, 1974.

⁵ Appointment terminated August 31, 1974, to accept position as Senior Research Associate, National Aeronautics and Space Administration Johnson Space Center, Houston, Texas.

⁶ Appointment from September 1, 1974.

⁷ Appointment terminated August 31, 1974, to accept Postdoctoral Fellowship at State University of New York at Stony Brook.

⁸ Appointment terminated June 30, 1975, to accept position as Assistant Professor at Purdue University.

⁹ Appointment from October 1, 1974.

¹⁰ Appointment terminated September 30, 1974, to accept position as Assistant Professor, Geology Department, University of Alberta, Edmonton, Canada.

¹¹ Appointment terminated March 31, 1975, to accept position as Associate Professor at the University of Tokyo, Japan.

¹² Appointment terminated June 30, 1975, to accept position as Crystallographer on temporary staff from July 1, 1975.

¹³ Appointment terminated August 31, 1974, to accept position as Senior Research Engineer with the Singer Corporation, Silver Spring, Maryland.

¹⁴ Appointment terminated August 31, 1974, to accept appointment as Postdoctoral Fellow from September 1, 1974.

¹⁵ Appointment terminated August 31, 1974.

¹⁶ Appointment from April 1, 1975.

¹⁷ Appointment from January 1, 1975.

Center; J. Benson, Stanford University; W. B. Bryan, Woods Hole Oceanographic Institution; I-Ming Chou, Johns Hopkins University; I. Ermanovics, Geological Survey of Canada; H. P. Eugster, Johns Hopkins University; G. W. Fisher, Johns Hopkins University; R. C. Fletcher, Department of Terrestrial Magnetism; T. Foster, Johns Hopkins University; B. M. French, National Science Foundation; J. M. Fuster, University of Madrid, Spain; W. Gardner, Skidaway Institute of Oceanography, University System of Georgia; J. J. Gurney, University of Cape Town, South Africa; S. E. Haggerty, University of Massachusetts; N. B. W. Harris, University of Toronto; B. Harte, University of Edinburgh, Scotland; Alice Hoersch, Johns Hopkins University; A. A. Kadik, Vernadsky Institute of Geochemistry and Analytical Chemistry, USSR Academy of Sciences, Moscow; G. Kullerud, Purdue University; M. Lafon, Johns Hopkins University; Dora Lee, Princeton University; Louise Levien, State University of New York at Stony Brook; V. R. Meenakshi, University of South Carolina; L. C. Ming, University of Rochester; A. Muan, Pennsylvania State University; K. Muehlenbachs, University of Alberta, Canada; M. Obata, Massachusetts Institute of Technology; R. W. Page, Australian Department of Minerals and Energy, Canberra; Barbara Pavlov, Johns Hopkins University; E. W. Roedder, U. S. Geological Survey; M. Rosenhauer, University of Frankfurt, Germany; G. Rossman, Cali-

fornia Institute of Technology; Th. G. Sahama, University of Helsinki, Finland; J. Smoot, Johns Hopkins University; Chien-Min Sung, Massachusetts Institute of Technology; Noreen Tuross, Trinity College; G. C. Ulmer, Temple University; A. Van Valkenburg, U. S. Bureau of Mines (retired); A. B. Vistelius, Laboratory of Mathematical Geology, Leningrad, USSR; J. Wehmiller, University of Delaware; B. Wyatt, Anglo-American Corporation, Johannesburg, South Africa

Operating and Maintenance Staff

Executive Officer: A. D. Singer
Accountant and Purchasing Agent: C. B. Petry
Editor and Librarian: Dolores M. Thomas
Stenographers: Marjorie E. Imlay, Mabel B. Mattingly
Typist-Clerk: Barbara B. Jones¹⁸
Clerk and Technician: H. J. Lutz
Electronic Technician: C. G. Hadidiacos
Laboratory Technician and Instrument Maker: G. E. Speicher
Instrument Maker: C. A. Batten
Machinist: W. R. Reed¹⁹
Apprentice Machinist: P. M. Vacchio
Building Engineer: H. L. Moore
Custodian and Painter: M. Ferguson
Custodian and Thin-Section Technician: D. Ratliff, Jr.
Custodian and Mechanic: L. B. Patrick

¹⁸ Temporary appointment from April 28, 1975.

¹⁹ Appointment terminated June 30, 1975.

Developmental Biology Research Group

Pasadena, California

Roy J. Britten

Senior Research Fellow

Contents

Introduction	655	Reassociation and Hybridization	699
DNA Sequence Arrangement	656	Rate of duplex formation in DNA	
DNA sequence organization in the		reassociation	699
mollusc <i>Aplysia californica</i>	656	Nucleic Acid Evolution	711
DNA sequence organization in the		Evolution of repetitive and nonrepetitive	
genomes of five marine invertebrates	669	DNA in two species of <i>Xenopus</i>	711
Comparative aspects of DNA organization		DNA sequence arrangement and	
in Metazoa	673	preliminary evidence on its evolution	723
DNA Sequence Expression Studied By		Acknowledgments	732
Transcription into RNA	678	References Cited	732
Sequence complexity of heterogenous		Recent Publications	734
nuclear RNA in sea urchin embryos.	678	Staff	735
Structural genes adjacent to interspersed			
repetitive DNA sequences	688		

INTRODUCTION

The work of this group has concentrated during the past year on four major areas: DNA sequence arrangement and its phyletic generality; studies of transcription in relation to DNA sequence arrangement; examination of the process and mechanism of DNA reassociation and RNA/DNA hybridization; and the evolutionary changes in DNA. The studies of sequence arrangement include a detailed examination of sequence interspersion in the DNA of a protostome, the Gastropod mollusc *Aplysia californica*, and studies of the DNA of eight other organisms in less detail. The conclusion from these measurements is that the DNA of all but two insects showed a great deal of similarity in sequence organization. In all of these cases the majority of the DNA consists of repeated sequences with a mode length of about 300 nucleotides interspersed with single-copy sequences of about 1000 nucleotide length. *Drosophila* and honey bee differ from the other species studied and lack a measurable quantity of short repeated DNA sequences. In contrast, the wild silk moth, a lepidopteran, shows a pattern of DNA sequence organization that is essentially identical to that of the majority of species studied. The insect sequence organization studies are relatively recent and are only briefly described here.

Our recent studies of the sequences transcribed into RNA during sea urchin development have led to several interesting conclusions. In earlier work we have shown that the great majority of structural gene sequences are transcribed from single-copy DNA sequences. (Goldberg, Galau, Britten, and Davidson, 1973). Only a few percent of the polysomal messages derived from sea urchin gastrulas hybridize to repetitive DNA. At this same stage the number of genes

expressed was measured by examining the fraction of the cellular single-copy DNA sequences which are transcribed into polysomal RNA. This earlier work showed that sea urchin gastrulas utilize 14,000 genes (Galau, Britten, and Davidson, 1974). The calculation assumes asymmetrical transcription and an average structural gene length of 1200 nucleotides. The work reported this year shows that about 10 times this amount of single-copy DNA sequence length is transcribed at the same stage to yield nuclear RNA which does not reach polysomes. Previous measurements had shown that much of this nuclear RNA consists of short-period, interspersed repetitive and single-copy sequence transcripts. (Smith, Hough, Chamberlin, and Davidson, 1974). Another set of measurements reported this year shows that the single-copy message sequences are typically transcribed from regions of the DNA immediately adjacent to repetitive sequences. This result confirms a prediction derived from the concept that repetitive sequences are involved in the regulation of the transcription (Britten and Davidson, 1969). It does not demonstrate, however, that the sequences are so involved. Projects are currently under way which will determine whether or not a specific set of repetitive sequences is adjacent to the sets of structural genes transcribed at particular stages.

Measurements have been made of the effects of length on the rate of DNA reassociation and on the rate of hybridization of RNA and DNA relative to the DNA reassociation rate. This is part of an ongoing study that retains a number of interesting if not exciting mysteries. The work reported here confirms previous measurements (Morrow, 1974) of the fraction of DNA actually remaining single stranded by single-strand nuclease

assay. Calculations from these results show that there is an inhibition in the rate of reassociation of single-strand ends of partially reassociated fragments. Measurements of hybridization rates were made as a part of the study of repeated sequences adjacent to structural genes. Under conditions in which an excess of DNA drives the reaction, the hybridization rate is about 4 times slower than the DNA reassociation rate.

Two aspects of our evolutionary studies are described here. Measurements of the sequence relationship of the DNAs of *Xenopus laevis* and *Xenopus borealis* (often mistakenly called *mulleri*). These measurements show that a great deal of divergence has occurred between the single-copy DNA sequences of these two congeners, which is consistent with the divergence observed by Donald Brown between the spaces of their ribosomal genes. Complete cross reassociation of repetitive sequences is observed but at rates which are strikingly slower than the homologous reassociation reaction. This observation indicates changes in the

number of certain sets of repetitive sequences while all sets of sequences remain represented.

In the final section of this Report, measurements of primate single-copy DNA relationships (Kohne, Chiscon, and Hoyer, 1970; Hoyer, van de Velde, Goodman, and Roberts, 1972) are reviewed, and the implied changes in the codogenic sequence are compared with the most rapidly changing amino acids in proteins. It is found that the rate of base substitution incorporated in the genes for fibrinopeptides and selected hemoglobin residues is about the same as the rate of base substitution in the average single-copy DNA. Evidence is assembled which implies that most of the single-copy DNA is not made up of structural gene sequences. The hypothesis is made that the rate observed for the principal part of the single-copy DNA is the "basal rate of nucleotide substitution" which is not significantly affected by selection based on changes in the phenotype.

DNA SEQUENCE ARRANGEMENT

DNA SEQUENCE ORGANIZATION IN THE MOLLUSC *Aplysia californica*

Robert C. Angerer, Eric H. Davidson, and
Roy J. Britten

A major fraction of the DNA of many organisms has been found to consist of short repetitive sequences (about 300 nucleotides long) alternating with single-copy sequences. Many of the single-copy sequences extend for less than about 2000 nucleotides before terminating in repeated sequence elements. This pattern is termed short-period interspersion. Short-period interspersion accounts for a large fraction of the DNA in a toad, *Xenopus laevis* (Davidson *et al.*, 1973), and a sea urchin, *Strongylocentrotus purpuratus* (Graham *et al.*, 1974), and is probably important in

mammalian DNA (Britten and Smith, 1970; Bonner *et al.*, 1974; Pearson, Wilkes, and Bonner, unpublished data). The DNA of the toad and the sea urchin includes, in addition, some longer single-copy sequences (up to 5000 nucleotides or more) interspersed with repetitive sequences.

The work reported here was undertaken to extend our knowledge of sequence organization to the second main branch of the animal kingdom, the protostomes, and includes extensive measurements which permit estimation of the length distribution of the interspersed single-copy sequences.

Reassociation Kinetics of *Aplysia* DNA

The reassociation kinetics of *Aplysia* DNA have been examined in several

ways. Figure 1 presents the results of three of these, extending over a factor of 10^{11} in C_0t . The reassociation of 400-nucleotide-long fragments assayed by hydroxyapatite (middle curve) shows that *Aplysia* DNA contains sequences with a broad range of repetition frequency. The curve represents the least-squares fit to this data with four second-order components. In this analysis only the rate constant of the single-copy component was fixed at $0.00055 \text{ l M}^{-1} \text{ sec}^{-1}$, the value expected from the genome size of 1.8 pg (Hinegardner, 1974). Table 1 lists the quantities and rate constants of the components of this least-squares solution. At this fragment length many of the single-copy sequences are present on the same fragments as repeated sequences and are thus bound to the hydroxyapatite at low C_0t , reducing the apparent size of the single-copy fraction. The rate constant for the single-copy sequences was determined by reassociating with total *Aplysia* DNA

a tracer preparation highly enriched for single-copy sequences. This tracer was the fraction of 400-nucleotide fragments not bound to hydroxyapatite after reassociation to C_0t 2000 (21% of the DNA). The right-hand curve of Fig. 1 shows the kinetics of reassociation of the tracer DNA with total *Aplysia* DNA. The curve shown is the least-squares solution for two second-order components. Table 1 shows the best solution for quantity and rate of both components. The single-copy component has a reassociation rate constant of $0.00073 \text{ l M}^{-1} \text{ sec}^{-1}$. If the rate constant is fixed at the value expected from the genome size ($0.00055 \text{ l M}^{-1} \text{ sec}^{-1}$), the root-mean-square error rises from 2.0% to 2.3%. This is hardly a significant increase in rms, and thus there is good agreement between the predicted and observed single-copy rates.

The 400-nucleotide fragment reassociation curve shows a wide range of reassociation rates. The measurements

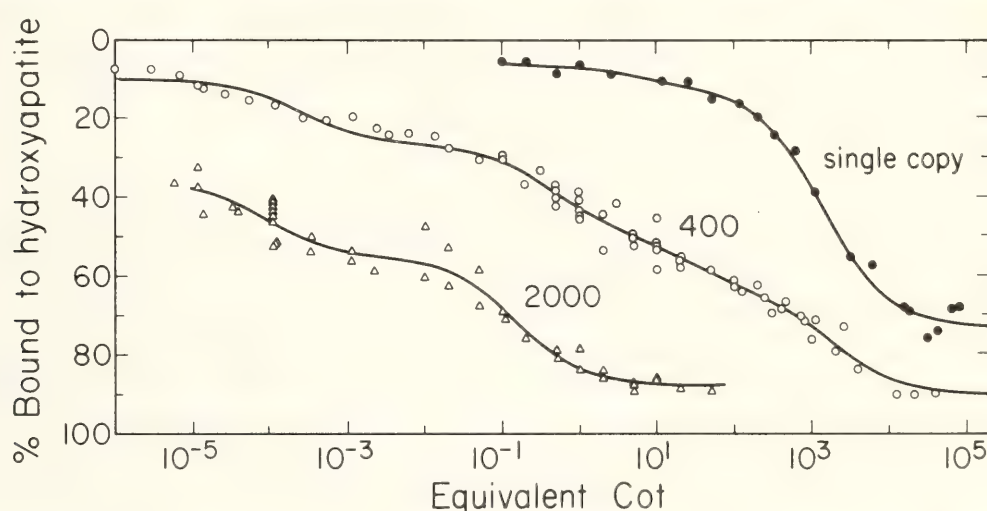


Fig. 1. Hydroxyapatite reassociation kinetics of *Aplysia* DNA. *Aplysia* DNA of fragment length 400 (open circles) or 2000 (open triangles) nucleotides was reassociated as described in "Experimental Procedures." The fraction of fragments containing duplex regions was measured at the indicated values of equivalent C_0t by hydroxyapatite column chromatography. The curve for 400-nucleotide fragments represents values determined by optical density or by radioactively labeled DNA using three different tracer preparations. Undiluted tracer at a concentration of $0.02 \mu\text{g/ml}$ was used for the low C_0t points. For higher C_0t s the tracer was mixed with unlabeled DNA up to an unlabeled DNA/labeled DNA ratio of 38 and a total DNA concentration of 4.4 mg/ml . For the 2000-nucleotide fragment curve, DNA concentrations were from $0.03 \mu\text{g/ml}$ to $132 \mu\text{g/ml}$ using unlabeled to labeled DNA ratios of 0 to 200.

The rate of reassociation of isolated single-copy sequences is also shown (solid circles). For this analysis the fraction of 400-nucleotide tracer not bound to hydroxyapatite at C_0t 2000 (21% of the DNA) was mixed with a 330-fold mass excess of total unlabeled driver DNA.

The lines drawn represent computer fits by least-squares analysis yielding the second-order components listed in Table 1.

TABLE 1. Kinetic Analysis of *Aplysia* DNA Reassociation

C_0t Curve	Component	Fraction of Fragments	k^c	$C_0t_{1/2} = 1/k$	Number of Copies	rms Deviation (%)
400 nucleotide	foldback	0.07	2.7
	very fast ^a	0.165	4.0×10^3	2.5×10^{-4}	7.1×10^6	
	fast	0.218	2.6	0.39	4.6×10^3	
	slow	0.158	4.7×10^{-2}	21	85	
	single copy ^b	0.263	5.6×10^{-4}	1.8×10^3	1 ^e	
2000 nucleotide	foldback	0.357	3.5
	very fast	0.192	1.2×10^4	8.3×10^{-5}	9.8×10^6 ^d	
	fast	0.329	6.6	0.150	5.4×10^3 ^d	
single copy	residual repeat	0.059	0.25	4.0	340	2.0
	single copy	0.638	7.3×10^{-4}	1.4×10^3	1 ^e	

^aA better fit to the data (rms = 2.4%) is obtained if the very fast fraction is divided into two components representing 13.1 and 4.7% of the genome and having k 's of 6.9×10^5 and 8.2×10^3 l M^{-1} sec⁻¹, respectively.

^bThe single-copy rate constant is fixed at 5.6×10^{-4} l M^{-1} sec⁻¹ as predicted from the genome size of 1.8 pg.

^cRate constant in whole DNA, l M^{-1} sec⁻¹.

^dBased on a theoretical single-copy rate constant of 1.2×10^{-3} l M^{-1} sec⁻¹ for 2000 nucleotide fragments.

^eAssumed value of 1 for the single-copy component.

imply that the *Aplysia* genome contains at least three major classes of repeated DNA sequence. We have identified these as the "slow," "fast," and "very fast" fractions with sequences present an average of 85, 4600, and 7,000,000 times per haploid genome. A better fit to the data is obtained if the very fast fraction is divided into two components as mentioned in the footnote to Table 1. In this case one of the components appears to have a complexity of less than 10 nucleotide pairs. Such simple sequences are known in satellite DNAs. However, neutral CsCl density gradient analysis did not reveal a density satellite in *Aplysia* DNA.

Measurements of the reassociation of the very fast fraction were made at several different DNA concentrations varying by a factor of 30. The data indicate that a collision-dependent reassociation process is involved since the observed hydroxyapatite binding depends on C_0t rather than the time of incubation. As shown in Fig. 2, the very fast component appears smaller when reassociation is monitored by S1 nuclease.

Since this fraction does not appear to be interspersed with extensive single-copy stretches, we have not further investigated its somewhat paradoxical properties.

Interspersed Studied by Reassociation Kinetics Using Hydroxyapatite and S1 Nuclease

Figure 1 (left-hand curve) shows the reassociation of 2000-nucleotide-long DNA fragments as measured by hydroxyapatite binding and provides clear evidence for the interspersed of rapidly reassociating sequences with single-copy DNA sequences. Nearly all the 2000-nucleotide fragments are bound as a result of reassociation of the repetitive regions. Table 1 shows the best least-squares solution for these measurements using two kinetic components. The rates appear to correspond to the fast and very fast components of the solution for the 400-nucleotide fragment measurements. If the fragments containing the very fast component contain no other sequences, then the rate corrected

for fragment length would be $(2000/400)^{1/2} \times 4 \times 10^3 = 9 \times 10^3 \text{ l M}^{-1} \text{ sec}^{-1}$, which is approximately what is observed ($1.2 \times 10^4 \text{ l M}^{-1} \text{ sec}^{-1}$).

We cannot easily calculate the effect of length on the rate of reassociation of the interspersed repetitive sequences. There seems no doubt, however, that the reaction of the 2000-nucleotide fragments between C_0t s 0.02 and 2 is due principally to the fast component. The reaction is 90% complete by C_0t 10, and the residual 10% is probably due to an unreassociating impurity rather than slow-fraction DNA sequences. Therefore, most or all of the single-copy DNA is

present on fragments that contain either foldback or repetitive sequences. At this stage it is reasonable to believe that single-copy DNA sequences are adjacent to both the fast fraction and to either or both of the very fast and foldback fractions. Measurements reported below will serve to identify the repetitive components that are interspersed.

The reassociation kinetics of *Aplysia* DNA have been assayed both by means of the single-strand-specific nuclease S1 and by optical hypochromicity, as shown in Fig. 2. Both methods show that the 2000-nucleotide fragments bound to hydroxyapatite by C_0t 10 are

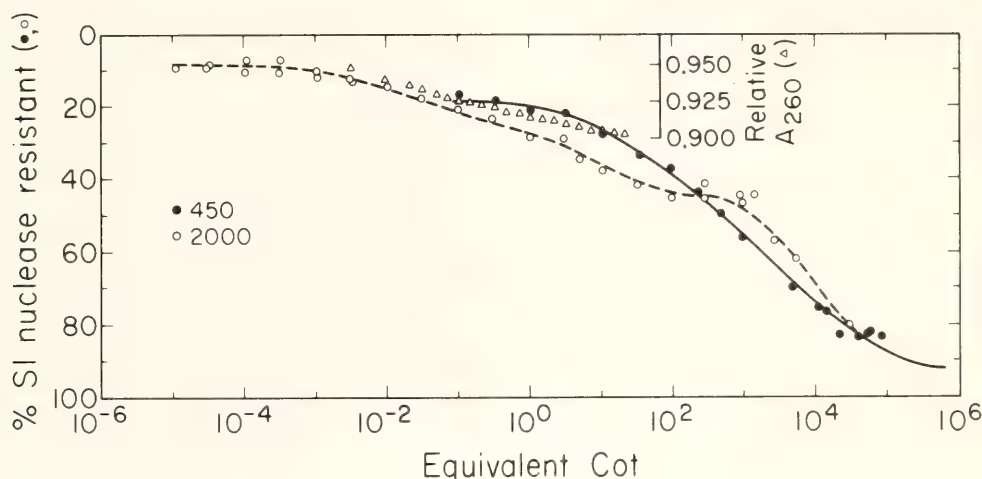


Fig. 2. S1 nuclease and optical reassociation kinetics of *Aplysia* DNA. *Aplysia* DNA of fragment length 450 (solid circles) or 2000 (open circles) nucleotides was reassociated as indicated in "Experimental Procedures." The fraction of the DNA in duplex was measured by digestion of single-stranded regions with single-strand-specific S1 nuclease and collection of duplex regions on hydroxyapatite. The curve through the 450 nucleotide data represents a least-squares computer analysis to two components of the appropriate form,

$$\frac{C}{C_0} = \left[\frac{1}{(1 + K C_0 t)} \right]^{0.44}$$

(Morrow, 1974; Britten, Smith and Davidson, this Report). For this analysis the rate constant of the single-copy component was fixed at $5.56 \times 10^{-4} \text{ l M}^{-1} \text{ sec}^{-1}$ as predicted from the genome size of 1.8 pg, yielding a component accounting for 0.45 of the genome. The repetitive component comprised .285 of the genome with a rate constant of $9.41 \times 10^{-2} \text{ l M}^{-1} \text{ sec}^{-1}$. The final fraction single stranded was 0.08 and the rms deviation for the fitted curve is 1.97%. The rms deviation does not vary appreciably for a single-copy component ranging from 0.4 to 0.55 of the genome.

The dashed line through the 2000-nucleotide data does not represent a computer-fitted curve. The retardation seen at high C_0t s may be due to large network structures formed from fragments containing more than one interspersed repetitive element.

The rate of duplex formation for 450-nucleotide fragments was also measured by optical hypochromicity (open triangles). The right-hand scale indicates the measured $A_{260} \text{ nm}$ relative to the $A_{260} \text{ nm}$ at 98°C . This scale has been adjusted to make the data directly comparable to the percentage of S1 nuclease resistance shown on the left-hand scale as follows: Twenty-five percent hypochromicity (relative $A_{260} = 0.75$) is taken to correspond to 100% S1 nuclease resistance. The zero percent nuclease resistance value is aligned with the 2.5% hypochromicity due to single-strand collapse.

predominantly single stranded, as expected if short, repetitive sequences are interspersed with longer, nonrepetitive sequences. For example, at C_0t 3, 85% of 2000-nucleotide fragments are bound to hydroxyapatite but only 30% of the DNA is resistant to S1 nuclease. Figure 3 shows the optical melting curve for 2000-nucleotide fragments which have been incubated to C_0t 10. The hyperchromicity from 60° to 95°C is 9% after correction for the fraction of the DNA in free single strands (0.17). The hyperchromicity of purely single-stranded DNA is about 2.5% and of native DNA is 25.5%. Thus, the fraction double stranded is about $(9 - 2.5)/(25.5 - 2.5) = .28$, which is in close agreement with the S1 measurement. Measurements

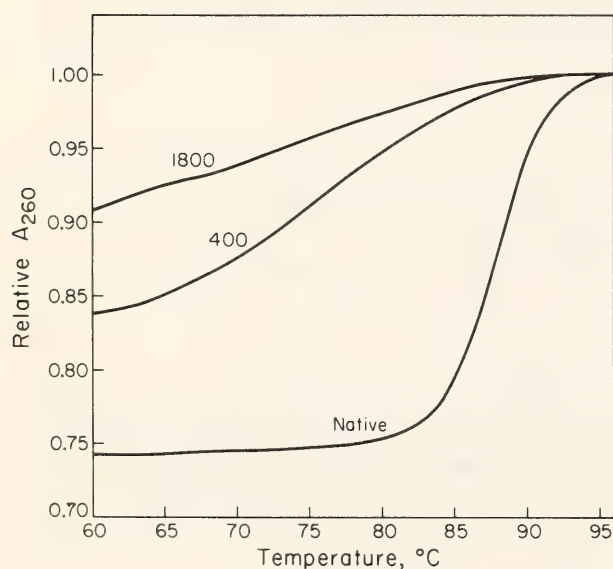


Fig. 3. Thermal denaturation of reassociated *Aplysia* DNA. DNA fragments 400 or 1800 nucleotides long were reassociated to C_0t 10. The 400-nucleotide fragments were isolated by binding to hydroxyapatite (41% of the genome). The 1800-nucleotide fragments included the whole reaction mixture since these fragments form extensive networks which cannot be eluted from hydroxyapatite except by denaturation. Thermal denaturation profiles of these fractions and of native *Aplysia* DNA were determined in 0.12 M PB. The curve for the 1800-nucleotide fragments has been corrected for the contribution of purely single-stranded fragments (16.8% of the DNA) to the thermal denaturation profile. This contribution was measured by means of an optical thermal denaturation profile of a single-stranded *Aplysia* DNA fraction (400 nucleotide, not bound to hydroxyapatite at C_0t 2000).

of the duplex content for two fragment lengths after renaturation to C_0t 10 are shown in Table 2. There it is seen that by both S1 nuclease assay and measurement of optical hyperchromicity only about 26%–28% of the fragments containing base-paired regions are actually in duplex.

At this stage we may estimate the fraction of the total single-copy DNA in the genome which is interspersed with repetitive sequences. Figure 1 shows that by hydroxyapatite assay at least 90% of 2000-nucleotide fragments contain repetitive sequences which reassociate by C_0t 10. Figure 2 shows that by S1 nuclease assay about 50% of the genome is made up of single-copy sequences in a short-period pattern. Thus, a possible $0.1/0.50 = 20\%$ of the single-copy DNA is not interspersed. In fact, much of the 10% which is not bound to hydroxyapatite at C_0t 10 may be an impurity which does not reassociate. Thus, we may conclude that between 80% and 100% of *Aplysia* single-copy sequences are interspersed with repetitive sequences with spacings of less than about 2000 nucleotides.

Interspersion of Foldback Sequences

Aplysia DNA has a particularly large amount of foldback, or zero-time binding DNA, accounting for 7% of 400 nucleotide fragments. When labeled 2000-nucleotide fragments are passed over hydroxyapatite with a C_0t of less than 10^{-5} , almost 40% of them bind. Under the same conditions about 9% of the genome is resistant to S1 nuclease. At least 75% of these S1-resistant foldback sequences will bind to hydroxyapatite after S1 treatment and a second denaturation (C_0t less than 10^{-5}). We do not know what sort of DNA sequences are responsible for the foldback fraction, but if there are tandem reverse repeats, few of them are separated by single-stranded loops sensitive to S1 nuclease. Such structures would not bind in the second hydroxyapatite test.

TABLE 2. Duplex Content of *Aplysia* DNA Fragments at C_0t 10

Fragment Length (nucleotides)	Assay	Hyperchromicity ^a (%)	Genome in Fraction ^b (%)	Genome, Base Paired (%)
400	Optical	16.2	41	25.5, 27 ^c
400	S1 nuclease	27 ^d
1800	Optical	9.2	84	28 ^c
2000	S1 nuclease	36 ^d

^aCalculated as $(A_{260} \text{ at } 98^\circ\text{C} - A_{260} \text{ at } 60^\circ\text{C})/A_{260} \text{ at } 98^\circ\text{C}$.
^bMeasured fraction of DNA fragments bindable to hydroxyapatite.
^cCalculated as $(H - 2.5)/(25.5 - 2.5)$, where H is the observed hyperchromicity, 25.5 is the hyperchromicity of native DNA, and 2.5 is the hyperchromicity due to single-strand collapse.
^dCalculated as (fraction of DNA bound to hydroxyapatite after S1 nuclease digestion) \times (% genome in fraction).

The fraction of fragments containing foldback sequences was measured for a variety of lengths by denaturing labeled DNA fragments and passing them over hydroxyapatite to an effective C_0t estimated to be 4×10^{-6} . Table 3 shows the increase in binding with length, and demonstrates that many of the foldback sequences are interspersed with other classes of DNA. Measurements of the kinetic characteristics of the *Aplysia* DNA sequences adjacent to foldback (not presented here) suggest that all classes of sequences are present and that the foldback sequences are interspersed throughout the genome. The length of the stretches of other kinds of sequence between the foldback sequences appears to be quite long since the fraction of DNA bound at C_0t 4×10^{-6} rises linearly with fragment length out to 4000 nucleotides. The data indicate that 50% binding occurs at 3500 nucleotides, and this suggests that the average length of the intervening sequences is 7000 nucleotides. Though there is no sugges-

TABLE 3. Fraction of Fragments Containing Repetitive Sequences

Fragment Length (nucleotides) ^a	Fraction Bound (F) ^b at			Binding Due to Repetitive Sequence (R) ^d at	
	C_0t 4×10^{-6} ^c	C_0t 10^{-2}	C_0t 10	C_0t 10^{-2}	C_0t 10
199	.023	.26	.38	0.27	0.40
435	.034	.28	.50	0.28	0.53
524	.058	.26	.63	0.23	0.67
945	.10	.32	.71	0.28	0.76
1374	.18	.43	.80	0.35	0.86
2089	.30	.48	.78	0.30	0.81
2487	.43	.61	.88	0.37	0.95
3919	.53	.65	.88	0.23	0.93

^aAverage of three determinations, each relative to two known markers.
^bAverage of two or more determinations except for 199-nucleotide tracer, which is a single value.
^cCalculated maximum C_0t based on the total time required for incubation and passage through the hydroxyapatite column.
^d
$$R = \frac{F(C_0t) - Z}{0.9 - Z}$$

Where Z is the fraction of the DNA bound as foldback at very low C_0t . The values for R are normalized to a value of 90% tracer reassociation which is the observed maximum value.

tion in the data of local clustering of the foldback sequences, this cannot be ruled out. Their length distribution is indicated in Fig. 5.

The Fraction of Fragments Containing Repeated Sequences as a Function of Length

The fraction of fragments containing repeated sequence elements was measured by hydroxyapatite binding of tracer fragments in the presence of a great excess of short-fragment (400

nucleotide) driver DNA. This method has previously been used for *Xenopus* and sea urchin DNA (Davidson *et al.*, 1973; Graham *et al.*, 1974). The measurements were made at driver C_0t 10^{-2} for the very fast fraction and C_0t 10 for the fast fraction. The results are shown in Table 3 and Fig. 4. Since the foldback sequences give increased binding as a function of fragment length, a correction has been made for the binding at very low C_0t using the following formula: $R = F_{(C_0t)} - Z/(.9 - Z)$, where $F_{(C_0t)}$ is the fraction of fragments binding at the selected C_0t and Z

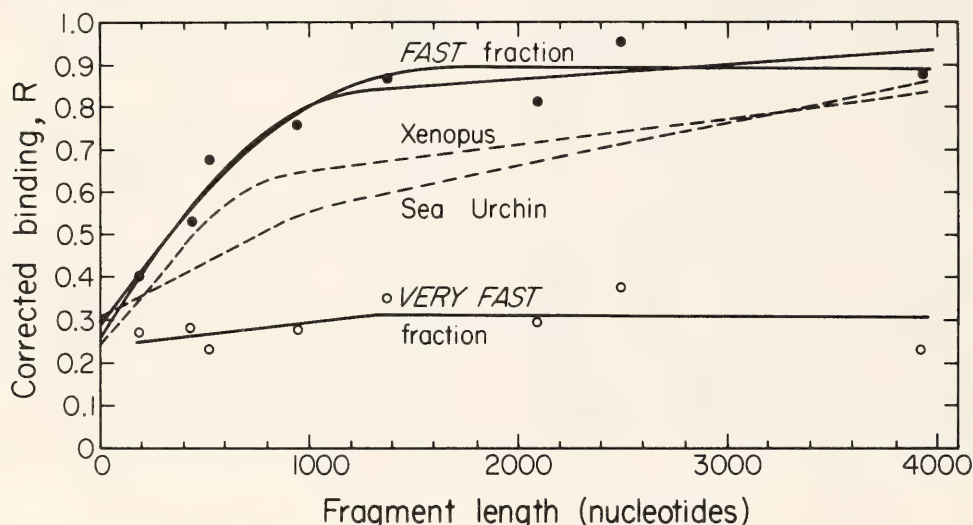


Fig. 4. Fraction of *Aplysia* DNA containing repetitive sequence elements as a function of fragment length. Labeled *Aplysia* DNA fragments of various lengths were mixed with unlabeled DNA driver of 400 nucleotide fragment length and reassociated to a driver C_0t of 10^{-2} (open circles) or 10 (solid circles). The mass ratio of driver to tracer was 1200 in the former case and 2300 in the latter. The fraction of DNA fragments containing duplex regions (F) was measured by hydroxyapatite chromatography. Values of F were corrected for the fraction of zero-time binding sequences (Z) and for 10% nonreactability of the tracer by the formula

$$R = \frac{F_{(C_0t)} - Z}{0.9 - Z}$$

as described in the text and in Table 3.

The lines drawn through the experimental points were generated by a least-squares computer program essentially as described in Graham *et al.*, (1974). The two curves for the fast fraction binding (C_0t 10) represent best solutions to the data (with approximately equivalent rms deviations) for two different conditions. One of these is a solution with a major component with single-copy interspersion lengths ranging from zero to 1300 nucleotides and a minor component with very long period interspersion. The other solution is for a distribution of single-copy lengths ranging from 200 to 1600 nucleotides, with no long-period interspersed component. The curve for the very fast fraction (C_0t 10^{-2}), is a solution containing only a small (7%) interspersed component with a single-copy length distribution centering around 1300 nucleotides.

For comparison, least-squares solutions (dashed curves) are included for similar data obtained for *Xenopus laevis* (Davidson *et al.*, 1973, Fig. 6, curve 2) and for the sea urchin, *Strongylocentrotus purpuratus* (Graham *et al.*, 1974, Fig. 3).

is the fraction binding at very low C_0t (Davidson *et al.*, 1973). The formula also corrects for the observation that the reassociation of these DNA preparations does not exceed 90%.

The very fast fraction (reassociating between C_0t s 10^{-6} and 10^{-2}) shows very little or no increase in binding with fragment length. The lower curve on Fig. 4 is the least-squares solution and

indicates an increase of about 7%, which is not significant. Therefore, we conclude that this fraction is not significantly interspersed with any other sequence classes of *Aplysia* DNA. The sequence complexity of the very fast fraction can be estimated to be about 23 nucleotides (see Table 4) from its average rate of reassociation, although as discussed above, it could be heterogeneous. The

TABLE 4. Components of *Aplysia* Genome

Component	Fraction of Genome	Complexity ^e
foldback	0.07 – 0.1 ^a	...
very fast	0.05 – 0.16 ^b	23
fast	0.11 – 0.17 ^c	5.1×10^4
slow	0.12 – 0.225 ^d	3.3×10^6
single copy	0.45 – 0.60 ^d	8.4×10^8

^aThe lower limit is the fraction of the genome bound to hydroxyapatite after incubation to $C_0t\ 10^{-5}$, digestion with S1 nuclease, denaturation, and reincubation to $C_0t\ 10^{-5}$. The upper limit is the fraction of the genome bound to hydroxyapatite after two incubations to $C_0t\ 10^{-5}$ and subsequent digestion with S1 nuclease.

^bThe lower limit is taken from the S1 nuclease assay of reassociation of 2000-nucleotide fragments shown in Fig. 2. The upper limit is taken from the data of Fig. 1 and Table 1 for 400 nucleotide fragments.

^cThe lower limit is the average total $C_0t\ 10$ duplex content of 30%, given in Table 2, minus the average values for foldback and very fast fractions given in this table. The upper limit is from the 400-nucleotide fragment data of Table 1 corrected for the effect of interspersion. Since the interspersed repeats are 300 nucleotides in length, about 0.75 of the fragments of this fraction represent duplexes of the fast fraction, and the remainder are single-copy (or slow) tails. The upper limit is therefore $(0.22) \times (0.75)$ or 17% of the genome.

^dThe upper limit is calculated as follows: The data of Table 2 and Fig. 2 show that about 70% of the DNA is not in duplex at $C_0t\ 10$. This fraction corresponds to all of the single-copy DNA and 0.67 of the slow fraction (which has a $C_0T_{1/2}$ of 20 and is therefore two-thirds unreacted at $C_0t\ 10$) as well as 10% nonreassociable tracer. The estimate for the single-copy content is the range of estimates with approximately equal rms deviation from the computer-fitted curve of Fig. 2 for 450-nucleotide fragments. We calculate the maximum size of the slow component as $70\% - (45\% + 10\%)/0.67 = 23\%$.

The lower limit is calculated using the value of 0.16 for the fraction of slow component in 400-nucleotide fragments from Table 1. Assuming this component is interspersed and of length similar to 300 nucleotides, then the minimum value is $0.16(0.75) = 0.12$.

^eComplexity values are calculated using the number of copies from Table 1 and the mean of the estimates in this table for fraction of the genome in each component.

lack of apparent increase in binding in the curve of Fig. 4 shows that the physical sequence length is greater than 4000 nucleotides. Therefore, we can conclude that the very fast fraction consists of tandemly duplicated sequences, and is analogous in this sense to previously observed satellite fractions, though as mentioned above, it was not resolved in CsCl density gradients.

The fast fraction (reassociating between C_0t s 0.01 and 10) shows a great deal of interspersion with other sequences in the genome. The binding vs. fragment-length curve on Fig. 4 rises to 90% or 95% (after the corrections mentioned above). Therefore, we can conclude that sequences of the fast fraction occur throughout the majority of the genome with spacings of less than a few thousand nucleotides. We have been unable to determine the spacing of the fast and single-copy interspersion in the neighborhood of the foldback sequences since these regions are bound to hydroxyapatite at very low C_0t . However, there is evidence that some fast fraction sequences occur in these regions from the reassociation kinetics of sheared foldback fraction DNA (Angerer, unpublished data). It should be pointed out that the foldback fraction accounts for only 17% of fragments 1400 nucleotides long (Table 3). Therefore, the interspersion of the fast fraction shown in Fig. 4 is representative of at least 83% of the genome.

The upper curves on Fig. 4 show that a major portion of *Aplysia* DNA is present as short-period interspersed repetitive and single-copy sequences. In fact, the principal part of the genome is included in this pattern. Comparison with the curves representing the *Xenopus* and sea urchin measurements (Davidson *et al.*, 1973; Graham *et al.*, 1974) shows that a larger fraction of the *Aplysia* genome is in the short-period spacing pattern. In fact, the data of Fig. 4 are not sufficient to determine whether or not *Aplysia* contains a small portion of the genome with a

pattern of long-period interspersion of repeated and single-copy DNA sequences. We return to the question of the length of the repeated and single-copy sequence elements below.

It is clear from the data of Table 3 and Fig. 4 that almost all of the single-copy DNA is interspersed with the fast fraction of repetitive sequences. This conclusion is, of course, consistent with that drawn from the measurements of the kinetics of reassociation of 2000-nucleotide fragments assayed by hydroxyapatite. There remains the question of the arrangement in the genome of the slow-fraction DNA sequences. They are obviously interspersed with the fast-fraction sequences, but without additional measurements we cannot determine if there are regions which contain short-sequence elements of fast, slow and single-copy sequences all interspersed with each other, or if the fast and slow are interspersed in some regions and the fast and single-copy are interspersed in other regions.

Repetitive Sequence Lengths Estimated with Single-Strand-Specific Nuclease

Aplysia DNA fragments of about 1800 nucleotides were incubated to C_0t s 10^{-5} , 10^{-2} , and 10 and then digested with S1 nuclease as described in "Experimental Procedures." The resistant duplex regions were collected on hydroxyapatite and chromatographed on agarose A-50. The extent of digestion with nuclease was sufficient to remove almost all of the single-strand tails as indicated by the hyperchromicity of the duplex regions. This was 87% of that of native DNA. Under the conditions used, relatively few strand scissions or duplex cuts occur (Davidson *et al.*, 1974; Chamberlin *et al.*, in press; Britten, Graham, Eden, and Davidson, in preparation) even in the divergent reassociated regions with melting temperatures 10° or 15°C less than that of perfectly paired DNA.

Figure 5 shows the agarose A-50 chromatography results. Under the condi-

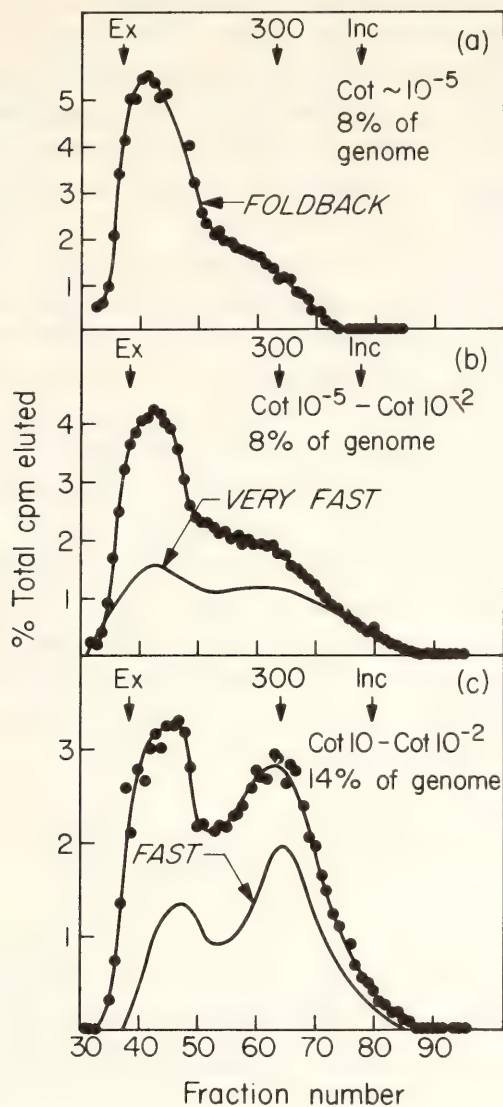


Fig. 5. Length distribution of *Aplysia* repeated DNA sequences. Total *Aplysia* DNA of 1800 nucleotide fragment length was reassociated to C_0t 10^{-5} (a), 10^{-2} (b) or 10 (c) as indicated in "Experimental Procedures." The single-stranded regions were removed by means of S1 nuclease and the duplexes recovered on hydroxyapatite and eluted with 0.4 M PB. The percentage of the DNA present in each fraction is indicated in the figure. The samples were chromatographed on a column of agarose A-50 with long native DNA as an exclusion marker and $^{32}\text{PO}_4^{3-}$ as an inclusion marker. The position of 300-nucleotide fragments in the column profile is indicated.

The lower curve of 5b indicates the distribution of very fast sequences reassociating between C_0t 10^{-5} and C_0t 10^{-2} . This distribution has been calculated by correcting the experimental curve shown in 5b for the contribution of foldback sequences shown in 5a.

The lower curve of 5c shows the distribution of fast sequences reassociating between C_0t 10^{-5} and C_0t 10^{-2} . This curve has been calculated by subtracting the contribution of sequences reassociating by C_0t 10^{-2} whose distribution is shown in 5b.

tions used, the left-hand peak consists of simple duplexes greater than about 1500 nucleotide pairs or of hyperpolymers consisting of multiple fragments paired in such a way as to be resistant to S1 nuclease. The foldback fraction shown in the curve in Fig. 5a consists of many long nuclease-resistant sequences, and this differs from foldback fractions observed in other animals, which are shorter (e.g., Wilson and Thomas, 1973). Each distribution of repetitive sequence lengths shown in Fig. 5 includes all sequences reassociating by the indicated C_0t . We have attempted to calculate the actual size distribution of the very fast and fast kinetic fractions by difference. The lower curves in Fig. 5b and 5c show these results. From the previous data indicating tandem repetition of the very fast fraction (Fig. 4) one might expect that these sequences would yield only long resistant regions, but the data show more than half of the fragments to be less than 1000 nucleotides long. We do not know the explanation of this size reduction, though it may indicate an interspersion of other sequences on a very short scale such as has been indicated for the mouse satellite (Rice, 1974).

The distribution of sequence lengths of the fast fraction is displayed in Fig. 5c. The curve corrected for the C_0t 10^{-2} contribution shows a significant peak at a size of about 300 nucleotides. This indicates that many of the interspersed fast fraction sequences are about 300 nucleotides long. This result is very similar to that obtained in the cases of *Xenopus* and the sea urchin (Davidson *et al.*, 1973; Chamberlin *et al.*, 1975; Graham *et al.*, 1974). There is an obvious risk that reassociated divergent repetitive DNA would contain structures with mispaired regions which could be digested by S1 nuclease. In fact, under some conditions it is possible with very extensive digestion to cut at single mispaired bases (Shenk *et al.*, 1975). However, with the light enzyme treatment and the salt and temperature conditions

used here, such strand scissions are minimized. With an even more extensive S1 nuclease digestion than used here, measurements with agarose A-50 of the size distribution of *Xenopus* interspersed repetitive sequences gave exactly the same mode size (Davidson *et al.*, 1974) as did measurements with the electron microscope (Chamberlin *et al.*, in press) which did not involve the use of any nuclease. We conclude that although there is probably a modest background of fragments due to strand scission at divergence points, the 300 base pair peak in Fig. 5c is actually a good measure of the length of fast fraction interspersed repetitive sequences.

The Fraction of the Genome in an Interspersed Pattern

Table 1 summarizes the reassociation kinetic measurements and the frequencies of the repetitive fractions that we are using to describe *Aplysia* DNA. Because of interspersion of the various sequence elements, the fraction of DNA fragments in the kinetic components does not accurately represent the fraction of the genome in these components. Correcting for interspersion and using the S1 measurements shown in Fig. 2 and Fig. 5 leads to the values for fraction of the genome in each component shown in Table 4. In every case except that of the single-copy sequences, the frequencies are average values for what may be in reality a range of frequencies. Measurements have not been made of the homogeneity of the repeated components. Thus, there is a considerable uncertainty in the complexity figures, since a minor amount of a more slowly reassociating component would not be recognized and could drastically alter the total amount of different sequences present. This *caveat* applies to most estimates of repetitive sequence complexity.

The measurements with S1 nuclease shown in Fig. 5 indicate that about two-thirds of the fast fraction is made

up of short interspersed sequences. This amounts to about 10% of the total DNA of *Aplysia*. The single-copy fraction amounts to 45%–60% of the genome as shown in Table 4. Most of these sequences are interspersed with the fast fraction and we may estimate as a lower limit that at least 55% of the genome is in this interspersion pattern. Another estimate can be made from the fact that 90% of fragments 2000 nucleotides long are bound to hydroxyapatite at C_0t 5, shown in Fig. 1. Twenty-two percent of the genome is in S1-resistant foldback and very fast fractions and noninterspersed fast sequences. The difference is 68%, which is a reasonable upper limit calculation. We conclude that between 55% and 70% of the DNA is made up of interspersed fast, single-copy, and slow sequences.

The Length and Spacing of the Interspersed Repetitive Sequences

The upper curves on Fig. 4 represent two least-squares solutions to the measurements of the variation with length of the fraction of fragments that contain fast-fraction repetitive sequences. These curves were fitted as described previously (Graham *et al.*, 1974). In one case it was assumed that there is a long-period pattern of interspersion which gives the later slope, and in the other case it was assumed that there is only a short-period pattern of interspersion. The root-mean-square deviations are essentially the same for both curves. It is clear that the short-period pattern is dominant and uncertain whether there are any long single-copy sequences without intervening repetitive sequences. Both solutions make use of a wide range of lengths of spacing in the short-period pattern: from zero to 1300 nucleotides in one case and from 200 to 1600 in the other. A solution using a narrow range of spacings (not shown) gives a slightly higher root-mean-square deviation, but the difference is not significant. The average short-period

spacing of the repeated sequences is 940 nucleotides in the solution that has an additional long-period component and 1190 for the case in which only the short-period component is included. It can be concluded that the average spacing of the short-period fast fraction interspersed repeated sequences is about 1000 nucleotides with an uncertainty of about 200 nucleotides. There is no significant difference between this conclusion and the length of the single-copy sequence calculated for the short-period interspersion patterns of *Xenopus* and sea urchin (Davidson *et al.*, 1973; Graham *et al.*, 1974). In the DNA of most of the other species examined it has been possible to state that the spacing between the repetitive sequences was the length of the interspersed single-copy sequences. However, in this case the slow fraction is also interspersed with fast sequences. We indirectly know that the slow fraction is interspersed from the fact that no slow component is seen in the reassociation kinetics of 2000-nucleotide DNA as shown in Fig. 1. Thus, the sequences of the slow fraction are almost entirely adjacent to fast fraction sequences on fragments of 2000-nucleotide length. This observation is suggestive of an interesting pattern from a functional point of view. The complexity of the slow fraction is apparently immense as demonstrated in Table 4, and thus many similar fast sequences must be near different slow sequences.

There are two sources of information on the lengths of the dominant fast interspersed repeated sequences. These are hyperchromicity measurements and size determination after S1 digestion. The S1 digestion measurements shown in Fig. 5 indicate a mode value for fast fraction lengths of about 300 nucleotides. This number is remarkably similar to that observed in a number of other cases (Davidson *et al.*, 1974; Goldberg *et al.*, in press). The hyperchromicity measurements do not permit as accurate a determination, but within a factor of 2 they are consistent with this value.

Conclusion

We have shown that about two-thirds of the genome of the mollusc *Aplysia californica* is made up of a highly ordered pattern of interspersed repeated and single-copy DNA sequences. This pattern is quantitatively similar to those determined in detail for *Xenopus laevis* and *Strongylocentrotus purpuratus* DNAs and shows considerable similarity to the less closely examined patterns in five other species scattered over many phylogenetic orders (Goldberg *et al.*, in press). These observations indicate that closely spaced interspersion of repeated and single-copy DNA sequences is very widespread. A comparison of the patterns observed and a discussion of their phylogenetic generality is given in a later section. The general occurrence of this pattern of sequence organization indicates that it carries out a significant role. The following argument suggests that this interspersion pattern is important to the regulation of genetic activity: While regulatory processes occur at many levels of cellular metabolism, the control of transcription is probably fundamental to the establishment of the pattern of gene expression of each cell type or state. In turn, transcriptional control very likely depends on the recognition by regulatory molecules of specific DNA sequences adjacent to or within the structural gene regions of the DNA. Specific sequence recognition in other regions of the genome is probably involved in the synthesis of the regulatory molecules themselves and thus in the integration of the whole regulatory process. It appears likely that a great many of the DNA sequences involved in the specific recognition processes occur in more than one place in the genome and therefore are repetitive sequences. Clearly if the interspersed repetitive sequences do carry out a regulatory function such as the control of transcription, it would be reasonable to expect that they would be adjacent to most, if not all, structural genes.

This proposal has recently been tested, and the results are described in a later section of this Report.

Experimental Procedures

Maintenance of animals and growth of embryos. *Aplysia californica* was collected locally and maintained in filtered seawater at ambient temperature of 14°–18°C. Egg masses were collected within a day after deposition, chopped or broken into approximately 0.5 cm pieces, washed repeatedly with Millipore-filtered seawater, and cultured at 15° or 22°C in Millipore-filtered seawater (containing 30 µg/ml streptomycin sulfate and 50 units/ml penicillin) as a 10%–20% suspension with vigorous aeration. The egg masses were washed every few days in order to reduce contamination. Just before hatching (about 21 days at 15°C or 7–9 days at room temperature) the egg masses were washed repeatedly with Millipore-filtered seawater, briefly with several changes of distilled water, and with SEDTA (0.075 M NaCl, 0.05 M EDTA, pH 8.0), and frozen with powdered dry ice. Embryos were stored at –70°C until use for DNA isolation.

Preparation of DNA. Frozen embryos were pulverized with dry ice in a Waring blender, suspended in a minimum volume of SEDTA (about 2 ml final volume/gm egg mass), brought to room temperature, and the nuclei lysed by the addition of 1% SDS. When a reasonably clear suspension was obtained, an equal volume of SEDTA-saturated phenol was added, and the phases were gently mixed for 2–3 hr and then separated by centrifugation. The aqueous phase was briefly reextracted with phenol: IAC (1:1) and IAC (24:1 chloroform:isoamyl alcohol), and the DNA spooled from the final aqueous phase after the addition of 2 vol of 95% ethanol. DNA was further purified by reprecipitation, treatment with 25 µg/ml RNase A (chromatographically pure, Worthington Biochemical Corp.), 100 µg/ml predigested

pronase (B grade, CalBiochem), extraction with phenol and IAC, and reprecipitation. An average yield was 150 µg DNA/gm egg mass, using egg masses from smaller animals which have a considerably higher embryo content/gm. When using egg masses from larger individuals, the large amount of capsule material made an additional purification step desirable. In this case the DNA was bound to hydroxyapatite at 60°C after shearing and washed with 0.12 M PB. This step resulted in marked increases in the 260/230 nm and 260/280 nm absorbance ratios and in the optical hyperchromicity.

To prepare radioactively labeled DNA, 5–6 day embryos (15°C) were suspended in enough Millipore-filtered seawater (containing penicillin and streptomycin) to cover them, and the suspension was made 50 µCi/ml in ³H-thymidine (Nuclear Dynamics, 24 Ci/mM). The embryos were grown with aeration for 4 days, washed repeatedly, and frozen. The culture supernatant was checked for contamination by microorganisms by measuring the counts retained by a 0.45 µ Millipore filter and by precipitating an aliquot of the seawater with 5% TCA. These values calculated for the total culture supernatant were less than 0.1% and 0.05% of the counts incorporated into the isolated DNA. A typical specific activity attained was 2.2×10^5 cpm/µg.

Preparation of DNA fragments. DNA fragments of desired sizes were produced by homogenization in a Virtis 60K homogenizer as previously described (Britten *et al.*, 1974) or by preparative alkaline sucrose gradient centrifugation.

Measurement of fragment lengths. The single-stranded fragment length of DNA preparations was determined on isokinetic alkaline sucrose gradients (Noll, 1967): $V_{\text{mix}} = 9.84$ ml, $C_{\text{res}} = 43\%$ w/v, $C_{\text{flask}} = 16\%$ w/v in 0.1 N NaOH. Gradients were centrifuged at 41,000 rpm for 20–24 hr at 20°C in the Beckman SW41 rotor. The weight average fragment length was determined in duplicate or triplicate with reference to

two known markers, using the equations of Studier (1965).

DNA reassociation techniques. DNA samples were reassociated in 0.12 M PB at 60°C or 0.4 M PB at 64°C. Values in the latter solution were corrected to equivalent C_0t in 0.12 M PB at 60°C by multiplying by a factor of 4.9. The fraction of molecules containing duplex regions was determined by hydroxyapatite column chromatography (Britten *et al.*, 1974). When using long DNA fragments the double-stranded fraction was eluted with 0.12 M PB at 100°C in order to attain complete recovery.

The fraction of base pairs in duplex in a reassociated DNA sample was quantitated by means of single-strand-specific S1 nuclease (Ando, 1966; Vogt, 1973). DNA samples to be assayed by this method were reassociated in 0.3 M NaCl, 0.01 M PIPES, pH 6.7, at 64°C, or in 0.15 M NaCl, 0.005 M PIPES at 60°C. After reassociation the reaction mixture was adjusted to final concentrations of 0.15 M NaCl, 0.005 M PIPES, 0.025 M sodium acetate, 0.1 mM ZnSO₄, pH 4.4. To this solution was added 0.05 vol of 0.5 M β -mercaptoethanol and sufficient S1 nuclease to remove all single-stranded DNA regions. The samples were digested for 45 min at 37°C, and the digestion was terminated by adjusting the samples to 0.12 M PB. Duplex material was then collected on hydroxyapatite.

The rate of DNA reassociation was monitored in some experiments by measuring the hypochromicity of denatured DNA samples at 260 nm in 0.12 M PB in a water-jacketed cell using an ACTA Mark III spectrophotometer (Beckman).

Agarose-50 chromatography. The size distribution of reassociated DNA duplexes was determined by agarose A-50 chromatography, using a column 2.2 × 100 cm. The gel bed was poured around a support of 6 mm glass beads. Samples were chromatographed in 0.12 M PB, using long native DNA and ³²PO₄³⁻ as exclusion and inclusion markers, respectively.

Optical melting. DNAs were melted in 0.12 M PB in water-jacketed cuvettes, and the hyperchromicity was monitored at 260 nm with an ACTA Mark III spectrophotometer modified for automatic data collection. Hyperchromicity was calculated according to the formula $H = (W - C)/(W - B)$; where H is hyperchromicity; C is the A_{260} at 60°C; W is the A_{260} at the highest temperature; and B is the A_{260} of the buffer.

DNA SEQUENCE ORGANIZATION IN THE GENOMES OF FIVE MARINE INVERTEBRATES

Robert B. Goldberg,¹ William R. Crain,²
Joan V. Ruderman,³ Gordon P. Moore,⁴
Thomas R. Barnett,⁵ Ratchford C. Higgins,⁶
Robert A. Gelfand,² Glenn A. Galau,²
Roy J. Britten,² and Eric H. Davidson²

This section briefly describes measurements of DNA sequence organization in the genomes of two molluscs, an arthropod, a nemertean worm, and a scyphozoan coelenterate. The work was mainly carried out during the 1974 Embryology Course at the Marine Biological Laboratory, Woods Hole, Massachusetts, and is fully reported elsewhere (Goldberg *et al.*, in press). The authors were among the trainees and staff on this course.

Experimental procedures applied in these studies were generally similar for all five DNAs. The methods used to study sequence organization were measurement of hydroxyapatite binding as a function of the fragment length after low C_0t renaturation, and measurement of the hyperchromicity and the single-strand-specific nuclease resistance of

¹Department of Biology, Wayne State University, Detroit, Michigan 48202.

²Division of Biology, California Institute of Technology, Pasadena, California 91125.

³Department of Biology, Massachusetts Institute of Technology, Cambridge, Massachusetts 02139

⁴Department of Biology, Syracuse University, Syracuse, New York 13210.

⁵Department of Biology, Yale University, New Haven, Connecticut 06520.

⁶Department of Biochemistry and Biophysics, University of California, Davis, California 95616.

those renaturation products. They have all been applied earlier and are extensively discussed in previous papers (Davidson *et al.*, 1973; Graham *et al.*, 1974; Davidson and Britten, 1973). Here we describe only the kinetics of reassociation of long and short fragments and the size of the single-strand-specific, nuclease-resistant fragments.

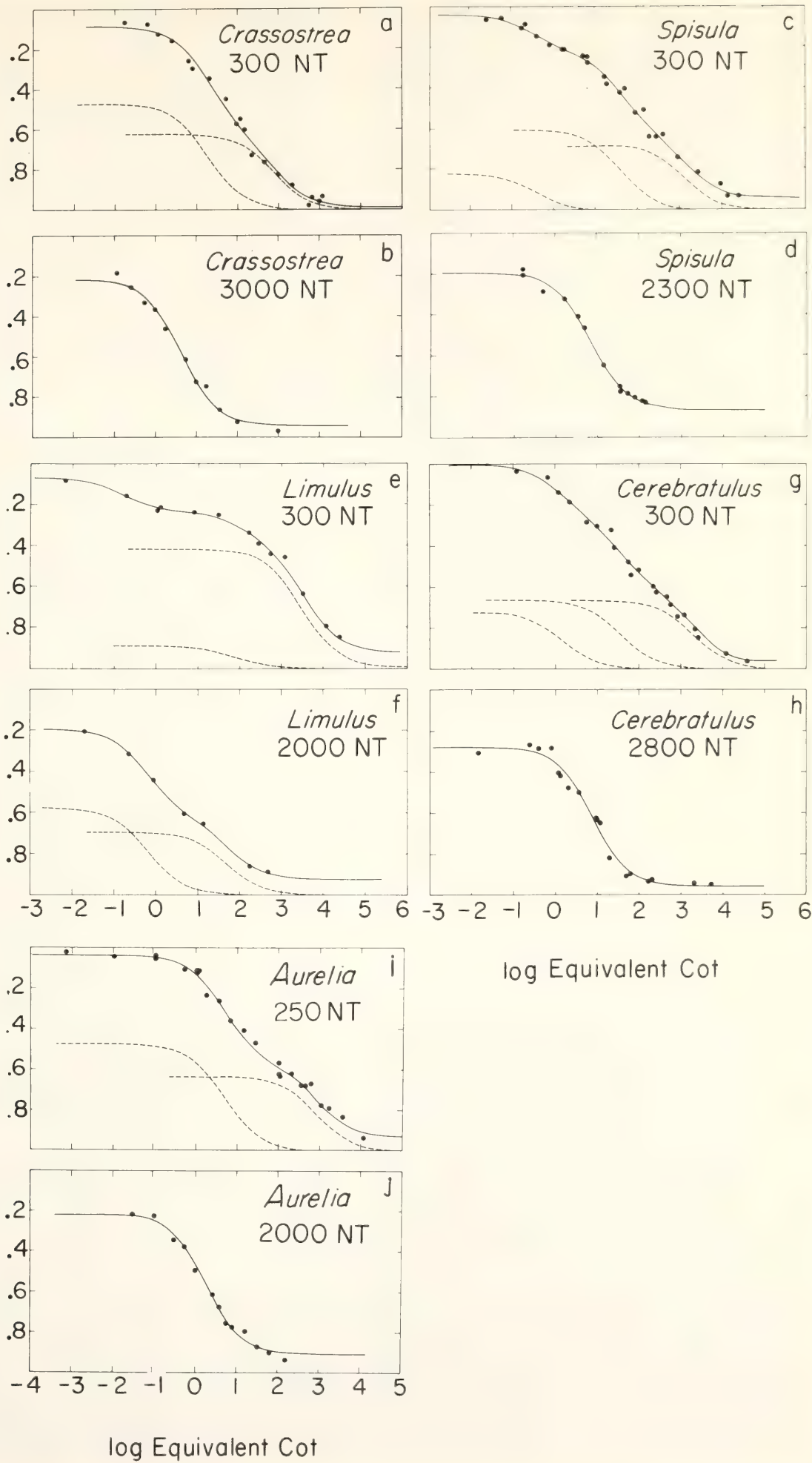
Measurements were made with the genomic DNA of the oyster (*Crassostrea virginica*), the surf clam (*Spisula solidissima*), the horseshoe crab (*Limulus polyphemus*), a nemertean worm (*Cerebratulus lacteus*), and a jellyfish (*Aurelia aurita*). Except for the jellyfish these animals belong to the protostomial branch of animal evolution, for which little information regarding DNA sequence organization has previously been available. The reassociation kinetics of short (250–300 nucleotide) and long (2000–3000 nucleotide) DNA fragments were studied by the hydroxyapatite method, and the results are assembled in Fig. 6. The comparison of the short-

fragment and long-fragment curves shows that in each case a major fraction of the DNA consists of single-copy sequences less than about 3000 nucleotides in length, interspersed with short repetitive sequences. The lengths of the repetitive sequences were estimated by optical hyperchromicity and S1 nuclease measurements made on renaturation products. In this brief report we show the results of the S1 nuclease measurements. The results shown in Fig. 7 show that all of the genomes studied include a prominent fraction of interspersed repetitive sequences about 300 nucleotides in length, as well as longer repetitive sequence regions.

The measurements with the DNA of all five of these animals indicate that they each have a pattern of sequence organization similar to that of the deuterostomes that have been examined in more detail. The comparison is extended and the significance discussed in the next section.

Fig. 6. Reassociation of DNA. DNA was reassociated in 0.12 M PB at 60°C. The fraction of the DNA fragments containing duplex regions was assayed by hydroxyapatite binding: (a) Reassociation of 300-nucleotide *Crassostrea* DNA. The solid curve is a two-component second-order least-squares fit to the data. The rate for the reassociation of the single-copy DNA fragments was held at that expected for 300-nucleotide long fragments for a genome of this size (0.69 pg). The dashed curves are the best choice of individual second-order kinetic components which can be summed to yield the total reaction. (b) Reassociation of 3000-nucleotide long *Crassostrea* DNA. The curve is a single-component least-squares fit to the data. (c) Reassociation of 300 nucleotide long *Spisula* DNA. The solid curve is a least-squares fit of three second-order kinetic components to the data. The dashed curves show the individual second-order kinetic components. The rate of the single-copy reaction was held at that expected for the length of DNA fragments used and the *Spisula* genome size (1.2 pg). (d) Reassociation of 2300 nucleotide long *Spisula* DNA. The curve is a least-squares fit of a single second-order kinetic component to the data. (e) Reassociation of 300 nucleotide long *Limulus* DNA. Three components are resolved in a least-squares fit of second-order kinetic components to the data. The solid line is the summed reaction while the dashed lines describe the reassociation of the individual kinetic components. The rate of the single-copy component was held constant in this analysis at the value calculated from the *Limulus* genome size (2.8 pg) and the DNA fragment length. (f) Reassociation of 2000 nucleotide long *Limulus* DNA. Two second-order kinetic components were resolved by a least-squares fit to the data. The dashed curves describe the reassociation of these components; the solid curve describes the total reaction. (g) Reassociation of 300 nucleotide long *Cerebratulus* DNA. The solid curve is a least-squares fit including the three second-order kinetic components indicated by the dashed curves. The genome size (1.4 pg) and fragment length were used to predict the reassociation of the single-copy component, which was fixed in the solution portrayed. (h) Reassociation of 2800 nucleotide long *Cerebratulus* DNA. The curve is a least-squares fit of a single second-order kinetic component. (i) Reassociation of 250 nucleotide long *Aurelia* DNA. The curve is a least-squares fit to the data. Two second-order kinetic components are resolved and are indicated by the dashed curves. The resolved rate of the slowest, the single-copy DNA, matches that expected for the fragment length and the *Aurelia* genome size (0.73 pg). (j) Reassociation of 2000 nucleotide long *Aurelia* DNA. The curve describes a single second-order kinetic component fit to the data by least squares.

Fraction of DNA Fragments bound to hydroxyapatite



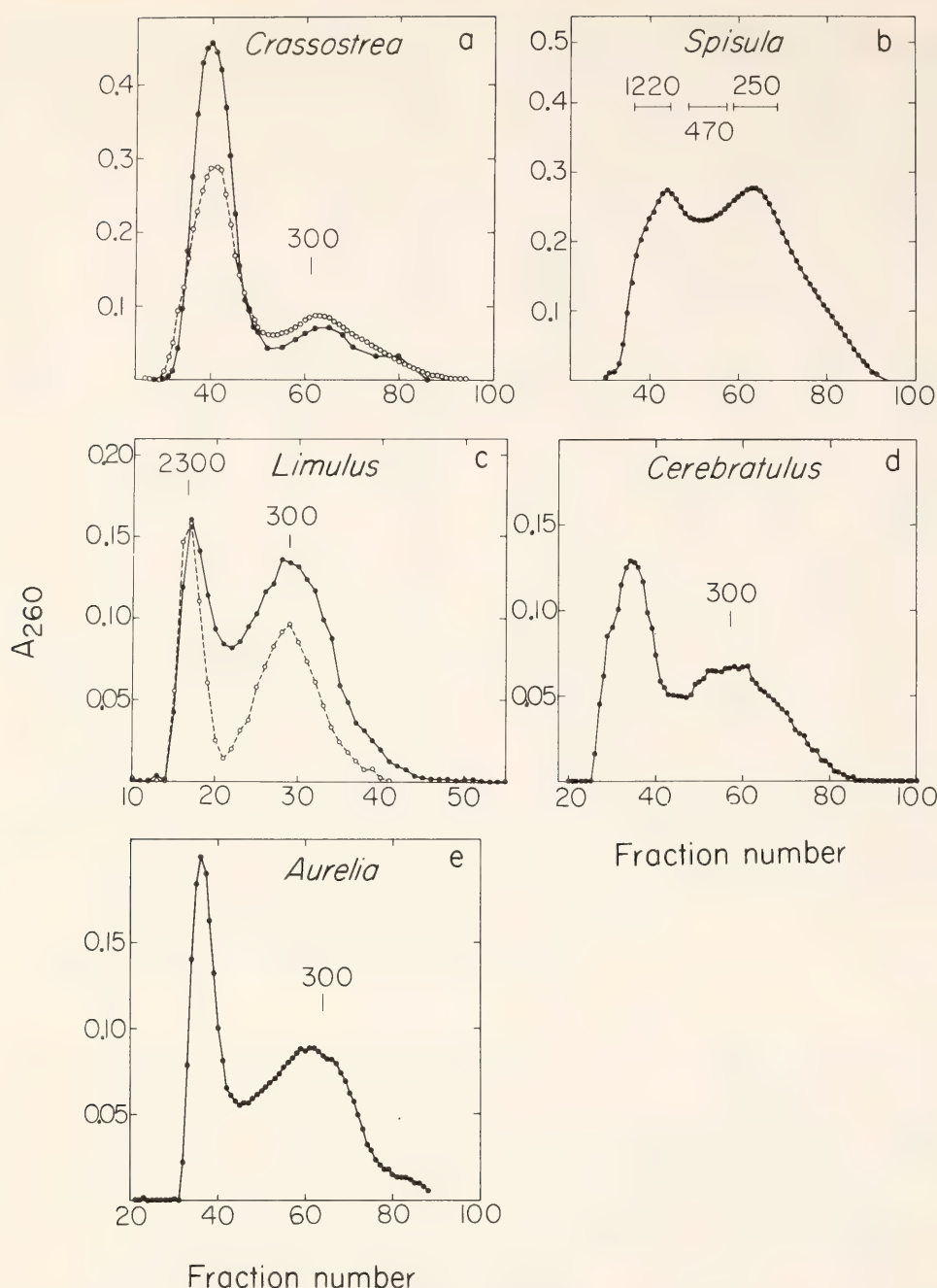


Fig. 7. Estimation of repetitive sequence length by Biogel A-50 chromatography: (a) 3000 nucleotide long *Crassostrea* DNA was reassociated to C_0t s of 20 and 138 and treated with S1 nuclease. The enzyme resistant DNA duplexes (41% and 57% of the total DNA at C_0t s 20 and 138, respectively) were isolated by Sephadex G-100 chromatography. These were then chromatographed on a calibrated Biogel A-50 column in 0.12 M PB. The position of a 300 nucleotide long DNA standard is indicated. Open circles, C_0t 20 duplexes; solid circles, C_0t 138 duplexes. (b) 2300-nucleotide long *Spisula* DNA was reassociated to a C_0t of 78 and then treated with single-strand-specific S1 nuclease. The enzyme-resistant repetitive DNA duplexes (20.5% of the total DNA) were isolated by hydroxyapatite chromatography. The resistant DNA was chromatographed on a calibrated Biogel A-50 column in 0.12 M PB. Pooled portions of the fractions indicated were sized independently by alkaline sucrose gradient centrifugation. The average single-strand nucleotide lengths of these pooled fractions are shown on the figure. Estimates of the size of individual fractions are listed in Table 4. (c) 2000 nucleotide long *Limulus* DNA was reassociated to C_0t 20. The reaction mixture was then treated with S1 nuclease and the resistant repetitive duplexes were isolated on hydroxyapatite. The duplexes (26% of the total DNA) were passed over a Biogel A-50 column in 0.12 M PB which had been calibrated in a previous run with 300 and 2300 nucleotide long double-strand DNA fragments. Solid circles, C_0t 20 S1-resistant DNA duplexes; open circles, 300 and 2300 nucleotide long DNA duplex standards. (d) *Cerebratulus* DNA 2800 nucleotides in length was incubated to C_0t 10 and the mixture treated with S1 nuclease. The enzyme-resistant duplexes (27% of the total DNA) were isolated by Sephadex G-100 chromatography and applied to a calibrated Biogel A-50 column run in 0.12 M PB. The position

COMPARATIVE ASPECTS OF DNA ORGANIZATION
IN METAZOA

Eric H. Davidson, Glenn A. Galau, Robert C.
Angerer, and Roy J. Britten

Transcription level control in animal genomes probably depends on the organization of sequences in the DNA. Study of sequence organization in animal DNA has been stimulated by the discovery of highly ordered patterns of sequence arrangement. Sufficient data are now available to permit significant comparisons across a wide phylogenetic area.

We are now aware of two distinct forms of DNA sequence organization. One of these is typified by the alternating interspersion of repetitive and nonrepetitive sequences demonstrated first for *Xenopus* DNA. For ease of communication we refer to this as "the *Xenopus* pattern." This form of sequence organization is characterized by single-copy sequence lengths of about 800 to several thousand nucleotides, with a large fraction of the single-copy sequence less than 1500 nucleotides in length. The single-copy sequences are terminated by repetitive sequence elements which themselves are typically only about 300 nucleotides long. Many diverse experimental approaches have been utilized in deriving the *Xenopus* pattern, including hydroxyapatite binding experiments, S1 nuclease and hyperchromicity measurements, kinetic studies, and electron microscope observations of renatured DNA (Davidson, Hough, Amenson, and Britten, 1973; Davidson *et al.*, 1974; Chamberlin, Britten, and Davidson, 1975).

A distinctly different pattern of sequence organization has been found in

Drosophila DNA. Here middle repetitive sequences are of an average length of 5600 nucleotides, though about 10% (only 2%–3% of the total DNA) are 500 nucleotides or less. The most fundamental difference, however, is in the length of single-copy sequence elements, which appear to extend for at least 10,000 nucleotides on the average without interruption by repetitive sequences (Manning, Schmid, and N. Davidson, 1975). These conclusions are based primarily on electron microscope data but are supported as well by hydroxyapatite binding studies which confirm the relative absence of sequence interspersion within a distance less than 2500 nucleotides. Pearson and Bonner (unpublished data) have carried out hyperchromicity measurements on renatured, middle repetitive *Drosophila* DNA, and obtained results in accordance with expectation for repetitive sequences which are much longer than a few hundred nucleotides. Furthermore only long repetitive sequences (>2000 nucleotides) lacking internal repetition have so far been identified in the experiments of Wensink, Finnegan, Donelson, and Hogness (1975). These workers have clonally replicated and characterized randomly chosen fragments of *Drosophila* DNA. Additional corroboration of the absence or relative scarcity of short interspersed repeats in *Drosophila* DNA derives from studies carried out in our laboratory (Crain, Eden, Davidson, and Britten, unpublished data). An earlier report that *Drosophila* DNA has essentially the same form of sequence organization as *Xenopus* DNA (Wu, Hurn, and Bonner, 1972), appears to have overestimated the quantity of short repetitive sequence elements. Though it remains

of a 300 nucleotide long DNA duplex standard run previously on the same column is shown. (e) Native *Aurelia* DNA approximately 10,000 nucleotides in single-strand length was reassociated to a C_0t of 14. The reaction mixture was treated with S1 nuclease, and the enzyme-resistant repetitive duplexes (22% of the total DNA) were isolated from the digest by hydroxyapatite. These duplexes were denatured in 0.12 M PB by boiling and then rapidly cooling in 4% formaldehyde. The column was run in 0.12 M PB in 4% formaldehyde. Also indicated is the relative position of a previously run, denatured 300-nucleotide-long DNA standard.

possible that such repeats exist in *Drosophila* DNA, they would have to be unusually divergent to have escaped detection by the usual procedures. It now appears that the *Drosophila* and *Xenopus* models of genomic organization are basically different.

Phylogenetic Considerations

A major object of the work described above has been expansion of present knowledge of sequence organization in order that the phylogenetic distribution of each form of sequence organization may be appreciated. This object has been accomplished, since it is now clear that the *Xenopus* form of sequence organization occurs in most major branches of the phylogenetic tree.

In Fig. 8 we present a phylogenetic tree showing the evolutionary position of animals whose genomes have been studied. Organisms whose DNA has been subjected to relatively extensive investigation are underlined. For the other organisms listed, partial data exist, in each case suggesting the presence of interspersed repetitive sequence elements only a few hundred nucleotides long. References are given in the legend to Fig. 8, as space does not permit a further review of these data here.

The inference suggested by Fig. 8 is that the *Xenopus* pattern of sequence organization stems from a remote evolutionary stage antedating the divergence of the Metazoa. Thus the DNA of a coelenterate (*Aurelia*) is organized in the same way as are the DNAs of higher animals. Similarly the genomes of both protostomial and deuterostomial animals, including an extremely primitive acoelomate protostome (*Cerebratulus*), are organized along the lines of the *Xenopus* pattern. The protostomial and deuterostomial evolutionary lines diverged before the beginning of the Cambrian fossil record. A possible interpretation is that interspersed sequence organization of the *Xenopus* type provided part of the basis for the evolution of multicellular

forms. This would be true, for example, if sequence interspersion is required for the regulation of gene activity which underlies cell differentiation, as suggested earlier (Britten and Davidson, 1969, 1971).

Summary of Sequence Organization Data and Some Generalizations

Table 5 collates key data from sequence organization studies on organisms whose generic names are underlined in Fig. 8. Several general conclusions can be drawn from this table:

1. *Genomic complexity.* There is no simple correlation between the sequence complexity of the genome and the apparent biological complexity of the animal. We have made this point earlier (Britten and Davidson, 1971) in comparing complexities of amphibian genomes of diverse sizes. However, it is now clear that the true genomic sequence complexity cannot be appreciated until the sequence interspersion pattern of the DNA is known so that the actual content of single-copy sequence (rather than the fraction of fragments bearing only single-copy sequence) can be measured. As can be seen in Table 5 the fraction of the genome that is single copy ranges around 70%. However, the complexity of the oyster genome, 3.8×10^8 nucleotide pairs, is only 46% of that of the surf clam genome, 8.2×10^8 nucleotide pairs; yet both belong to the same molluscan class, Bivalvia. The complexity of the *Aurelia* genome is almost six times that of *Drosophila*, and yet *Aurelia* totally lacks organ systems. The complexity of the *Cerebratulus* genome is greater than that of *Aplysia* (a gastropod mollusc), or *Drosophila*, and yet the acoelomate nemertean would appear to be a less biologically complex animal in terms of construction, organ systems, developmental pathways, and capabilities. Single-copy complexity is thus to be regarded as a measure of the *potential*, rather than the actual (i.e., utilized) genomic information content.

2. *Frequency of occurrence of repet-*

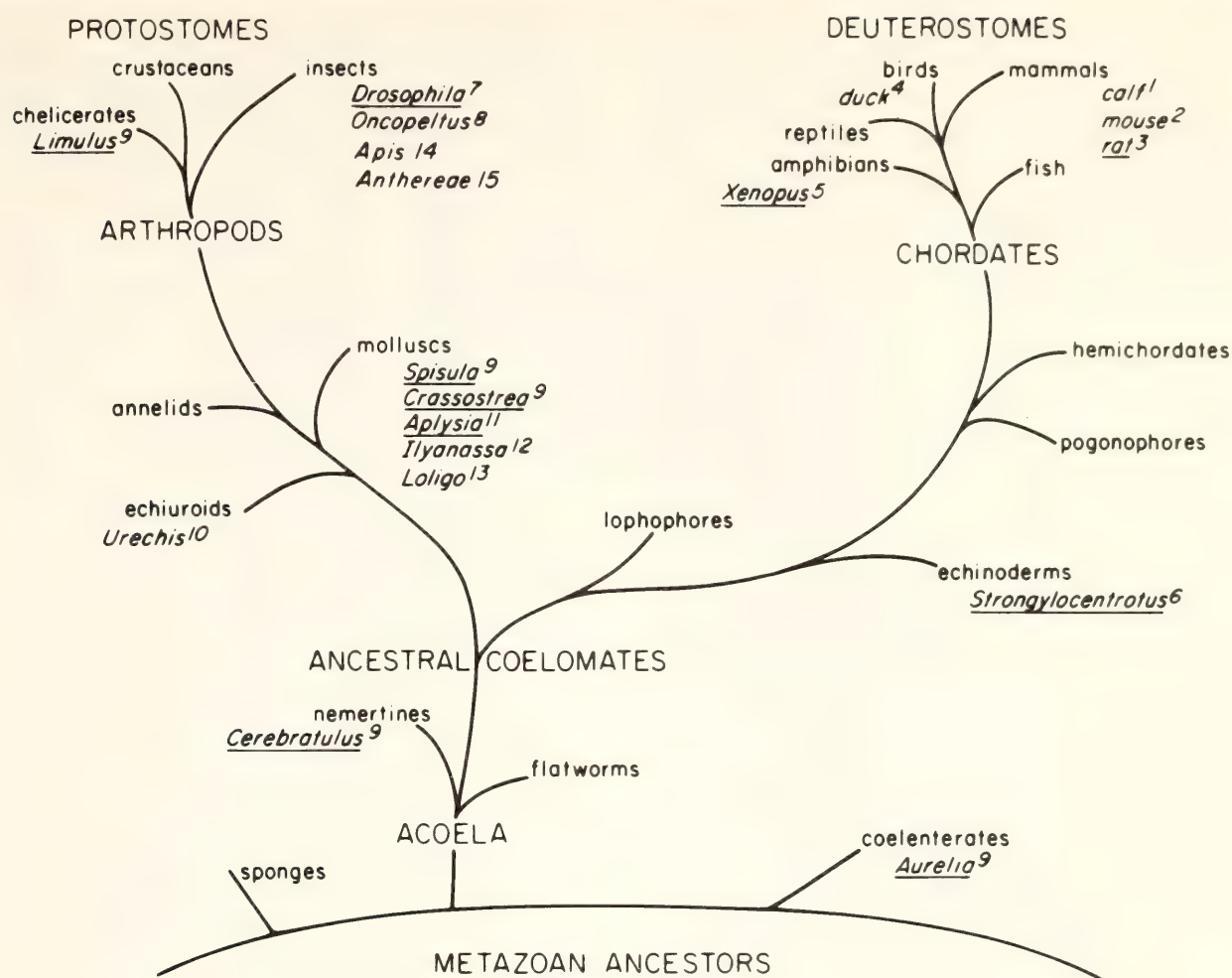


Fig. 8. Phylogenetic tree, essentially after Hyman (1940), showing positions of organisms for which information on genomic sequence organization exists. DNAs studied at least as extensively as those in the accompanying papers are underlined. Only generic or common names are given.

References:

- ¹ Britten and Smith, 1970; Britten, unpublished data.
- ² Rice, 1971a; Britten, 1972.
- ³ Rice, 1971a; Bonner *et al.*, 1974; Pearson, Wilkes and Bonner, unpublished data.
- ⁴ Bishop and Freeman, 1974; Bishop, personal communication.
- ⁵ Davidson *et al.*, 1973; Chamberlin *et al.*, 1975.
- ⁶ Graham *et al.*, 1974.
- ⁷ Manning *et al.*, 1975; Wu *et al.*, 1972; Wensink *et al.*, 1975.
- ⁸ Lagowski *et al.*, 1973.
- ⁹ Goldberg *et al.*, 1975.
- ¹⁰ Neufeld, Smith, Davidson, and Britten, unpublished data.
- ¹¹ Angerer, Davidson, and Britten, in preparation.
- ¹² Davidson *et al.*, 1971.
- ¹³ Galau, unpublished data.
- ¹⁴ Crain, unpublished data.
- ¹⁵ Efstratiadis, unpublished data.

itive sequences. A striking fact emerging from Table 5 is that most of the organisms listed possess a repetitive sequence class in which the sequences are present between 30 and 200 times per genome. Such components, which are apparent exceptions, may also exist in the organism. In addition most genomes include

sequences present 1000-4000 times. Much more highly repetitive frequency classes such as those found in some mammalian genomes, for example the 66,000 repeat class studied extensively in cow DNA by Britten and Smith (1970), occur only sporadically, or if present generally are in very small quantity.

TABLE 5. Approximate Parameters of the Sequence Content and Sequence Organization for Fourteen Animal DNAs

1	2	3	4			5	6	7
Organism	Genome Size (pg)	Fraction of DNA in Non-repetitive Sequence	Repetitive Frequency Classes Observed by Reassociation Kinetics (copies per genome)			Fraction of Total Repetitive DNA in 200-400 Nucleotide Long Sequence Elements	Fraction of Single-Copy DNA Interspersed with Repetitive DNA in 2000-3500 Nucleotide Fragments	References
			<10 ³	10 ³ -10 ⁴	10 ⁴ -10 ⁶			
<i>Spisula</i> (clam)	1.2	0.75	30			0.60	>0.70	Goldberg <i>et al.</i> , 1975
<i>Crassostrea</i> (oyster)	0.69	0.60	40	3700		0.35	>0.75	Goldberg <i>et al.</i> , 1975
<i>Aplysia</i> (sea hare)	1.8	0.55	85	4600	7,000,000	0.60	>0.80	Angerer <i>et al.</i> , 1975
<i>Loligo</i> (squid)	2.8	0.75	100	4100	230,000	0.60	>0.85	Galau, unpublished
<i>Limulus</i> (horseshoe crab)	2.8	0.70	50	2000		0.75	>0.70	Goldberg <i>et al.</i> , 1975
<i>Cerebratulus</i> (nemertean worm)	1.4	0.60	40	1200		0.55	>0.70	Goldberg <i>et al.</i> , 1975
<i>Aurelia</i> (jellyfish)	0.73	0.70	180			0.60	>0.80	Goldberg <i>et al.</i> , 1975
<i>Strongylocentrotus</i> (sea urchin)	0.89	0.75	100	1500		0.75	>0.70	Graham <i>et al.</i> , 1974; Britten, Graham, Eden, and Davidson, in preparation
<i>Xenopus</i> (clawed toad)	2.7	0.75	100	2100	290,000	0.75	>0.70	Davidson <i>et al.</i> , 1973, 1974; Chamberlin <i>et al.</i> , 1975
<i>Rattus</i> (rat)	3.2	0.75	70	2000		?	>0.65	Bonner <i>et al.</i> , 1974; Pearson, Gottsfield, Wilkes, and Bonner, unpublished
<i>Bos</i> (cow)	3.2	0.65	?	?	60,000 1,000,000	0.55	>0.65	Britten and Smith, 1970; Britten, unpublished
<i>Drosophila</i> (fruit fly)	0.12	0.75	35			0.10	none observed	Manning <i>et al.</i> , 1975; Crain, Eden, Davidson, and Britten, unpublished; Pearson and Bonner, unpublished
<i>Apis</i> (honey bee)	0.3-0.4	0.9	not determined			?	none observed	Crain, Britten, and Davidson, unpublished
<i>Anthereae</i> (moth)	0.8	0.5-0.6	15	1600		0.12-0.15	>0.75	Efstathiadis, Crain, Britten, Davidson, and Kafatos, unpublished

Low and moderate repetition frequency sequences could thus be regarded as a basic requirement though present data suggest that some exceptions, such as cow DNA, may exist. There is also evidence for the interspersion with single-copy DNA of either or both classes of repetitive sequence in various genomes. The usual interspersion experiments tend to detect only the more highly repetitive interspersed sequences, since if less repetitive sequence elements are present on the same fragments they will be carried along at the faster rate.

3. *Repetitive sequence length.* Though all organisms listed contain some repetitive sequence in the 200–400 nucleotide range, the proportion varies sharply. Except for *Drosophila*, all show a peak in the repetitive sequence length distribution at about 300 nucleotides. The quantity of short repetitive sequences in the genome always suffices to account for the amount of interspersion of single-copy DNA observed (Goldberg *et al.*, 1975). The longer repetitive sequences terminate eventually and thus are also interspersed with single-copy DNA, provided one considers a great enough length. However, it is obvious that the far more numerous 300 nucleotide repetitive sequences account for most of the interspersed repeats. The fraction of the repetitive DNA in long middle repetitive sequence is not correlated in any simple way with the genome size. For example, in the small oyster genome about 65% of the repetitive sequence is found in long sequence elements, while in *Spisula* DNA, which has a genome almost twice as large, only 40% of the repetitive sequences are long. However, the absolute quantity of short interspersed repetitive sequence appears to be correlated with the quantity (complexity) of single-copy DNA.

4. *Correlation between mismatch and repetitive sequence length.* In the DNAs of *Xenopus* (Davidson *et al.*, 1974), *Spisula* (Goldberg *et al.*, 1975), calf (Britten, unpublished data), and sea urchin (Britten, Graham, Eden, and Davidson,

in preparation), it has been found that longer repetitive sequences melt with higher T_m 's. This is true even after correction for the effect of duplex length on melting temperature. We conclude that there is a correlation, as yet not understood, between repetitive sequence organization and sequence divergence during evolution.

5. *Length of interspersed single-copy sequence elements.* As Table 5 shows, in all of the organisms studied (except *Drosophila*) over 70% of the single-copy DNA is included in sequence elements of 3000 nucleotides or less, terminated by repetitive sequence. In no case are we able to show that all the nonrepetitive sequence is included in this category, though of course it is possible that this is actually the case and technical problems have simply interfered with the demonstration. Such problems might include strand scission and interspersion of sequences of very low repetitive frequency or highly divergent repetitive sequences. We have recently reported that in the sea urchin genome the single-copy sequence contiguous to the interspersed repetitive sequence includes most or all of those structural genes which are active in embryogenesis (Davidson, Hough, Klein, and Britten, 1975). This may also be true for other organisms whose DNA is organized similarly. The observed single-copy sequence element length distribution would fit well with this view, since a small fraction of structural genes are longer than 3000 nucleotides while most are shorter (the modal size is probably about 1200 nucleotides). Rationalization of sequence organization in such terms, however, awaits another crucial item of evidence. This is knowledge of the fraction of the total single-copy sequence which is present in functional structural genes.

The Xenopus and Drosophila Patterns of Sequence Organization.

Recently we have been examining the patterns of DNA sequence organization

in the DNA of a number of insects. As shown in Table 5, the honey bee appears not to have a detectable quantity of short interspersed repetitive sequences. However the wild silk moth *Anthereae pernyi*, which is also a holometabolous insect and therefore fairly closely related to both *Drosophila* and honey bee, has a pattern which is not detectably different from that of *Xenopus* DNA. It appears

that the *Drosophila* pattern is not limited to the Diptera but is not widespread. Studies of other Diptera are underway. Even without these results it is hard to avoid the suggestion that the *Drosophila* pattern is a relatively modern offshoot from evolutionarily older patterns which have led to the dominant *Xenopus* pattern observed in most modern species.

DNA SEQUENCE EXPRESSION STUDIED BY TRANSCRIPTION INTO RNA

SEQUENCE COMPLEXITY OF HETEROGENEOUS NUCLEAR RNA IN SEA URCHIN EMBRYOS

Barbara R. Hough, Michael J. Smith,
Roy J. Britten, and Eric H. Davidson

In this section we report a measurement of the sequence complexity of the rapidly labeled, heterogeneous nuclear RNA in sea urchin gastrulas. Sequence complexity is defined as the number of nucleotide pairs of diverse DNA sequence represented in the RNA. RNAs that are heterogeneous in sequence and that label rapidly and turn over rapidly (hnRNA) are known to be synthesized actively in sea urchin embryo nuclei (Aronson and Wilt, 1969; Brandhorst and Humphreys, 1971, 1972; Smith *et al.*, 1974). Messenger RNA synthesis also occurs in these cells. The sequence complexity of polysomal messenger RNA extracted from embryos of the gastrula stage has recently been measured and found to be about 1.7×10^7 nucleotide pairs, the equivalent of about 14,000 different structural genes of a median length of 1200 nucleotide pairs (Galau, Britten, and Davidson, 1974). The opportunity thus exists to compare the complexity of the nuclear RNA with that of the messenger RNA being translated in the same cells. A question of considerable interest and one which has received a great deal of attention is whether the mRNA is synthesized as a separate class of molecules or is derived from a portion

of each hnRNA molecule as proposed for example by Scherrer *et al.* (1970) and Soeiro and Darnell (1970). The present hnRNA complexity measurement was undertaken to provide further quantitative insight into the comparison between hnRNA and mRNA. The only direct measurement of hnRNA and mRNA complexity in the same cells available at this writing is that of Getz *et al.* (1975), who found that nuclear poly-A-containing RNA is at least five times more complex than polysomal poly-A RNA in Friend cells. A number of previous observations also have suggested that hnRNA complexity might be higher than mRNA complexity (see review by Lewin, 1975). Here we show that hnRNA is more than ten times as complex as the polysomal mRNA in the *Strongylocentrotus purpuratus* gastrula.

The Complexity Measurement

The sequence complexity of the nuclear RNA was determined by measuring the amount of nonrepetitive ^3H -DNA complementary to the RNA in RNA excess hybridization reactions. The kinetics of the reaction provides an estimate of the concentration of the reacting sequences in the nuclear RNA preparation. Since the concentration of unhybridized RNA remains virtually constant, RNA-DNA duplex formation follows

pseudo first-order kinetics and can be described by the equation

$$D/D_0 = e^{-kR_0t} \quad (1)$$

where D is the concentration of unhybridized DNA, D_0 is the initial DNA concentration, k is the rate constant, R_0 is the RNA concentration, and t is time. As R_0t (RNA C_0t) increases, the fraction of the DNA which is hybridized approaches a constant value.

The ^3H -DNA fraction used in these experiments is mainly nonrepetitive (Galau *et al.*, 1974). Sheared, labeled DNA was fractionated on hydroxyapatite after incubation to C_0t 200, and the single-stranded portion was incubated again to C_0t 200. The ^3H -DNA remaining nonreassociated after the second incubation was used for the complexity measurement. The upper curve in Fig. 9 (dotted line) shows the reassociation of the ^3H -DNA preparation with whole 450-nucleotide sea urchin DNA (data are presented in Galau *et al.*, 1974). The second-order rate constant is $0.91 \times 10^{-3} \text{ l } M^{-1} \text{ sec}^{-1}$. This is close to the expected rate of reaction of the nonrepetitive sequence component for fragment lengths of 200–300 nucleotides (see "Experimental Procedures"). The small fragment length of this preparation probably accounts for its 25% nonreactability. The reassociation kinetics indicate that at least 95% of the reactable ^3H -DNA consists of nonrepetitive sequences.

To determine the fraction of the nonrepetitive ^3H -DNA complementary to the hnRNA, the hybridization mixtures were incubated to increasing RNA C_0t s. The quantities of ^3H -DNA included in the reactions were kept as low as possible in order to minimize DNA self-reaction. The fraction of ^3H -DNA in duplexes with complementary strands of ^3H -DNA and with RNA was measured for each sample by binding to hydroxyapatite, as described in "Experimental Procedures." Data from these experiments are listed in Table 6 along with the calculated fraction in hybrids, which is

also displayed in Fig. 10. A curve of the form of Equation 1 was fitted to the fractions hybridized by a least-squares method. The rate constant is $1.11 \times 10^{-4} \text{ l } M^{-1} \text{ sec}^{-1}$.

The best least-squares solution indicates that the extent of the reaction is 12.4% of the ^3H -DNA hybridized (Fig. 10). This level is reached at an RNA C_0t of about 40,000. However, at very high RNA C_0t s the data are sufficiently scattered so that the termination estimate is not precise. At low RNA C_0t s (400 and 600 in Table 6), 1.7% of the ^3H -DNA is bound. As shown below, this can be assumed to be due to a small amount of repetitive sequence contamination in the nonrepetitive tracer. Thus the hybridi-

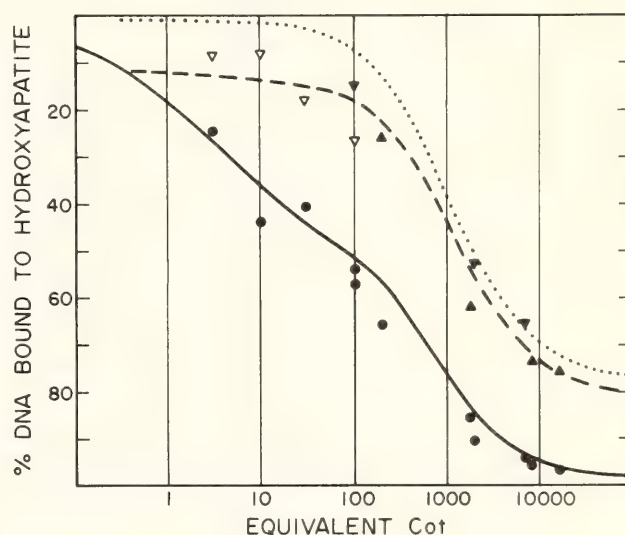


Fig. 9. Reassociation with whole DNA of nonrepetitive ^3H -DNA recovered from hybridization with nuclear RNA. The upper curve (dotted line) describes the reassociation of nonrepetitive ^3H -DNA with a 10,000 fold excess of 450-nucleotide long whole DNA. This curve is the best least-squares second-order fit to data presented in Galau *et al.* (1974). The rate constant for this reaction is $0.91 \times 10^{-3} \text{ l } M^{-1} \text{ sec}^{-1}$. Open and solid triangles show the results with three different preparations of previously hybridized ^3H -DNA. These data fit a second-order reassociation curve (dashed line) with an imposed rate constant of $0.91 \times 10^{-3} \text{ l } M^{-1} \text{ sec}^{-1}$ corresponding to the rate constant of the reaction of this ^3H -DNA preparation with whole DNA. The solid circles show the reassociation of the whole DNA which was reacted with the ^3H -DNA extracted from RNA-DNA hybrids. The curve (solid line) is a least-squares fit to previously published data (Galau *et al.*, 1974; Smith *et al.*, 1974; Graham *et al.*, 1974) including more than 70 points (data not reproduced here).

TABLE 6. Hybridization of Nonrepetitive ³H-DNA with Nuclear RNA

RNA Preparation	RNA C ₀ t	³ H-DNA C ₀ t	% ³ H-DNA in Duplex		
			Total	DNA-DNA	DNA-RNA
a	400	0.75	3.3	1.6	1.7
	943	8.8	3.8	1.4	2.4
	1032	2.3	5.4	1.6	3.8
	1500	14.4	9.3	5.8	3.5
	3036	7.1	7.7	3.2	4.5
	3967	3.8	6.0	1.6	4.4
	4000	7.5	7.0	1.8	5.2
	8000	15.0	9.9	2.5	7.4
	10,000	18.7	12.1	4.8	7.3
	10,022	23.4	12.1	2.7	9.4
	14,400	17.2	13.0	3.2	9.8
	14,583	27.2	16.4	5.5	10.9
b	600	3.0	2.4	0.7	1.7
	1608	13.4	5.7	(2.0)	3.7
	3135	26.0	6.7	(2.5)	4.2
	4717	39.0	9.3	(3.5)	5.8
	6205	52.0	10.8	(4.0)	6.8
	8516	71.0	13.3	(5.0)	8.3
	9410	78.0	14.6	(6.0)	8.6
	10,200	51.7	14.6	5.6	9.0
	20,604	53.0	16.8	(4.0)	12.8
	32,966	172.0	19.0	8.4	10.6
	33,916	85.0	25.3	14.1	11.2
	38,485	96.0	17.6	7.0	10.6
	40,188	103.0	24.0	12.0	12.0
	47,495	247.0	25.5	11.9	13.6
	48,634	119.0	23.0	10.0	13.0
	50,000	125.0	21.2	9.3	11.9

* DNA-DNA duplex values in parentheses were estimated from control data obtained from separate measurements of nonrepetitive ³H-DNA self-reassociation (Galau *et al.*, 1974) rather than by direct measurements made on the RNA-DNA hybridization mixtures (see "Experimental Procedures"). Counts in DNA-RNA hybrids were in the range 150-1500 per sample.

zation reaction described by the curves of Fig. 10 accounts for 10.7% of the total ³H-DNA.

Nuclear RNA Hybridizes with Nonrepetitive ³H-DNA

The ³H-DNA used to measure RNA complexity in the experiments reported here reacts as a nonrepetitive component with whole DNA (Galau *et al.*, 1974, and Fig. 9). However, repetitive sequences present as low-level contaminants in the ³H-DNA preparation are probably also present in the hybridized fraction, particularly since sea urchin nuclear RNA is known to contain repetitive

sequence transcripts (Smith *et al.*, 1974). To test for this possibility, ³H-DNA was incubated with RNA to an RNA C₀t of 10,000, and the hybridized ³H-DNA was extracted. This was done by eluting the DNA-DNA and DNA-RNA duplexes bound to hydroxyapatite and removing the RNA from the DNA-RNA hybrids by low-salt RNAase treatment, as described in "Experimental Procedures." In a second passage over hydroxyapatite the single-stranded ³H-DNA released by RNAase was recovered as the unbound fraction.

The previously hybridized ³H-DNA was reassociated with whole sea urchin DNA in the experiments shown in Fig. 9.

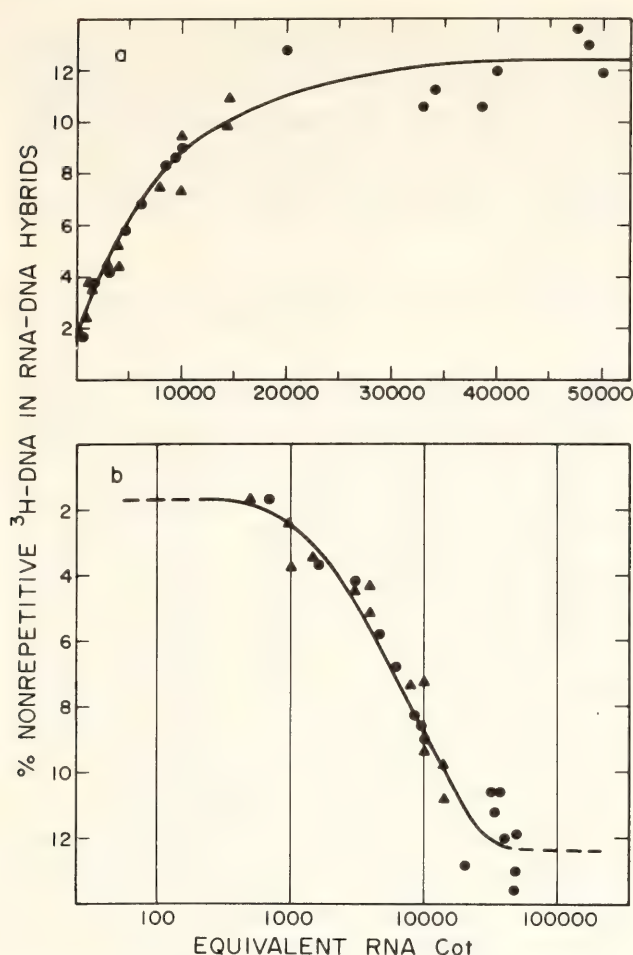


Fig. 10. Hybridization of nonrepetitive ^3H -DNA with nuclear RNA. Data are listed in Table 6. Nuclear RNA preparations are symbolized as follows: preparation a, solid triangles; preparation b, solid circles. Two methods of presenting the same data are shown in 10a and 10b. The pseudo first-order curves are calculated according to Equation 1. Solid lines represent the least-squares solution for the data. The rate constant for this fit is $1.11 \times 10^{-4} \text{ l M}^{-1} \text{ sec}^{-1}$. The hybridization reaction extends from 1.7% to 12.4% of the nonrepetitive ^3H -DNA. The extent of the observed reaction is 10.7% of the ^3H -DNA in the experiment. RNA equivalent C_0t on the abscissa is RNA C_0t corrected for reassociation in salt concentrations higher than 0.18 M Na^+ .

The rate of the principal part of this reaction is consistent with the rate of reaction of nonrepetitive sequences in whole DNA (dashed line, Fig. 9), which means that most of the hybridized ^3H -DNA is itself nonrepetitive sequence. 67% of the previously hybridized ^3H -DNA takes part in the nonrepetitive phase of the reaction, and 20% is unable to react. The remaining 13% of the ^3H -DNA extracted from the DNA-RNA

hybrids reacts with whole DNA at lower C_0t s. The ^3H -DNA reassociating with whole DNA at C_0t s ≤ 50 (Fig. 9) is to be considered a repetitive sequence fraction present in the hybridized ^3H -DNA which has reacted with repetitive transcripts in the nuclear RNA. This portion of the ^3H -DNA is the same fast-hybridizing DNA as the fraction which binds by RNA C_0t 400 in the RNA excess reactions of Fig. 10 since the 1.7% initial binding calculated in the least-squares solution equals about 13% of the ^3H -DNA bound at high RNA C_0t . Therefore, our best estimate of the extent of nonrepetitive sequence representation in the hnRNA is 10.7% of the ^3H -DNA.

It is now possible to calculate the minimum sequence complexity of the hnRNA. Allowing for 75% terminal reactivity of the nonrepetitive ^3H -DNA, and assuming single-strand transcription, at least $(10.7 \times 2)/0.75$ or 28.5% of the nonrepetitive complexity of the genome is expressed in the nuclear RNA. The nonrepetitive complexity of the sea urchin DNA is 6.1×10^8 nucleotide pairs, 75% of the haploid genome size (Graham *et al.*, 1974), which is $8.9 \times 10^{-13} \text{ g}$ (Hinegardner, 1968). It follows that the sequence complexity of the hnRNA is at least 1.74×10^8 nucleotides.

Proportion of Nuclear RNA Driving the Reaction

Since we know the complexity of the hnRNA and the rate constant from the least-squares solution shown in Fig. 10, we can calculate the fraction of the RNA which drives the hybridization reaction. To do this, we compare the observed rate of reaction (k_{obs}) with the rate expected if all of the RNA consisted of the complex sequences driving the reaction (k_{exp}). The fraction of RNA driving is then $k_{\text{obs}}/k_{\text{exp}}$.

The expected reaction rate for 220-nucleotide tracer ^3H -DNA with an excess of 800-nucleotide RNA of complexity 1.74×10^8 nucleotides is $4.41 \times 10^{-3} \text{ l M}^{-1} \text{ sec}^{-1}$. For this calculation the com-

plexity of *E. coli* DNA is taken as 4.2×10^6 nucleotide pairs, and for 450-nucleotide fragment length and standard conditions the reassociation rate is $0.25 \text{ l } M^{-1} \text{ sec}^{-1}$. For an RNA-driven reaction the rate constant is twice that of the DNA self-reaction of equivalent complexity, since the one strand representing any given sequence is present twice as often in RNA as in DNA per unit mass. The basic rate of RNA-DNA hybrid formation in an RNA-driven reaction is at least 80% of that of DNA-DNA duplex formation and may be 100% [Hutton and Wetmur, 1973; also shown in our laboratory in experiments of the same design as those reported here but carried out with ϕ X174 nucleic acids (Galau, Britten, and Davidson, in preparation)]. For the present calculation we assume that the DNA-RNA nucleation rate equals the DNA-DNA nucleation rate under the same conditions. The mean length of the RNA is about 800 nucleotides, and of the ^3H -DNA, 220 nucleotides. Recent studies with prokaryote nucleic acids (Galau, Britten, and Davidson, in preparation) have shown that the appropriate length correction for this case is the ratio of tracer (^3H -DNA) to driver (RNA) fragment lengths. The rate constant for the driver nucleic acid is calculated in relation to the *E. coli* complexity standard as usual, with a correction factor equal to the square root of the ratio of fragment lengths. Thus

$$k_{\text{exp}} = \frac{2 \times 0.25 \times 4.2 \times 10^6}{1.74 \times 10^8} \\ \times \left(\frac{800}{450} \right)^{1/2} \times \left(\frac{220}{800} \right) = 4.41 \times 10^{-3},$$

while

$$k_{\text{obs}} = 1.11 \times 10^{-4} \quad (\text{Fig. 10}).$$

Then

$$k_{\text{obs}}/k_{\text{exp}} = .025.$$

If it is assumed that the RNA-DNA nucleation rate is 80% of the DNA-DNA nucleation rate, the result becomes 0.031. Thus we find that 2.5%–3.1% of the nuclear RNA drives the hybridization reaction.

hnRNA is the High-Complexity Fraction

If only 2.5–3.1% of the RNA in the reaction mixtures drives the hybridization reaction with nonrepetitive ^3H -DNA, it cannot be assumed that the measured complexity belongs to the rapidly labeled (hnRNA) portion of the nuclear RNA rather than to some other nuclear RNA fraction. To investigate this question, nonrepetitive DNA was reacted with an excess of nuclear RNA in which the rapidly turning over hnRNA was labeled for 10 min to relatively high specific activity with ^{32}P . The hybridized RNA was assayed for increased ^{32}P specific activity compared to the ^{32}P specific activity of the whole nuclear RNA.

The results of these experiments are shown in Table 7. Here the ^{32}P specific activity of hybridized RNA sequences is significantly increased over the specific activity of the original preparation. Therefore the ^{32}P -labeled RNA sequences are hybridized with nonrepetitive DNA to a much greater extent (27.4–42.3 times more in these experiments) than unlabeled sequences. Essentially all the ^{32}P counts are incorporated in hnRNA, due to the rapid turnover of the latter fraction. The enrichment in ^{32}P cpm is seen at RNA C_0t 1000 as well as at C_0t 10,000, demonstrating that the same population of RNA molecules drives the reaction at low and high C_0ts . The increase in specific activity of the hybridized RNA compared to that of the total RNA extracted can be used as a measure of the fraction of total RNA which is able to hybridize with the nonrepetitive DNA, i.e., the fraction of the total RNA driving the hybridization reaction. This fraction is the inverse of the enrichment in ^{32}P specific activity,

TABLE 7. Rapidly Labeled RNA Is the Complex Component of Nuclear RNA ^a

	RNA C ₀ t 10,000	RNA C ₀ t 10,000	RNA C ₀ t 1000
Input RNA ³² P (10 min label)	9.03 × 10 ⁵	6.59 × 10 ⁵	9.45 × 10 ⁵
³ H (total)	6.01 × 10 ⁵	3.94 × 10 ⁵	7.73 × 10 ⁵
³ H-cpm hybridized ^b	6.4 × 10 ²	3.4 × 10 ²	1.6 × 10 ²
μg DNA hybridized ^c (percent of DNA)	0.17 (10.6)	0.09 (8.6)	0.04 (1.9)
³² P-cpm hybridized ^b	2.7 × 10 ⁴	1.54 × 10 ⁴	0.73 × 10 ⁴
³² P-specific activity of RNA hy- bridized cpm/μg	1.59 × 10 ⁵	1.70 × 10 ⁵	1.82 × 10 ⁵
³² P-specific activity in starting nuclear RNA preparation (cpm/μg) ^d	5.8 × 10 ³	4.5 × 10 ³	4.3 × 10 ³
Specific activity of input RNA/ Specific activity of hybridized RNA	0.036	0.027	0.024

^ahnRNA was labeled in vivo with a 10 min pulse of ³²P-phosphate and in vitro with ³H-dimethyl sulfate. About 250 μg RNA was used to drive hybridization reactions with unlabeled nonrepetitive DNA at an RNA/DNA ratio of 100/1. After incubation, the reaction mixtures were treated with RNAase A (10 μg/ml, 0.24 M phosphate buffer, room temperature, 1 hr) to destroy all unhybridized ³²P-RNA. Digestion products were removed by passage over a Sephadex G-200 column. The exclusion peak was then placed on a hydroxyapatite column at 60°C in order to select duplexes at the same criterion as in the complexity measurements.

^bControl experiments showed that 0.18% of unhybridized ³H input and 0.72% of ³²P input bound nonspecifically to hydroxyapatite after the RNAase treatment described in footnote a. These background values were calculated from the input cpm in each experiment and subtracted from the total counts bound to obtain the number of counts hybridized.

^cAbout 2.5 μg nonrepetitive DNA was used for each determination. The ³H-specific activity of the RNA was 3750 cpm/μg. The amount of DNA hybridized (in μg) was calculated from the RNA ³H-cpm hybridized, after RNAase treatment in high salt, assuming 1:1 RNA-DNA hybrids. It is important to note that the fraction of DNA in hybrid calculated from the ³H-cpm in these experiments agrees closely with the fraction of DNA hybridized at RNA C₀t's 1000 and 10,000 according to the data of Fig. 10.

^dDifferences are due to ³²P decay.

and as shown in Table 7 is calculated as 2.4%–3.6%, almost exactly the fraction of the total RNA driving the hybridization reaction according to the kinetic calculation above. That calculation indicated a driver fraction of 2.5%–3.1% of the RNA. The experiment therefore proves that it is the hnRNA which contains the complex sequence set in the nuclear RNA preparation. The remaining RNA in the preparation is probably ribosomal and other nuclear RNAs. This contamination does not affect the complexity measurement but simply reduces the measured driver concentration.

Discussion

Complexity of sea urchin gastrula hnRNA. The complexity measurement described here is based on the amount of nonrepetitive ³H-DNA which hybridizes with hnRNA (Table 6 and Fig. 10), and on the kinetics of reassociation between the hybridized ³H-DNA and whole DNA (Fig. 9). Figure 9 shows that a small amount of repetitive ³H-DNA is included in the total hybridized DNA. The remainder of the hybridized DNA reacts as nonrepetitive sequence. The least-squares fit to the hybridization measurements suggests that 10.7% of

the nonrepetitive ³H-DNA is complementary to nuclear RNA. For the single-component fit the rms (root-mean-square) error rises steeply when the size of the hybridized fraction is varied more than ±5%. For example, a 15% increase in rms error occurs when the size of the hybridized component is set at 9.4% or 12% rather than the best value, 10.7%.

It is generally assumed that hnRNA is an asymmetric transcript, but this point has not often been demonstrated. The present study provides such a demonstration. In the experiment of Table 8, hnRNA labeled with ³²P was incubated to an RNA C₀t of 10,000, which is sufficient to permit the reaction of most nonrepetitive sequences of the complexity measured in these RNA preparations. Yet more than 9% of the ³²P-RNA remained sensitive to RNAase digestion carried out under high-salt conditions which spare duplex structures (Table 8); that is, the RNAase-resistant fraction is only the approximately 3% of the ³²P-RNA hybridized to DNA. Therefore both the repetitive and the

nonrepetitive sequences present in the hnRNA preparation are almost completely single-strand transcripts. Utilizing this fact and taking into account the 75% reactivity of the ³H-DNA, we conclude that about 28.5% of the total complexity of the sea urchin genome is represented in the nuclear RNA of the 600-cell gastrula.

The hybridization reaction illustrated in Fig. 10 appears to follow the expected first-order kinetics. Only one kinetic component is visible, though as noted below, others may of course be present. The kinetics of hybridization show that most of the hybridizing sequences are probably present in the hnRNA in about the same number of copies. This is consistent with the results of the ³²P-hnRNA experiment described in Table 7, which shows that the hybridizing RNA is the RNA that is labeled rapidly and therefore turns over rapidly. Berridge *et al.* (1974) have reported that hnRNA molecules are synthesized in sea urchin embryos at a rate of about 6 nucleotides per sec. At this rate it would require several minutes to complete the

TABLE 8. Sequence Content of hnRNA and mRNA of Sea Urchin Gastrulas

	hnRNA	mRNA
Approximate nonrepetitive sequence complexity	≥1.74 × 10 ⁸ nucleotides	1.7 × 10 ^{7a} nucleotides
Total amount	2 × 10 ⁸ nucleotides per nucleus ^b 1.2 × 10 ¹¹ nucleotides per embryo ^c	1.17 × 10 ⁸ nucleotides per cell ^a 7 × 10 ¹⁰ nucleotides per embryo ^c (5.6 × 10 ⁹ of complex mRNA class)
Number of sequences of each kind per embryo ^d	690 ^d	330 (of complex mRNA class) ^a
Repetitive sequence content	about 8% ^e 12-14% ^g	less than 3% ^f about 2% ^g

^aGalau *et al.* (1974).

^bData of Brandhorst and Humphreys (1971, 1972) interpolated for gastrula stage.

^cThe gastrula stage embryo contains about 600 cells (Hinegardner, 1967).

^dCalculated by dividing total nucleotides by complexity.

^eSmith *et al.* (1974).

^fGoldberg *et al.* (1973).

^gData of McColl and Aronson (1974), recalculated assigning nonhybridized RNA cpm to non-repetitive class as in Smith *et al.* (1974).

synthesis of a large molecule. On the other hand, Brandhorst and Humphreys (1971) have shown that this hnRNA appears to decay stochastically with a half time in the range of 5–15 min. It would follow that not many molecules of most hnRNA species could accumulate. Another argument to the effect that not many copies of each hnRNA molecule exist per nucleus is derived from the hybridization experiments of Smith *et al.* (1974). These authors showed that much of the non-repetitive hnRNA transcript in sea urchin gastrulas can be hybridized at relatively low DNA/RNA ratios. It was calculated that about 1–10 copies of each nonrepetitive hnRNA transcript should be present. The same conclusion can be reached independently by dividing the number of hnRNA nucleotides per embryo by the total hnRNA complexity, as shown in Table 8. The average frequency of occurrence of each non-repetitive sequence in the hnRNA is 690 per embryo, or approximately one per cell if all cells contain the same transcripts.

Comparison of hnRNA with mRNA. Table 8 shows that hnRNA and mRNA are strikingly different populations of molecules. The total amounts of each RNA class per cell are about the same, but their complexity differs by more than an order of magnitude. The turnover time for hnRNA is 7–15 min, while that of mRNA is measured in hours (Aronson and Wilt, 1969; Brandhorst and Humphreys, 1971; Galau, G. A., unpublished experiments). An additional difference is found in the repetitive sequence content of the two classes of RNA. The small amount of repetitive sequence in mRNA is found on molecules wholly transcribed from repetitive sequences of DNA (Klein *et al.*, 1974; Goldberg *et al.*, 1973; Campo and Bishop, 1974). In hnRNA, the repetitive sequence elements are interspersed with non-repetitive sequences present in the same molecules. This has been shown for sea urchin hnRNA (Smith *et al.*, 1974)

as well as other hnRNAs (Holmes and Bonner, 1974; Darnell and Balint, 1970; Molloy *et al.*, 1974).

Are there very high complexity components in hnRNA or mRNA? It is appropriate to ask whether an hnRNA component of greater complexity might be observed if the measurements were carried out to higher RNA C_0t s. To test this possibility the data of Fig. 10 and Table 7 were fitted by least-squares methods with two first-order components. The best fit is actually the single component with the complexity of 28.5% of the genome discussed above. For this fit rms error was 0.025 (in terms of the total genomic complexity). Thus our measurements do not suggest any heterogeneity in the hybridization curve such as could indicate a more complex component. However, the hybridization measurements themselves do not rule out such a possibility. If a very small fraction of the RNA were to belong to a more complex class of sequences, the change in slope of the overall curve would of course be small. This would mean that only fractional quantities of each sequence are present per cell. Figure 11 shows a calculation in which the maximum slope is fitted to the hybridization data, using two kinetic components, in order to display the consequences of the proposition that the hnRNA actually represents the whole of the genomic complexity. Thus the sum of the two components is set equal to 100% of the complexity of the genome. When this is done the rms error increases about 15% from its value for the single-component fit. For steeper slopes the rms error rises sharply, showing that a more prevalent class of complex RNA species than that referred to in Fig. 11 is unlikely to exist. Calculation shows, however, that there would be fewer than 20 copies of each sequence of the complex class per 600-cell embryo, or 0.03 copies per cell, even for the component used in the calculation of Fig. 11. This seems to be an unlikely possibility, but it cannot be ruled out

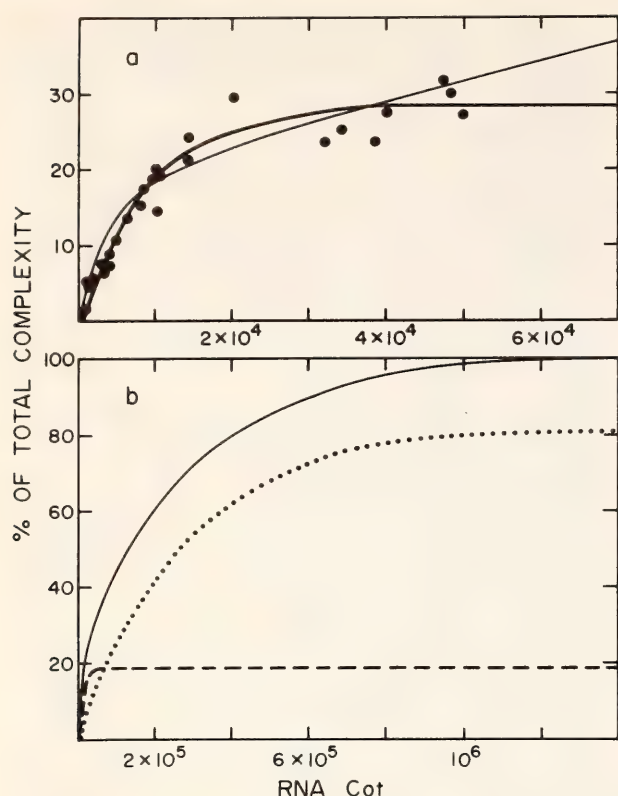


Fig. 11. Calculation of the hybridization kinetics of possible components in hnRNA. (a). Data of Table 6 are fitted by least-squares methods to a curve representing two first-order components (light line) for comparison with the one-component fit of Figure 10, shown here by the heavy line. The root-mean-square error of the two-component fit is 15% higher than that of the one-component fit. The data have been replotted as percent of total genome complexity. (b) The two-component curve of 11a is further extrapolated to 100% of genome complexity, and the kinetic components are depicted separately. The components represent 19% (dashed line) and 81% (dotted line) of total complexity. The pseudo first-order rate constant of the more rapidly hybridizing 19% component is $2.1 \times 10^{-4} \text{ l M}^{-1} \text{ sec}^{-1}$. For the slow component the pseudo first-order rate constant is $3.8 \times 10^{-6} \text{ l M}^{-1} \text{ sec}^{-1}$. The sum of the two components is shown by the solid curve, the extension of the light curve of 11a.

that a few cells of the embryo produce hnRNA with a complexity approaching that of the full nonrepetitive DNA complement. We conclude on the basis of the best single-component solution that most of the hnRNA has a sequence complexity that results from the transcription of $28.5 \pm 5.7\%$ of the nonrepetitive DNA sequences and is equal to $1.74 \pm .34 \times 10^8$ nucleotide pairs.

We may ask the same question about

the messenger RNA of the sea urchin gastrula. From the measurement of mRNA complexity reported by Galau *et al.* (1974), it can be calculated that putative messages with a complexity near that of the hnRNA (i.e., about 28%) would be present in less than one copy per 5000 cells and in much less than one copy per embryo. Such a result would not be physiologically meaningful. We conclude that the complexity of the hnRNA in these embryos is at least an order of magnitude higher than that of the polysomal mRNA. The absolute value of the hnRNA complexity seems too large to be considered in terms of its capacity to code for proteins. Even at a single stage of embryogenesis, the hnRNA represents a large fraction of the interspersed nonrepetitive and repetitive sequences in the sea urchin genome. The significance of hnRNA sequence content may lie in the functional meaning of the interspersed genomic sequence organization.

Experimental Procedures

Preparation of embryos. *Strongylocentrotus purpuratus* embryos were cultured by standard methods (Smith *et al.*, 1974). At early gastrula stage, about 5 mCi ^{32}P (carrier-free) were added to one-fifth of the culture, and the embryos were labeled for 10 min. Incorporation was stopped by dilution with unlabeled embryo suspension, and immediate centrifugation at 4000 rpm. After pelleting, the embryos were disrupted by 40-sec homogenization in a Waring blender.

Preparation of nuclear RNA. Nuclei were isolated and RNA extracted essentially as described by Smith *et al.* (1974). After two washes in 1.5 M glucose, nuclei were pelleted, resuspended in cold buffer, and treated for 4 min with Tween and Na-deoxycholate (Smith *et al.*, 1974). The nuclear pellet of the preparation designated preparation a in Table 6 was resuspended in a low-salt buffer (0.05 M Na-acetate, pH 5.1, 0.01 M EDTA, 0.05% SDS, and 10 $\mu\text{g/ml}$ poly-

vinyl sulfate). For preparation *b* of Table 6, and the double-labeled RNA preparation referred to in Table 7, the nuclei were suspended in the same buffer containing in addition 7 *M* urea (Holmes and Bonner, 1973). The nucleic acids were extracted with phenol-cresol and chloroform-isopentyl alcohol. The aqueous phase was precipitated and treated with DNAase (Smith *et al.*, 1974). The RNA preparations were further purified by passage over Sephadex G-200 or by preparative sucrose gradient centrifugation.

In one preparation ^{32}P -RNA was additionally labeled after extraction by reaction with ^3H -dimethyl sulfate in 0.3 *M* phosphate buffer as described previously (Hough and Davidson, 1972). After the final purifications the mean length of the ^{32}P -labeled RNA fragments in preparations *a* and *b* of Table 6 was estimated at about 800 nucleotides by sedimentation analysis carried out in formaldehyde sucrose gradients (Fenwick, 1968).

Unlabeled and tritium-labeled DNA. Unlabeled DNA was purified by standard methods from *Strongylocentrotus purpuratus* sperm (Smith *et al.*, 1974). The DNA was sheared to 450-nucleotide average length in a high-pressure press. Tritium-labeled DNA was extracted from sea urchin blastulas, sheared in a Virtis homogenizer, and the nonrepetitive fraction isolated, exactly as described by Galau *et al.* (1974). The DNA was re-associated to C_0t 200, and the unre-associated portion was harvested. These sequences were again incubated to a C_0t equivalent to C_0t 200 in whole DNA, and the single-stranded fraction isolated as nonrepetitive ^3H -DNA. The specific activity of the ^3H -DNA was 2.4×10^5 cpm/ μg under our scintillation counting conditions. The fragment length of the final preparation was about 220 nucleotides according to several determinations in alkaline sucrose gradients. Similar procedures were applied in the preparation of the unlabeled nonrepetitive fraction used in the experiments of Table 7.

RNA-driven DNA-RNA hybridization reactions. RNA-DNA reactions were carried out and analyzed as described by Galau *et al.* (1974). Three 10 μl mixtures containing driver amounts of RNA and trace quantities of nonrepetitive ^3H -DNA were denatured by heat and incubated in sodium phosphate buffer at 60°C to the desired RNA C_0t . Phosphate buffer concentrations range from 0.4 *M* to 0.55 *M*. The mass ratio of RNA to DNA varied from 120 to 1060. Samples were quenched in dry ice-acetone, diluted to 0.1 ml 0.12 *M* phosphate buffer, and divided for analysis. A 10 μl portion was counted directly as an input sample. A second 10 μl portion was passed over a Sephadex G-200 column in order to monitor possible RNA degradation in all samples. Half of the remaining sample was diluted to 0.05 *M* phosphate buffer and treated overnight at 37°C with RNAase A at 10 $\mu\text{g}/\text{ml}$ to destroy DNA-RNA hybrids. It was passed over hydroxyapatite in 0.12 *M* phosphate buffer at 60°C, and the bound DNA-DNA duplexes were measured. The remaining half was passed over hydroxyapatite directly and the binding of DNA-DNA plus DNA-RNA duplexes measured. The difference in binding between the two samples is the fraction of the nonrepetitive DNA in RNA-DNA hybrids.

Isolation of ^3H -DNA from RNA-DNA hybrids. To isolate nonrepetitive ^3H -DNA from ^3H -DNA-RNA hybrids (Galau *et al.*, 1974; Hough and Davidson, 1972; Gelderman, Rake, and Britten, 1971), RNA and nonrepetitive ^3H -DNA were incubated (at an RNA/DNA ratio of about 200) to C_0t 10,000, and the double-stranded nucleic acids (DNA-RNA and DNA-DNA duplexes) were eluted in 0.5 *M* phosphate buffer. This eluate was incubated with RNAase A (10 $\mu\text{g}/\text{ml}$) in 0.05 *M* phosphate buffer at 37°C for 15 hr to destroy hybridized RNA. The mixture was further diluted to 0.02 *M* phosphate buffer, and all the DNA bound to hydroxyapatite at room temperature. The DNA which had been

rendered single stranded by the low-salt RNAase treatment was then washed from the column at 60°C in 0.12 *M* phosphate buffer. The ³H-DNA thus harvested from hybrids was precipitated and later used in reactions with whole, sheared sea urchin DNA.

STRUCTURAL GENES ADJACENT TO INTERSPERSED REPETITIVE DNA SEQUENCES

*Eric H. Davidson, Barbara R. Hough,
William H. Klein, and Roy J. Britten*

The observation that repetitive and single-copy sequences are interspersed in animal DNAs has suggested that repetitive sequences are adjacent to single-copy structural gene sequences. To test this concept single-copy DNA sequences contiguous to interspersed repetitive sequences were prepared from sea urchin DNA and hybridized with labeled messenger RNA prepared from sea urchin gastrulas. These experiments were briefly mentioned in last year's Report. Here we present the central measurements which establish the conclusion that repetitive sequences are adjacent to a large fraction of the structural genes expressed at this stage of urchin development. A complete description of the measurements has been published (Davidson *et al.*, 1975).

In the genome of the sea urchin *Strongylocentrotus purpuratus* short repetitive DNA sequence elements averaging 300 nucleotides in length are extensively interspersed among non-repetitive sequences of one to several thousand nucleotides. At least 70% or 80% of the DNA is organized in this way (Graham *et al.*, 1974). A striking aspect of the observations is the rough correspondence between the inter-repeat distances and the length of typical animal structural genes.

We here define the animal structural gene specifically as the DNA sequence from which a functional polysomal

mRNA is transcribed. Most (though clearly not all) animal structural genes appear to be single-copy sequence elements (compare with Galau, Britten, and Davidson, 1974; Klein *et al.*, 1974; Sullivan *et al.*, 1973; Harrison *et al.*, 1974; previous studies reviewed in Davidson and Britten, 1973). The number average length of animal structural gene sequences is about 2000-2500 nucleotides, with about half of the individual sequences 1200-1500 nucleotides or less, while others are many thousands of nucleotides long. This sequence length distribution is crudely similar to that we have estimated for interspersed single-copy sequence in the DNAs of the two animals thus far studied. It is therefore a reasonable proposition that most structural genes are single-copy sequences which are immediately contiguous to repetitive sequence elements.

Structural gene sequences can be detected empirically by their ability to hybridize with polysomal mRNA, here extracted from sea urchin embryos. To determine whether the structural gene sequences are located next to repetitive sequences, we have isolated that fraction of nonrepetitive DNA which is contiguous to interspersed repetitive sequence elements in the genome. For convenience we term this preparation the repeat-contiguous DNA fraction. We then compare the hybridization of mRNA with the repeat-contiguous DNA fraction to the hybridization obtained with whole DNA. Though only about 30% of the nonrepetitive sequences in whole DNA are highly represented in repeat-contiguous DNA, almost as much mRNA hybridization is obtained with repeat-contiguous single-copy sequences as with whole DNA. It follows that at least a large majority of the expressed structural gene sequences are located next to repetitive elements in the genome. We believe that this pattern of organization may be involved in structural gene regulation in animal cells.

The Repeat-Contiguous DNA Fraction

A series of five fractionations was employed in the preparation of repeat-contiguous DNA. These are diagrammed together with yields at each step and fragment lengths in Fig. 12. The two initial fractionations (stages B1 and B2 of Fig. 12) were for the purpose of isolating moderately long fragments which contain both interspersed repetitive sequence elements and flanking nonrepetitive sequence (B fragments). The double fractionation is necessary to remove all fragments that fail to bind reproducibly to hydroxyapatite after low C_0t incubations. However, when fraction B2 DNA was incubated to C_0t 20 again, 98%–100% of the fragments are found to bind. Special care had to be exercised to avoid strand scission during these hydroxyapatite fractionations. Not surprisingly, we found that the most important factors in this respect were minimum length of exposure to high temperature and avoidance of external pressure during elution of the DNA from the column.

The third fractionation was designed to strip the DNA of fragments binding to hydroxyapatite because of the presence of intrastrand duplexes (Wilson and Thomas, 1973; Davidson *et al.*, 1973; Graham *et al.*, 1974). The DNA was denatured, cooled rapidly to 60°C in a coiled heat-exchange tube, and passed quickly over the column. Effective C_0t was about 6×10^{-3} , and as Fig. 12 shows, about 70% of the fragments were not bound (fraction B3). The fragment length was close to 1800 nucleotides at this stage, and thus the 30% of the DNA which bound at C_0t 6×10^{-3} is within a few percent of the expected "zero-time binding" according to previous experience with unfractionated sea urchin DNA fragments of a similar length (Graham *et al.*, 1974).

The next fractionation was carried out for the purpose of increasing the homogeneity of the preparation by re-

moving those sequences present least frequently. The DNA was sheared to 450 nucleotides and incubated to C_0t 500. After this incubation, close to 70% of the fragments contained duplex (fraction B4 of Fig. 12). The terminal reassociation value for the preparation as a whole was about 90% at this stage (Fig. 13). Therefore, by C_0t 500 approximately two-thirds of the single-copy fragments had reacted. Since single-copy sequences that are present very rarely (for example, at less than 10^{-2} of the concentration of the prevalent sequences in the preparation) will not yet have reassociated by this point, any such sequences will be excluded as unbound DNA when the preparation is passed over hydroxyapatite. Similarly, the concentration of less rare but still relatively infrequent sequences will be further reduced by the C_0t 500 fractionation.

The final fractionation accomplished the removal of most of the repetitive sequences. The DNA was incubated to C_0t 10 and again fractionated on hydroxyapatite. The nonbound fraction (B5 in Fig. 12) contains the single-copy sequences originally present on the same fragments as the repetitive sequences before shearing to 450 nucleotides. This fraction was the repeat-contiguous DNA preparation used in subsequent experiments. Both calculation and measurement show that a maximum of 15% of the fragments in this fraction contain recognizable repetitive sequence. Since, as shown earlier (Goldberg *et al.*, 1973) and confirmed below, the sea urchin mRNA hybridizes significantly only with nonrepetitive sequences, the presence in repeat-contiguous DNA fraction of these repetitive sequence contaminants does not affect the results in any way.

As discussed in the preceding section, the repeat-contiguous DNA fraction B5 contains at least a portion of all single-copy sequences near (within an average of 1800 nucleotides) repetitive sequence elements. However, lacking from the

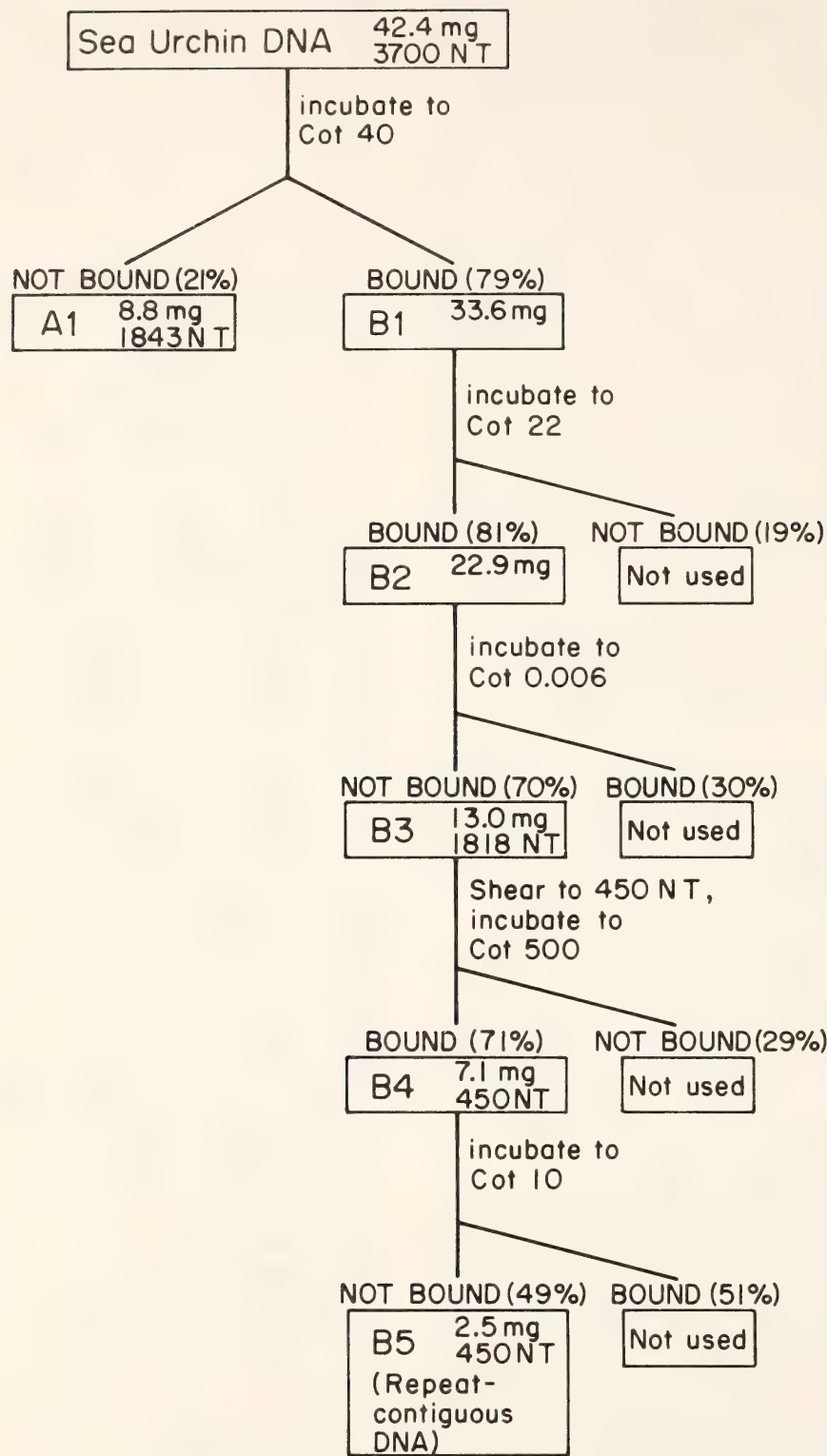


Fig. 12. Preparation of repeat-contiguous DNA and related fractions. All stages of the fractionation on the right-hand branch of the column descend from fragments containing repetitive sequence elements and are labeled *B*. Unbound fragments contain no repetitive sequences and are labeled *A*. Stages of the fractionation are denoted by numbers. Yields and mean fragment lengths in nucleotides (NT) for the DNA (where available) are given in the boxes. The lengths were determined by alkaline sucrose gradient measurements.

prevalent sequence class of the repeat-contiguous DNA are the more distant regions of nonrepetitive sequences as well as those flanking foldback regions.

Characterization of Repeat-Contiguous DNA

If the fractionation procedure for repeat-contiguous DNA is meaningful, a minor fraction of the total single-copy sequence in the genome will be prevalent in the final preparation. The theoretical size of this fraction can be roughly estimated from what is known about sequence organization in sea urchin DNA (Graham *et al.*, 1974), given the fragment length after the low C_0t fractionations (that is, fraction B3 in Fig. 12). According to Graham *et al.* (1974), about 0.65 of 1800-nucleotide DNA

fragments not containing foldbacks include repetitive sequence regions. Repetitive sequence accounts for about 0.25 of the total DNA, and all of these sequences should be included in the 1800-nucleotide bound fraction. To proceed, we assume that the sequences flanking foldback structures in the 1800-nucleotide fragments are proportionately representative of repetitive and nonrepetitive sequence classes. This assumption is based somewhat tenuously on experiments with *Xenopus* DNA (Davidson *et al.*, 1973), in which it was found that the sequences flanking foldbacks in 3700-nucleotide fragments (mean length) reassociated with excess whole DNA exactly like the whole DNA driver. About 30% of 1800-nucleotide fragments at stage B2 of Fig. 12 include foldback structures. We argue that if foldbacks are indeed distributed

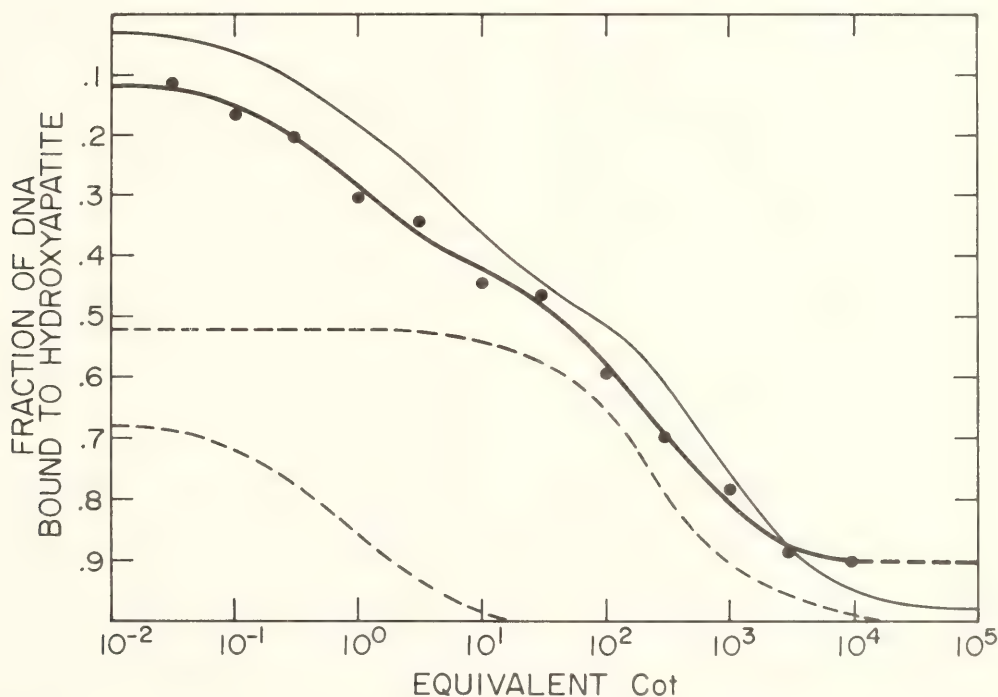


Fig. 13. Self-reassociation of DNA fraction B3. The 1800-nucleotide fragments were sheared to 450 nucleotides in a high pressure press. Samples containing DNA concentrations ranging from 0.06 mg/ml to 12 mg/ml were incubated at 60°C at salt concentrations between 0.12 M and 0.46 M phosphate buffer to the identical equivalent C_0t . Following incubation the samples were diluted to 0.12 M phosphate buffer and passed over a hydroxyapatite column at 60°C in 0.12 M phosphate buffer. Duplex containing fragments were eluted at 95°C. Data obtained are represented by solid circles. The curve (thick line) is a least-squares fit to these data utilizing two kinetic components (dashed lines). The faster reassociating component represents 31.6% of the DNA and reacts with a rate constant of $1.2 M^{-1} sec^{-1}$. The slower reassociating component represents 47.5% of the DNA and reacts with a rate constant of $4.2 \times 10^{-3} M^{-1} sec^{-1}$. Reassociation of unfractionated sea urchin DNA sheared to 450 nucleotides is shown for comparison and is represented by the thin solid line. This curve was derived from the data of Galau *et al.* (1974).

proportionately, the same fraction, 30%, of the single-copy sequence will be removed when the 1800 nucleotide fragments containing foldbacks are extracted. The fraction of the total single-copy sequence remaining should then be $[0.7(0.65 - 0.25)]/0.75 = 0.37$. Since the actual disposition of foldbacks in sea urchin DNA is unknown, this calculation can only be regarded as a crude approximation. However, if the decrease in single-copy complexity associated with removal of foldbacks and their flanking sequences is ignored, the fraction of single-copy sequence expected to be present in repeat-contiguous DNA would be as high as 0.55 instead of 0.37. As the data presented below indicate, such a value lies far above the range obtained by direct complexity measurements.

We can also estimate the prevalent sequence complexity from the fractionation recoveries summarized in Fig. 12. This calculation follows the same route as the previous one, and is detailed in footnote 6 of Table 9. Calculated in this way the prevalent sequence complexity of the repeat-contiguous DNA preparation is expected to be about 0.32 of that of the whole genome.

To obtain empirical complexity estimates, the reassociation kinetics of repeat-contiguous DNA were measured in several ways. These measurements, together with the calculated estimates just described, are summarized in Table 9. By definition the prevalent sequence complexity is the complexity of the large majority of fragments, and thus observations of renaturation kinetics made on an absorbance basis should provide the required information. Table 9 includes data from three experiments of this kind. In each case self-reaction kinetics of the single-copy DNA component were measured by hydroxyapatite chromatography. The first of these determinations was carried out with the 450-nucleotide fragments formed by shearing fraction B3 (Fig. 12). This fraction contains both single-copy and repetitive

sequences. Its reassociation is shown in Fig. 13 (heavy solid line). For comparison the reassociation kinetics of whole sea urchin DNA are also shown (thin solid line). As expected, most of the single-copy sequences present in the B3 DNA fraction renature somewhat more rapidly than the single-copy fraction of whole DNA. Repetitive and nonrepetitive kinetic components are indicated by the dashed lines. The best rate constant for the nonrepetitive component in this fraction is $4.2 \times 10^{-3} M^{-1} \text{ sec}^{-1}$. Appropriate calculations based on this rate constant (Table 9) suggest that the complexity of the bulk of the DNA included in the repeat-contiguous fraction is only about 20% of that of the total single-copy DNA.

A second estimate is derived from some of the data shown in Fig. 15. The lower curve in this figure represents the self-reassociation of the final repeat-contiguous DNA fraction (fraction B5 of Fig. 12). The samples in this experiment were assayed on hydroxyapatite in urea-phosphate medium (see "Experimental Procedures"). About 15% of the DNA apparently consists of fragments bearing repetitive sequence, as a result of their incomplete elimination by the C_0t 10 preparative incubation (see Fig. 12). The remaining DNA fragments reassociate at a rate of 3.5×10^{-3} , indicating a complexity of about 34% of the total. This estimate, which falls between the two calculated estimates, is probably the most reliable of the values in Table 9, since the purified repeat-contiguous DNA rather than its precursor is used, and since it is based on the most data. A further estimate is based on the self-reaction of the repeat-contiguous DNA illustrated in Fig. 14a. Here the reassociated samples were assayed in 0.12 *M* phosphate buffer (rather than urea-phosphate as in Fig. 15), and the best-fit rate constant for the major fraction of the DNA is 7×10^{-3} , suggesting that about 19% of the total complexity is represented in the bulk DNA of the sample (see calculation in Table

TABLE 9. Estimations of the Complexity of Prevalent Sequences in Repeat-Contiguous DNA

DNA Fraction	Data Used for Complexity Estimation	Rate Constant of Major Non-repetitive Component ($M^{-1} \text{ sec}^{-1}$)	Rate Constant Corrected for 100% Purity ($M^{-1} \text{ sec}^{-1}$)	Apparent Complexity of Major Non-repetitive Component (Nucleotides)	Percent of Total Nonrepetitive Complexity ¹
1800 nucleotide fragments bearing repetitive sequence ²	DNA sequence length and organization ³	2.22×10^8	37%
	Reassociation kinetics after shearing to 450 nucleotides ⁴	0.0042	0.0089	1.24×10^8	19.7%
Repeat-contiguous DNA ⁵	Recoveries during DNA fractionation ⁶	1.95×10^8	32% ⁶
	Self-reassociation kinetics ⁷	0.0035	0.0051	2.17×10^8	34%
	Self-reassociation kinetics ⁸	0.0070	0.0098	1.12×10^8	18.5%
	³ H nonrepetitive DNA tracer re-association with excess repeat-contiguous DNA ⁸	0.0070	. . .	1.32×10^8	24.1%

¹The complexity of *S. purpuratus* total single-copy DNA is 6.1×10^8 nucleotides (Graham *et al.*, 1974).
²Fraction B3 of Fig. 12.
³Data of Graham *et al.* (1974). The calculation is described in the text.
⁴Data from Fig. 13. Observations were carried out on fraction B3 of Fig. 12, after shearing to 450 nucleotides.
⁵Fraction B5 of Fig. 12.
⁶The fraction of nonrepetitive sequences removed at each fractionation is calculated as follows: 0.75 of the starting DNA is nonrepetitive. 0.21 of the DNA, i.e., 0.28 of the nonrepetitive sequence, is lost at the initial fractionation. At the second fractionation fragment size decreased and therefore the further loss of 0.19 of the remaining DNA (i.e., 0.15 of the original DNA) represents loss of 0.21 of the original single-copy sequence. At the third fractionation 0.30 of the DNA was discarded with the fold-back fraction, and 0.75 of this is expected to fall within nonrepetitive sequence regions, since fold-backs are considered to be distributed proportionally among all classes of sequence (see text). The 0.3 of the DNA excluded here represents 0.19 of the starting material, and if 0.75 of this is considered as loss of nonrepetitive sequence, $0.19 \times 0.75/0.75 = 0.19$ of the original nonrepetitive sequence is removed at this step. Thus the total nonrepetitive sequence loss in these three fractionations is $0.28 + 0.21 + 0.19 = 0.68$, leaving 0.32 as the estimated recovery of starting complexity. No significant loss of prevalent sequence complexity is expected in the fourth fractionation since the C_0t to which the reaction is run was sufficient to ensure that about $\frac{2}{3}$ of the prevalent sequences reassociated.
⁷Data from Fig. 15.
⁸Data from Fig. 14.

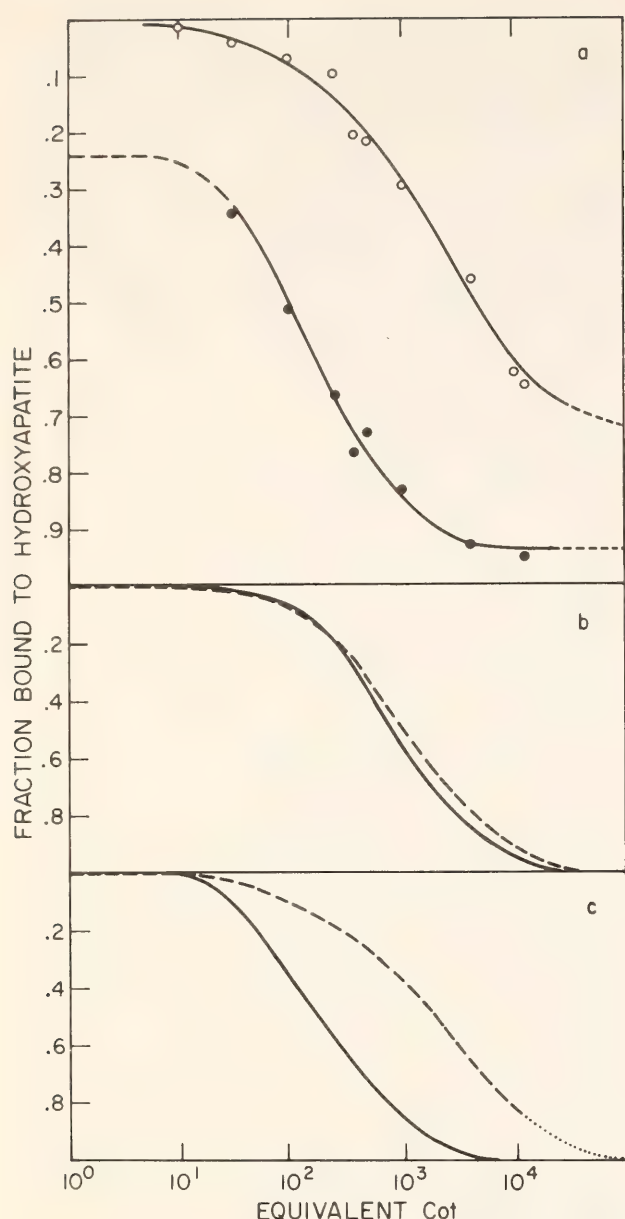


Fig. 14. (a) Reassociation of nonrepetitive ^3H -DNA with repeat-contiguous DNA. 0.01 ml samples containing 4.3 mg/ml of repeat-contiguous DNA and 3×10^3 cpm of nonrepetitive ^3H -DNA in 0.44 M phosphate buffer were incubated at 60° to the indicated equivalent C_0t s greater than 100. For incubations to equivalent C_0t less than 100, 0.035 ml samples were used containing 1.3 mg/ml of repeat-contiguous DNA and 3.3×10^3 cpm of nonrepetitive ^3H -DNA in 0.12 M phosphate buffer. Following incubation the samples were analyzed on hydroxyapatite at 60°C . Closed circles represent the self-reassociation of the repeat-contiguous DNA fraction. The solid line through the points represents a least squares fit to the data on the basis that 15% of the repeat-contiguous fragments bear a repetitive sequence. This amount of repetitive sequence is the expected quantity according to calculation from both the fractionation of Fig. 12 and the renaturation data of Fig. 13. The best-fit size of the repetitive component observed in the self-reaction data in Fig. 15 is also 15%. Reaction of this repetitive

9). However, low C_0t renaturation data needed for a more reliable fit are not available, and this estimate is therefore somewhat less firm.

The experiment of Fig. 14 provides an additional and independent assessment of the prevalent sequence complexity of repeat-contiguous DNA. A measure of the total complexity of this DNA fraction can be derived from the same experiment. Here purified single-copy DNA tracer prepared from whole ^3H -

component was not measured in the present experiment. A rate constant of $7 \times 10^{-3} M^{-1} \text{sec}^{-1}$ for the repeat-contiguous DNA was obtained from this curve. This rate was then used to fit the reaction of the nonrepetitive ^3H -DNA with repeat-contiguous DNA (open circles). The curve drawn through the latter data represents a least-squares fit of two kinetic components, the rate constant of one fixed at $7 \times 10^{-3} M^{-1} \text{sec}^{-1}$. By this procedure the fraction of nonrepetitive ^3H -DNA reacting with the main component of the repeat-contiguous DNA (i.e., with a rate constant of $7 \times 10^{-3} M^{-1} \text{sec}^{-1}$) could be determined. The tracer fragments average only 200 nucleotides in length and hence react at only about 0.73 of the driver DNA rate (rates given in 14b below). Correcting for this minor difference, the fraction of tracer being driven by most of the nonrepetitive sequences in the repeat contiguous on a fraction is determined to represent 18% of the reacting nonrepetitive ^3H -DNA. However, only 75% of the nonrepetitive ^3H -DNA is reactable with whole DNA at our criterion conditions, and thus a total of 24.1% of the reactable tracer DNA reassociated with the driver component reacting with itself at the rate of $7 \times 10^{-3} M^{-1} \text{sec}^{-1}$. The second component of the tracer DNA reassociated at a rate of $2.9 \times 10^{-4} M^{-1} \text{sec}^{-1}$, and represented 75% of the reactable nonrepetitive ^3H -DNA.

(b) Normalized reassociation of nonrepetitive ^3H -DNA with nonrepetitive sequences in whole, sheared sea urchin DNA. The solid line represents the normalized self-reassociation of the nonrepetitive component of whole sea urchin DNA. Its rate is $1.25 \times 10^{-3} M^{-1} \text{sec}^{-1}$. The dashed line represents the normalized reassociation reaction of nonrepetitive ^3H -DNA with whole sea urchin DNA. Its rate is $0.91 \times 10^{-3} M^{-1} \text{sec}^{-1}$. These curves are derived from data of Galau *et al.* (1974).

(c) Normalized reassociation reaction of repeat-contiguous DNA with nonrepetitive ^3H -DNA. Data are from 14a. The solid line represents the normalized self-reassociation of the nonrepetitive component of repeat-contiguous DNA. The dashed line represents the normalized reassociation reaction of nonrepetitive ^3H -DNA with repeat-contiguous DNA.

DNA is permitted to react with a large excess of repeat-contiguous DNA. The tracer reaction is shown by the upper curve in Fig. 14a (open circles). It is clear that the labeled DNA fails to react completely and that much of its reaction is extremely slow relative to the reaction rate of the bulk of the repeat-contiguous DNA. Control experiments have shown that this tracer preparation is only able to react with whole DNA to about 75% (Galau *et al.*, 1974), probably due to the presence of many very short fragments (the mean fragment length is only about 200 nucleotides).

The two curves of Fig. 14a are redrawn in Fig. 14c normalized to a 75% terminal value for the tracer. For comparison, Fig. 14b describes the reaction of the tracer with the single-copy component of whole DNA similarly normalized. Figure 14c shows that 80%–90% of the reactable single-copy tracer is eventually able to find homologous sequences in repeat-contiguous DNA, though this requires very high driver DNA C_0t . By this measure the total complexity of repeat-contiguous DNA is at least 80%–90% of the total genomic complexity. However, the driver sequences required for reaction of most of the tracer must be present at concentrations at least an order of magnitude less than that of the bulk of the driver DNA. Thus, at C_0t 10^3 , for example, when more than 90% of the driver DNA fragments carry duplex regions, less than 40% of the reassociable tracer is bound. The tracer reaction approaches completion only at C_0t s over 3×10^4 . Curve fitting shows that about 24% of the reassociable tracer reacts at the rate of the bulk of the driver DNA (Fig. 14). The rate constant that best describes the reassociation of the tracer with the slower kinetic component in the driver DNA (that is, the rare sequences) is about 3×10^{-4} . Since all single-copy sequences in the genome are included in the tracer preparation of Fig. 14, the experiment indicates that the bulk of the driver

DNA fragments represents about 24% of the whole genome complexity.

From Table 9 we conclude that the prevalent sequence complexity of the repeat-contiguous DNA fraction lies in the range 19%–34%. The most reliable measurement yields the 34% value, and this result agrees satisfactorily with calculations based on knowledge of sequence organization and actual fractionation yields. Rare sequences of additional complexity are also present. However, due to the nature of the fragment length distributions and the C_0t 500 fractionation step (fraction B4 of Fig. 12), these sequences exist in the preparation at significantly lower concentrations. Therefore, their participation in a reaction with tracer (either DNA or RNA) can be distinguished clearly on the basis of their extremely slow kinetics. For this reason the reaction kinetics are of significance for the interpretation of the mRNA–repeat-contiguous DNA hybridization experiments which are the main contribution of this study. We next describe detailed measurements aimed at establishing the kinetics of hybridization of sea urchin embryo mRNA with whole DNA at a level of precision greater than has heretofore been possible.

Hybridization of mRNA with Repeat-Contiguous DNA

Figure 15 shows an experiment in which repeat-contiguous DNA was incubated to various equivalent C_0t s with trace amounts of ^3H -labeled mRNA. The mRNA used in these hybridization experiments was a Sephadex-excluded fraction. These experiments were assayed by hydroxyapatite chromatography carried out at 40°C in urea-phosphate buffer. The left ordinate refers to the mRNA hybridization. The experiment shows that the maximum extent to which the mRNA hybridizes is $50\% \pm 5\%$. The curve was fitted to the form of Equation 1, and the best-fit rate constant R computed for the hybridization reaction is 4.5×10^{-4} . Very little heterogeneity in

rate could be detected in the RNA-DNA hybridization data of Fig. 15 ($h = 1.5$).

The stability of the RNA-DNA hybrid duplexes formed at C_0t 5300 was measured by thermal elution from a hydroxyapatite column. Duplex-containing molecules were initially bound to the column in 0.2 *M* phosphate buffer-8 *M* urea at 40°C as usual, and then the elution medium was replaced by 0.12 *M* phosphate buffer and the temperature raised. The experiment is shown in Fig. 16. The melting profile of the repeat-contiguous DNA duplexes (filled circles) and of RNA-DNA hybrids (open circles) is almost indistinguishable, as can be seen in Fig. 16. For both types of duplex, the T_m was 82°C. The mRNA hybrids formed with repeat-contiguous DNA are thus well matched and are at least a few hundred nucleotides in length.

The experiments presented in Figs. 15 and 16 show that gastrula mRNA hybridizes extensively with single-copy sequences contiguous to repetitive sequences in the genome. The extent of the reactions is about 50%, compared with the 65% reaction observed with whole DNA at similar mRNA/DNA sequence ratios. The form of the kinetics of hybridization is similar to that of the whole DNA-mRNA reactions. The hybridization rate of the mRNA with repeat-contiguous DNA was retarded compared to the kinetics of the driver single-copy DNA renaturation. The latter reacted at a rate of $3.5 \times 10^{-3} M^{-1} \text{ sec}^{-1}$ in this experiment (Table 9). The rate of hybridization of repeat-contiguous DNA with the mRNA was $4.5 \times 10^{-4} M^{-1} \text{ sec}^{-1}$. A very similar degree of retardation of the hybridization reaction rela-

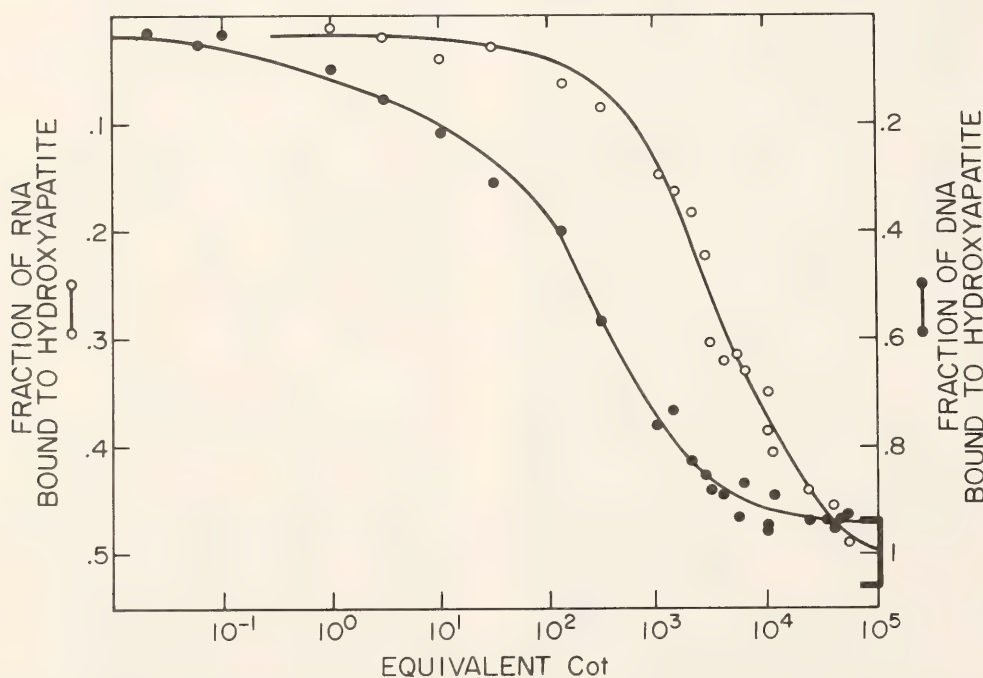


Fig. 15. Hybridization of sea urchin gastrula mRNA with repeat-contiguous DNA. The DNA/RNA ratio ranged from 20,000 to 25,000. After incubation at 60°C to the indicated equivalent C_0t , the samples were brought to 0.2 *M* phosphate buffer, 8 *M* urea, 1% SDS, and the hybrid content assayed by hydroxyapatite chromatography at 40°C in the urea-phosphate buffer. Closed circles represent the self-reassociation of repeat-contiguous DNA (right ordinate). The line drawn through the points is a least-squares fit to the data, which includes a 15% repetitive component, reacting with a rate constant of $7.2 \times 10^{-1} M^{-1} \text{ sec}^{-1}$. The main sequence component of repeat-contiguous DNA includes 70% of the DNA in the preparation. Its rate of renaturation is $3.5 \times 10^{-3} M^{-1} \text{ sec}^{-1}$, in accord with other observations (see Table 9). The final 2-5% of the DNA can be considered to contain rare sequences reassociating at a 10-fold slower rate than the prevalent sequence class. Open circles represent the hybridization of Sephadex G-200-excluded mRNA of preparation 3 with repeat-contiguous DNA (left ordinate). The line drawn through the points is a least squares fit to the data according to Equation 5 of the Appendix of Davidson *et al.* (1975). The bracket indicates the range of terminal extents permitted by the acceptable solutions.

tive to the DNA reassociation rate is observed with whole sea urchin as the driver (Davidson *et al.*, 1975). This means that the bulk of the repeat-contiguous DNA which is observed to reassociate in Fig. 15 must include the expressed structural gene sequences. Put another way, since whole DNA contains no "rare" single-copy sequences and yet drives mRNA hybridization with a certain retardation, the observation of a similar retardation in the experiment of Fig. 15 precludes significant hybridization of the mRNA with rare sequences in the repeat-contiguous DNA preparation. We conclude from the reaction kinetics that the mRNA hybridizes mainly or exclusively with the prevalent sequence class in repeat-contiguous DNA.

These are the sequences that lie mainly within 0-1800 nucleotides of a repetitive sequence element.

*Sequence Organization in the
Strongylocentrotus purpuratus Genome
and the Sequence Content of Repeat-
Contiguous DNA*

The significance of these experiments depends essentially on two points. The first is the demonstration that the prevalent sequence complexity in repeat-contiguous DNA is about 34% of the total genomic complexity. The second is that the mRNA has indeed hybridized with the prevalent sequences in the repeat-contiguous DNA preparation.

The measurements presented in Figs. 13, 14, and 15 and summarized in Table 9 indicate that 18.5%-34% of the complexity of whole DNA is present in the prevalent sequences of the repeat-contiguous DNA fraction. Of these four experimental complexity measurements, the 34% value derived from the relatively extensive self-reassociation data of Fig. 15 appears the most reliable. Calculations based on knowledge of sequence organization studies and of fractionation recoveries suggest values of 32% and 37%. It is worth underlining, however, that both the latter calculations require a simplifying assumption. This is that

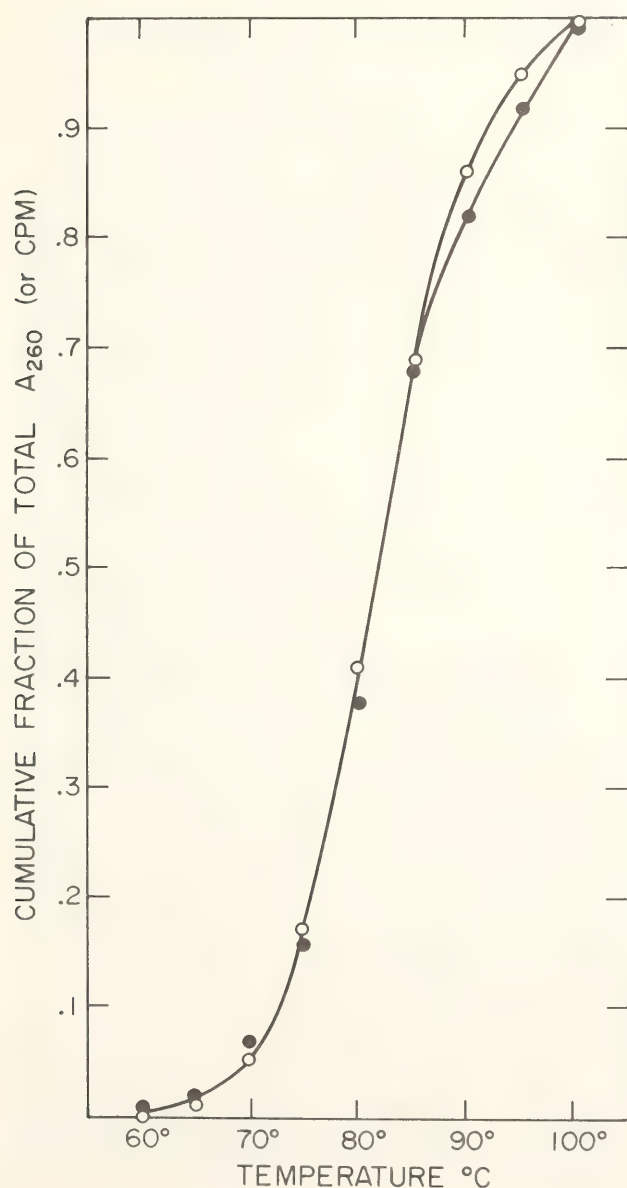


Fig. 16. Thermal elution of mRNA-repeat-contiguous DNA hybrids and DNA duplexes from hydroxyapatite. A 0.01 ml sample containing 40 μ g of repeat-contiguous DNA and 6.8×10^3 cpm of Sephadex G-200 excluded mRNA preparation 3 in 0.42 M phosphate buffer was incubated at 60°C to an equivalent C_0t of 5300. The sample was then brought to 8 M urea, 0.2 M phosphate buffer, 1% SDS, and bound to hydroxyapatite in this buffer at 40°C. The urea phosphate buffer was then replaced with 0.12 M phosphate buffer and the temperature raised to 60°C. No nucleic acids were eluted in this interval. The temperature was then increased in 5°C increments and 2 ml fractions were eluted up to 100°C. Closed circles represent the elution profile of the DNA duplexes. Open circles represent the elution profile of the RNA-DNA hybrids. T_m for both species of duplex was 82°C.

foldback sequences are distributed proportionately in DNA of all sequence classes, and hence that removal of foldback regions entails a proportional decrease in the remaining single-copy complexity. Furthermore, it is assumed that the DNA fragment length distribution gives rise to no serious errors in the calculation of prevalent sequence complexity. Considering these uncertainties, it is surprising that the calculated estimates of prevalent sequence complexity and the kinetic measurements for the complexity of the bulk of the repeat-contiguous DNA agree as closely as they do.

Sequence Organization around the Structural Genes Expressed in the Sea Urchin Embryo

The amount of hybridization obtained with repeat-contiguous DNA must be adjusted in order to account for the effect of structural gene sequence length. However, the main result is obvious even without this refinement, since 50% of the mRNA hybridized with repeat-contiguous DNA compared to 65% with whole DNA. Thus, 80% as much mRNA hybridization was obtained with a DNA fragment population which includes only 34% or less of the non-repetitive sequence. It is therefore immediately evident that structural gene sequences are located primarily in the vicinity of repetitive sequence elements.

Calculations taking the effect of structural gene sequence length into account have been made (Davidson *et al.*, 1975). A striking result is that even if all structural genes had repetitive sequences at one end, the length of the sequence domain represented in repeat-contiguous DNA is such that no more than 50% hybridization could have been obtained. Needless to say, this calculation suffers from uncertainties and possible errors. Nonetheless, the general conclusion seems inescapable, since the structural gene length distribution clearly includes sequences longer than the region repre-

sented by the prevalent sequences in repeat-contiguous DNA. The data are consistent with a form of genomic sequence organization in which all or almost all structural gene sequences are bordered by a repetitive sequence element on one end. On the other hand, if we suppose that every structural gene sequence has a repetitive sequence on both ends, calculation suggests that about 62% rather than 50% of the mRNA would have hybridized with the repeat-contiguous DNA. This assumes that 100% efficiency has been achieved throughout the experiment and that the genes have either two or zero repetitive sequences near them. Clearly, this calculation derives from a rather extreme model. Even so, this model demands that about 80% of structural genes be contiguous to repetitive sequences. If in fact structural genes tend to be bordered on both ends by repetitive sequence elements, the mRNA length distribution tells us that both short-period and long-period interspersed single-copy sequences must be included in the structural gene class. About half of the individual gene sequences would fall within the short-period class (1200–1400 nucleotides or less), and the remainder would fall in a range of lengths stretching out to many thousands of nucleotides. We conclude that 80–100% of the mRNA molecules derive from structural gene sequences which begin within a few hundred nucleotides of the repeat terminations, if they are not immediately contiguous to them. This conclusion, of course, refers only to the structural genes whose transcripts are present on polysomes in the sea urchin gastrula. That sample is fairly diverse, since the study of Galau *et al.* (1974) shows that at least 14,000 ($\pm 20\%$) distinct structural gene sequences of an average length of 1200 nucleotides are represented in this mRNA population. However, we cannot exclude the possibility that not all the mRNA complexity is represented in the hybridized mRNA population.

Implications for Structural Gene Regulation

We have argued that the physical basis for coordinated structural gene regulation in animal cells is the presence of repetitive receptor sequences near the 5' end of structural genes (Britten and Davidson, 1969, 1971; Davidson and Britten, 1973). In this model, binding of diffusible regulatory macromolecules to these sequences would result in transcriptional activation of the contiguous structural genes. A crucial and inescapable prediction of this theory is that structural gene sequences are contiguous in the genome to interspersed repetitive

sequence elements. The findings reported are consistent with this prediction. However, we stress the fact that no information regarding the functional role played by the contiguous repetitive sequences is available. It is not known whether their position is 5' (with respect to the transcript) or whether they really are involved in control of the activity of these genes. The fact that interspersed repetitive sequences are contiguous to expressed genes, however, means that the latter issues now become matters of primary interest for those concerned with the system properties of animal gene regulation.

REASSOCIATION AND HYBRIDIZATION

RATE OF DUPLEX FORMATION IN DNA REASSOCIATION

*Roy J. Britten, Michael J. Smith, and
Eric H. Davidson*

The methods most commonly used for the measurement of eukaryotic DNA reassociation kinetics are binding to hydroxyapatite, measurement of hypochromicity, and assay of resistance to single-strand-specific nucleases. Generally the S1 nuclease of *Aspergillus oryzae* is used (Vogt, 1973; Ando, 1966), although other single-strand-specific nucleases such as Mung bean nuclease (Ardelt and Laskowski, 1971) have also been applied. The nuclease procedures measure the fraction of DNA nucleotides in duplex at each point in the renaturation reaction. At least to a first approximation this should also be true of the optical hypochromicity method. On the other hand, hydroxyapatite chromatography measures the fraction of DNA fragments that are totally single stranded. For randomly sheared DNA, the structures bound to hydroxyapatite must contain both single-stranded and duplex regions, since in general no two reacting fragments begin and end at the same point in the DNA sequence.

When renaturation reactions are assayed by the hydroxyapatite method, second-order kinetics are observed (Britten and Kohne, 1968). These workers also measured the rate of formation of duplex by optical hyperchromicity. In the initial part of the reaction, the rate of duplex formation was shown to be about half the rate at which DNA becomes able to be bound to hydroxyapatite. During the first two-thirds of the reaction it was found that duplex formation assayed in this way followed second-order kinetics, but this result depended on an assumed terminal value corresponding to about 80% completion. Second-order kinetics were also reported for the initial phase of optically monitored renaturation reactions by Wetmur and Davidson (1968). The correct form of the kinetics in the later part of the reaction as assayed by optical hyperchromicity remains an open question which we bypass. It has been the practice to assume that there is a factor of 2 in rate between hydroxyapatite binding and duplex formation assayed by optical hyperchromicity and for many purposes this is sufficiently accurate.

With the increasing use of S1 nuclease for the assay of duplex formation, some-

what better accuracy is possible, and it has become useful to consider the actual kinetics of duplex formation. Morrow (1974) reported that the kinetics of reassociation of randomly sheared SV40 DNA fragments assayed with S1 nuclease are significantly different from second order. After the early part of the reaction a slower rate of formation of duplex is observed than would be predicted from the initial rate if second-order kinetics were followed. In the experiments described here we have directly compared the kinetics of *Escherichia coli* DNA reassociation as measured by hydroxyapatite and by S1 nuclease resistance. Our results for the appearance of S1 nuclease resistance show quantitatively the same kinetic form as do Morrow's measurements.

In order to understand the causes of the observed kinetics a number of further studies have been undertaken. In particular we have explored the rates of reaction of the single-strand ends of partially reassociated structures. These are termed particles since late in the reaction they can grow to fairly large size (Graham, Eden, Davidson, and Britten, in preparation). Reactions of such unpaired regions with each other and with single strands on totally unpaired fragments (termed free) form an important part of the reassociation process which has not been fully analyzed in previous treatments.

In an earlier analysis (Britten *et al.*, 1974; Britten and Kohne, 1968) a simple approximation was used to account for the reduction in yield of duplex in later collisions. It was assumed that effective nucleation rate is proportional to the square of the concentration of unpaired nucleotides and that the yield of duplex per nucleation is reduced as the reaction proceeds in proportion to the fraction of unpaired nucleotides remaining. The form of the resulting equation predicted fairly well the kinetics of duplex formation observed by Morrow (1974). However this analysis provides little insight into the mechanisms responsible. In

the current work we have taken into account the variation in length of the free single strands and of the single strands remaining on particles. The variation in length during the reaction was estimated using a computer program which models the reassociation reaction by a "Monte Carlo" method. These length changes, of course, retard the reassociation rate at later times. We show in addition that, probably due to some form of steric interference, the per nucleotide rate of reaction of the particle single strands is inhibited. This inhibition is required to explain quantitatively the observed forms of both hydroxyapatite and S1 nuclease kinetics. A full description of this work is being prepared, and here we only briefly discuss the results.

The Empirical Expressions for Analysis of Reassociation Measurements

In 1968 Britten and Kohne introduced the useful and now familiar form

$$\frac{C}{C_0} = \frac{1}{1 + kC_0t} \quad (1)$$

to describe second-order DNA reassociation reactions. Here C represents the concentration of totally single-stranded fragments; C_0 is the total DNA nucleotide or starting single-stranded nucleotide concentration; t is time; and k is the empirically observed second-order rate constant. As shown originally by Britten and Kohne and later by many other authors, the kinetics of reassociation of almost totally nonrepetitive DNAs such as that of *E. coli* follow Equation 1 when strand pair formation is assayed by hydroxyapatite binding. Recently Morrow (1974) found that when duplex formation is measured by S1 nuclease resistance, the reassociation kinetics of randomly sheared DNA follows a form which can be described by the non-second-order form

$$\frac{S}{C_0} = \left(\frac{1}{1 + kC_0t} \right)^n \quad (2)$$

*Kinetics of E. coli DNA Reassociation
Measured by S1 Nuclease Resistance
and by Hydroxyapatite Binding*

Samples of sheared, denatured *E. coli* DNA were allowed to renature as described in "Materials and Methods," and at appropriate C_0t values the reactions were stopped by quick freezing in dry ice-acetone. The samples were later thawed, diluted, and divided into two portions. One of these was assayed for S1 nuclease resistance, and the other was passed over a hydroxyapatite column. The results of this experiment are shown in Fig. 17. As expected, the kinetics of appearance of hydroxyapatite binding follow a second-order form. In Fig. 17 the hydroxyapatite data are fitted with Equation 1, using the least-squares procedures referred to in "Materials

and Methods." The kinetics of appearance of S1 nuclease resistance are fitted with Equation 2. Our data follow the form of Equation 2 reasonably well, though the unavoidable scatter precludes a very accurate comparison. Least-squares analysis shows that the best value for the n of Equation 2 is 0.45. These results are therefore in excellent quantitative agreement with those reported by Morrow for randomly sheared SV40 DNA.

*Computer Simulation of the
Reassociation Reaction by a Monte Carlo
Procedure*

The reassociation reaction was modeled in a computer in the following way. Two arrays of 5000 elements, representing the complementary strands of DNA were established in the computer. The array

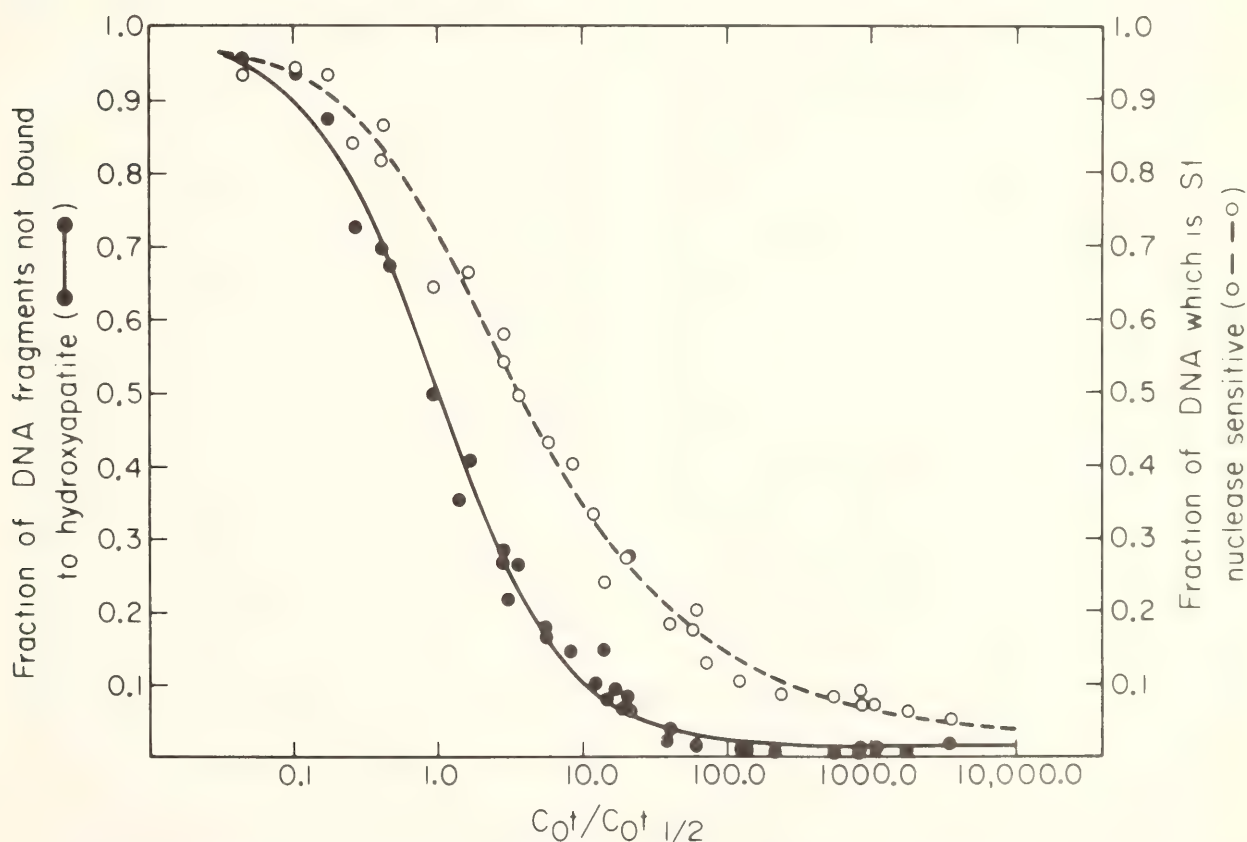


Fig. 17. Reassociation of *E. coli* DNA fragments. DNA duplex formation was assayed on hydroxyapatite at 60°C in 0.12 *M* PB (solid circles) and by resistance to S1 nuclease digestion (open circles) (see "Materials and Methods"). Two sets of data were pooled by normalizing both to a hydroxyapatite $C_0t_{1/2}$ of 1.0 (i.e., $C_0t/C_0t_{1/2}$). The solid line represents a computer least-squares solution for reassociation assayed by hydroxyapatite binding, according to Equation 1 in text. The dashed line represents the best least-squares solution for the S1 nuclease kinetics, according to Equation 2 in text. The normalized rate constant K is, of course, 1.0 for both curves and the best value of n for the S1 nuclease data is 0.453.

is divided into fragments, using a random number generator according to a Gaussian distribution of lengths with the average and standard deviation specified for each run. For the results utilized in this paper the average was 20 elements long, and the standard deviation was 10. The distribution was truncated so that no lengths below 2 or above 40 were included. This distribution matched fairly closely the length distribution of sheared fragments determined by electron microscopy (Chamberlin *et al.*, 1975). The array of 5000 elements was assumed to repeat every 31 elements in order to increase the effective rate of nucleation to a practical value. The ratio of the repeat length to the average fragment length was chosen so that the fragments terminated randomly within the repeat length. A run is done as follows. A random number generator selects an element out of the total 5000; if it has been paired already, a second is selected again at random; when an unpaired element is found, one of the complementary elements in the other strand is selected at random; if it is paired the process starts over by calling a random element in the first strand; when two unpaired elements have been selected in this totally random fashion, the two fragments are "zippered" to the two ends of their overlap; each of the included elements is marked as paired. The number of elements paired is scored for duplex formation and the total length of the two fragments is scored for hydroxyapatite binding. Where inhibition of particle single-strand ends is to be included, a chosen fraction of the nucleations are dissociated and no scoring or marking is done. The process of selecting a random nucleotide in the first strand starts over. Each such try is considered a collision and is the measure of the C_0t . When the simulated rate is calculated so that the probability of nucleation is proportional to the square root of the fragment length rather than to the fragment length itself there is little change in the result. At periodic intervals in $\log C_0t$

the information is read out and stored in files that are available to the least-squares programs for kinetic analysis. It is to be noted that collisions that lead to overlap of less than one element are not recorded since the elements are counted as integers. From this point of view, one element can be considered equivalent to about 30 nucleotides.

Fraction of Duplex-Containing Fragments Which Remain Single Stranded

The renaturation begins with a first collision and nucleation, the result of which is the formation of a length of duplex equal to the overlap between the strands. In later collisions the single-stranded regions become filled in as successive nucleation events occur. Thus the fraction of DNA which is S1 nuclease sensitive progressively decreases. Figure 17 shows that about 94% of the DNA becomes S1 nuclease resistant when the reaction approaches completion (the remaining 6% may be contaminated with unreactable DNA fragments and is not necessarily true terminal value). The *initial value* for the fraction of hydroxyapatite-bound fragments which is S1 nuclease insensitive should equal the average amount of overlap which occurs when two fragments containing complementary sequence collide, since early in the reaction only first collision products are present in the duplex fraction. We define the parameter α as the sequence paired per nucleation event (i.e., the overlap), expressed as a function of the single-strand fragment length. For fragments terminating at the same place in the sequence, for example, restriction enzyme fragments or whole genomes, $\alpha = 1.0$. Wetmur and Davidson (1968) calculated that for an ideal case of randomly sheared fragments of uniform length, $\alpha = 0.66$. In other words two-thirds of each fragment would be included in duplex in an average collision between such fragments. We have confirmed this result using an independent method of calculation and have

extended it to the case of a range of fragment lengths. The effect of a distribution of fragment lengths is to decrease the value of α . For fragment length distributions roughly similar to that of the randomly sheared DNAs used in this study the computer simulation provides values for α in the range 0.55–0.6. The exact value depends on the fragment length distribution imposed.

Theoretically the value of α could be obtained directly by measuring the S1 nuclease sensitivity of hydroxyapatite-bound DNA early in the reaction. In practice this is difficult with fragment lengths of the range used in this study. Quantitative elution of the reassociated DNA (i.e., with 0.5 M phosphate buffer) cannot always be achieved. Hence our best empirical estimate of α is derived from the data of Fig. 17. To obtain this estimate, the S1 nuclease resistance of a portion of the reaction mixture at each C_0t is subtracted from the amount bound to hydroxyapatite. The difference is

plotted in Fig. 18. Earlier than $0.5 \times$ the $C_0t_{1/2}$ the difference between the two measurements is too small in absolute terms to be estimated reliably, and thus the ordinate intercept in Fig. 18 is set at this point in the reaction. Here about 33% of the DNA is bound to hydroxyapatite but only about 18% is S1 nuclease resistant. However at $0.5 \times$ the $C_0t_{1/2}$ almost none of the duplex-containing particles include more than two fragments. Thus, these particles are mainly the products of first collisions. Figure 18 shows that the fraction of bound fragments which is S1 nuclease sensitive at relatively low C_0t is about 0.45. The value of α obtained from these is then $(1 - 0.45)$ or 0.55. This result is consistent with the value calculated on a statistical basis in the computer simulation, as noted above.

At this point a contradiction is apparent between the best estimates of α (0.55–0.6) and the value of the exponent n in Equation 2 fitted to the S1 nuclease

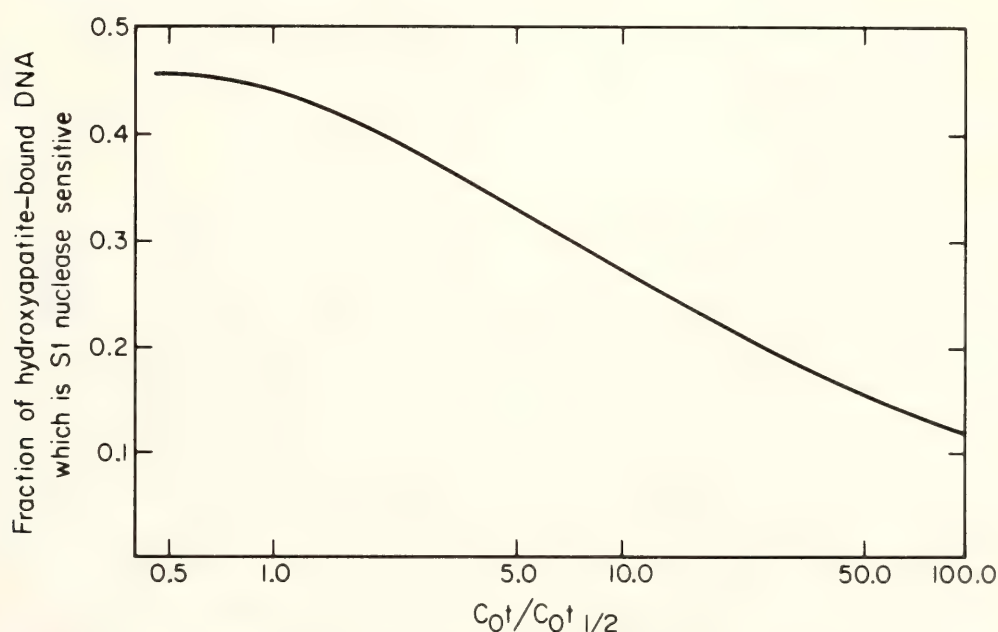


Fig. 18. Fraction of hydroxyapatite bound DNA which remains single stranded as a function of C_0t . The fraction of hydroxyapatite bound DNA which is S1-nuclease sensitive was calculated from the computer least-squares fits shown in Fig. 17. At each C_0t the fraction of the total DNA in fragments bearing duplex was determined from the curve describing the hydroxyapatite kinetics in Fig. 17 (hydroxyapatite bound fraction). At the same C_0t the fraction of the total DNA which was S1 nuclease resistant was calculated from the line describing the S1 nuclease kinetics (S1-resistant duplex). The fraction of hydroxyapatite-bound DNA which is single stranded at this C_0t is therefore $[1 - (\text{S1-resistant duplex/hydroxyapatite-bound fraction})]$. A series of such calculations were made from approximately one-half the normalized hydroxyapatite $C_0t_{1/2}$ (i.e., C_0t 0.5) to 100 times the $C_0t_{1/2}$.

data (0.45). For the initial few percent of the reaction, n should equal α .^{*} It follows that Equation 2, when $n = 0.45$, is an erroneous form for the early part of the reaction and more importantly, that there is no simple physical meaning for the measured value of n . We show below that several complex factors are indeed involved. For the moment we retain Equation 2 as an adequate empirical description of single strand remaining for most, if not all, of the course of the reaction.

Figure 18 shows that as the reaction proceeds the fraction of the bound fragments which are S1 nuclease sensitive decreases from the maximum value of $(1 - \alpha)$. Since this is mainly the result of successive nucleations on the same fragments, the expected consequence is the buildup of large hyperpolymers late in the reaction. These have been observed both in the electron microscope and by physical-chemical means, and will be the subject of a separate report (Graham, Eden, Davidson, and Britten, in preparation).

Comparison of Observed and Ideal Reaction Kinetics

The computer simulation of the reassociation reaction has been used to calculate the expected or ideal reaction kinetics. By summing up the fraction of simulated fragments which contain duplex regions, the ideal rate of appearance of hydroxyapatite binding is calculated. A similar calculation in which the duplex content is summed provides the ideal rate of appearance of S1 nuclease resistance as a function of the number of fruitful collisions ($C_0 t$). The cal-

culated kinetics are compared to the observed kinetics in Fig. 19.

Figure 19 shows that the measured kinetics of the reaction are of different form than the expected kinetics. These two sets of curves are plotted with the same hydroxyapatite rate. Given the same initial rate, the calculated reaction would proceed more rapidly than the observed second-order form. Thus, when Equation 2 is used to fit the simulated hydroxyapatite binding curve, the value obtained for n is 1.85 rather than 1.0 as in Equation 1. Similarly, when Equation 2 is used to fit the simulated S1 nuclease curve, the value obtained for n is 0.55 rather than the measured 0.45. We now consider the implications of the disagreement between the ideal and the observed kinetic calculations.

As pointed out above, the rate of disappearance of free single strands depends not only on the reaction between free single strands but also on the reaction between free single strands and the single-stranded regions on particles. A correct description of this process would take the form

$$\frac{dC}{dt} = -kC^2 - kC(S - C) \quad (3)$$

where the meaning of k and C are as above and $(S - C)$ is the concentration of single-stranded nucleotides on particles. As a first approximation the same rate constant, k , is used for both terms of the expression. Equation 3 is, of course, a non-second-order form, and it predicts that measurements of single-stranded DNA concentration made with hydroxyapatite should display faster than second-order kinetics, given the same initial rates. The effect of fragment length variation is to blur this distinction somewhat by slowing down the reaction as it approaches termination. This is because longer fragments tend to react first so that the mean free fragment length and the reaction rate decrease. However, a realistic fragment length distribution is already included in the

^{*} This can be shown in the following way. From Equation 1, the initial rate of disappearance of single strands is $dC/dt = -kC_0^2$. Thus for the first collision case the disappearance of single-stranded DNA nucleotides should be $dS/dt = -\alpha kC_0^2$. On the other hand, from Equation 2, $dS/dt = -nkC_0^2(1 + kC_0 t) - 1 - n$. Early in the reaction when t is small, $dS/dt = -nkC_0^2$. Therefore early in the reaction, $\alpha = n$.

simulated reactions illustrated in Fig. 19. The conclusion is that the reaction as measured with hydroxyapatite has a rate which in the second half of the reaction is slower than the prediction even when the effect of fragment length distribution is included. This result strongly implies the existence of some form of inhibition which retards the later phase of the reaction.

Similar considerations apply to the comparison of calculated and observed S1 nuclease kinetics. Here again it is evident that there is some inhibition,

which has the effect of retarding the actual appearance of S1 nuclease resistance. The calculated uninhibited case begins at the expected rate, with the n of Equation 2 at 0.55 (i.e., the same as α). The simulated reaction continues throughout in accordance with this function. The observed reaction must also begin at this rate since α is measured empirically at 0.55 (Fig. 18). For the initial phase of the reaction the difference between an n value of 0.45 and one of 0.55 is of course almost purely theoretical, since low C_0t data accurate

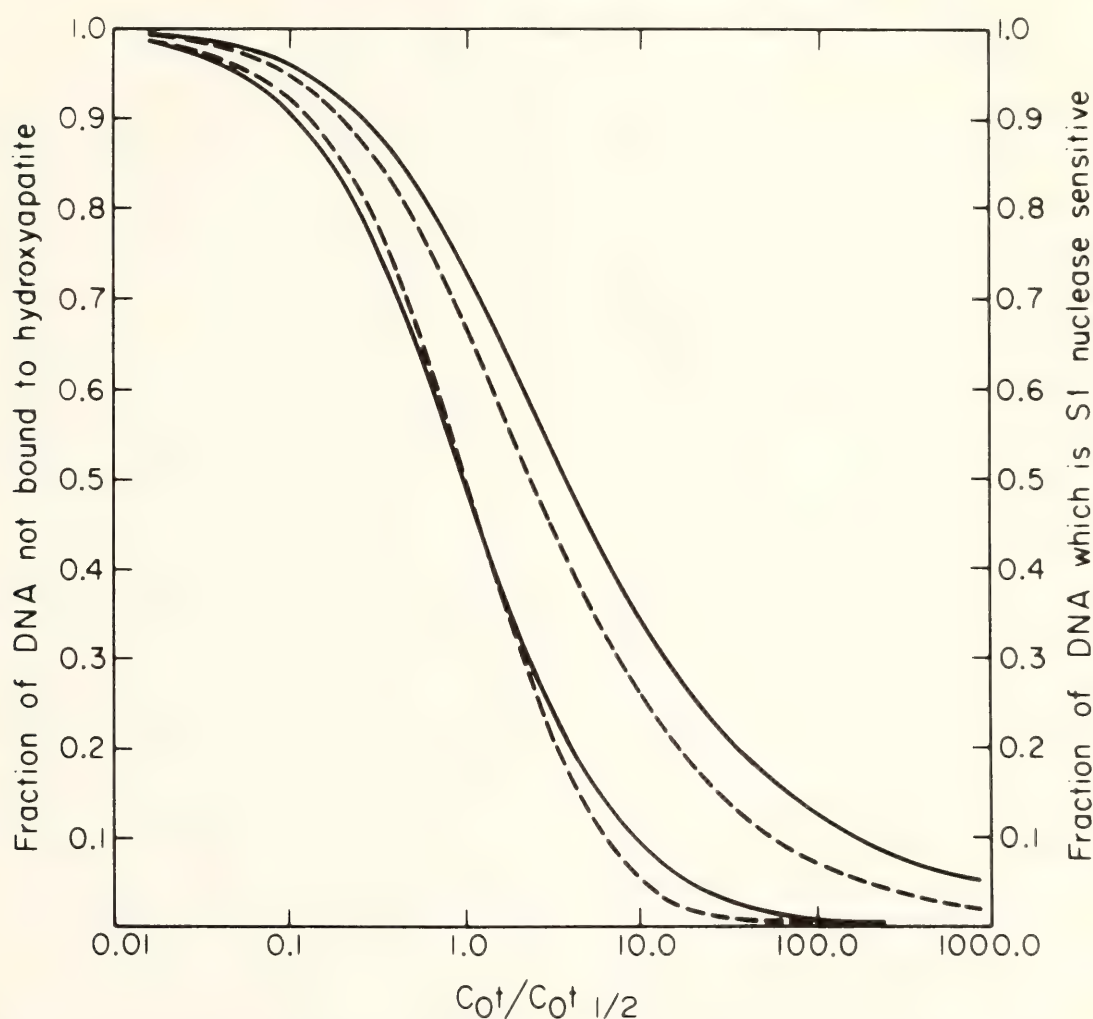


Fig. 19. Comparison of calculated and observed reassociation kinetics. The solid lines describing the reassociation of *E. coli* DNA as measured by S1 nuclease resistance and by hydroxyapatite binding are reproduced from Fig. 17. The calculated curves are shown by dashed lines. These are the hydroxyapatite binding curve (inner curve) and the calculated S1 nuclease resistance curve (outer curve). The calculation was carried out by a computer program which simulates the reassociation reaction using a realistic fragment size distribution as described in "Materials and Methods." The computer calculations presented are the average of 8 runs of the simulation program, all closely agreeing. Both sets of curves are normalized to a hydroxyapatite rate constant of 1 to facilitate comparison. When Equation 2 is used to fit the computer-generated curves, setting $K = 1.0 \text{ l M}^{-1} \text{ sec}^{-1}$, the calculated hydroxyapatite binding curve has $n = 1.85$, and the calculated S1 nuclease curve has $n = 0.55$.

enough to distinguish these initial rates are almost impossible to obtain. Soon, however, the overall rate declines, due to some form of inhibition, and the best-fit value of n for the whole reaction drops to 0.45. We conclude that an inhibition affecting the later part of the reassociation reaction is required in order to explain the experimental measurements of both hydroxyapatite and S1 nuclease kinetics. Neither the apparent second-order form described by Equation 1 for hydroxyapatite kinetics nor the use of Equation 2 with $n = 0.45$ for S1 nuclease measurements can be quantitatively understood without considering such an inhibition.

Reaction of Particle Single Strands with Free Single Strands

A reasonable explanation of the above results is the proposition that the reaction of particle single strands is inhibited relative to that of free single strands. To test this idea the following experiments were carried out. *E. coli* DNA was allowed to renature to a point where almost all the DNA was present in particles, as judged by its binding to hydroxyapatite. In one case the particles were physically isolated from the small amount of free single-stranded DNA remaining. Trace amounts of labeled single-stranded DNA were then added, and the rate of reaction of the tracer with the already renatured driver DNA was measured. The quantity of particle single strands in the driver DNA preparation at the point of addition of the tracer was estimated as its S1 nuclease sensitivity. Details of three such experiments are presented in Table 10, and an example of the kinetics obtained is presented in Fig. 20. Here the reassociation kinetics of the driver DNA are shown, and in addition the tracer DNA reactions beginning at driver DNA C_0 ts 20 and 1000 are illustrated.

The results of these experiments are presented in Table 10. An expected rate for the tracer-particle single-strand

reaction is calculated, on the basis that particle single strands of given length are as effective in initiating nucleation as if they were free single strands of the same length and at the same concentration (column 7, Table 10). When the observed tracer rate (column 8, Table 10) is compared to this calculated free strand rate it is found that the observed tracer rate is about one half the calculated rate (column 9, Table 10). That is, the tracer reacts about two times more slowly than if it had been added to a single-strand driver of equivalent length at the beginning of the reaction. This provides a direct measure of the relative inhibition in the reaction of free single strands with particle single strands. The measurement is not of very high accuracy because of the several quantitative assumptions required in carrying out the appropriate calculations (see footnotes to Table 10). However we believe it to be reliable with an error of about $\pm 20\%$. This calculation provides an estimate of inhibition *after* the best length correction possible at our present stage of knowledge has been made. The roughly twofold inhibition observed is therefore due to some factor other than progressive shortening of the driver particle single strands. We stress that these measurements provide only an average, or overall estimate of the inhibition, which is likely to change during the course of the reaction as a function of strand length, size of particle, and possibly other factors, such as ionic strength and temperature, as well.

Calculation of Hydroxyapatite and S1 Nuclease Renaturation Kinetics

It is clear from the foregoing that neither the traditional second-order expression (Equation 1) nor the modified form proposed by Morrow (1974) (Equation 2) provides a description of reassociation kinetics which is satisfactory from a mechanistic point of view. Both Equation 1 and Equation 2 are of course

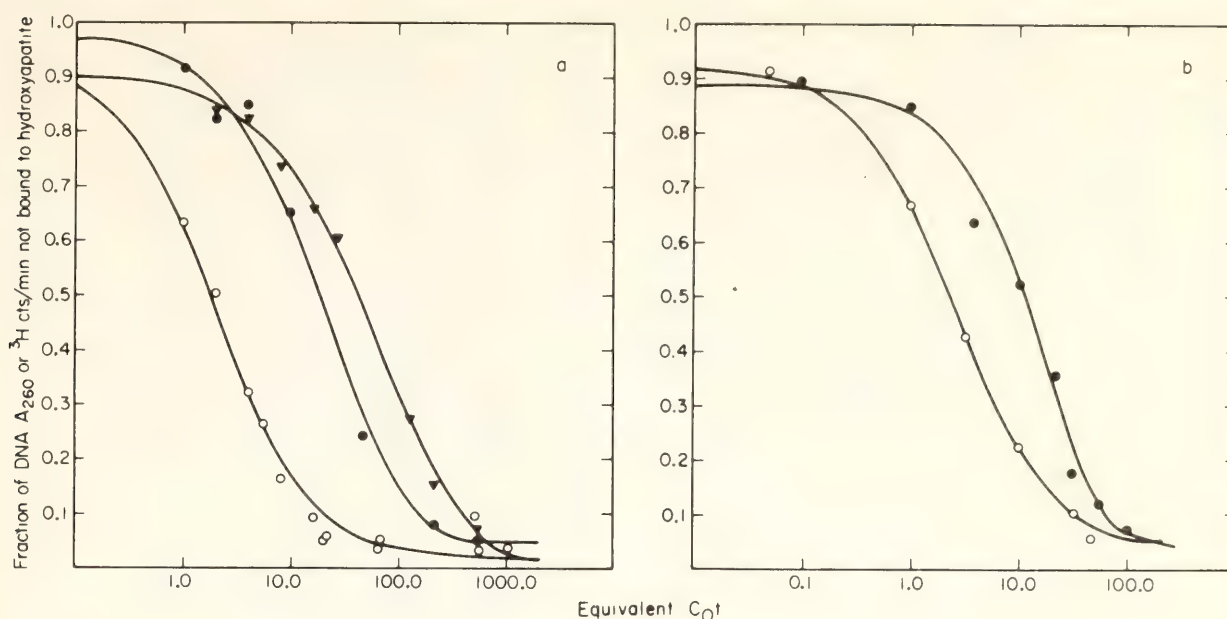


Fig. 20. Tracer DNA reaction with particle single strands: (a) Open circles show reassociation of 1000-nucleotide *E. coli* DNA measured by the portion of A_{260} bound to hydroxyapatite ("driver DNA"). The best least-squares fits are shown by the lines. Solid circles describe the reaction of 300-nucleotide ^3H -DNA fragments added to the driver at C_0t 0. Solid triangles show the reaction of the same tracer added to the driver DNA in a separate series of samples when the driver DNA has attained C_0t 1000. At this stage 6.4% of the driver DNA is single stranded (Table 10). For comparison, the latter two curves are plotted together with the driver DNA curve by regarding the time of tracer addition as C_0t 0 and the single-strand concentration at the time of tracer addition as C_0 . The calculated rates are shown in Table 10. (b) Open circles show reassociation of 600-nucleotide *E. coli* DNA measured by hydroxyapatite binding as in 20a. At C_0t 20 the fraction which binds was isolated and reacted with the 300-nucleotide long tracer DNA. Reassociation of the tracer with this particle driver is indicated by the open circles. The calculated rates of these reactions are shown in Table 10. As above, the single-strand driver concentration at time of tracer addition is taken as C_0 to permit a comparable plot.

empirically useful for data reduction. However, neither explicitly takes into account reactions other than the initial nucleation of two free single strands. Furthermore, we know from the comparison in Fig. 19 between the kinetics obtained in a computer simulation of the reassociation reaction and the kinetics observed experimentally that the kinetics described by Equations 1 and 2 include the effects of retardation in the course of the reaction, contrary to simple prediction. The experiments described in Table 10 provide direct evidence for such an inhibition.

There are two classes of explanation for the overall retardation revealed by these investigations. One of these we shall term "length effects" and the other "particle inhibition." By length effects we mean a decrease in the rate of successful nucleation between single

strands which is due simply to the progressive shortening of the single-stranded regions. The expected length effects for single strands on particles is assumed to be the same as for free single strands. We use the term "particle inhibition" to denote decrease in the per nucleotide reactivity (i.e., per nucleotide nucleation probability) of single strands which belong to duplex-containing particles, due to the presence of the duplex. For example, one could imagine the rigid duplex regions affecting the excluded volume parameters of neighboring single-stranded regions. Particle inhibition is measured directly in the experiments of Table 10, and was estimated to result in about a twofold rate decrease for reactions in which particles participate. It now appears that both length effects and particle inhibition are required to account for the observed kinetics.

TABLE 10. Experimental Observation of Rate Inhibition in Reaction of Particle Single Strands Compared to Free Single Strands. 300-nucleotide-long tracer DNA is added to driver DNA at indicated driver DNA C_0t s and rate of association with driver DNA is measured by hydroxyapatite chromatography.

1	2	3	4	5	6	7	8	9
Driver DNA Equivalent C_0t When Tracer DNA Added (M^{-1} sec)	Starting Driver Fragment Length L_D (NT)	Calculated Length of Single-Stranded Regions on Driver Particles at C_0t^a L_R (NT)	Fraction of Driver DNA at C_0t		Self-Reassociation Rate of Driver DNA ^c K_D ($1 M^{-1} \text{ sec}^{-1}$)	Expected Rate of Tracer Association with Driver ^d K_T (exp) ($1 M^{-1} \text{ sec}^{-1}$)	Observed Rate of Tracer Association with Driver ^h K_T (obs) ($1 M^{-1} \text{ sec}^{-1}$)	Minimum Inhibition K_T (exp) K_T (obs)
			Hydroxyapatite Unbound	S1 Nuclease Sensitive ^b				
20	1000	250	0.055	0.277	0.516	0.0791 ^e	0.044	1.8 ×
1000		100	0.025	0.067		0.0328 ^f	0.013	2.5 ×
20	600	160	0.02	(0.39)	0.393	0.148 ^g	0.064	2.3 ×
(hydroxyapatite-bound DNA used as driver)								

^a Average length of single-strand regions on particles (L_R) was calculated by Equation 6 in text.

^b S1 sensitivity was measured directly except for value in parentheses, which was calculated from Equation 2 using the measured driver rate ($0.393 \text{ l } M^{-1} \text{ sec}^{-1}$). For the other cases the measured values compare closely to the expected values calculated from Equation 2. Thus expected values for the driver reacting at the rate of $0.516 \text{ l } M^{-1} \text{ sec}^{-1}$ are 0.34 for $C_0t \text{ 20}$ and 0.076 for $C_0t \text{ 1000}$.

^c Driver reassociation rates (K_D) were obtained as usual from hydroxyapatite measurements. The values given are the best least-squares fits to Equation 1.

^d Calculations of the expected rates of tracer-driver association [K_T (exp)] on hydroxyapatite utilize a result presented in Galau, Klein, Smith, Davidson, and Britten, 1975. There it is shown that for the case where driver DNA is longer than tracer, the rate of reaction of a tracer of length L_T with a driver of length L_D is given approximately by $K_D(L_T/L_D)$ where K_D is the driver rate constant. For the $C_0t \text{ 0}$ tracer additions, K_D is the measured driver rate (column 6). Where the tracer is added at $C_0t \text{ 20}$ or $C_0t \text{ 1000}$ K_D must be calculated from the lengths shown in column 3 since the length of the particle single strands, L_R , is less than the starting length, L_0 . Here the usual $L^{-1/2}$ relationship must be applied. Thus for these cases

$$K_D = K_D \text{ (column 6)} \left[\frac{300}{L_R \text{ (column 3)}} \right]^{1/2}$$

(tracer length L_T is 300 nucleotides throughout). Individual calculations are given in the following notes.

^eTo calculate the expected tracer rate we must know that fraction of the total single-stranded DNA driver (0.277, column 5) which is particle single strand and that fraction which is free single strand, since the rates of these two components of the overall tracer reaction will be different. The reason for this is that the average length of the free single-strand driver is different from that of the particle single-strand driver. We calculate the average free single-strand length is 440 nucleotides at $C_0 t$ 20, while that of the particle single strand is 250 nucleotides. Equation 1 tells us that 0.088 of the DNA fragments renaturing at a rate of $0.516 \text{ l } M^{-1} \text{ sec}^{-1}$ is present as free single strands at $C_0 t$ 20 (this is a more reliable value for the calculation than the terminal estimate seen in column 4, 0.055). Thus about 0.189 of the DNA is particle single strand ($0.277 - 0.088 = 0.189$). For each fraction of the tracer reaction we calculate the expected driver rate K_D as in note d above: For the free single strands $K_D = 0.088 \times 0.516 \text{ l } M^{-1} \text{ sec}^{-1} \times (440/1000)^{1/2} = 0.0301 \text{ l } M^{-1} \text{ sec}^{-1}$, for the particle single strands $K_D = 0.189 \times 0.516 \text{ l } M^{-1} \text{ sec}^{-1} \times (250/1000)^{1/2} = 0.0488$. $K_{T(\text{exp})}$ for the free single strands is then $0.0301 \text{ l } M^{-1} \text{ sec}^{-1} (300/440) = 0.0205 \text{ l } M^{-1} \text{ sec}^{-1}$ and $K_{T(\text{exp})}$ for the particle single strands is $0.0488 \text{ l } M^{-1} \text{ sec}^{-1} (300/250) = 0.0586$. The overall value of $K_{T(\text{exp})}$ is the sum of these two reactions or $0.079 \text{ l } M^{-1} \text{ sec}^{-1}$.

^fThe fraction of free single strands at $C_0 t$ 1000 is so small that only the particle single strand reaction need be considered. The calculation is otherwise the same as in note f. Thus $K_{T(\text{exp})} = 0.516 \text{ l } M^{-1} \text{ sec}^{-1} \text{ (column 6)} \times 0.067 \text{ (column 5)} \times [100 \text{ (column 3)}]/1000 \text{ (column 2)}^{1/2} \times [300/100 \text{ (column 3)}] = 0.0328 \text{ l } M^{-1} \text{ sec}^{-1}$.

^gSince hydroxyapatite-bound DNA was used as driver, no free single strands participate in the tracer reaction. Thus as in note g only particle single strands need be considered to calculate $K_{T(\text{exp})}$ (see notes e and f). K_D is first calculated using L_R , the average particle single-strand length. $K_{T(\text{exp})} = 0.393 \text{ l } M^{-1} \text{ sec}^{-1} \text{ (column 6)} \times 0.39 \text{ (column 5)} \times [160 \text{ (column 3)}]/600 \text{ (column 2)}^{1/2} \times [300/160 \text{ (column 3)}] = 0.148 \text{ l } M^{-1} \text{ sec}^{-1}$.

^hObserved tracer rates were calculated by using the equation

$$\frac{T}{T_0} = \exp \frac{K_T [1 - (1 + K_D C_0 t)^{1-n}]}{K_D (1 - n)}$$

where T is unhybridized tracer concentration, T_0 is starting tracer concentration, K_T is the rate of tracer-driver reaction, and other symbols are as in Equations 1 and 2. K_T is different from K_D since $L_T \neq L_D$. Equation 10 is obtained by integrating the equation $dT/dt = -K_T ST$, where S is total single strand concentration (Equation 2). The derivation of the equation is given in Davidson *et al.* (1975). This equation does not include the effects of the particle single strand inhibition noted in this paper. However the rates obtained in this experiment are very insensitive to the exact form used to fit the data, and for this case even second order fits (Equation 1) give closely equivalent results. For the calculations in this column, the values of K_D are those calculated in footnotes e, f, and g. The listed values of $K_{T(\text{obs})}$ are the best least-squares fits to this equation.

We have developed new differential equations for the disappearance of free single strands (hydroxyapatite kinetics) and the disappearance of single-stranded nucleotides (S1 nuclease kinetics). These equations include appropriate terms for the reaction of free single strands with particle single strands and for the reaction of particle single strands with each other. They permit a more detailed analysis of the nature of the apparent inhibition evident in the observed reassociation kinetics than has previously been possible. For brevity we have not reproduced here the equations or their derivation which will be published in the near future. (Smith, Britten and Davidson; Britten and Davidson, con-

tributed to *Proceedings of the National Academy of Sciences*).

Evaluation of the Particle Inhibition, E

In Fig. 22 the data of Fig. 17 are replotted with the best least-squares fits of the equation for single-strand nuclease resistance. The form can be seen to fit the data excellently. The value of α was taken as 0.55 (Figs. 19 and 21) and K is normalized to 1.0 for ease of calculation.

Slightly less than a twofold particle inhibition factor has been used. The main feature of the calculation illustrated in Fig. 22 is that it shows that the

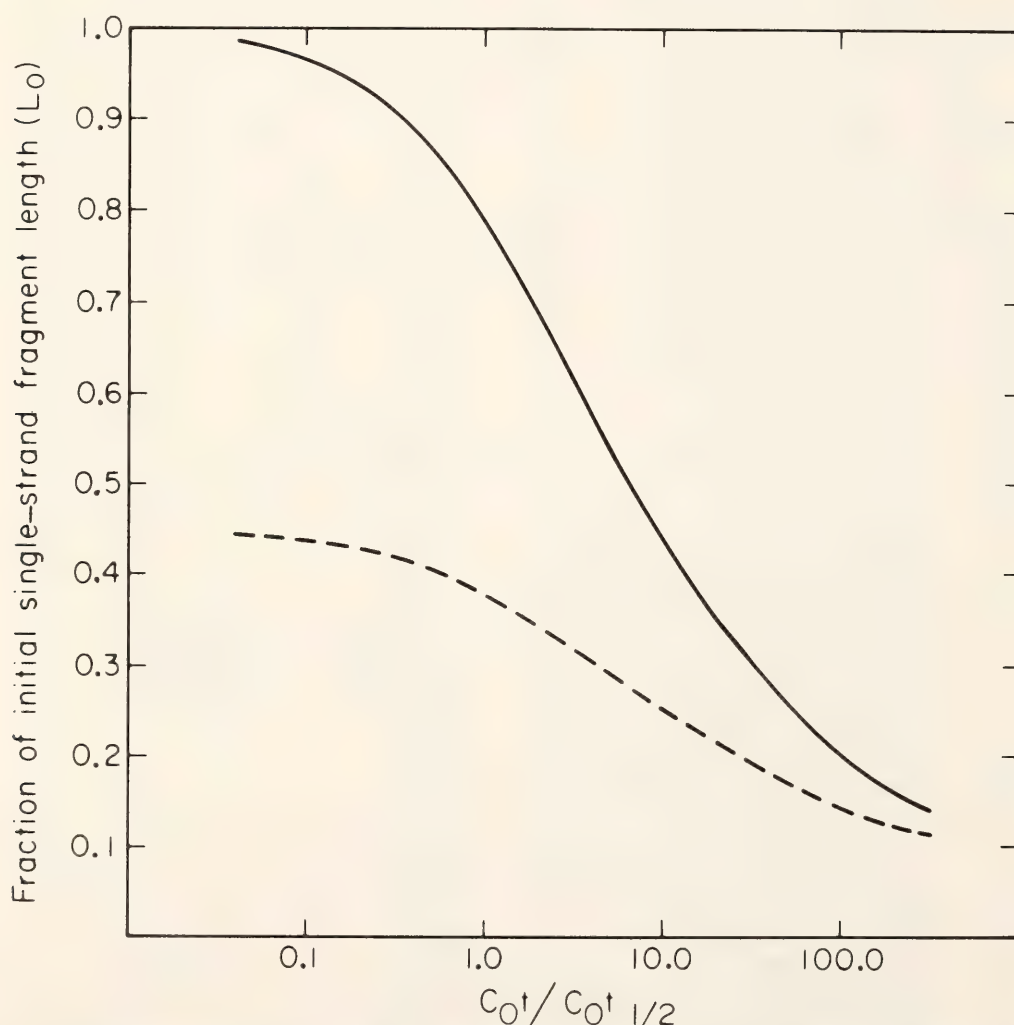


Fig. 21. Calculated change in length of free single strands (L/L_0) and single-strand regions in particles (L/L_R) with C_0t . The ordinate is expressed as the single-strand lengths relative to the starting fragment length, L_0 . The calculations were carried out with the computer simulation of the reassociation reaction described in the text. The abscissa is expressed in terms of C_0t normalized to a simulated hydroxyapatite binding rate of $1.0 \text{ l } M^{-1} \text{ sec}^{-1}$. The functions used to generate the lines plotted are Equation 6 for L_R/L_0 (dashed line) and Equation 7 for L/L_0 (solid line), from Britten, Smith, and Davidson, 1975.

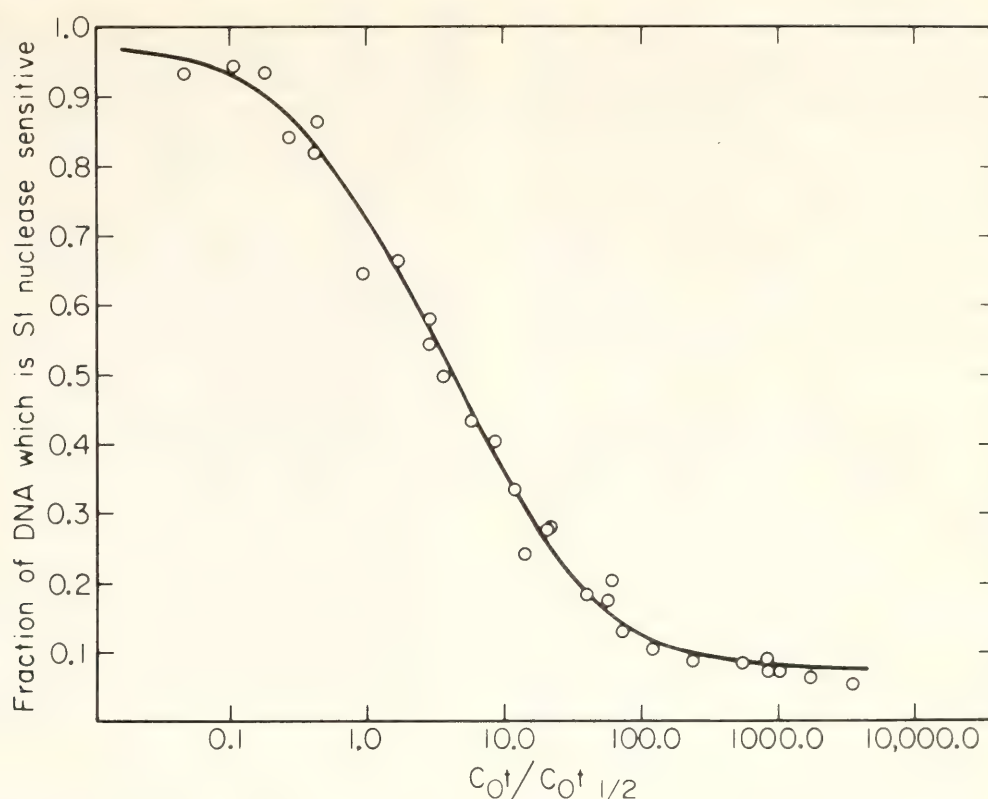


Fig. 22. S1 nuclease reassociation data compared to calculation including inhibition. Data are transcribed directly from the curve in Fig. 17. The line is calculated from equations (Britten, Smith, and Davidson, 1975) including the effect of length of single-strand regions available for re-association and including an inhibition of about a factor of 2 in the rate of nucleation of single-strand ends of partially reassociated fragments.

length effect built into the equations, combined with the particle inhibition, suffices to explain the observed S1 nuclease kinetics. It is possible that the length effect is slightly different from that we have calculated. New evidence (Galau, Klein, Smith, Britten, and Davidson, in preparation) shows that the dimensions of the longer strand may have to be taken into account in considering reactions between longer and shorter strands. We find that a slightly

larger inhibition is also needed to explain the observed hydroxyapatite kinetics, but less discrimination is possible than with the S1 nuclease kinetics (Fig. 19). Furthermore, the variation in root-mean-square error in fitting the calculated curves to the data with change in E is gradual. The most conservative conclusion is that an inhibition of 1.8- to 4-fold is required in order to provide a quantitative interpretation of the observed kinetics.

NUCLEIC ACID EVOLUTION

EVOLUTION OF REPETITIVE AND NONREPETITIVE DNA IN TWO SPECIES OF *Xenopus*

Glenn A. Galau, Margaret E. Chamberlin,
Barbara R. Hough, Roy J. Britten, and
Eric H. Davidson

This section is a very brief adaptation of Galau *et al.* (1975). The comparison of various rodent DNAs has shown that

the high thermal stability fraction of the repetitive sequence in each genome tends to be species specific, while the lower thermal stability fraction is more extensively shared between related species (Rice, 1971 *a, b*; 1972). Among the species for which a typical interspersed sequence arrangement has been demonstrated is the rat studied by Bonner *et al.* (1974). From the data reviewed in

the next section we may associate the high thermal stability fraction with the long repetitive sequences, and the lower thermal stability fraction with the short interspersed sequences. We conclude that at least some of the short repetitive sequence families present in a given genome tend to be older in evolution than most of the long repetitive sequence sets.

In *Xenopus laevis* 75% of the repetitive DNA is included in the 300-nucleotide interspersed sequence class. This amounts to about 18% of the genome, or some 4.9×10^8 nucleotides. Therefore the genome contains some 1.6×10^6 300-nucleotide repetitive sequence elements. The major frequency of repetition averages 2000 copies of each sequence (Davidson *et al.*, 1973) so in this repetitive class there are about 800 distinct repetitive sequence families. In addition, there is a complex class of long repetitive sequences. In the following section we consider some experimental evidence on the evolution of this huge library of repetitive sequences. Our approach has been to measure the changes that have occurred in the repetitive sequence components since the divergence of *Xenopus laevis* from one of its closer congeners, *Xenopus borealis* (sometimes misnamed *Xenopus mulleri*). As we now show, these changes have affected both the nucleotide sequences themselves and the frequency with which related repetitive sequences occur in the two genomes.

Reassociation Kinetics of *X. laevis* and *X. borealis* DNAs

The rates of reassociation of the various classes of repetitive sequence in *X. laevis* DNA have been studied previously, and extant data are summarized by Davidson *et al.* (1973). Figure 23 displays the reassociation of whole *X. laevis* DNA sheared to 450 nucleotides (solid circles, solid line) as well as the various kinetic components fitted to the *X. laevis* data (dashed lines, curves *a*, *b*, *c*, and *d*). While these components are

not unique choices and may in some cases represent averages rather than discrete frequency classes, they portray the best least-squares fits to the data assuming a small number of components. The major repetitive sequence class in which each sequence occurs about 2000 times (curve *b*) is present on about 31% of the 450-nucleotide fragments. In addition there are smaller repetitive components in which the sequences are present an average of 100 times (curve *c*) and over 10,000 times (curve *a*). The most slowly renaturing component is single-copy sequence (curve *d*). The actual amount of single-copy sequence in the genome is of course underestimated in an experiment like the one in Fig. 23 because of sequence interspersion. About a third of the total single-copy sequence is included in fragments that also contain repetitive sequence elements and hence bind at lower C_0t s than do fragments containing only single-copy sequences.

The reassociation profile for *X. borealis* DNA (open circles, dotted line) is remarkably similar to that of *X. laevis* DNA. In fact the *X. borealis* data can easily be fitted assuming exactly the same rates of reaction for the *X. borealis* kinetic components as for the *X. laevis* genome. When this is done the rms (root-mean-square) error of the fit remains the same as if the components were left free. As Fig. 23 shows, only slight or imperceptible differences may exist in the quantity of each repetitive sequence class in these two congeners.

Isolation of repetitive DNA fractions from X. laevis and X. borealis genomes. The isolation and characterization of *X. laevis* repetitive ^3H -DNA has been previously described (Hough and Davidson, 1972). Repetitive DNA is prepared by collecting from a hydroxyapatite column those DNA fragments which form duplex structures during incubation to C_0t 50 (*X. laevis*) or C_0t 100 (*X. borealis*). This C_0t is sufficient for the reaction of the small, very fast component (curve *a* in Fig. 23) and the major repetitive

class (curve *b* in Fig. 23) but not for the entire slow repetitive class (curve *c* in Fig. 23). The reaction of this isolated repetitive DNA fraction with whole *X. laevis* DNA is shown in Fig. 24. A repetitive *X. borealis* fraction was prepared similarly, and its reaction with whole *X. borealis* DNA is also shown in Fig. 24. 60%–70% of both tracers contain sequences present about 1000–2000 times per genome, reassociating with second-order kinetics at the rate characteristic of the major repetitive sequence class ($0.72\text{ M}^{-1}\text{ sec}^{-1}$). The reaction of the small portion of these tracers which belongs to the slow repetitive component (curve *c* of Fig. 23) is undetectable due to scatter in the terminal portions of the data. Completion of

the reaction at 75%–80% of tracer bound is due principally to its short fragment size, which also decreases its thermal stability.

Fig. 24 provides additional evidence for the similarity in repetitive sequence content suggested by the overall reassociation profiles in Fig. 23. Thus the isolated repetitive DNA fractions of both genomes renature with their respective whole DNAs at identical rates.

Interspecific reassociation of repetitive DNA fractions. Fig. 25a shows the reassociation of *X. laevis* repetitive DNA tracer with an excess of *X. borealis* DNA, and Fig. 25b shows the reassociation of *X. borealis* repetitive DNA tracer with an excess of *X. laevis* DNA. These reactions may be compared with

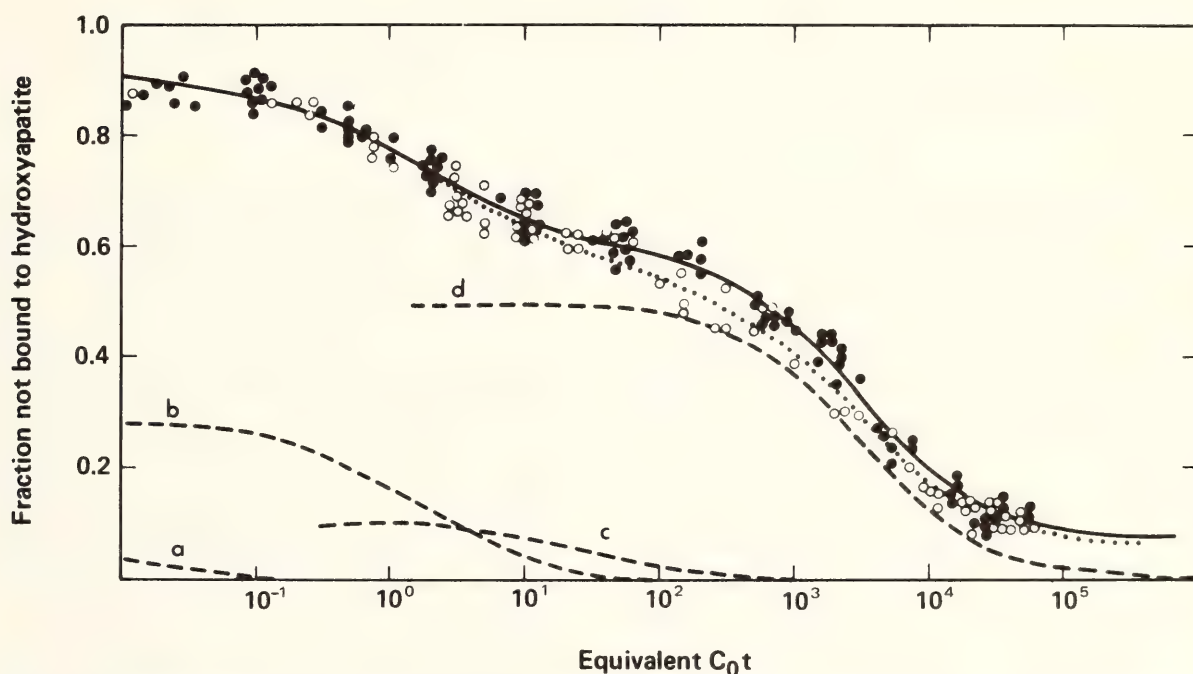


Fig. 23. Reassociation of 450-nucleotide long *X. laevis* and *X. borealis* DNAs. Reactions were carried out in 0.12–0.41 *M* phosphate buffer at 60°C and were analyzed by hydroxyapatite chromatography in 0.12 *M* phosphate buffer at 60°C. Incubations to C_0t s less than 100–1000 were carried out in 0.12 *M* phosphate and higher C_0t incubations in higher salt concentrations up to 0.41 *M* phosphate buffer. The C_0t values plotted have been corrected for the accelerating effect of higher salt concentrations (Britten *et al.*, 1974). That is, all C_0t values presented are calculated as the C_0t which would have been required to obtain the same amount of reassociation under standard 60°C, 0.12 *M* phosphate buffer conditions (equivalent C_0t). The solid and dotted curves represent the best least-squares solutions obtained with a computer assuming second-order kinetic components (Britten *et al.*, 1974). The components are as follows: Curve *a*, 6% of fragments reacting at a rate of $103\text{ M}^{-1}\text{ sec}^{-1}$; curve *b*, 31% of fragments reacting at $0.72\text{ M}^{-1}\text{ sec}^{-1}$; curve *c*, 10% of the fragments reacting at $0.036\text{ M}^{-1}\text{ sec}^{-1}$; curve *d*, 54% of the fragments reacting at $0.00035\text{ M}^{-1}\text{ sec}^{-1}$. The latter is the single-copy rate for the *X. laevis* genome. These kinetic components were derived by Davidson *et al.* (1973), where a more detailed description of the procedures and the data shown here can also be found. The components shown are those calculated for the *X. laevis* reaction (solid circles), and the same rates were also used to obtain the fit shown for *X. borealis* DNA (open circles).

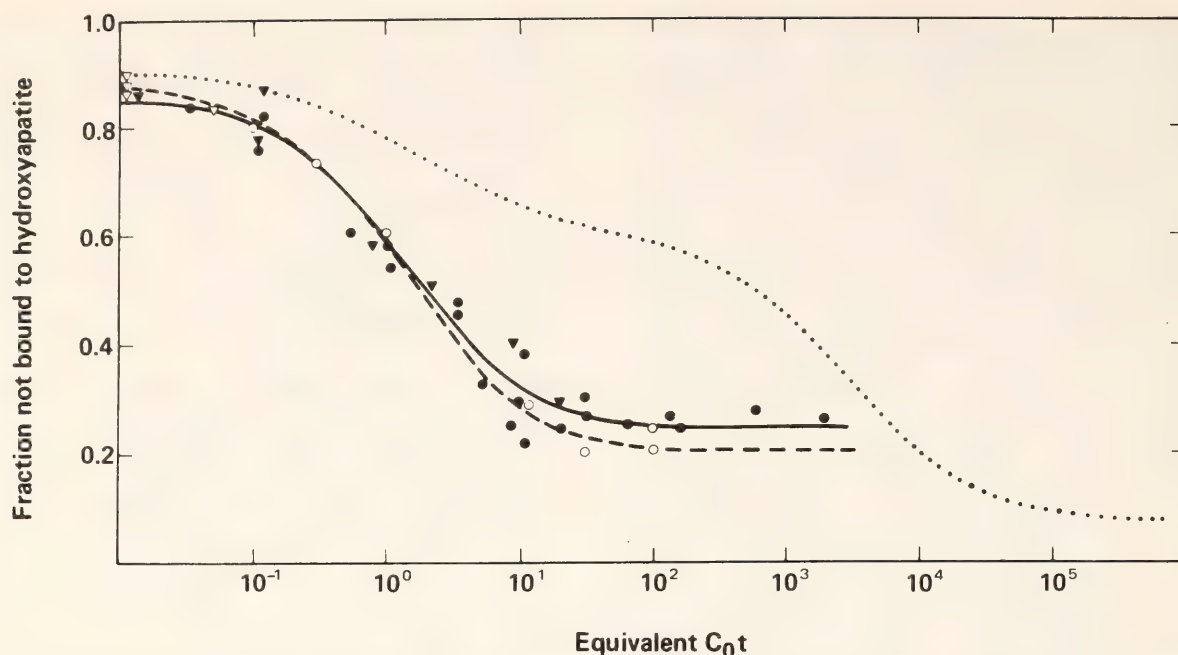


Fig. 24. Reassociation of isolated repetitive DNA fractions with homologous whole DNA. Reaction of isolated repetitive ^3H -DNA from *X. laevis* (solid circles) and from *X. borealis* (open circles) with their respective whole homologous DNA are shown. Conditions and data reduction were as in Fig. 23. Also indicated is the self-reassociation of *X. laevis* (solid triangles) and *X. borealis* (open triangles) repetitive DNA in the absence of whole DNA driver. The *X. laevis* data are reproduced from Hough and Davidson (1972). For comparison, the reassociation of whole *X. laevis* DNA (from Fig. 23) is illustrated as well (dotted line).

the reassociation of the same tracer preparations with an excess of homologous DNA as shown in Fig. 24 and reproduced on Fig. 25 as dotted curves. All four reactions appear to approach the same degree of completion (about 75%–80%). The relative retardation of at least part of the interspecies reactions is clearly evident. From the similar extent of reaction we infer that there are representatives of all repetitive sequence families in the DNA of both species. However, the two sets of repetitive sequences evidently differ in their repetition frequency and as a result of base substitution as well.

The retardation in the rate of interspecies reaction suggests that there have been some changes in the number of members of some of the sets of repeated sequences. The kinetic analyses shown on Fig. 25 are the simplest ways to represent the interspecies reaction kinetics, namely in terms of two components, one of which has the rate of the homologous reaction, and one of which is retarded. This solution suggests

that there are components with up to a 100-fold retardation in rate of reassociation. In reality there may be a wide range of different degrees of retardation in the interspecies reactions for different sets of repeated sequences. The thermal stability of the resulting duplexes has to be taken into account in order to derive the frequency of occurrence of repetitive sequences from the rates of reassociation measured in the experiments.

Even at its optimum temperature the renaturation rate for severely mismatched duplexes is somewhat retarded compared to the rate for perfectly matched duplexes (Wetmur and Davidson, 1968; Bonner *et al.*, 1973). Furthermore the rate begins to approach its maximum value only when the incubation temperature is about 15°C below the melting temperature of the duplexes.

An analysis of the melting characteristics of the hybrids formed by the *X. laevis* repetitive ^3H -DNA with whole *X. laevis* DNA and with whole *X. borealis* DNA was therefore carried out, and

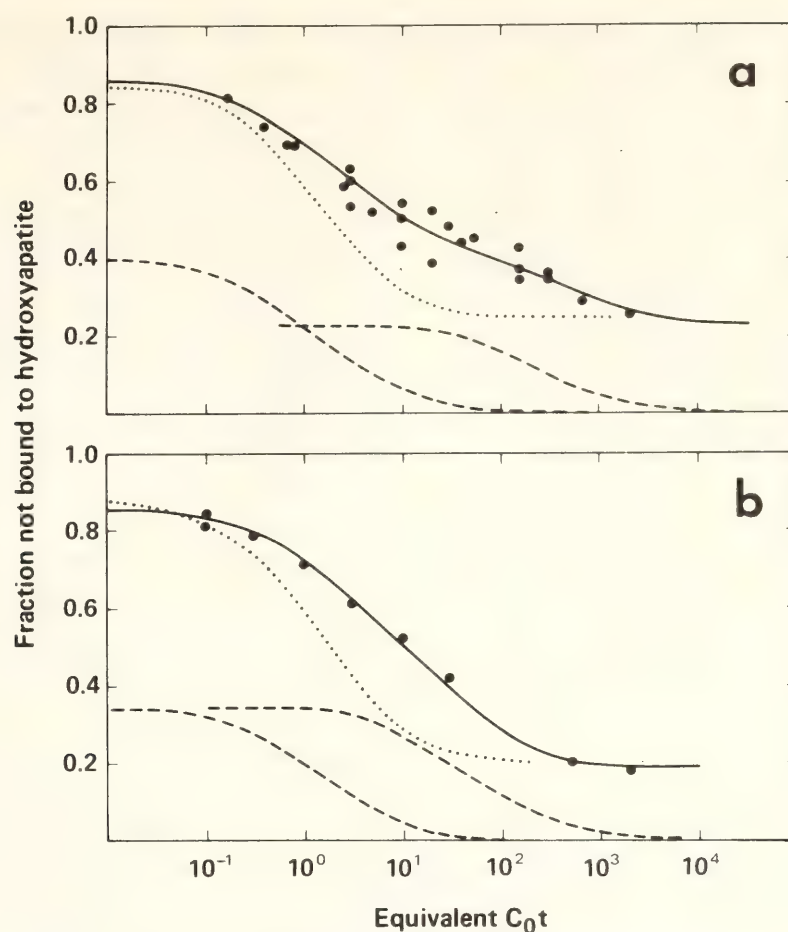


Fig. 25. Hybridization of repetitive ^3H -DNA fractions with heterologous whole DNA. Repetitive *X. laevis* and *X. borealis* ^3H -DNA were incubated separately with at least 6600-fold excesses of unlabeled, whole heterologous DNA in 0.12 *M* phosphate buffer at 60°C. The fraction of tracer hybridized was assayed by hydroxyapatite in 0.12 *M* phosphate buffer at 60°C. Self-reaction of the tracers (calculated to be less than 3% beyond the very rapid binding material) has not been subtracted from the hybrid data.

(a) Hybridization of repetitive *X. laevis* ^3H -DNA with *X. borealis* DNA. The solid curve through the data is the sum of two second-order kinetic components fit by least-squares methods to the data. These components are indicated by the dashed curves. This particular solution was obtained by holding the rate of the major fast component at $0.72\text{ M}^{-1}\text{ sec}^{-1}$, which is the rate of the major repetitive sequence component in both DNAs (Fig. 23). The least-squares rate for the smaller component is $0.004\text{ M}^{-1}\text{ sec}^{-1}$. If both rates and quantities are free to change, an equally good fit is obtained with rate constants of $1.02\text{ M}^{-1}\text{ sec}^{-1}$ and $0.003\text{ M}^{-1}\text{ sec}^{-1}$. The dotted line is the reaction of the repetitive *X. laevis* ^3H -DNA fraction with whole *X. laevis* DNA reproduced from Fig. 24.

(b) Hybridization of repetitive *X. borealis* ^3H -DNA with whole unlabeled *X. laevis* DNA. The data are again fit with two second-order components by least squares. These are indicated by the dashed lines, and the solid curve is the summed reaction. The rate of the faster component was held at $0.72\text{ M}^{-1}\text{ sec}^{-1}$ in this particular solution, and the best-fit rate for the slower component is then $0.02\text{ M}^{-1}\text{ sec}^{-1}$. Equally good fits can be obtained by allowing both rates to change, yielding rates of $1.2\text{ M}^{-1}\text{ sec}^{-1}$ and $0.02\text{ M}^{-1}\text{ sec}^{-1}$. The dotted line is the reassociation of repetitive *X. borealis* ^3H -DNA with whole *X. borealis* DNA reproduced from Fig. 24.

representative thermal elution profiles are shown for both homologous and heterologous duplexes in Fig. 26. The melting temperature of the homologous duplexes is about 3.5°C lower than that of the repetitive driver DNA. It is probable that this difference is due to the shorter mean fragment length of the

final tracer preparation. Figs. 26c and d show that the heterologous tracer-driver DNA duplexes melt very similarly to the homologous ones. Only a 1°-2°C depression in melting temperature is noted relative to the homologous tracer duplexes. This very slight temperature reduction is also independent of C_0t

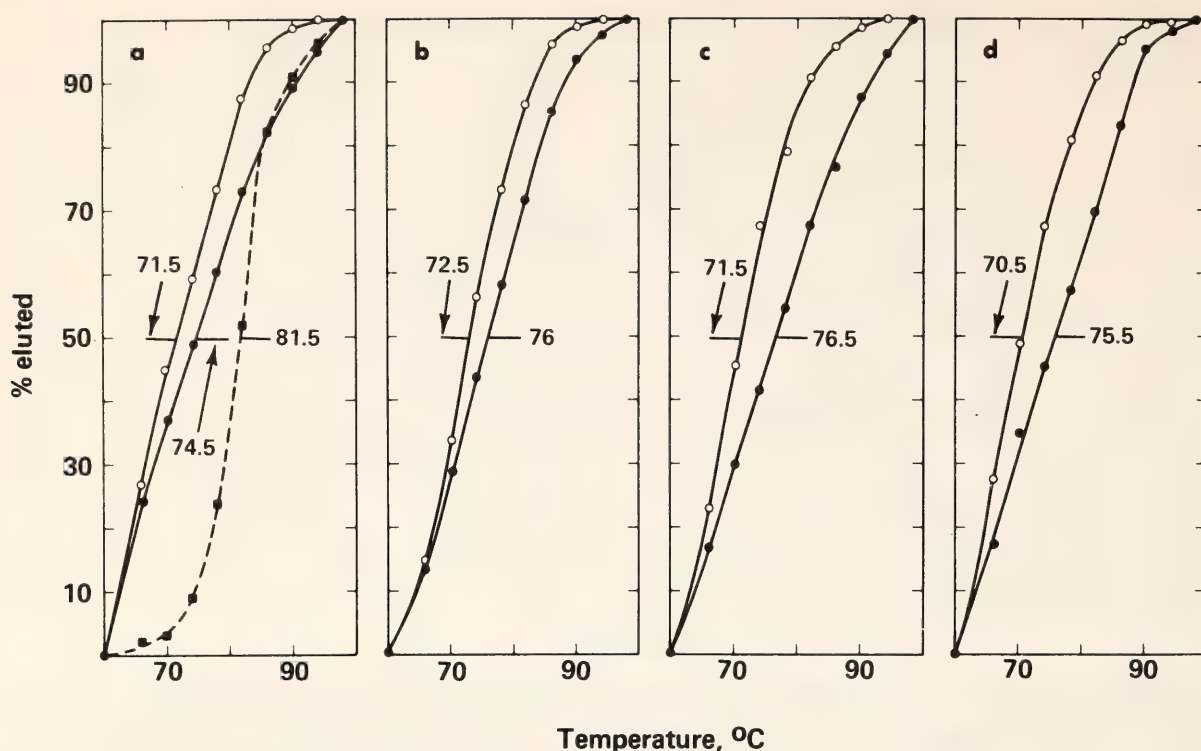


Fig. 26. Representative melts of repetitive *X. laevis* ^3H -DNA hybrids. Repetitive *X. laevis* ^3H -DNA was incubated with whole *X. laevis* or *X. borealis* DNA as described in the legends to Figs. 24 and 25. These reaction mixtures were placed over hydroxyapatite in 0.12 *M* phosphate buffer at 60°C and the single strand DNA fragments washed through the column with 0.12 *M* phosphate buffer. The temperature was then increased in 4°–6°C increments. The DNA fragments rendered entirely single stranded at each temperature interval were eluted from the column with 0.12 *M* phosphate buffer. The numbers near each curve indicate the temperature at which one-half of the DNA has eluted (T_m).

(a, b) Thermal elution of repetitive *X. laevis* ^3H -DNA duplexes with driver *X. laevis* DNA after incubation to C_0t s 3 and 150, respectively. The elution profiles of the repetitive ^3H -DNA duplexes (open circles) and the driver *X. laevis* DNA (solid circles) duplexes are shown. Included for comparison is the elution from a parallel column of unlabeled nonrepetitive *X. laevis* DNA duplexes (solid squares).

(c, d) Thermal elution of repetitive *X. laevis* ^3H -DNA duplex with driver *X. borealis* DNA after incubation to C_0t s 3 and 150, respectively. The elution profiles of the repetitive ^3H -DNA hybrids (open circles) and the driver *X. borealis* DNA duplexes (solid circles) are shown.

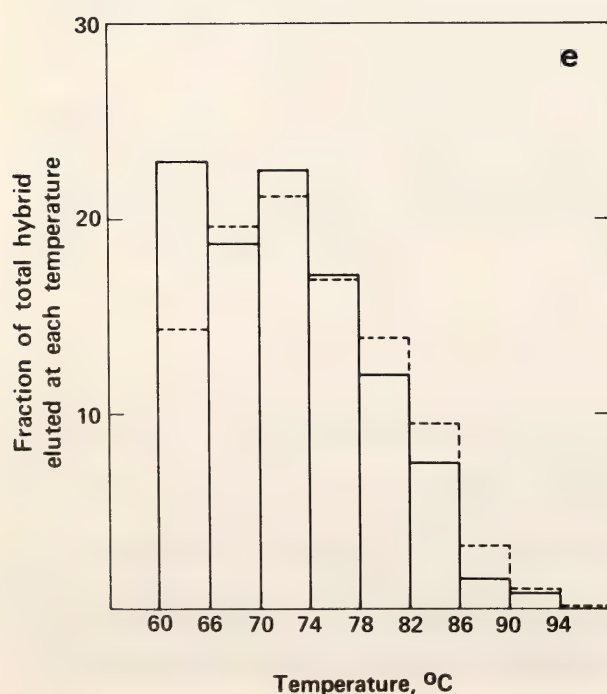


Fig. 26e. Comparison of the thermal stability of homologous and heterologous repetitive ^3H -DNA duplexes. The thermal elution profile of repetitive *X. laevis* ^3H -DNA hybrids formed at C_0t 150 with excess *X. laevis* (dashed lines) and with *X. borealis* DNA (solid lines) are replotted incrementally from b and d. The graph shows the fraction of the total material which elutes in each temperature interval. To facilitate the direct comparison, the elution of the *X. laevis*-*X. borealis* hybrids was slightly adjusted by normalizing the driver elution profiles to that of the *X. laevis* driver DNA and then apportioning the *X. laevis* ^3H -DNA radioactivity in each temperature increment in the same ratio to its driver DNA as in the original data. Within experimental error the two driver DNAs melted similarly. The elution profiles of the unlabeled driver DNAs are not shown. Similar results are obtained when C_0t 20 rather than C_0t 150 duplexes are compared.

over the range from C_0t 3 (Fig. 26c) to C_0t 150 (Fig. 26d). It is evident that any more divergent heterologous duplexes would not be observed in these experiments because their thermal stability would be too close to the experimental incubation temperature. The result is that this procedure possibly provides an artificially high estimate of the mean heterologous duplex stability.

The differential melting profile of the C_0t 150 homologous and heterologous reactions are compared in Fig. 26e. Clearly, only a small fraction of the observed heterologous duplexes melt at significantly lower temperatures than do the homologous duplexes. Therefore any correction for the effect of divergence on the rate of the homologous reaction compared to the heterologous reaction is likely to be small. We are thus left with a rather surprising conclusion. This is that while most or all of the repetitive sequence families of *X. laevis* are represented in *X. borealis* DNA, many of the sequences are present at 10–100 times lower frequencies in the latter genome. Furthermore, the results are complementary, so that an equivalent amount of the *X. borealis* repetitive sequences also seem to occur at much lower frequencies in the *X. laevis* genome than they do in the *X. borealis* genome. Two mechanisms could be responsible for the observed evolutionary decrease in repetitive sequence frequency. These are (1) divergence of a large portion of the repetitive sequences in some families so that heterologous duplexes are no longer stable under our conditions, and (2) reduction in copy number of some sequences as a result of unequal crossover and selection. The first of these mechanisms can apply either to interspersed or to long repetitive sequences while the second must refer mainly to long, tandemly repeated regions. The present data do not permit us to decide which of these mechanisms has been more important in the evolution of the *Xenopus* genome.

Interspecific Reaction of Nonrepetitive DNA Sequences

To provide a standard of comparison for the results obtained with the repetitive sequence fractions, the homology between *X. laevis* and *X. borealis* nonrepetitive DNAs was also measured. A mainly nonrepetitive fraction was isolated from *Xenopus laevis* DNA by passing the DNA over hydroxyapatite after incubation to C_0t 2500. The DNA that failed to bind to the column was harvested. The reaction of this nonrepetitive *X. laevis* tracer with excess whole homologous *X. laevis* DNA is shown in Fig. 27a. About 75% of the tracer reassociates as single-copy sequence. In addition, about 10% may be complementary to the slow repetitive component in whole DNA, the sequences of which are present about 100 times per genome (see curve *c* of Fig. 23). The nonrepetitive *X. laevis* 3H -DNA was reacted with a large excess of whole *X. borealis* DNA in 0.41 *M* phosphate buffer at 60°C (equivalent to about 53°C in 0.12 *M* phosphate buffer). This experiment is shown in Fig 27b. Duplex formation was measured as usual by binding to hydroxyapatite in 0.12 *M* phosphate at 60°C. From this reaction we conclude that most of the nonrepetitive sequence is shared between these two species. The arguments leading to this conclusion are now considered.

Within the range of C_0ts technically accessible, the reaction of the nonrepetitive *X. laevis* tracer with *X. borealis* DNA is incomplete. Only about 40% of the tracer reacts by C_0t 50,000 (Fig. 27b). The melting profiles of the heterologous duplexes and of the homologous tracer-driver duplexes are shown in Fig. 28. Duplexes formed between *X. laevis* nonrepetitive tracer and homologous whole DNA melt at about 77°C (Fig. 28a). For comparison this is about 4°C below the melting temperature of single-copy DNA duplexes, 81.5°C (dotted line, Fig. 28a). Figures 28b, 28c, and 28d show the melting pro-

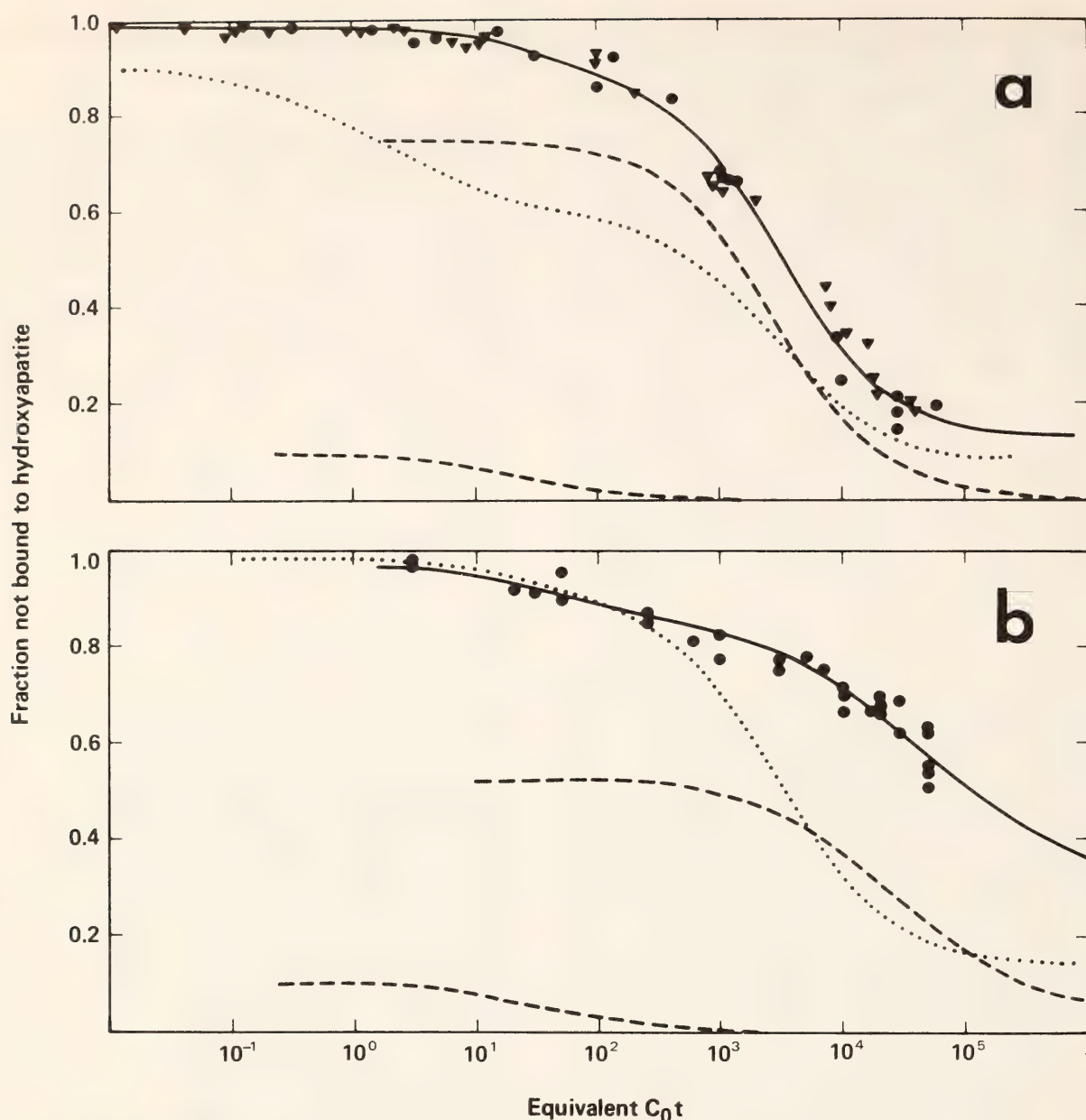


Fig. 27. Hybridization of nonrepetitive *X. laevis* ^3H -DNA with whole *X. laevis* and *X. borealis* DNA:

(a) Reassociation of nonrepetitive *X. laevis* ^3H -DNA with whole *X. laevis* DNA. Nonrepetitive *X. laevis* ^3H -DNA was incubated in 0.12–0.41 *M* phosphate buffer at 60°C with excess *X. laevis* DNA, and the fraction of repetitive DNA in hybrid was assayed by hydroxyapatite (solid circles). High C_0t data are from reactions run in 0.41 *M* phosphate buffer. Also indicated are self-reassociation data for nonrepetitive *X. laevis* DNA (solid triangles) in the absence of whole driver DNA. The data are reproduced from Hough and Davidson (1972). The solid curve is the result of a least-squares fit including two second-order components, indicated by the dashed lines. This particular solution is the result of fixing the rate of the main component at 0.00035 $M^{-1} \text{ sec}^{-1}$ (the rate of the single-copy DNA in whole DNA from Fig. 27). Included for comparison is the reassociation of whole *X. laevis* DNA (dotted line) reproduced from Fig. 23.

(b) Hybridization of nonrepetitive *X. laevis* ^3H -DNA with whole *X. borealis* DNA. Nonrepetitive *X. laevis* ^3H -DNA was incubated with a 5,000–10,000-fold excess of whole *X. borealis* DNA in 0.41 *M* phosphate buffer at 60°C, and the fraction of tracer hybridized was measured by hydroxyapatite. The solid curve is the result of a fit of two components to the data. The rate of the small repetitive component is fixed at 0.036 $M^{-1} \text{ sec}^{-1}$, which is the rate of the slow repetitive DNA driver component (see Fig. 23). The second component is a least-squares fit to the data obtained at higher C_0t values using the expression

$$\frac{G}{G_0} = V^{-.75T} \exp \left[\frac{.25TV^{.56}}{.56} \right]$$

files of the heterologous tracer-driver duplex fractions at C_0t s 3000, 16,000, and 30,000, respectively. In all three samples 50% of the tracer becomes single stranded at 67°C, 10°C lower than the homologous tracer-driver duplexes. The shape of the heterologous melts shows that a substantial fraction of the hybrid may have formed duplexes at the 53°C incubation criterion, but were melted at 60°C when loaded on the hydroxyapatite columns. Even for a duplex population melting at 67°C the rate of hybridization of tracer with the carrier should be only about 0.28 of that of the self-reassociation of the driver DNA under the conditions used (Bonner *et al.*, 1973). The appropriate mathematical form for the reduction of such heterologous kinetic data is shown in the legend to Fig. 27. When the rate reduction of 0.28 times the homologous rate is included, the calculation shows that the reaction would have terminated with 60%–70% of the heterologous tracer in duplex. However, it can be argued that the mean melting temperature would have been only 64°C had the thermal stability measurement been made from 53°C rather than from 60°C. On this basis (i.e., since the reactions were carried out at 53°C criteria), the curve shown in Fig. 27b (solid line) is calculated for the reassociation of DNAs so divergent in sequence as to melt (50%) at 64°C. The renaturation rate for such a DNA fraction would be approximately 0.2 times that for the single-copy sequences in the driver DNA (Bonner *et al.*, 1973), and it can be seen

that with this assumption almost complete heterologous cross-reaction of those sequences able to react with homologous DNA would have been attained at completion.

Further experiments are shown in Table 11. The *X. laevis* nonrepetitive tracer was reacted to C_0t 30,000 with *X. borealis* DNA (Reaction 1 of Table 11), and the hybridized tracer and unhybridized tracer were separately recovered and rereacted with *X. laevis* and *X. borealis* DNA. Rereaction of the *X. laevis* tracer with *X. laevis* driver DNA provides a control for the fraction of the tracer which has survived the long incubations and chromatography steps and remains reactable. Thus the tracer which reacted with the *X. borealis* DNA is still over 80% reactable (Reaction 2 of Table 11). However, the fraction which failed to react with *X. borealis* DNA by C_0t 30,000 remains only about 52% reactable when assayed at 60°C (Reaction 4, Table 11) and 73% reactable when assayed at 50°C (Reaction 6, Table 11). Now if the fraction of the *X. laevis* tracer which reacted with *X. borealis* DNA were a selected fraction of more homologous sequences, all of the reactable tracer, or over 80% of the total tracer, should have been able to rereact with the *X. borealis* DNA. On the other hand, if the failure to achieve complete heterologous reaction the first time (i.e., in Reaction 1 of Table 11) is merely kinetic, only about 40% of the single-copy sequence should again have been able to react on a second exposure to *X. borealis* DNA. Considering

where G and G_0 are the concentrations of single stranded nonrepetitive tracer at various times and at time zero, respectively; $V = 1 + k C_0 t$, where k is the second-order rate constant of the driver DNA and C_0 its concentration; and $T = R/k$, where R is the rate constant for the reaction of the tracer with the driver DNA. The derivation of this expression is presented by Galau, Klein, Smith, Britten, and Davidson (in preparation). In this instance R was fixed at $0.2 k$, where k = the homologous driver rate of $0.00036 M^{-1} \text{ sec}^{-1}$. The ratio 0.2 is calculated from the data of Bonner *et al.* (1973) for the incubation conditions and the thermal stability of the hybrids taken as $T_m = 64^\circ\text{C}$. The solid curve thus provides the best estimate of the total reaction kinetics, taking into account the extent of binding observed and the characteristics of the heterologous duplexes at the highest C_0t s possible, as well as our current understanding of the nature of retarded reaction kinetics. Included for comparison is the reassociation of nonrepetitive *X. laevis* ^3H -DNA with unlabeled *X. laevis* DNA (dotted line) reproduced from 27a.

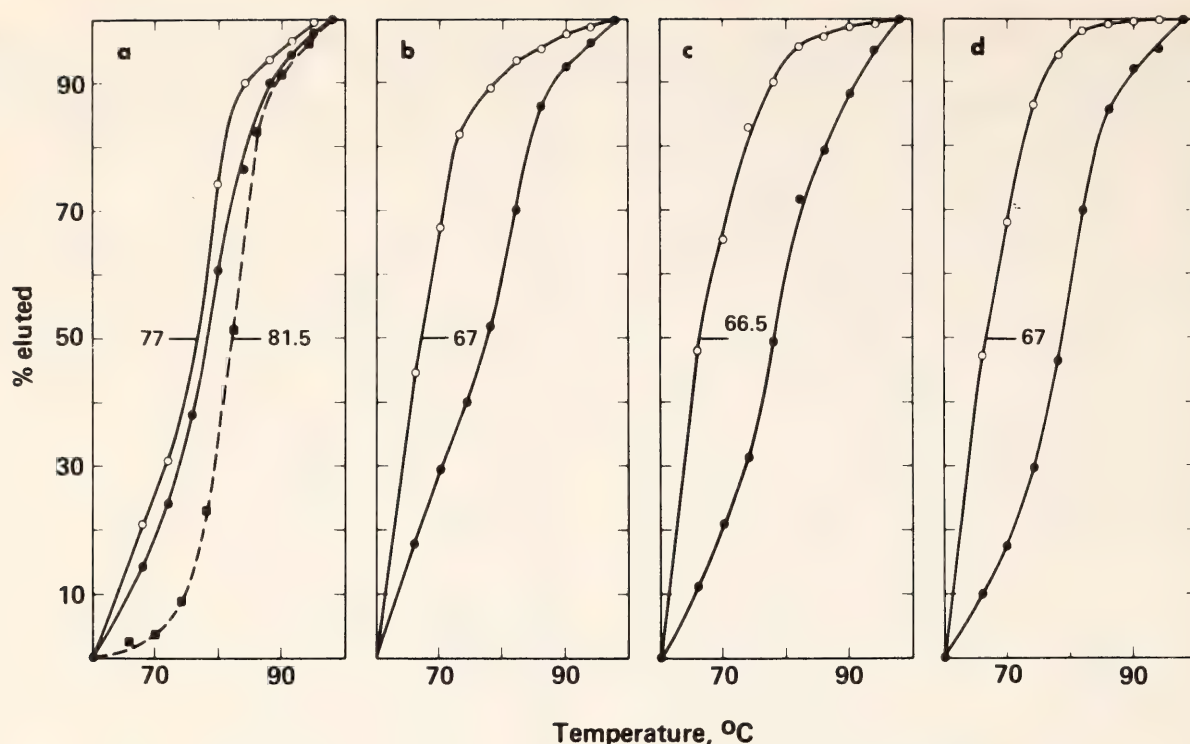


Fig. 28. Representative melts of nonrepetitive *X. laevis* ^3H -DNA duplexes. Nonrepetitive *X. laevis* ^3H -DNA was incubated separately with excess *X. laevis* DNA or *X. borealis* DNA in 0.41 M phosphate buffer at 60°C as described in the legend to Fig. 27. The reaction mixtures were then applied to hydroxyapatite and thermally eluted as described in the legend to Fig. 26.

(a) Thermal elution of nonrepetitive *X. laevis* ^3H -DNA duplexes with driver *X. laevis* DNA formed at C_0t 10,000. The elution profiles of nonrepetitive ^3H -duplexes (open circles) and driver *X. laevis* DNA duplexes (solid circles) are shown. Included for comparison is the elution from a parallel column of unlabeled nonrepetitive *X. laevis* DNA duplexes (solid squares).

(b-d) Thermal elution of nonrepetitive *X. laevis* ^3H -DNA hybrids with driver *X. borealis* DNA after incubation to C_0ts 3000, 16,000, and 30,000. The elution profiles of nonrepetitive ^3H -DNA duplexes (open circles) and driver *X. borealis* DNA duplexes (filled circles) are shown.

that the starting tracer includes about 10% repetitive sequence (Fig. 27a), the expected amount of reaction in the latter case is around 68%. Reaction 3 of Table 11 shows that the kinetic explanation is probably the correct one, since the average value obtained, 66%, is close to prediction. This interpretation is strengthened by the results of Reaction 5 in Table 11. Here the fraction of *X. laevis* tracer not reacting with *X. borealis* DNA on first exposure is re-associated once more with *X. borealis* DNA. Again we are faced with two distinct predictions. If the *X. laevis* DNA which initially reacts with *X. borealis* DNA is a special set of sequences, rereaction of the nonbound tracer with *X. borealis* DNA should yield no duplex. If, however, failure of the initial reaction was kinetic, rereac-

tion to C_0t 30,000 should again yield about 40% of the reactable single-copy sequence present.

In the latter case we expect about 20% total reaction, since only half the DNA remains reactable at this stage (shown in Reaction 4 of Table 11). This is exactly what is found. When the incubation and assay temperature are both decreased by 10°C, more tracer reacts with both homologous and heterologous DNAs. However there is proportionately more reaction with the heterologous DNA (Reaction 7, Table 11). This finding confirms the presence of marginally stable heteroduplexes.

To summarize these experiments we may make the following points. At least 70% and possibly all of the single-copy DNA sequences of *X. laevis* are represented in *X. borealis* DNA, and

TABLE 11. Reassociation of Nonrepetitive *X. laevis* ³H-DNA with *X. laevis* and *X. borealis* DNA

Selected Nonrepetitive <i>X. laevis</i> ³ H-DNA Tracer	Reaction	Excess DNA Driver ¹	Temperature of Incubation and Assay ² (°C)	Fraction of Selected Tracer in Hybrid at C ₀ t 30,000
Starting unfractionated tracer	1	<i>X. borealis</i>	60	0.38
Tracer in heterologous hybrid at C ₀ t 30,000	2	<i>X. laevis</i>		0.82, 0.85 (av. 0.83)
	3	<i>X. borealis</i>		0.54, 0.77 (av. 0.66)
Tracer not in heterologous hybrid at C ₀ t 30,000	4	<i>X. laevis</i>	60	0.51, 0.51, 0.54 (av. 0.52)
	5	<i>X. borealis</i>		0.16, 0.18, 0.25 (av. 0.20)
	6	<i>X. laevis</i>	50	0.73
	7	<i>X. borealis</i>		0.32, 0.37 (av. 0.34)

¹Excess DNA was added to the fractionated tracer to 50,000 times the tracer concentration and 20–200 times the residual unfractionated *X. borealis* carrier DNA.

²Incubation was in 0.41 M phosphate buffer, and the hydroxyapatite assay was conducted in 0.12 M phosphate buffer.

most of the sequences have diverged greatly since the separation of the two species. It can be calculated that the average sequence divergence is at least 10%–15% of the base pairs in the single-copy fraction. Unfortunately the relatedness of all the single-copy sequences in the *X. laevis* genome to sequences in the *X. borealis* genome is difficult to prove, since the kinetic retardation observed would require impracticably high C₀t_s in order to obtain complete reaction. The interpretation we present here is nonetheless quantitatively consistent with the experimental data.

According to the albumin divergence studies of Wilson and his associates (unpublished), about 15–20 million years have elapsed since the divergence of *X. laevis* and *X. borealis*. The gross rate of change in single-copy sequence in the genus *Xenopus* thus seems significantly more rapid than in the primates, which have a genome size only about 20% larger than *Xenopus*. Single-copy heteroduplexes formed between the DNAs of primate species whose common ancestor

existed in the range 16–20 million years ago display only about 1°–2°C reduction in melting temperature when compared to the homologous duplexes (Kohne *et al.*, 1970). This is in contrast to the 10°–13°C depression in heteroduplex melting temperature reported here. It is difficult to account for this large difference in divergence rate between primates and *Xenopus* species on the basis of differences in generation time alone. Whether it is a function of the amphibian DNA replication and repair mechanisms or has other sources cannot at present be judged. In any case it is clear that no safe generalization with regard to the rate of DNA sequence change can be derived from studies on any one taxon.

Conclusions

Male hybrids of *X. laevis* and *X. borealis* are totally sterile, though some fertile female hybrids can be produced. However, the fertility of these hybrid animals is in a sense an accident of an abnormal meiotic prophase. Although

the *X. borealis* and *X. laevis* chromosomes in some of the oocytes of these hybrids fail to synapse with each other, the fertile eggs develop from tetraploid primary oocytes. In such oocytes two sets of *X. borealis* and two sets of *X. laevis* chromosomes are later found synapsed, each with homologues of its own species. At ovulation and reduction divisions a diploid egg is formed which, when fertilized by a normal haploid sperm, can develop into a mature but triploid adult. This account is based on studies of M. Fischberg (personal communication). Its significance for us is that by the usual criterion the two organisms whose DNA we have studied here are clearly distinct species. They are closely related morphologically, though key species differences exist. The main point is that in ontogenic terms they are sufficiently compatible to develop into hybrid adults whether fertile or not.

As shown above, a large amount of total DNA sequence divergence has occurred since the evolutionary separation of these two anuran congeners. Brown *et al.* (1972) and Brown and Sugimoto (1973) have shown that the ribosomal and 5S-RNA-DNA spacer sequences in the same two species (referred to by them as *Xenopus laevis* and *Xenopus mulleri*) are so different that they fail to display any heterologous cross reaction. Various evidence suggests that the mechanism of such changes in the content of tandem repetitive sequence clusters has been unequal crossover. Here we have reported that most of the single-copy sequence has diverged at a high rate as well. There has been at least 10%-15% nucleotide substitution. Replication error, failure of repair processes, and random insertion of base transitions and transversions rather than unequal crossover are evidently among the responsible mechanisms here. Among the most significant aspects of the findings reported here is the conclusion that two genomes capable of cooperating to produce an adult hybrid can tolerate

such a large amount of genomic sequence alteration. Only one interpretation seems reasonable, and it is that the specific sequence of much of the single-copy DNA is not functionally required during the life of the animal. This is not to say that this DNA is functionless, only that its specific sequence is not important. Such would be the case, for example, if some of the single-copy sequence served as a form of spacer sequence. Obviously selection will play a direct role in maintaining at least some of the specific sequence of structural gene elements. These are expected to constitute a minor fraction of the single-copy DNA, probably less than 10%. Thus we would expect that a small portion of the nonrepetitive sequence must exist which shows far less divergence between the two species, but isolation of the structural gene sequences would be necessary to demonstrate this.

A particularly interesting observation is that most of the repetitive sequences present in each genome are able to cross-react with those of the other genome. It is clear that most or all of the repetitive sequence families are present in both genomes. There are two explanations for this conclusion: Either these families are required physiologically or they have been protected by linkage to the single-copy regions in which many of them are embedded so that they could not be lost in the time since divergence. Sharing among related species of the interspersed repetitive sequences has been demonstrated in studies of rodent DNAs as well (Rice, 1972). However, in contrast to the latter studies we found here that the repetitive heteroduplex structures display about the same thermal stability as the homologous repetitive duplexes. To some extent this impression may result from the relatively stringent pairing criterion at which the observations were made. The main fact remains, however, that most of the medium and higher stability homologous reaction with repetitive DNA is also

found with the heterologous reaction (e.g., see Fig 26e). If we better understood the function of the interspersed repetitive sequences, it would be easier to interpret the meaning of this result.

The kinetic experiments on the heterologous repetitive DNA reactions shown in Fig. 25 led us to the conclusion that the frequency of occurrence of some repetitive sequences has changed since the divergence of the two species. After correcting for the effect of divergence on reaction rate, we are still left with the conclusion that a significant fraction of the repetitive sequences appear to have changed in frequency. This fraction may fall in the long repeat class (about 25% of the total repetitive sequence), but whether this is true is unknown. The unequal crossover mechanism provides a means by which the number of copies of given sequences can be rapidly altered, but this explanation pertains only to tandemly repetitive sequence clusters. To explain changes in frequency of occurrence of interspersed repetitive sequences presents a new problem of formidable dimensions.

DNA SEQUENCE ARRANGEMENT AND PRELIMINARY EVIDENCE ON ITS EVOLUTION

Roy J. Britten and Eric H. Davidson

The Role (or Roles) of Nonrepetitive DNA Sequences

This section has been modified from Britten and Davidson (1975). Most structural genes are nonrepetitive DNA sequences. In sea urchin gastrulas (Galau, Britten, and Davidson, 1974; Goldberg *et al.*, 1973), HeLa cells (Klein *et al.*, 1974), rat cells (Campo and Bishop, 1974), and several other systems (Davidson and Britten, 1973; Lewin, 1975) most of the polysomal message is transcribed from single-copy DNA sequences. A number of purified messenger RNA preparations derived from particular genes have also been shown to be transcribed from single-copy DNA sequences,

and this subject has recently been reviewed (Davidson and Britten, 1973; Lewin, 1975). The histone genes are present in sea urchin in a few hundred copies (Kedes and Birnstiel, 1971; Weinberg *et al.*, 1972). This is the only known case of structural genes for proteins that are present in many copies, though it is clear that others exist (e.g., Klein *et al.*, 1974). The fact that most structural genes are single-copy DNA sequences does not at all imply that most single-copy DNA sequences are structural genes, as the following discussion will show.

The genome sizes of animals range from about 10^8 nucleotide pairs per haploid set for *Drosophila melanogaster* to 8×10^{10} for *Amphiuma*. Even among vertebrates the range is from 4×10^8 (the minimum for bony fish) to 8×10^{10} nucleotide pairs. Studies of the reassociation kinetics of nuclear DNA indicate that even in the large genomes a significant fraction is nonrepetitive DNA. Comparison of morphological organization does not imply that one vertebrate can make use of 10 to 100 times as many structural genes as another. The large quantity of single-copy DNA and the variation in quantity from species to species thus suggests that much of it is not made up of structural genes. These observations force us to consider other roles for the single-copy DNA. Hinegardner (1968) has shown in several groups that while there is a sharply defined minimum for a given taxon, many are characterized by genomes several times larger than the minimum. It follows directly that much of the DNA in these large genomes is not needed to specify the basic features of the taxon. In fact they suggest that only a minority of the single-copy DNA is made up of structural genes coding for protein amino acid sequences.

Measurements have recently been made of the complexity (i.e., total length of different sequences) of the DNA transcribed into RNA in sea urchin embryos. Galau *et al.* (1974) determined

that the purified polysomal message from gastrula hybridizes with only 1.35% of a single-copy DNA tracer. Assuming asymmetric transcription, we estimate that 2.7% of the single-copy DNA is expressed as structural genes at this stage. This is a complexity of 1.7×10^7 nucleotide pairs or 14,000 genes of typical length of 1200 nucleotide pairs. Similar measurements of the complexity of the nuclear RNA present in embryos of the same stage show that 28.5% of the single-copy DNA sequence complexity is transcribed. This corresponds to 1.74×10^8 nucleotide pairs, almost exactly 10 times the sequence complexity which is transcribed into messenger RNA. It is certain that at least 90% of the sequences are restricted to the nucleus, or at least do not reach the polysomes. This evidence again strongly suggests that the great majority of the nonrepetitive sequences in the genome play a role different from that of a structural gene and shows that many of them are transcribed to yield nuclear RNA.

Measurements have not yet been made which provide an estimate of the total number of structural genes in the genome of any species. As a crude initial approach we can assume that the ratio of nuclear RNA complexity to messenger RNA complexity observed at gastrula is maintained at other stages. If during the whole life cycle 100% of the single-copy sequences were transcribed we could estimate that $2.7\% / .285 = 9.5\%$ of the nonrepetitive DNA is potentially structural gene sequences. No convincing proposal can be made at this time for the actual role of the remaining 90% or so of the nonrepetitive sequences in the DNA, much of which we know is transcribed.

Evolution of Single-Copy DNA Sequences

Single-copy DNA sequence relationships among primate species have been studied (Hoyer *et al.*, 1972; Kohne,

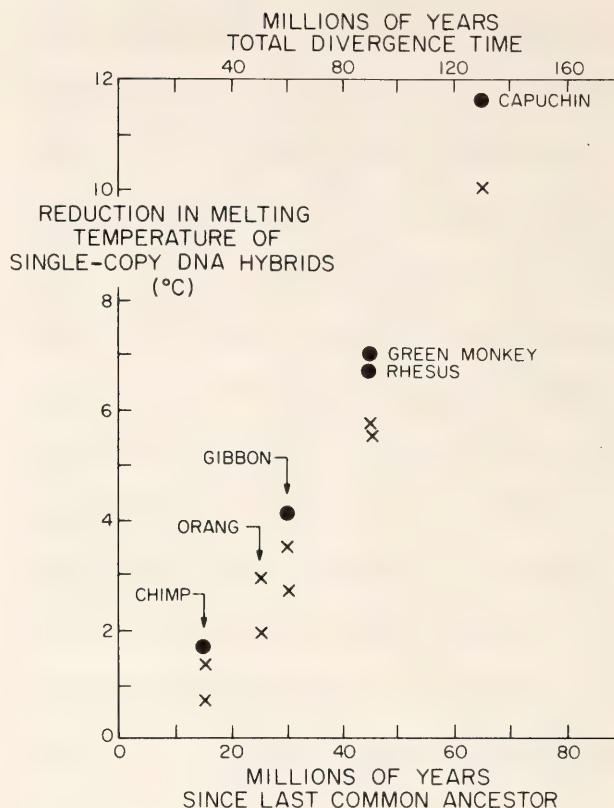


Fig. 29. Measurements of primate single-copy DNA sequence divergence, relative to human DNA. The reduction in thermal stability of hybrids between labeled single-copy DNA of the listed species and human DNA is compared to the thermal stability of single-copy human DNA from Kohne *et al.*, 1970, and Hoyer *et al.*, 1972. The lower points (crosses) represent the actual reduction in thermal stability of the fraction of the heterologous tracer DNA that was bound to hydroxyapatite, based on the temperatures at which 50% of the duplex DNA has been eluted. The two points for chimp and gibbon come from the two references listed. Shown for orang are human tracer with orang driver and *vice versa* (Goldberg *et al.*, 1973). The upper points (solid circles) represent the temperature at which 50% of the total original labeled DNA remained in duplex. This method of calculation was chosen (Kohne *et al.*, 1970) to correct for the fraction of the potential DNA hybrids which were so divergent as to be unstable at the incubation temperature. The correction may be excessive, and we use the average of the uncorrected (crosses) values for the comparisons shown in Fig. 30.

The lower time scale indicates the time based on the paleontological record since the latest common ancestor for both human and the species indicated. The upper time scale has twice this value and represents the total time of divergence between the two species.

Chiscon, and Hoyer, 1970). A few measurements exist for other vertebrates (Galau *et al.*, 1975; Laird, McConaughy, and McCarthy, 1969; Mazrimas and Hatch, 1972; McCarthy and Farquhar, 1972; Rice, 1971 *a, b*; Rice, 1972; Rice, 1974; Rice and Esposito, 1973); we discuss only the primate data. Figure 29 shows the relationship of single-copy DNA sequence divergence to the divergence times of evolutionary lines of descent leading to the modern species. The data are presented as the decrease in melting temperature of labeled human DNA fragments reassociated with the DNA of various species. The melting temperature reduction is a good measure of the sequence divergence, but the conversion factor is not accurately known. For this discussion we assume that a reduction of 1°C in T_m corresponds to about 1% nucleotide substitution in the two ancestral species lines since their divergence from a common ancestor (Britten, Graham, and Neufeld, 1974; Laird *et al.*, 1969). During much of the period of primate evolution the average rate of base substitution implied is about 0.1% per million years of total divergence time. This represents three to four nucleotide pairs mutated per haploid genome per year.

A preliminary measurement has been made of the relative rate of base substitution in structural gene sequences compared to that in total single-copy DNA (Rosbash, Campo, and Gummerston; personal communication). For this purpose rat myoblast tissue culture cell messenger RNA was copied with reverse transcriptase to yield ^3H -labeled DNA fragments. This DNA preparation and ^{32}P -labeled single-copy fraction rat DNA were incubated with an excess of mouse DNA fragments to high C_0t . Hydroxyapatite thermal chromatography of the reassociated DNA indicated that the sequence divergence between average rat and mouse single-copy DNA sequences was perhaps three times as great as that for this set of expressed structural gene sequences.

Kohne and Byers (1971) have examined the relative rate of base substitution in single-copy DNA sequences which are transcribed in specific tissues. In these measurements total calf kidney and brain RNA were hybridized to labeled calf DNA to prepare "expressed DNA fragments." When these were reassociated with calf, sheep, and pig DNA, no difference in reduction of thermal stability of the expressed DNA was observed relative to total calf single-copy DNA. It is now clear that these measurements were dominated by nuclear RNA transcripts. The measurements thus suggest that the sequences which are transcribed into nuclear RNA are not strongly conserved in evolution. The sea urchin nuclear RNA complexity measurements mentioned above lead to a similar conclusion, since nearly a third of the single-copy DNA sequences are included in the transcripts present in the gastrula. The total fraction transcribed throughout the life cycle is surely larger, and it is very unlikely that so large a fraction of the single-copy DNA has a rate of base substitution different from the whole. Thus the rapid rate of sequence change characteristic of most of the single-copy DNA must also characterize those sequences transcribed into hnRNA.

Rate of Alteration in Single-Copy DNA and in Rapidly Changing Protein Sequences

The rate of amino acid substitution during the evolution of proteins is widely different for different proteins. Previous comparisons between the rates of DNA base substitution and protein evolution have been made (Laird *et al.*, 1969), but here we examine only rapidly changing protein sequences. Figure 30 shows the rate of change of these rapidly evolving proteins compared to that of the total single-copy DNA sequence. Protein sequences are from Dayhoff (1972). The figure shows the percentage of amino acid substitution divided by

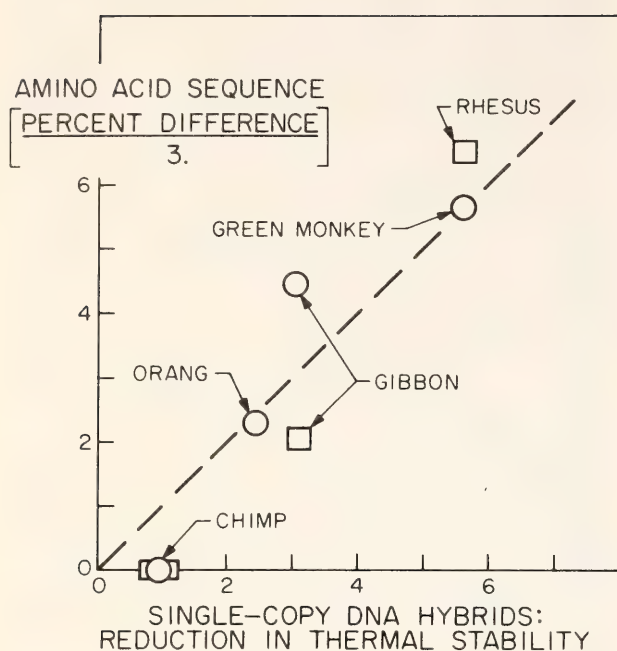


Fig. 30. Comparison of the degree of substitution of amino acid residues which change rapidly in evolution with the degree of substitution in single-copy DNA for some primates relative to man. The single-copy DNA reduction in thermal stability of 1°C represents about 1% difference in nucleotide sequence (Britten *et al.*, 1974). The open circles represent fibrinopeptides α and β with a total sequence length of 30 residues. For example, green monkey peptides differ from human in five residues (Dayhoff, 1972), and thus the amino acid sequences differ by 17%. Thus we estimate the minimum change in the codogenic sequences required would be $17/3 = 5.6\%$.

The open squares represent a rapidly changing set of residues in α and β hemoglobin, selected in the following way. The sequences of α and β hemoglobin in man, rhesus monkey, mouse, rabbit, dog, horse, pig, cow, sheep, kangaroo, and chicken (Dayhoff, 1972) were compared, and two or more alternate amino acids were observed in a total of 45 positions. (β 2, 5, 9, 10, 12, 13, 16, 19, 20, 21, 43, 50, 52, 56, 69, 75, 76, 87, 110, 112, 116, 120, 125, 126, 129, 130, 139, and α 4, 8, 12, 15, 19, 22, 23, 34, 61, 66, 70, 73, 84, 113, 117, 118, 132, 133).

The sequences were compared for man, rhesus monkey and gibbon, and it was found that all but one of the differences among these three species occurred in this set of positions. The change in the one exceptional position (β 104) was not included in the calculation. Thus the percent difference in the codogenic sequence for rhesus and man was calculated as $100 \times 8/45 \times 3 = 5.9\%$.

3.0 versus the single-copy DNA sequence divergence for several primates relative to man. We have chosen to divide the percentage of amino acid substitution by 3 as a first approximation of the effect of base substitutions on the amino acid coding of a structural gene sequence. Base substitutions incorporated in the first two positions of a codon usually lead to amino acid substitutions, but those in the third position do so to a smaller extent. The appropriate factor thus lies between 2 and 3, but the accuracy of the data plotted in Fig. 30 does not justify use of a more precise estimate. The use of the factor of 3 probably gives a slight overestimate of the rate of change of the codogenic sequence.

The evolutionary rate of amino acid substitution in hemoglobin is less than that of the fibrinopeptides. However, the rate of change of certain residues is faster than the average (Jukes and Holmquist, 1972), and the rate of change may relate to the function of the residues (Sullivan, 1972; Goodman, Moore, and Matsuda, 1975). For Fig. 30 we selected the 34 positions in α and β hemoglobin sequences in which three or more alternate amino acids have been found (see legend to Fig. 30). This totally arbitrary division simply serves to select a rapidly changing set of positions in a statistically valid way. In other words, we used the total vertebrate data to avoid being affected in the choice of these positions by alterations occurring only during primate evolution. The point on Fig. 30 for Rhesus represents an actual difference between Rhesus and human of nine amino acid substitutions out of the 45 selected residues. With such small numbers it is clear that large statistical variations are likely. The same problem exists for the fibrinopeptides which include only 30 residues. Even if there were a well-defined average rate of amino acid substitution in these residues, a large amount of scatter is expected in a comparison such as Fig. 30.

At this limited level of accuracy the

conclusion can be drawn that the rate of amino acid substitution in the rapidly changing primate hemoglobin and fibrinopeptide residues is just what would be expected from the average rate of base substitution in the single-copy DNA. In other words, the rate of base substitution in the selected locations of the structural genes for α and β hemoglobin and for fibrinopeptide is about the same as the average rate of base substitution in the total primate single-copy DNA. As discussed above, the majority of the single-copy DNA sequences are probably not structural genes.

It seems likely that the nature of the functions which led to possible selection pressure on the majority of single-copy DNA sequences differs from those that affect the fibrinopeptide structural gene regions. In addition, the functional reasons for possible selection pressure on the 45 rapidly changing residues of α and β hemoglobin should be different from either of the above. Yet all three have about the same rate. Either these three rates are the result of coincidentally similar selection pressure or all represent the rate of change in the absence of selection pressure.

Since these arguments are suggestive rather than convincing, we propose the following "basal rate" hypothesis. The majority of the single-copy DNA does not have a strongly sequence-dependent effect on the phenotype, even if it is transcribed into nuclear RNA. The same is true for certain protein regions which can be identified by their rapid evolutionary change. The rates of change of all of these sequences are considered to be unaffected by selection pressure. The actual rate of incorporation of nucleotide substitutions into such regions of the genome probably depends on the precision of DNA replication and repair as well as the generation time, population size, and potential sequence-specific effects of processes such as synapsis and crossover. We refer to the resultant rate of change as the "basal rate of incorporation of nucleotide substitutions."

This basal rate may well vary from species to species or between populations. Where nucleotide substitutions do affect the phenotype in significant ways, then selective pressure would reduce the rate of change at these sites to less than the basal rate.

The hypothesis presented above is quite different from the so-called neutralist hypothesis (Fitch, 1972; King and Jukes, 1969) which proposes that a majority of the amino acid residues are not under selection pressure. We do not make any comment here about selective pressure on the majority of amino acid residues. We simply note that a fraction of them (perhaps a small fraction) exhibits about the same rate of change as does total single-copy DNA sequence, and hence that they display little effect of selective pressure.

Evolution of Repetitive DNA Sequences

Investigation of the evolution of repeated sequence is still at an early stage of advancement. Quantitative measurements of rates are not yet available, and almost nothing can be said about the mechanisms involved. However, the evidence clearly shows that two major processes generally occur in the evolution of higher organism genomes: Repeated DNA sequences are added at significant rates; base substitution occurs, and members of a related set of sequences within the genome diverge from each other. Eventually the latter process leads to loss of sequences from the observable repetitive sequence class and their appearance in the single-copy fraction. It is not known if selection is important in the divergence of repetitive sequences nor what the rate of base substitution is compared to the single-copy substitution rate. Nor is it known whether repeated sequences are lost by deletion from the genome.

While these processes were recognized early (Britten and Kohne, 1968), the clearest evidence for addition of repeated sequences to the genome comes from

studies of the thermal stability of intergeneric hybrids of repeated DNA fragments (Rice, 1972). These measurements show that rat and mouse DNA have a significant fraction of repeated sequences which self-reassociate to give relatively well paired double-strand DNA having melting temperatures within 10°C of native DNA. However, when labeled mouse DNA is reassociated with excess rat DNA or *vice versa*, few if any of the sequences match with this accuracy. Most of the intergeneric repetitive DNA duplex melts at temperatures between 10°C and 30°C below that of native DNA.

The precise matching of some of the repetitive sequences within each genome shows that they are new additions to the genome since they are not shared between the two species at this high level of precision. The more precisely matching sets of sequences could be multiple copies of divergent preexisting ancestral repetitive sequences. In this case the same sequences which show precise intraspecies relationships could show divergent interspecies relationships (Rice, 1971 *a, b*; Klein *et al.*, 1974; Lewin, 1975; Sutton and McCallum, 1971). If the precise sets of sequences were each copied from a preexisting nonrepetitive sequence, interspecies relationships of these sets would be difficult or impossible to measure. In any case, selection alone cannot account for the existence of sets of sequences which differ in two related species but are precisely matched within each species. Some sort of multiplication mechanism is required. Calculation from these measurements indicates that about 9% of the total rat genome is made up of repetitive sequences that have been added since the species lines leading to mouse and rat diverged about 10 million years ago. About 20% of the mouse genome is made up of such sequences, but about half of this is the mouse satellite. In comparison, single-copy DNA interspecies hybrids between rat and mouse melt about 25°C below native DNA (Rice and Paul, 1972).

The general occurrence of interspersion of repetitive and single-copy sequences strongly indicates that events of sequence rearrangement or translocation have occurred. It is hard to imagine that a large number of short (300 nucleotide) similar sequences could arise *de novo* interspersed among single-copy sequences. Recent measurements apply more directly to the question of sequence rearrangement. These measurements show that there is a correlation between the organization of the repeated sequences in the genome and the degree of base substitution that has occurred. The short interspersed repeated sequences are typically divergent from each other in sequence, and the long regions are made up of sequences which are more precisely related to each other. Figure 31 shows the spectrophotometric melting curve of repetitive fractions of sea urchin DNA which have been allowed to reassociate. The left curve (Fig. 31) describing the melting of short interspersed sequences shows a reduction in T_m of about 7°C to 10°C below perfectly paired DNA of the same fragment size, implying about 10% average sequence divergence between homologous repeats. In contrast the sample of long repetitive regions shows very little reduction in T_m and there is probably not more than 1% to 2% divergence among these sequences.

Tests have been made to be certain that the correlation between length of repeated regions and thermal stability was not an artifact of the enzyme S1. Measurements such as those shown in Figure 31 were repeated on sea urchin DNA replacing the S1 nuclease with *E. coli* exonuclease VII (Chase and Richardson, 1974*a* and 1974*b*), and essentially identical results were obtained. In another set of experiments no enzyme at all was used, and advantage was taken of the ability of hydroxyapatite to fractionate DNA on the basis of thermal stability. For this purpose 2000-nucleotide-long labeled sea urchin DNA fragments were reassociated to repetitive C_0t with an excess of 400-nucleotide sea

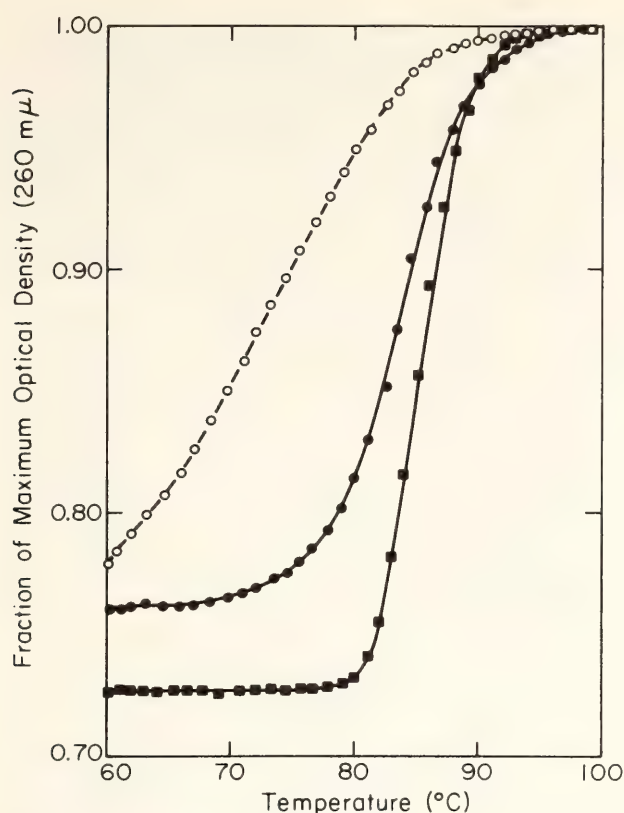


Fig. 31. Spectrophotometric melting curves (260 nm) of long and short sea urchin repetitive regions. Right-hand curve (solid squares) is for long native sea urchin. DNA fragments were incubated to $C_0t\ 4$ (moles nucleotides \times sec $^{-1}$ liters $^{-1}$) in (0.01 M PIPES, 0.3 M NaCl) at 64°C and then treated to 45 min with S1 nuclease (in 0.025 M Na acetate, 0.1 mM ZnSO $_4$, 0.15 M NaCl, 5 mM mercaptoethanol, pH 4.4) at 37°C with an amount of enzyme sufficient to convert about 70% of the single-strand DNA present to acid soluble. The digestion mixture was adjusted to 0.12 M neutral phosphate buffer and passed over hydroxyapatite at 60°C. The bound fraction (19%) was eluted with 0.4 M phosphate buffer and chromatographed on agarose A-50. Solid circles, exclusion region (greater than 1500 nucleotide pairs) melting curve after shearing to 300 nucleotides; Open circles, melting curves of DNA fragments with mode value of 300-nucleotide pairs ($k_{av} = 0.7$). These results are for a light S1 nuclease digestion, and therefore the hyperchromicity is reduced to 88% and 81% of native DNA due to remaining single-strand regions attached to these duplexes. With heavier digestion these values reach 98% and 90% of that of native DNA without appreciably affecting the T_m of either class of fragments.

urchin DNA and fractionated by hydroxyapatite thermal chromatography. The relatively divergent fractions which melted between 60°C and 70°C and the more precisely paired DNA fragments which melted above 80°C were isolated and sheared to 400 nucleotides. They

were then analyzed for repetitive and single-copy DNA sequence content. The low thermal stability fraction was almost completely composed of repetitive DNA sequences, showing perhaps 5% single-copy DNA. These are the results expected if the interspersed short repetitive sequences are divergent, while the long repeated regions are made up of more precisely repetitive sequences.

The same correlation between length and thermal stability has been observed with S1 nuclease method for calf (Britten, unpublished data), *Xenopus* (Davidson *et al.*, 1973), and the clam *Spisula* (Goldberg *et al.*, 1975), as well as the sea urchin. A related observation was made with mouse DNA (Britten, 1972). Such observations indicate that in a number of species the long repetitive regions are relatively recent in origin while the short interspersed regions are of relatively ancient origin. They also suggest that some form of sequence rearrangement as well as nucleotide substitution occurs.

The evidence summarized here indicates that the repetitive DNA is undergoing a number of changes in evolution, including addition and loss of copies, base substitutions and rearrangements. We do not know, however, whether the genome is in a dynamic steady state with the repeated DNA being continuously replaced and remaining approximately constant in quantity and characteristics. Alternatively, the amount of repetitive DNA could be growing as the organization of the genome evolves or could be shrinking during the long aftermath of some massive past events of multiplication. Decisive evidence of such possibilities is difficult to obtain by comparing modern species.

The long, precisely repeated regions are probably the source of the short, divergent, interspersed sequences. This leads directly to the conclusion that events of sequence rearrangement occur. In other words, repeated sequences are probably added to the genome as long regions of tandem sequence repetition which then undergo base substitution

and translocation to yield interspersed short repetitive sequences.

Much of the DNA in the long repetitive regions can be accounted for as regions of tandem repetition of known function, for example, rRNA and tRNA cistrons with repetitive spacers. The histone genes are also clustered together. Recent evidence (D. D. Brown, 1975) indicates that 5S ribosomal RNA regions may undergo multiplication by unequal crossover (Smith, 1974) and selection in favor of a high degree of multiplicity of the relevant genes. It seems likely that the spacers are important to this process, but their function is not known. It is tempting to speculate that other long repetitive regions are added to the genome by a similar process. If parts of the long precise repetitive regions are precursors to the short interspersed repetitive sequences, other parts of these regions carry out known genetic functions.

Though its role remains unproven, sequence rearrangement appears to be a widely occurring and significant process in the evolution of the genome. Future measurements are required to establish the significance of rearrangement relative to other modes of repetitive DNA sequence evolution.

The Potential Significance of Rearrangement to Evolutionary Processes

At the present time the principal sources of variation in the genome which supply the raw material for evolutionary change are unknown. A variety of changes are known to be incorporated into the genome during evolution: base substitution, multiplication and possibly deletion of sequences, and sequence rearrangement. In this section we comment on the evolutionary significance of sequence rearrangement, with particular emphasis on changes affecting short regions of the DNA that change the organization of repeated sequences

relative to single-copy sequences. In making this emphasis we are not denying the significance to fertility and speciation of gross rearrangement events leading to visible changes in the karyotype, although we feel that they represent a relatively minor source of changes that affect genetic regulation.

It is very probable that the organization of different classes of DNA sequences in relation to each other is important to the regulation of genetic activity. This concept has been developed to a testable model of genetic regulation (Britten and Davidson, 1969). The model has been discussed in relation to current evidence (Britten and Davidson, 1971; Davidson and Britten, 1973), and here only two aspects will be described briefly: the organization of sensor and integrator sequences and that of receptor sequences in relationship to structural genes. In the model, sensor sequences facilitate the control of transcription of sets of adjacent integrator sequences. The transcription of the integrator sequences yields regulatory molecules which diffuse through the nucleus, bind to receptor sequences, and thus establish control of the transcription of structural genes adjacent to these receptor sequences. In this way a hormone molecule, for example, could initiate the transcription of a number of regulatory molecules, each of which could turn on the transcription of a battery of unlinked structural genes. What we emphasize here are the branching characteristics of the model by which the transcription of many individual genes is controlled in an integrated fashion and the importance of sequence organization to this set of processes. We feel that these two characteristics of the model are necessary to any model of gene regulation and thus would survive even if some of the more detailed proposals were proved wrong. However, the model forms a convenient framework for the examination of the evolutionary implication of sequence rearrangements.

We proposed that sequence rearrange-

ment would have great evolutionary potential (Britten and Davidson, 1969):

"A peculiar combination of conservatism and flexibility is supplied by the model system. Preexisting useful batteries of genes will tend to remain integrated in function. At the same time, there is the potentiality of formation of new integrative combinations of preexisting producer genes. These combinations would be the result of translocations, principally among the integrator gene sets. Less often, new producer gene batteries would result from events in which receptor genes are translocated into positions contiguous to other producer genes. . . .

"Changes in the integrator systems make possible the origin of new functions and possibly even of new tissues and organs. In other words, the model supplies an avenue for the appearance of novelty in evolution by combining into new systems the already functioning parts of preexisting systems."

These ideas were carried further (Britten and Davidson, 1971):

"Since the developmental process is inherited, the genome must contain the regulative programs with which to control the pattern of genetic activity as well as the genes individually called upon to function in these patterns. Evolutionary changes in the developmental process could certainly come about by alterations of individual genes expressed at given stages of development. It is clear, however, that alterations in the genes which determine the regulative programs could cause enormous changes in the developmental process and that this would be a much more potent source of evolutionary change. We feel that to explain the magnitude of the functional and structural change which has occurred in evolution it is necessary to postulate changes in the regulatory apparatus. A basic property is the potentiality for evolutionary modification of the regulatory systems that were envisioned. In

this model important parts of the regulative relationships depend on the location of sequences in the genome, and a variety of changes can be caused by sequence translocation. As a result, a great many individual cellular properties could be affected by genomic alterations of a type which may occur relatively frequently, namely translocations and chromosomal rearrangements. It is quite plausible that selectively favorable changes of the former type are much more frequent. Furthermore, the model regulatory system is receptive to the incorporation of new sequences and sets of sequences, and through these additions can achieve new functional interrelationships. It can grow as well as become rearranged. Whether or not the particular gene regulation system that we have proposed turns out to occur in living systems, the properties of growth and change by genomic rearrangement are likely to be necessary attributes of evolving regulatory systems."

An additional argument (Britten and Davidson, 1971) was made that the classes of enzymatic function were highly conserved in living systems, with the implication that amino acid substitution in proteins has had a minor effect on evolution of form and function in comparison with changes in the regulatory networks. While many authors in recent years have emphasized the importance of changes in gene regulation to evolution, we are pointing out the relationship between regulatory evolution and changes in DNA sequence organization.

From these concepts can be derived some clear and testable predictions. Among these is the prediction that sequence rearrangement has occurred in evolution on the appropriate length scale required to change the receptor sequences adjacent to structural genes and the sequence arrangement of those DNA regions involved in the integration of genetic activity. Significant changes of this kind will obviously be under strong selection pressure so that con-

servation of sequence arrangement should be observed in relation to the function of the DNA sequences. A general and important conclusion is that sequence rearrangement may be the mechanism providing the major source of variation of the phenotype, far more important than that induced by amino

acid substitution in proteins. Modern techniques supply the opportunity to actually measure the changes in sequence arrangement by determining, for example, which sequences are adjacent to selected repeated sequences in the DNAs of two related animals.

ACKNOWLEDGMENTS

Support for the research reported here was furnished by the National Institutes of Health (NIH), Grants nos. HD-05753 and GM-20927; a National Science Foundation Grant, no. GB-33441; and NIH Training Grant no. HD 00014 to the Woods Hole Marine Biological Laboratory's Embryology Course. Glenn A. Galau was a predoctoral fellow on a National Institutes of Health Training Grant, no. GM-00086. Robert C. Angerer holds a postdoctoral

fellowship from the American Cancer Society, no. PF-925. William H. Klein holds a postdoctoral fellowship from the Damon Runyon Memorial Fund, no. DRG-19-F. Amy Shiu Lee holds a postdoctoral fellowship from the American Cancer Society, California, no. J-289. Francine C. Eden holds a postdoctoral fellowship from American Cancer Society, no. PF-955. William R. Crain holds a postdoctoral fellowship from the National Institutes of Health, no. GM-55726-01.

REFERENCES CITED

- Ando, T., *Biochim. Biophys. Acta*, **114**, 158, 1966.
- Angerer, R. C., E. H. Davidson, and R. J. Britten, *Cell*, **6**, 29, 1975.
- Ardelt, W., and M. Laskowski, Sr., *Biochem. Biophys. Res. Commun.*, **44**, 1205, 1971.
- Aronson, A. I., and F. H. Wilt, *Proc. Nat. Acad. Sci. USA.*, **62**, 186, 1969.
- Berridge, M. V., D. D. Loewensteiner, and A. I. Aronson, *Biochemistry*, **13**, 2520, 1974.
- Bishop, J. O., and K. B. Freeman, *Cold Spring Harb. Symp. Quant. Biol.*, **38**, 707, 1974.
- Bonner, J., W. T. Garrard, J. Gottesfeld, D. S. Holmes, J. S. Sevall, and M. Wilkes, *Cold Spring Harb. Symp. Quant. Biol.*, **38**, 303, 1974.
- Bonner, T. I., D. J. Brenner, B. R. Neufeld, and R. J. Britten, *J. Mol. Biol.*, **81**, 123, 1973.
- Brandhorst, B. P., and T. Humphreys, *Biochemistry*, **10**, 877, 1971.
- Brandhorst, B. P., and T. Humphreys, *J. Cell Biol.*, **53**, 474, 1972.
- Britten, R. J., in *Evolution of Genetic Systems* (Brookhaven Symp. no. 23), H. H. Smith, ed., Gordon and Breach, New York, p. 80, 1972.
- Britten, R. J., and E. H. Davidson, *Science*, **165**, 349, 1969.
- Britten, R. J., and E. H. Davidson, *Quart. Rev. Biol.*, **46**, 111, 1971.
- Britten, R. J., and E. H. Davidson, *FASEB*, 4th Conference, in press, 1975.
- Britten, R. J., D. E. Graham, and B. R. Neufeld, in *Methods in Enzymology*, L. Grossman and K. Moldave, eds., Vol. 29, Part E, Academic Press, New York, p. 363, 1974.
- Britten, R. J., and D. E. Kohne, *Science*, **161**, 529, 1968.
- Britten, R. J., and J. Smith, *Carnegie Inst. Wash. Year Book* **68**, p. 378, 1970.
- Britten, R. J., M. J. Smith, and E. H. Davidson, *J. Mol. Biol.*, in press, 1975.
- Brown, D. D., *FASEB*, 4th Conference, in press, 1975.
- Brown, D. D., and K. Sugimoto, *J. Mol. Biol.*, **78**, 397, 1973.

- Brown, D. D., P. C. Wensink, and E. Jordan, *J. Mol. Biol.*, **63**, 57, 1972.
- Campo, M. S., and J. O. Bishop, *J. Mol. Biol.*, **90**, 649, 1974.
- Chamberlin, M. E., R. J. Britten, and E. H. Davidson, *J. Mol. Biol.*, in press, 1975.
- Chase, J. W., and C. C. Richardson, *J. Biol. Chem.*, **249**, 4545, 1974a.
- Chase, J. W., and C. C. Richardson, *J. Biol. Chem.*, **249**, 4553, 1974b.
- Darnell, J. E., and R. Balint, *J. Cell Physiol.*, **76**, 349, 1970.
- Davidson, E. H., and R. J. Britten, *Quart. Rev. Biol.*, **48**, 565, 1973.
- Davidson, E. H., B. R. Hough, M. E. Chamberlin, and R. J. Britten, *Devel. Biol.*, **25**, 445, 1971.
- Davidson, E. H., B. R. Hough, C. S. Amenson, and R. J. Britten, *J. Mol. Biol.*, **77**, 1, 1973.
- Davidson, E. H., D. E. Graham, B. R. Neufeld, M. E. Chamberlin, C. S. Amenson, B. R. Hough, and R. J. Britten, *Cold Spring Harb. Symp. Quant. Biol.*, **38**, 295, 1974.
- Davidson, E. H., B. R. Hough, W. H. Klein, and R. J. Britten, *Cell*, **4**, 217, 1975.
- Dayhoff, M. O., *Atlas of Protein Sequence and Structure, Vol. 5*, The National Biomedical Research Foundation, Silver Spring, Md., 1972.
- Fenwick, M. L., *Biochem. J.*, **107**, 851, 1968.
- Fitch, W. M., in *Evolution of Genetic Systems* (Brookhaven Symp. No. 23), H. H. Smith, ed., Gordon and Breach, New York, p. 186, 1972.
- Galau, G. A., R. J. Britten, and E. H. Davidson, *Cell*, **2**, 9, 1974.
- Galau, G. A., M. E. Chamberlin, B. R. Hough, and E. H. Davidson, in *Molecular Studies of Biological Evolution*, F. J. Ayala, ed., Sinauer Press, in press, 1975.
- Getz, M. J., G. D. Birnie, B. D. Young, E. MacPhail, and J. Paul, *Cell*, **4**, 121, 1975.
- Gelderman, A. H., A. V. Rake, and R. J. Britten, *Proc. Nat. Acad. Sci. USA*, **58**, 172, 1971.
- Goldberg, R. B., G. A. Galau, R. J. Britten, and E. H. Davidson, *Proc. Nat. Acad. Sci. USA*, **70**, 3516, 1973.
- Goldberg, R. B., W. R. Crain, J. V. Ruderman, G. P. Moore, T. R. Barnett, R. C. Higgins, R. A. Gelfand, G. A. Galau, R. J. Britten, and E. H. Davidson, *Chromosoma* (Berlin), in press, 1975.
- Goodman, M., G. W. Moore, and G. Matsuda, *Nature*, **253**, 603, 1975.
- Graham, D. E., B. R. Neufeld, E. H. Davidson, and R. J. Britten, *Cell*, **1**, 127, 1974.
- Harrison, P. R., G. D. Birnie, A. Hell, S. Humphries, B. D. Young, and J. Paul, *J. Mol. Biol.*, **84**, 539, 1974.
- Hinegardner, R. T., in *Methods in Developmental Biology*, F. H. Wilt and N. K. Wessells, eds., Thomas Crowell, New York, p. 139, 1967.
- Hinegardner, R. T., *Am. Nat.*, **102**, 517, 1968.
- Hinegardner, R. T., *Comp. Biochem. Physiol.*, **47A**, 447, 1974.
- Holmes, D. S., and J. Bonner, *Biochemistry*, **12**, 2330, 1973.
- Holmes, D. S., and J. Bonner, *Proc. Nat. Acad. Sci. USA*, **71**, 1108, 1974.
- Hough, B. R., and E. H. Davidson, *J. Mol. Biol.*, **70**, 491, 1972.
- Hoyer, B. H., N. W. van de Velde, M. Goodman, and R. B. Roberts, *Carnegie Inst. Wash. Year Book* **71**, p. 260, 1972.
- Hutton, J. R., and J. G. Wetmur, *J. Mol. Biol.*, **77**, 495, 1973.
- Hyman, L. H. *The Invertebrates: Protozoa through Ctenophora*, vol. 1, ch. 2, McGraw-Hill, New York, 1940.
- Jukes, T. H., and R. Holmquist, *J. Mol. Biol.*, **64**, 163, 1972.
- Kedes, L. H., and M. L. Birnstiel, *Nature (London) New Biol.*, **230**, 165, 1971.
- King, J. L., and T. H. Jukes, *Science*, **164**, 788, 1969.
- Klein, W. H., W. Murphy, G. Attardi, R. J. Britten, and E. H. Davidson, *Proc. Nat. Acad. Sci., USA*, **71**, 1785, 1974.
- Kohne, D. E., and M. J. Byers, *Carnegie Inst. Wash. Year Book* **70**, p. 378, 1971.
- Kohne, D. E., J. A. Chiscon, and B. H. Hoyer, *Carnegie Inst. Wash. Year Book* **69**, p. 488, 1970.
- Lagowski, J. M., M. Y. Yu, H. S. Forrest, and C. D. Laird, *Chromosoma* (Berlin), **43**, 349, 1973.
- Laird, C. D., B. L. McConaughy, and B. J. McCarthy, *Nature*, **224**, 149, 1969.
- Lewin, B., *Cell*, **4**, 77, 1975.
- Manning, S. E., C. W. Schmid, and N. Davidson, *Cell*, **4**, 141, 1975.
- Mazrimas, J. A., and F. T. Hatch, *Nature (London) New Biol.*, **240**, 102, 1972.
- McCarthy, B. J., and M. N. Farquhar, in *Evolution of Genetic Systems* (Brookhaven Symp. No. 23), H. H. Smith, ed., Gordon and Breach, New York, p. 1, 1972.
- McColl, R. S., and A. Aronson, *Biochem. Biophys. Res. Commun.*, **56**, 47, 1974.
- Molloy, G. R., W. Jelinek, M. Dalditt, and J. E. Darnell, *Cell*, **1**, 43, 1974.

- Morrow, J., PhD. Thesis, Stanford University, Stanford, California, 1974.
- Noll, H., *Nature*, 215, 360, 1967.
- Rice, N. R., *Carnegie Inst. Wash. Year Book* 69, p. 472, 1971a.
- Rice, N. R., *Carnegie Inst. Wash. Year Book* 70, p. 366, 1971b.
- Rice, N. R., in *Evolution of Genetic Systems* (Brookhaven Symp. No. 23), H. H. Smith, ed., Gordon and Breach, New York, p. 44, 1972.
- Rice, N. R., *Carnegie Inst. Wash. Year Book* 73, p. 1088, 1974.
- Rice, N. R., and P. Esposito, *Carnegie Inst. Wash. Year Book* 72, p. 200, 1973.
- Rice, N. R., and P. Paul, *Carnegie Inst. Wash. Year Book* 71, p. 262, 1972.
- Scherrer, K., G. Spohr, N. Granboulan, C. Morel, J. Grosclaude, and C. Chezzi, *Cold Spring Harb. Symp. Quant. Biol.* 35, 539, 1970.
- Shenk, T. E., C. Rhodes, P. W. J. Rigby, and P. Berg, *Proc. Nat. Acad. Sci. USA.*, 72, 989, 1975.
- Smith, G., *Cold Spring Harb. Symp. Quant. Biol.*, 38, 501, 1974.
- Smith, M. J., B. R. Hough, M. E. Chamberlin, and E. H. Davidson, *J. Mol. Biol.*, 85, 103, 1974.
- Soeiro, R., and J. E. Darnell, *J. Cell Biol.*, 44, 467, 1970.
- Studier, F. W., *J. Mol. Biol.*, 11, 373, 1965.
- Sullivan, B., *J. Mol. Evol.*, 1, 295, 1972.
- Sullivan, D., R. Palacios, J. Stavnezer, J. N. Taylor, A. J. Faras, N. L. Kiely, N. M. Summers, J. M. Bishop, and R. T. Schimke, *J. Biol. Chem.*, 248, 7530, 1973.
- Sutton, W. D., and M. McCallum, *Nature (London) New Biol.*, 232, 83, 1971.
- Vogt, V. M., *Eur. J. Biochem.*, 33, 192, 1973.
- Weinberg, E. S., M. L. Birnstiel, D. R. Purdom, and R. Williamson, *Nature (London)* 240, 225, 1972.
- Wetmur, J. G., and N. Davidson, *J. Mol. Biol.*, 31, 349, 1968.
- Wensink, P. C., D. J. Finnegan, J. E. Donelson, and D. S. Hogness, *Cell*, 3, 315, 1975.
- Wilson, D., and C. A. Thomas, *Biochim. Biophys. Acta*, 331, 333, 1973.
- Wu, J.-R., J. Hurn, and J. Bonner, *J. Mol. Biol.*, 64, 211, 1972.

RECENT PUBLICATIONS

- Anderson, D. M., Galau, G. A., Britten, R. J., and Davidson, E. H., Informational content of the RNA accumulated in oocytes of the sea urchin, in preparation, 1975.
- Angerer, R. C., Davidson, E. H., and Britten, R. J., DNA sequence organization in the mollusc *Aplysia californica*, *Cell*, in press, 1975.
- Britten, R. J., and Davidson, E. H., DNA sequence arrangement and preliminary evidence on its evolution, *Fed. Proc.*, in press, 1975.
- Britten, R. J., Smith, M. J., and Davidson, E. H., Experimental studies on nucleic acid reassociation kinetics. I. Rate of duplex formation in DNA-DNA reactions, submitted to *J. Mol. Biol.*, 1975.
- Chamberlin, M. E., Britten, R. J., and Davidson, E. H., Sequence organization in *Xenopus* DNA studied by the electron microscope, *J. Mol. Biol.*, in press, 1975.
- Davidson, E. H., and Britten, R. J., Molecular aspects of gene regulation in animal cells. *Cancer Res.*, 34, 2034-2043, 1974.
- Davidson, E. H., Galau, G. A., Angerer, R. C., and Britten, R. J., Comparative aspects of DNA organization in metazoa, *Chromosoma*, in press, 1975.
- Davidson, E. H., Hough, B. R., Klein, W. H., and Britten, R. J., Structural genes adjacent to interspersed repetitive DNA sequences. *Cell*, 4, 217-238, 1975.
- Galau, G. A., Chamberlin, M. E., Hough, B. R., Britten, R. J., and Davidson, E. H., Evolution of repetitive and nonrepetitive DNA in two species of *Xenopus*, in *Molecular Studies of Biological Evolution*, F. J. Ayala, ed., Sinauer Associates, in press, 1975.
- Goldberg, R. B., Crain, W. R., Ruderman, J. V., Moore, G. P., Barnett, T. R., Higgins, R. C., Gelfand, R. A., Galau, G. A., Britten, R. J., and Davidson, E. H., DNA sequence organization in the genomes of five marine invertebrates, *Chromosoma*, in press, 1975.
- Hough, B. R., and Davidson, E. H., The RNA of the mature *Xenopus* oocyte, in *Handbook of Genetics*, R. C. King, ed., vol. 4, Plenum Press, New York, 1975.
- Hough, B. R., Smith, M. J., Britten, R. J., and Davidson, E. H., Sequence complexity of heterogeneous nuclear RNA in sea urchin embryos, *Cell*, 5, 291-299, 1975.

S T A F F

Roy J. Britten, *Senior Research Associate*
Eric H. Davidson, *Professor*
Barbara R. Hough, *Senior Research Fellow*
Michael J. Smith, *Senior Research Fellow*
Robert C. Angerer, *Research Fellow—American Cancer Society Fellowship*
William R. Crain, *Research Fellow—National Institutes of Health Fellowship*
Francine C. Eden, *Research Fellow—American Cancer Society Fellowship*
William H. Klein, *Research Fellow—Damon Runyon Fellowship*
Amy Shiu Lee, *Research Fellow—American Cancer Society, California, Fellowship*

Frank Costantini, *Graduate Research Assistant*
Mark M. Davis, *Graduate Research Assistant*
Glenn A. Galau, *Graduate Research Assistant*
Barbara J. Wold, *Graduate Research Assistant*
Margaret E. Chamberlin, *Senior Research Assistant*
Jane Rigg, *Senior Research Assistant*
Denise M. Painchaud, *Research Assistant*
Michael R. Kozlowski, *Undergraduate Assistant*
John Mamin, *Undergraduate Assistant*
Dennis B. Cochran, *Laboratory Assistant*
Charles F. Collett, *Laboratory Assistant*

Department of Plant Biology

Stanford, California

Winslow R. Briggs

Director

Contents

Introduction (Briggs)	739
Photosynthetic responses of plants from habitats with contrasting thermal environments	743
Comparison of photosynthetic characteristics of intact plants (Björkman, Mooney, and Ehleringer)	743
Thermal stability of the photosynthetic apparatus in intact leaves (Björkman) ...	748
Mechanistic studies of thermal damage to leaves (Berry, Fork, and Garrison)	751
Comparison of the quantum yields for CO ₂ uptake in C ₃ and C ₄ plants (Björkman and Ehleringer)	760
Chromosomal numbers in <i>Atriplex</i> (Nobs)	762
Control of photosynthesis by temperature (Murata, Fork, and Troughton)	766
The effect of growth temperature on the transition of the physical phase of membrane lipids as detected by electron spin resonance spectrometry and chlorophyll <i>a</i> fluorescence (Murata, Fork, and Troughton)	766
The relationship between the physical phase of membrane lipids, electron transport, oxygen evolution, and quantum distribution in the photosynthesis of <i>Anacystis nidulans</i> and in lettuce and spinach chloroplasts (Murata, Fork, and Troughton)	771
A comparison of light-induced shifts in carotenoid absorption in representatives of different algal groups (Fork and Brown)	776
Metabolism and photocharacteristics of chlorophyll-protein complexes (Brown)	779
Formation of aggregates from short fragments of plant DNA (Thompson)	783
Comparison of DNA base sequences in three species of the genus <i>Osmunda</i> (Stein and Thompson)	786
DNA hybridization studies in <i>Atriplex</i> species (Strong and Thompson)	789
Bacterial plasmids of <i>Agrobacterium tumefaciens</i> and their role in crown gall disease (Rogler, Thompson, and DeVay)	791
A model system to simulate chloroplast movement and accompanying transmittance changes in <i>Ulva</i> (Britz)	794
Inhibitor studies on the mechanism of chloroplast movement in <i>Ulva</i> (Britz)	803
Localization of some new phytochrome reactions within the cell (Mackenzie and Briggs)	805
Studies on a possible photoreceptor for phototropism in corn (Briggs)	807
Staff activities	809
Bibliography	811
Speeches	812
Personnel	814

INTRODUCTION

It is with both pleasure and relief that the Department of Plant Biology announces completion of construction and renovation and the resumption of a more normal scientific program. The last items are out of storage, and the last inspection completed. During the current fiscal year, we anticipate about 15 scientific visitors—predoctoral fellows, postdoctoral fellows, or visiting investigators. With the physical plant in order, most new equipment on hand and in operation, and the influx of visitors started, the scientific challenge now remains before us.

The architectural design of the present facility is intended to encourage the continual interaction between visitor, staff, and fellows that has been one of the attractive features of the Department.

Interaction between Plant Biology and the Department of Biological Sciences at Stanford is also increasing. Next year we will have three Carnegie Predoctoral Fellows in the Department of Biology, and it is probable that all three will work with staff members in Plant Biology. Plans are currently under way for a collaborative course in photosynthesis and another general course in photobiology, both to be taught in our new seminar room, and a research level seminar in experimental botany will continue, in collaboration with botanists at Stanford.

Despite the rigors of construction and moving, the staff and visitors to the Department were able to accomplish a substantial amount of research. Dr. Björkman, together with Professor H. A. Mooney of Stanford University and Mr. James Ehleringer, a Stanford graduate student, continued studies in progress last year on the photosynthetic properties of plants from contrasting thermal environments. Direct measurement of

photosynthesis corresponded well with previous growth studies, indicating that the temperature dependence of dry matter production is closely related to the temperature dependence of photosynthetic capacity, whether the plant studied used the C_3 or the C_4 pathway of carbon fixation, and whether it was a native of a cool coastal climate or a native of the extremes of temperature found in the bottom of Death Valley. When the various plants were all grown under similar conditions, whether warm or cool, some showed the capability of adapting the photosynthetic machinery to growth under temperature regimes far removed from normal, while others did not. Plants which could perform excellently under the most extreme conditions, however, seemed the least adaptive.

Further studies by Björkman indicate that the high temperature inhibition of photosynthesis is not caused by a decrease in stomatal conductance, nor by temperature-induced alteration of diffusive transport of CO_2 fixation sites within the cells. Neither is it caused by a general breakdown of cellular integrity, since inhibition of respiration cannot be detected until temperatures are raised significantly above those at which inhibition of photosynthesis is found. Under rate-limiting light intensities, however, the quantum yield for photosynthesis falls off sharply at the temperature at which inhibition of photosynthesis is first found. Likewise, the quantum yield of the extraordinary desert plant *Tidestromia oblongifolia*, which can flourish at temperatures of $47^\circ C$, is sharply reduced when the plant is grown at lower temperature, e.g., $22^\circ C$. The cause cannot be alteration of any barriers to CO_2 movement into the cell, or reduction in chlorophyll, protein, or carboxylation enzymes. Björkman hypothesizes that

the membrane properties which permit photosynthesis at high temperatures preclude effective function at low temperatures.

Drs. Fork and Berry and Ms. Garrison then heat-treated leaves and examined various properties of chloroplasts isolated from them. It was clear that photosystem II electron transport was strongly inhibited by treatments which did not affect photosystem I. The temperature at which this effect was first noted corresponded fairly well with the temperature at which inhibition of photosynthesis is first observed. Changes in the fluorescence kinetics of intact leaves also occur at temperatures at which thermal inhibition of photosynthesis is found. These results also implicate system II. Overall fluorescence yield is also affected by temperature, but transitions in fluorescence yield occur at temperatures significantly above those at which damage to photosynthesis occurs. Likewise, studies on ion leakage show that cell permeability is also normal at temperatures above which photosynthetic damage occurs. It is clear that photosynthetic membranes are more sensitive to thermal injury than the plasma membrane.

Björkman and Ehleringer also examined the quantum yield for CO_2 uptake in a number of C_3 and C_4 plants at 2% and 21% O_2 , under conditions of limiting light intensity. They used intact attached leaves in the measurements. Surprisingly, all species measured showed quantum yields between 0.051 and 0.055 at atmospheric oxygen concentration. Only at 2% oxygen was there a significant difference, with the values for the C_4 species remaining unchanged and those for the intact plants increasing to about 0.073. Thus the advantage in C_4 plants conferred by lack of O_2 inhibition of photosynthesis is almost exactly offset by the increased energy cost of CO_2 fixation in these species. Only at high light intensity do they possess an advantage.

Dr. Nobs has continued his cytological studies on the genus *Atriplex*, on which so much of the experimental work is done. The base chromosome number is nine pairs, with no evidence for aneuploidy in any of the natural species (though it occurs strikingly in certain artificial hybrids). The pairing pattern in the tetraploids suggests that at least partial autopolyploidy has been a major factor in the evolution of the polyploids.

Visiting investigators Drs. Murata and Troughton, together with Dr. Fork, grew the blue-green alga *Anacystis nidulans* under different temperatures selected to bring about known variation in the fatty acid composition of their membranes. Studies using electron spin resonance spectrometry on isolated lamellar fragments suggested that in cells grown at higher temperatures, the marked change in the environment of the spin label with increasing temperature occurred at higher temperatures. Maximum fluorescence yield also occurred at higher temperatures for cells grown at higher temperatures, as was the case for lamellar fragments or for structures formed by reaggregation of extracted galactolipids and chlorophyll *a*. Fluorescence of the extracted chlorophyll alone, however, or extracted phycobilins, showed no effect of growth temperature. Thus the changes observed in fluorescence yield in intact cells must be produced by interaction between the pigments and membrane lipids. The changes are probably caused by transition of membrane lipids between the liquid-crystalline state and the mixed solid-liquid-crystalline state.

Further studies on electron transport as indicated by P700 reduction, oxygen evolution, and the shift of the thylakoid membranes from pigment state 1 to pigment state 2, also gave clear evidence of the membrane phase transition at roughly the same temperatures. These studies complement those by the physiological ecology group on temperature effects on photosynthesis under condi-

tions of thermal inhibition, concentrating instead on events occurring at temperatures below optimum instead of above. Both studies indicate the wisdom of an approach which combines studies on intact plants with careful biochemical and biophysical studies. They also strengthen the notion that fluorescence measurement can be a powerful tool to investigate the state of the photosynthetic apparatus in intact cells and plants.

Drs. Fork and Brown have continued studies on light-induced shifts in carotenoid absorption in a wide variety of different algal groups. Included were representatives of a newly identified algal group, the *Eustigammatophyceae*, plants containing only chlorophyll *a*, β -carotene, and a major xanthophyll. Both light-minus-dark difference spectra and kinetics of the changes were examined. It is clear that such shifts occur in virtually all photosynthetic organisms, with the blue-green algae standing as the single exception. Further study is needed, however, to understand the physicochemical events which underlie these changes.

Dr. Brown has continued studies on the properties of chlorophyll-protein complexes isolated from higher plants. One of these, CPI, is rich in P700 and contains only chlorophyll *a*. The other, CPII, contains all of the chlorophyll *b* plus an equimolar concentration of chlorophyll *a*. Studies with Mme. Suzanne Acker and Dr. Jacques Duranton at the French Atomic Energy Center, Saclay, near Paris, show clearly that CPI is metabolically isolated from the rest of the chlorophyll-containing membranes in the plastid. Its pigments are both synthesized and degraded more slowly than the rest of the pigments. CPI preparations also show two distinct light-induced changes in absorbance, with half-lives of 8 milliseconds and 50 milliseconds, respectively. The changes probably represent direct oxidation of P700 on the one hand and cytochrome *f*-limited oxida-

tion on the other. The CPI preparations would also very effectively oxidize cytochrome *c*, a test frequently used to monitor photosystem I activity. The capacity to oxidize cytochrome *c* seems to parallel the P700 concentration.

Fluorescence emission spectra at room temperature and at -190° were measured both for CPI and CPII. Though the spectra are not yet sufficiently clear to permit curve analysis, it should be possible to relate the various peaks with the various forms of chlorophyll *a* seen previously in absorption spectra. Dilution of CPII did not alter the fluorescence emission spectra whether excitation occurred with 420 nm or 470 nm light (preferential chlorophyll *a* or chlorophyll *b* excitation, respectively). Thus the two chlorophylls are clearly on the same protein (though not necessarily on the same polypeptide chain), since otherwise dilution would have decreased energy transfer between chlorophyll *b* and chlorophyll *a*.

Dr. Thompson, who joined the Department of Plant Biology this year, has initiated extensive studies of plant nucleic acids, concentrating particularly on DNA hybridization techniques. Studies on reaggregation of pea DNA suggest that the genome is organized with many clusters of repetitive sequences, providing a first clue to the possible linear arrangement of genetic information along the DNA strand. Studies with Ms. Diana Stein, a graduate student at the University of Massachusetts at Amherst, show that three species of the fern genus *Osmunda* can be clearly distinguished in DNA hybridization experiments, though two are extremely similar in morphology. The results suggested that the technique might be useful in studying relationships between the various species of *Atriplex* under investigation by the physiological ecology group. Preliminary indications are that the technique will work very well indeed with *Atriplex*, and should enable comparison between morphologically similar and dis-

similar species as well as between those which do either C₃ or C₄ photosynthesis. Ms. Heather Strong, another graduate student from the University of Massachusetts at Amherst, now has the system characterized for four species, and detailed analysis can begin. Thus one major goal has been reached—a demonstration that these techniques would be useful adjuncts to the other kinds of evolutionary and ecological research in progress in the Department.

Mr. Steven Britz has continued studies begun at Harvard University on the nature of chloroplast movement in the green alga *Ulva lactuca*. The chloroplasts move in synchrony according to a circadian rhythm, when held under continuous conditions of temperature and illumination (or darkness). Sensitivity of the movement to the inhibitor colchicine, but not to cytochalasin B, suggests that microtubules are involved in the process. Mr. Britz has also developed a computer model for the observed changes in transmittance that accompany chloroplast movement, and the model could be extremely useful in determining whether or not there are also changes in pigment orientation or amount accompanying the movement. He has recently completed a device for automatic monitoring of transmittance changes through 30 samples and is now in a position to do some precise quantitative work on the phenomenon.

Mr. John Mackenzie completed some studies in the laboratory of Dr. Lee H. Pratt, Vanderbilt University, on localization of phytochrome, the pigment mediating so many light-triggered reactions in plants, using a sensitive immunospecific technique developed at Vanderbilt by Dr. Richard A. Coleman. Mr. Mackenzie has been able to demonstrate some striking changes in intra-

cellular distribution following photo-transformation of the pigment to its biologically active form in oat and rice seedlings. Further changes occur depending upon whether the pigment is allowed to remain in its active form, or is transformed back to its inactive form. He has thus discovered several previously undescribed reactions for this important pigment, and has laid the groundwork for investigations in several new directions.

Dr. Briggs has been able to resume work started last year in the laboratory of Professor Rainer Hertel, University of Freiburg, Germany, on a promising candidate for the phototropic photoreceptor. With a visiting investigator, Dr. Jack Freeberg, he has obtained preliminary evidence for a light-induced absorbance change in a membrane fraction from corn coleoptiles. The change, which decays in the dark, suggests the light-induced reduction of a flavoprotein with subsequent reduction of a *b*-type cytochrome. Though other workers have seen such changes and related them to the phototropic photoreceptor, the present work represents the first demonstration of such changes outside the fungi, and the first suggestion that the pigment is membrane-associated. Mr. Robert Brain, a Stanford undergraduate visiting the laboratory this summer, has been able to show these same changes in a membrane fraction from the fungus *Neurospora crassa*.

As the above paragraphs suggest, several of the projects currently under way are really only in their earliest stages. However, given the difficulties of research during the past year of construction, one should be optimistic that the intensity of work on basic problems of plant biology will now increase rapidly. The Director finds this trend gratifying.

PHOTOSYNTHETIC RESPONSES OF PLANTS FROM
HABITATS WITH CONTRASTING THERMAL
ENVIRONMENTSCOMPARISON OF PHOTOSYNTHETIC
CHARACTERISTICS OF INTACT PLANTS

Olle Björkman, Harold A. Mooney,¹
and James Ehleringer

Last year we reported on the responses of growth and development of a number of species native to habitats with contrasting thermal regimes in our experimental stations on the hot desert floor of Death Valley and the cool oceanic bluff of Bodega Head (*Year Book* 73, p. 748). On the basis of their growth response under adequate water supply in the Death Valley garden, the 17 species tested could be separated into three main categories: (1) those which are unable to survive the hottest period of the year, (2) those which are able to survive this period but do not grow, and (3) those whose growth mainly occurs during the hottest part of the year. All of the species native to cool oceanic habitats and several of those native to warm-temperate environments, including both C₃ and C₄ species, fall in the first category. All species native to the floor of Death Valley, except *Tidestromia oblongifolia*, fall in category 2. This C₄ species which is summer active and winter deciduous in its native Death Valley habitat, is the only one that falls into category 3. This plant exhibited a very fast growth rate under the extreme summer heat in the Death Valley garden.

In contrast, all of the species tested, except *T. oblongifolia*, were able to grow in the cool Bodega Head garden. Here the species native to cool coastal habitats such as *Atriplex glabriuscula* (C₃) and *A. sabulosa* (C₄) had the highest productivities.

On the basis of these transplant experiments *Atriplex glabriuscula* (cool coastal C₃), *A. sabulosa* (cool coastal C₄), *A. hymenelytra* (Death Valley ever-

green C₄), and *Tidestromia oblongifolia* (Death Valley summer active C₄) were selected for further detailed comparative studies of productivity under contrasting controlled thermal regimes and for investigation of the photosynthetic and other physiological mechanisms that underlie the striking differences in the ability of plants to grow in contrasting natural thermal environments. The comparative growth experiments in which temperature was the only variable and in which other stress factors, including atmospheric drought, were completely eliminated clearly show that the widely different abilities of these species to grow in the contrasting habitats of Bodega Head and the Death Valley floor are primarily due to intrinsic differences in their response to temperature (*Year Book* 73, p. 757). For example, under a 16°C day/10°C night regime, simulating a cool coastal environment, the daily growth rates of coastal *A. glabriuscula* and *A. sabulosa* were as high as 0.16 g⁻¹day⁻¹ or 65% to 75% of the maximum growth rate which occurred at about 25°C day/17°C night. *T. oblongifolia* proved to be incapable of sustained growth under the 16°/10°C regime. In contrast, under a very hot 45°C day/31°C night regime, simulating a typical summer day in Death Valley, *T. oblongifolia* is very near its optimum temperature for growth and under these conditions its growth rate was a record high of 0.26 g⁻¹ day⁻¹, i.e., this extraordinary plant doubled its dry matter content in less than 3 days. This high temperature regime is lethal to both of the coastal species. *A. hymenelytra* grew under both of these extremes of temperature, but the growth rates were lower than those of the coastal species under the cool regime and much lower than that of *T. oblongifolia* under the hot regime.

¹ Department of Biological Sciences, Stanford University, Stanford, California.

Our growth analyses further show that although temperature has a marked influence on the growth habits and other morphological characteristics, the strikingly different temperature dependences of dry matter production among the four species analyzed in detail cannot even in part be due to differences in the allocation of carbon to the leaves in relation to nonphotosynthetic organs. These results indicate that the contrasting interspecific responses of dry matter production to temperature must be the result of intrinsic differences in the temperature dependence of primary growth processes. During the year detailed studies of the photosynthetic and respiratory characteristics of the four species have been conducted both in the field and on plants grown under controlled temperature regimes in the laboratory. Since processing of the field data was not yet completed when this report was prepared (May 1975) the results presented here will concentrate on the characteristics of material grown under controlled conditions. It is evident, however, that these results are consistent with the field data.

The photosynthetic performances of the different species discussed in the following section, are compared under similar conditions of irradiance, CO_2 and O_2 concentrations, water vapor pressure, stomatal conductance, and plant water status. These results, therefore, reflect intrinsic characteristics of the photosynthetic apparatus. A detailed account of these studies will be published elsewhere.

The striking differences that can exist in the photosynthetic temperature dependence of higher plants native to habitats with contrasting thermal regimes are illustrated in Fig. 1. The curve for *T. oblongifolia* was obtained at the peak of summer heat in Death Valley, while that for coastal *A. glabriuscula* was measured on a plant grown under a thermal regime simulating a cool oceanic environment.

The coastal C_3 species, *A. glabriuscula*, and the coastal C_4 species, *A. sabu-*

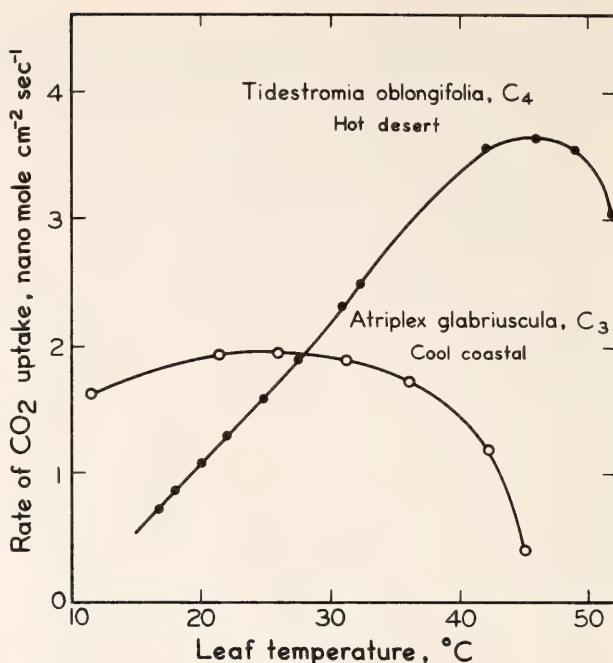


Fig. 1. Temperature dependence of photosynthesis in *Tidestromia oblongifolia* and *Atriplex glabriuscula* at a high light intensity of 160 nanoeinstein $\text{cm}^{-2}\text{sec}^{-1}$, a CO_2 partial pressure of approximately 320 μbar , and an O_2 concentration of 21%. Stomatal conductance values were almost identical in the two species.

losa (not shown), are capable of high photosynthetic rates at low and moderate temperatures but the rates do not increase with increased temperature beyond 25° to 30°C; they decline above 35°C and rapidly fall to zero at 45°C. The photosynthetic performance of *T. oblongifolia* is in sharp contrast with the coastal plants. When grown in a hot temperature regime either in Death Valley or under controlled conditions in the laboratory, the photosynthetic rate is poor at low and moderate temperatures but increases steeply with increased temperature to reach a very high maximum rate at about 45°C, and even at 50°C the rate exceeds that of *A. glabriuscula* at its optimum temperature. Total inhibition of photosynthesis in *T. oblongifolia* does not occur until 52° to 54°C.

Both curves shown in Fig. 1 were determined at a high light intensity of 160 nanoeinstein $\text{cm}^{-2}\text{sec}^{-1}$, which is approximately equal to 80% of maximum noon sunlight. This light intensity is rate-saturating for *A. glabriuscula* but

is insufficient to provide maximum photosynthetic rate at the temperature optimum for *T. oblongifolia*. The latter species is thus capable of even higher photosynthetic rates. Rates in excess of 5 nanomole CO₂ cm⁻²sec⁻¹ (80 mg CO₂ dm⁻²hr⁻¹) are not uncommon for *T. oblongifolia*.

The temperature regime under which the plants are grown markedly affects the temperature dependence of photosynthesis in all of the species examined. Comparisons of the different species grown at a temperature regime simulating the summer in Death Valley cannot be made, since this is lethal to the coastal plants. The comparisons were therefore carried out under 40°C day/30°C night and 16°C day/11°C night, the highest and lowest temperature regime at which all four species are able to survive. As shown in Table 1, growth at 40°C results in strikingly reduced photosynthetic rates both at high and low temperatures in the two coastal species. In *T. oblongifolia*, on the other hand, growth at the low temperature regime causes a drastic reduction in photosynthetic capacity. This low temperature inhibition of photosynthesis is present at low, intermediate, and high temperatures, irradiances, and CO₂ concentrations.

Atriplex hymenelytra (C₄) is capable of a wider range of photosynthetic acclimation to temperature than either the two coastal *Atriplex* species or *T. oblongifolia*. Growth under the cool tem-

perature regime results in a somewhat higher photosynthetic capacity at low temperature than does growth under the hot regime and vice versa. However, the photosynthetic capacity of this species is lower than the capacity of the coastal plants when grown under a low temperature regime and greatly inferior to that of *T. oblongifolia* when grown under a hot regime. Although *A. hymenelytra* can tolerate higher temperatures than the coastal *Atriplexes* without permanent damage, it is less extreme in this respect than *T. oblongifolia* and it is incapable of sustained net photosynthesis above 47°C.

These and other results show that the responses of photosynthesis to different temperatures are quite similar to those of overall growth rates and thus provide further evidence that the temperature dependence of dry matter production is closely linked to the temperature dependence of photosynthetic capacity. Also, the genetically determined range of environmentally induced photosynthetic acclimation to temperature is strikingly different among the study species. This undoubtedly reflects profound adaptive differentiations of the photosynthetic machinery to the contrasting thermal regimes of the respective native environments and indicates that these adaptations are major determinants in the different abilities of the plants to grow and succeed in their widely diverse habitats. The results further suggest that excellence in photosyn-

TABLE 1. Effect of Temperature for Growth on Photosynthetic Rates*

Species	Photosynthesis at 16°C			Photosynthesis at 40°C		
	A: Grown at 16°C	B: Grown at 40°C	Ratio A/B	C: Grown at 40°C	D: Grown at 16°C	Ratio C/D
<i>A. glabriuscula</i>	2.20	0.73	3.01	1.01	1.80	0.56
<i>A. sabulosa</i>	2.80	0.70	4.00	1.54	2.80	0.55
<i>A. hymenelytra</i>	1.62	1.10	1.47	2.41	2.18	1.11
<i>T. oblongifolia</i>	0.42	1.70	0.25	5.00	0.42	11.90

* Rates measured at a high light intensity of 150 nanoeinstein cm⁻²sec⁻¹, 320 microbar CO₂, and a water vapor pressure deficit ≤ 15 millibar. Rates are given in nanomole CO₂ cm⁻²sec⁻¹.

thetic performance in one extreme may preclude excellence in the opposite extreme.

The superior photosynthetic performance of *T. oblongifolia* at high temperature is not caused by differences in stomatal conductance to CO_2 diffusion. Figure 2 shows the relationship between the photosynthetic and stomatal conductance at 40°C leaf temperature of plants grown at this temperature. The data are derived from experimental determinations of the rate of CO_2 uptake as a function of the CO_2 concentration in the intercellular spaces in the leaf. It is clear that *T. oblongifolia* is superior to *A. hymenelytra* at any stomatal conductance at which either plant is capable of a substantial rate of CO_2 uptake. Recent field measurements on these two species in Death Valley show that the responses are similar to those of the laboratory grown material but the differences between the two species are somewhat greater with even higher rates for *T. oblongifolia* and lower rates for *A. hymenelytra*. The rates of the coastal C_3 plant *A. glabriuscula* are lower than those of the other species at any stomatal conductance. Clearly, the interspecific differences in photosynthetic performance are unrelated to differences in stomatal characteristics.

From the results presented in Fig. 2 it also follows that for any given photosynthetic rate and any given water vapor pressure difference between the leaves and the air, the photosynthetic water use efficiency (CO_2 fixed/water transpired) is considerably greater in *Tidestromia* than in *A. hymenelytra* and much greater than in the coastal C_3 species. It is interesting to note that the stomatal conductance values usually found under optimal conditions in the two Death Valley species are so adjusted that they permit a near maximum photosynthetic water use efficiency together with a high photosynthetic rate. A further increase in stomatal conductance would lead to a proportional increase in

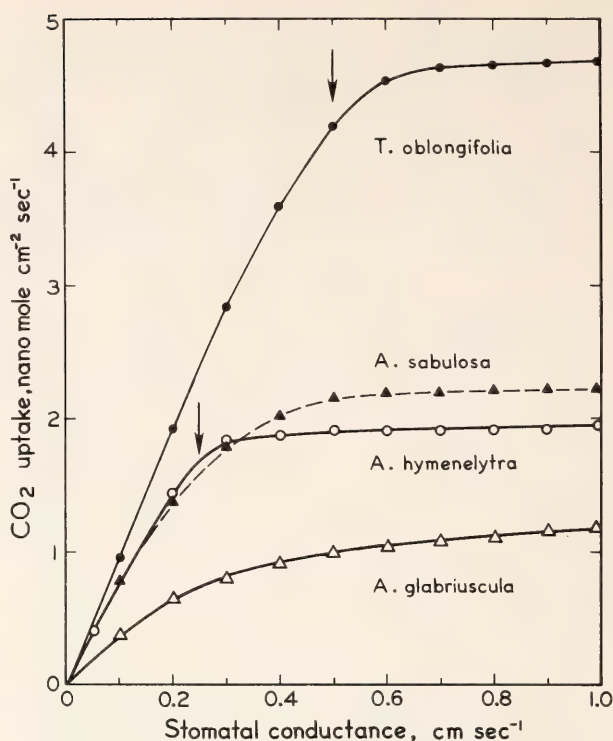


Fig. 2. Rate of net photosynthesis as a function of stomatal conductance to water-vapor diffusion in *T. oblongifolia*, *A. hymenelytra*, *A. sabulosa*, and *A. glabriuscula*. Light intensity was 160 nanoeinstein $\text{cm}^{-2}\text{sec}^{-1}$, the CO_2 partial pressure of the external air was 325 μbar , and leaf temperature was 40°C. The plants were grown at a 40°C day/30°C night regime. The relationship was determined from measurements of CO_2 uptake as a function of CO_2 concentration at known stomatal conductances. Arrows indicate the stomatal conductance values usually found in *T. oblongifolia* and *A. hymenelytra* under optimum conditions both in the field and in the laboratory.

water loss but a much smaller increase in photosynthesis. A decrease in conductance would, on the other hand, result in a decreased photosynthetic rate with little improvement in water use efficiency.

There is now little doubt that C_4 photosynthesis is an important mechanism underlying the capacity for a high photosynthetic water use efficiency. Photosynthetic gas exchange studies on a great number of C_3 and C_4 plants including the heat-adapted *T. oblongifolia* and the cool-adapted *A. sabulosa* show without exception that C_4 photosynthesis is markedly superior in utilizing low CO_2 concentrations in the leaf intercellular spaces. This is illustrated in Fig. 3 which

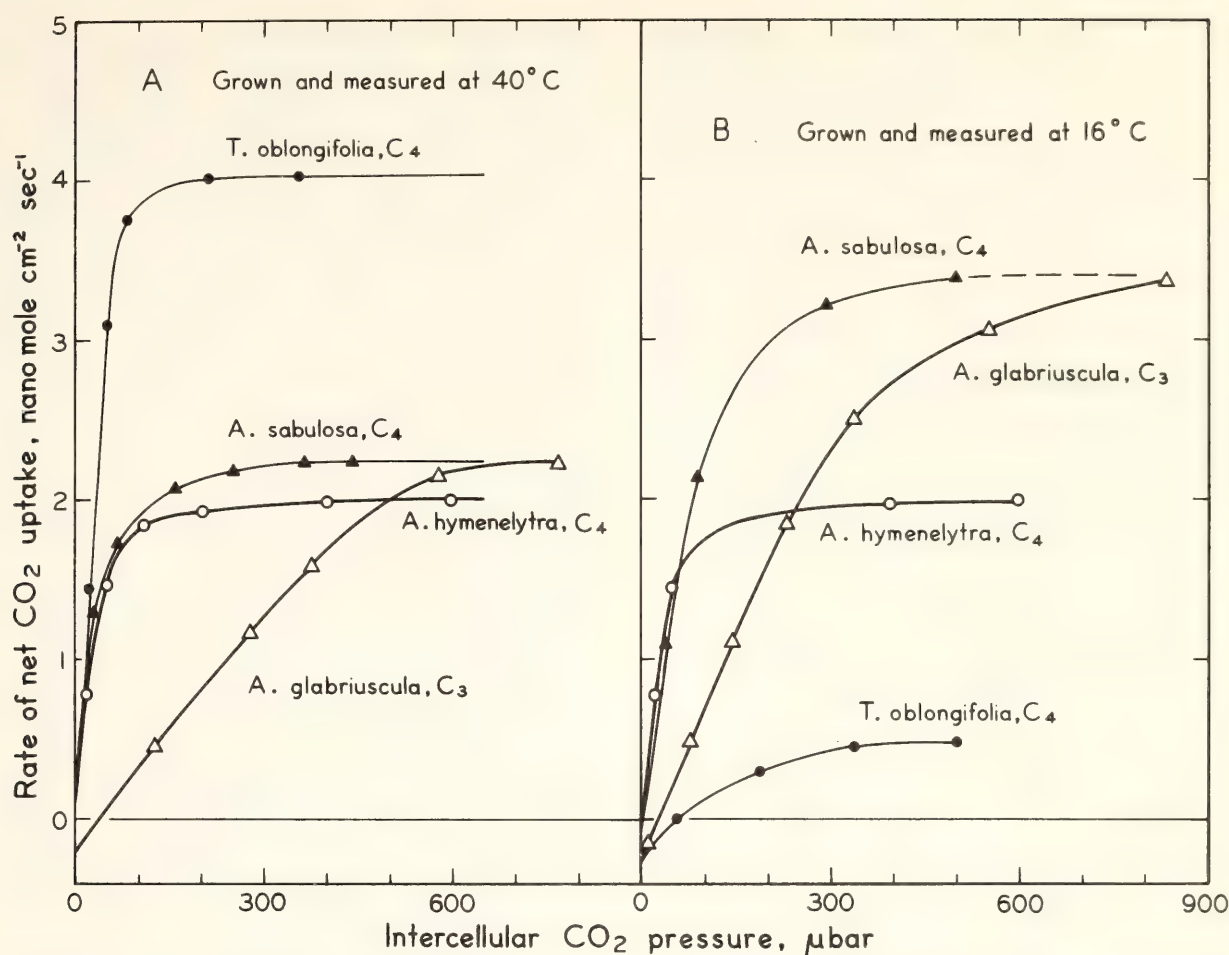


Fig. 3. Photosynthesis as a function of the CO₂ partial pressure in the intercellular spaces for different C₃ and C₄ species. Measurements were made at a high light intensity of 160 nanoeinstein cm⁻²sec⁻¹, an O₂ concentration of 21%, and two different leaf temperatures, 40°C and 16°C.

shows the rate of photosynthesis as a function of intercellular space CO₂ concentration in the four species grown and measured at 40°C and at 16°C. At the high temperature the C₄ species are greatly superior to the C₃ plant. With the exception of *T. oblongifolia*, which does not tolerate extended periods at low temperatures, this difference between C₃ and C₄ plants is also present at 16°C although it is not as pronounced as at the higher temperature.

One would thus predict that the C₄ pathway would confer an adaptive advantage under any condition where photosynthesis in the absence of this pathway would be markedly limited by the intercellular space CO₂ concentration. Where this concentration exerts no effect or only a small effect, as is the case at low light intensities or low tempera-

tures, the advantage would of course be at best marginal, but there is no reason to assume that C₄ photosynthesis *per se* would be disadvantageous in any terrestrial environment. All of our experimental results to date are in full agreement with these predictions. Conversely, one would also predict that the advantages of the C₄ pathway would be maximal under conditions where photosynthesis is limited largely by the intercellular CO₂ concentration. Such conditions are present when photosynthesis is operating at high light intensities and temperatures and in particular when stomatal conductance to the exchange of CO₂ and water vapor is low. Thus, for a given high light intensity and leaf temperature and a given rate of water loss, a C₄ plant should have a higher photosynthetic rate and, consequently, a

higher water use efficiency. However, this can only be realized if other essential adaptations are also present. For example, the high thermal stability of the photosynthetic apparatus of *T. oblongifolia* permits a full expression of the adaptive advantage of C_4 photosynthesis at very high temperatures. In *Atriplex sabulosa*, which lacks this thermal stability, the photosynthetic rate at high temperatures is limited by factors other than intercellular CO_2 concentration, and the potential advantage of C_4 photosynthesis cannot be fully realized.

THERMAL STABILITY OF THE PHOTOSYNTHETIC APPARATUS IN INTACT LEAVES

Olle Björkman

In the preceding pages we reported on the dramatic differences that exist in the temperature dependence of photosynthesis among plants from habitats with contrasting thermal regimes. It seems evident that the truly remarkable performance at high temperatures and normal air of *Tidestromia oblongifolia* is dependent on the presence of the C_4 pathway of photosynthesis but that other independent adaptations, such as an unusually high thermal stability of the photosynthetic apparatus, must also be present. This year several studies have been initiated in an effort to uncover the biochemical and biophysical mechanisms that underlie the differences among our study species in their genetically determined abilities to photosynthesize and grow at extreme temperatures, as well as the changes induced by the temperature under which a given genotype is grown. Brief accounts of some of the early results are given here and in the following reports.

Measurements of CO_2 and water vapor exchange rates clearly show that in none of the four species analyzed is the decline in photosynthetic rate at high temperatures due to a decreased con-

ductance of the stomata to CO_2 diffusion. On the contrary, conductances reached their maximum values at the highest measurement temperatures.

Temperature dependence curves of photosynthesis determined at rate-saturating CO_2 concentrations in the leaf intercellular spaces rather than in normal air show that high CO_2 does not prevent high-temperature inhibition in any of the four species. Although, as expected, high CO_2 greatly increases the absolute photosynthetic rate at high but noninhibiting temperatures in the C_3 species, *Atriplex glabriuscula*, and little or not at all in the three C_4 species, there is scarcely any effect of CO_2 concentration on the leaf temperature at which a rapid high-temperature-induced decline of photosynthesis sets in. For plants grown at 40°C day/30°C night regime these critical temperatures are: *A. glabriuscula*, 36°–37°C; *A. sabulosa*, 37°–38°C; *A. hymenelytra*, 41°–42°C; and *T. oblongifolia*, 46°–47°C. For plants grown under 16°C day/10°C night regime these temperatures are 2° to 3°C lower.

These results show that the high-temperature-induced decline in photosynthesis is unrelated to changes in the *diffusive* transport of CO_2 fixation sites inside the parenchyma cells. Further experiments show that a reduction of the oxygen concentration from the usual 21% to 2% at normal atmospheric CO_2 concentration did not significantly change the temperature at which thermal inhibition occurred in the C_3 or in the C_4 species. This indicates that factors associated with the O_2 inhibition of CO_2 fixation, catalyzed by RuDP carboxylase, and the O_2 -stimulated photorespiratory CO_2 release via the glycolate pathway are not responsible for high-temperature inhibition of photosynthesis. (It should be noted, however, that in *A. glabriuscula* and other C_3 plants, these factors are almost certainly partly responsible for the relatively low net photosynthetic rates in normal air at

moderate temperate temperatures and at high but noninhibitory temperatures.)

All the results presented above suggest that the intraspecific differences in the ability to maintain a high photosynthetic rate at high temperatures largely reside in the thermal stability of one or several constituents of the photosynthetic apparatus at the subcellular levels. This, of course, may involve a number of factors ranging from the thermal stability of enzymes associated with carbon fixation and reduction to electron carriers and other membrane-bound components including the photochemical reaction centers. Comparative studies of the temperature stability of various component reactions have therefore been initiated.

The possibility also exists that high-temperature-induced inhibition of photosynthesis results from a general breakdown of cellular components such as, for example, loss of the semipermeability of the cell membrane. Comparative studies of high temperature effects on the high-temperature-adapted C_4 species, *T. ob-*

longifolia, and the cool-temperate C_4 species, *A. sabulosa*, show that these plants indeed differ in several features of high temperature inhibition: damage to and death of leaves, leakage of solutes from the leaves, inhibition of respiration, and inhibition of photosynthesis. All occur at considerably lower temperatures (7° – 10°C) in *A. sabulosa* than in *T. oblongifolia*. However, photosynthesis is especially sensitive because in both species this process is completely inhibited before other symptoms of high-temperature injury can be detected. For example, as shown in Fig. 4, inhibition of either respiratory CO_2 evolution or O_2 uptake in intact leaves of *A. sabulosa* cannot be detected at temperatures lower than 46°C , but inhibition of photosynthesis occurs at 37°C . In *T. oblongifolia* the corresponding temperatures are 55° and 47°C . Thus, it appears highly unlikely that high temperature inhibition of photosynthesis is a result of a general breakdown of the integrity of the cell.

The photosynthetic characteristics discussed above were determined at high

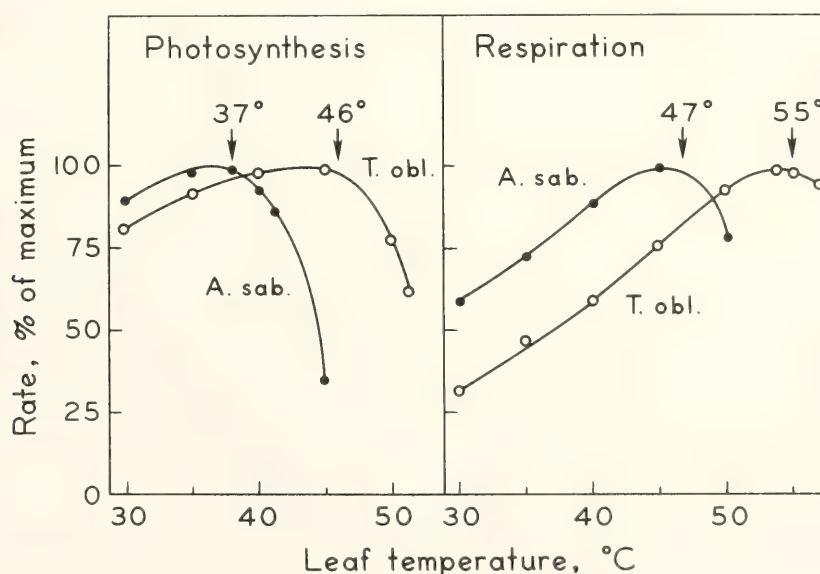


Fig. 4. High temperature response of photosynthesis and respiration in the two C_4 species *Atriplex sabulosa* and *Tidestromia oblongifolia*. Photosynthetic CO_2 uptake was measured at a high light intensity of $160 \text{ nanoeinstein cm}^{-2}\text{sec}^{-1}$ and saturating CO_2 concentration. Respiratory O_2 uptake was measured in the dark in air of normal O_2 and CO_2 concentration. Measurements proceeded from low to high temperature. The leaves were kept at each temperature for 15 minutes, and the plotted rates are those recorded at the end of each 15-minute period.

light intensities. In an attempt to delimit the component steps of photosynthesis that are responsible for the high-temperature-induced decline in photosynthesis, comparative measurements of the quantum yield of photosynthesis at rate-limiting light intensities were also made. On theoretical grounds one would expect that the quantum yield would remain independent of temperature as long as the chloroplast membranes remain intact. An inhibition of enzyme reactions of CO_2 fixation and reduction should not influence the quantum yield as long as photosynthesis remains light-limited.

Figure 5 shows the quantum yield (slope of the curve for CO_2 uptake as a function of quanta absorbed by the leaf) for *A. sabulosa* and *T. oblongifolia*. The quantum yield is the same in these species and remains constant with temperature over a wide range. However, when the temperature exceeds 40°C , there is a sharp reduction in the quantum yield for *A. sabulosa*, whereas in *T. oblongifolia* a decline does not occur until the leaf temperature exceeds 47°C (At pres-

ent, we can offer no explanation for the observation that the slopes below the light compensation point are less affected by high temperature than they are above this point).

The results shown in Fig. 5 strongly suggest that photochemical membrane-bound reactions in intact leaves of *T. oblongifolia* are able to tolerate higher temperatures without loss of activity than those of *A. sabulosa*. If the inhibition is caused by an inactivation of the reaction centers, this could explain the high temperature inhibition of the photosynthetic rate at intermediate and rate-saturating light intensities as well. Results show that the inhibition is remarkably independent of the light intensity at which the rate of photosynthesis is measured. In this respect the high temperature inhibition closely resembles photoinhibition caused by excessively high light intensities. It should be pointed out, however, that the present data do not in any way exclude the possibility that photosynthetic enzymes and other nonphotochemical components are equally or even more severely inacti-

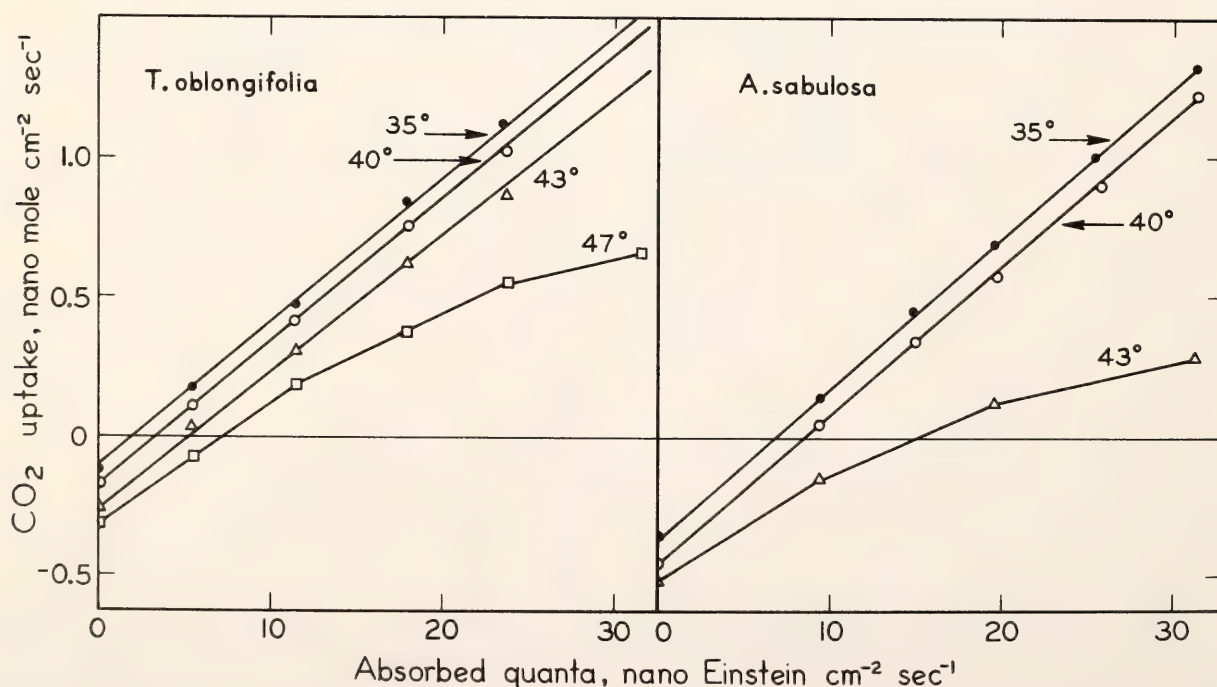


Fig. 5. Effect of high temperatures on the quantum yield for CO_2 fixation in *Tidestromia oblongifolia* and *Atriplex sabulosa*. Rates were measured in 21% O_2 and approximately 325 μbar CO_2 partial pressure. Plants were grown under a 40°C day/ 30°C night regime.

vated by high temperature than photochemical components and hence are responsible for the high-temperature-induced inhibition of photosynthesis in its light-saturated state. Further extensive studies utilizing a wide range of methods and approaches are needed to elucidate this problem.

As was mentioned in the preceding article, the remarkable performance of *T. oblongifolia* at high temperatures with record rates of both photosynthesis and growth under conditions that are lethal to most other plants is contrasted with its extremely poor performance at low temperatures. Growth of *T. oblongifolia* at 22°C, which is near the optimum for many other plants, is very slow, and at a few degrees below this temperature there is no measurable net growth. As shown in Fig. 6, the photosynthetic performance of *T. oblongifolia* plants, maintained at a 16°C day/10°C night regime for several weeks, is extremely poor. Detailed analyses of the gas exchange characteristics of these plants show that their poor photosynthetic performance is not attributable to a low stomatal conductance or other internal barriers to the diffusion of CO₂ into the cell. Dark respiration also is normal. Leaf anatomical examinations by Dr. Nobs did not reveal any aberrations in the anatomy of these plants. Total leaf chlorophyll and protein contents are also the same as in plants grown under a 40°C day/16°C night regime, and analyses by Dr. Berry indicate that the activities of the carboxylation enzymes, PEP and RuDP carboxylase, as well as the content of soluble protein are normal. Thus, we have so far been unable to pinpoint the causes underlying the exceedingly poor performance of *T. oblongifolia* at low temperatures. It is nevertheless noteworthy that the quantum yield is strongly inhibited in these plants (Fig. 6), suggesting that the photochemical activity of the chloroplast membranes may be impaired. This result points to the possibility that the

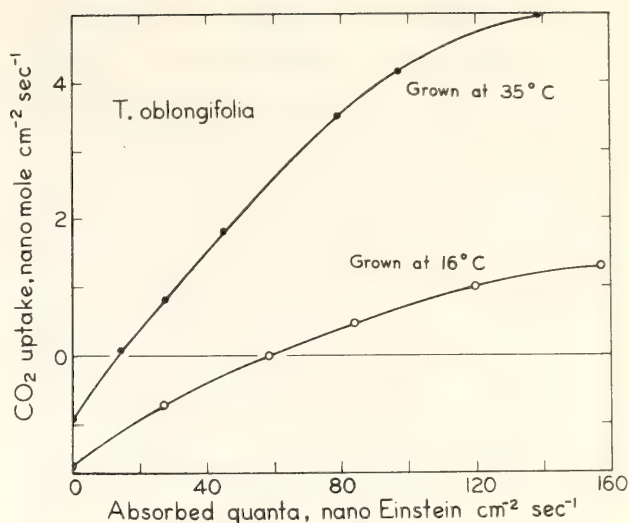


Fig. 6. Effect of growth temperature regime on the light dependence of photosynthesis in *Tidestromia oblongifolia*. Measurements were conducted at 35°C, 21% O₂, and approximately 325 μ bar CO₂.

composition or organization necessary for maintaining the structural integrity and functional efficiency of these membranes in *T. oblongifolia* at very high temperatures precludes their effective function at low temperatures.

MECHANISTIC STUDIES OF THERMAL DAMAGE TO LEAVES

J. A. Berry, D. C. Fork, and S. Garrison

Introduction

It is clear from studies of the photosynthetic characteristics of plants native to cool and hot habitats that adaptations have occurred which enable plants to function more efficiently under the environmental limitations typically imposed by their native environments. The functional specializations which are involved in photosynthetic adaptation to different thermal regimes are obviously complex and relate to the interacting effects of temperature on individual component steps of the photosynthetic process. Thus, descriptive studies do not by themselves provide a basis for a mechanistic understanding of the functional specializations which these adaptations involve. The experiments reported here

are intended to expose, characterize, and make understandable more specific physical and functional differences among plants, which can be related on the one hand to the effects of temperature on simple systems and on the other hand to the integrated functioning of the entire photosynthetic process.

Much of this work has focused upon differences between *Atriplex sabulosa* and *Tidestromia oblongifolia*. Both are C₄ species and are native to cool marine and hot desert habitats, respectively. The photosynthetic characteristics of these plants have been extensively studied (see Björkman, Mooney, and Ehleringer, this Year Book). The results form a starting point for additional studies, and are summarized here.

Atriplex sabulosa has high rates of photosynthesis at temperatures below 20°C, while *Tidestromia* has very poor rates under these conditions and is in fact injured by exposure to these cool temperatures. At the other extreme, *Tidestromia* has extremely high rates of photosynthesis, much higher than those of *A. sabulosa*, at high temperatures. Excessively high temperatures cause photosynthetic rates of both species to decline. This occurs at temperatures above 36°–40°C with *A. sabulosa* but not until 46°–49°C with *Tidestromia*. This effect of high temperature cannot be reversed by high humidity or high CO₂ concentrations. Further study has shown that the efficiency with which the plant can utilize light energy to fix CO₂ is unaffected by temperatures within the normal physiological range. However, this efficiency declines sharply at temperatures which cause total photosynthetic capacity to fall (42°C for *A. sabulosa* and 46°C for *Tidestromia*). This indicates that the inhibiting effect of high temperature on these plants is at least in part due to an effect on the basic efficiency of light energy conversion; and differences in the mechanisms which convert light to chemical energy within the chloroplasts may account for the dif-

ference between these plants in their resistance to high temperature.

Photochemical Activities of Isolated Chloroplasts

Numerous studies of isolated spinach chloroplasts indicate that the coupling of electron transport to photophosphorylation and the capacity of electron transport by photosystem II are more susceptible to damage by high temperature than other activities which can be assayed. However, chloroplasts once isolated from the leaf might respond differently to heating than in the intact leaf, and since species-to-species differences might be expected, we have chosen to reexamine the effect of heat treatment on the activity of chloroplasts by heat treating the intact leaves of *A. sabulosa* and *Tidestromia* and subsequently assaying the activity of chloroplasts isolated from them.

Leaves were detached and submerged for four minutes in water heated to the treatment temperature. The leaves were then transferred to ice water. Chloroplasts were isolated from these leaves, and photosystem I electron transport (ascorbate to methyl viologen), coupled and uncoupled photosystem II electron transport (water to ferricyanide or dichlorophenolindophenol), and fluorescence induction kinetics were assayed.

The activity of photosystem I electron transport in chloroplasts isolated from leaves of *A. sabulosa* which had been heated at 44°C was unaffected, while that for photosystem II electron transport retained only 25% of the activity of unheated control leaves. Addition of the uncoupler, methylamine, stimulated electron transport by chloroplasts from unheated leaves but inhibited electron transport by chloroplasts which had been severely heat damaged. Quite similar results were obtained with *Tidestromia* leaves heated to 52°C. These results are similar to those obtained by Yamashita and Butler (1969) and Mukohata *et al.* (1974) with isolated spinach chloro-

plants. The effect of heat damage is similar in both *A. sabulosa* and *Tidestromia*; however, the temperature sensitivity differs.

It is of interest to compare the heat sensitivity of the chloroplast activities to that of the photosynthetic activities of the intact leaf. Treatment of leaves of *A. sabulosa* to 38°C did not alter the properties of the chloroplasts isolated from them, while treatment at 41°C resulted in a 50% decline in photosystem II activity. Chloroplasts from *Tidestromia* leaves heated at 43°C were similar to those of control leaves, while those from leaves treated at 49°C were heat damaged. By comparison the quantum yield for CO₂ fixation by intact leaves declines above 46°C for *Tidestromia* and 42°C for *A. sabulosa*. These temperatures are at least very close to those which cause detectable damage to isolated chloroplasts, and it seems reasonable to postulate that the decline in photosynthetic performance at high temperature is due to damage to chloroplast components which are required for photosystem II.

Studies with isolated chloroplasts are laborious and even in the absence of heat treatment are subject to rather large variations from one chloroplast preparation to the next. These variations make it difficult to specify accurately the temperatures at which chloroplasts begin to be damaged by heat treatment. For the same reasons this technique is not well suited for routine assays to assess damage to plants by high temperature. The fluorescence of the chlorophyll *a* of photosynthetic membranes is known to be quite sensitive to the state of the reaction centers of photosystem II, and fluorescence can be measured rapidly and accurately on intact tissue or isolated chloroplasts. If a correlation between changes in the fluorescence properties and damage to photosystem II could be established, this could lead to a rapid routine assay for heat damage which could be conducted with intact tissue.

Studies of Fluorescence Induction

The time course of the induction of fluorescence from dark-adapted leaves or chloroplasts was monitored on an oscillographic recorder. These studies were conducted in the presence of 10⁻⁵ M 3(3',4'dichlorophenyl)-1, dimethyl-urea (DCMU) which appears to block electron transport at a point just beyond photosystem II and eliminates fluorescence changes due to steady-state electron transport. Immediately upon illuminating, fluorescence rises to an initial level (F_0), and then climbs over several tenths of a second (depending upon the light intensity) to a final value (F_{max}) (Fig. 7).

With heat treatment the value of the ratio of (F_0/F_{max}) increases from 40%–50% for undamaged tissue or chloroplasts to 70%–90% for severely damaged chloroplasts. The data obtained

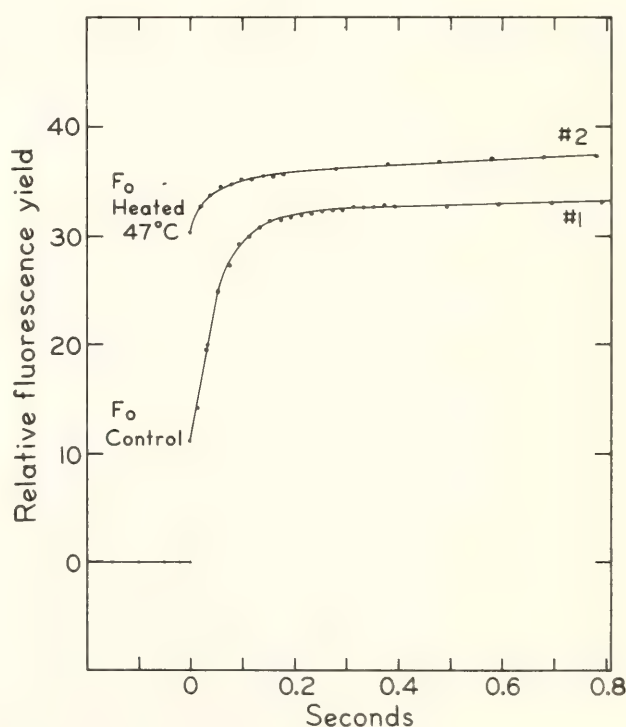


Fig. 7. Time course for the induction of fluorescence at 685 nm from chloroplasts of *Atriplex sabulosa* isolated from a control leaf and from a leaf heated to 47°C. The assays contained approximately 1 μ g chlorophyll/ml, 10⁻⁵ M DCMU, 0.025 M KH₂PO₄, 0.025 M K₂HPO₄, 0.01 M KCl, 0.3 M sucrose, and were conducted at 25°C with blue actinic light of 0.37 nanoeinstein cm⁻²sec⁻¹.

with isolated chloroplasts indicate that the loss of system II activity is directly correlated with changes in the ratio of (F_0/F_{\max}). A linear regression of the two variables predicts a 2.06% loss in photosystem II activity for an increase of 1% in the ratio (F_0/F_{\max}). The correlation coefficient for the relationship is high (0.91). However, there is some scatter in the data because each point is based upon a separate chloroplast isolation. The correlation is being reexamined to test its validity as a technique for assay of heat damage.

Since fluorescence changes can be measured quickly on intact leaves, this technique lends itself to direct examination of heat treatment on large numbers of leaves. Figure 8 shows data from two experiments in which the ratio of (F_0/F_{\max}) was studied as a function of the temperature of heat pretreatment of single leaves. It is clear that the ratio (F_0/F_{\max}) increases sharply above ap-

proximately 41°C in *A. sabulosa* and above 46°C in *Tidestromia*. It is also clear that there is considerable leaf-to-leaf variation even among untreated leaves. It is not yet possible to separate this random variation from systematic variation in the actual temperature that any one leaf may tolerate without damage. These studies show that the ratio of (F_0/F_{\max}) begins to increase with heat treatment at temperatures that are quite similar to the temperatures at which quantum yield for CO₂ uptake of the intact leaf is inhibited (Björkman *et al.*, this Year Book) and at which photosystem II activity of isolated chloroplasts also begins to change as a function of heat treatment.

No change in the relative fluorescence yield at F_{\max} was detected with heat-treated chloroplasts. Thus, the change in (F_0/F_{\max}) ratio is probably due to a change which occurs with heat treatment in the processes which quench vari-

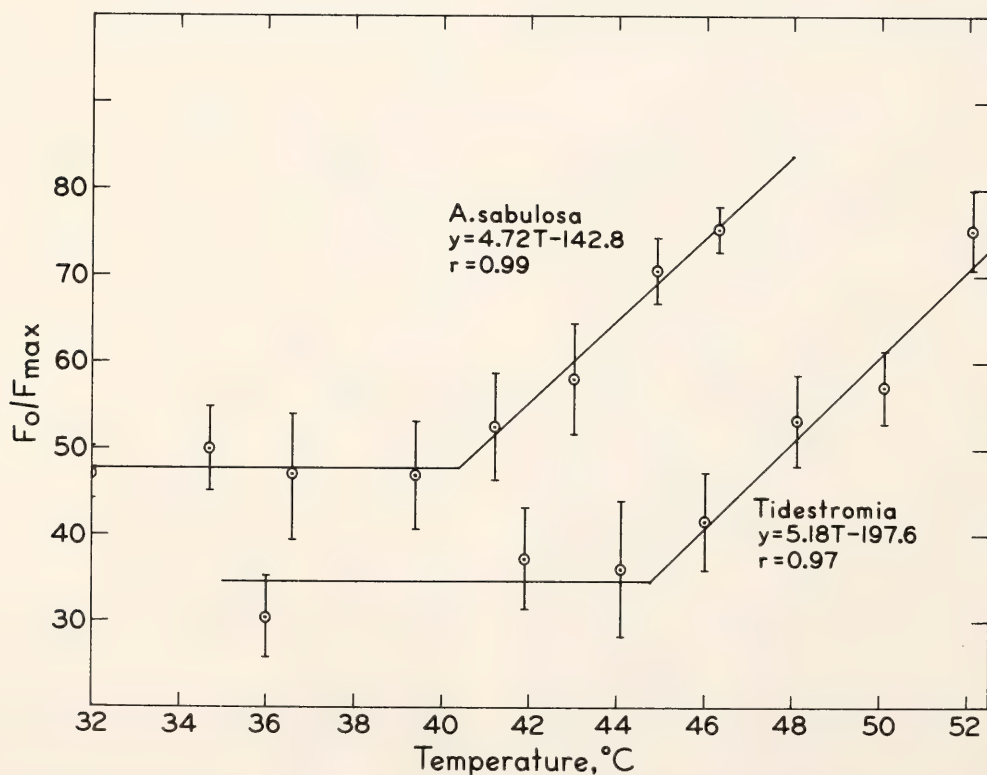


Fig. 8. Change in the ratio (F_0/F_{\max}) of single leaves of *A. sabulosa* or *Tidestromia oblongifolia* with heat treatment for 4 minutes. The mean and standard deviation of the fluorescence ratio of nine leaves is plotted for each treatment. The horizontal lines are the means of the treatments which did not differ from the control, and the sloping lines are linear regression lines fitted to the data. Leaves were vacuum infiltrated with DCMU before heat treatment, and fluorescence was measured at 22–25°C.

able fluorescence in the chloroplasts. It is generally believed that this quenching is due to the photochemical reaction center of photosystem II (Butler and Kitajima, 1975). The reaction center traps become open (oxidized) in dark-adapted tissue, and because DCMU prevents subsequent electron transport they become filled (reduced) by photochemical reactions during the induction phase. These photochemical reactions quench fluorescence. At the beginning of the illumination period the quenching capacity is high, and as the photochemical reaction centers become filled and the traps close, the capacity for photochemical quenching falls to a minimum.

The change in fluorescence kinetics with heat damage could be caused by damage to the photochemical reaction center or by a change which prevents oxidation of the trap in the dark. Yamashita and Butler (1968) showed that electron transport in heat-damaged chloroplasts is blocked by a lesion in the electron transport reactions which remove electrons from water and transfer them to the photochemical reaction center of photosystem II. This function is thought to reside in a mangano-protein which is bound to the inside surface of the thylakoid membrane. Heat treatment may give rise to denaturation of this protein, causing it to disassociate from the membrane, or it may cause a liquefying of the membrane lipids, permitting them or other components to move and disrupt necessary spatial relationships of electron carrier components. The similarity of heat damage to damage caused by lipid specific agents (Mukohata, 1974) suggests that the lipids of the thylakoid membrane are involved either via lipid-lipid interactions or lipid-protein interactions in the structure which is damaged.

The Dependence of Fluorescence on Temperature in Higher Plants and Algae

The previous studies indicate that physical changes of the thylakoid mem-

branes may be responsible for thermal damage to the photosynthetic apparatus. Among the most likely possibilities is that the temperature at which damage occurs corresponds to the temperature at which the membrane lipids change from the liquid-crystalline phase to a liquid phase.

Studies by Murata and Fork, this Year Book, indicate that the fluorescence of chlorophyll *a* may be used as a native probe for detecting phase transitions of the thylakoid membranes. It is clear that the physical state of the membrane affects its biological properties (see Murata and Fork, this Year Book) and that the temperatures at which these transitions occur can be manipulated by changing the fatty acid composition of the lipids. Most work to date has focused upon the temperature of the transition from the mixed solid-liquid-crystalline to the liquid-crystalline states. This transition temperature appears to be at the lower limit for normal physiological functioning of the membrane. It is possible, as mentioned previously, that the upper temperature limit of physiological activity is also related to a phase transition either of the lipids or of the lipid-protein associations which form the thylakoid membrane. In these studies we have extended the approach of Murata and Fork to higher temperatures near the upper limit for growth. Reproducible discontinuities in the graphs of temperature versus fluorescence yield of chlorophyll *a* of intact leaves and algae were detected. Because of the (unknown) physical basis of this phenomenon several other species of higher plants and algae were also examined.

Higher plant leaves were vacuum-infiltrated with a solution of 10^{-5} M DCMU in distilled water and a 7 mm disc of leaf material was cut with a cork borer. Algae were separated from their growth medium by centrifugation and resuspended in fresh medium containing 10^{-5} M DCMU. The leaf discs in infiltration medium or the algae suspensions

were contained in a single-sided cuvette constructed of a microscope cover-slip attached with epoxy adhesive to a machined brass block. A rectangular slot 7 mm wide by 2 mm deep was milled in the front face of the block to permit insertion of the leaf disc between the block and the cover slip. Channels were drilled through the block, and water from a constant temperature bath was circulated through the block to control the temperature. The temperature of the leaf or algal suspension was monitored by a fine gauge copper-constantan thermocouple which contacted the back of the leaf or was inserted into the algal suspension.

The cuvette was positioned vertically at an angle of 45° to both the excitation and emission light paths of a Perkin-Elmer MPD-3L Spectrofluorimeter. Fluorescence was excited by 480 nm light of 20 mm half bandwidth which fully illuminated the leaf disc. Intensity of the exciting light was attenuated to maintain $0.25 \text{ nanoeinstein cm}^{-2}\text{sec}^{-1}$. Rela-

tive fluorescence emission was monitored at 682 nm with a Corning 2030 cutoff filter to reduce stray actinic light reaching the phototube. The fluorescence yield of leaves or algae under continuous illumination was constant at constant temperature but declined as the temperature increased. Figure 9 illustrates this change of fluorescence with temperature with *A. sabulosa* and *Tidestromia*. Note the discontinuity in the fluorescence yield in the range of 35° to 47°C for *A. sabulosa* and 51° to 59°C for *Tidestromia*. This type of discontinuity was detected with several other species, including both higher plants and algae. Most showed a minimum followed by a maximum in fluorescence yield. The temperature of the midpoint of this transition for several species is given in Table 2.

The physical basis of this phenomenon is not clear. There are indeed differences among species, and they correspond in a qualitative way with what is known about the thermal stability of their pho-

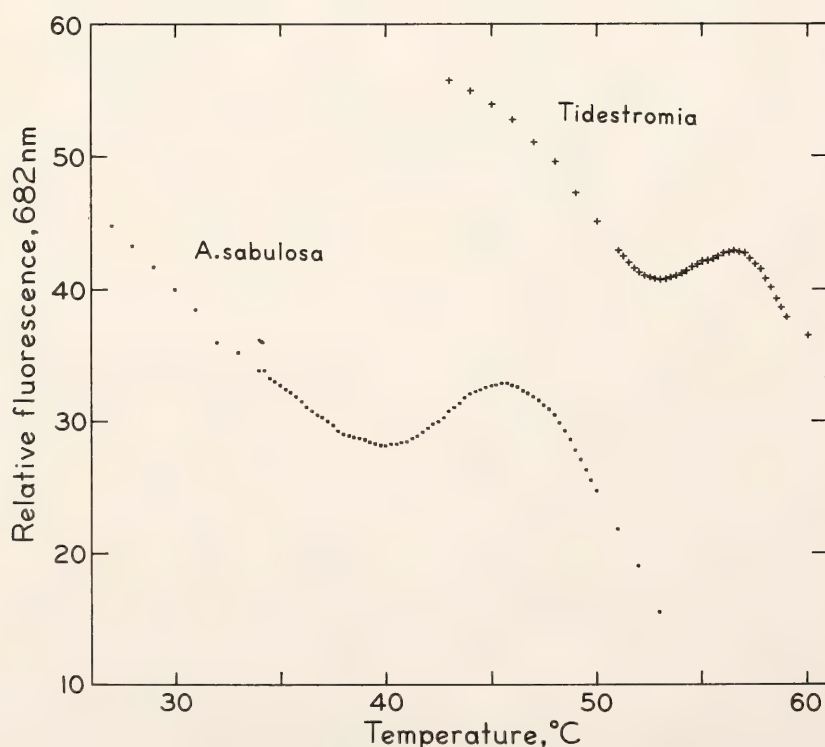


Fig. 9. Change in the apparent fluorescence yield of leaf discs under constant illumination as temperature is increased. Leaves were vacuum infiltrated with $10^{-5} M$ DCMU, and fluorescence at 682 nm was monitored in a Perkin-Elmer MPD-3L Spectrofluorimeter. Temperature was increased at a constant rate of $1^\circ\text{C}/\text{min}$.

TABLE 2. Midpoint Temperatures of Fluorescence Transitions of Chlorophyll *a* in Intact Leaves as a Function of Species and Growth Conditions

Species	Growth Conditions	Midpoint Temperature (°C)
<i>Atriplex glabriuscula</i>	phyto cell, 22°/18°C	not typical
<i>A. hortensis</i>	greenhouse	46
<i>A. sabulosa</i>	phyto cell, 22°/18°	42.1 ± 1.0
<i>Tidestromia oblongifolia</i>	phyto cell, 47°/31°	53.4 ± 1.2
<i>Tidestromia oblongifolia</i>	phyto cell, 22°/18°	49.8 ± 1.4
<i>Atriplex hymenelytra</i>	greenhouse	51.3
<i>Atriplex lentiformis</i>	greenhouse	47.6
<i>Anacystis nidulans</i>	culture, 26° or 36°	54.3 ± 2.3
<i>Cyanidium caldarium</i>	culture, 36°	49.8 ± 1.9

tosynthetic mechanisms. In *A. glabriuscula*, *A. hymenelytra*, *A. sabulosa*, and *Tidestromia*, damage was detected at temperatures below that of the midpoint of this transition. So far, we have not found a clear relationship between the specific temperature dependence of this phenomenon and the temperature for damage to photosynthesis in the intact leaf. For example, in the case of *A. sabulosa*, the midpoint of the fluorescence transition occurs at 42°C, while damage to photosynthesis occurs at 41°C. In *Tidestromia* the midpoint of the transition is at 53.4°C, and damage to photosynthesis was detected at 46°C.

It is tempting to postulate that this fluorescence transition is the result of a phase transition of the chlorophyll-containing membranes that alters the physical environment and hence the fluorescence of the chlorophyll molecules. Attempts to obtain similar fluorescence transitions in chlorophyll-containing liposomes are in progress, but to date these have not been successful. It is possible that the fluorescence transition results from other changes within the leaf, causing alterations of the optical properties of the leaf rather than changes in fluorescence yield. For example, a change in the amount of light scattered from the leaf cells or subcellular membranes could change the amount of fluorescence that is reabsorbed and thus change the apparent fluorescence yield. Until we can

assign a physical meaning to this phenomenon, the data on the midpoint temperatures for fluorescence transition cannot be reliably correlated to mechanisms of thermal acclimation.

Temperature Dependence of Cell Permeability

If damage to membranes is the cause of the inhibition of photosynthesis by high temperature, then damage to other membrane systems might also be expected. In fact there is no reason to expect *a priori* that the photosynthetic membranes would be any more labile at high temperature than other membranes, and further it is likely that damage to other membrane systems could have secondary effects upon photosynthesis that would be difficult to distinguish from a primary effect of temperature. Damage to the plasma membrane, for example, could allow the contents of the leaf cells to escape, dramatically changing the intracellular environment and leading to secondary effects upon other physiological processes, including photosynthesis. A technique originally applied to monitoring thermal damage to algal cell membrane by Kleinschmidt and McMahon (1970) was adapted to the study of leaves. The object of these studies was to determine the temperature at which the plasma membranes of leaf cells lose their semipermeability.

Leaves were vacuum-infiltrated with

distilled water, and washed with 0.2 *M* mannitol to remove extra-cellular ionic substances until the conductivity of the medium bathing the leaves approached that of the mannitol solution. Single leaves were then placed in test tubes with 20 ml of medium, placed in a thermostated water bath and the temperature was increased in 5°C increments. The ratio of the conductivity of the solution bathing the intact leaf to that bathing a similar leaf at the same temperature, but which had been heated in boiling water for 30 min to release the ions of the leaf cells, was determined with a YSI microconductivity probe. The use of this ratio provided a convenient means of compensating for the effect of temperature on conductivity and for differences among species in their salt content. Assuming that the initial conductivity of the bathing solution is very low in comparison to the conductivity when the leaf contents have escaped, and that the concentration is directly proportional to conductivity, the ratio of the conductivity of the bathing solution to that of the boiled leaf indicates the fraction of leaf contents

which have escaped to the bathing medium. Figure 10 is a plot of the data from such an experiment. Note that there are sharp inflections of the curves as the temperature is increased. Above a certain temperature ionic materials rapidly accumulate in the medium and the conductivity approaches that of the boiled leaf. The experiments were done under room light without aeration. No effect of aeration was observed in experiments which compared aerated and unaerated leaves. Since aeration caused complications to the temperature control, aeration was not used for routine studies. The temperature at which ion leakage was detected from several duplicate determinations on leaves from different species are presented in Table 3. It should be noted that leakage probably begins quite gradually, and more sensitive techniques or longer exposures could probably detect thermal damage at lower temperatures.

In all these cases the temperature at which thermal damage to the cell membranes is evident is higher than that at which thermal damage to photosynthesis is complete. *Atriplex sabulosa* is remark-

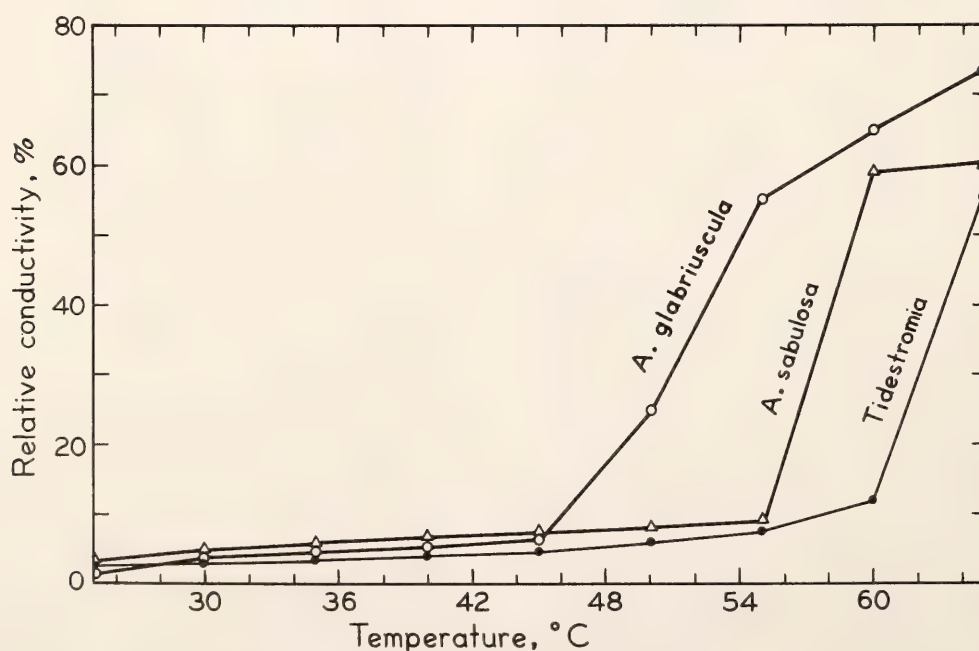


Fig. 10. Changes in the relative conductivity with increasing temperature of the solution bathing a single vacuum-infiltrated leaf (percentage of total ionic contents leaked from the leaf). Temperature was increased in 5°C increments. 30 min elapsed between each measurement.

TABLE 3. Temperature at Which Ion Leakage Is Detected by Measurement of the Conductivity of a Solution Bathing Vacuum-Infiltrated Leaves or Algae

Species	Growth Conditions	Inflection Temperature (°C)
<i>Atriplex glabriuscula</i>	phytoCELL, 22°/18°C	48.7 ± 1.3
<i>Atriplex sabulosa</i>	phytoCELL, 22°/18°	53 ± 1
<i>Tidestromia oblongifolia</i>	phytoCELL, 47°/31°	52.4 ± 2.4
<i>Tidestromia oblongifolia</i>	phytoCELL, 22°/18°	58.9
<i>Anacystis nidulans</i>	culture, 35°	48 ± 3
<i>Cyanidium caldarium</i>	culture, 35°	58

able in this respect. Photosynthetic activity declines rapidly above 42°C but the leaves do not begin to lose ions rapidly until 53°C. *A. glabriuscula* is the most sensitive of the higher plants in this respect. Ion leakage was indicated at approximately 48°C in these assays. Leakage sufficient to have a physiological effect may occur at temperatures below this. Leaves of this plant wilt at 44°C even in moist air and at comparatively low rates of transpiration. Although wilting is normally attributed to water stress, it could also be caused by loss of semipermeability of the cell membranes. This would dissipate the osmotic gradient necessary to maintain turgor.

Clearly there are differences among these species in the thermal stability of their cell membranes, and the substantial differences between leaves of *Tidestromia* grown at high temperature and at low temperature indicate a “hardening” of the plant by growing it in high temperatures. It is interesting that leaves of *Tidestromia* have resistance to high temperature similar to that of the thermophilic alga *Cyanidium caldarium*.

These studies indicate that an increased thermal stability of the plasma membrane is probably involved in adaptation to environments with high thermal loads. It is clear, however, that these membranes are more stable than the photosynthetic membranes. The reason for this difference is difficult to under-

stand unless there is a requirement placed upon photosynthetic membranes which could not be served by a membrane of higher thermal stability. Lenaz (1973) has suggested that there may be a requirement of a specific degree of fluidity of very active membranes such as those of the chloroplasts and mitochondria. Increasing the proportion of long-chain, saturated fatty acids to confer greater thermal stability could also decrease fluidity at low temperature. This may explain the fact that plants such as *Tidestromia* which are adapted to high temperatures are also subject to chilling injury at low temperatures. The interplay between these factors could explain the obvious trend toward specialization of plants to a particular thermal regime.

REFERENCES

Butler, W. L., and M. Kitajima, *Biochim. Biophys. Acta*, 376, 116, 1975.
Kleinschmidt, M. G., and V. A. McMahon, *Plant Physiol.*, 40, 290, 1970.
Lenaz, G., in *Membrane Structure and Mechanisms of Biological Energy Transduction*, J. Avery, ed., Plenum Press, New York, p. 456, 1973.
Mukohata, Y., in *Organization of Energy-Transducing Membranes*, M. Nakao and L. Parker, eds., University of Tokyo Press, p. 219, 1974.
Yamashita, T., and W. L. Butler, *Plant Physiol.*, 44, 435, 1969.

COMPARISON OF THE QUANTUM YIELDS FOR CO₂ UPTAKE IN C₃ AND C₄ PLANTS

O. Björkman and J. Ehleringer

It is now well established that the C₄ pathway of photosynthesis enables the plant to photosynthesize more efficiently under conditions where, in the absence of this pathway, the rate would be severely limited by the CO₂ concentration in the intercellular spaces. Thus, the advantages of C₄ photosynthesis are maximal under conditions of high light intensities, high temperatures, and limited water supply. There is, however, no evidence to support the converse supposition that the C₄ pathway would in itself be disadvantageous in other natural environments such as cool coastal habitats. Hatch (1970) discussed the possibility that the higher intrinsic energy requirement of C₄ photosynthesis (two additional ATP molecules per CO₂ fixed) in comparison with conventional C₃ photosynthesis might result in lower efficiency of light utilization at low light intensities by C₄ plants. A lower quantum efficiency for CO₂ fixation would of course be an important disadvantage in shaded habitats. It could also have a significant effect under moderate light intensities and could at least in part be responsible for the unusually high light intensities required for saturation of photosynthesis in many C₄ plants.

To elucidate this question precise measurements of the quantum yield of CO₂ uptake at rate-limiting light intensities were made on intact, attached leaves of a number of C₃ and C₄ plants, including our principal study species, *Tidestromia oblongifolia*, *Atriplex glabriuscula*, and *A. sabulosa*. *T. oblongifolia* belongs to a group of C₄ plants utilizing NADP malic enzyme for decarboxylation of C₄ acids in the bundle sheath cells (Year Book 69, p. 649), while *A. sabulosa* and the other C₄ *Atriplex* species analyzed appear to belong to a group utilizing NAD malic enzyme.

Photosynthetic rates on the basis of absorbed quanta were obtained from CO₂-uptake rates measured as a function of incident quantum flux in the spectral range 400–700 nm (Xenon arc) and from the light absorptance values of the same leaves, determined with an Ulbricht integrating sphere using a Xenon light source with the same spectral distribution used in the photosynthesis measurements. Since photosynthesis is inhibited by the atmospheric O₂ concentration in C₃ plants even at rate-limiting light intensities, quantum yields were determined in both 21% and 2% O₂. The CO₂ partial pressure was that of normal air (310–330 μ bar), and leaf temperature was 27°C.

The typical responses of photosynthesis of C₃ and C₄ plants to changes in the quantum flux absorbed by the leaves in the rate-limiting range are shown in Fig. 11. In the C₃ species *Atriplex glabriuscula* the quantum yield (slope of the curve) is 0.051 mole CO₂/absorbed einstein in normal air. A decrease in the O₂ concentration to 2% results in an increase in the quantum yield to 0.073 mole CO₂/absorbed einstein. In the C₄ species *Atriplex argentea* the quantum yield is 0.052 moles CO₂/absorbed einstein, and no enhancement is observed when the O₂ concentration is reduced. These results are very similar to those previously determined for *Atriplex patula* (C₃) and *A. rosea* (C₄) in monochromatic light (Year Book 68, p. 630).

Table 4 summarizes the results obtained with a number of C₃ and C₄ species. The quantum yields of the C₃ plants are consistently about one-third higher than in the C₄ plants under a low O₂ concentration. This higher energy requirement of the C₄ plants is consistent with the notion that C₄ photosynthesis requires two more ATP molecules per

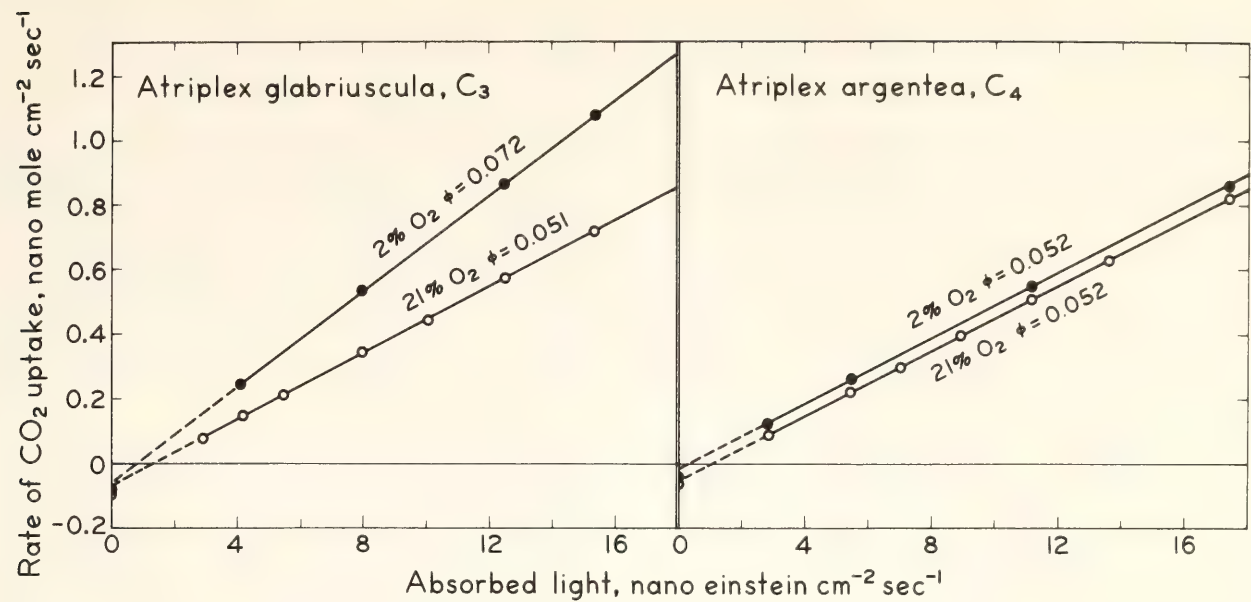


Fig. 11. Initial slopes for the rate of photosynthesis as a function of absorbed quantum flux in *Atriplex glabriuscula* (C₃) and *A. argentea* (C₄).

TABLE 4. Quantum Yields (mole CO₂/absorbed einstein) of Different C₃ and C₄ Species

C ₃ Species	Quantum Yield		C ₄ Species	Quantum Yield	
	2% O ₂	21% O ₂		2% O ₂	21% O ₂
<i>Atriplex glabriuscula</i>	0.072	0.051	<i>Atriplex argentea</i>	0.052	0.052
<i>Atriplex heterosperma</i>	0.073	0.053	<i>Atriplex rosea</i>	0.054	0.053
<i>Atriplex hortensis</i>	0.073	0.055	<i>Atriplex sabulosa</i>	0.054	0.054
<i>Atriplex triangularis</i>	0.073	0.051	<i>Atriplex serenana</i>	0.055	0.054
<i>Plantago lanceolata</i>	0.074	0.053	<i>Tidestromia oblongifolia</i>	0.054	0.054

CO₂ fixed than does C₃ photosynthesis; the extra ATP molecules are needed for the regeneration of the CO₂ acceptor phospho(enol)pyruvate from pyruvate. However, oxygen causes an inhibition of the quantum yield in the C₃ plants but not in the C₄ plants, and as a result their quantum yields *in normal air* are practically identical (C₃: 0.0526 ± 0.0017; C₄: 0.0534 ± 0.0009 mole/einstein). It certainly seems remarkable that the benefit of the abolishment of O₂ inhibition of photosynthesis conferred by the C₄ pathway is almost exactly offset by the higher intrinsic energy cost of this

pathway. One can speculate that it may be more than fortuitous that the quantum yields of C₃ and C₄ plants are so similar in normal air. There very likely exist strong selective pressures against the quantum yields of C₄ plants falling below those of C₃ plants, since photosynthesis in natural canopies is often light limited.

REFERENCES

Hatch, M. D., in *Prediction and Measurement of Photosynthetic Productivity*, Pudoc, Wageningen, p. 215, 1970.

CHROMOSOMAL NUMBERS IN *Atriplex*

Malcolm A. Nobs

Six years ago at the start of our physiological studies on the *Atriplex* the cytological data on this genus were extremely limited with only 11 chromosome numbers reported in the two major chromosome atlases (Tischler, 1950; Darlington and Wylie, 1956). Since that time the Canadian species have been well studied (Frankton and Bassett 1968, 1970; Basset and Crompton, 1973; Tischereau, 1972) and their taxonomy clarified. Likewise the species found in northern Europe are now well known (Gustafsson, 1973, 1974, 1975). It is appropriate now to present the cytological data that have accumulated from our studies during this period.

The purpose of these studies was two-

fold: first to fill partially the gap in our cytological knowledge of the California species, and second, to form a foundation for choosing the most promising material to use in hybridizations between C₃ and C₄ species for genetic studies on these two photosynthetic pathways.

All chromosome counts were determined from acetocarmine squashes of pollen mother cells fixed in Aceticalcohol from plants grown in the experimental garden or greenhouses of the Carnegie Institution at Stanford.

The phylogenetic groups of Hall and Clements (1923) have been followed in the presentation of the data (Table 5).

The Hortensis group contains three

TABLE 5. Chromosome Numbers in *Atriplex*

Group and Species	Number	Origin	Chromosome Number
Hortensis			
<i>A. hortensis</i> L.	8127	Palo Alto Yacht Harbor, Santa Clara, Calif.	n = 9 II
<i>A. heterosperma</i> Bunge	8128	Los Banos, Merced Co., Calif.	n = 18 II
<i>A. heterosperma</i> Bunge	8129	Tracy, San Joaquin Co., Calif.	n = 18 II*
<i>A. heterosperma</i> Bunge	8130	Walley's Hot Springs, Douglas Co., Nevada	n = 18 II*
Patula			
<i>A. patula</i> L.	8131	Yellow Springs, Ohio	n = 18 II*
<i>A. triangularis</i> Wildenoo	8132	Pescadero, San Mateo Co., Calif.	n = 9 II
<i>A. triangularis</i> Wildenoo	8133	Davis, Yolo Co., Calif.	n = 9 II
<i>A. patula</i> ssp?	8139	Canby, Modoc Co., Calif.	n = 18 II
<i>A. glabriuscula</i> Edm.	8134	Great Britain	n = 9 II
<i>A. gmelinii</i> C. A. Mey	8137	Ciba, Japan	n = 18 II*
<i>A. patula</i> ssp. <i>spicata</i> (Watson) Hall and Clements	8141	Davis, Yolo Co., Calif.	n = 9 II
Californica			
<i>A. californica</i> Moquin	8142	Indian Beach, Pt. Reyes, Marin Co., Calif.	n = 9 II
Endolepis			
<i>A. dioica</i> (Nutt) Macbride	8145	Medicine Bow, Carbon Co., Wyoming	n = 9 II
Phyllostegia			
<i>A. phyllostegia</i> (Torrey) Watson	8144	Panama, 10 m South of Bakersfield, Kern Co., Calif.	n = 9 II

TABLE 5 continued

Group and Species	Number	Origin	Chromosome Number
Rosea			
<i>A. rosea</i> L.	8146	Palo Alto Yacht Harbor, Santa Clara Co., Calif.	n = 9 II
<i>A. rosea</i> L.	8147	Los Banos, Merced Co., Calif.	n = 9 II
<i>A. rosea</i> L.	8148	Topaz Lake, Mono Co., Calif.	n = 9 II
<i>A. laciniata</i> L.	8149	Le Priex, France	n = 9 II
<i>A. laciniata</i> L.	8150	Gettersson, Sweden	n = 9 II
Truncata			
<i>A. truncata</i> (Torrey) Gray	8156	Mono Lake, Mono Co., Calif.	n = 9 II
<i>A. truncata</i> (Torrey) Gray	8158	Walley's Hot Springs, Douglas Co., Nevada	n = 9 II
<i>A. truncata</i> (Torrey) Gray	8159	Loyalton, Sierra Valley, Sierra Co., Calif.	n = 9 II
<i>A. truncata</i> (Torrey) Gray	8160	Alturas, Modoc Co., Calif.	n = 9 II
Argentea			
<i>A. argentea</i> ssp. <i>expansa</i> (Watson) Hall and Clements	8151	Los Banos, Merced Co., Calif.	n = 18 II
<i>A. argentea</i> ssp. <i>expansa</i> (Watson) Hall and Clements	8152	Davis, Yolo Co., Calif.	n = 18 II
<i>A. argentea</i> ssp. <i>expansa</i> (Watson) Hall and Clements	8153A	Visalia, Tulare Co., Calif.	n = 18 II
<i>A. argentea</i> ssp. <i>expansa</i> (Watson) Hall and Clements	8154	Palo Alto Yacht Harbor, Santa Clara Co., Calif.	n = 18 II
<i>A. coronata</i> Watson	8155	Wasco, Kern Co., Calif.	n = 18 II
<i>A. coronata</i> Watson	8162	Lost Hills, Kern Co., Calif.	n = 18 II
Pusilla			
<i>A. cordulata</i> Jepson	8163	12 m east of Firebaugh, Madera Co., Calif.	n = 18 II
Pentandra			
<i>A. elegans</i> ssp. <i>fasciculata</i> (Watson) Hall and Clements	8165	Johannesburg, Kern Co., Calif.	n = 9 II
<i>A. elegans</i> ssp. <i>fasciculata</i> (Watson) Hall and Clements	8166	Panimint Valley, Inyo Co., Calif.	n = 9 II
<i>A. pacifica</i> Nels.	8167	El Consuela, Baja California	n = 9 II
<i>A. serenana</i> A. Nels.	8170	Firebaugh, Fresno Co., Calif.	n = 9 II
<i>A. serenana</i> A. Nels.	8171	Stockton, San Joaquin Co., Calif.	n = 9 II
<i>A. serenana</i> A. Nels.	8153B	Visalia, Tulare Co., Calif.	n = 9 II
<i>A. fruticulosa</i> Jep.	8172	Altimont Pass, Alameda Co., Calif.	n = 9 II
Dioecious shrubs			
<i>A. parryi</i> Wats.	8179	Saratoga Springs, Death Valley, San Bernadino, Co., Calif.	n = 9 II
<i>A. lentiformis</i> ssp. <i>breweri</i> (Wats.) Hall and Clements	7972	Point Mugu, Ventura Co., Calif.	n = 9 II

* One to three multivalents are occasionally present.

European and Asian annual species. Two of these, *Atriplex hortensis* L., a diploid, and *Atriplex heterosperma* Bonge, a tetraploid, have become relatively widespread in northern North America. Frankton and Bassett (1968) have called attention to *Atriplex heterosperma*; it does not appear in any of our American floras because it has previously been confused with forms of *Atriplex patula* or *Atriplex hortensis*. In California it is frequent in saline soils both in the Great Valley and on the east side of the Sierra Nevada from Merced and Inyo Counties north. The third species, *Atriplex nitens* L., is a diploid (Wulff, 1936) and has not appeared in North America. All three species have non-Kranz leaf anatomy.

The Patula group (Hall and Clements, 1923) is highly polymorphic and is found on all continents except Antarctica. Chromosome numbers range from diploid to hexaploid (Tischereau, 1972; Bassett and Crompton, 1973). Our counts agree with those of the previous workers with the exception of *Atriplex gmelinii* from Japan, which is a tetraploid, in contrast to the Alaskan material of Bassett and Crompton, which is hexaploid. All species have non-Kranz leaf anatomy.

Atriplex californica, a small perennial herb, is the only member of this group. It is restricted to sandy beaches along the Pacific coast from Marin County, California, into Baja California. It is diploid with non-Kranz leaf anatomy.

The Rosea group contains three annual species which are all of European origin. These are *Atriplex rosea*, *Atriplex laciniata* (*Atriplex sabulosa* Rouy), and *Atriplex tatarica* L. All are diploids (cf. Bassett, 1969, for *Atriplex tatarica*), and have Kranz-type leaf anatomy. The most widespread is *Atriplex rosea*, which has become a common weed of roadsides and waste places in western United States. *Atriplex laciniata* and *Atriplex tatarica* are restricted; the former is con-

fined to the northeastern Atlantic seaboard while the latter occurs sporadically along the entire Atlantic coast.

The Endolepis group contains only two species, *Atriplex dioica* and *Atriplex monolifera* Wats. The former occurs from Alberta and Saskatchewan in Canada south into Nebraska, while the latter is known from only one specimen from Chihuahua, Mexico. The leaf anatomy of *Atriplex dioica* is non-Kranz. Our material from Wyoming is diploid, as is the material from Saskatchewan reported by Frankton and Bassett (1970).

Atriplex phyllostegia is the only species in its group. It is an annual diploid with non-Kranz leaf anatomy and is found primarily in the Great Basin but also in the southern San Joaquin Valley.

Of the five species in the Pusilla group, only one, *Atriplex cordulata* has been grown; it is a tetraploid with Kranz leaf anatomy. Anatomical studies of leaves of herbarium material of *Atriplex tulerensis* Coville and *Atriplex parishii* Wats. also show Kranz anatomy. The remaining species, *Atriplex pusilla* (Torr.) Wats. and *Atriplex tenuissima*, remain to be studied.

The Truncata group contains four annual species: *Atriplex truncata*, *Atriplex wolfii* Wats., *Atriplex graciflora* Jones, and *Atriplex saccaria* Wats. Only *Atriplex truncata* is present in California and occurs on the east side of the Sierra Nevada. It is a diploid with Kranz-type leaf anatomy, as is the Canadian material reported by Frankton and Bassett (1970).

Two annual species are present in the Argentea group. *Atriplex argentea* has two subspecies, *Atriplex argentea* Nutt. and *Atriplex argentea* ssp. *expansa* (Wats.) Hall and Clements. The former is common in waste saline areas in western North America. It is a diploid (Frankton and Bassett, 1970). The subspecies *expansa* is a tetraploid and is predominantly Californian. *Atriplex coronata* also is a tetraploid and is com-

monly found in the Great Valley of California. Both species have Kranz-type leaf anatomy.

Atriplex powellii Wats. is the only member of its group. It occurs from Alberta in Canada south into Colorado and Arizona. It is a diploid with Kranz-type leaf anatomy (Frankton and Bassett, 1970).

The Pentandra group contains nine species and is extremely polymorphic with both annuals and perennials. In all species the staminate and pistillate flowers are separated in the inflorescence, the former being terminal, while the latter are in the axil of the leaves. The four studied by us are all diploid, as is *Atriplex coulteri* (Moq.) Dietr. (Bassett, 1969), *Atriplex leucophylla* (Moq.) Dietr., *Atriplex wrightii* Wats., *Atriplex linifolia* Humb., and the highly polymorphic *Atriplex pentandra* (Jacq.) Stand. have not been grown at this time. Anatomical studies from herbarium leaf material all show Kranz-type leaf anatomy.

The Decumbens group includes only *Atriplex decumbens* Wats. and *Atriplex matamorensis* Nels. Because these species have not yet matured, no counts are available; however, both have Kranz-type leaf anatomy.

Only five of the twelve species in the Shrubby Dioecious group have been counted. Bassett (1969) reports $2n = 18$ for *Atriplex hymenelytra* (Torr.) Wats., *Atriplex barclayana* ssp. *palmerii* (S. Wats.) Hall and Clements, and *Atriplex lentiformis* (Torr.) Wats. ssp. *breweri* (Wats.) Hall and Clements. The latter agrees with our count (Table 5). *Atriplex parryi* is likewise a diploid. *Atriplex canescens* (Pursh) Nutt., the most widely spread species in this group which ranges from Canada into Mexico, is tetraploid through this wide range except for one local population in Juab County, Utah, that is diploid (Stutz *et al.*, 1975). All members of this group have Kranz-type leaf anatomy.

It is clearly evident that *Atriplex*,

similar to the majority of the Chenopodiaceae, has a base chromosome number of nine pairs. In the natural taxa no aneuploidy has been found. This is in striking contrast to the artificial hybrids between *Atriplex rosea* and *Atriplex triangularis* (*Atriplex patula* ssp. *hastata* Gray), where in the second and third generations an aneupolyploid series was found with chromosome numbers ranging from 22 to 52 (Björkman *et al.*, 1971). This suggests that in the evolution of *Atriplex*, amphiploidy has not been a dominant factor. Since the majority of the tetraploids do exhibit a high frequency of multivalents, it is suggested that at least partial autopolyploidy has been the major factor in the evolution of the polyploids.

REFERENCES

- Bassett, I. J., *Taxon*, 18, 310, 1969.
 Bassett, I. J., and C. W. Crompton, *Can. J. Bot.*, 51, 1715, 1973.
 Björkman, O., M. A. Nobs, and J. Berry, *Carnegie Inst. Wash. Year Book* 70, p. 501, 1971.
 Darlington, C. D., and A. P. Wylie, in *Chromosome Atlas of Flowering Plants*, MacMillan Publishers, New York, p. 76, 1956.
 Frankton, C., and I. J. Bassett, *Can. J. Bot.*, 46, 1309, 1968.
 Frankton, C., and I. J. Bassett, *Can. J. Bot.*, 48, 981, 1970.
 Gustafsson, M., *Bot. Not.*, 126, 345, 1973.
 Gustafsson, M., *Bot. Not.*, 127, 125, 1974.
 Gustafsson, M., *Opera Bot.*, Prepublication, 1975.
 Hall, H. M., and F. E. Clements, *Carnegie Inst. Wash. Publ. No.* 326, 1923.
 Stutz, H. C., J. M. Melby, and G. K. Livingston, *Am. J. Bot.*, 62, 236, 1975.
 Tischereau, P. M., *Can. J. Bot.*, 50, 1571, 1972.
 Tischler, G., *Die Chromosomenzahlen der Gefäßpflanzen Mitteleuropas*, Junk. 5 Gravenhage, 1950.
 Wulff, H. D., *Planta*, 26, 275, 1936.

CONTROL OF PHOTOSYNTHESIS BY TEMPERATURE

Norio Murata, David C. Fork,
and John Troughton

INTRODUCTION

Since photosynthetic reactions take place in the lipo-protein matrix of thylakoid membranes, the physical phase of the membrane lipids must play an important role in the proper functioning of these reactions.

Lipids show a change of phase with a change of temperature. When lipids are in lamellar or vesicular structures in water at low temperatures they are in the solid state and are in the (smectic) liquid-crystalline state at high temperatures. It has been established for model membranes that the temperature of the phase transition from the liquid-crystalline state to the solid state depends upon the lipid species as well as the fatty acid composition (Barratt *et al.*, 1969; Chapman *et al.*, 1974; Ladbroke and Chapman, 1969; Träuble, 1971). In general, the higher the degree of unsaturation of the fatty acid the lower the temperature for phase transition. A similar correlation between the phase transition temperature and the fatty acid composition has been found in biological membranes where drastic changes of physiological activities are observed at the phase transition temperatures. This has been observed as changes in rates of growth, transport, and respiration in the bacterium *Escherichia coli* (Overath *et al.*, 1970; Wilson *et al.*, 1970), as well as by changes in rates of phosphorylation and respiration in mitochondria (Kemp *et al.*, 1969; Lyons and Raison, 1970; Lyons *et al.*, 1964; Raison *et al.*, 1971).

In photosynthetic systems such as chloroplasts or thylakoid membranes, however, there has not been a good demonstration of a relationship between the transition of the physical phase of membrane lipids and photosynthetic activities. In chloroplasts of higher plants and most algae there is a high content

of unsaturated lipids (Benson, 1964). This suggests that the transition of the physical phase of lipids in these plants would occur far below room temperatures. In the blue-green alga *Anacystis nidulans*, however, there is a high degree of saturation of the major fatty acids (Hirayama, 1967), suggesting that the transition of phase of lipids may occur at room temperatures. Moreover, it has been found by Holton and co-workers (1964) that the fatty acid content of *Anacystis* changes with growth temperature. Since the fatty acid composition of this alga can be varied by growing it at different temperatures, it seemed to be a good organism to use to measure phase transition of lipids as a function of growth temperature to see if a correlation could be found between the temperature for phase transition and the photosynthetic reactions in these algae.

THE EFFECT OF GROWTH TEMPERATURE
ON THE TRANSITION OF THE PHYSICAL
PHASE OF MEMBRANE LIPIDS AS DE-
TECTED BY ELECTRON SPIN RESONANCE
SPECTROMETRY AND CHLOROPHYLL *a*
FLUORESCENCE

Anacystis used in these experiments was grown at 19°, 28°, and 38°C in Kratz and Myers' C medium. In order to determine the temperature of phase transition by a spin-probe method, fragments of lamellar membranes were prepared by passing harvested cells twice through the French pressure cell. Centrifugation of the homogenate for 10 min at 2000 *g* removed whole cells and large fragments. Membrane fragments were recovered from the supernatant by centrifuging at 105,000 *g* for 45 min. After adding the spin-labeling reagent *N*-oxyl-4',4'-dimethyl-oxazolidine derivative of 5-ketostearic acid (5-SAL) to a highly concentrated suspension of membrane

fragments, it was possible to measure at various temperatures the ESR spectra of 5-SAL bound to membrane fragments thanks to the courtesy of Dr. Toru Kihara of the Ames Research Center, Moffett Field, California.

In Fig. 12 the shape of the ESR signal reveals how the mobility of the spin label in the membrane changes with temperature. The distance between the two vertical lines (hyperfine splitting or $2T'_{II}$) is an indicator of the mobility of the nitroxide group in the hydrophobic region of the membrane (Sackmann *et al.*, 1973). The wider the separation the more immobilized is the spin label. Figure 13 shows a plot of $2T'_{II}$ against the reciprocal of the absolute temperature. In *Anacystis* grown at 28°C there are two straight lines and a jump around 13°C. In the cells grown at 38°C, however, there is a jump near 24°C. In addition to the jump, the slopes of the lines change. The temperature at which the abrupt jump occurs probably indicates the temperature of phase transition. Below the break the membrane lipids are in the solid state and above the break in the liquid-crystalline state, as will be discussed in the next section. Only one transition point appeared in the curve for the ESR hyperfine splitting vs. temperature in each sample.

Chlorophyll a Fluorescence as an Indicator of Phase Transition of Lipids

Fluorescence measurements were all done in the presence of 10 μ M DCMU to inhibit electron transport. The temperature vs. fluorescence curves for *Anacystis* grown at 19°, 28°, and 38°C are given in Fig. 14. In cells grown at 38°C a maximum appeared at 16°C on decreasing and at 21°C on increasing the temperature. For the cells grown at 38°C a shoulder was occasionally seen upon decreasing the temperature, as can be seen in Fig. 14. No such shoulder was seen in curves obtained from cells grown at lower temperatures, however. In *Ana-*

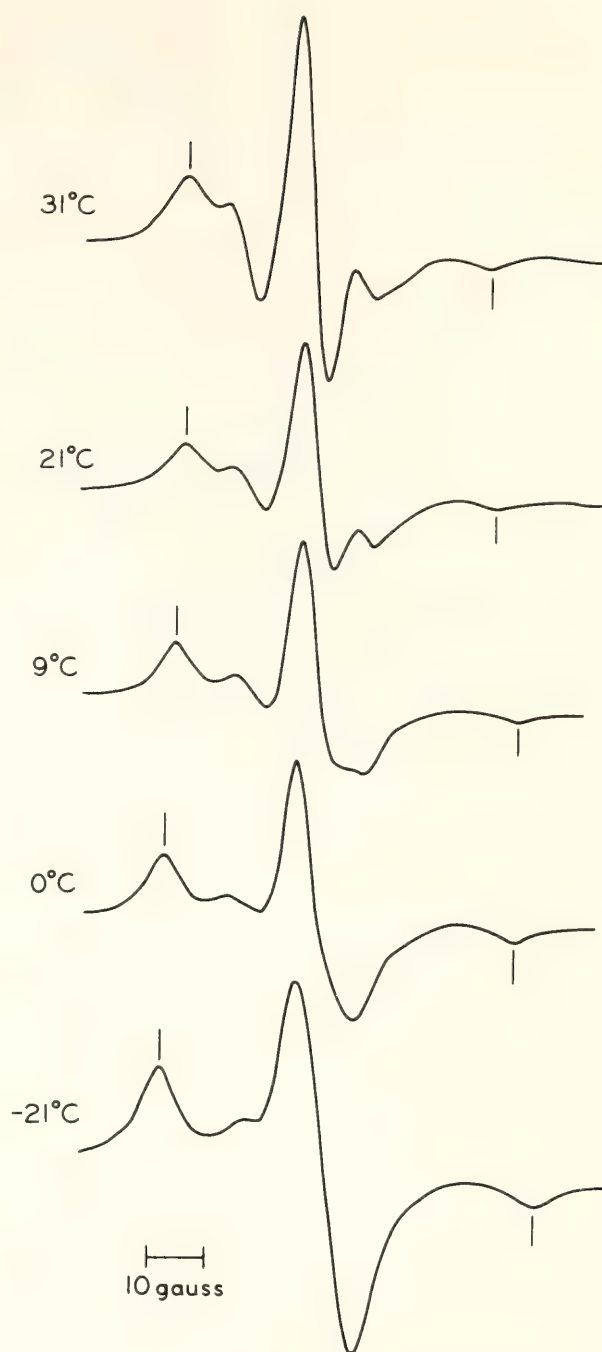


Fig. 12. ESR spectra of *N*-oxyl-4',4'-dimethyl-oxazolidine derivative of 5 ketostearic acid (5-SAL) at various temperatures in a suspension of membrane fragments of *Anacystis* grown at 28°C. Concentrations of chlorophyll *a* and 5-SAL were 650 and 20 μ g/ml, respectively, the molar ratio of chlorophyll *a* to 5-SAL being 10. The distance between the vertical lines in each spectrum indicates the maximum hyperfine splitting $2T'_{II}$.

cystis grown at 28°C the maximum appeared at 11°C on decreasing the temperature and at 14°C on increasing it. Cells grown at 19°C had maxima at 9°C on decreasing the temperature and at

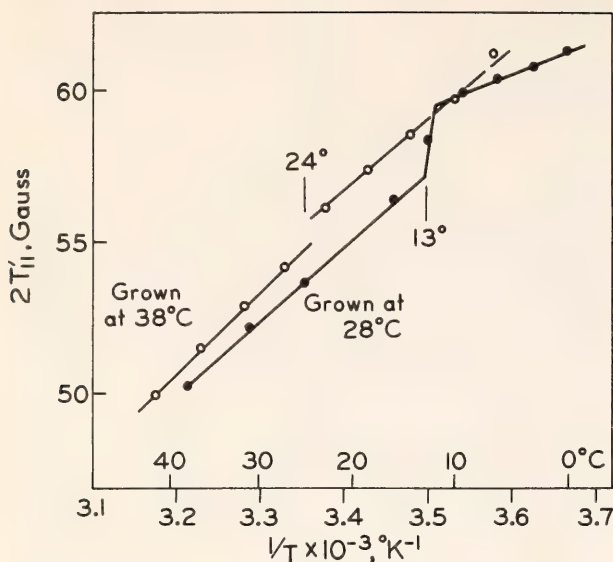


Fig. 13. The maximum hyperfine splitting of ESR spectrum, $2T'_{II}$, plotted against the reciprocal of absolute temperature. 5-SAL was added to the suspension of membrane fragments of *Anacystis* grown at 28° and 38°C. Concentration of 5-SAL was 20 $\mu\text{g/ml}$. Concentration of chlorophyll *a* was 650 and 445 $\mu\text{g/ml}$ in the samples grown at 28° and 38°C, respectively.

12°C on increasing it. No minima were seen in the fluorescence curves measured in the room temperature region. In an experiment with cells grown at 38°C the temperature was lowered to -5°C , and even then no minimum was seen.

It can be seen in Fig. 14 that the fluorescence maxima appeared at lower temperatures when the temperature was lowered and at higher temperatures when the temperature was increased. The extent of this hysteresis effect is shown for the culture grown at 28°C by the dotted line in Fig. 14. It can be noted that Overath and Träuble (1973) and Sackmann *et al.* (1973) observed a hysteresis effect for artificial fluorescent probes in model and in biological membranes.

Figure 15 shows for *Anacystis* cells grown at 38°C the temperature dependence of chlorophyll *a* fluorescence measured at 684 nm and of allophycocyanin fluorescence measured at 655 nm when phycocyanin excitation was provided at 560 nm. Chlorophyll *a* fluorescence appeared at about 10°C higher tempera-

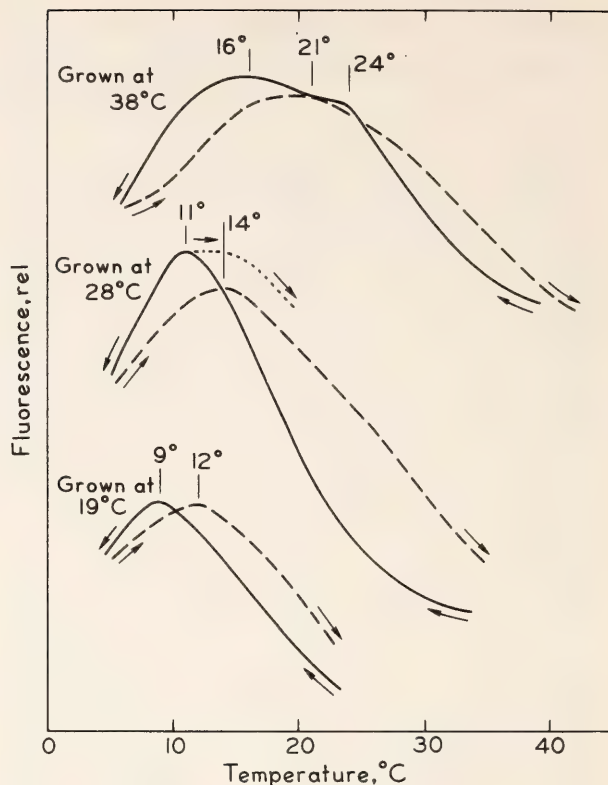


Fig. 14. Temperature dependence of chlorophyll *a* fluorescence in *Anacystis* grown at 38°, 28°, or 19°C upon excitation of chlorophyll *a*. Fluorescence was excited at 430 nm and measured at 684 nm. Solid and dashed lines indicate decreasing and increasing temperature, respectively. Rates of temperature decrease and increase were 0.5°C/min and 2°C/min, respectively. The dotted line shows the temperature dependence of chlorophyll *a* fluorescence when cells grown at 28°C were cooled until the fluorescence became maximum and then were heated.

tures when phycocyanin was excited than when chlorophyll *a* was excited (compare with Fig. 14).

Figure 15 (lower part) also shows the temperature dependence of the yield of allophycocyanin fluorescence in *Anacystis* grown at 38°C. No maxima were seen. Instead there was a steep rise in fluorescence when the temperature was decreased below 5°C.

The temperature dependence of fluorescence yield was also measured in the membrane fragments obtained by fragmenting *Anacystis* cells in the French pressure cell followed by differential centrifugation. The temperatures for maximum fluorescence appeared at 11° and 19°C in membrane fragments ob-

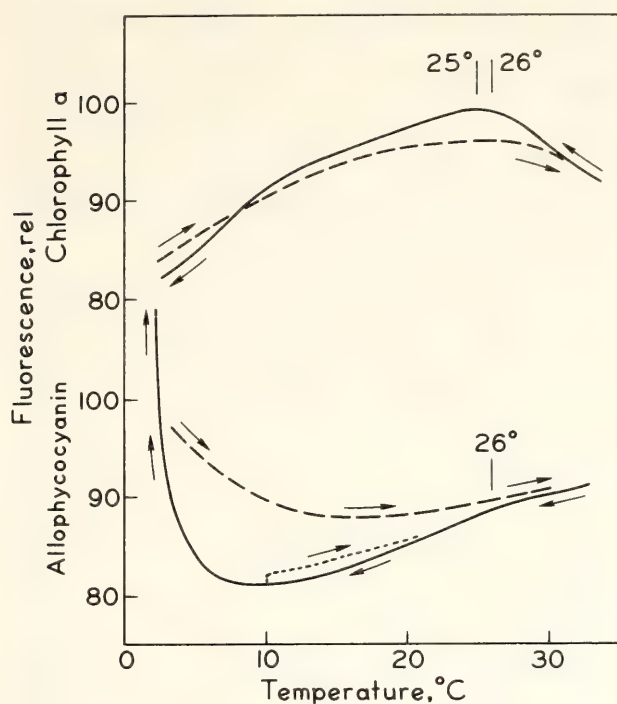


Fig. 15. Temperature dependence of sensitized fluorescence of chlorophyll *a* and allophycocyanin in *Anacystis* grown at 38°C upon excitation of phycocyanin. Phycocyanin was excited at 560 nm, and the fluorescence of chlorophyll *a* and allophycocyanin was measured at 684 nm and 655 nm, respectively. Rates of temperature change were 2°C/min.

tained from cells grown at 28° and 38°C, respectively.

In addition preparations were made by extracting chlorophyll *a* and most of the galactolipids from the thylakoid membranes in a small volume of 80% acetone and adding this extract to a large volume of buffer solution. We may assume by analogy to the phospholipid model membrane of Colbow (1973) that the galactolipids and chlorophyll *a* formed lamellar or vesicular structures. In the lipid/chlorophyll mixtures in buffer obtained from cells grown at 28° and 38°C the temperature maxima for fluorescence appeared at 10° and 18°C, respectively.

No characteristic changes in fluorescence yield with temperature change were observed with extracted chlorophyll *a* in 80% acetone or phycobilins in aqueous solution. Instead the fluorescence of both compounds decreased

monotonically with increase in temperature (Fig. 16).

It can be concluded from all of these results that the fluorescence maxima are produced by the interaction of chlorophyll *a* and membrane lipids and are not due to the nature of chlorophyll *a* or to the phycobilins by themselves.

The temperature dependence of chlorophyll *a* fluorescence was investigated in isolated chloroplasts obtained from a number of higher plants such as spinach (chilling resistant), lettuce (chilling resistant) grown at 15° and 25°C, tomato (chilling sensitive) grown at 15° and 25°C, and *Tidestromia oblongifolia* obtained from Death Valley, California, and grown at 44°C. Figure 17 shows that for all of these plants no maxima in the fluorescence vs. temperature curves occurred over the range from about 0° to 20°C. These findings suggest that the phase transition of the lipids in the thylakoid membranes occurs below the freezing point in all of these plants.

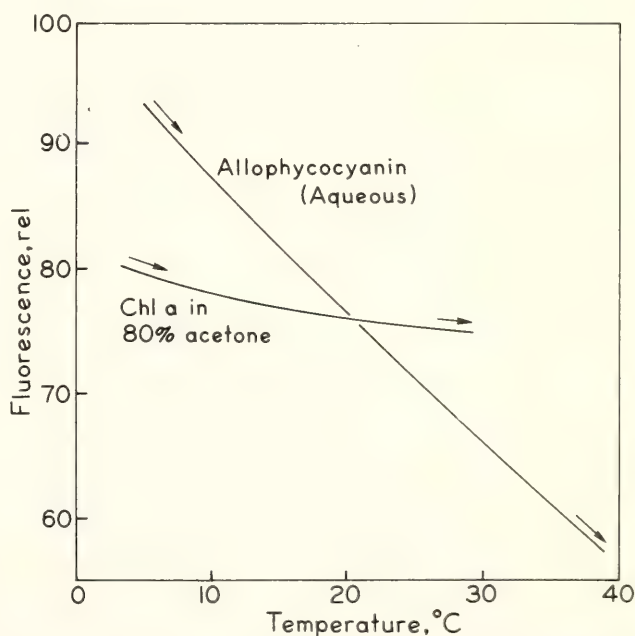


Fig. 16. Temperature dependence of chlorophyll *a* fluorescence in 80% acetone and allophycocyanin in an aqueous solution. The chlorophyll *a* and phycobilins were obtained from *Anacystis* grown at 38°C. The chlorophyll *a* fluorescence was excited at 430 nm and measured at 675 nm. The allophycocyanin fluorescence was excited at 560 nm and measured at 655 nm. Temperature was increased at the rate of 2°C/min.

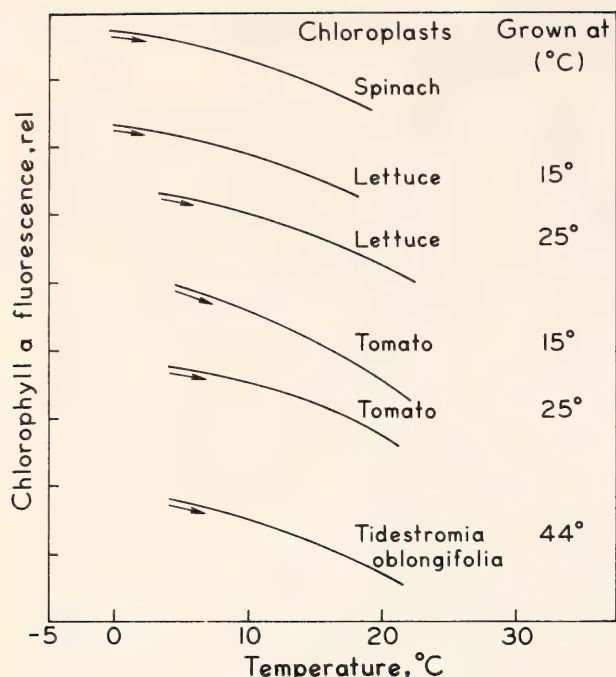


Fig. 17. Temperature dependence of chlorophyll *a* fluorescence in chloroplasts of spinach, lettuce, tomato, and *Tidestromia oblongifolia*. Fluorescence was excited at 430 nm and measured at 684 nm. Rate of temperature change was 2°C/min.

As mentioned earlier, the transition of the spin-probe signal in membrane fragments of *Anacystis* occurred at 24°C in cells grown at 38°C and at 13°C in cells grown at 28°C. These discontinuity points are characteristic of a transition of the physical phase of the hydrocarbon regions of membrane lipids and probably represent a change from the liquid-crystalline to the mixed solid-liquid-crystalline states. In other words, the transition temperature corresponds to a beginning of local solidification of membrane lipids. The fluorescence yield vs. temperature curves shows that the temperature of maximum fluorescence, especially upon increasing the temperature, was close to the phase transition temperatures as determined by the spin-labeling method. These findings suggest that the fluorescence yield of chlorophyll *a* is a sensitive method to detect the phase transition of lipids in the thylakoid membrane.

As noted previously, the fatty acid composition of *Anacystis* changes with growth temperature (Holton *et al.*,

1964). Cells grown at lower temperatures have a higher content of unsaturated fatty acids than do cells grown at higher temperatures. It was seen here that the fluorescence maxima as well as the discontinuity of the spin-label signal appeared at a lower temperature when *Anacystis* was grown at a lower temperature. This would seem to be related to the change of fatty acid composition of the thylakoid membranes with growth temperature.

Colbow (1973) has found that chlorophyll *a* in phospholipid model membranes functioned as a fluorescent probe just like added artificial fluorescent probes and that the fluorescence yield of chlorophyll *a* was drastically decreased when the temperature passed through the phase transition point from the high to the low.

It would appear that the fluorescence of chlorophyll *a* is a better probe for detecting the transition of the phase of membrane lipids than is the fluorescence from artificial probes such as ANS and NPN (Overath and Träuble, 1973). In intact cells many kinds of membranes and cell organelles are included and added artificial probes are not necessarily bound only to chloroplast membranes. Chlorophyll *a* molecules, on the other hand, are localized exclusively in the chloroplasts and thus provide information about the physical state of thylakoid membranes. The artificial probes do not work well even in extracted chloroplasts or in thylakoid membranes because the efficient energy transfer from the probes to chlorophyll almost completely quenches the fluorescence of the membrane-bound probes.

The very large increase of fluorescence from allophycocyanin in *Anacystis* below 0°C must be a reflection of the suppression of excitation transfer from the allophycocyanin to chlorophyll *a* in pigment system 2. At temperatures near 0°C the lipid areas of the membrane are probably largely in the solid state and this may influence the binding be-

tween the phycobilisomes and the thylakoid membrane. *Anacystis* is known to be especially sensitive to chilling. When cells are exposed to low temperature they lose photosynthetic activity as well as release considerable amounts of pteridines (Forrest *et al.*, 1957).

THE RELATIONSHIP BETWEEN THE PHYSICAL PHASE OF MEMBRANE LIPIDS, ELECTRON TRANSPORT, OXYGEN EVOLUTION, AND QUANTUM DISTRIBUTION IN THE PHOTOSYNTHESIS OF *Anacystis nidulans* AND IN LETTUCE AND SPINACH CHLOROPLASTS

As discussed in the previous section, the transition of the physical phase of membrane lipids between the liquid-crystalline state and the mixed solid-liquid-crystalline state can be shown by spin label and fluorescence measurements to occur at different temperatures in *Anacystis*, depending upon the temperature used for growth. This transition of the physical phase of membrane lipids appeared around 10°C in cells grown at 28°C and around 20°C in cells grown at 38°C and appears to be a reflection of the growth temperature-dependent alteration of the fatty acid composition of membrane lipids.

In this study we have investigated the relationship between the transition of the physical phase of membrane lipids and photosynthetic activities.

Photosynthetic Electron Transport
Measured by P700 Reduction in
Anacystis

The effect of the transition of the physical phase of membrane lipids in electron transport reactions was followed by measuring the oxidation-reduction reactions of P700 at various temperatures. In this experiment a suspension of algal cells was illuminated for 15 sec by intense actinic light having wavelengths longer than 620 nm that was absorbed by both pigment systems. The rate of P700 reduction was followed as

the rate of absorbance increase at 435 nm when the actinic light was turned off. Light-minus-dark difference spectra were very similar in shape and magnitude when measured at either 30° or 12°C. P700 reduction measured at 435 nm is only slightly contaminated by the cytochrome *f* change since the latter change contributes very little to the absorbance change measured at this wavelength.

The Arrhenius plot of the rate of P700 reduction in the dark given in Fig. 18 shows two straight lines with a break at 10°C for the cells grown at 28°C and at 20°C for the cells grown at 38°C. The values for the activation energy above the transition temperatures were 14 and 13 kcal/mole for cells grown at 28° and 38°C, respectively, and below the transition temperatures were 21 and 16 kcal/

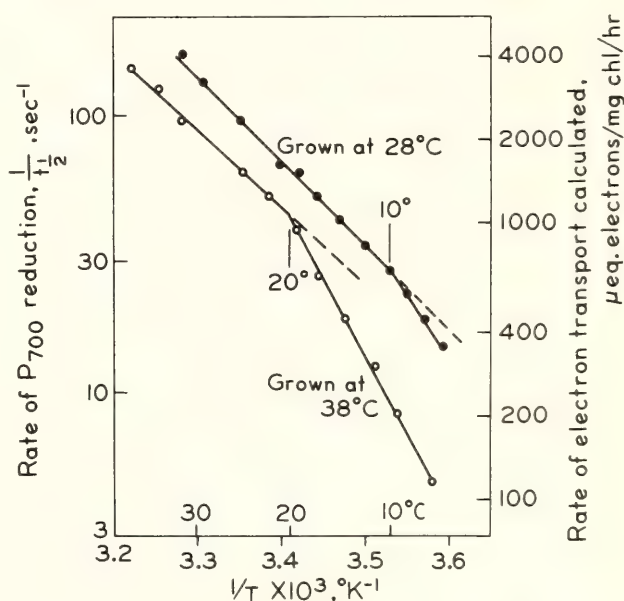


Fig. 18. Arrhenius plot of P700 reduction after turning off the 15 sec red actinic illumination (620 to 750 nm; 1.8×10^5 ergs cm⁻²sec⁻¹) in intact cells of *Anacystis* grown at 28° and 38°C. The rate of P700 reduction was plotted as the reciprocal of the half-decay time of the absorbance change at 435 nm. The rate of electron transport presented on the right side of the figure was calculated from the half-decay time of P700 reduction, using the assumption that P700 reduction is a monomolecular reaction and that the molar ratio of chlorophyll *a* to P700 is 100 (Inoue *et al.*, 1973). The temperature of the sample was changed from high to low.

mole in cells grown at 28° and 38°C, respectively. Although the transition of P700 reduction appeared at different temperatures, the activation energy in the liquid-crystalline state was about the same for the two cultures. The calculated rate of electron transport through P700 is about 3000 μeq electrons/mg chlorophyll/hr at the growth temperature in the two cultures (assuming the molar ratio of chlorophyll *a* to P700 is 100 as shown by Inoue *et al.*, 1973, for *Anacystis*). As will be shown in Fig. 19, this value corresponded rather well to the rate of photosynthesis measured by O_2 evolution.

Figure 18 was measured by decreasing the temperature from the high to the low. In another experiment the algae were cooled from their growth temperature and then heated up after reaching 6°C. The break in the line occurred at the same temperature as before, and the values for the activation energy were the same at temperatures below the break point. However, at temperatures above the break point the activation energy was lower, suggesting that the chilling treatment had induced some damaging effects on the thylakoid membrane that slowed down electron transport reactions at higher temperatures.

When DCMU was added to inhibit electron transport from photoreaction 2 to plastoquinone (Amesz, 1964), the dark reduction of P700 was greatly retarded. Dark reduction in this case comes from an unknown endogenous electron donor or donors. For *Anacystis* grown at 28°C the discontinuity in the Arrhenius plot occurred at 12°C, and for cells grown at 38°C it appeared at 20°C. Again these break points occurred near the transition temperature of the lipid phase for the two cultures.

O₂ Evolution as a Function of Growth Temperature in Anacystis

The Arrhenius plots of the rates of O_2 evolution in cultures grown at 28° and 38°C are given in Fig. 19. The transition

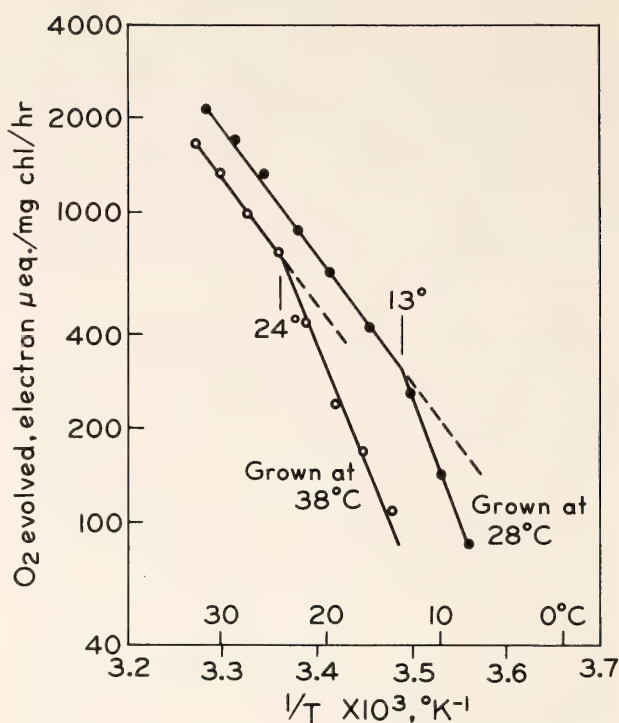


Fig. 19. Arrhenius plot of photosynthesis of *Anacystis* grown at 28° and 38°C. White actinic light of a sufficient intensity to saturate photosynthesis was used. Chlorophyll concentration was 21 and 12 $\mu\text{g}/\text{ml}$ for cells grown at 28° and 38°C, respectively.

of the activation energy appeared at 13° and 24°C for cultures grown at 28° and 38°C, respectively. Again these temperatures occurred near the transition temperatures of the lipid phase. Above the transition temperature the values for the activation energy were 19 kcal/mole for both cultures, showing that the activation energy of the reaction is constant in the liquid-crystalline state regardless of the growth temperature. But below the transition temperature the values for the activation energy were 37 and 34 kcal/mole in cells grown at 28° and 38°C, respectively.

Pigment State 1 and State 2 Shifts in Anacystis

When plants are illuminated for several seconds with light absorbed preferentially by pigment system 2, a special kind of configurational alteration of the thylakoid membrane takes place, resulting in a change in light quantum distribution between the two pigment systems so that more light quanta are diverted

to photosystem I (Bonaventura and Myers, 1969; Murata, 1969a, 1970). The effect of this change is to stimulate the system 1 reaction that would be the rate-limiting step of the overall electron transport reaction. This state is called Pigment State 2. When cells are illuminated by light absorbed preferentially by pigment system 1 the reverse change of light quantum distribution occurs. This state is called Pigment State 1. This flexibility of quantum redistribution is advantageous for plants, since it allows them to utilize available light energy efficiently.

Fluorescence transients reflecting State 1, State 2 shifts were measured at 33° and 17°C in *Anacystis* grown at 38°C. For this experiment weak light preferentially absorbed by pigment system 2 was given continuously to excite chlorophyll *a* fluorescence. This brought the cells into State 2. A beam of rather intense light absorbed by pigment system 1 was turned on for 1 min in addition to the excitation light absorbed by system 2. At 33°C the fluorescence yield after turning off the system 1 light increased from an initial level (*I*) to a peak (*P*) afterward decreasing to a steady-state level (*S*) the same as seen before illumination of pigment system 1 (Fig. 20). The appearance of the peak suggests a shift from State 2 to State 1 during illumination with overlapped system 1 light, and the slow decrease from *P* to the *S* level indicates a shift from State 1 back to State 2 again. At 17°C the state shifts are almost completely lacking (lower part of Fig. 20). Figure 21 shows for *Anacystis* the Arrhenius plot of the rate of the State 1 to State 2 shift represented by:

$$R = \frac{d(\Delta F)/dt_{\max}}{\Delta F}$$

where *R* is equal to the maximum rate of fluorescence yield change after the peak, $d(\Delta F)/dt_{\max}$, divided by the difference of fluorescence yields *P* and *S* (ΔF). Figure 21 shows discontinuity

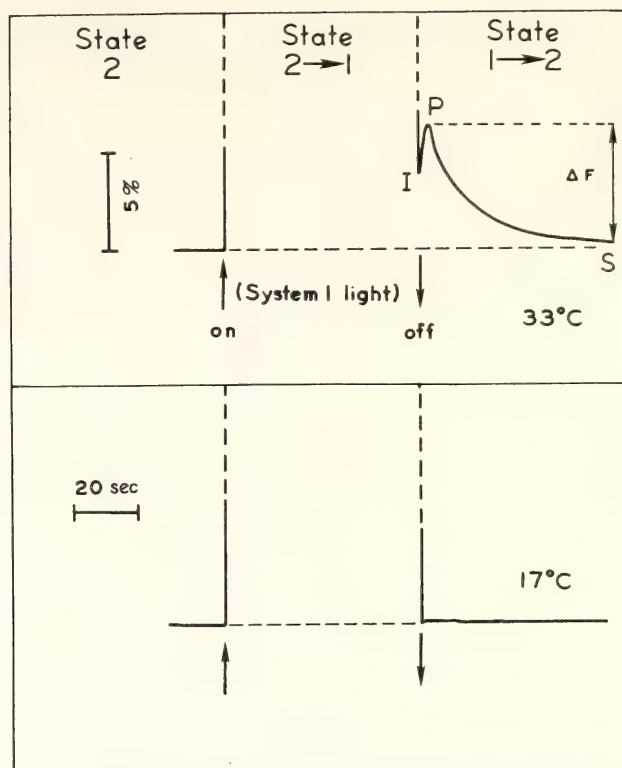


Fig. 20. Time course of fluorescence transients due to the State 1 and State 2 shift at 33° and 17°C in *Anacystis* cells grown at 38°C. The monochromatic light (620 nm, 800 ergs/cm²/sec) used for excitation of pigment system 2 was obtained from a Bausch and Lomb grating monochromator used in conjunction with a Corning glass filter 9788. Blue actinic light to excite pigment system 1 was obtained by filtering light from a halogen lamp through two filters of Corning 9782, a Corning 5543 filter, and a Calflex C filter and had an intensity of 5000 ergs/cm²/sec.

points of the lines, although no more than one data point was obtained below the transition temperature because of the difficulty in obtaining exact values for very slow State 1 and State 2 shifts. The transition temperature appeared at 13°C for cells grown at 28°C and at 22°C for cells grown at 38°C. Here again the dramatic change in the Arrhenius plot occurred at the temperature of the transition of the physical phase of membrane lipids for the two cultures.

Electron Transport Reactions in Higher Plant Chloroplasts

Electron transport reactions were studied in a higher plant (lettuce) by measuring the rate of DCIP reduction. In addition the rate of P700 reduction

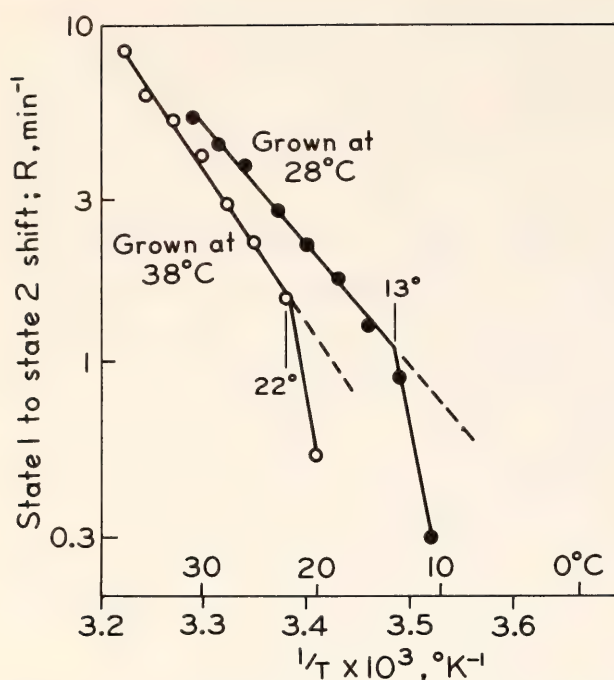


Fig. 21. Arrhenius plot of the shift of State 1 to State 2 in *Anacystis* cells grown at 28° and 38°C. R represents the rate of shift from State 1 to State 2. The experimental conditions were the same as in Fig. 20 except for temperature.

was measured by first oxidizing P700 in far-red light, and after a 30 msec dark period during which time most of the P700 and other electron transport components remained oxidized, a 3 μ sec flash of red light was given to reduce P700.

The Arrhenius plots of both the Hill reaction with DCIP and the rate of reduction of oxidized P700 that was induced by a red flash gave straight lines with no break points over the temperature range from about 8° to 33°C. The values of the activation energy were 28 kcal/mole for P700 reduction induced by a red flash and 10 kcal/mole for the Hill reaction with DCIP. This difference may not be unexpected since the reactions of P700 reduction and DCIP reduction may include different pathways of electron transport.

We also measured the cation-induced configurational change of the thylakoid membrane that is reflected by a change in the efficiency of excitation transfer between the two pigment systems and can be monitored as fluorescence changes

(Murata, 1969b, 1970; Murata *et al.*, 1970). For lettuce and spinach chloroplasts Arrhenius plots in both cases gave straight lines with no break points. Moreover, for chloroplasts made from lettuce grown at 15° and 25°C the points for the Mg^{++} -induced fluorescence change followed the same straight line.

Figure 22 summarizes the temperatures for the transition in the Arrhenius plots for the various parameters measured. For *Anacystis* grown at 28°C the transition temperatures appeared between 10° and 13°C, and for organisms grown at 38°C, between 18° and 24°C.

It can be noted that the characteristic transition temperatures appeared at 13° C (the upper limit) in the spin-label mobility, chlorophyll *a* fluorescence in intact cells, and O_2 evolution and for the State 1 to State 2 shift. Measurements of fluorescence in lipid water mixtures and electron transport in the absence of DCMU gave transition temperatures near the lower limit (10°C). Other parameters studied appeared at intermediate temperatures. The same pattern, but with more scatter, appeared when cells grown at 38°C were used. These results would seem to indicate that these photosynthetic parameters respond slightly differently to the transition of the physical phase of membrane lipids.

As mentioned previously the transitions appearing in *Anacystis* at 10° and at 20°C for cells grown at 28° and 38°C, respectively, probably reflect the growth temperature-dependent alteration of the fatty acid composition of the membrane lipids (Holton *et al.*, 1964). This finding with *Anacystis* is in contrast to the finding in lettuce chloroplasts that the Arrhenius plots of the $MgCl_2$ -induced fluorescence changes followed the same line regardless of the growth temperature. Thus the fluidity of lettuce chloroplast membranes does not seem to be influenced by growth temperature, and the transition of phase of the membrane lipids must occur below 0°C.

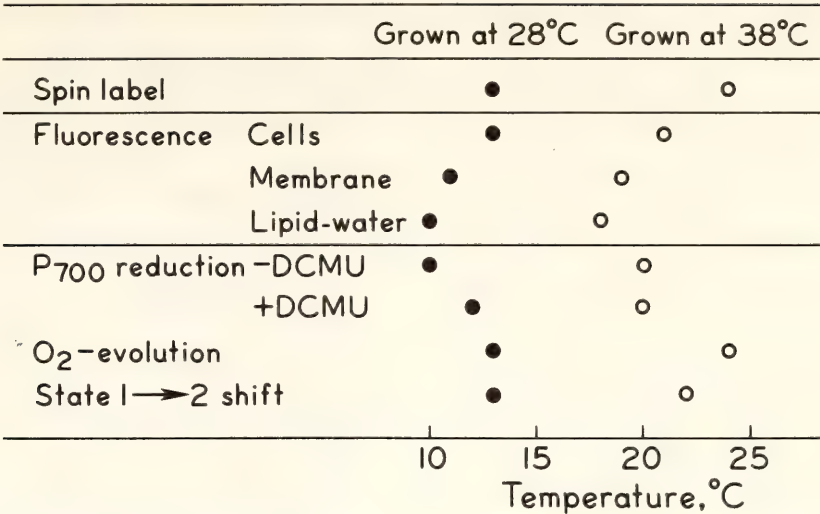


Fig. 22. Summary of the transition temperatures of photosynthetic parameters in *Anacystis nidulans*.

It is of interest to estimate the site of electron transport that is influenced by the transition of the lipid phase of the thylakoid membrane. It is known from studies of the red alga *Porphyridium cruentum* (Amesz *et al.*, 1972) and spinach chloroplasts (Haehnel, 1973) that the site of plastoquinone oxidation is the rate-determining step in overall electron transport. This may also be the case for *Anacystis*. After turning off the red actinic light that causes P700 and cytochrome *f* to become oxidized and plastoquinone to become reduced, the dark reduction of P700 is controlled by the rate of plastoquinone oxidation. The appearance of a change in the rate of P700 reduction corresponding to a transition in the phase of membrane lipids leads to the conclusion that this part of electron transport including plastoquinone is influenced by the phase transition of the lipids. Moreover, plastoquinone is the most lipophilic component in the electron transport system, suggesting that this compound would be most likely to be influenced by the fluidity of membrane lipids. It has been noted in the respiratory electron transport of mitochondria (Raison *et al.*, 1971) as well as in bacterial membranes (Esfahani *et al.*, 1972) that the oxidation-reduction reactions including ubiquinone show a transition in the activation energy that

is related to the transition of the physical phase of membrane lipids.

The State 1 to State 2 shift of light quantum distribution between the two pigment systems was highly dependent upon the fluidity of membrane lipids. This effect almost disappeared when the membrane lipids were in the mixed solid and the liquid-crystalline state. Thus the State 1 to State 2 shift is very much dependent upon the physical state of the membrane lipids.

It appears that the transitions of the hyperfine splitting of the ESR signal, the photosynthetic electron transport, the configurational changes leading to quantum redistribution, as well as the maximum of chlorophyll *a* fluorescence in the thylakoid membranes of *Anacystis* are all affected by transitions of the physical phase of membrane lipids between the liquid-crystalline state and the mixed liquid-crystalline and the solid state.

REFERENCES

Amesz, J., *Biochim. Biophys. Acta*, 79, 257, 1964.
Amesz, J., J. W. M. Visser, G. J. Vanden Engh, and M. P. Dirks, *Biochim. Biophys. Acta*, 256, 370, 1972.
Barratt, M. D., D. K. Green, and D. Chapman, *Chem. Phys. Lipids*, 3, 140, 1969.

- Benson, A. A., *Ann. Rev. Plant Physiol.*, **15**, 669, 1964.
- Bonaventura, C., and J. Myers, *Biochim. Biophys. Acta*, **189**, 366, 1969.
- Chapman, D., J. Urbina and K. M. Keough, *J. Biol. Chem.*, **249**, 2512, 1974.
- Colbow, K., *Biochim. Biophys. Acta*, **318**, 4, 1973.
- Esfahani, M., P. D. Crowfoot, and S. J. Wakil, *J. Biol. Chem.*, **247**, 7251, 1972.
- Forrest, H. S., C. Van Baalen, and J. Myers, *Science*, **125**, 699–700, 1957.
- Haehnel, W., *Biochim. Biophys. Acta*, **305**, 618, 1973.
- Hirayama, O., *J. Biochem.*, **61**, 179–185, 1967.
- Holton, R. W., H. H. Blecker, and M. Onore, *Phytochem.*, **3**, 595, 1964.
- Inoue, Y., T. Ogawa, and K. Shibata, *Biochim. Biophys. Acta*, **305**, 483, 1973.
- Kemp, A., Jr., G. S. P. Groot, and H. J. Reitsma, *Biochim. Biophys. Acta*, **180**, 28, 1969.
- Ladbrooke, B. D., and D. Chapman, *Chem. Phys. Lipids*, **3**, 304, 1969.
- Lyons, J. M., and J. K. Raison, *Plant Physiol.*, **45**, 386, 1970.
- Lyons, J. M., T. A. Wheaton, and H. K. Pratt, *Plant Physiol.*, **39**, 262, 1964.
- Murata, N., *Biochim. Biophys. Acta*, **172**, 242, 1969a.
- Murata, N., *Biochim. Biophys. Acta*, **189**, 171, 1969b.
- Murata, N., *Biochim. Biophys. Acta*, **205**, 379, 1970.
- Murata, N., H. Tashiro, and A. Takamiya, *Biochim. Biophys. Acta*, **197**, 250, 1970.
- Overath, P. and H. Träuble, *Biochemistry*, **12**, 2625, 1973.
- Overath, P., H. U. Schairer, and W. Stoffel, *Proc. Nat. Acad. Sci. USA*, **67**, 606, 1970.
- Raison, J. K., J. M. Lyons, and W. W. Thompson, *Arch. Biochem. Biophys.*, **142**, 83, 1971.
- Sackmann, E., H. Träuble, H.-J. Galla, and P. Overath, *Biochem.*, **12**, 5360, 1973.
- Träuble, H., *Naturwissen.*, **58**, 277, 1971.
- Wilson, G., S. P. Rose and C. F. Fox, *Biochem. Biophys. Res. Commun.*, **38**, 617, 1970.

A COMPARISON OF LIGHT-INDUCED SHIFTS IN CAROTENOID ABSORPTION IN REPRESENTATIVES OF DIFFERENT ALGAL GROUPS

David C. Fork and Jeanette S. Brown

Little is known about the functioning of carotenoids in photosynthesis. These pigments appear to be essential components for the process, and all photosynthetically active plants examined so far contain β -carotene. However, only the two xanthophylls fucoxanthin and peridinin have been shown to act directly as light-harvesting pigments by transferring their absorbed light energy to chlorophyll *a*. Except for the phycobilin pigments all of the photosynthetically active plant pigments are embedded in the thylakoid membranes. Light reactions of photosynthesis appear to produce physiochemical change(s) in these mem-

branes leading to wavelength shifts in the absorption maxima of the embedded pigments (Schliephake *et al.*, 1968; Jackson and Crofts, 1969). The first recorded absorbance change seen in a green alga had a large positive maximum near 515 nm and a kinetically similar change with a negative peak near 475 nm (Duysens, 1954; *Year Book* **53**, p. 166). These changes are thought to be caused by shifts in absorption towards longer wavelength in the light of both chlorophyll *b* and carotenoids and a return again in the dark (Hildreth *et al.*, 1966; Hildreth, 1970; for a review, see Fork and Ames, 1969). Ames and

Visser (1971) reported shifts of chlorophyll *a* forms occurring in the red part of the spectrum. Some of these changes were also seen in the green alga *Ulva* (Year Book 72, p. 374).

We have compared a number of different algae, some of them previously unexamined. Three of the algae used belong to the newly established class, the *Eustigmatophyceae* (Hibberd and Lee-dale, 1970, 1971, 1972) and apparently have a very simple pigment composition containing only chlorophyll *a*, β -carotene, and a major xanthophyll (Norgård *et al.*, 1974; Guillard and Lorenzen, 1972). We have examined the light-induced shifts in several algae belonging to this new class and have compared them with light-induced changes in representatives of other algal groups having more elaborate pigmentation, such as the green algae that contain chlorophyll *b*, the brown algae and diatoms that contain chlorophyll *c*, and the yellow-green algae (*Xanthophyceae*). Some members of the latter group have recently been shown to contain chlorophyll *c* (Guillard and Lorenzen, 1972).

Figure 23 shows the light-induced difference spectra obtained for the algae used. The large minimum at 420 nm can be attributed to the light-induced oxidation of cytochrome *f*. All of the algae belonging to the *Eustigmatophyceae* produced difference spectra that are caused apparently by red shifts of carotenoid bands and have maxima and minima separated by about 30 nm. In *Pleurochloris magna*, for example, the positive peaks at 450, 485, and 515 nm are separated by 35 and 30 nm, and the two negative peaks at 468 and 498 nm, by 30 nm. The kinetics of the absorbance changes at all of these wavelengths were similar, suggesting that they all were produced by the same reaction. Also in *Polyedriella* the positive peaks are separated by about 35 nm and the negative peaks by 30 nm. Another organism examined, "GSB Sticho," class unknown (Guillard and Lorenzen, 1972) but prob-

ably a member of the *Eustigmatophyceae* was found to have a difference spectrum with positive peaks separated by 33 and 37 nm and the negative peaks by 30 nm. In all three of these organisms the positive peak (or shoulder) near 515 nm (or 520 nm) can clearly be seen to be associated with the carotenoid changes. Another peak seen in the difference spectrum of each organism near 535 nm cannot be attributed yet to a particular compound.

The xanthophyte *Tribonema* had positive peaks at 450 and 482 nm and a shoulder at around 517 nm. In addition it had minima at 463 and 496 nm, making this portion of the difference spectrum like the spectra of the *Eustigmatophyceae*. No contribution of chlorophyll *c* to this difference spectrum is evident.

The diatom (*Phaeodactylum*) and brown alga (*Macrocystis*) had difference spectra very different from the other algae. The maxima near 475, 512, and 525 nm as well as the minima near 490 nm and 538 nm in the case of *Phaeodactylum* probably represent carotenoid, chlorophyll *c*, and fucoxanthin changes mixed together. A large positive band was seen in both algae at 562 nm. A relatively large change at 561 nm has been described by Nakayama *et al.* (1974) in chloroplasts of the coenocytic green alga *Bryopsis*. The kinetic properties of the change were reported to be like those of the 515 nm change in this same alga. Similarly, both changes were affected by inhibitors and uncouplers of photophosphorylation. Perhaps the change seen at 537 nm in *Tribonema* and in the *Eustigmatophytes* will also be closely correlated with the behavior of the carotenoid bands in these algae.

The most commonly observed difference spectrum in higher plants and green algae is represented by that shown for the green alga *Stichococcus bacillaris*. Here the positive and negative peaks are not so uniformly separated by about 30 nm as are those of the organisms described above. It would seem that the

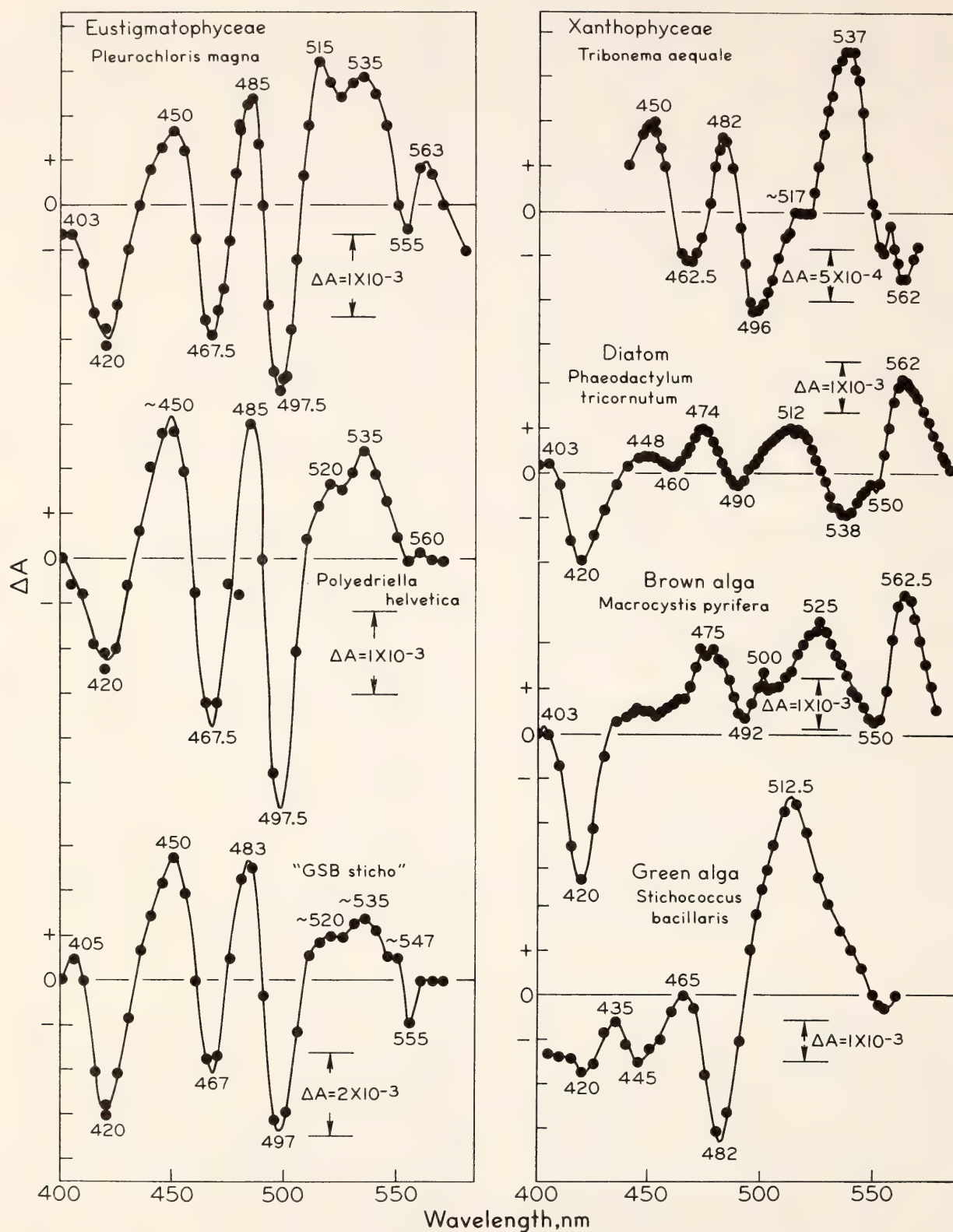


Fig. 23. Light-induced changes of absorbance produced in a number of variously pigmented algae. Exposures to 0.3 to 3 sec flashes of red actinic light of saturating intensity were used. The largest absorbance change attained in the light was plotted. Temperature, 20°C; gas phase, air. *Macrocystis* (giant kelp) was collected at Half-Moon Bay, California. The other algae were obtained from the Culture Collection of Algae at Indiana University except for "GSB Sticho," which was obtained from the Woods Hole Oceanographic Institution and cultured in appropriate liquid media.

minimum near 482 and the maximum near 515 nm in organisms containing chlorophyll *b* is produced by both carotenoids and chlorophyll *b*.

The light-induced difference spectra given here show that pigment shifts are seen even in plants that have a very simple complement of photosynthetically active pigments. These light-induced pigment shifts seem to be almost universally present in photosynthetic organisms. Carotenoid and chlorophyll shifts have been observed in purple photosynthetic bacteria (Smith and Ramírez, 1960; Clayton, 1963; Ames and Vredenberg, 1966); and carotenoid shifts have been observed in red and brown algae (Fork and Ames, 1967), in a higher plant mutant (Fork, 1969), and in the algae described here. It is noteworthy that the blue-green algae have so far not been shown to have light-induced carotenoid band shifts but only chlorophyll band shifts (Ames and Visser, 1971). Further study will be needed to determine why such an otherwise universal phenomenon is not also found in these primitive algae and to understand more fully the physicochemical nature of the events that produce these changes.

REFERENCES

- Ames, J., and J. W. M. Visser, *Biochim. Biophys. Acta*, **234**, 62, 1971.
- Ames, J., and W. J. Vredenberg, in *Currents in Photosynthesis*, J. B. Thomas and J. C. Goedheer, eds., Ad. Donker, Rotterdam, p. 75, 1966.
- Clayton, R. K., *Proc. Natl. Acad. Sci. USA*, **50**, 583, 1963.
- Duysens, L. N. M., *Science*, **120**, 353, 1954.
- Fork, D. C., in *Progress in Photosynthesis Research*, H. Metzner, ed., International Union of Biological Sciences, Tübingen, vol. 2, p. 800, 1969.
- Fork, D. C., and J. Ames, *Photochem. Photobiol.*, **6**, 913, 1967.
- Fork, D. C., and J. Ames, *Ann. Rev. Plant Physiol.*, **20**, 305, 1969.
- Guillard, R. R. L., and C. J. Lorenzen, *J. Phycol.*, **8**, 10, 1972.
- Hibberd, D. J., and G. F. Leedale, *Nature*, **225**, 758, 1970.
- Hibberd, D. J., and G. F. Leedale, *Taxon*, **20**, 523, 1971.
- Hibberd, D. J., and G. F. Leedale, *Ann. Bot.*, **36**, 49, 1972.
- Hildreth, W. W., *Arch. Biochem. Biophys.*, **139**, 1, 1970.
- Hildreth, W. W., M. Avron, and B. Chance, *Plant Physiol.*, **41**, 983, 1966.
- Jackson, J. B., and A. R. Crofts, *FEBS Letters*, **4**, 185, 1969.
- Nakayama, K., M. Okada, and A. Takamiya, *Plant Cell Physiol.*, **15**, 799, 1974.
- Norgård, S., W. A. Svec, S. Liaaen-Jensen, A. Jensen, and R. R. L. Guillard, *Biochem. System. and Ecol.*, **2**, 3, 1974.
- Schliephake, W., W. Junge, and H. T. Witt, *Z. Naturforsch.*, **23b**, 1571, 1968.
- Smith, L., and J. Ramírez, *J. Biol. Chem.*, **235**, 219, 1960.

METABOLISM AND PHOTOCHARACTERISTICS OF CHLOROPHYLL-PROTEIN COMPLEXES

J. S. Brown

In last year's Annual Report (*Year Book 73*, p. 694), we presented the results of a collaborative study of chlorophyll-protein complexes with Professor Philip Thornber's group at the University of California, Los Angeles. Two

main chlorophyll-protein complexes have been isolated from a number of different kinds of higher plants and algae (Brown *et al.*, 1975a; Thornber, 1975). CPI is high in P700 and contains only chlorophyll *a*, which suggests that it is the re-

action center complex for photosystem I. CPII contains all the chlorophyll *b* in the plant and an equimolar amount of chlorophyll *a*; it appears to function in a light-harvesting capacity. Study of these pigment complexes, isolated by hydroxylapatite chromatography from detergent-solubilized spinach chloroplasts, has been continued this year.

Metabolism of CPI

With Mme. Suzanne Acker and Dr. Jacques Duranton at the French Atomic Energy Center, Saclay, near Paris, I isolated CPI from young corn leaves that had incorporated tritiated δ -amino-levulinic acid, a precursor of chlorophyll. We measured and compared the specific activities of the chlorophyll *a* in CPI with the total chlorophyll *a* in the Triton-solubilized chloroplast membranes.

The results showed that the radioactive label was incorporated into CPI at about half the rate of total incorporation. After 48 hr when the cut leaves were senescing, the breakdown of the chlorophyll *a* in CPI was slower than the overall degradation state. Thus it was demonstrated that the P700-chlorophyll-protein complex in vivo is isolated metabolically from the rest of the chlorophyll-containing membrane. For more details see Brown *et al.* (1975b).

Light-Induced Absorption Changes of CPI

Absorbance changes in a spinach CPI preparation induced by flashing light

were measured in collaboration with Dr. Fork (*Year Book* 71, p. 183). The preparation contained 12 μ g chlorophyll *a* per ml and had a chlorophyll-to-P700 ratio of 37. Sodium ascorbate and diaminodurene (DAD) were added as artificial electron donors and methylviologen as an acceptor. The absorbance was measured during a one second sweep following a 350 msec flash of saturating red or blue light. The averaged signal from 4 flashes with 12 sec dark time between flashes was recorded. Difference spectra between 400 and 470 nm and between 660 and 725 nm were measured.

Two kinetically distinct changes were observed at both the beginning and end of the flash. A semi-log reciprocal plot of these two changes showed that the rapid change had a half-time of less than 8 msec. Probably this change is limited by the response of the apparatus and is in reality faster. The slower change had a half-time of about 50 msec. Difference spectra for the two light-on changes are shown in Fig. 24. Spectra of the fast and the slow light-off changes were mirror images of the two spectra shown.

The spectrum of the rapid change with its negative peaks at 430 and 700 nm is identical with that first shown for P700 by Kok and Hoch, 1961, and repeated in many laboratories since. The slower change has a negative peak at 420 and a broad positive band near 450 nm, suggesting the involvement of cyt *f*. The broad band of the slow change near 700 nm and shoulder near 430 nm may

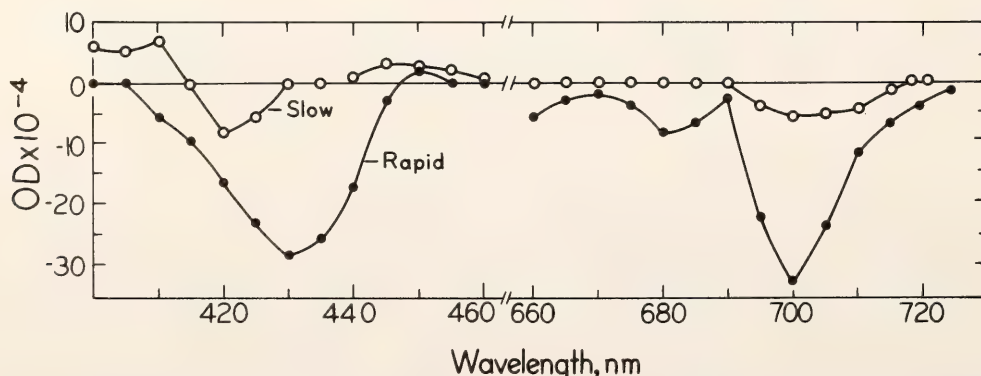


Fig. 24. Difference spectra of CPI induced by flashing light. See text for details.

be a component of the change due to P700 that is limited by its close association with cyt *f*.

Shiozawa *et al.* (1974) found that P700 and cyt *f* are present in approximately equimolar amounts in purified CPI. The results presented here suggest that whereas most of the P700 is oxidized rapidly in the light, about 10%–15% may be coupled closely to cyt *f*, and therefore its rate of oxidation is limited by the speed at which cyt *f* can be oxidized. After the flash, electrons from ascorbate and DAD rapidly reduce most of the P700 but reduce cyt *f* more slowly, and cyt *f*, in turn, reduces additional P700.

Photooxidation of Cytochrome c by CPI

The photooxidation of mammalian cytochrome *c* has frequently been used to measure photosystem I activity (Year Book 69, p. 678; Year Book 70, p. 499). Reinvestigation of this reaction revealed a mistake in previous calculations by a factor of 1000. Thus in the previous reports the rate of cyt *c* oxidation should have been given in mmoles rather than μ moles. Because rates between various preparations were compared, the error does not change any of the conclusions in those experiments. The same concentrations of reactants were used as before, but the Perkin-Elmer 356 Two-Wavelength Double Beam Spectrophotometer with the Actinic Light Accessory was used to measure the rate of change of absorption of the cyt *c* as it was photooxidized. A red Shott filter RG-2 was placed over the actinic light, and a blue Corning filter no. 9782 was placed over the photomultiplier tube.

CPI preparations, having about 45 chlorophyll *a* molecules for each P700, oxidized cyt *c* at about 25 mmole/mg chl \cdot hr, and with saturating amounts of plastocyanin this rate increased to about 50 mmole/mg chl \cdot hr. The reaction was not saturated by the 10^5 erg/cm² \cdot sec of

red light available unless the preparation contained less than about 1 μ g chl/ml. Kok *et al.* (1964) also found some difficulty in saturating the rate of cyt *c* oxidation with detergent-treated spinach chloroplasts and viologen, but estimated the maximum rate to be in excess of 5 mmole/mg chl \cdot hr. Since CPI is approximately 10 times enriched in P700 compared to whole chloroplasts on a chlorophyll basis, values of 50 mmole/mg chl \cdot hr are to be expected.

In some experiments with very dilute but highly reactive CPI preparations, rates of nearly 200 mmole/mg chl \cdot hr were observed. These rates were unstable, probably due to photoinhibition, and were not stimulated by plastocyanin. Further investigation is required to explain these curious results.

Fluorescence Emission Spectra of CPI and CPII

CPI and CPII were prepared from spinach by hydroxylapatite chromatography according to Shiozawa *et al.* (1974) and Kung and Thornber (1971). Fluorescence emission spectra were recorded with a Perkin-Elmer Model MPF-3L Fluorimeter and a Phosphorescence Accessory for measuring at the temperature of liquid N₂ (–190°C). Samples of CPI and CPII were placed in 5 mm OD, NMR tubes, and their fluorescence was measured first at room temperature, then in liquid N₂. At least two dilutions were measured to ensure that error due to reabsorption was not distorting the spectrum. The samples for spectra shown in Fig. 25 contained less than 3 μ g chl/ml. In each case a baseline was measured with buffer in the cuvette, and this was subtracted from the sample curve run at the same sensitivity.

At room temperature (22°C) both CPI and CPII have their main emission at 685 nm. In addition, CPI has a second emission peak at 725 nm and shoulder near 735 nm, while CPII has only the broad low emission beyond 700 nm characteristic of most chloroplast prepara-

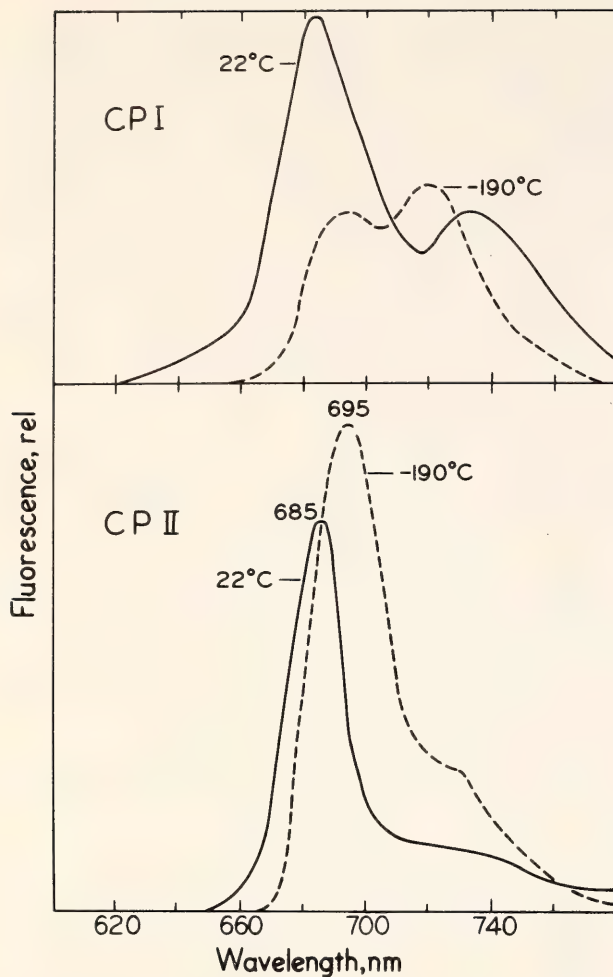


Fig. 25. Fluorescence emission spectra of CPI and CP II at 22°C and -190°C. Excitation at 438 nm. Slit width: excitation, 10–16 nm; emission, 2 nm. Spectra were corrected by subtracting the apparent emission spectrum of ice recorded under identical conditions.

tions. The 725 nm peak of CPI was evident in two different, freshly prepared samples. This result may indicate that photosystem I has a second emission band near 725 nm that is normally masked by the much more fluorescent photosystem II.

At low temperature the apparent fluorescence yield of CP II increased, but the yield of CPI decreased by several-fold. In each sample the 685-band decreased relative to a new band at 695 nm. CPI showed other distinct bands near 705, 720 and 735 nm which varied somewhat in proportion between different preparations. A shoulder near 730 nm became apparent in the spectrum of CP II at low temperature.

The increase in apparent fluorescence yield seen in CP II and most chloroplast preparations upon freezing is probably due to the increase in optical path-length caused by light-scattering of the ice. The unexpected observation was the decrease in fluorescence yield of CPI preparations. This decrease in total fluorescence was also observed when CPI was mixed in a one-to-one ratio with glycerol, but the proportion of the 720 nm band in relation to the other bands was greater in the 50% glycerol. It may be that this chl-protein complex aggregates more readily than other chl-containing particles or detergent complexes, and that this causes a quenching of the fluorescence. When CPI is frozen or lyophilized, a portion cannot be redissolved in buffer, indicating that the complex becomes aggregated or denatured rather easily.

With previously frozen and thawed preparations of CPI and those in which the chl-to-P700 ratio was high (~ 70), a distinct emission band was seen at 680 nm and the fluorescence yield was higher at both temperatures. Probably this higher emission and shift in peak position is due to detergent-solubilized chl detached from the protein complex.

The fluorescence yield of both chl-protein complexes was relatively low, causing the recorded spectra to be noisy. For this reason accurate curve analysis is not yet feasible, but it seems likely that a correlation between these emission bands and the forms of chl *a* shown in absorption spectra last year may exist.

The light-harvesting chlorophyll-protein complex, CP II, has equimolar amounts of chls *a* and *b* attached to a protein with a molecular weight of about 30,000 daltons. The possibility existed that the two chls might be attached to different protein molecules that were otherwise similar. Normally in vivo, excitation energy absorbed by chl *b* is transferred to and emitted by chl *a*. If, however, the two chls are on separate protein molecules, these would be sepa-

rated by dilution to a point where excitation of chl *b* would result in its own emission. To test this possibility the fluorescence emission of CPII was measured at different dilutions and with excitation at both 430 nm (chl *a* absorption) and 470 nm (chl *b* absorption).

The spectra were identical for excitation at 430 and 470 nm even at the highest dilutions, indicating that the two chls are indeed attached to the same protein but not necessarily to the same polypeptide chain. This fact is relevant to hypotheses concerning the arrangement of chls in the photosynthetic structure.

REFERENCES

- Brown, J. S., R. S. Alberty, and J. P. Thornber, in *Proc. 3rd Intern. Congr. Photosynthesis*, M. Avron, ed., pp. 1951–1962, 1975a.
- Brown, J., S. Acker, and J. Duranton, *Biochem. Biophys. Res. Commun.*, **62**, 336–341, 1975b.
- Kok, B., and G. Hoch, in *Light and Life*, W. D. McElroy and B. Glass, eds., Johns Hopkins Press, pp. 397–417, 1961.
- Kok, B., H. Ruaiski, and E. A. Harmon, *Plant Physiol.*, **39**, 513–520, 1964.
- Kung, S. P., and J. P. Thornber, *Biochim. Biophys. Acta*, **253**, 285–289, 1971.
- Shiozawa, J. A., R. S. Alberty, and J. P. Thornber, *Arch. Biochem. Biophys.*, **165**, 388–397, 1974.
- Thornber, J. P., *Ann. Rev. Plant Physiol.*, **26**, 127–158, 1975.

FORMATION OF AGGREGATES FROM SHORT FRAGMENTS OF PLANT DNA

W. F. Thompson

Research conducted at the University of Massachusetts resulted in the observation that plant DNA fragments at least as short as 350 nucleotides could aggregate during reassociation to form large particulate structures. Evidence for such structures was obtained using DNA prepared from a variety of vascular plants, including dicots, monocots, and ferns, and the process of aggregation was studied in more detail with pea DNA. Aggregation was especially pronounced when high concentrations of DNA were reassociated, and structures large enough to pellet at $40,000 \times g$ (30–60 min) frequently accounted for up to about 40% of the pea genome. In contrast to previously described pelletable structures involving long DNA fragments, DNA in these aggregate preparations appeared to be extensively base-paired. The mean thermal stability was about equal to that of repetitive sequence duplexes formed from total pea DNA.

Since aggregate formation may cause technical difficulties in various kinds of DNA reassociation experiments, and also because we hoped that aggregates might prove to be of some use in future work on sequence organization in plant genomes, further studies were conducted in which the process of aggregate formation was investigated in more detail. Figure 26 shows that aggregates form prior to reassociation of the unique, or slowly reassociating, sequences in the pea genome. However, at least when measured by the standard centrifugation assay, aggregates do not begin to appear until after most repetitive sequences have already formed duplexes which bind to hydroxylapatite (and therefore contain at least some double-stranded DNA). In addition, the kinetics of pelletable aggregate formation are complex. As indicated in Fig. 26, pelletable structures are observed at lower C_0t values in more concentrated DNA solutions. Thus, the apparent rate constant

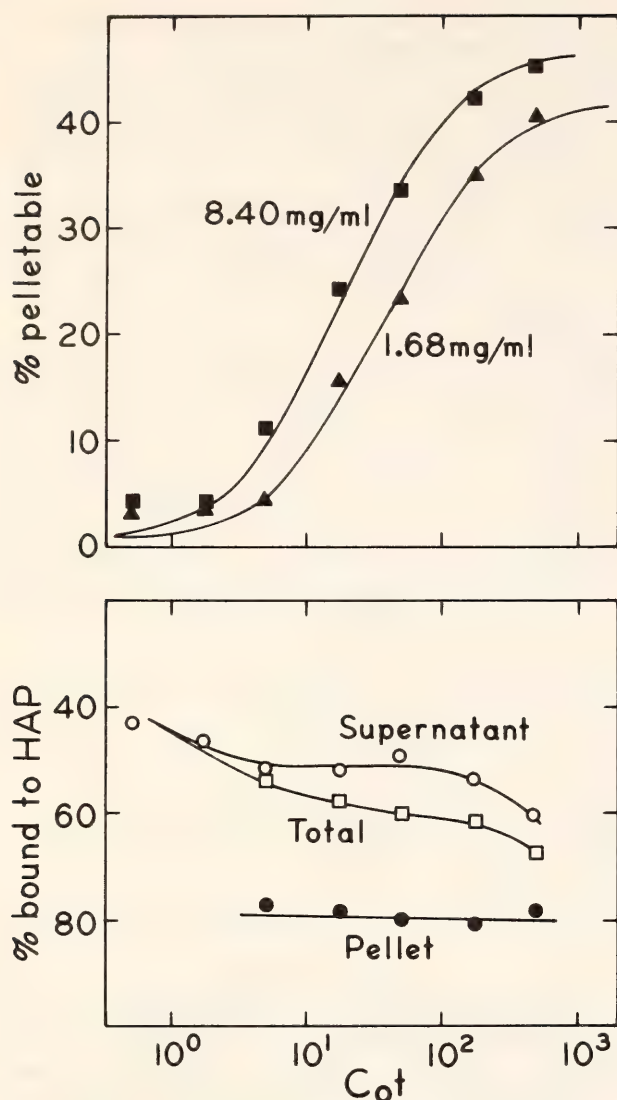


Fig. 26. Kinetics of aggregate and total duplex formation. DNA sheared to approximately 500 nucleotides was reassociated in SP buffer, 0.6 *M* NaCl, 10 mM PIPES (*pH* 6.8) containing 50% formamide for various times at 35° (29° below the T_m of native DNA). At each time, aliquots were removed, and the aggregate and supernatant fractions were separated by centrifugation. Each fraction was then sonicated and applied to hydroxylapatite. In the upper portion of the figure the solid lines depict theoretical second-order kinetics for final values of 47.5% aggregate at 8.4 mg/ml and 42.5% at 1.68 mg/ml. In the lower portion, total duplex (as hydroxylapatite binding) is plotted against C_0t for total DNA and the separated aggregate and supernatant fractions.

depends on the DNA concentration employed, which suggests a complex reaction involving one or more intermediates. Aggregate formation is presently visualized as involving secondary reassociation reactions between single-stranded

regions remaining on fragments which have already become double stranded over part of their length. These secondary reactions would eventually result in production of long hyperpolymers containing many DNA fragments (Graham and Britten, 1973), with interactions among these hyperpolymers resulting in particulate structures.

Aggregate formation is most significant when DNA is incubated under conditions establishing a reassociation criterion of low to moderate stringency, and the fraction of DNA in pelletable structures falls rapidly as the incubation temperature is increased. Relative to controls reassociated at $T_m - 29^\circ$ (29° below the mean dissociation temperature for native DNA fragments), for example, aggregates formation is reduced by about 40% at $T_m - 24^\circ$, and little or no pelletable DNA can be detected after reassociation at $T_m - 15^\circ$. In contrast, under the conditions employed (50% formamide, 0.6 *M* Na⁺, temperatures between 35 and 50°, $C_0t = 100$) total duplex formation is measured by hydroxylapatite binding is relatively little affected, being reduced by only about 10% even at $T_m - 15^\circ$. This dramatic temperature sensitivity of aggregate formation could be explained if the postulated secondary duplexes were shorter and/or more poorly matched than the majority of primary duplexes, and therefore of lower thermal stability. Raising the incubation temperature would then preferentially inhibit secondary duplex reassociation, thus reducing hyperpolymer and aggregate formation.

It is also possible that increased DNA degradation at higher temperatures leads to a more rapid disruption of hyperpolymers, which would have similar results. However, the experiments mentioned above were conducted under mild conditions (using formamide to permit reassociation at low temperature) and involve incubations of 1 hour or less. Extensive aggregate formation also occurs at much higher temperatures (in aqueous

buffers) in experiments involving up to at least 3 hours incubation. Therefore, it seems unlikely that thermal degradation alone can explain the observed temperature effects.

Hyperpolymer formation would be expected after extensive reassociation of randomly sheared simple DNA (that is, DNA without sequence repetition) (Britten *et al.*, 1974), and both hyperpolymers (Graham and Britten, 1973) and aggregates (A. Bendich, personal communication) have been observed in reassociated DNA preparations from T4 bacteriophage. Short repeated sequences interspersed with unique elements would not be expected to form hyperpolymers or aggregates when only the repeated DNA is allowed to reassociate (as in the present experiments). However, DNA fragments obtained by random shearing of regions of the genome containing clustered (or very long) repeated sequences might be expected to mimic simple DNA with regard to hyperpolymer and aggregate formation, and short fragments of sea urchin DNA have been shown to form hyperpolymers in amounts consistent with the fraction of that genome characterized by other techniques as clustered repeats (Graham and Britten, 1973).

The fact that a large fraction of pea DNA fragments form aggregates therefore suggests that the pea genome may contain many clusters of repetitive sequences. This view is supported by the fact that isolated aggregate DNA is highly enriched in repetitive sequences, as shown by its rapid and extensive reassociation (Fig. 27). Clustered repeats would seem likely on *a priori* grounds in many plant genomes, since in most plants so far examined a majority of the DNA is made up of repetitive sequences (Flavell *et al.*, 1974; and unpublished observations). However, our knowledge of sequence organization in plant genomes is still extremely limited, and more direct evidence on repetitive sequence clusters as well as other aspects

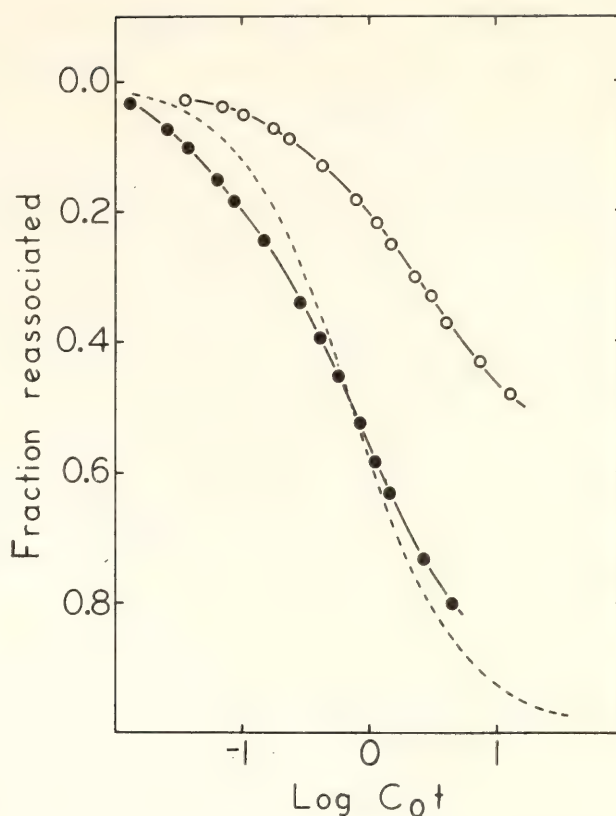


Fig. 27. Optical reassociation kinetics of separated aggregate and supernatant DNA sequences. Aggregates were formed from 350 nucleotide fragments incubated at $T_m - 24^\circ$ in buffer containing 70% formamide and isolated by centrifugation in the same buffer at the same temperature. About 25% of the DNA was pelletable, as expected at this incubation criterion. Aliquots of each fraction were then heat-denatured and reassociated in the same buffer, with reassociation being followed in the Gilford spectrophotometer by means of hypochromicity at 270 nm. After correction for collapse hyperchromicity, the estimated fraction reassociated was calculated by assuming that fully reassociated, randomly sheared DNA fragments will regain 80% of the hypochromicity observed in native DNA. Filled circles, aggregate DNA; open circles, supernatant DNA. The dotted line represents theoretical second-order kinetics for purposes of comparison.

of DNA organization is clearly required. At present, we are initiating experiments in these areas which we hope will begin to provide information useful in both evolutionary and developmental studies.

REFERENCES

- Britten, R. J., D. E. Graham, and B. R. Neufeld, *Methods in Enzymology*, 29, 363, 1974.

Flavell, R. B., M. D. Bennett, J. B. Smith, and D. B. Smith, *Biochem. Genet.*, 12, 257, 1974.

Graham, D. E., and R. J. Britten, *Carnegie Inst. Wash. Year Book* 72, p. 223, 1973.

COMPARISON OF DNA BASE SEQUENCES IN THREE SPECIES OF THE GENUS *Osmunda*

D. B. Stein¹ and W. F. Thompson

Miller (1967, 1971) has recently suggested that evolutionary lines leading to *Osmunda claytoniana* (interrupted fern) and *cinnamomea* (cinnamon fern) diverged more than 70 million years ago, but that only about one million years have elapsed since the *O. claytoniana* last shared a common ancestor with *regalis* (royal fern). This proposed phylogeny is based on the most extensive fossil record found among the ferns (Arnold, 1964) as well as on anatomical features of living representatives. However, the interrupted ferns and the cinnamon ferns are very similar morphologically in many respects (to the extent that the fronds are nearly impossible to distinguish in the field unless fertile pinnae are present), while the royal fern has a strikingly different leaf morphology. Since previous classifications (Hewitson, 1962) have considered interrupted fern to be more closely related to cinnamon fern than to royal fern, we felt it would be useful to attempt an assessment of the relative relationships of these three species based on interspecific DNA hybridization experiments.

DNA from all three species was extracted and purified using a combination of gel filtration and hydroxylapatite chromatography techniques. This procedure was developed after considerable preliminary experimentation. It permits high yields of pure DNA to be recovered from mature frond tissue collected from the field and stored after freeze-drying, thus eliminating the need for fresh material. In addition, it proved possible to separate the DNA from the large

amounts of polyphenolic compounds present in our initial extracts. Polyphenols have been a persistent problem in attempts to purify DNA from a number of plant species, especially ferns. In *Osmunda*, a variety of attempts to reduce the level of polyphenols by inhibiting polyphenol oxidase were uniformly unsuccessful.

Briefly, the procedure involves homogenizing the dried tissue in buffer containing sodium dodecyl sulfate at 60° in order to obtain efficient DNA extraction and minimize enzyme activity; after extraction with chloroform/octanol, the extract is concentrated by dialysis against polyethylene glycol, and the majority of the polyphenols and low molecular weight contaminants removed by chromatography on a column of polyacrylamide or agarose gel (Bio Gel P-200 or A-50 m). Final purification is then accomplished by hydroxylapatite chromatography in 8 M urea, using a procedure similar to that of Britten *et al.* (1974). It appears to be essential to avoid alcohol precipitation at least until after the gel filtration step, since numerous attempts to separate DNA from coprecipitated polyphenols were unsuccessful. We prefer to avoid precipitation until after the hydroxylapatite step, at which point the DNA is free of UV-absorbing contaminants as well as detectable polyphenols. For reassociation and hybridization experiments, the DNA was then sheared in the Virtis 60 homogenizer to a mean fragment length of about 400–500 nucleotides, and passed over columns of AG-50WX8 cation exchange resin and Chelex-100 chelating resin (Bio Rad).

In order to measure relationships

¹Department of Botany, University of Massachusetts, Amherst 01002.

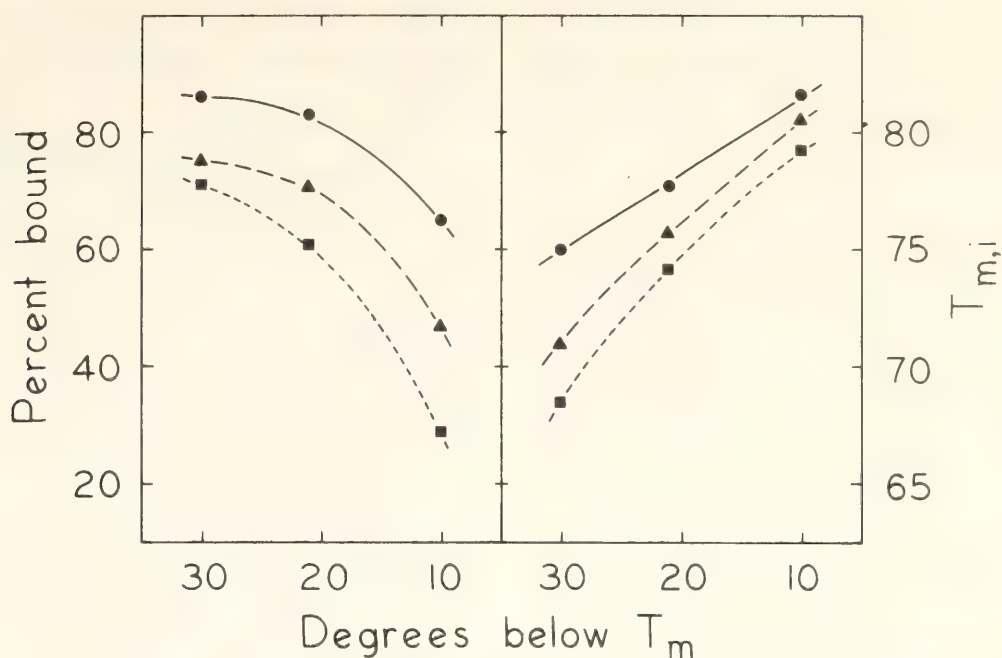


Fig. 28. Extent of duplex formation, and thermal stability of duplexes formed, between ^{125}I DNA from *O. claytoniana* and DNA from *O. claytoniana* (open circles), *O. cinnamomea* (open triangles) or *O. regalis* (open squares) after reassociation to $C_0t = 1.6 \times 10^4$ at three different temperatures in buffer containing 50% formamide, 1 M NaCl, 10 mM PIPES, pH 6.7. The T_m of native DNA fragments in this buffer was 64°.

among the three species, DNA from either *O. claytoniana* or *O. regalis* was labeled in vitro (while still double stranded) with ^{125}I following published procedures (Commerford, 1969; Prenskey *et al.*, 1973), and the labeled DNA was mixed with a 1000-fold excess of unlabeled DNA from the species to be compared. Aliquots of these mixtures in buffer containing 50% formamide and 1 M NaCl, 10 mM PIPES, pH 6.7, were heat denatured and then allowed to reassociate for appropriate times. Incubation periods of up to 5 days and concentrations of up to about 10 mg/ml were employed in order to achieve nearly complete reassociation. (The genome size of *O. cinnamomea* has been reported to be about 10,000 times that of *E. coli*; Sparrow, 1972). Reassociated duplexes, both homologous and heterologous (interspecific) were isolated by hydroxylapatite chromatography following dilution into 0.12 or 0.14 M Na phosphate buffer, and the precision of base-pairing analyzed by means of thermal elution from the hydroxylapatite columns.

Results of several experiments are

summarized in Fig. 28. In these experiments, mixtures of unlabeled DNA and *O. claytoniana* tracer were incubated to the same C_0t (with respect to the unlabeled DNA) and then applied to hydroxylapatite. Both the total amount of interspecific reaction (fraction of the tracer binding to hydroxylapatite) and the mean thermal stability ($T_{m,i}$) of the interspecific duplexes were determined. Similar measurements were made using the homologous mixture of *O. claytoniana* tracer with unlabeled *O. claytoniana* DNA. Incubations were conducted at three different temperatures; the higher temperatures establish a more stringent criterion for recognition of sequence homology, while the lower temperatures permit duplex formation between more widely divergent sequences.¹

¹ Reassociation at $T_m - 30^\circ$ resulted in extensive aggregate formation. In the experiments described here, aggregates were disrupted by briefly sonicating the reassociated DNA prior to application to hydroxylapatite. In similar experiments without sonication the melting profiles were altered in some respects, but interspecific differences were maintained. At $T_m - 20^\circ$, sonication had no effect on the melting profiles.

As the reassociation temperature is increased, the fraction of DNA forming duplexes is reduced, while the thermal stability of those duplexes which do form is increased. These effects are obvious in the homologous reaction but are even more pronounced in cross reactions between species. For example, the extent of interspecific duplex formation between *O. claytoniana* tracer and *O. regalis* DNA drops from 83% of the homologous value at $T_m - 30^\circ$ to 45% at $T_m - 10^\circ$, while the homologous value decreases by only 24%. In addition, it is worth noting that differences in cross-reactivity are still apparent at $T_m - 30^\circ$, and differences in thermal stability are detectable even at $T_m - 10^\circ$. Thus, DNA sequence differences between these

closely related species are clearly detectable under widely different reaction conditions.

Genome sizes in the three species are probably similar, since the number and size of the chromosomes are the same in all three, and we have shown that the DNA reassociation kinetics are virtually indistinguishable. Melting profiles of reassociated DNA are identical for all three species under all conditions and do not show any distinct, high-stability components which might represent recent, large-scale addition of repeated sequences to the genome. Furthermore, we have seen no indication of distinct thermal stability classes in interspecific hybrids (Fig. 29). Reciprocal experiments using *O. claytoniana* and *O. cin-*

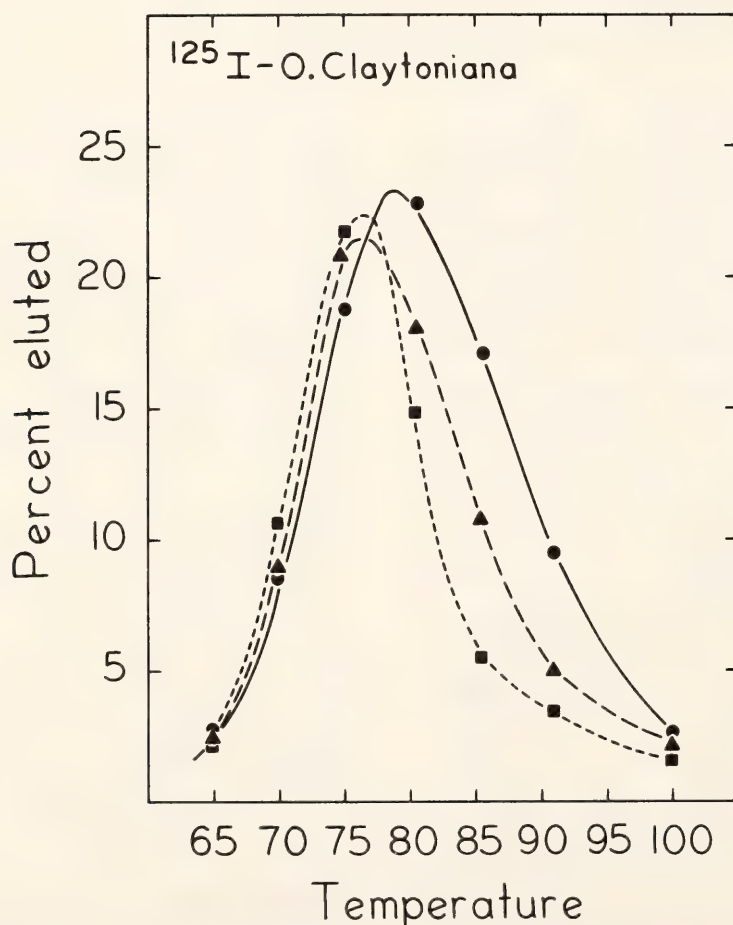


Fig. 29. Thermal elution profiles for duplexes formed between ^{125}I DNA from *O. claytoniana* and unlabeled DNA from *O. claytoniana* (open circles), *O. cinnamomea* (open triangles), or *O. regalis* (open squares). Reassociation was as described for Fig. 28, at $T_m = -21^\circ$. After dilution into 0.12 M Na phosphate buffer, samples were applied to hydroxylapatite at 60° , and the bound material was eluted by raising the temperature in 5° increments. Each point represents the percentage of total ^{125}I DNA in the reaction which eluted at the indicated temperature.

namomea as the source of labeled DNA yield essentially the same values for cross-reactivity and hybrid thermal stability.

From the data of Fig. 28, it is clear that DNA from *O. regalis* has less homology with *O. claytoniana* than does DNA from *O. cinnamomea* at all three temperatures and by both criteria of measurement. Thus we conclude that *O. claytoniana* is more closely related to *O. cinnamomea* than to *O. regalis*, and we support the earlier classifications (Hewitson, 1962) which placed *O. regalis* in a separate subgenus. Miller's proposed phylogeny (Miller, 1967, 1971) is inconsistent with our data unless it is assumed that (a) divergence between *O. regalis* and *O. claytoniana* during the last million years has involved more DNA change than that which occurred between *O. claytoniana* and *O. cinnamomea* over more than 70 million years, or (b) that parallel evolution produced a secondary increase in DNA homology between *O. claytoniana* and *O. cinnamomea*. Neither of these alternatives appears likely. Distinctions between closely related species are necessarily subjective in fossil material where the sample size is limited and preservation is often incomplete. DNA comparisons,

on the other hand, provide a more objective measure of overall relatedness, at least when the comparisons involve species with similar genome size and organization, under conditions in which most of the genome is included in the analysis. We feel that this technique will be increasingly important in studies of plant evolution at the species level, where the above conditions seem most likely to be met.

REFERENCES

- Arnold, C. A., *Mem. Torrey Bot. Club*, 21, 58, 1964.
 Britten, R. J., D. E. Graham, and B. R. Neufeld, *Methods in Enzymology*, 29, 363, 1974.
 Commerford, S. L., *Biochem.*, 10, 1993, 1969.
 Hewitson, W., *Ann. Mo. Bot. Gard.*, XLIX, 57, 1962.
 Miller, C. N., *Contrib. Mus. Paleontol. Univ. Mich.*, 21 (8), 139, 1967.
Ibid., 25 (8), 105, 1971.
 Prensky, W., D. M. Steffenson, and W. L. Hughes, *Proc. Natl. Acad. Sci. USA*, 70, 1860, 1973.
 Sparrow, A. H., H. J. Price, and A. G. Underbrink, *Brookhaven Symp. Biol.*, 23, 451, 1972.

DNA HYBRIDIZATION STUDIES IN *Atriplex* SPECIES

Heather G. Strong and William F. Thompson

Atriplex is a cosmopolitan genus, some species of which have adapted to marginal or extreme environments including salt marshes and deserts. Both C₃ and C₄ photosynthetic systems have evolved in the genus, and evidence is accumulating to indicate that C₄ photosynthesis has developed independently at least twice within the genus (Björkman *et al.*, 1973). It is of interest to understand relationships and the evolutionary distances between species of moderate and extreme habitats and between C₃ and C₄ species. Ideally, knowledge of these rela-

tionships will further efforts to understand evolutionary mechanisms and, perhaps, lead to improved breeding methods for crop plants which are photosynthetically more efficient and better adapted to restrictive environments (Berry, 1975). The most recent and complete phylogeny of *Atriplex* (Hall and Clements, 1923) predates the discovery of C₃ and C₄ photosynthesis. Although considered by systematists to represent the likely qualitative phylogeny based on morphological characteristics, the monograph states nothing

quantitative about the evolutionary distance between species.

DNA sequence comparisons have been undertaken among several *Atriplex* species. The reasons for such a study are twofold. Of primary concern is the question of interspecies relatedness. Since DNA is the basis of heritable changes during evolution, comparisons of DNA sequences should reflect evolutionary divergence. Molecular hybridization techniques permit various measures of sequence similarity or difference between genomes, depending on assay conditions used, and we hope that experiments using these techniques will be useful in evaluating evolutionary relationships between *Atriplex* species.

The second reason for *Atriplex* DNA comparisons is an extrapolation of the first. In addition to contributing to our understanding of systematic relationships, DNA comparisons within the genus should also advance our understanding of molecular events associated with speciation in plants. There is very little information concerning the magnitude of DNA sequence differences between closely related plant species. Such information would be especially valuable in a genus such as *Atriplex* where data from extensive studies of physiological adaptations are already available (Björkman *et al.*, 1971; Björkman *et al.*, 1973; Hatch *et al.*, 1972), and systematic genetic studies are currently in progress (Nobs, 1975).

Thus far, methods have been developed for extracting and purifying DNA from four species: *Atriplex hortensis* (C₃), *A. triangularis* (C₃), and *A. sabulosa* (C₄) (all of the subgenus *Euatriplex*); and *A. seranana* (C₄) (subgenus *Obione*), chosen to represent several habitats and diverse placements in the current phyletic scheme. The procedure involves extraction of freeze-dried tissue at 60°C and extensive deproteinization of the crude homogenate by treatment with pronase and subsequent extraction in 5 M NaClO₄-5% SDS (Wilcockson,

1973). Further purification steps include chromatography on hydroxylapatite in 8 M Urea-0.24 M Na-phosphate buffer and agarose gel chromatography. Optical reassociation experiments using 4 M NaClO₄-0.4 M Na-phosphate buffer, pH 6.8 (Hoyer and van de Velde, 1974) have been done to assess the feasibility of using this buffer system in interspecific hybridizations. The perchlorate anion lowers mean duplex thermal stability (T_m) and permits reassociation at lower temperatures than those required in the standard 0.12 M Na-phosphate buffer system (T_m -25°C is 60°C and 39°C in the standard phosphate and perchlorate buffer systems, respectively).

Results of preliminary hybridizations substantiate our expectation that the sensitivity of the technique is great enough to distinguish species differences. DNA from *A. hortensis* labeled with ¹²⁵Iodine was mixed with an excess of each of the four purified *Atriplex* DNA's. The mixtures were heat-denatured and allowed to reassociate at 39°C (T_m -25°). Homologous and heterologous duplex formation was measured between C_0t values (DNA concentration in moles/l \times reassociation time in sec) of 5.5×10^{-2} and 5.5×10^3 . Thermal stability profiles of homologous and heterologous duplexes were examined after reassociation to C_0t values of approximately 0.135, 55, and 1300 by thermal elution from hydroxylapatite.

Generally, our results are consistent with the Hall and Clements phyletic scheme in that I¹²⁵-DNA from *A. hortensis* appears to be more similar to that from *A. triangularis* than it is to DNA from either *A. sabulosa* or *A. seranana*. This conclusion is based on measurements of the extent of interspecific reaction and hybrid thermal stability after very extensive reassociation. Data from short incubations, in which only highly repeated sequences would be expected to reassociate, follow the same pattern.

However, after incubation to intermediate C_0t values to permit reassocia-

tion of less frequently repeated sequences, a high thermal stability component is observed in melting profiles of duplexes formed between the *A. hortensis* tracer and *A. serenana* DNA. The presence of this component raises the mean thermal stability of the hybrids to such an extent that *A. hortensis* DNA appears more similar to *A. serenana* than to either of the other species. Thus it would seem that *A. hortensis* total DNA contains some sequences which are more closely related to *A. serenana* DNA and others which are more closely related to sequences of *A. triangularis* and *A. sabulosa*. This suggests that the evolution of repeated sequences in *Atriplex* has not been a uniform process, and we believe that future studies of repeated sequence evolution in this genus should prove extremely interesting.

We are now turning our attention to the preparation of tracer DNA in which the repeated sequences have been separated from the unique sequences by preparative reassociation and hydroxylapatite fractionation. It is our expecta-

tion that hybridization experiments with these preparations will allow comparative studies of sequence evolution in these two portions of the genome.

REFERENCES

- Berry, J., *Science*, **188**, 644, 1975.
 Björkman, O., M. Nobs, R. Pearcy, J. Boynton, and J. Berry, in *Photosynthesis and Photorespiration*, M. D. Hatch, C. B. Osmond, and R. O. Slayter, eds., pp. 105–119, Wiley-Interscience, New York, 1971.
 Björkman, O., J. Troughton, and M. Nobs, in *Brookhaven Symp. Biol.*, **25**, 206, 1973.
 Hall, H. M., and F. E. Clements, *Carnegie Inst. Wash. Publ.*, **326**, p. 235, 1923.
 Hatch, M. D., *Carnegie Inst. Wash. Year Book* **71**, p. 135, 1972.
 Hoyer, B. H., and N. W. van de Velde, *Carnegie Inst. Wash. Year Book* **73**, p. 1102, 1974.
 Wilcockson, J., *Biochem. J.*, **135**, 559, 1973.

BACTERIAL PLASMIDS OF *Agrobacterium tumefaciens* AND THEIR ROLE IN CROWN GALL DISEASE

C. E. Rogler, W. F. Thompson, and J. E. DeVay¹

During the past few years there has been a rebirth of interest in research on the mechanism of crown gall tumor induction in plants. This has been stimulated primarily by two important discoveries. The first was the report from Schell's laboratory in Belgium (Zaenen *et al.*, 1974) which showed that all the pathogenic strains of *Agrobacterium tumefaciens* studied contained a covalently closed circular DNA plasmid (mol wt 1.12×10^8) and all the non-pathogenic strains studied did not contain the plasmid. The same group has

also reported that the pathogenic strains may lose the plasmid during growth at elevated temperature, with a concomitant loss of pathogenicity (Van Larebeke *et al.*, 1974).

The second discovery was initially reported by Kerr (1971) and has been further supported by Hamilton and Chopan (1975). These investigators have reported the development of a virulence transfer system for *Agrobacterium* which involves growth of the donor and recipient strains of bacteria in the presence of an actively growing crown gall tumor. Under these conditions, initially non-pathogenic strains of *Agrobacterium* have acquired virulence at a very high

¹ Department of Plant Pathology, University of California, Davis, California 95616.

frequency. Recent unpublished work by the Belgian group and also by Dr. E. W. Nester and co-workers at the University of Washington in Seattle has provided further support of the hypothesis that plasmid transfer is involved in the acquisition of virulence in this system.

Dr. Rogler's work on this project was

begun at the University of California at Davis in collaboration with Dr. DeVay, and we have continued the work with two main objectives in mind. The first objective is to study the function of the *A. tumefaciens* plasmid by comparing the plasmid species present in several attenuated mutants. Methods of attenu-

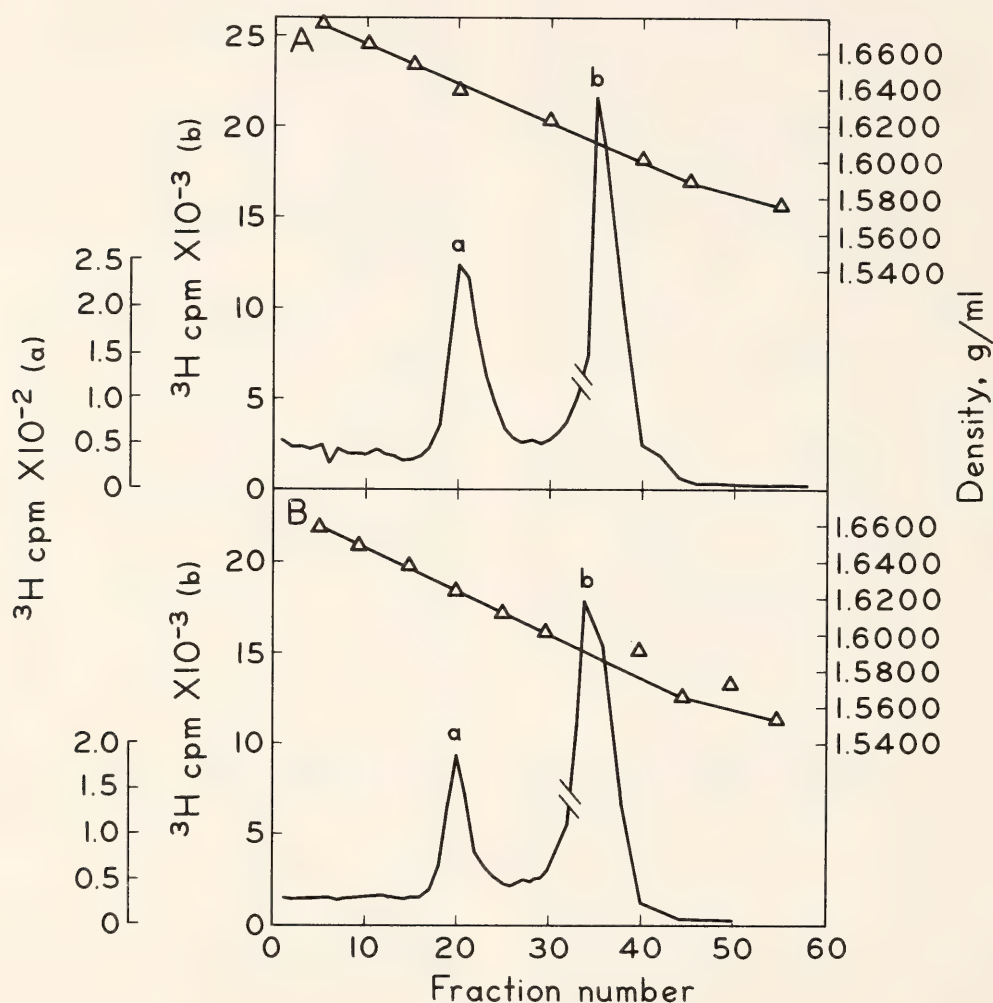


Fig. 30. Cesium chloride-ethidium bromide density gradient profiles of DNA preparations from two pathogenic strains of *Agrobacterium*. (A) Strain 209 isolated from a tomato gall (USA). (B) Strain K27 isolated from a peach gall in Australia. Cell cultures were grown and labelled with ^3H -thymidine in peptone medium according to the method of Zaenen *et al.* (1974). DNA preparations were obtained as follows: Washed cells (30 ml culture) were suspended in 1 ml 25% sucrose in 0.05 M Tris, pH 8.0, at 4°C. 5 mg Lysozyme (Worthington, salt free) was added, and the solution was incubated for 15 min. 0.05 ml of 0.25 M EDTA, pH 8.0, was added, and after further 15 min incubation 0.06 ml 20% Sarkosyl NL-30 was added to achieve lysis. After lysis was complete NaCl was added to 1 M, and the DNA was centrifuged at $48,000 \times g$ for 70 min in a Sorvall Model RC2B. The pellet was dissolved in TES buffer (Tris, 0.05 M, pH 8; EDTA, 0.005 M; NaCl, 0.05 M), NaCl added to 0.5 M and extracted 2 times with TES-saturated phenol. The DNA was precipitated with ethanol, dissolved in TES, and mixed with CsCl-ethidium bromide. Density gradient centrifugation was carried out in a Beckman 50°K fixed angle rotor at 44,000 rpm for 40 hr at 20°C. 50 μl aliquots of each gradient fraction were counted according to the method of Zaenen *et al.* (1974). Note the scale change between plasmid (a) and main-band (b) DNA peaks.

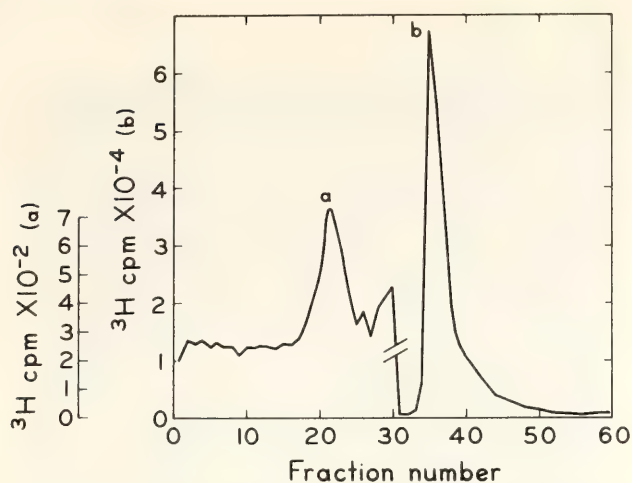


Fig. 31. Cesium chloride-ethidium bromide density gradient profile of a DNA preparation from nonpathogenic strain 210. Strain 210 was obtained by attenuation of strain 209 on high-glycine media (Van Lanen *et al.*, 1952) and retains its nonpathogenic character when transferred to nutrient agar. DNA preparation and centrifugation were carried out as in Fig. 30.

ation have included growth on high-glycine media, which may result primarily in alteration of the bacterial cell wall, and ultraviolet irradiation, which induces mutations in the DNA. The results of our initial studies show that plasmid species are present in two pathogenic strains we have studied (Fig. 30) and also in the glycine-attenuated mutant (Fig. 31), as judged by the presence of a second band of DNA at a higher buoyant density than chromosomal DNA in CsCl-ethidium bromide density gradients. These results show that an *Agrobacterium* strain can be attenuated without the complete loss of plasmid molecules from its genome. We are planning to conduct further studies to determine if the plasmid species in each isolate are identical. This system may enable us to obtain evidence bearing on the hypothesis that crown gall tumor induction involves a two-step process in which the pathogenic bacteria first binds specifically to the plant cell as shown by Yajko

and Hegeman (1971) and then transfers new genetic information. The glycine-attenuated mutant may be deficient only in the first step of this process.

The second objective of our work is to study the direction of information flow (DNA transfer) in a crown gall virulence transfer system similar to that developed by Kerr. Direct DNA transfer between donor and recipient strains in this system could involve conjugation, phage-mediated transduction, or transformation by naked DNA. However, Kerr (1971) has presented strong arguments which suggest that none of these mechanisms are responsible for the acquisition of virulence by initially nonpathogenic strains in this case. We are therefore beginning investigation of the possibility that the recipient bacteria acquire virulence directly from crown gall tumor cells which have previously acquired the tumor-inducing principle (perhaps an *A. tumefaciens* plasmid) from the donor bacteria.

REFERENCES

- Hamilton, R. H., and M. N. Chopan, *Biochem. Biophys. Res. Commun.*, **63**, 349-354, 1975.
- Kerr, A., *Physiol. Plant Path.*, **1**, 241-246, 1971.
- Van Lanen, J. M., I. L. Baldwin, and A. J. Riker, *J. Bacteriol.*, **63**, 715-721, 1952.
- Van Larebeke, N., G. Engler, M. Hols- ters, S. Von den Elsocher, I. Zaenen, R. H. Schilperoot, and J. Schell, *Nature*, **252**, 169-170, 1974.
- Yajko, D. M., and G. D. Hegeman, *J. Bot.*, **108**, 973-979, 1971.
- Zaenen, I., N. Van Larebeke, H. Teuchy, M. Van Montagu, and J. Schell, *J. Mol. Biol.*, **86**, 109-127, 1974.

A MODEL SYSTEM TO SIMULATE CHLOROPLAST MOVEMENT AND ACCOMPANYING TRANSMITTANCE CHANGES IN *Ulva*

S. J. Britz

Several aspects of a circadian rhythm of chloroplast orientation in the green alga *Ulva lactuca* var. *latissima* (Britz and Seliger, 1973; Britz and Briggs, in preparation; Britz *et al.*, in preparation) are under investigation. The thallus of this macroscopic alga has two layers of cells, each cell possessing one very large, cup-shaped chloroplast. The chloroplasts occupy the exterior cell face during the day and move at night into a profile orientation along the side walls (Fig. 32), these arrangements being termed "face" and "profile," respectively. The effect is to open an optical window in the cell which increases light transmittance through the thallus (as much as 200%). The movement continues in constant conditions and can be monitored readily by transmittance measurements (Fig. 33).

Transmittance changes occurring upon chloroplast orientation are the result of the sieve effect (Rabinowitch, 1951), that is, an alteration in the nonhomogeneous distribution of pigments in the cell. The involvement of the sieve effect has been tacitly assumed in past discussions, for example, the model system calculations by Pfau (1974). Figure 34 demonstrates a similar model and the calculations involved. Note that "non-homogenous" refers only to the lateral distribution of pigment across the light path. Thus, the face position chloroplast is equivalent to the pigment being spread evenly through the cell (using the Beer-Lambert Law, doubling the pathlength cancels halving the concentration). In the profile situation, there is an exposed area, r , having a transmittance of 1.0. The transmittance of the pigment package decreases, but the latter effect is greatly outweighed by the former, with the result being an overall increase in

transmittance. This process for an entire cell is described by the function:

$$(r \cdot 1) + (1 - r) \cdot T^{1/(1 - r)} \quad (1)$$

where T is the starting transmittance. For a given area exposed, the net ΔT is greatest when $T = 0$. ΔT decreases to 0 as T goes to 1.0.

The consequences of the sieve effect have been discussed mainly in terms of spectroscopy artifacts. For example, absorbance maxima are suppressed by light escaping around pigmented organelles or cells (Rabinowitch, 1951; Duysens, 1956) or being light-piped through cuvette walls (Butler, 1964). Dichroic orientation of pigments can produce a sieve effect (Slayter, 1970) if a rearrangement of pigment transition moments allows one or both components of the electric vector of light to pass differentially. Distortion of difference spectra may result for photochromic molecules localized in an organelle with a stable, high background absorbance (Spruit, 1972).

The sieve effect does play a role in more biological functions. Animals whose skin darkens or changes color do so by controlling the position of pigmented melanosomes which, when dispersed, absorb more light and reduce reflectance. There may be an interesting analogy to chloroplast orientation in *Ulva* in terms of movement mechanisms (utilization of microtubules and/or microfilaments, reported elsewhere in this Year Book) and circadian rhythms (*Uca*, the fiddler crab, possesses a well-known rhythm of color change due to the movement of melanosomes).

The chloroplasts of many plants orient with respect to light intensity or direction, usually so that in weak light the chloroplasts accumulate on the illu-

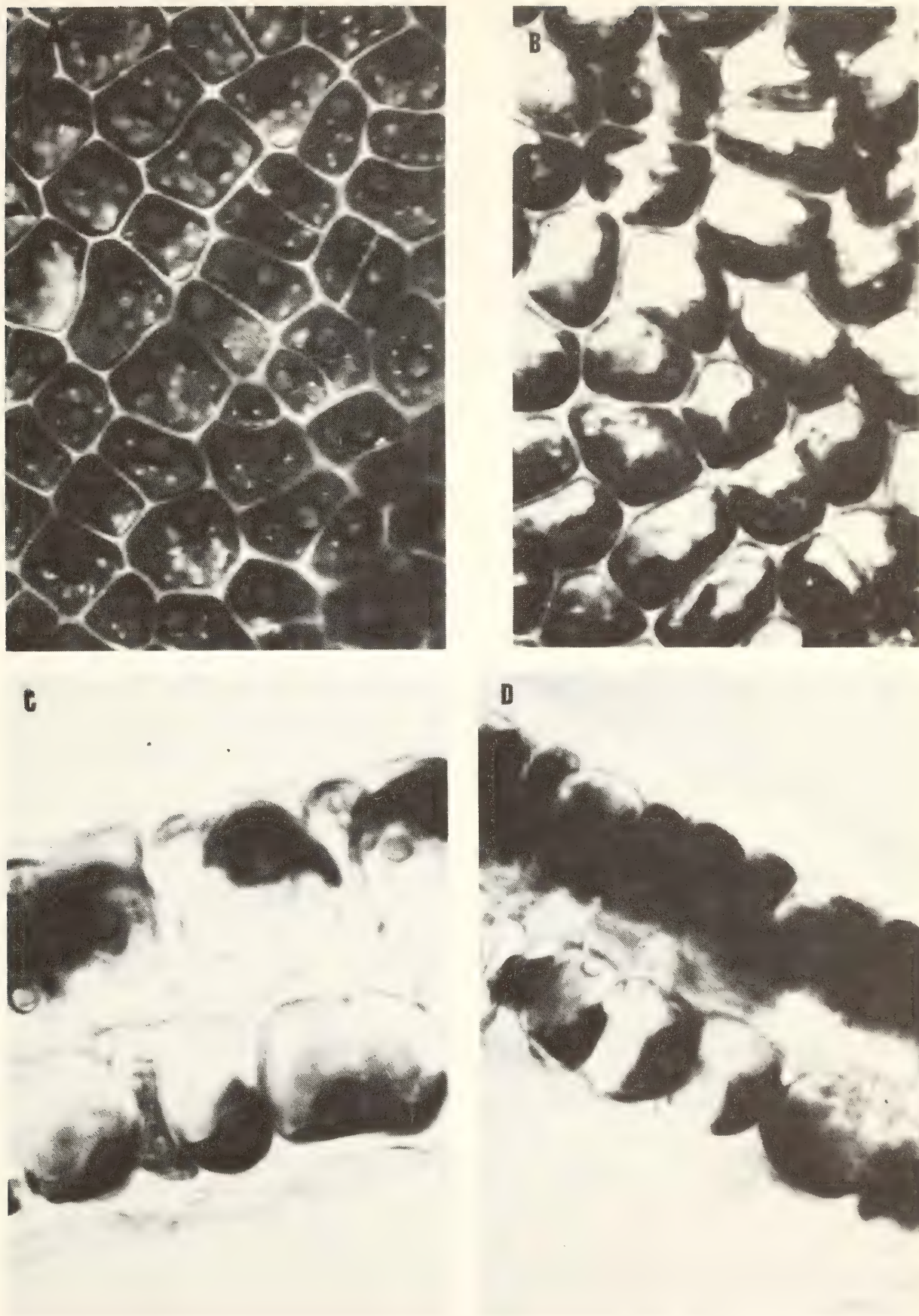


Fig. 32. *A* and *B* are in vivo whole-mount photomicrographs of *Ulva*; *C* and *D* are razor blade sections about 20 μm thick. *A* and *C* represent chloroplasts in face position; *B* and *D* represent chloroplasts in profile position.

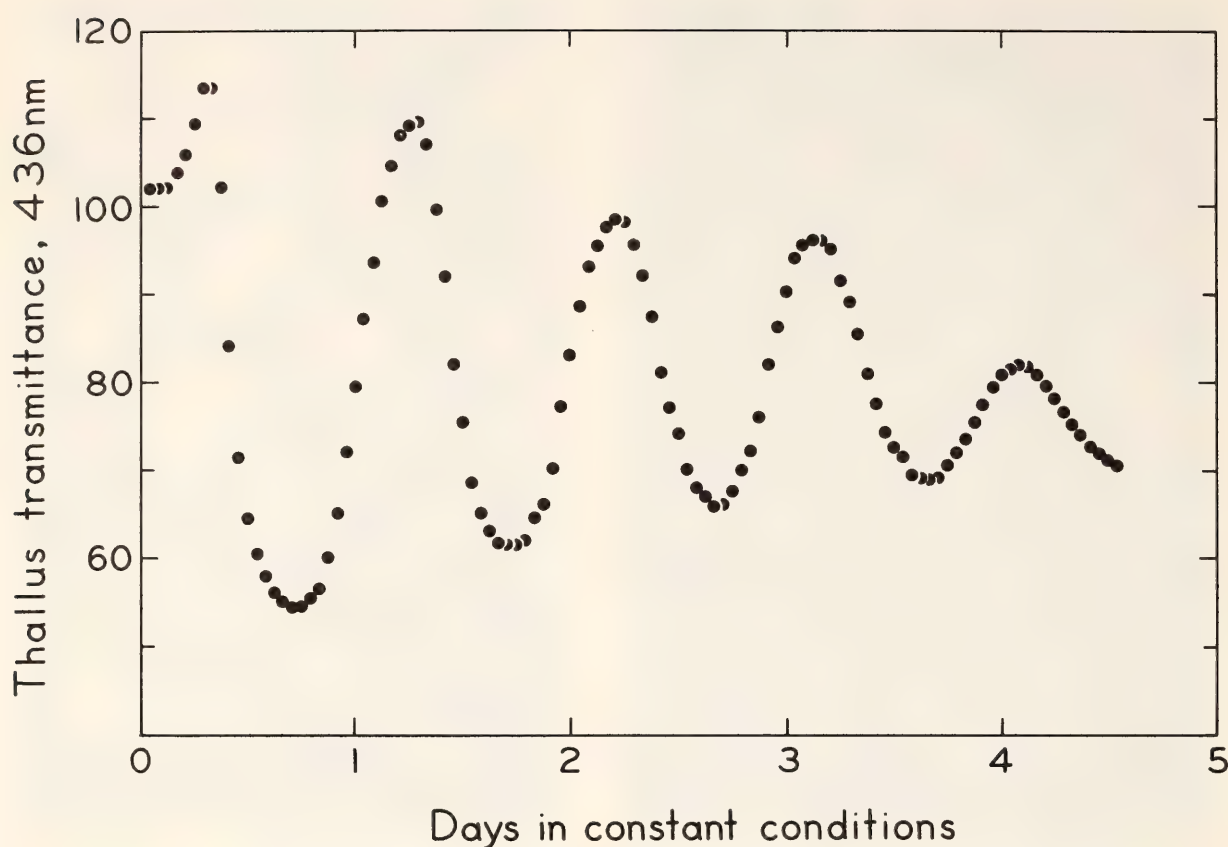


Fig. 33. The *Ulva* transmittance rhythm in continuous, dim 436 nm light. The results are from a prototype instrument designed to monitor long-term changes in up to 30 samples, each maintained in a small cuvette. Due to technical problems, the light intensity was not measured. Depending on the constant conditions chosen, the period (termed free-running) can have values between 21 and 27 hr. The period here was about 22.8 hr.

minated side of cells and intercept the maximum amount of incident light, while in strong light the chloroplasts retreat to walls parallel to the direction of illumination where by various means (shading, lens effects) they escape the full intensity. The concomitant changes in light absorption properties might be expected to influence photosynthesis. In fact, non-light-saturated photosynthesis in several plants was shown to be dependent on chloroplast position, while light-saturated photosynthesis was not (Zurzycki, 1955). This has led to the notion that control of chloroplast arrangement enables the optimization of photosynthesis in dim light and protection from possible damage (photobleaching, etc.) in strong light. While most investigations of chloroplast movement have been conducted on water plants or

algae whose thin leaves or thalli without air spaces facilitate direct microscope observation, land plants demonstrate the phenomenon as well (Biebl, 1954, 1955; Honda *et al.*, 1964; Inoue and Shibata, 1973, 1974). The adaptive significance of rhythmic chloroplast orientation in *Ulva* and its relation to the above-described phenomena is not clear, but it would seem that chloroplast orientation and the accompanying transmittance changes are of general importance.

Further progress in the field would benefit from a firm theoretical basis for the generation of transmittance changes that would take into account possible complications from chloroplast volume and pigment changes, dichroism, light scattering, more complex chloroplast shapes, etc. The ultimate importance of these parameters must be reckoned by

correlating them with transmittance as done by Zurzycki (1961) for chloroplast position, but it is not expected that this approach would be easy or that the re-

sult would be necessarily clear-cut. To aid in identifying and dealing with important variables, a computer program was designed to simulate chloroplast ori-

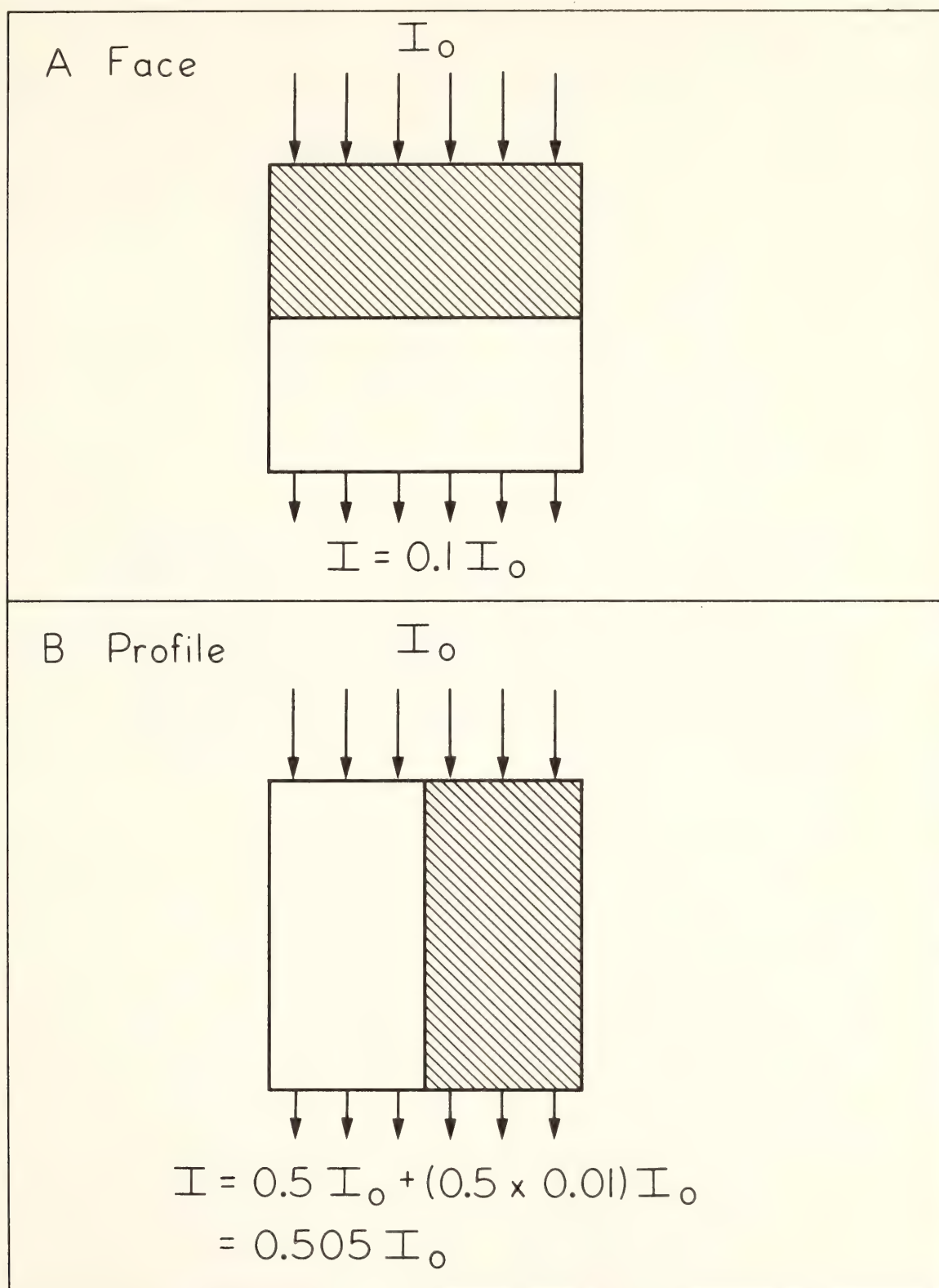


Fig. 34. Generation of transmittance changes by the sieve effect. A. Face position transmittance (I/I_0) is set to 0.1. B. In profile position, one-half the light goes by the chloroplast without being absorbed ($0.5 \times I_0$) while 1% of the other half is transmitted ($0.5 \times 0.01 \times I_0$). The net transmittance of the cell is the sum of the two sides and shows an increase ($\Delta T = 0.405$) in going from face to profile.

entation in *Ulva*. The model may serve a diagnostic function as well; using a simple system as in Fig. 34, it was possible to distinguish between a pure sieve effect and an effect complicated by simultaneous changes in any of the Beer-Lambert Law coefficients (concentration, extinction coefficient, and pathlength, referred to as CEL). The distinction was based on qualitative differences in the shape of the curves obtained from two different ways in which the data was manipulated. In a transmittance-dependent mode, the change in transmittance (ΔT) between extreme face and profile positions of the chloroplast is plotted against the face position transmittance (T_{face} , which is the minimum transmittance). In a position-dependent mode, the transmittance is plotted as a function of cell surface area exposed. Thus, the computer data can be correlated with measurable parameters.

The results presented here have been obtained using a more realistic model consisting of two layers of rectangular cells with irregular, cup-shaped chloroplasts. The effects of light leaking through cell walls, a possible pigment dichroism, and increases or decreases in the CEL factor are considered. The model cell itself is composed of 96 cubic units (4×4 across $\times 6$ deep) of which the chloroplast occupies 30. Figure 35 shows a perspective view of the cell with a face position chloroplast and top views of a cell with chloroplasts in face, intermediate, and profile positions. The model cell can be broken up into columns of chloroplast material which can be handled independently. The movement exposes 50% of the cell surface and is accomplished by a lateral shrinkage of one-half of the chloroplast coupled to a vertical extension of the other half. The transmittance, T , of a cubic unit of chloroplast is defined at the outset of a movement series. As in Expression 1, the transmittance of the cell, T_{cell} , is based on the sum of the fractional contributions of columns of chloroplast material

of the same CEL value. For example, the contribution of a segment which halves its lateral area while doubling its depth is

$$(a - \frac{a}{2} \cdot v_i) \cdot T^{(1 + v_i)} \quad (2)$$

where a is the fractional area occupied at the outset of a series and v_i is the fractional extent of movement.

CEL is varied by a factor which appears as an additional exponent of the transmittance

$$(1 + v_i \cdot s) \quad (3)$$

where s is chosen at the start of a series to be any value greater than -1 . Note that as movement proceeds, $v_i \cdot s$ goes from 0 to s and the CEL factor goes from 1 to $1 + s$. CEL is programmed to covary with the orientation which is the simplest alternative. While a change in CEL cannot distinguish between its three components, pigment concentration is independently measurable and a large-scale change in the extinction coefficient seems unlikely. It is hoped that this method would evaluate the effective pathlength of light through the chloroplast which might be modified by light scattering.

It is thought that the porphyrin ring of at least some of the chlorophyll molecules is oriented parallel to the plane of the thylakoid membrane. In *Ulva* the thylakoids run parallel to the length of the chloroplast. The potential for a variable dichroism would reduce light absorption because chromophores in the lip of the cup-shaped chloroplast would have only one component of their transition moment in the plane of the electric vector of the light. The effect would increase as the chloroplasts moved down the side of the cell into profile. In the model it is assumed the transition moments of the top layer of chloroplast material are all in the plane of the thallus and not affected by the dichroism. The expression for a column of chloroplast material would be

$$D \cdot T^n + (1 - D) \cdot T \tag{4}$$

where n is the number of layers of chloroplast and D is the dichroism factor which varies between 0.5 and 1.0. In a perfect dichroism ($D = 0.5$), half of the light would interact with all layers while the other half would interact with only the top layer of the chloroplast.

The cell wall allowance, w , corresponds to a certain fraction of incident light bypassing the chloroplast independently of its position. It is calculated as

$$(1 - w) \cdot T_{\text{cell}} + w \tag{5}$$

which also allows the consideration of incomplete movement to face by the

chloroplast, since the net effect is the same.

As a final consideration, the transmittance of the thallus is calculated as the square of Expression 5. This has the effect of treating each layer of cells independently, that is, assuming a random orientation of the wall space, cells, and chloroplasts of one layer with respect to those of the other, as actually appears to be the case. It also demonstrates a property of the sieve effect; the transmittance changes due to orientation decrease as the number of participating layers increases. Consider two cubical cells, as in Fig. 34, stacked one upon the other. The rectangular profile chloro-

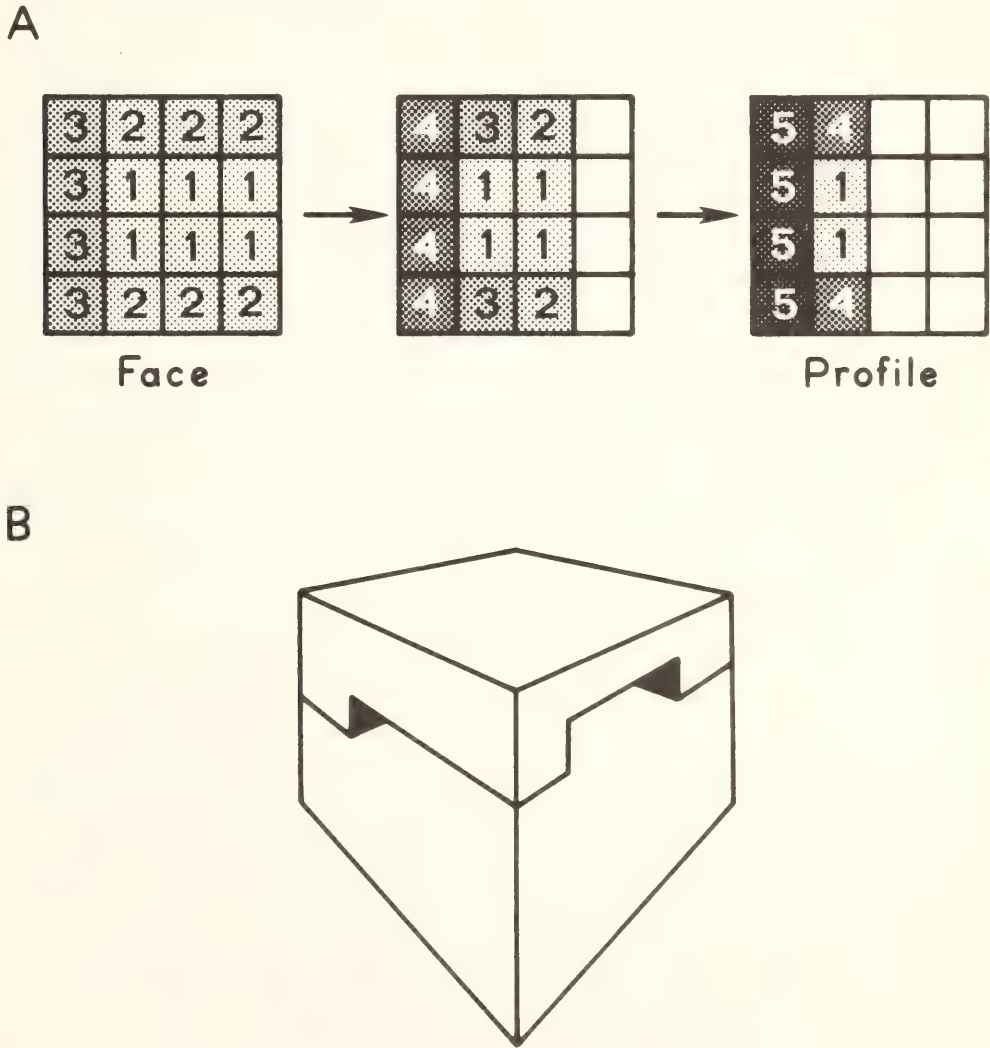


Fig. 35. Model system cell with cup-shaped chloroplast. (A) Top views of a cell with chloroplast going from face to profile. The number of layers of chloroplast material in each column is identified by number. (B) Perspective view of a cell with a cup-shaped chloroplast in face position.

plasts could line up one on top of the other, end over end, or on opposite sides of their respective cells. The probabilities of these states would be 0.25, 0.5, and 0.25, respectively, and the areas exposed would be 0.5, 0.25, and 0. The average total area exposed for two layers would be 0.25, or the square of what it would be for one layer (0.5). The multiplication of the transmittance of successive layers was used with empirical justification by Duysens (1956) and was recently proven in theory by Stokes (1975).

Some results for the transmittance mode of the model system are shown in Fig. 36 using CEL factors of 0.5, 1.0, and 2.0 and dichroism factors of 0.5 and 1.0. These extreme values are designed to demonstrate the range of effects. A 5% cell wall allowance was used which results in a shift of the minimum T_{face} to 0.0025 when $T = 0$. Otherwise, the cell wall allowance did not produce significant alteration of the results.

As discussed above, ΔT is generally greater when T_{face} is small. Also, all the

curves converge at the minimum and maximum T_{face} values. The CEL and dichroism factors have no effect then because they appear in or modify the use of exponents to calculate the transmittance.

The "control" curve (d) shows a ΔT maximum shifted away from the minimum T_{face} value, an effect not predicted by a simple model system. It is due to the cup-shaped chloroplast being a non-homogenous pigment distribution itself. That is, for a given number of cubic units of chloroplast material of some transmittance (not 0 or 1.0), the cup-shaped chloroplast has a higher transmittance than if the units were spread evenly across the cell like the model in Fig. 34. Conversely, the even distribution model would require about 21% less chloroplast material to give the same T_{face} as the cup-shaped model, but when shifted to a simple profile position the net cell transmittance (and hence ΔT) would be slightly lower than for the corresponding profile position cup-shaped chloroplast. Since this effect re-

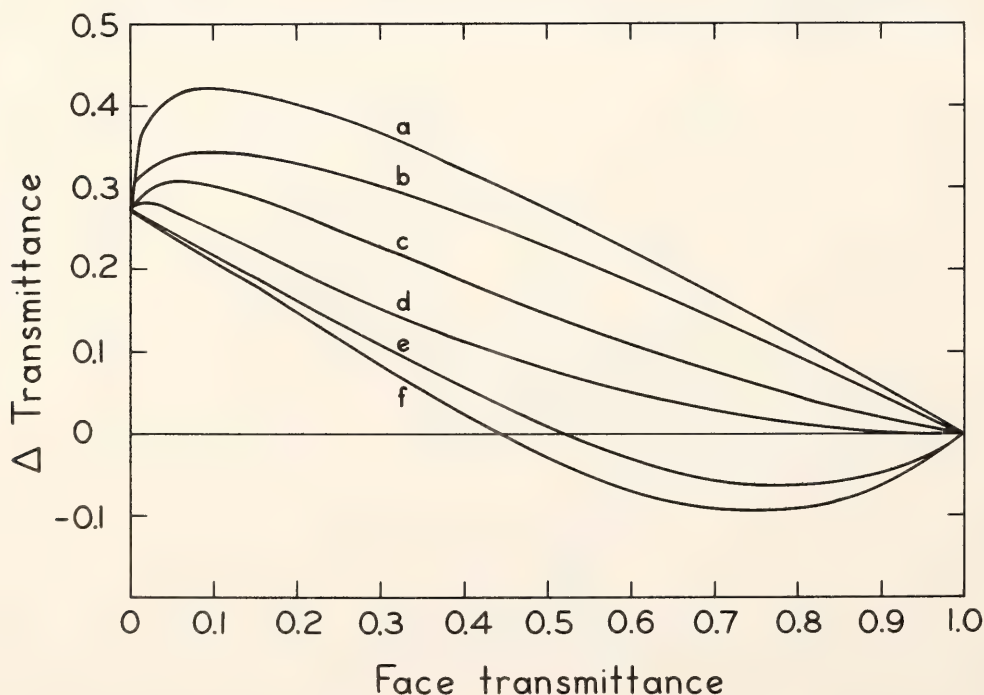


Fig. 36. Computer simulation data of transmittance changes for chloroplast orientation in the model system shown in Fig. 34 using the transmittance mode. The CEL factors are 0.5 for curves *a* and *b*, 1.0 for *c* and *d*, and 2.0 for *e* and *f*. The dichroism factors are 0.5 for curves *a*, *c*, and *e*, and 1.0 for *b*, *d*, and *f*.

lies on the exponential treatment of successive layers of chloroplast material, it falls away as T goes to 0 and 1.0 and reaches an optimum at some T_{face} determined by the parameters of the model.

Decreasing CEL (curves a and b) or using a dichroism (curves a , c , and e) yield greater ΔT 's because they increase the transmittance of profile position over face. They also shift the ΔT maximum to higher T_{face} values, which results again from optimizing the exponential effect at certain T_{face} values. Increasing CEL (curves e and f) decreases ΔT because the profile transmittance is decreased relative to the control. In these cases the optimization can result in minima at negative ΔT , that is, face-to-profile orientation is accompanied by a net decrease in transmittance—the opposite of what would be predicted by a simple sieve effect.

These data, which would appear even more characteristic in a first derivative plot, may be useful in diagnosing the involvement and/or significance of possible influencing factors. Aside from the presence and position of ΔT maxima or minima, the shape of the curves can be quite different. For example, curves c and d go through an inflection point where the slope of the declining ΔT curve becomes less negative; curves a and b do not. Preliminary results from *Ulva* show curves similar to d , but with the ΔT maximum shifted to somewhat higher T_{face} value and with a steeper ΔT decline. Whether ΔT might become negative cannot be determined, because of a lack of suitable T_{face} values in the appropriate range. However, too detailed a comparison would serve no purpose until the parameters of the model (relative chloroplast thickness, cell wall allowance, area exposed, etc.) can be adjusted to fit observations more closely.

Alternative transforms of the data, such as $\Delta T/T$ or $\Delta A = \log [(\Delta T/T) + 1]$, do not seem as sensitive to diagnostic treatment. Since data is expressed frequently in absorbance units, it should

be pointed out that ΔA is usually very small until about $A_{\text{face}} = 0.3$ when a rapid increase occurs. Above 0.8 to 1.0, the increase in ΔA is nearly linear in all cases.

The use of the position mode is shown in Fig. 37 starting at three T_{face} values spaced at critical intervals. It can be noted again the effects of CEL and dichroism are programmed to increase with increasing profile position. At low, starting T_{face} , the variables considered change mainly the rate of transmittance increase, a dichroism and decreased CEL giving somewhat flatter curves at the profile end. Transmittance measurements would tend to emphasize movement near profile position while minimizing changes around face position. Absorbance units would reverse this tendency, which is an important consideration in evaluating kinetics of chloroplast movement. At the highest T_{face} value, all the curves are essentially flat and show small ΔT increases except for an increased CEL which results in a steep transmittance decrease. This is as predicted from the transmittance mode data. Less expected was the behavior at an intermediate T_{face} value, where increasing the CEL resulted in a clear dip below the starting value even though the recovery yielded a net positive ΔT . This effect appears for both large (2.0) and moderate (1.5) increases in CEL. Of course, the minima occur when the total CEL change is only about one-half accomplished.

The position mode may provide a good means of detecting an increase in the CEL. This would be valuable because the negative ΔT minima seen in the transmittance mode occur at high transmittance values where a convenient marker wavelength may not be available.

In conclusion, it can be seen that the prediction of a simple model system (that face-to-profile movement should lead to transmittance increases) can fail under the influence of various factors.

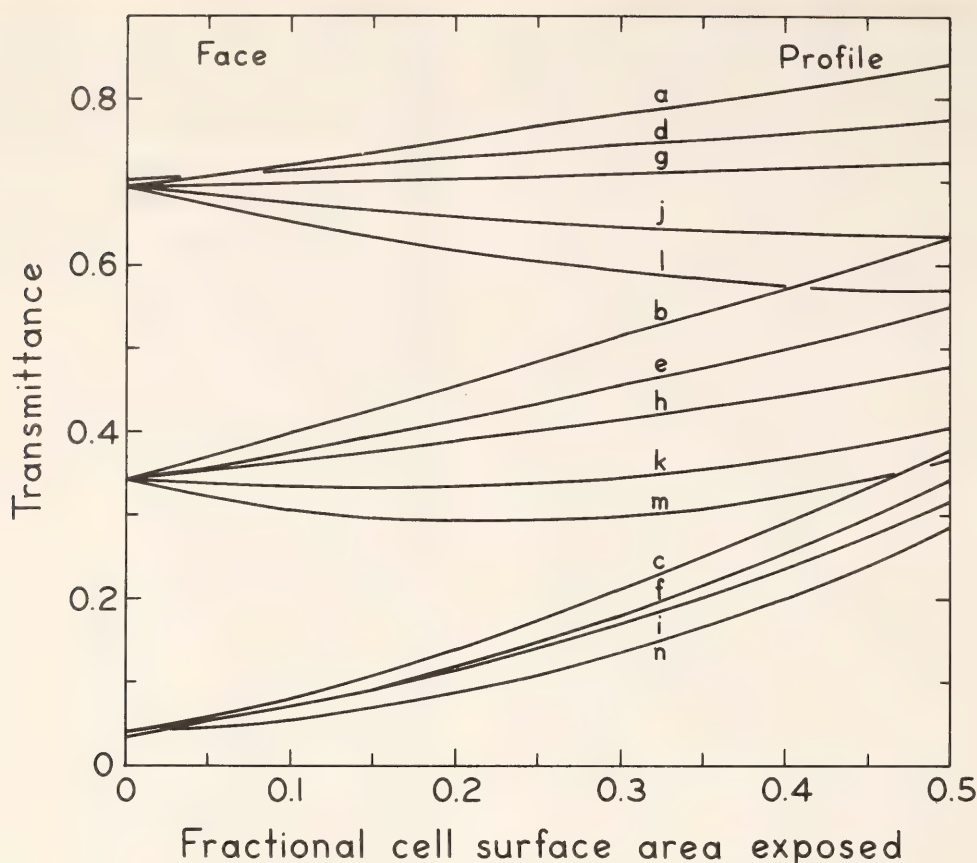


Fig. 37. Computer-simulation data of transmittance changes for chloroplast orientation in the model system shown in Fig. 34, using the position mode. The CEL and dichroism factors, respectively, for the following curves are: *a*, *b*, and *c*, 0.5 and 1.0; *d*, *e*, and *f*, 1.0 and 0.5; *g*, *h*, and *i*, 1.0 and 1.0; *j* and *k*, 1.5 and 1.0; and *l*, *m*, and *n*, 2.0 and 1.0.

However, fairly drastic changes in these factors are required. Significant deviations from the prediction could probably be avoided by making measurements at wavelengths where transmittance is low. Conveniently, it is these wavelengths that show the greatest changes, although the changes may not be directly proportional to chloroplast position.

The usefulness of the model can be further seen in considering some past reports. Biebl (1955) examined a number of land plants for transmittance change and chloroplast orientation and found that movement could be demonstrated in some species for which white light transmittance measurements yielded contrary indications. White light (coupled with photocell sensitivity) might select for changes at wavelengths of higher transmittance which, as considered above, would be more susceptible to modification by CEL changes.

The results of Inoue and Shibata (1973, 1974) give fairly small ΔA 's which might be expected from the model based on multilayer systems with a greater amount of light scattering. Scattering decollimates light and causes a loss of positional information as demonstrated by the data of Zurzycki (1961). The opal glass and dual beam method used by Inoue and Shibata corrects only for the artifacts in collecting and measuring scattered light and not for the effects of scatter within the tissue.

The benefits of a more complex model system seem clear. Aside from helping to demonstrate how transmittance changes are generated, the diagnostic potential is improved. Future developments might take into account possible chloroplast volume changes and light scattering along with CEL changes not in phase with movement. Breaking the chloroplast into small cubes also facilitates the

application of the model to organisms whose cells contain many small chloroplasts.

REFERENCES

- Biebl, R., *Flora*, 141, 163, 1954.
 Biebl, R., *Flora*, 142, 280, 1955.
 Britz, S. J., and H. H. Seliger, *Biol. Bull.*, 144, 12, 1973.
 Butler, W. L., *Ann. Rev. Plant Physiol.*, 15, 451, 1964.
 Duyser, L. N. M., *Biochim. Biophys. Acta*, 19, 1, 1956.
 Honda, S. I., T. Hongladarom, and S. G. Wildman, in *Primitive Motile Systems in Cell Biology*, R. D. Allen and N. Kamiya, eds., Academic Press, London, 1964.
 Inoue, Y., and K. Shibata, *Planta*, 114, 341, 1973.
 Inoue, Y., and K. Shibata, *Plant Cell Physiol.*, 15, 717, 1974.
 Rabinowitch, E. I., *Photosynthesis and Related Processes*, Vol. II(1), Wiley-Interscience, New York, 1951.
 Pfau, J., Ph.D. Thesis, Philipps-Universität Marburg, 1974.
 Slayter, E. M., *Optical Methods in Biology*, Wiley-Interscience, New York, 1970.
 Stokes, A. N., *Arch. Biochem. Biophys.*, 167, 393, 1975.
 Spruit, C. J. P., in *Phytochrome*, K. Mitrakos and W. Shropshire, eds., Academic Press, London, 1972.
 Zurzycki, J., *Acta. Soc. Bot. Pol.*, 24, 27, 1955.
 Zurzycki, J., *Acta. Soc. Bot. Pol.*, 30, 503, 1961.

INHIBITOR STUDIES ON THE MECHANISM OF CHLOROPLAST MOVEMENT IN *Ulva*

S. J. Britz

An important and fascinating aspect of cells and organelles is their ability to move, a function believed to result from the action of two general classes of fibrillar, polymeric proteins—microtubules and microfilaments. For a comprehensive review of the properties of these proteins and for references pertinent to the discussion below, see the review by Hepler and Palevitz (1974).

Inhibitor studies were undertaken as a preliminary investigation into the possible involvement of microtubules and/or microfilaments in rhythmic chloroplast movement in *Ulva*. The plant alkaloid colchicine binds irreversibly to tubulin dimers, the subunits of microtubules, and disrupts the equilibrium between polymer and subunit. The fungal metabolite cytochalasin B inhibits many apparently microfilament-related movement phenomena in plants and animals, but it may be much less specific than colchicine, since cytochalasin B in-

hibits other processes not readily associated with motility.

Sodium azide, a terminal respiratory inhibitor, was applied to see if metabolic energy was required for either or both phases of movement. [Ethylenbis(oxyethylenenitrilo)] tetraacetic acid (EGTA) is a calcium chelator. The regulation of calcium concentration is important in the control of contraction in muscle and may also be a regulatory factor for microfilaments which appear to be composed of the muscle thin-filament protein actin. Calcium may play a similar role with microtubules; isolated spindles possess calcium-stimulated ATPase activity. On the other hand, even micromolar concentrations of calcium may inhibit the in vitro assembly of tubules from subunits. A positive EGTA effect might be difficult to interpret, since calcium may affect membranes or metabolic energy supply through the binding of coupling factor.

The results (Fig. 38) indicate that colchicine, given at the start of continuous darkness or at the absorbance minimum (profile position), inhibited profile-to-face movement, but not the reverse. Fifty percent inhibition was achieved at about 3 mM. In addition, if the thalli were washed after one cycle (24 hr), the colchicine remained bound and the percentage of inhibition was seen to remain constant for the second and third cycles, indicating little new tubulin production. If the colchicine were kept in the medium, a large increase in the inhibition was seen in the second cycle, which could

be reversed by prior UV irradiation (which forms nonbinding lumi-colchicine).

The inhibition of only one direction of movement (profile to face) may be due to the microtubules being involved in only that aspect, or perhaps the tubules are not sensitive to colchicine during face-to-profile movement. The increase in inhibition on the second cycle may be because the colchicine is slow in entering the cells or because only some of the tubules are sensitive at certain times. The latter view is supported because the degree of inhibition did not

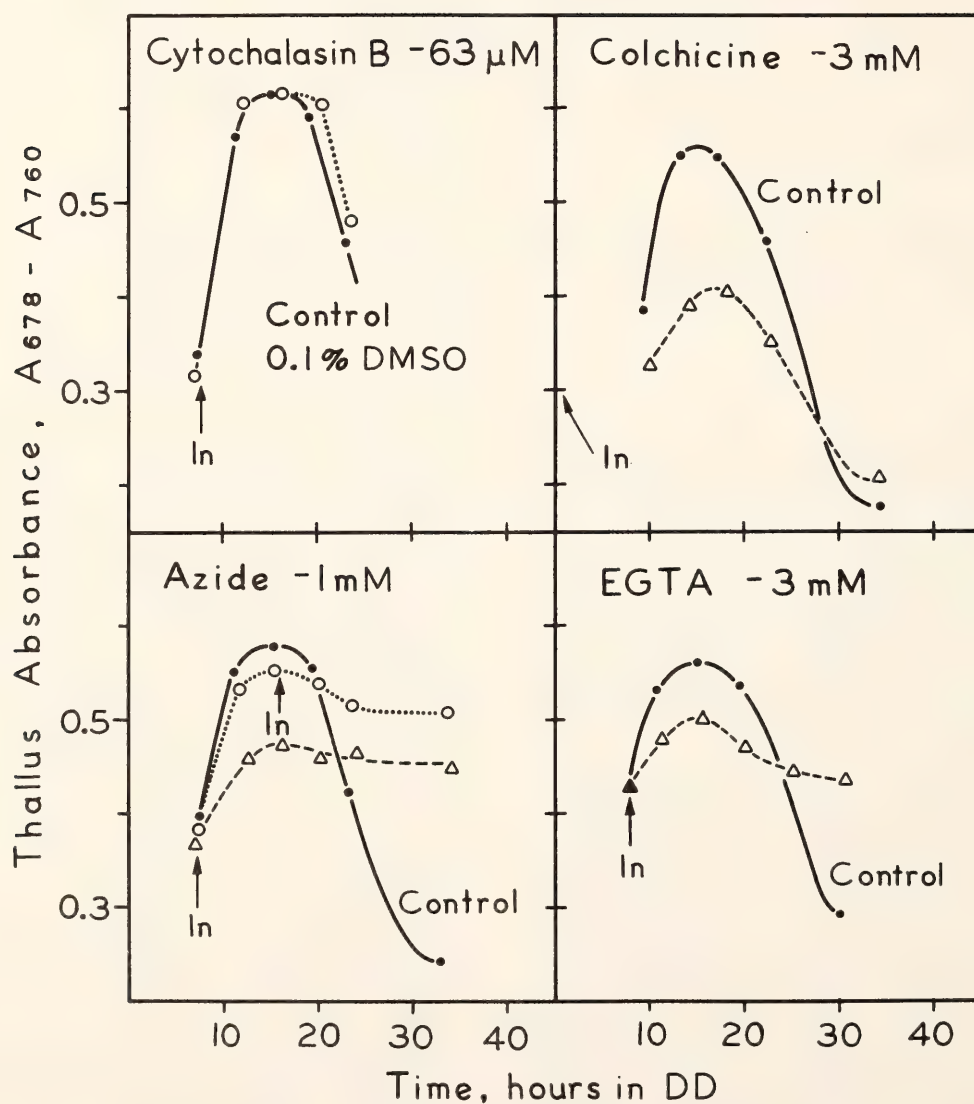


Fig. 38. The effect of inhibitors on rhythmic *Ulva* chloroplast movement. The inhibitors were added at times marked by the arrows and "In"; concentrations are as shown. Absorbance measurements (as described in Britz and Briggs, in preparation) were used to monitor the movement which was verified by direct microscope observation. Constant darkness (DD) was chosen to avoid complications from metabolic energy supply, possible light-induced pigment or chloroplast volume changes, etc. Colchicine is also somewhat light sensitive.

seem to depend on whether the colchicine was added at the start of the dark period or 7.5 hr later during maximum profile position. If the microtubules have polarity and one end undergoes a colchicine-sensitive assembly-reassembly process, this feature might account for the failure to achieve full face position without any effect on completing the movement to profile.

Microtubules do show variable drug sensitivity. Intact cilia and flagella are insensitive to colchicine, but their isolated tubulin will bind colchicine, which can inhibit the assembly reaction. Cytoplasmic microtubules are generally sensitive to colchicine, but this need not be the case. Microtubules involved in pigment granule movement in cells of a teleost fish (Murphey, 1973) were colchicine sensitive only after first being depolymerized in the cold. In this sense they are more like the microtubules of cilia and flagella. It is thought an increase in cross-bridging between tubules may stabilize them.

Although microtubules are involved in at least one direction of movement, they might not be generating the motive force. It has been suggested they may function alternatively as guide elements for directed vesicle transport. If so, then motility in one or both directions might actually be caused by some other system, perhaps microfilaments. However, cytochalasin B had no effect on movement in either direction even at relatively high concentration. Based on its rapid inhibitory action on cytoplasmic streaming in a variety of plants and algae, it seems

unlikely that the drug is not getting into the cell or that *Ulva* possesses a cytochalasin B-insensitive microfilament system. Since *Ulva* does not have observable cytoplasmic streaming, this possibility cannot be tested further.

Azide inhibits movement in both directions, indicating an active mechanism is involved in both phases of the movement. Interestingly, the final arrangement of chloroplasts under azide inhibition was not random, but intermediate. The EGTA results are quite similar to the azide effect, suggesting a role for calcium in the movement process. However, what this role might be cannot be specified.

The results suggest that microtubules are active in movement in at least one and perhaps both directions. Thus, rhythmic *Ulva* chloroplast movement would seem to be mechanistically different from light-induced chloroplast movement in *Mougeotia* (Wagner *et al.*, 1972) and *Funaria* (Schönbohm, 1973), which are both cytochalasin B-sensitive. Regardless of whether this difference holds up in other cases, *Ulva* seems well suited for further motility studies.

REFERENCES

- Hepler, P. K., and B. A. Palevitz, *Ann. Rev. Plant Physiol.*, **25**, 309, 1974.
Murphey, D. B., *Abstr. 13th Ann. Mtg. Am. Soc. Cell Biol.*, **239**, 1973.
Schönbohm, E., *Ber. dtsh. bot. Ges.*, **86**, 407, 1973.
Wagner, G., W. Haupt, and A. Laux, *Science*, **176**, 808, 1972.

LOCALIZATION OF SOME NEW PHYTOCHROME REACTIONS WITHIN THE CELL

John M. Mackenzie, Jr., and Winslow R. Briggs

The intracellular localization of phytochrome was visualized in dark-grown oat (*Avena sativa* L., cv. Garry) coleoptiles and rice (*Oryza sativa*, L.) inter-

modes following various light treatments with an indirect peroxidase-antiperoxidase antibody-labeling method (Coleman and Pratt, 1974; Pratt and Cole-

man, 1971; Pratt and Coleman, 1974). Phytochrome is generally distributed throughout the cytoplasm in cells which have not been exposed to light prior to fixation. Within at most 8 min following the onset of saturating red irradiation, phytochrome, now present in its far red-absorbing form (Pfr), becomes associated with discrete regions of the cell. These regions do not appear to be nuclei, plastids, or mitochondria. Following phototransformation back to the red-absorbing form (Pr), phytochrome gradually relaxes back to its general distribution, a process requiring about 2 hr at room temperature. For details, see Mackenzie *et al.* (1975).

The redistribution of phytochrome was next studied at 3°C following a very brief but high-intensity and saturating dose of red light. The purpose was to determine the rate of phytochrome redistribution following its transformation to the far red-absorbing form. Even at 3°C, the redistribution is complete within 2 min. Both sodium azide (Butler and Lane, 1965) and mercaptoethanol (Furuya *et al.*, 1965) retard another known reaction of phytochrome *in vivo*—namely the dark destruction of Pfr. They both slightly retarded the redistribution phenomenon but did not prevent it when used at concentrations which completely inhibited destruction. The two inhibitors also had no effect on the subsequent relaxation reaction following reconversion of Pfr to Pr and a subsequent dark period of 2 hr.

The reactions studied in oats and rice could not be observed in corn, zucchini squash, or barley seedlings, at least under the light microscope. Before one assumes that the redistribution and relaxation phenomena are not general properties of phytochrome in all species, however, and hence a part of normal cellular events, one must study the phenomenon at the electron microscope level. Such studies are planned.

The localization reaction was also used to follow the course of events dur-

ing the destruction in oat coleoptiles of Pfr in continuous illumination. The very densely stained areas were the first to disappear. They were gone within 90 min, but activity now appeared associated with nuclei and plastids not previously labeled. This association remained evident for the next 6 hr but by 12 hr, all activity had vanished.

If tissue samples of oat coleoptiles were held at -1°C, the redistribution phenomenon could be completely prevented. Hence it was possible to see whether the redistribution into small dense packages within the cell had any effect on the apparent amount of phytochrome measurable by dual wavelength spectrophotometry. Spruit (1972) had indeed proposed that the phytochrome destruction might represent not actual destruction of the pigment but rather loss of measurable photoreversibility caused by sequestering of phytochrome into small and discrete particles. However, the present results showed no difference in measurable photoreversibility whether the samples were measured at temperatures at which sequestering occurred (3°C or higher) or did not occur (-1°C). In all cases samples were fixed immediately for the localization procedure following the reversibility measurement to verify that the phytochrome either was or was not sequestered according to the temperature at which the phototransformation was accomplished.

When phytochrome in oats is transformed to Pfr, allowed to become sequestered, and then reconverted to Pr, about 30% of this Pr is destroyed. The time course showed a 15 min lag period followed by log-linear first-order kinetics for an additional 1½ hr. At the end of this period destruction of Pr ceased, and the remaining population of phytochrome remained stable. There is a striking similarity between the sequestering of phytochrome and its destruction as Pr. However, the same phenomenon could not be detected in barley seedlings. Barley does not show the re-

distribution phenomenon reported above for oats. Thus the redistribution phenomenon may be related to the Pr destruction mechanism. Similar studies on rice (in which phytochrome does become redistributed following red light treatment) and corn (in which the phytochrome does not appear to become redistributed) are planned.

Most of these studies were done while the senior author was in the laboratory of Dr. Lee H. Pratt at Vanderbilt University and will be published jointly with Dr. Pratt and Dr. Coleman who collaborated in the research in its early stages and developed the antibody-labeling method for use in phytochrome studies.

STUDIES ON A POSSIBLE PHOTORECEPTOR FOR PHOTOTROPISM IN CORN

Winslow R. Briggs

In addition to the photosynthetic pigments and phytochrome, there exists in higher plants a photoreceptor which is excited only by blue and ultraviolet light and which mediates a variety of physiological and chemical reactions including phototropism in coleoptiles (Thimann and Curry, 1960). The action spectrum shows a single broad band near 370 nm, and a second band between 400 and 500 nm with considerable fine structure. Over the years there has been a considerable controversy as to whether this photoreceptor is a carotenoid or a flavin of some sort.

The pigment also occurs widely in the fungi. Recently Poff and Butler (1974, 1975) have published evidence that blue light, absorbed possibly by a flavin, brings about the photoreduction of a *b*-type cytochrome in the cellular slime mold *Dictyostelium discoideum* and the filamentous fungus *Phycomyces blakesleeianus*. A crude action spectrum for the photoreduction showed a maximum near 465 nm, a wavelength at which the cytochrome itself did not absorb appreciably.

REFERENCES

- Butler, W. H., and H. C. Lane, *Plant Physiol.*, **40**, 13, 1965.
Coleman, R. A., and L. H. Pratt, *J. Histochem. Cytochem.*, **22**, 1039, 1974.
Furuya, M., W. G. Hopkins, and W. S. Hillman, *Arch. Biochem. Biophys.*, **112**, 180, 1965.
Mackenzie, J. M., Jr., R. A. Coleman, W. R. Briggs, and L. H. Pratt, *Proc. Nat. Acad. Sci. USA*, **72**, 799, 1975.
Pratt, L. H., and R. A. Coleman, *Proc. Nat. Acad. Sci. USA*, **68**, 2431, 1971.
Pratt, L. H., and R. A. Coleman, *Am. J. Bot.*, **61**, 195, 1974.
Spruit, C. J. P., In *Phytochrome*, K. Mitrakos and W. Shropshire, Jr., eds., p. 77, 1972.

Muñoz and Butler (1975) carried these studies somewhat further with the fungus *Neurospora crassa*, showing that the action spectrum for photoinduction of the cytochrome reduction in vivo is very similar to the action spectrum for suppression of expression of a circadian rhythm of conidiation in *Neurospora* (Sargent and Briggs, 1967). They also showed that light treatments which produced bleaching in the samples also appropriately reduced the size of the signal inducible by 465 nm light. The bleaching difference spectrum was consistent with the photolysis of a flavin.

The purpose of the present study was to investigate certain membrane fractions obtained from corn coleoptiles to see whether they might have a pigment with the properties of such a photoreceptor. Dark-grown corn coleoptiles were harvested under dim green light and chopped and ground in the following buffer: morpholinopropane sulfonic acid buffer, pH 7.4, 0.1 mM MgCl₂, 3 mM EDTA, 14 mM 2-mercaptoethanol, and 8% sucrose (4 ml buffer/g tissue). After

filtration to remove large particles, the crude extract was successively centrifuged at 500, 9000, and $21,000 \times g$ (15 min each) and $50,000 \times g$ for 1 hr. The two final pellets (designated 21KP and 50KP) were then resuspended in the same buffer but at pH 7.0 and without mercaptoethanol. The turbid solutions could then be examined in a Perkin-Elmer Model 356 Dual Wavelength Spectrophotometer designed for measurement of samples with substantial light scattering. Both pellets had a major absorption band near 420 nm plus minor bands at 445 and 475 nm. Both clearly contained a *b*-type cytochrome, accounting for the 420 nm band, as judged by oxidized-minus-reduced difference spectra; and both contained $1\text{--}2 \times 10^{-7} M$ flavin (converted to lumiflavin by alkaline photolysis and assayed by fluorescence) on a tissue basis, accounting for the 445 and 475 nm bands (Fig. 39). Over 60% of the cytochrome in the 50KP could be reduced by NADH, while less than 30% could be reduced in the 21KP. The 50KP was enriched for endoplasmic reticulum (assayed by measuring NADH-dependent cytochrome-*c* reductase after Lord *et al.*, 1973), and the 21KP was enriched in a membrane fraction which would bind naphthylphthalamic acid, considered by Hertel *et al.* (1972) to be a marker for plasma membrane. Sucrose gradients (20%–50% sucrose) were layered with supernatant following the $9000 \times g$ centrifugation and run to equilibrium in the ultracentrifuge to determine the location of the two membrane fractions. The NADH-reducible cytochrome was clearly superimposed over the endoplasmic reticulum marker, while the non-NADH-reducible cytochrome coincided with naphthylphthalamic acid binding. Both fractions contained an electron transport chain from NADH to molecular oxygen, in both cases cyanide resistant. Mitochondria, located by assaying cytochrome-*c* oxidase, banded well below both fractions.

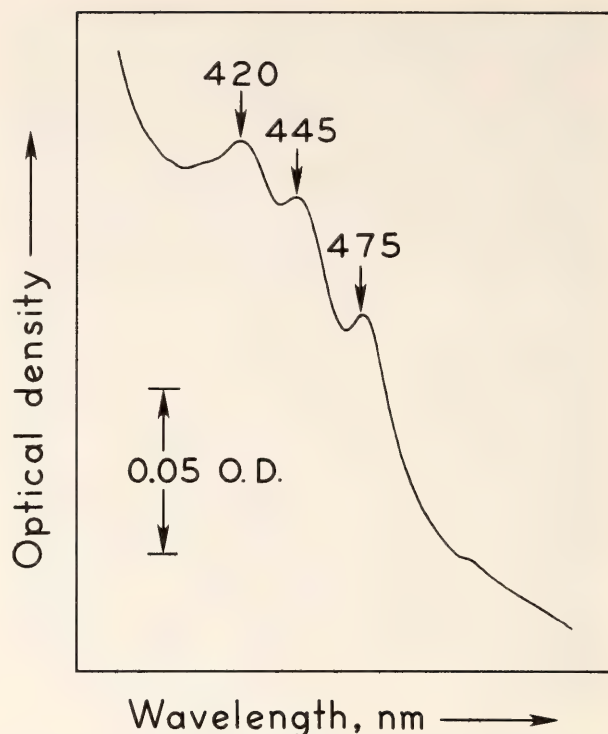


Fig. 39. Absorption spectrum of resuspended $21,000 \times g$ pellet. That of the $50,000 \times g$ pellet was identical.

Recently Hertel (personal communication) has demonstrated that both fractions have binding sites for riboflavin. The affinity of these sites for riboflavin is only one-tenth that for the naturally occurring (and currently unidentified) major soluble flavin in corn and the fungus *Phycomyces*. With the naturally occurring flavin, the sites are saturated when the flavin concentration is roughly $10^{-5} M$.

Briggs (1960) showed that a brief (e.g., 2 min), very high intensity exposure of blue light not only did not induce phototropic curvature in corn coleoptiles but also left them insensitive to normally effective phototropic stimuli. Recovery of phototropic sensitivity required about 40 min darkness. Thus the properties of the two pellets were examined following extraction from plants which had received the same brief, high-intensity light treatment to see whether their pigment composition was in any way altered, and if so, whether it showed the same pattern of dark recovery as phototropic sensitivity. In the 21KP the

light treatment induced an increase of between 20% and 30% in flavin (with respect to total protein) over dark controls. The extra flavin had decayed back to the dark level within 1 hr in darkness preceding extraction.

Briggs (1963) also showed that red-light treatment prior to phototropic induction would decrease the phototropic sensitivity of corn coleoptiles by an order of magnitude, though in this case the decrease was not immediate but required an hour to go to completion. Preliminary experiments indicate that such a red-light treatment also brings about a substantial increase (30%–40%) in flavin, but the effect has not been measured in the two types of pellets to determine in which fraction it occurs, nor have the kinetics been measured.

Recently, light-induced absorbance changes have been seen in the 21KP which are consistent with the light-mediated reduction of a *b*-type cytochrome. The dark reoxidation has a half-life of about 30 sec, roughly the same as that reported by Muñoz and Butler (1975) for the signal measured in *Neurospora*. However, further work is necessary to characterize these light-induced absorbance changes before one can be certain that one is dealing with a similar system.

The results to date are consistent with the notion that corn coleoptiles contain a photoreceptor system similar to that observed in the various fungi studied and that it may be localized in the plasma membrane fraction. It has an affinity for flavin and contains an NADH oxidase and a *b*-type cytochrome. Treatments which alter the phototropic sensitivity of the intact coleoptiles also change the amount of flavin bound to

this fraction upon extraction. Preliminary studies suggest that the kinetics for the flavin change may parallel the phototropic sensitivity change. Thus it is reasonable to hypothesize that this fraction may indeed contain the photoreceptor system for phototropism. The flavin itself must be protein bound or in some way restricted to provide the fine structure seen in the absorption spectrum (see Song and Moore, 1974). Such restriction would account for the fine structure in the action spectrum (Thimann and Curry, 1960). The distribution of this fraction in sucrose gradients does not coincide with the distribution of carotenoids; hence it seems unlikely that a carotenoid is involved in the light-induced reduction of the cytochrome.

REFERENCES

- Briggs, W. R., *Plant Physiol.*, **35**, 951, 1960.
Briggs, W. R., *Am. J. Bot.*, **50**, 196, 1963.
Hertel, R., K. St. Thomson, and V. Russo, *Planta*, **107**, 325, 1972.
Lord, J. M., T. Tagawa, T. S. Moore, and H. Beevers, *J. Cell Biol.*, **57**, 659, 1973.
Muñoz, V., and W. L. Butler, *Plant Physiol.*, **55**, 421, 1975.
Poff, K. L., and W. L. Butler, *Nature*, **248**, 799, 1974.
Poff, K. L., and W. L. Butler, *Plant Physiol.*, **55**, 427, 1975.
Sargent, M. L., and W. R. Briggs, *Plant Physiol.*, **42**, 1504, 1967.
Song, P.-S., and T. A. Moore. *Photochem. Photobiol.*, **19**, 435, 1974.
Thimann, K. V., and G. M. Curry, in *Comparative Biochemistry*, M. Florin and H. S. Mason, eds., Academic Press, New York, p. 243, 1960.

STAFF ACTIVITIES

A highlight of the year was a visit by six plant scientists from the People's Republic of China in December 1974. The group, headed by Professor Shen,

Head of the Photosynthesis Laboratory, Shanghai Institute of Plant Physiology, were all actively involved in research in photosynthesis. Department members

found the visit an important scientific and cultural communication and hope that some contact can continue in the future.

In August 1974, Dr. Björkman gave the inaugural address at a symposium on Environmental and Biological Control of Photosynthesis at the opening of Limburg University, Hasselt, Belgium. Dr. Briggs gave a symposium talk at the annual meeting of the Society for Physical Biology, in Freiburg, Germany, on "Photobiologically relevant blue-absorbing pigments" in October 1974. He gave a review lecture on a similar topic at the 22nd Easter School of Agricultural Science at the University of Nottingham, Nottingham, England. Dr. Björkman also was an invited participant at a workshop on "Improving the photosynthetic capability and biological conversion of solar energy by crops" organized by the Agricultural Research Service of the U.S. Department of Agriculture. In addition to these invited lectures, staff members gave 45 seminars to various university departments or research groups.

Dr. Jeanette Brown spent a very successful summer doing research with Dr. Jacques Duranton at the Centre D'Etudes Nucléaire de Saclay, in Gif-sur-Yvette, France.

Dr. French was awarded an honorary Ph.D. by the University of Göteborg in November 1974. He made an extensive lecture tour in Europe after accepting the honor. Dr. Briggs was elected president-elect by the American Society of Plant Physiologists and will assume his duties on October 1, 1975. Dr. Briggs was elected a member of the American Academy of Arts and Sciences at their spring meeting, 1975.

Dr. Jack Freeberg, from the Department of Biology, University of Massachusetts, Boston, Massachusetts, arrived in June to spend his sabbatical leave working with the plant development

group. Dr. Alan Stemler, from the University of Illinois, arrived recently to begin tenure as a Research Fellow in photosynthesis. Dr. Bruce Mahall completes his fellowship to accept a position as assistant professor in the Department of Biology, University of California, Santa Barbara, California. Dr. Richard Carey, assistant professor of Plant Physiology at San José State University has joined the Department as a Visiting Investigator working with the physiological ecology group.

There are currently six graduate students associated with the Department. Mr. Steven Britz and Mr. John Mackenzie are working with Dr. Briggs to complete the work for a Ph.D. from Harvard University. Ms. Heather Strong and Ms. Diana Stein are working with Dr. Thompson for a doctorate from the University of Massachusetts. Mr. James Ehleringer and Mr. Daniel Cosgrove are both Stanford University graduate students, interested in physiological ecology and plant development, respectively. In addition to these six graduate students there are two undergraduate special research students, Mr. Jay Schramm, working with Dr. Berry, and Mr. Robert Brain, working with Dr. Briggs.

During the construction of the past year, the Department of Plant Biology was able to do a substantial amount of housecleaning. A great deal of obsolete equipment was donated to a local high school for their industrial arts and science programs; and herbarium material of great historical interest was put permanently into the care of the Dudley Herbarium of Stanford University. A large number of old records and notebooks were donated to the Stanford University archives, and miscellaneous chemicals were given to the Chemistry Department of Stanford University. Some equipment was also given to the University of California at Santa Cruz.

BIBLIOGRAPHY

- Acker, S., *see* Brown, J. S.
 Alberte, R. S., *see* Brown, J. S.
 Bartholomew, B., *see* Percy, R. W.
 Berry, J. A., *see* Percy, R. W.
- 545* Berry, Joseph A., Adaptation of photosynthetic processes to stress, *Science*, 188, 644-650, 1975.
- Björkman, O., *see* Hall, A. E.; Osmond, C. B.; Percy, R. W.
- 533 Björkman, O., Environmental and biological control of photosynthesis: inaugural address, in *Environmental and Biological Control of Photosynthesis*, R. Marcelle, ed., Dr. W. Junk B. V., The Hague, The Netherlands, pp. 1-16, 1975.
- 547 Björkman, O., Adaptive and genetic aspects of C₄ photosynthesis, in *CO₂ Metabolism and Productivity of Plants*, R. H. Burris and C. C. Black, eds., University Park, Baltimore, in press, 1975.
- Boisard, J., *see* Marme, D.
- 536 Boisard, J., D. Marme, and W. R. Briggs, *In vivo* properties of membrane-bound phytochrome, *Plant Physiol.*, 54, 272-276, 1974.
- Briggs, W. R., *see* Gardner, G.; Garrison, R.; Hagar, W. G.; Mackenzie, J. M.; Marme, D.; Negbi, M.
- 519 Brown, J. S., R. S. Alberte, and J. P. Thornber, Comparative studies on the occurrence and spectral composition of chlorophyll-protein complexes in a wide variety of plant material, *Proc. III Int. Congr. Photosynthesis, Israel*, 3, 1951-1964, 1975.
- 529 Brown, J. S., R. S. Alberte, and J. P. Thornber, Chlorophyll protein complexes in some eucaryotic algae, *Plant Physiol. Supp.*, A360, p. 63, 1974.
- 534 Brown, J. S., S. Acker, and J. Duranton, The difference in turnover rate between the chlorophyll *a* in the P700-chlorophyll *a*-protein and in the total chloroplast membranes, *Biochem. Biophys. Res. Commun.*, 62, 336-341, 1975.
- Card, K. A., *see* Troughton, J. H.
- Chang, F. H., *see* Troughton, J. H.
- Coleman, R. A., *see* Mackenzie, J. M.
- Duranton, J., *see* Brown, J. S.
- 538 Ehleringer, James R., and Philip C. Miller, A simulation model of plant water relations and production in the Alpine tundra, Colorado, *Oecologia (Berlin)*, in press, 1975.
- Fork, D., *see* Murata, N.; Troughton, J. H.
- 524 Gardner, G., and W. R. Briggs, Some properties of phototransformation of rye phytochrome *in vitro*, *Photochem. Photobiol.*, 19 (5), 367-377, 1974.
- 526 Gardner, G., W. F. Thompson, and W. R. Briggs, Differential reactivity of the red- and far-red absorbing forms of phytochrome to [¹⁴C] N-Ethyl Maleimide, *Planta*, 117, 367-372, 1974.
- 549 Garrison, R., and W. R. Briggs, The growth of internodes in *Helianthus* in response to far red light, *Bot. Gaz. (Chicago)*, in press, 1975.
- Hackett, W., *see* Rogler, C.
- 530 Hagar, W. G., and W. R. Briggs, Light induced conformational changes of *Chenopodium* chlorophyll protein 668, *Plant Physiol. Supp.*, A13, p. 4, 1974.
- Harrison, A. T., *see* Percy, R. W.
- 552 Hall, A. E., and O. Björkman, Model of leaf photosynthesis and respiration, in *Perspectives in Biophysical Ecology: Ecological Studies Series*, D. M. Gates and R. B. Schmerl, eds., Springer Verlag, New York, pp. 55-72, 1975.
- Hopkins, David W., *see* Negbi, M.
- Mackenzie, J. M., *see* Marme, D.
- 539 Mackenzie, J. M., R. A. Coleman, W. R. Briggs, and L. H. Pratt, Reversible redistribution of phytochrome within the cell upon conversion to its physiologically active form, *Proc. Nat. Acad. Sci. USA*, 72, 799-803, 1975.
- Marme, D., *see* Boisard, J.
- 535 Marme, D., J. M. Mackenzie, Jr., J. Boisard, and W. R. Briggs, The isolation and partial characterization of a membrane fraction containing phytochrome, *Plant Physiol.*, 54, 263-271, 1974.
- Miller, P., *see* Ehleringer, J.
- Mooney, H. A., *see* Percy, R. W.
- 542 Murata, N., J. H. Troughton, and D. C. Fork, The relationship between the transition of the physical phase of membrane lipids and photosynthetic parameters in *Anacystis nidulans* and lettuce and spinach chloroplasts, *Plant Physiol.*, in press, 1975.
- 554 Negbi, Moshé, David W. Hopkins, and Winslow R. Briggs, Acceleration of dark reversion of phytochrome *in vitro* by calcium and magnesium, *Plant Physiol.*, 56, 157-159, 1975.
- 516 Osmond, C. B., and O. Björkman, Pathways of CO₂ fixation in the CAM plant *Kalanchoe daigremontiana*. II. Effects of O₂ and CO₂ concentration on light and dark CO₂ fixation, *Aust. J. Plant Physiol.*, 2, 155-162, 1975.
- 498 Percy, R. W., J. A. Berry, and B. Bartholomew, Field photosynthetic performance and leaf temperature of

* Department of Plant Biology publication number.

- Phragmites communis* in Death Valley, California, *Photosynthetica*, 8 (2), 104–108, 1974.
- 527 Percy, R. W., A. T. Harrison, H. A. Mooney, and O. Björkman, Seasonal changes in net photosynthesis of *Atriplex hymenelytra* shrubs growing in Death Valley, California, *Oecologia (Berlin)*, 17, 111–121, 1974.
- Pratt, L. H., see Mackenzie, J. M.
- 543 Rogler, C., and W. Hackett, Phase change in *Hedera helix*. I. Induction of the mature to juvenile phase change by Gibberellin A₃, *Physiol. Plant.*, in press, 1975.
- 544 Rogler, C., and W. Hackett, Phase change in *Hedera helix*. II. Stabilization of the mature form with abscisic acid and growth retardants, *Physiol. Plant.*, in press, 1975.
- 552 Stein, D. B., and W. F. Thompson, Isolation and initial characterization of DNA in the three species of the Osmundaceae, *Plant Physiol. Supp.*, A145, p. 26, 1974.
- 546 Stein, D. B., and W. F. Thompson, DNA hybridization and evolutionary relationships in three *Osmunda* species, *Science*, in press, 1975.
- Thompson, W. F., see Gardner, G.; Stein, D. B.
- Thornber, J. P., see Brown, J. S.
- Troughton, J. H., see Murata, N.
- 521 Troughton, J. H., and K. A. Card, Temperature effects on the carbon-isotope ratio of C₃, C₄ and Crassulacean-acid-metabolism (CAM) plants, *Planta (Berlin)* 123, 185–190, 1975.
- 531 Troughton, J. H., and D. C. Fork, Quantum efficiency states of photosynthesis, *Plant Physiol. Supp.*, A114, p. 21, 1974.
- 550 Troughton, J. H., D. C. Fork and F. H. Chang, in *Environmental and Biological Control of Photosynthesis*, Part II, R. Marcelle, ed., Dr. W. Junk B. V., The Hague, The Netherlands, 300 pp., 1974.

SPEECHES

- Berry, Joseph A., Inhibition of Photosynthesis by Atmospheric Oxygen. Joint Session of Western Section of the American Society of Plant Physiologists and Pacific Slope Biochemical Conference at the University of California, Riverside, California, August 28, 1974.
- Berry, Joseph A., Plant Performance in Relation to the Environment. Department of Botany and Microbiology, University of Arizona, Tempe, Arizona, October 2, 1974.
- Berry, Joseph A., Alternate Pathways of Photosynthesis in Relation to Plant Environment. Department of Biology, Simon Fraser University, Vancouver, B.C., Canada, November 21, 1974.
- Björkman, Olle, Environmental and Biological Control of Photosynthesis: Inaugural Address. Limburg Universitaire Centrum, Hasselt, Belgium, August 25, 1974.
- Björkman, Olle, Adaptive and Genetic Aspects of C₄ Photosynthesis. Fifth Steinbock Symposium, University of Wisconsin, Madison, Wisconsin, June 9, 1975.
- Briggs, Winslow R., and A. J. Jesaitus, Photo-biologically Relevant 'Blue-Absorbing Pigments. Symposium on "Primärreaktionen von Photoreceptoren," University of Freiburg, Freiburg, West Germany, October 6, 1974.
- Briggs, Winslow R., The Question of the Phototropic Photoreceptor. Laboratory of Chemical Biodynamics, University of California, Berkeley, California, November 22, 1974.
- Briggs, Winslow R., Pigment-Membrane Associations and Photomorphogenesis (seminar). Department of Botany and Microbiology, Arizona State University, Tempe, Arizona, March 31, 1975.
- Briggs, Winslow R., The Blue-Absorbing Photoreceptor—Structure and Properties. University of Nottingham, School of Agriculture, Sutton Bonington, Loughborough, England, April 7, 1975.
- Briggs, Winslow R., Pigment Excitation and Rapid Plant Responses. Office of Administration, Carnegie Institution of Washington, Washington, D.C., May 1, 1975.
- Briggs, Winslow R., Pigment-Membrane Associations and Photomorphogenesis. Department of Botany, University of California, Davis, California, May 7, 1975.
- Briggs, Winslow R., Phytochrome—Chemistry and Properties. Department of Botany, University of California, Davis, California, May 8, 1975.
- Briggs, Winslow R., Pigment-Membrane Associations and Photomorphogenesis. Department of Botany, University of Washington, Seattle, Washington, May 12, 1975.
- Briggs, Winslow R., Recent Advances in Photomorphogenesis. Department of Botany, University of Washington, Seattle, Washington, May 13, 1975.
- Briggs, Winslow R., Pigment-Membrane Associations and Photomorphogenesis. Department of Botany, University of California, Berkeley, California, May 16, 1975.

- Briggs, Winslow R., Pigment-Membrane Associations and Photomorphogenesis. Department of Biology, University of California, Santa Cruz, California, May 22, 1975.
- Briggs, Winslow R., Pigment-Membrane Associations and Photomorphogenesis. Monsanto Agricultural Products Co., St. Louis, Missouri, May 29, 1975.
- Briggs, Winslow R., Membrane-Associated Yellow Pigments and Blue Light Photoresponses. Annual Meeting of the American Society for Photobiology, Louisville, Kentucky, June 23, 1975.
- Britz, S. J., Studies on a Circadian Rhythm of Chloroplast Orientation in *Ulva*. 8th International Seaweed Symposium, Bangor, Wales, August 22, 1974.
- Britz, S. J., Circadian Rhythms in Chloroplast Movement in *Ulva* (seminar). Stanford-Carnegie Plant Physiology Graduate Seminar, Department of Plant Biology, Carnegie Institution, Stanford, California, October 9, 1974.
- Brown, Jeanette S., Comparative Studies of the Occurrence and Spectral Forms of Chlorophyll in Pigment-Protein Complexes of a Wide Variety of Plants. 3rd International Congress on Photosynthesis, Rehovot, Israel, September 5, 1974.
- Brown, Jeanette S., Chlorophyll-Protein Complexes From Diverse Plants. Stanford-Carnegie Plant Physiology Graduate Seminar, Department of Plant Biology, Carnegie Institution, Stanford, California, February 12, 1975.
- Brown, Jeanette S., Chlorophyll: The Natural Energy Trap. San Diego State University, San Diego, California, April 7, 1975.
- French, C. S., Trends, Fads, and Progress in Photosynthesis Research since 1900. American Society for Photobiology, Vancouver, B.C., Canada, July 23, 1974.
- French, C. S., Different Forms of Chlorophyll *a* in Plants. Copenhagen Biological Club, Copenhagen, Denmark, October 9, 1974.
- French, C. S., History of Photosynthesis Research since 1900. Department of Plant Physiology and Anatomy, Royal Veterinary and Agricultural College, Copenhagen, Denmark, October 11, 1974.
- French, C. S., History of Photosynthesis Research since 1900 with a Discussion of Methods for Cellular Disintegration. Department of Plant Physiology, University of Oslo, Oslo, Norway, October 14, 1974.
- French, C. S., History of Photosynthesis Research since 1900. Department of Plant Physiology, Botanical Institute, University of Göteborg, Göteborg, Sweden, October 18, 1974.
- French, S. C., History of Photosynthesis Research since 1900. Institute for Physiological Botany, University of Lund, Lund, Sweden, October 23, 1974.
- French, C. S., Different Forms of Chlorophyll *a* in Plants. Institute for Physiological Botany, University of Lund, Lund, Sweden, October 23, 1974.
- French, C. S., History of Photosynthesis Research since 1900. Institute of Physiological Botany, University of Uppsala, Uppsala, Sweden, October 24, 1974.
- French, C. S., History of Photosynthesis Research since 1900. Institute of Physiological Botany, University of Stockholm, Stockholm, Sweden, October 25, 1974.
- French, C. S., History of Photosynthesis Research since 1900. Department of Plant Physiology, University of Umeå, Umeå, Sweden, October 28, 1974.
- French, C. S., Different Forms of Chlorophyll *a* in Plants. Department of Plant Physiology, University of Umeå, Umeå, Sweden, October 29, 1974.
- Hiyama, Tetsuo, Chlorophyll Proteins That Have Little to Do with Photosynthesis. Stanford-Carnegie Plant Physiology Graduate Seminar, Department of Plant Biology, Carnegie Institution, Stanford, California, November 20, 1974.
- Mahall, Bruce E., Ecological and Physiological Factors Influencing the Ecotone between *Spartina foliosa* and *Salicornia virginica* in Salt Marshes in Northern San Francisco Bay. Department of Botany, University of California, Berkeley, California, October 11, 1974.
- Mahall, Bruce E., The Ecotone between *Spartina* and *Salicornia* in Tidal Marshes of Northern San Francisco Bay. Department of Biological Sciences, University of California, Santa Barbara, California, March 12, 1975.
- Mahall, Bruce E., The Ecotone between *Spartina* and *Salicornia* in Tidal Marshes of Northern San Francisco Bay. Department of Biology, University of Michigan, Ann Arbor, Michigan, March 24, 1975.
- Nobs, Malcolm A., and Bruce E. Mahall, Transplants, Past, Present, and Future. San Jose State University, Department of Biology, held at the Carnegie Institution of Washington's Mather and Timberline Transplant Stations, October 24, 1974.
- Nobs, Malcolm A., The Ecotype, History, Genetic Structure, and Future Research Potentials. Department of Biology, University of California, Santa Cruz, California, April 8, 1975.
- Rogler, Charles, Physiological and Molecular Aspects of Gibberellic Acid-Induced Phase Change in *Hedera helix*. Stanford-Carnegie Plant Physiology Graduate Seminar, Department of Plant Biology, Carnegie Institution, Stanford, California, August 22, 1974.

Rogler, Charles, Molecular Studies on Crown Gall Induction, Stanford-Carnegie Graduate Seminar, Department of Plant Biology, Carnegie Institution, Stanford, California, March 5, 1975.

Thompson, W. F., Network Formation during Reassociation of Plant DNA. Joint Session of Western Section of the American Society of Plant Physiologists and Pacific Slope Biochemical Conference at the University of

California, Riverside, California, August 28, 1974.

Thompson, W. F., Genome Organization and Regulation. Department of Botany, University of Massachusetts, Amherst, Massachusetts, February 27, 1975.

Thompson, W. F., DNA Hybridization Studies in the Neglected Kingdom. Department of Biological Sciences, Stanford University, Stanford, California, June 2, 1975.

PERSONNEL

Photosynthesis Group

Staff: Jeanette S. Brown; David C. Fork; C. Stacy French, Director Emeritus

Carnegie Institution Research Fellows: William G. Hagar,¹ Tetsuo Hiyama,² Norio Murata³

Technical Assistant: Charles V. Weiss⁴

Physiological Ecology Group

Staff: Joseph A. Berry; Olle Björkman; Malcolm A. Nobs; William M. Hiesey, Emeritus

Carnegie Institution Research Fellows: Bruce E. Mahall, John H. Troughton⁵

Technical Assistants: Edward G. Gausden, James Johnson,⁶ Frank Nicholson, William E. Ward⁷

Visiting Investigators: Richard Carey,⁸ Harold A. Mooney⁹

¹ To August 31, 1974.

² To September 30, 1974.

³ To August 31, 1974.

⁴ From March 1, 1975.

⁵ To September 30, 1974.

⁶ From December 1, 1974.

⁷ To November 30, 1974.

⁸ From January 1, 1975. From San Jose State University, San Jose, California.

⁹ From April 1, 1975. From Stanford University, Stanford, California.

Plant Development Group

Staff: Winslow R. Briggs, Director; William F. Thompson

Carnegie Institution Research Fellow: Charles Rogler¹⁰

Visiting Investigator: John Freeberg¹¹

Administrative and Operating Staff

Administrative Secretary-Accountant: Ruth Fischer

Department Secretary: Donna C. Moore

Clerical Assistant: Kathleen Keller¹²

Mechanical Engineer: Richard W. Hart

Technical Assistants (Illustrators): Steven Coffee¹³, Ann Ewart¹⁴

Custodian: Jan Kowalik

Predoctoral Fellows

Steve Britz¹⁵, Dan Cosgrove¹⁶, James Ehleringer¹⁷, John Mackenzie¹⁸, Heather Strong¹⁹

¹⁰ From January 13, 1975. From University of California, Davis, California.

¹¹ From June 24, 1975. From University of Massachusetts, Boston, Massachusetts.

¹² From March 1, 1975.

¹³ From May 27, 1975.

¹⁴ From January 29, 1975, to April 30, 1975.

¹⁵ From July 1, 1974.

¹⁶ From July 1, 1974.

¹⁷ From July 1, 1974.

¹⁸ From July 1, 1974.

¹⁹ From October 1, 1974.

Bibliography

July 1, 1974–June 30, 1975

PUBLICATIONS OF THE INSTITUTION

Carnegie Institution of Washington Year Book 73. Octavo, vii + 32 + 1158 pages, 577 figures. December 1974.

An Atlas of Galactic Hydrogen I. The Region $0^\circ \leq l \leq 12^\circ$, $+3^\circ \leq b \leq +17^\circ$. By W. G. L. Pöppel and E. R. Vieira. Publication 633. Octavo, 47 pages, 42 figures. December 1974.

Geochemical Transport and Kinetics. Edited by A. W. Hofmann, B. J. Giletti, H. S. Yoder, Jr., and R. A. Yund. Publication 634. Octavo, vii + 353 pages, 144 figures. December 1974.

Carnegie Institution of Washington Catalogue 1975–1976. Octavo, 81 pages, 21 figures. June 1975.

Carnegie Institution Newsletter. Issued in November and April.

Continental Drilling. Edited by E. M. Shoemaker. Octavo, xi + 56 pages, 8 figures. June 1975. Reprinted in July 1975.

Carnegie Institution of Washington. 1st edition. $3\frac{1}{2} \times 4\frac{1}{2}$ inches, 15 pages, 3 figures. September 1974.

Carnegie Institution of Washington. 2nd edition. $3\frac{1}{2} \times 4\frac{1}{2}$ inches, 18 pages, 4 figures. November 1974.

Drosophila Guide: Introduction to the Genetics and Cytology of Drosophila melanogaster. 8th edition. By M. Demerec and B. P. Kaufmann. Octavo, ii + 45 pages, 14 figures. Reprint. November 1974.

PUBLICATIONS BY THE PRESIDENT OF THE INSTITUTION

Philip H. Abelson

Meeting energy needs. *Eos*, Transactions of the American Geophysical Union, Vol. 56, July 1974, pp. 644–647.

Energy for the 70s. *Field Museum of Natural History Bulletin*, Vol. 45, July–August 1974, pp. 7–9, 15.

Informing the intellectual community on science, technology, and public policy. *Technical Communication*, Fourth Quarter, 1974, pp. 2–4.

Energy supply and demand during the next decade. *A.G.A. Monthly*, Vol. 56, December 1974, pp. 12–15, 36.

Foreword to *Energy: Use Conservation and Supply* (editor). American Association for the Advancement of Science, 1974, pp. v–vi.

Report of the President. Reprinted from *Carnegie Institution of Washington Year Book* 73, December 1974, 32 pp.

Report of the Association. *Science*, 187, March 21, 1975, pp. 1109–1114.

Energy for Tomorrow. The Jessie and John Danz Lectures. University of Washington Press. ix + 78 pp., 1975.

A graduate student with Ernest O. Lawrence. Chapter 2 in *All In Our Time*, The Reminiscences of Twelve Nuclear Pioneers. (Jane Wilson, editor), reprinted by *Bulletin of the Atomic Scientists*, Chicago, 1975, pp. 22–34.

Foreword to *Continental Drilling* (E. M. Shoemaker, editor), Carnegie Institution of Washington, 1975, pp. v–vi.

Editorials in *Science*

Volume 185:

The deteriorating energy position, July 26, 1974, p. 309; Hemispheric cooperation in science, August 9, 1974, p. 485; Mr. Ford and science policy, August 22, 1974, p. 651; Two digit inflation, September 20, 1974, p. 1040.

Volume 186:

Circum-Pacific energy and mineral resources, October 4, 1974, p. 11; Troublesome portents for scientific journals, November 22, 1974, p. 683; Declining years of hydrocarbon production, December 13, 1974, p. 969.

Volume 187:

Delays in tapping energy sources, January 10, 1975, p. 17; Science advice for the Executive Branch, January 17, 1975, p. 119; The world's disparate food supplies, January 24, 1975, p. 217; President Ford's energy initiatives, February 7, 1975, p. 391; Mineral research in Turkey, March 7, 1975, p. 793; Life members of AAAS, March 21, 1975, p. 1035.

Volume 188:

Food and nutrition, May 9, 1975, p. 501; Energy and the shape of society, May 30, 1975, p. 889; Changing climate for medicine, June 6, 1975, p. 975; International cooperation in geology, June 20, 1975, p. 1169.

Administrative Reports

Report of the Executive Committee

To the Trustees of the Carnegie Institution of Washington

Gentlemen:

In accordance with the provisions of the By-Laws, the Executive Committee submits this report to the Annual Meeting of the Board of Trustees.

During the fiscal year ending June 30, 1975, the Executive Committee held four meetings. Printed accounts of these meetings have been or will be mailed to each Trustee.

The estimate of expenditures for the fiscal year beginning July 1, 1975, has been reviewed by the Executive Committee.

In a letter dated September 12, 1974, Keith S. McHugh tendered his resignation as a member of the Board of Trustees and indicated his desire to be relieved of his responsibilities on the Standing Committees immediately. In accordance with Article V, Section 2 of the By-Laws, the vacancies were filled by the Executive Committee by temporary appointment as follows: Member of the Executive Committee, Hanna H. Gray; member of the Finance Committee, William McChesney Martin, Jr.; Chairman of the Auditing Committee, Juan T. Trippe; and member of the Auditing Committee, Robert C. Seamans, Jr.

In addition to the vacancy caused by the resignation of Mr. McHugh, vacancies exist in the membership of the Board of Trustees resulting from the resignations of Lord Ashby in June 1974 and of Charles P. Taft in April 1975.

The terms of all Committee Chairmen and the following members of Committees also expire on May 2, 1975:

Executive Committee

Michael Ference, Jr.
Hanna H. Gray
Crawford H. Greenewalt

Finance Committee

William McChesney Martin, Jr.
Robert M. Pennoyer
Richard S. Perkins

Nominating Committee

Caryl P. Haskins

Auditing Committee

Robert C. Seamans, Jr.

Frank Stanton, *Chairman*

May 2, 1975

Abstract of Minutes

of the Seventy-Seventh Meeting of the Board of Trustees

The annual meeting of the Board of Trustees was held in the Board Room of the Administration Building on Friday, May 2, 1975. The meeting was called to order by Chairman William McChesney Martin, Jr.

The following Trustees were present: Lewis M. Branscomb, Michael Ference, Jr., Carl J. Gilbert, William T. Golden, Hanna H. Gray, Crawford H. Greenewalt, Caryl P. Haskins, William McChesney Martin, Jr., Henry S. Morgan, Walter H. Page, Robert M. Pennoyer, Richard S. Perkins, Robert C. Seamans, Jr., Frank Stanton, Charles H. Townes, Juan T. Trippe, and James N. White. Garrison Norton, Trustee Emeritus, and the President, Philip H. Abelson, were also in attendance.

The minutes of the Seventy-Sixth Meeting were approved.

The Chairman notified the Trustees of the death of Vannevar Bush and spoke of the Trustees' high esteem for Dr. Bush and of his service to the Institution as President from 1939 to 1955 and as Trustee from 1958 to 1971. The Trustees passed the following resolution:

Be It Therefore Resolved, That we, the Trustees of Carnegie Institution of Washington, record our deep sense of loss in the death of Vannevar Bush.

And Be It Further Resolved, That this resolution be entered on the minutes of the Board of Trustees and that copies be sent to the members of the family of Dr. Bush.

The resignations of Eric Ashby, Keith S. McHugh, and Charles P. Taft were accepted with regret. Mr. McHugh and Mr. Taft were designated Trustees Emeritus.

On the recommendation of the Nominating Committee, John T. Connor, John Diebold, and William C. Greenough were elected members of the Board of Trustees.

The following were elected for one year terms: Frank Stanton, as Chairman of the Executive Committee; Richard S. Perkins, as Chairman of the Finance Committee; Juan T. Trippe, as Chairman of the Auditing Committee; William R. Hewlett, as Chairman of the Nominating Committee; and Carl J. Gilbert, as Chairman of the Retirement Committee.

Vacancies in Standing Committees, with terms ending in 1978, were filled as follows: Michael Ference, Jr., Hanna H. Gray, Crawford H. Greenewalt, and Richard S. Perkins were elected members of the Executive Committee; Richard S. Perkins, William McChesney Martin, Jr., and Robert M. Pennoyer were elected members of the Finance Committee; Crawford H. Greenewalt and Robert C. Seamans, Jr., were elected members of the Auditing Committee; and Hanna H. Gray was elected a member of the Nominating Committee.

The reports of the Executive Committee, the Finance Committee, the Retirement Committee, and the Auditing Committee were accepted. On recommendation of the latter, it was resolved that Arthur Andersen & Co. be reappointed as public accountants for the fiscal year beginning July 1, 1975.

The annual report of the President was accepted.

To provide for the operation of the Institution for the fiscal year beginning July 1, 1975, and upon recommendation of the Executive Committee, the sum of \$6,534,715 was appropriated. To provide for construction expenses of the Irénée du Pont Telescope project at the Las Campanas Observatory for the fiscal year beginning July 1, 1975, and upon recommendation of the Executive Committee, the sum of \$906,203 was appropriated from the Unrestricted Capital Fund for use at the discretion of the President.

Financial Statement

CARNEGIE INSTITUTION OF WASHINGTON
TEN-YEAR FINANCIAL SUMMARY, 1966-1975
All Figures are Thousands of Dollars

<i>Fiscal Year Ended June 30</i>	1975*	1974*	1973	1972	1971	1970	1969	1968	1967	1966
<i>Income</i>										
Realized capital gain or loss, net	(\$ 1,369)	\$ 4,762	\$ 6,576	\$ 2,328	\$ 2,924	(\$ 117)	\$ 360	\$ 581	(\$ 307)	\$ 731
Interest and dividends	3,295	3,356	3,647	3,863	4,127	4,077	4,213	4,092	4,091	4,026
Other	83	60	58	65	90	45	59	53	41	45
Total	2,009	8,178	10,281	6,256	7,141	4,005	4,632	4,726	3,825	4,802
<i>Expenditures (Includes Plant Fund)</i>										
Terrestrial Magnetism	1,188	1,025	1,022	937	909	801	844	845	839	757
Mount Wilson Observatory	1,027	1,051	1,016	992	930	1,154	762	781	688	647
Las Campanas Observatory	2,138	2,572	2,559	1,075	1,184	466	126	—	—	—
Geophysical Laboratory	1,136	964	984	770	779	768	761	762	727	711
Embryology	851	791	718	699	668	613	618	562	557	510
Plant Biology	1,270	673	330	271	252	244	253	244	221	184
Genetics Research Units	24	70	65	68	165	151	142	147	166	153
Research Projects, etc.	51	98	29	22	61	63	86	118	151	67
Office of Administration	571	520	592	583	559	469	433	455	410	403
General publications	78	57	79	58	98	111	45	70	95	49
Consulting fees, insurance, taxes . . .	134	95	62	67	75	44	80	38	78	50
Employee benefits, special	81	89	97	78	77	71	77	78	82	91
Financial advisory services	213	199	195	108	66	70	74	71	72	78
Total	8,762	8,204	7,748	5,728	5,823	5,025	4,301	4,171	4,086	3,700
<i>Restricted Grants</i>										
Grants received	815	505	544	444	483	437	678	464	417	527
Expenditures	447	484	554	470	517	517	566	576	458	532
<i>Gifts received</i>	146	330	377	354	611	5	66	38	660	9
<i>Endowment and Special Funds</i>										
Endowment Fund	75,048	79,852	79,322	76,863	76,649	75,641	76,157	76,542	76,019	76,065
Special Funds	1,188	1,049	1,007	947	934	893	888	1,505	1,453	797
Total	76,236	80,901	80,329	77,810	77,583	76,534	77,045	78,047	77,472	76,862
Total market value of investments	\$93,719	\$98,200	\$124,770	\$128,826	\$113,042	\$89,000	\$109,262	\$114,796	\$109,188	\$104,189

*Accrual Basis; prior years are stated on a Cash Basis.

ARTHUR ANDERSEN & Co.

1666 K STREET, N.W.
WASHINGTON, D. C. 20006

August 29, 1975

REPORT OF INDEPENDENT PUBLIC ACCOUNTANTS

To the Auditing Committee of
Carnegie Institution of Washington:

We have examined the statement of assets, liabilities and funds of CARNEGIE INSTITUTION OF WASHINGTON (a non-profit corporation chartered by Act of the United States Congress) as of June 30, 1975, and June 30, 1974, the related summary statement of changes in funds for the year ended June 30, 1975, and the supporting exhibits and schedules, all of which are set forth on the thirteen immediately following pages. Our examination was made in accordance with generally accepted auditing standards, and accordingly included such tests of the accounting records and such other auditing procedures as we considered necessary in the circumstances.

In our opinion, the financial statements and supporting exhibits and schedules referred to above present fairly the assets, liabilities and funds of Carnegie Institution of Washington as of June 30, 1975, and June 30, 1974, and the changes in funds for the year ended June 30, 1975, in conformity with generally accepted accounting principles consistently applied during the periods.

Arthur Andersen & Co.

CARNEGIE INSTITUTION OF WASHINGTON
SUMMARY OF SIGNIFICANT ACCOUNTING POLICIES

Basis of Accounting

The financial statements of the Institution are prepared on the accrual basis of accounting. The Institution follows a policy of reporting all commitments outstanding at year-end as liabilities for financial statement purposes.

Land, Buildings and Equipment

The Institution capitalizes expenditures for land, buildings, telescopes and other significant equipment, and construction projects in progress. Expenditures for other equipment are charged to current operations as incurred, and the cost of such equipment is not capitalized. The Institution follows the policy of not depreciating its buildings, telescopes and significant equipment.

Retirement Plan

The Institution has a noncontributory retirement plan in which all regularly employed United States personnel are eligible to participate. Voluntary contributions may also be made by employees. Actuarially determined contributions are funded currently by the Institution, and there are no unfunded past service costs. The total contributions made by the Institution were \$453,684 in 1975 and \$425,249 in 1974. Benefits under the plan upon retirement are dependent upon the investment performance of the Institution's Retirement Trust. After four years' participation, benefits are fully vested.

During 1975, the plan was modified in order to comply with the Employees Retirement Income Security Act of 1974. The modifications were generally of a technical nature and had no significant impact on the plan.

CARNEGIE INSTITUTION OF WASHINGTON
STATEMENT OF ASSETS, LIABILITIES AND FUNDS
JUNE 30, 1975 AND 1974

ASSETS

	1975	1974
Cash	\$ 145,588	\$ 169,952
Accrued interest	403,145	296,327
Grants receivable	428,509	40,142
Advances	47,227	41,754
Investments (cost),* Schedule 2:		
Governmental bonds	5,047,113	2,492,031
Nongovernmental bonds	23,487,483	20,489,912
Common stocks	49,286,443	61,184,698
Total investments	<u>77,821,039</u>	<u>84,166,641</u>
Land	766,402	763,816
Buildings	4,603,555	3,524,961
Equipment	8,211,486	6,494,696
Total assets	<u>\$92,426,951</u>	<u>\$95,498,289</u>

LIABILITIES AND FUNDS

Appropriated funds:

Accounts payable and accrued expenses—		
Operating Fund	\$ 528,950	\$ 230,696
Restricted Grants	73,786	2,052
Total liabilities	<u>602,736</u>	<u>232,748</u>
Operating Fund, Exhibit 1	1,603,090	3,544,917
Restricted Grants, Exhibit 2	403,922	35,713
Unappropriated Funds, Exhibit 3	76,235,760	80,901,438
Plant Fund	13,581,443	10,783,473
Total liabilities and funds	<u>\$92,426,951</u>	<u>\$95,498,289</u>

*Approximate market value on June 30, 1975: \$93,719,359 (July 31, 1975: \$88,135,054); on June 30, 1974: \$98,200,017.

CARNEGIE INSTITUTION OF WASHINGTON
SUMMARY STATEMENT OF CHANGES IN FUNDS
FOR THE YEAR ENDED JUNE 30, 1975

	<i>Appropriated Funds</i>		<i>Unappropriated Funds</i> (Exhibit 3)	<i>Plant Fund</i>	<i>Total</i>
	<i>Operating Fund</i> (Exhibit 1)	<i>Restricted Grants</i> (Exhibit 2)			
Balance, July 1, 1974	\$3,544,917	\$ 35,713	\$80,901,438	\$10,783,473	\$95,265,541
<i>Additions</i>					
Realized capital loss, net	—	—	(1,369,473)	—	(1,369,473)
Investment income					
Interest	—	—	1,623,707	—	1,623,707
Dividends	—	—	1,671,587	—	1,671,587
Gifts	—	—	145,516	—	145,516
Other income	—	—	82,795	—	82,795
Land, buildings and equipment, capitalized					
Current year	—	—	—	2,294,818	2,294,818
Prior years	—	—	—	511,224	511,224
Appropriations					
Budget	6,374,810	—	(6,374,810)	—	—
Las Campanas Observatory	445,000	—	(445,000)	—	—
Restricted grants	—	814,962	—	—	814,962
	6,819,810	814,962	(4,665,678)	2,806,042	5,775,136
<i>Deductions</i>					
Expenditures	8,761,637	446,753	—	—	9,208,390
Building written-off	—	—	—	8,072	8,072
	8,761,637	446,753	—	8,072	9,216,462
Net change during year	(1,941,827)	368,209	(4,665,678)	2,797,970	(3,441,326)
Balance, June 30, 1975	\$1,603,090	\$403,922	\$76,235,760	\$13,581,443	\$91,824,215

CARNEGIE INSTITUTION OF WASHINGTON

EXHIBIT 1

APPROPRIATED FUNDS

CHANGES IN OPERATING FUND
FOR THE YEAR ENDED JUNE 30, 1975

Balance, July 1, 1974			\$ 3,544,917
<i>Appropriations</i>			
Budget, July 1, 1974 to June 30, 1975	\$6,374,810		
Las Campanas Observatory			
Unrestricted Capital Fund	445,000		6,819,810
Total available for expenditures			10,364,727
<i>Expenditures</i>			
Salaries	\$2,942,369		
Employee benefits	570,930		
Building maintenance	555,209		
Equipment	539,771		
Educational and research supplies	444,404		
Administrative	315,427		
Financial advisory services	213,084		
Fellowship grants	195,135		
Taxes	169,820		
Publications	138,504		
Travel	122,987		
Insurance	100,960		
Consulting fees	56,041		
Commissary	35,889		
Awards	30,948		
Shop	19,295		
Entertainment	8,549		
Fellowship travel	7,397		
Rent	100	6,466,819	
<i>Transfers to Plant Fund</i>			
Construction in progress:			
Equipment	1,231,438		
Building	864,610		
Salaries	168,860		
Employee benefits	16,682		
Taxes	9,375		
Land	2,586		
Building	1,267	2,294,818	
Total expenditures			8,761,637
Balance, June 30, 1975			\$ 1,603,090

EXHIBIT 2

CARNEGIE INSTITUTION OF WASHINGTON

APPROPRIATED FUNDS

CHANGES IN RESTRICTED GRANTS

FOR THE YEAR ENDED JUNE 30, 1975

	<i>Balance July 1, 1974</i>	<i>Grants</i>	<i>Expenditures</i>		<i>Balance June 30, 1975</i>
			<i>Salaries</i>	<i>Other</i>	
Carnegie Corporation of New York	\$ 336	\$ 80,000	—	\$ 80,142	\$ 194
Geological Survey	1,452	—	—	1,452	—
Golden Gift	29	—	—	29	—
Jet Propulsion Laboratory	73	—	—	36	37
Moseley Gift	1,199	—	—	—	1,199
Muscular Dystrophy Association	—	500	—	500	—
National Academy of Sciences	31,412	10,000	—	18,214	23,198
National Aeronautics & Space Administration	—	115,247	\$ 34,600	62,096	18,551
National Cystic Fibrosis Research Foundation	—	54,459	—	29,459	25,000
National Science Foundation . .	—	445,475	48,252	85,245	311,978
Office of Naval Research	—	24,624	16,900	7,724	—
Public Health Service	—	4,834	—	4,834	—
Whitehall Foundation	—	40,000	—	31,148	8,852
Wistar Institute	<u>1,212</u>	<u>39,823</u>	<u>14,700</u>	<u>11,422</u>	<u>14,913</u>
Total	<u>\$35,713</u>	<u>\$814,962</u>	<u>\$114,452</u>	<u>\$332,301</u>	<u>\$403,922</u>

EXHIBIT 3

CARNEGIE INSTITUTION OF WASHINGTON
CHANGES IN UNAPPROPRIATED FUNDS
FOR THE YEAR ENDED JUNE 30, 1975

	Balance July 1, 1974	Investment Income	Gifts and Other Income	Realized Capital Loss, net	Appropriations	Transfers	Balance June 30, 1975
<i>Endowment Fund</i>							
<i>Gift</i>							
Andrew Carnegie	\$22,000,000	—	—	—	—	—	\$22,000,000
Realized capital gain, net	32,011,681	—	—	\$ 813,928	—	—	31,197,753
Unrestricted Capital Fund							
Carnegie Corporation of New York	10,000,000	—	—	—	—	—	10,000,000
Other gifts	157,226	—	\$ 1,000	—	\$ 158,226	—	—
Realized capital gain, net	15,683,048	—	—	541,729	3,291,155	—	11,850,164
Working Capital Fund							
Income	—	\$3,255,414	—	—	3,338,209	\$82,795	—
Sales							
Assets	—	—	26,806	—	—	(26,806)	—
Publications	—	—	17,187	—	—	(17,187)	—
Optical services	—	—	1,896	—	—	(1,896)	—
University of Toronto	—	—	20,000	—	—	(20,000)	—
Royalties	—	—	9,118	—	—	(9,118)	—
Refunds	—	—	5,940	—	—	(5,940)	—
Rent	—	—	1,560	—	—	(1,560)	—
Miscellaneous	—	—	288	—	—	(288)	—
<i>Special Funds</i>							
Bush Bequest	—	3,785	100,000	1,630	—	—	102,155
Bush Gift	26,801	1,641	—	620	—	—	27,822
Colburn	226,717	9,060	—	3,423	9,491	—	222,863
Hale Relief	6,577	199	—	80	189	—	6,507
Harkavy	11,063	396	—	150	414	—	10,895
Lundmark	23,948	938	19,516	(130)	754	—	43,778
Martin	—	570	25,000	(757)	—	—	26,327
Morgenroth	38,248	1,062	—	401	1,112	—	37,797
Special Instrumentation	95,493	2,889	—	1,092	—	—	97,290
Wood	620,636	19,340	—	7,307	20,260	—	612,409
Total	\$80,901,438	\$3,295,294	\$228,311	\$1,369,473	\$6,819,810	\$ —	\$76,235,760

CARNEGIE INSTITUTION OF WASHINGTON
APPROPRIATED FUNDS
BUDGET SUMMARY OF OPERATING FUND
FOR THE YEAR ENDED JUNE 30, 1975

SCHEDULE 1

	<i>Unexpended Appropriations July 1, 1974</i>	<i>Appropriations</i>	<i>Transfers and Allotments</i>	<i>Total Expenditures</i>	<i>Unexpended Appropriations June 30, 1975</i>
Terrestrial Magnetism	\$ 67,945	\$1,079,182	\$ 41,182	\$1,188,309	—
Mount Wilson Observatory	57,220	1,041,809	(29,141)	1,026,823	\$ 43,065
Las Campanas Observatory	1,332,361	755,000	202,564	2,138,180	151,745
Geophysical Laboratory	76,301	999,097	73,216	1,136,190	12,424
Embryology	45,612	838,643	(29,262)	850,729	4,264
Plant Biology	778,940	546,979	17,916	1,269,567	74,268
Genetics Research Units	—	24,500	(1,118)	23,382	—
Research Projects, etc.	68,387	50,400	1,585	51,363	69,009
Office of Administration	71,335	590,200	(90,441)	571,094	—
General publications	25,447	65,000	(1,509)	78,169	10,769
Consulting fees, insurance, taxes	3,223	90,000	40,777	134,000	—
Employee benefits, retirees	85,000	84,000	(17,579)	77,621	73,800
Employee benefits, special	11	6,000	(2,885)	3,126	—
Financial advisory services	45,076	249,000	(80,992)	213,084	—
Contingent operating fund	5,000	400,000	(367,394)	—	37,606
Unallocated appropriations	883,059	—	243,081	—	1,126,140
Total	\$3,544,917	\$6,819,810	\$ —	\$8,761,637	\$1,603,090

CARNEGIE INSTITUTION OF WASHINGTON

SCHEDULE 2

INVESTMENTS, JUNE 30, 1975

<i>Description</i>	<i>Par</i>	<i>Cost</i>	<i>Approximate Market</i>
Federal Agency Bonds			
Federal Home Loan Banks, Cons., 7.30s, 1983	\$1,000,000	\$ 999,375	\$ 960,000
Federal Home Loan Banks, Cons., 7.80s, 1976	1,000,000	992,656	1,006,250
Federal Home Loan Banks, Cons., 7.80s, 1980	500,000	501,719	498,750
Federal Home Loan Banks, Cons., 9.50s, 1979	200,000	199,925	209,500
Federal National Mortgage Assn., 7.95s, 1984	500,000	496,250	492,500
Federal National Mortgage Assn., Cons., 9.80s, 1979	200,000	200,000	211,000
Twelve Federal Land Banks, Cons., 7.30s, 1982	500,000	500,000	481,875
USA Treasury, Notes, 8s, 1982	1,150,000	1,157,188	1,157,901
Total		<u>5,047,113</u>	<u>5,017,776</u>
Foreign Bonds			
Alcan Aluminum Corporation, Prom. Note, 4 ¾ s, 1984	606,000	606,000	481,770
Aluminum Co. of Canada, Ltd., S. F. Deb., 9 ½ s, 1995	500,000	517,267	475,000
Churchill Falls (Labrador) Corp. Ltd., 1st Mtg. Series A, 7 ¾ s, 2007	800,000	800,000	606,000
IAC Ltd., Sec. Note, Series Z, 5 ¼ s, 1982	750,000	750,000	532,500
Quebec Hydro-Electric Commission, S. F. Deb., 5s, 1988	640,000	628,083	440,000
Quebec Hydro-Electric Commission, Deb. Series BN, 9 ¼ s, 1995	500,000	504,126	477,500
Total		<u>3,805,476</u>	<u>3,012,770</u>
Public Utility Bonds			
American Telephone & Telegraph Company, Deb., 8.70s, 2002	925,000	925,000	926,156
American Telephone & Telegraph Company, Deb., 8 ¾ s, 2000	375,000	375,500	380,156
Minnesota Power & Light Co., 1st Mtg., 3 ½ s, 1975	200,000	200,510	200,000
Pacific Gas & Electric Co., 1st & Ref. Mtg. Series BB, 5s, 1989	250,000	251,050	170,000
Pacific Power & Light Co., 1st Mtg., 4 ¾ s, 1986	250,000	251,551	170,938
Potomac Electric Power Co., Deb., 4 ¾ s, 1982	210,000	212,225	162,225
Washington Water Power Co., 1st Mtg., 4 ¾ s, 1987	300,000	300,000	208,500
Total		<u>2,515,836</u>	<u>2,217,975</u>

CARNEGIE INSTITUTION OF WASHINGTON

INVESTMENTS—Continued

<i>Description</i>	<i>Par</i>	<i>Cost</i>	<i>Approximate Market</i>
Industrial and Miscellaneous Bonds			
American Express Credit Corp., Sr. Note, 9 ½ s, 1982	\$ 500,000	\$ 500,000	\$ 506,250
American Hoechst Corp., Note, 5 ¾ s, 1986	802,000	802,000	671,675
Arco Pipe Line Co., Note, 8s, 1982	300,000	298,500	299,250
Atlantic Richfield Co., Demand Note	199,000	199,000	199,000
Bank of America NT & SA San Francisco, Ctf. of Dep., 7s, 1976	500,000	500,000	499,300
Boeing Co., Notes, 6 ¾ s, 1986	636,000	636,000	440,430
Chase Manhattan Bank, Ctf. of Dep., 6 ½ s, 1975	500,000	500,000	499,980
Columbia Broadcasting System Inc., Prom. Note, 5 ½ s, 1991	720,000	720,000	549,000
Commercial Credit Co., Note, 3 ⅝ s, 1976	400,000	401,381	390,500
Continental Illinois Nat'l Bank & Trust Co., Ctf. of Dep., 5 ⅝ s, 1975	500,000	500,000	499,875
Crown Zellerbach Corp., Prom. Note, 4 ⅝ s, 1981	175,000	175,000	150,938
Crown Zellerbach Corp., S. F. Deb., 8 ⅞ s, 2000	1,000,000	1,026,929	971,250
Erie Mining Company, 1st Mtg. Series B, 4 ½ s, 1983	291,000	280,662	189,878
First International Bancshares Inc., Notes, 9s, 1983	450,000	450,000	454,500
First National City Bank of New York, Ctf. of Dep., 5 ⅞ s, 1975	500,000	500,000	499,725
First National City Bank of New York, Ctf. of Dep., 6 ⅞ s, 1975	500,000	500,000	498,705
Fischbach & Moore Inc., Conv. Sub. Deb., 4 ¾ s, 1997	238,000	246,725	176,120
Four Corners Pipe Line Co., Sec. Note, 5s, 1982	80,000	80,000	69,600
General Electric Credit Corp., Notes, 8.60s, 1985	500,000	500,500	505,000
General Motors Acceptance Corp., 4 ⅝ s, 1982	480,000	390,912	385,200
General Motors Acceptance Corp., Deb., 5s, 1977	200,000	195,000	190,250
General Motors Acceptance Corp., Deb., 5s, 1981	200,000	199,000	172,000
General Telephone & Electronics Corp., Demand Note	491,000	491,000	491,000
Inter-American Development Bank, Notes, 8 ½ s, 1985	500,000	502,500	499,375
Intl. Bank for Reconstruction and Development, Notes, 8.15s, 1985	400,000	400,000	398,500
International Harvester Credit Corp., Demand Note	91,000	91,000	91,000
Kaiser Aluminum & Chemical Corp., 1st Mtg., 5 ½ s, 1987	174,000	174,000	124,410

CARNEGIE INSTITUTION OF WASHINGTON

INVESTMENTS—Continued

<i>Description</i>	<i>Par</i>	<i>Cost</i>	<i>Approximate Market</i>
Industrial and Miscellaneous Bonds —Continued			
Kresge (S. S.) Company, Prom. Note, 4 $\frac{7}{8}$ s, 1983	\$ 536,667	\$ 536,667	\$ 415,916
Manufacturers Hanover Trust Co., Ctf. of Dep., 6.55s, 1976	500,000	500,000	498,780
Mercantile Stores Co., Inc., S. F. Deb., 8.70s, 1995	500,000	500,000	450,000
Montgomery Ward Credit Corp., Deb., 4 $\frac{7}{8}$ s, 1980	200,000	199,000	162,000
NCNB Corp., S. F. Deb., 8.40s, 1995	500,000	497,500	430,000
Sears Roebuck Acceptance Corp., Sub. Deb., 4 $\frac{7}{8}$ s, 1977	525,000	511,505	496,781
Sears Roebuck Acceptance Corp., Sub. Deb., 8 $\frac{3}{8}$ s, 1986	400,000	399,200	402,000
Sears Roebuck & Co., 7 $\frac{3}{4}$ s, 1985	500,000	491,250	487,500
Shell Funding Corp., Collat. Tr. Note, 4 $\frac{3}{4}$ s, 1985	648,000	648,000	521,640
Trailer Train Co., 4 $\frac{7}{8}$ s, 1976	64,709	64,709	62,768
United Air Lines Inc., Notes, 5s, 1984	630,000	630,000	448,875
Weyerhaeuser Co., Notes, 8s, 1985	500,000	498,750	497,500
Woolworth (F. W.) Company, Prom. Note, 5s, 1981	429,481	429,481	339,290
Total		<u>17,166,171</u>	<u>15,635,761</u>
Bonds, funds invested		<u>\$28,534,596</u>	<u>\$25,884,282</u>

	<i>Shares</i>	<i>Cost</i>	<i>Approximate Market</i>
Common Stocks			
Air Products & Chemicals, Inc.	18,360	\$ 875,222	\$ 1,383,885
Alcon Laboratories, Inc.	8,000	261,374	219,000
American Home Products Corp.	25,000	1,010,058	1,043,750
AMP Incorporated	32,000	694,753	1,192,000
A T Cross Co.	4,000	238,000	129,500
Automatic Data Processing Inc.	3,000	80,182	174,375
Baker Oil Tools, Inc.	20,000	551,538	1,097,500
Cameron Iron Works, Inc.	2,000	228,900	364,000
Caterpillar Tractor Co.	19,000	1,164,340	1,270,625
Central Telephone & Utilities Corp.	40,000	596,511	850,000
Charles River Breeding Labs, Inc.	6,000	221,784	150,000
Chemed Corporation	8,000	276,762	164,000
Chesebrough-Pond's, Inc.	23,000	769,130	1,477,750

CARNEGIE INSTITUTION OF WASHINGTON

INVESTMENTS—*Continued*

<i>Description</i>	<i>Shares</i>	<i>Cost</i>	<i>Approximate Market</i>
Common Stocks — <i>Continued</i>			
Christiana Securities Company	6,221	\$ 820,683	\$ 762,073
Citicorp	50,000	896,429	1,925,000
Coca-Cola Company (The)	19,000	304,865	1,721,875
Connecticut General Insurance Corp.	20,000	1,056,250	885,000
Data General Corp.	4,000	124,672	137,500
Disney (Walt) Productions	20,000	695,864	1,010,000
Dow Chemical Co.	18,000	1,064,836	1,615,500
Drexler Technology Corporation	50	81	113
Eastman Kodak Company	30,000	404,533	3,097,500
Eli Lilly & Co.	10,000	799,125	783,750
Exxon Corporation	23,000	668,525	2,127,500
First Alabama Bancshares, Inc.	5,000	166,600	88,750
Ford Motor Co.	25,000	1,063,396	1,028,125
General Electric Company	30,000	581,734	1,578,750
General Motors Corporation	30,000	900,794	1,462,500
Genuine Parts Co.	25,000	687,353	1,000,000
Gilbert Associates, Inc.	9,000	355,363	216,000
Goodyear Tire & Rubber Co.	40,000	557,439	760,000
Halliburton Company	7,000	917,001	1,312,500
Helmerich & Payne, Inc.	4,500	195,652	172,125
Hewlett-Packard Co.	5,000	306,643	595,625
International Business Machines Corp.	22,000	594,926	4,598,000
International Nickel Co. of Canada, Ltd.	35,000	1,182,229	975,625
International Paper Co.	15,000	667,500	765,000
John H. Harland	5,000	130,137	132,500
Johnson & Johnson	12,000	232,795	1,168,500
Kaiser Aluminum & Chemical Corp.	25,000	781,075	806,250
Kresge (S. S.) Co.	40,000	1,405,036	1,285,000
Lawter Chemicals Inc.	10,937	249,989	147,650
Mary Kay Cosmetics Inc.	4,000	63,438	76,000
McDonalds Corp.	15,000	801,282	855,000
Merck & Co., Inc.	20,000	350,862	1,700,000
Minnesota Mining & Manufacturing Co.	34,000	1,735,833	2,286,500
National Chemsearch Corp.	28,000	1,117,808	1,407,000
Northrup & King Co.	9,000	223,500	204,750
Ocean Drilling & Exploration Co.	2,500	105,075	100,625
Peabody Galion Corporation	30,000	1,027,857	600,000
Penny (J. C.) Company, Inc.	20,000	1,124,042	1,160,000
Petrie Stores Corp.	2,000	136,781	136,500
Philip Morris, Inc.	15,000	967,725	800,625
Pickwick International, Inc.	20,000	724,354	347,500
Potlatch Corp.	20,000	797,717	972,500

CARNEGIE INSTITUTION OF WASHINGTON

INVESTMENTS—*Continued*

<i>Description</i>	<i>Shares</i>	<i>Cost</i>	<i>Approximate Market</i>
Common Stocks — <i>Continued</i>			
Procter & Gamble Co.	17,000	\$ 1,687,475	\$ 1,668,125
Puritan Bennett Corp.	4,000	248,675	174,000
Ralston Purina Co.	35,000	1,538,856	1,575,000
Reynolds & Reynolds Co.	6,000	264,188	96,000
Sabine Royalty Corp.	4,635	190,821	179,606
Schering-Plough Corp.	15,000	1,175,897	873,750
Schlumberger, Ltd.	30,000	596,423	2,610,000
Sears Roebuck and Co.	20,000	1,821,704	1,467,500
Snap-on Tools Corp.	6,000	332,225	187,500
Squibb Corp.	25,000	1,163,536	950,000
Standard Oil Co. of California	35,000	1,394,986	1,111,250
Standard Oil Co. of Ohio	18,000	1,254,381	1,377,000
Tennant Co.	5,000	209,525	135,000
Tennessee Valley Bancorp, Inc.	8,000	231,638	120,000
Union Camp Corp.	12,000	790,419	823,500
Union Carbide Corp.	10,000	627,500	618,750
Waste Management, Inc.	14,000	296,000	143,500
Xerox Corp.	20,000	1,505,841	1,402,500
Common stocks, funds invested		<u>49,286,443</u>	<u>67,835,077</u>
Aggregate investments		<u><u>\$77,821,039</u></u>	<u><u>\$93,719,359</u></u>

SCHEDULE 3

CARNEGIE INSTITUTION OF WASHINGTON
SUMMARY OF INVESTMENT TRANSACTIONS
FOR THE YEAR ENDED JUNE 30, 1975

Cash awaiting investment, July 1, 1974 \$ 298

Sales and Redemptions

	<i>Gain</i>	<i>Capital Loss</i>	<i>Book Value</i>
Bonds	—	\$ 151,306	\$25,462,129
Common stocks	<u>\$4,911,598</u>	<u>6,129,765</u>	<u>17,828,216</u>
	4,911,598	6,281,071	43,290,345
Realized capital loss, net	<u>—</u>	<u>(1,369,473)</u>	<u>(1,369,473)</u>
	<u><u>\$4,911,598</u></u>	<u><u>\$4,911,598</u></u>	
Total sales and redemptions			41,920,872
Cash transferred to Operating Fund			<u>(4,975,000)</u>
Total			36,946,170

Acquisitions

Bonds	\$31,014,781
Common stocks	<u>5,929,962</u>
Total acquisitions	<u>36,944,743</u>
Cash awaiting investment, June 30, 1975	<u><u>\$ 1,427</u></u>

Articles of Incorporation

Fifty-eighth Congress of the United States of America;

At the Second Session,

Begun and held at the City of Washington on Monday, the seventh day of December, one thousand nine hundred and three.

AN ACT

To incorporate the Carnegie Institution of Washington.

Be it enacted by the Senate and House of Representatives of the United States of America in Congress assembled, That the persons following, being persons who are now trustees of the Carnegie Institution, namely, Alexander Agassiz, John S. Billings, John L. Cadwalader, Cleveland H. Dodge, William N. Frew, Lyman J. Gage, Daniel C. Gilman, John Hay, Henry L. Higginson, William Wirt Howe, Charles L. Hutchinson, Samuel P. Langley, William Lindsay, Seth Low, Wayne MacVeagh, Darius O. Mills, S. Weir Mitchell, William W. Morrow, Ethan A. Hitchcock, Elihu Root, John C. Spooner, Andrew D. White, Charles D. Walcott, Carroll D. Wright, their associates and successors, duly chosen, are hereby incorporated and declared to be a body corporate by the name of the Carnegie Institution of Washington and by that name shall be known and have perpetual succession, with the powers, limitations, and restrictions herein contained.

SEC. 2. That the objects of the corporation shall be to encourage, in the broadest and most liberal manner, investigation, research, and discovery, and the application of knowledge to the improvement of mankind; and in particular—

(a) To conduct, endow, and assist investigation in any department of science, literature, or art, and to this end to cooperate with governments, universities, colleges, technical schools, learned societies, and individuals.

(b) To appoint committees of experts to direct special lines of research.

(c) To publish and distribute documents.

(d) To conduct lectures, hold meetings, and acquire and maintain a library.

(e) To purchase such property, real or personal, and construct such building or buildings as may be necessary to carry on the work of the corporation.

(f) In general, to do and perform all things necessary to promote the objects of the institution, with full power, however, to the trustees hereinafter appointed and their successors from time to time to modify the conditions and regulations under which the work shall be carried on, so as to secure the application of the funds in the manner best adapted to the conditions of the time, provided that the objects of the corporation shall at all times be among the foregoing or kindred thereto.

SEC. 3. That the direction and management of the affairs of the corporation and the control and disposal of its property and funds shall be vested in a board of trustees, twenty-two in number, to be composed of the following individuals: Alexander Agassiz, John S. Billings, John L. Cadwalader, Cleveland H. Dodge, William N. Frew, Lyman J. Gage, Daniel C. Gilman, John Hay, Henry L. Higginson, William Wirt Howe, Charles L. Hutchinson, Samuel P. Langley, William Lindsay, Seth Low, Wayne MacVeagh, Darius O. Mills, S. Weir Mitchell, William W. Morrow, Ethan A. Hitchcock, Elihu Root, John C. Spooner, Andrew D. White, Charles D. Walcott, Carroll D. Wright, who shall constitute the first board of trustees. The board of trustees shall have power from time to time to increase its membership to not more than twenty-seven members. Vacancies occasioned by death, resignation, or otherwise shall be filled by the remaining trustees in such manner as the by-laws shall prescribe; and the persons so elected shall thereupon become trustees and also members of the said corporation. The principal place of business of the said corporation shall be the city of Washington, in the District of Columbia.

SEC. 4. That such board of trustees shall be entitled to take, hold and administer the securities, funds, and property so transferred by said Andrew Carnegie to the trustees of the Carnegie Institution and such other funds or property as may at any time be given, devised, or bequeathed to them, or to such corporation, for the purposes of the trust; and with full power from time to time to adopt a common seal, to appoint such officers, members of the board of trustees or otherwise, and such employees as may be deemed necessary in carrying on the business of the corporation, at such salaries or with such remuneration as they may deem proper; and with full power to adopt by-laws from time to time and such rules or regulations as may be necessary to secure the safe and convenient transaction of the business of the corporation; and with full power and discretion to deal with and expend the income of the corporation in such manner as in their judgment will best promote the objects herein set forth and in general to have and use all powers and authority necessary to promote such objects and carry out the purposes of the donor. The said trustees shall have further power from time

to time to hold as investments the securities hereinabove referred to so transferred by Andrew Carnegie, and any property which has been or may be transferred to them or such corporation by Andrew Carnegie or by any other person, persons, or corporation, and to invest any sums or amounts from time to time in such securities and in such form and manner as are permitted to trustees or to charitable or literary corporations for investment, according to the laws of the States of New York, Pennsylvania, or Massachusetts, or in such securities as are authorized for investment by the said deed of trust so executed by Andrew Carnegie, or by any deed of gift or last will and testament to be hereafter made or executed.

SEC. 5. That the said corporation may take and hold any additional donations, grants, devises, or bequests which may be made in further support of the purposes of the said corporation, and may include in the expenses thereof the personal expenses which the trustees may incur in attending meetings or otherwise in carrying out the business of the trust, but the services of the trustees as such shall be gratuitous.

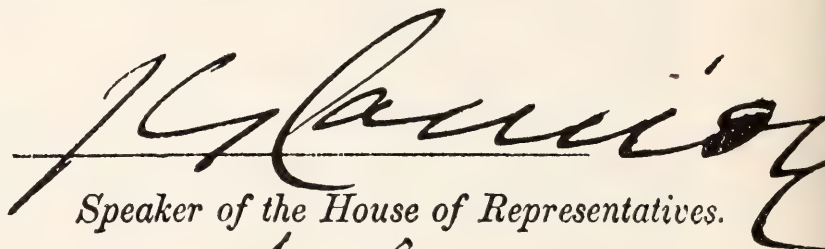
SEC. 6. That as soon as may be possible after the passage of this Act a meeting of the trustees hereinbefore named shall be called by Daniel C. Gilman, John S. Billings, Charles D. Walcott, S. Weir Mitchell, John Hay, Elihu Root, and Carroll D. Wright, or any four of them, at the city of Washington, in the District of Columbia, by notice served in person or by mail addressed to each trustee at his place of residence; and the said trustees, or a majority thereof, being assembled, shall organize and proceed to adopt by-laws, to elect officers and appoint committees, and generally to organize the said corporation; and said trustees herein named, on behalf of the corporation hereby incorporated, shall thereupon receive, take over, and enter into possession, custody, and management of all property, real or personal, of the corporation heretofore known as the Carnegie Institution, incorporated, as hereinbefore set forth under "An Act to establish a Code of Law for the District of Columbia, January fourth, nineteen hundred and two," and to all its rights, contracts, claims, and property of any kind or nature; and the several officers of such corporation, or any other person having charge of any of the securities, funds, real or personal, books or property thereof, shall, on demand, deliver the same to the said trustees appointed by this Act or to the persons appointed by them to receive the same; and the trustees of the existing corporation and the trustees herein named shall and may take such other steps as shall be necessary to carry out the purposes of this Act.

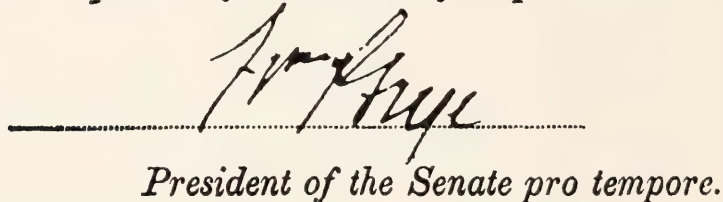
SEC. 7. That the rights of the creditors of the said existing corporation known as the Carnegie Institution shall not in any manner be impaired by the

passage of this Act, or the transfer of the property hereinbefore mentioned, nor shall any liability or obligation for the payment of any sums due or to become due, or any claim or demand, in any manner or for any cause existing against the said existing corporation, be released or impaired; but such corporation hereby incorporated is declared to succeed to the obligations and liabilities and to be held liable to pay and discharge all of the debts, liabilities, and contracts of the said corporation so existing to the same effect as if such new corporation had itself incurred the obligation or liability to pay such debt or damages, and no such action or proceeding before any court or tribunal shall be deemed to have abated or been discontinued by reason of the passage of this Act.

SEC. 8. That Congress may from time to time alter, repeal, or modify this Act of incorporation, but no contract or individual right made or acquired shall thereby be divested or impaired.

SEC. 9. That this Act shall take effect immediately.


Speaker of the House of Representatives.


President of the Senate pro tempore.

Approved,
April 28, 1904.

Theodore Roosevelt

By-Laws of the Institution

Adopted December 13, 1904. Amended December 13, 1910, December 13, 1912, December 10, 1937, December 15, 1939, December 13, 1940, December 18, 1942, December 12, 1947, December 10, 1954, October 24, 1957, May 8, 1959, May 13, 1960, May 10, 1963, May 15, 1964, March 6, 1967, May 3, 1968, May 14, 1971, August 31, 1972, and May 9, 1974.

ARTICLE I

The Trustees

1. The Board of Trustees shall consist of twenty-four members with power to increase its membership to not more than twenty-seven members. The Trustees shall hold office continuously and not for a stated term.

2. In case any Trustee shall fail to attend three successive annual meetings of the Board he shall thereupon cease to be a Trustee.

3. No Trustee shall receive any compensation for his services as such.

4. All vacancies in the Board of Trustees shall be filled by the Trustees by ballot at an annual meeting, but no person shall be declared elected unless he receives the votes of two-thirds of the Trustees present.

5. If, at any time during an emergency period, there be no surviving Trustee capable of acting, the President, the Director of each existing Department, and the Executive Officer, or such of them as shall then be surviving and capable of acting, shall constitute a Board of Trustees *pro tem*, with full powers under the provisions of the Articles of Incorporation and these By-Laws. Should neither the President, nor any such Director, nor the Executive Officer be capable of acting, the senior surviving Staff Member of each existing Department shall be a Trustee *pro tem* with full powers of a Trustee under the Articles of Incorporation and these By-Laws. It shall be incumbent on the Trustees *pro tem* to reconstitute the Board with permanent members within a reasonable time after the emergency has passed, at which time the Trustees *pro tem* shall cease to hold office. A list of Staff Member seniority, as designated annually by the President, shall be kept in the Institution's records.

6. A Trustee who resigns after having served at least five years and having reached age seventy shall be eligible for designation by the Board as a Trustee Emeritus. A Trustee Emeritus shall be entitled to attend the annual meeting of the Board but shall have no vote and shall not be counted for purposes of ascertaining the presence of a quorum. A Trustee Emeritus may be invited to serve in an advisory capacity on any committee of the Board of Trustees except the Executive Committee.

ARTICLE II

Officers of the Board

1. The officers of the Board shall be a Chairman of the Board, a Vice-Chairman, and a Secretary, who shall be elected by the Trustees, from the members of the Board, by ballot to serve for a term of three years. All vacancies shall be filled by the Board for the unexpired term; provided, however, that the Executive Committee shall have power to fill a vacancy in the office of Secretary to serve until the next meeting of the Board of Trustees.

2. The Chairman shall preside at all meetings and shall have the usual powers of a presiding officer.

3. The Vice-Chairman, in the absence or disability of the Chairman, shall perform the duties of the Chairman.

4. The Secretary shall issue notices of meetings of the Board, record its transactions, and conduct that part of the correspondence relating to the Board and to his duties.

ARTICLE III

Executive Administration

The President

1. There shall be a President who shall be elected by ballot by, and hold office during the pleasure of, the Board, who shall be the chief executive officer of the Institution. The President, subject to the control of the Board and the Executive Committee, shall have general charge of all matters of administration and supervision of all arrangements for research and other work undertaken by the Institution or with its funds. He shall prepare and submit to the Board of Trustees and to the Executive Committee plans and suggestions for the work of the Institution, shall conduct its general correspondence and the correspondence with applicants for grants and with the special advisers of the Committee, and shall present his recommendations in each case to the Executive Committee for decision. All proposals and requests for grants shall be referred to the President for consideration and report. He shall have power to remove, appoint, and, within the scope of funds made available by the Trustees, provide for compensation of subordinate employees and to fix the compensation of such employees within the limits of a maximum rate of compensation to be established from time to time by the Executive Committee. He shall be *ex officio* a member of the Executive Committee.

2. He shall be the legal custodian of the seal and of all property of the Institution whose custody is not otherwise provided for. He shall sign and execute on behalf of the corporation all contracts and instruments necessary in authorized administrative and research matters and affix the corporate seal thereto when necessary, and may delegate the performance of such acts and other administrative duties in his absence to the Executive Officer. He may execute all other contracts, deeds, and instruments on behalf of the corporation and affix the seal thereto when expressly authorized by the Board of Trustees or Executive Committee. He may, within the limits of his own authorization, delegate to the Executive Officer authority to act as custodian of and affix the corporate seal. He shall be responsible for the expenditure and disbursement of all funds of the Institution in accordance with the directions of the Board and of the Executive Committee, and shall keep accurate accounts of all receipts and disbursements. Following approval by the Executive Committee he shall transmit to the Board of Trustees before its annual meeting a written report of the operations and business of the Institution for the preceding fiscal year with his recommendations for work and appropriations for the succeeding fiscal year.

3. He shall attend all meetings of the Board of Trustees.

4. There shall be an officer designated Executive Officer who shall be appointed by and hold office at the pleasure of the President, subject to the approval of the Executive Committee. His duties shall be to assist and act for the President as the latter may duly authorize and direct.

5. The President shall retire from office at the end of the fiscal year in which he becomes sixty-five years of age.

ARTICLE IV

Meetings and Voting

1. The annual meeting of the Board of Trustees shall be held in the City of Washington, in the District of Columbia, in May of each year on a date fixed by the Executive Committee, or at such other time or such other place as may be designated by the Executive Committee, or if not so designated prior to May 1 of such year, by the

Chairman of the Board of Trustees, or if he is absent or is unable or refuses to act, by any Trustee with the written consent of the majority of the Trustees then holding office.

2. Special meetings of the Board of Trustees may be called, and the time and place of meeting designated, by the Chairman, or by the Executive Committee, or by any Trustee with the written consent of the majority of the Trustees then holding office. Upon the written request of seven members of the Board, the Chairman shall call a special meeting.

3. Notices of meetings shall be given ten days prior to the date thereof. Notice may be given to any Trustee personally, or by mail or by telegram sent to the usual address of such Trustee. Notices of adjourned meetings need not be given except when the adjournment is for ten days or more.

4. The presence of a majority of the Trustees holding office shall constitute a quorum for the transaction of business at any meeting. An act of the majority of the Trustees present at a meeting at which a quorum is present shall be the act of the Board except as otherwise provided in these By-Laws. If, at a duly called meeting, less than a quorum is present, a majority of those present may adjourn the meeting from time to time until a quorum is present. Trustees present at a duly called or held meeting at which a quorum is present may continue to do business until adjournment notwithstanding the withdrawal of enough Trustees to leave less than a quorum.

5. The transactions of any meeting, however called and noticed, shall be as valid as though carried out at a meeting duly held after regular call and notice, if a quorum is present and if, either before or after the meeting, each of the Trustees not present in person signs a written waiver of notice, or consent to the holding of such meeting, or approval of the minutes thereof. All such waivers, consents, or approvals shall be filed with the corporate records or made a part of the minutes of the meeting.

6. Any action which, under law or these By-Laws, is authorized to be taken at a meeting of the Board of Trustees may be taken without a meeting if authorized in a document or documents in writing signed by all the Trustees then holding office and filed with the Secretary.

7. During an emergency period the term "Trustees holding office" shall, for purposes of this Article, mean the surviving members of the Board who have not been rendered incapable of acting for any reason including difficulty of transportation to a place of meeting or of communication with other surviving members of the Board.

ARTICLE V

Committees

1. There shall be the following Standing Committees, *viz.* an Executive Committee, a Finance Committee, an Auditing Committee, a Nominating Committee, and a Retirement Committee.

2. All vacancies in the Standing Committees shall be filled by the Board of Trustees at the next annual meeting of the Board and may be filled at a special meeting of the Board. A vacancy in the Executive Committee and, upon request of the remaining members of any other Standing Committee, a vacancy in such other Committee may be filled by the Executive Committee by temporary appointment to serve until the next meeting of the Board.

3. The terms of all officers and of all members of Committees, as provided for herein, shall continue until their successors are elected or appointed.

Executive Committee

4. The Executive Committee shall consist of the Chairman, Vice-Chairman, and Secretary of the Board of Trustees, the President of the Institution *ex officio*, and, in addition, not less than five or more than eight Trustees to be elected by the Board by ballot for a term of three years, who shall be eligible for re-election. Any member elected

to fill a vacancy shall serve for the remainder of his predecessor's term. The presence of four members of the Committee shall constitute a quorum for the transaction of business at any meeting.

5. The Executive Committee shall, when the Board is not in session and has not given specific directions, have general control of the administration of the affairs of the corporation and general supervision of all arrangements for administration, research, and other matters undertaken or promoted by the Institution. It shall also submit to the Board of Trustees a printed or typewritten report of each of its meetings, and at the annual meeting shall submit to the Board a report for publication.

6. The Executive Committee shall have power to authorize the purchase, sale, exchange, or transfer of real estate.

Finance Committee

7. The Finance Committee shall consist of not less than five and not more than six members to be elected by the Board of Trustees by ballot for a term of three years, who shall be eligible for re-election. The presence of three members of the Committee shall constitute a quorum for the transaction of business at any meeting.

8. The Finance Committee shall have custody of the securities of the corporation and general charge of its investments and invested funds, including its investments and invested funds as trustee of any retirement plan for the Institution's staff members and employees, and shall care for and dispose of the same subject to the directions of the Board of Trustees. It shall have power to authorize the purchase, sale, exchange, or transfer of securities and to delegate this power. It shall consider and recommend to the Board from time to time such measures as in its opinion will promote the financial interests of the Institution and of the trust fund under any retirement plan for the Institution's staff members and employees, and shall make a report at each meeting of the Board.

Auditing Committee

9. The Auditing Committee shall consist of three members to be elected by the Board of Trustees by ballot for a term of three years.

10. Before each annual meeting of the Board of Trustees, the Auditing Committee shall cause the accounts of the Institution for the preceding fiscal year to be audited by public accountants. The accountants shall report to the Committee, and the Committee shall present said report at the ensuing annual meeting of the Board with such recommendations as the Committee may deem appropriate.

Nominating Committee

11. The Nominating Committee shall consist of the Chairman of the Board of Trustees *ex officio* and, in addition, three Trustees to be elected by the Board by ballot for a term of three years, who shall not be eligible for re-election until after the lapse of one year. Any member elected to fill a vacancy shall serve for the remainder of his predecessor's term, provided that of the Nominating Committee first elected after adoption of this By-Law one member shall serve for one year, one member shall serve for two years, and one member shall serve for three years, the Committee to determine the respective terms by lot.

12. Sixty days prior to an annual meeting of the Board the Nominating Committee shall notify the Trustees by mail of the vacancies to be filled in membership of the Board. Each Trustee may submit nominations for such vacancies. Nominations so submitted shall be considered by the Nominating Committee, and ten days prior to the annual meeting the Nominating Committee shall submit to members of the Board by mail a list of the persons so nominated, with its recommendations for filling existing vacancies on the Board and its Standing Committees. No other nominations shall be received by the Board at the annual meeting except with the unanimous consent of the Trustees present.

Retirement Committee

13. The Retirement Committee shall consist of three members to be elected by the Board of Trustees by ballot for a term of three years, who shall be eligible for re-election and the Chairman of the Finance Committee *ex officio*. Any member elected to fill a vacancy shall serve for the remainder of his predecessor's term.

14. The Retirement Committee shall, subject to the directions of the Board of Trustees, be responsible for the maintenance of a retirement plan for staff members and employees of the Institution and act for the Institution in its capacity as trustee under any such plan, except that any matter relating to investments under any such plan shall be the responsibility of the Finance Committee subject to the directions of the Board of Trustees. The Committee shall submit a report to the Board at the annual meeting of the Board.

ARTICLE VI

Financial Administration

1. No expenditure shall be authorized or made except in pursuance of a previous appropriation by the Board of Trustees, or as provided in Article V, paragraph 8, hereof.

2. The fiscal year of the Institution shall commence on the first day of July in each year.

3. The Executive Committee shall submit to the annual meeting of the Board a full statement of the finances and work of the Institution for the preceding fiscal year and a detailed estimate of the expenditures of the succeeding fiscal year.

4. The Board of Trustees, at the annual meeting in each year, shall make general appropriations for the ensuing fiscal year; but nothing contained herein shall prevent the Board of Trustees from making special appropriations at any meeting.

5. The Executive Committee shall have general charge and control of all appropriations made by the Board. Following the annual meeting, the Executive Committee may allocate these appropriations for the succeeding fiscal year. The Committee shall have full authority to reallocate available funds, as needed, and to transfer balances.

6. The securities of the Institution and evidences of property, and funds invested and to be invested, shall be deposited in such safe depository or in the custody of such trust company and under such safeguards as the Finance Committee shall designate, subject to directions of the Board of Trustees. Income of the Institution available for expenditure shall be deposited in such banks or depositories as may from time to time be designated by the Executive Committee.

7. Any trust company entrusted with the custody of securities by the Finance Committee may, by resolution of the Board of Trustees, be made Fiscal Agent of the Institution, upon an agreed compensation, for the transaction of the business coming within the authority of the Finance Committee.

8. The property of the Institution is irrevocably dedicated to charitable purposes, and in the event of dissolution its property shall be used for and distributed to those charitable purposes as are specified by the Congress of the United States in the Articles of Incorporation, Public Law No. 260, approved April 28, 1904, as the same may be amended from time to time.

ARTICLE VII

Amendment of By-Laws

1. These By-Laws may be amended at any annual or special meeting of the Board of Trustees by a two-thirds vote of the members present, provided written notice of the proposed amendment shall have been served personally upon, or mailed to the usual address of, each member of the Board twenty days prior to the meeting.

Index of Names

- Aaronson, M., 308, 334, 360
publications, 370
- Abelson, P. H., v, vii, 17, 173, 179, 821
publications, 815
Report of the President, 1–35
- Acero, S., 140
- Acker, S., 24, 741, 780
publications, 811
- Adams, J. B., 396, 648
studies, 590–593
- Adams, W. M., 376
- Adelman, S. J., 349
- Adkins, J. M., 377
- Adler, W. H., 27, 10, 12, 103
publications, 101, 102
studies, 88, 88–90
- Agassiz, A., vi
- Akella, J., 33, 648
- Alberte, R. S., 811
- Alberts, B., 100
- Albuquerque, E. X., 100
- Alcaino, G., 349
- Aldous, E., 180
- Aldrich, L. T., 15, 35, 110, 180, 181, 299
publications, 296
studies, 291–293
- Aller, L. H., 353
- Altschuler, M. D., 315, 370
- Andersen, C. A., 296, 297
- Anderson, D. M., 734
- Angel, J. R. P., 349
- Angerer, R. C., 735
publications, 734
studies, 656–669, 673–678
- Aquirre, B., 300
- Arculus, R. J., 33, 390, 628, 630, 648
studies, 504–507, 507–512, 512–515
- Arnal, E., 300
- Arnold, L. G., 113, 300
publications, 296
studies, 146–148, 148–149
- Aronson, A. I., 180
- Arp, H. C., 34, 308, 335, 341, 365, 376
publications, 370
- Asch, E., 103
studies, 53–54, 54–60
- Ashby, E., v, 30, 819, 821
- Assousa, G. E., 35, 112, 113, 299
publications, 296, 298
studies, 126–129
- Aumento, F., 627
- Austin, T. B., 350
- Avery, R. J., 180
- Axelrod, D., 180
- Babcock, H. W., 19, 34, 376
report of the Director, Hale Observatories, 303–378
- Bahcall, J., 319, 350
- Bahcall, N., 350
- Bajaja, E., 140, 300
- Baldwin, G. J., vi
- Balick, B., 113, 296
- Bannister, J. R., 180, 291, 292, 299
- Barbour, T., vi
- Barnes, H. L., 627
- Barnett, T. R., 734
studies, 669–673
- Barry, A., 97
- Bartholomew, B., 811
- Barton, P., 627
- Bass, M. N., 109, 180, 181, 299
studies, 234–240
- Bassett, W. A., 628, 629
- Beach, L., 180, 183, 291, 292, 299, 301
publications, 296, 297
studies, 293–294
- Bechtold, J., 34, 377
- Becklin, E. E., 34, 308, 324, 326, 329, 331, 334, 360, 376
publications, 370
- Beckwith, S. V. W., 34, 326, 327, 377
- Bedke, J. R., 366, 377
- Bell, J. F., vi
- Bell, P. M., 11, 33, 383, 393, 394, 396, 628, 630, 633, 634, 648
studies, 399–402, 402–405, 555–557, 557–559, 559–561, 590–593, 593–595, 595–598
- Bennett, C. L., 35, 300
- Benson, J., 633, 649
- Berg, E., 300
- Bergstrahl, J., 317, 350
- Berry, J. A., 22, 23, 34, 740, 814
publications, 811
studies, 751–759
- Bertola, F., 337
- Bhatnagar, A., 351
- Billings, J. S., vi
- Biroc, S. L., 33, 12, 27, 103
studies, 26–27, 33–35
- Björkman, O., 22, 23, 34, 739, 740, 810
publications, 811, 812
studies, 743–748, 748–751, 760–761
- Bliss, R. W., vi
- Blumenthal, T., 100
- Boder, C., 100
- Boezi, J. A., 180
- Böhm, K.-H., 351
- Boise, J. W., vii

- Boksenberg, A., 307, 311, 319, 332, 333, 342, 343, 357
 publications, 371
- Bolton, E. T., 14, 15, 17, 35, 175, 179, 299
- Bonner, T. I., 112, 150, 180, 299
 publications, 296
 studies, 151-158
- Boroson, T., 343
- Borra, E. F., 34, 319, 344, 376
 publications, 371
- Böving, B. G., 102
- Bowen, I. S., 18
- Bowen, N. L., 630
- Boyd, F. R., Jr., 33, 391, 392, 631, 648
 studies, 519-525, 525-528, 536-539
- Boyden, J. E., 377
- Bracamonte, M., 300
- Bradford, A. H., vi
- Bradford, L., vi
- Bradley, O. N., vi
- Brady, J. B., 626, 627
- Brain, R., 24, 742, 810
- Branscomb, L. M., v, 821
- Braunstein, R., 352
- Brenner, D. J., 180
- Bresnahan, R. E., 180
- Bridgman, P. W., 12
- Briggs, W. R., 24, 31, 34, 810, 814
 publications, 811
 report of the Director, Department of Plant Biology, 739-742
 studies, 805-807, 807-809
- Britten, R. J., vii, 17, 28, 29, 177, 179, 655, 735
 report of the Developmental Biology Research Group, 655-735
 studies, 656-669, 669-673, 673-678, 678-688, 688-699, 699-711, 711-723, 723-732
- Britz, S., 34, 742, 810, 814
 studies, 794-803, 803-805
- Brookings, R. S., vi
- Brooks, C., 110, 111, 180, 182, 300
 publications, 296
 studies, 240-247, 247-250
- Brown, D. D., 25, 26, 32, 33, 7, 8, 11, 14, 102, 656
 publications, 101, 102
 studies, 12, 13, 19, 19-26
- Brown, J. S., 24, 741, 814
 publications, 811
 studies, 776-779, 779-783
- Brown, L., 17, 35, 113, 385
 publications, 296
 studies, 141, 141-146, 146-148, 148-149, 149-150
- Brown, R. D., 26, 33, 9, 11, 12, 15, 102
 publications, 101
 studies, 12, 13, 13-14
- Brownlee, G., 12, 14, 103
 publications, 101
- Brucato, R. J., 21, 34, 312, 347, 376
- Bryan, W. B., 628, 649
 publications, 633
- Burnham, C. W., 627, 628
- Burrhus, K. D., 180
- Burstein, D., 364
- Burt, D. M., 626, 627
- Bush, V., vi, 10, 173, 821
- Cabre, R., 300
- Cadwalader, J. L., vi
- Campbell, W. W., vi
- Caponi, M., 140
- Card, D., 100
- Card, K. A., 811, 812
- Carey, R., 810, 814
- Carnegie, A., 4, 10
- Carpenter, R., 341
- Carroll, D., 25, 26, 33, 8, 9, 11, 12, 102
 publications, 101
 studies, 12, 13, 14-19
- Carswell, R. F., 311, 342
- Carter, F. L., 628
- Carty, J. J., vi
- Casaverde, M., 180, 291, 299
- Cathles, L., 625, 626, 627
- Chamberlin, M. E., 180, 655, 735
 publications, 734
 studies, 711-723
- Chang, F. H., 811, 812
- Charles, R. W., 633
- Charlu, T. V., 515
- Chase, J. W., 103
- Chayes, F., 33, 392, 631, 648
 studies, 542-550
- Cherry, S., 103
 studies, 67-68
- Chinner, G., 516
- Chiscon, J. A., 180
- Chou, I.-M., 649
- Clardy, K. D., 377
- Clayton, D., 100
- Cochran, D. B., 735
- Cohen, G. N., 151, 180, 300
 publications, 296
 studies, 165-172
- Cole, W. R., vi
- Coleman, R. A., 742, 811
- Collett, C. F., 735
- Colomb, R., 140, 300
- Comaford, D., 296, 297
- Connes, P., 351
- Connor, J. T., v, 31, 821
- Constantini, F., 735
- Coon, H. G., 12, 103
 publications, 101
- Cordova, F., 34, 377
- Cosgrove, D., 34, 810, 814
- Costrejean, J.-M., 296
- Coutts, C., 352
- Cowie, D. B., 35, 113, 150, 151, 173, 179, 299
 publications, 296
 studies, 165-172
- Cowley, A., 296
- Cragg, T. A., 377
- Crain, W. R., 735
 publications, 734
- Craine, E. R., 296, 298

- Creaser, E. H., 180
 Crippa, M., 100
 Cronin, J. R., 33, 384, 398, 631, 648
 studies, 415–416, 617–619
 Crutcher, R. M., 352
 Currie, D. G., 352
 Cuyubamba, A., 35, 110, 180, 182, 299
 publications, 296
 studies, 247–250
 Czyzak, S. J., 353
- Danziger, J., 353
 Darby, H. H., 17, 173, 180
 Darnell, J., 100
 Datlowe, D. W., 314, 371
 David, M. M., 735
 Davidson, E. H., 28, 29, 180, 655, 735
 publications, 734
 studies, 656–669, 669–673, 673–678, 678–688,
 688–699, 699–711, 711–723, 723–732
 Davidson, N., 12, 103
 publications, 101
 Davis, G. L., 12, 15, 33, 180, 300, 384, 399, 649
 studies, 416–417, 619–623, 623–625
 Davis, M. B., 180, 299
 Dawid, I. B., 25, 33, 8, 11, 12, 102
 publications, 101, 102
 studies, 19–26, 46, 47–48
 de Francesca, L., 100
 DeHaan, R. L., 102
 Delano, F. A., vi
 del Pozo, S., 180, 292, 300
 Demarque, P., 323, 354, 376
 Demerec, M., 172
 publications, 815
 Demers, S., 354
 Dennison, E. W., 34, 376
 De Noyer, L. K., 113, 129, 300
 de Ruiter, H. R., 340, 364, 365, 370
 Deslattes, R., 628
 De Vay, J. E., 791
 Devreotes, P. N., 26, 33, 9, 12, 103
 publications, 101
 studies, 67–68, 68–73, 74–78
 Dickens, R. J., 352
 Diebold, J., v, 31, 821
 Dimroth, E., 629
 Diner, D., 316, 371
 Dodge, C. H., vi
 Dodge, W. E., vi
 d'Odorico, S., 337
 Dodson, M. H., 180, 300, 629
 publications, 296
 studies, 210–217
 Doering, C., 35, 300
 Donoghue, T. R., 296
 Drachman, D. B., 26, 9, 12, 103
 studies, 81–85
 Duerksen, J. D., 180
 Duggan, J. L., 296, 297
 Duncan, W. H., 103
 studies, 53–54, 64–65, 67–68
 Durantón, J., 24, 741, 780, 810, 811
- Duryee, W. R., 17, 173, 180
- Eames, J. H., 180
 Ebert, J. D., 24, 27, 31, 33, 10, 102
 publications, 101, 102
 report of the Director, Department of Em-
 bryology, 3–103
 studies, 88, 88–90, 90–92, 93–94, 94–97
 Ecklund, E. T., 113, 301
 studies, 131–133, 138–139
 Eden, F. C., 735
 Edgell, M., 100
 Edidin, M., 103
 Eggen, O., 19, 307, 322
 Eggler, D. H., 13, 14, 33, 388, 389, 628, 631, 648
 studies, 468–474, 474–479, 479–484
 Ehleringer, J., 22, 34, 739, 740, 810, 814
 publications, 811
 studies, 743–748, 760–761
 Ekers, R., 340
 El Goresy, A., 620, 633
 Elias, J. H., 34, 325, 371, 377
 Emmons, S., 33, 11, 12, 102
 studies, 12, 19
 Endow, S., 100
 Epps, E., 352
 Erkes, J. W., 113, 129, 300
 Erlank, A. J., 297, 300
 Ermanovics, I., 399, 649
 studies, 623–625
 Eugster, H. P., 625, 649
 Evans, N. J., 327, 354
 Evertson, D. W., 180, 300
- Fambrough, D. M., 26, 33, 9, 11, 102
 publications, 101
 studies, 67–68, 68–73, 74–78, 81–85
 Fanti, R., 340
 Fenner, C. P., vi
 Ference, M., Jr., v, 819, 821, 822
 Ferguson, H. L., vi
 Ferry, J., 627
 Filloy, E. M., 140, 300
 Finger, L. W., 33, 391, 392, 394, 395, 628, 631,
 648
 publications, 633, 634
 studies, 519–525, 539–542, 564–569, 569–572,
 572–575
 Fischberg, M., 722
 Fisher, G. W., 625, 626, 649
 Fiske, R. S., 628
 Fitzgerald, M. P., 355
 Fletcher, R. C., 180, 300, 385, 625, 626, 627, 629,
 631, 649
 publications, 296
 studies, 424–428
 Flexner, J. B., 178, 179, 300
 Flexner, L. B., 178, 179, 180, 300
 Flexner, S., vi
 Flores, A., 35, 180, 300
 Forbes, W. C., vi
 Forbush, S. E., 35, 180, 181, 183, 300
 studies, 293–294

- Ford, W. K., Jr., 16, 17, 35, 111, 112, 113, 125, 299, 369
 studies, 113-118, 120-123, 123-125, 135-137, 137-138
- Fork, D. C., 22, 23, 24, 34, 740, 741, 814
 publications, 811-812
 studies, 751-759, 766-776, 776-779
- Forrestal, J., vi
- Forsheit, A., 12, 101, 103
- Foster, T., 649
- Foukal, P., 355
- Franco, M., 140, 141
- Frantz, J. D., 33, 385, 436, 625, 626, 627, 630, 631, 648
 publications, 634
 studies, 417-424
- Freeberg, J., 24, 742, 810, 814
- French, B. M., 649
- French, C. S., 22, 32, 34, 810, 814
- French, E. F., 180
- Frew, W. N., vi
- Fricke, K. J., 355
- Fridenberg, J. T., 18, 349
 publications, 371
- Friedman, M., 33, 103
- Frogel, J., 308, 334, 360
 publications, 371
- Fujita, Y., 355
- Fuster, J. M., 628, 649
- Gage, L. J., vi
- Galau, G. A., 655, 735
 publications, 734
 studies, 669-673, 673-678, 711-723
- Garavito, C., 300
- Gardner, E., 12, 97, 98, 102
 publications, 101
 studies, 97-98
- Gardner, G., 811
- Gardner, R. K., 296, 297
- Gardner, W., 649
- Garrison, R., 740, 811
 studies, 751-759
- Garrison, S., 23
- Gasser, R. F., 98, 101
- Gausden, E. G., 814
- Gatley, I., 326, 371
- Gazze, L. A., 180, 301
- Gehrels, T., 356
- Gelderman, A., 180
- Gelfand, R. A., 734
 studies, 669-673
- Gélinas, L., 180, 300
 studies, 240-250
- George, J. M., 180
- Gergely, T., 140
- Gezari, D. Y., 325, 376
 publications, 371
- Giesecke, A. A., 180, 300
- Gifford, W. S., vi
- Gil, M., 140, 300
- Gilbert, C., vi
- Gilbert, C. J., v, 821
- Giletti, B. J., 296, 297
 publications, 815
- Gillett, F. H., vi
- Gilman, D. C., vi
- Giza, P., 41, 103
 studies, 36, 36-38, 41-42
- Gladwin, M. T., 296, 298
- Godwin, J. G., 350
- Goldberg, R. B., 655
 publications, 734
 studies, 669-673
- Golden, W. T., v, 821
- Goldich, S. S., 296, 297
- Goodwin, A. M., 399, 623
- Gordon, M., 141, 300
- Gott, J. R., 19, 307, 338
 publications, 371
- Grady, N. J., 180
- Graham, J. A., 113, 114, 300
- Grauert, B., 296
- Gray, H. H., v, 819, 821, 822
- Gray, J., 180
- Gray, T. J., 296, 297
- Green, R., 342, 343, 377
 publications, 371
- Greene, T. B., 362
- Greenewalt, C. H., v, 819, 821, 822
- Greenough, W. C., v, 31, 821
- Greenstein, J. L., 20, 34, 310, 311, 320, 376
 publications, 371
- Gregory, T. S., 377
- Griffin, R. F., 356, 371
- Griffin, W., 180
- Guidotti, C. V., 630
- Guiso, N., 296
- Gulkis, S., 341
- Gunn, J. E., 20, 21, 34, 309, 312, 322, 323, 339, 345, 346, 347, 349, 356, 376
- Gurney J. J., 392, 649
 studies, 528-536
- Hackett, W., 811, 812
- Hagar, W. G., 34, 814
 publications, 811
- Haggerty, P. E., v, 30
- Haggerty, S. E., 396, 649
 studies, 593-595
- Hall, A. E., 811
- Hänny, R., 296
- Haraburda, J. M. S., vii
- Hardy, E., 34, 337, 344, 376
- Hare, P. E., 33, 397, 629, 631, 648
 publications, 634
 studies, 609-612, 612-617
- Harris, J. W. S., 103
- Harris, N. B. W., 399, 623, 649
 studies, 623-625
- Harrison, A. T., 811, 812
- Harrison, D., 100
- Hart, M. H., 34, 376
- Hart, S. R., 15, 16, 35, 109, 110, 111, 180, 181, 252, 299
 publications, 297
 studies, 195-210, 218-224, 224-234

- Harte, B., 387, 392, 628, 631, 649
 studies, 438–446, 528–536
 Hartwick, F. D. A., 331, 334, 356
 Harvey, E. N., 30
 Haskins, C. P., v, 819, 821
 Hass, J., 627
 Hastie, L. M., 297, 298
 Hauser, M., 325
 Hay, J., vi
 Haynes, C. V., 629
 Hedges, J. I., 33, 396, 629, 648
 studies, 604–609
 Heiles, C., 113, 127, 140, 300
 Helgeson, H., 625, 626
 Helin, E. F., 362
 Helsley, C. E., 300
 Hemley, J., 627
 Henard, K. R., vii
 Henry, B. M., vi
 Herrick, M. T., vi
 Hershey, A. D., vii, 8
 Hertel, R., 24, 742
 Hertig, A. T., 97, 102
 Hewitt, A. S., vi
 Hewitt, D., 626
 Hewitt, R. E., vii
 Hewlett, W. R., v, 821
 Hickson, P., 34, 372, 377
 Hiesey, W. M., 34, 814
 Higashinakagawa, T., 33, 11, 102
 publications, 101–102
 studies, 26–27, 28–33
 Higgins, R. C., 734
 studies, 669–673
 Higginson, H. L., vi
 Hinthorne, J. R., 297
 Hitchcock, E. A., vi
 Hitchcock, H., vi
 Hiyama, T., 22, 34, 814
 Hodges, F. N., 33, 648
 publications, 634
 Hoering, T. C., 33, 386, 396, 629, 631, 648
 studies, 436–438, 598–604
 Hoersch, A., 649
 Hoessel, J. G., 34, 377
 Hofmann, A. W., 34, 110, 180, 181, 252, 253, 299,
 625, 626, 627
 publications, 297
 studies, 183–189, 195–210
 Hogan, M. E., 103
 studies, 26–27
 Holden, F., 356
 Hölzl, E., 395
 studies, 579–585
 Hoover, H., vi
 Hopkins, D. W., 811
 Hornblower, M., vii
 Hough, B. R., 655, 735
 publications, 734
 studies, 678–688, 688–699, 711–723
 Howard, R. F., 34, 314, 315, 316, 351, 376
 publications, 372
 Howe, W. W., vi
 Hoyer, B. H., 15, 35, 112, 150, 179, 299
 studies, 158–159, 165
 Huaco, D., 300
 Huang, L., 27, 33, 10, 11, 75, 102
 publications, 101
 studies, 53–54, 54–60, 60–64, 66–67, 88, 94–97
 Hubble, E. P., 19
 Huchra, J. P., 34, 328, 377
 publications, 372
 Huckenholz, H., 387, 395
 studies, 446–453, 579–585
 Huggins, F. E., 12, 33, 384, 393, 395, 648
 studies, 402–405, 551–555, 575–579, 579–585,
 585–590
 Humphreys, R., 296, 297
 Hurford, G. J., 376
 Hurrell, E. E., 140
 Hutchinson, C. L., vi
 Hutchinson, Clyde, 100

 Imhoff, C., 357
 Irvine, T. N., 33, 389, 625, 629, 630, 631, 649
 publications, 634
 studies, 484–492, 492–500
 Irving, A. J., 513

 James, D. E., 110, 180, 182, 299
 publications, 297
 studies, 247–250, 250–256
 Jessup, W. A., vi
 Jewitt, F. B., vi
 Joesten, R., 626
 Johnson, D., 180
 Johnson, J., 814
 Johnson, P., 362
 Johnson, T., 357
 Jordan, E., 8, 26, 103
 studies, 12, 13, 19

 Kable, E. J. D., 297
 Kadik, A. A., 389, 649
 studies, 479–484
 Kamper, K., 364
 Katem, B. N., 377
 publications, 372
 Kato, A., 394
 studies, 561–564
 Katz, M., 377
 Kaufmann, J. P., 355, 815
 Kaushagen, C., 33, 12, 103
 studies, 46–47, 49–53
 Kedes, L., 100
 Keenan, P. C., 357, 370, 372
 Kelley, M. L., 180
 Kempner, E. S., 180
 Kerrick, D., 626
 Khachikian, E. Y., 372
 Kihara, T., 767
 Kirshner, R. P., 328, 333
 publications, 372
 Klein, M., 341
 Klein, W. H., 735

- publications, 734
 studies, 688-699
 Kleinmann, D. E., 357
 Kleppa, O. J., 515
 Knapp, S. L., 352, 376
 Knox, G. V., 377
 Kohne, D. E., 179
 Konigsberg, I. R., 102
 Kormendy, J., 339, 377
 Korn, L., 100
 Kowel, C., 316, 327, 332, 363, 377
 publications, 372
 Kozłowski, M. R., 735
 Kristian, J., 311, 312, 327, 339, 346, 347, 348, 376
 publications, 372
 Krogh, T. E., 12, 15, 33, 180, 300, 384, 385, 398,
 399, 629, 648
 studies, 416-417, 619-623, 623-625
 Kroon, A. A., 100
 Kullerud, G., 626, 627, 649
 publications, 634
 Kumar, C. K., 111, 113, 299
 publications, 297
 studies, 125-126, 141-146
 Kupferman, P. N., 377
 Kushiro, I., 110, 180, 181, 301, 648
 publications, 634
 studies, 189-195
 Kwast, T., 357
- Labeyrie, A., 357
 LaBonte, B., 313, 348
 Lafon, M., 649
 Lajoie, K., 629
 Landstreet, J. D., 319, 349, 357
 Langley, S. P., vi
 Lari, C., 340
 Lawrence, E. O., vi
 Leahy, J. J., 180
 Lear, R. D., 297
 Lee, A. S., 735
 Lee, D., 33, 649
 Leighton, R. B., 34, 376
 Lenhoff, H. M., 180
 Levien, L., 649
 Liewer, K. M., 352
 Light, G. M., 297
 Lindbergh, C. A., vi
 Linde, A. T., 35, 111, 180, 182, 299
 publications, 297
 studies, 273-274, 281-286
 Lindsay, W., vi
 Lipin, B. R., 33, 648
 Little, C., 113
 studies, 131-133
 Liu, S.-Y., 351, 372, 376
 Lodge, H. C., vi
 Lohman, S., 180
 Loomis, A. L., v, 29, 30
 Loomis, D., 367
 Lovett, R. A., vi
 Lövdtrup, S., 180
 Low, F., 324, 331, 361
- Low, S., vi
 Lowen, A. L., 377
 Lynds, B., 296, 297
- Mabin, A., 103
 studies, 67-68
 Mackenzie, J., 34, 742, 810, 814
 publications, 811
 studies, 805-807
 MacVeagh, W., vi
 Mahall, B. E., 34, 810, 814
 Mahoney, J. W., Jr., 297
 Mamin, J., 735
 Mao, H. K., 11, 12, 33, 383, 384, 385, 393, 394,
 396, 625, 626, 627, 629, 648
 publications 633, 634
 studies, 399-402, 402-405, 405-410, 413-415,
 417-424, 555-557, 557-559, 559-561, 590-593,
 593-595, 595-598
 Marme, D., 811
 Marsh, B., 629
 Martin, M. A., 180
 Martin, W. M., Jr., v, 819, 821, 822
 Massey, P., 34, 377
 Matson, D., 357, 358
 Matsubara, S., 394
 studies, 561-564
 Matthews, K., 308, 334, 360, 370
 Mattinson, J. M., 12, 634
 McBirney, A. R., 629, 631, 648
 McCallister, R. H., 33, 296, 297, 386, 392, 625,
 626, 627, 628, 630, 632, 648
 studies, 433-436, 536-539, 539-542
 McCarthy, B. J., 15, 175, 179
 McCarthy, M. F., 358
 McClintock, B., vii
 McClure, F. T., 180
 McClure, R. D., 356
 McCord, T. B., 358
 McDaniel, F. D., 297
 McGough, S. A., vii
 McHugh, K. S., v, 29, 819, 821
 McKavanagh, B., 297, 298
 McMahan, U. J., 11, 12, 103
 studies, 85-88
 McNamara, D. H., 358
 McQuillen, K., 180
 Medenbach, O., 620
 Meenakshi, V. R., 649
 Melean, M., 180
 Mellon, A. W., vi
 Melnick, J., 34, 377
 publications, 373
 Mendes, R. H., 322, 373
 Merriam, J. C., vi
 Meyer, R. P., 300
 Michalitsanos, A. G., 313, 351, 373, 376
 Midgley, J. E., 175, 180
 Mignacco, J. J., 140
 Miller, G. H., 33, 397, 648
 studies, 609-612, 612-617
 Miller, M. C., vi
 Miller, P. C., 811

- Miller, R., vi
 Miller, W. C., 365, 366
 Mills, D. O., vi
 Ming, L. C., 649
 Minkowski, R., 333
 Mirabel, I., 140, 300
 Miranda, M., 180
 Mitchell, S. W., vi
 Montague, A. J., vi
 Mooney, H. A., 22, 34, 739, 814
 publications, 811, 812
 studies, 743–748
 Moore, G. P., 734
 studies, 669–673
 Moore, R., 314, 373, 376
 Morgan, B., 626
 Morgan, H. S., v, 821
 Morganti, H. O., 140
 Morras, R., 140, 301
 Morrow, J. F., 33, 11, 102
 studies, 45–46
 Morrow, W. W., vi
 Morton, D. C., 342, 359
 Motoya, Y., 180, 300
 Muan, A., 649
 Mudd, S. G., vi
 Muehlenbachs, K., 33, 386, 648, 649
 studies, 436–438
 Muller, K. J., 33, 11, 102
 studies, 85–88
 Münch, G., 34, 317, 325, 326, 346, 350, 376
 publications, 373
 Murata, N., 23, 34, 740, 814
 publications, 811
 studies, 766–776
 Murray, S., 350
 Mutti, L., 630
 Myers, W. I., v
 Mysen, B. O., 13, 33, 387, 388, 516, 628, 630, 632, 648
 publications, 634
 studies, 454–468

 Nakamura, Y., 33, 629, 648
 Naslund, H. R., 33, 648
 Negbi, M., 811
 Nelson, J., 297
 Neugebauer, G., 34, 308, 324, 325, 326, 329, 331, 334, 360, 376
 publications, 373
 Newkirk, G., Jr., 315
 publications, 373
 Ney, E. P., 373
 Nicholson, F., 814
 Nobs, M. A., 34, 751, 814
 studies, 762–765
 Norris, J., 308, 338
 North, B. D., 180
 Norton, D., 627
 Norton, G., v, 821
 Novick, R., 100

 Obata, M., 649
 Ocola, L., 180, 299

 O'Connell, R. W., 373
 Oertel, G., 630
 Ohashi, Y., 33, 392, 394, 629, 632, 649
 publications, 634
 studies, 536–539, 539–542, 561–564, 564–569, 569–572
 Ohi, S., 33, 11, 102
 studies, 46, 47–48
 Ohmoto, H., 436, 625, 626, 627
 Oinas, V., 360
 Okada, H., 180, 299
 publications, 297
 Okada, T., 33, 11, 100, 102
 Oke, J. B., 20, 34, 309, 323, 328, 333, 334, 340, 345, 348, 361, 376
 publications, 373
 Olafsson, G., 180, 301
 Olano, C. A., 140, 141
 Oosterbaan, C. E., 364
 O'Rahilly, R., 12, 97, 98, 102
 publications, 101
 studies, 97–98
 Osborn, E. F., 33, 390, 516, 627, 632, 648
 publications, 634
 studies, 504–507, 507–512
 Osborn, W. C., vi
 Osmond, C. B., 811
 Ostriker, J., 331, 360, 363
 Ozato, K., 27, 33, 10, 11, 102
 publications, 101
 studies, 53–54, 60–64, 66–67, 88, 88–90, 90–92, 93–94, 94–97

 Pagano, R. E., 27, 33, 10, 102
 publications, 101
 studies, 53–54, 54–60, 60–64, 64–65, 65–66
 Page, R. W., 649
 Page, W. H., v, 821
 Painchaud, D. M., 735
 Parmelee, J., vi
 Parsons, W. B., vi
 Pascue, D., 316
 Paton, S., vi
 Paul, P., 180
 Pavlov, V., 649
 Percy, R. W., 811, 812
 Pennoyer, R. M., v, 819, 821, 822
 Penston, M. V., 333
 publications, 371
 Pepper, G. E., vi
 Pepper, G. H., 35, 113, 150, 299
 publications, 297
 studies, 146–148, 149–150
 Perkins, R. S., v, 819, 821, 822
 Pershing, J. J., vi
 Persson, E., 308, 334, 360
 publications, 370
 Peterson, C. J., 35, 111, 112, 113, 299
 studies, 120–123, 123–125, 133–135
 Philip, A. G. D., 360
 Pimental, E., 301
 Pogo, A., 377
 Pollock, H. E. D., vii
 Pöppel, W., 140, 141, 301, 815

- Prager, L., 180
 Pratt, L. H., 742, 807, 812
 Prentis, H. W., Jr., vi
 Preston, G. W., 20, 34, 310, 318
 publications, 371
 Priedhorsky, W. C., 34, 377
 Prince, E., 628, 633, 634
 Pritchett, H. S., vi
 Proskouriakoff, T., vii

 Rabin, D. M., 34, 377
 Rake, A. V., 180
 Ramirez, J., 33, 12, 103, 180, 301
 studies, 46, 46-47
 Ramsey, E. M., 101
 Rankin, D. W., 627
 Ratkowski, A. J., 150, 301
 Reeber, R. R., 629
 Reeder, R. H., 25, 33, 8, 12, 102
 publications, 101, 102
 studies, 19-26, 26-27, 27-28
 Rentschler, G. S., vi
 Revzin, A., 100
 Rice, N. R., 35, 112, 113, 150, 151, 179, 299
 studies, 159-161, 161-164, 164-165, 165
 Richer, H. B., 361
 Richstone, D. O., 323, 343, 359, 376
 Rieke, G., 324, 331, 361
 Rigg, J., 735
 Ritchie, A. K., 33, 11, 79, 103
 studies, 67-68
 Roberts, I. Z., 180
 Roberts, M. S., 113, 301
 Roberts, R. B., 17, 18, 35, 112, 113, 114, 150,
 151, 173, 179, 299
 studies, 164-165, 165, 172-180
 Rock, J., 97
 Rockefeller, D., vi
 Roddy, P., 180
 Rodriguez, A., 180
 Roedder, E. W., 649
 Roeder, R., 100
 Roesler, F., 317
 Rogler, C., 34, 814
 publications, 812
 studies, 791-793
 Rohrer, U., 301
 publications, 297
 studies, 148-149
 Root, E., vi
 Root, E., Jr., vi
 Rosenhauer, M., 384, 389, 633, 649
 studies, 410-412, 413-415, 474-479
 Rosenwald, J., vi
 Rossman, G., 634, 649
 Roth, W. M., v
 Roy, J.-R., 373, 376
 Rubey, W. W., vi
 Rubin, V. C., 16, 111, 113, 125, 299
 publications, 297
 studies, 113-118, 120-123, 123-125
 Ruderman, J. V., 669
 Ruiz, M. T., 34, 376
 Rule, B. H., 18, 34, 366, 367, 376

 Rumble, D. III, 33, 386, 625, 626, 627, 630, 633,
 648
 publications, 634
 studies, 436-438
 Ryerson, M. A., vi

 Sacks, I. S., 16, 35, 110, 111, 180, 182, 299
 publications, 297
 studies, 256-266, 266-273, 273-274, 281-286,
 287-291
 Sahade, J., 322, 373
 Sahama, T. G., 629, 649
 Salgueiro, R., 292
 Sandage, A. R., 19, 20, 32, 34, 307, 309, 311, 328,
 329, 337, 339, 344, 347, 364, 376
 publications, 373, 374
 Sanders, R. H., 113, 127, 301
 Sanders, W. L., 361
 Sands, M. K., 180
 Sanz, A. J., 140
 Sargent, A. I., 34, 377
 Sargent, W. L. W., 34, 307, 311, 327, 331, 333,
 334, 340, 342, 343, 376
 publications, 374
 Scargle, J. D., 343, 374
 Schairer, J. F., 516
 Schilling, J. G., 16, 110, 180, 181, 224, 301
 publications, 297
 studies, 224-234
 Schmidt, H. H., Jr., 595
 Schmidt, M., 34, 310, 323, 328, 342, 343, 376
 publications, 374
 Schmucker, U., 291
 Schramm, J., 810
 Schwarzschild, M., 20, 309, 334, 361
 publications, 374
 Schweizer, F., 308, 336, 337, 376
 publications, 374
 Schwerer, F. C., 634
 Seamans, R. C., Jr., v, 819, 821, 822
 Searle, L., 19, 34, 307, 332, 333, 376
 publications, 374
 Sebok, W. L., 34, 377
 Seifert, F. A., 634
 Seitz, M. G., 33, 296, 297, 648
 publications, 634
 Seyler, R. G., 297, 301
 Shaffer, D., 342
 Sheckman, S. A., 34, 361, 376
 Shepley, H. R., vi
 Shields, G., 20, 308, 332, 333
 publications, 374
 Shimizu, N., 110, 180, 299
 publications, 298
 studies, 189-195
 Shirven, A., 180
 Shleser, R. A., 180
 Shoemaker, E. M., 362, 815
 Shorthill, R. W., 362
 Shortridge, K., 307, 333
 Siegmund, W. A., 351
 Sigtrygsson, H., 180, 301
 Simoni, D., 180, 301

- Smith, B., 108
 studies, 88
 Smith, D., 362
 Smith, J., 180
 Smith, M. J., 655, 735
 publications, 734
 studies, 678–688, 699–711
 Smith, T., vi
 Smoot, J., 649
 Snoke, J. A., 16, 35, 110, 111, 180, 182, 299
 publications, 298
 studies, 266–273, 273–274, 274–278, 278–281,
 281–286, 287–291
 Somerville, D., 103
 studies, 43–54, 66–67, 88
 Soptrajanova, G., 296, 298
 Spiegelman, S., 174, 180
 Spinrad, H., 329, 365
 Spooner, J. C., vi
 Stacey, F. D., 298
 Stambrook, P. J., 102
 publications, 101–102
 Stanton, F., v, 819, 821
 Stefansson, R., 180, 301
 Stein, D. B., 741, 810, 812
 studies, 786–789
 Steiner, E., 298
 Stemler, A., 810
 Stern, E., 180
 Storey, W. B., vi
 Straus, N. A., 180
 Strong, H., 34, 742, 810, 814
 Strong, R. P., vi
 Sung, C.-M., 649
 Suyehiro, S., 180, 299
 publications, 298
 studies, 287–291
 Suzuki, Y., 33
 publications, 102
 studies, 36, 36–38, 38–39, 39–40, 41
 Swings, J.-P., 362
 Swope, H. H., 32, 376
 publications, 374
 Szafranski, P., 180

 Taft, C. P., v, 30, 819, 821
 Taft, W. H., vi
 Takeichi, M., 27, 33, 10, 11, 103
 studies, 53–54, 64–65, 65–66
 Tamayo, L., 180, 301
 Tammann, G. A., 362, 364
 publications, 374
 Tang, F. Y. C., 374, 377
 Tapia, M. D., 225
 Taylor, K., 325, 326, 346, 376
 publications, 374
 Taylor, L. A., 634
 Taylor, R. E., 634
 Telleria, J. L., 301
 Tepperman, K., 26, 33, 9, 11, 103
 studies, 67–68, 78–81
 Thayer, W. S., vi
 Thomas, C., 37, 103
 studies, 42–44

 Thomas, T., 100
 Thompson, A. B., 626
 Thompson, J. E., 32
 Thompson, W. F., 24, 741, 810, 814
 publications, 811, 812
 studies, 786–789, 791–793
 Thonnard, N., 16, 35, 111, 113, 299
 publications, 296, 298
 studies, 113–118, 118–120, 120–123, 138–139,
 141–146
 Thorber, J. P., 811, 812
 Thuan, T. X., 19, 307, 331, 334, 338, 339, 359, 376
 Thurston, W., 599
 Tinsley, B. M., 309, 346
 publications, 374
 Tovmassian, H. M., 342
 publications, 374
 Townes, C. H., v, 821
 Trauger, J., 317
 Trippe, J. T., v, 819, 821
 Trotter, D. E., 315, 374
 Troughton, J. H., 23, 34, 740, 814
 publications, 812
 studies, 766–776
 Truffa-Bachi, P., 151, 301
 publications, 296, 298
 studies, 165–172
 Tunell, G., 629
 Turner, E. L., 34, 374, 377
 Turner, K. C., 35, 111, 112, 113, 299
 studies, 118–120, 129–130, 138–139, 139
 Turnrose, B. E., 34, 375, 377
 Tuross, N., 33, 397, 649
 studies, 609–612
 Tuve, M. A., 10, 14, 17, 35, 112, 113, 172, 173,
 183, 299
 publications, 298
 studies, 131–133

 Ulmer, G. C., 649
 publications, 634
 Ulrich, M. H., 340
 Upholt, W. B., 11, 103
 studies, 46, 48–49

 van den Bergh, S., 334, 363, 364
 van der Kruit, P. C., 34, 309, 335, 376
 publications, 372
 van de Velde, N. W., 180, 301
 studies, 158–159, 164–165, 165
 Van Rinsvelt, H. A., 301
 publications, 298
 Van Valkenberg, A., 649
 Vaughan, A. H., Jr., 20, 310, 318, 322, 367, 369,
 376
 Veeder, G., 350, 357
 publications, 375
 Vidale, R. J., 33, 385, 386, 625, 626, 627, 629, 630,
 633, 648
 studies, 424–428, 428–432
 Vieira, E. R., 140
 publications, 815
 Virgo, D., 12, 33, 384, 395, 628, 633

- publications, 634
 studies, 405–410, 575–579, 579–585, 585–590
 Vistelius, A. B., 649
 Visvanathan, N., 376
 publications, 375
 Volponi, F., 301
 Vota, M. D., 141
- Wadsworth, J. W., vi
 Wagner, M. E., 296, 298
 Wahn, H., 100
 Walburn, M. J., vii
 Walcott, C. D., vi
 Walcott, F. C., vi
 Walcott, H. P., vi
 Walker, M. F., 364
 Wallace, D. G., 180, 299
 Wallerstein, G., 364
 Walter, R. L., 149, 301
 Walton, B. P., 180
 Wampler, E. J., 333
 publications, 375
 Ward, W. E., 814
 Waring, M. J., 180
 Warner, J. W., iii, 35, 113, 299
 publications, 298
 Wasilewsky, P., 634
 Watson, E. B., 33, 390, 648
 studies, 500–504
 Weare, J., 625
 Weber, H. P., 395
 studies, 575–579
 Weed, L. H., vi
 Wehmiller, J., 649
 Weisbrod, A., 634
 Weiss, C. V., 814
 Welch, W. H., vi
 Wellauer, P. K., 25, 33, 8, 11, 12, 15, 19, 103
 publications, 101–102
 studies, 19–26
 Werner, M. W., 34, 324, 325, 326, 376
 publications, 375
 Westbrook, W. E., 34, 324, 325, 377
 publications, 375
 Westpfahl, D., Jr., 35, 300
 publications, 298
 Westphal, J. A., 21, 34, 311, 312, 316, 339, 346,
 347, 348, 349, 376
 publications, 371, 375
 Wetherill, G. W., 14, 35, 299
- Wey, C. A., 33, 103
 publications, 101–102
 White, A. D., vi
 White, E. D., vi
 White, H., vi
 White, J. N., v, 821
 White, R. E., 20, 310, 318
 White, W. M., 16, 35, 110, 180, 181, 224, 233, 299
 publications, 298
 studies, 224–234
 Wickersham, G. W., vi
 Wickes, W. C., 364
 Wilkinson, A., 346, 376
 Williams, T. B., 34, 377
 Willis, A. G., 340, 364, 365
 publications, 375
 Willner, S. P., 34, 331, 377
 Wilson, C. P., 21, 34, 307, 312, 333, 347, 376
 Wilson, O. C., 311, 323, 327, 376, 357
 Wilson, R. E., vi
 Wishner, B., 628
 Wold, B. J., 735
 Woodward, R. S., vi
 Wozniak, W., 98, 103
 Wright, C. D., vi
 Wright, E. L., 357
 Wright, T. L., 628
 Wyatt, B., 392, 649
 studies, 536–539
- Yamagishi, Y., 180, 301
 studies, 287–291
 Yoder, H. S., Jr., 13, 33, 187, 391, 413, 625, 626,
 627, 629, 633, 648
 report of the Director, Geophysical Labora-
 tory, 379–649
 publications, 815
 studies, 515–519
 Yoshimura, H., 34, 315, 316, 376
 Young, J., 180
 Yund, R. A., 386, 628
 studies, 433–436
 publications, 815
- Zen, E., 625
 Zies, E. G., 33, 648
 Zinn, R. J., 34, 308, 323, 338, 354, 359, 376
 Zirin, H., 34, 310, 313, 322, 376
 publications, 375
 Zwicky, F., 332
 publications, 375

